USAAMRDL TECHNICAL REPORT 71-25

FULL-SCALE WIND-TUNNEL INVESTIGATION OF THE ADVANCING BLADE CONCEPT ROTOR SYSTEM

By

Vincent M. Paglino
Edward A. Beno

August 1971

EUSTIS DIRECTORATE
U. S. ARMY AIR MOBILITY RESEARCH AND DEVELOPMENT LABORATORY
FORT EUSTIS, VIRGINIA

829

CONTRACT DAAJ02-67-C-0102
UNITED AIRCRAFT CORPORATION
SIKORSKY AIRCRAFT DIVISION
STRATFORD, CONNECTICUT

Approved for public release;
distribution unlimited.

UNCLASSIFIED

Security Classification

DOCUMENT CONTROL DATA - R & D

(Security classification of title, body of abstract and indexing annotation must be entered when the overall report is classified)

1. ORIGINATING ACTIVITY (Corporate author) ikorsky Aircraft ivision of United Aircraft Corporation Stratford, Connecticut	2a. REPORT SECURITY CLASSIFICATION UNCLASSIFIED 2b. GROUP

3. REPORT TITLE

FULL-SCALE WIND TUNNEL INVESTIGATION OF THE ADVANCING BLADE CONCEPT ROTOR SYSTEM

4. DESCRIPTIVE NOTES (Type of report and inclusive dates)

Final Report

5. AUTHOR(S) (First name, middle initial, last name)

Vincent M. Paglino
Edward A. Beno

6. REPORT DATE	7a. TOTAL NO. OF PAGES	7b. NO. OF REFS
August 1971	827	6

8a. CONTRACT OR GRANT NO. DAAJ02-67-C-0102 b. PROJECT NO. Task 1F162203A14302 c. d.	9a. ORIGINATOR'S REPORT NUMBER(S) USAAMRDL Technical Report 71-25 9b. OTHER REPORT NO(S) (Any other numbers that may be assigned this report) Sikorsky Engineering Report 50705

10. DISTRIBUTION STATEMENT

Approved for public release; distribution unlimited.

11. SUPPLEMENTARY NOTES	12. SPONSORING MILITARY ACTIVITY
	Eustis Directorate U. S. Army Air Mobility R&D Laboratory Fort Eustis, Virginia 23604

13. ABSTRACT

A 40-foot-diameter ABC (coaxial) rotor system was tested in the NASA/Ames Research Center 40 ft x 80 ft Wind Tunnel. The six rigid blades were instrumented to measure flatwise, edgewise, and torsional strain. Advance ratios up to 0.91 and tip Mach numbers to 0.83 were tested. Lateral displacement of individual rotor lift was varied. The performance, control, stress, and vibration data recorded during these tests are presented and discussed.

The blade lift capacity was found to be significantly greater than in the case of articulated rotors, and design lift coefficient was maintained to an advance ratio of 0.91 with good power efficiency. Measured and predicted performance were in good agreement.

Large control power in pitch and roll was available at all advance ratios, and yaw control diminished at low power settings. Little or no undesirable control coupling existed except for yaw-roll and the effect of lift and lift offset controls on pitching moment. The control derivatives and longitudinal stability characteristics were as predicted by theory.

At design lift coefficient and optimum L/D, the measured blade stresses indicate an unlimited operating capability at advance ratios up to approximately 0.6.

DD FORM 1 NOV 65 1473 REPLACES DD FORM 1473, 1 JAN 64, WHICH IS OBSOLETE FOR ARMY USE.

UNCLASSIFIED

Security Classification

DISCLAIMERS

The findings in this report are not to be construed as an official Department of the Army position unless so designated by other authorized documents.

When Government drawings, specifications, or other data are used for any purpose other than in connection with a definitely related Government procurement operation, the U. S. Government thereby incurs no responsibility nor any obligation whatsoever; and the fact that the Government may have formulated, furnished, or in any way supplied the said drawings, specifications, or other data is not to be regarded by implication or otherwise as in any manner licensing the holder or any other person or corporation, or conveying any rights or permission, to manufacture, use, or sell any patented invention that may in any way be related thereto.

Trade names cited in this report do not constitute an official endorsement or approval of the use of such commercial hardware or software.

DISPOSITION INSTRUCTIONS

Destroy this report when no longer needed. Do not return it to the originator.

UNCLASSIFIED
Security Classification

14 KEY WORDS	LINK A		LINK B		LINK C	
	ROLE	WT	ROLE	WT	ROLE	WT
Helicopter						
Rotor						
Advancing Blade Concept						
Rigid Rotor						
Wind Tunnel Tests						
Performance						
Vibratory Stress						

UNCLASSIFIED
Security Classification

DEPARTMENT OF THE ARMY
U. S. ARMY AIR MOBILITY RESEARCH & DEVELOPMENT LABORATORY
EUSTIS DIRECTORATE
FORT EUSTIS, VIRGINIA 23604

This report has been reviewed by the U. S. Army Air Mobility Research and Development Laboratory and is considered to be technically sound. The purpose of the research was to experimentally investigate the aerodynamic and dynamic characteristics of a full-scale advancing blade concept rotor system, both statically and throughout the maximum forward speed range of the 40-by-80-foot wind tunnel.

The report is published to provide information for the evaluation of this rotor concept. The program was conducted under the technical management of Mr. John L. Shipley and Mr. John E. Yeates of the Aeromechanics Division of this Directorate.

Task 1F162203A14302
Contract DAAJ02-67-C-0102
USAAMRDL Technical Report 71-25
August 1971

FULL-SCALE WIND-TUNNEL INVESTIGATION OF THE ADVANCING BLADE CONCEPT ROTOR SYSTEM

SER-50705

by

Vincent M. Paglino
Edward A. Beno

Prepared by

United Aircraft Corporation
Sikorsky Aircraft Division
Stratford, Connecticut

for

EUSTIS DIRECTORATE
U. S. ARMY AIR MOBILITY RESEARCH AND DEVELOPMENT LABORATORY
FORT EUSTIS, VIRGINIA

SUMMARY

A 40-foot-diameter ABC (coaxial) rotor system was tested in the NASA/Ames Research Center 40 ft x 80 ft Wind Tunnel. The six rigid blades, tapered in both planform and thickness, were instrumented to measure flatwise, edgewise, and torsional strain. Advance ratios up to 0.91 and tip Mach numbers to 0.83 were tested over a wide range of collective pitch and shaft angle of attack. Lateral displacement of individual rotor lift was varied from 1 percent to 70 percent of rotor radius. The performance, control, stress, and vibration data recorded during these tests are presented and discussed. Selected data are compared with theoretical predictions over a range of advance ratios from 0.21 to 0.91.

The blade lift capacity was found to be significantly greater than in the case of articulated rotors, and design lift coefficient was maintained to an advance ratio of 0.91 with good power efficiency. Measured and predicted performances were in good agreement.

Large control power in pitch and roll was available at all advance ratios, and yaw control diminished at low power settings. Little or no undesirable control coupling existed except for yaw-roll and the effect of lift and lift offset controls on pitching moment. Control mixing may be desirable to reduce these effects. The control derivatives and longitudinal stability characteristics were as predicted by theory.

At design lift coefficient and optimum L/D, the measured blade stresses indicate an unlimited operating capability at advance ratios up to approximately 0.6. The blade and hub stresses were lower than predicted and the control loads, although higher than predicted, were below allowable. Total fixed system vibration was usually low. No structural instabilities were detected anywhere in the operating range.

FOREWORD

Mr. Robert Burgess was the Sikorsky project engineer for development of the ABC rotor. Mr. Alfred Lizak was the principal wind tunnel test coordinator and supervised the assembly and preparation of the test article at Ames. Mr. John Leary was the principal instrumentation engineer and contributed to the instrumentation section of this report.

Mr. John Shipley and Mr. John Yeates monitored this program for the Eustis Directorate, U. S. Army Air Mobility Research and Development Laboratory, and the NASA/Ames project engineer for the wind tunnel testing was Mr. Robert Stroub.

This report was prepared under Contract DAAJ02-67-C-0102, Task 1F162203A14302.

TABLE OF CONTENTS

LIST OF ILLUSTRATIONS

LIST OF TABLES

LIST OF SYMBOLS AND ABBREVIATIONS

Symbols

A_{1s}	longitudinal cyclic pitch, $(A_{1s_{UR}} + A_{1s_{LR}})/2$, deg
$A_{1s_{LR}}$	lower rotor longitudinal cyclic pitch, deg
$A_{1s_{UR}}$	upper rotor longitudinal cyclic pitch, deg
A'_{1s}	lift longitudinal displacement control, $(A_{1s_{UR}} - A_{1s_{LR}})/2$, deg
B_{1s}	lateral cyclic pitch, $(B_{1s_{UR}} - B_{1s_{LR}})/2$, deg
$B_{1s_{LR}}$	lower rotor lateral cyclic pitch, deg
$B_{1s_{UR}}$	upper rotor lateral cyclic pitch, deg
B'_{1s}	lift lateral displacement control, $(B_{1s_{UR}} + B_{1s_{LR}})/2$, deg
b	number of blades (6 for dual rotor, 3 for single rotor)
C_D/σ	rotor drag coefficient, $D/\sigma\pi R^2 \rho(\Omega R)^2$
C_{HF}/σ	hub pitching moment coefficient, $\dfrac{(b/2)\times(\text{1st harmonic COS component of UR SLV flatwise moment})}{\sigma\pi R^3 \rho(\Omega R)^2}$, based on single rotor b and σ
C_{HR}/σ	hub rolling moment coefficient, $\dfrac{(b/2)\times(\text{1st harmonic SIN component of UR SLV flatwise moment})}{\sigma\pi R^3 \rho(\Omega R)^2}$, based on single rotor b and σ
C_L/σ	rotor lift coefficient, $L/\sigma\pi R^2 \rho(\Omega R)^2$
C_M/σ	rotor pitching moment coefficient, $PM/\sigma\pi R^3 \rho(\Omega R)^2$
C_{MZ}/σ	rotor yawing moment coefficient, $YM/\sigma\pi R^3 \rho(\Omega R)^2$
C_Q/σ	rotor torque coefficient, $(\text{rotor torque})/\sigma\pi R^3 \rho(\Omega R)^2$
C_R/σ	rotor rolling moment coefficient, $RM/\sigma\pi R^3 \rho(\Omega R)^2$
C_Y/σ	rotor side force coefficient, $SF/\sigma\pi R^2 \rho(\Omega R)^2$
c	rotor blade chord, in. or ft

D	rotor drag, lb ,wind axis
D_e	equivalent drag, lb
E_n	blade n-th edgewise mode
F_n	blade n-th flatwise mode
Hp	rotor shaft horsepower
L	rotor lift, lb, wind axis
M_t	advancing blade tip Mach number
PM	rotor pitching moment, ft-lb, positive nose up
R	rotor radius, in.
R	distance from center of rotation to blade radial station, in. (Appendix only)
r	distance from center of rotation to blade radial station, in.
RM	rotor rolling moment, ft-lb, positive roll right, shaft axis
SF	rotor side force, lb, positive right, wind axis
T_n	blade n-th torsional mode
t	blade thickness, in.
V	forward velocity, kn or ft/sec
YM	rotor yawing moment, ft-lb, positive nose right, shaft axis
α_s	rotor shaft angle of attack, ALPHA SHAFT, deg
$\Delta\theta$	differential collective pitch, $(\theta_{c_{UR}} - \theta_{c_{LR}})/2$, deg
θ_c	blade collective pitch at 0.75R $(\theta_{c_{UR}} + \theta_{c_{LR}})/2$, deg
$\theta_{c_{LR}}$	lower rotor blade collective pitch at 0.75R, deg
$\theta_{c_{UR}}$	upper rotor blade collective pitch at 0.75R, deg
θ_1	blade twist, deg
μ	advance ratio, $V/\Omega R$
ρ	air density, slug/ft^3

σ	rotor solidity, SIGMA, $bc/\pi R$ (based on $c_{.75R} = 1.165$ ft)
Ω	rotor angular velocity, rad/sec

<u>Abbreviations</u>

ACC	acceleration
BL	module butt line
BLD	blade
CYCL	cyclic
DISPL	displacement
ES	edgewise stress
FA	fore and aft
FS	flatwise stress
GB	gearbox
LAT	lateral
LD	load
LR	lower rotor
LONG	longitudinal
PSHRD	pushrod
PTP	peak-to-peak
RL	right lateral
RS	right strut
SLV	sleeve
SRV	servo
STA	module station
TM	torsional moment
TS	total stress
UR	upper rotor

INTRODUCTION

The Advancing Blade Concept (ABC) for helicopter design uses coaxial, counterrotating, rigid rotors. The use of this concept reduces rotor retreating blade stall by unloading the retreating blade and loading the advancing blade without increasing advancing blade tip Mach number. Two rotors are used to balance the resulting roll moments. The coaxial (rather than biaxial) configuration is considered to be optimum since it has the shortest load path between rotors. Besides the alleviation of retreating blade stall and its implicit performance gains, other advantages are predicted for this rotor system, arising out of the rigid root retention of the blades and the coaxial arrangement of the rotors. These include greater load factor capability, increased control power and center-of-gravity travel, reduction of rotor head complexity (through elimination of flapping and lagging hinges), elimination of antitorque power requirements, and the potential of cancelling particular frequencies of vibration through control of relative rotor motion.

Although the basic theoretical advantages of the ABC system are readily understandable, several complex problems had to be resolved to realize these benefits: (1) The rotor blades had to be rigid enough to sustain the anticipated load offsets, yet light enough for practical use on an aircraft; (2) the rotors had to be spaced for low profile but with minimum aerodynamic interference and with safe tip clearances; (3) the rotors and control system had to be dynamically stable, despite the elimination of lag dampers and the use of long control rods; (4) the method of pilot control had to be similar to that of conventional single rotors, despite the addition of another rotor; and (5) the system had to operate at acceptable vibration levels. In order to resolve these and other questions, Sikorsky Aircraft and United Aircraft Research Laboratories began in 1965 a series of analytical and experimental programs to develop and test dynamically scaled ABC hardware. Much of this early work is discussed in Reference 1. It was concluded from these and other investigations that the ABC system was practical and that full-scale hardware could be developed.

The purpose of the present investigation was to experimentally evaluate a full-scale ABC rotor system both statically and over a substantial forward speed range. The rotor built for this program was designed for an operating lift of 14,500 pounds and a maximum speed of 230 knots. A description of the rotor static test, including a transmissibility study of the supporting module, is given in Reference 2. Briefly, the system was found to be capable of operating at extreme conditions of power and blade bending moment for substantial periods of time. The rotor also was found to respond in a stable fashion when subjected to step and sinusoidal control excitations.

To evaluate the system in forward flight, the strain-gage-instrumented ABC rotor was installed in the NASA/Ames Research Center 40 ft x 80 ft Wind Tunnel. Advance ratios up to 0.91 and tip Mach numbers to 0.83 were tested over a wide range of collective pitch and shaft angle of attack.

Lateral displacement of individual rotor lift was varied from 1 percent to 70 percent of rotor radius. This report examines the performance, control, and stress data recorded during these tests, and compares test results with theoretical predictions.

The static and wind tunnel tests were jointly sponsored by USAAMRDL and Sikorsky Aircraft. The wind-tunnel test was conducted by the Ames Research Center of the National Aeronautics and Space Administration.

DESCRIPTION OF FACILITIES AND EQUIPMENT

WIND TUNNEL

The full-scale wind tunnel located at the NASA/Ames Research Center is a closed-throat, closed-return type, with a test section 40 feet high and 80 feet wide. This tunnel has a nominal maximum speed capability of 200 knots and is powered by six 6000-horsepower electric motors. Model forces and moments are measured by a six-component mechanical balance, with the readings punched directly on computer cards for processing.

ROTOR DRIVE AND CONTROL SYSTEM

The rotor system and its supporting module are shown as installed in the wind tunnel in Figure 1. The rotor system is mounted on a specially designed coaxial gearbox, with provision for two separate power inputs. A removable gear coupling provided the option of powering the rotors either separately or in combination. The latter method was employed throughout the coaxial rotor tests. Power to the gearbox inputs was supplied by two NASA 1500-horsepower variable-speed electric motors. The six-bladed coaxial hub is shown enclosed by a slip-ring assembly and slip-ring fairing. Terminal boxes are mounted between the upper rotor blades to accommodate instrumentation leads from the rotating system through the slip rings to the fixed system. An additional slip-ring assembly with its fairing is located directly below the gearbox. All components are mounted on a triangular I-beam frame, and the complete assembly is enclosed in a streamlined fairing. The model is supported on the tunnel balance by two faired forward struts and one faired, telescoping tail strut. A self-centering, hydraulic vibration isolation system was installed at the tail strut attachment point. This isolator was used only as a rigid link, however, since such isolation was found to be not required during the test.

Control to each rotor was supplied by three remotely operated electro-mechanical actuators which introduced longitudinal, lateral, and collective pitch through typical aircraft type linkages. CH-54 standard hydraulic servos were employed to react the rotor forces. To reduce the possibility of the rotors inadvertently being set to unreasonably different operating conditions, and to simplify control settings, the electro-mechanical actuators of the upper and lower rotor were electrically ganged such that an upper rotor actuator and the corresponding lower rotor actuator responded simultaneously to one signal, producing appropriate motions of equal magnitude. One type of signal (or control switch) caused an actuator pair to move in opposite directions, while another type of signal caused this actuator pair to move in the same direction. Thus, there were six operator's rotor control switches (two for longitudinal, two for lateral, and two for collective pitch).

ROTOR BLADES AND HUB

The test was conducted using six rigidly attached, 20-foot-radius rotor blades, which were balanced both statically and aerodynamically. The upper rotor hub arms are preconed 5 degrees, while the lower rotor hub

arms are not preconed. The blades are tapered in both planform and thickness, having an airfoil contour of NACA 0030 near the root and a contour of 0006 at the tip. They are of -10 degrees, nonlinear, aerodynamic twist. The primary structural member of the blade is a titanium alloy spar, retained at the root end by two sets of radially loaded, tapered roller bearings and four thrust bearings. The loads are transmitted through the bearings to a cylindrical sleeve which is bolted to the rotor hub. Further details of blade geometry are given in Figure 2. The blade structural properties are given in Figure 3; the blade natural frequency diagram is shown in Figure 4.

INSTRUMENTATION AND DATA ACQUISITION SYSTEM

Five of the six blades on the rotor system were strain-gaged to measure eight flatwise and eight chordwise normal bending loads, three torsional moments, and sixteen total stresses. One blade of each rotor was designated as the primary instrumented blade. Figure 5 shows the location of the principal operative blade and sleeve gages on either the primary or the secondary blade. Three servo loads and one rotating pushrod load of each rotor were recorded, as well as rotating and stationary scissors loads. Fifteen vibration measurements, three of which rotated with the hub, were also recorded during the test. Blade tip clearance was measured continuously by means of six specially modified electronic blade tracker units located on the tunnel floor, below the six blade cross-over points (see Figure 1). Individually controlled tilt-tables provided alignment for various shaft angles. Four remotely controlled closed-circuit television cameras also were used to monitor blade tip paths.

A modular control console was used to provide rotor control and monitoring functions. The displays available included rotor tip clearance, rotor rpm, gearbox temperatures and oil pressures, chip detector, first- and second-stage servo hydraulic pressure, indicators for primary and secondary power for the module and data acquisition system, indicators for pitching and rolling moments of each rotor, actuator position indicators, and resolved blade pitch angle indicators for each rotor.

A resistance transducer was employed to measure blade pitch. This signal was also electrically resolved into the first-harmonic sine and cosine amplitudes. These components were displayed on the control console for use in setting test points. The blade sleeves of each rotor were instrumented for flatwise bending, and this measurement was resolved into individual rotor pitching and rolling moments for console display. Secondary measurements of rotor blade pitch and moments were available for instantaneous backup. Additional on-line monitoring of critical gages was provided by 16 channels of peak-to-peak and steady information. Eight channels at a time were recorded on a 16-channel oscillograph.

Rotating electrical signals from the lower rotor were brought down by first going through an assembly of 112 slip rings located between the rotors, and then through the upper rotor assembly of 442 slip rings attached to the bottom of the gearbox. The synchro-resolvers and rotor azimuth hardware were driven by gears off the bottom of the rotor gearbox.

Time-averaged six-component rotor static force and moment data were recorded by the wind-tunnel balance and processed by NASA/Ames. Rotor power was determined by visual recording of the drive motor wattmeters.

The dynamic data acquisition system is diagrammed in Figure 6. The principal acquisition device was a magnetic tape recorder which had a capacity of 14 tracks. The recording system was a narrow-band FM multiplex using standard subcarrier oscillators. Ten channels of information, bands 7 through 16, were recorded on individual tape tracks. Ten direct record tracks were used for dynamic data. In addition, one track was used for audio comments, another for rotor azimuth reference information, and another for data run commands to be used in processing. All dynamic measurements were recorded simultaneously to provide proper time correlation of the data. Signal conditioning for the strain-gage instrumentation channels was accomplished using Sikorsky-designed electronic modules.

DATA PROCESSING SYSTEM

The dynamic test data were processed by means of the technique block-diagrammed in Figure 7. A single tape track, which contained a maximum of ten measurements in an FM multiplex, was played back into a bank of narrow-band FM discriminators. The discriminator outputs were then fed into normalizing amplifiers that scaled all measurements to a common signal level (10 volts = full scale). These outputs were presented to a solid-state multiplex with sample and hold amplifiers. The sampling rate of the multiplexer was controlled by hardware that utilized control signals from the analog tape. The control signals, 72 azimuth pulses per rotor revolution, and a data run command were combined to generate 720 data sampling pulses for 10 data cycles within a given data burst. The multiplexer output was digitized by a nine-bit (eight-bit plus sign) analog to digital converter and put into format on digital tape through a Scientific Data System Computer, Model 910. This digital tape was then processed to engineering units by a computer, with calibration constants incorporated in the digital computations. The computations also included averaging of the individual data cycles within a data run to yield an average cycle. Peak-to-peak and harmonic content were then calculated from these average cycles.

TEST PROCEDURE AND ANALYTICAL METHODS

TEST PROCEDURE

The method of operating the rotor was to set a desired tip speed, shaft angle of attack, forward speed, collective pitch, and lift lateral displacement control (B'_{1s}). Collective pitch (θ_c) and/or B'_{1s} was then varied by increments not exceeding two degrees, with each setting representing a data recording point. Coupled longitudinal and lateral cyclic pitch (A_{1s} and B_{1s}) were adjusted at each point to provide nominally zero (± 5000 ft-lb) overall module rolling and pitching moments, read from resolved blade root bending gages. The other two rotor controls, lift longitudinal displacement (A'_{1s}) and differential collective pitch ($\Delta\theta$), were generally left at zero (± 1 degree). At 15 selected points in the test spectrum, substantial overall module moments were generated in order to evaluate rotor control and static stability characteristics.

Five combinations of tip speed and forward speed were tested; they are shown graphically in Figure 8. Average values of air density, advancing tip Mach number, and advance ratio at all flight conditions are given in Table I. Conditions 6 and 7 are reruns of conditions 1 and 2, with the lower rotor blades removed. Testing procedure varied somewhat for these last two cases in that all six rotor controls were set to duplicate those of selected test points of the corresponding dual rotor condition.

Tares

At the conclusion of all dynamic testing, the rotor blades were removed and the module/rotor head combination was tested over a range of forward speed and shaft angle of attack to determine its lift, drag, and moment characteristics. The tare values thus obtained were represented by a mathematical curve fit and used in the NASA/Ames performance data reduction program. The performance data thus reflect only the forces generated by the rotor. The six hub arms for the tare test extended 19.5 inches from the center of rotation.

ANALYTICAL METHODS

Both a rigid blade approach and a flexible blade approach are used in the subsequent theoretical calculations. Rigid blade theory is used for performance and control derivative calculations, while flexible blade theory is used to calculate stresses, structural loads, and static stability.

Rigid Blade Theory

The theory used for correlation with the performance and control data was the Yawed Blade Element Rotor Performance Method. The method assumes rigid blades (which may or may not be hinged) subjected to uniform momentum inflow. The blades are mathematically divided into a number of segments, each of which is treated as if immersed in a three-dimensional flow field, including the effects of stall and compressibility. When applied to ABC rotor

calculations, variable-thickness airfoil section data are used (compiled from a number of wind-tunnel tests), and the effects of upper and lower rotor interaction are approximated by allowing the wake from the upper rotor to pass through a portion of the lower rotor.

Flexible Blade Theory

The method used for correlation with the structural loads and stability data is the Normal Modes Aeroelastic Blade Analysis. This analysis is a numerical method for integrating the fully coupled flatwise, edgewise, and torsional equations of motion of a flexible rotor blade. As applied to the computations in this report, the aerodynamic portions of the analysis are similar to those of rigid blade theory with the following exceptions: NACA 0012 airfoil data are used throughout instead of variable-thickness section data; no upper-lower rotor interaction is assumed; and a two-dimensional, rather than three-dimensional, flow field is assumed to act at each blade element. For this investigation, three flapwise modes, two edgewise modes, and one torsional mode of flexure were used to represent the rotor blade motion.

DISCUSSION OF PERFORMANCE

BASIC PERFORMANCE DATA

Complete nondimensional performance data (drag, power, L/D, side force, and rolling, pitching, and yawing moments) from these tests are presented in the Appendix, plotted versus rotor lift coefficient (C_L/σ) for lines of constant shaft angle. Also plotted are the principal rotor operating parameters, θ_c, A_{1s}, and lift lateral displacement. All of these data are grouped according to flight condition (combination of forward velocity, tip speed, and configuration) and subdivided according to lift lateral displacement control setting (B'_{1s}). In all, there are data for 25 combinations of flight condition/B'_{1s} setting. A sample combination of these data, depicting a velocity of 179 knots and with B'_{1s} set at 6 degrees, is given in Figure 9. These data are typical of other conditions as well, and were chosen since they represent the highest forward velocity tested (although not the highest advance ratio tested). A velocity of 179 knots was the maximum speed attained by the tunnel with the module and its associated monitoring equipment installed. The B'_{1s} setting of 6 degrees yielded the highest rotor L/D's for this velocity.

Figures 9(a) through 9(c) show the rotor drag coefficient, shaft torque (power) coefficient, and lift-drag ratio characteristics as a function of shaft angle and lift coefficient. Figure 9(a) also contains lines of nominal collective pitch (θ_c) at 75 percent blade radius. The ABC rotor reacts to changes in shaft angle and collective pitch in much the same manner as conventional rotors, in that tilting the shaft into the wind ($-\alpha_s$) increases power and propulsive force (negative drag), while increases in collective pitch cause an increase in lift. The magnitude of the effect, however, is considerably greater than in the case of articulated rotors when the latter have the tip path plane held constant. For example, Figure 15 of Reference 3 depicts performance data of an articulated rotor for a similar tip speed (651 ft/sec) and a similar forward speed (177 kn). For the articulated case, increasing collective pitch by 2 degrees (at constant shaft angle) typically produced an increase in lift coefficient of 0.02. For the ABC rotor, a similar increase in collective pitch produces approximately twice (0.04) the increase in lift coefficient at this forward speed (see Figure 9(a)). On a dimensional basis, the lift increase per degree collective is over 90 percent greater for the ABC. Moment control characteristics will be discussed in a later section.

A comparison of the ABC and articulated rotor lift coefficient data of Reference 3 reveals that the test spectrum for the ABC rotor begins at lift coefficients that represent the upper limits of the articulated rotor test spectrum. Such large lift generating capacity of the rotor system was obtained at all advance ratios tested with little evidence of stall-associated vibration or control load increase (see Discussion of Stresses and Loads). A 1g lift coefficient capability was established to advance ratios of at least 0.91. Model tests (Reference 1) have revealed that peak vibratory blades stresses (and approximately the critical load limit) occur at an advance ratio of 1.0 and decrease thereafter. For the present investigation, tunnel balance resonance at low rotor tip speeds prevented

further verification of this behavior for steady-state conditions. However, future tests might avoid this difficulty by rapidly slowing the rotor as it passes through the μ = 1.0 flight regime, or by approaching it from the stopped-rotor state.

The variation in rotor equivalent lift-drag ratio with shaft angle and lift coefficient is shown in Figure 9(c). The denominator of this ratio contains the actual rotor drag (negative for propulsive force), plus the rotor shaft horsepower converted to an equivalent drag (D_e = 550 Hp/V). The L/D parameter is useful for choosing the combination of shaft angle and B'_{1s} that produces the most efficient airload distribution at a desired lift coefficient. For example, the zero shaft angle curve of Figure 9(c) is seen to be optimum at lower lift coefficients while 4 degrees appears better at higher lift coefficients. These distributions change at other combinations of velocity/B'_{1s}, as may be seen from the Appendix. In general, the lift coefficient at which maximum L/D occurs increases with advance ratio, for any given shaft angle or B'_{1s}. In particular, at μ = 0.91, maximum L/D was encountered at a lift coefficient of about 0.18 (see Appendix). Since this lift coefficient is about 10 percent greater than that required to achieve design rotor lift at this advance ratio, some refinement in the blade aerodynamic design may be indicated for high-advance-ratio operation. The definition of the upper limit on L/D obtainable through changes in blade geometry is still under investigation analytically.

Figure 9(d) shows the variation in lift lateral displacement as a function of lift coefficient and shaft angle. This quantity was calculated by dividing the upper rotor rolling moment (derived from resolved blade root bending gages) by the upper rotor lift (assumed equal to one-half of the system lift). It may be noted for this case that lift lateral displacement increases with lift (i.e., collective pitch) when shaft angle is held constant, and increases with negative shaft tilt (i.e., propulsive force) when lift is held constant. This, and data at other velocity/B'_{1s} combinations, substantiates the basic ABC premise that for a given lift and propulsive requirement there exists a unique optimum lift lateral displacement which varies with advance ratio and which can be achieved through proper combination of shaft angle and B'_{1s}.

As described in the Test Procedure, the method of operation called for trimming to zero overall (net) aircraft moments before taking each data point. The control system is designed such that net pitching, rolling, and yawing moments are controlled through application of A_{1s}, B_{1s}, and $\Delta\theta$, respectively. Figure 9(e) depicts the amount of A_{1s} needed to trim net pitching moment for each data point. There is little variation with shaft angle, but significant variation with lift as anticipated. The magnitude of negative A_{1s} shown is proportional to the magnitude of nose-up pitching moment which the A_{1s} control cancelled. Most of this moment is caused by the lift of the advancing blades, some of which translates into longitudinal moment through phase lag due to blade flexibility. For a coaxial system, such precession effects are additive as affecting longitudinal moments and subtractive for lateral moments. This behavior was confirmed in the present investigation. In fact, no B_{1s} control is plotted, since

blade root bending gages did not indicate any significant lateral unbalance in upper-lower rotor rolling moments for any flight condition, and thus little or no B_{1s} control was applied. Subsequent to the tests, some discrepancies were noted between those roll moments derived from blade root bending gages and those recorded by the wind-tunnel balance system. These differences are generally small and have little bearing on the analyses presented herein. In any case, were any net roll moments actually present, they could easily have been trimmed to zero through the large roll control power afforded by B_{1s}. Such control derivatives are discussed in a subsequent section of this report.

Figure 9(f) presents the net side force coefficient as recorded by the wind-tunnel balance. Cancellation of side force would take place for a coaxial system with identical, noninterfering rotors. One mechanism by which this small side force could have been produced is the difference in upper and lower rotor precones. Dissymmetry in upper and lower rotor aerodynamics or some small offset in the resolution of balance forces may also contribute to side force.

Figures 9(g), 9(h), and 9(i) depict the net rolling, pitching, and yawing moments recorded by the wind-tunnel balance. As has been mentioned, the intent was to trim these moments to approximately zero at each data point. The net balance moments recorded are presented for reference at all flight conditions in the Appendix. It is seen for this example that recorded pitching and yawing moments did remain nominally zero (Figures 9(h) and 9(i)), and that balance rolling moment remained somewhat negative. However, as previously discussed, blade root bending gages showed zero net rolling moment, and thus no B_{1s} control was applied. Further exploration of this discrepancy between balance and blade root rolling moment measurements is beyond the interest of this report, since, as will subsequently be shown, more than ample roll control was available in any case. The resolution of the question may be related to the balance side-force measurement discussed in connection with Figure 9(f). The reader is also referred to the single-rotor flight conditions (numbers 6 and 7 of Table I) in the Appendix, where balance moments are plotted against blade root moments and wattmeter readings are plotted against balance yaw measurements.

The near-zero yawing moments of Figure 9(i), achieved with little or no application of $\Delta\theta$ control, demonstrate the in-plane symmetry of upper and lower rotor aerodynamics. Conventional rotor antitorque power requirements are thus largely eliminated for the ABC system.

The measured stresses and loads corresponding to the performance results of Figure 9 are presented in the section "Discussion of Stresses and Loads".

A qualitative summary of the preceding discussion of the effect of major test variables on measured rotor performance parameters is given in Table II. Additional trends are also shown in this table which may be verified by a study of the presentations in the Appendix. The effect of any variable shown is valid only when all other variables are held simultaneously fixed.

CORRELATION OF PERFORMANCE DATA WITH THEORY

In order to evaluate the capability of predicting ABC performance, stresses, and loads over a wide range of advance ratio, measured results were cross-plotted versus advance ratio at nominal design lift coefficient. The shaft angle and B'_{1s} combination chosen at each advance ratio was that yielding the highest tested L/D at the design lift coefficient. Theoretical calculations were then performed, constraining the lift, shaft angle, and B'_{1s} schedules to be the same as for the test data. Figure 10 shows the variation with advance ratio of the independent variables chosen. As seen in Figure 10(a), a lift value of 14,500 lb was used at the first three advance ratios. At the two highest advance ratios (0.70 and 0.91), the lift is scaled down (short dotted line) in accordance with the reduced tip speeds used to achieve these high advance ratios in the tunnel test. The lift coefficients, however, are higher for the high μ conditions than for the low μ cases. Also shown at high μ's is a line of constant lift (dashed line). Additional calculations were performed at this lift, with advancing tip Mach number increased to full-scale values, in order to demonstrate the high forward speed characteristics predicted for the rotor system operating at the same lift coefficients and advance ratios as the tunnel test article. The Mach number schedule for the test data and the two schedules for theory are given in Figure 10(b).

Figures 10(c) and 10(d) indicate the shaft angle and B'_{1s} schedules employed. Note that the theoretical inputs for both the high tip Mach number case and the reduced tip Mach number case were chosen to follow the test data.

Further details of the inputs for the theoretical calculations are given in Table III. Conditions A and B in this table represent the full-scale tip Mach number calculation inputs. Also shown is the longitudinal cyclic pitch (A_{1s}) necessary to trim out pitching moment for each test condition. A value of zero was assumed, however, for all performance calculations, since these calculations were carried out using rigid blade theory. As discussed in the preceding section, the A_{1s} control was needed in practice to counteract phase lag effects caused by blade flexibility. In the theory used for the performance calculations, no such coupled moments are generated and so no A_{1s} is required to counteract them. The correlation obtained in this manner thus typifies the results which would be obtained by a preliminary designer employing rigid blade theory to predict performance for a projected configuration. For the stress and load correlation (discussed in a later section), the test values of longitudinal cyclic pitch were used with flexible blade theory.

The results of the performance correlation study are given in Figure 11. They are shown in dimensional form to provide for easy application of the results to aircraft performance computations, if desired. The circled points again represent test data, the short dotted line represents calculations at the wind-tunnel tip Mach numbers, and the dashed lines are calculations at full-scale tip Mach number. Figure 11(a) shows the variation with advance ratio of measured and predicted rotor shaft horsepower. The unusual variation of the horsepower (and other parameters of Figure 11) with advance ratio is due to the varying combinations of shaft angle and

B'_{1s} required for best rotor L/D (see Table III). In addition, the reduction in tip speed at the two highest advance ratios causes a change in the character of the curves above $\mu = 0.5$.

The rotor power characteristics are seen to be well defined by theory. At two advance ratios ($\mu = 0.35$ and $\mu = 0.70$) the theory predicts somewhat higher than measured power. As expected, increases in power are predicted for the full-scale Mach number cases, with power requirements falling off at $\mu = 0.7$ as tip speed is decreased to keep M_t from exceeding 0.9 (see Table III, cases A and B).

The measured and predicted rotor drag force characteristics are in excellent agreement for the cases investigated, as shown in Figure 11(b). The variation in rotor drag forces expected at full-scale lift and Mach number is also shown at the high advance ratios.

The measured and predicted lateral bending moments experienced by each rotor shaft are depicted in Figure 11(c). The predicted moments are somewhat less than those measured in the wind tunnel, possibly because the effects of blade flexibility are not accounted for in this particular method. Moments of approximately 70,000 foot-pounds are seen to be predicted at full-scale Mach number, since higher dimensional lifts are generated. To verify the system's capacity to support such moments, conditions were explored during the test with lateral bending moments greater than 70,000 foot-pounds. This may be verified by moment computations using the data of Figure 9(d) or similar figures in the Appendix. For example, at C_L/σ = 0.16 in Figure 9(d), the lift lateral displacement is 0.37 for $\alpha_s = -4$ degrees. Thus,

$$\text{Lateral Moment} = \left\{\text{upper rotor lift}\right\} \left\{\text{lift offset}\right\}$$

$$= \left\{\tfrac{1}{2}\,(C_L/\sigma)\;\; \sigma\pi R^2 (\Omega R)^2 \rho\right\}\left\{(.37)(20)\right\}$$

$$\approx 74{,}000 \text{ foot-pounds}$$

Figure 11(d) shows the lift lateral displacement for best L/D with this blade geometry, as a function of advance ratio. There is evidence that the test spectrum at the two highest advance ratios did not include the optimum lateral displacement setting. True optimum displacement at high μ may be up to 30 percent less than that shown in Figure 11(d). The theoretical calculations indicate that optimum lift lateral displacement is expected to remain substantially unchanged at full-scale values of lift and Mach number.

The collective pitch, θ_c, required to produce the desired lift is depicted in Figure 11(e). Theory and experiment are in good agreement, with the theory specifying approximately one degree more than actually required at the higher advance ratios. Predicted collective pitch requirements decrease slightly for full-scale lift and tip Mach number.

Tip Clearance

As discussed previously, blade tip clearance was monitored continuously throughout the test using television cameras and electronic blade trackers. The closest approach of the rotor tip path planes at design lift coefficient and optimum lift lateral displacement was 20 inches. To simulate blade overload and nonoptimum lateral displacement operation, the tip paths were brought to within 9 inches for several test points at an advance ratio of 0.7. For these conditions, the tip paths were observed to be steady, predictable, and controllable.

To summarize the preceding discussion, it has been shown that the wind-tunnel performance of the ABC rotor followed qualitative expectations to a high degree. A wide range of operating regimes was explored experimentally, and the measured and predicted performances were shown to be in good agreement for the cases illustrated. The data presented in the Appendix should provide an ample source of material for future quantitative studies. It is presented in a form suitable for cross-plotting at any desired lift coefficient, and for easy reference to the corresponding structural loads.

DISCUSSION OF STRESSES AND LOADS

MEASURED STRESS AND LOAD DATA

The stress and load data measured during the wind-tunnel tests are shown in final form in the Appendix. From the 95 measurements recorded on magnetic tape, 24 were chosen to represent the major areas of stress, load, and vibration interest. The remaining measurements were either approximate duplications of the ones chosen or the gages were not operative for sufficient periods of time to provide for meaningful analysis. Included in the presentations are blade flatwise and edgewise stresses, torsional moments, pushrod loads, servo loads, and hub stresses. The one-half peak-to-peak values of each of the 24 parameters are plotted versus C_L/σ for each of 25 test condition/B'_{1s} combinations. In some instances all 24 parameters are not plotted because of insufficient data or an inoperative strain gage. A typical sample of the data presented in the Appendix is given in Figure 12 for one of the test condition/B'_{1s} combinations.

Figure 12 includes the measured vibratory stress and loads data at 179 knots with 6 degrees of B'_{1s}. This figure represents the maximum wind-tunnel velocity condition and contains the highest rotor L/D data obtained at that velocity. Each plot shows the effects of α_s and C_L/σ on the measured quantities.

Upper and lower rotor blade flatwise stresses are shown in Figures 12(a) through 12 (f) at different blade radial stations. With two exceptions, these stresses continuously increase with increasing C_L/σ at most radial locations. There is evidence, Figure 12(d), that some stresses, at the lowest tested values of C_L/σ, decrease slightly and then increase with increased C_L/σ. This point of minimum stress between C_L/σ of 0.08 and 0.12 corresponds to the region in which the rotor was designed to operate. Also the outboard stresses, at a radial station of 204 inches, are relatively insensitive to changes in C_L/σ. The highest flatwise stresses occur over the inboard half of the blade. Also evident in these plots is the decrease in vibratory flatwise stress when shaft angle is tilted backward. The lower rotor stresses are lower than the corresponding upper rotor stresses for the same control settings.

Vibratory edgewise stresses on the upper rotor blade are shown at several radial stations in Figures 12(g) through 12(i). The edgewise stresses generally increase with C_L/σ but also demonstrate a minimum stress region as was seen in the flatwise stresses. The edgewise stresses decrease fairly consistently with increase in positive shaft angle. Edgewise stresses are considerably lower than the corresponding flatwise stresses.

The vibratory torsional moment near midspan of the upper rotor blade increases with C_L/σ as indicated in Figure 12(j). As with the flatwise and edgewise stresses, the torsional response decreases with an increase in shaft angle. These torsional response characteristics of the upper rotor blade are also demonstrated in the upper rotor pushrod load which is shown in Figure 12(k).

Lower rotor pushrod load data are given in Figure 12(l). The lower and upper rotor vibratory pushrod loads are of approximately the same magnitude, about 1000 to 1500 pounds.

Upper and lower rotor servo loads are compared in Figures 12(m) through 12(p). The lower rotor servo loads are greater than the corresponding upper rotor loads, especially the fore and aft servo loads. All loads increase with increasing C_L/σ but generally decrease with positive change in α_s.

The vibratory total stress at one of the most highly stressed points on the upper rotor hub is shown in Figure 12(q). Like much of the other stress and load data, the hub stresses generally increase with C_L/σ but also exhibit the trend of first decreasing and then increasing at low values of C_L/σ. At constant B_{1s}', decreased vibratory stress is generally achieved by increasing shaft angle.

In general, Figure 12(a-q) exhibits the predominant trends of the blade response, control loads, and hub stresses to increase with increase of C_L/σ and to decrease with increasing α_s. The trends of the condition shown are typical of other conditions included in the Appendix.

The plots in the Appendix for all test condition/B_{1s}' combinations were examined to determine any further trend information exhibited by the measured data. Table IV shows qualitatively the effects of the major test variables on this data. The test variables chosen are α_s, B_{1s}', C_L/σ, and μ. Table IV gives the change in each of the major types of measurements due to a positive change in each of the four test variables. The information is only useful for general trend effects of all the data. For specific effects at a particular operating point, the pertinent plots in the Appendix should be used.

CORRELATION OF STRESS AND LOAD DATA WITH THEORY

Measured blade stress and load data were compared to results of analytical studies, using the Normal Modes Aeroelastic Blade Analysis. Measured rotor hub stresses were compared to predictions based on a photoelastic model study of the upper rotor hub (Reference 4). Theoretical calculations were performed for the five tunnel test conditions listed in Table III. No corrections for wind-tunnel wall interference were made to the control settings. The results of the correlation study are presented in Figure 13. The measured and analytical values of each parameter are plotted as a function of advance ratio (μ). Conditions A and B, also indicated in Table III, correspond to theoretical calculations at a full-scale lift of 14,500 pounds and an advancing blade tip Mach number of 0.90. These are the same high Mach number conditions used in the performance calculations of the preceding section. Condition A corresponds to a forward velocity of 255 knots with a rotor tip speed of 615 ft/sec at an advance ratio of 0.70. Condition B represents a forward velocity condition at 294 knots having a tip speed of 546 ft/sec with an advance ratio of 0.91. Calculations at these conditions are included in Figure 13.

Vibratory flatwise stresses on the upper rotor blade are correlated with theory and are shown in Figures 13(a) through 13(d). The normal modes analysis is generally conservative in the prediction of these stresses at each blade station. However, the analysis does exhibit the same trend as the test data as advance ratio is increased. Theory is also in agreement with the test data by predicting that the highest flatwise stresses occur over the inboard half of the blade. Higher flatwise stresses are predicted to occur at the full-scale lift and Mach number conditions (A and B in Table III) than at the corresponding advance ratio conditions reached in the wind tunnel.

Maximum upper rotor blade centrifugal force at the highes rotor speed tested is calculated to be 58,900 pounds at the blade root. This condition results in a maximum blade centrifugal stress of 11,830 psi at a radial station of 156 inches, or about 10 percent of the spar's tensile strength. The maximum vibratory stress for the tested rotor blades occurs at 60 inches of radius, principally in the flatwise mode. Since the station-60 gage was not operating properly throughout the advance ratio range, station 84 is assumed to represent the approximate critical stress location. Stresses at this location are calculated to differ from station 60 by only 1600 psi (at $\mu = 0.7$). The measured and predicted variation of this stress with advance ratio is shown in Figure 13(a). Unlimited operating life is predicted for these rotor blades if maximum vibratory stress remains less than ± 18,000 psi at maximum steady loads. Higher vibratory loads are allowable at lower steady loads. Allowing for an increase in stress at full-scale Mach number, the measured data of Figure 13(a) indicate that the present blades can operate up to an advance ratio of between 0.6 and 0.7 for an unlimited period. Higher advance ratios are possible if finite life limits are set, and advanced composite materials offer promise of still higher stress allowables. Variations in blade geometry to decrease high advance ratio stresses might also be considered.

The one-half peak-to-peak edgewise blade stress correlation on an upper rotor blade is shown in Figures 13(e) through 13(g). As in the case of the flatwise stresses, theory predicts higher than measured edgewise response. As advance ratio increases, the variation of the theorectical edgewise stresses is comparable to the measured stresses, except at the highest advance ratio. At $\mu = 0.91$, the theoretical stress is larger than that predicted at $\mu = 0.70$, while the test data decreases in this region. The full-scale Mach number condition at $\mu = 0.91$ is predicted to have higher edgewise stresses than the low Mach number calculation condition at the same advance ratio, while there is little difference at $\mu = 0.70$.

A possible explanation for the highly conservative edgewise stresses predicted at $\mu = 0.91$ is the proximity of the first edgewise mode frequency of the analytical blade to a multiple of the 1/rev rotor frequency causing an analytical edgewise resonance. The first edgewise mode frequency of the wind-tunnel condition, at a tip speed of 325 ft/ sec, is 2.842/rev, while the full-scale condition, at 546 ft/sec tip speed, is 1.771/rev. These frequencies are indicated in Figure 4. An earlier ABC model rotor test, Reference 5, indicated that edgewise stress amplification could occur at rotor rotational speeds corresponding to the natural frequency of the first

edgewise bending mode. Although there are large third and second harmonics of edgewise stress in the analytical prediction of the wind tunnel and full-scale conditions respectively, the tunnel test data do not indicate these large vibratory stresses. This indicates that an inaccurate description of the analytical blade properties may have been used in the theoretical calculations. Another possible contribution to the differences noted in the correlation of both edgewise and flatwise stresses is that the conditions compared are not tunnel test points but are conditions whose control settings and loads were found by interpolation of the data between measured test points. But this interpolation of the data is believed to result only in a 0- to 1000-psi uncertainty in the stresses that were correlated. An additional 0- to 2000-psi inaccuracy of the flatwise and edgewise stresses is possible due to cross-talk interactions between the strain gages. It is recommended that a further correlation study be performed, especially in the high μ region.

Figure 13(h) compares the measured and analytical vibratory torsional moment near the blade midspan. Analysis predicts significantly lower torsional response than actually measured at each condition and indicates only a slight increase in torsional response as advance ratio is increased. The full-scale Mach number conditions are predicted to have slightly lower moments than their corresponding wind-tunnel cases.

Because of the large differences that exist in the correlation of the measured and predicted torsional moments, the measured data were reevaluated to determine their reliability. Examination of the torsional moment measurements at other blade radial stations indicated a different radial trend than that predicted. Analytically, the blade torsional moment steadily decreased along the blade from root to tip. The measured torsional moments, however, indicated first a large increase and then a decrease along the blade from root to tip. This led to an investigation of the torsional moment measurements themselves.

For the same percentage of full-scale load, the flatwise and edgewise bending moment measurements indicate a true strain of 250 and 180 microinches/inch respectively, whereas only 33 microinches/inch true strain is received by the torsion gages. The low torsional strain is due to the relatively stiff torsional properties of an ABC blade and results in low sensitivity of the torsional bending measurements.

It was also found during the blade calibration that, due to the low sensitivity of the torsion measurements, flatwise and edgewise blade moments substantially influence the torsional strain gage outputs. As an example, for the conditions correlated in Figure 13, at the radial station at 132 inches the average measured one-half peak-to-peak flatwise moment is approximately 25,000 in.-lb, while the corresponding average edgewise moment is about 17,000 in.-lb. The blade calibration indicated a cross-talk effect of 0.092 in.-lb of torsional moment per in.-lb of applied flatwise moment, and 0.053 in.-lb of torsional moment per in.-lb of applied edgewise moment, at the 130-inch radial station. For the conditions shown in Figure 13 this results in 2300 in.-lb of torsional moment due to flatwise cross talk and 900 in.-lb of torsion due to edgewise cross talk, creating a

maximum cross-talk error of 3200 in.-lb of torsional moment. This is approximately the magnitude of the torsional moment measurements for the conditions shown in Figure 13(h). This is a 'worst case' example, but it does indicate that due to the low sensitivity and the susceptibility of the torsion measurements to flatwise and edgewise moment cross talk, all of the data obtained from the torsional moment measurements should be considered unreliable.

Blade torsional response was also studied by correlation of the upper rotor vibratory pushrod load shown in Figure 13(i). The analytical prediction of the pushrod loads was generally lower than the test loads with the exception of the condition at the highest advance ratio. The test data indicated that the load decreased over most of the advance ratio range, while theoretical pushrod loads increased. The failure of the predicted pushrod loads to diminish at the highest advance ratios may be due to the resonance effect noted for the analytical edgewise stresses at high μ. Due to mode coupling, this edgewise resonance could have affected the torsional moment calculation, which in turn was used to predict the pushrod loads. Although the measured pushrod loads shown in Figure 13(i) are higher than predicted, they are still below the allowable limit for continuous operation of ±1500 pounds. The pushrod loads were measured independently of blade torsional moment and thus contain none of the inaccuracies discussed in connection with torsional moment measurement. Compared to the low Mach number predictions, lower pushrod loads are predicted for the corresponding full-scale Mach number cases. This is probably due to the removal of the analytical blade modes from the vicinity of a resonance condition for the full-scale Mach number conditions.

Correlation of measured upper rotor hub total stress with the photoelastic prediction method is shown in Figure 13(j). The stress shown was measured in a region where high stresses were found to occur in the photoelastic study, Reference 4. The study indicated that the hub stress at this location is primarily a linear function of the applied head moment. The stress-to-load ratio was found in that study to be 0.026 psi/in.-lb of head moment. The use of this factor with the theoretical head moment yields the hub stress prediction shown in Figure 13(j). This method predicts conservative stresses when compared to the measured data. Based on this method, the full-scale Mach number condition hub stresses are significantly higher than those at the lower tip speed wind tunnel conditions.

In general, the behavior of measured ABC rotor blade stresses, loads, and hub stresses is as anticipated. With the exception of the pushrod loads, the loadings were lower than predicted. A more extensive correlation study is recommended that would include the effects of variable airfoil section data, the determination of rotor-rotor interaction, and the inclusion of variable inflow effects along with a reevaluation of the analytical blade description.

ROTOR SYSTEM STRUCTURAL INTEGRITY

During rotor operation at 180 knots, three instrumentation terminal boxes which were attached to the rotor head became unfastened and impacted upon

the rotor blades. One of these boxes, weighing 24 pounds, struck the leading edge of one blade near the tip, which was moving at approximately 650 feet per second. The system was brought to a safe stop without blade failure or excessive vibration. Two blades were replaced and the other four were repaired without removal, and testing was continued.

DISCUSSION OF STABILITY AND CONTROL

STABILITY AND CONTROL DATA

In order to validate the high control powers predicted for the ABC rotor system, out-of-trim moments of up to 20,000 foot-pounds were generated, for selected cases, about the three primary body axes. With all other controls fixed, increments of A_{1s}, B_{1s}, and $\Delta\theta$ were introduced in turn to produce pitching, rolling, and yawing moments, respectively. The principal moment control derivatives thus generated were:

Pitching Moment/A_{1s}

Rolling Moment/B_{1s}

Yawing Moment/$\Delta\theta$

In addition, the six control coupling derivatives were measured:

Pitching Moment/B_{1s}, /$\Delta\theta$

Rolling Moment/A_{1s}, /$\Delta\theta$

Yawing Moment/A_{1s}, /B_{1s}

These nine control derivatives were evaluated at 15 rotor initial operating conditions, which correspond to trim points in the normal test spectrum. The control derivatives, along with initial trim point information (μ, B'_{1s}, α_s, and θ_c), are presented in Table V. Also shown in this table are three longitudinal stability derivatives:

Pitching Moment/α_s

Pitching Moment/θ_c

Pitching Moment/B'_{1s}

These are defined as "stability" derivatives to differentiate them from controls specifically designed for moment generation. They were not evaluated by holding all other controls fixed, but rather were computed from the measured moment control derivatives, in combination with information from adjacent rotor trim points. For example, if the subscripts correspond to adjacent trim points,

$$PM_2 = PM_1 + \frac{\partial PM}{\partial A_{1s}}\left[A_{1s_2} - A_{1s_1}\right] + \frac{\partial PM}{\partial B_{1s}}\left[B_{1s_2} - B_{1s_1}\right]$$

$$+ \frac{\partial PM}{\partial \Delta\theta}\left[\Delta\theta_2 - \Delta\theta_1\right] + \frac{\partial PM}{\partial \alpha_s}\left[\alpha_{s_2} - \alpha_{s_1}\right]$$

Solving for $\frac{\alpha PM}{\partial \alpha_s}$,

$$\frac{\partial PM}{\partial \alpha_s} = \left[\frac{PM_2 - PM_1}{\alpha_{s_2} - \alpha_{s_1}}\right] - \frac{\partial PM}{\partial A_{1s}} \left[\frac{A_{1s_2} - A_{1s_1}}{\alpha_{s_2} - \alpha_{s_1}}\right]$$

$$- \frac{\partial PM}{\partial B_{1s}} \left[\frac{B_{1s_2} - B_{1s_1}}{\alpha_{s_2} - \alpha_{s_1}}\right] - \frac{\partial PM}{\partial \Delta\theta} \left[\frac{\Delta\theta_2 - \Delta\theta_1}{\alpha_{s_2} - \alpha_{s_1}}\right]$$

Since the control partial derivatives in this expression are known, the derivative on the left side may be computed directly. The trim points chosen for such a calculation would necessarily be such that they had differing shaft angles but the same values of A_{1s}', B_{1s}', and θ_c. Similar expressions may be derived for computation of $\partial PM/\partial \theta_c$ and $\partial PM/\partial B_{1s}'$, depicted in Table V.

A study of the derivatives in Table V reveals that the principal control derivatives ($\partial RM/\partial B_{1s}$, $\partial PM/\partial A_{1s}$, $\partial YM/\partial \Delta\theta$) are of generally large magnitude and are consistent in both sign and magnitude for a given advance ratio. Of these, the yawing moment control power is, as anticipated, substantially smaller than control power about the other two axes. The smallest values of yaw control power occurred at lower collective pitch (low power) settings. The $\Delta\theta$ control was not investigated at the higher advance ratios since airplane-type rudder control would be used in such flight regimes.

The six control coupling derivatives of Table V (defined in paragraph 2 on page 20) are generally of low magnitude for all conditions except for the $\partial RM/\partial \Delta\theta$ derivative, where substantial negative roll is introduced through application of $\Delta\theta$ control. This undesirable coupling will not be a problem if a rudder is the primary yaw control at high speed. However, the relatively low yaw control afforded by $\Delta\theta$ at low power settings indicates that development of an alternate yaw control method should be considered. A possible alternative presently under investigation is differential rpm. Some of the remaining control coupling derivatives of Table V may be noted to display occasional increases in magnitude. These deviations are thought to result from small random measurement errors in moment and/or control settings, which may sometimes be cumulative in the computation of the derivatives. This conclusion is supported by the seemingly random nature of the sign and magnitude of the deviations, in contrast to the consistent nature of the principal control derivatives. Further investigation of such effects is beyond the scope of this report, but a statistical analysis of large samples of the data, currently under way, tends to support the viewpoint that all of the moment coupling derivatives except $\partial RM/\partial \Delta\theta$ are generally small.

Of the three longitudinal stability derivatives shown in Table V ($\partial PM/\partial \alpha_s$, $\partial PM/\partial \theta_c$, $\partial PM/\partial B_{1s}'$), the two relating to θ_c and B_{1s}' are less

critical, because the induced pitching moments can be anticipated and nullified by proper application of A_{1s} control when changes of collective pitch or lift lateral displacement control (B_{1s}') are necessary. Such longitudinal trimming is also typically necessary for conventional rotors when collective pitch is altered. In the case of B_{1s}' (not present on conventional rotors), swashplate reorientation should minimize the effect of this control on pitching moment. In any case, as exemplified by the data in a preceding section dealing with rotor performance, more than ample A_{1s} control was available at each trim data point to nullify the ABC system pitching moment. For example, in Figure 9(e), the maximum A_{1s} control required at the maximum lift coefficient is -8 degrees. Since the present control system has an A_{1s} range of ±10 degrees, an additional 2 degrees is available for nose-down maneuvers. From Table V at the corresponding speed ($\mu = 0.47$), it is seen that 2 degrees of A_{1s} can produce a pitching moment of about 30,000 to 40,000 foot-pounds.

The angle-of-attack derivative of the rotor system, $\partial PM/\partial \alpha_s$, is seen from Table V to be destabilizing, as in the case of conventional rotors. The rigidness of the ABC rotor produces an effect approximately an order of magnitude greater than that of an articulated rotor of equivalent disc loading. As a result, an aircraft with an ABC rotor will probably require a larger horizontal tail than the same aircraft with an articulated rotor. There are, however, two important considerations which may alleviate this requirement. First, the magnitudes of the α_s derivatives shown in Table V are probably conservative. More complex methods of calculating these derivatives have been undertaken which involve larger samples of the wind-tunnel data that are resolved through simultaneous solution of control input and moment equations. The results obtained to date produce α_s derivatives about 30 percent smaller than those depicted in Table V, at $\mu = 0.47$. The reason for the differences is still under investigation, but possibly it is related to the elimination of cumulative errors. As previously discussed, such errors can be generated in the method of computation presented herein. The second mitigating consideration is the rigidness of the system itself, which contributes to a high value of damping in the pitching mode, which in turn should improve dynamic stability characteristics. Reference 6 has shown that increasing the hinge offset (i.e.,rigidity) of a rotor enables it to withstand increasing degrees of static instability without becoming dynamically unstable (Figure 13 of Reference 6).

CORRELATION OF DERIVATIVES WITH THEORY

All of the stability and control characteristics of the ABC system as measured in the wind tunnel are substantially as expected. To illustrate this, Figure 14 presents the more important derivatives as a function of advance ratio, and compares them to theoretical predictions. The theoretical derivatives are computed at the same initial trim conditions that are used in the performance calculations of Figure 11. These conditions are listed in Table III. Changes of one degree in the appropriate control were used to calculate the derivatives. The test data shown in Figure 14 are the maximum and minimum values of the derivatives listed in Table V, at the appropriate advance ratio. The range of test data includes points with initial control settings that are the same or close to the control settings

used for the theoretical calculations. This may be verified by a comparison of the α_s and B'_{1s} settings listed in Tables III and V.

The principal rolling, pitching, and yawing moment control derivatives are plotted in Figures 14(a), 14(b), and 14(c), respectively. Qualitatively, the test data and theory are in good agreement. The largest quantitative differences occur in the case of the rolling moment control (Figure 14(a)) at lower advance ratios, where the measured derivatives are about 5000 foot-pounds less than predicted. This difference, however, is not considered significant, in view of the relatively high control power available. For example, the maximum measured out-of-trim rolling moment coefficient in the sample 179-knot performance data (Figure 9(g)) is -0.009. This is equivalent to approximately 23,000 foot-pounds of rolling moment. As seen from Figure 14(a) at $\mu = 0.47$, a moment of this magnitude can be counteracted with less than 2 degrees of B_{1s} control. Since the present control system provides a B_{1s} control range of ±10 degrees, there is ample authority remaining for roll maneuvers.

The degree of correlation shown in Figure 14(a) would possibly be improved by the use of flexible blade theory, rather than rigid blade theory as used herein. Such an approach should be investigated for detailed stability and control design work. However, rigid blade theory and test results are seen to be in good agreement in the case of pitching moment control (Figure 14(b)) and yawing moment control (Figure 14(c)). As previously mentioned, $\Delta\theta$ control is of practical interest only at low advance ratios, and this control was not experimentally investigated above $\mu = 0.21$. The theoretical curves of Figure 14(c) are extended to high advance ratio for completeness.

Figure 14(d) depicts the measured and predicted values of the coupling derivative, $\partial RM/\partial\Delta\theta$, which correlate well at $\mu = 0.21$, where the measured coupling is slightly less in magnitude than predicted. The high advance ratio calculations are, again, of little practical interest.

Angle-of-attack stability is seen from Figure 14(e) to correlate well with that predicted by flexible blade theory throughout the advance ratio range. Rigid blade theory cannot be used to compute this derivative, since much of the moment is caused by precession effects previously discussed.

The results of this preliminary stability and control study indicate that the ABC system has large control power in pitch and roll at all advance ratios, but that the $\Delta\theta$ control provides adequate yawing moments only at higher rotor power settings. Coupling of the controls is minimal with the exception of a $\Delta\theta$-rolling moment coupling and the effect of θ_c and B'_{1s} on pitching moment. Control mixing may be desirable to reduce these effects. All trends measured in the wind tunnel are predictable by theory, and the theoretical methods in conjunction with the acquired data appear to provide a sound basis for on-going simulation and control system design work.

DISCUSSION OF VIBRATION

MEASURED VIBRATION DATA

Wind-tunnel data from four vibration measurements are included in the Appendix. Accelerometers measured lateral and longitudinal acceleration on both the gearbox and the right strut of the module. The Appendix shows plots of the one-half peak-to-peak values of each of these measurements as a function of C_L/σ, at each of the 25 test condition/B'_{1s} combinations. The vibration data for the test condition at 179 knots with B'_{1s} = 6 degrees are presented in Figures 12(r) through 12(u).

These plots indicate that the average one-half peak-to-peak vibration is approximately ±0.4g at each location. Examination of the vibration plots included in the Appendix indicates that, at the conditions for which blade stresses and control loads were correlated (Table III), the vibration was also usually ±0.4g or less. Figures 12(r) through 12(u) indicate that there is no consistent effect on vibration due to an increase in C_L/σ. In some instances, vibration is insensitive to change in lift while for other control positions it either increases or decreases as C_L/σ increases. Similarly, there is no consistent effect on vibration due to a change in shaft angle, although the general trend is for vibration to decrease as α_s is tilted backward. An attempt was made to determine if these apparently changeable trends were applicable to all of the measured vibration data.

Table IV shows the general effects (non-numerical) of the major test variables on total vibratory gearbox longitudinal and lateral accelerations. The conclusions are based on the vibration characteristics of all of the test condition/B'_{1s} combinations in the Appendix. The general trends attributed to all of the data are similar to those found in Figures 12(r) through 12(u) which correspond to one specific operating point. Table IV indicates that no consistent trend of vibration due to change in shaft angle is apparent except that generally it decreases as α_s is tilted backward. Table IV also indicates that gearbox response is minimum in the C_L/σ region (0.08 to 0.12) corresponding to the lowest measured blade stresses but increases as lift is increased or decreased from this region.

The above results and those indicated in Table IV due to changes in B'_{1s} and μ indicate that in general the one-half peak-to-peak vibration data follow few obvious patterns with changes in the major test variables. This may in small part be due to the averaging of the data cycles to create an average cycle of each parameter. It was determined that a 0- to 10-percent reduction in the one-half peak-to-peak vibration occurred during the cycle averaging process because of high harmonic content and relatively less cycle-to-cycle repeatability of the vibration measurements compared to stress and load data. Since this occurred randomly, it may partially account for the scarcity of obvious vibration trends. Another influencing factor may be the changes in forced response characteristics of the balance structure, when subjected to varying combinations of forces and moments. Analysis of such effects is beyond the interest of the present study, since vibration levels were generally low.

HARMONICS OF VIBRATION

In order to determine the principal harmonic orders contributing to the total one-half peak-to-peak vibration in the fixed system, the average cycle time histories were harmonically analyzed to obtain the first ten harmonics. Figure 15 depicts harmonic content at four accelerometer stations on the gearbox and on the right strut of the module. For each harmonic, a bar indicates the range of vibratory amplitude recorded for the 8 data points at the 179-knot, B'_{1s} = 6-degree condition.

Figure 15 indicates that the 2, 3, 6, and 9/rev harmonics reached the highest amplitudes. For the ABC rotor, with 3 blades on each of the upper and lower rotors, the third, sixth, and ninth harmonics are theoretically at the primary response frequencies, but the large second harmonic is not expected.

As shown in Figure 15, the ninth harmonic of vibration is generally the largest in magnitude. The 9/rev vibration is significant in both the longitudinal and lateral directions at the gearbox and at the right strut of the module. At each station, the third and sixth harmonics are smaller in magnitude than the ninth. The third harmonics of vibration are larger than the sixth in the lateral direction, while the opposite trend occurs in the longitudinal direction. The measured blade response data do not indicate an appreciable amount of high-frequency content that could cause 9/rev excitation of the gearbox or module. It is believed that the source of the large ninth harmonic vibration may be due to operation near a module resonance condition, although no shake test data for the module are available at the frequency associated with 9/rev to verify this opinion. Such resonances are usually minimized by appropriate fuselage design in aircraft.

As previously noted, the existence of an appreciable second harmonic vibration content in the accelerometer measurements was not expected. As indicated in Figure 15, this occurred at three of the four stations shown. The gearbox longitudinal acceleration was the exception, having little 2/rev vibration content. The fact that this accelerometer location was at the zero butt line of the module (along the axis perpendicular to the rotor shaft), while the other three locations were displaced from this axis, indicated a possible vibration due to rotor head vibratory moment. It was found that the second harmonic of each of the three affected accelerometer measurements increased as the magnitude of the rotor head rolling moment increased. This suggests that one of the three blades in either the upper or lower rotor had an unbalance of some type or a 1/rev lift variation that was of different magnitude than the other two blades. This would result in a 1/rev moment in the rotating system which would cause a 2/rev vibratory roll moment in the fixed system, which in turn would cause the second harmonic vibration. Examination of the sleeve flatwise bending time histories for the data included in Figure 15 indicates that they are primarily 1/rev in vibratory content.

Harmonic analyses of the remaining test conditions indicate that the high-speed condition shown in Figure 15 exhibits the largest 2/rev vibration content. The 2/rev content decreases as either velocity or tip speed

decreases. The second harmonic of vibration is in fact larger than the third harmonic only for the 179-knot condition. The 2/rev vibration occurring in the test data is therefore most significant at high forward velocity and high tip speed, and its cause should be investigated further.

CONCLUSIONS

Analysis of the measured ABC performance data leads to the following principal conclusions:

1. The Advancing Blade Concept is a feasible design approach from the standpoint of performance, structural integrity, and aeromechanical stability characteristics exhibited in the full-scale wind-tunnel tests.

2. The blade lift capacity of the ABC system is significantly greater than in the case of an articulated rotor operating at the same forward speed and tip speed, as is lift response to collective pitch inputs. Design lift coefficients for the present configuration can be maintained to advance ratios of at least 0.91, with tip clearances of 20 inches or greater.

3. Both shaft angle and B'_{1s} are effective in varying lift lateral displacement. As expected, the lift lateral displacement for optimum L/D increases with advance ratio in the range considered.

4. Little or no imbalance occurs between upper and lower rotor rolling moments when either lift or lift lateral displacement is varied. Imbalances that do exist may be trimmed with small control inputs.

5. The requirement for conventional rotor antitorque power is largely eliminated.

6. Measured rotor power and propulsive force characteristics are in generally good agreement with those predicted by rigid blade theory at all advance ratios investigated. Increased power requirements are predicted at high advance ratios if tip Mach number is increased to 0.9.

Analysis of the measured ABC stress and load data leads to the following principal conclusions:

7. Characteristics of the measured ABC rotor blade stresses, control loads, and hub stresses are as expected from earlier model tests and analysis. An exception is the blade torsional moments, which are found to be unreliable due to inadequate gage sensitivity and high cross-talk interference.

8. Blade stresses and control loads tend to increase as C_T/σ or advance ratio increases, and they tend to decrease as the shaft is tilted back or as lift lateral displacement is decreased. Many blade stresses achieve a relative minimum at design lift coefficients.

9. At design rotor lift coefficient and optimum L/D, the present rotor blades have an unlimited operating capability at advance ratios up to approximately 0.6.

10. The measured rotor blade and hub stresses are lower than predicted by flexible blade theory. Measured control loads are higher than predicted but below allowable at all advance ratios.

Analysis of the measured ABC stability and control data leads to the following principal conclusions:

11. Large control powers about the system's pitch and roll axes are available at all advance ratios through application of A_{1s} and B_{1s}, respectively. There is little or no mutual coupling between these controls.

12. Yaw control power (as produced by $\Delta\theta$) is less than that of pitch and roll, and diminishes at low power settings. An alternate means of yaw control in such regimes should be considered. The $\Delta\theta$ control also introduces negative rolling moment in forward flight.

13. Because of phase lag effects, significant system pitching moments are produced when collective pitch, shaft angle, or lift lateral displacement control (B'_{1s}) is varied. These moments can be nullified through application of longitudinal cyclic pitch (A_{1s}). Reorientation of the swashplates may also be used to minimize the effect of B'_{1s} on pitching moment.

14. Because of the greater pitching moment response to shaft angle change, an aircraft with an ABC rotor will probably require a larger horizontal tail than the same aircraft with an articulated rotor.

15. The principal control derivatives measured in the wind tunnel are well approximated by rigid blade theory to advance ratios of 0.7. Measured longitudinal static stability characteristics are in very good agreement with flexible blade theory.

Analysis of the measured ABC vibration data leads to the following principal conclusions:

16. Total fixed system vibration is usually low ($\leq$ 0.4g vibratory amplitude) at design lift coefficients. It consists primarily of third-, sixth-, and ninth-harmonic content, with the ninth being generally the largest. At high-velocity conditions, the second harmonic content is also large, possibly due to a 1/rev unbalance in the rotating system.

17. Gearbox vibration generally decreases as the rotor shaft is tilted back. Minimum vibration occurs at lift coefficients corresponding to minimum blade stress.

18. The full-scale ABC rotor system was found to be capable of operating over a substantial range of wind-tunnel conditions without any major mechanical or structural problems, and without evidence of divergent stresses or vibrations.

TABLE I. AVERAGE VALUES OF TEST CONDITIONS

Test Condition	Rotor Configuration	Forward Velocity (kn)	Advance Ratio	Advancing Tip Mach Number	Tip Speed (ft/sec)	Air Density (slugs/ft^3)	Speed of Sound (ft/sec)
1	Dual	82	.21	.69	650	.002246	1143
2	Dual	136	.35	.77	650	.002184	1148
3	Dual	179	.47	.83	650	.002140	1149
4	Dual	165	.70	.59	400	.002118	1160
5	Dual	175	.91	.54	325	.002118	1158
6	Single	82	.21	.69	650	.002243	1144
7	Single	136	.35	.77	650	.002184	1148

TABLE II. QUALITATIVE EFFECT OF MAJOR TEST VARIABLES ON ROTOR PERFORMANCE

Measurement(1)	Test Variable			
	α_s	$\dot{B}_{1s}$	C_L/σ	μ
Propulsive Force	decreases	increases	increases(2)	decreases
Lift-Drag Ratio	(3)	(3)	(3),(4)	(3)
Lift Lateral Displacement	decreases	decreases	increases	increases
Negative A_{1s} Required	decreases slightly	decreases slightly	increases	increases slightly

Notes:
(1) All entries indicate change in measurement due to positive change in test variable with all else held constant.

(2) Only if α_s is sufficiently negative; otherwise decreases.

(3) Maximizes at a point which is dependent upon the settings of the other three test variables.

(4) Maximizes at higher values of C_L/σ and lift lateral displacement as μ is increased.

TABLE III. INPUT VARIABLES FOR THEORETICAL CALCULATIONS

Cond.(1)	V (kn)	ΩR (ft/sec)	μ	M_t	α_s (deg)	Rigid Blade(2)		Flexible Blade(3)		C_L/σ	Lift (lb)
						A_{1s} (deg)	B_{1s}' (deg)	$A_{1s_{UR}}$ (deg)	$B_{1s_{UR}}$ (deg)		
1	82	650	.21	.69	4	0	1.6 [2]	-4.0	1.2	.110	14,500
2	136	650	.35	.77	4	0	1.6 [2]	-5.2	1.3	.113	14,500
3	179	650	.47	.83	0	0	5.9 [6]	-5.6	5.5	.115	14,500
4	165	400	.70	.59	-4	0	5.4 [6]	-6.3	3.9	.130	6,146
5	175	325	.91	.54	0	0	1.5 [2]	-6.9	- .2	.165	5,137
A	255	615	.70	.90	-4	0	5.4	-6.3	3.9	.130	14,500
B	294	546	.91	.90	0	0	1.5	-6.9	- .2	.165	14,500

NOTES:

(1) Condition numbers correspond to Table I. Conditions A and B do not have corresponding test data. Density and speed of sound were chosen for A and B equal to those for 4 and 5, respectively (see Table I).

(2) A_{1s} inputs for rigid blade calculations were set to zero although test values of A_{1s} were non-zero; see text, page [illegible], for explanation. B_{1s}' inputs correspond to actual test values (average B_{1s} of both rotors). Nominal test values of B_{1s}' are shown in brackets for reference.

(3) $A_{1s_{UR}}$ and $B_{1s_{UR}}$ inputs for flexible blade calculations correspond to actual test values for the upper rotor.

TABLE IV. QUALITATIVE EFFECT OF MAJOR TEST VARIABLES ON ROTOR STRESSES, LOADS, AND VIBRATION

Measurement[1]	Test Variable			
	α_s	B_{1s}'	C_L/σ	μ
UR ½ PTP BLD FS	Decrease[2]	Decrease	Increase[2]	Increase
UR ½ PTP BLD ES	Decrease[2]	Decrease	Increase[2]	Increase/ Decrease[4]
UR ½ PTP BLD TM	Decrease[2]	Decrease	Increase[2]	Increase[5]
UR ½ PTP PUSHRD LD	Decrease[2]	No Consistent Trend[3]	Increase[2]	Increase/ Decrease[4]
UR ½ PTP SRV LD	No Consistent Trend[3]	No Consistent Trend[3]	Increase[2]	Increase/ Decrease[6]
GB ½ PTP LONG ACC	No Consistent Trend[3]	No Consistent Trend	Increase[2]	No Consistent Trend[7]
GB ½ PTP LAT ACC	No Consistent Trend[3]	No Consistent Trend[3]	Increase[2]	No Consistent Trend

(1) All entries indicate change in measurement due to positive change in test variable.

(2) Except at some lowest values of C_L/σ where trend tends to reverse.

(3) But generally decrease.

(4) Increase but begins to decrease at $\mu \approx 0.7$.

(5) Except at $\mu \approx 0.7$.

(6) Increase but begins to decrease at $\mu \approx 0.5$.

(7) But generally increase.

TABLE V. MEASURED STABILITY AND CONTROL DERIVATIVES

					LONGITUDINAL STABILITY			ROLL CONTROL			PITCH CONTROL			YAW CONTROL		
μ	σ (x 10^2)	Nominal B_{1s}' (deg)	α_s (deg)	Nominal θ_c (deg)	$\partial PM/\partial \alpha_s$ (1)	$\partial PM/\partial \theta_c$	$\partial PM/\partial B_{1s}'$	$\partial RM/\partial A_{1s}$ Coupling	$\partial RM/\partial B_{1s}$ Principal	$\partial RM/\partial \Delta\theta$ Coupling	$\partial PM/\partial A_{1s}$ Principal	$\partial PM/\partial B_{1s}$ Coupling	$\partial PM/\partial \Delta\theta$ Coupling	$\partial YM/\partial A_{1s}$ Coupling	$\partial YM/\partial B_{1s}$ Coupling	$\partial YM/\partial \Delta\theta$ Principal
.21	.2302	2	-4	10	1,137.	7,746.	-4,986.	-1,234.	11,006.	-5,734.	13,371.	58.	-2,069	472.	-534.	3,668.
	.2220	2	4	6	1,719.	8,882	-6,586.	439.	11,439.	-6,392.	14,176.	157.	- 185.	-193.	174.	601.
	.2216	2	4	10	1,133.	7,497	-5,142.	555.	8,764.	-5,863.	12,684.	582.	-1,503.	436.	-616.	3,808.
	.2253	2	8	8	941.	7,267.	-5,726.	808.	10,026.	-6,627.	13,767.	258.	- 777.	203.	140.	1,930.
	.2269	4	-4	10	(3)	6,703.	-4,553.	-1,179.	8 961.	-8,212.	12,248.	-867.	-1,934.	-231.	550.	3,741.
	.2224	4	4	8	1,809.	10,284.	-5,503.	263.	10,742.	-7,556.	14,014.	9.	- 83.	104.	441.	1,834.
	.2236	4	8	8	1,722	9,170.	-5,492	- 5.	10,700.	-9,323.	13,206.	232.	175.	322.	805.	2,066.
.47	.2074	2	4	4	(3)	24,496.	-18,852.	-2,343.	19,413.	(2)	22,507.	287.	(2)	-193.	324.	(2)
	.2154	4	8	4	8,458.	19,345.	(3)	- 638.	15,[illegible]03.		19,462.	-1,896.		124.	705.	
	.2077	6	0	8	8,385.	14,930.	-11,655.	346.	18,076.		15,736.	- 240.		-166.	754.	
	.2131	6	4	6	8,680.	24,971.	-17,816.	- 831.	18,360.		20,290.	564.		-816.	988.	
	.2122	8	-4	12	9,077.	19,392.	-13,877.	7,491.	16,905.		18,716.	2,599.		373.	-939.	
	.2105	10	-9	14	(3)	16,099.	-11,932.	76.	18,229.		16,367.	158.		130.	-1,345.	
.70	.2117	4	0	6	2,947.	6,178.	- 3,376.	360.	11,331.		8,010.	1,939.		-303.	15.	
.70	.2088	4	4	4	3,961.	5,675.	- 3,537.	131.	11,333.		8,036.	931.		49.	213.	

Notes: (1) All derivatives have the units of ft-lb/deg.
(2) $\Delta\theta$ control not investigated at the higher advance ratios.
(3) Information not available due to insufficient data.

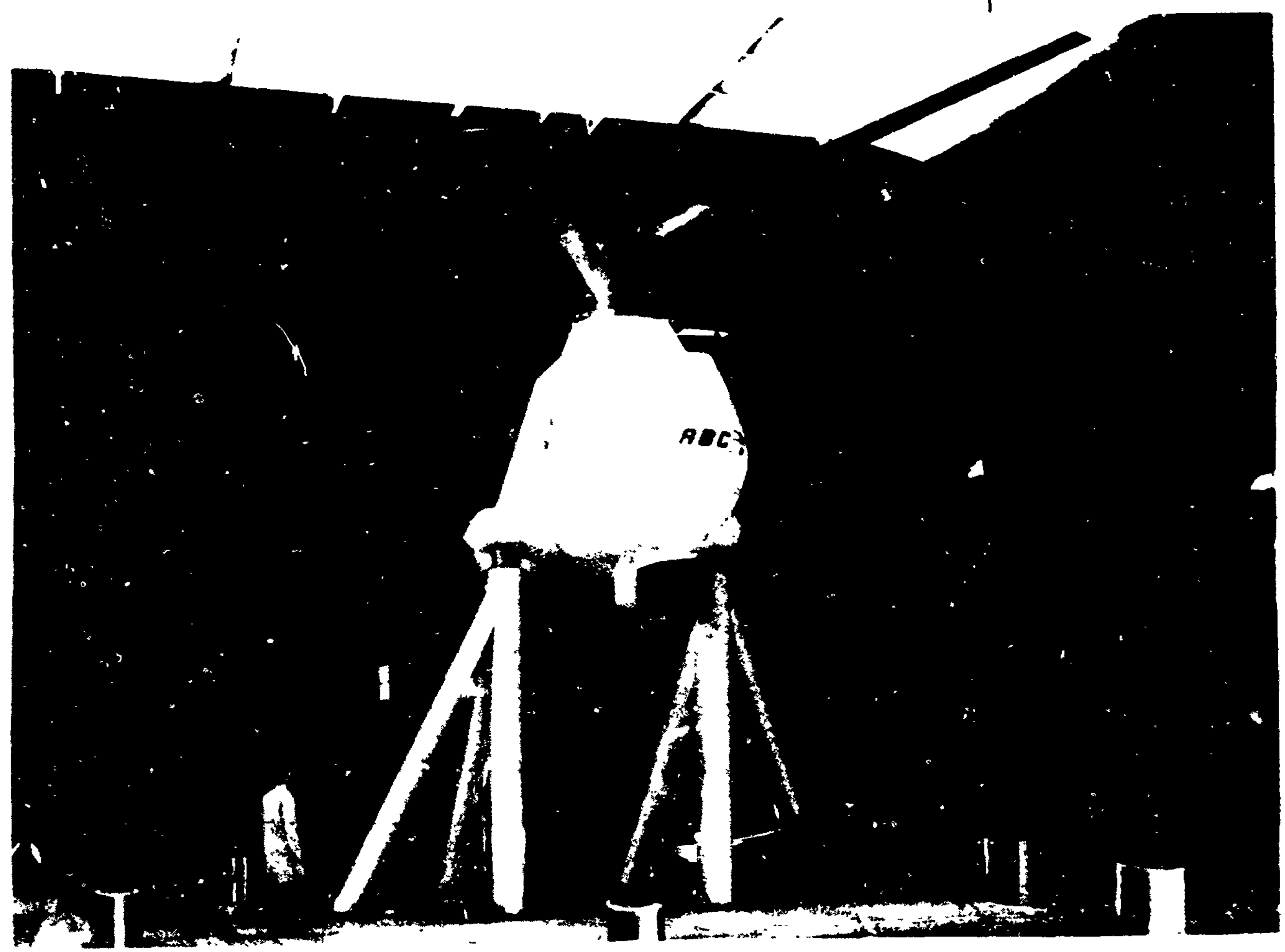

Figure 1. Advancing Blade Concept (ABC) Rotor System Installed in the NASA/Ames Full-Scale Wind Tunnel.

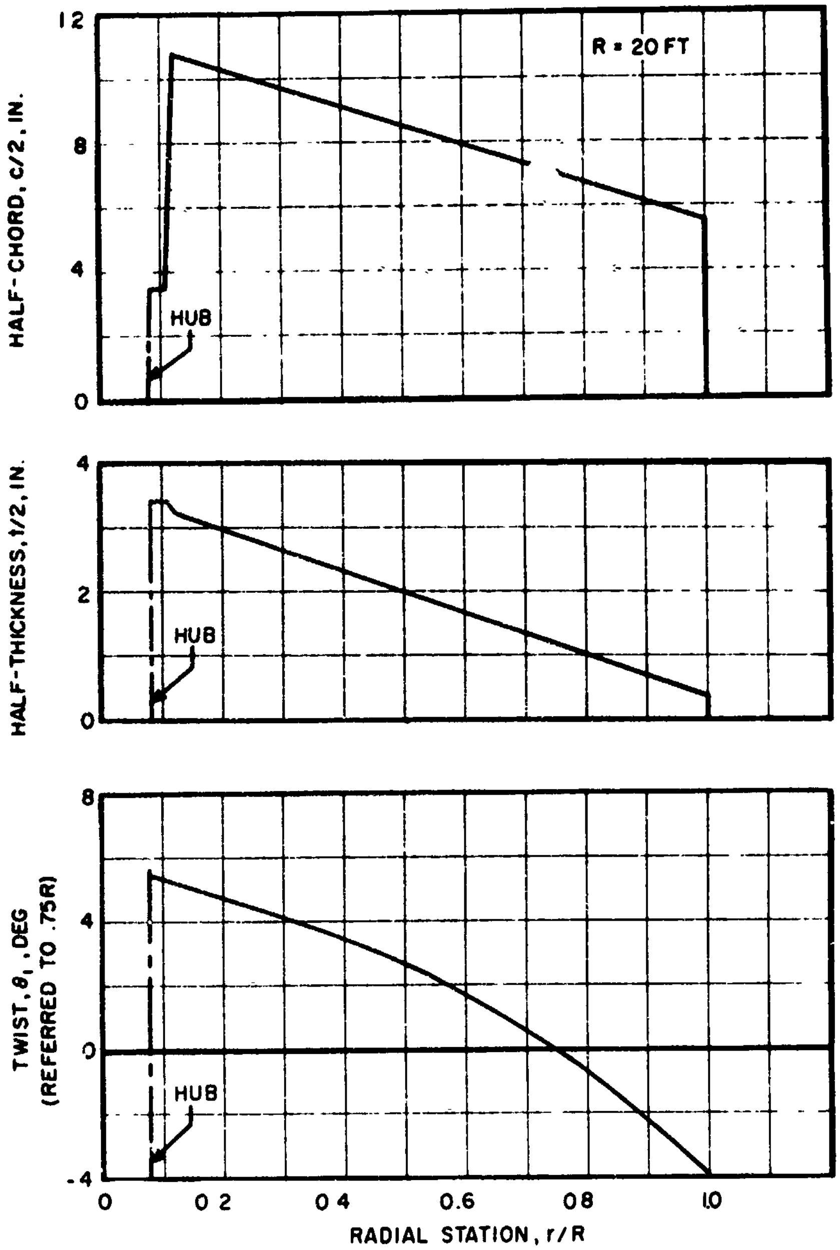

Figure 2. Rotor Blade Geometrical Properties.

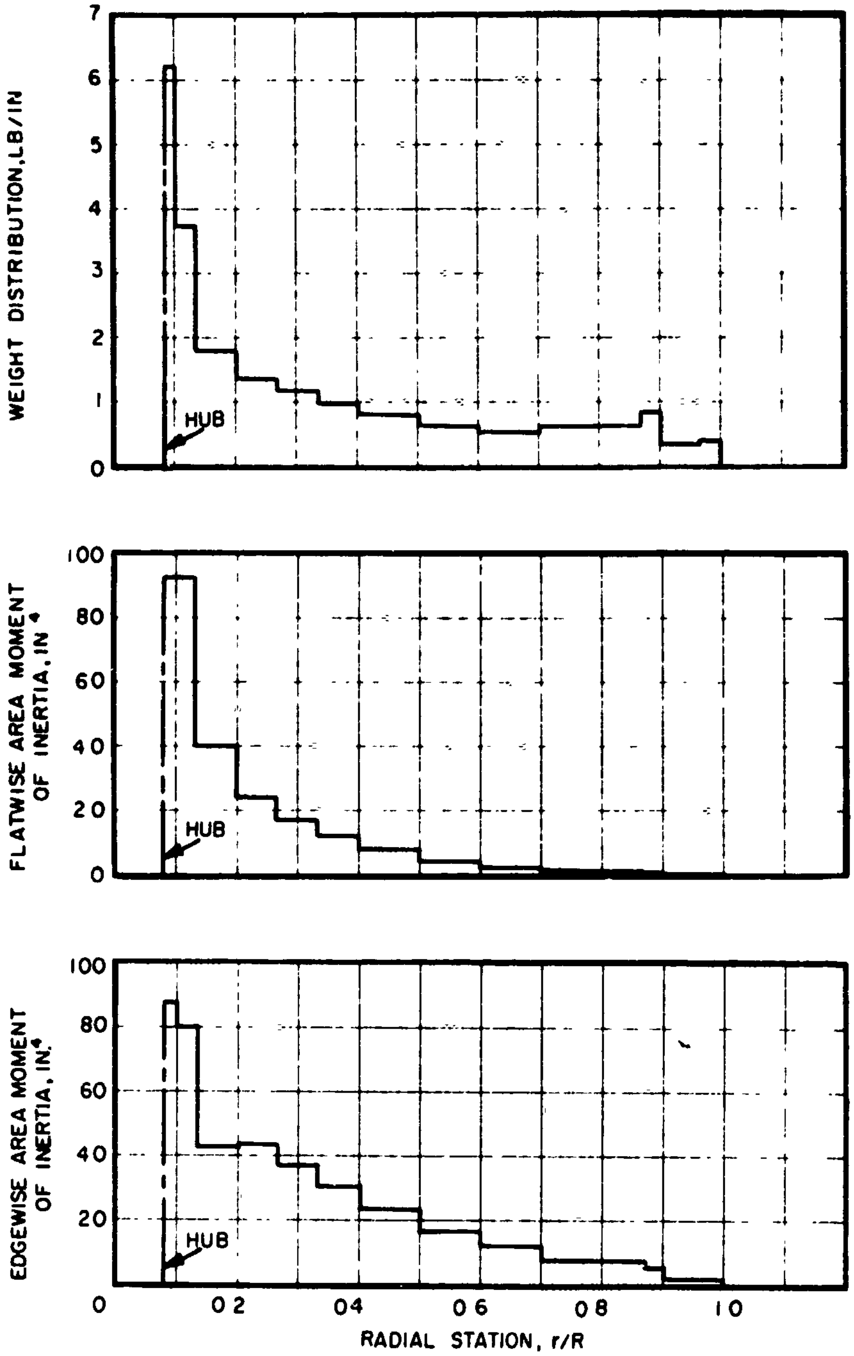

Figure 3. Rotor Blade Structural Properties.

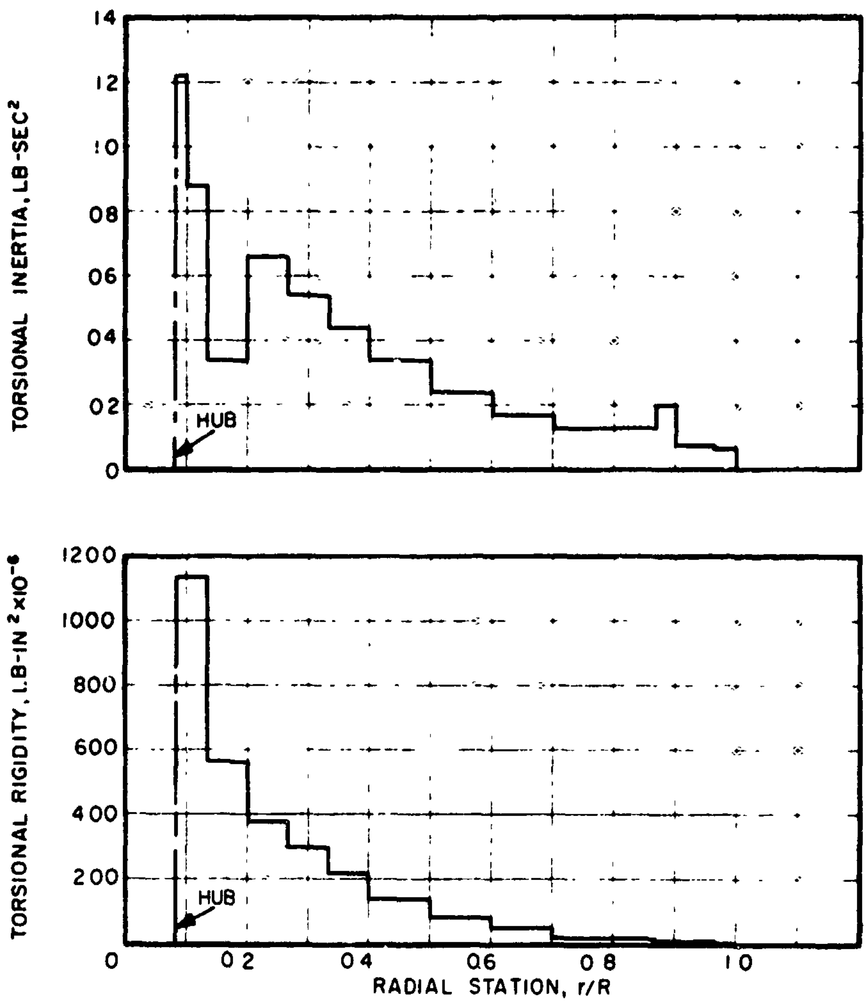

Figure 3. Concluded.

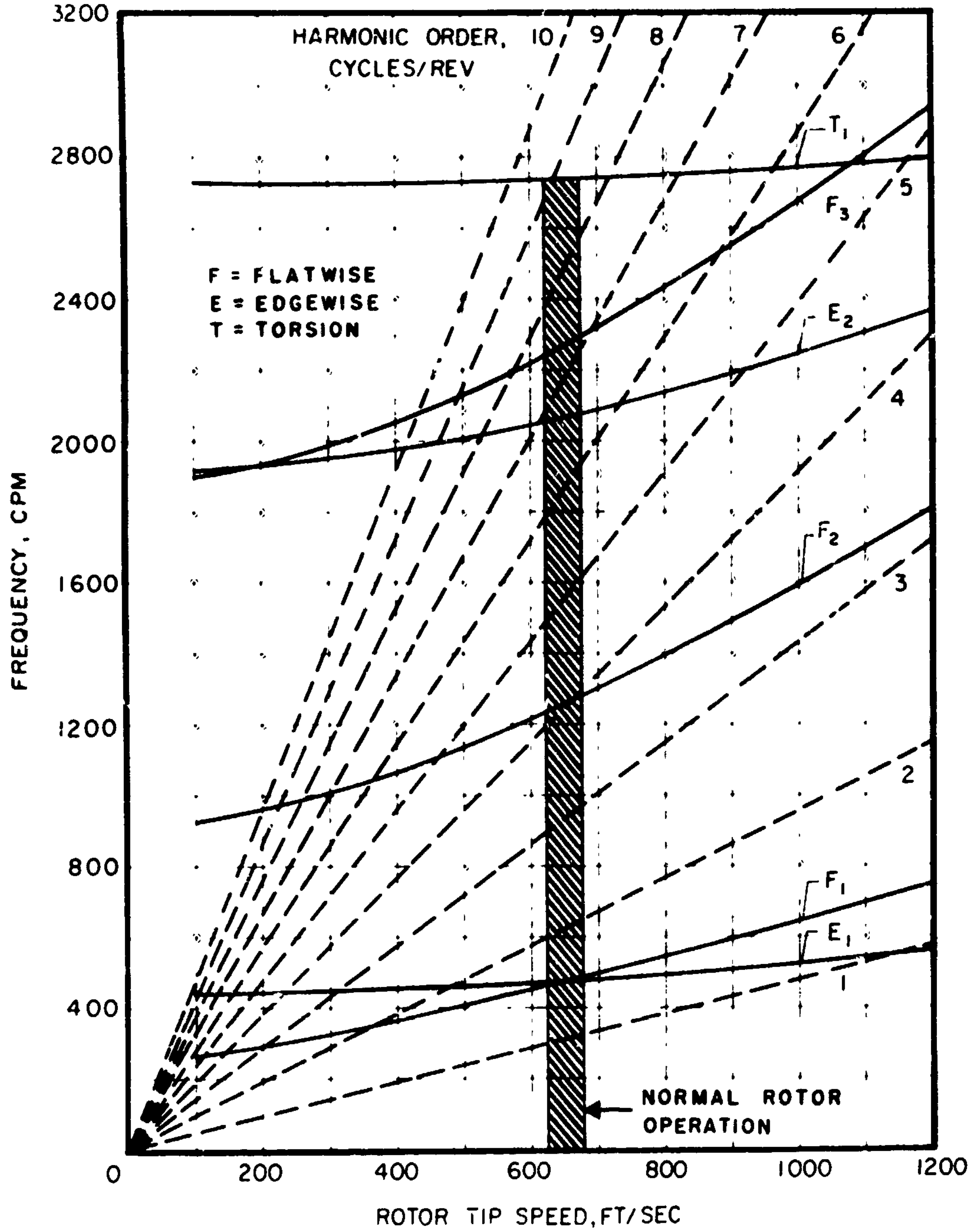

Figure 4. Rotor Blade Natural Frequency Diagram.

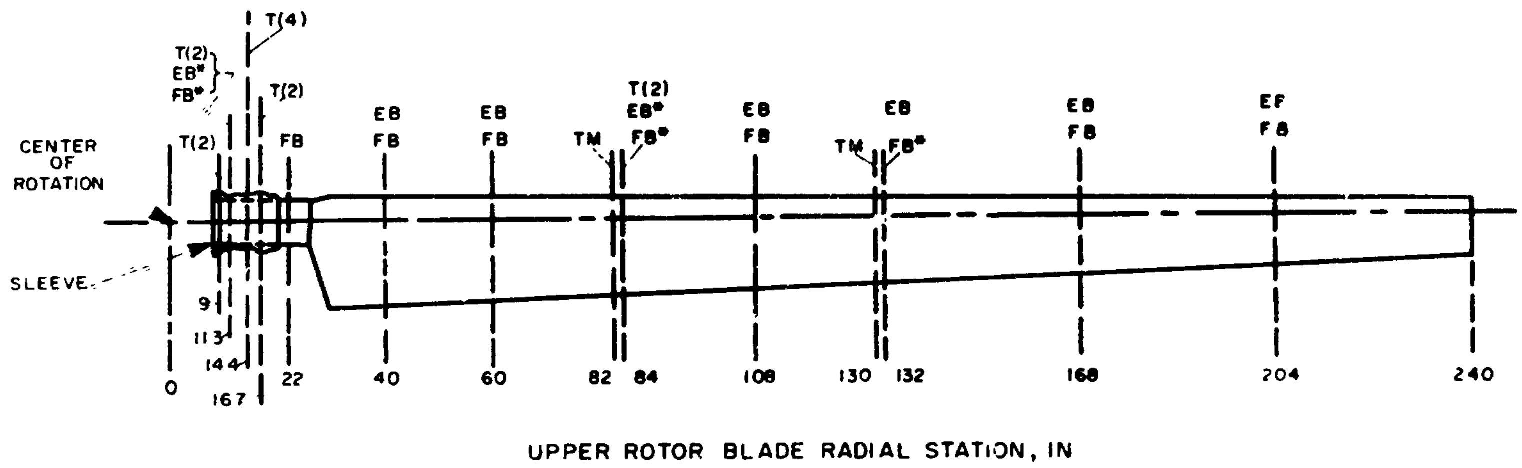

FB = FLATWISE BENDING
EB = EDGEWISE BENDING
TM = TORSION
T = TOTAL STRESS
TS2 (NOT SHOWN) = GAGE LOCATED ON HUB FOR MEASUREMENT OF HUB TOTAL STRESS

* INDICATES STRAIN GAGE ALSO ON LOWER ROTOR BLADE
( ) INDICATES NUMBER OF TOTAL STRESS GAGES INSTALLED AT THE RADIAL STATION

Figure 5. Location of Blade Strain Gages.

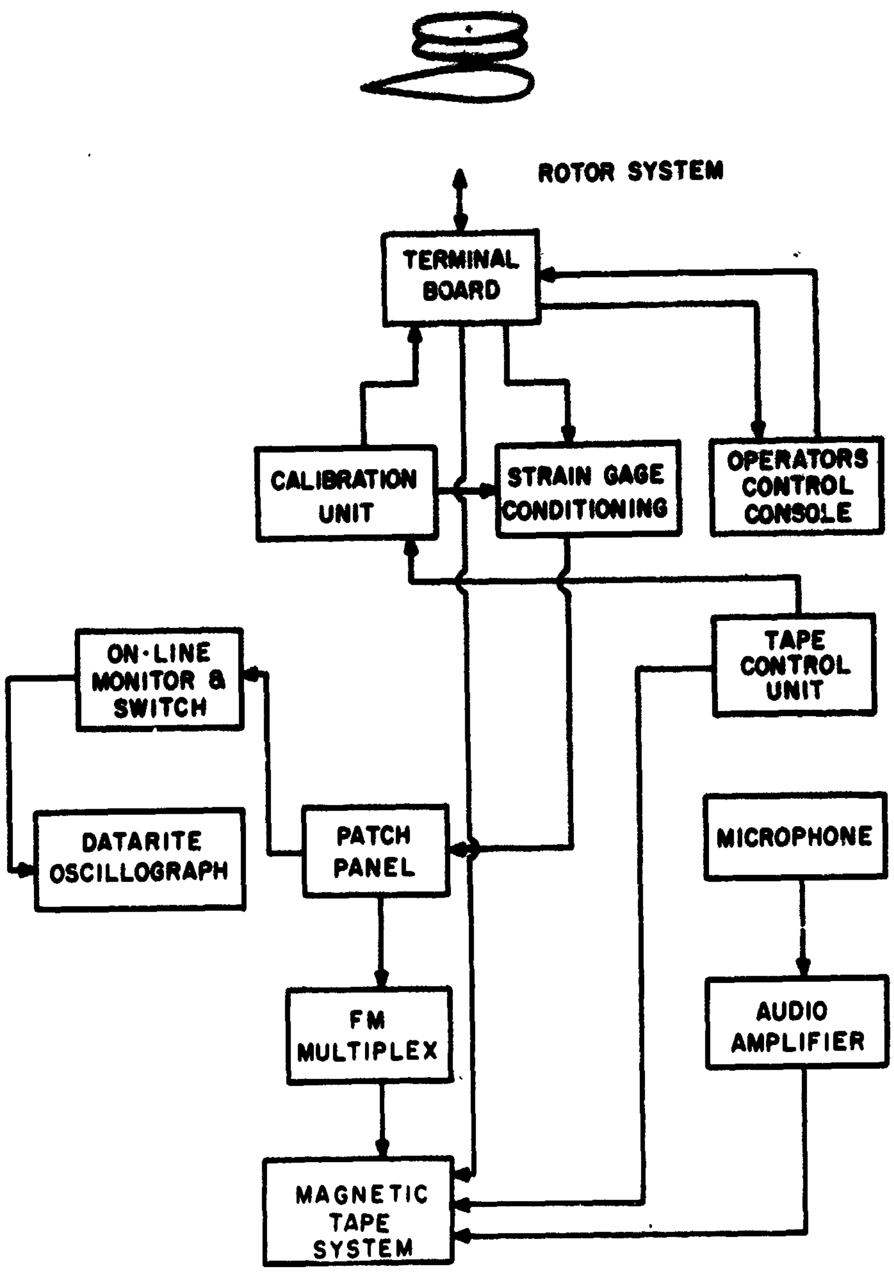

Figure 6. Flow Chart of Data Acquisition System.

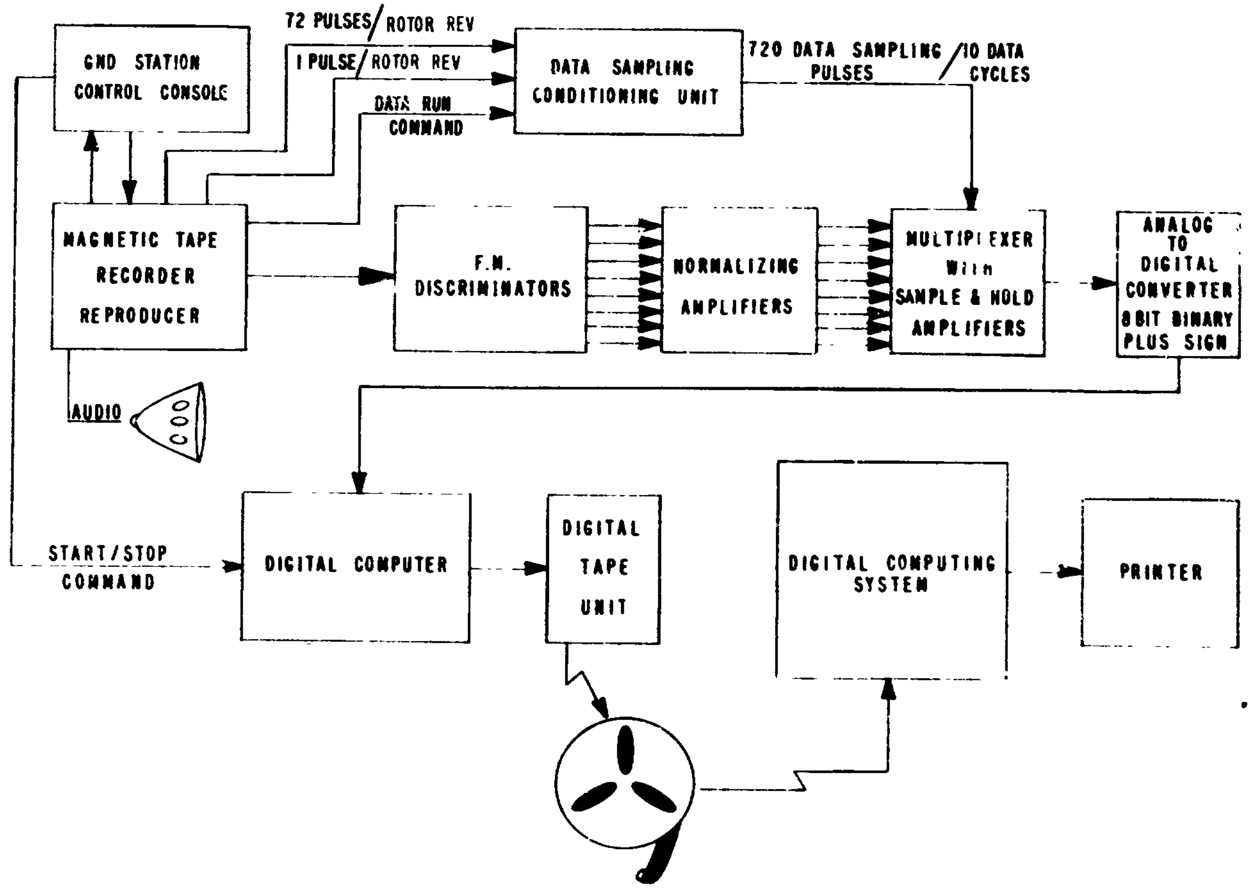

Figure 7. Flow Chart of Data Processing System.

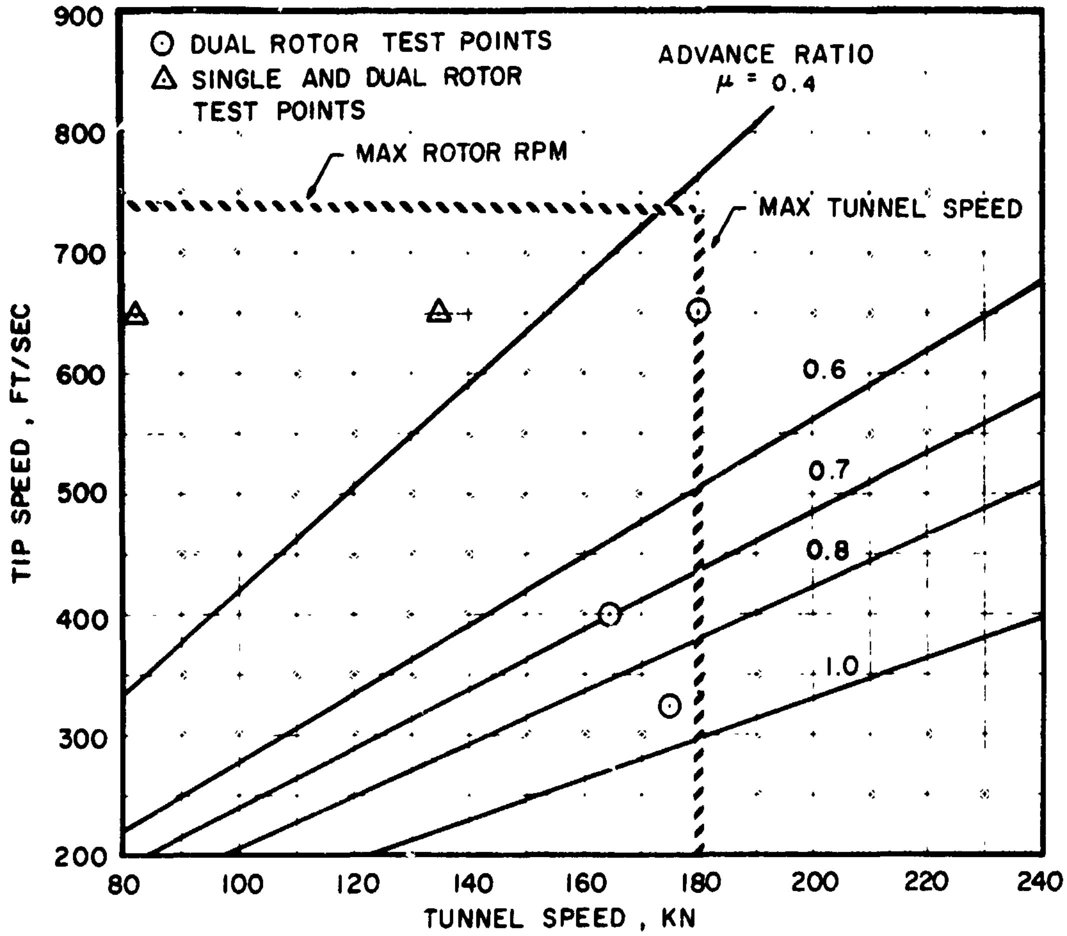

Figure 8. Diagram of the Combinations of Tip Speed and Forward Velocity Investigated.

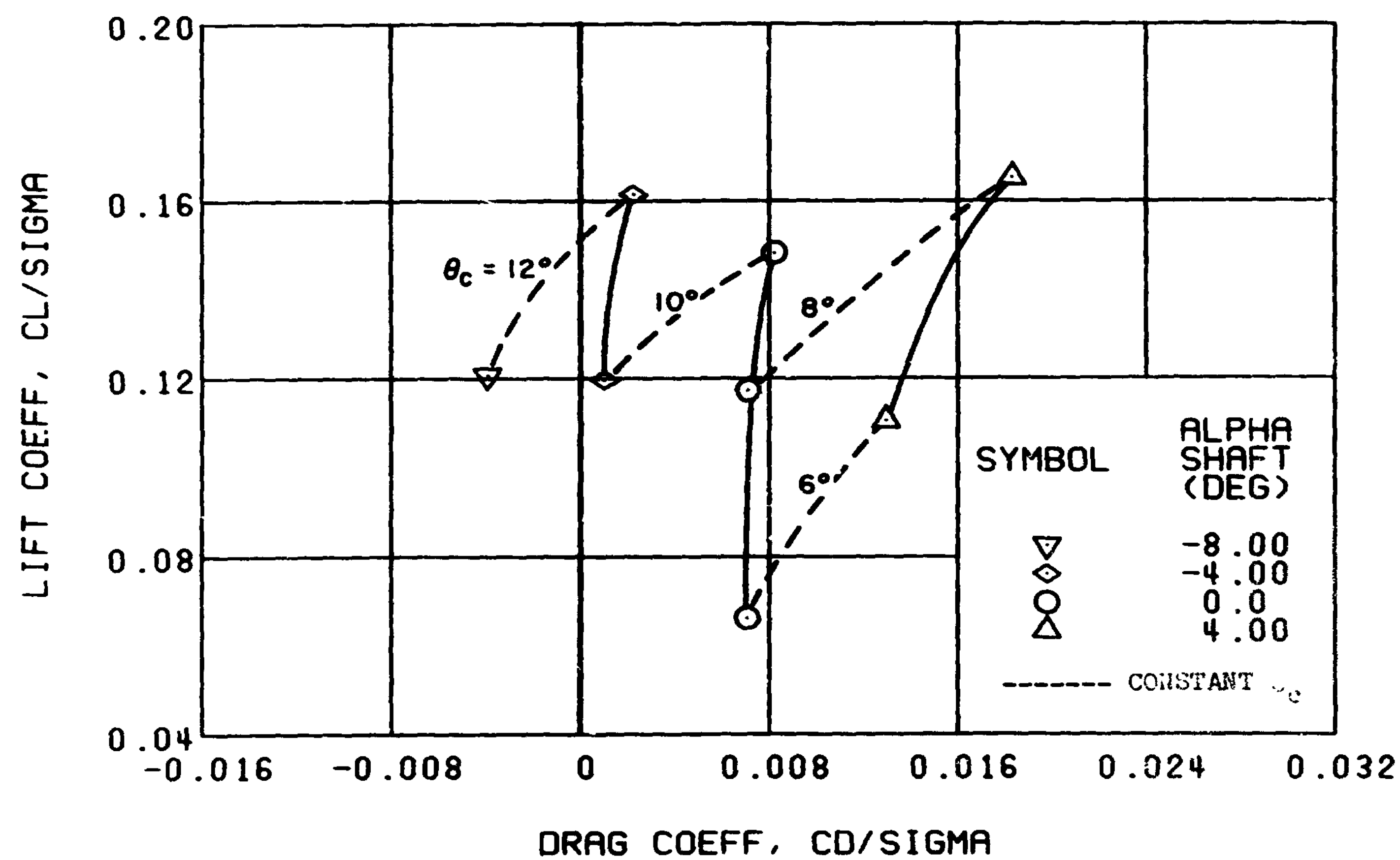

(a) DRAG COEFFICIENT

Figure 9. Performance Data at a Velocity of 179 Knots With the Lateral Displacement Control (B_{1s}) Set at 6 Degrees; μ =0.47, M_t = 0.83.

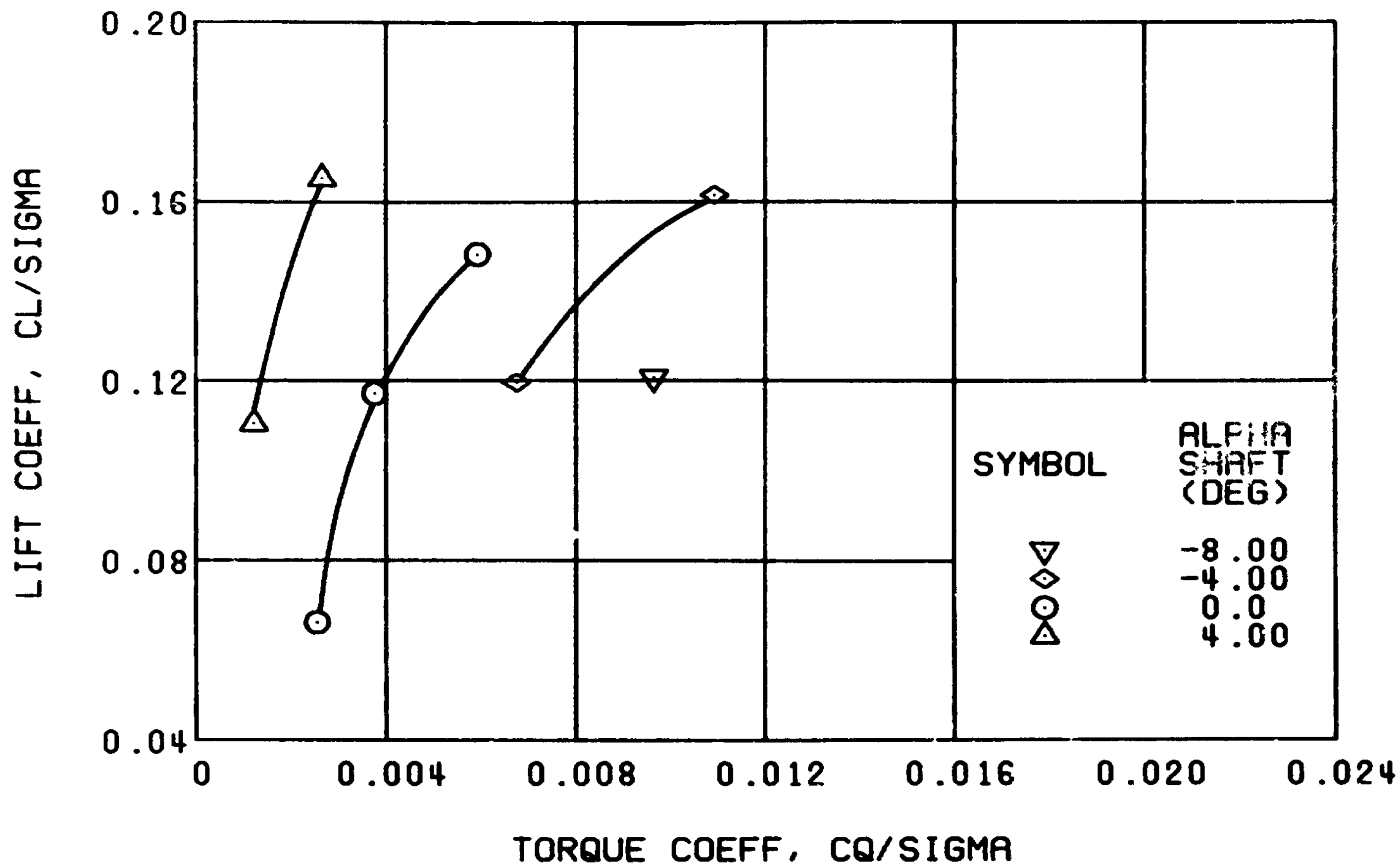

(b) TORQUE COEFFICIENT

Figure 9. Co tinued.

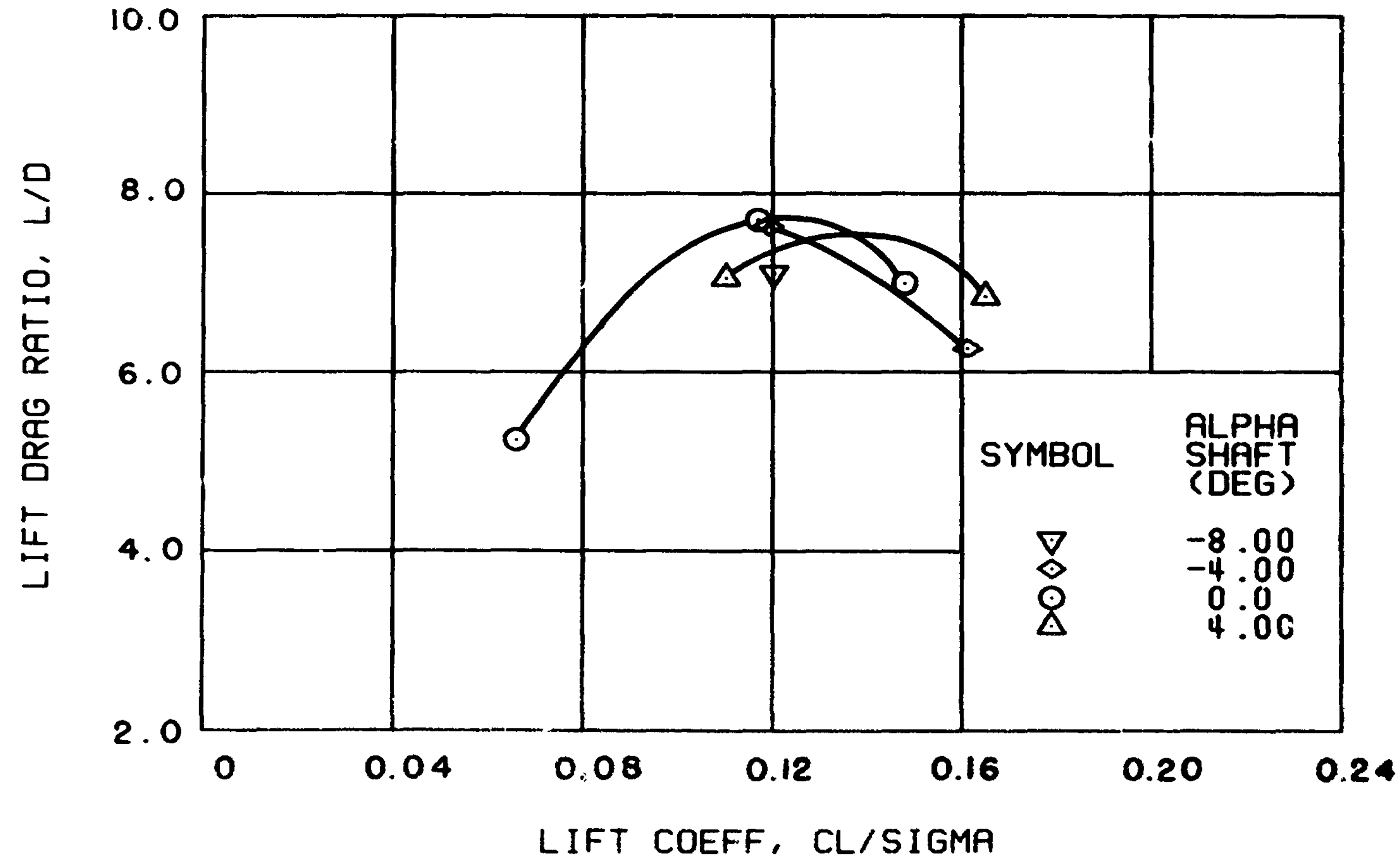

(c) LIFT-DRAG RATIO

Figure 9. Continued.

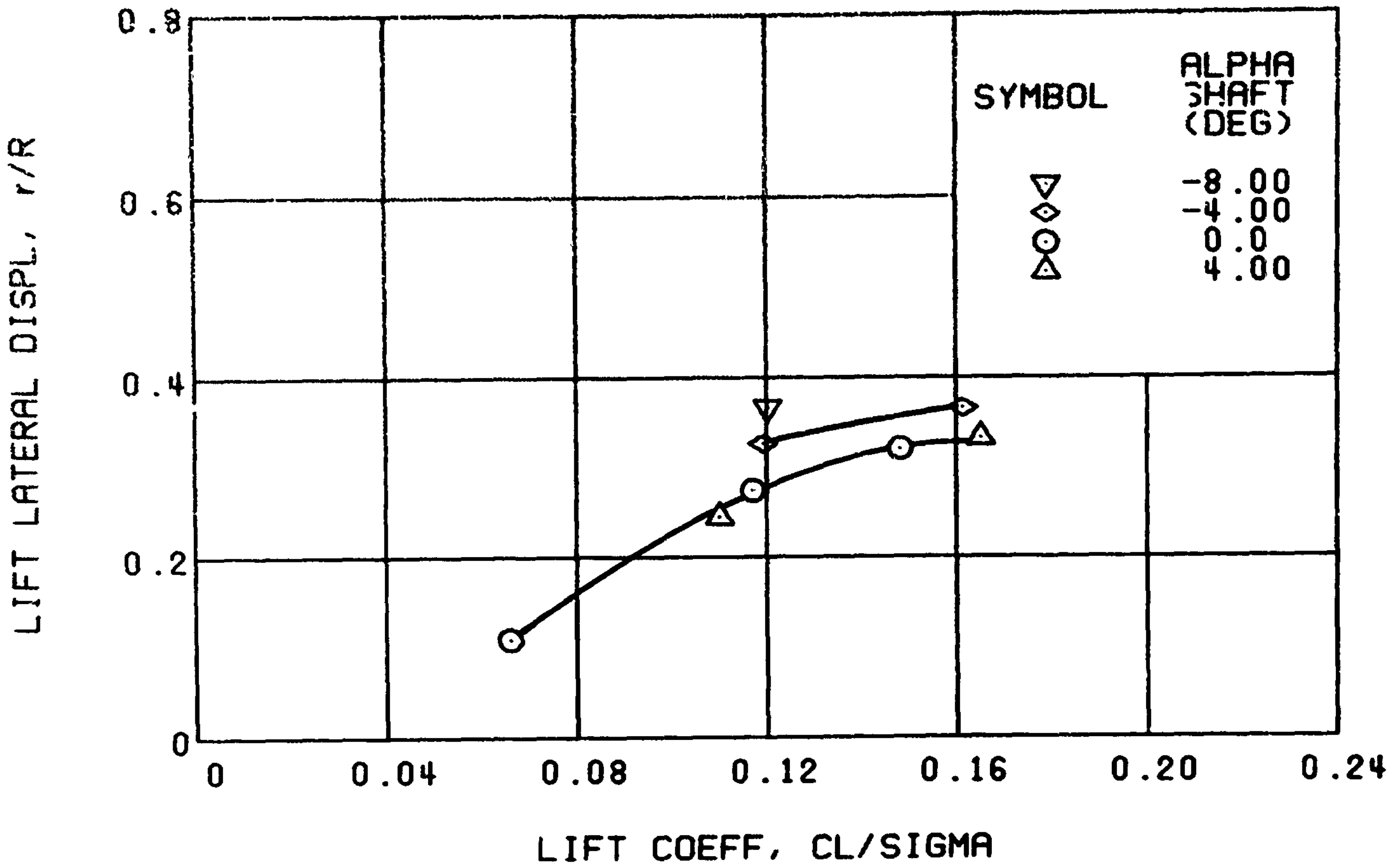

(d) LIFT LATERAL DISPLACEMENT

Figure 9. Continued.

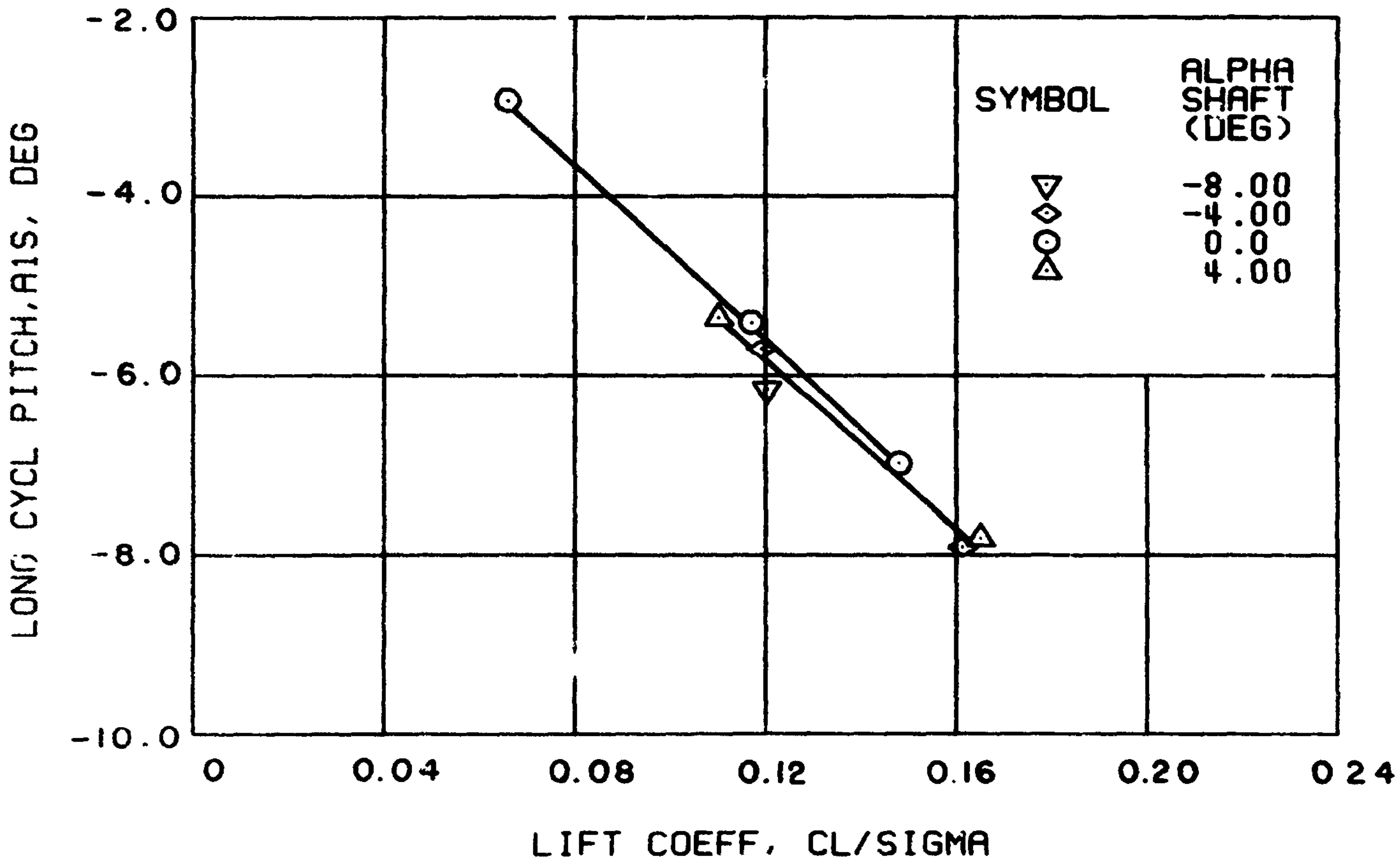

(e) LONGITUDINAL CYCLIC PITCH

Figure 9. Continued.

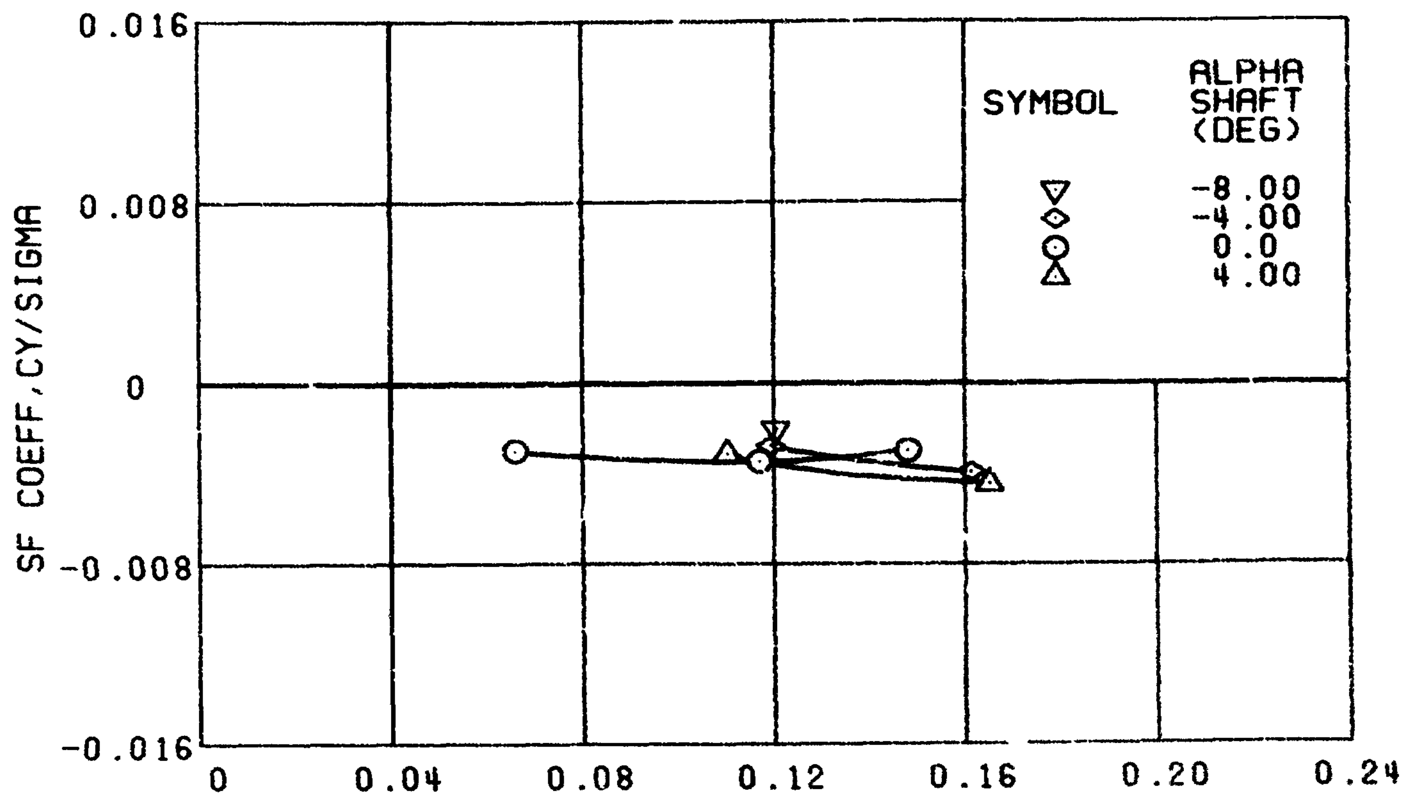

(f) SIDE FORCE COEFFICIENT

Figure 9. Continued.

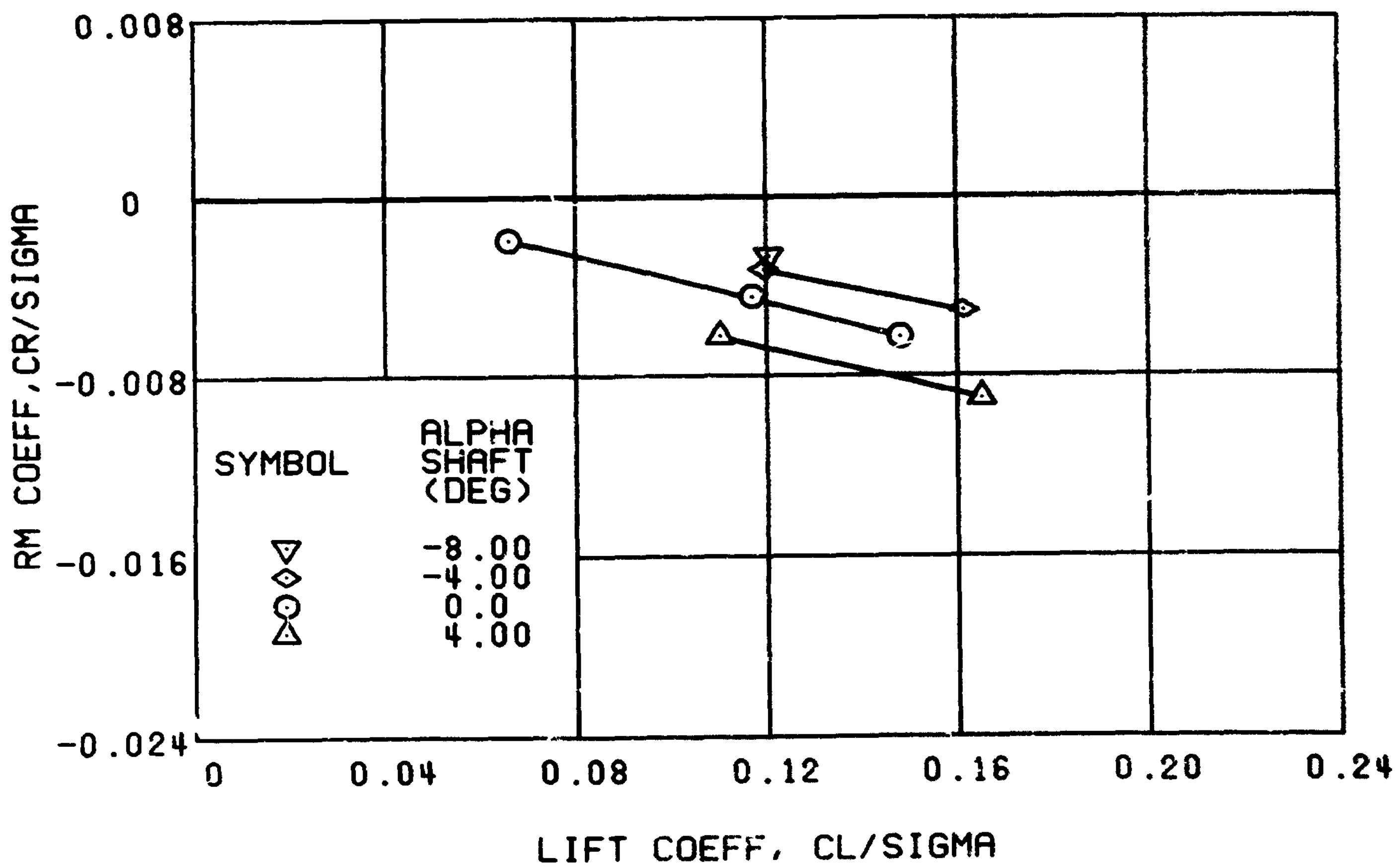

(g) ROLLING MOMENT COEFFICIENT

Figure 9. Continued.

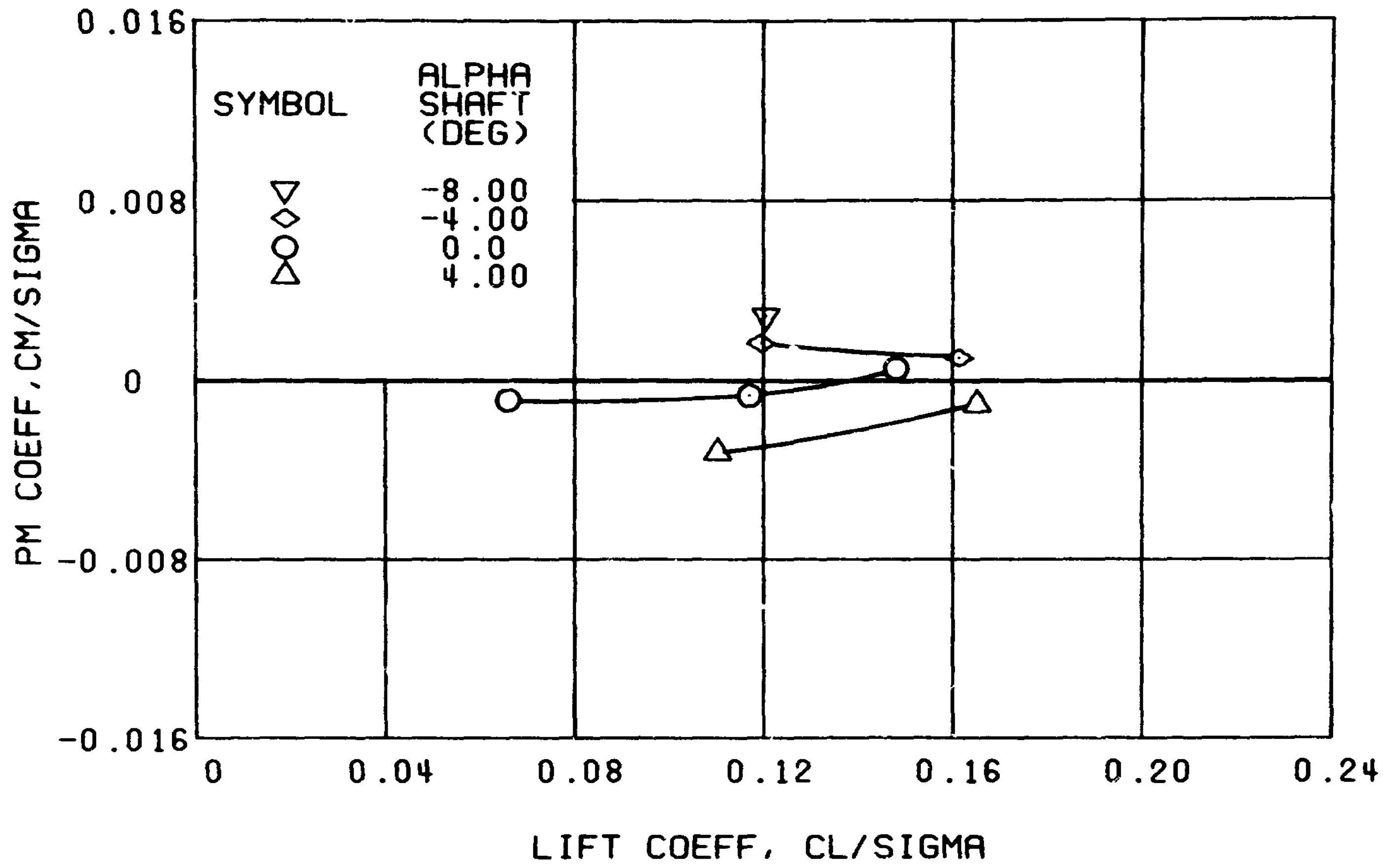

(h) PITCHING MOMENT COEFFICIENT

Figure 9. Continued.

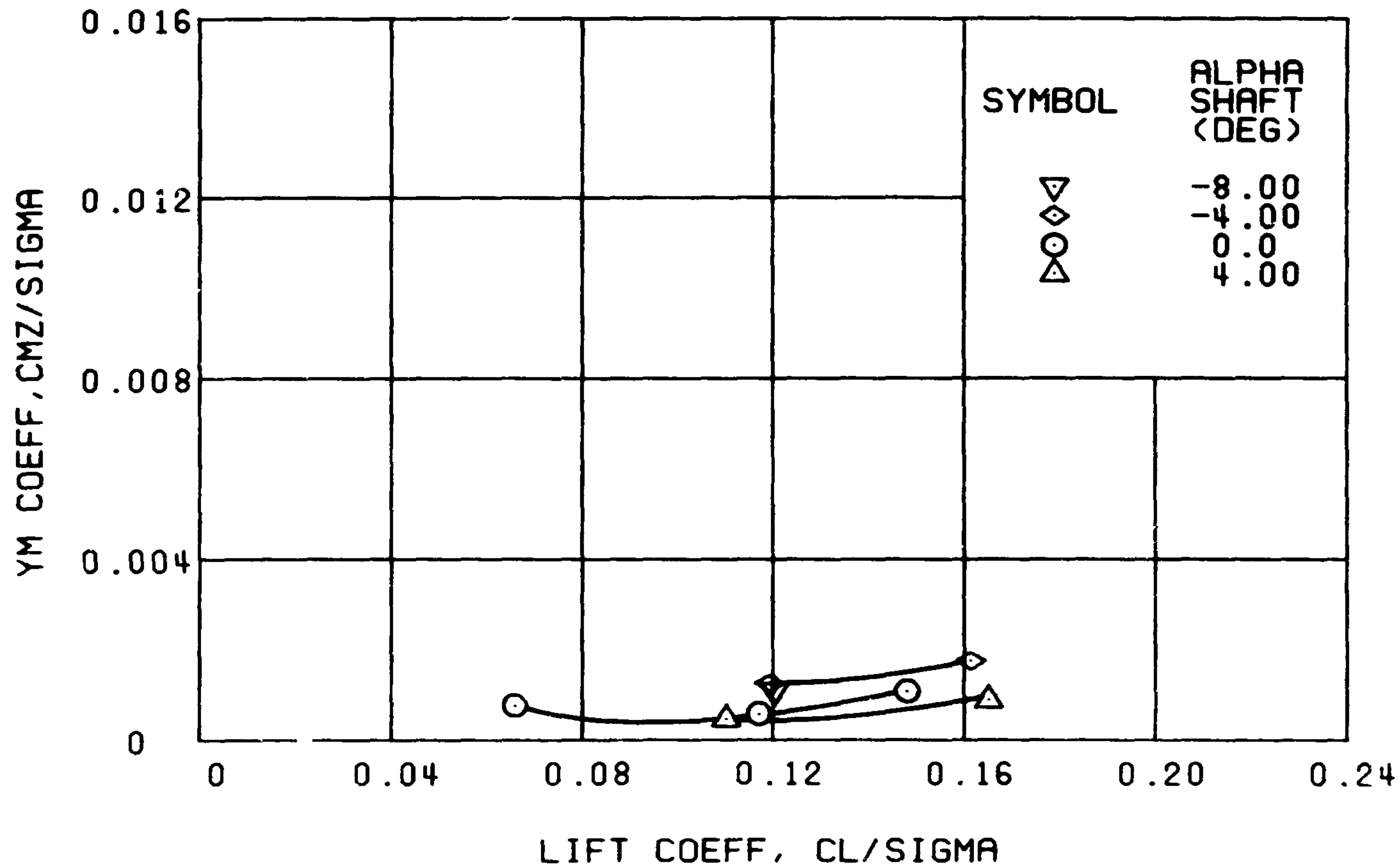

(i) YAWING MOMENT COEFFICIENT

Figure 9. Concluded.

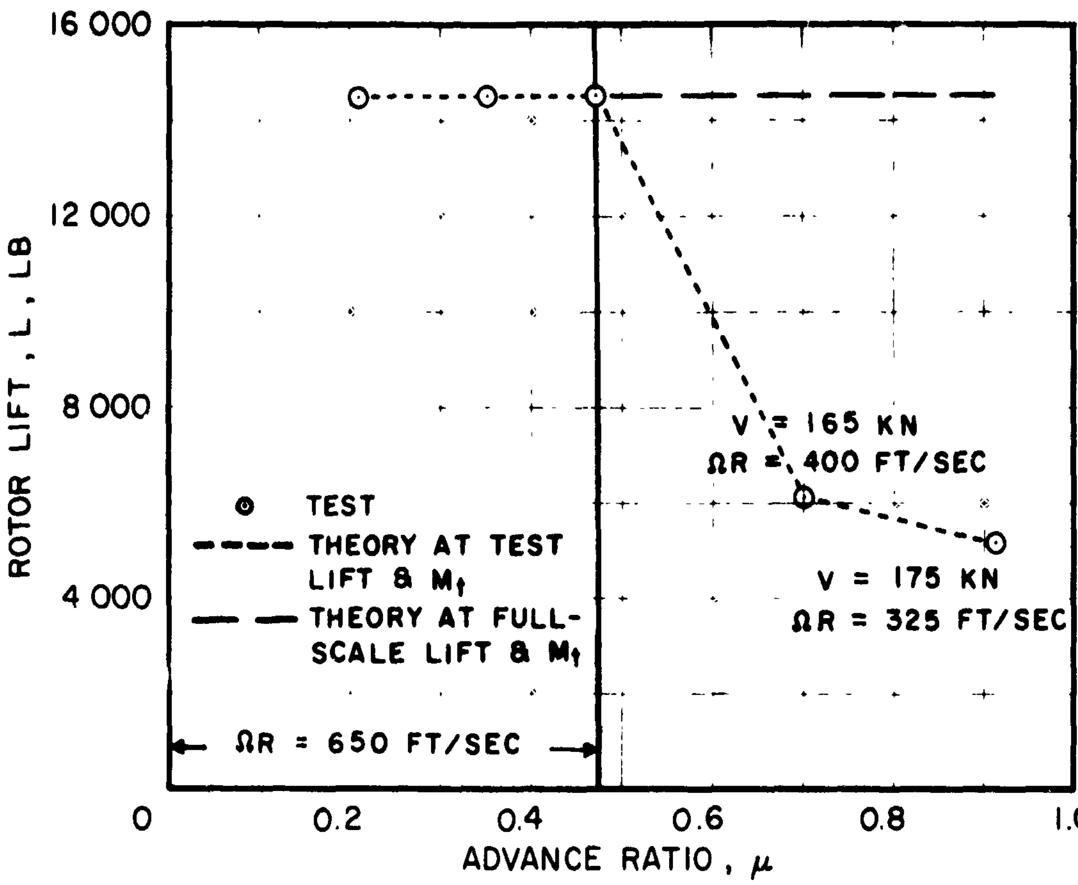

(a) LIFT SCHEDULE

Figure 10. The Variation With Advance Ratio of the Independent Variables Chosen for Correlating Measured and Predicted Rotor Performance and Stresses.

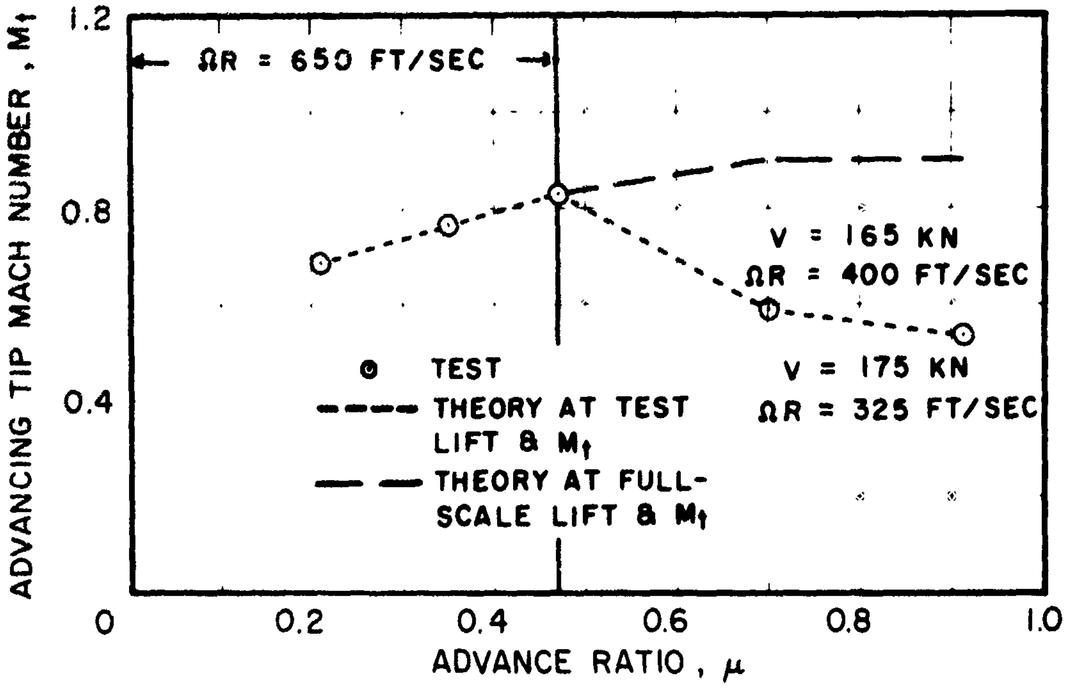

(b) ADVANCING TIP MACH NUMBER SCHEDULE

Figure 10. Continued.

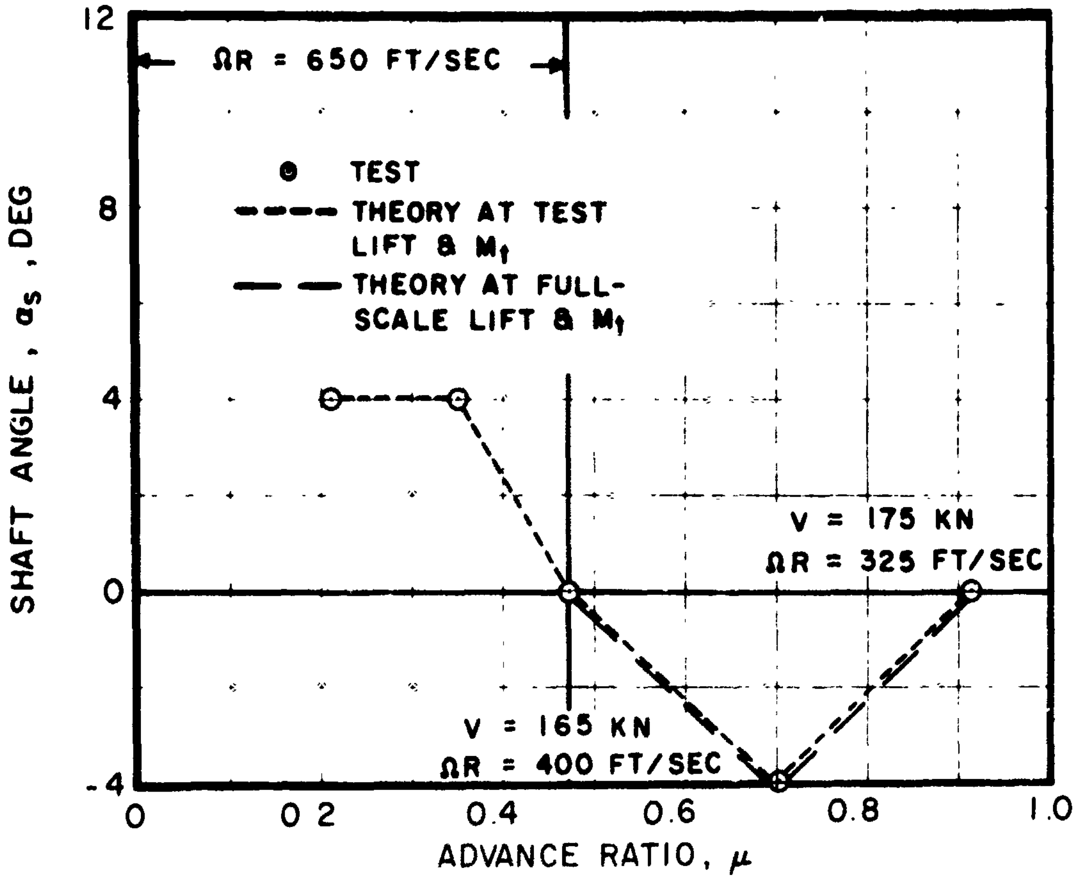

(c) SHAFT ANGLE SCHEDULE

Figure 10. Continued.

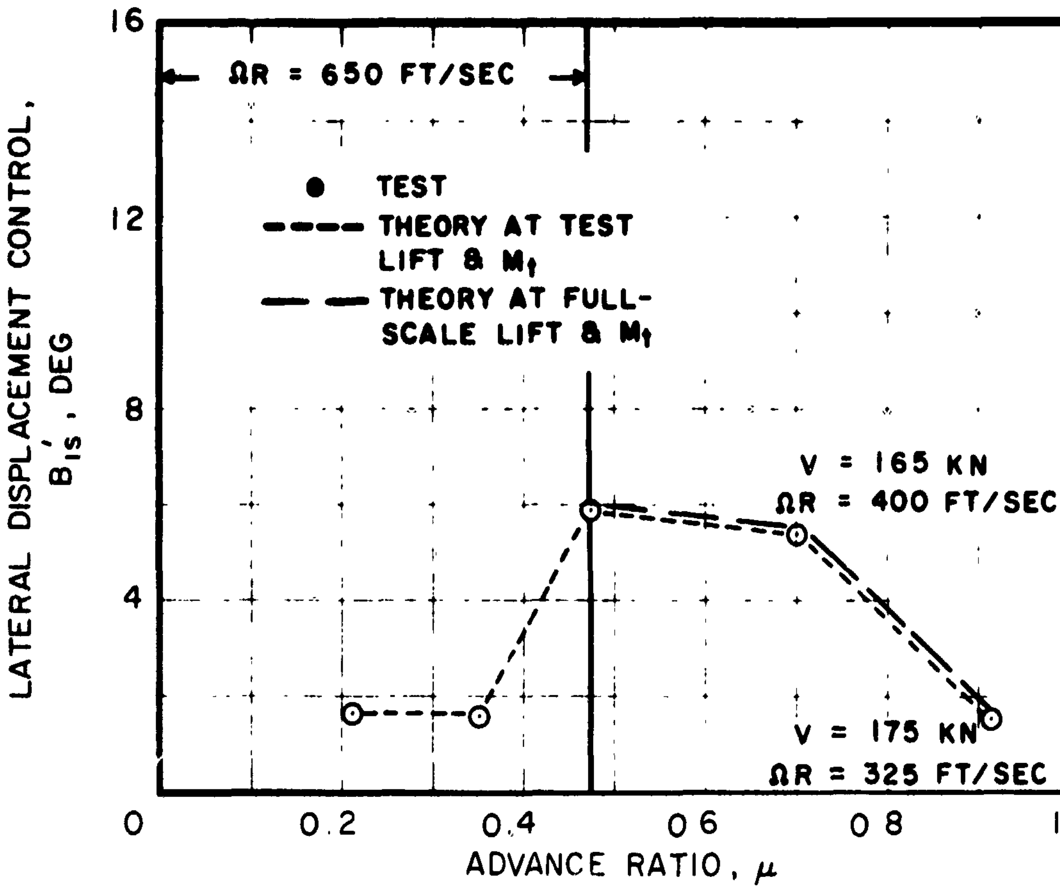

(d) LATERAL DISPLACEMENT CONTROL SCHEDULE

Figure 10. Concluded.

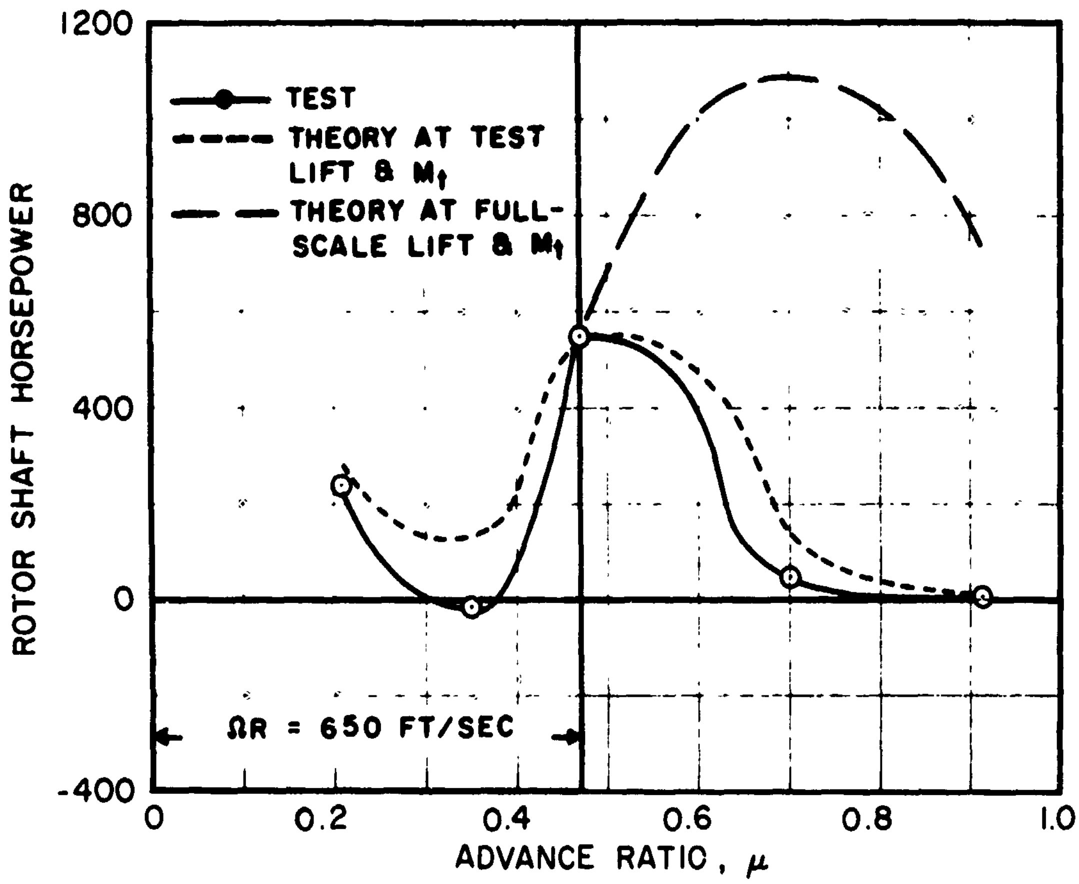

(a) ROTOR SHAFT HORSEPOWER

Figure 11. The Effect of Advance Ratio on Measured and Predicted Performance.

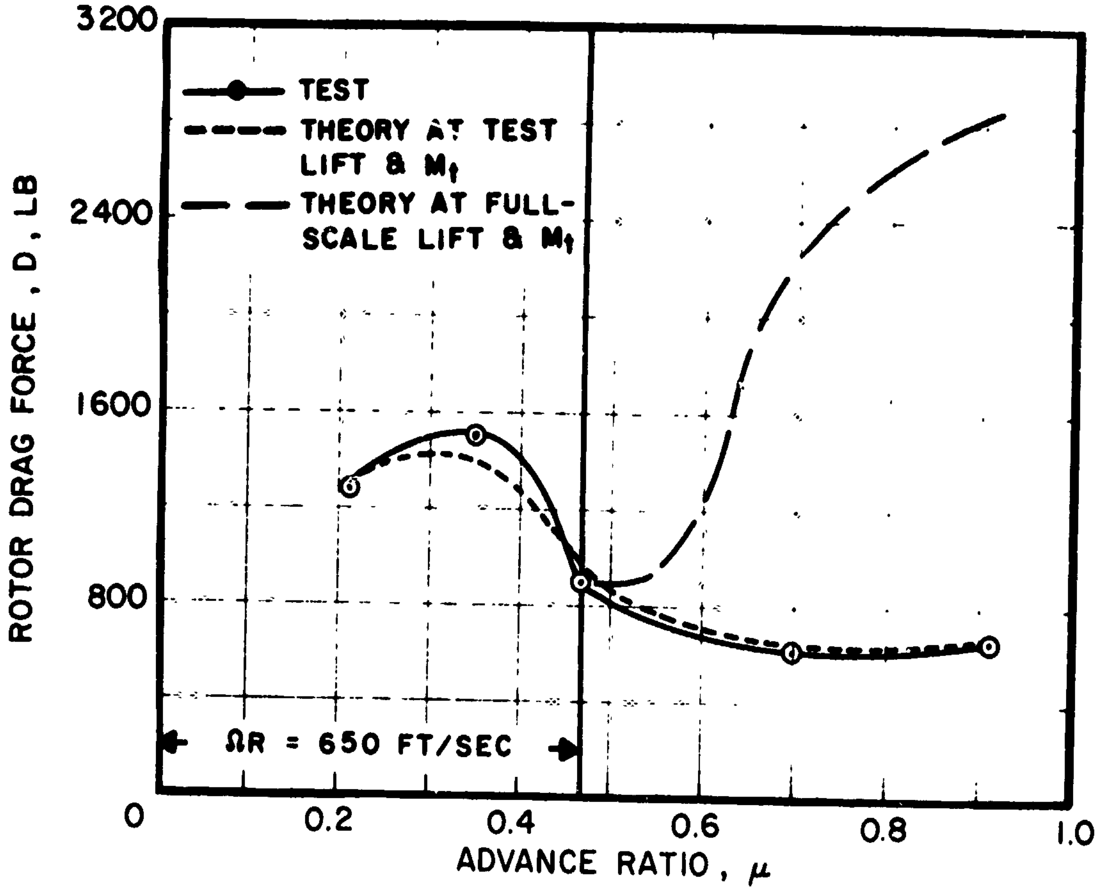

(b) ROTOR DRAG FORCE

Figure 11. Continued.

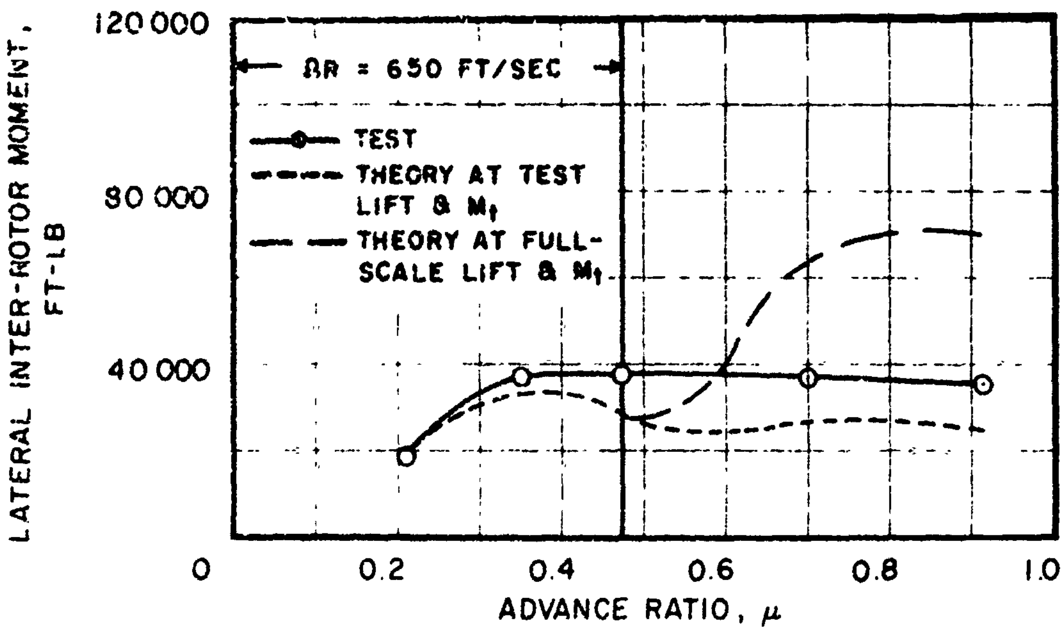

(c) LATERAL INTER-ROTOR MOMENT

Figure 11. Continued.

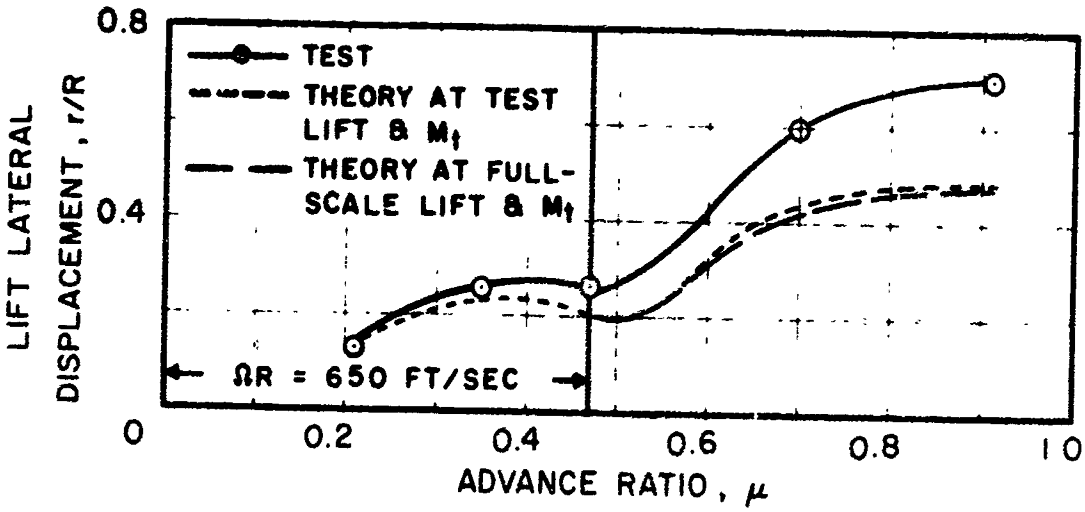

(d) LIFT LATERAL DISPLACEMENT

Figure 11. Continued.

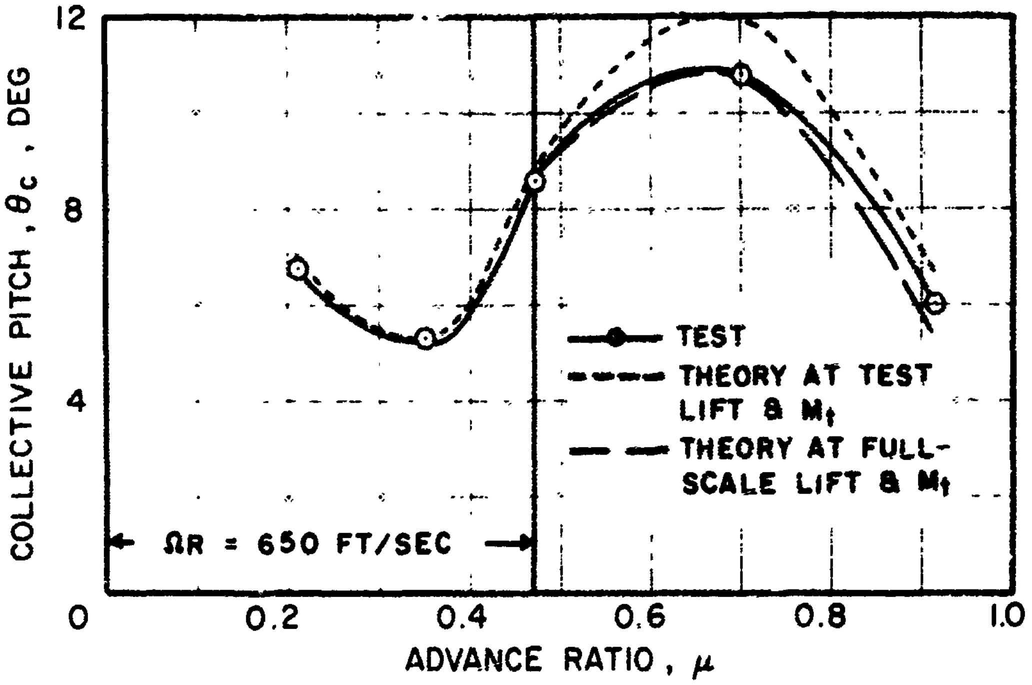

(e) COLLECTIVE PITCH REQUIRED

Figure 11. Concluded.

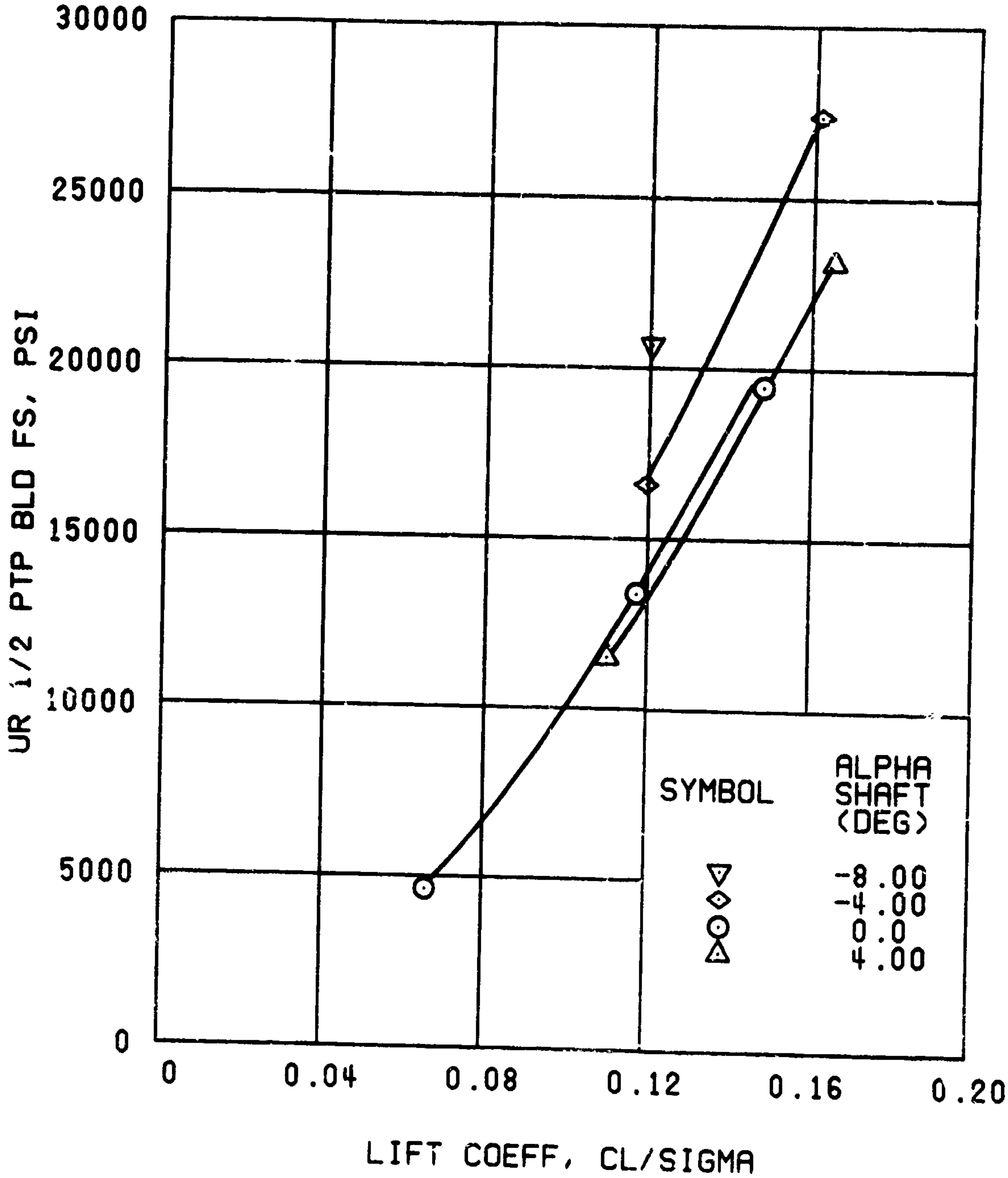

(a) UPPER ROTOR FLATWISE STRESS, r = 84 IN.

Figure 12. Stress, Load, and Vibration Data at a Velocity of 179 Knots, With the Lateral Displacement Control (B'_{1s}) Set at 6 Degrees; μ = 0.47, M_t = 0.83.

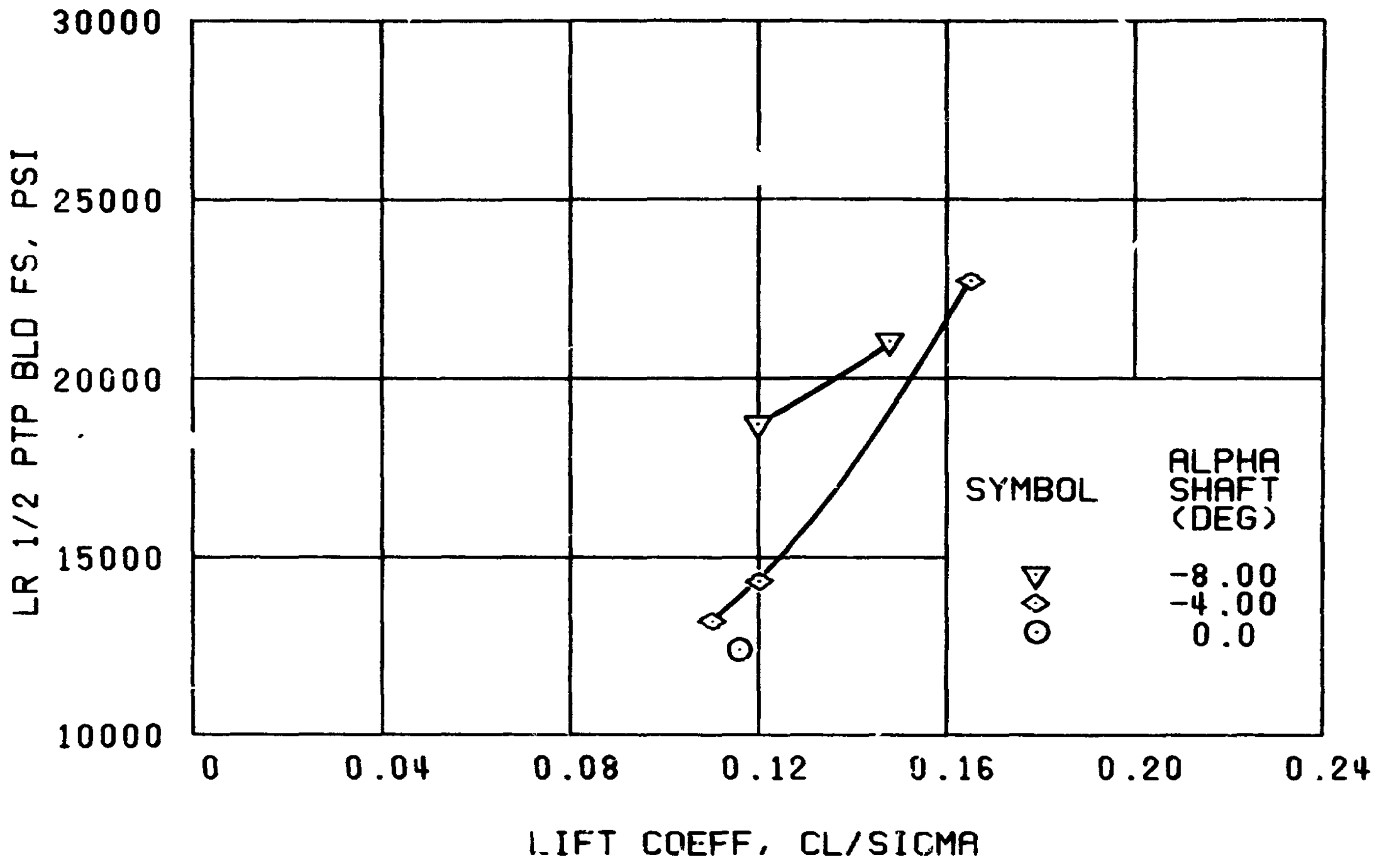

(b) LOWER ROTOR FLATWISE STRESS , r = 84 IN.

Figure 12. Continued.

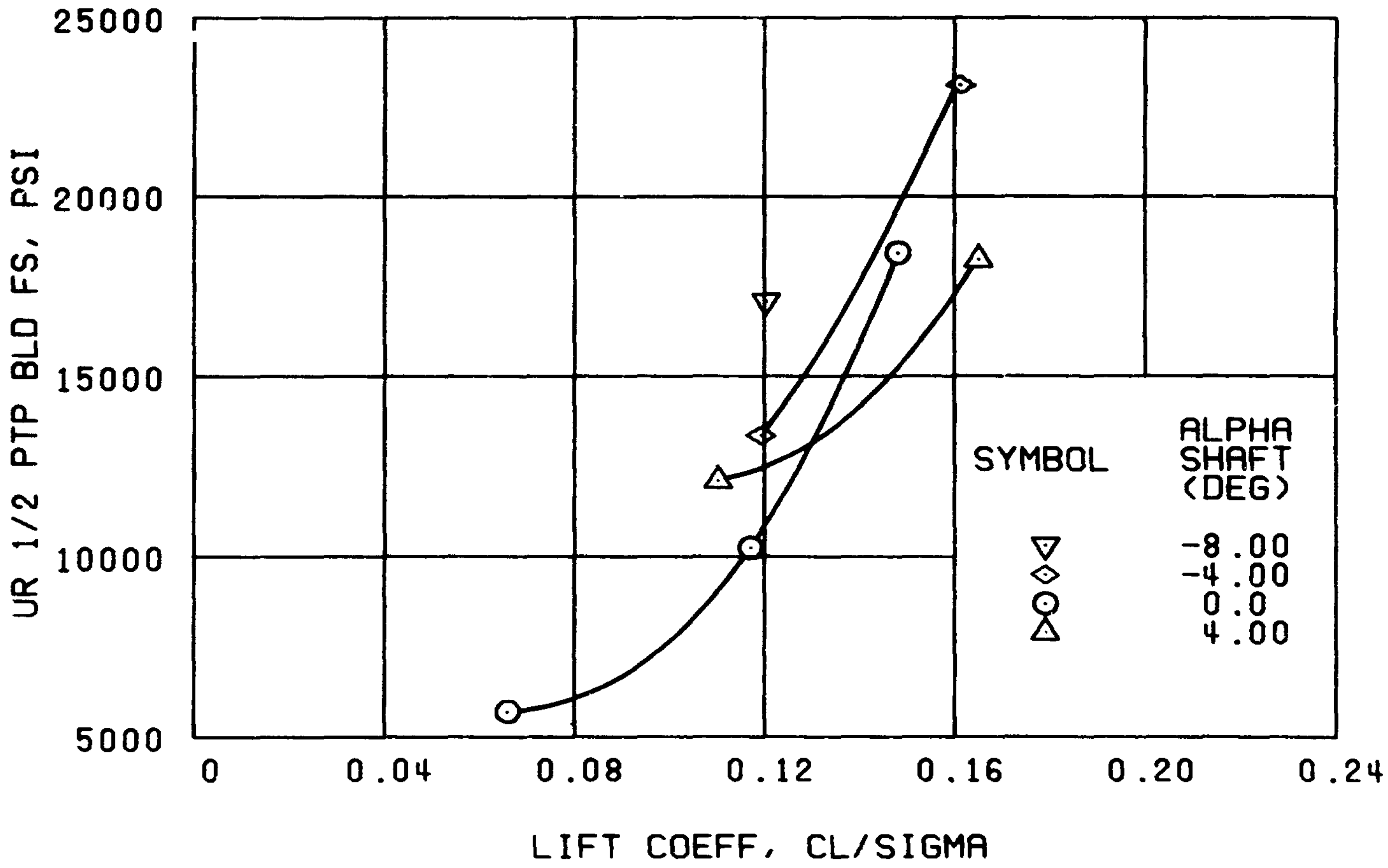

(c) UPPER ROTOR FLATWISE STRESS , r = 108 IN.

Figure 12. Continued.

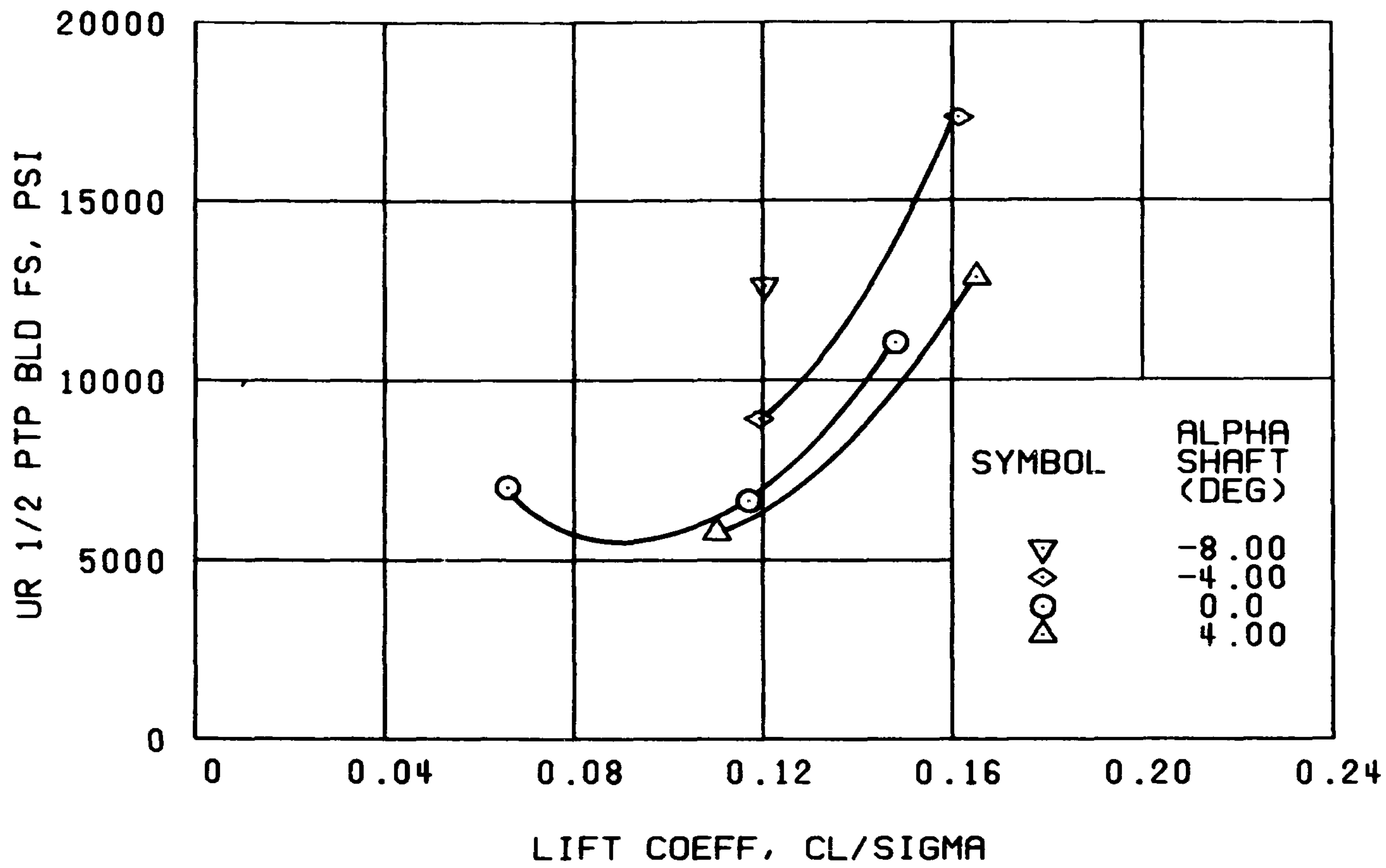

(d) UPPER ROTOR FLATWISE STRESS , r = 132 IN.

Figure 12. Continued.

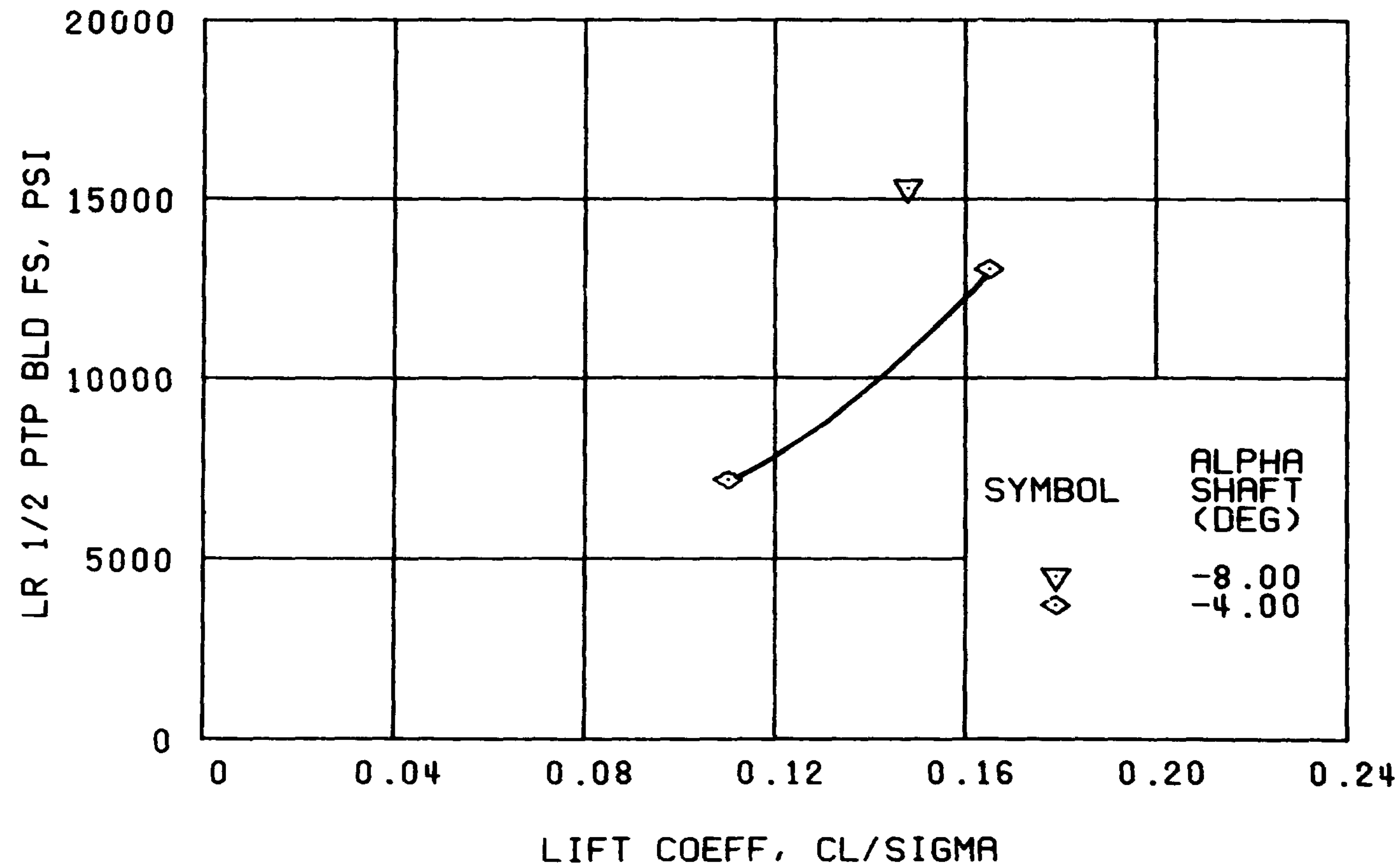

(e) LOWER ROTOR FLATWISE STRESS , r = 132 IN.

Figure 12. Continued.

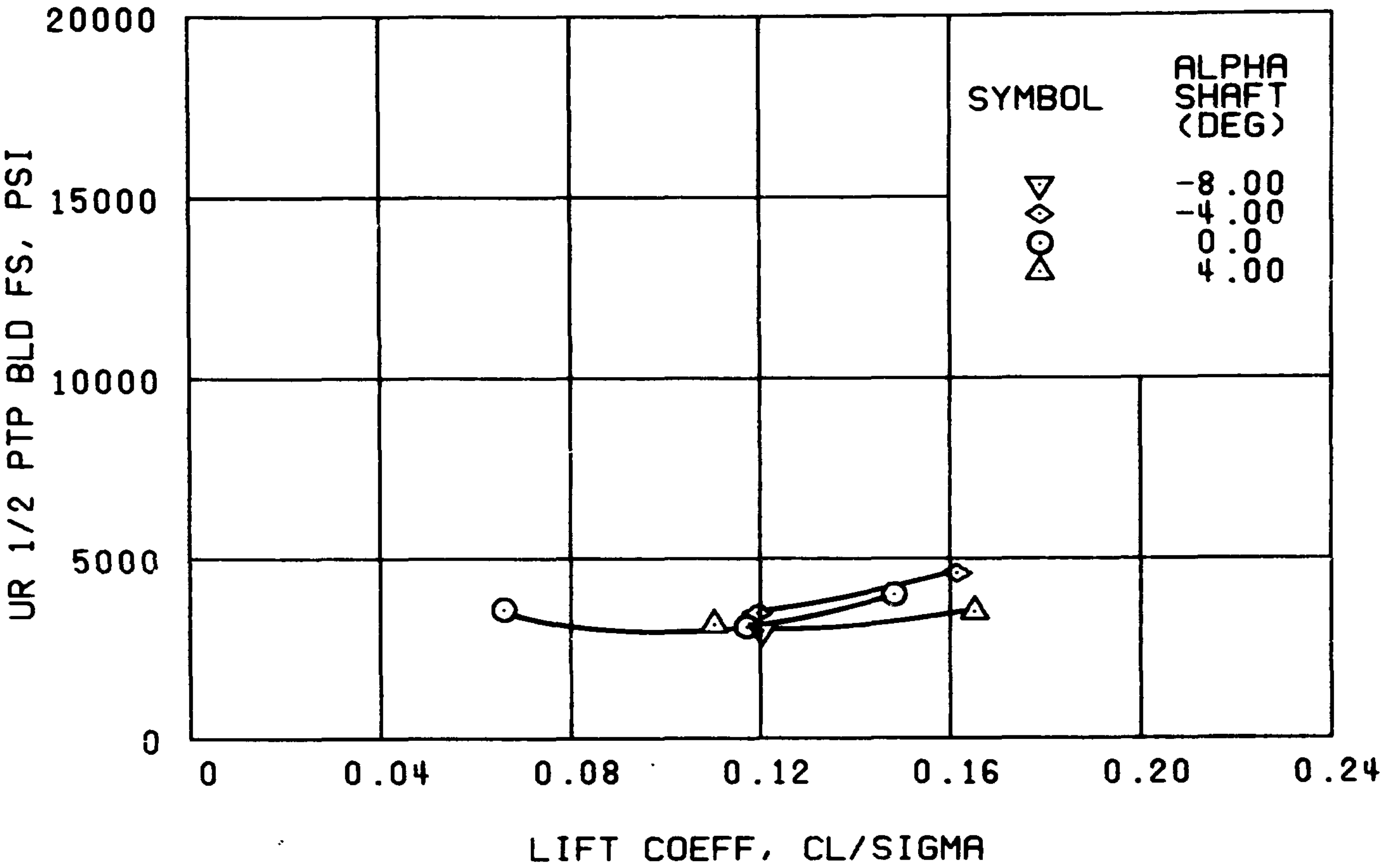

(f) UPPER ROTOR FLATWISE STRESS , r = 204 IN.

Figure 12. Continued.

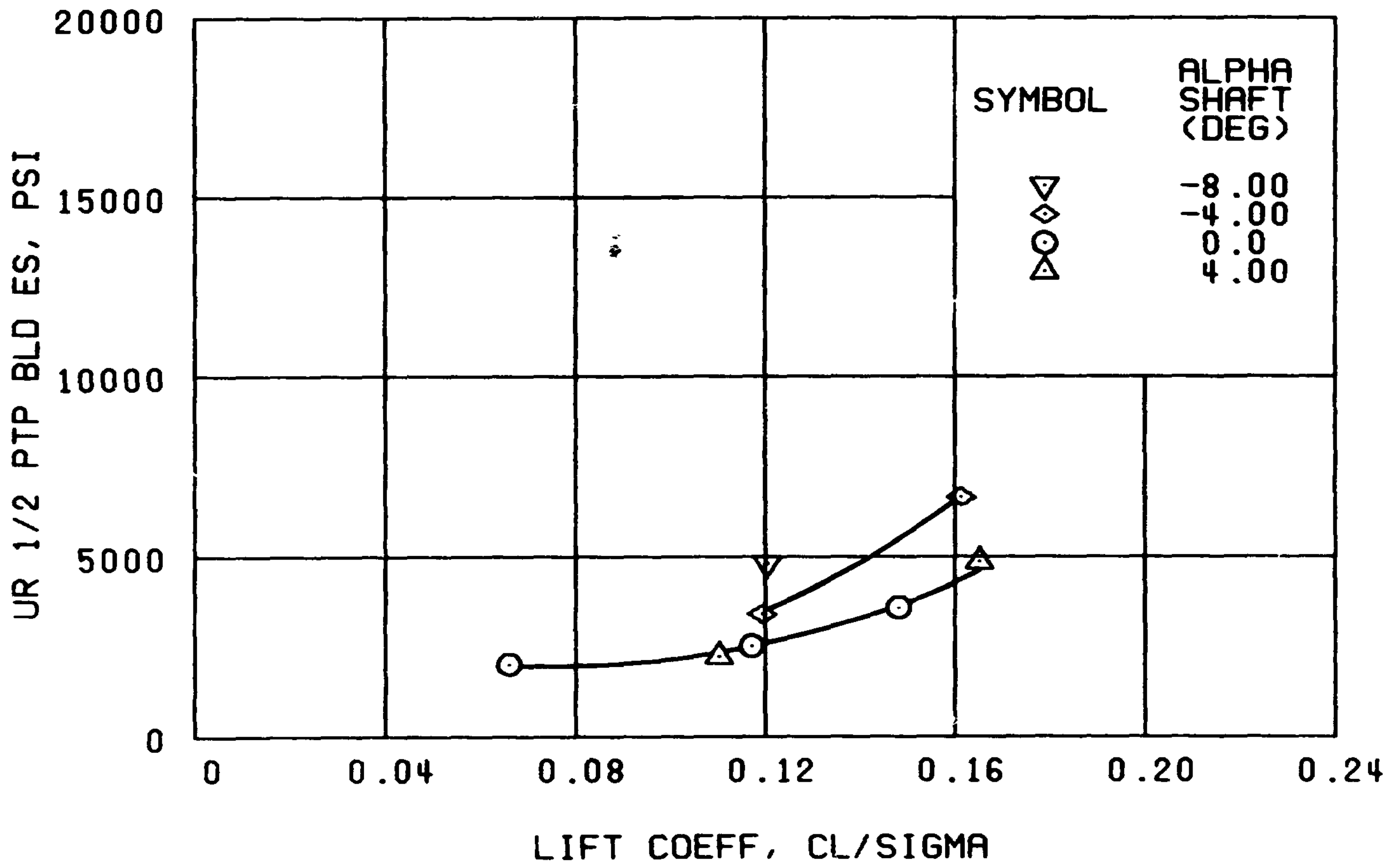

(g) UPPER ROTOR EDGEWISE STRESS , r = 84 IN.

Figure 12. Continued.

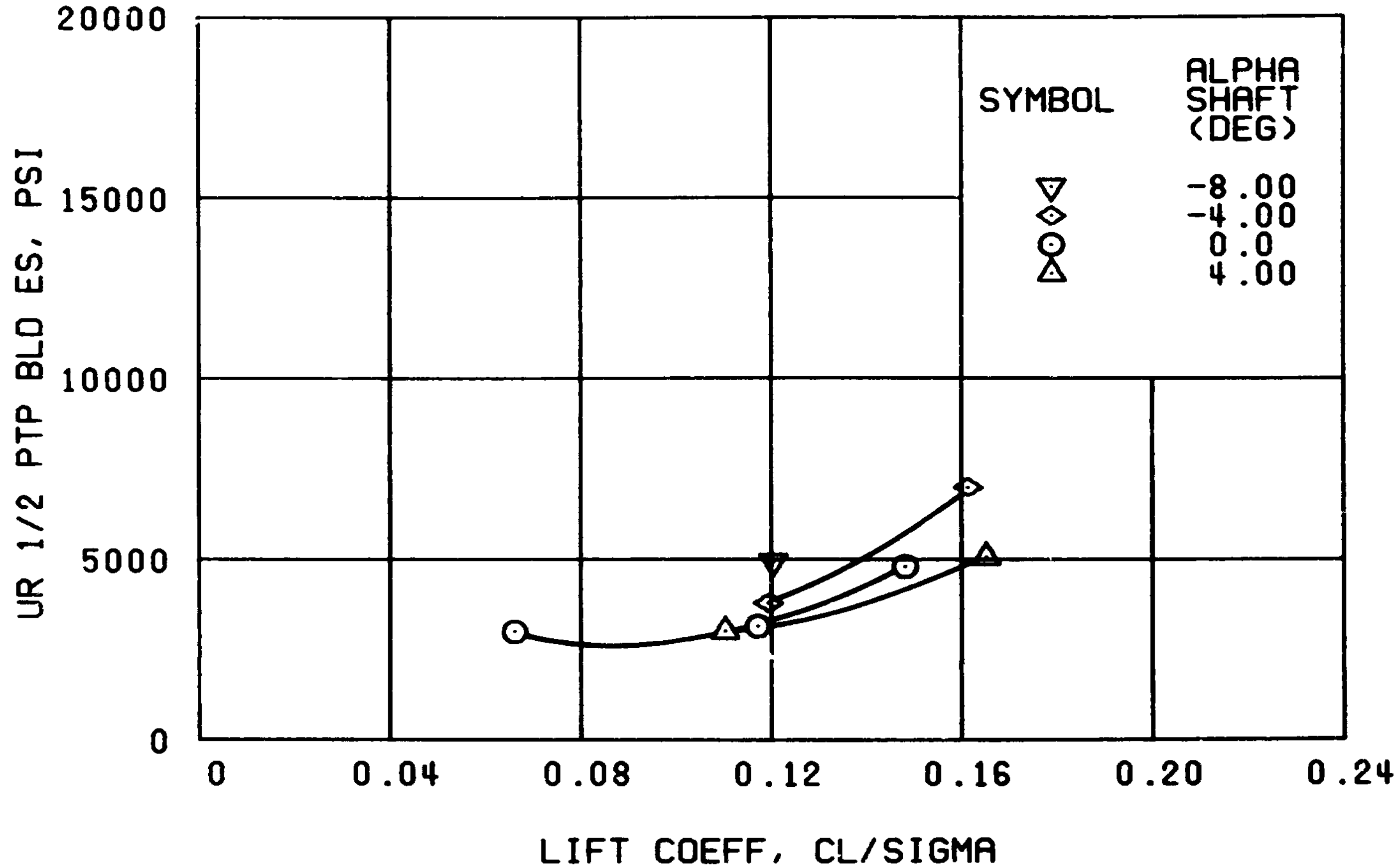

(h) UPPER ROTOR EDGEWISE STRESS , r = 132 IN.

Figure 12. Continued.

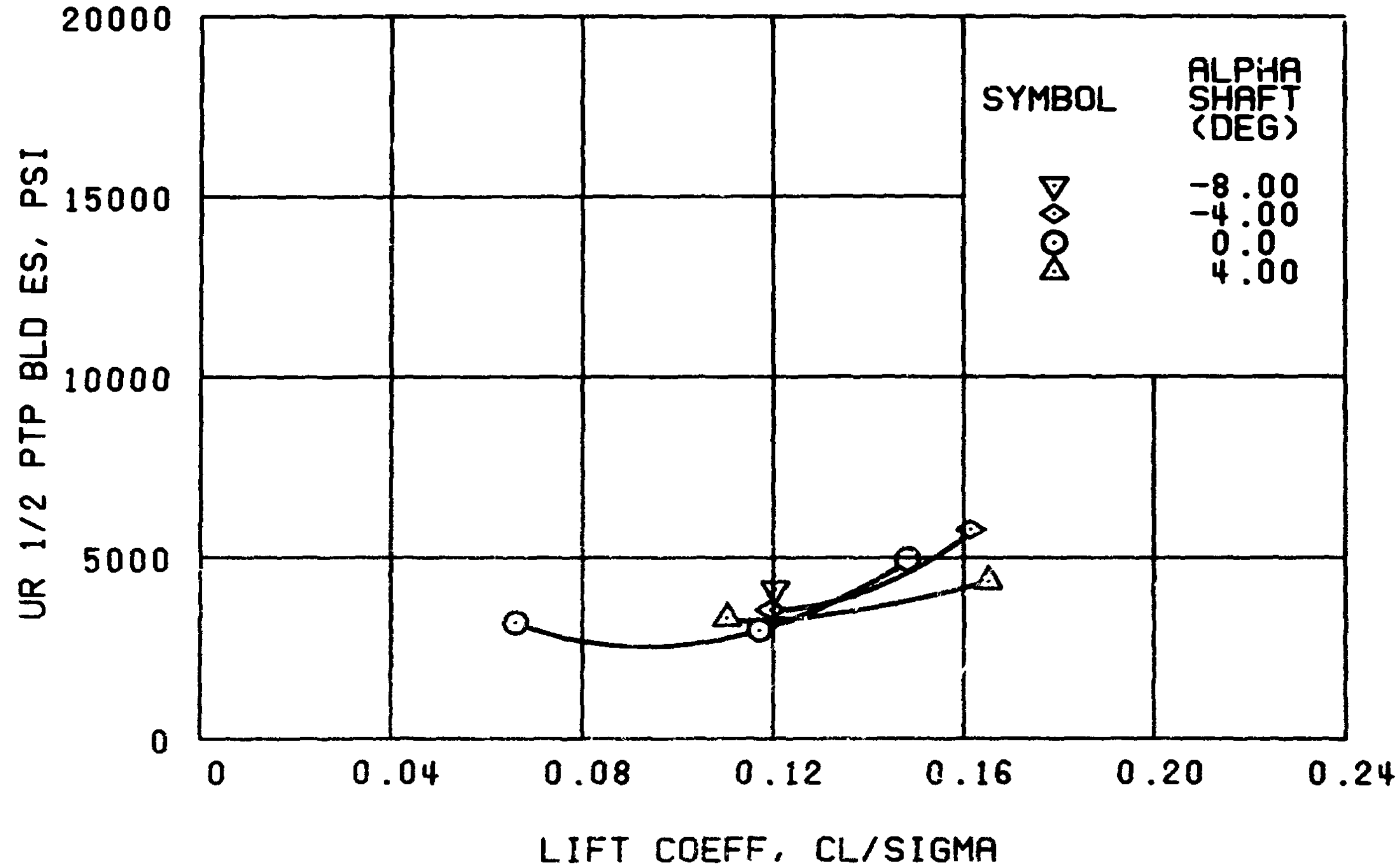

(i) UPPER ROTOR EDGEWISE STRESS , r = 168 IN.

Figure 12. Continued.

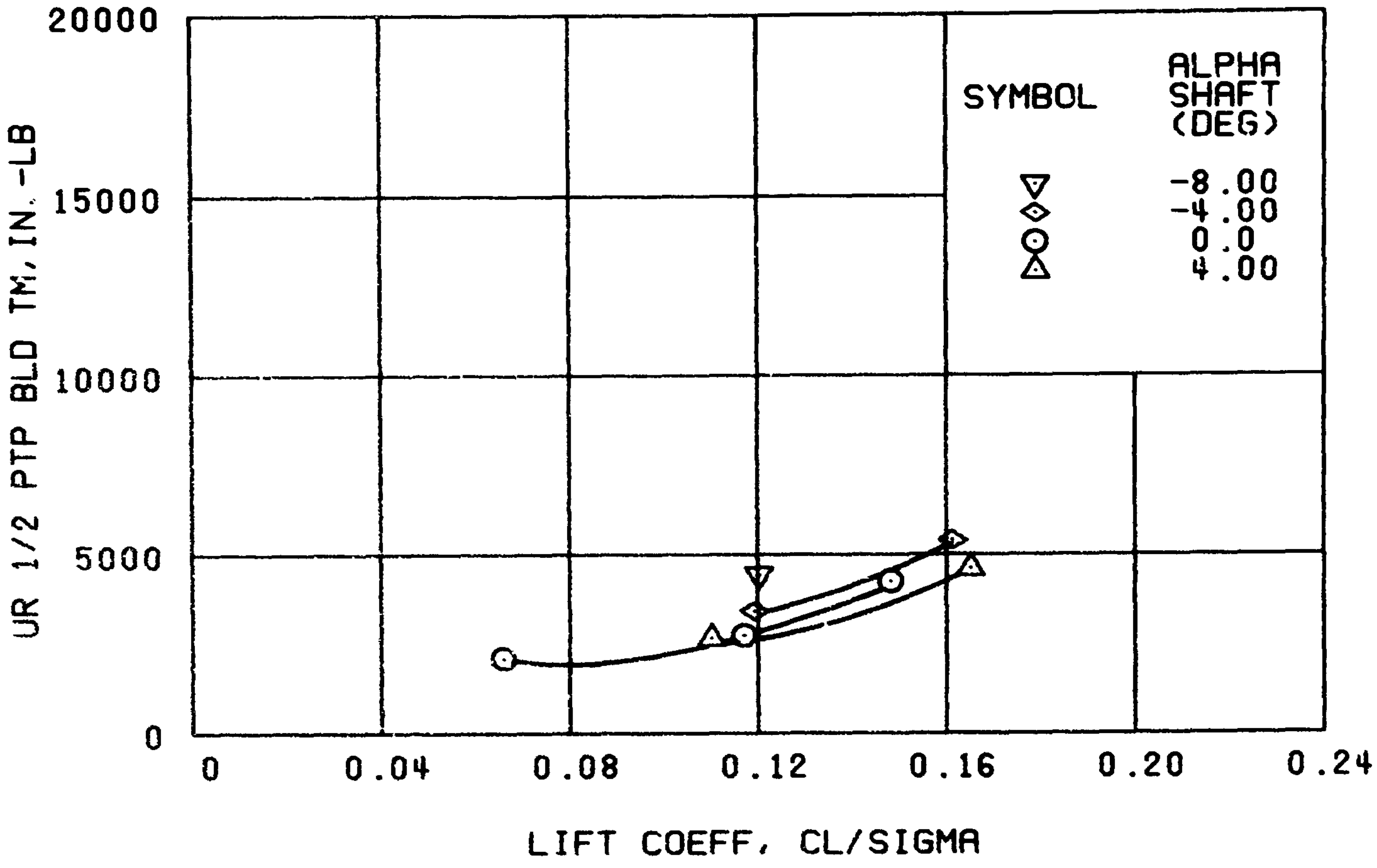

(j) UPPER ROTOR TORSIONAL MOMENT, r = 130 IN.

Figure 12. Continued.

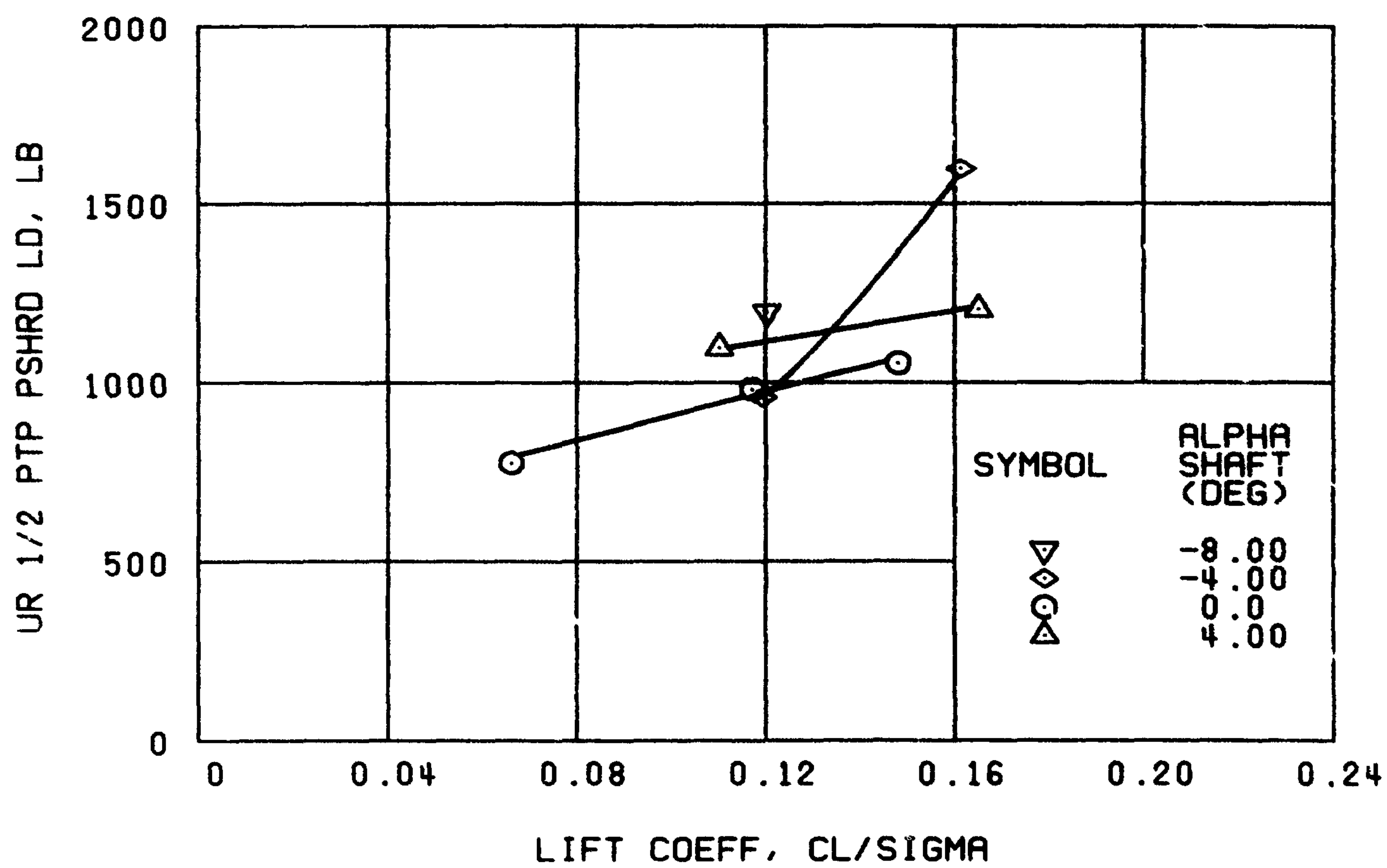

(k) UPPER ROTOR PUSHROD LOAD

Figure 12. Continued.

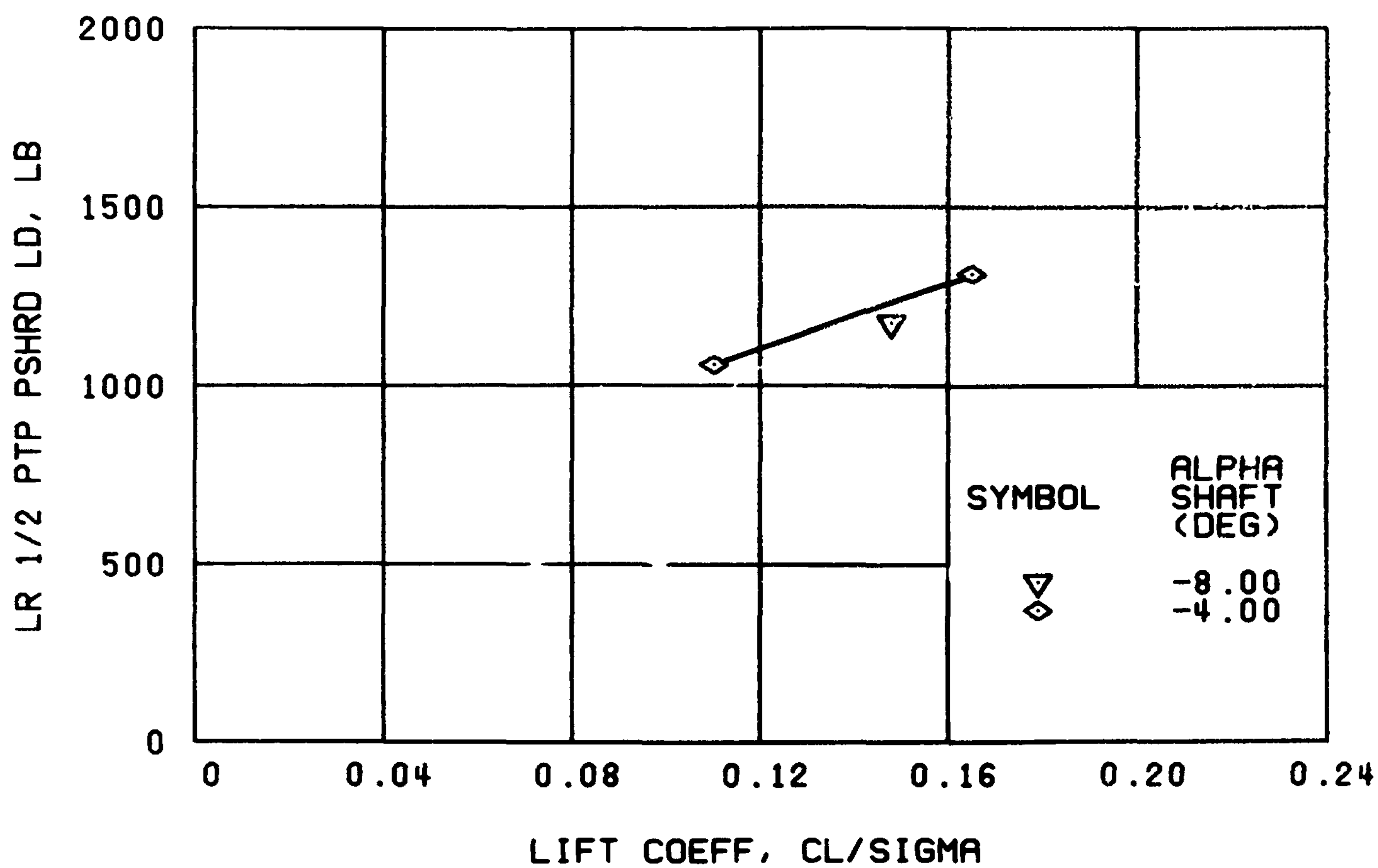

(l) LOWER ROTOR PUSHROD LOAD

Figure 12. Continued.

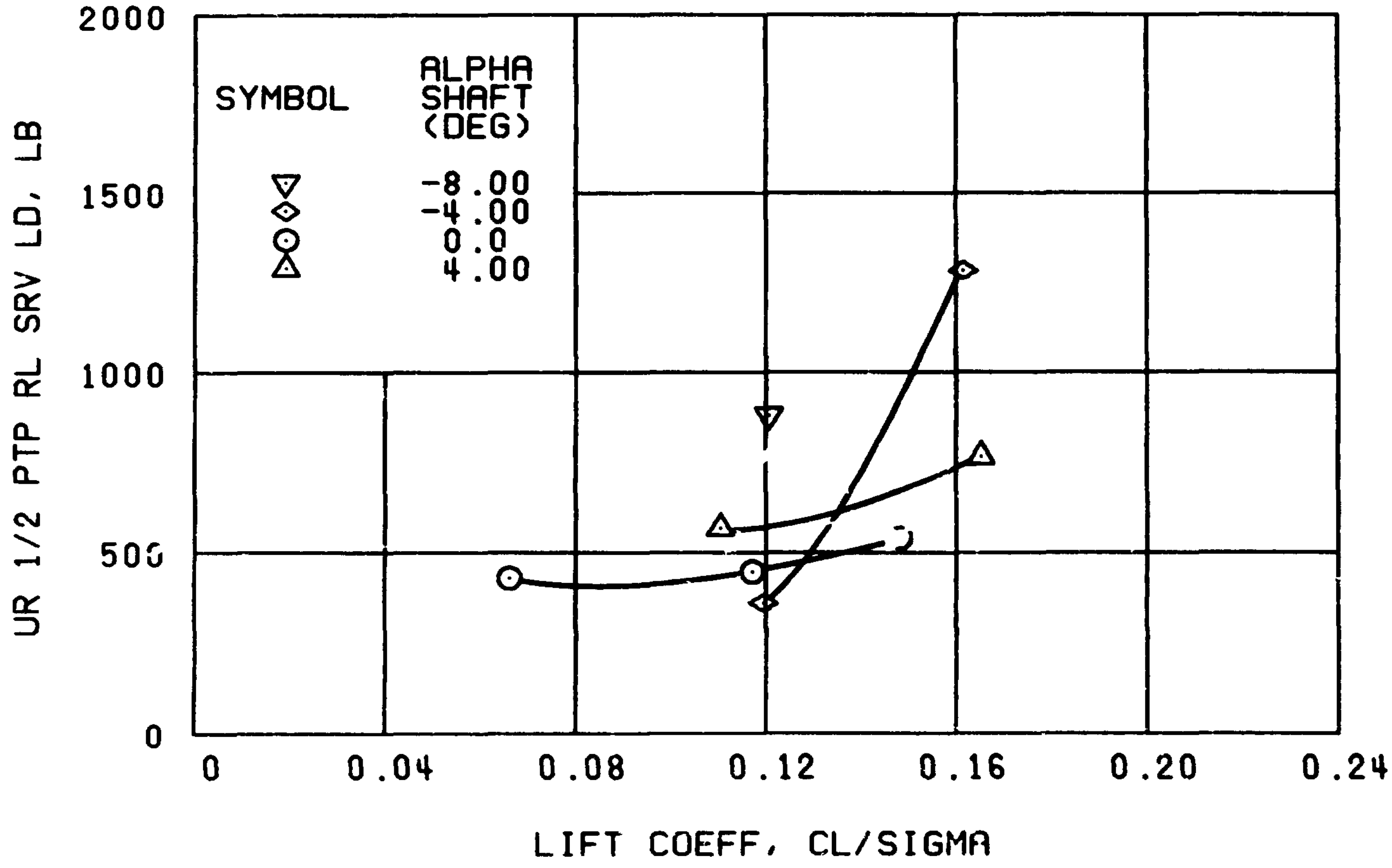

(m) UPPER ROTOR RIGHT LATERAL SERVO LOAD

Figure 12. Continued.

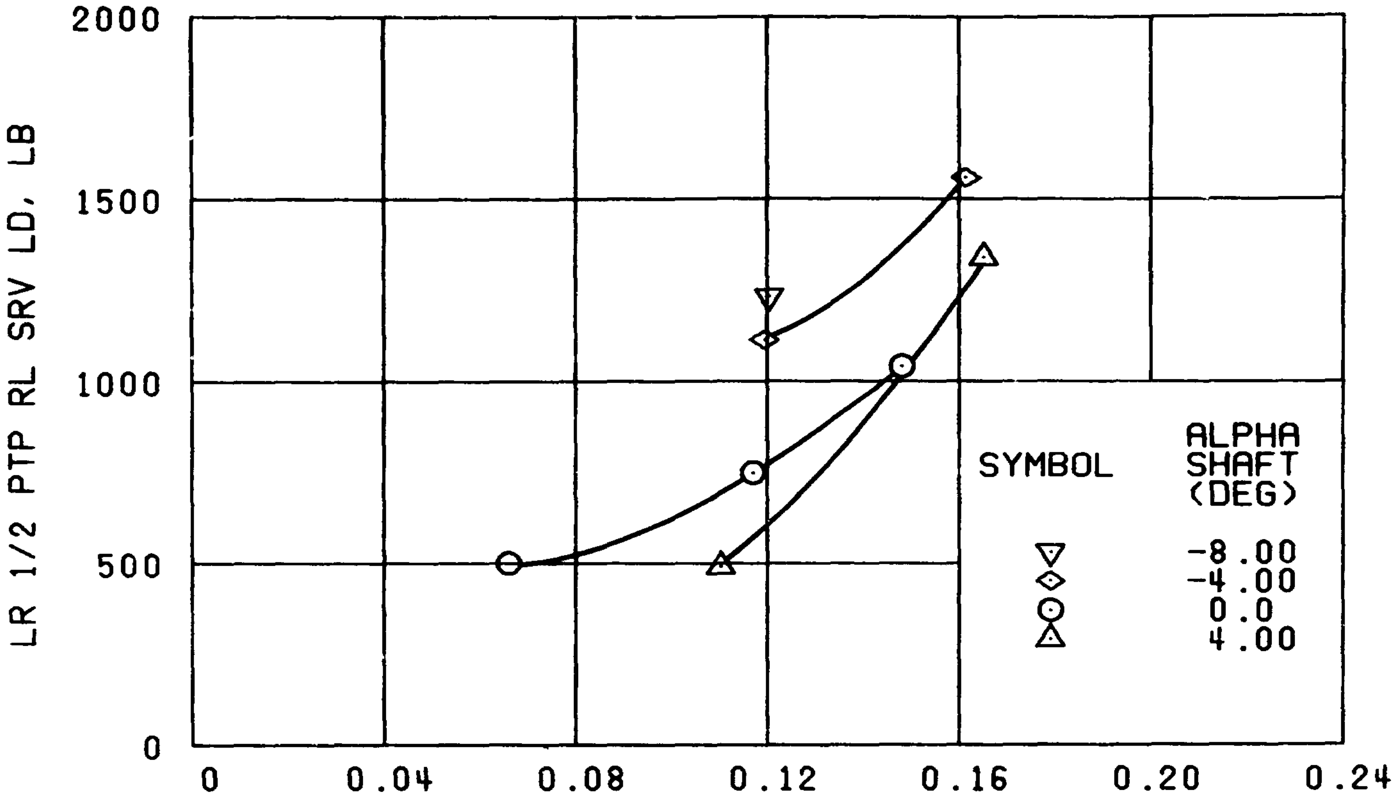

(n) LOWER ROTOR RIGHT LATERAL SERVO LOAD

Figure 12. Continued.

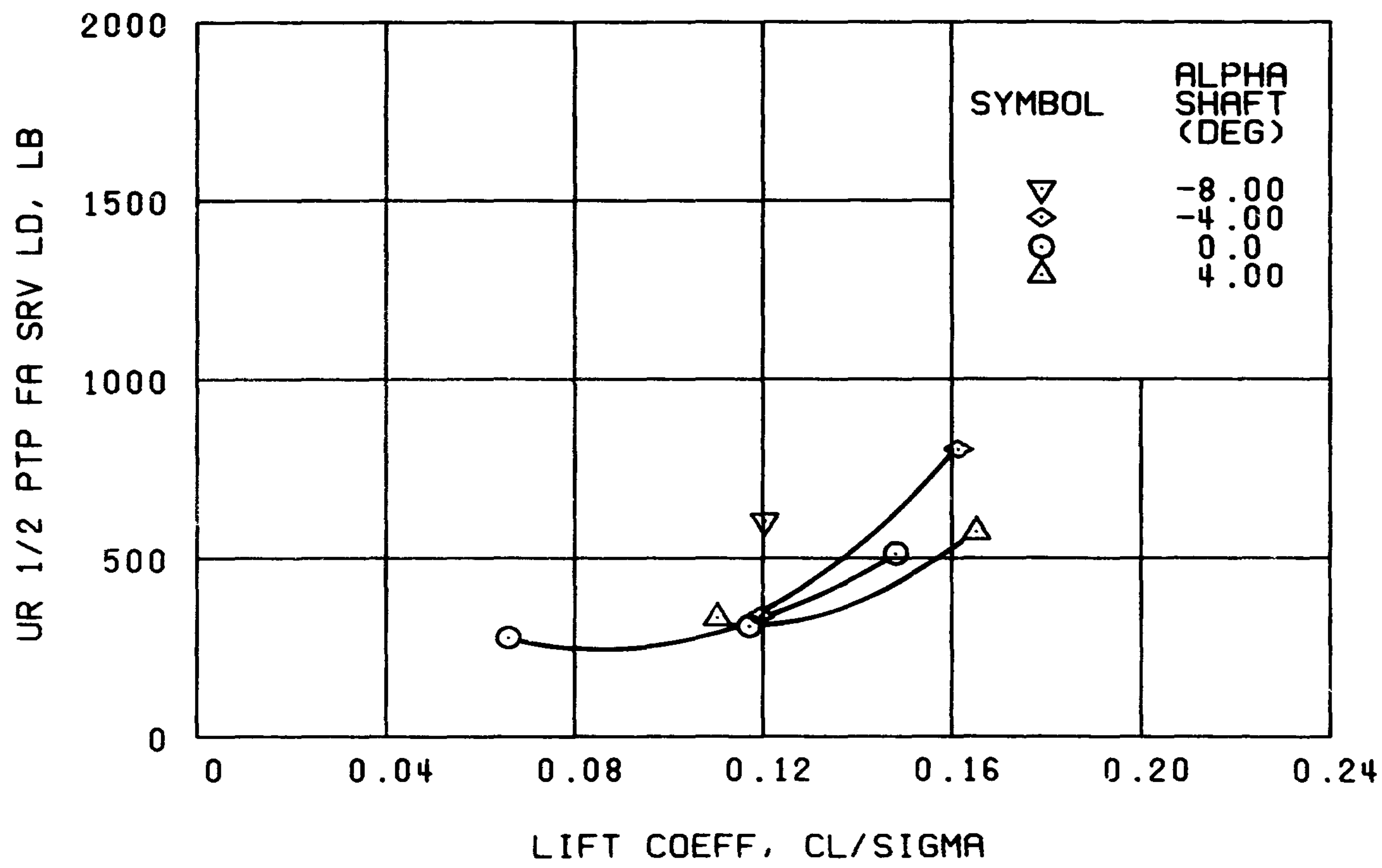

(o) UPPER ROTOR FORE AND AFT SERVO LOAD

Figure 1?. Continued.

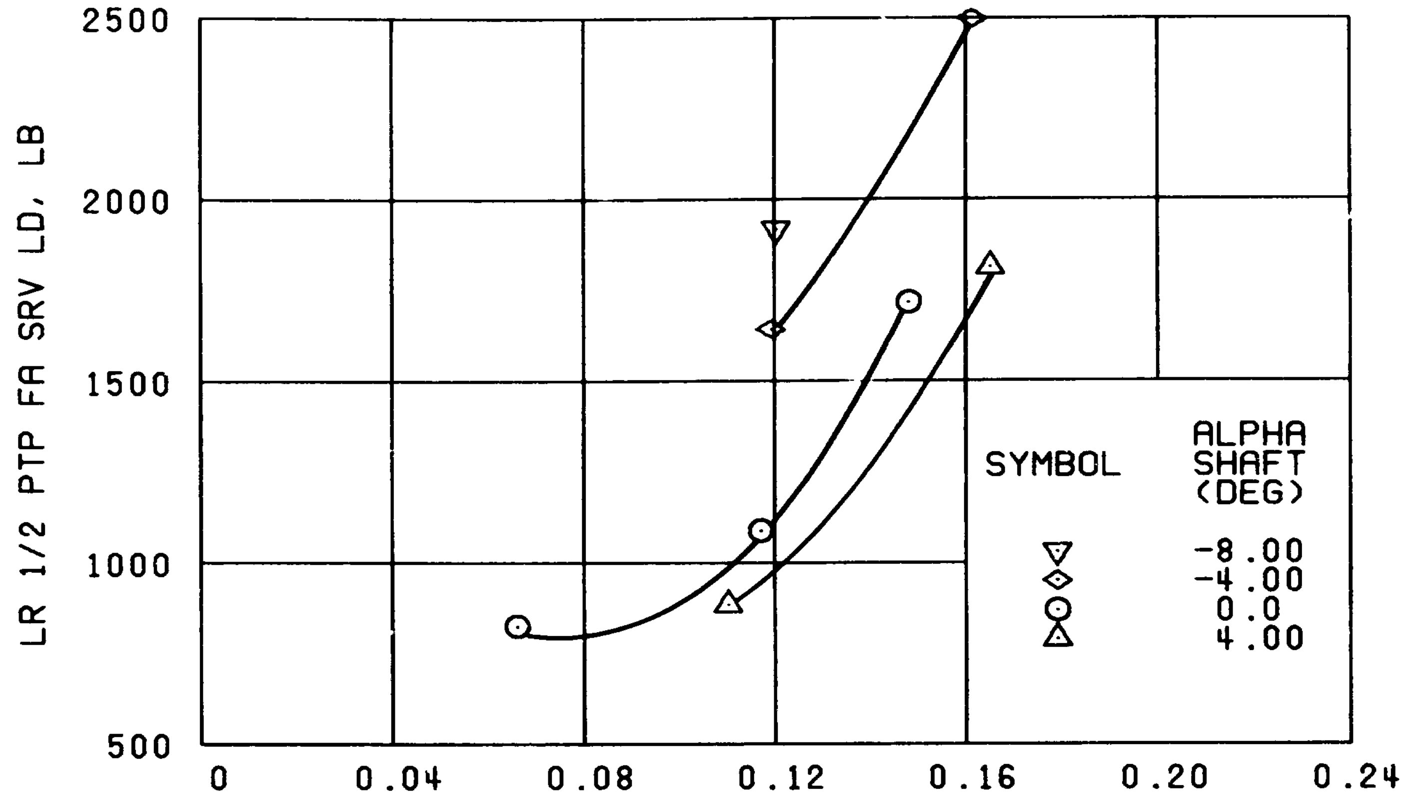

(p) LOWER ROTOR FORE AND AFT SERVO LOAD

Figure 12. Continued.

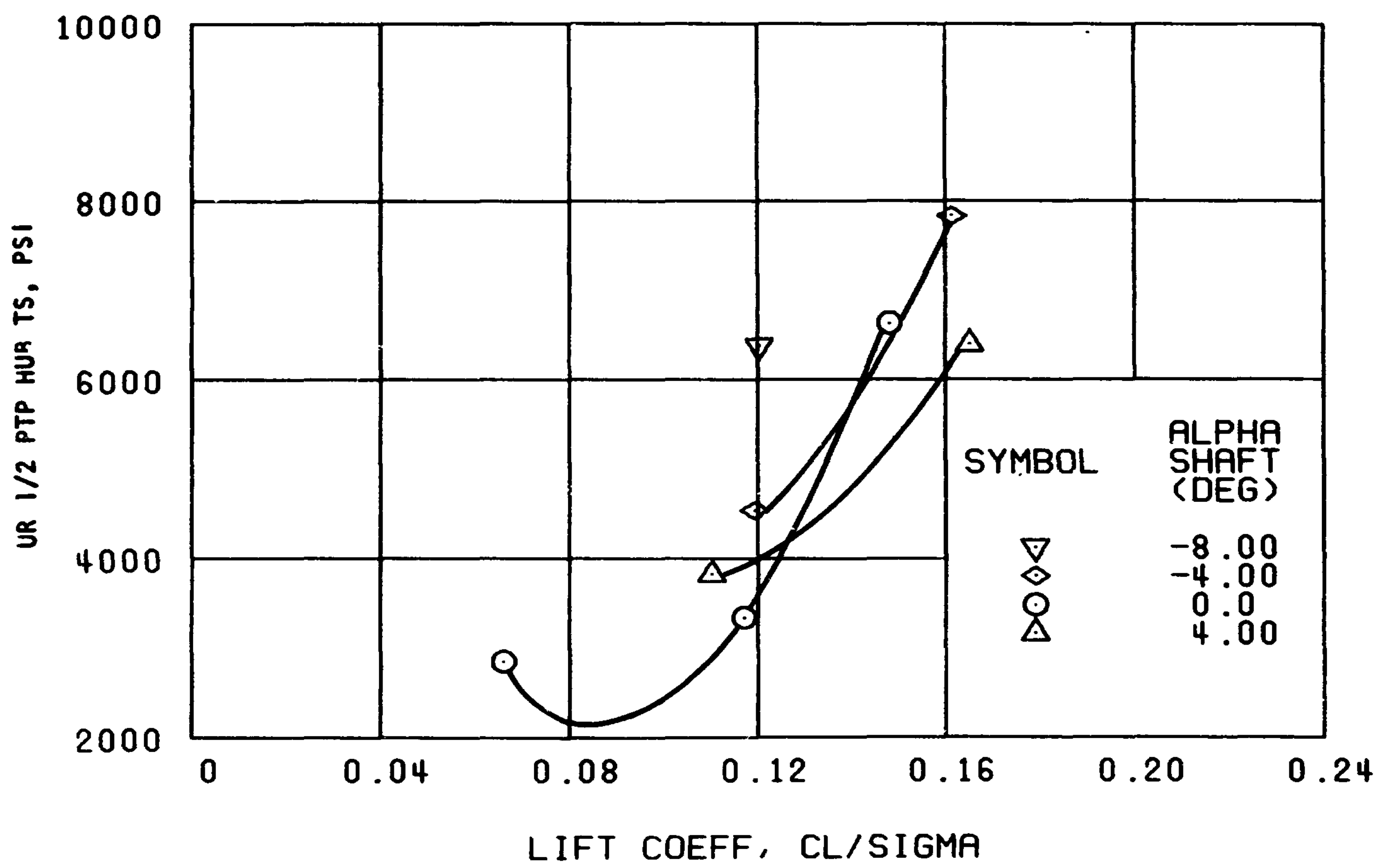

(Q) MAXIMUM MEASURED UPPER ROTOR HUB TOTAL STRESS

Figure 12. Continued.

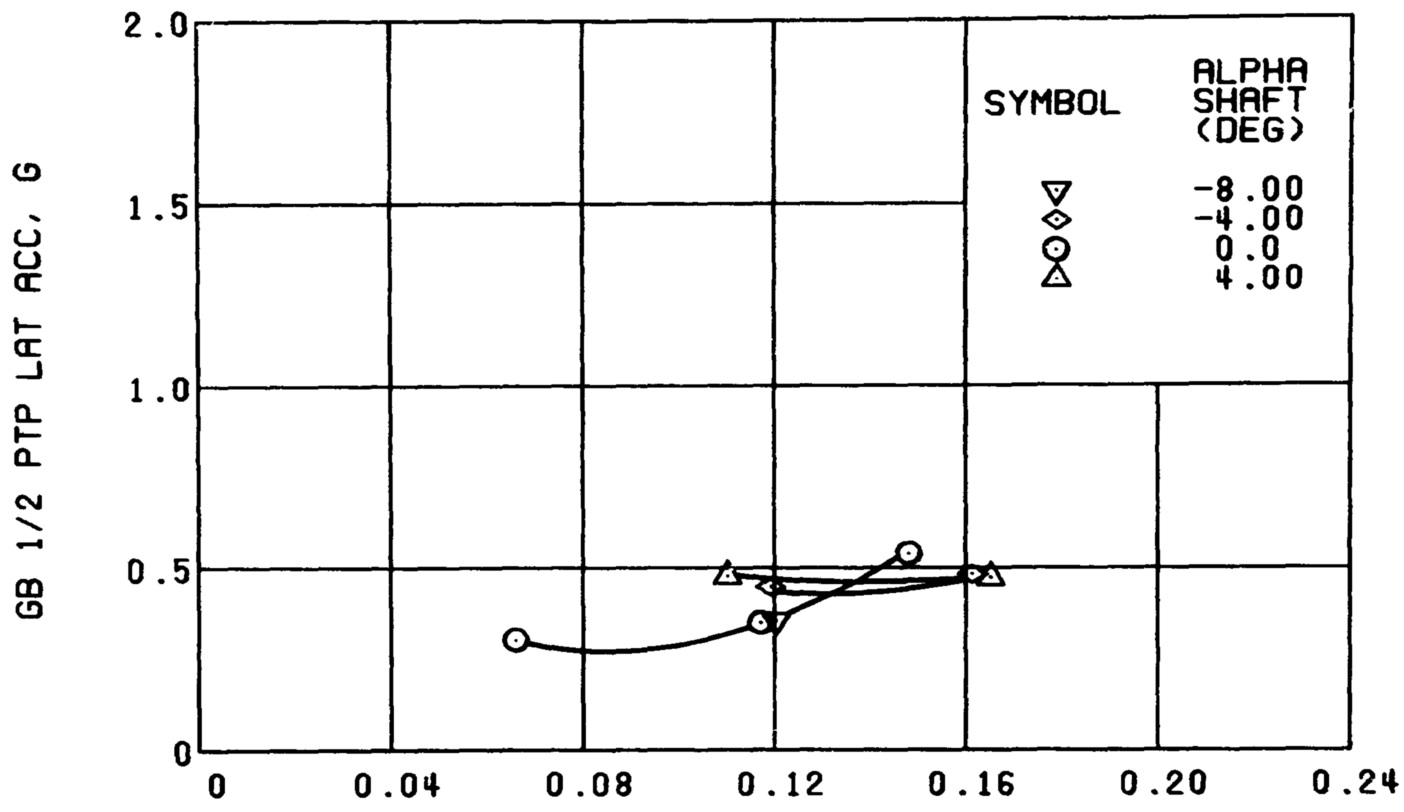

(r) GEARBOX LATERAL ACCELERATION

Figure 12. Continued.

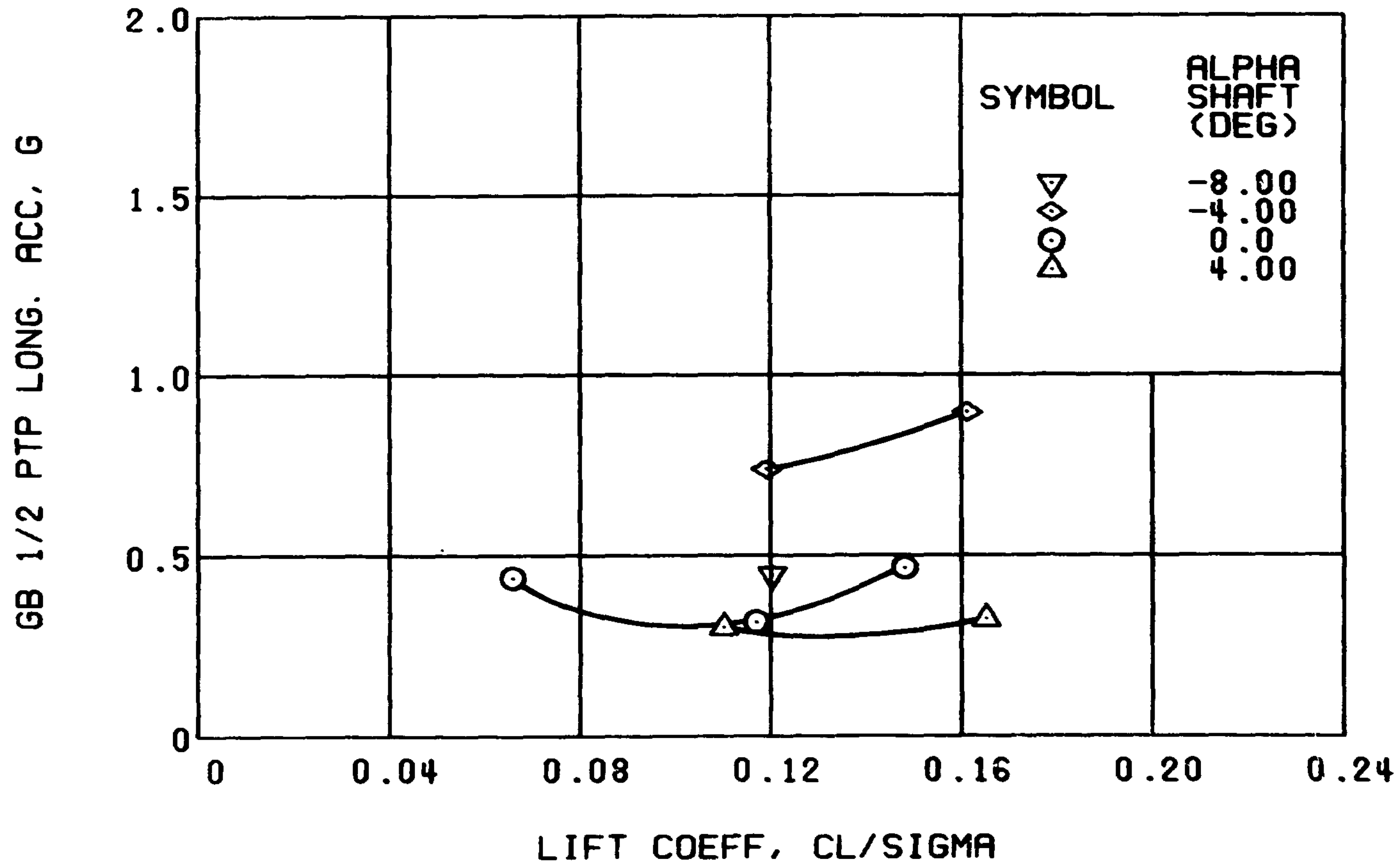

(s) GEARBOX LONGITUDINAL ACCELERATION

Figure 12. Continued.

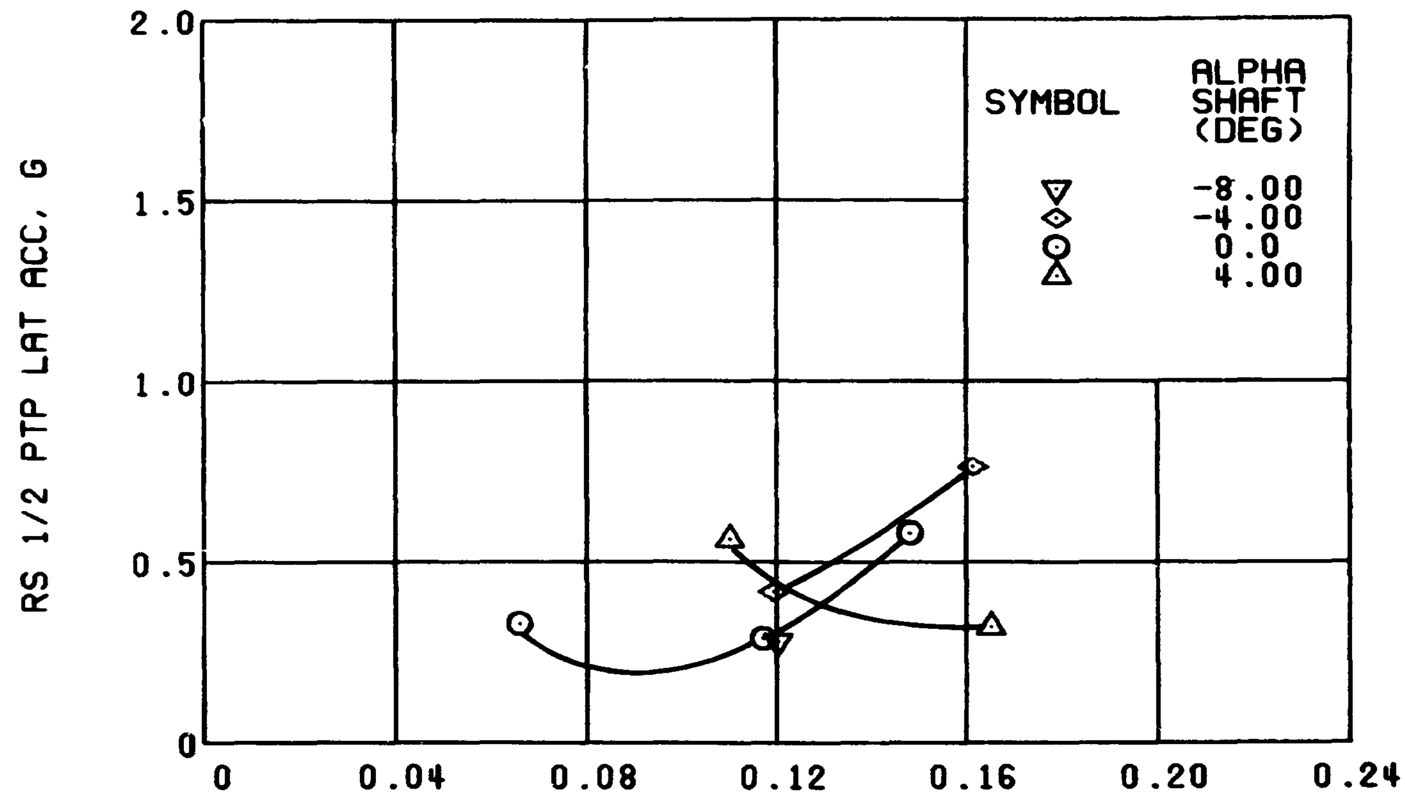

(t) RIGHT STRUT LATERAL ACCELERATION

Figure 12. Continued.

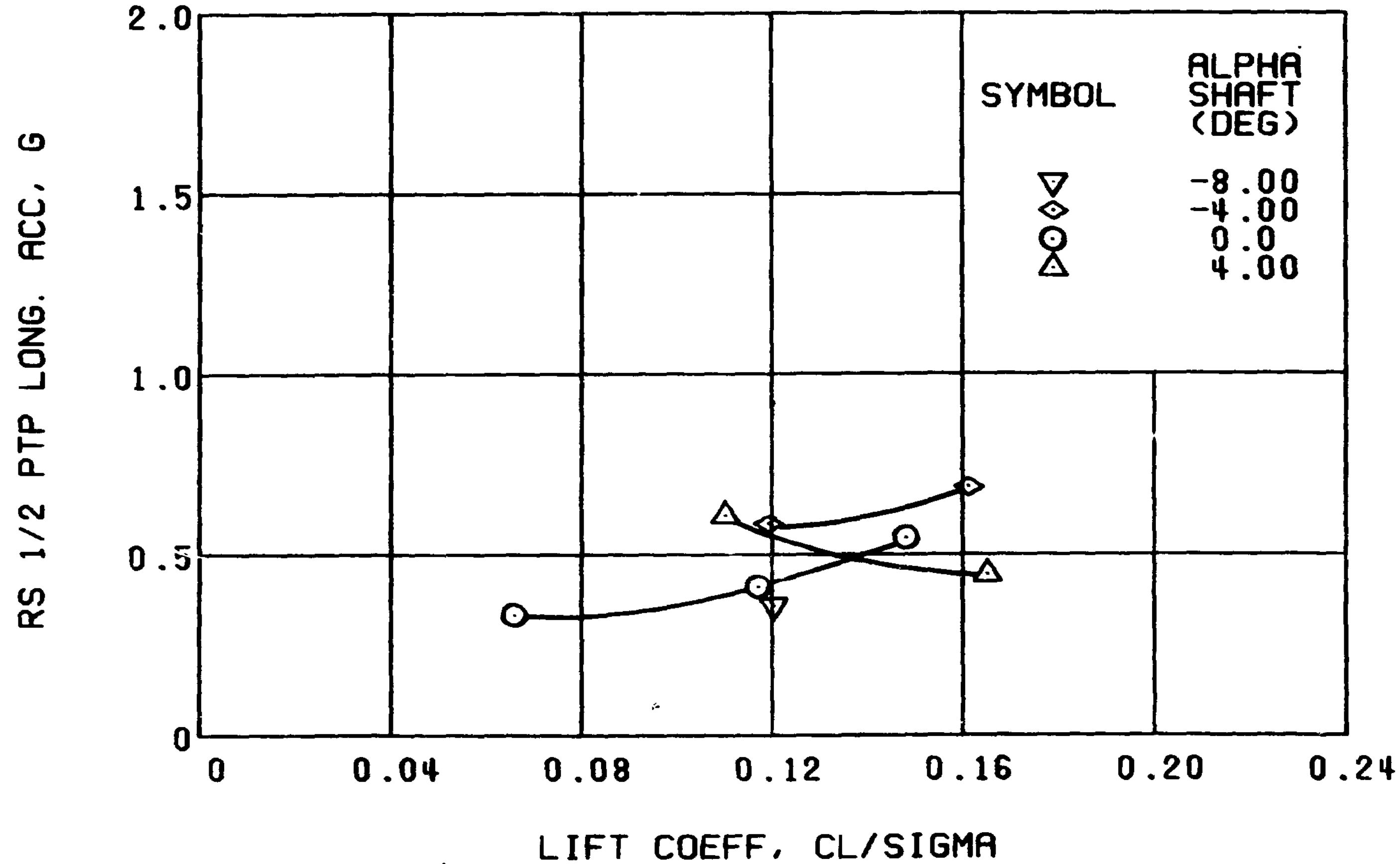

(u) RIGHT STRUT LONGITUDINAL ACCELERATION

Figure 12. Concluded.

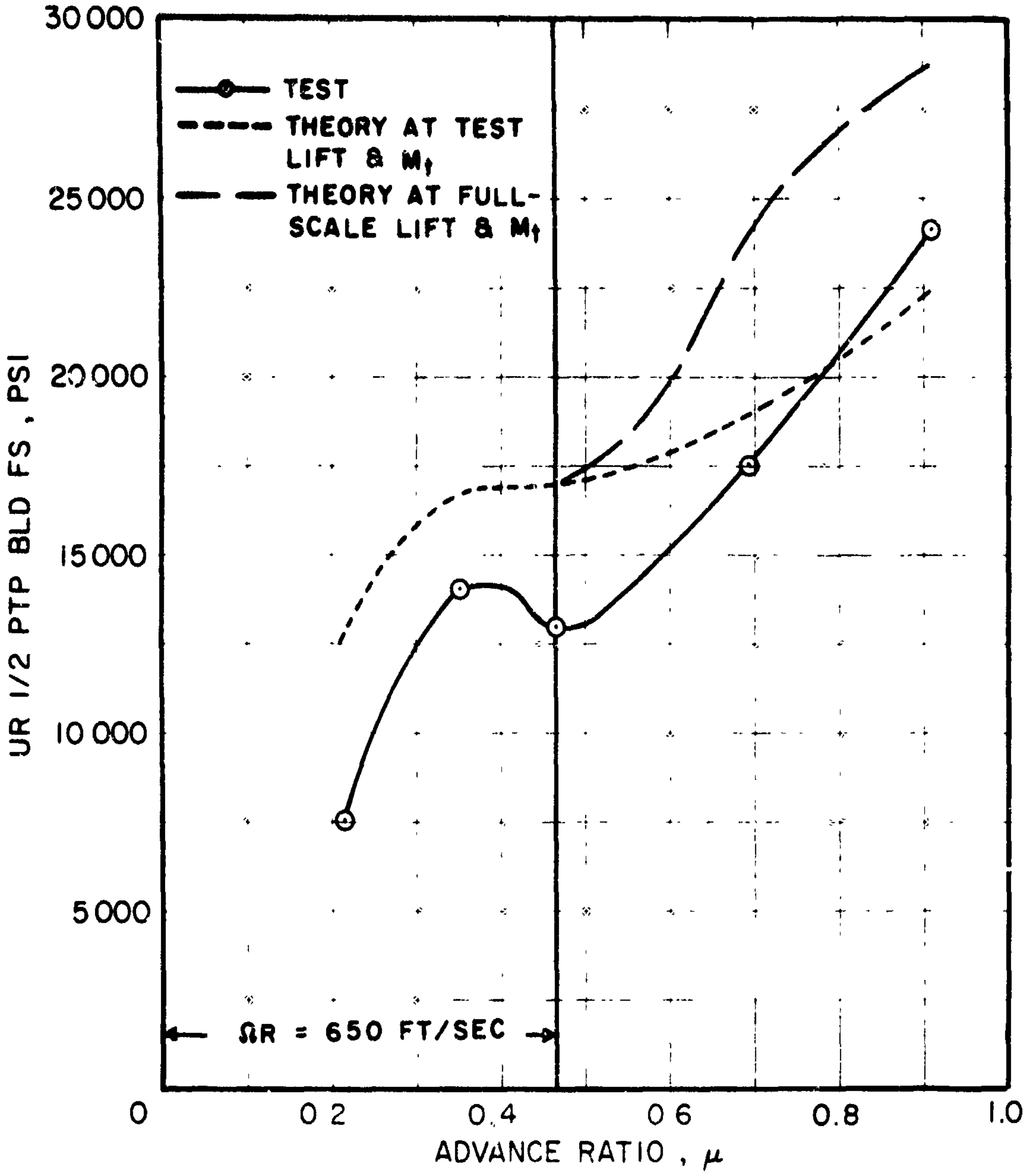

(a) UPPER ROTOR FLATWISE STRESS, r = 84 IN.

Figure 13. The Effect of Advance Ratio on Measured and Predicted Stresses and Loads.

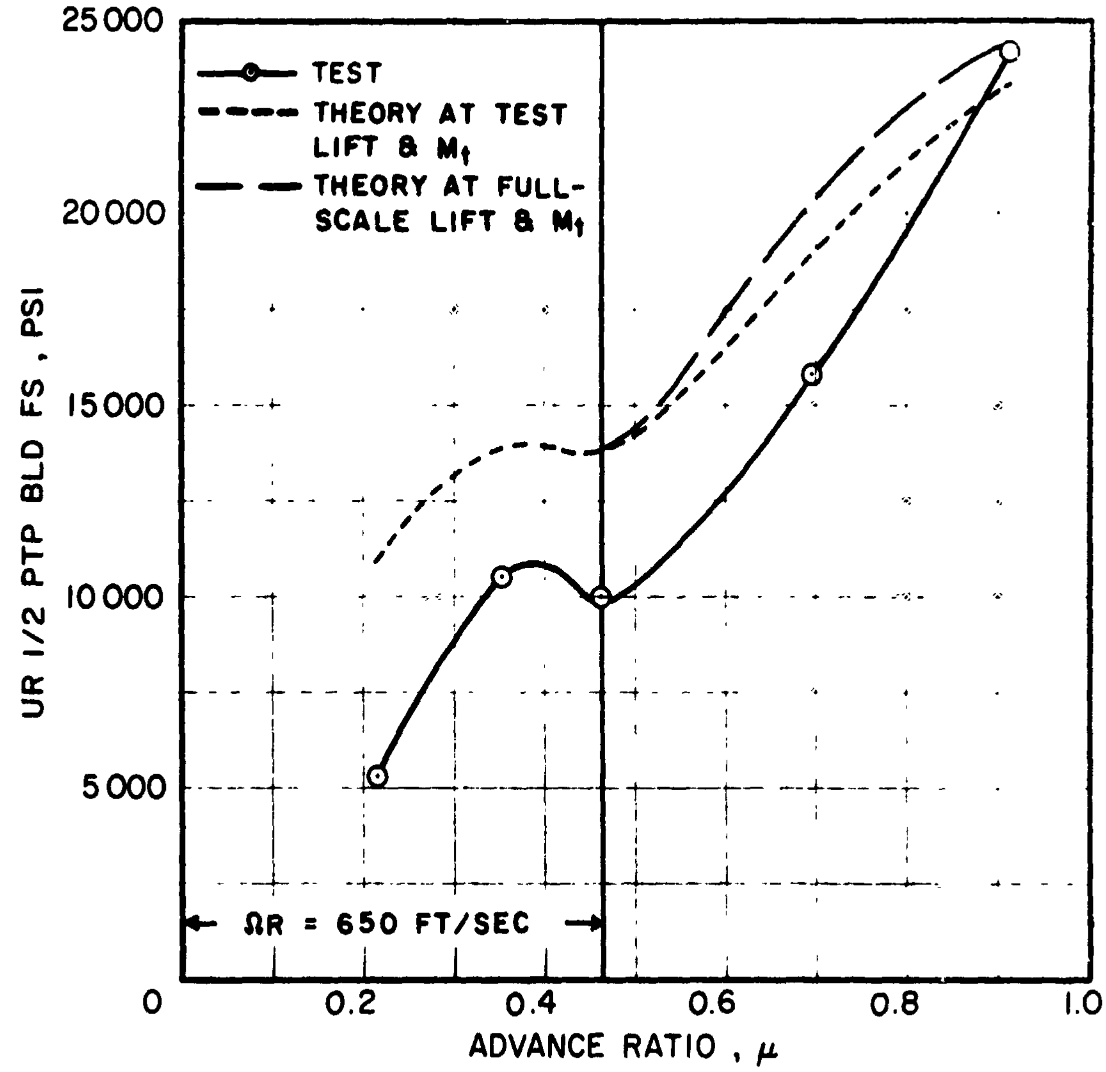

(b) UPPER ROTOR FLATWISE STRESS, r = 108 IN.

Figure 13. Continued.

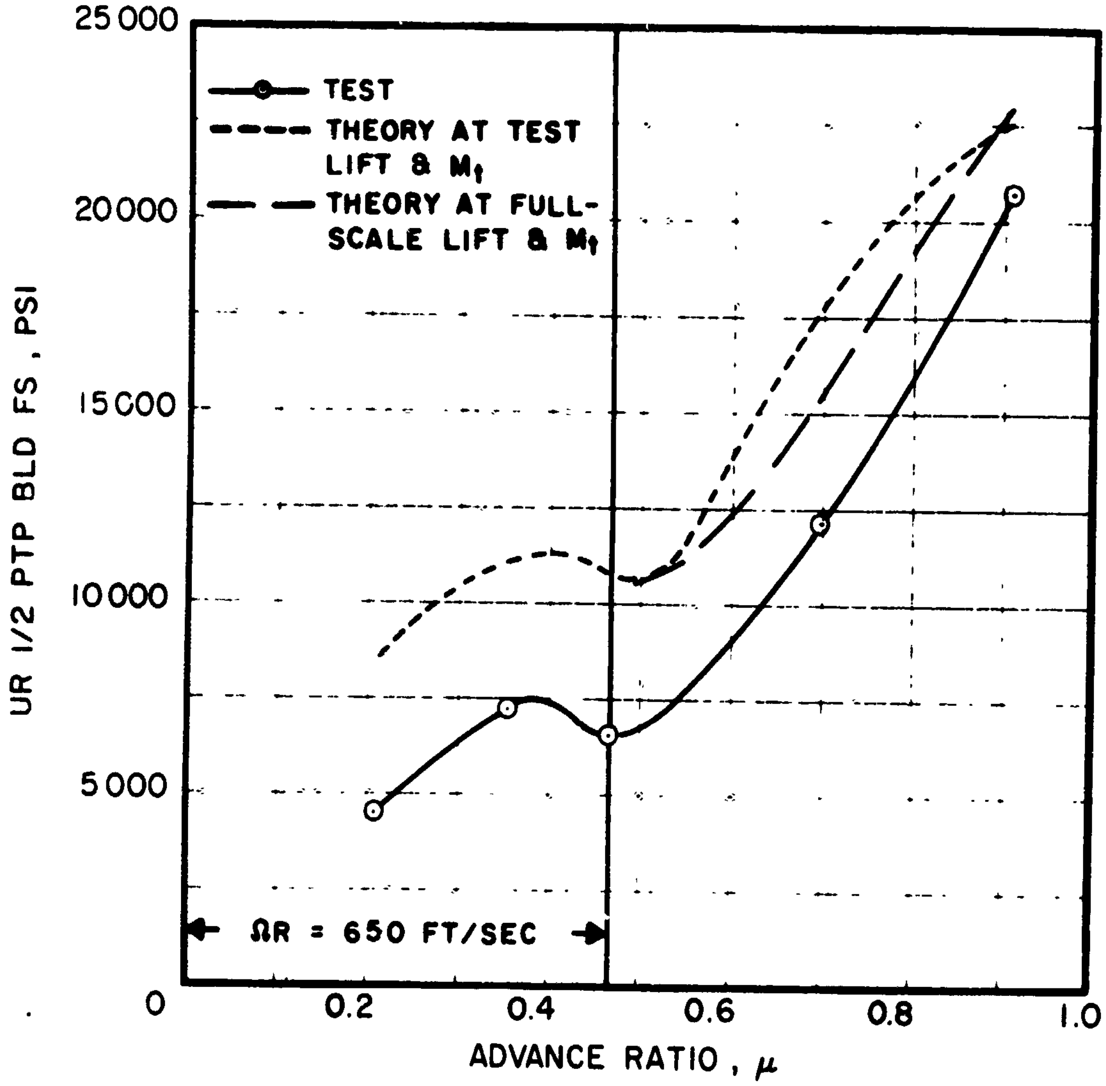

(c) UPPER ROTOR FLATWISE STRESS , r = 132 IN.

Figure 13. Continued.

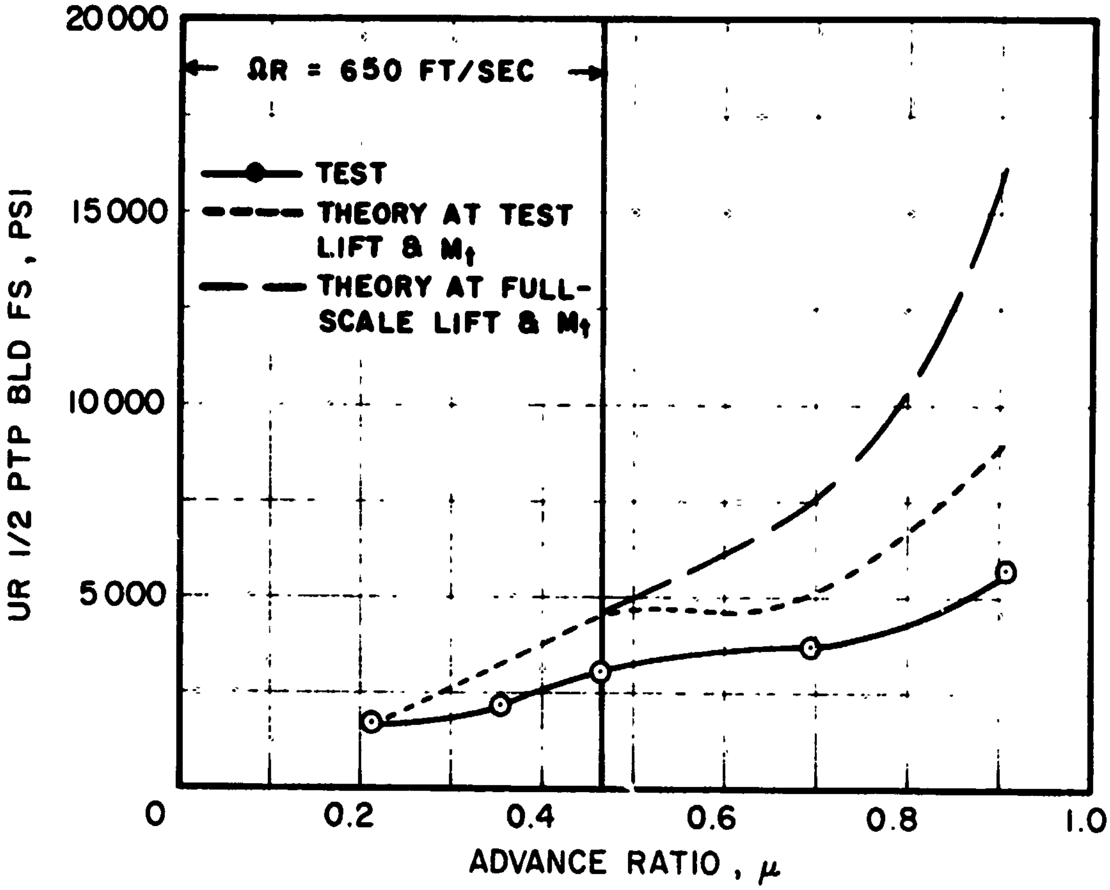

(d) UPPER ROTOR FLATWISE STRESS, r = 204 IN.

Figure 13. Continued.

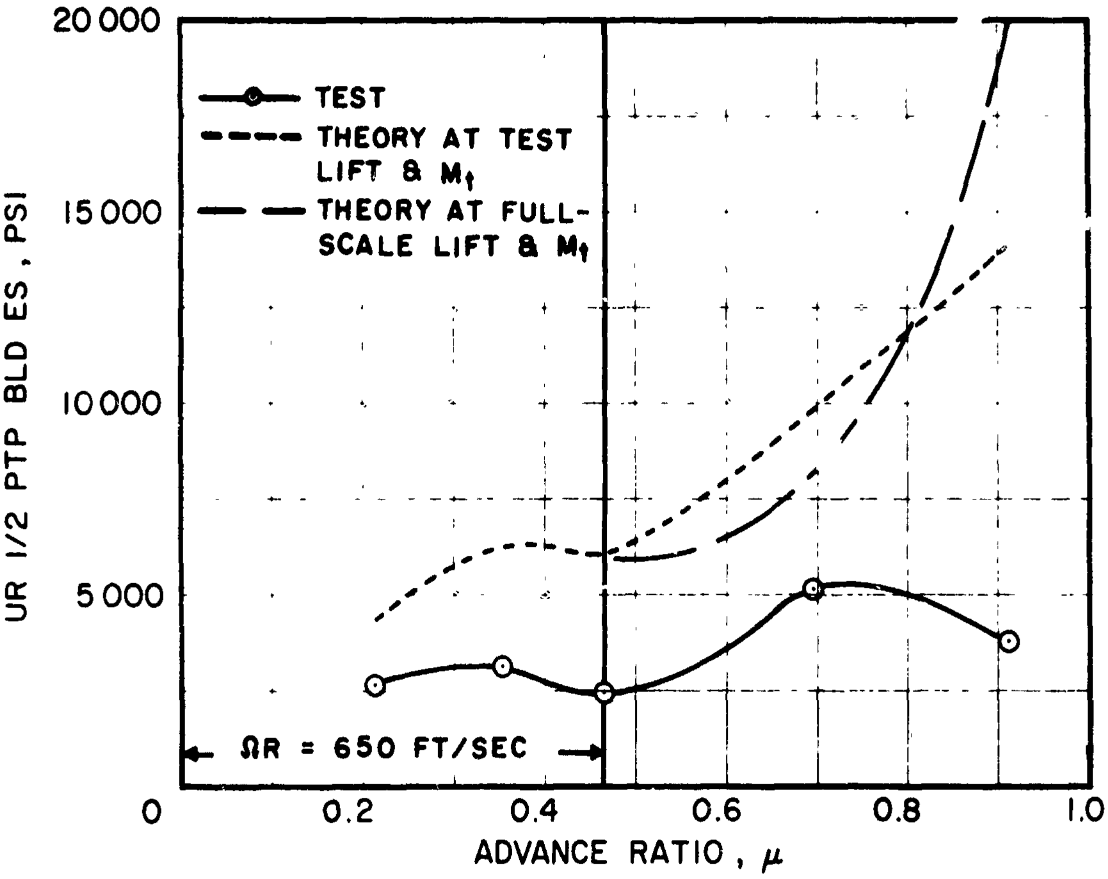

(e) UPPER ROTOR EDGEWISE STRESS, r = 84 IN.

Figure 13. Continued.

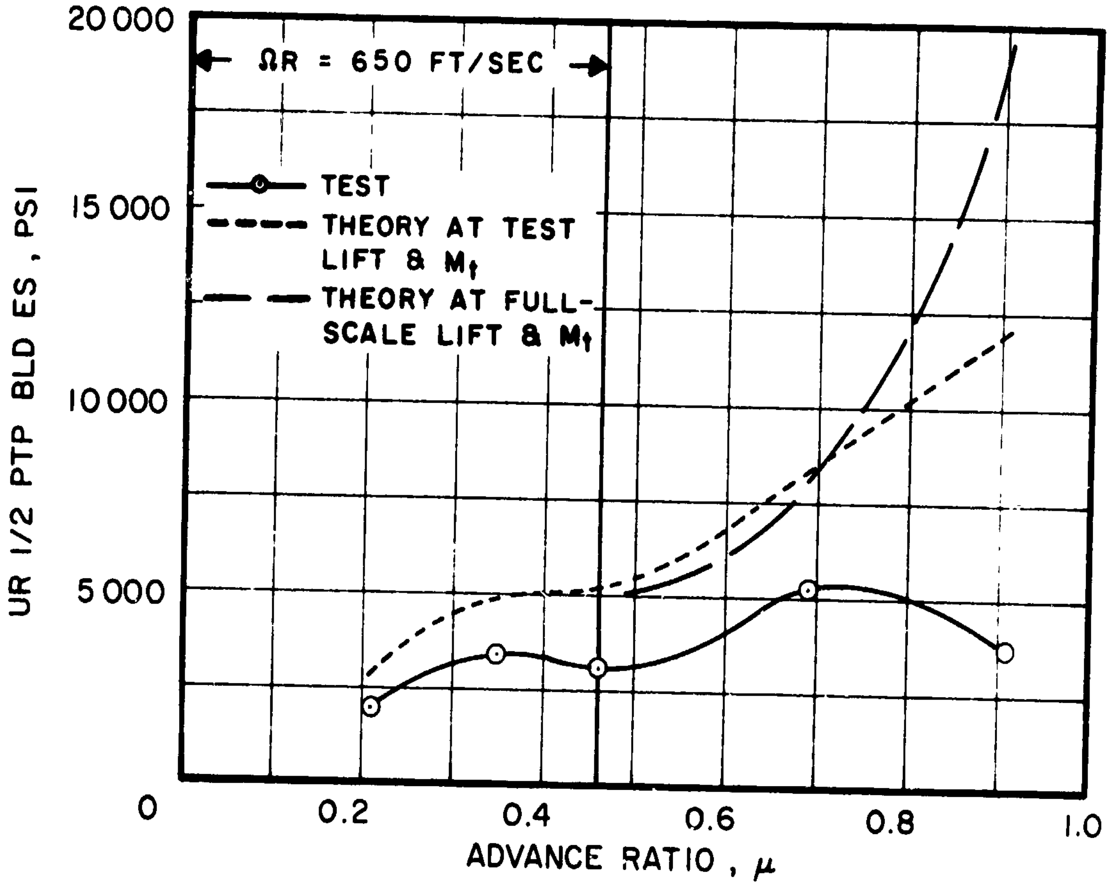

(f) UPPER ROTOR EDGEWISE STRESS , r = 132 IN.

Figure 13. Continued.

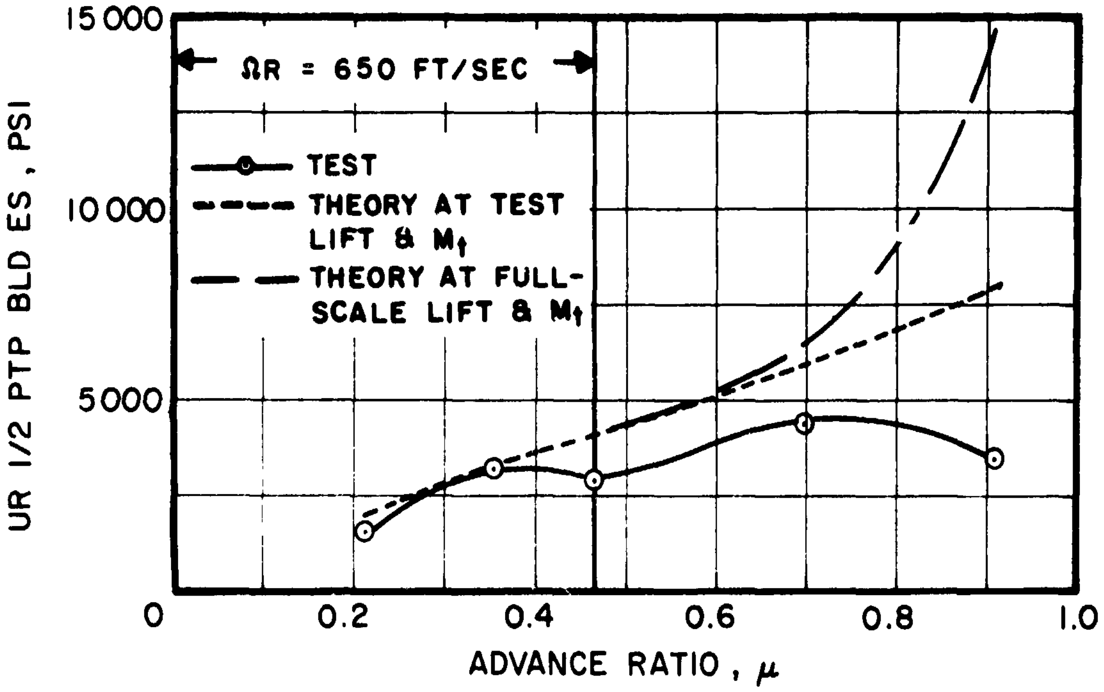

(g) UPPER ROTOR EDGEWISE STRESS , r = 168 IN.

Figure 13. Continued.

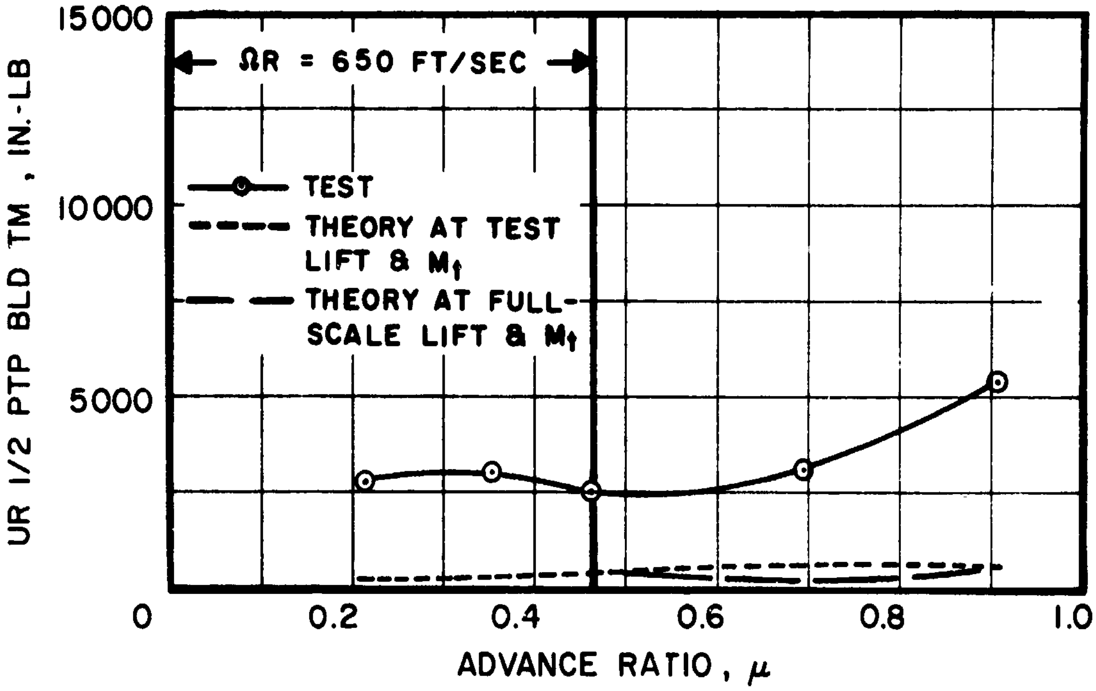

(h) UPPER ROTOR TORSIONAL MOMENT , r = 130 IN.

Figure 13. Continued.

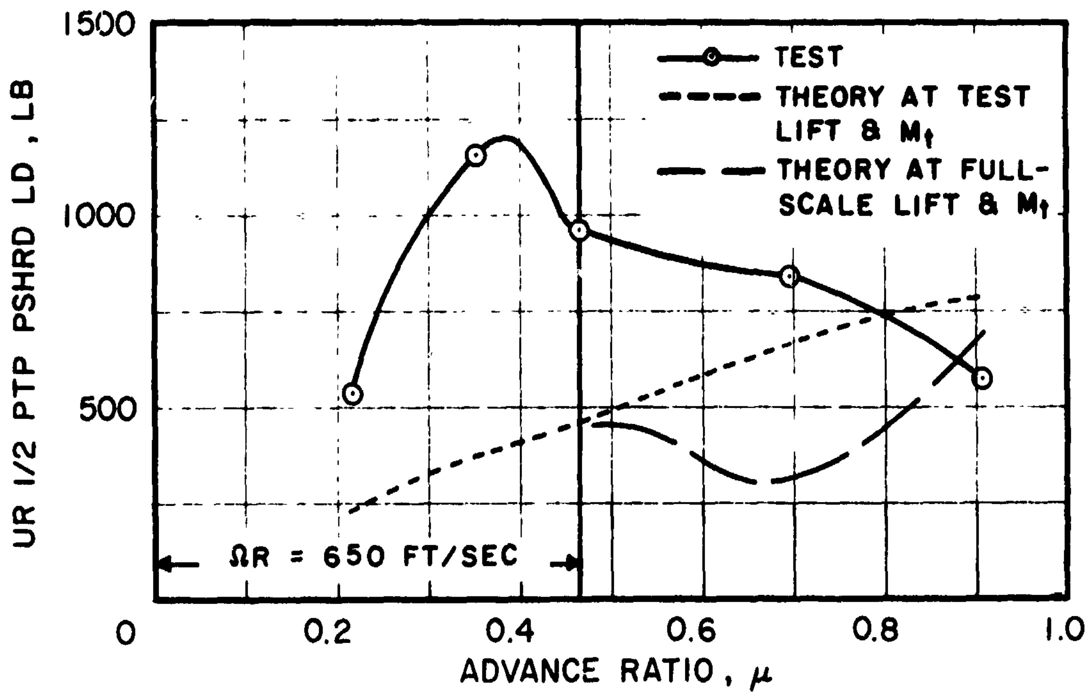

(i) UPPER ROTOR PUSHROD LOAD

Figure 13. Continued.

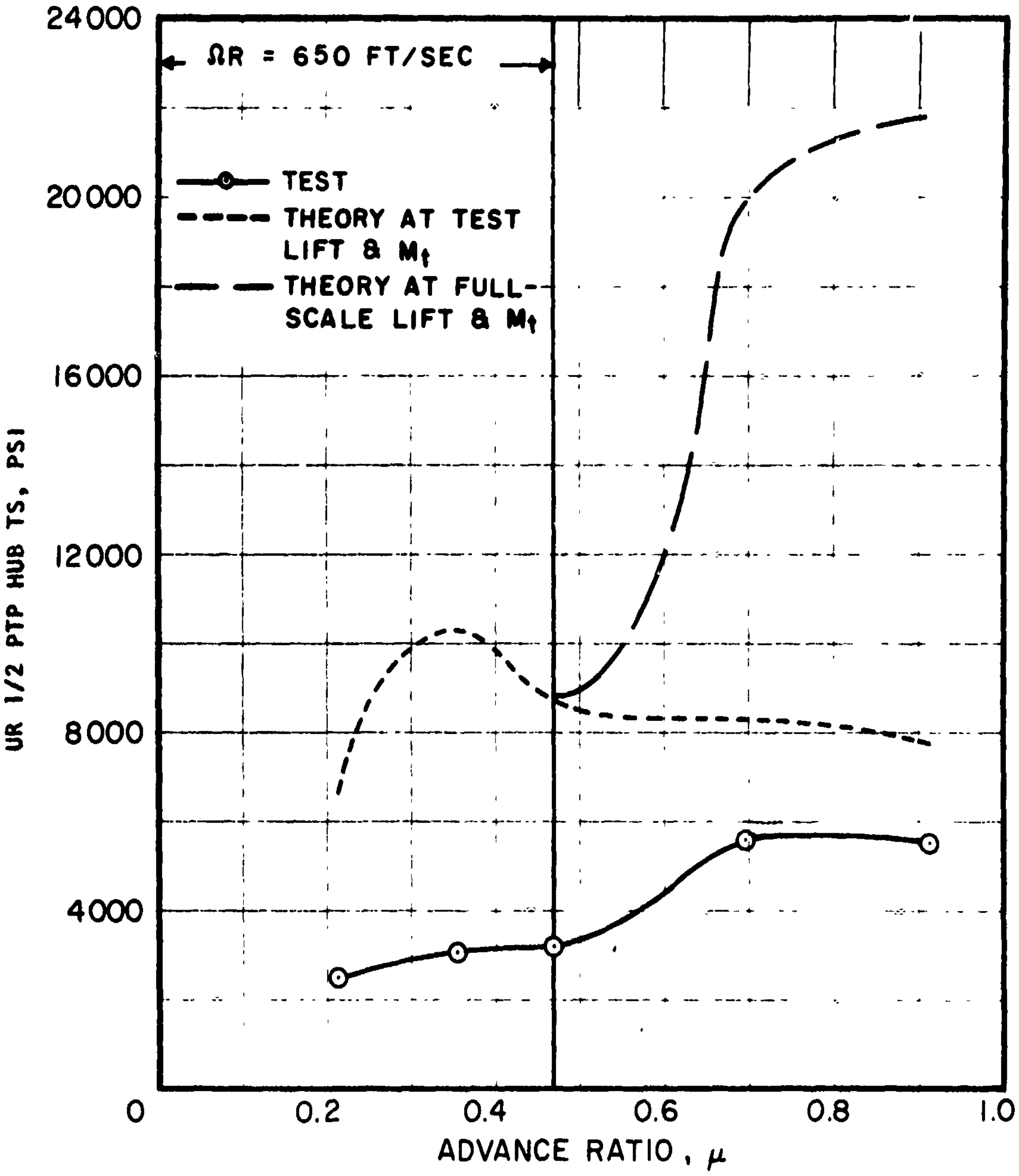

(J) MAXIMUM MEASURED UPPER ROTOR HUB TOTAL STRESS

Figure 13. Concluded.

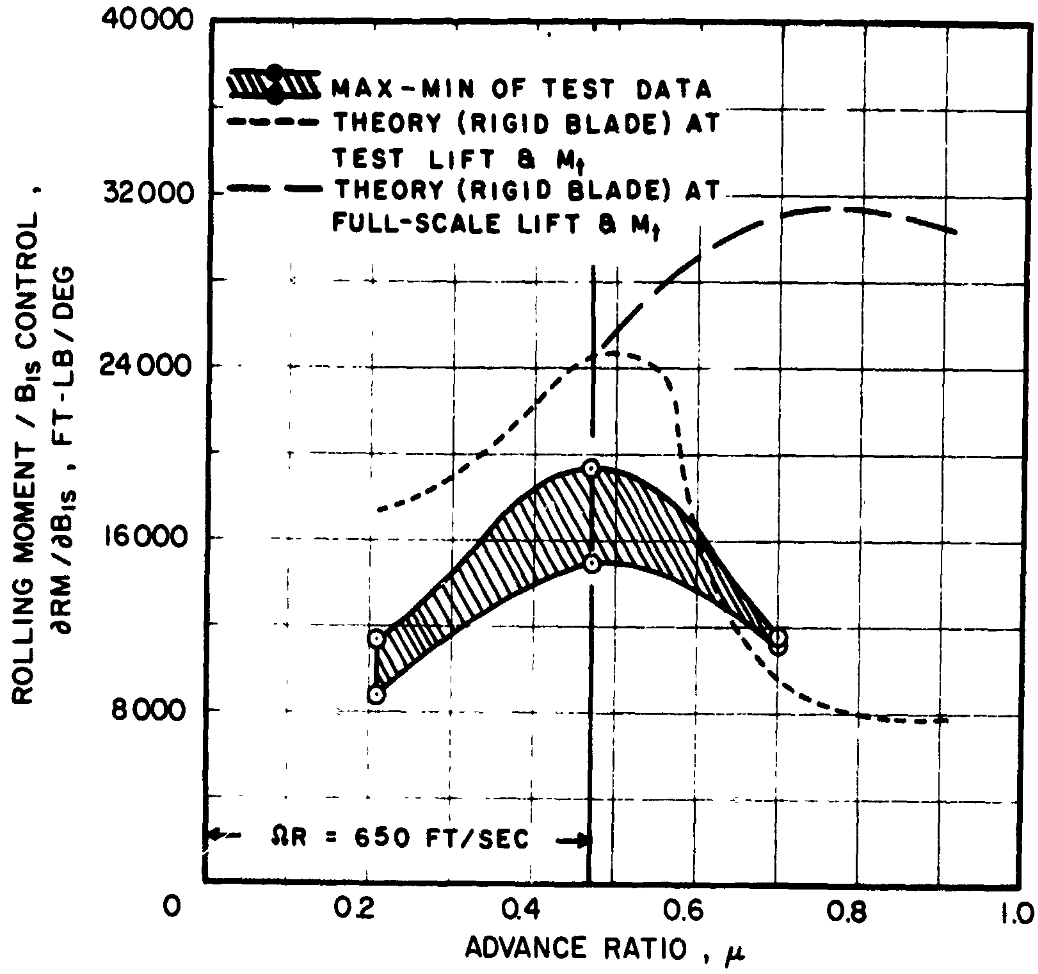

(a) ROLLING MOMENT CONTROL

Figure 14. The Effect of Advance Ratio on Measured and Predicted Stability and Control.

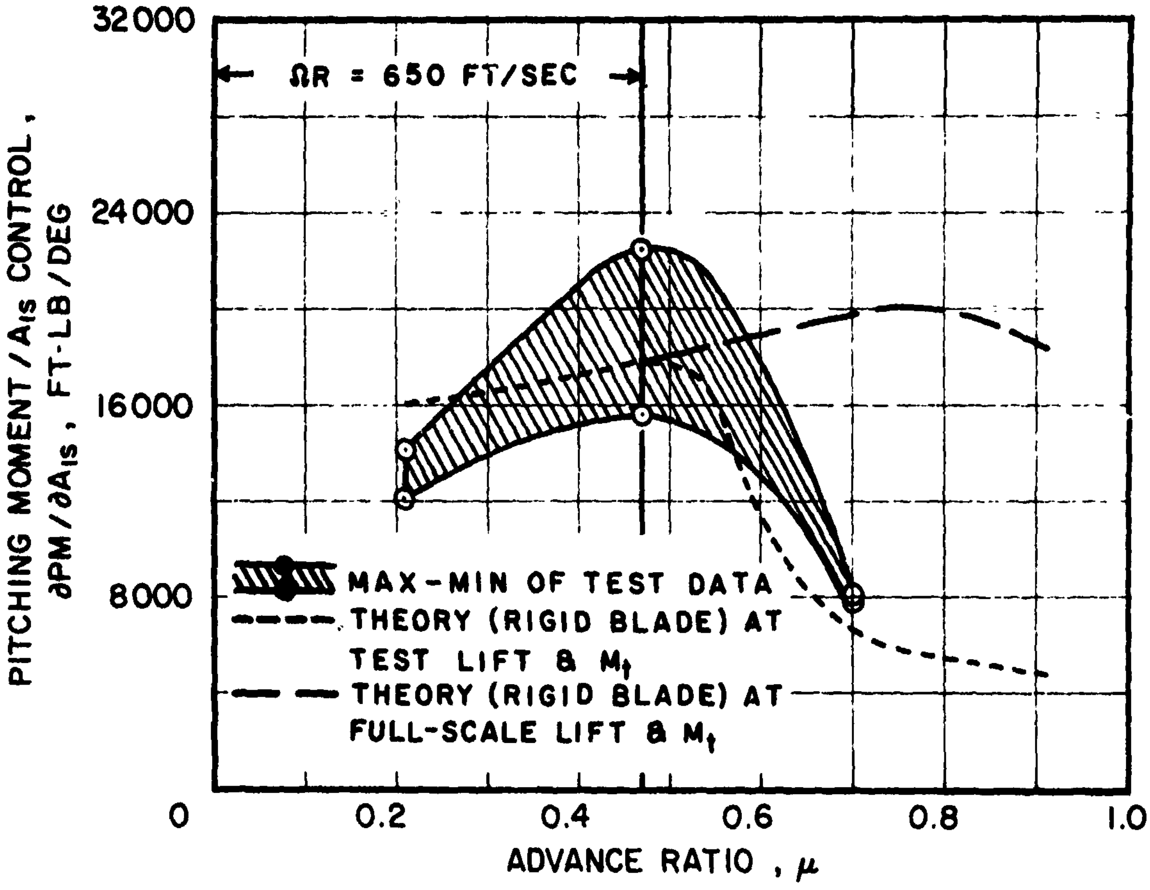

(b) PITCHING MOMENT CONTROL

Figure 14. Continued.

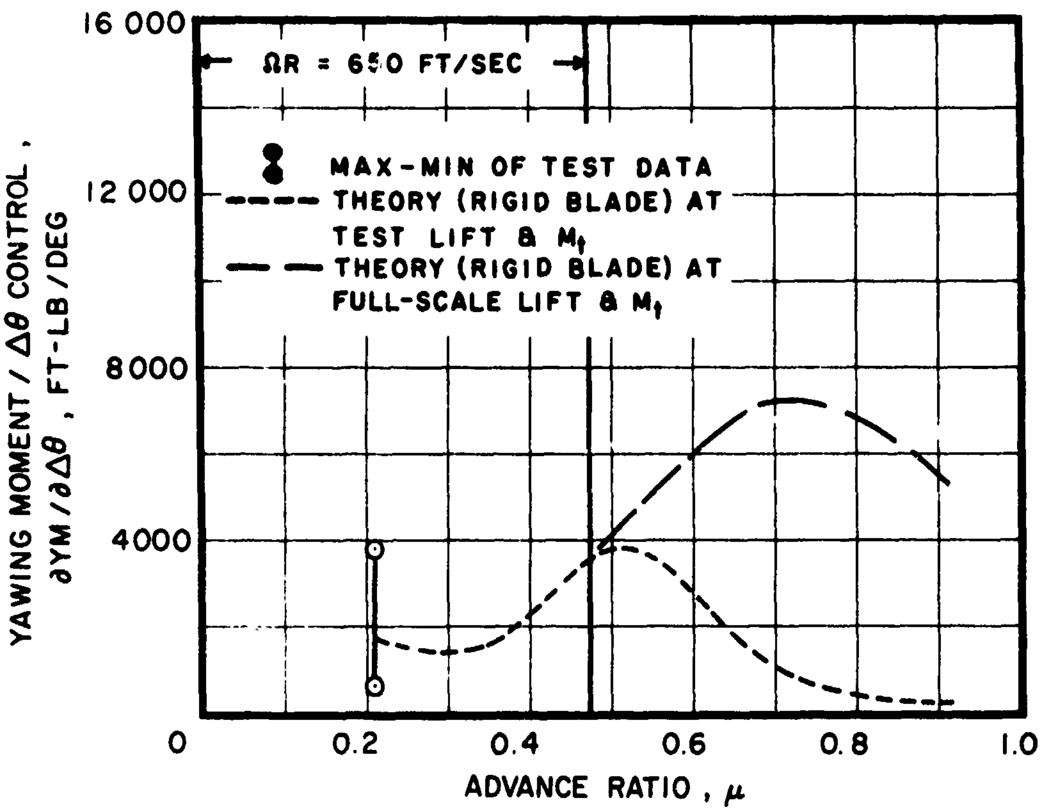

(c) YAWING MOMENT CONTROL

Figure 14. Continued.

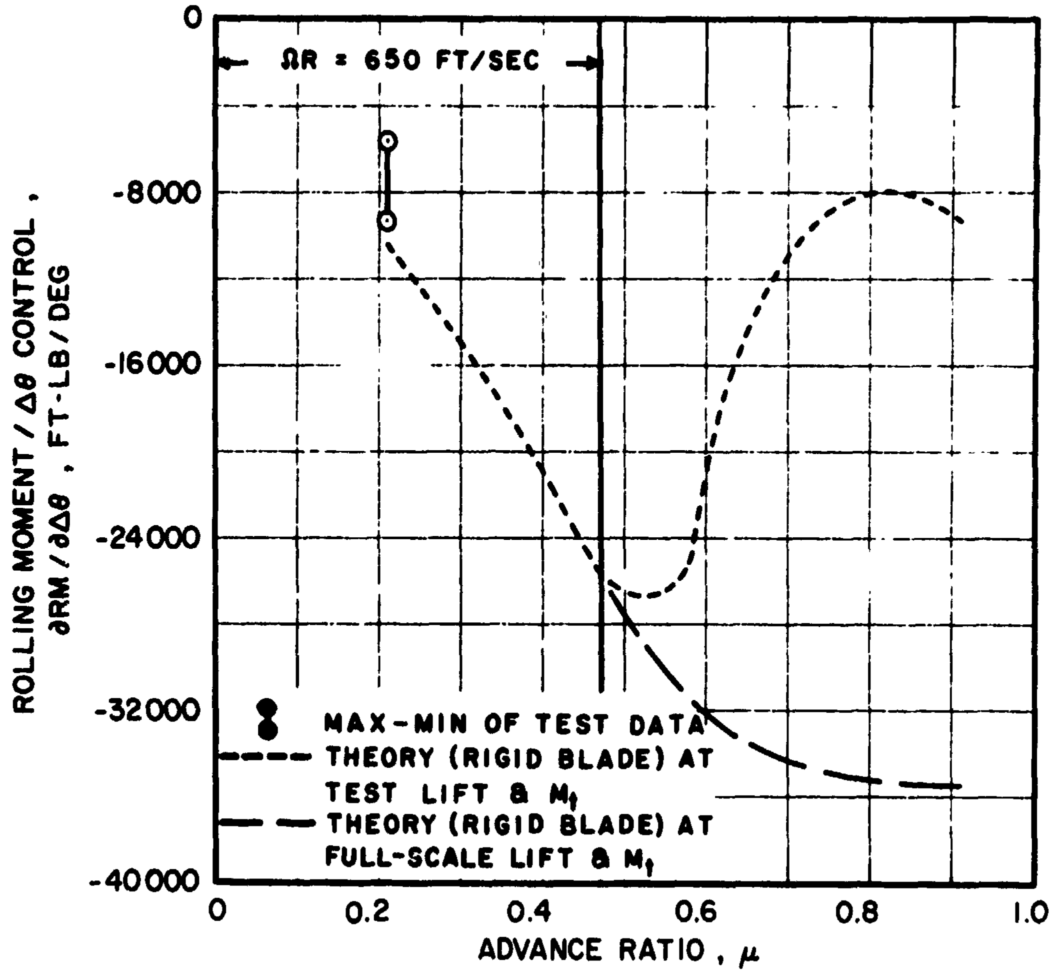

(d) ROLLING MOMENT / Δθ CONTROL COUPLING

Figure 14. Continued.

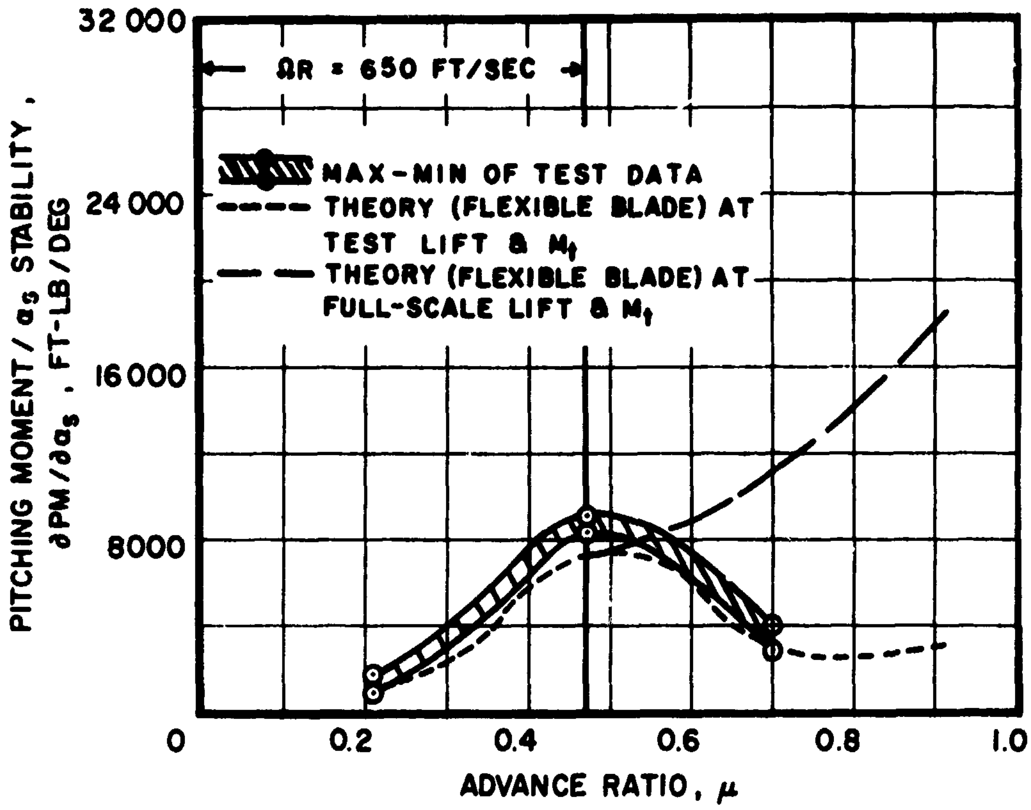

(e) ANGLE-OF-ATTACK STABILITY

Figure 14. Concluded.

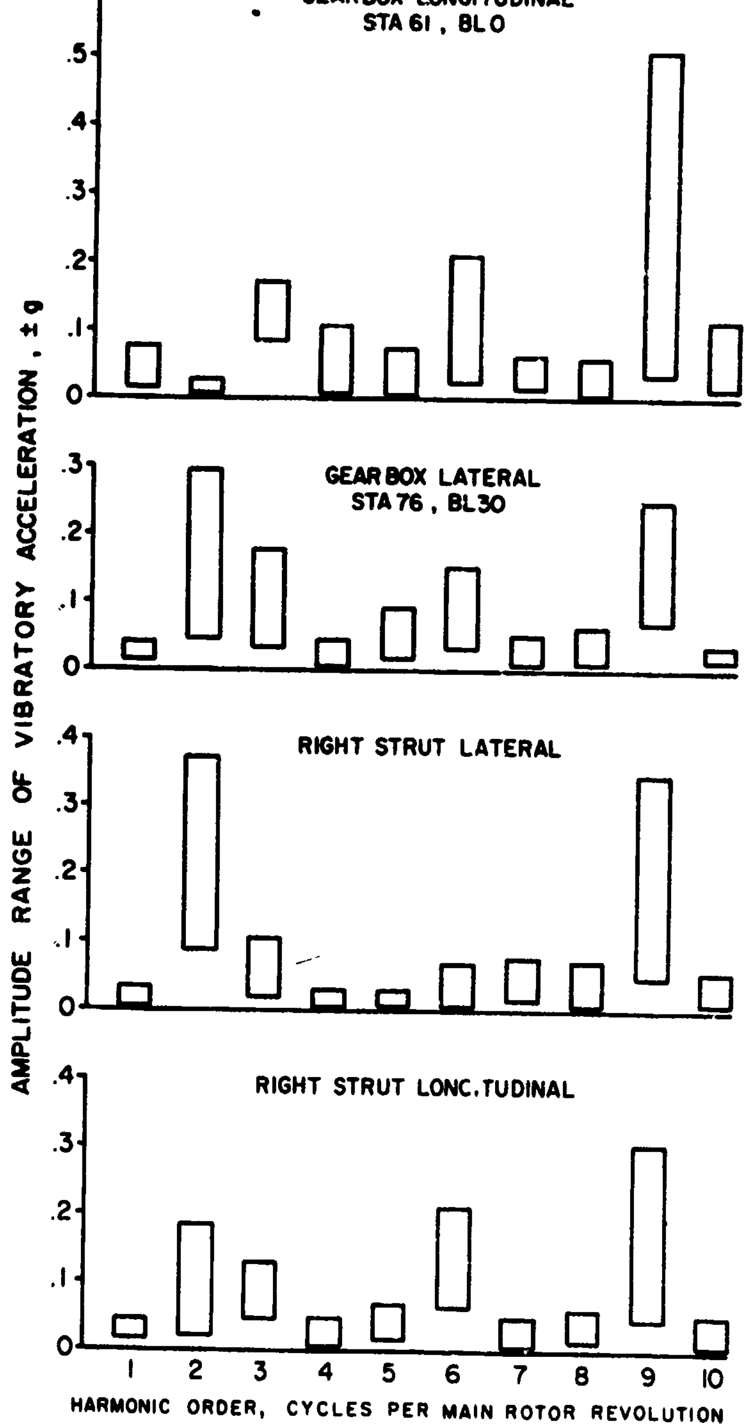

Figure 15. Range of Vibration Encountered at a Velocity of 179 Knots With the Lateral Displacement Control (B'_{1s}) Set at 6 Degrees; $\mu = 0.47$, $M_t = 0.83$. (Data (point) scatter reflects variations in αs and θ_c settings. All vibrations shown have a zero "g" steady reference.)

LITERATURE CITED

1. Cheney, M. C., Jr., THE ABC HELICOPTER, Journal of the American Helicopter Society, Vol. 14, No. 4, New York, New York, October 1969.

2. Paglino, V. M., et al., ABC WHIRL TEST SUMMARY REPORT, SER-50653, Sikorsky Aircraft Division of United Aircraft Corporation, Stratford, Connecticut, March 1970.

3. Paglino, V. M., and Logan, A. H., AN EXPERIMENTAL STUDY OF THE PERFORMANCE AND STRUCTURAL LOADS OF A FULL-SCALE ROTOR AT EXTREME OPERATING CONDITIONS, SER-50505, Sikorsky Aircraft Division of United Aircraft Corporation, Stratford, Connecticut; USAAVLABS Technical Report 68-3, U. S. Army Aviation Materiel Laboratories, Fort Eustis, Virginia, July 1968, AD 674187.

4. Burger, W. G., PHOTOELASTIC ANALYSIS OF ONE-HALF SCALE MODEL OF ABC UPPER ROTOR HUB, SER-50556, Sikorsky Aircraft Division of United Aircraft Corporation, Stratford, Connecticut, June 1968.

5. Cheney, M. C., ANALYTICAL AND EXPERIMENTAL INVESTIGATION OF A MODEL RIGID ROTOR AT STOPPED AND LOW ROTOR SPEED CONDITIONS, H-410779-1, United Aircraft Research Laboratories Division of United Aircraft Corporation, East Hartford, Connecticut, June 1969.

6. Cooper, D. E., and Szustak, L.S., SEVERAL MAN/MACHINE CONSIDERATIONS FOR HELICOPTERS, AGARD Conference Proceedings No. 55, March 1970.

APPENDIX

PRESENTATION OF MEASURED DATA

Presented in Figures 16 through 39 are the primary nondimensional performance and control measurements: drag, torque, L/D, lift lateral displacement, longitudinal cyclic pitch, side force, rolling moment, pitching moment, and yawing moment. In addition, for the single-rotor conditions (Figures 36 through 39), balance moments are compared to sleeve bending moments and balance torque is compared to wattmeter reading. Figures 40 through 63 show recorded vibratory blade stresses, control loads, and fixed system vibration.

All data are plotted as a function of lift coefficient and shaft angle of attack for ease of cross plotting at any lift coefficient. The presentaticns are grouped according to the flight conditions of Table I and subdivided according to lateral displacement control setting (B'_{1s}). In all, there are data for 25 combinations of flight condition/B'_{1s} settings.

Table VI (Page 100) lists all of the parameters plotted, together with their letter designations within each figure. For example, "Upper Rotor 1/2 PTP Flatwise Stress, R108" may be found in Part (c) of Figures 40 through 63. Table VI also indicates when a measurement is unavailable due to an inoperative gage or insufficient data. The letter designations for the data in the Appendix are held fixed, despite missing data, to provide for rapid reference to a particular measurement at different flight conditions.

TABLE VI. INDEX OF MEASURED DATA

Performance Data

Figure Letter	Parameter	Test Cond 1				Test Cond 2					Test Cond 3						Test Cond 4					Test Cond 5	Test Cond 6		Test Cond 7	
	B'_{1s}	0	2	4	6	0	2	4	6	8	0	2	4	6	8	10	0	2	4	6	8	2	2	4	2	4
	Figure	16	17	18	19	20	21	22	23	24	25	26	27	9	28	29	30	31	32	33	34	35	36	37	38	39
(a)	Drag Coefficient	Y	Y	Y	Y	Y	Y	Y	Y	Y	Y	Y	Y	Y	Y	Y	Y	Y	Y	Y	Y	Y	Y	Y	Y	Y
(b)	Torque Coefficient	Y	Y	Y	Y	Y	Y	Y	Y	Y	Y	Y	Y	Y	Y	Y	Y	Y	Y	Y	Y	Y	Y	Y	Y	Y
(c)	Lift-Drag Ratio	Y	Y	Y	Y	Y	Y	Y	Y	Y	Y	Y	Y	Y	Y	Y	Y	Y	Y	Y	Y	Y	Y	Y	Y	Y
(d)	Lift Lateral Displacement	Y	Y	Y	Y	Y	Y	Y	Y	Y	Y	Y	Y	Y	Y	Y	Y	Y	Y	Y	Y	Y	Y	Y	Y	Y
(e)	Longitudinal Cyclic Pitch	Y	Y	Y	Y	Y	Y	Y	Y	Y	Y	Y	Y	Y	Y	Y	Y	Y	Y	Y	Y	Y	Y	Y	Y	Y
(f)	Side Force Coefficient	Y	Y	Y	Y	Y	Y	Y	Y	Y	Y	Y	Y	Y	Y	Y	Y	Y	Y	Y	Y	Y	Y	Y	Y	Y
(g)	Rolling Moment Coefficient	Y	Y	Y	Y	Y	Y	Y	Y	Y	Y	Y	Y	Y	Y	Y	Y	Y	Y	Y	Y	Y	Y	Y	Y	Y
(h)	Pitching Moment Coefficient	Y	Y	Y	Y	Y	Y	Y	Y	Y	Y	Y	Y	Y	Y	Y	Y	Y	Y	Y	Y	Y	Y	Y	Y	Y
(i)	Yawing Moment Coefficient	Y	Y	Y	Y	Y	Y	Y	Y	Y	Y	Y	Y	Y	Y	Y	Y	Y	Y	Y	Y	Y	Y	Y	Y	Y
(j)	Hub vs Balance RM Coefficient	N	N	N	N	N	N	N	N	N	N	N	N	N	N	N	N	N	N	N	N	N	Y	Y	Y	Y
(k)	Hub vs Balance PM Coefficient	N	N	N	N	N	N	N	N	N	N	N	N	N	N	N	N	N	N	N	N	N	Y	Y	Y	Y
(l)	Wattmeter vs Balance YM Coeff	N	N	N	N	N	N	N	N	N	N	N	N	N	N	N	N	N	N	N	N	N	Y	Y	Y	Y

TABLE VI - Concluded

Stress, Load, and Vibration Data

Figure Letter	Parameter	Test Cond 1, B'_{1s} 0	2	4	6	Test Cond 2, B'_{1s} 0	2	4	6	8	Test Cond 3, B'_{1s} 0	2	4	6	8	10	Test Cond 4, B'_{1s} 0	2	4	6	8	Test Cond 5, B'_{1s} 2	Test Cond 6, B'_{1s} 2	4	Test Cond 7, B'_{1s} 2	4
		Figure 40	41	42	43	Figure 44	45	46	47	48	Figure 49	50	51	12	52	53	Figure 54	55	56	57	58	Fig 59	Figure 60	61	Figure 62	63
(a)	UR Flatwise Stress, R84	Y	Y	Y	Y	Y	Y	Y	Y	Y	Y	Y	Y	Y	Y	Y	Y	Y	Y	Y	Y	Y	Y	Y	Y	Y
(b)	LR Flatwise Stress, R84	N	N	N	N	Y	Y	Y	N	N	N	Y	Y	Y	Y	Y	Y	Y	Y	Y	N	Y	N	N	N	N
(c)	UR Flatwise Stress, R108	Y	Y	Y	Y	Y	Y	Y	Y	Y	Y	Y	Y	Y	Y	Y	Y	Y	Y	Y	Y	Y	Y	Y	Y	Y
(d)	UR Flatwise Stress, R132	Y	Y	Y	Y	Y	Y	Y	Y	Y	Y	Y	Y	Y	Y	Y	Y	Y	Y	Y	Y	Y	Y	Y	Y	Y
(e)	LR Flatwise Stress, R132	N	N	N	N	N	N	N	N	N	Y	Y	Y	Y	Y	N	Y	Y	Y	Y	Y	Y	N	N	N	N
(f)	UR Flatwise Stress, R204	Y	Y	Y	Y	Y	Y	Y	Y	Y	Y	Y	Y	Y	Y	Y	Y	Y	Y	Y	Y	Y	Y	Y	Y	Y
(g)	UR Edgewise Stress, R60	Y	Y	Y	Y	N	N	N	N	N	N	N	N	N	N	N	N	N	N	N	N	N	N	N	N	N
(h)	UR Edgewise Stress, R84	Y	Y	Y	Y	Y	Y	Y	Y	Y	Y	Y	Y	Y	Y	Y	Y	Y	Y	Y	Y	Y	Y	Y	Y	Y
(i)	LR Edgewise Stress, R84	N	Y	Y	Y	N	Y	Y	Y	Y	N	N	N	N	N	N	N	N	N	N	N	N	N	N	N	N
(j)	UR Edgewise Stress, R132	Y	Y	Y	Y	Y	Y	Y	Y	Y	Y	Y	Y	Y	Y	Y	Y	Y	Y	Y	Y	Y	Y	Y	Y	Y
(k)	UR Edgewise Stress, R168	Y	Y	Y	Y	Y	Y	Y	Y	Y	Y	Y	Y	Y	Y	Y	Y	Y	Y	Y	Y	Y	Y	Y	Y	Y
(l)	UR Torsional Moment, R82*	Y	Y	Y	Y	N	Y	Y	Y	Y	N	N	N	N	N	N	N	N	N	N	N	N	N	N	N	N
(m)	UR Torsional Moment, R130*	Y	Y	Y	Y	Y	Y	Y	Y	Y	Y	Y	Y	Y	Y	Y	Y	Y	Y	Y	Y	Y	Y	Y	Y	Y
(n)	UR Pushrod Load	Y	Y	Y	Y	Y	Y	Y	Y	Y	Y	Y	Y	Y	Y	Y	Y	Y	Y	Y	Y	Y	Y	Y	Y	Y
(o)	LR Pushrod Load	Y	Y	Y	Y	N	Y	Y	Y	Y	Y	Y	Y	Y	Y	N	N	Y	N	Y	Y	N	N	N	N	N
(p)	UR Right Lat Servo Load	Y	Y	Y	Y	Y	Y	Y	Y	Y	Y	Y	Y	Y	Y	Y	Y	Y	Y	Y	Y	Y	Y	Y	Y	Y
(q)	LR Right Lat Servo Load	Y	Y	Y	Y	Y	Y	Y	Y	Y	Y	Y	Y	Y	Y	Y	Y	Y	Y	Y	Y	Y	N	N	N	N
(r)	UR Fore and Aft Servo Load	Y	Y	Y	Y	Y	Y	Y	Y	Y	Y	Y	Y	Y	Y	Y	Y	Y	Y	Y	Y	Y	Y	Y	Y	Y
(s)	LR Fore and Aft Servo Load	Y	Y	Y	Y	Y	Y	Y	Y	Y	Y	Y	Y	Y	Y	Y	Y	Y	Y	Y	Y	Y	N	N	N	N
(t)	UR Hub Total Stress No. 2	Y	Y	Y	Y	Y	Y	Y	Y	Y	Y	Y	Y	Y	Y	Y	Y	Y	Y	Y	Y	Y	Y	Y	Y	Y
(u)	Gearbox Lat Acceleration	Y	Y	Y	Y	Y	Y	Y	Y	Y	Y	Y	Y	Y	Y	Y	Y	Y	Y	Y	Y	Y	Y	Y	Y	Y
(v)	Gearbox Long. Acceleration	Y	Y	Y	Y	Y	Y	Y	Y	Y	Y	Y	Y	Y	Y	Y	Y	Y	Y	Y	Y	Y	Y	Y	Y	Y
(w)	Right Strut Lat Acceleration	Y	Y	Y	Y	Y	Y	Y	Y	Y	Y	Y	Y	Y	Y	Y	Y	Y	Y	Y	Y	Y	Y	Y	Y	Y
(x)	Right Strut Long.Acceleration	Y	Y	Y	Y	Y	Y	Y	Y	Y	Y	Y	Y	Y	Y	Y	Y	Y	Y	Y	Y	Y	Y	Y	Y	Y

NOTES:
- Y Plot available
- N Plot not available
- R Distance from center of rotation to blade radial station, in.
- * Torsional moment data unreliable due to sensitivity and crosstalk (See "Discussion of Stresses and Loads" section)

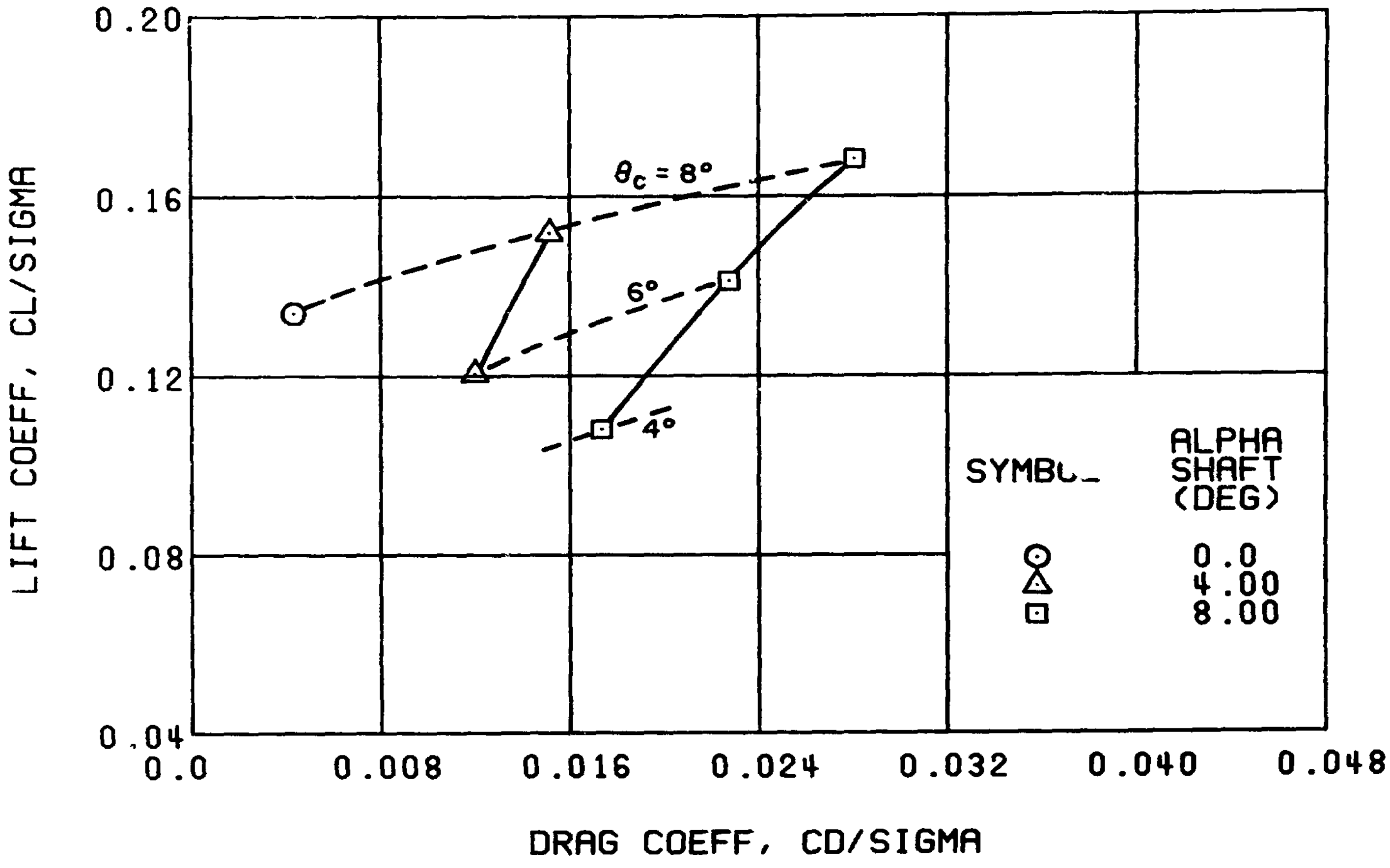

(a) DRAG COEFFICIENT

Figure 16. Performance Data at an Advance Ratio of 0.21 With the Lateral Displacement Control (B'_{1s}) Set at 0 Degrees.

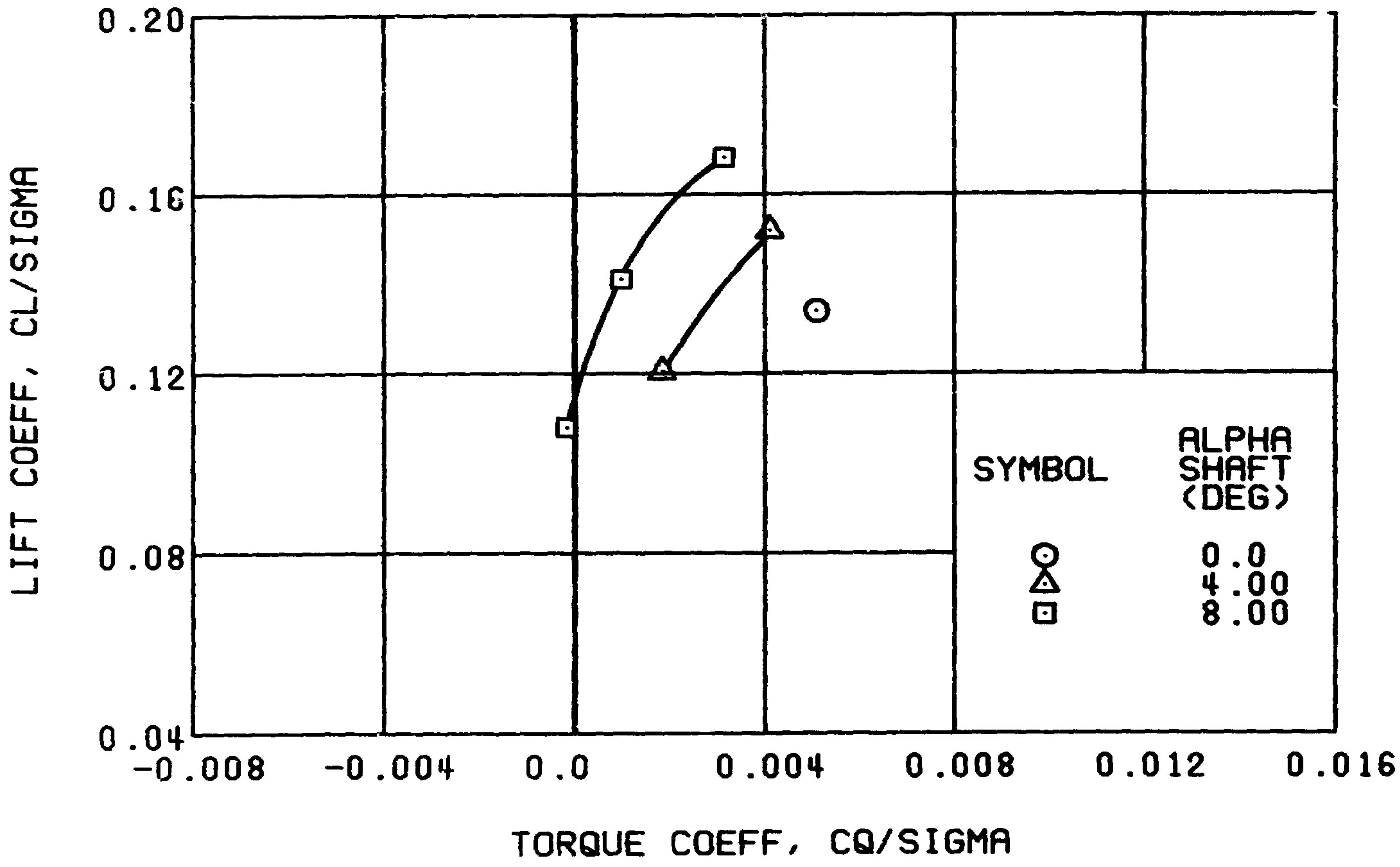

(b) TORQUE COEFFICIENT

Figure 16. Continued.
$\mu = 0.21 \quad B'_{1s} = 0$ Deg

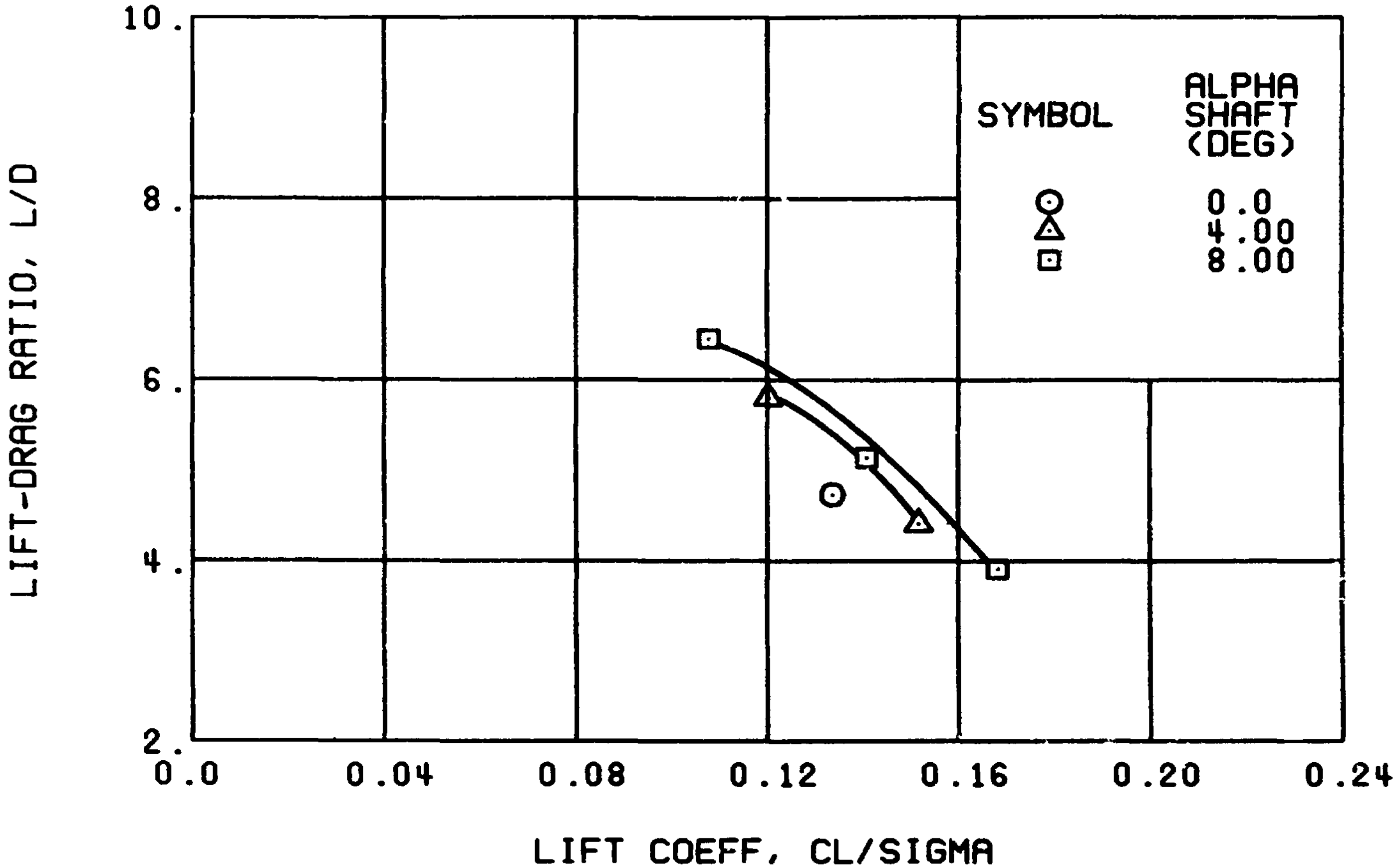

(c) LIFT-DRAG RATIO

Figure 16. Continued.
μ = 0.21 B'_{1s} = 0 Deg

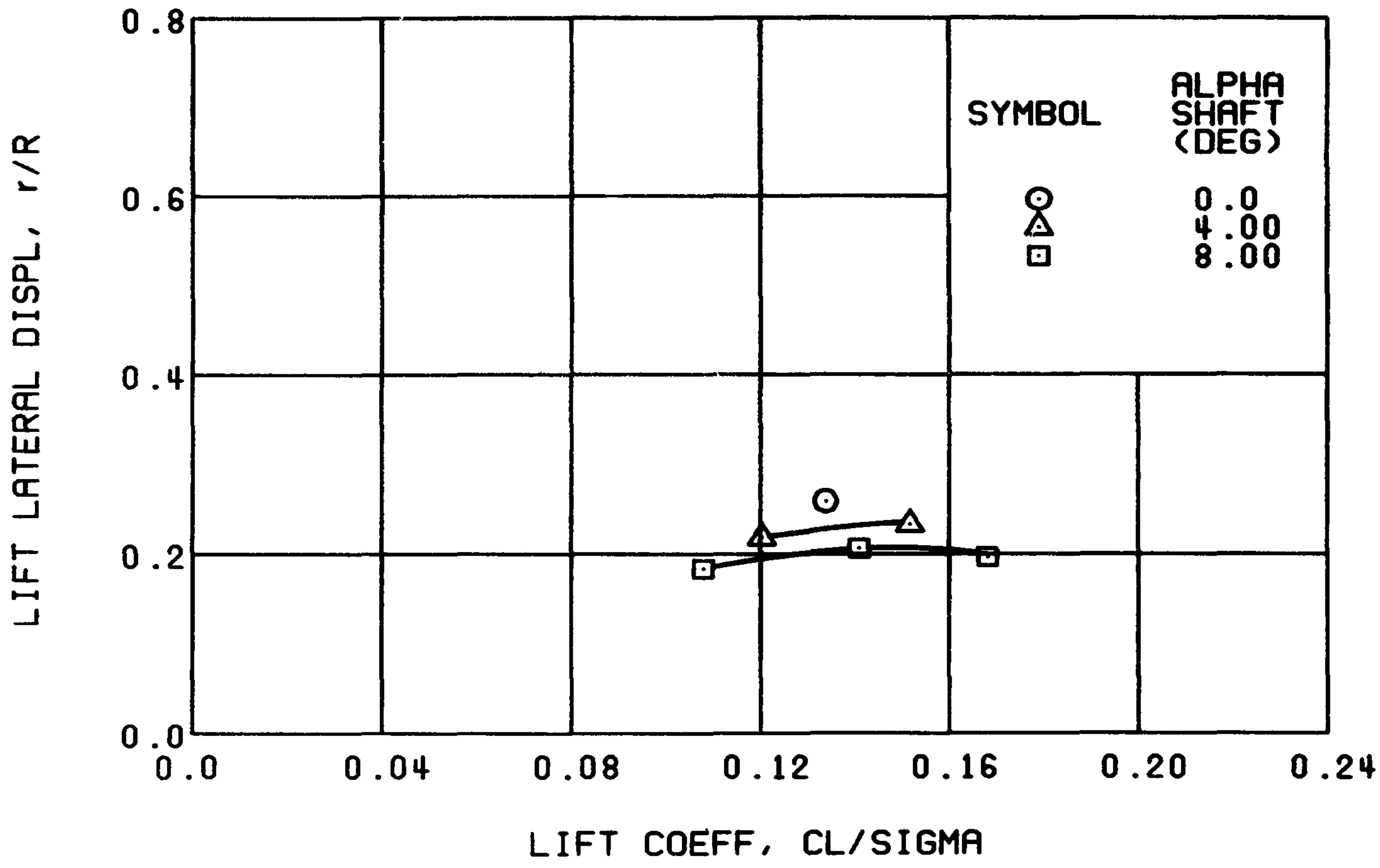

(d) LIFT LATERAL DISPLACEMENT

Figure 16. Continued.
μ = 0.21 B'_{1s} = 0 Deg

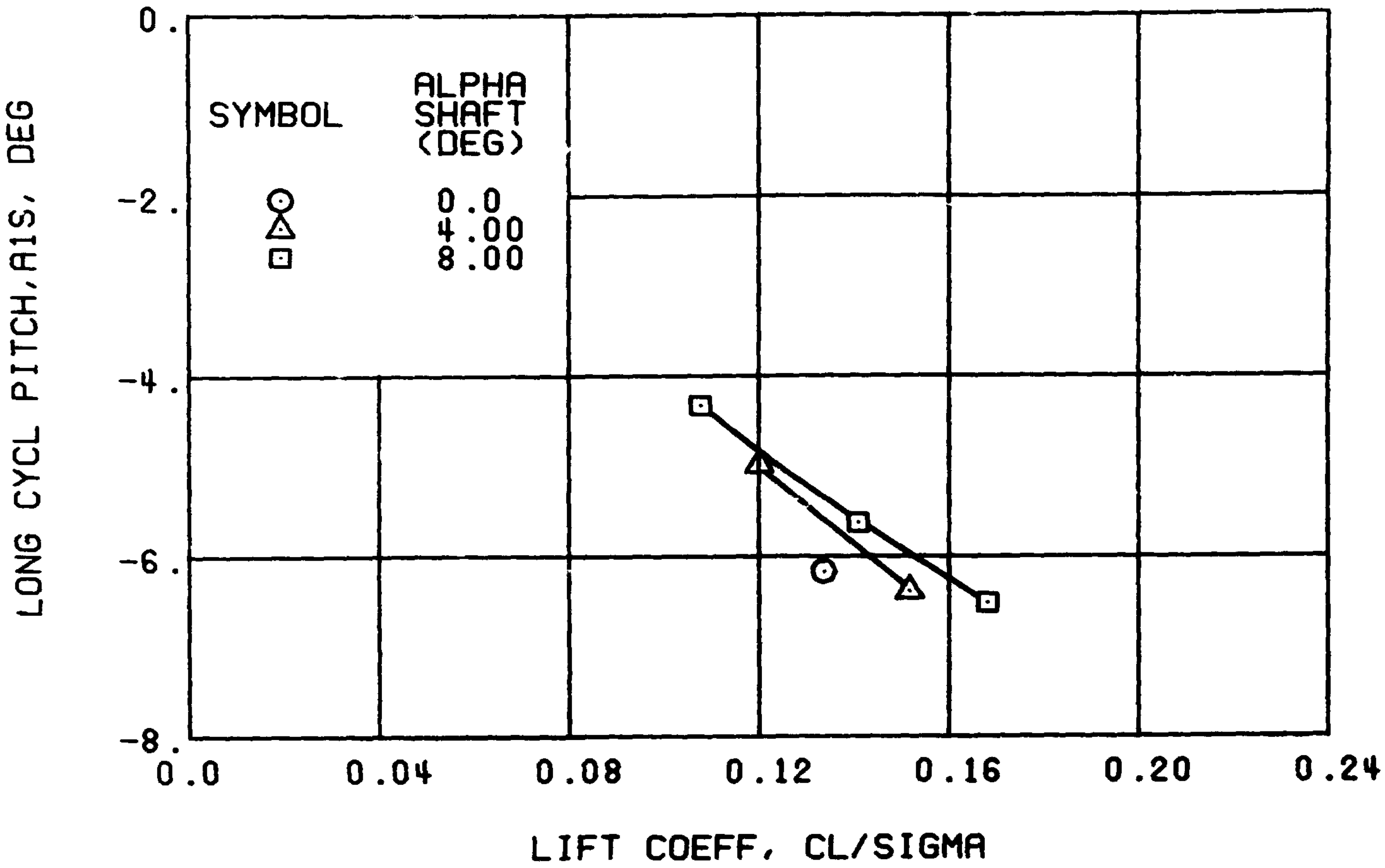

(e) LONGITUDINAL CYCLIC PITCH

Figure 16. Continued.
$\mu = 0.21 \quad B'_{1s} = 0$ **Deg**

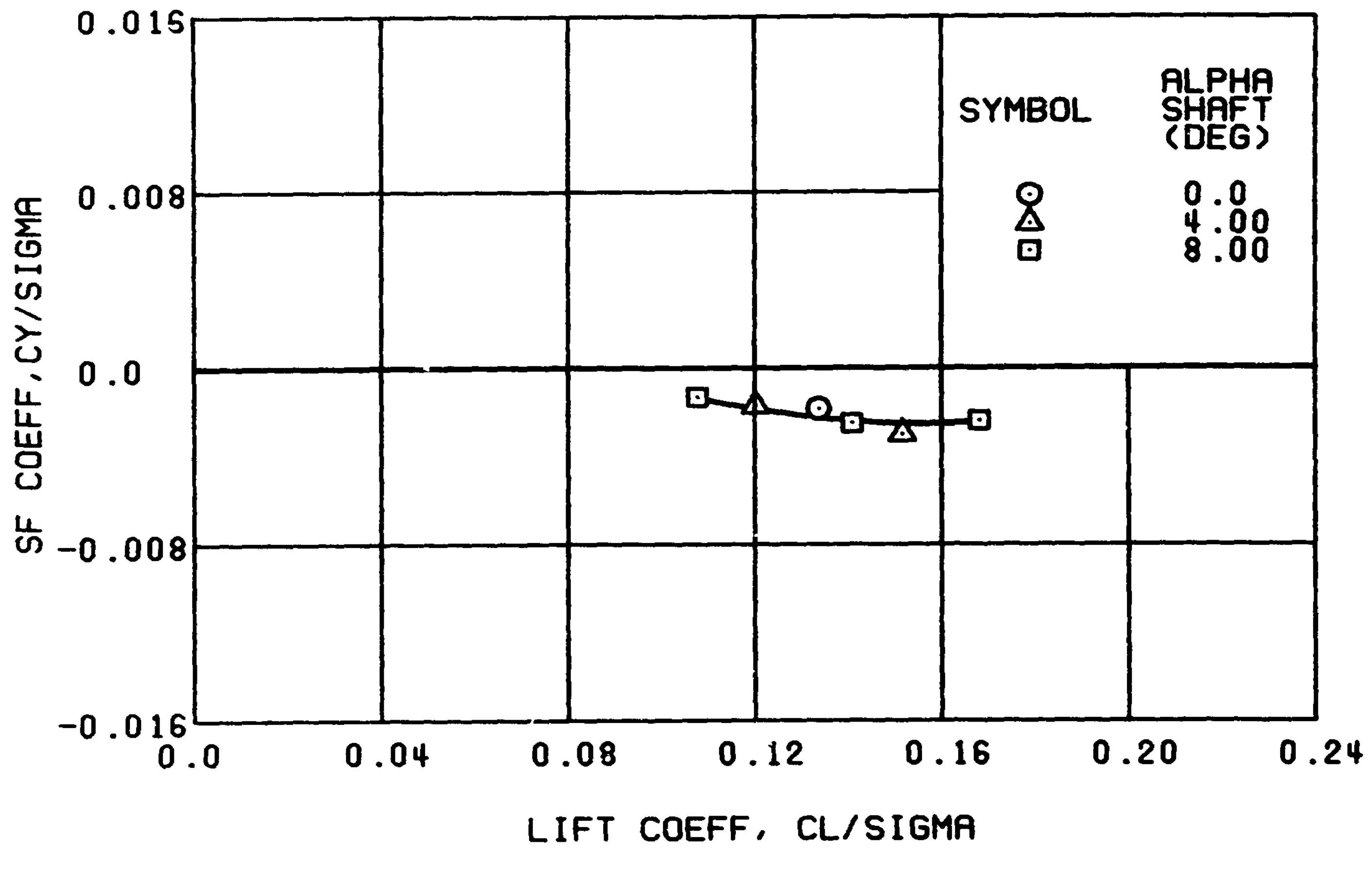

(f) SIDE FORCE COEFFICIENT

Figure 16. Continued.
μ = 0.21 B'_{1s} = 0 Deg

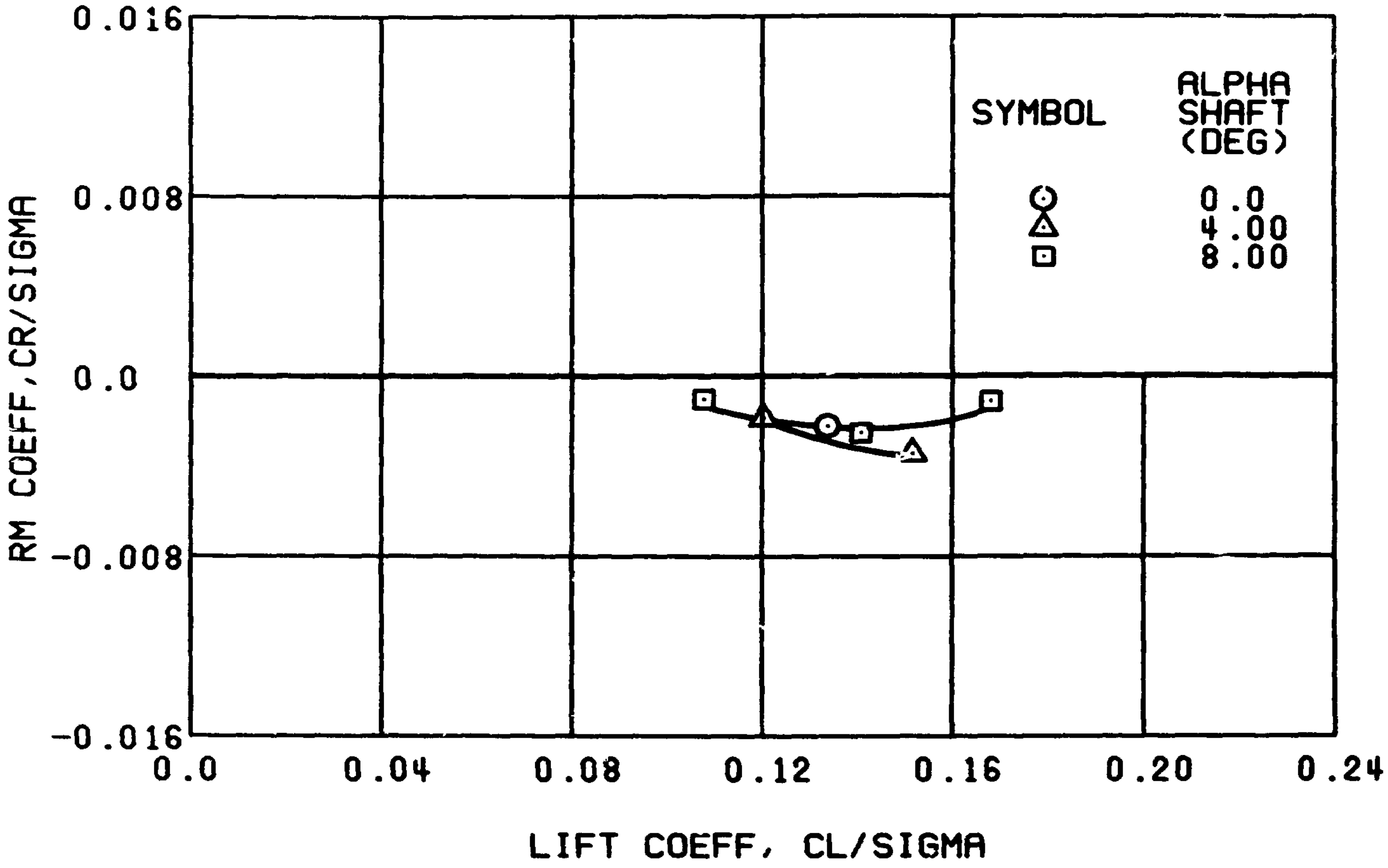

(g) ROLLING MOMENT COEFFICIENT

Figure 16. Continued.
$\mu = 0.21 \quad B'_{1s} = 0$ Deg

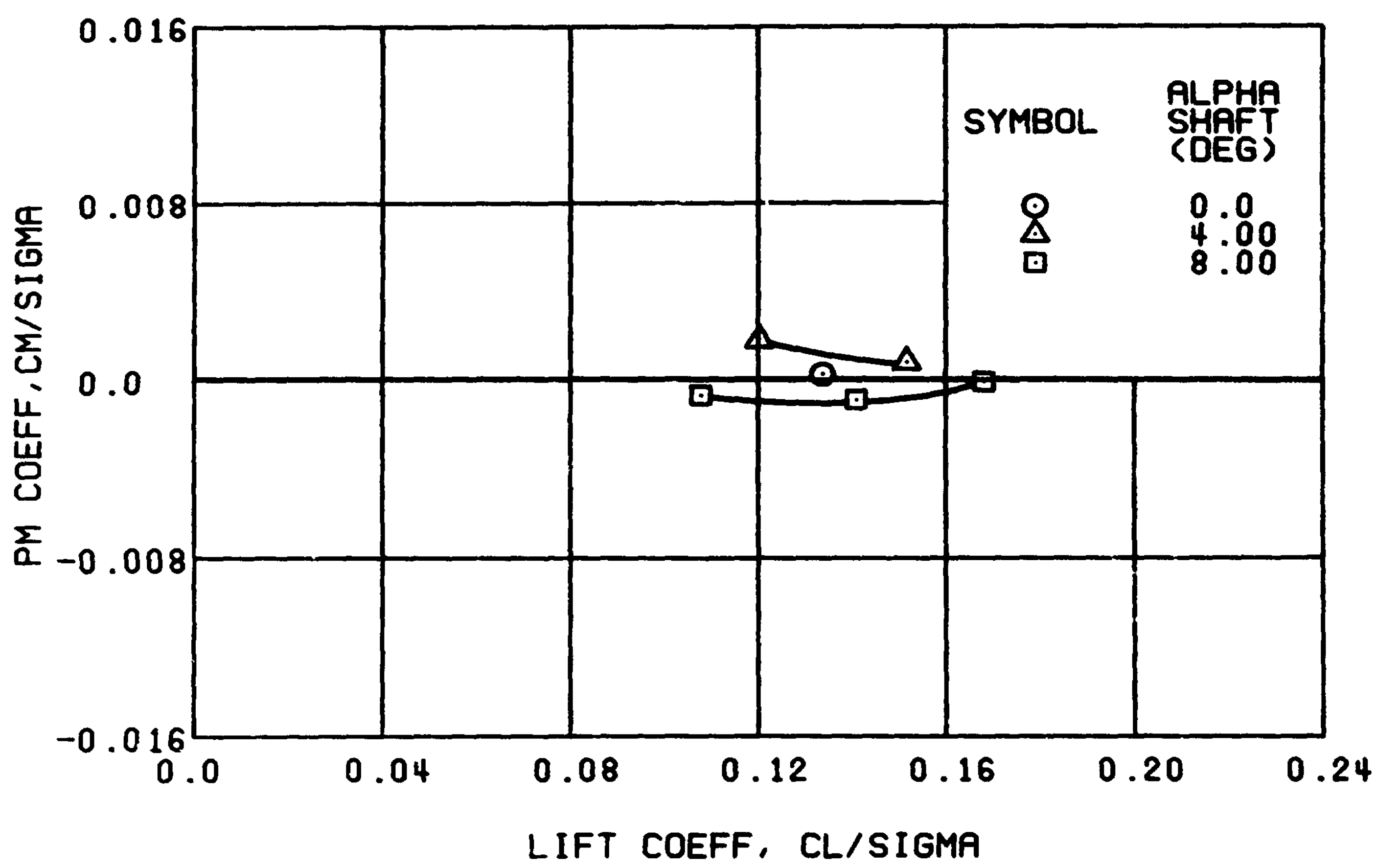

(h) PITCHING MOMENT COEFFICIENT

Figure 16. Continued.
$\mu = 0.21$ $B'_{1s} = 0$ Deg

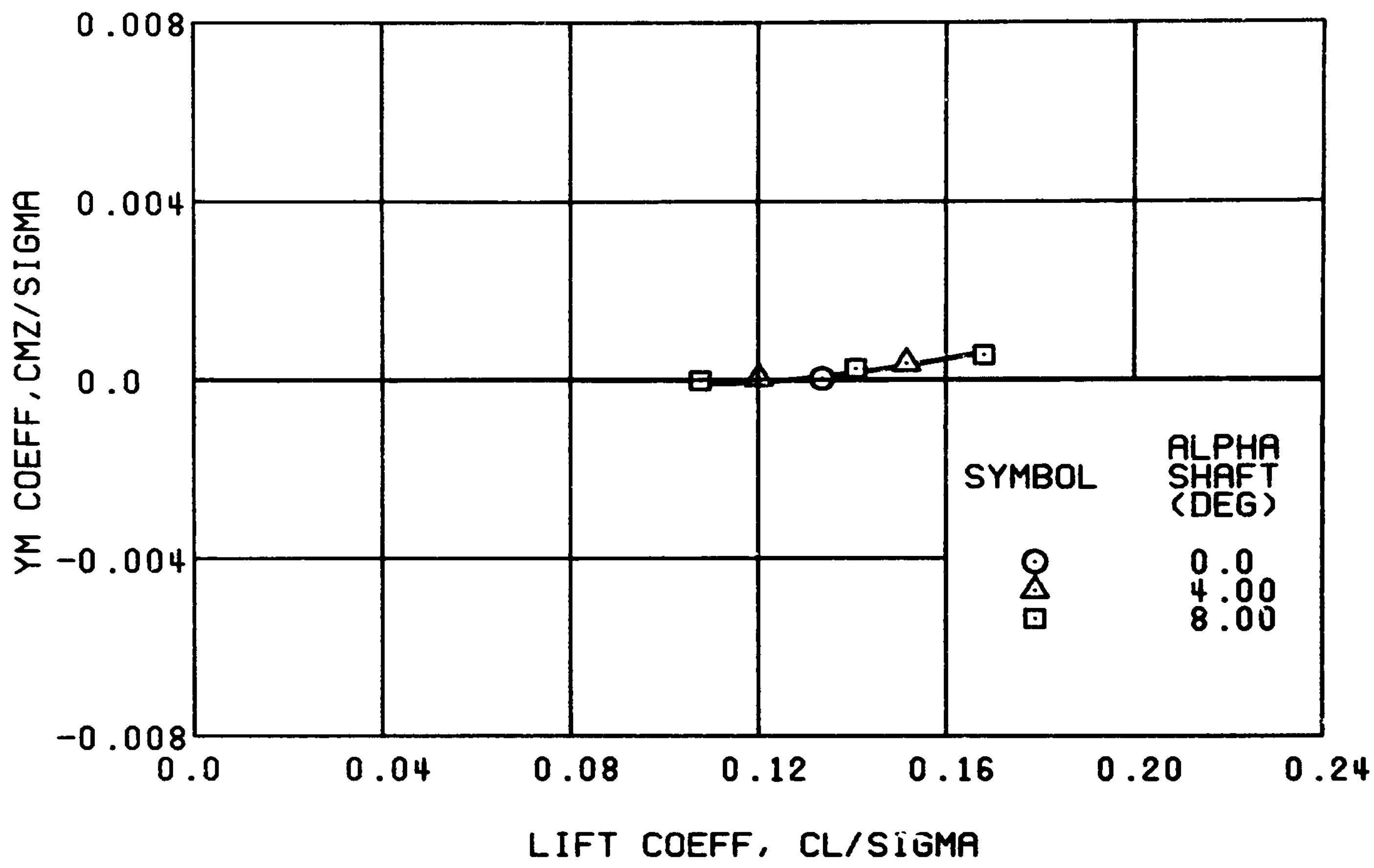

(i) YAWING MOMENT COEFFICIENT

Figure 16. Concluded.
$\mu = 0.21 \quad B'_{1s} = 0$ Deg

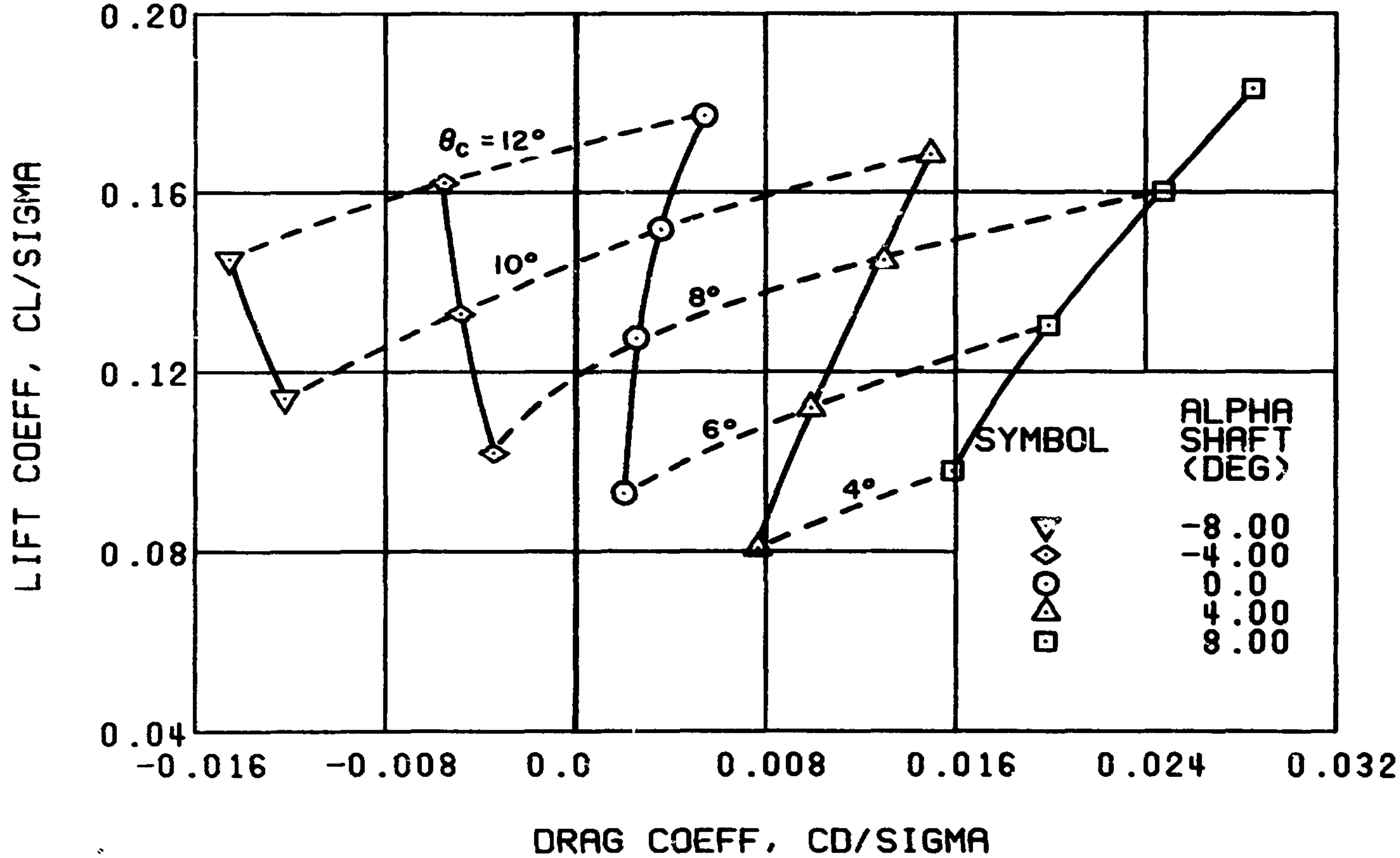

(a) DRAG COEFFICIENT

Figure 17. Performance Data at an Advance Ratio of 0.21 With the Lateral Displacement Control (B'_{1s}) Set at 2 Degrees.

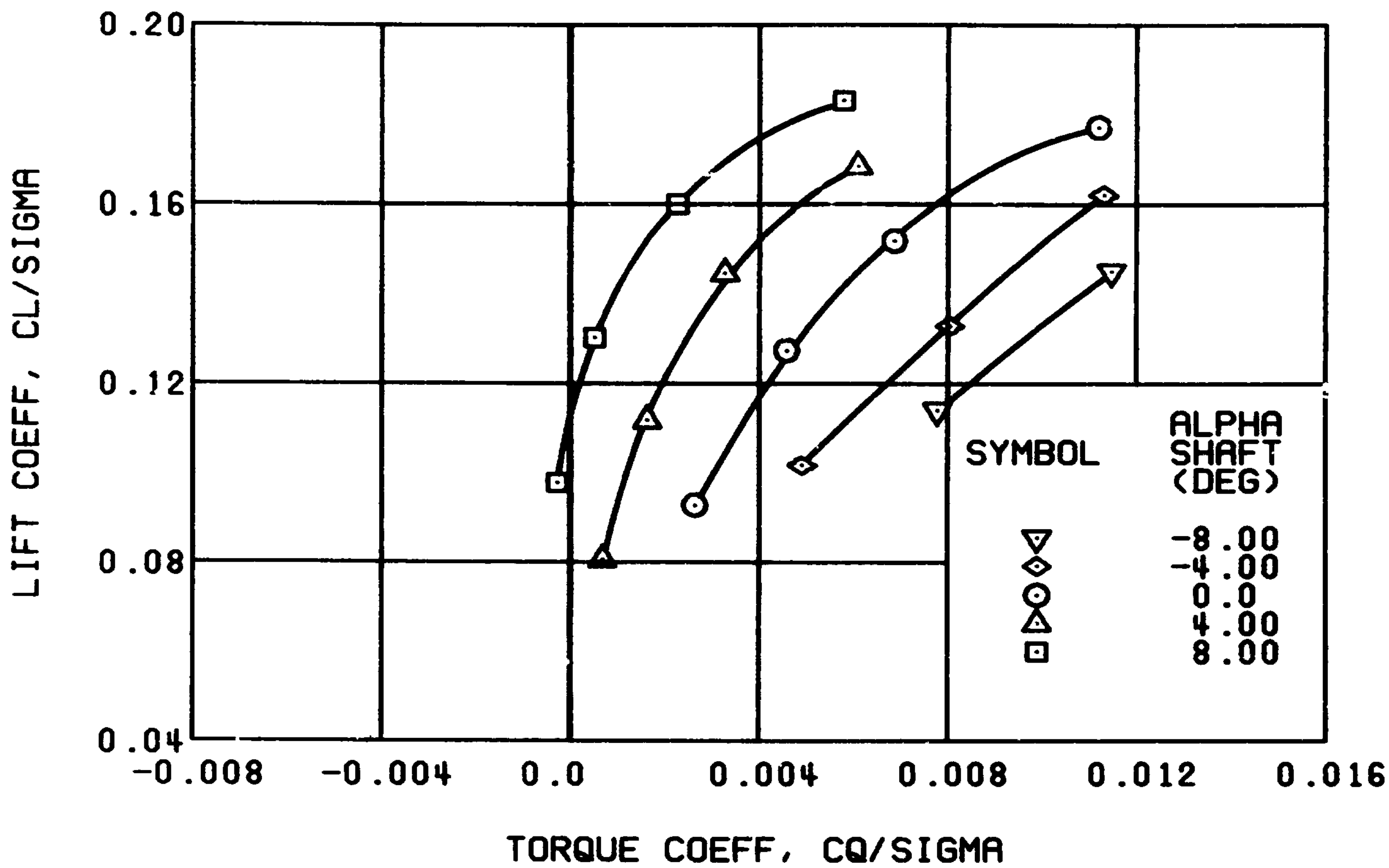

(b) TORQUE COEFFICIENT

Figure 17. Continued.
$\mu = 0.21 \quad B'_{1s} = 2$ Deg

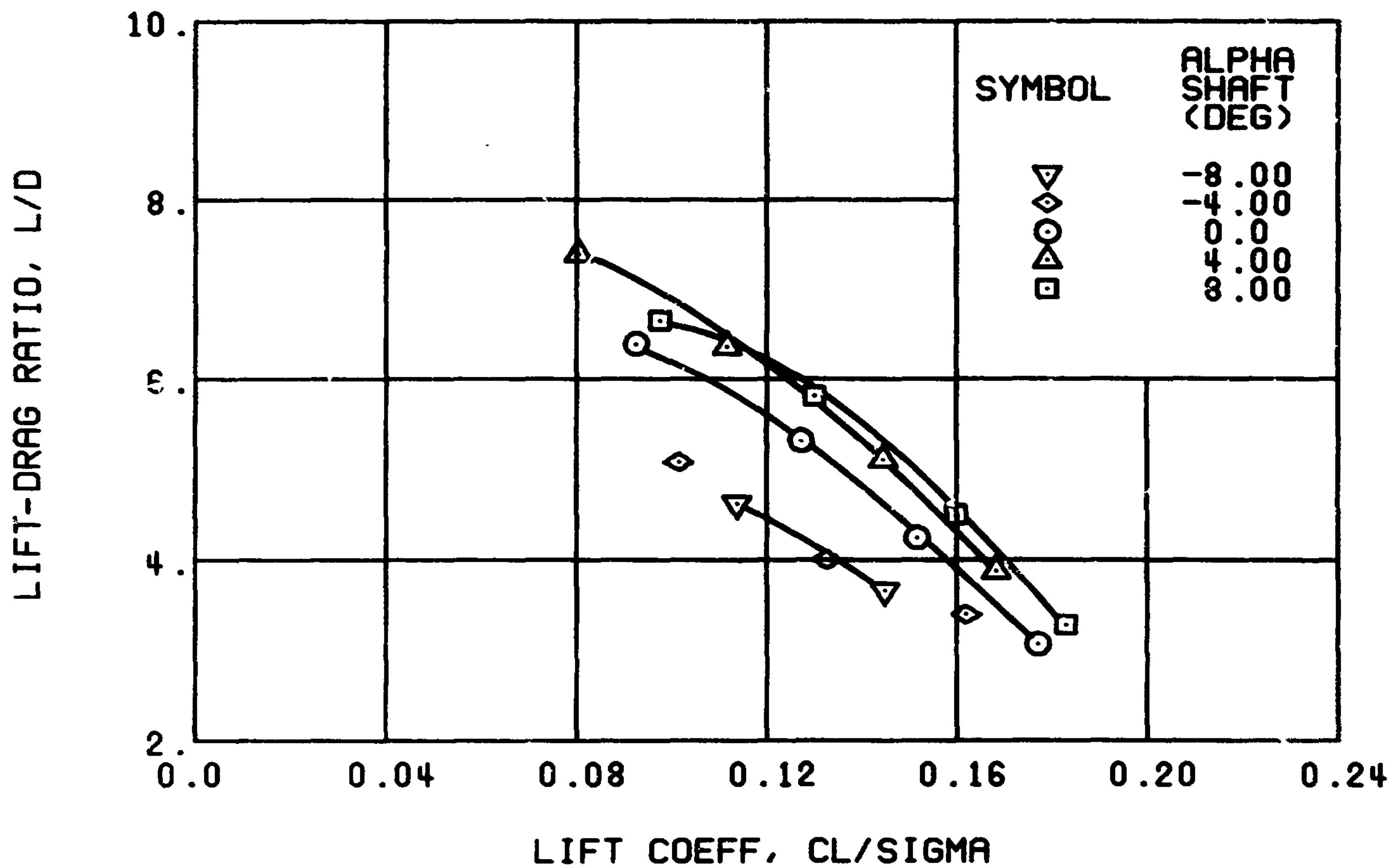

(c) LIFT-DRAG RATIO

Figure 17. Continued.
$\mu = 0.21 \quad B'_{1s} = 2$ Deg

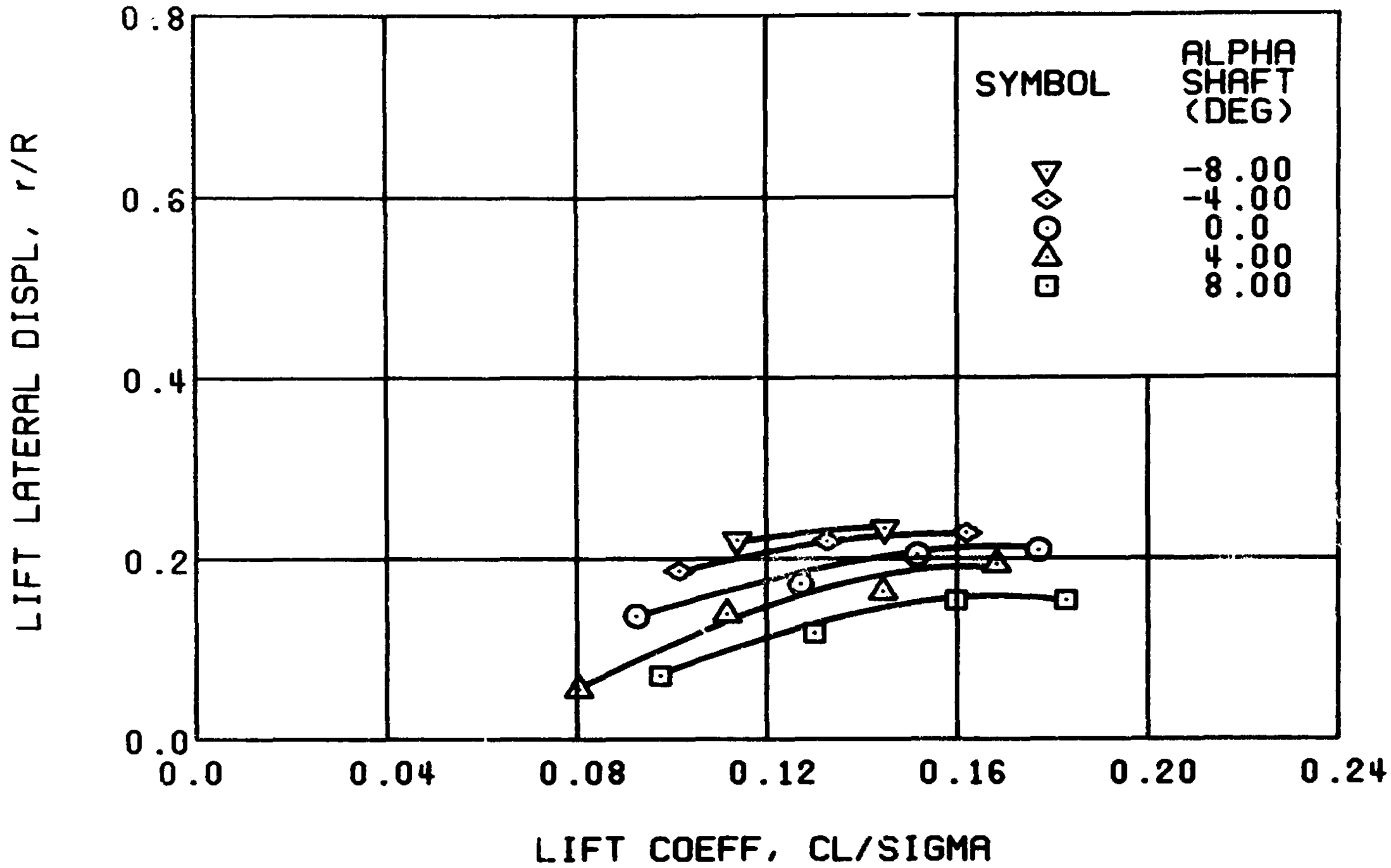

(d) LIFT LATERAL DISPLACEMENT

Figure 17. Continued.
$\mu = 0.21$ $B'_{1s} = 2$ Deg

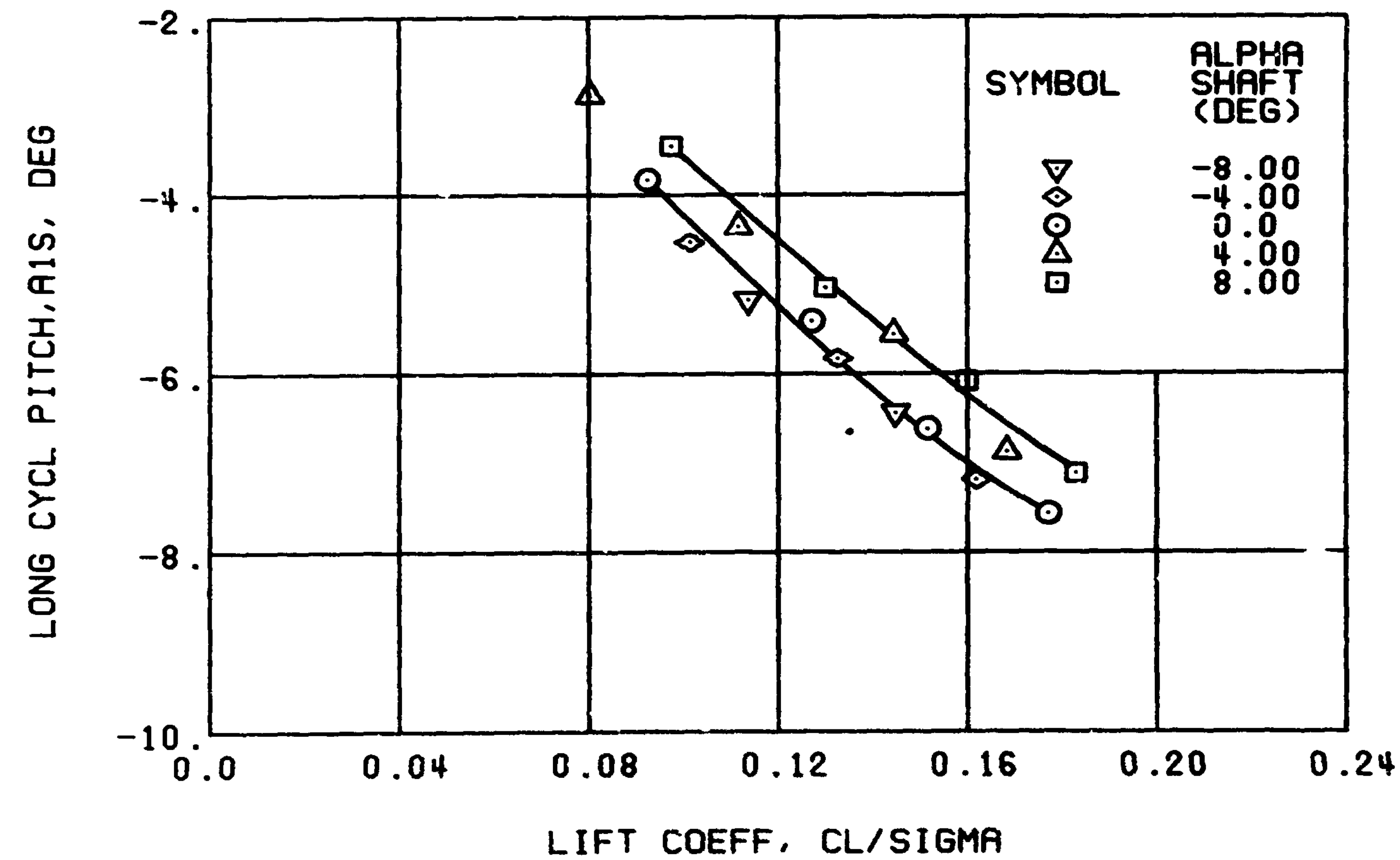

(e) LONGITUDINAL CYCLIC PITCH

Figure 17. Continued.
$\mu = 0.21$ $B'_{1s} = 2$ Deg

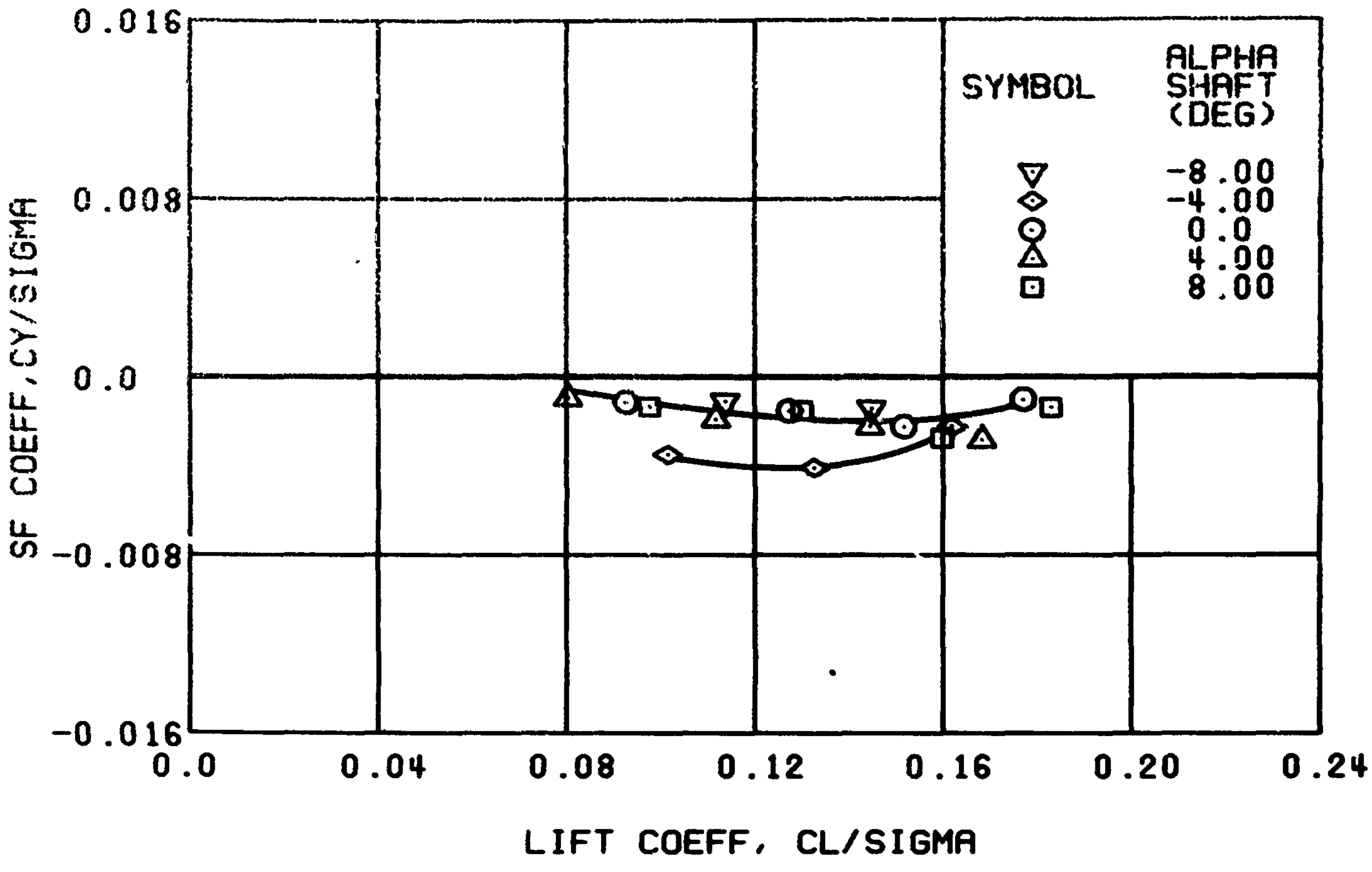

(f) SIDE FORCE COEFFICIENT

Figure 17. Continued.
μ = 0.21 B'_{1s} = 2 Deg

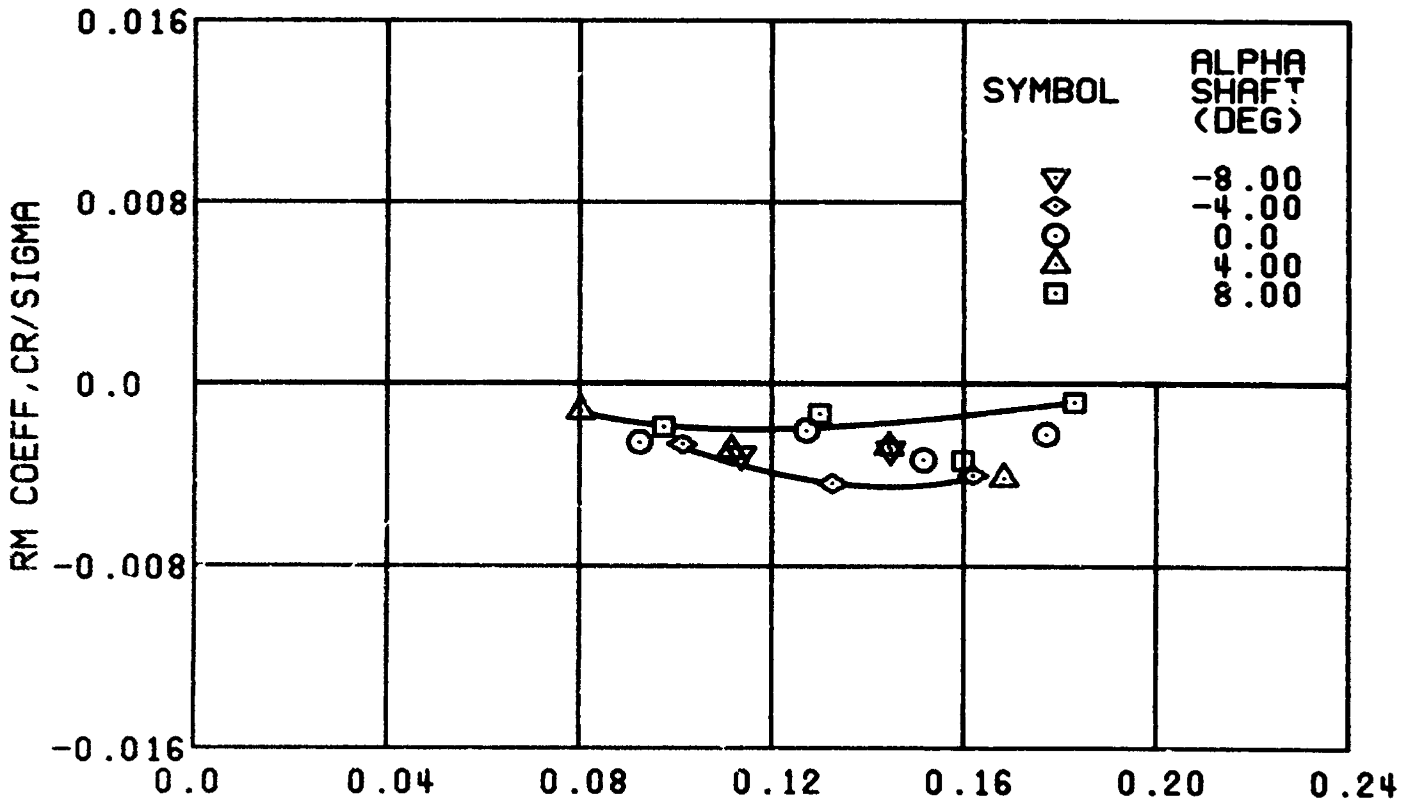

(g) ROLLING MOMENT COEFFICIENT

Figure 17. Continued.
$\mu = 0.21$ $B'_{1s} = 2$ Deg

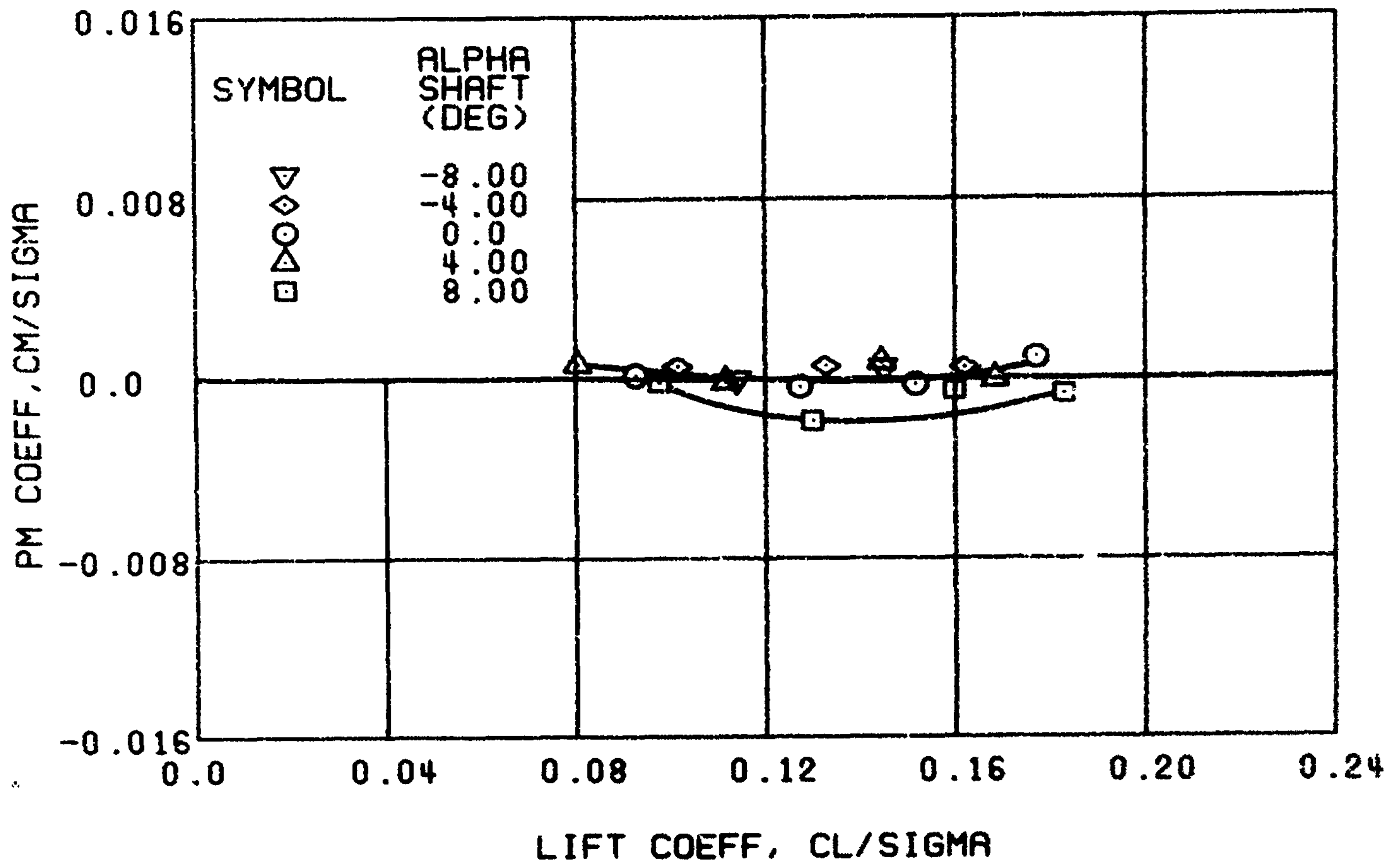

(h) PITCHING MOMENT COEFFICIENT

Figure 17. Continued.
μ = 0.21 B'_{1s} = 2 Deg

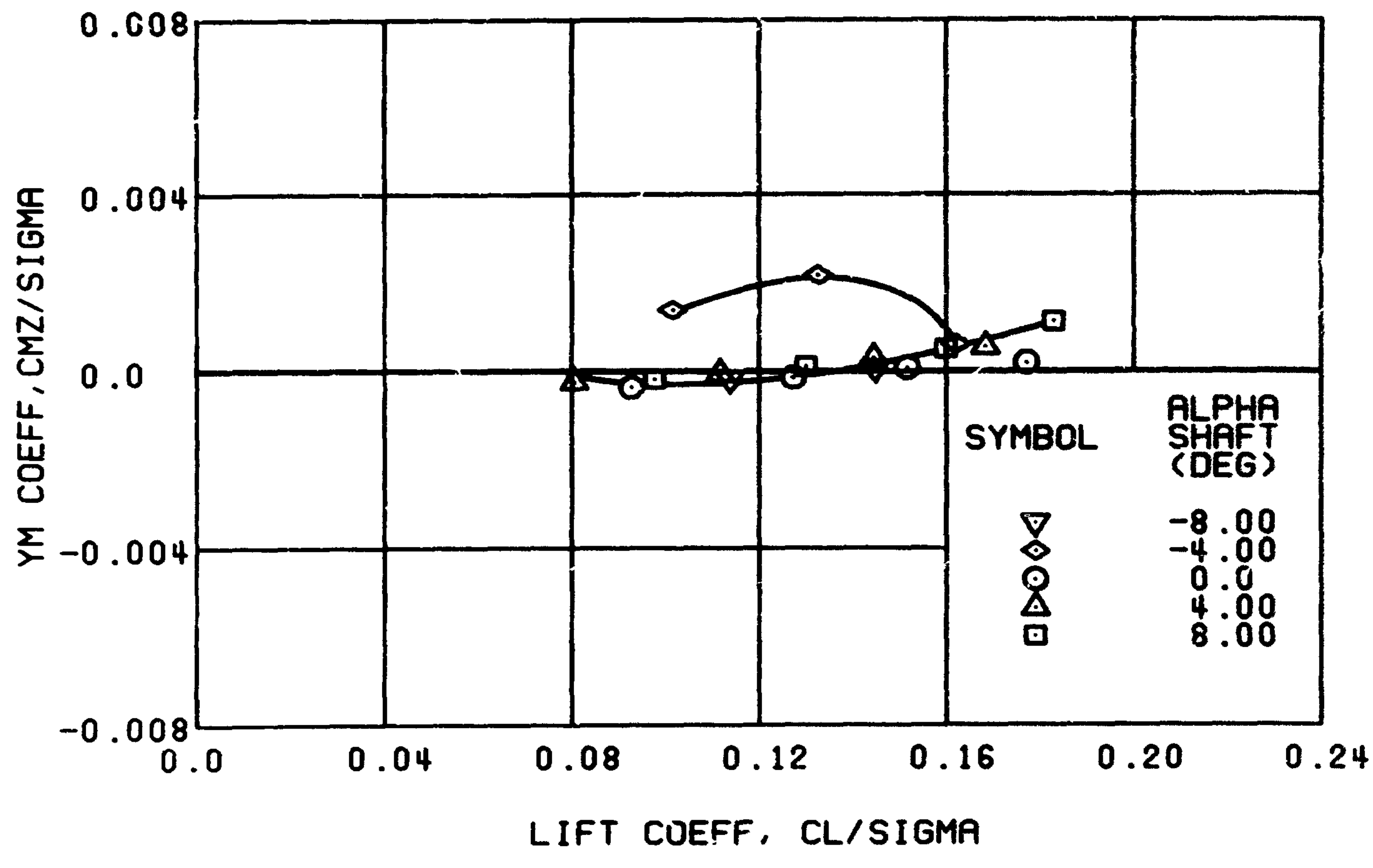

(i) YAWING MOMENT COEFFICIENT

Figure 17. Concluded.
$\mu = 0.21 \quad B'_{1s} = 2$ Deg

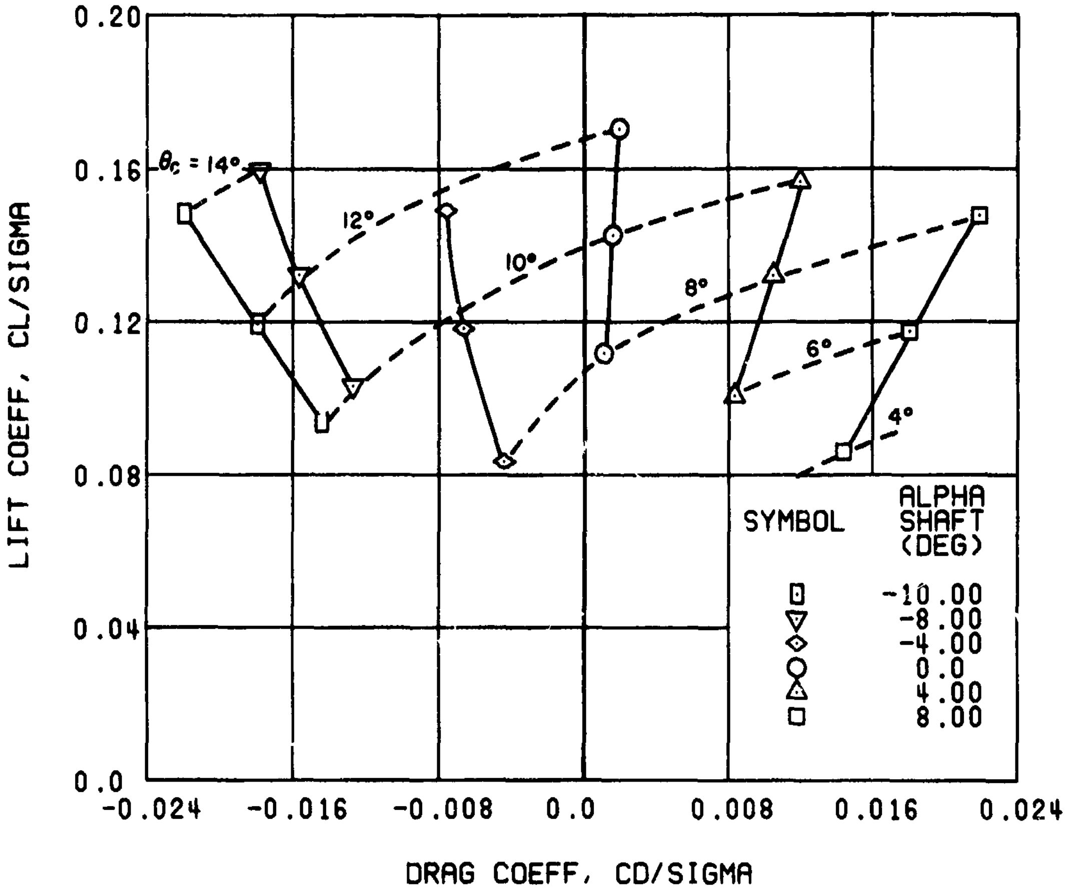

(a) DRAG COEFFICIENT

Figure 18. Performance Data at an Advance Ratio of 0.21 With the Lateral Displacement Control (B'_{1s}) Set at 4 Degrees.

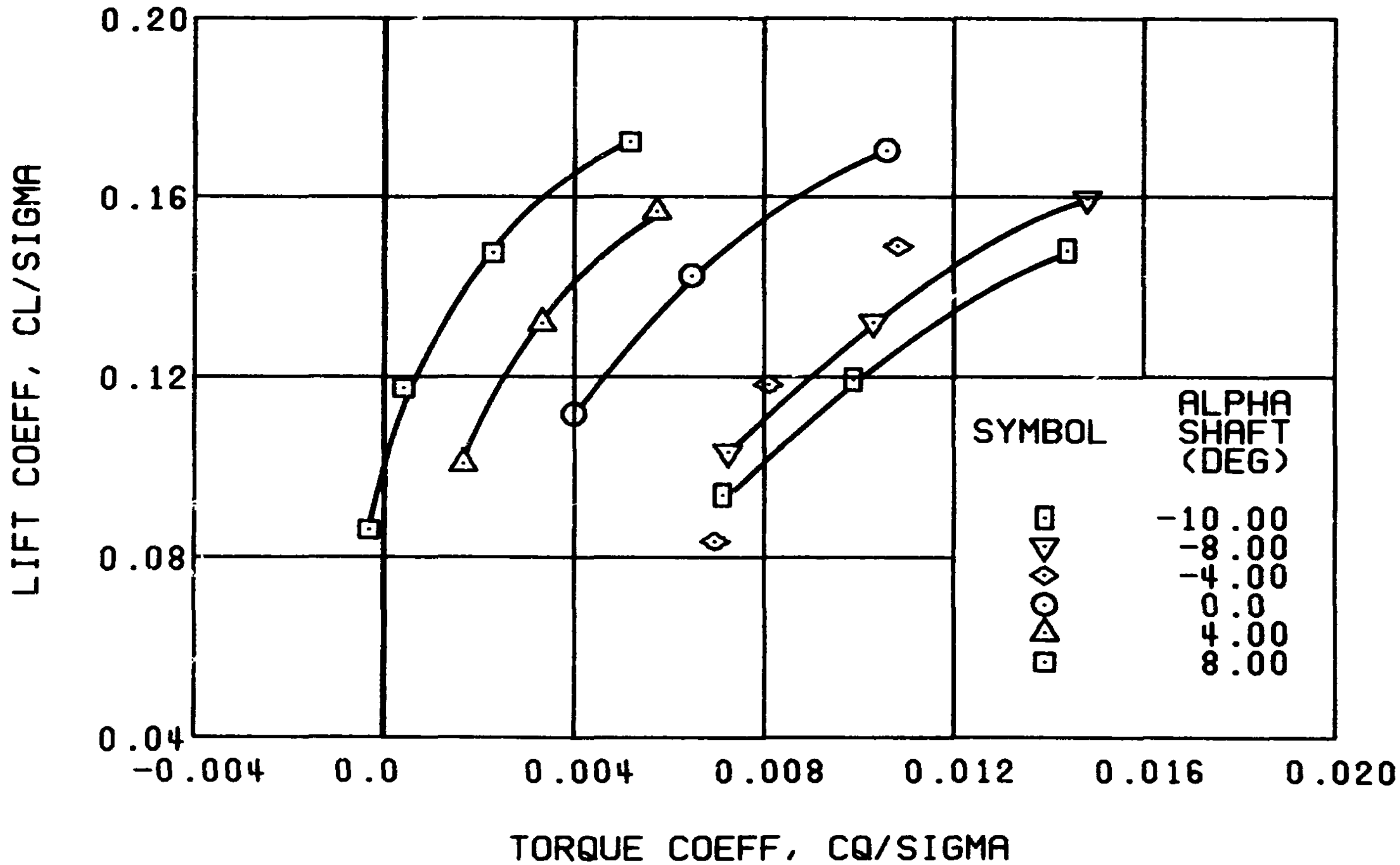

(b) TORQUE COEFFICIENT

Figure 18. Continued.
$\mu = 0.21 \quad B'_{1s} = 4$ **Deg**

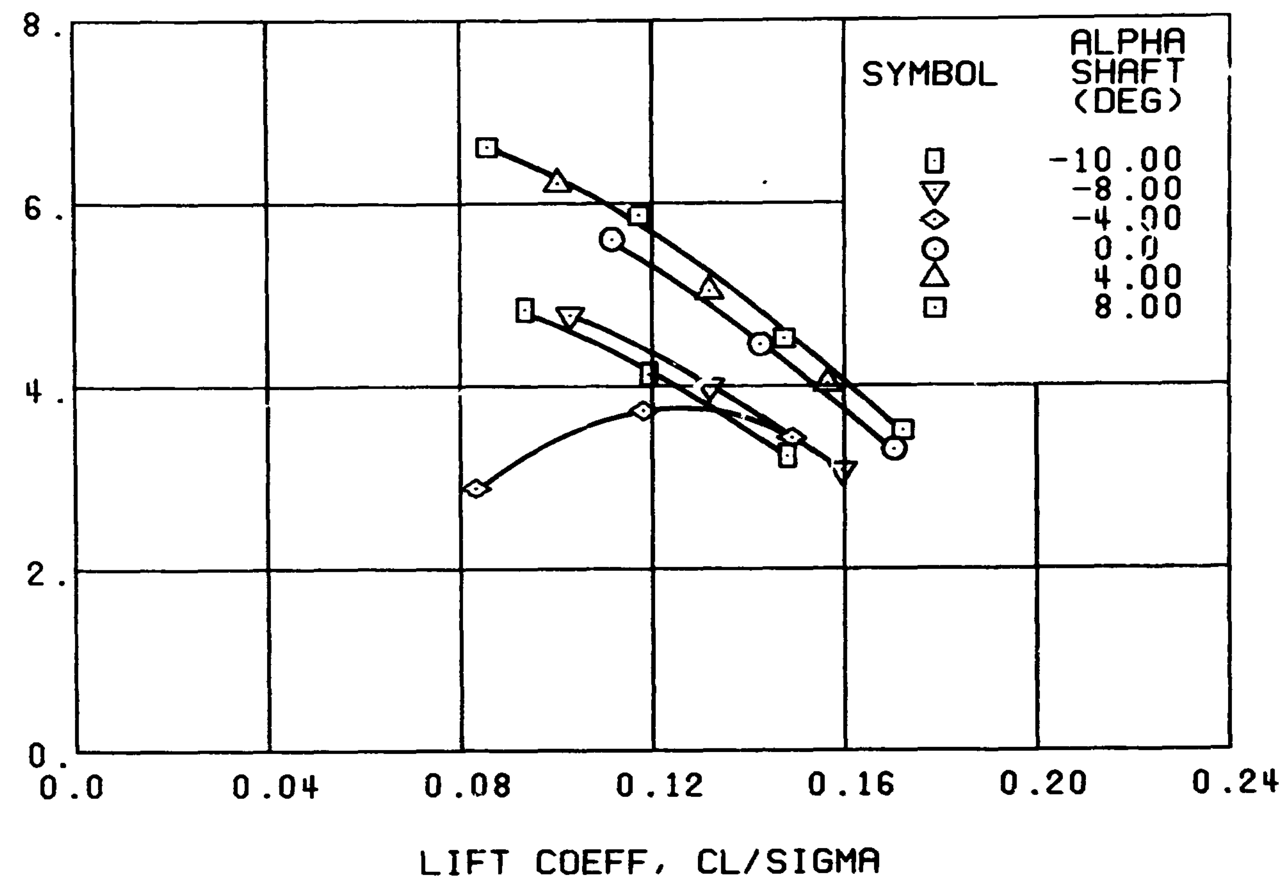

(c) LIFT-DRAG RATIO

Figure 18. Continued.
$\mu = 0.21 \quad B'_{1s} = 4$ Deg

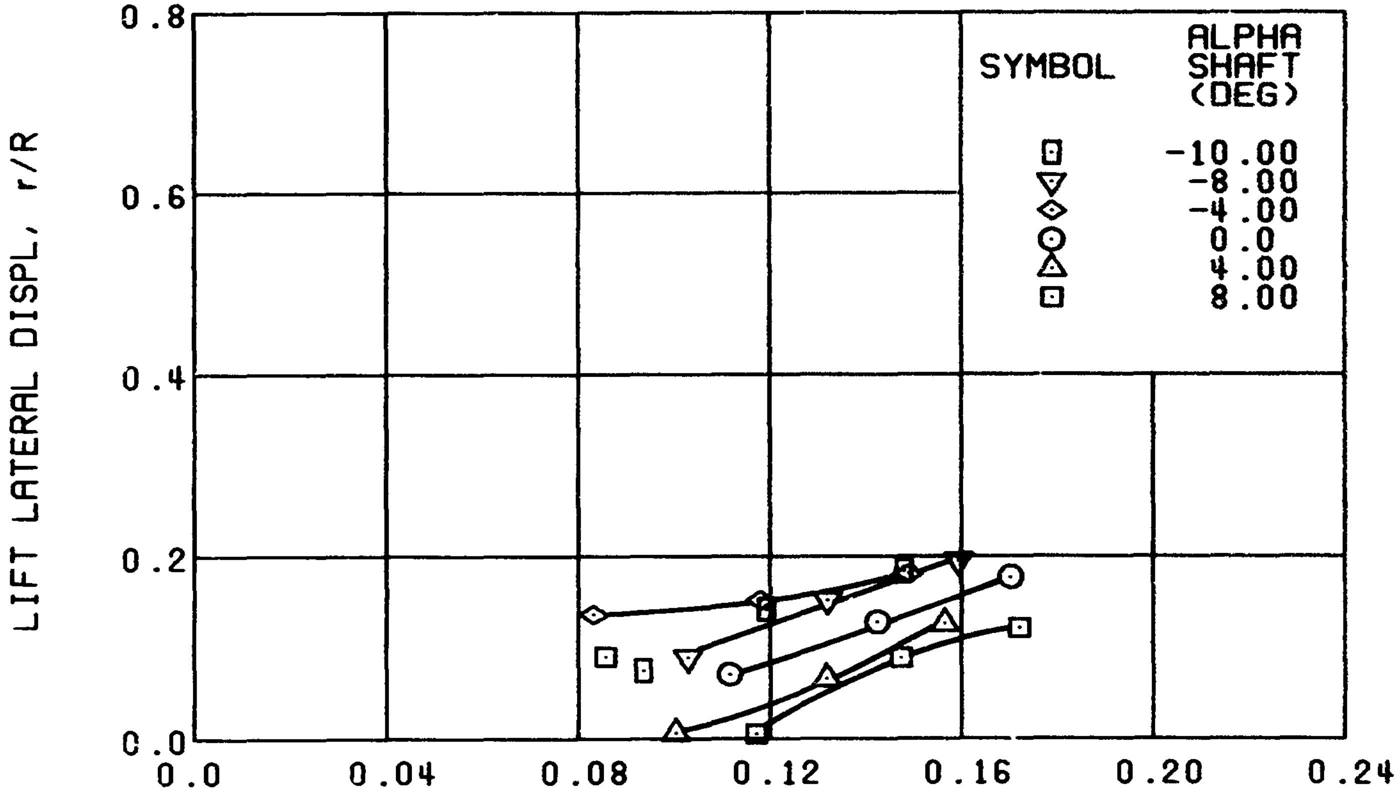

(d) LIFT LATERAL DISPLACEMENT

Figure 18. Continued.
$\mu = 0.21 \quad B'_{1s} = 4$ Deg

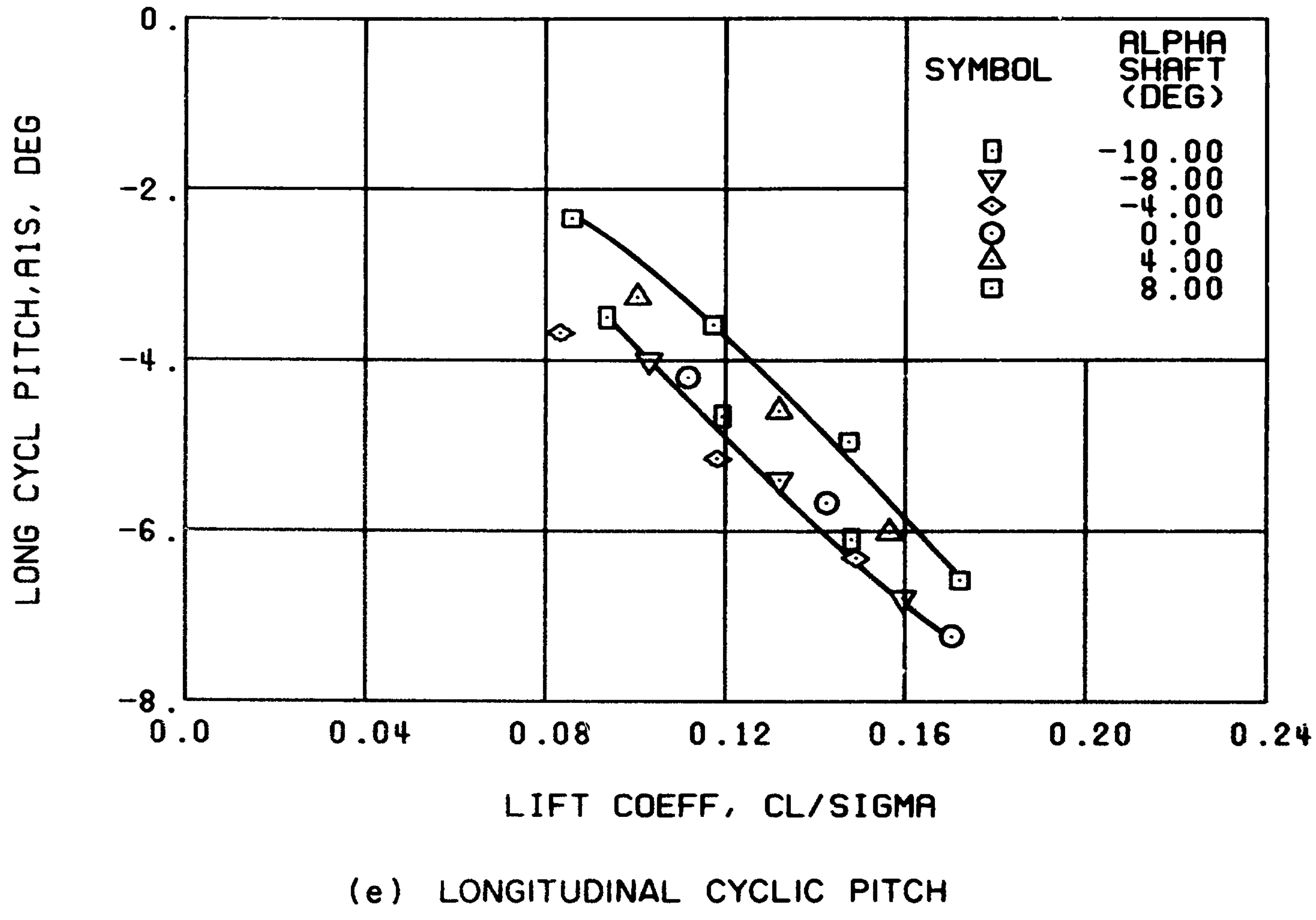

Figure 18. Continued.
$\mu = 0.21 \quad B'_{1s} = 4$ Deg

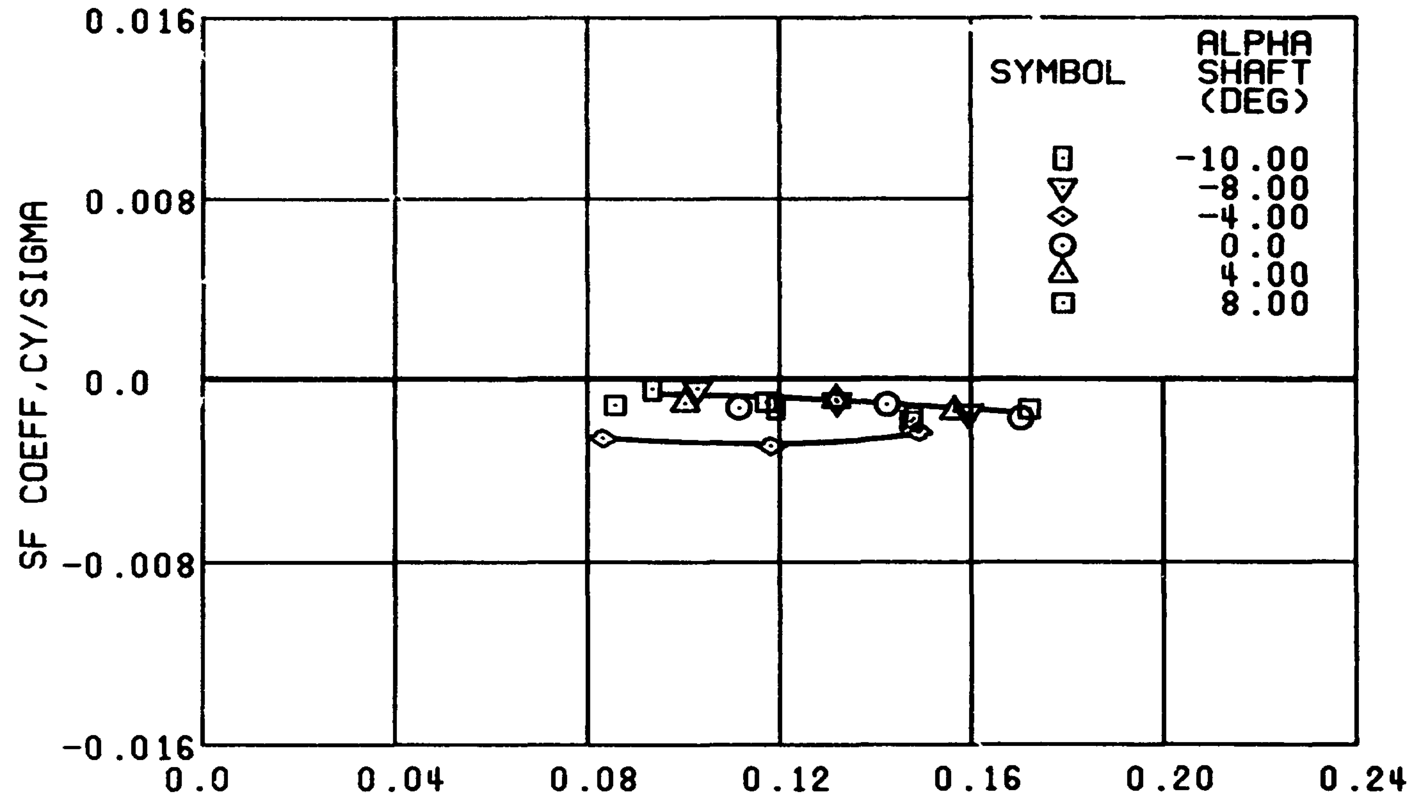

(f) SIDE FORCE COEFFICIENT

Figure 18. Continued.
$\mu = 0.21 \quad B'_{1s} = 4$ Deg

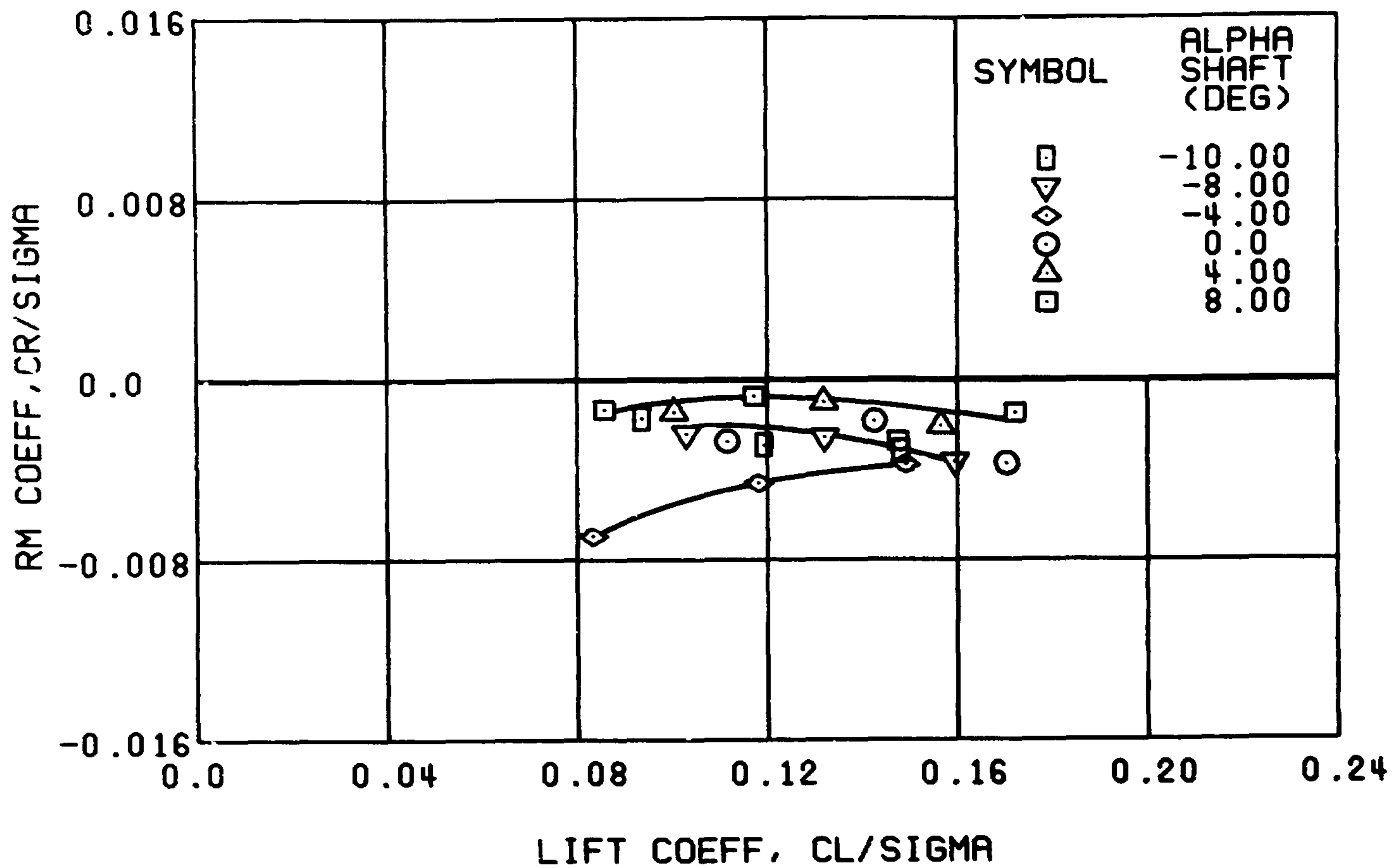

(g) ROLLING MOMENT COEFFICIENT

Figure 18. Continued.
$\mu = 0.21 \quad B'_{1s} = 4$ Deg

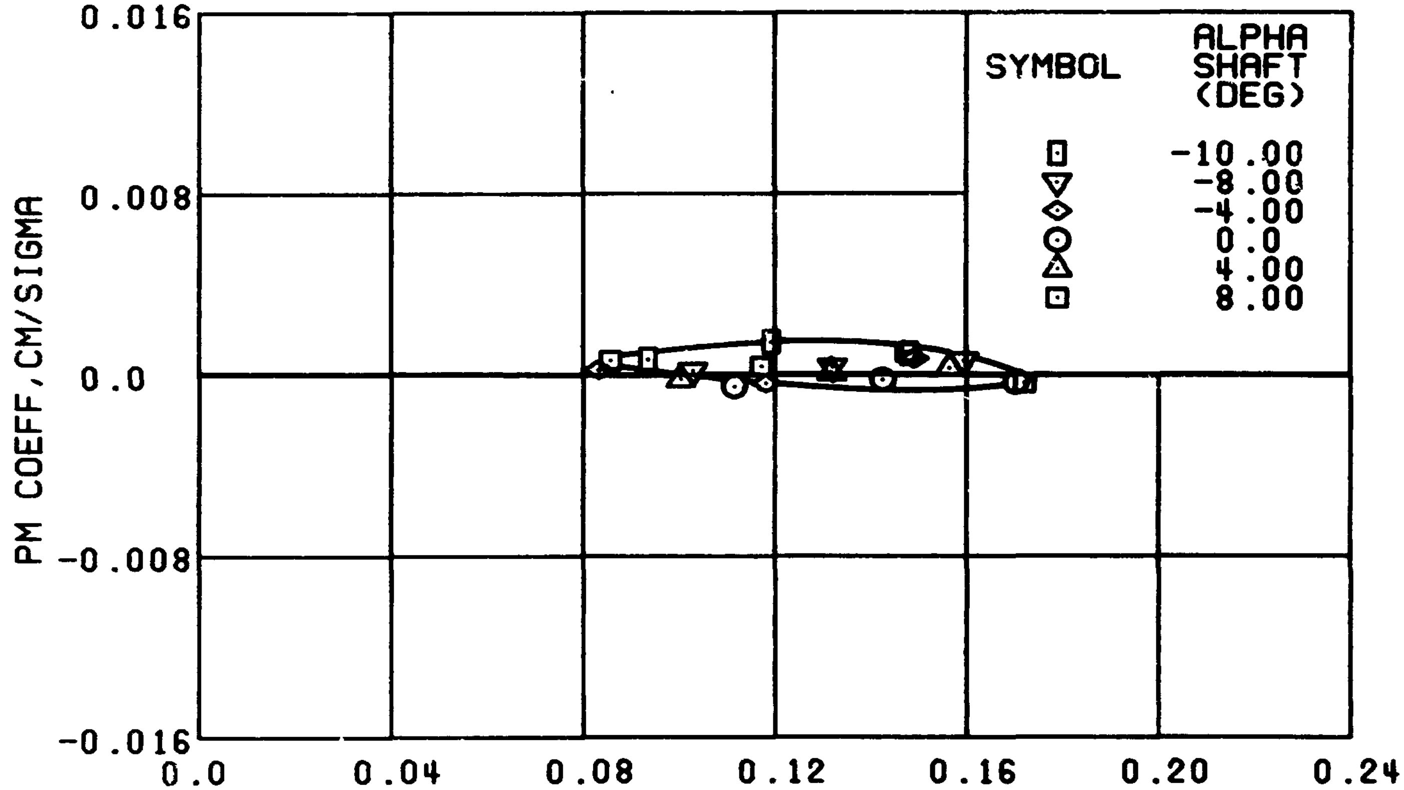

(h) PITCHING MOMENT COEFFICIENT

Figure 18. Continued.
$\mu = 0.21 \quad B'_{1s} = 4$ Deg

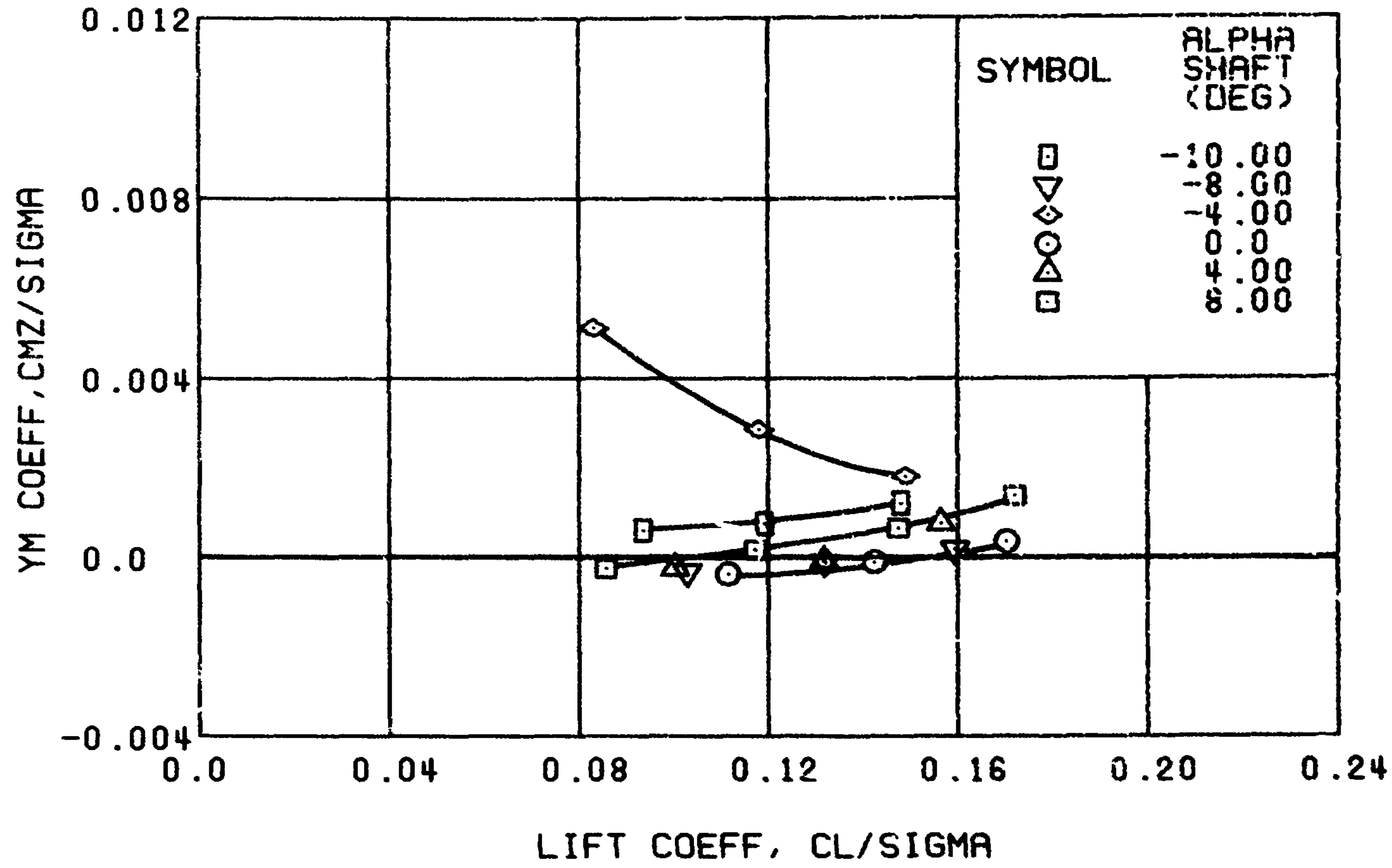

(i) YAWING MOMENT COEFFICIENT

Figure 18. Concluded.
$\mu = 0.21 \quad B'_{1s} = 4$ Deg

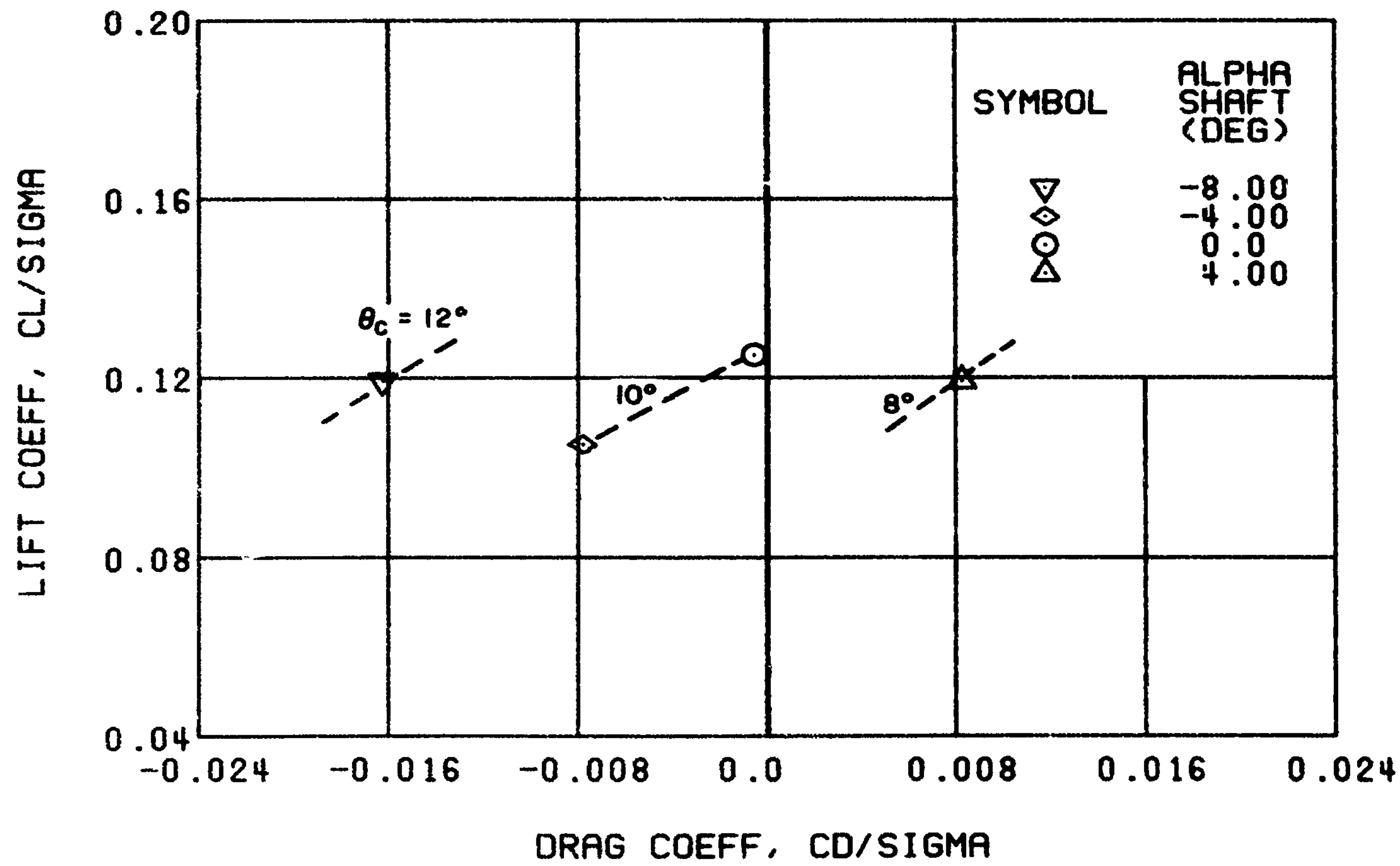

(a) DRAG COEFFICIENT

Figure 19. Performance Data at an Advance Ratio of 0.21 With the Lateral Displacement Control (B'_{1s}) Set at 6 Degrees.

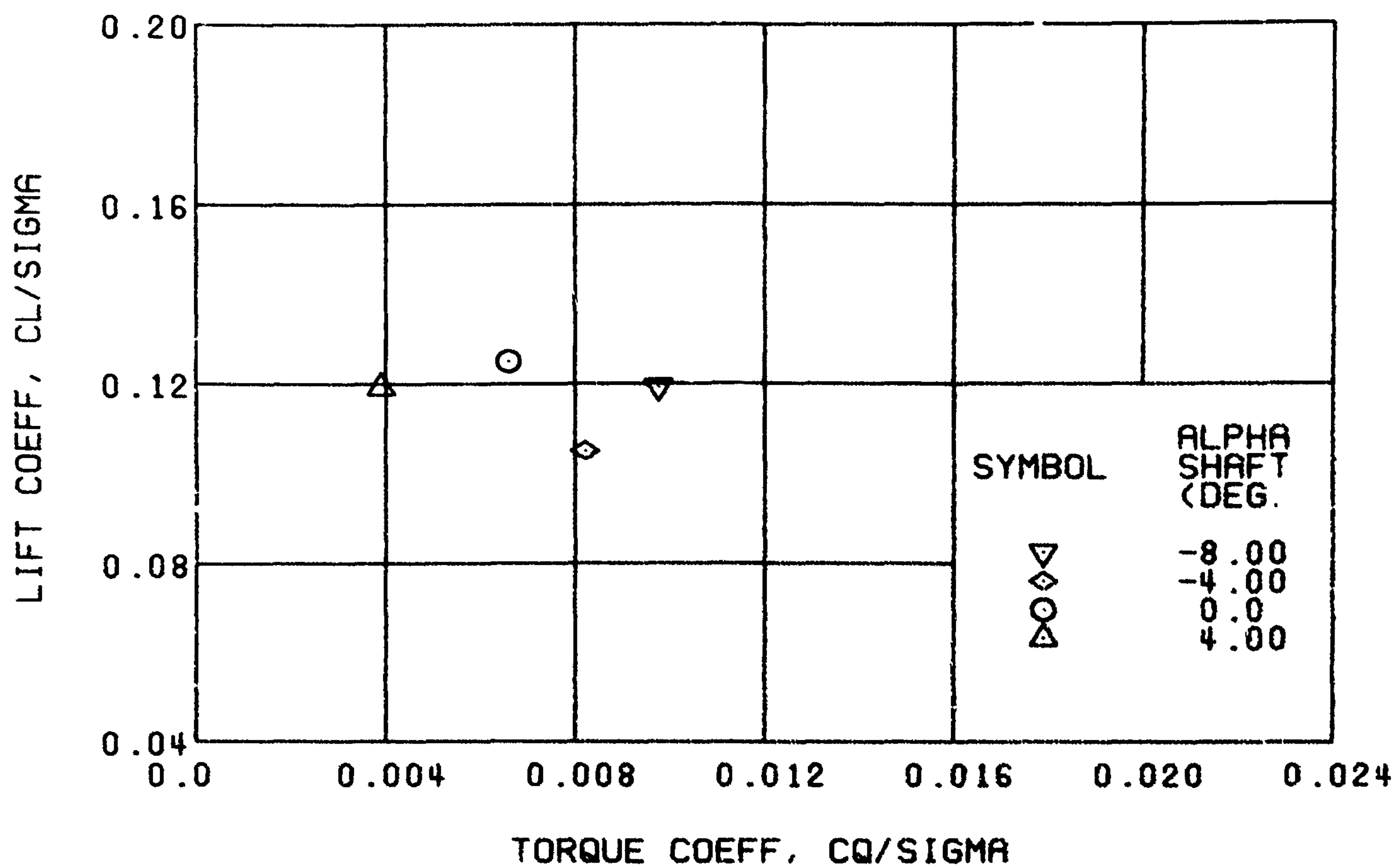

(b) TORQUE COEFFICIENT

Figure 19. Continued.
$\mu = 0.21 \quad B'_{1s} = 6$ Deg

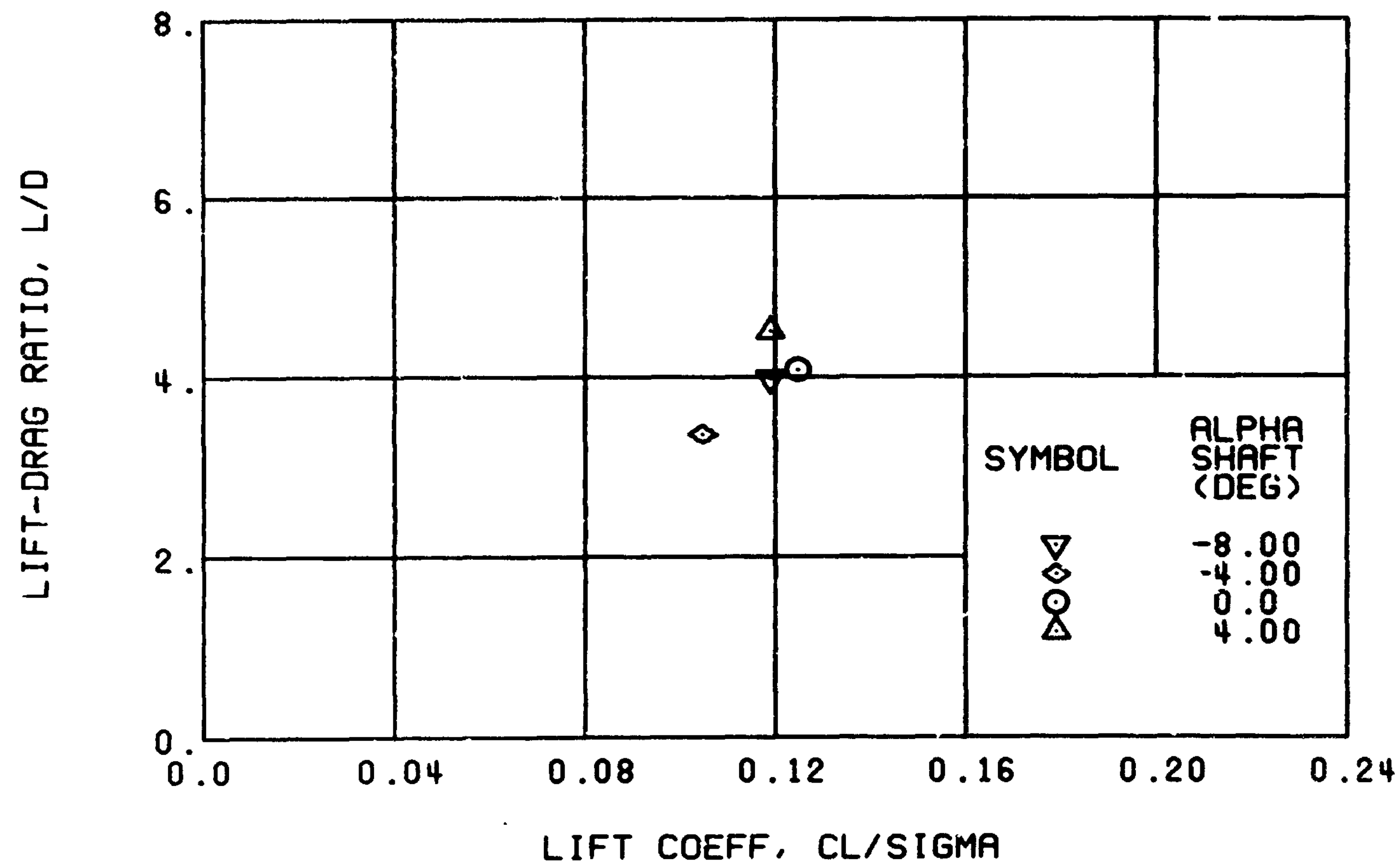

(c) LIFT-DRAG RATIO

Figure 15 Continued.
$\mu = 0.21$ $B'_{1s} = 6$ Deg

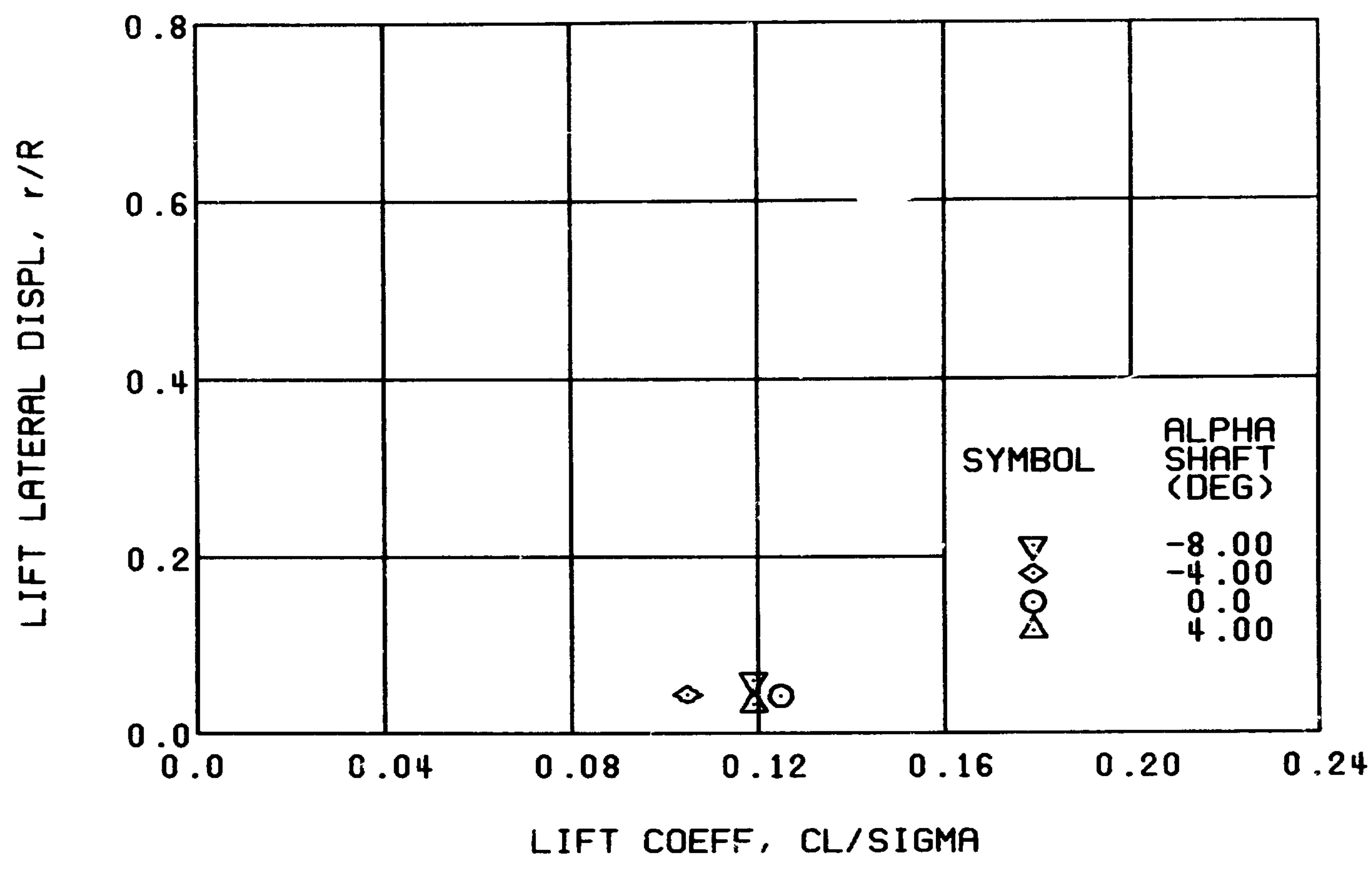

(d) LIFT LATERAL DISPLACEMENT

Figure 19. Continued.
$\mu = 0.21$ $B'_{1s} = 6$ Deg

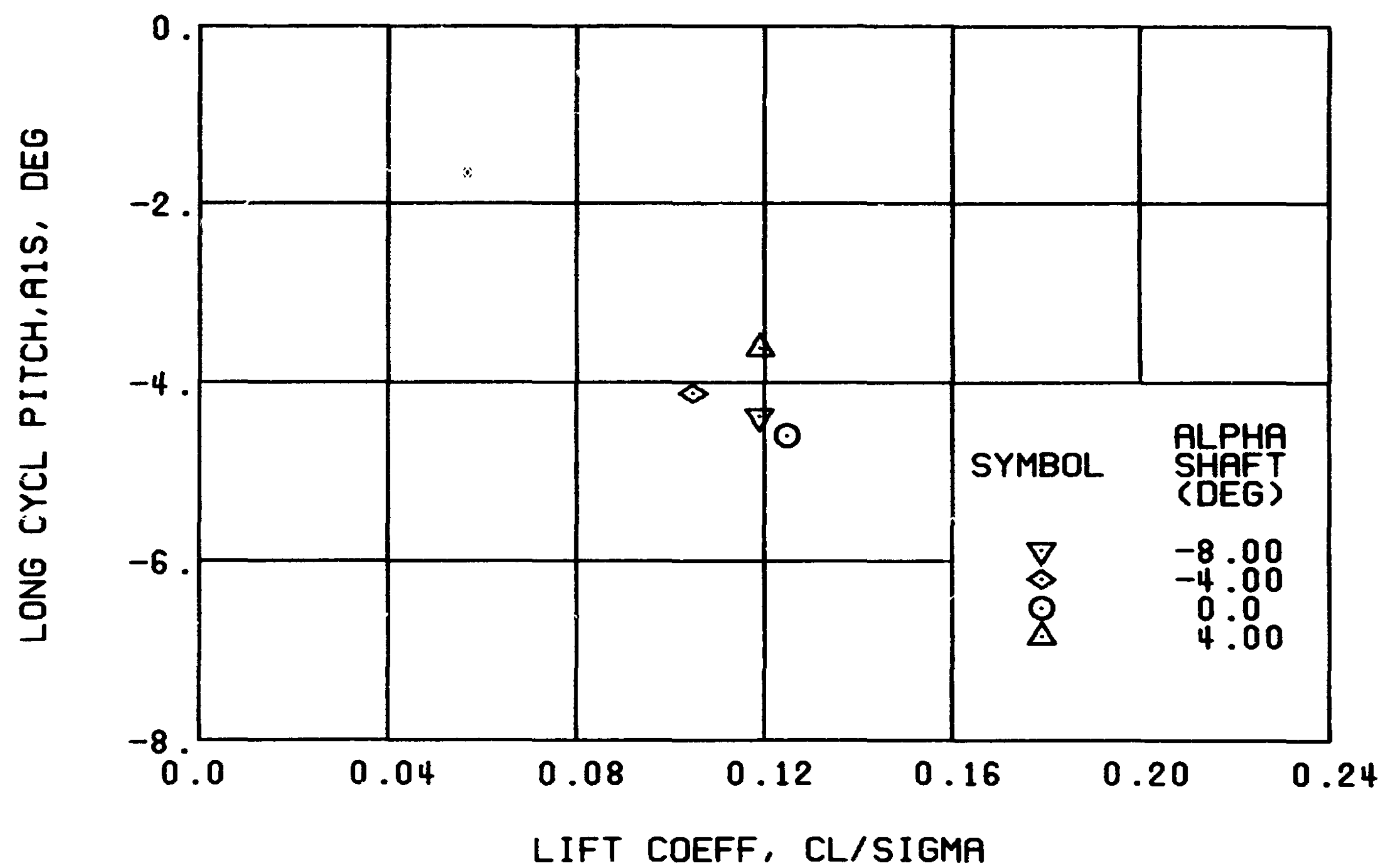

(e) LONGITUDINAL CYCLIC PITCH

Figure 19. Continued.
$\mu = 0.21 \quad B'_{1s} = 6$ Deg

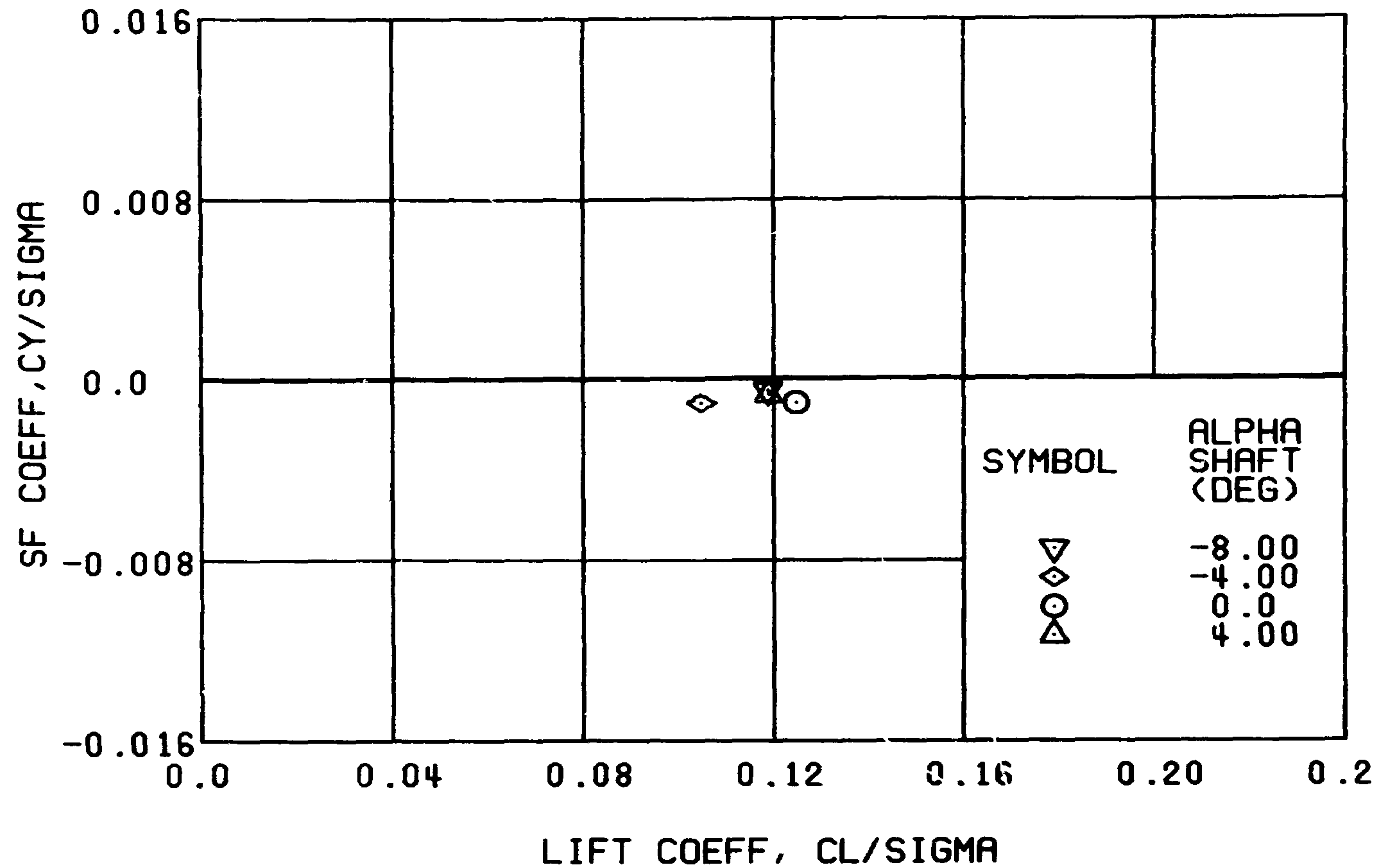

(f) SIDE FORCE COEFFICIENT

Figure 19. Continued.
$\mu = 0.21$ $B'_{1s} = 6$ Deg

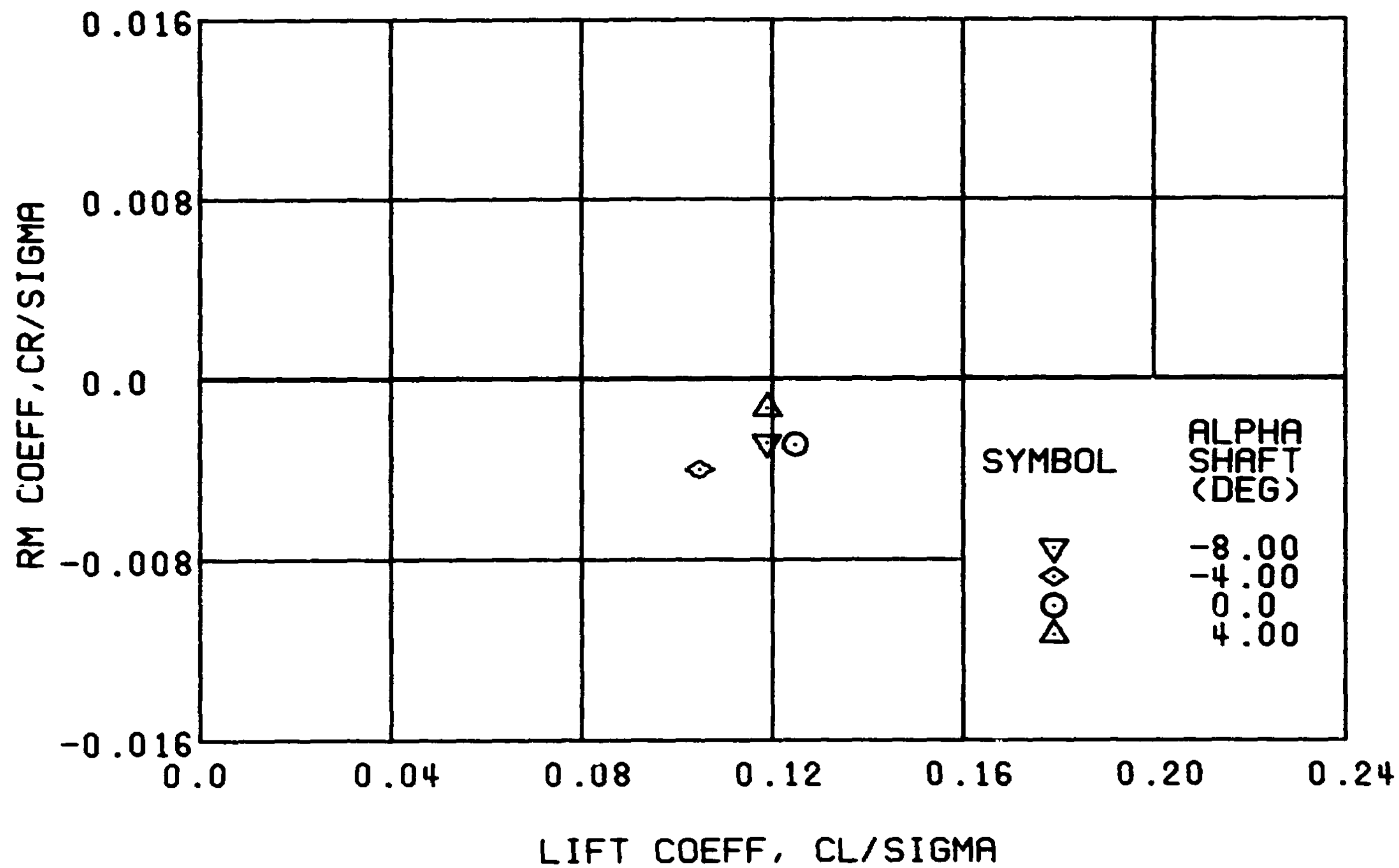

(g) ROLLING MOMENT COEFFICIENT

Figure 19. Continued.
$\mu = 0.21 \quad B'_{1s} = 6$ **Deg**

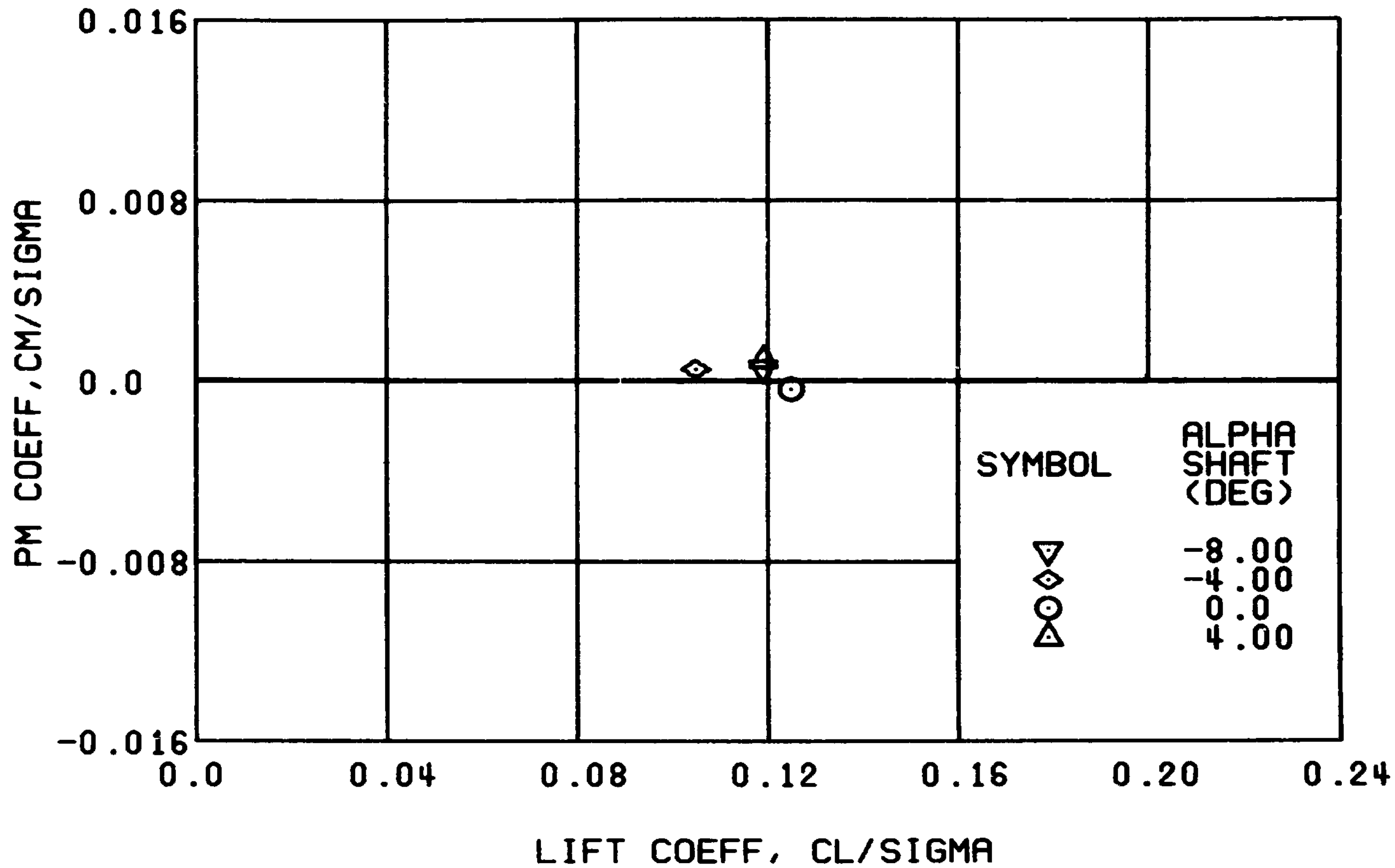

(h) PITCHING MOMENT COEFFICIENT

Figure 19. Continued.
$\mu = 0.21 \quad B'_{1s} = 6$ Deg

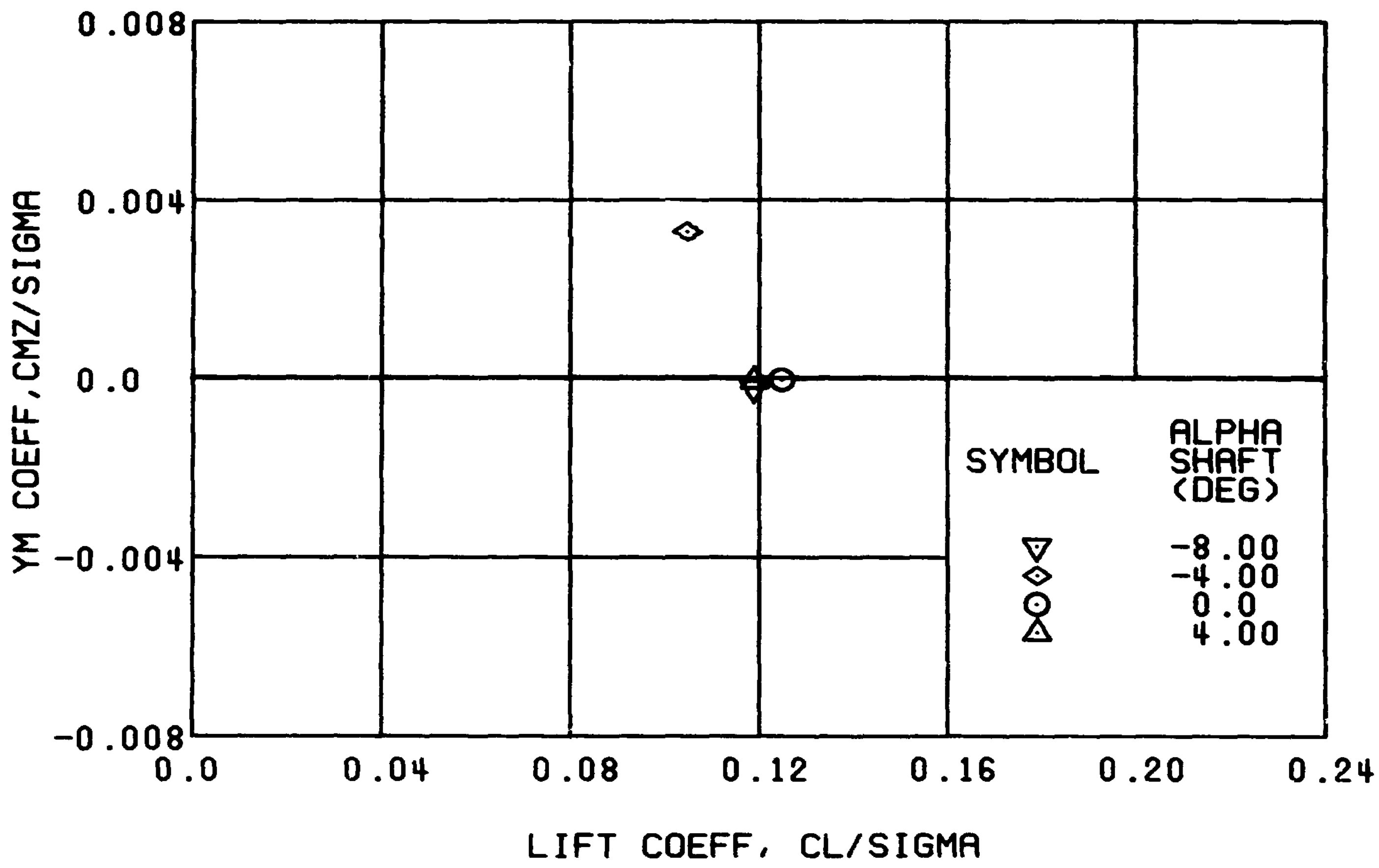

(i) YAWING MOMENT COEFFICIENT

Figure 19. Concluded.
$\mu = 0.21$ $B'_{1s} = 6$ Deg

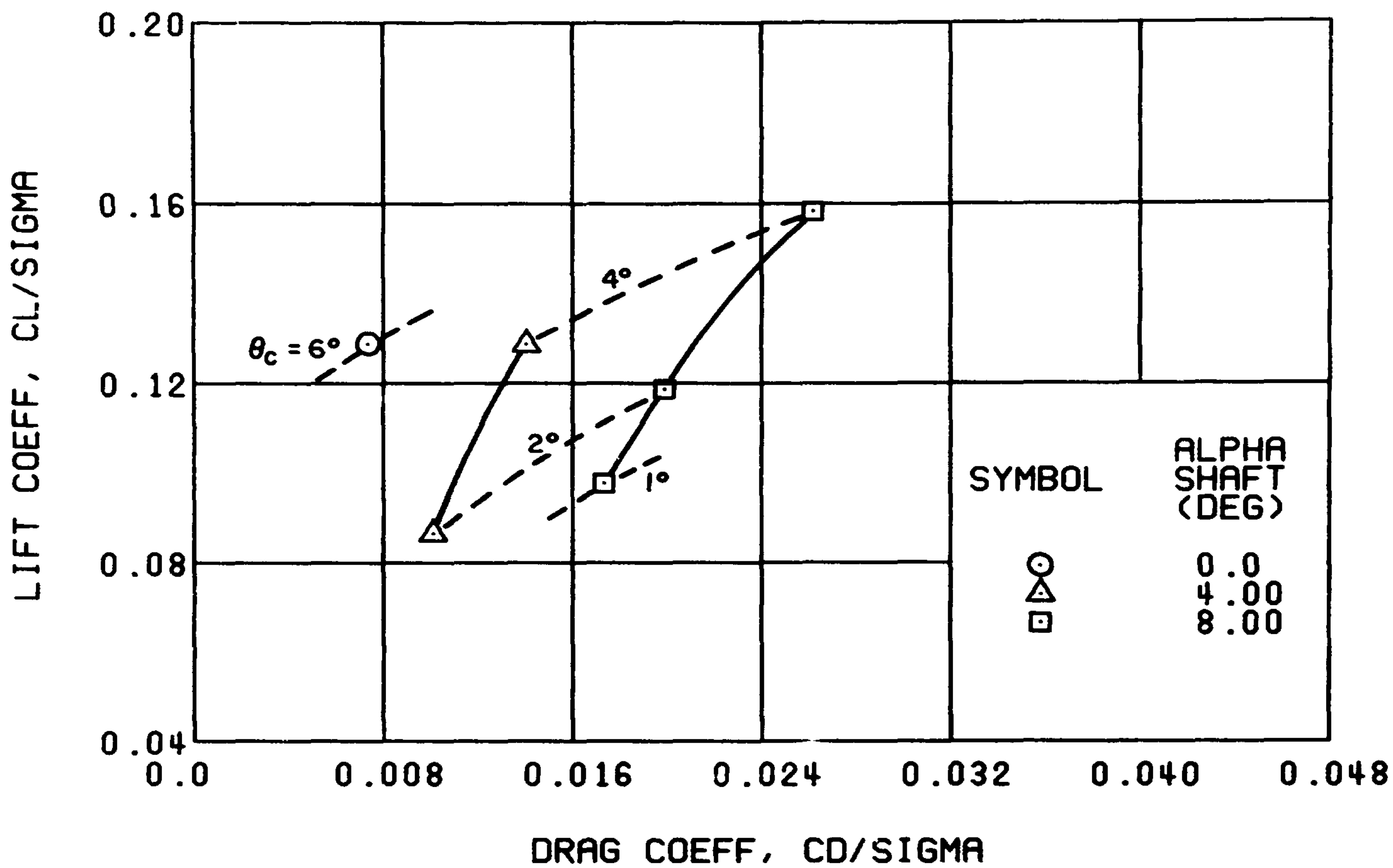

(a) DRAG COEFFICIENT

Figure 20. Performance Data at an Advance Ratio of 0.35 With the Lateral Displacement Control (B'_{1s}) Set at 0 Degrees.

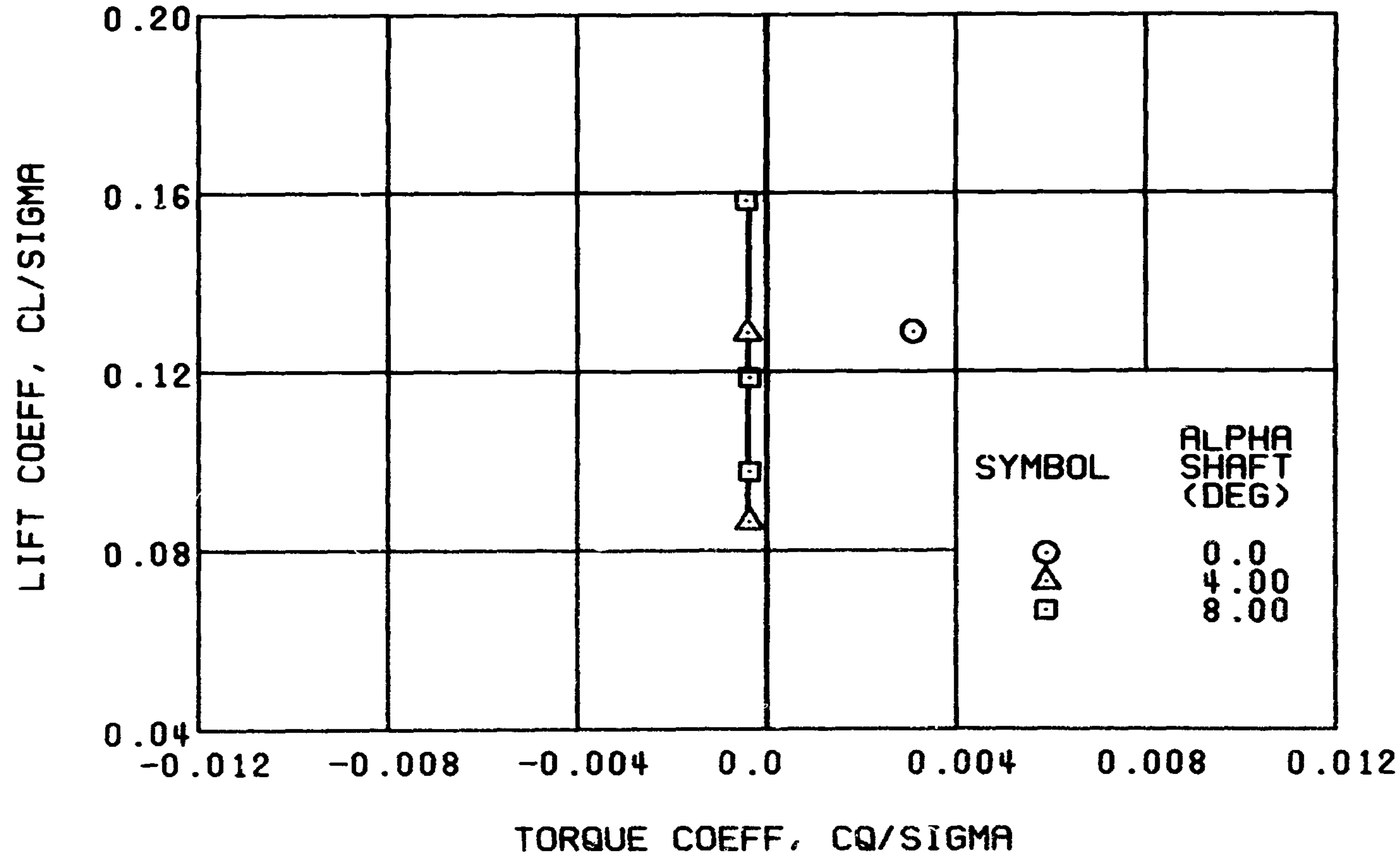

(b) TORQUE COEFFICIENT

Figure 20. Continued.
$\mu = 0.35$ $B'_{1s} = 0$ Deg

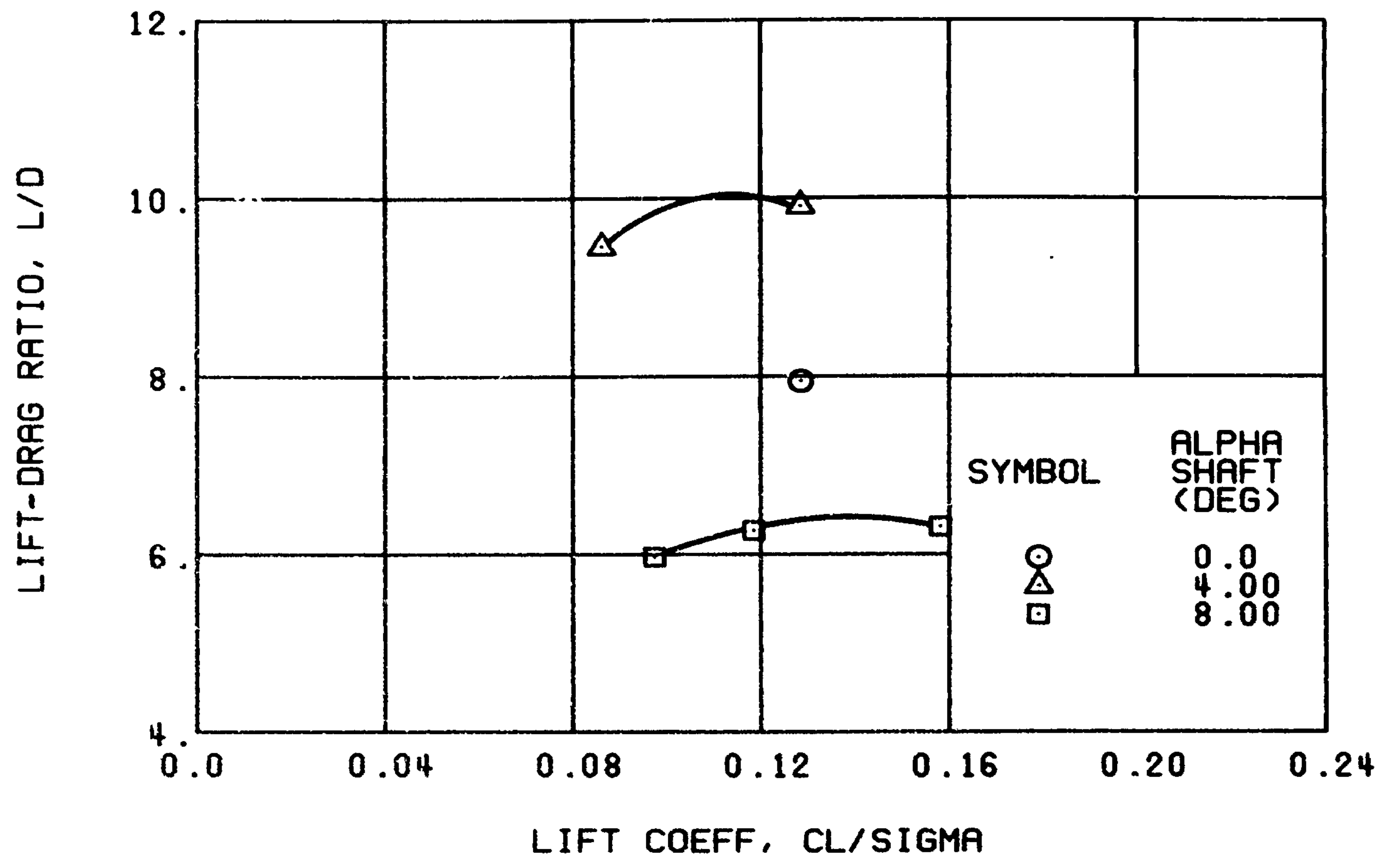

(c) LIFT-DRAG RATIO

Figure 20. Continued.
$\mu = 0.35 \quad B'_{1s} = 0$ Deg

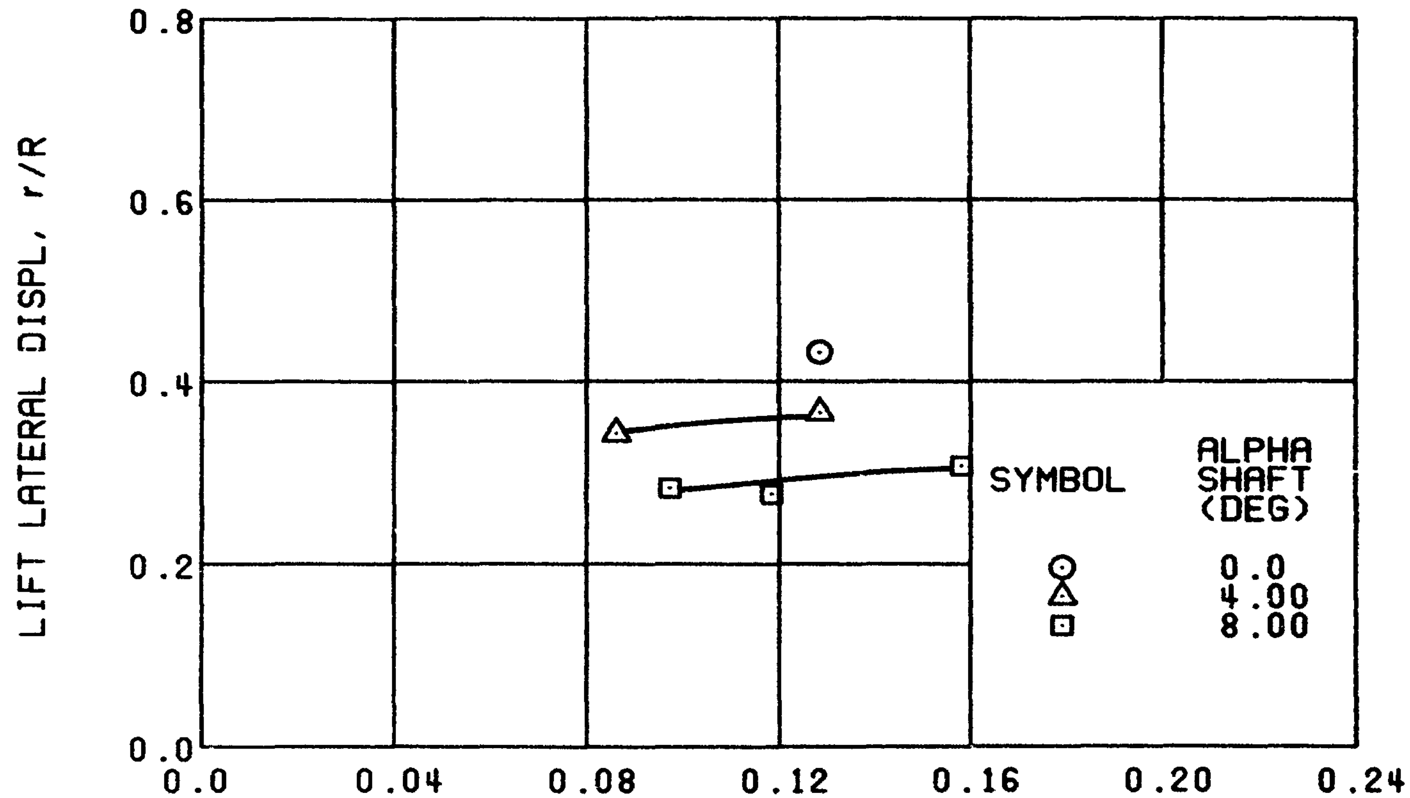

(d) LIFT LATERAL DISPLACEMENT

Figure 20. Continued.
$\mu = 0.35 \quad B'_{1s} = 0$ Deg

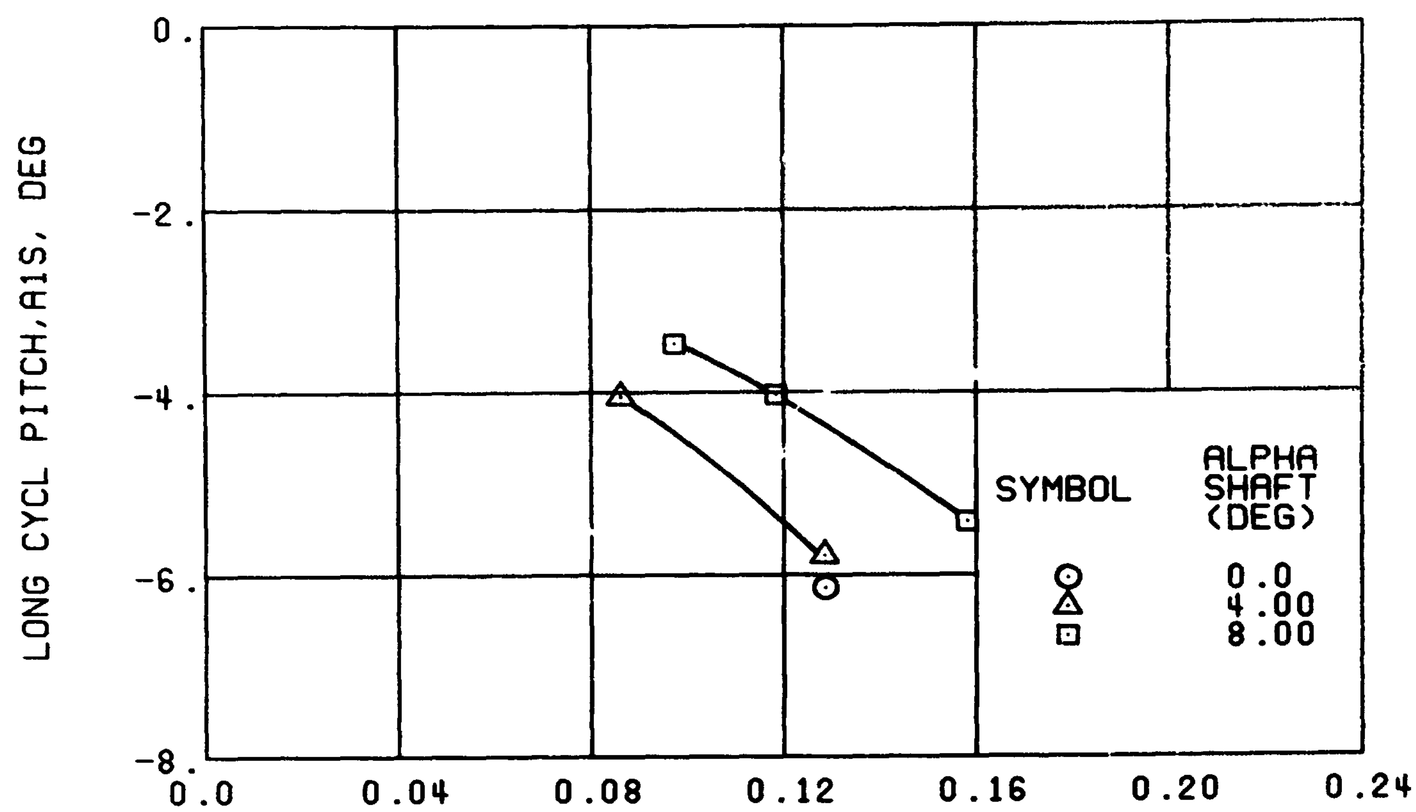

(e) LONGITUDINAL CYCLIC PITCH

Figure 20. Continued.
μ = 0.35 B'_{1s} = 0 Deg

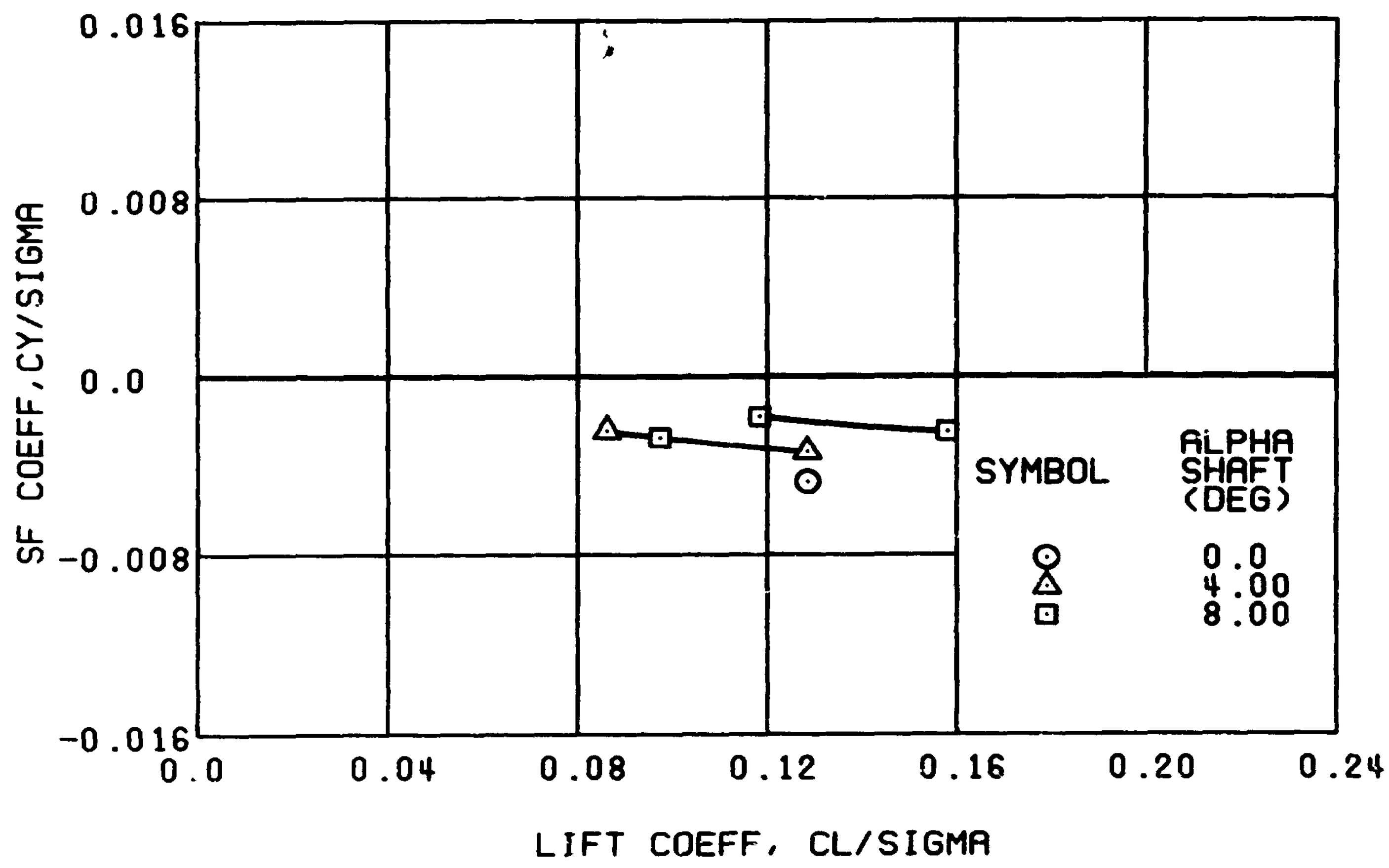

(f) SIDE FORCE COEFFICIENT

Figure 20. Continued.
$\mu = 0.35$ $B'_{1s} = 0$ **Deg**

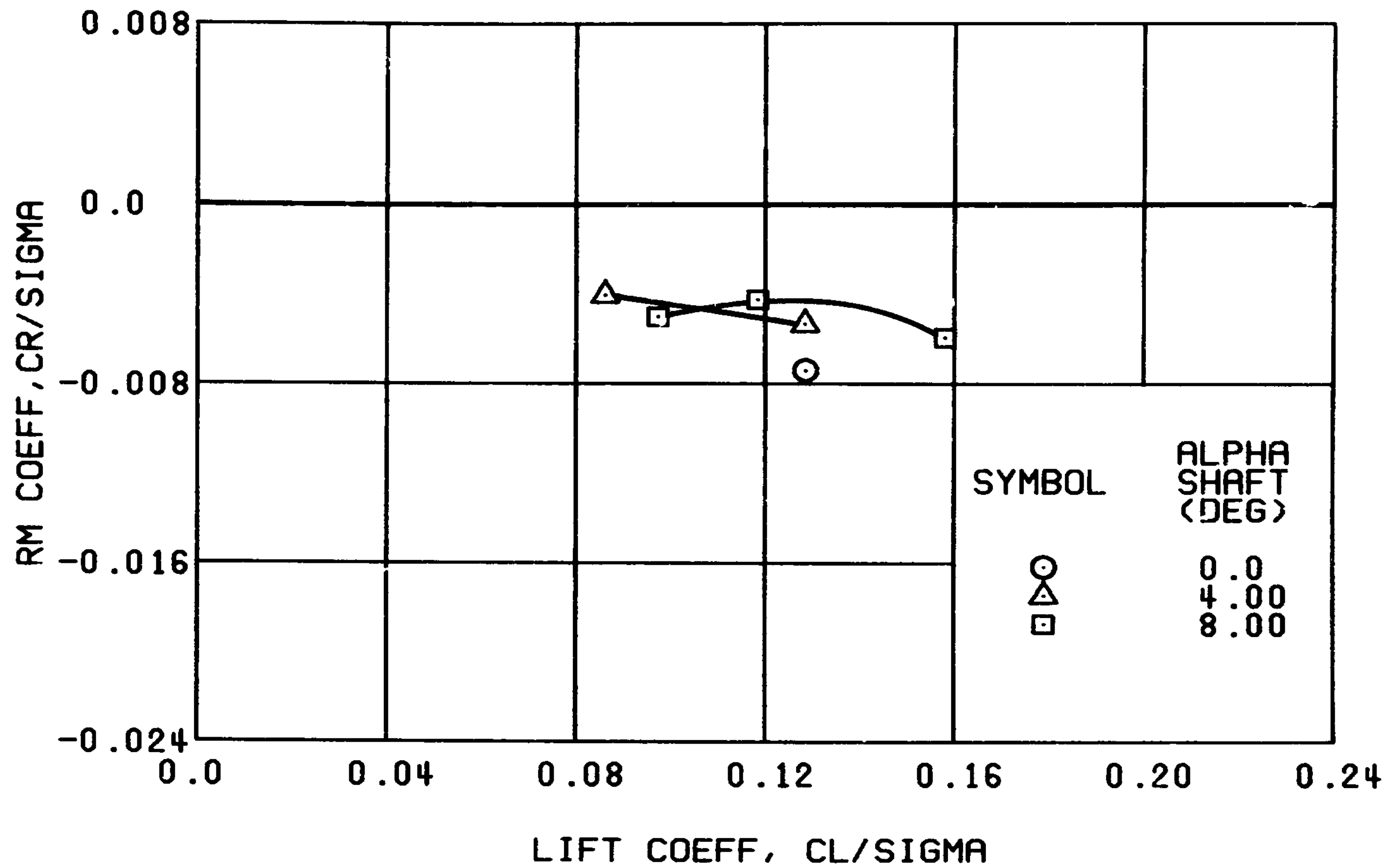

(g) ROLLING MOMENT COEFFICIENT

Figure 20. Continued.
$\mu = 0.35$ $B'_{1s} = 0$ Deg

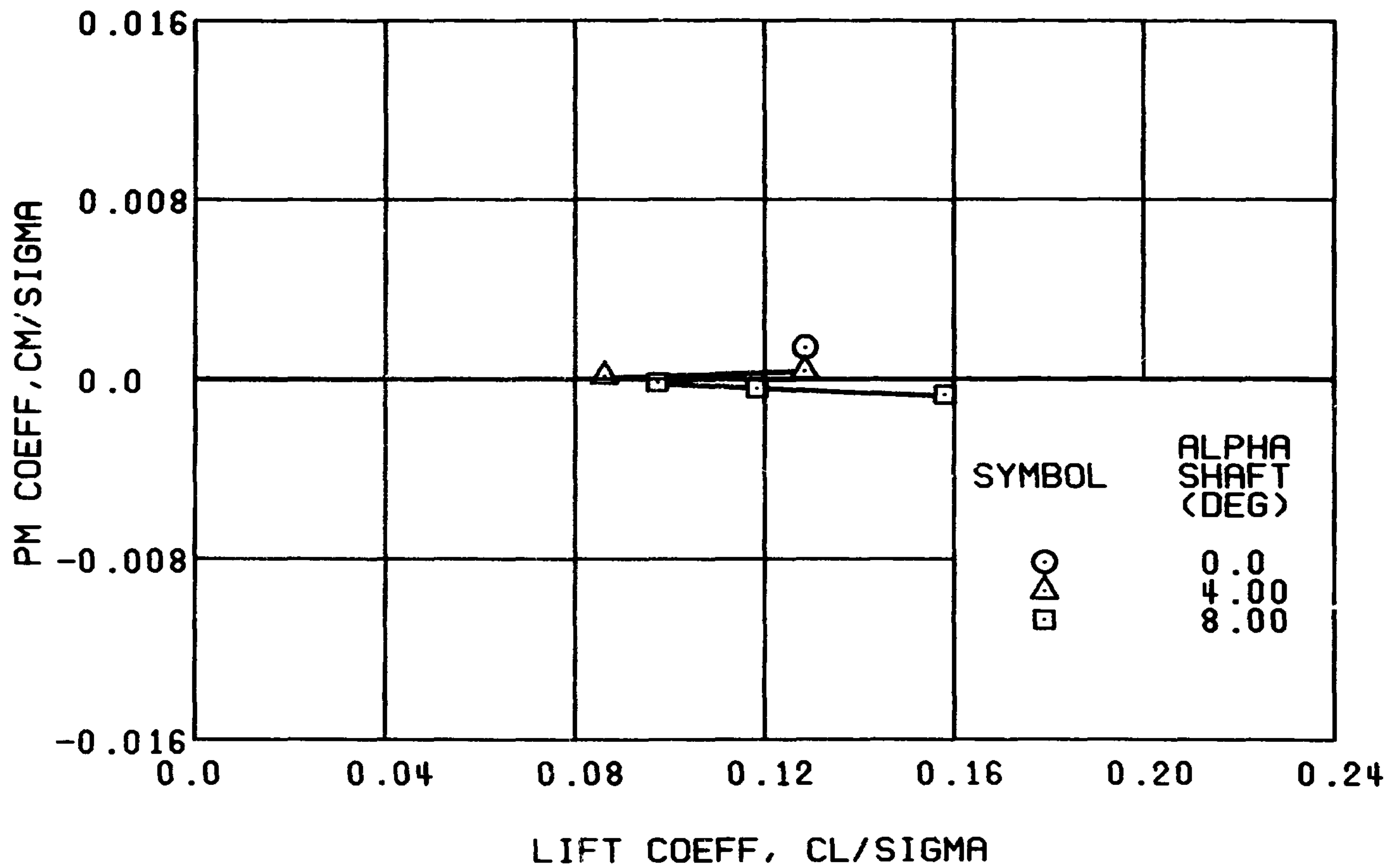

(h) PITCHING MOMENT COEFFICIENT

Figure 20. **Continued.**
μ = 0.35 B'_{1s} = 0 **Deg**

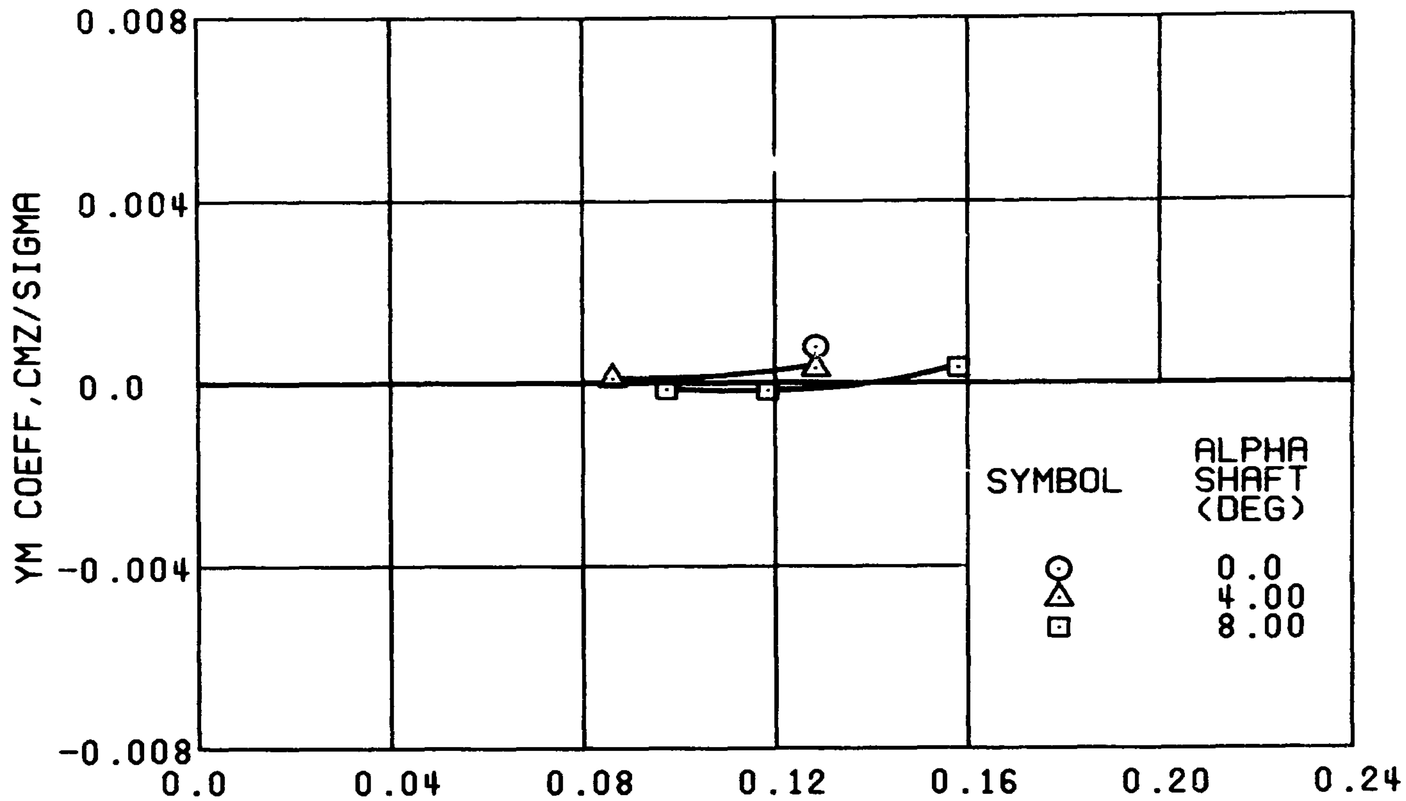

(i) YAWING MOMENT COEFFICIENT

Figure 20. Concluded.
$\mu = 0.35$ $B'_{1s} = 0$ Deg

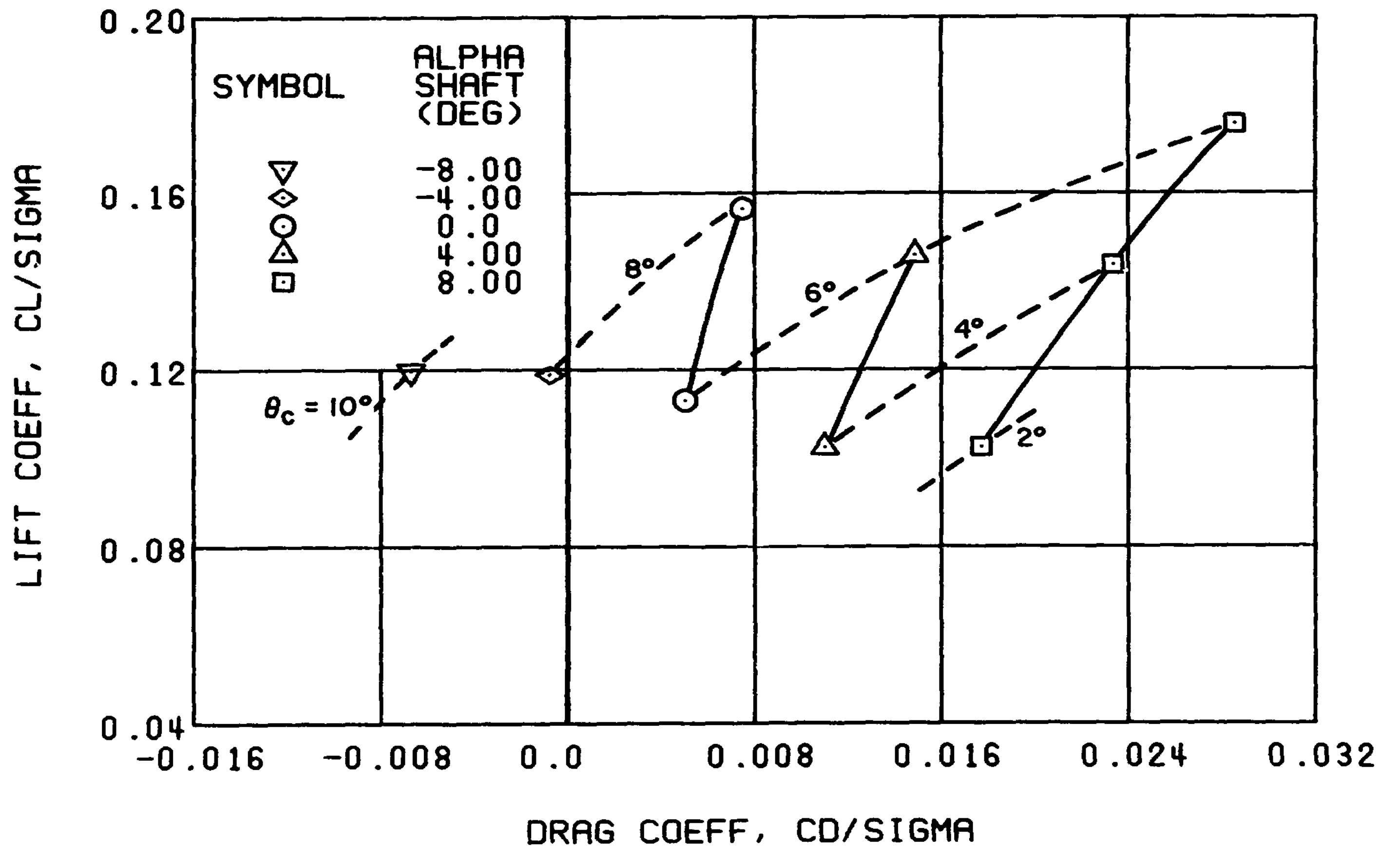

(a) DRAG COEFFICIENT

Figure 21. Performance Data at an Advance Ratio of 0.35 With the Lateral Displacement Control (B'_{1s}) Set at 2 Degrees.

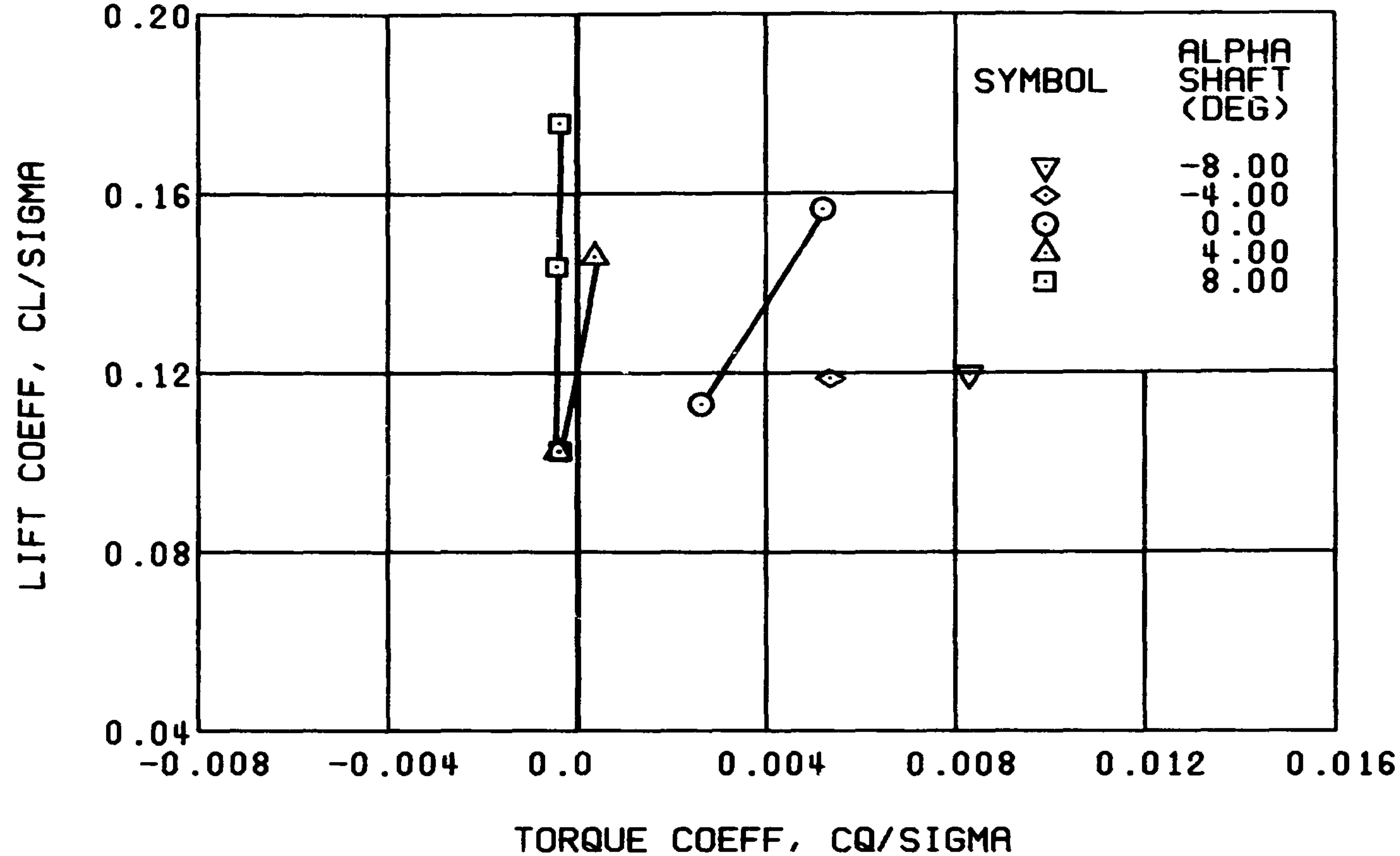

(b) TORQUE COEFFICIENT

Figure 21. Continued.
$\mu = 0.35 \quad B'_{1s} = 2$ Deg

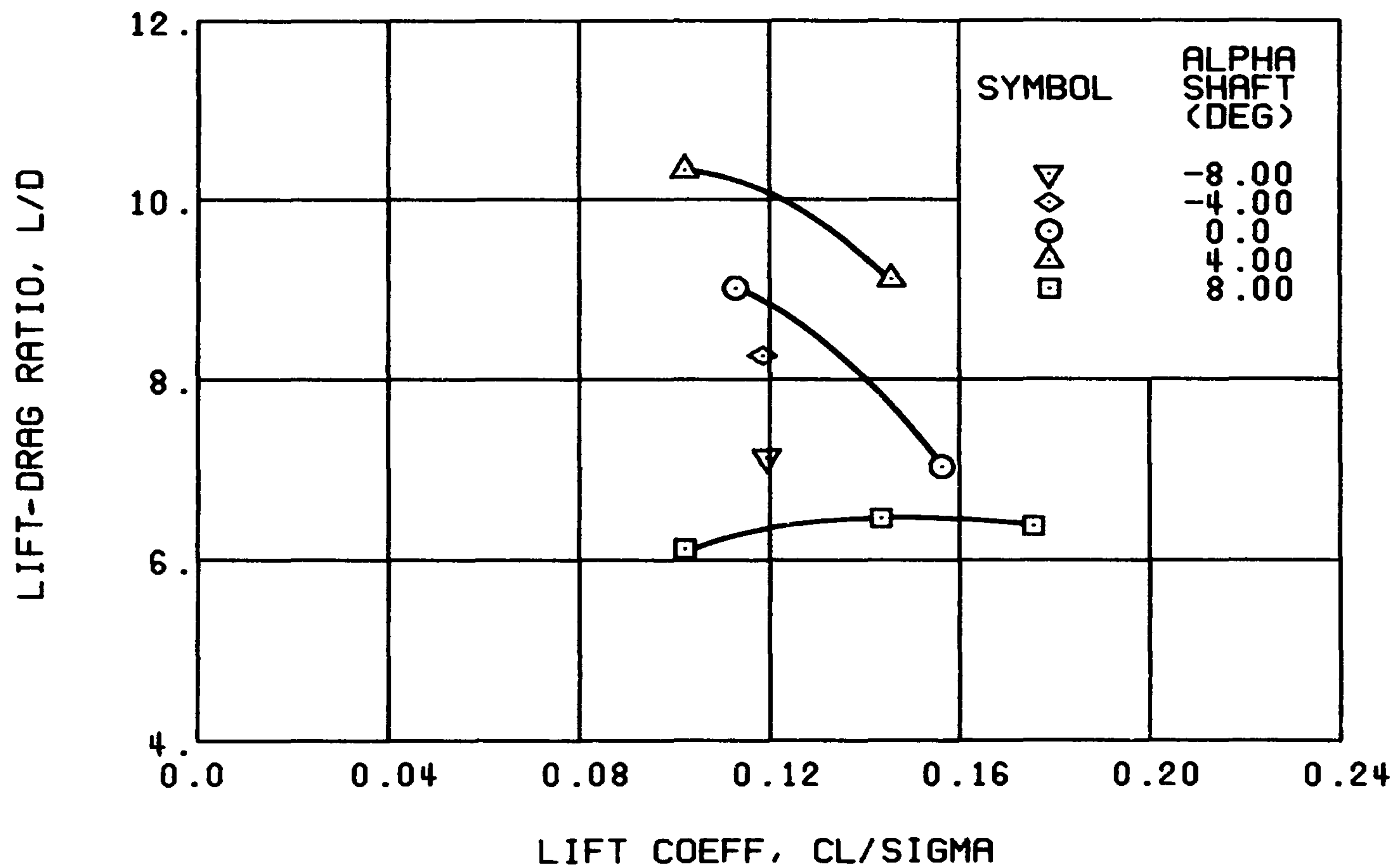

(c) LIFT-DRAG RATIO

Figure 21. Continued.
μ = 0.35 B'_{1s} = 2 Deg

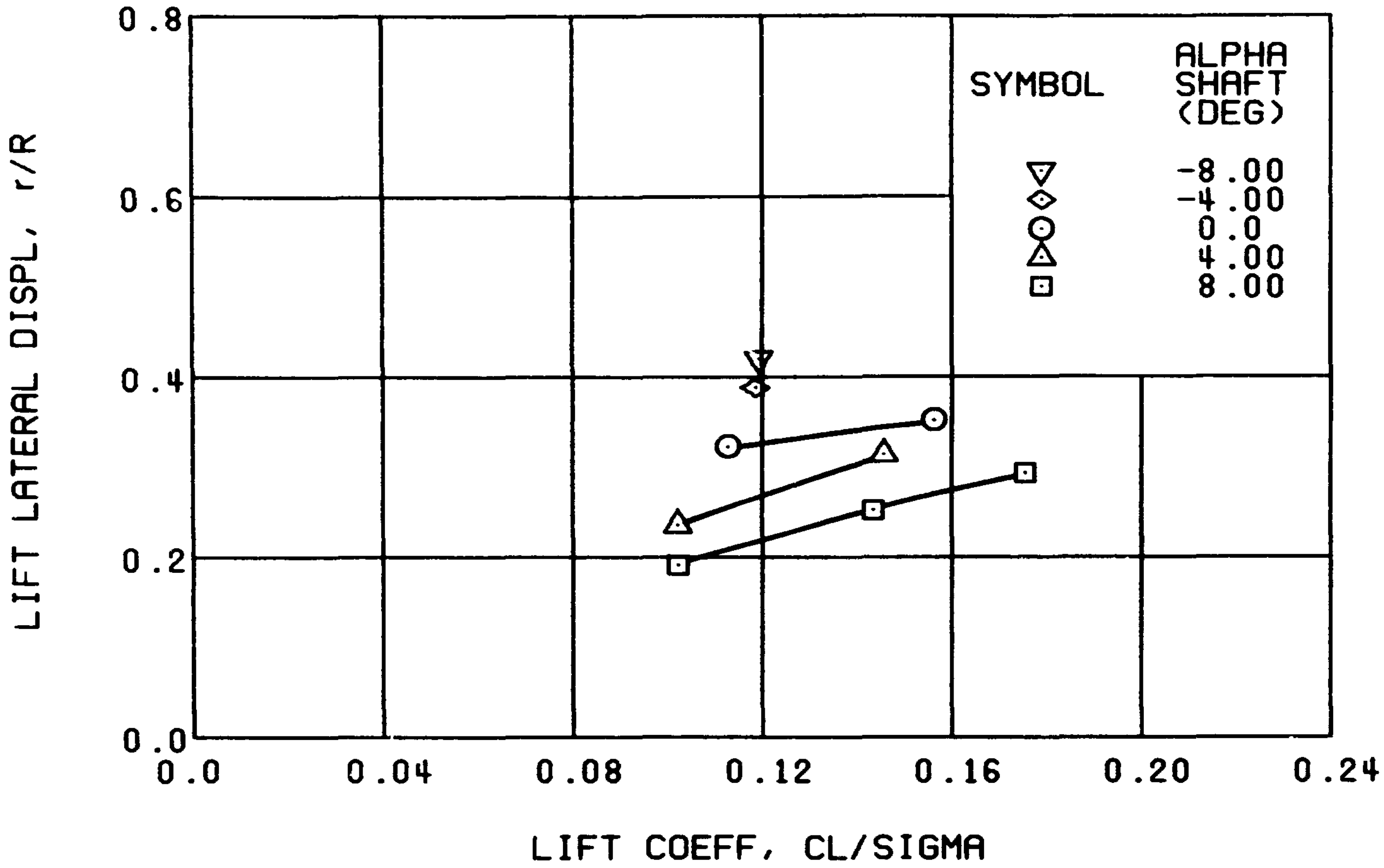

(d) LIFT LATERAL DISPLACEMENT

Figure 21. Continued.
$\mu = 0.35 \quad B'_{1s} = 2$ Deg

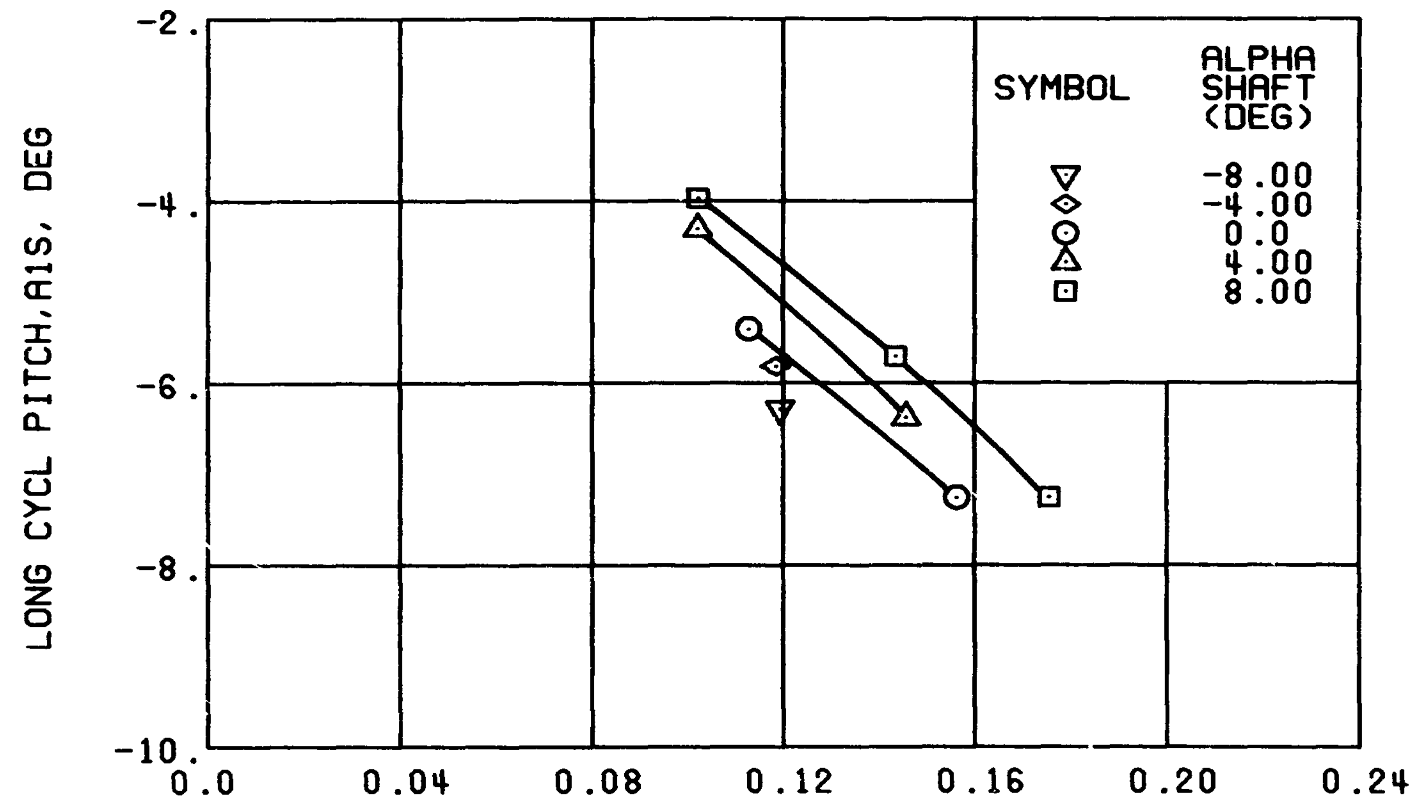

(e) LONGITUDINAL CYCLIC PITCH

Figure 21. Continued.
$\mu = 0.35$ $B'_{1s} = 2$ Deg

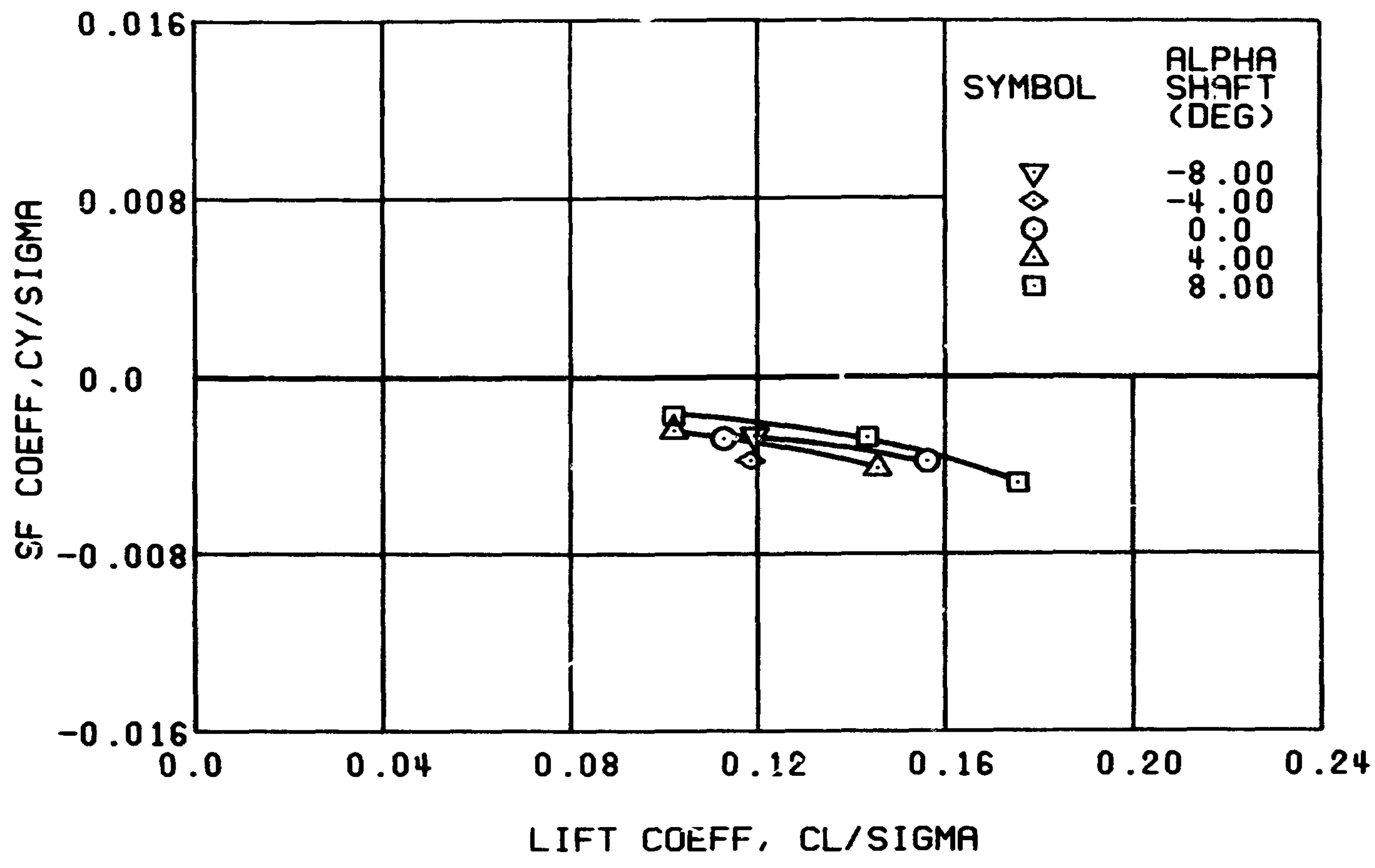

(f) SIDE FORCE COEFFICIENT

Figure 21. Continued.
$\mu = 0.35 \quad B'_{1s} = 2$ Deg

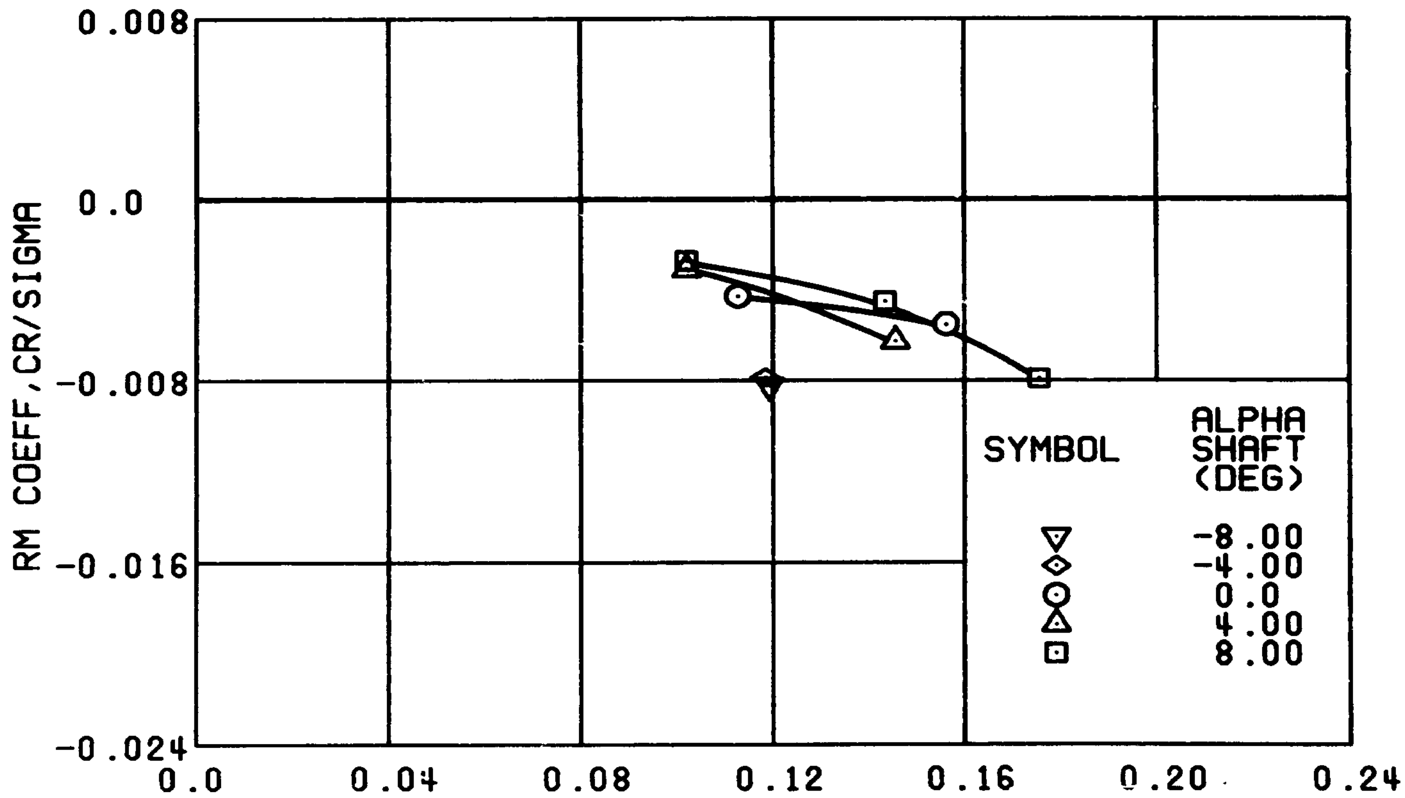

(g) ROLLING MOMENT COEFFICIENT

Figure 21. Continued.
$\mu = 0.35 \quad B'_{1s} = 2$ **Deg**

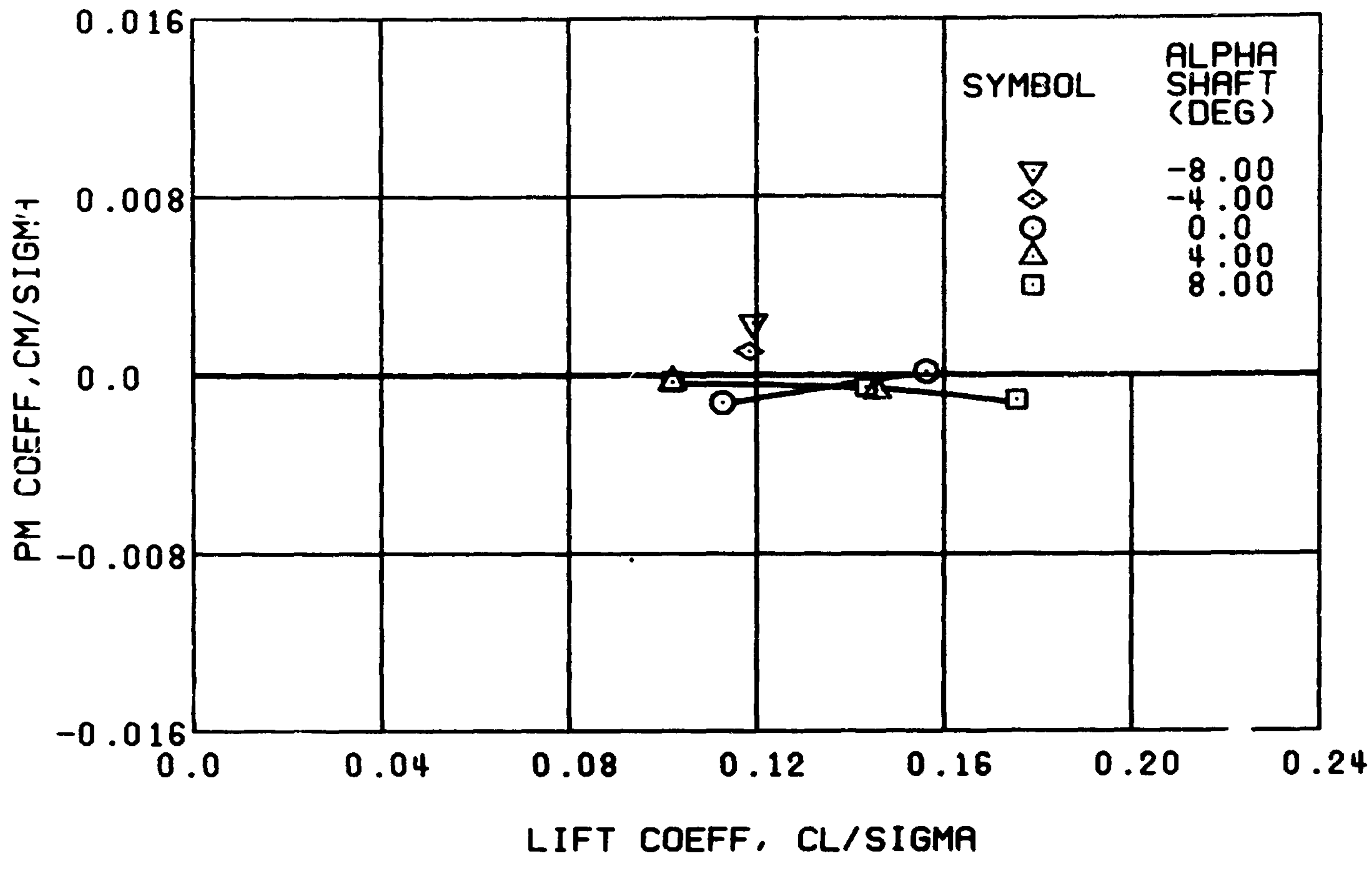

(h) PITCHING MOMENT COEFFICIENT

Figure 21. Continued.
$\mu = 0.35$ $B'_{1s} = 2$ Deg

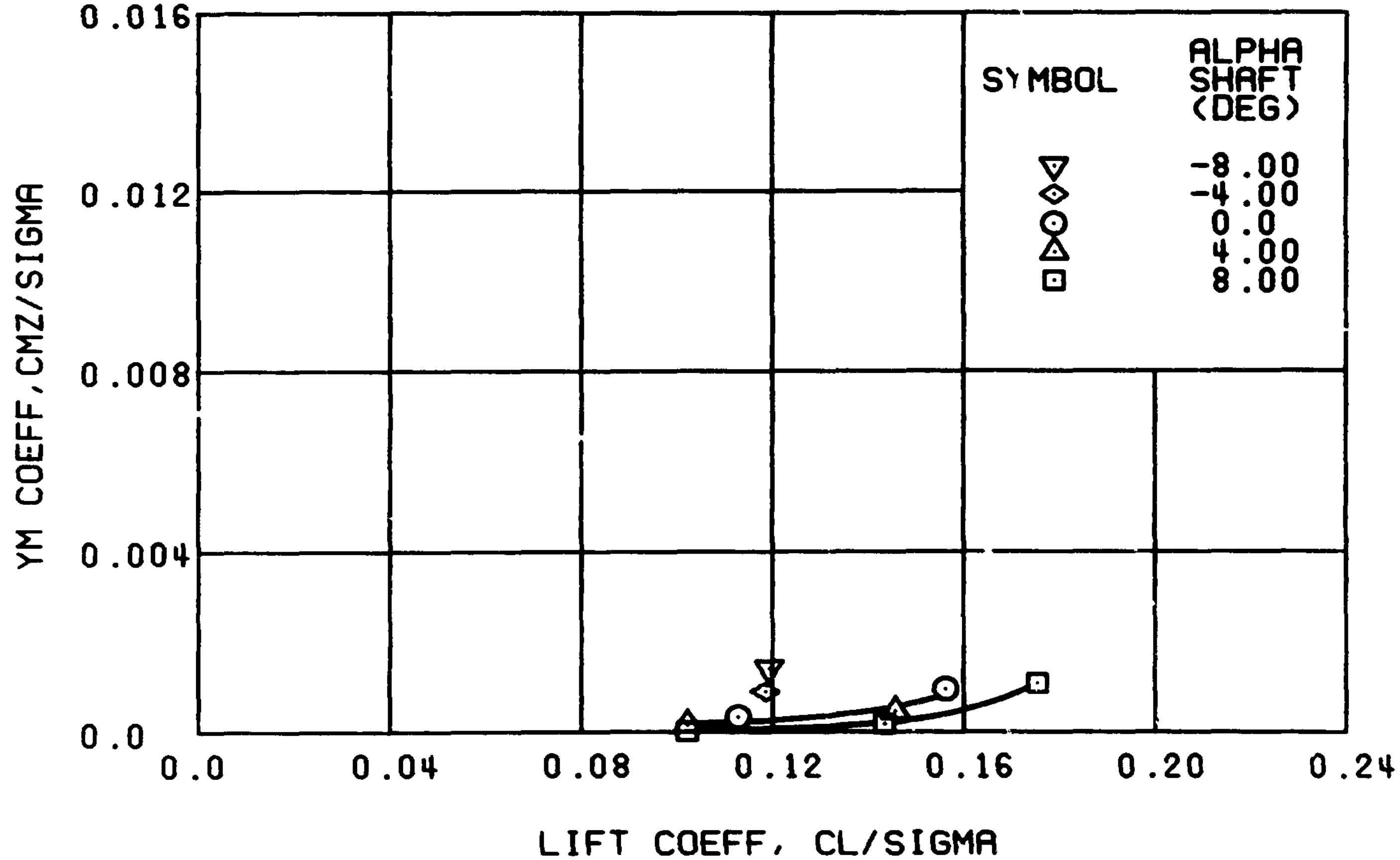

(i) YAWING MOMENT COEFFICIENT

Figure 21. Concluded.
$\mu = 0.35$ $B'_{1s} = 2$ Deg

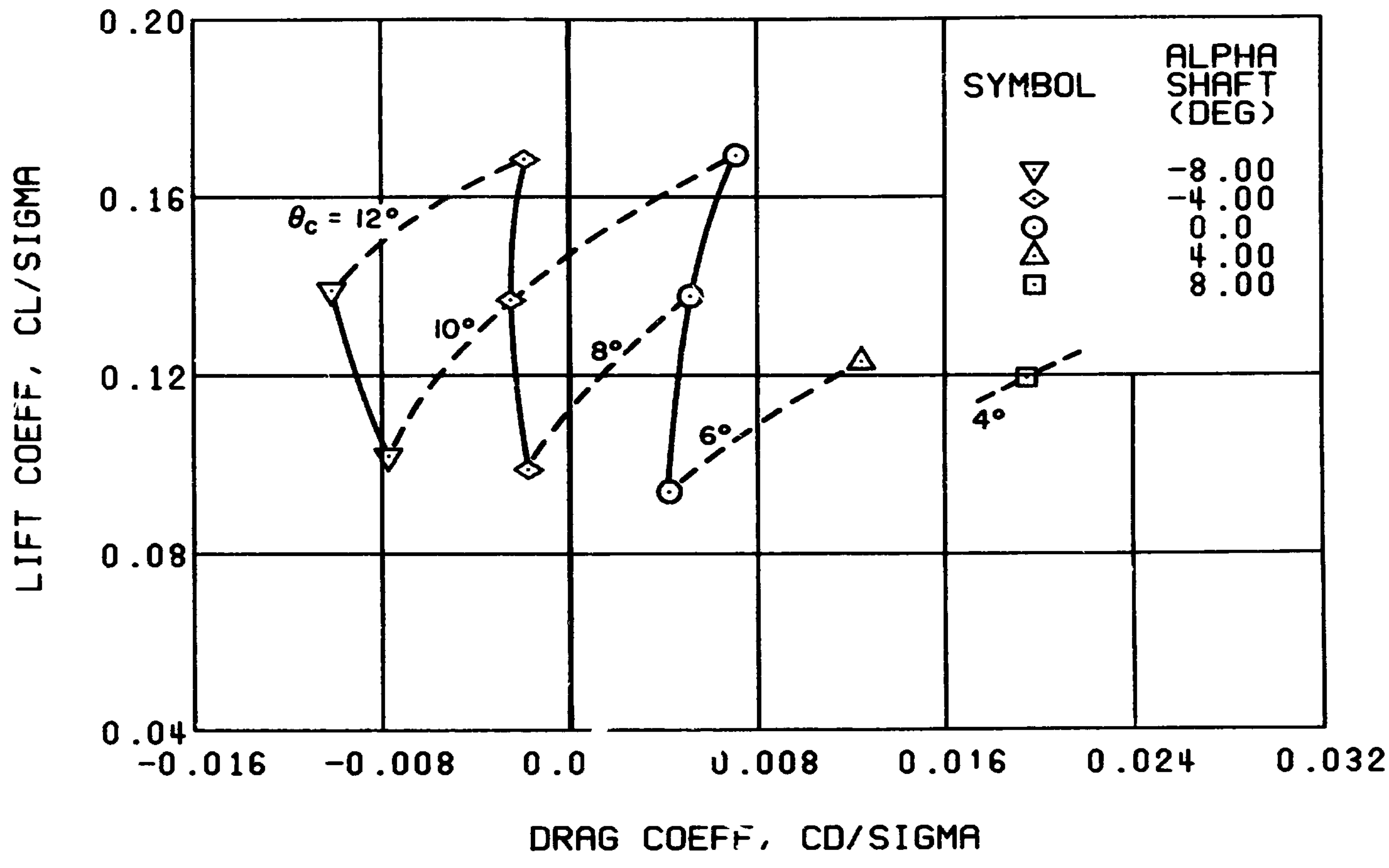

(a) DRAG COEFFICIENT

Figure 22. Performance Data at an Advance Ratio of 0.35 With the Lateral Displacement Control (B'_{1s}) Set at 4 Degrees.

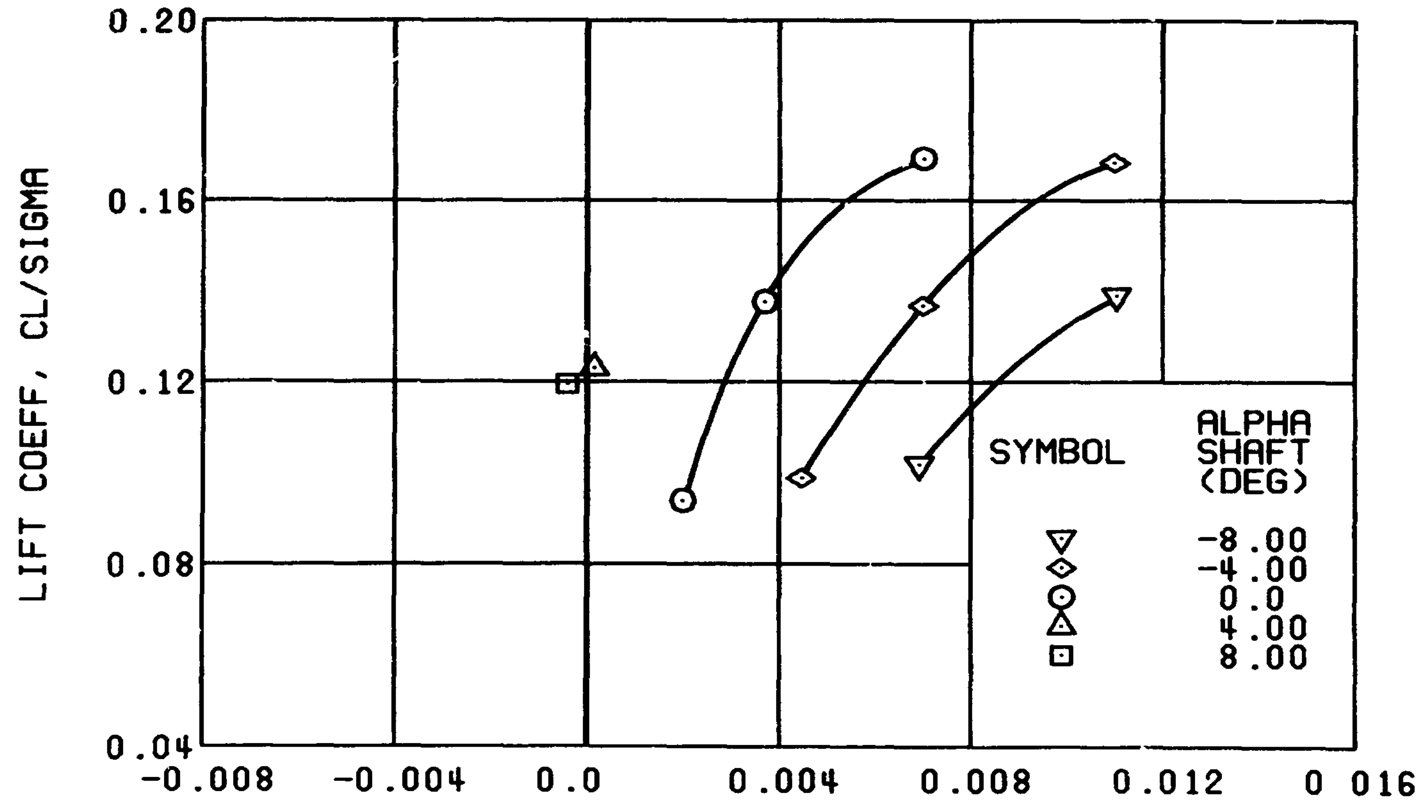

(b) TORQUE COEFFICIENT

Figure 22. Continued.
$\mu = 0.35 \quad B'_{1s} = 4$ Deg

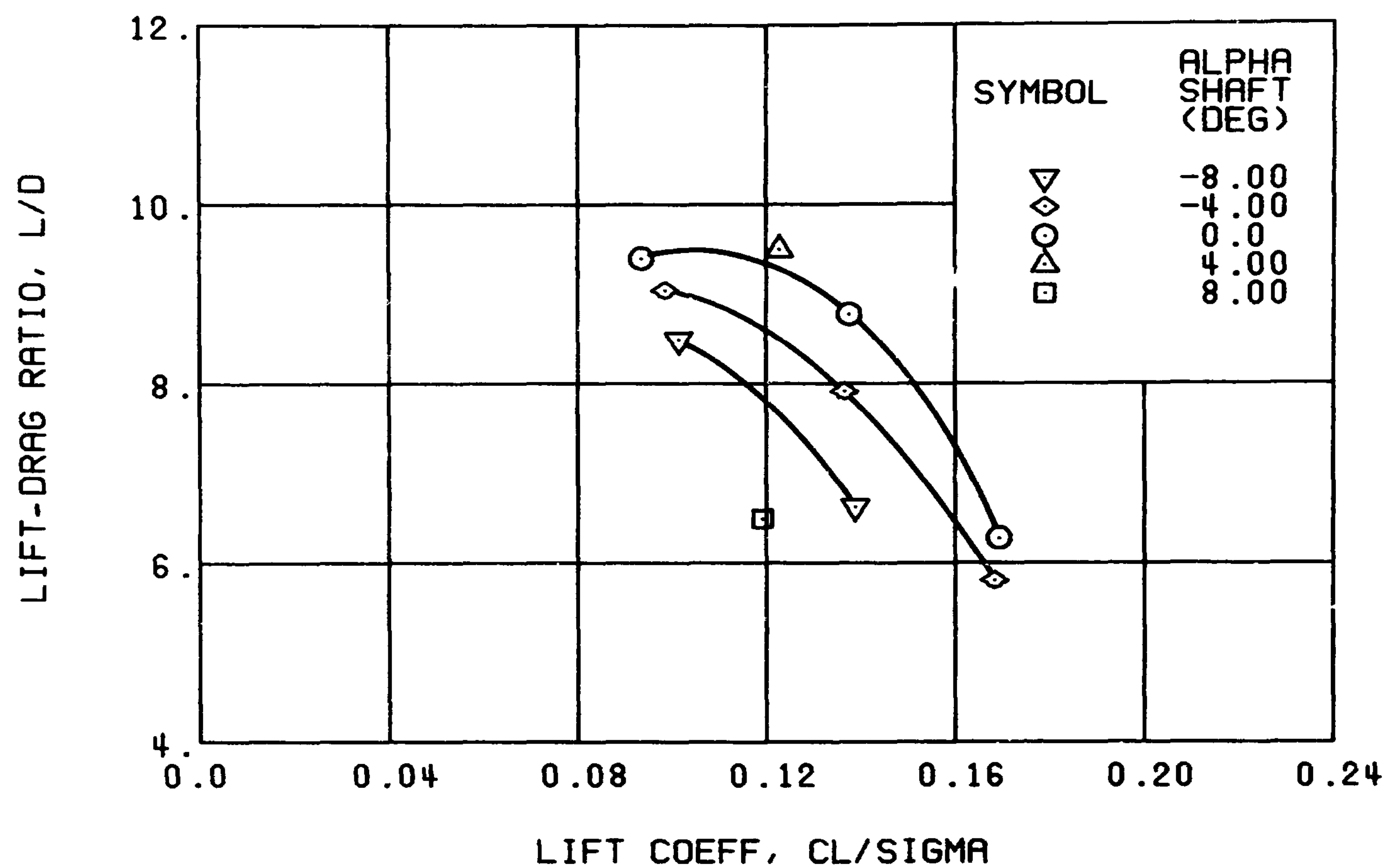

(c) LIFT-DRAG RATIO

Figure 22. Continued.
μ = 0.35 B'_{1s} = 4 Deg

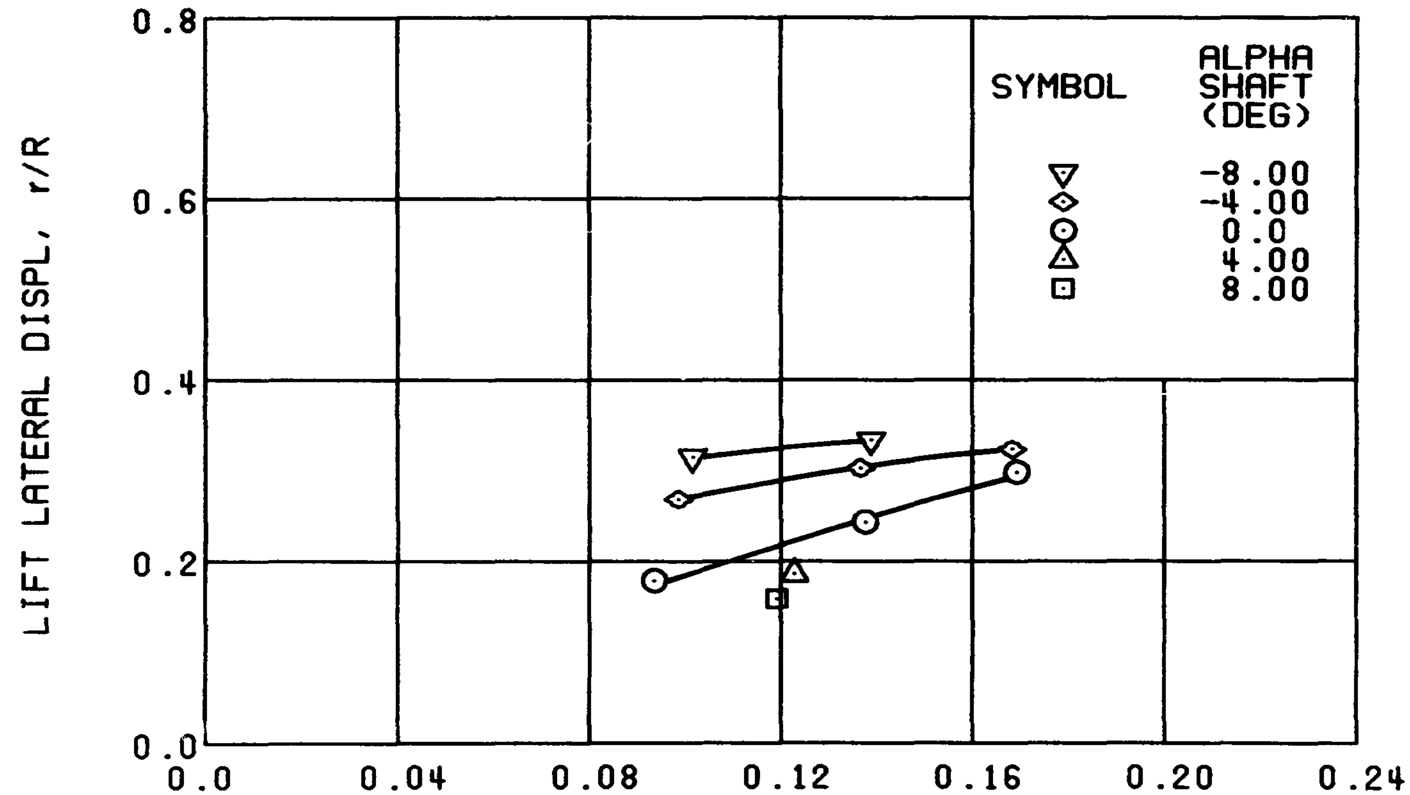

(d) LIFT LATERAL DISPLACEMENT

Figure 22. Continued.
$\mu = 0.35 \quad B'_{1s} = 4$ Deg

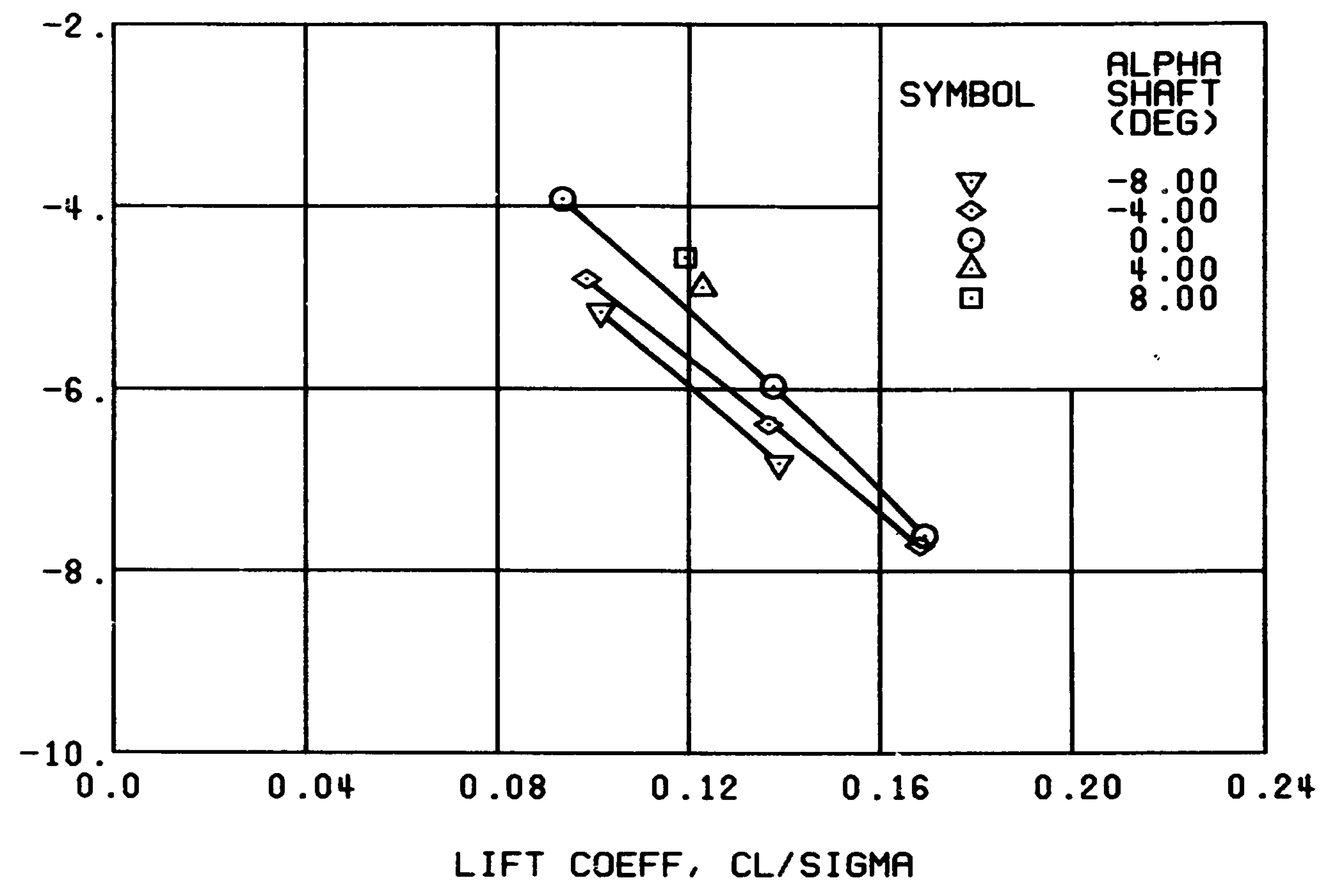

(e) LONGITUDINAL CYCLIC PITCH

Figure 22. Continued.
$\mu = 0.35 \quad B'_{1s} = 4$ Deg

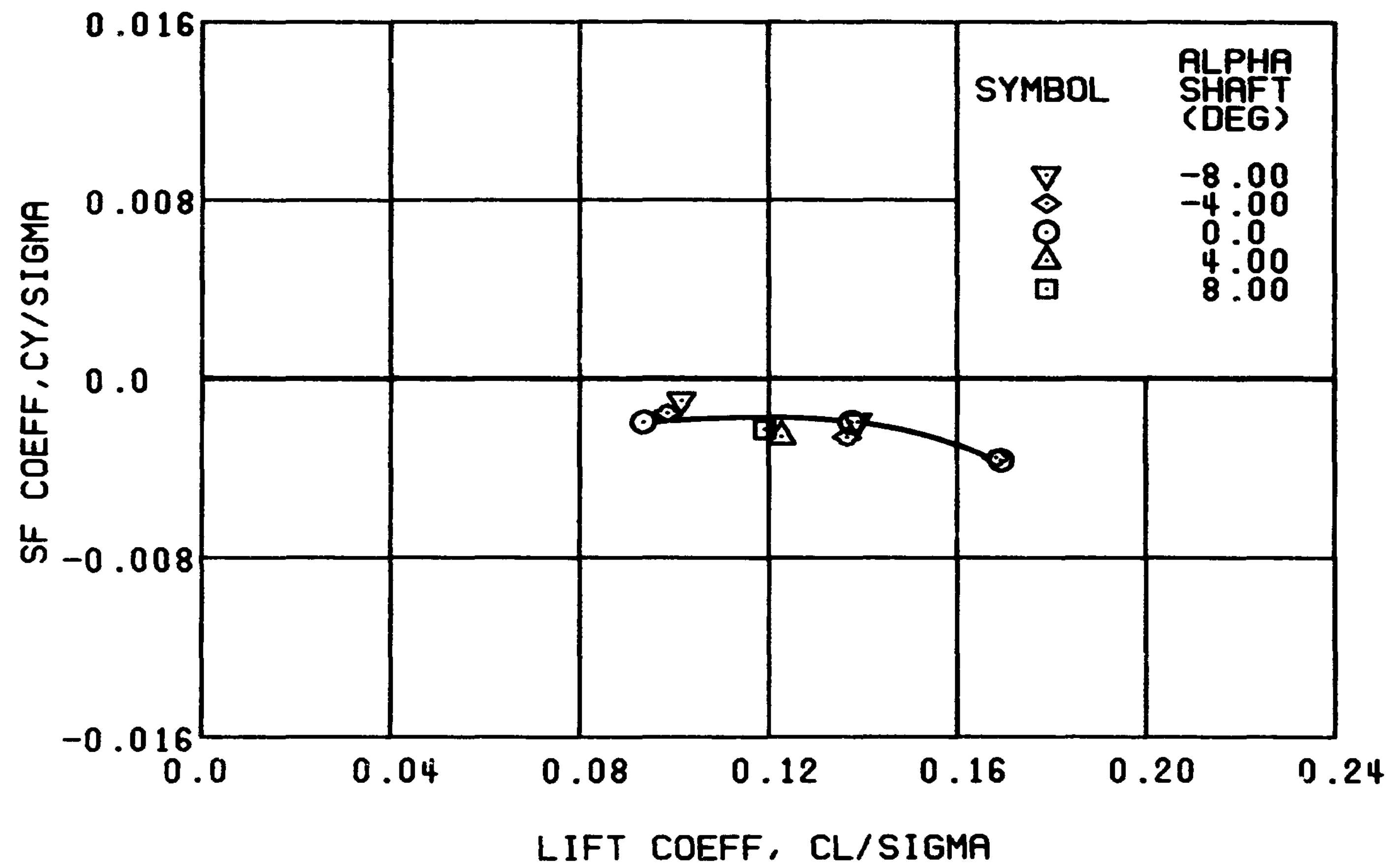

(f) SIDE FORCE COEFFICIENT

Figure 22. Continued.
$\mu = 0.35$ $B'_{1s} = 4$ Deg

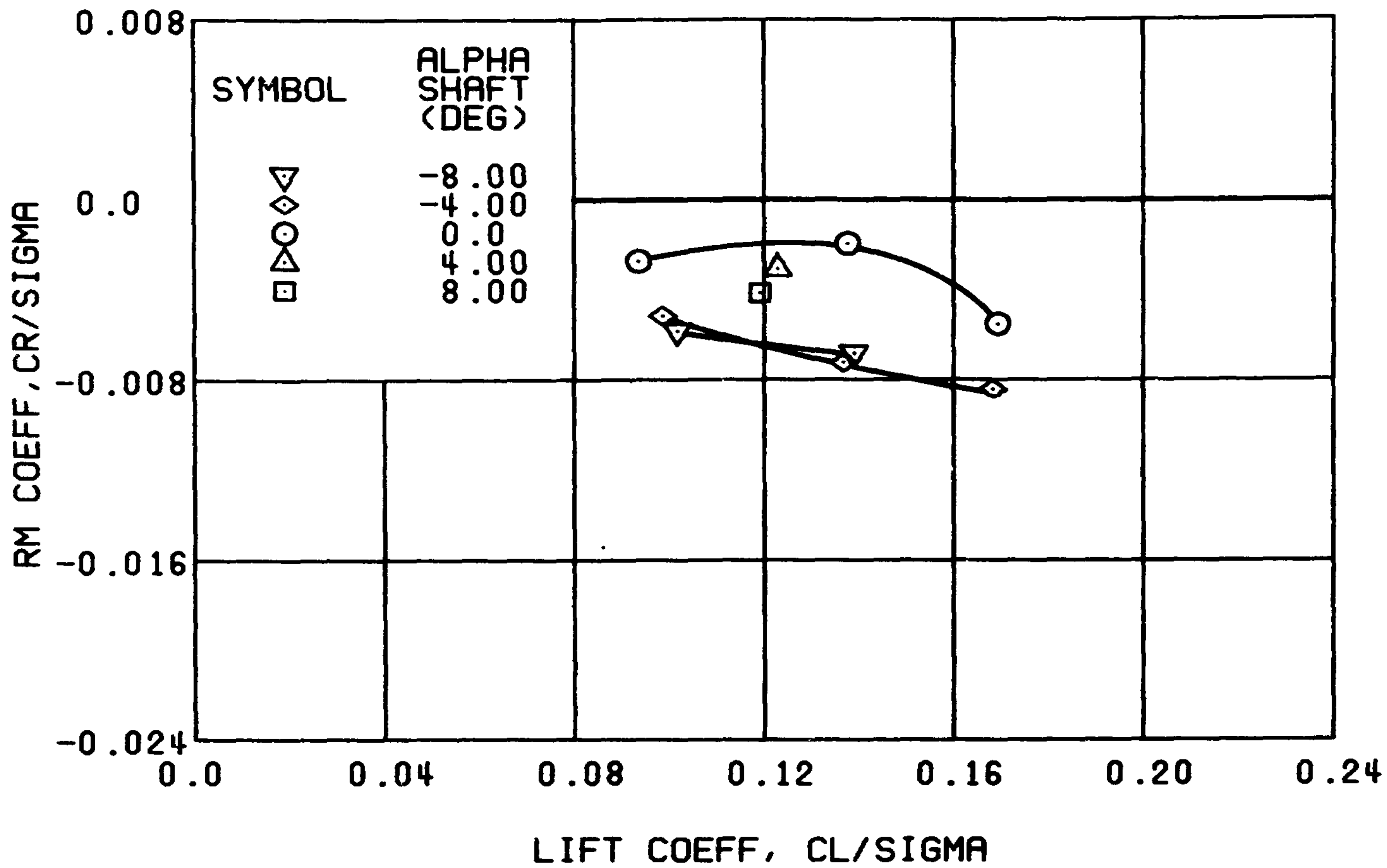

(g) ROLLING MOMENT COEFFICIENT

Figure 22. Continued.
$\mu = 0.35$ $B'_{1s} = 4$ Deg

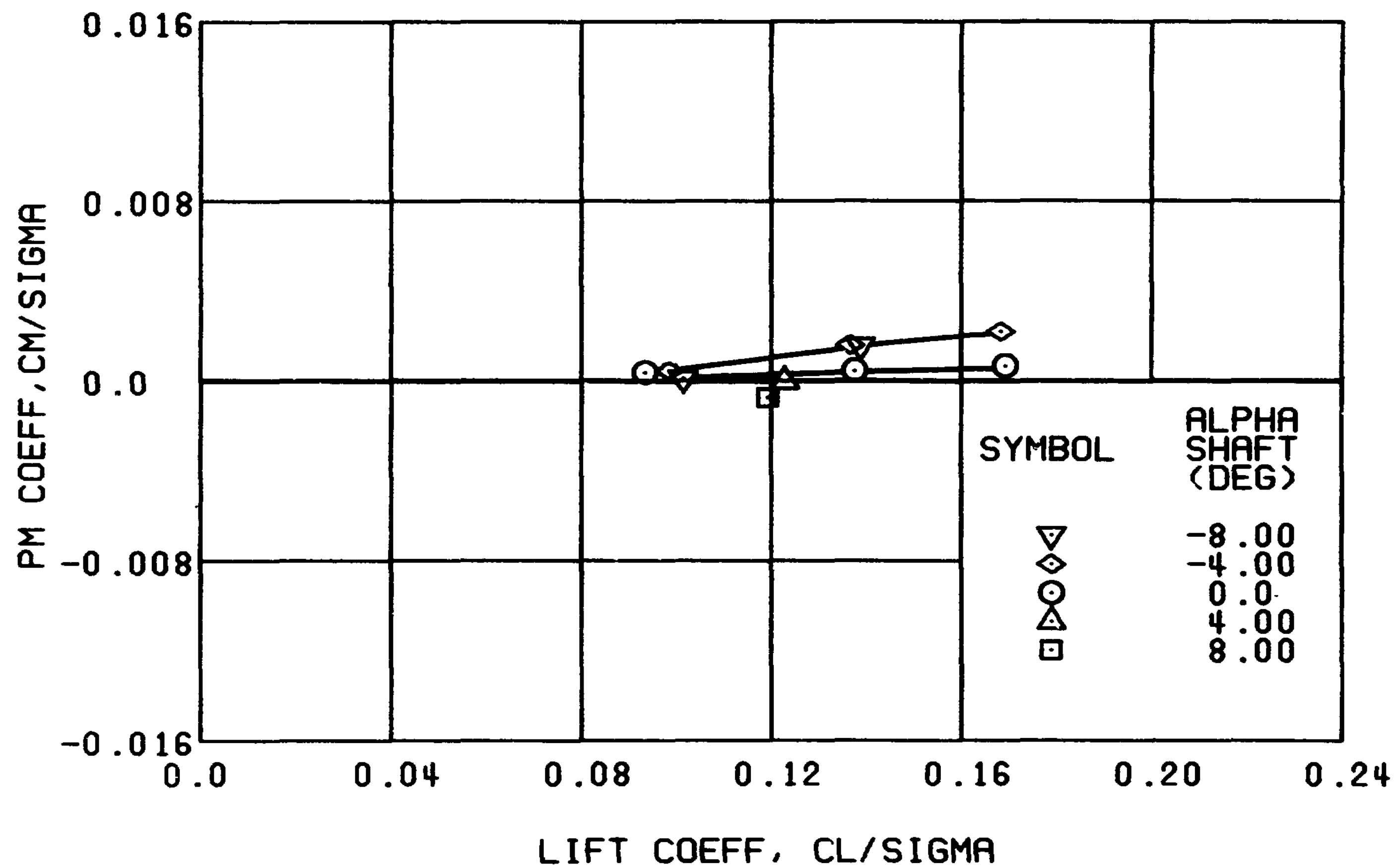

(h) PITCHING MOMENT COEFFICIENT

Figure 22. Continued.
$\mu = 0.35$ $B'_{1s} = 4$ Deg

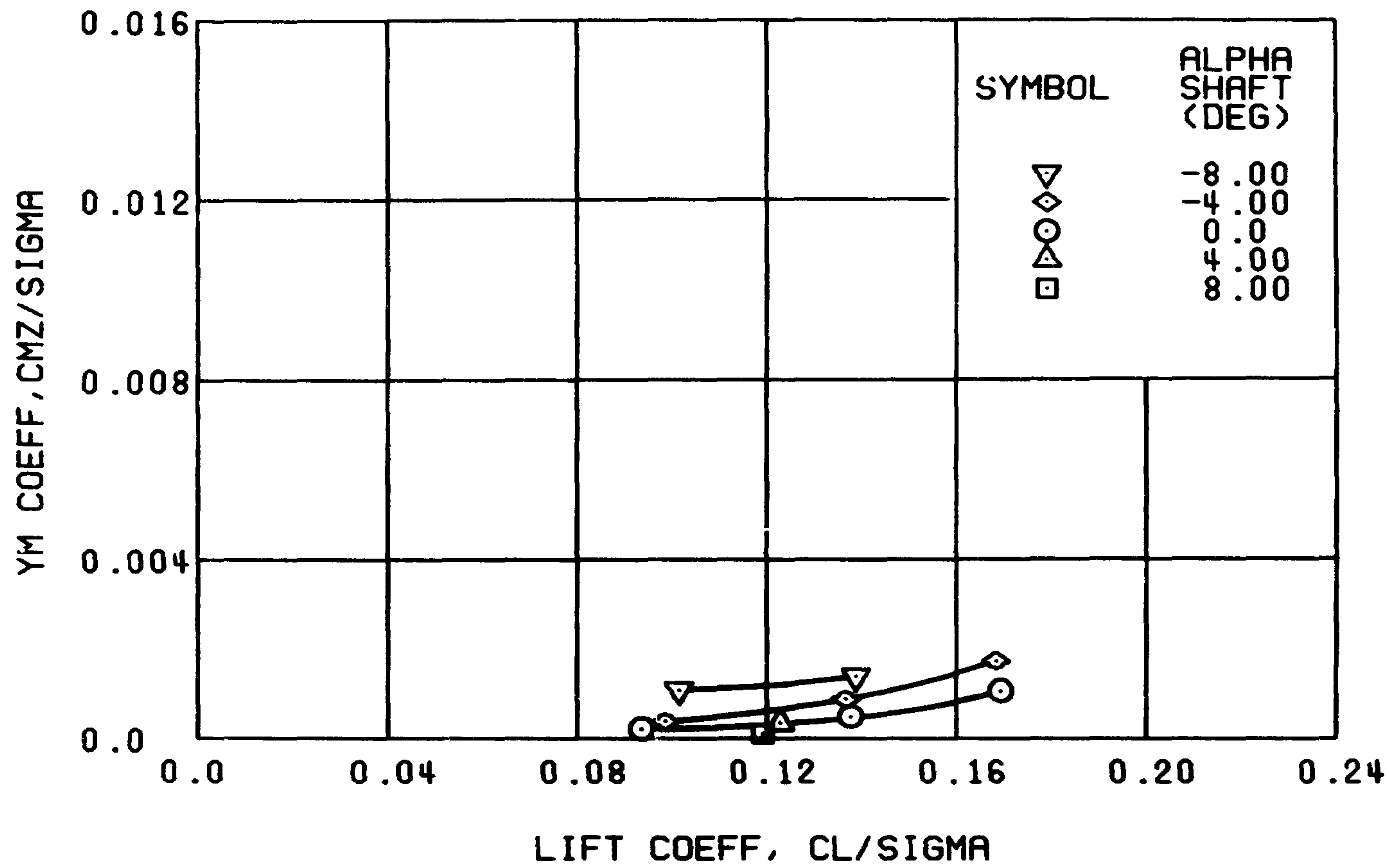

(i) YAWING MOMENT COEFFICIENT

Figure 22. Concluded.
$\mu = 0.35 \quad B'_{1s} = 4$ Deg

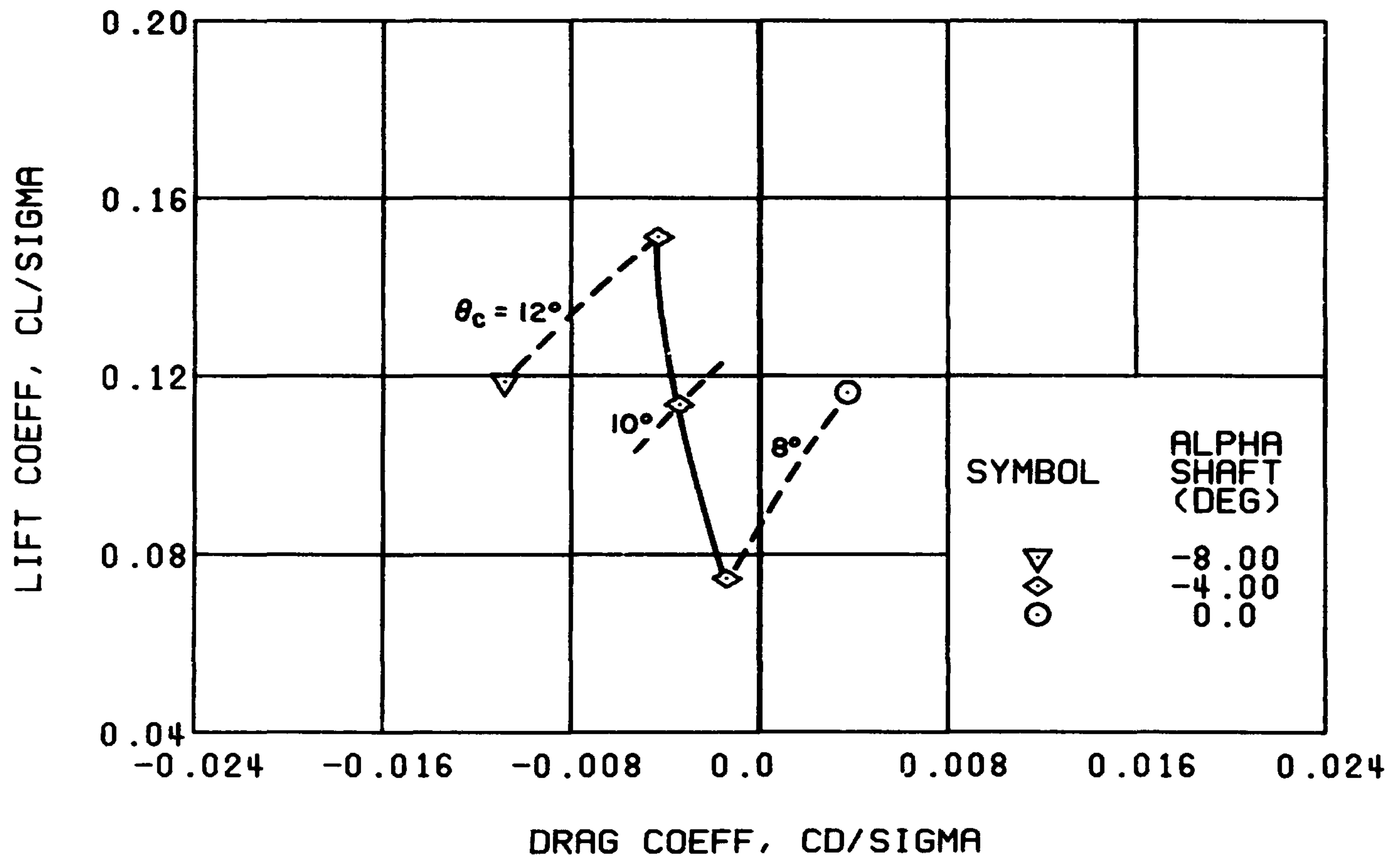

(a) DRAG COEFFICIENT

Figure 23. Performance Data at an Advance Ratio of 0.35 With the Lateral Displacement Control (B'_{1s}) Set at 6 Degrees.

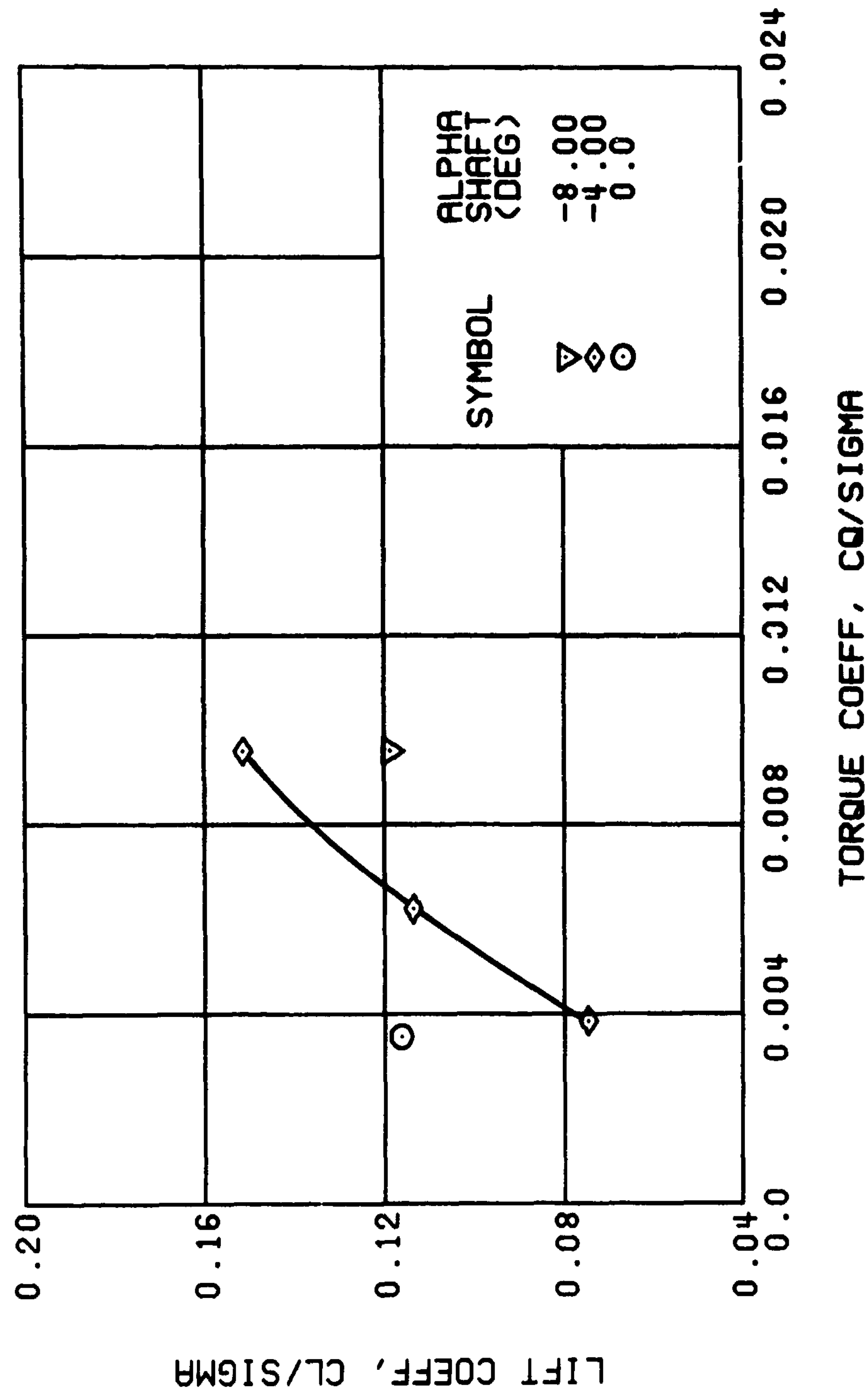

(b) TORQUE COEFFICIENT

Figure 23. Continued.
$\mu = 0.35$ $B'_{1c} = 6$ Deg

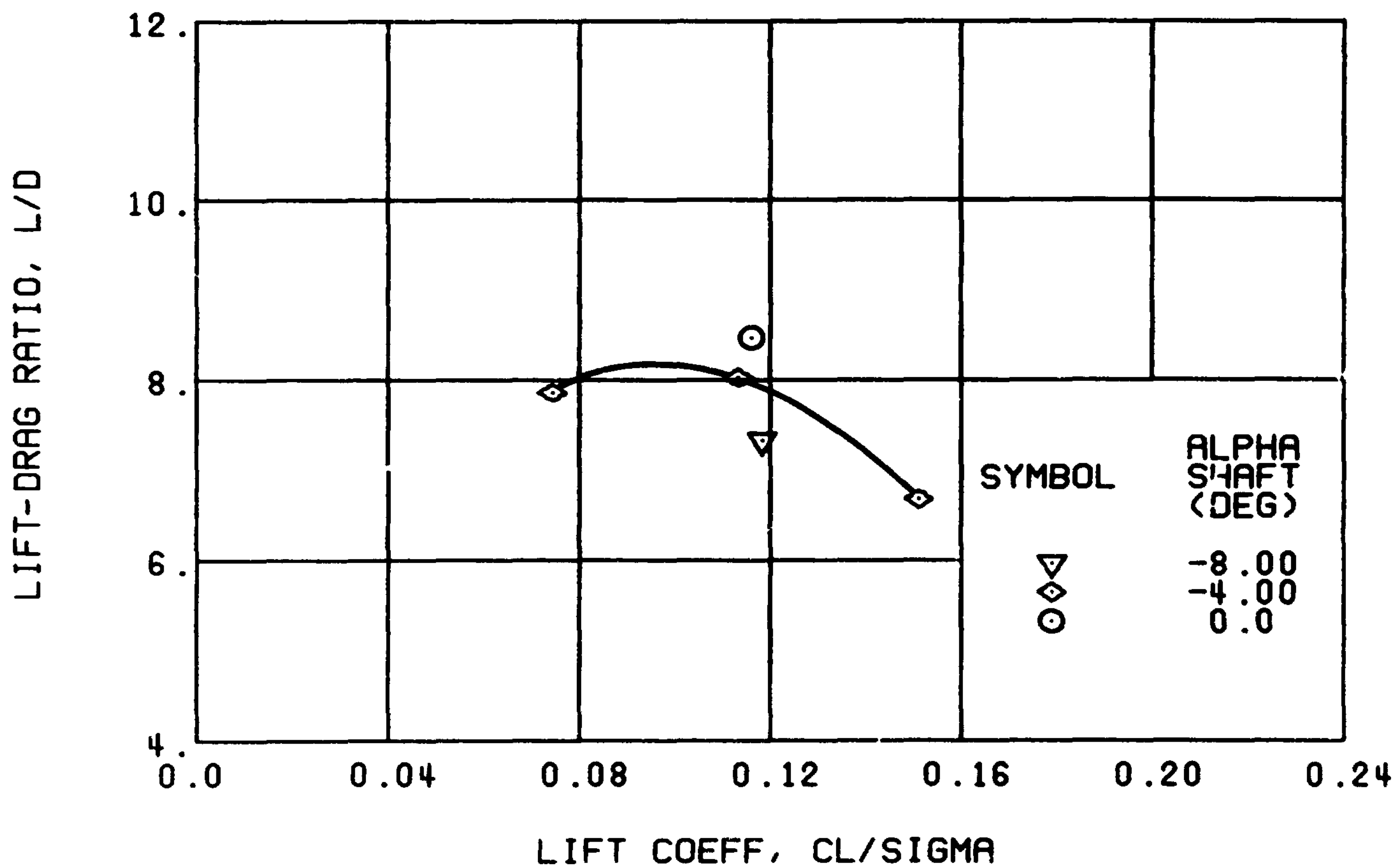

(c) LIFT-DRAG RATIO

Figure 23. Continued.
$\mu = 0.35$ $B'_{1s} = 6$ Deg

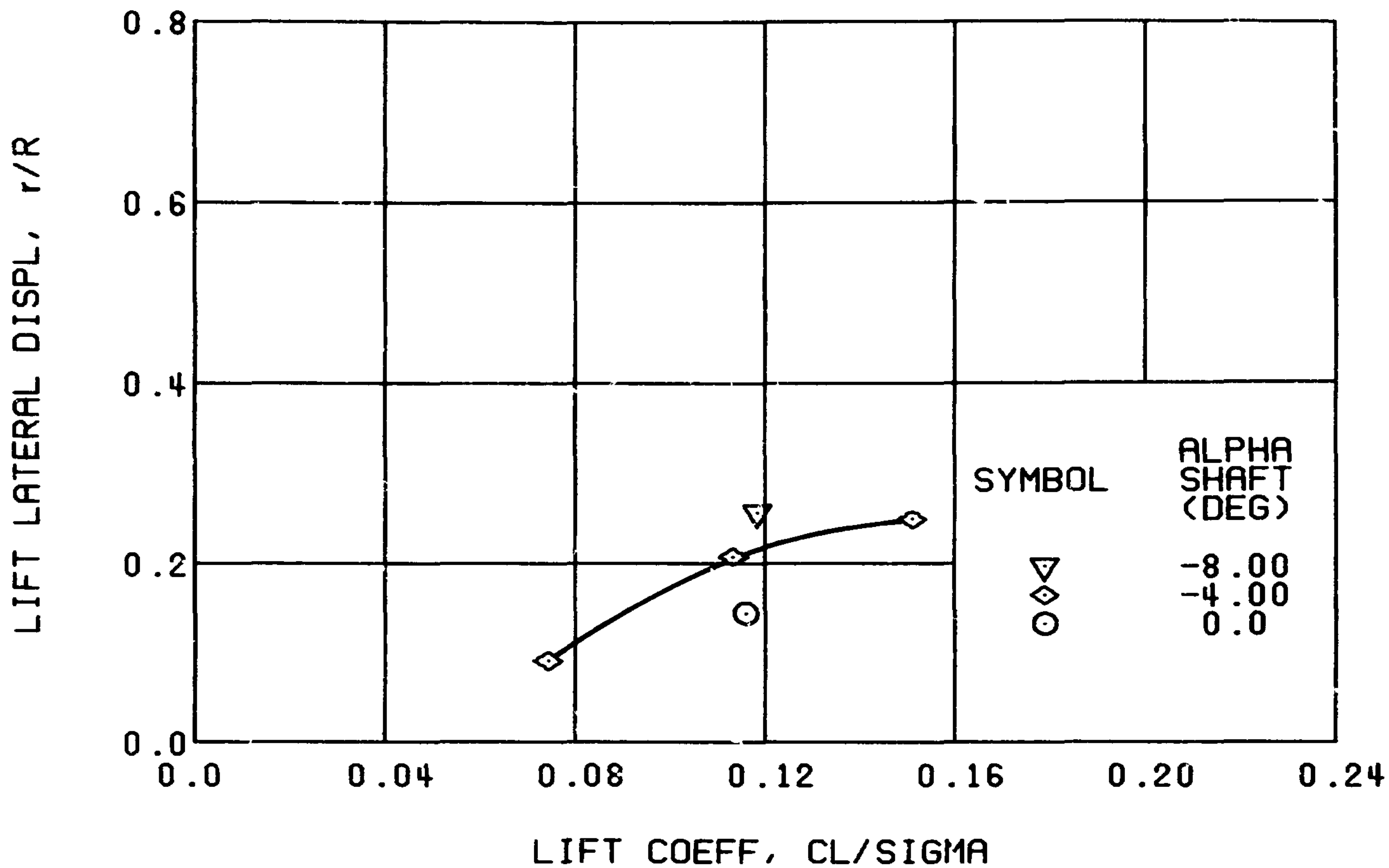

(d) LIFT LATERAL DISPLACEMENT

Figure 23. Continued.
$\mu = 0.35$ $B'_{1s} = 6$ Deg

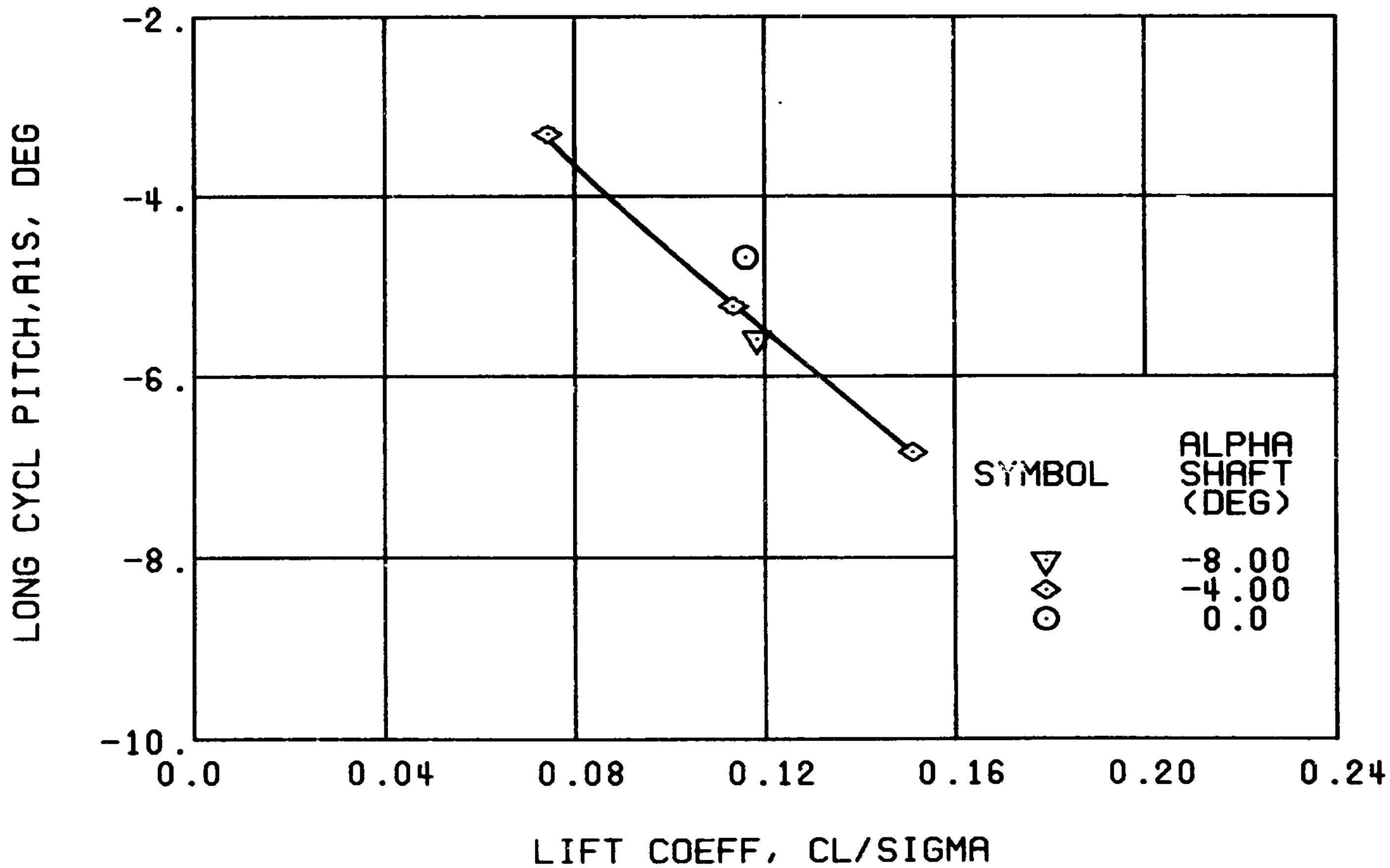

(e) LONGITUDINAL CYCLIC PITCH

Figure 23. Continued.
$\mu = 0.35$ $B'_{1s} = 6$ Deg

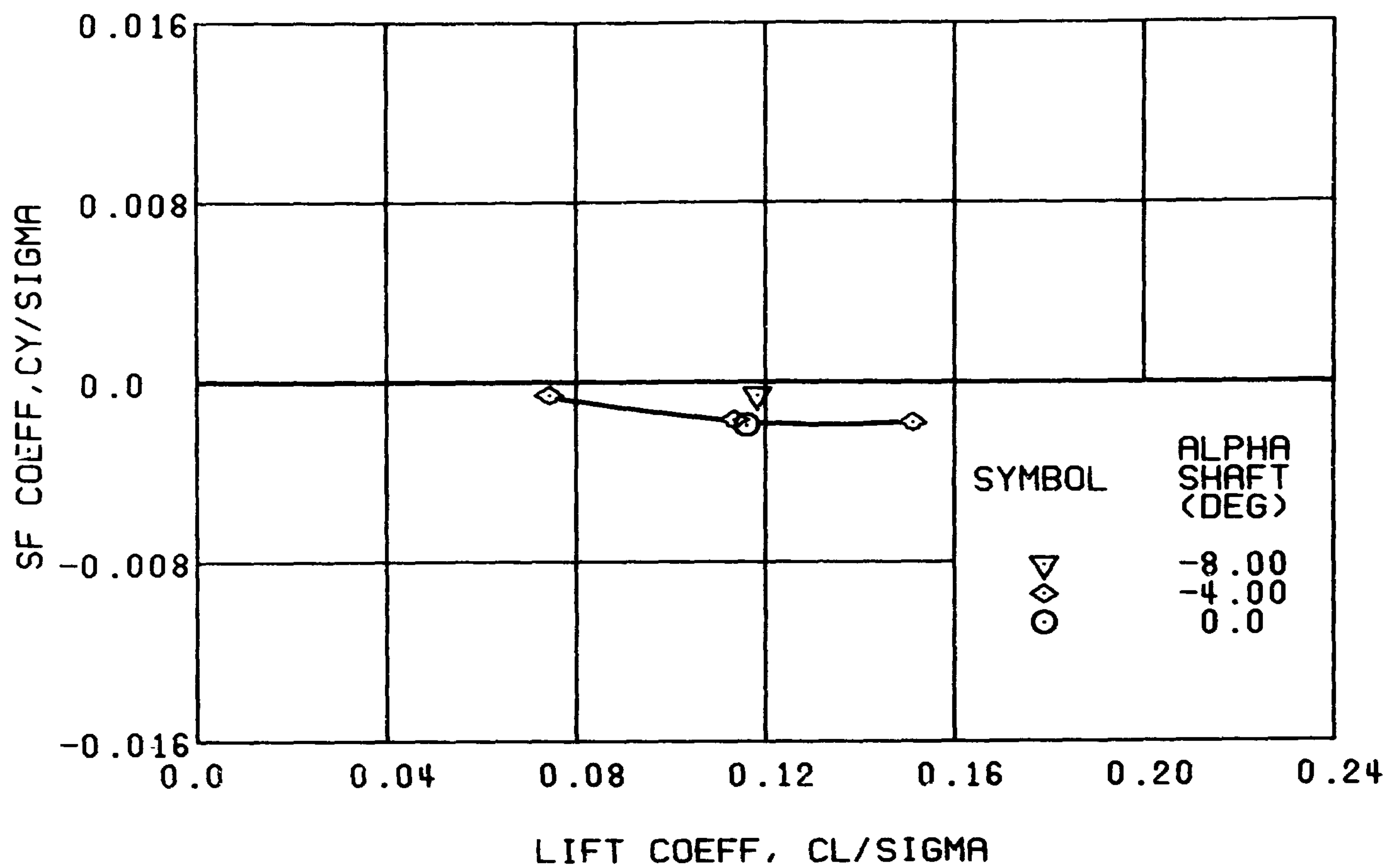

(f) SIDE FORCE COEFFICIENT

Figure 23. Continued.
$\mu = 0.35$ $B'_{1s} = 6$ Deg

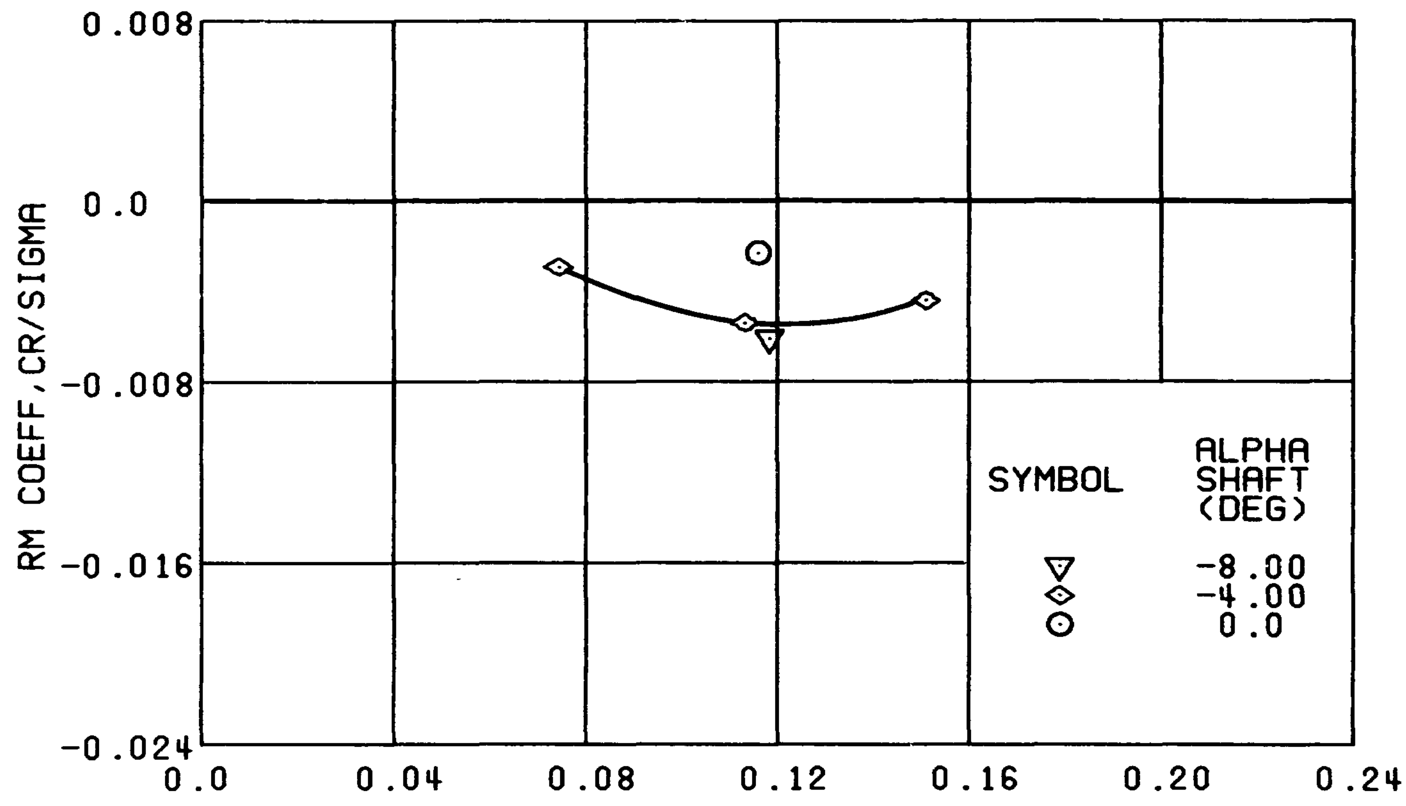

(g) ROLLING MOMENT COEFFICIENT

Figure 23. Continued.
$\mu = 0.35 \quad B'_{1s} = 6$ Deg

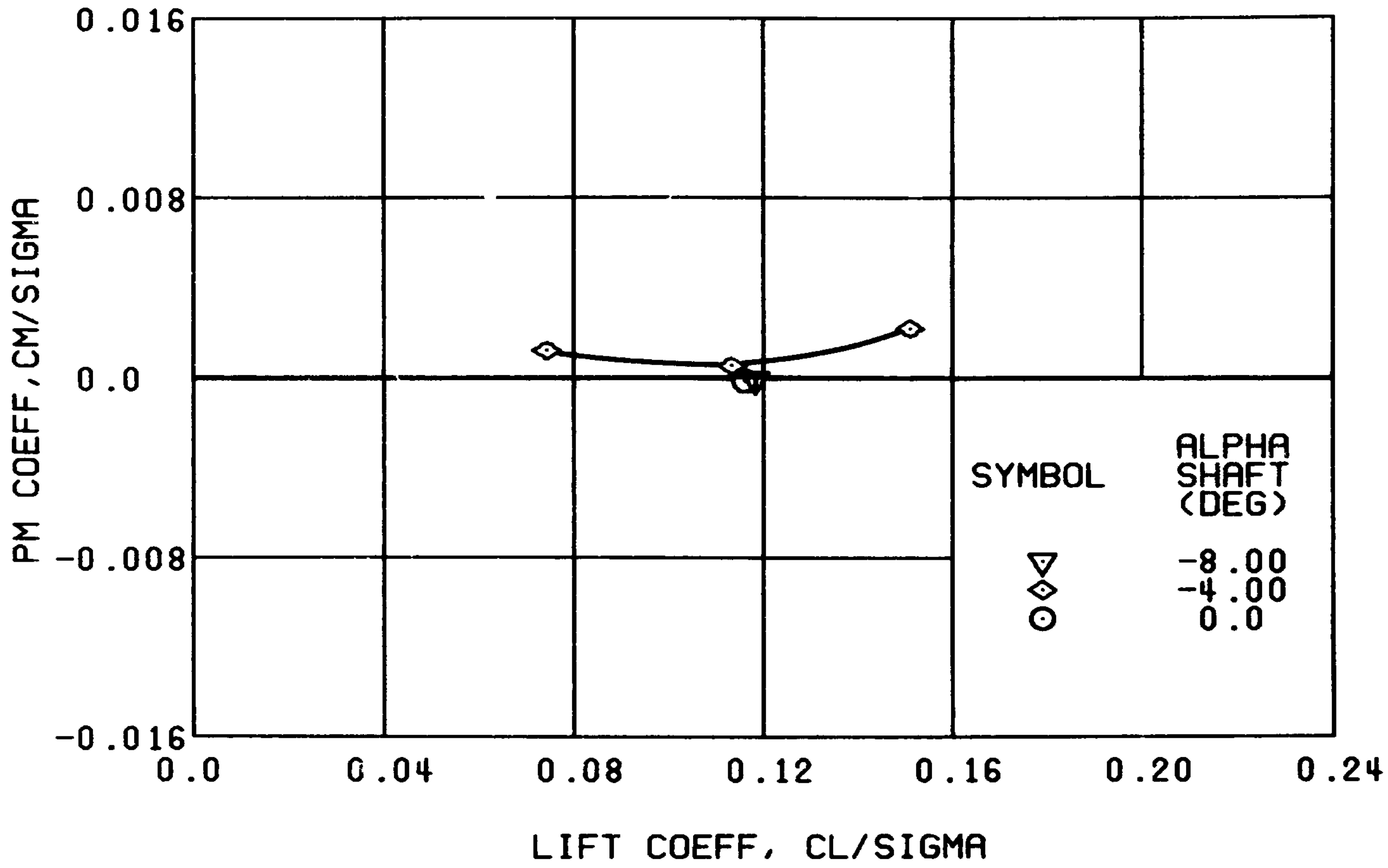

(h) PITCHING MOMENT COEFFICIENT

Figure 23. Continued.
$\mu = 0.35$ $B'_{1s} = 6$ Deg

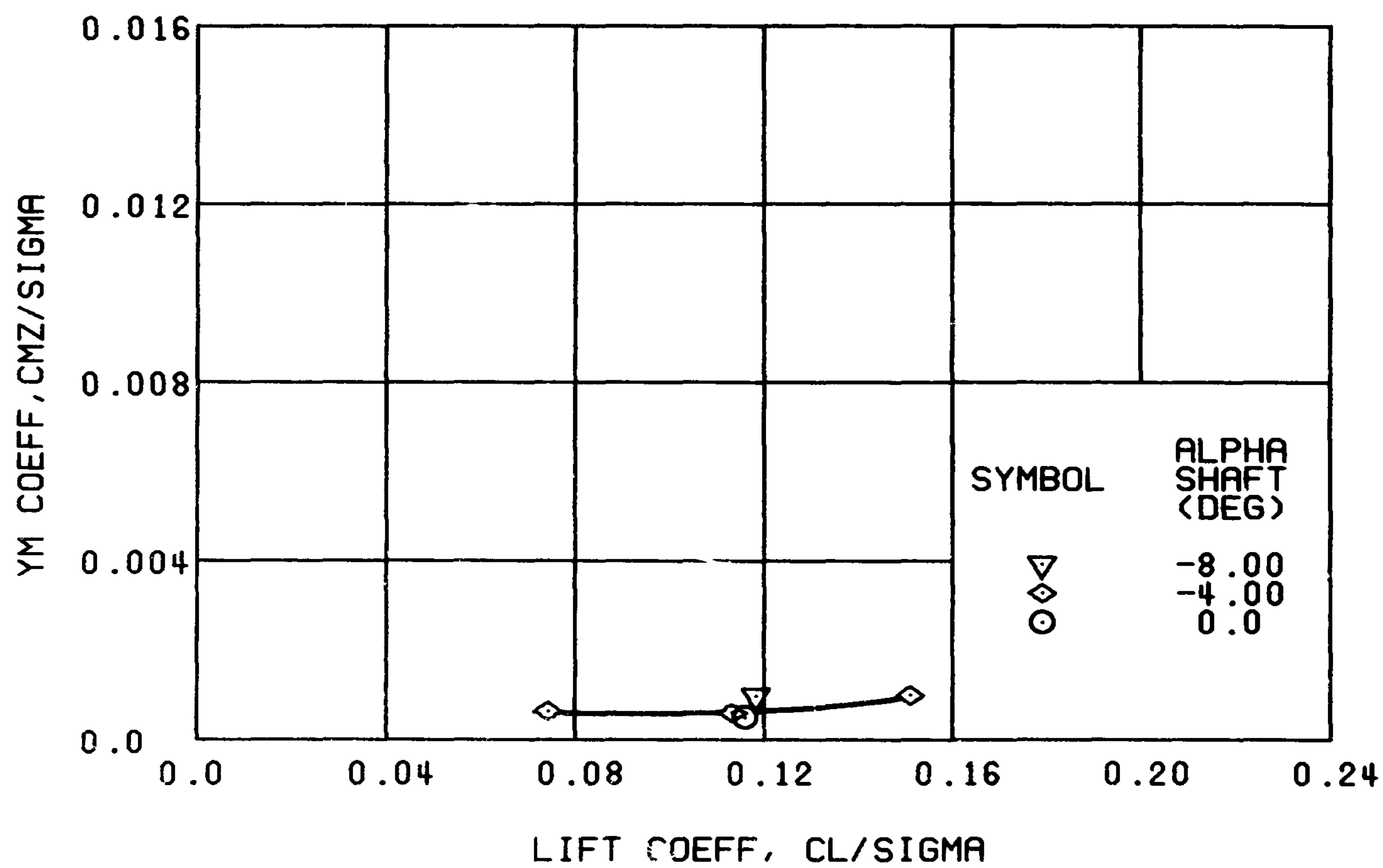

(i) YAWING MOMENT COEFFICIENT

Figure 23. Concluded.
$\mu = 0.35$ $B'_{1s} = 6$ Deg

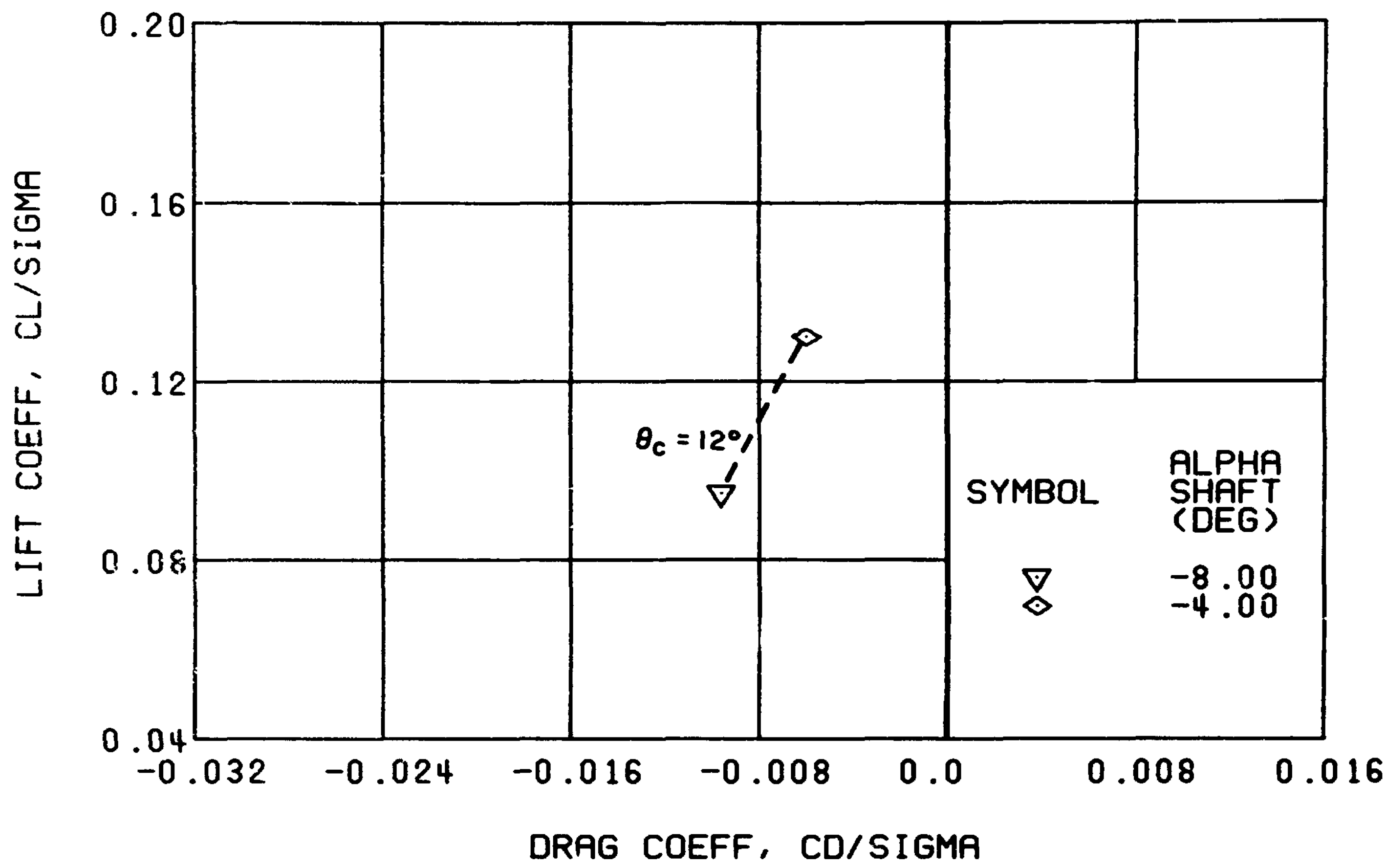

(a) DRAG COEFFICIENT

Figure 24. Performance Date at an Advance Ratio of 0.35 With the Lateral Displacement Control (B'_{1s}) Set at 8 Degrees.

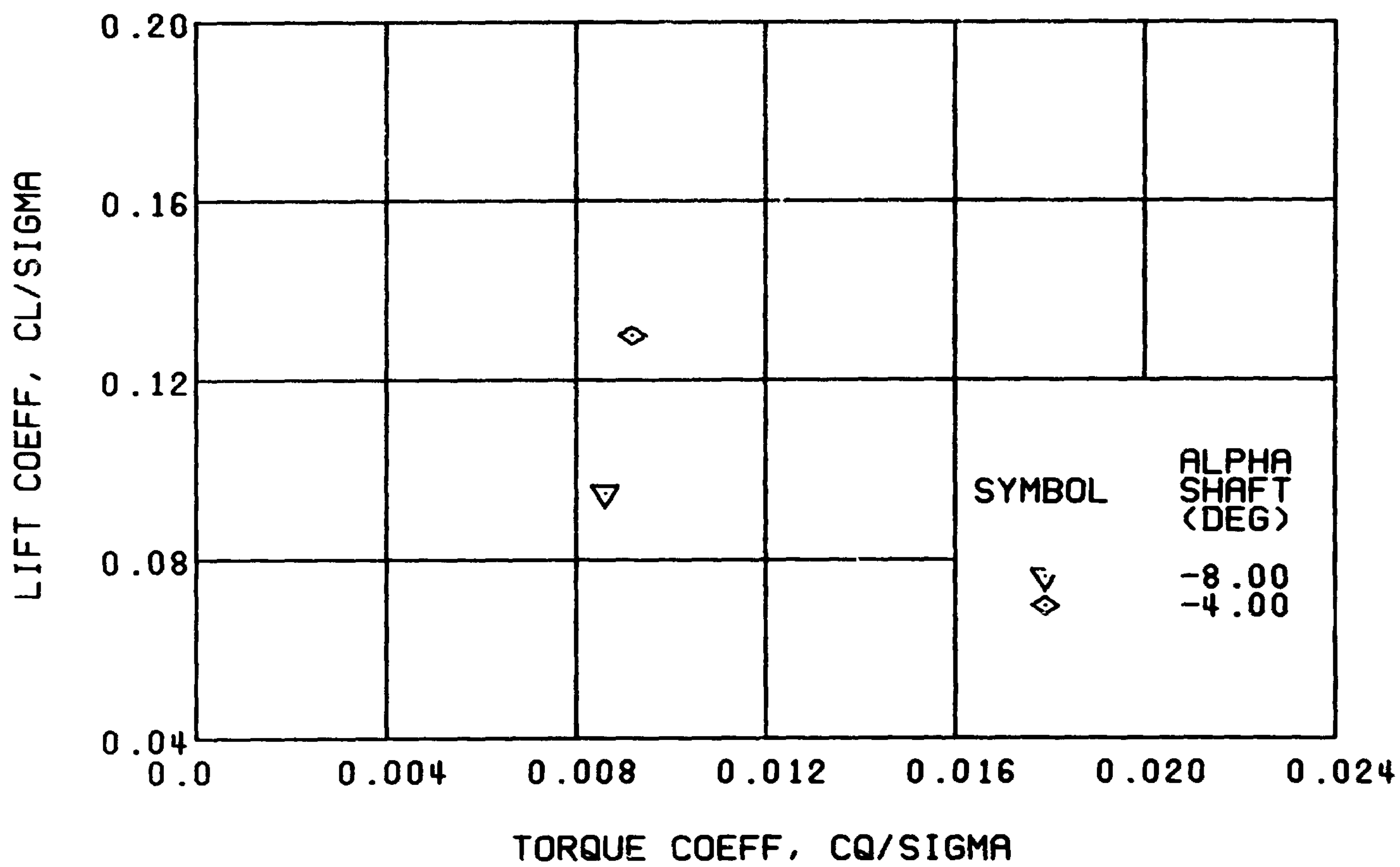

(b) TORQUE COEFFICIENT

Figure 24. Continued.
$\mu = 0.35 \quad B'_{1s} = 8$ Deg

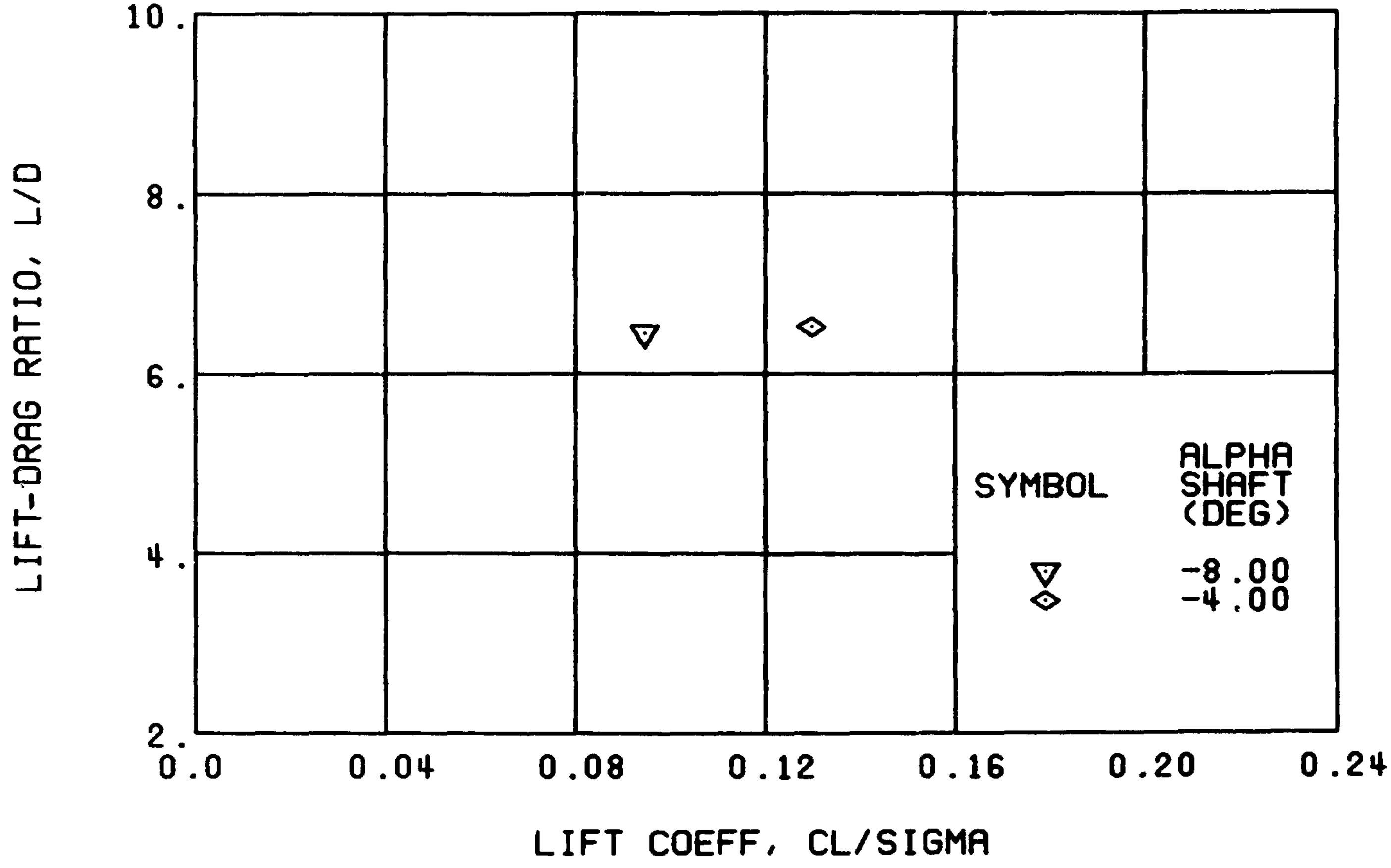

(c) LIFT-DRAG RATIO

Figure 24. Continued.
$\mu = 0.35$ $B'_{1s} = 8$ Deg

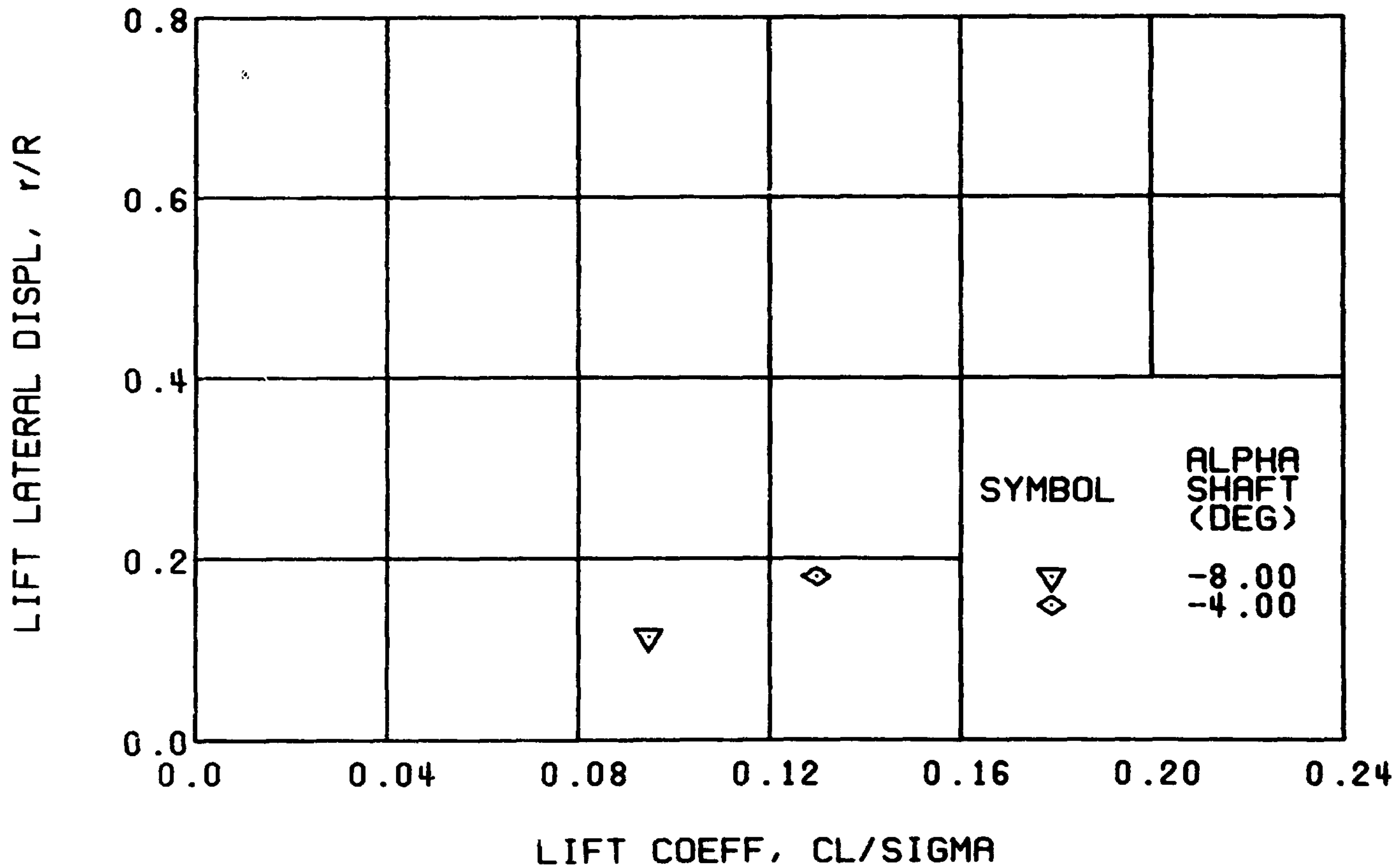

(d) LIFT LATERAL DISPLACEMENT

Figure 24. Continued.
$\mu = 0.35 \quad B'_{1s} = 8$ Deg

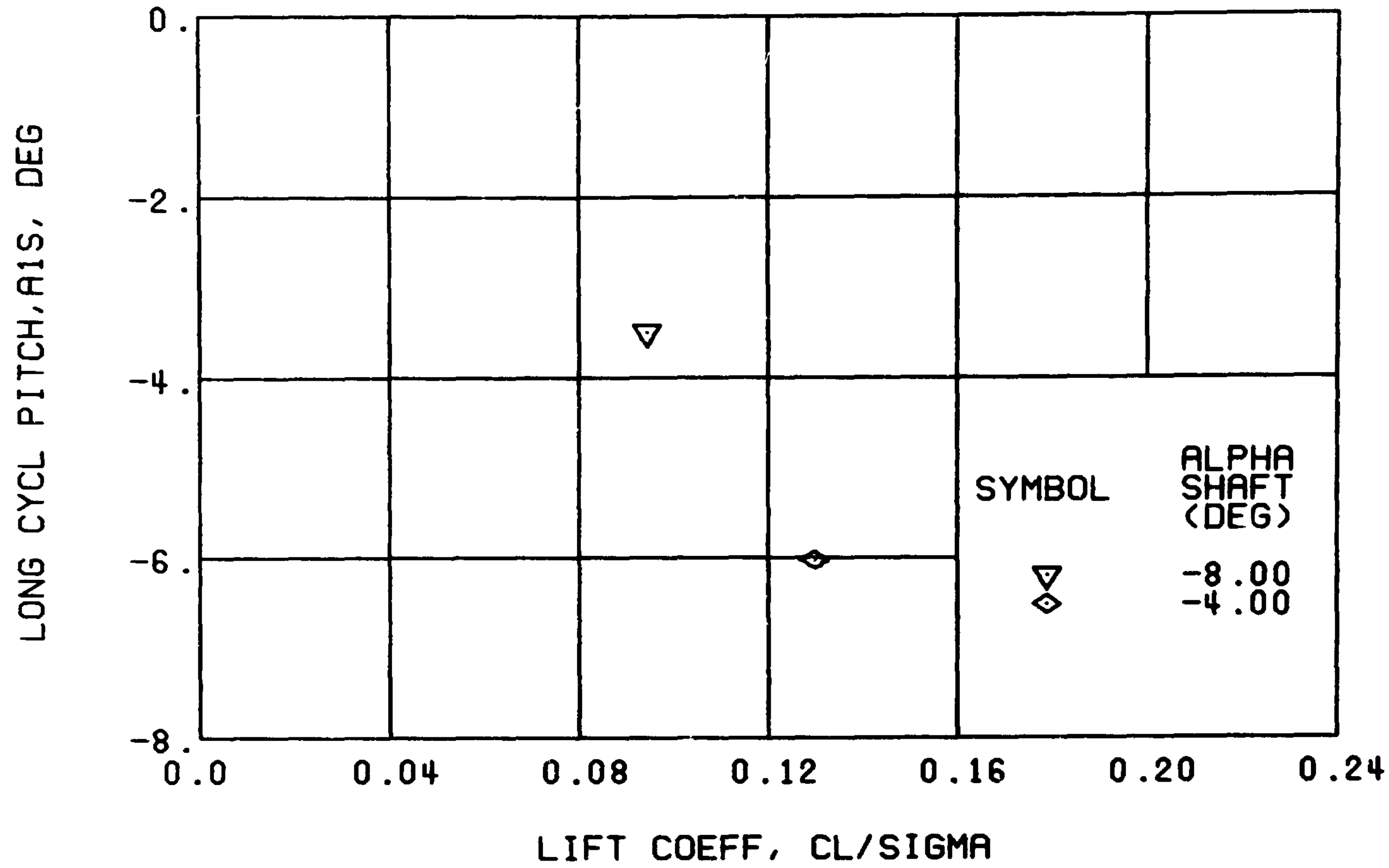

(e) LONGITUDINAL CYCLIC PITCH

Figure 24. Continued.
$\mu = 0.35$ $B'_{1s} = 8$ Deg

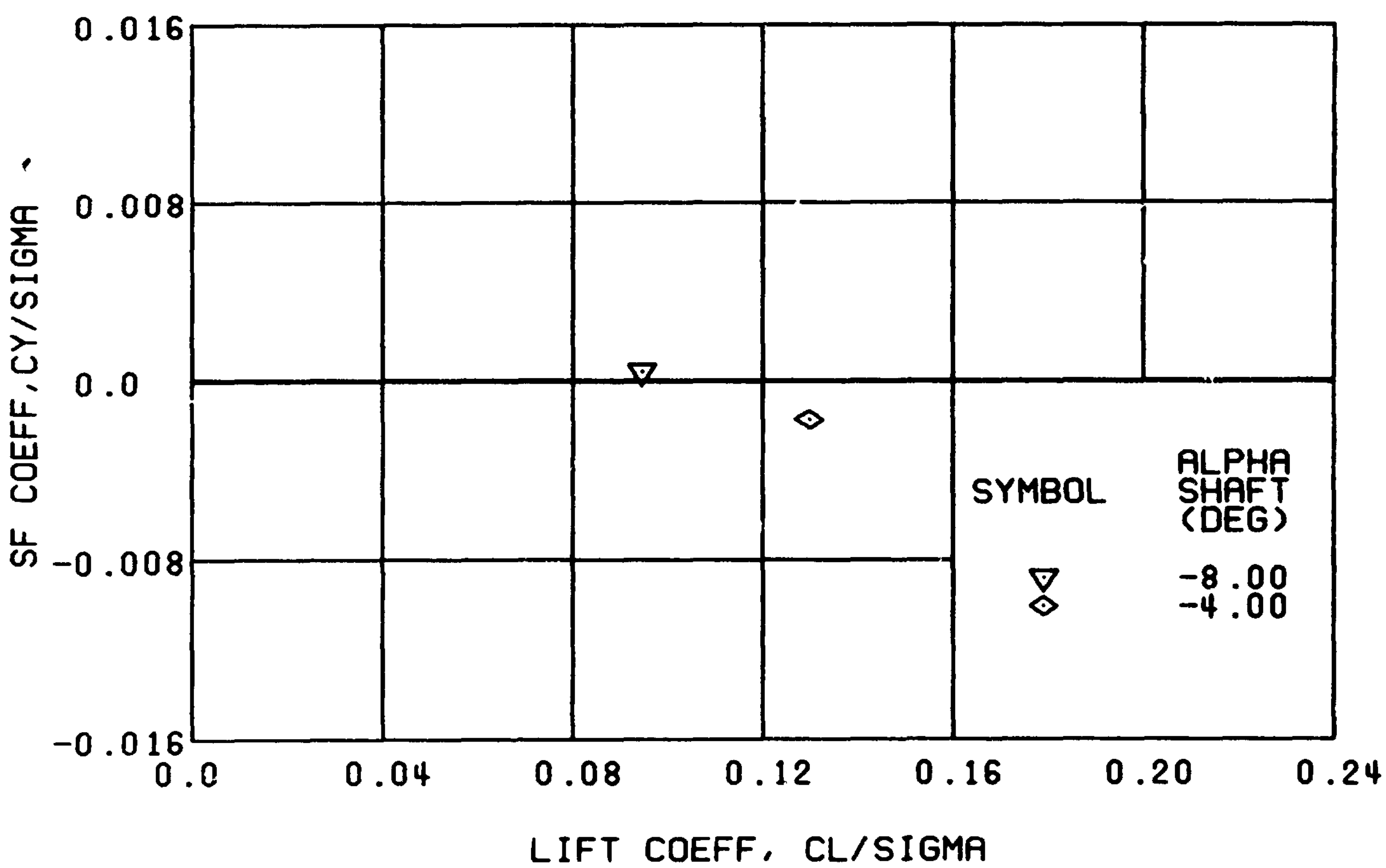

(f) SIDE FORCE COEFFICIENT

Figure 24. Continued.
$\mu = 0.35$ $B'_{1s} = 8$ Deg

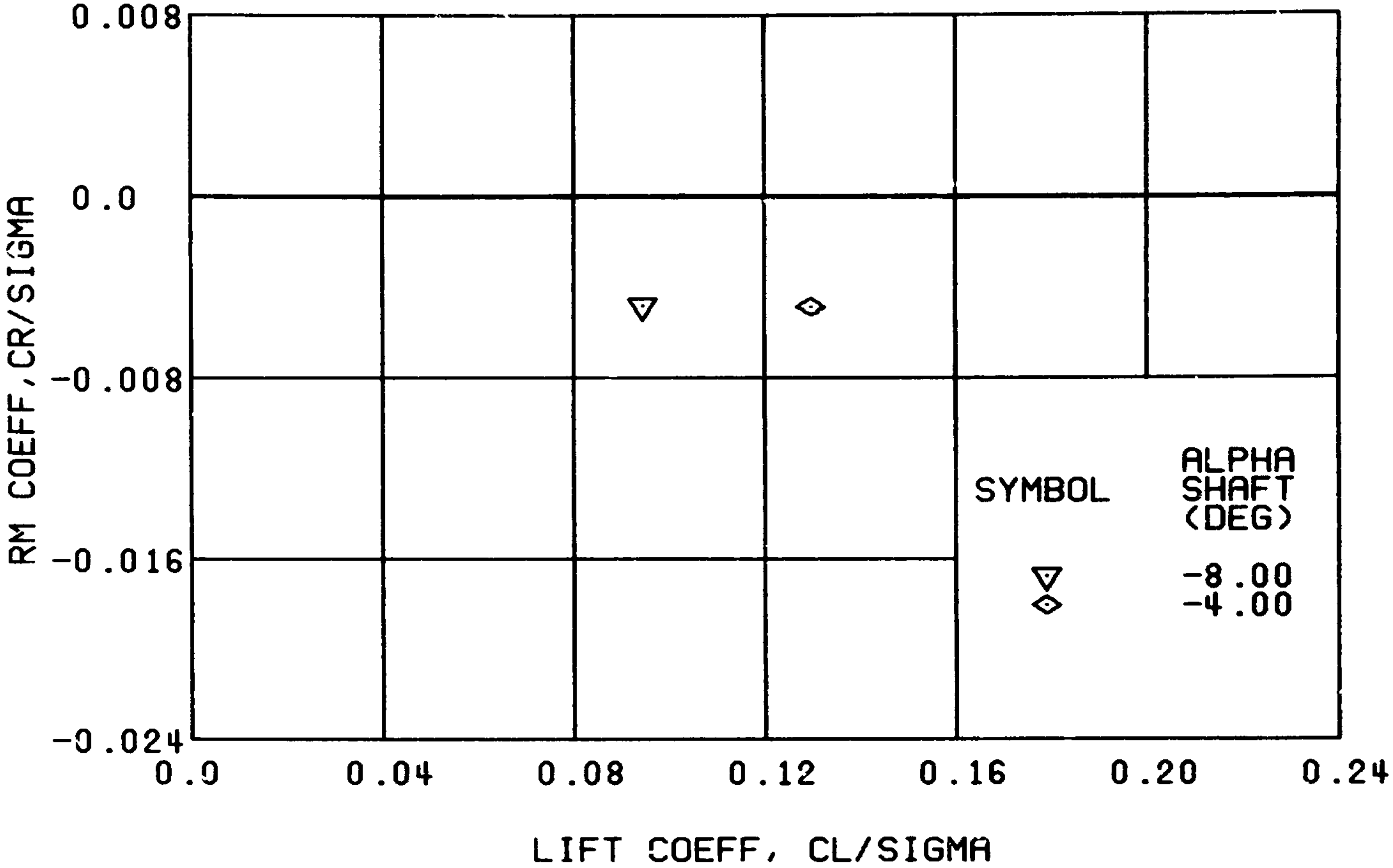

(g) ROLLING MOMENT COEFFICIENT

Figure 24. Continued.
$\mu = 0.35$ $B'_{1s} = 8$ Deg

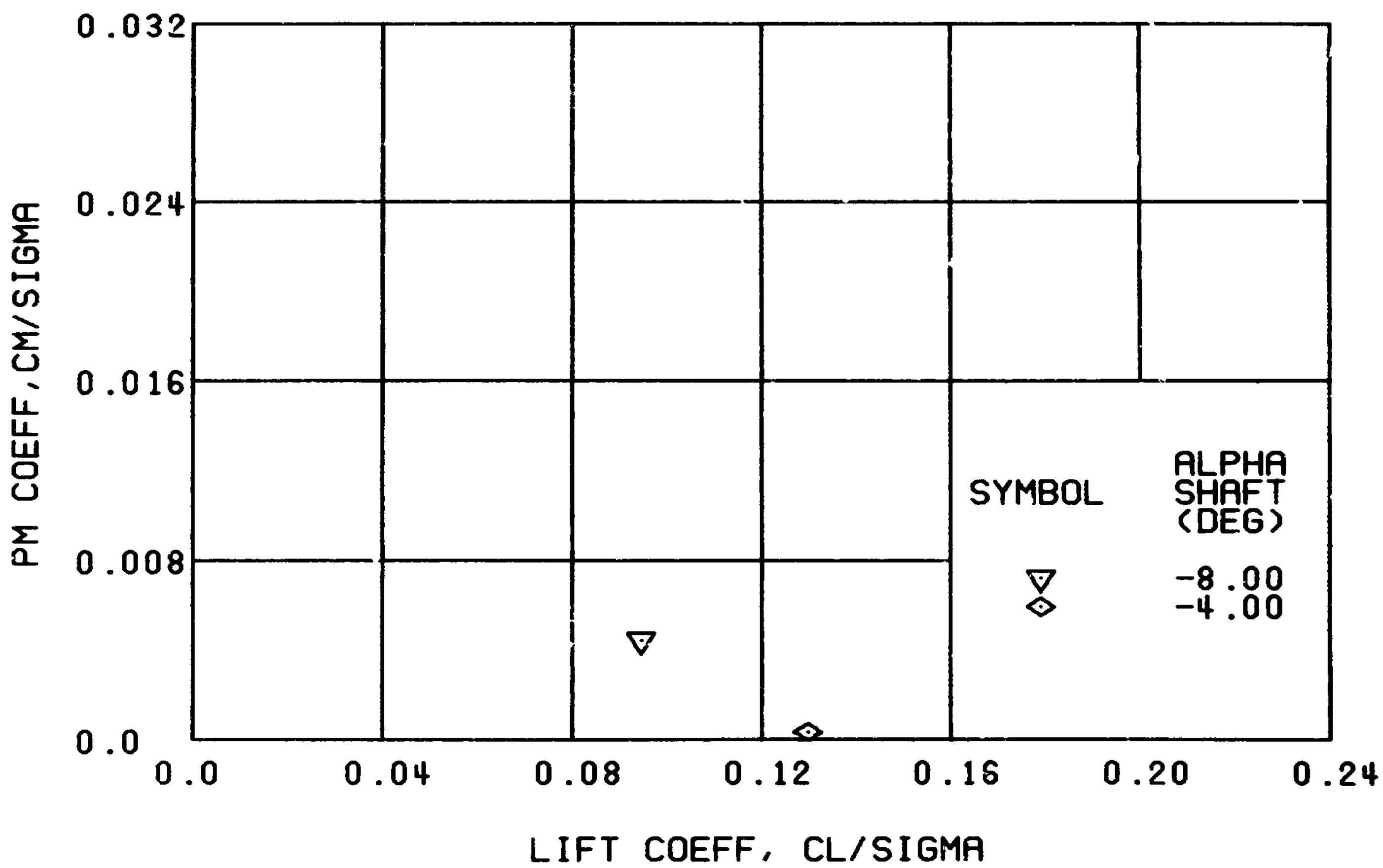

(h) PITCHING MOMENT COEFFICIENT

Figure 24. Continued.
$\mu = 0.35 \quad B'_{1s} = 8$ Deg

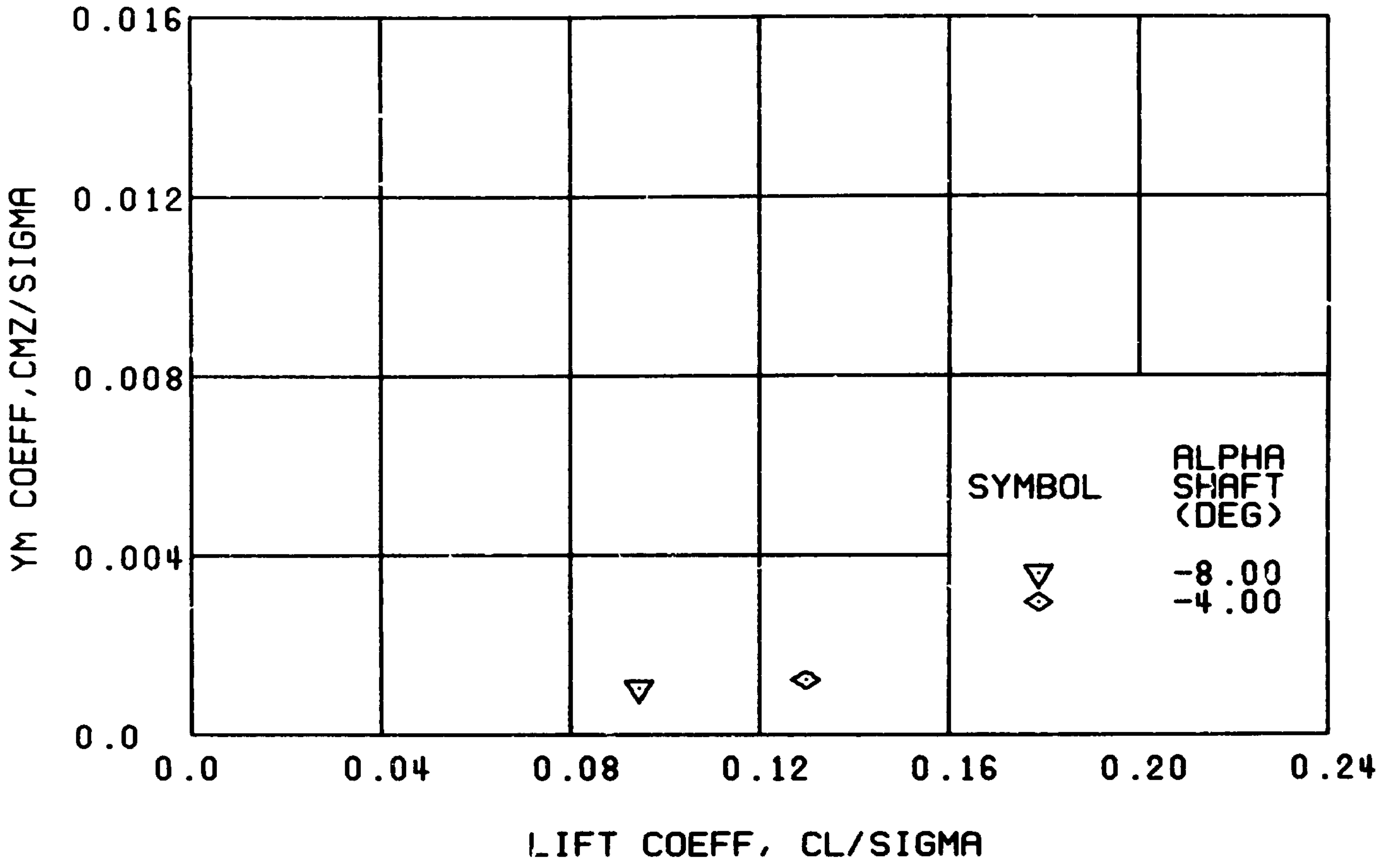

(i) YAWING MOMENT COEFFICIENT

Figure 24. Concluded.
$\mu = 0.35$ $B'_{1s} = 8$ Deg

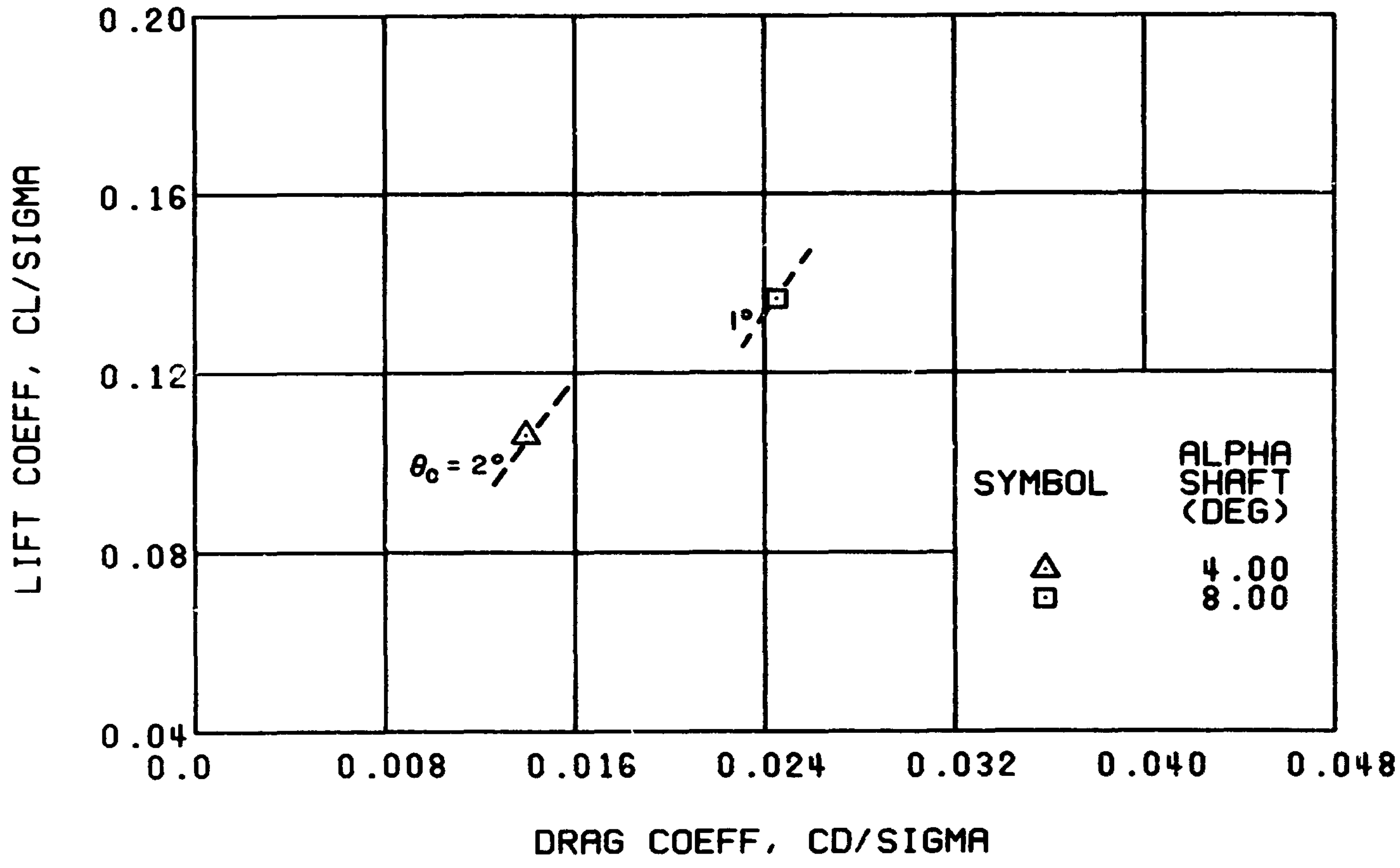

(a) DRAG COEFFICIENT

Figure 25. Performance Data at an Advance Ratio of 0.47 With the Lateral Displacement Control (B'_{1s}) Set at 0 Degrees.

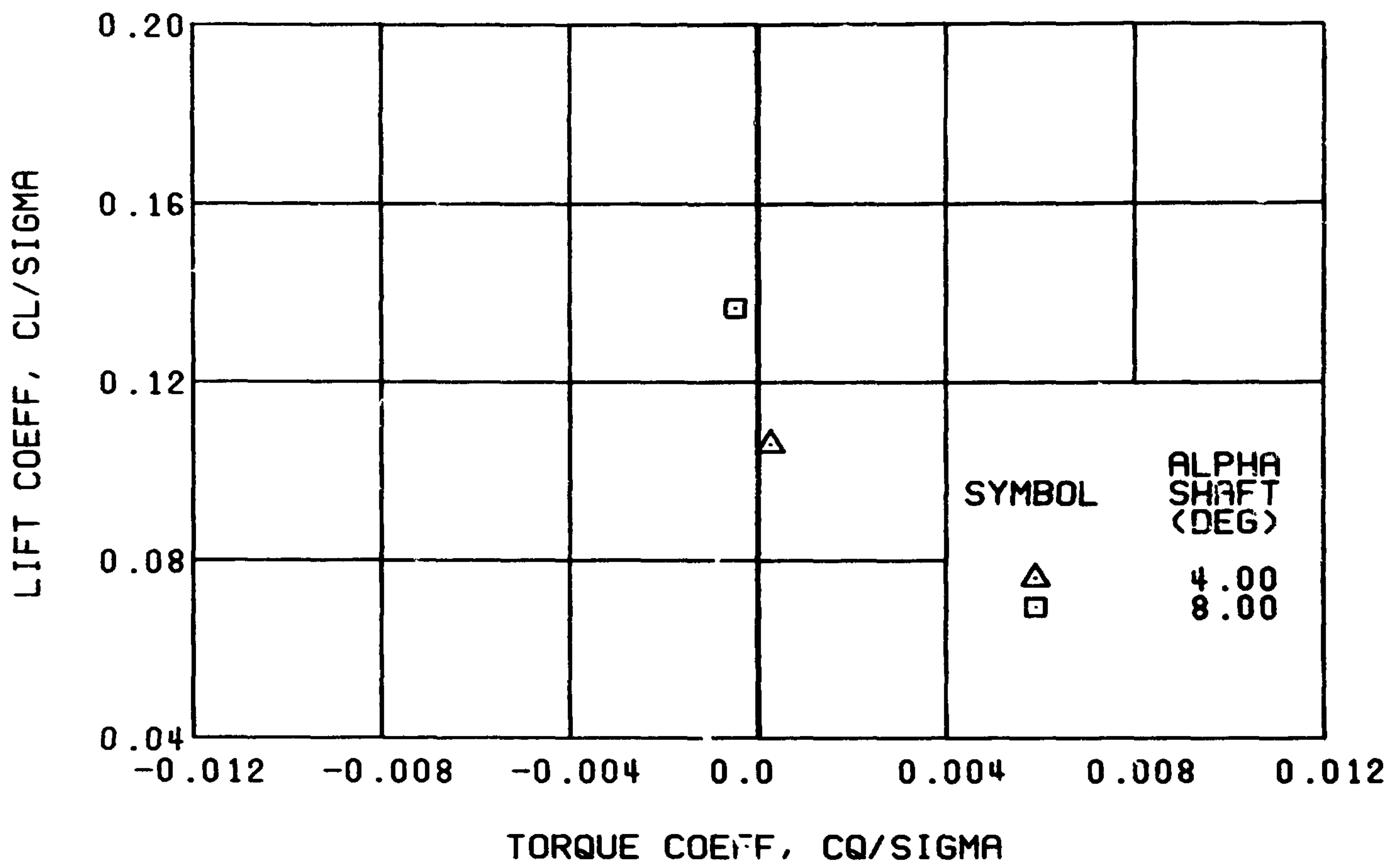

(b) TORQUE COEFFICIENT

Figure 25. Continued.
$\mu = 0.47 \quad B'_{1s} = 0$ Deg

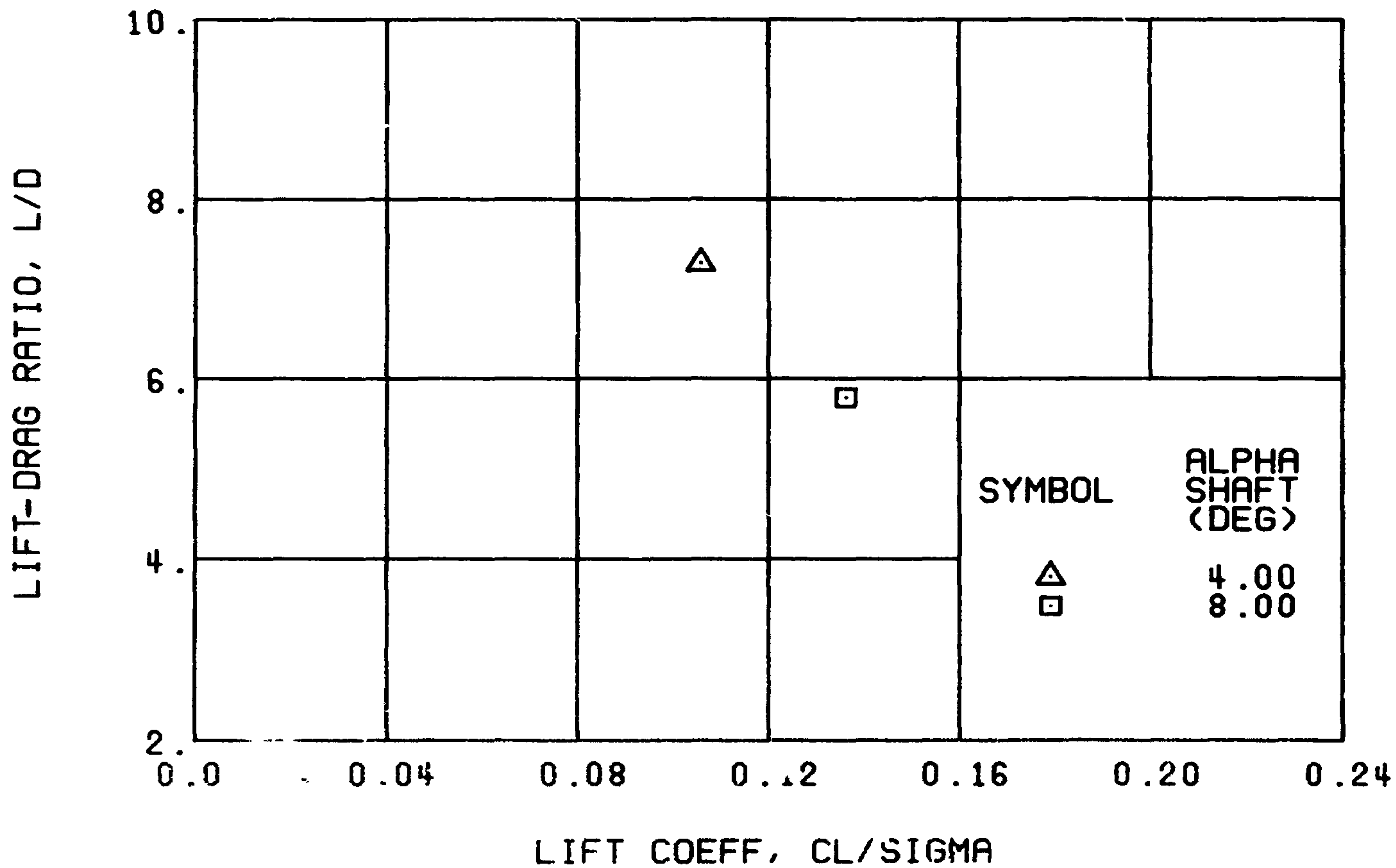

(c) LIFT-DRAG RATIO

Figure 25. Continued.
$\mu = 0.47 \quad B_{1s}' = 0$ Deg

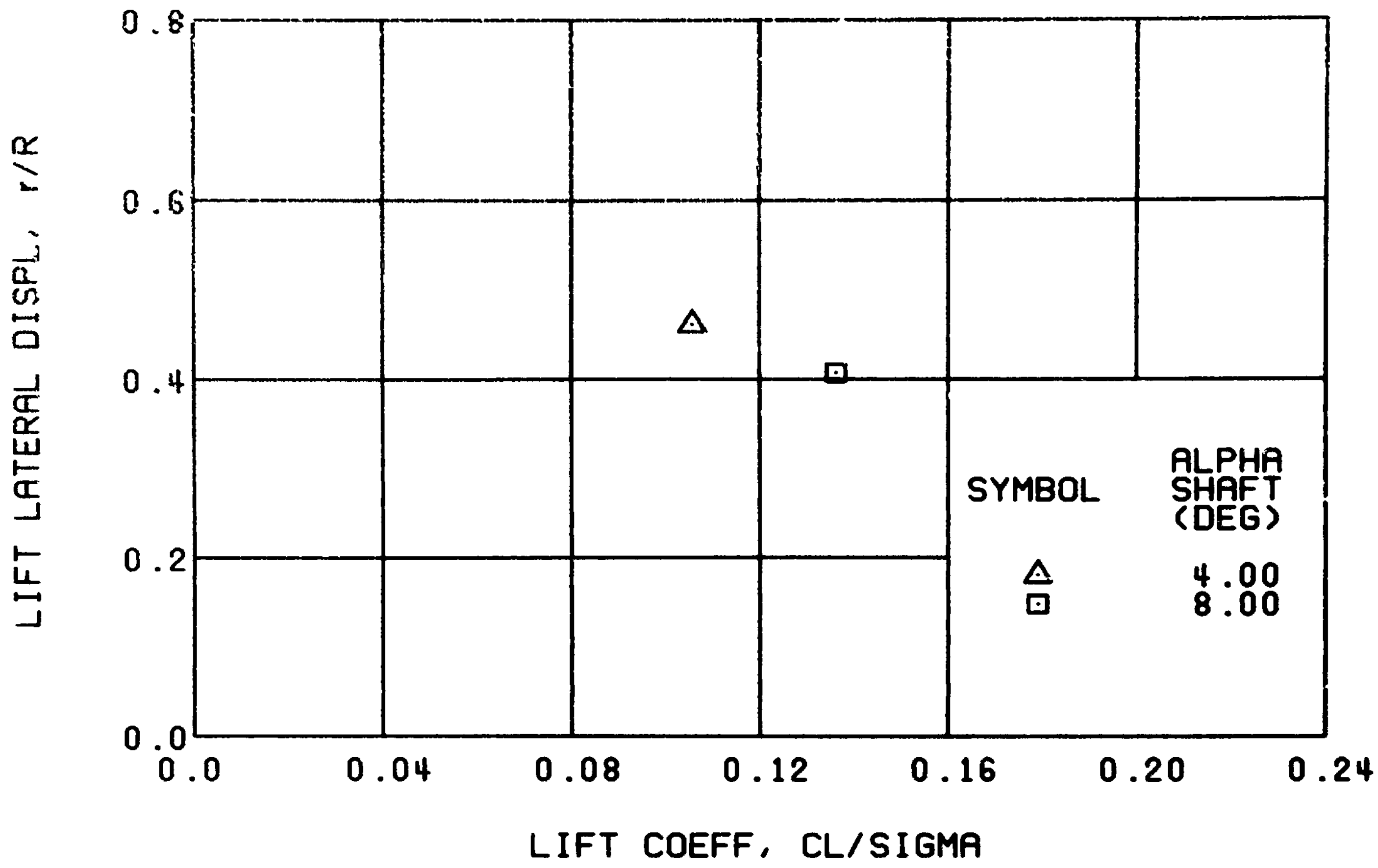

(d) LIFT LATERAL DISPLACEMENT

Figure 25. Continued.
$\mu = 0.47 \quad B'_{1s} = 0$ Deg

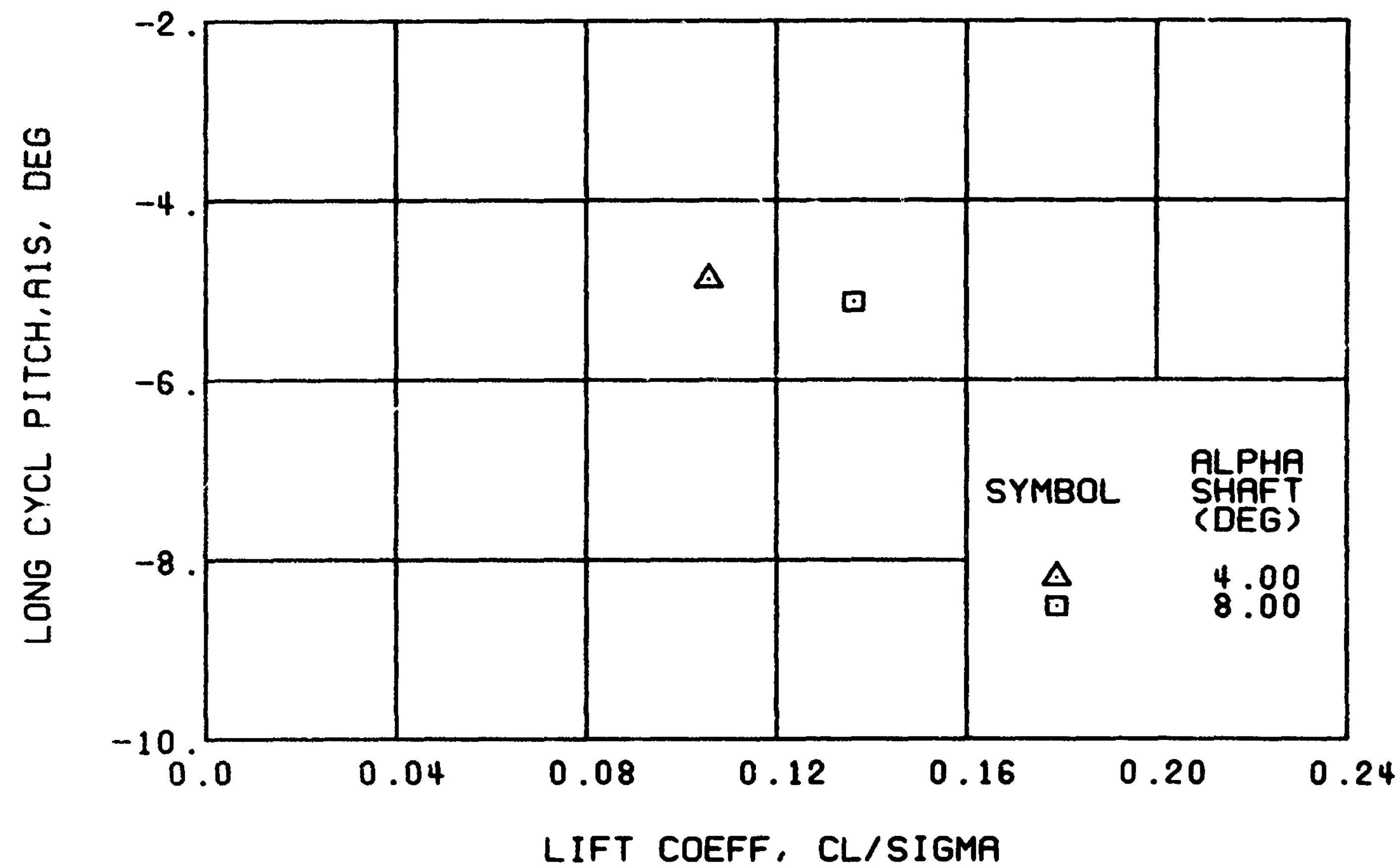

(e) LONGITUDINAL CYCLIC PITCH

Figure 25. Continued.
μ = 0.47 B'_{1s} = 0 Deg

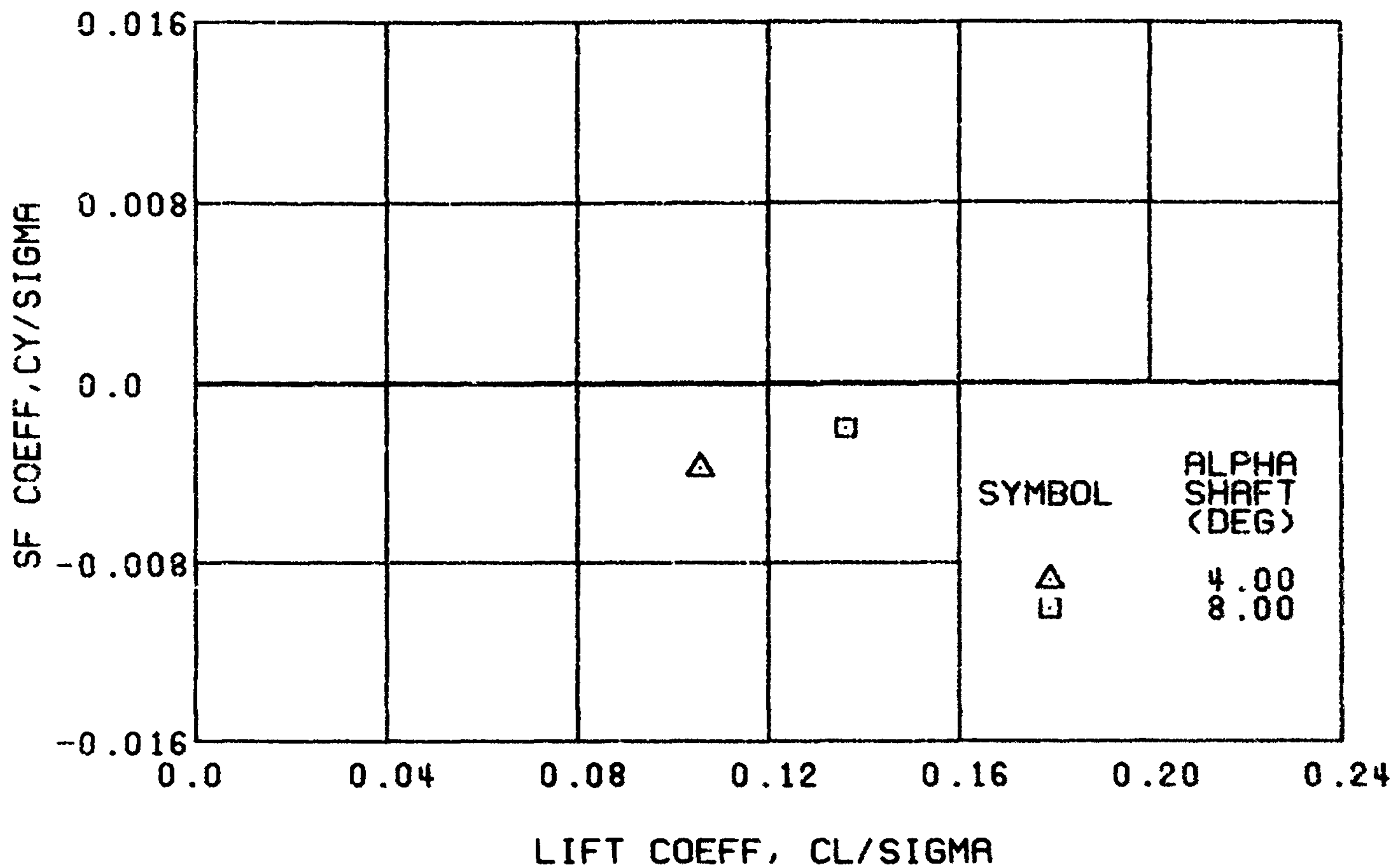

(f) SIDE FORCE COEFFICIENT

Figure 25. Continued.
$\mu = 0.47$ $B'_{1s} = 0$ Deg

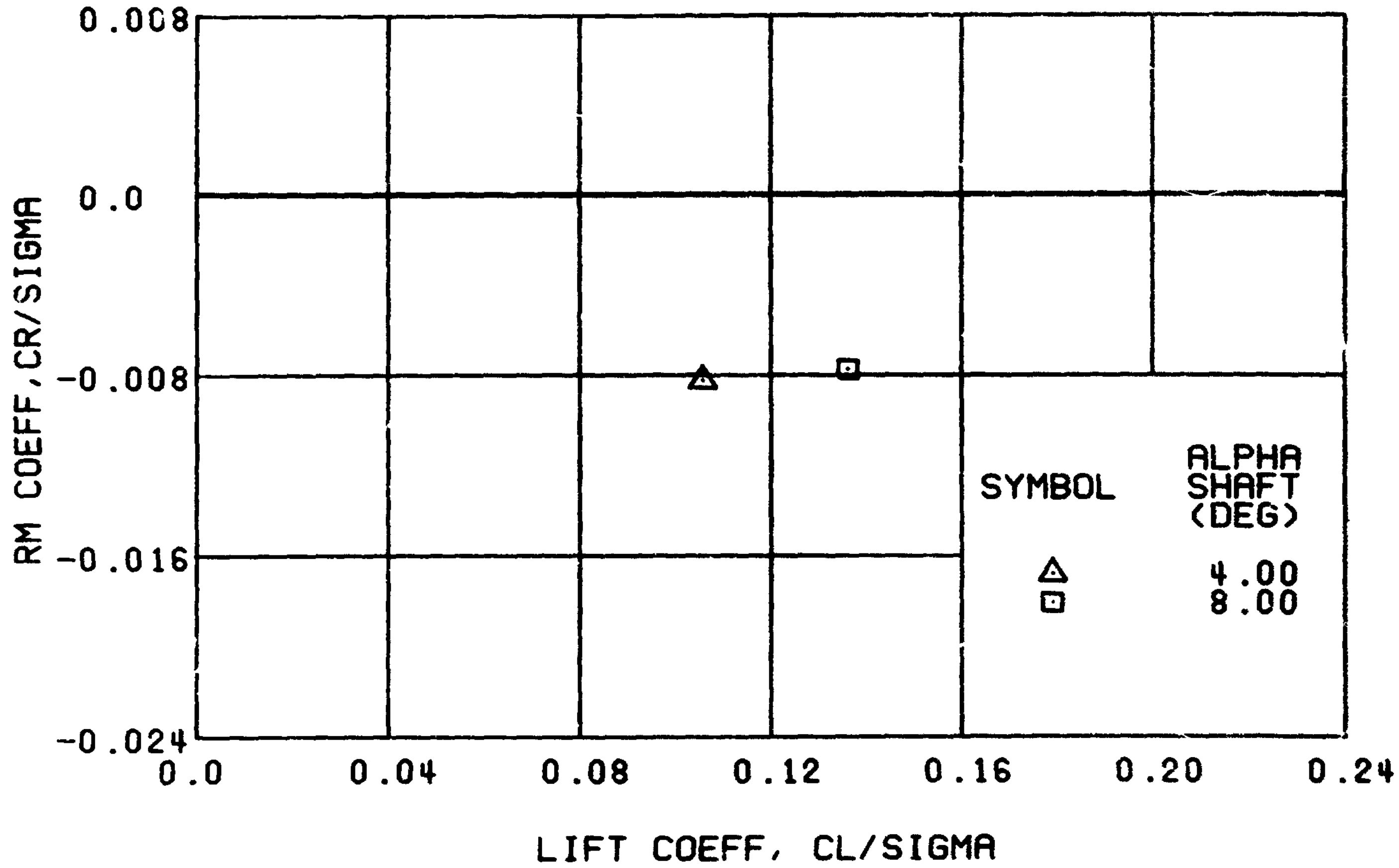

(g) ROLLING MOMENT COEFFICIENT

Figure 25. Continued.
$\mu = 0.47 \quad B'_{1s} = 0$ Deg

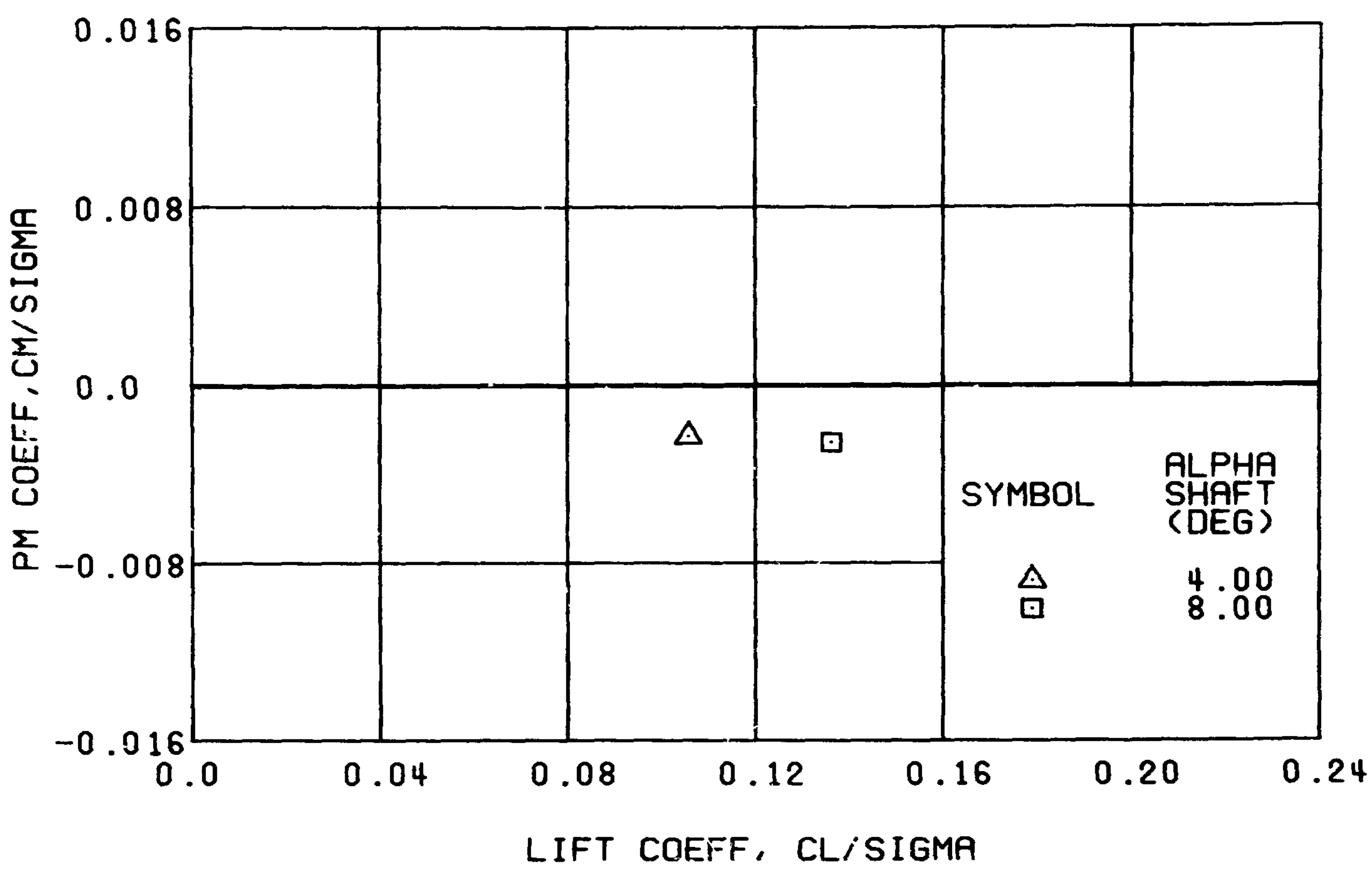

(h) PITCHING MOMENT COEFFICIENT

Figure 25. Continued.
$\mu = 0.47$ $B'_{1s} = 0$ Deg

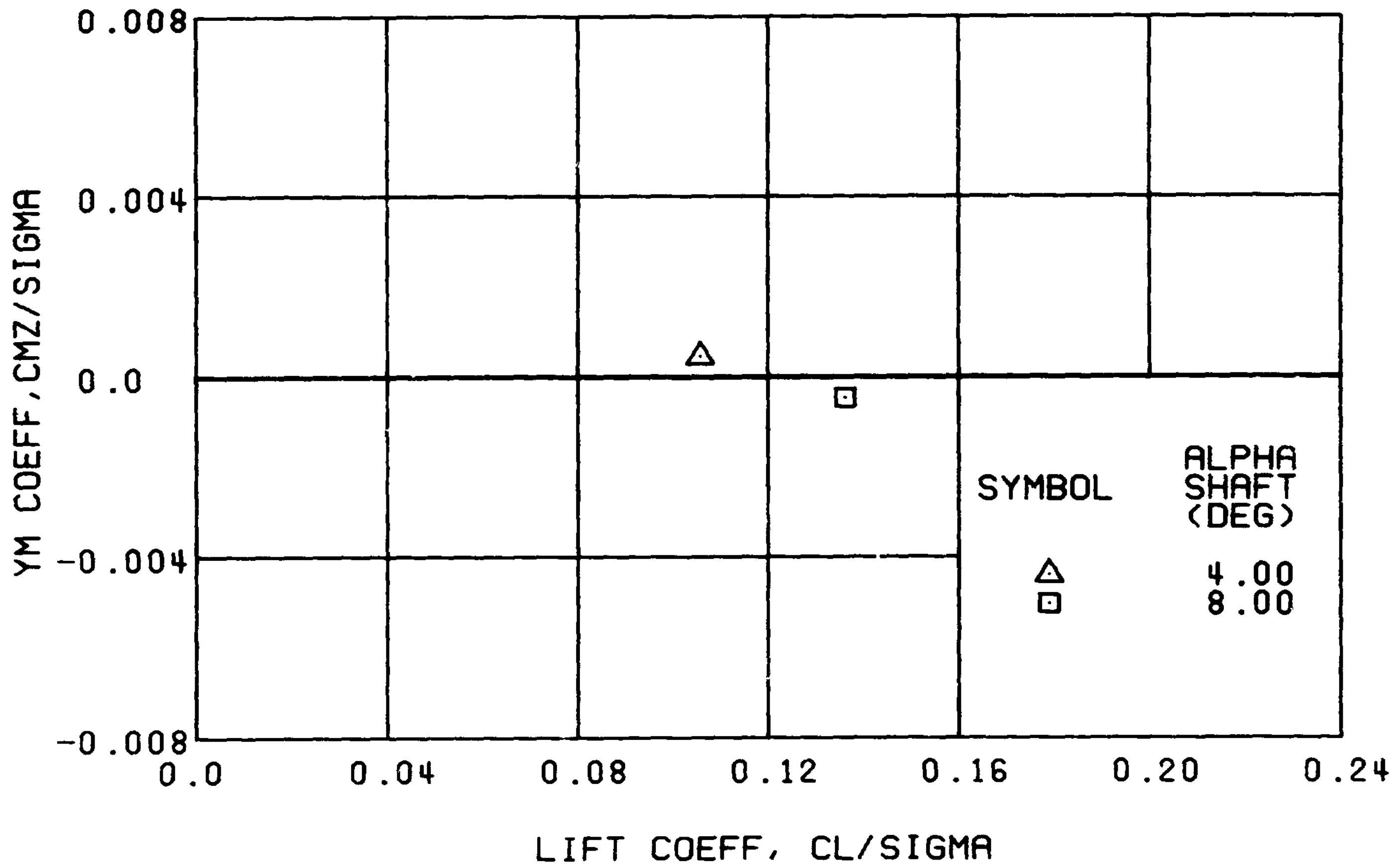

(i) YAWING MOMENT COEFFICIENT

Figure 25. Concluded.
$\mu = 0.47 \quad B_{1s}' = 0$ Deg

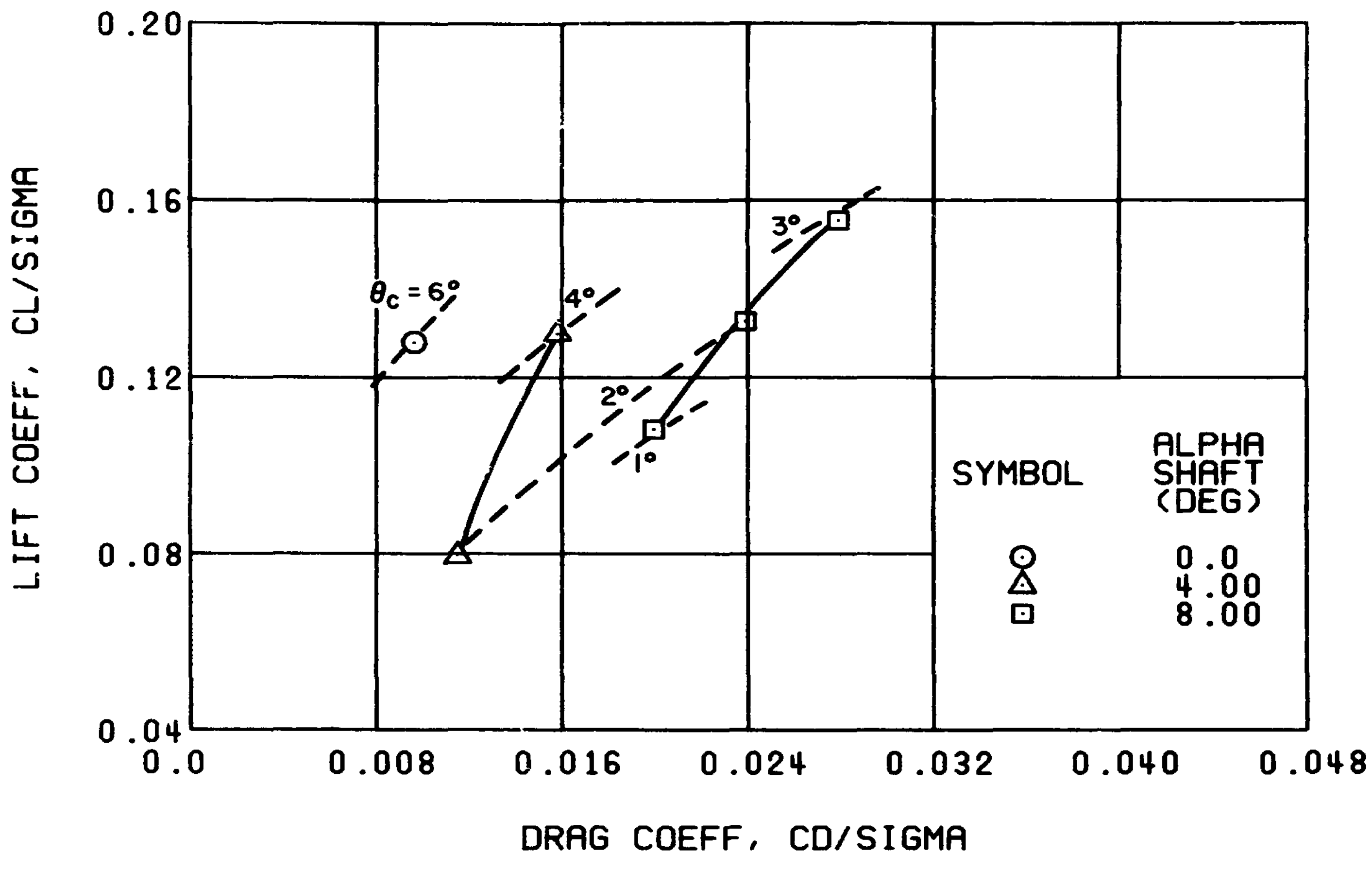

(a) DRAG COEFFICIENT

Figure 26. Performance Data at an Advance Ratio of 0.47 With the Lateral Displacement Control (B'_{1s}) Set at 2 Degrees.

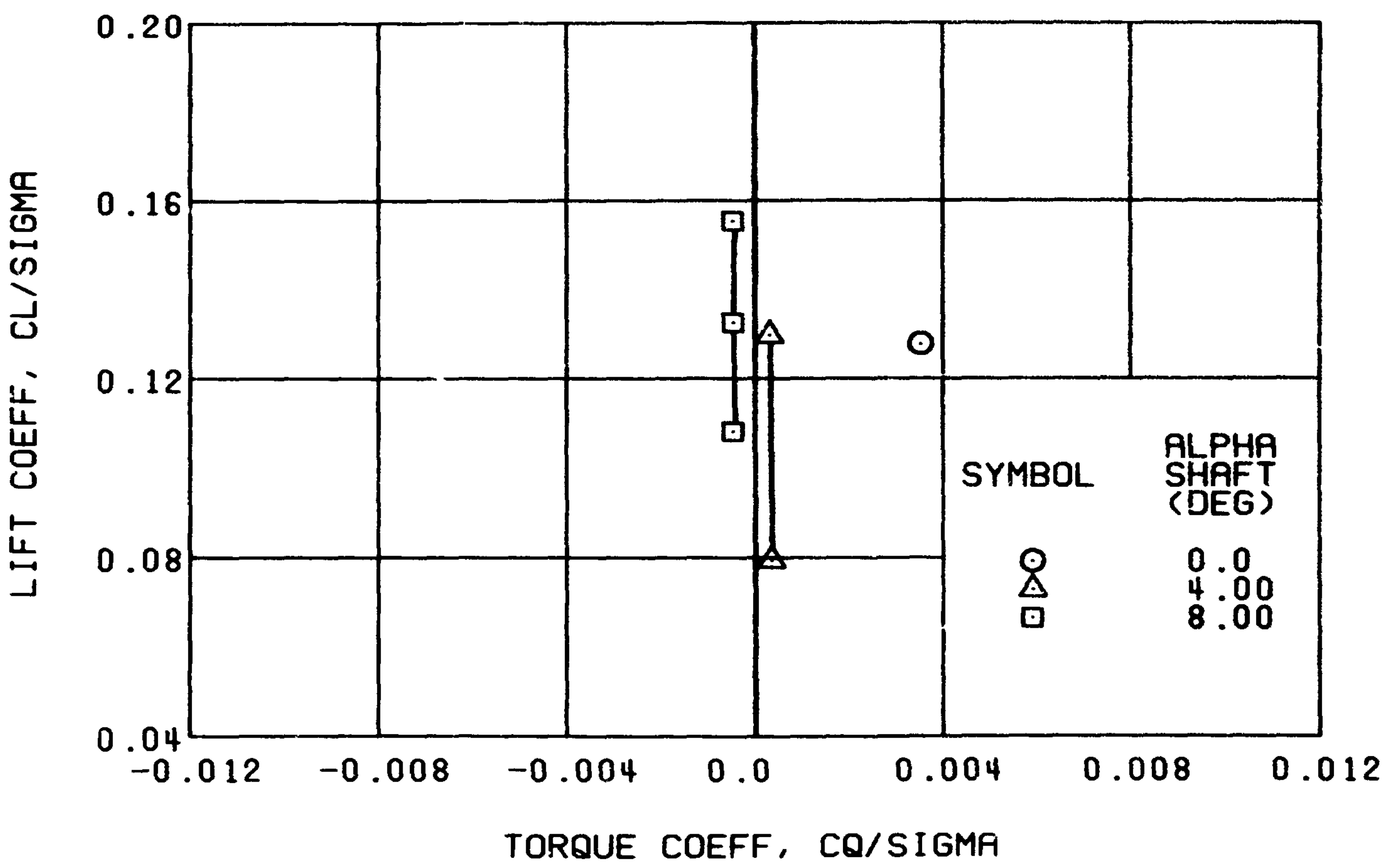

(b) TORQUE COEFFICIENT

Figure 26. Continued.
$\mu = 0.47$ $B'_{1s} = 2$ Deg

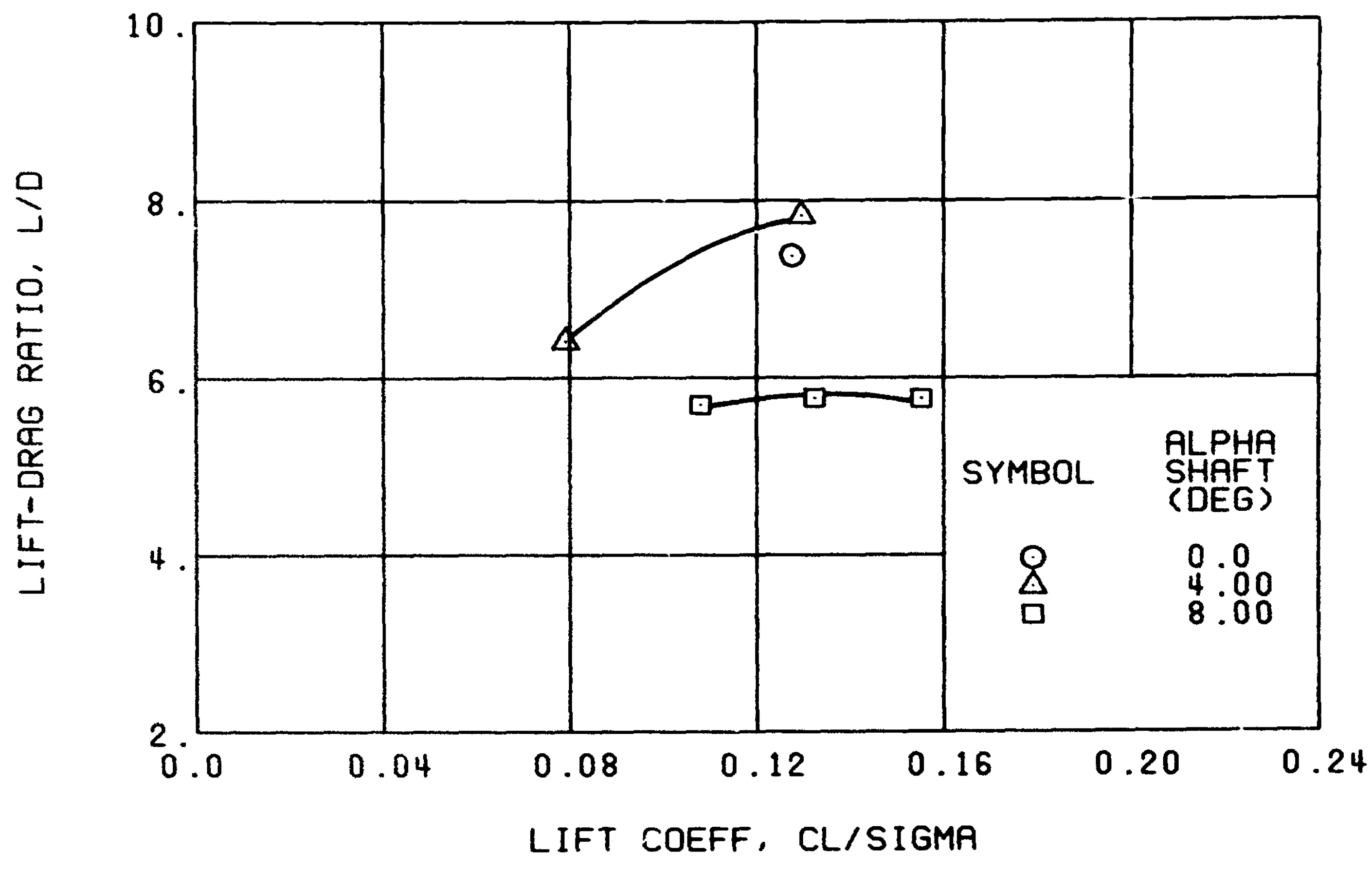

(c) LIFT-DRAG RATIO

Figure 26. Continued.
$\mu = 0.47 \quad B'_{1s} = 2$ Deg

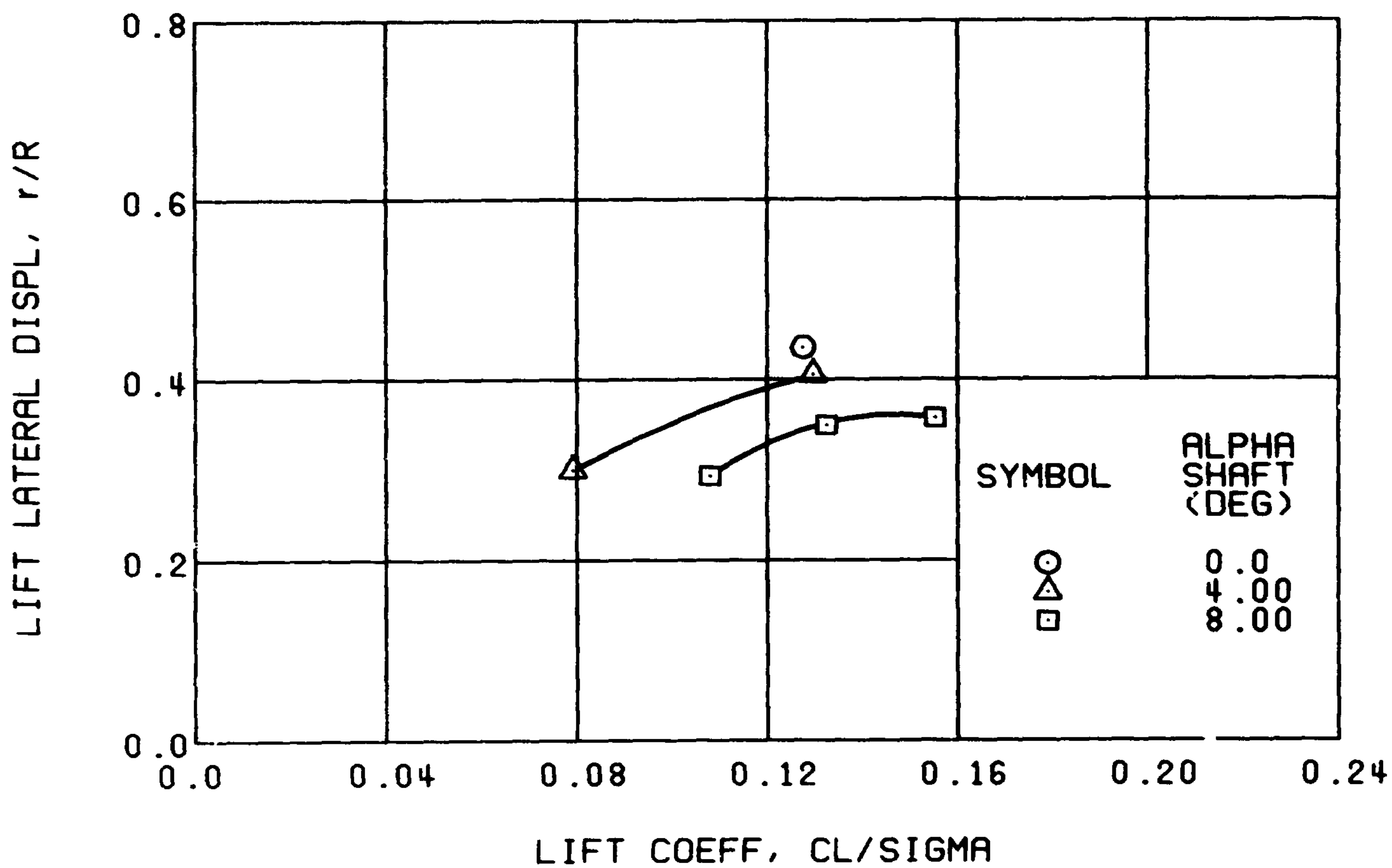

(d) LIFT LATERAL DISPLACEMENT

Figure 26. Continued.
$\mu = 0.47$ B'_{1s} = 2 Deg

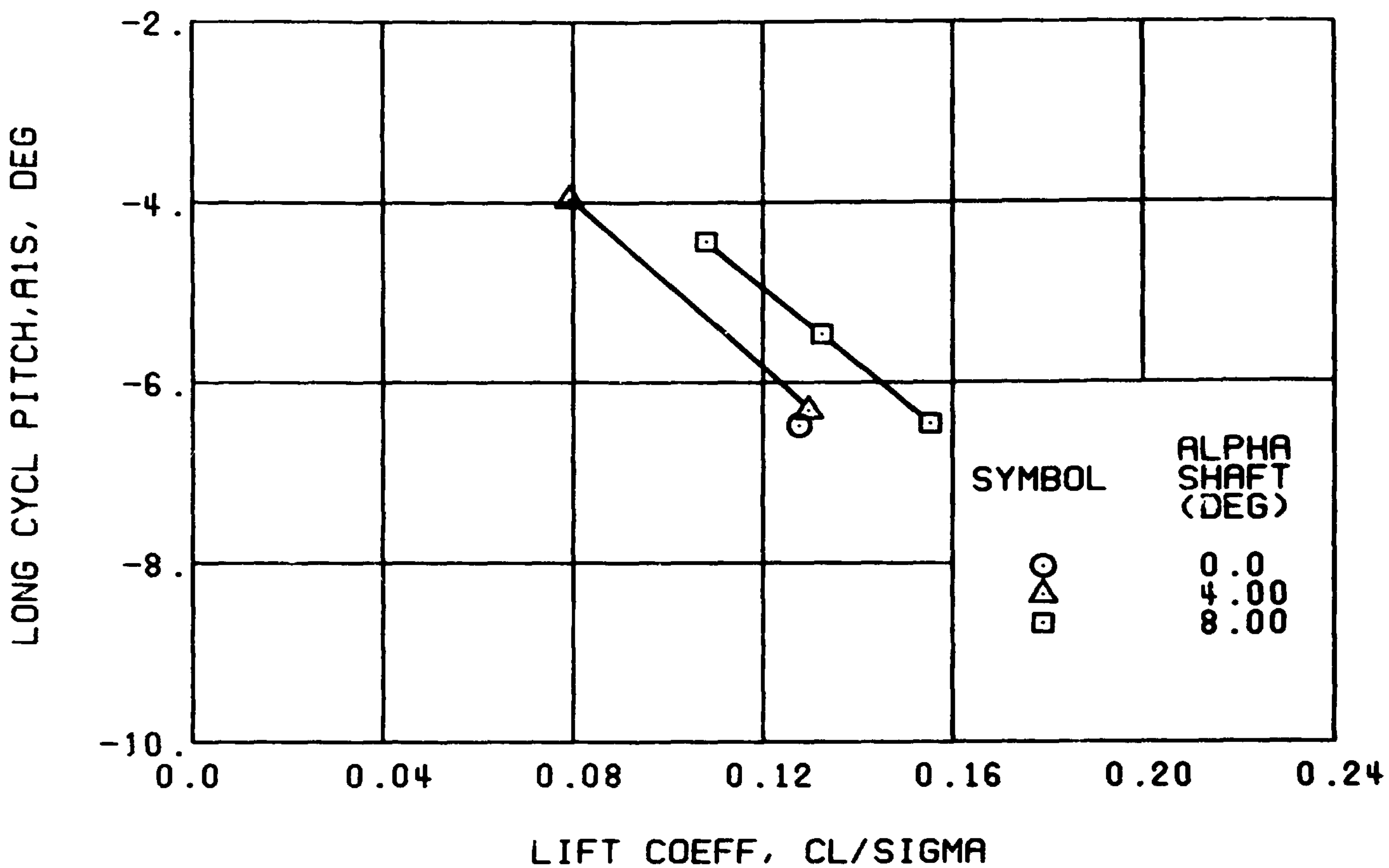

(e) LONGITUDINAL CYCLIC PITCH

Figure 26. Continued.
$\mu = 0.47 \quad B'_{1s} = 2$ Deg

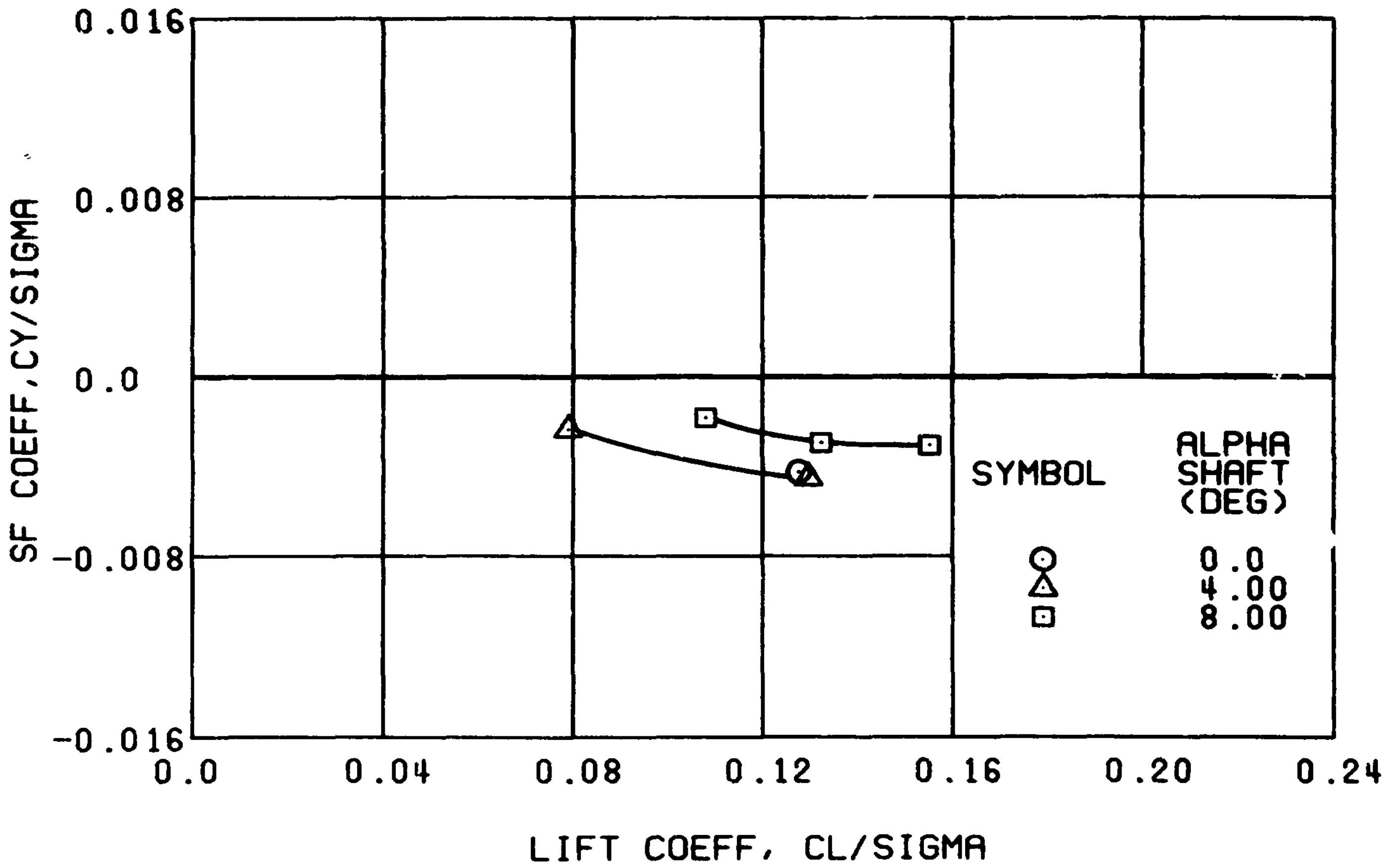

(f) SIDE FORCE COEFFICIENT

Figure 26. Continued.
$\mu = 0.47$ $B'_{1s} = 2$ Deg

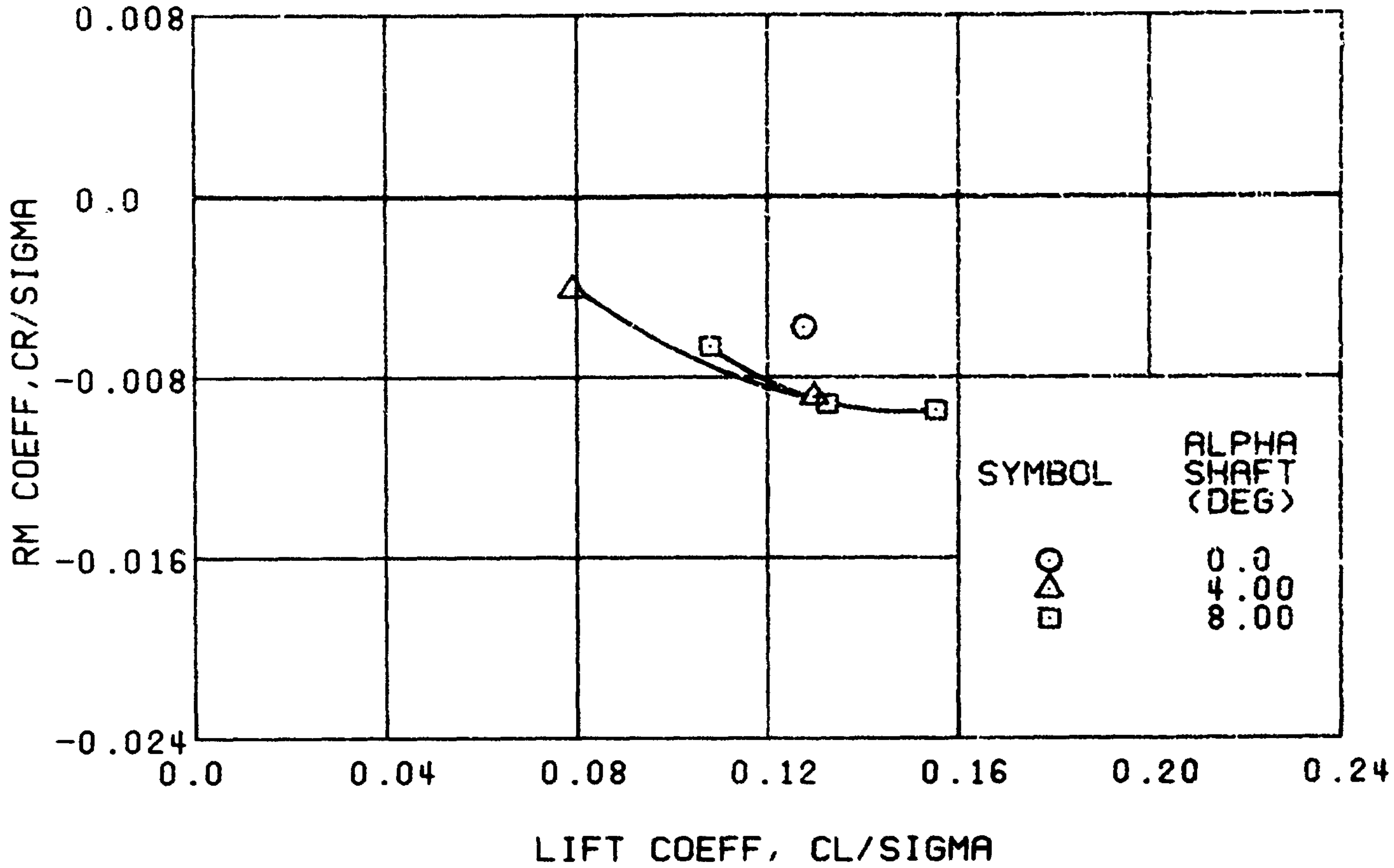

(g) ROLLING MOMENT COEFFICIENT

Figure 26. Continued.
$\mu = 0.47$ $B'_{1s} = 2$ Deg

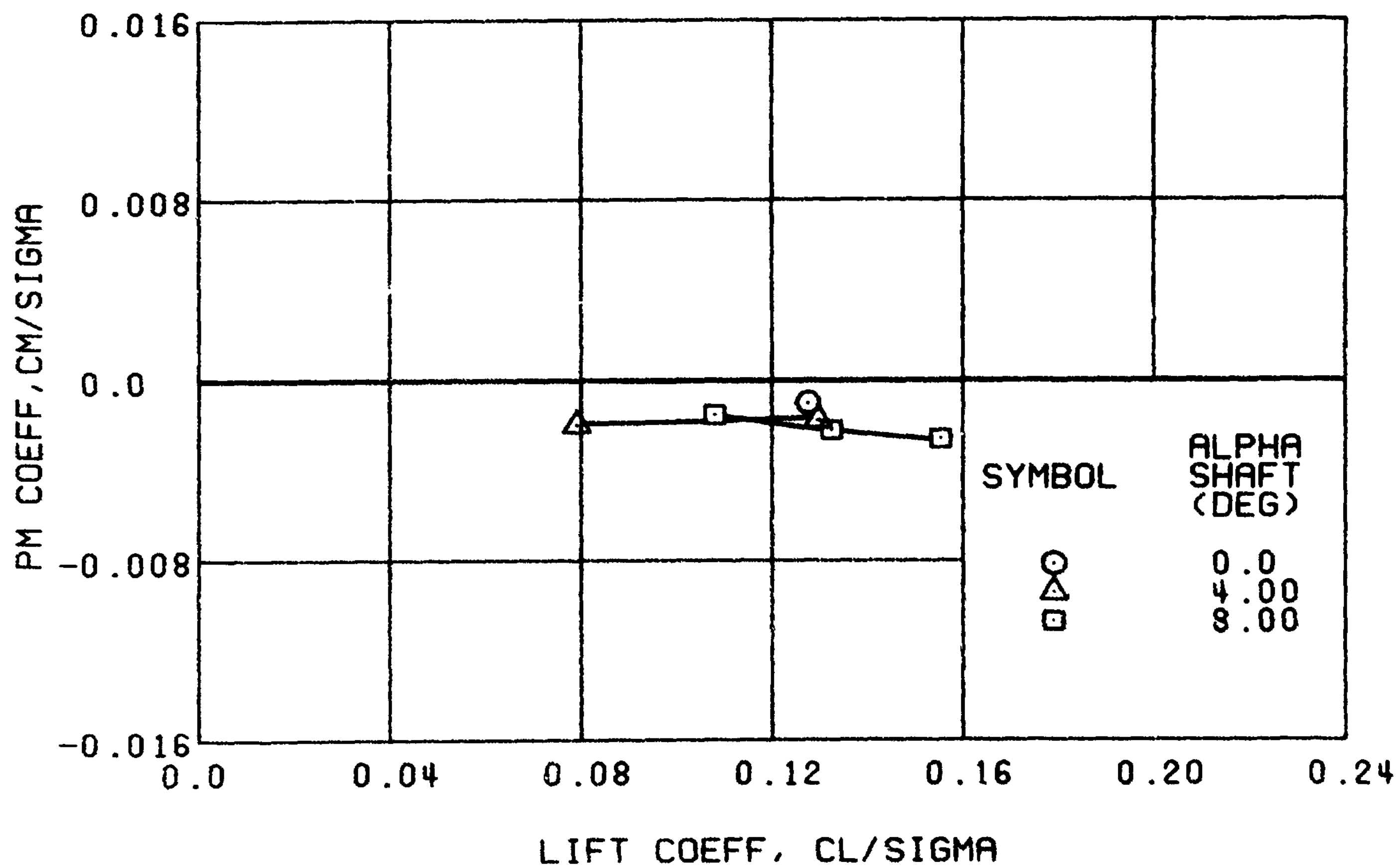

(h) PITCHING MOMENT COEFFICIENT

Figure 26. Continued.
$\mu = 0.47 \quad B'_{1s} = 2$ Deg

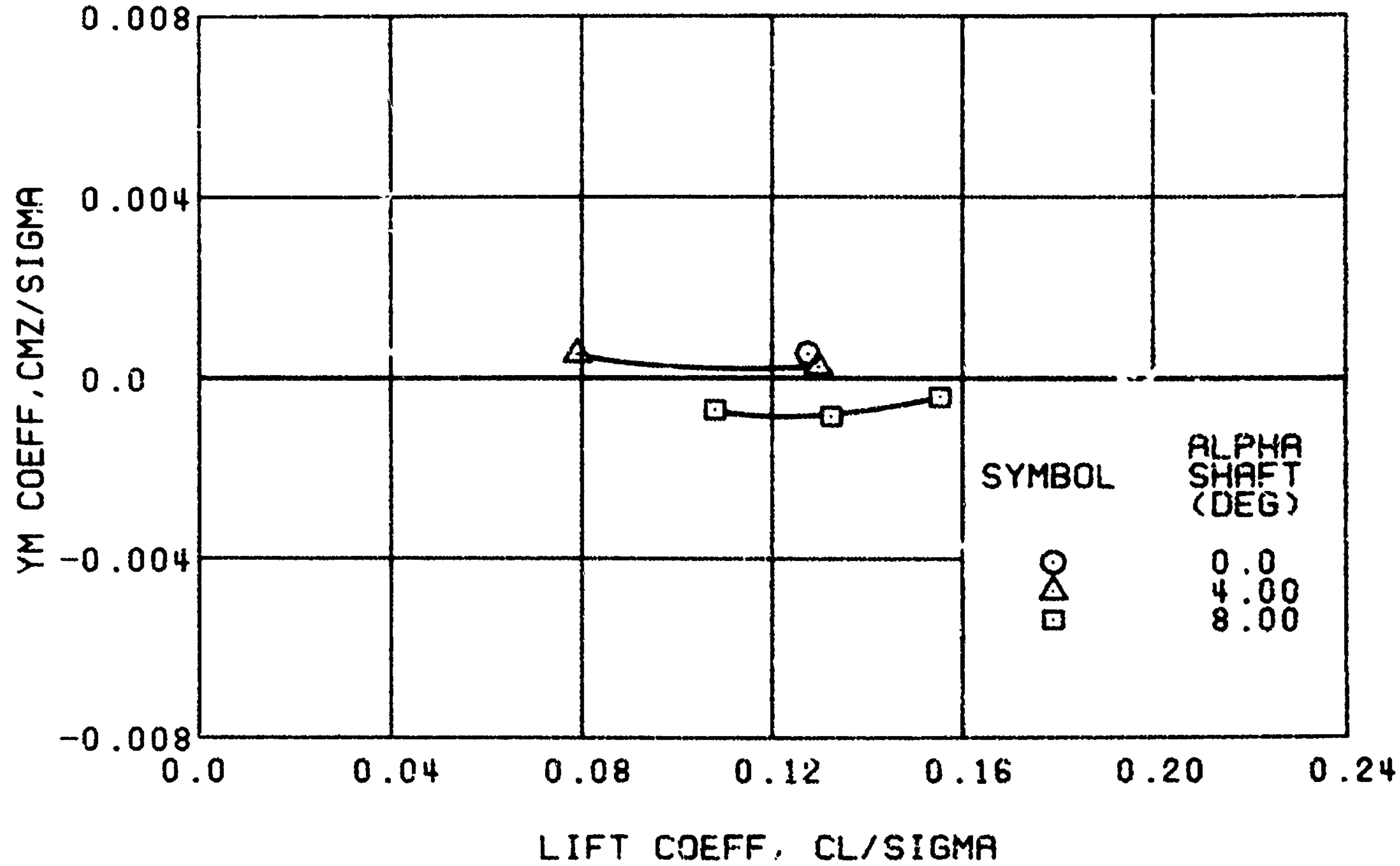

(i) YAWING MOMENT COEFFICIENT

Figure 26. Concluded.
$\mu = 0.47$ $B'_{1s} = 2$ Deg

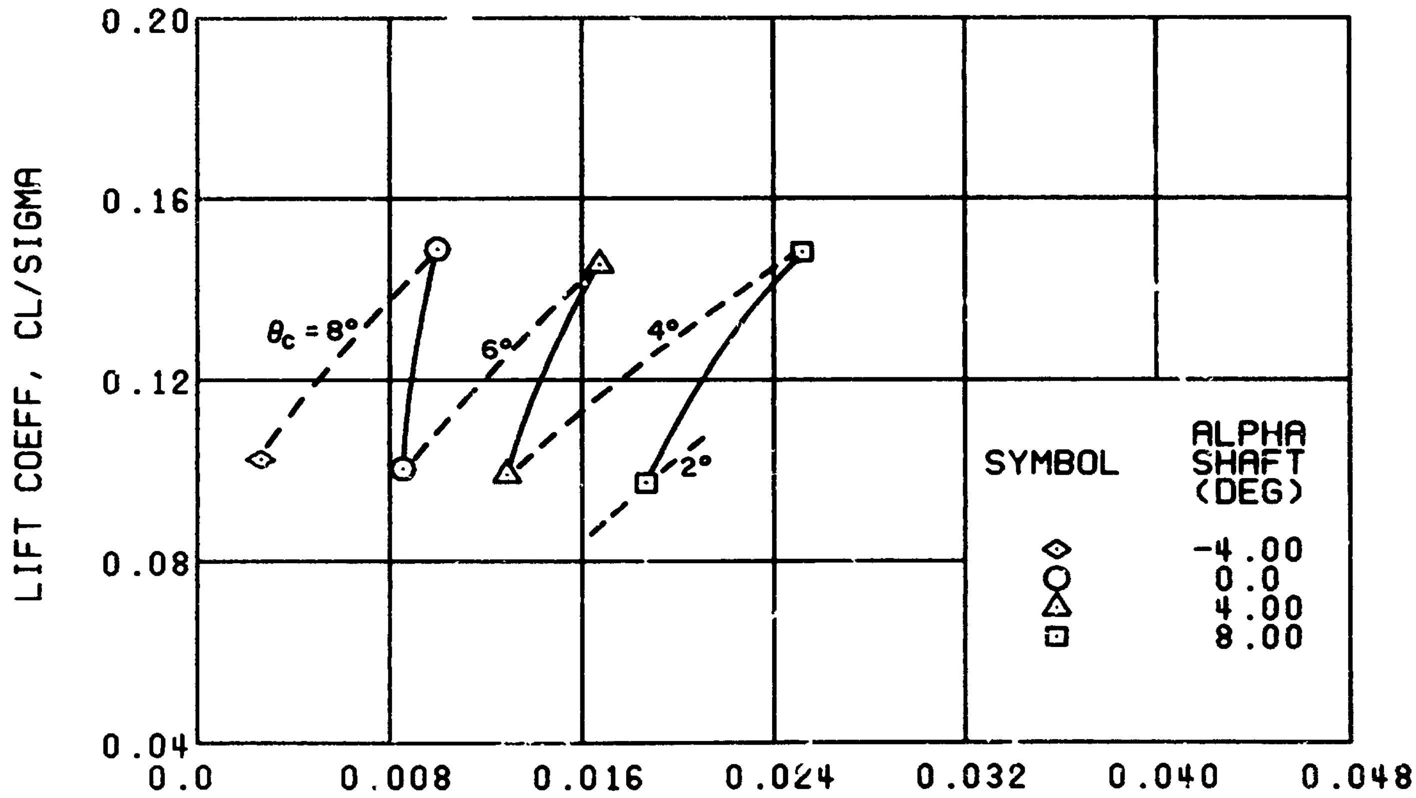

(a) DRAG COEFFICIENT

Figure 27. Performance Data at an Advance Ratio of 0.47 With the Lateral Displacement Control (B'_{1s}) Set at 4 Degrees.

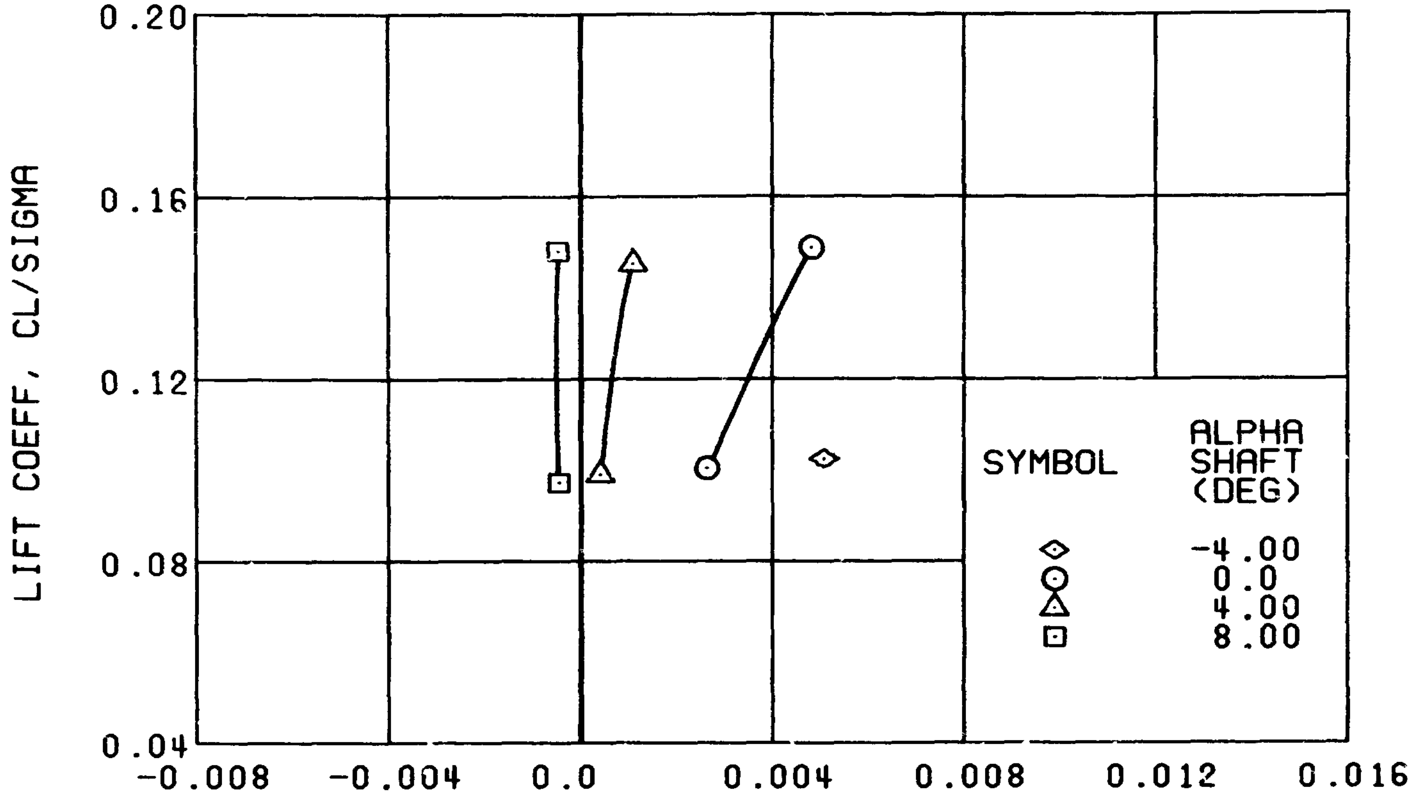

(b) TORQUE COEFFICIENT

Figure 27. Continued.
$\mu = 0.47$ $B'_{1s} = 4$ Deg

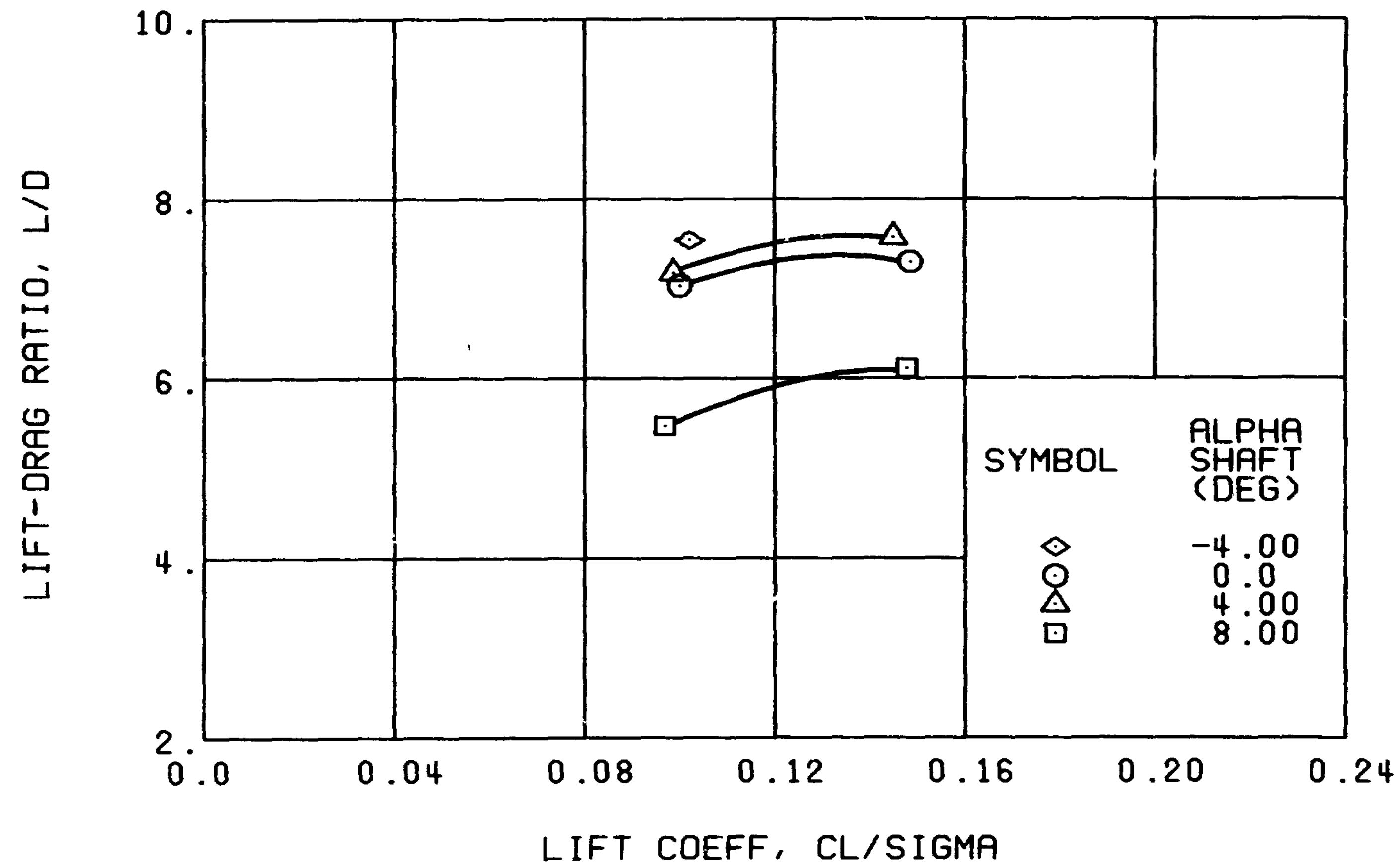

(c) LIFT-DRAG RATIO

Figure 27. Continued.
$\mu = 0.47 \quad B'_{1s} = 4$ Deg

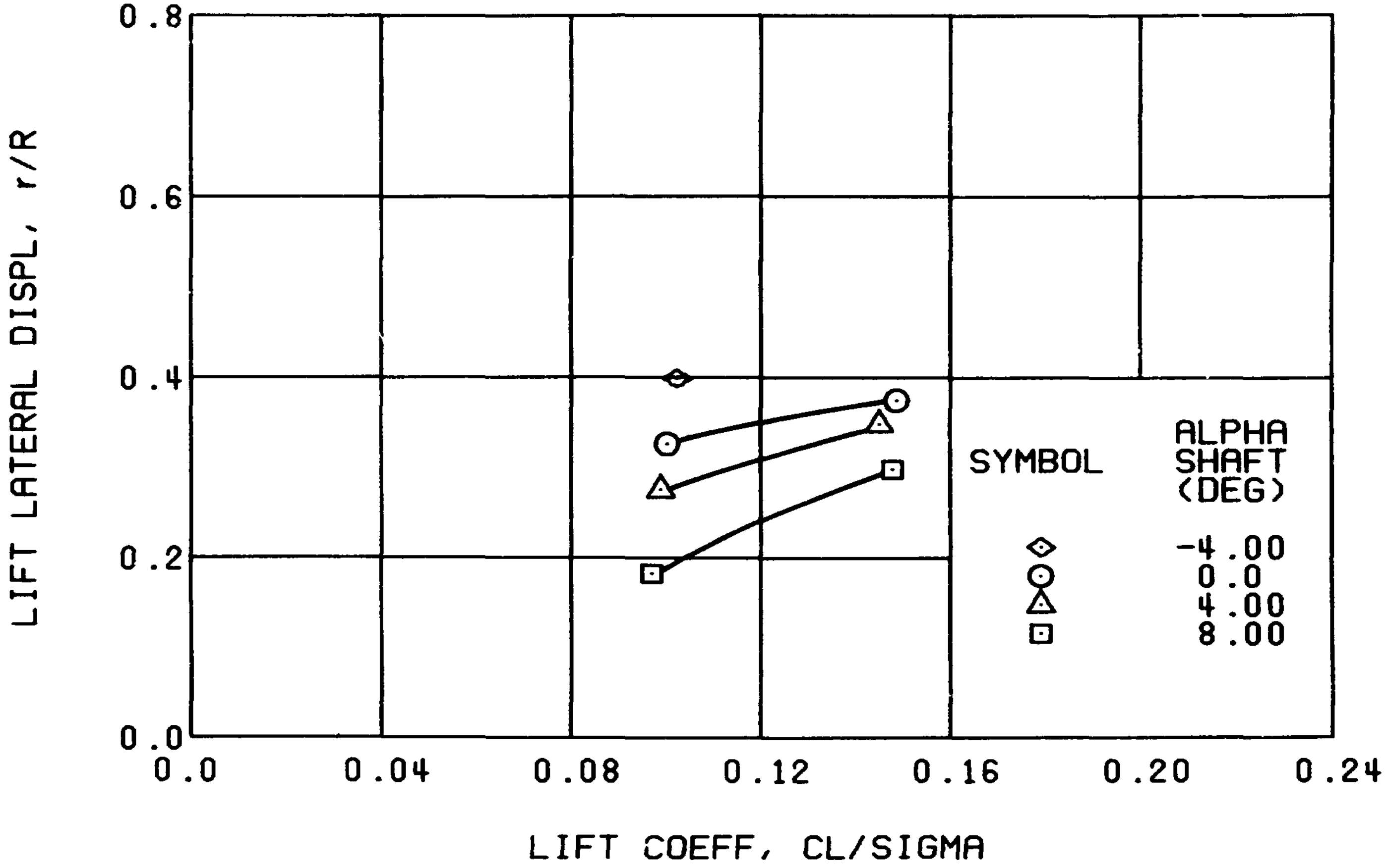

(d) LIFT LATERAL DISPLACEMENT

Figure 27. Continued.
$\mu = 0.47 \quad B'_{1s} = 4$ Deg

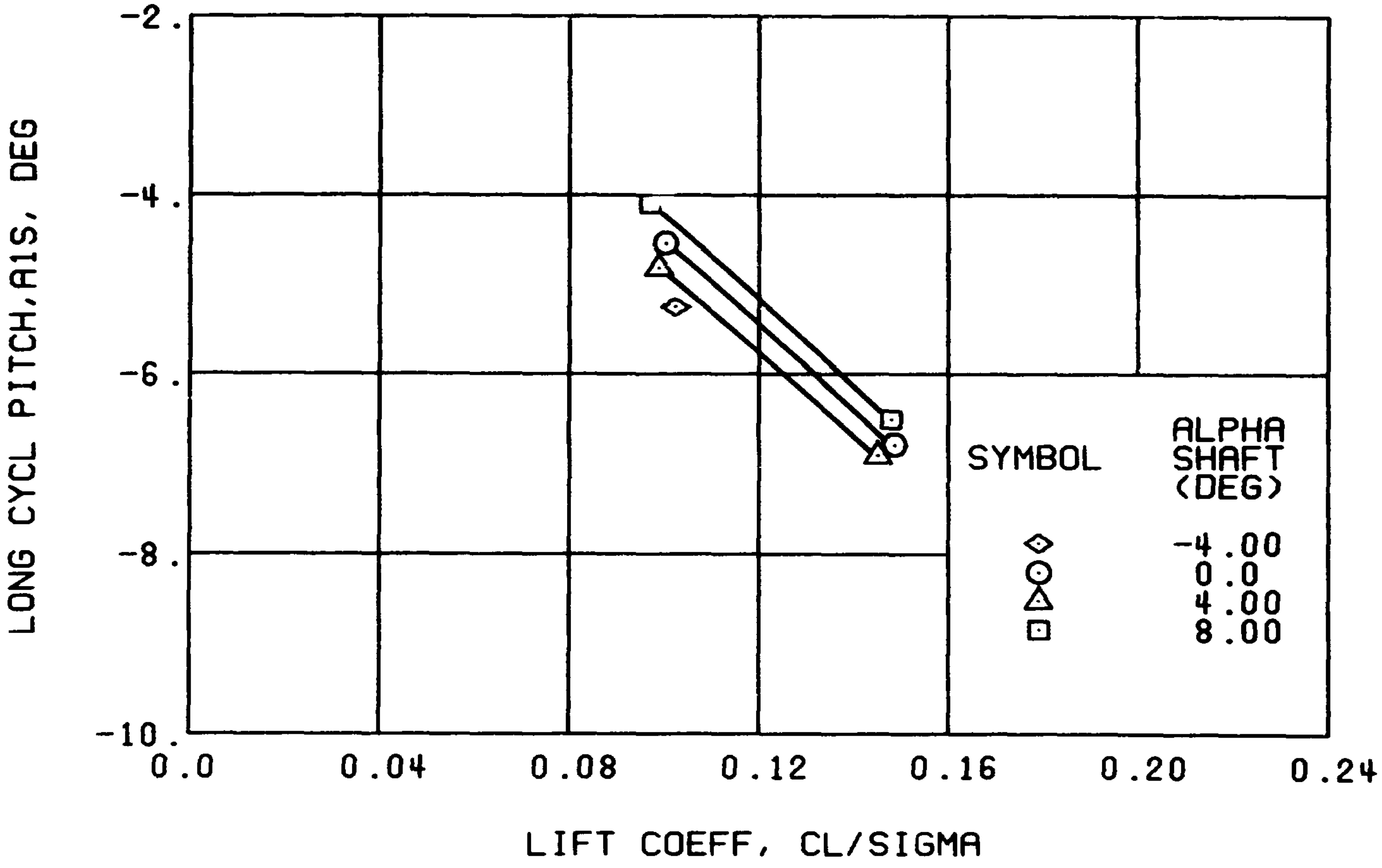

(e) LONGITUDINAL CYCLIC PITCH

Figure 27. Continued.
$\mu = 0.47$ $B'_{1s} = 4$ Deg

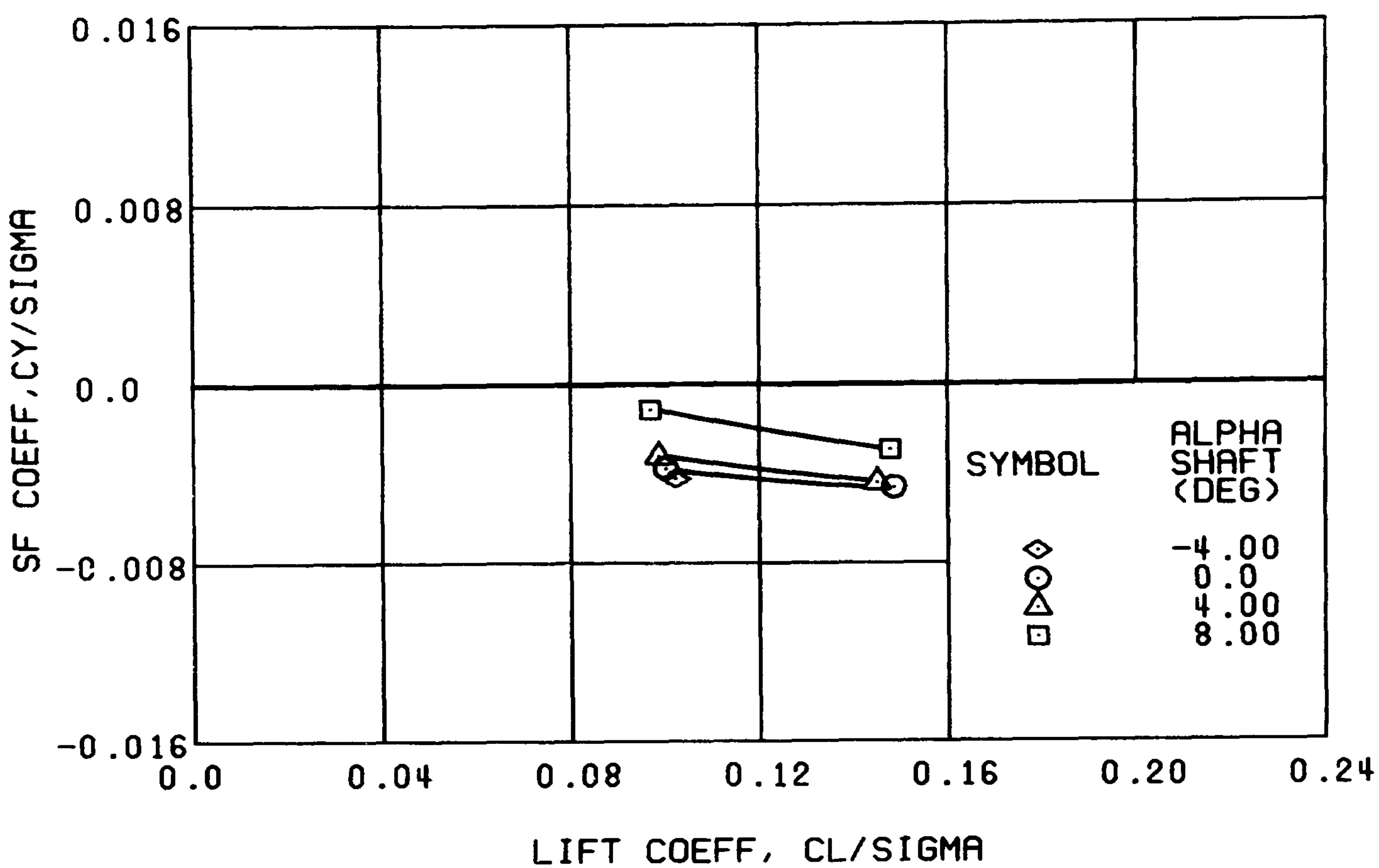

(f) SIDE FORCE COEFFICIENT

Figure 27. Continued.
$\mu = 0.47$ $B'_{1s} = 4$ Deg

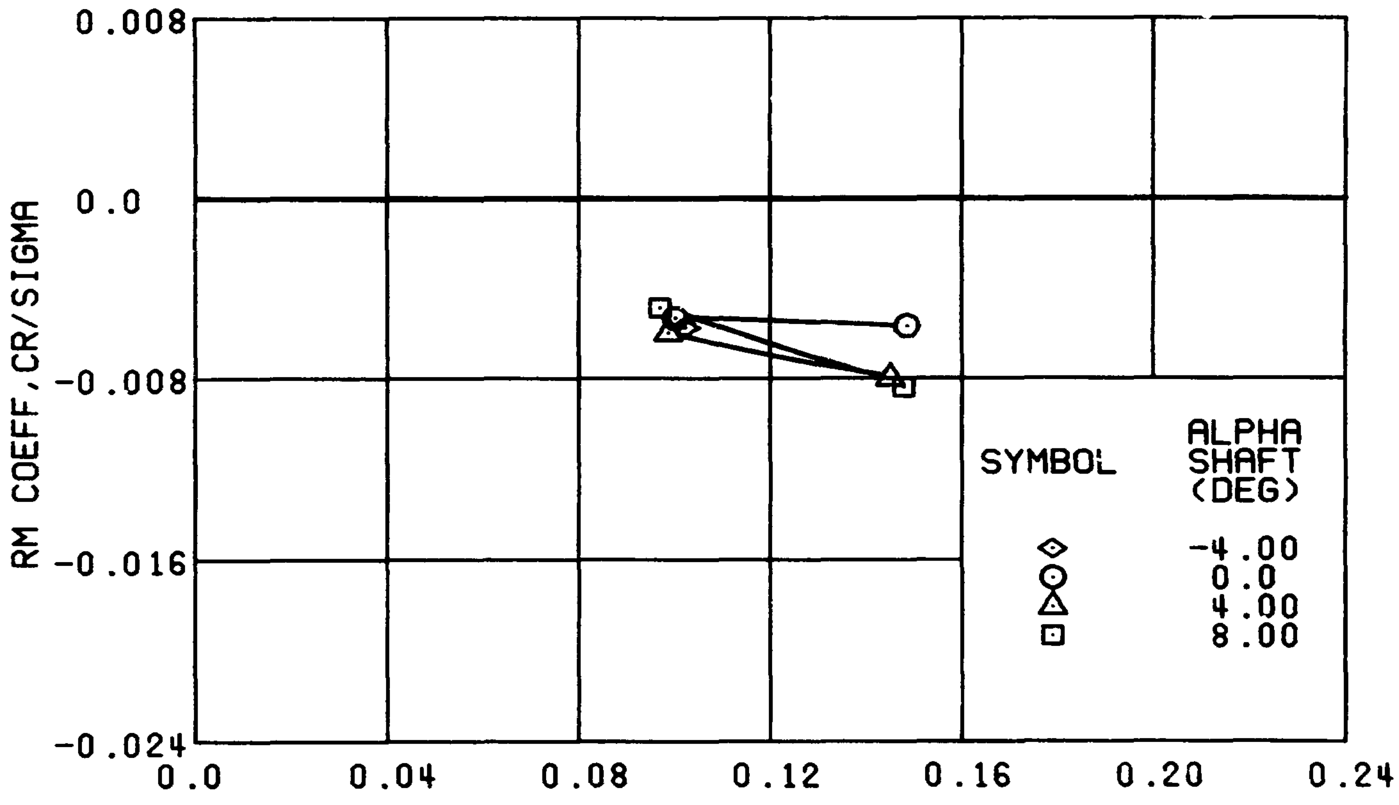

(g) ROLLING MOMENT COEFFICIENT

Figure 27. Continued.
$\mu = 0.47 \quad B'_{1s} = 4$ Deg

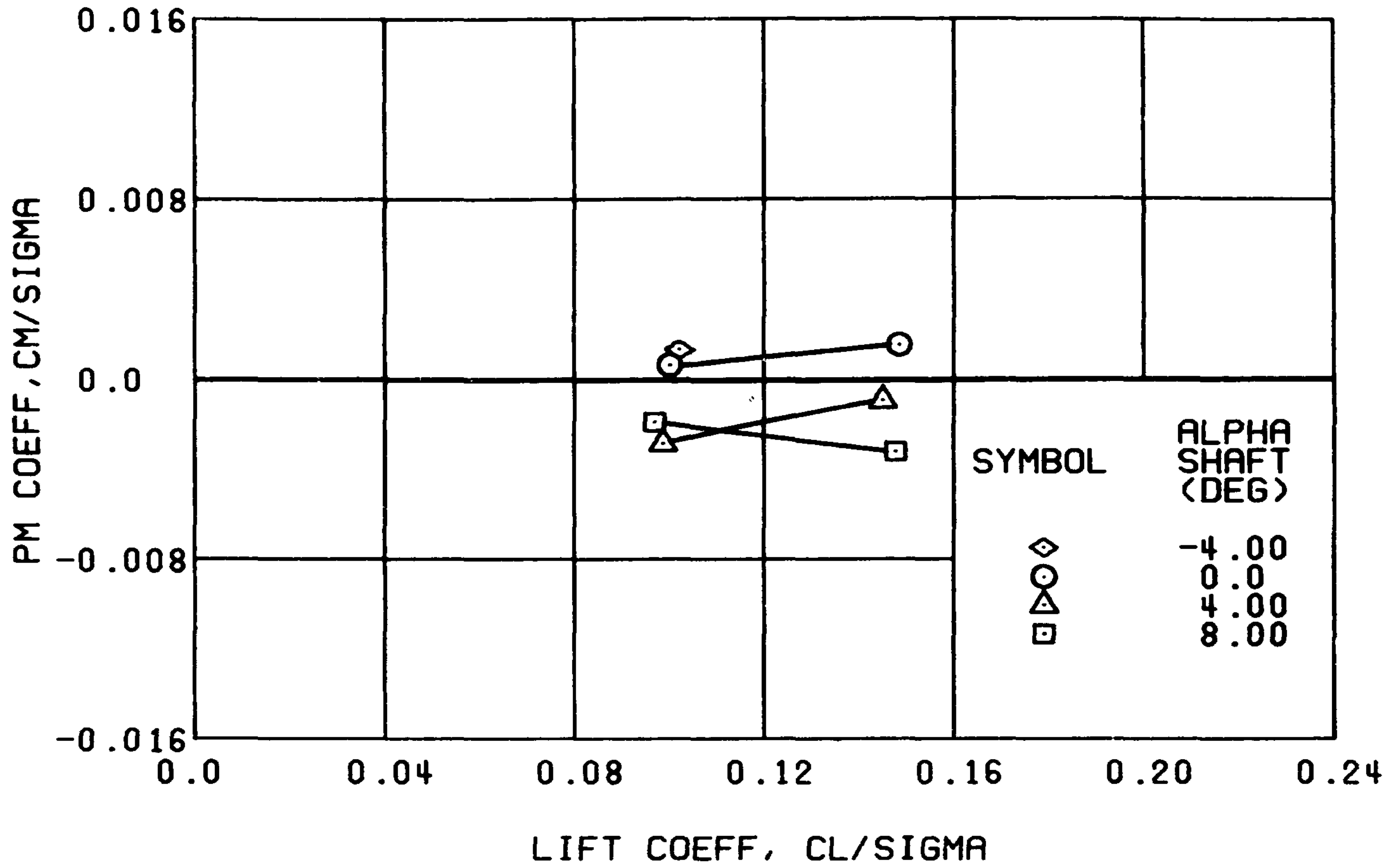

(h) PITCHING MOMENT COEFFICIENT

Figure 27. Continued.
$\mu = 0.47$ $B'_{1s} = 4$ Deg

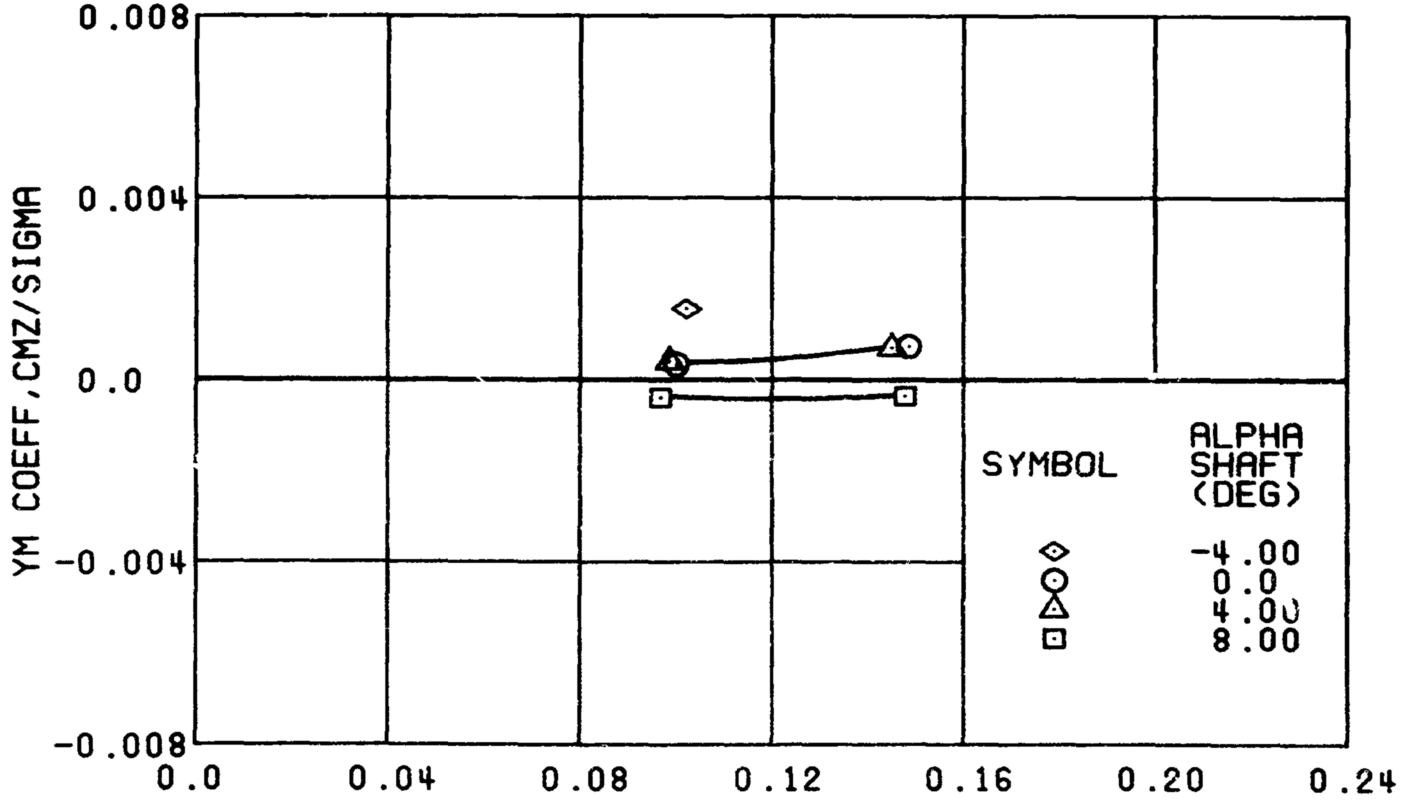

(i) YAWING MOMENT COEFFICIENT

Figure 27. Concluded.
$\mu = 0.47$ $B'_{1s} = 4$ Deg

Note: Performance data at an advance ratio of 0.47 with the lateral displacement control (B'_{1s}) set to 6 degrees is contained in Figure 9, page 43.

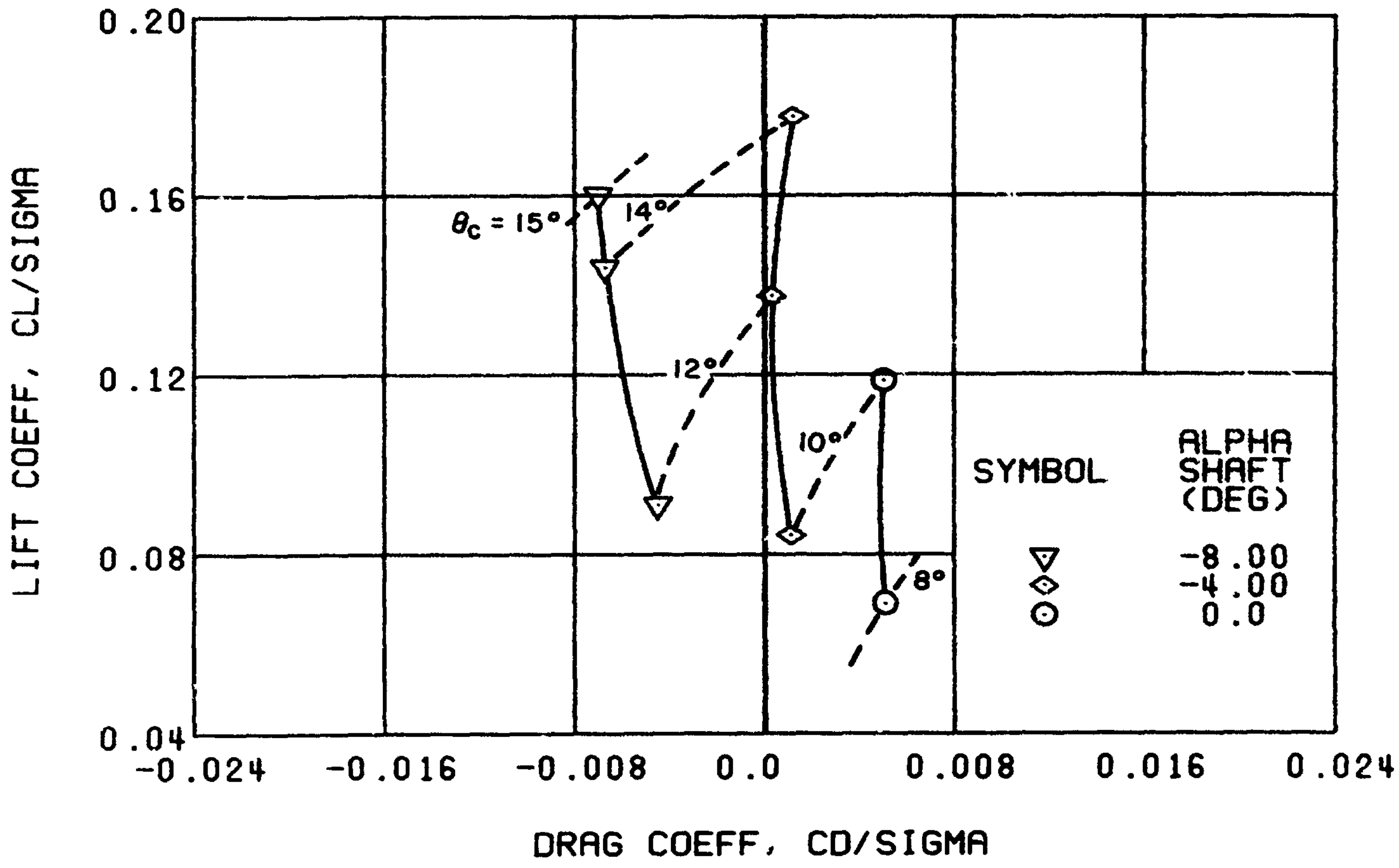

(a) DRAG COEFFICIENT

Figure 28. Performance Data at an Advance Ratio of 0.47 With the Lateral Displacement Control (B'_{1s}) Set at 8 Degrees.

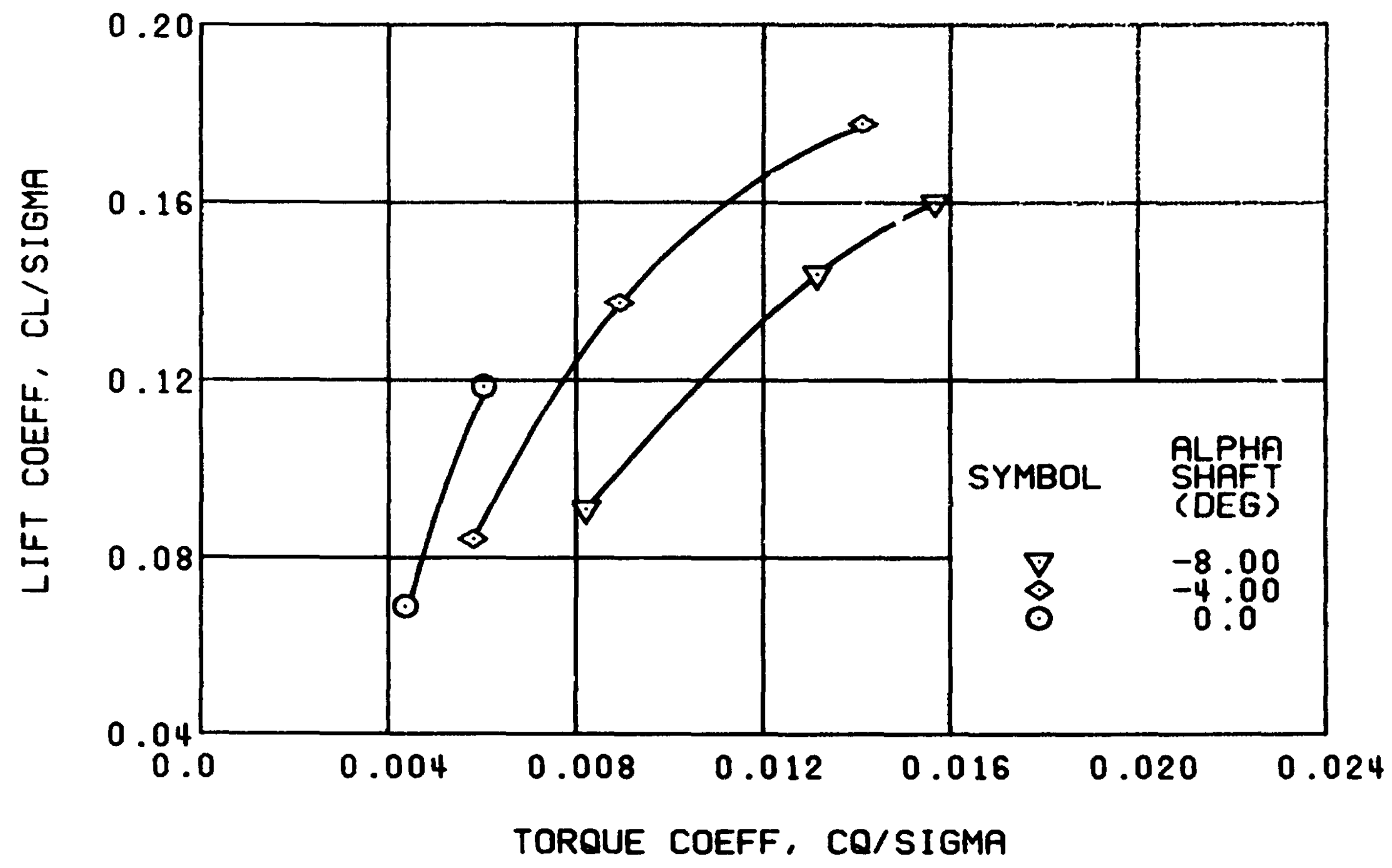

(b) TORQUE COEFFICIENT

Figure 28. Continued.
$\mu = 0.47$ $B'_{1s} = 8$ Deg

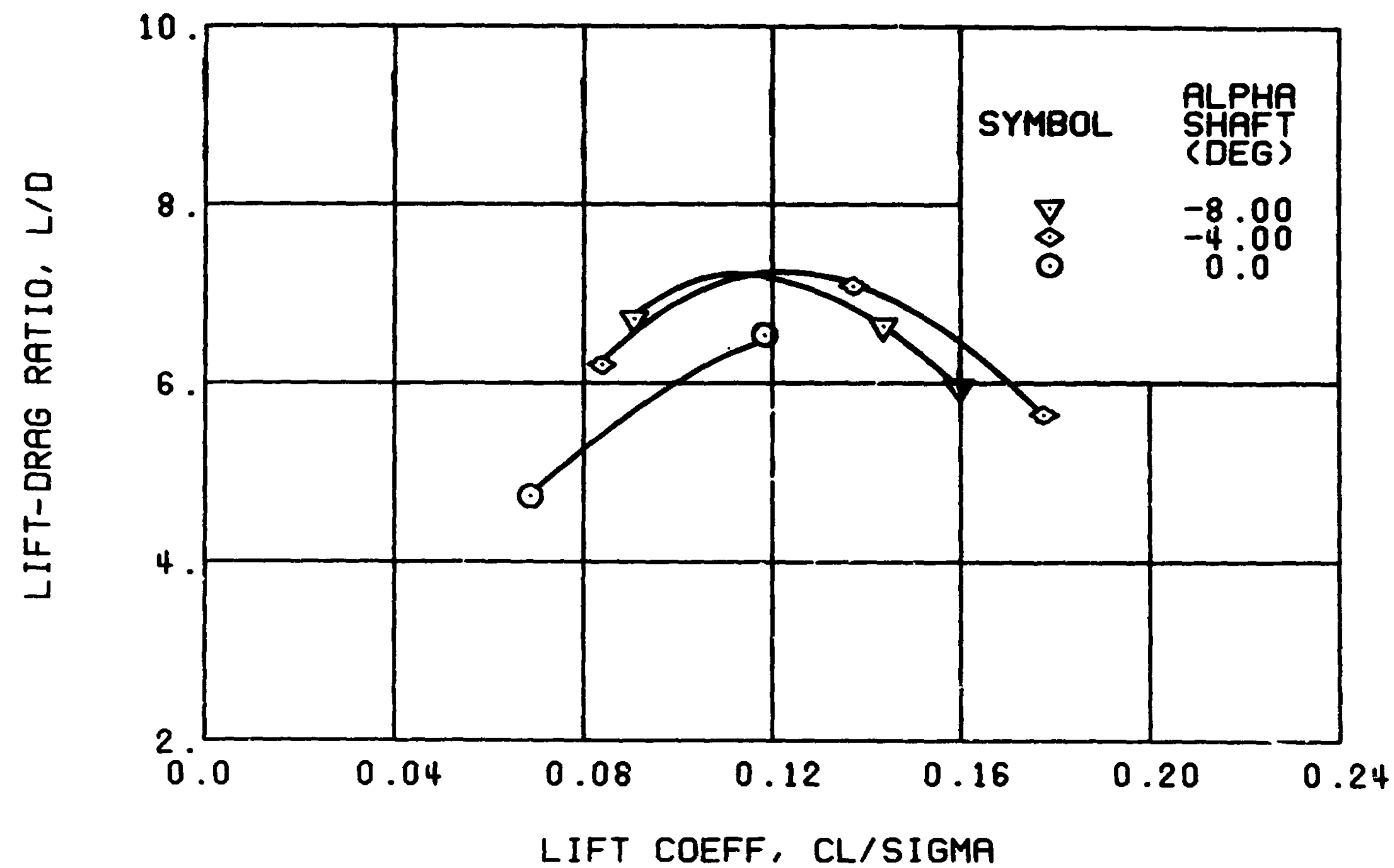

(c) LIFT-DRAG RATIO

Figure 28. Continued.
$\mu = 0.47 \quad B'_{1s} = 8$ Deg

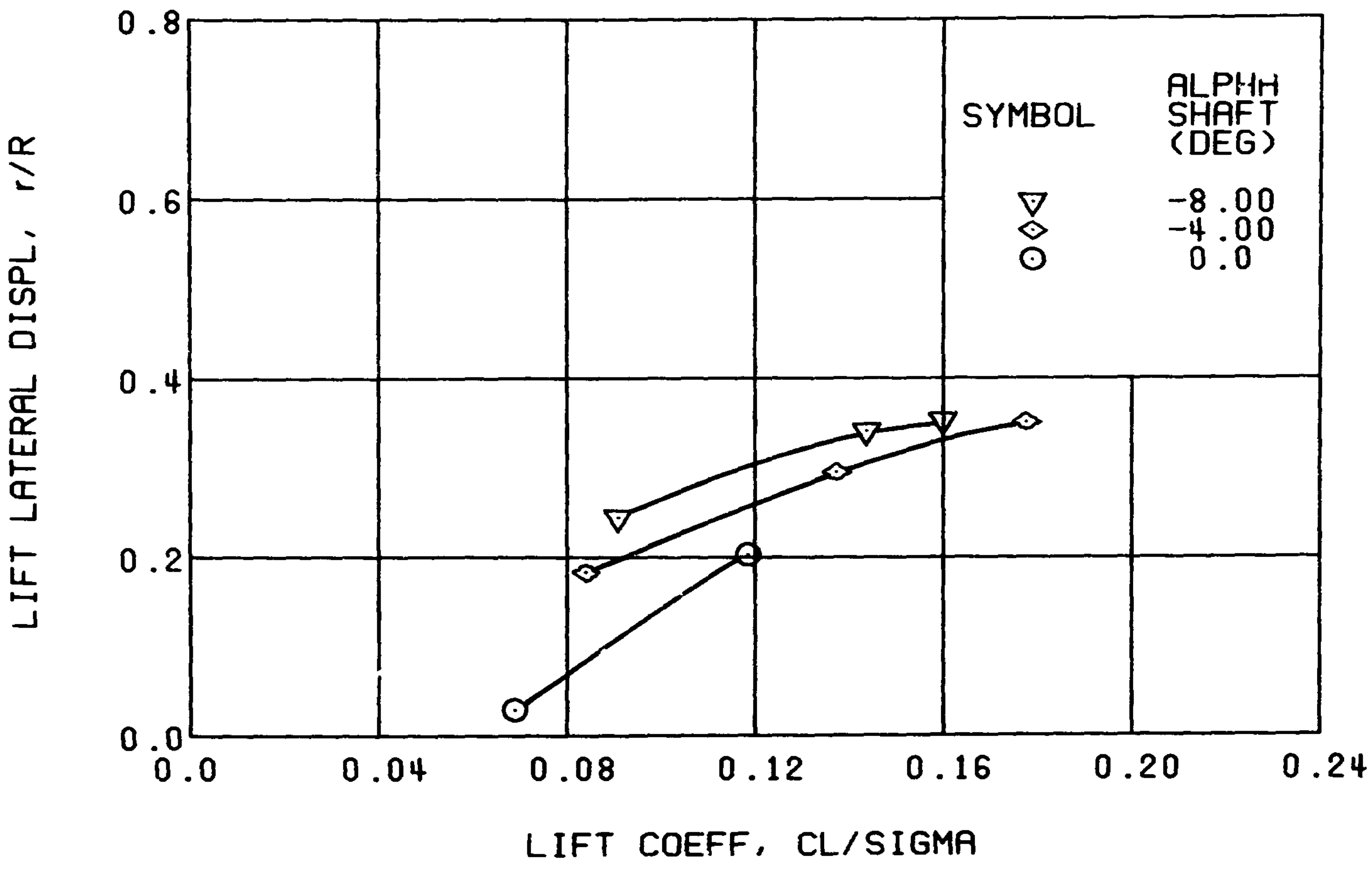

(d) LIFT LATERAL DISPLACEMENT

Figure 28. Continued.
$\mu = 0.47 \quad B'_{1s} = 8$ Deg

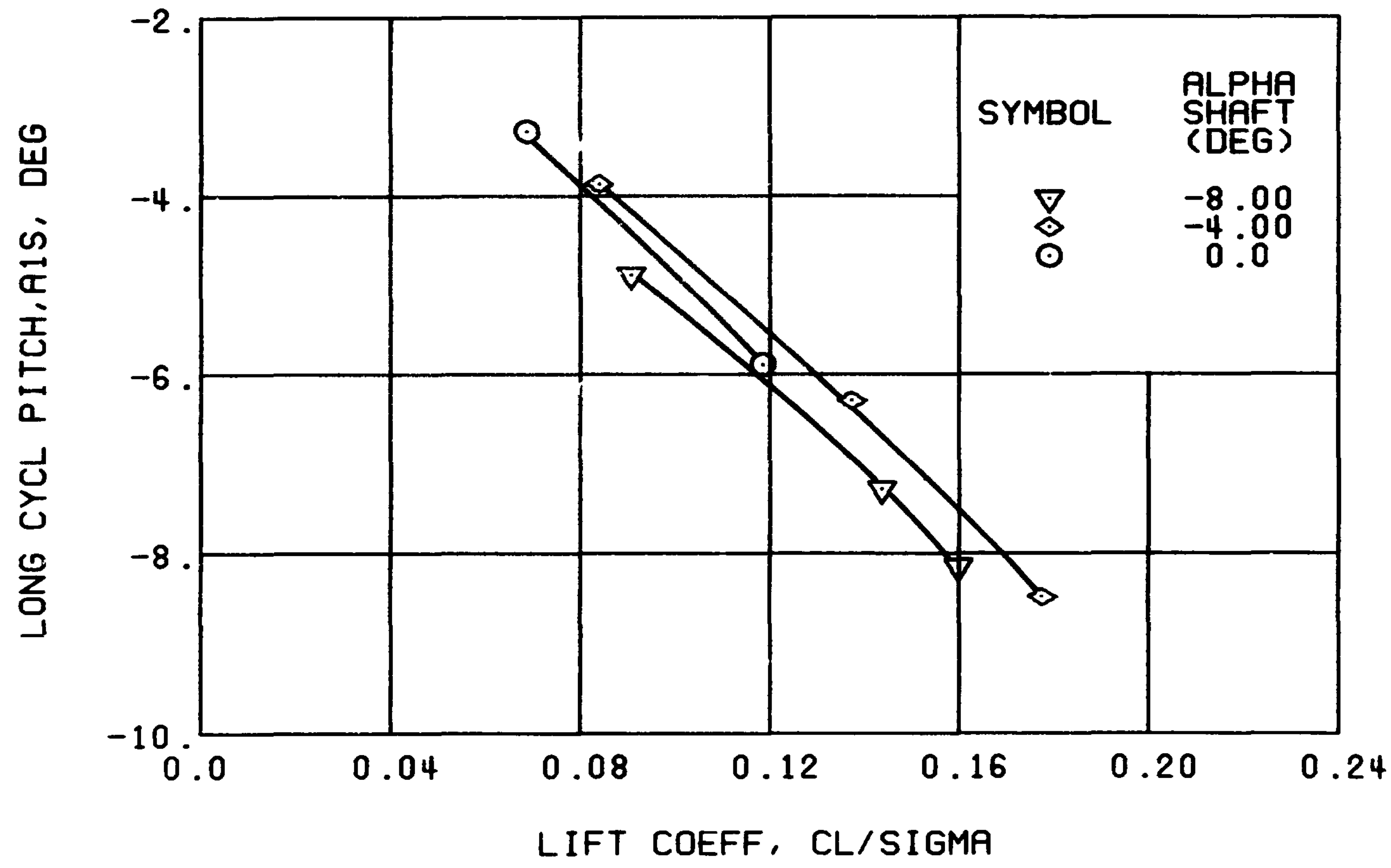

(e) LONGITUDINAL CYCLIC PITCH

Figure 28. Continued.
$\mu = 0.47 \quad B'_{1s} = 8$ Deg

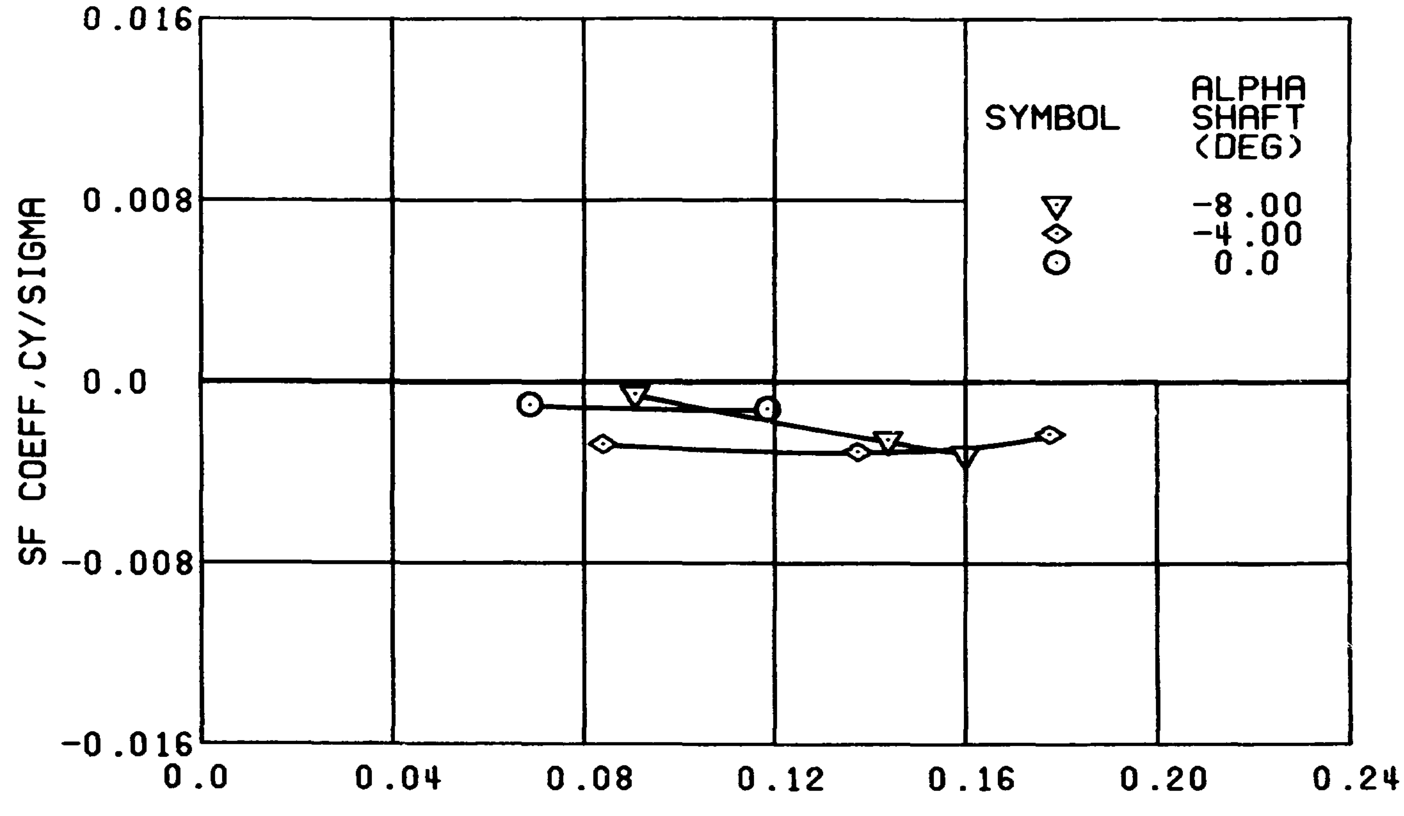

(f) SIDE FORCE COEFFICIENT

Figure 28. Continued.
$\mu = 0.47 \quad B'_{1s} = 8$ Deg

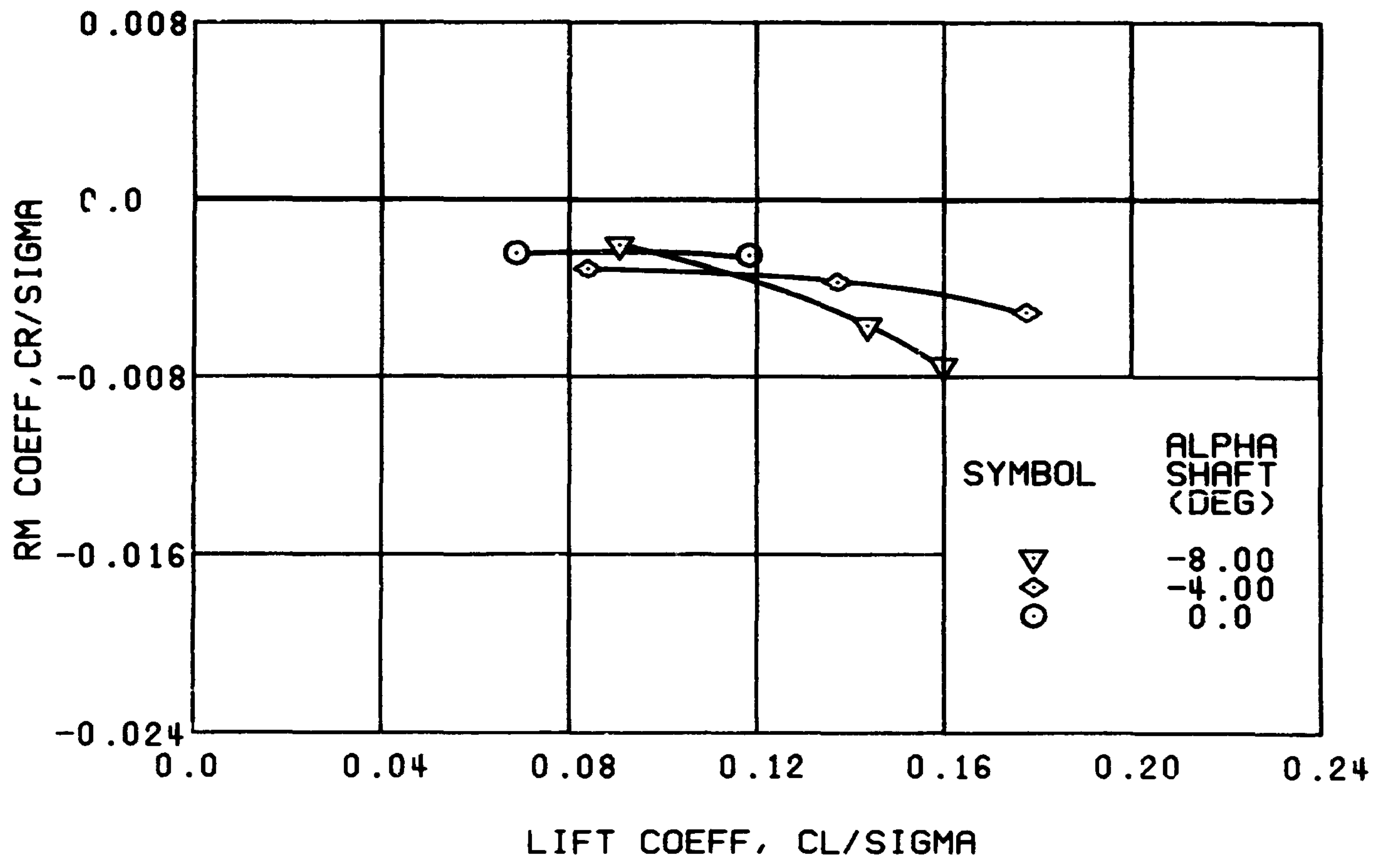

(g) ROLLING MOMENT COEFFICIENT

Figure 28. Continued.
$\mu = 0.47$ $B'_{1s} = 8$ Deg

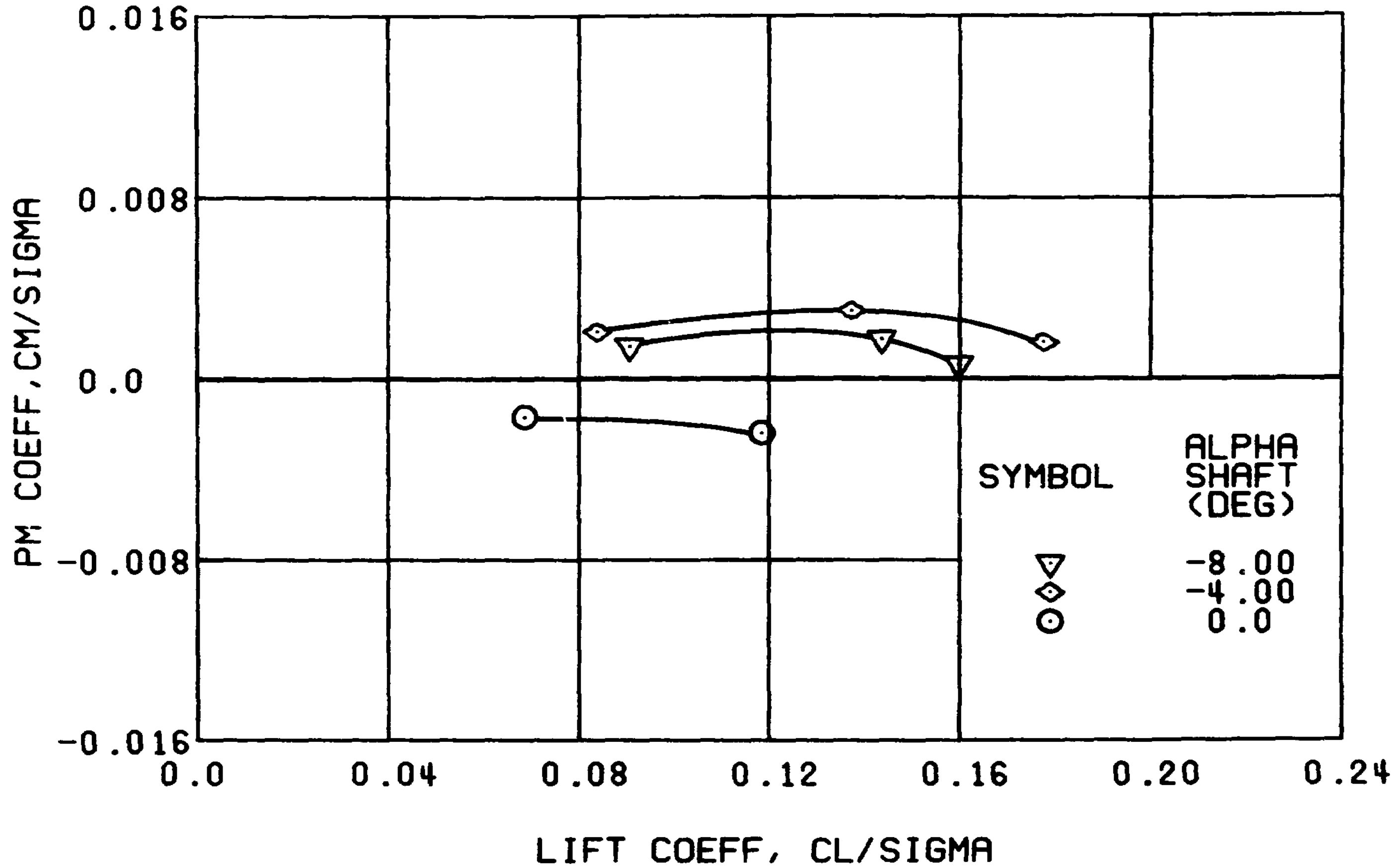

(h) PITCHING MOMENT COEFFICIENT

Figure 28. Continued.
$\mu = 0.47$ $B'_{1s} = 8$ Deg

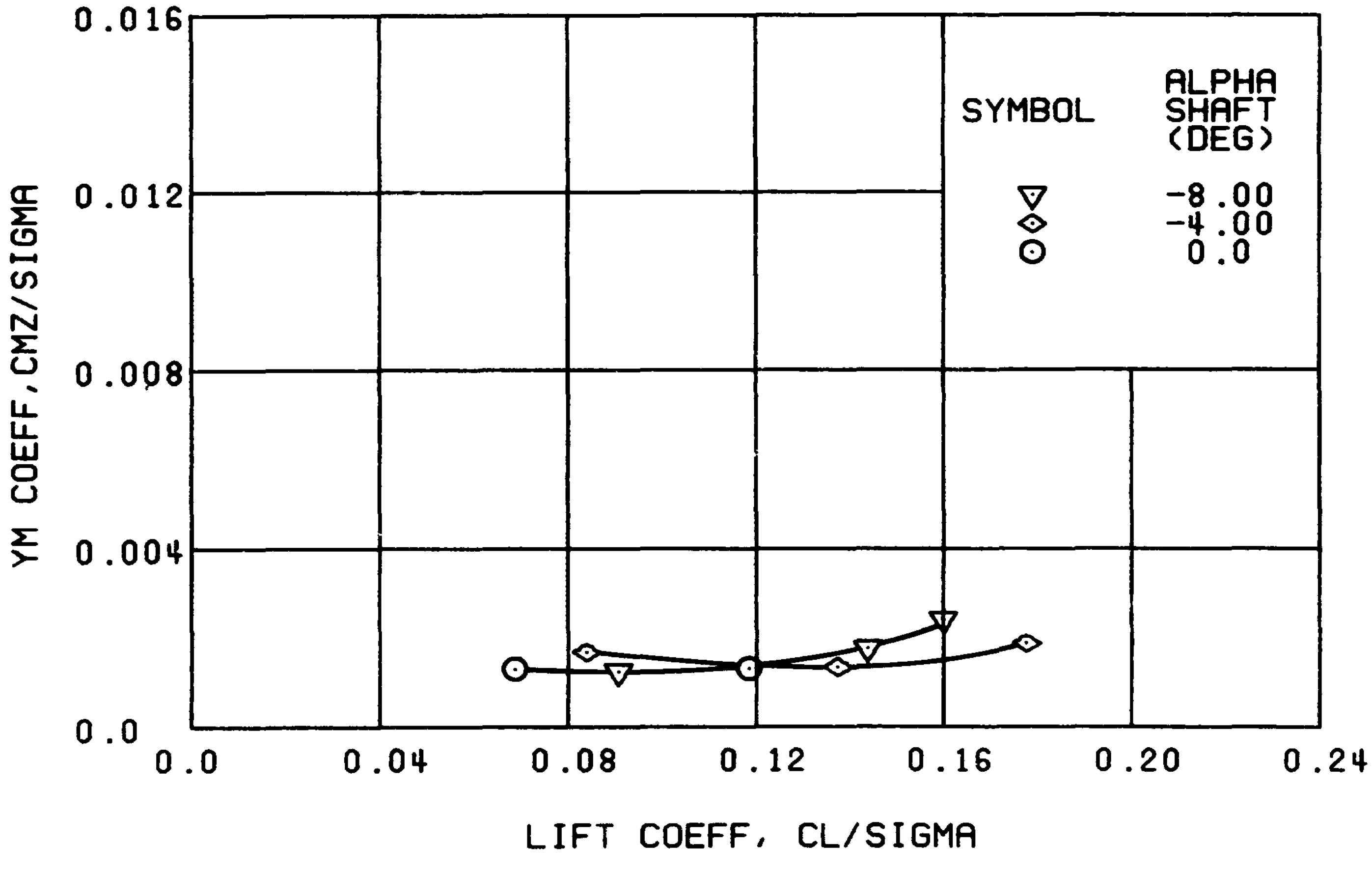

(i) YAWING MOMENT COEFFICIENT

Figure 28. Concluded.
$\mu = 0.47 \quad B'_{1s} = 8$ Deg

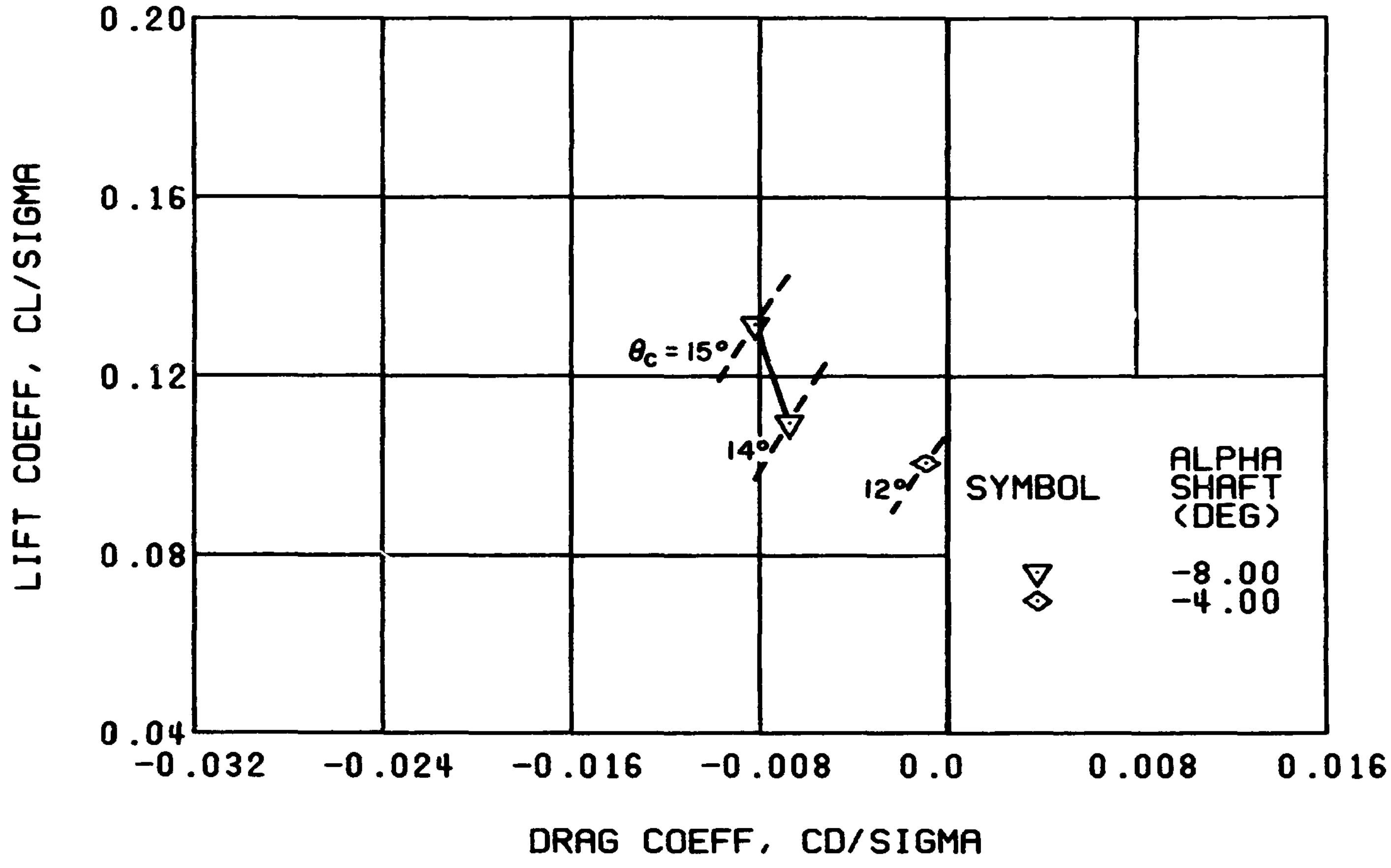

(a) DRAG COEFFICIENT

Figure 29. Performance Data at an Advance Ratio of 0.47 With the Lateral Displacement Control (B'_{1s}) Set at 10 Degrees.

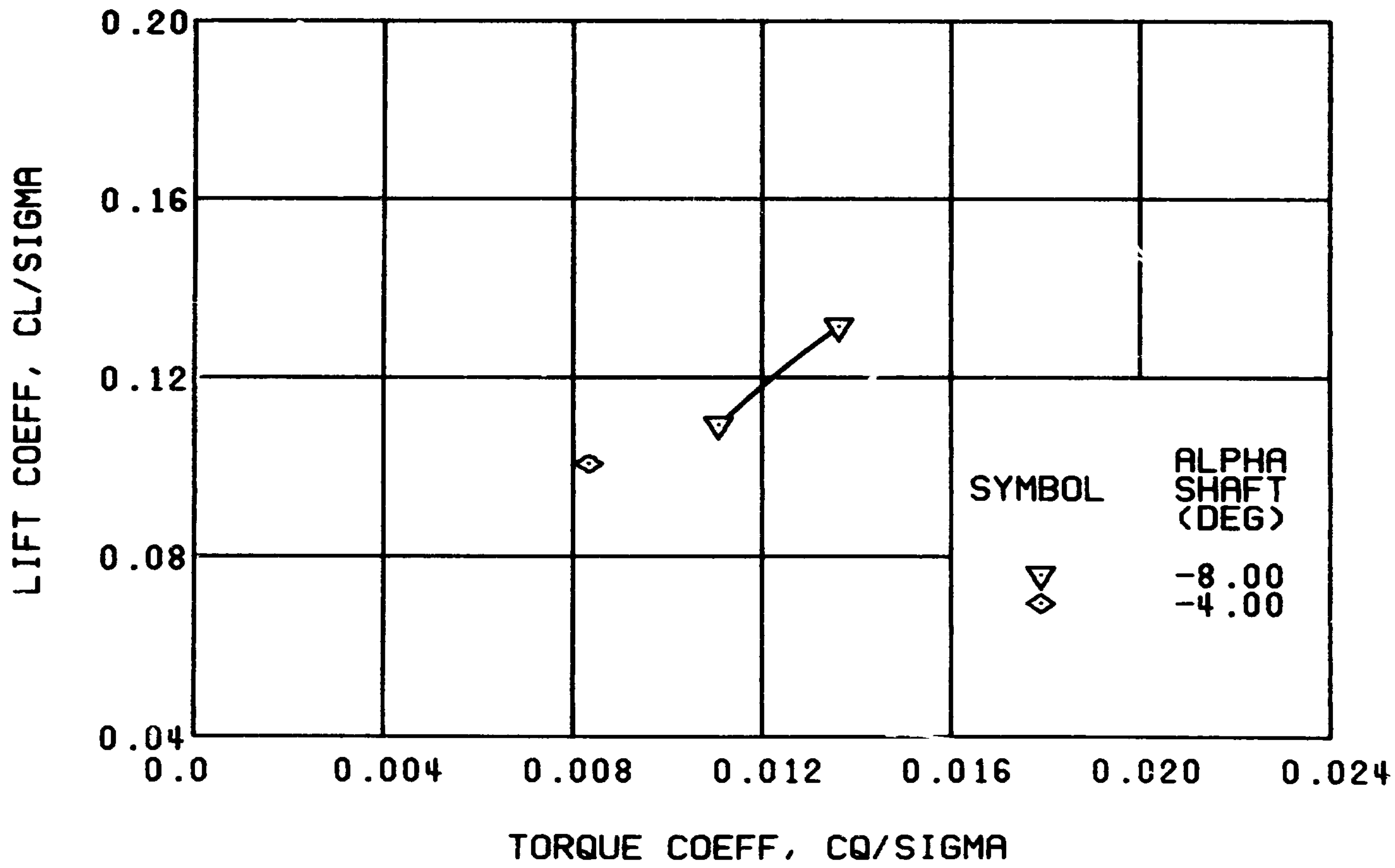

(b) TORQUE COEFFICIENT

Figure 29. Continued.
$\mu = 0.47 \quad B'_{1s} = 10$ Deg

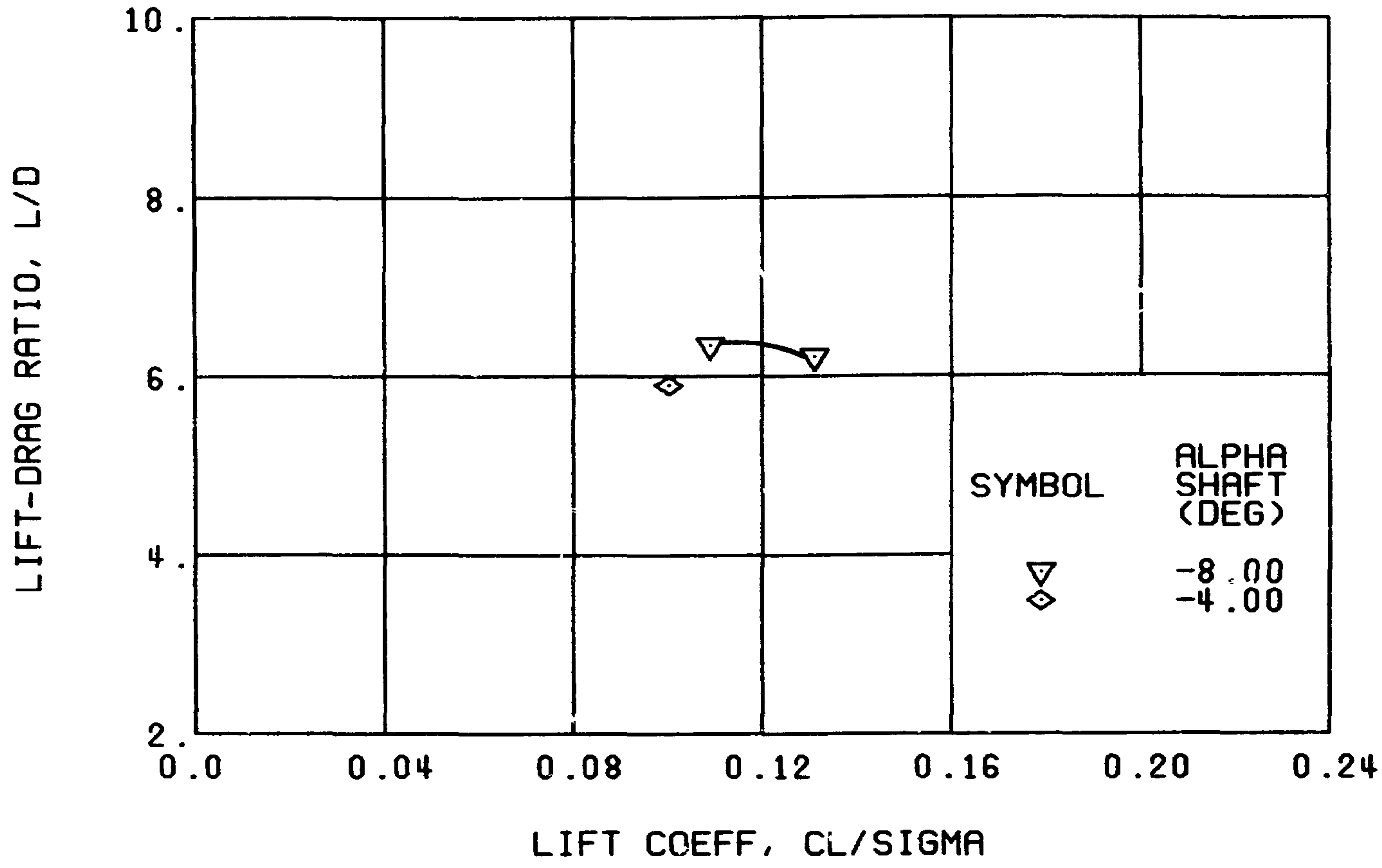

(c) LIFT-DRAG RATIO

Figure 29. Continued.
$\mu = 0.47 \quad B'_{1s} = 10$ **Deg**

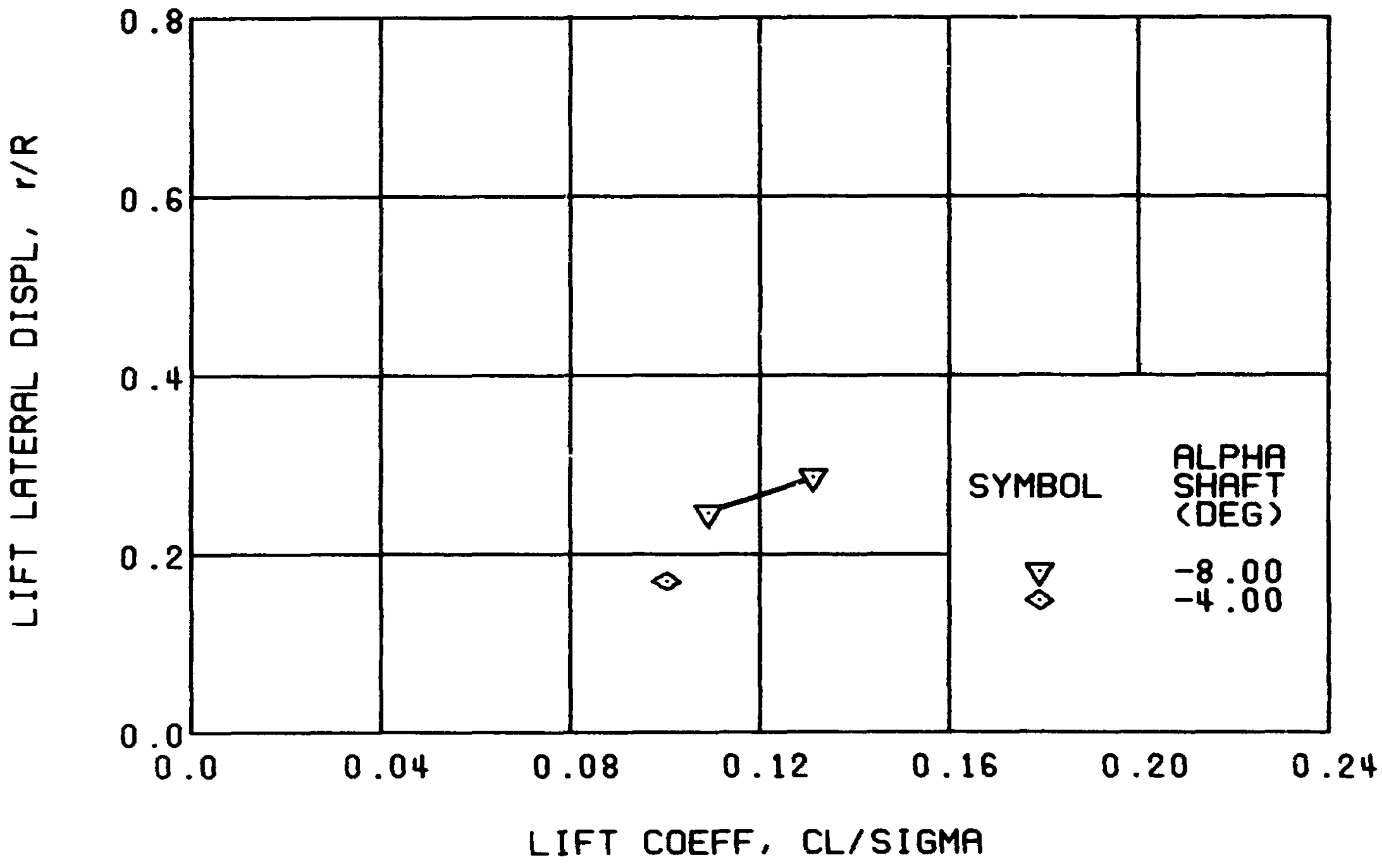

(d) LIFT LATEF.AL DISPLACEMENT

Figure 29. Continued.
$\mu = 0.47$ $B'_{1s} = 10$ Deg

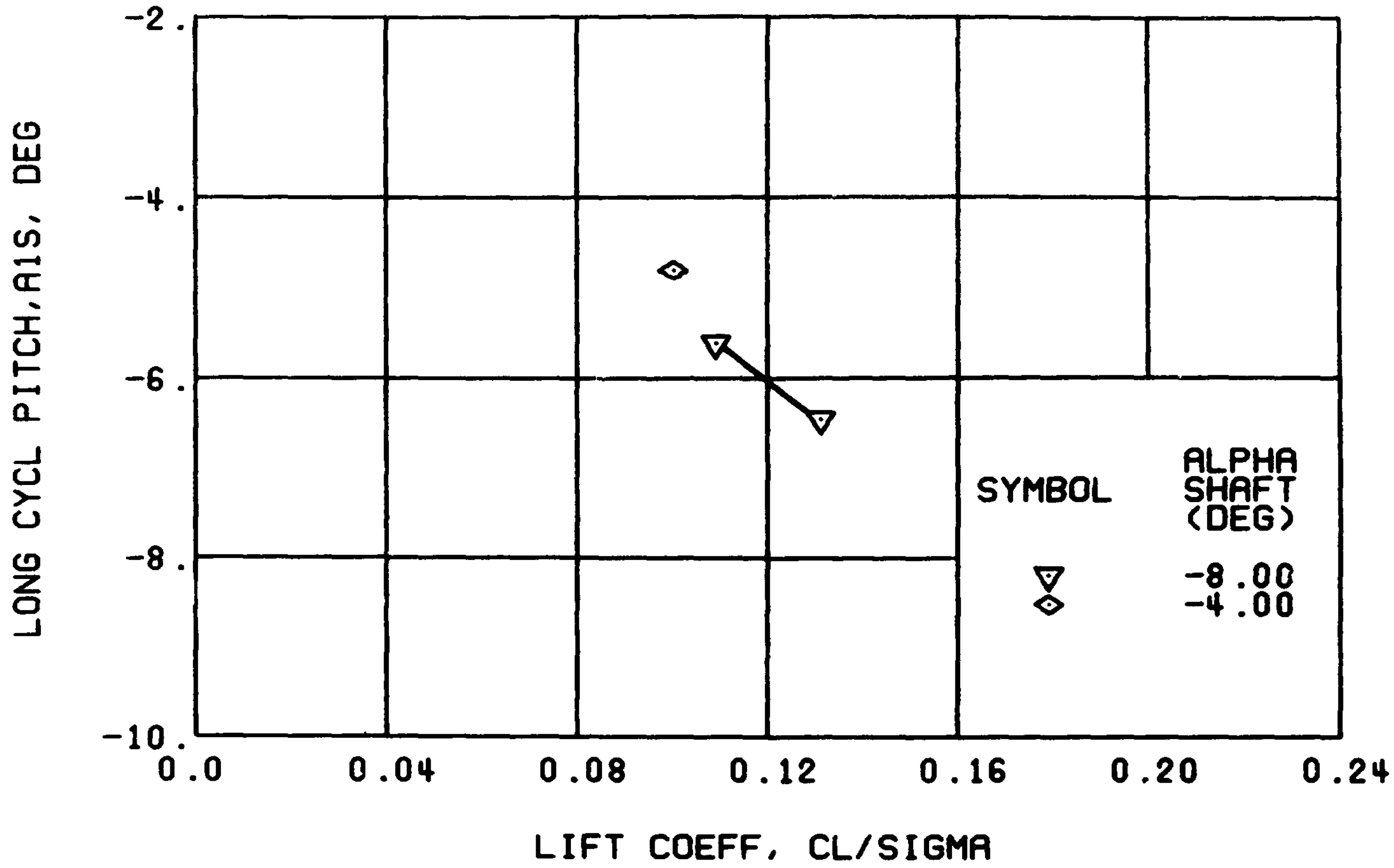

(e) LONGITUDINAL CYCLIC PITCH

Figure 29. Continued.
$\mu = 0.47$ $B'_{1s} = 10$ Deg

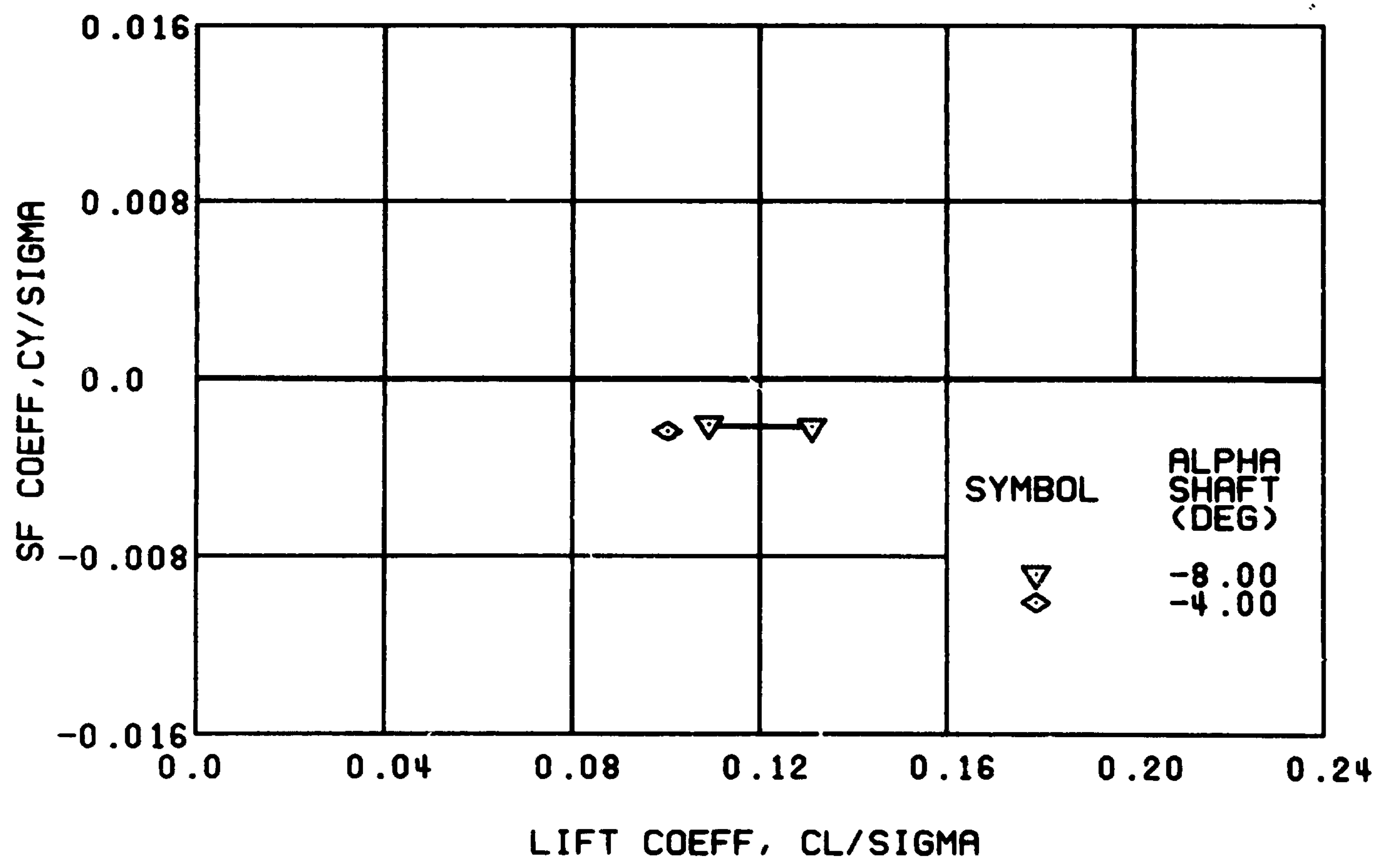

(f) SIDE FORCE COEFFICIENT

Figure 29. Continued.
μ = 0.47 B'_{1s} = 10 Deg

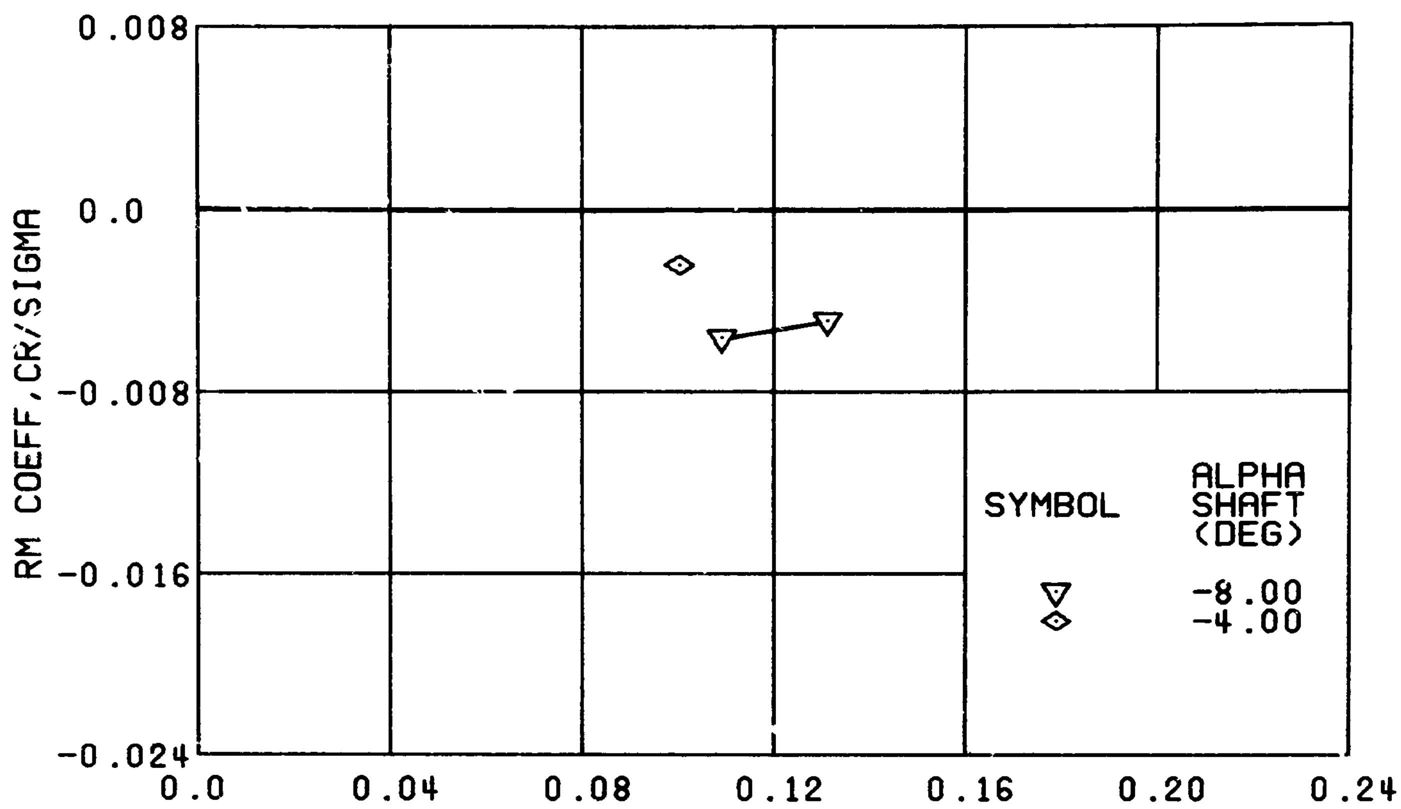

(g) ROLLING MOMENT COEFFICIENT

Figure 29. Continued.
$\mu = 0.47 \quad B'_{1s} = 10$ Deg

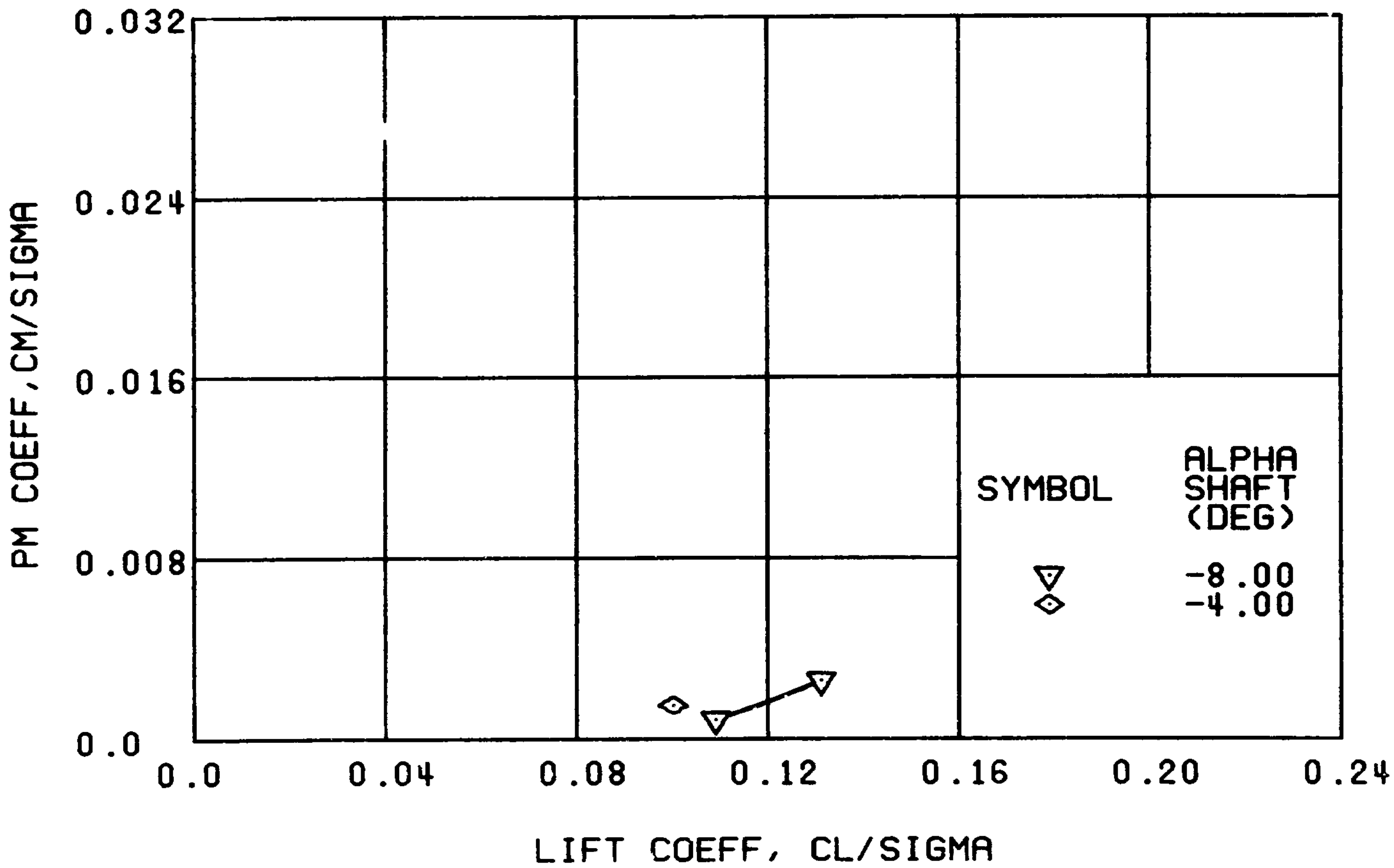

(h) PITCHING MOMENT COEFFICIENT

Figure 29. Continued.
$\mu = 0.47$ $B'_{1s} = 10$ Deg

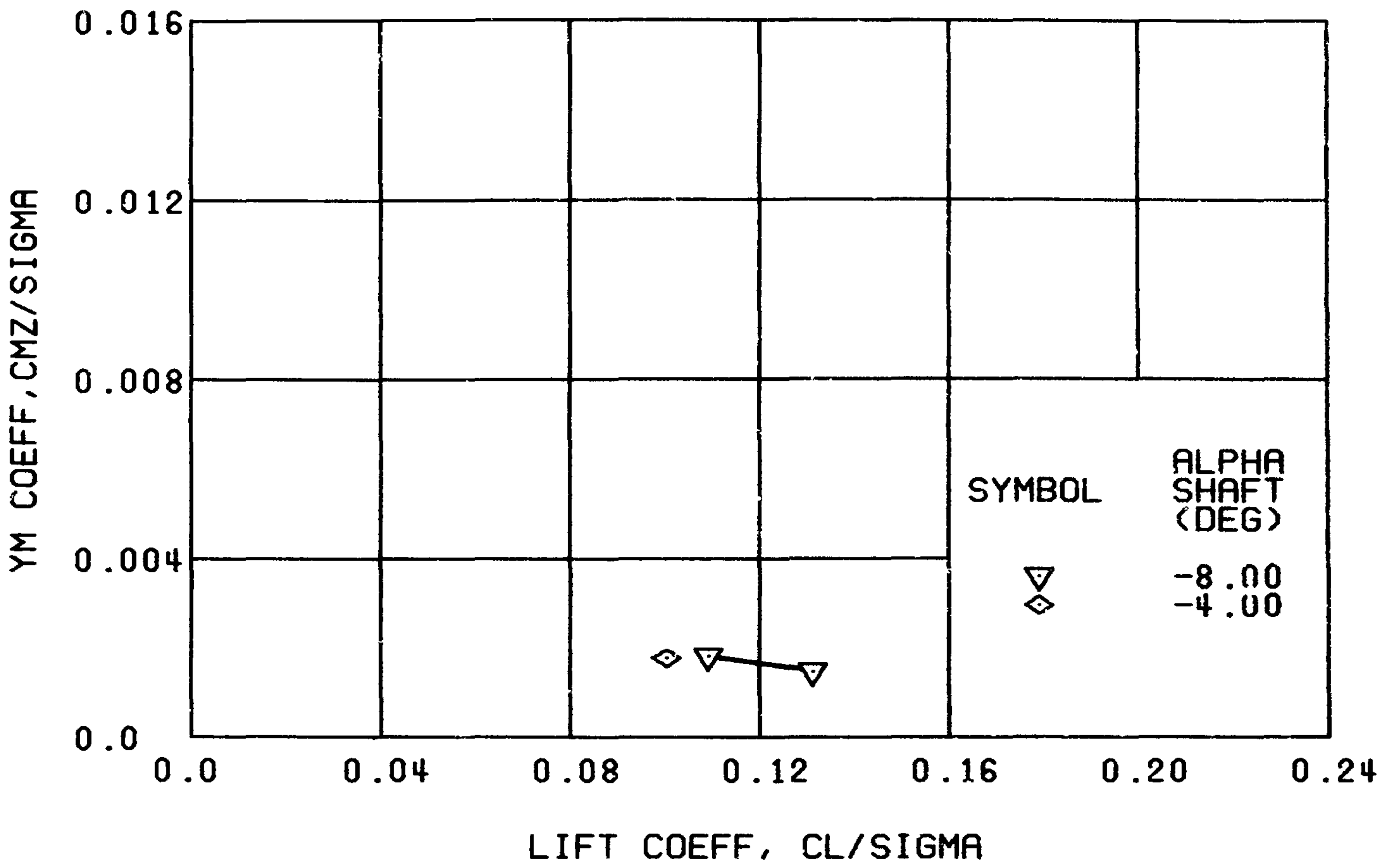

(i) YAWING MOMENT COEFFICIENT

Figure 29. Concluded.
$\mu = 0.47 \quad B'_{1s} = 10$ Deg

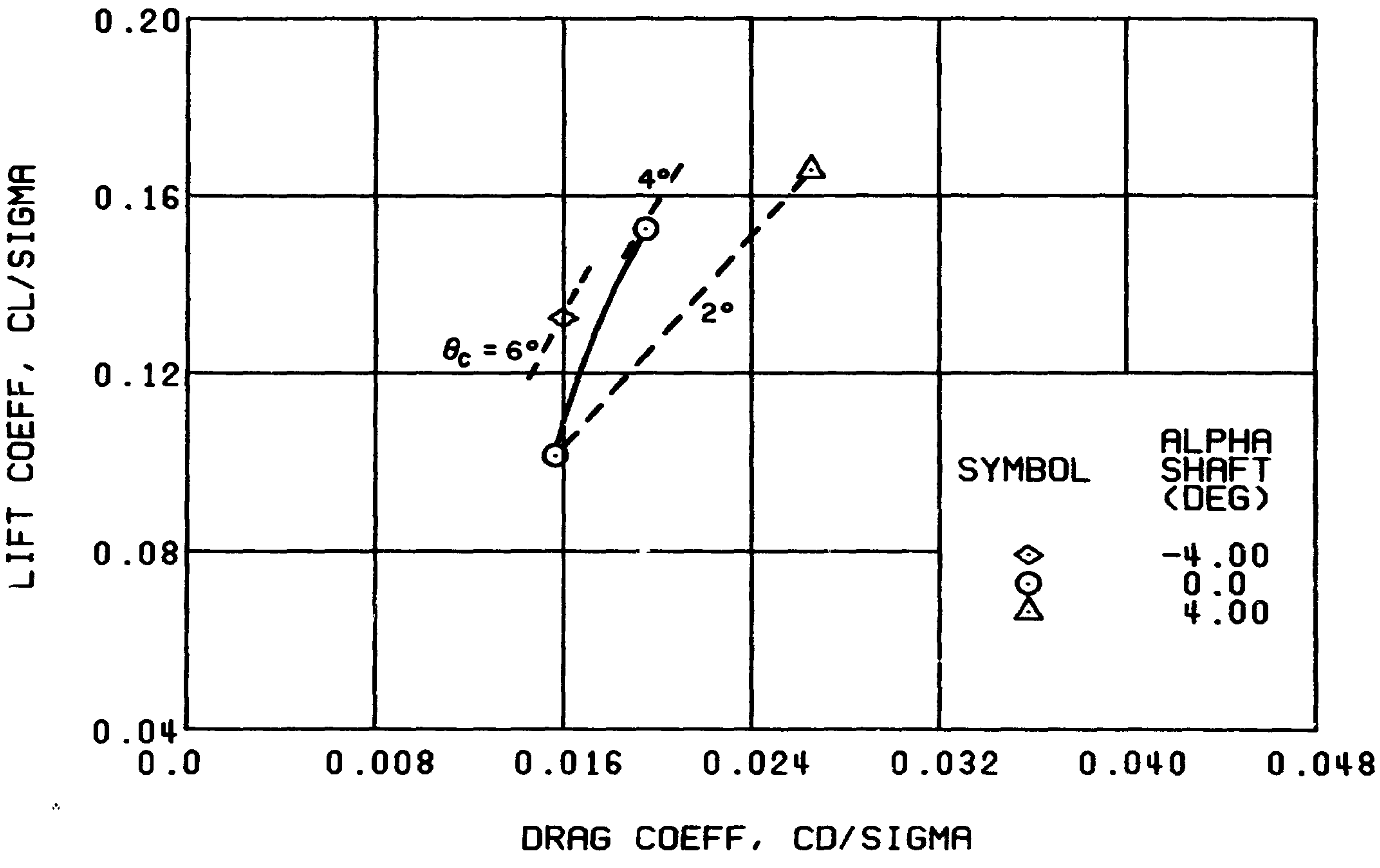

(a) DRAG COEFFICIENT

Figure 30. Performance Data at an Advance Ratio of 0.70 With the Lateral Displacement Control (B'_{1s}) Set at 0 Degrees.

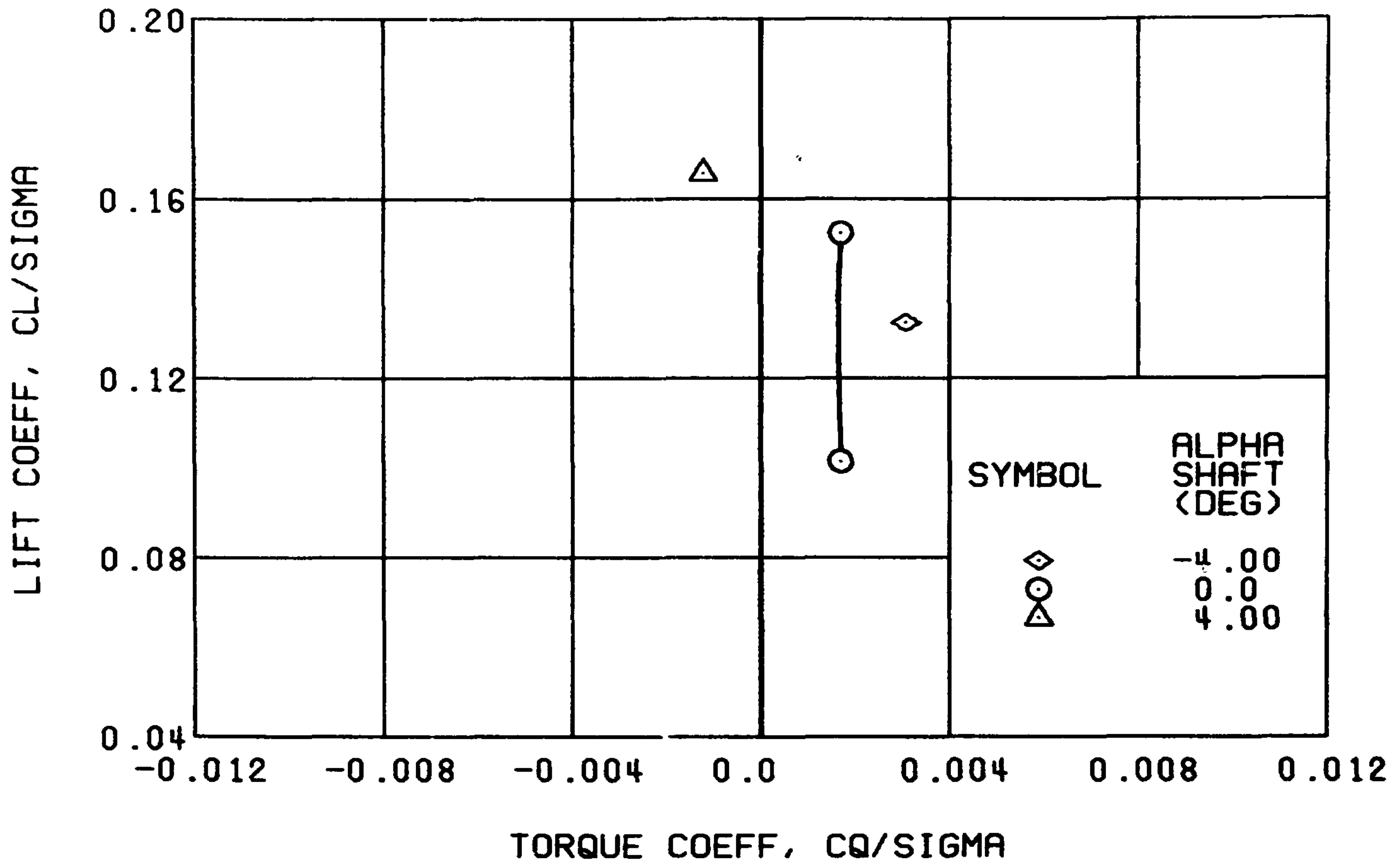

(b) TORQUE COEFFICIENT

Figure 30. Continued.
μ = 0.70 B'_{1s} = 0 Deg

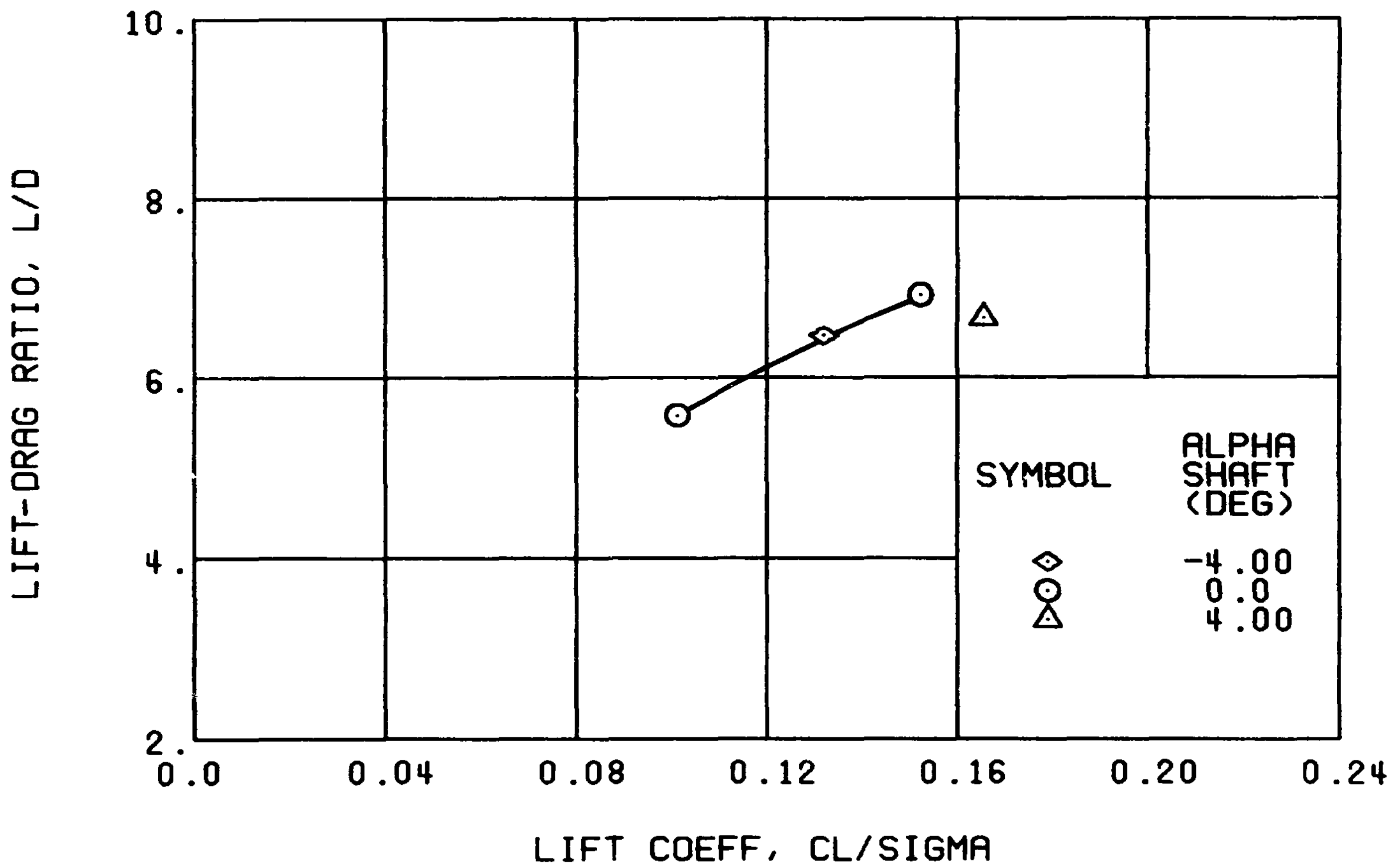

(c) LIFT-DRAG RATIO

Figure 30. Continued.
$\mu = 0.70$ $B'_{1s} = 0$ Deg

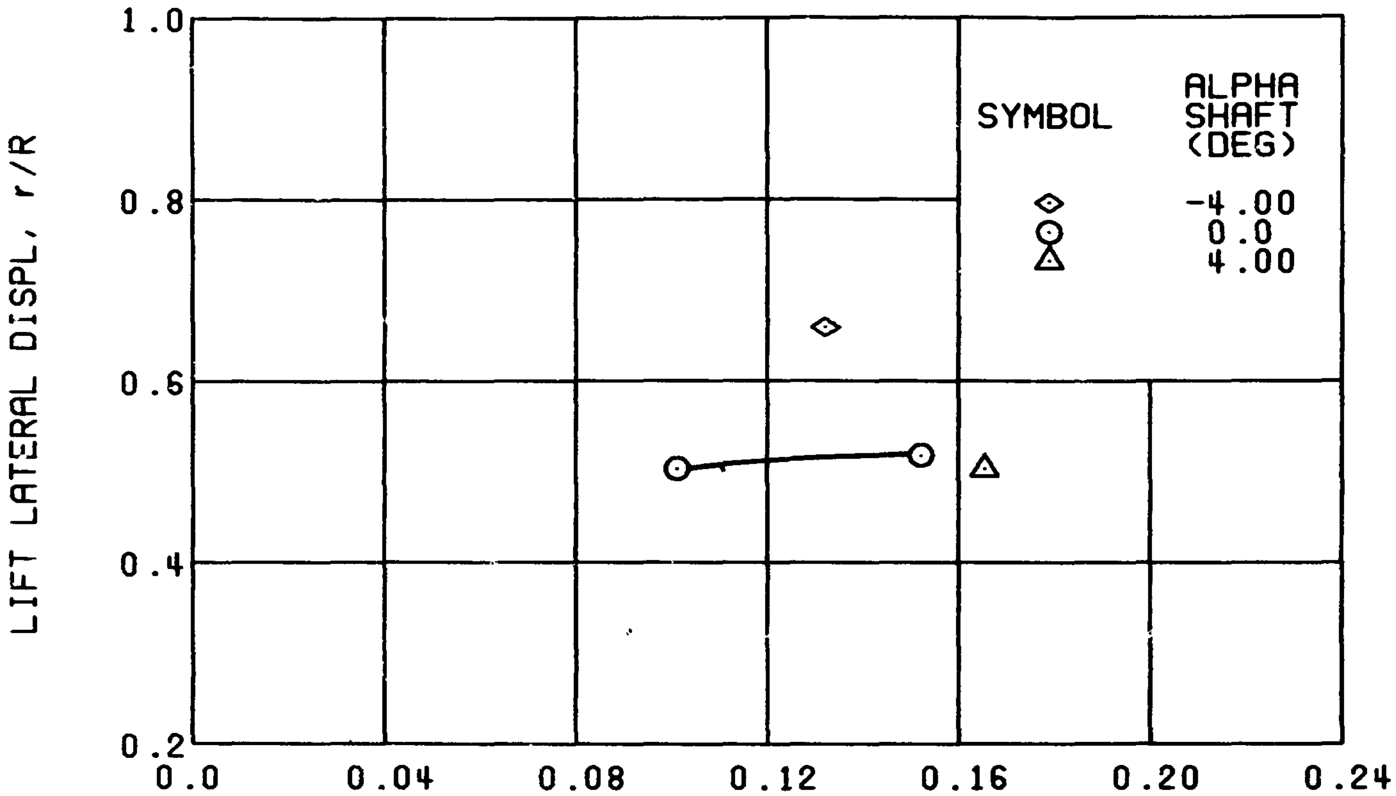

(d) LIFT LATERAL DISPLACEMENT

Figure 30. Continued.
$\mu = 0.70$ $B'_{1s} = 0$ Deg

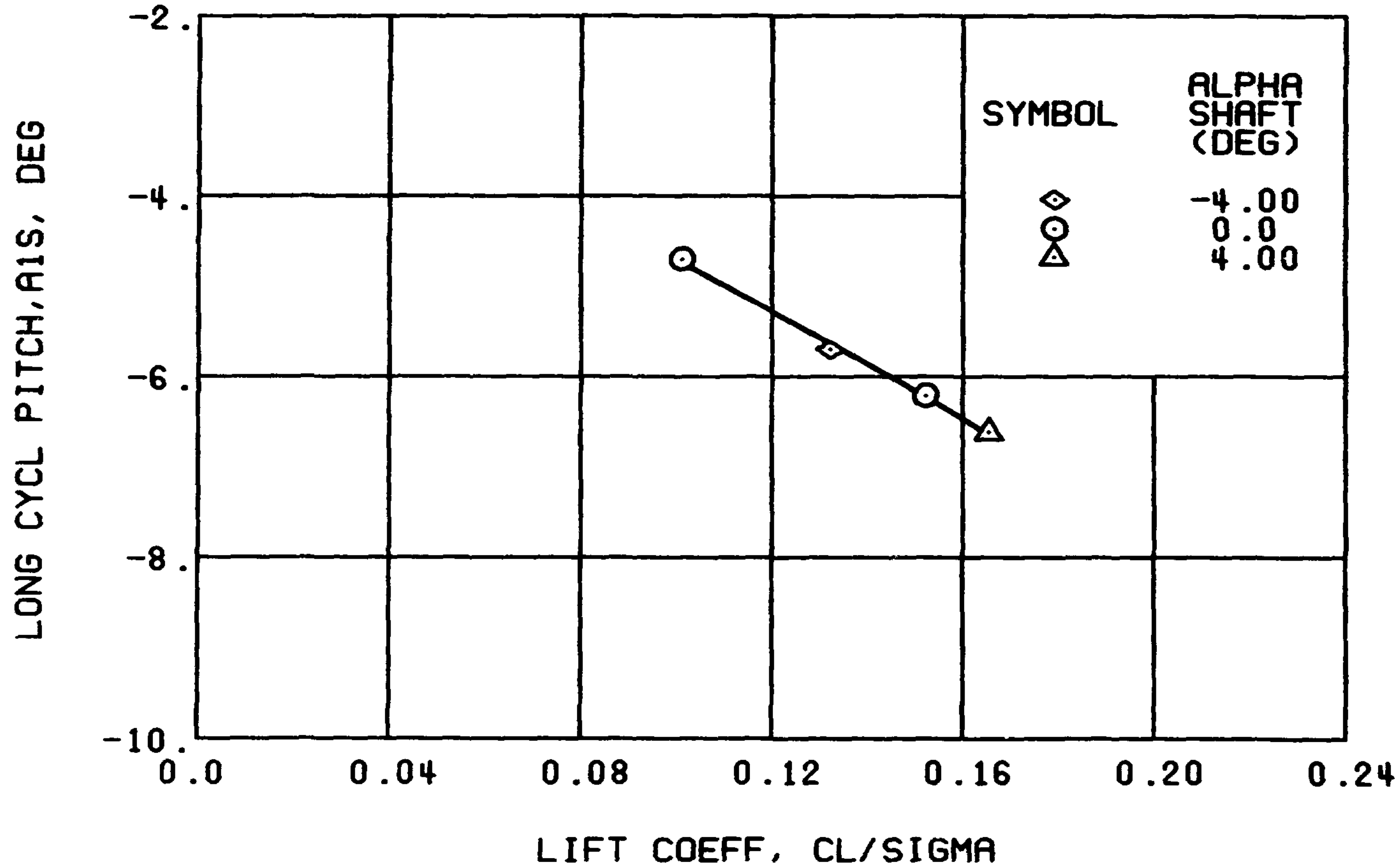

(e) LONGITUDINAL CYCLIC PITCH

Figure 30. Continued.
μ = 0.70 B'_{1s} = 0 Deg

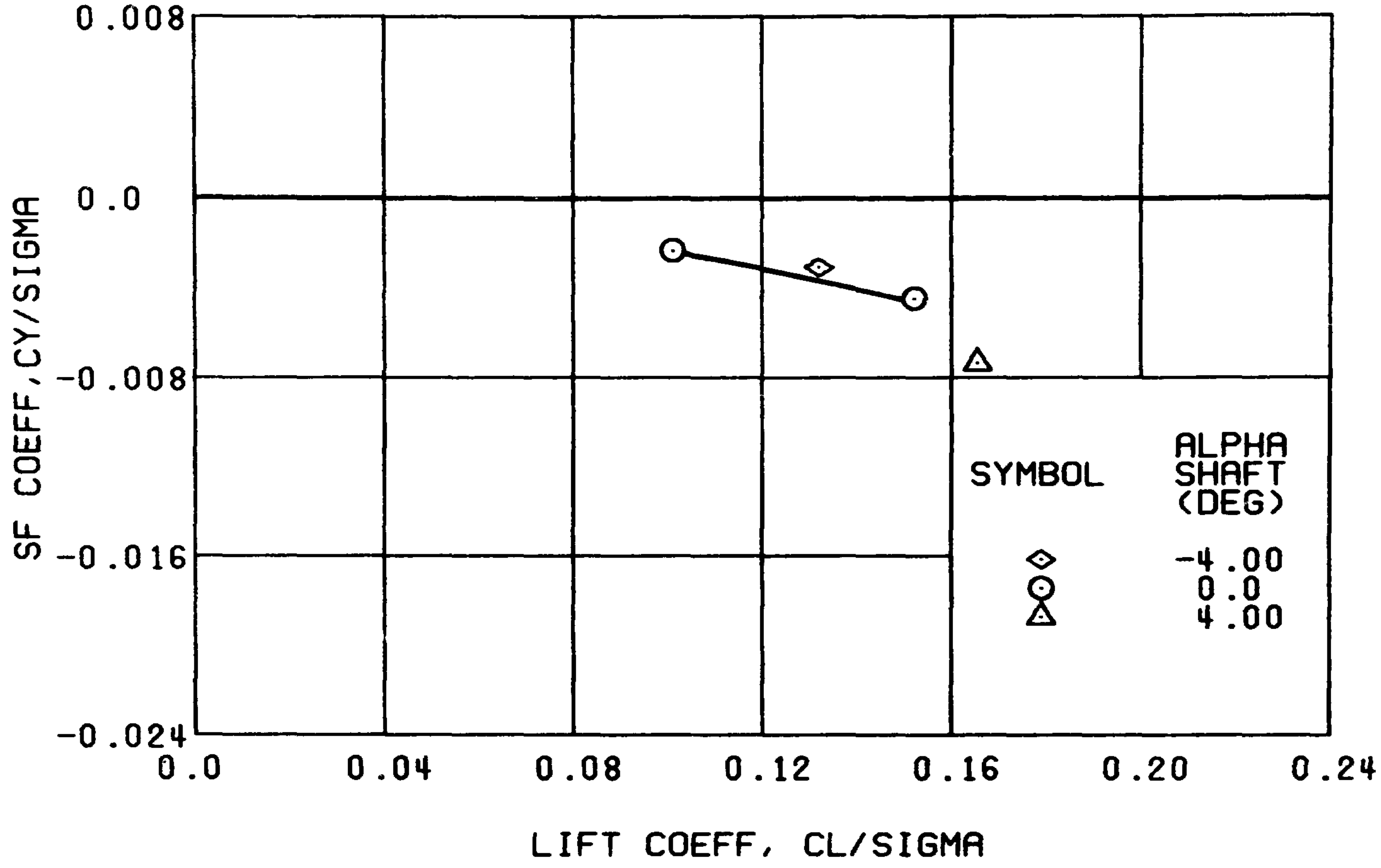

(f) SIDE FORCE COEFFICIENT

Figure 30. Continued.
$\mu = 0.70$ $B'_{1s} = 0$ Deg

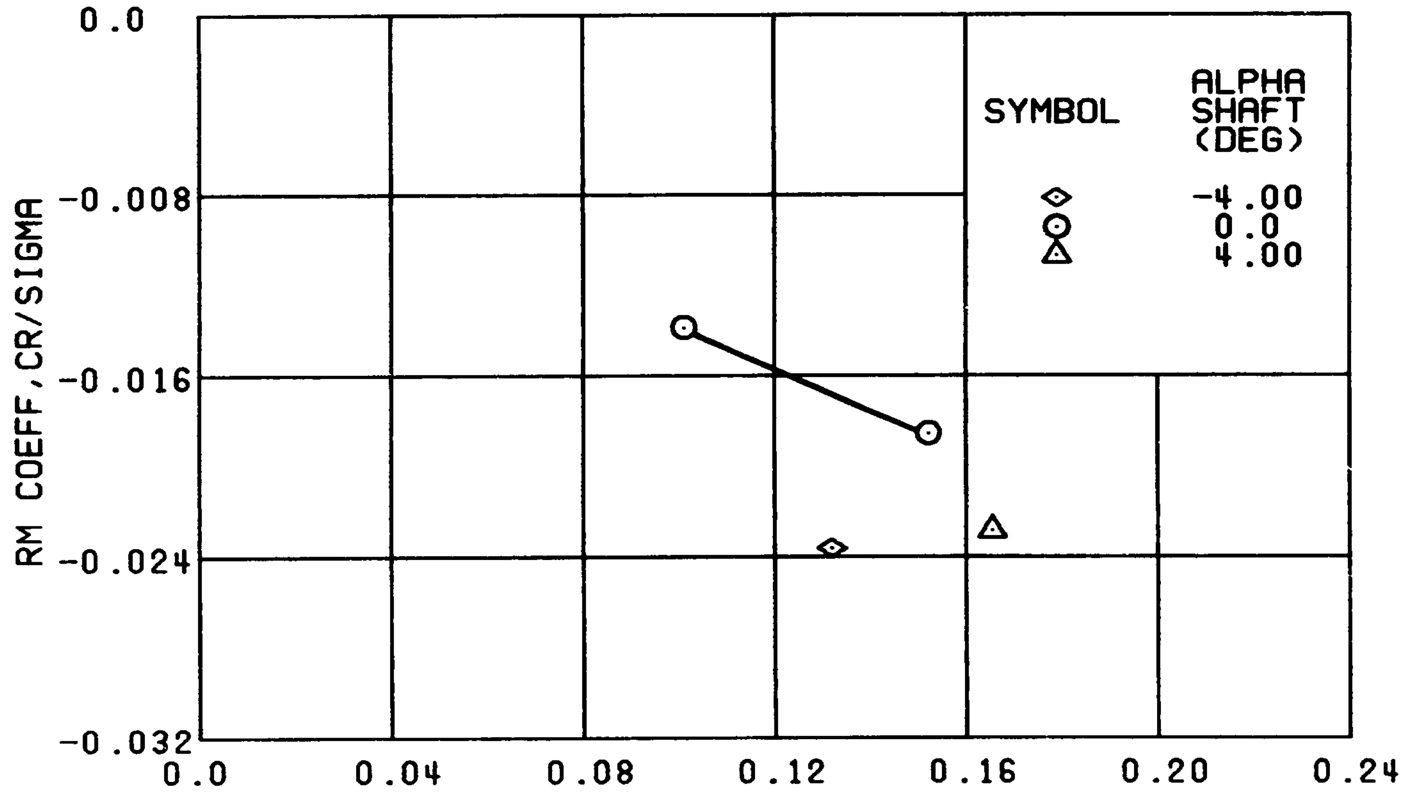

(g) ROLLING MOMENT COEFFICIENT

Figure 30. Continued.
$\mu = 0.70 \quad B'_{1s} = 0$ Deg

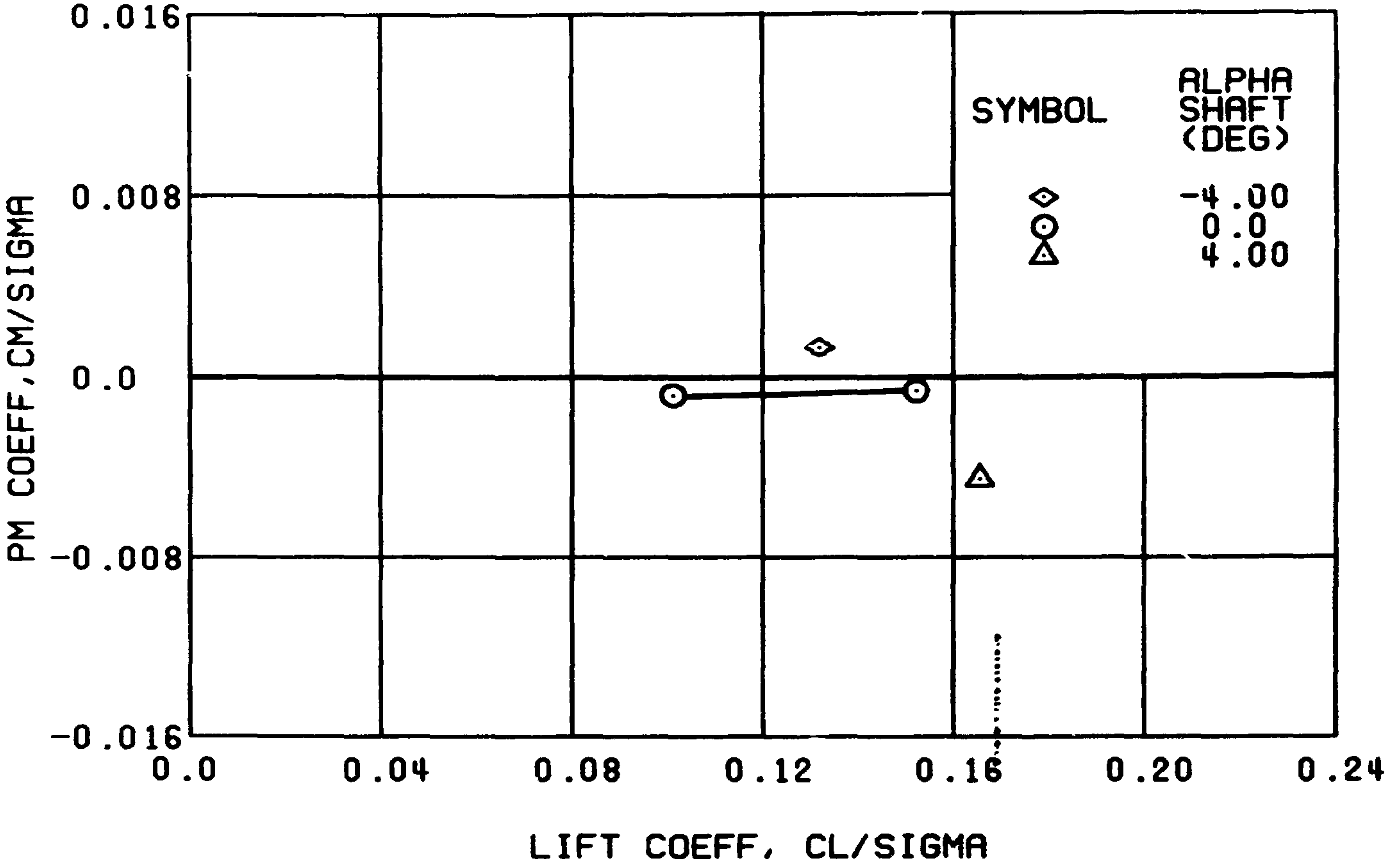

(h) PITCHING MOMENT COEFFICIENT

Figure 30. Continued.
$\mu = 0.70 \quad B'_{1s} = 0$ Deg

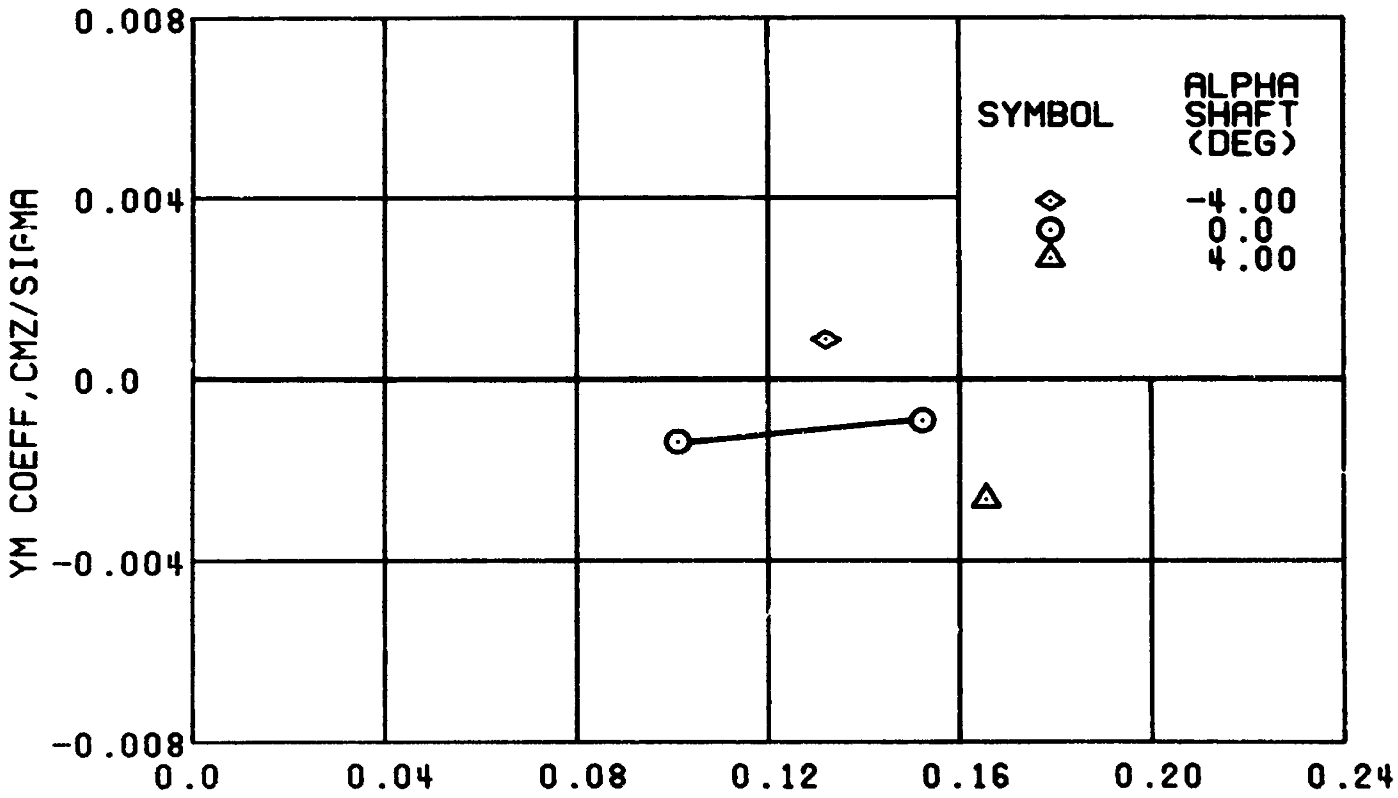

(i) YAWING MOMENT COEFFICIENT

Figure 30. Concluded.
μ = 0.70 B'_{1s} = 0 Deg

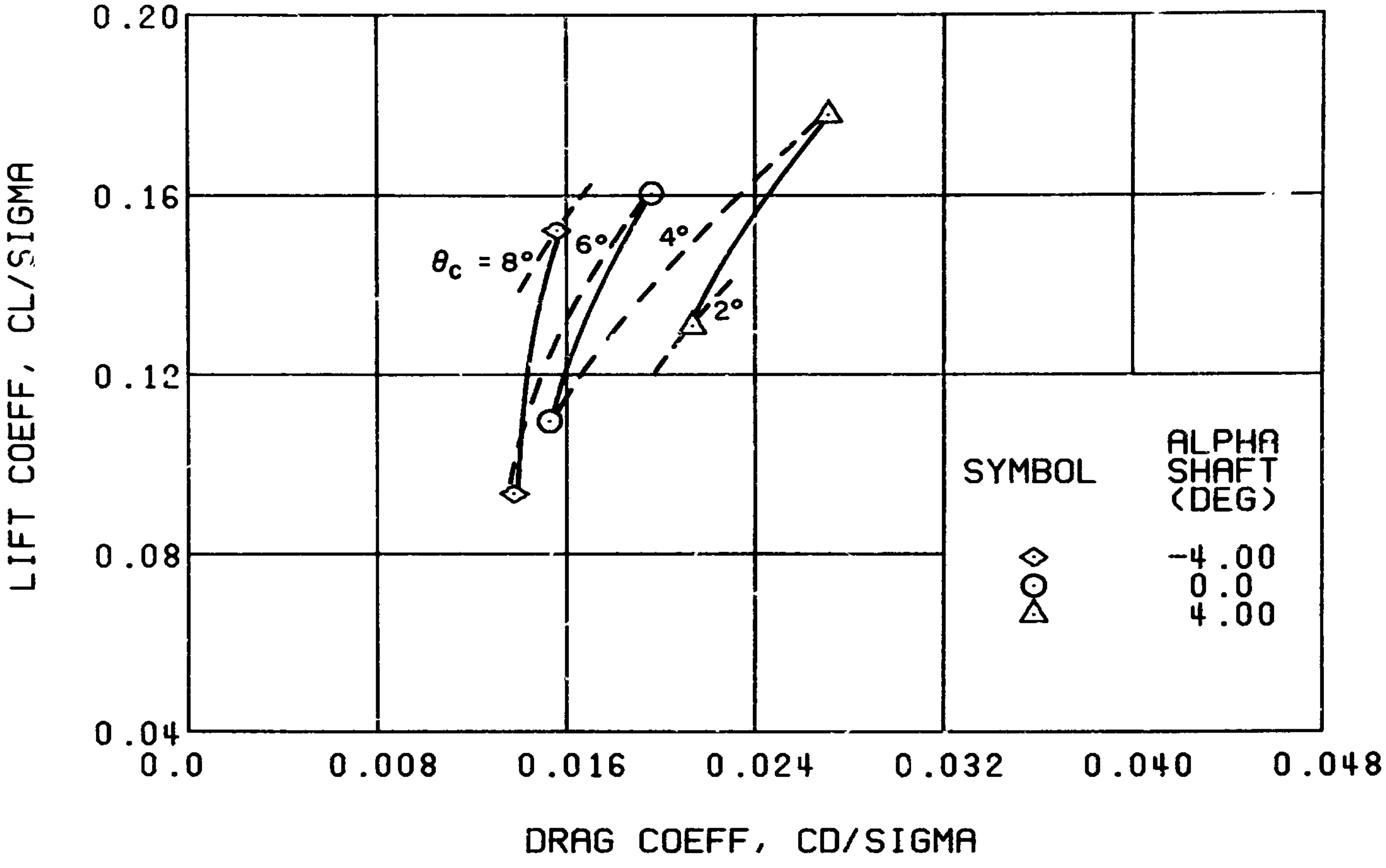

(a) DRAG COEFFICIENT

Figure 31. Performance Data at an Advance Ratio of 0.70 With the Lateral Displacement Control (B'_{1s}) Set at 2 Degrees.

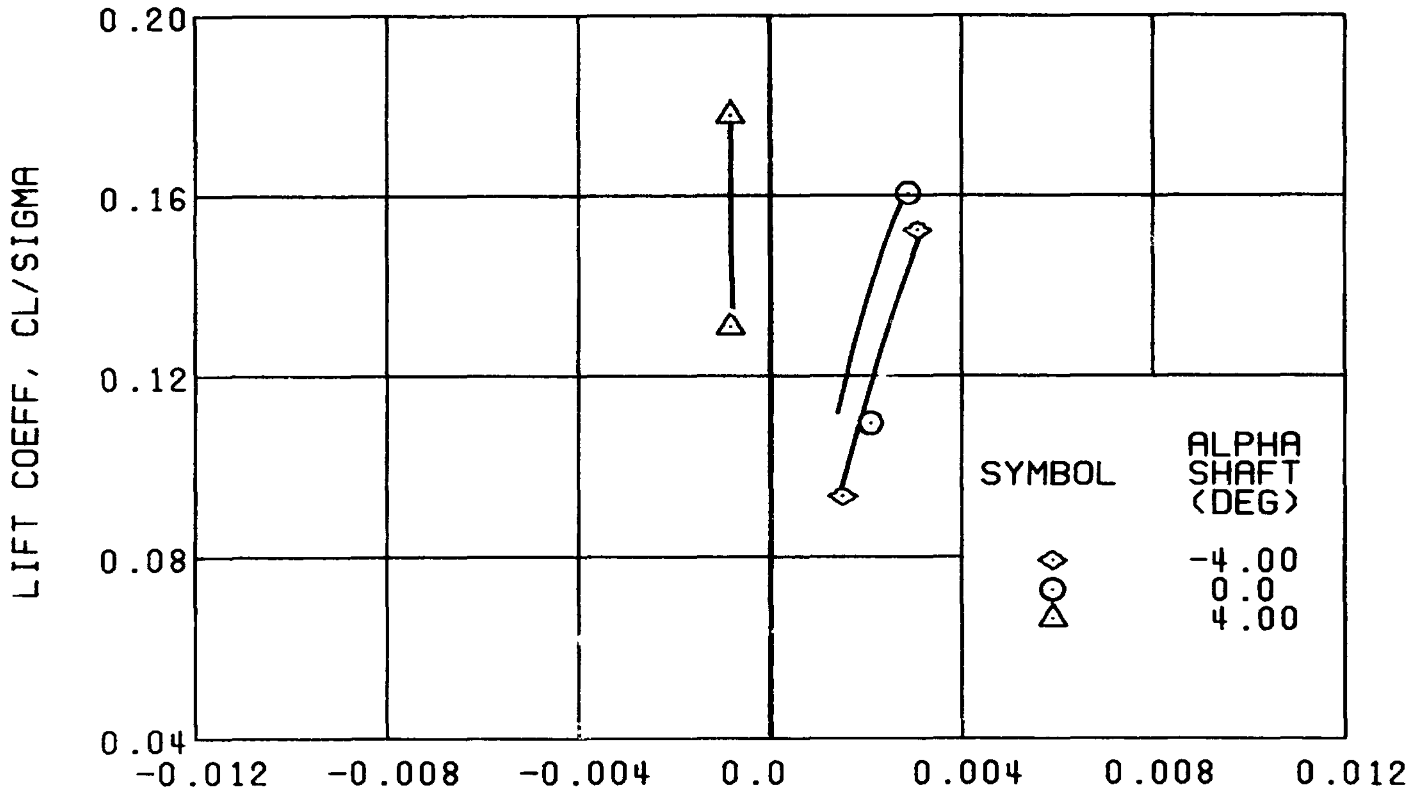

(b) TORQUE COEFFICIENT

Figure 31. Continued.
$\mu = 0.70 \quad B'_{1s} = 2$ Deg

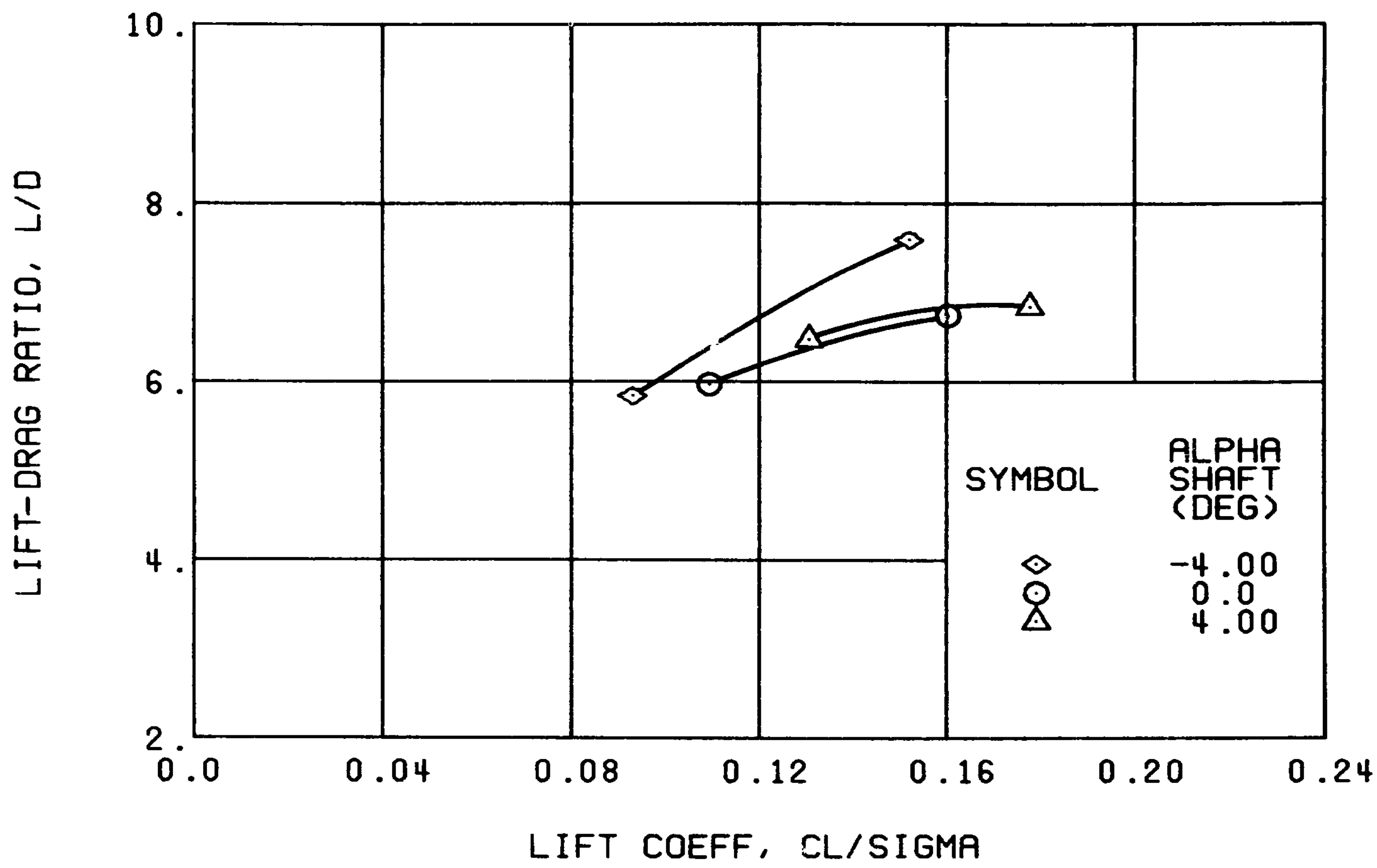

(c) LIFT-DRAG RATIO

Figure 31. Continued.
μ = 0.70 B'_{1s} = 2 Deg

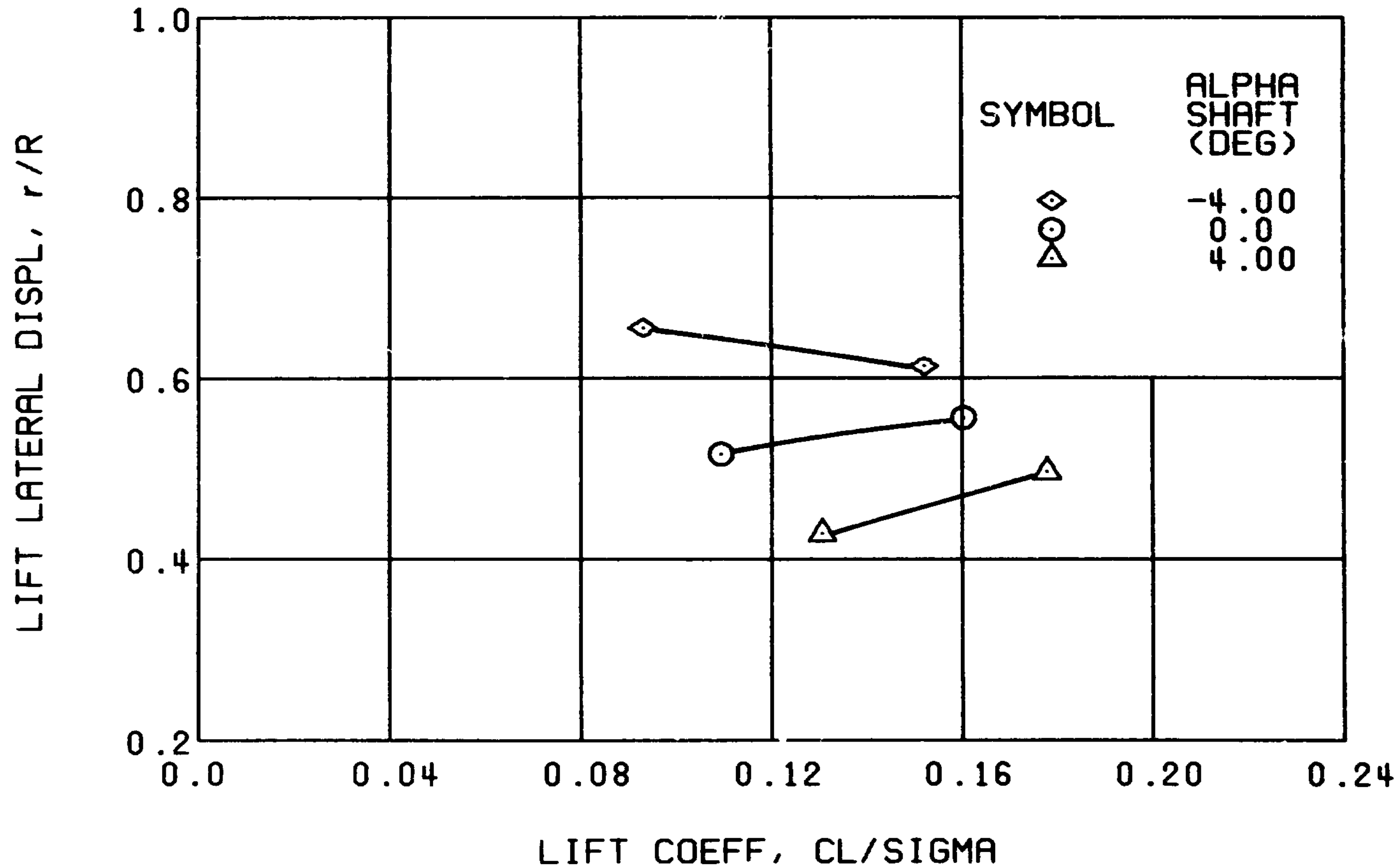

(d) LIFT LATERAL DISPLACEMENT

Figure 31. Continued.
$\mu = 0.70 \quad B'_{1s} = 2$ Deg

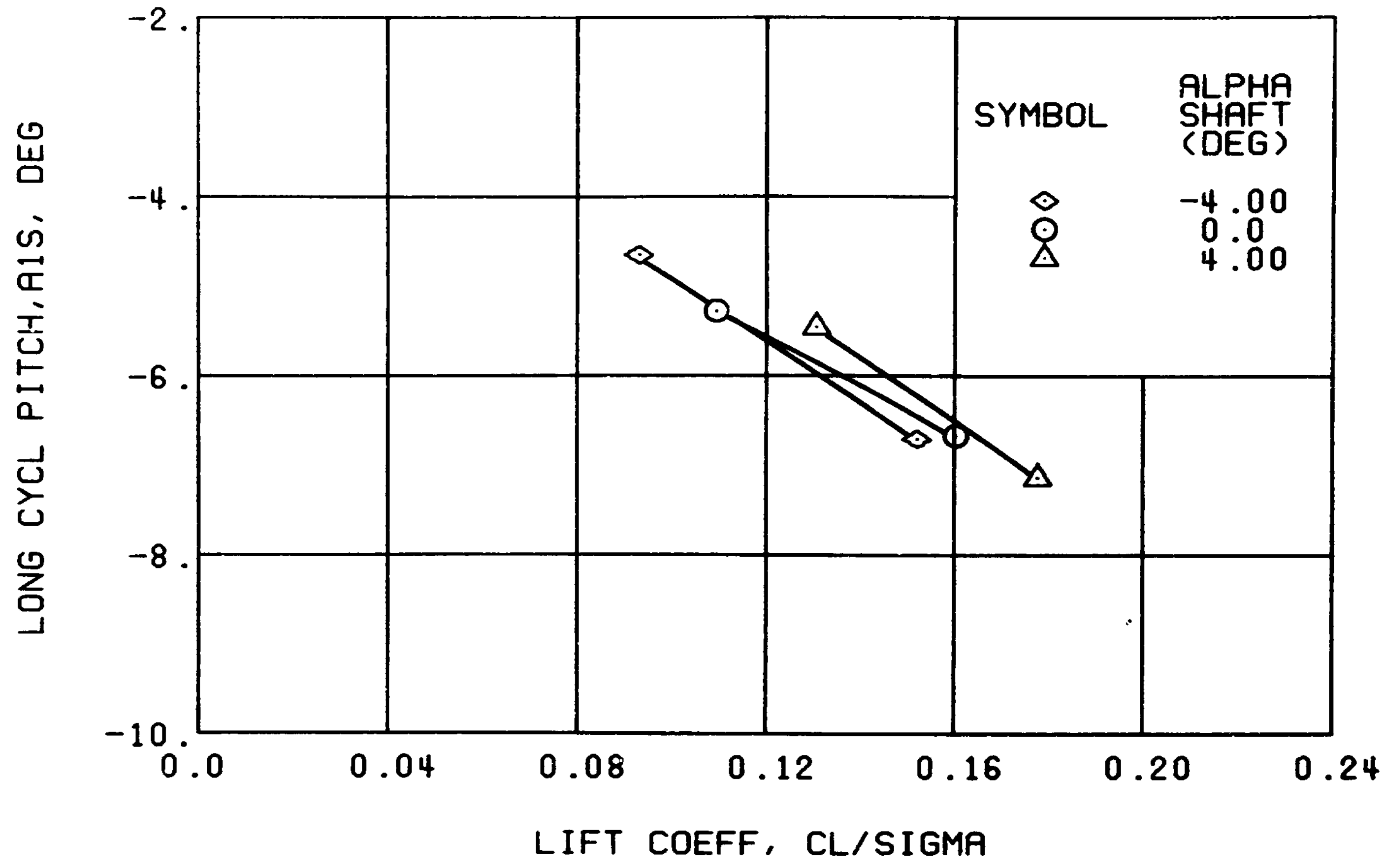

(e) LONGITUDINAL CYCLIC PITCH

Figure 31. Continued.
$\mu = 0.70$ $B'_{1s} = 2$ Deg

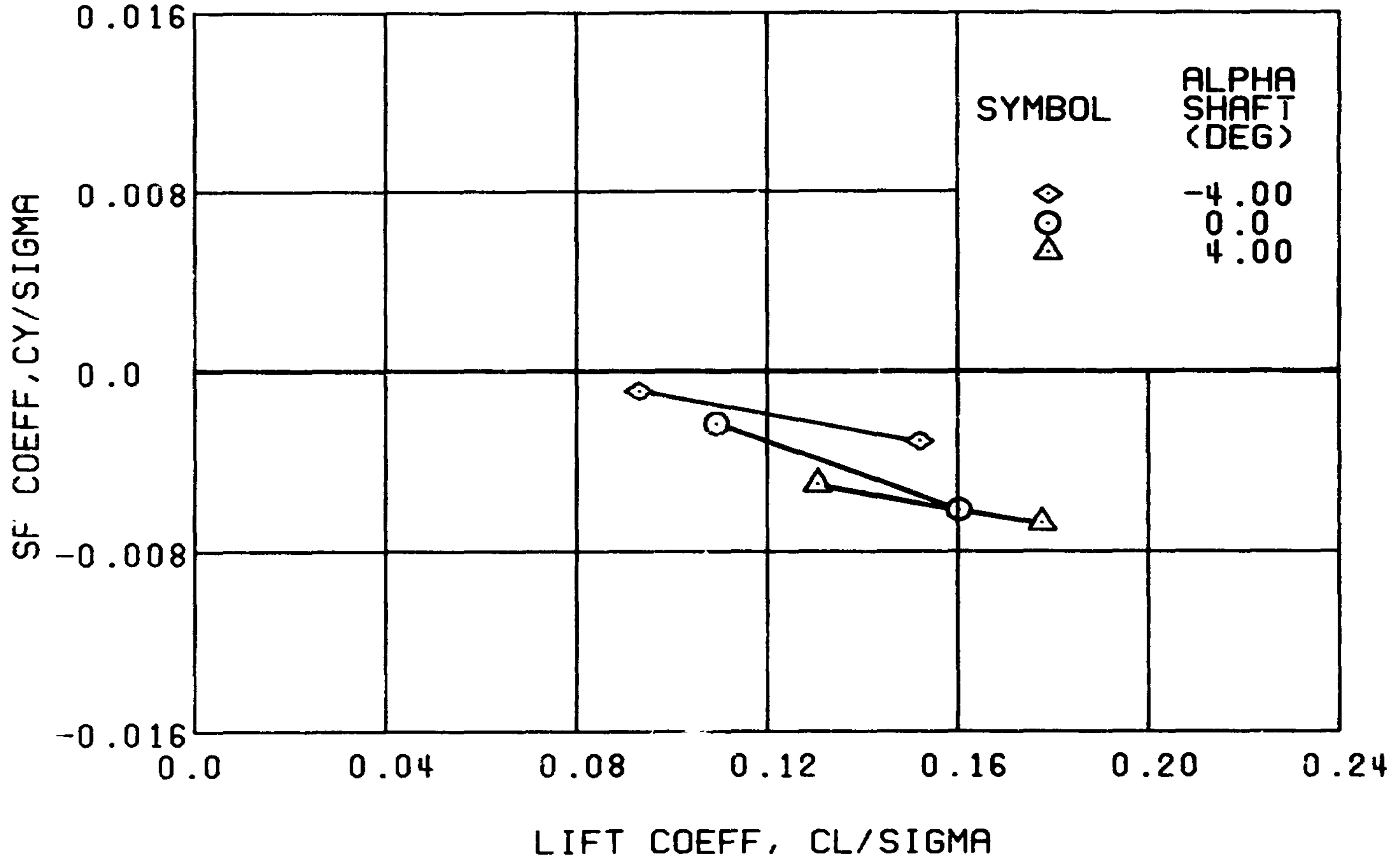

(f) SIDE FORCE COEFFICIENT

Figure 31. Continued.
$\mu = 0.70 \quad B'_{1s} = 2$ Deg

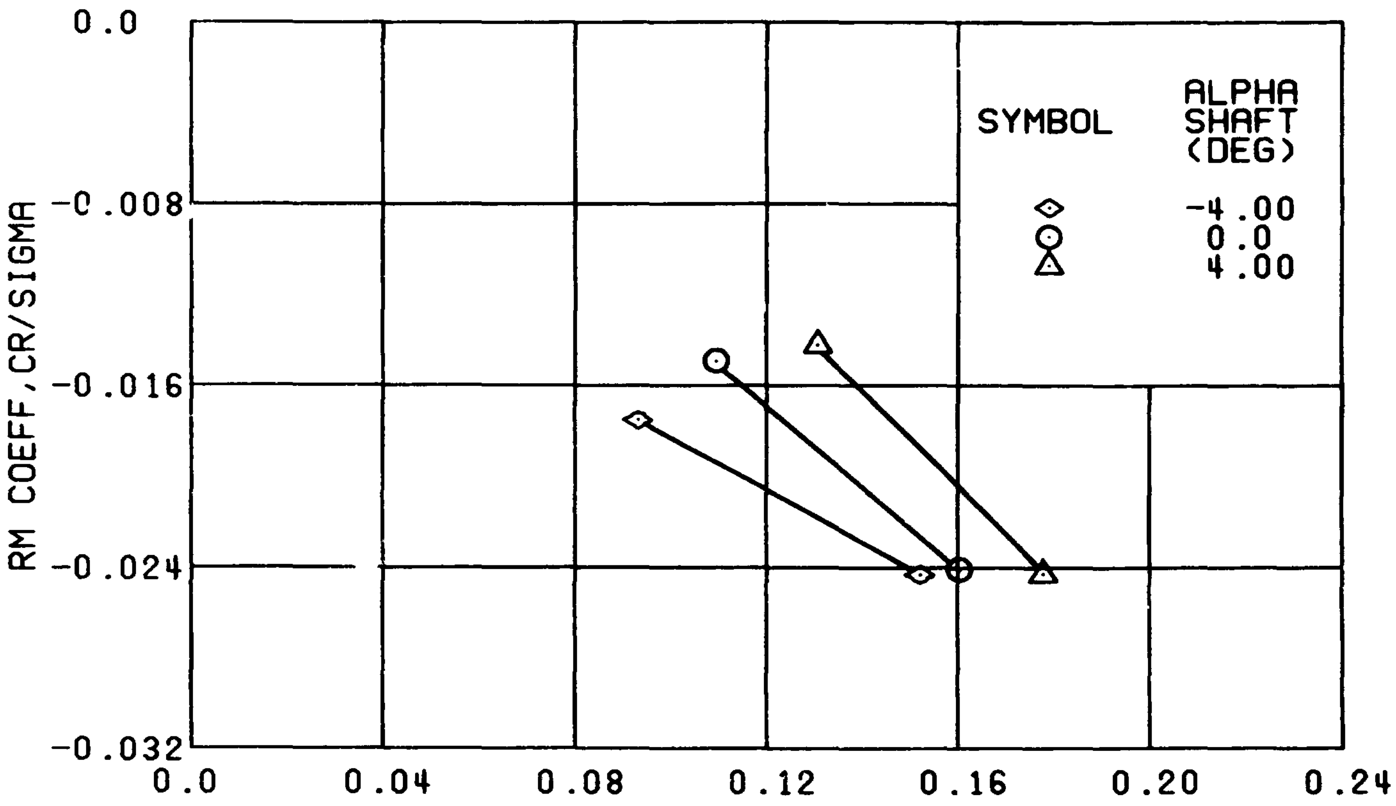

(g) ROLLING MOMENT COEFFICIENT

Figure 31. Continued.
$\mu = 0.70 \quad B'_{1s} = 2$ **Deg**

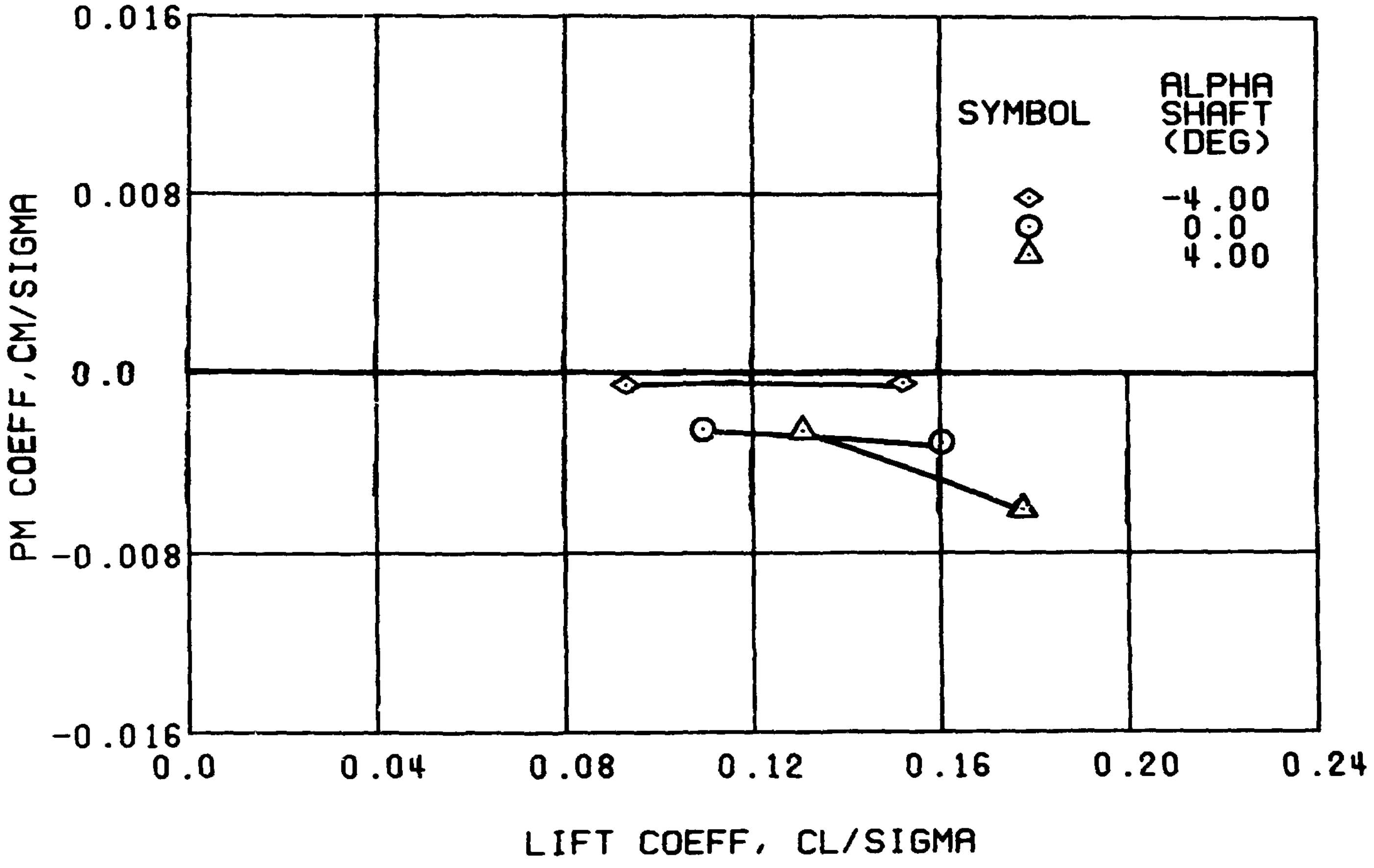

(h) PITCHING MOMENT COEFFICIENT

Figure 31. Continued.
$\mu = 0.70 \quad B'_{1s} = 2$ Deg

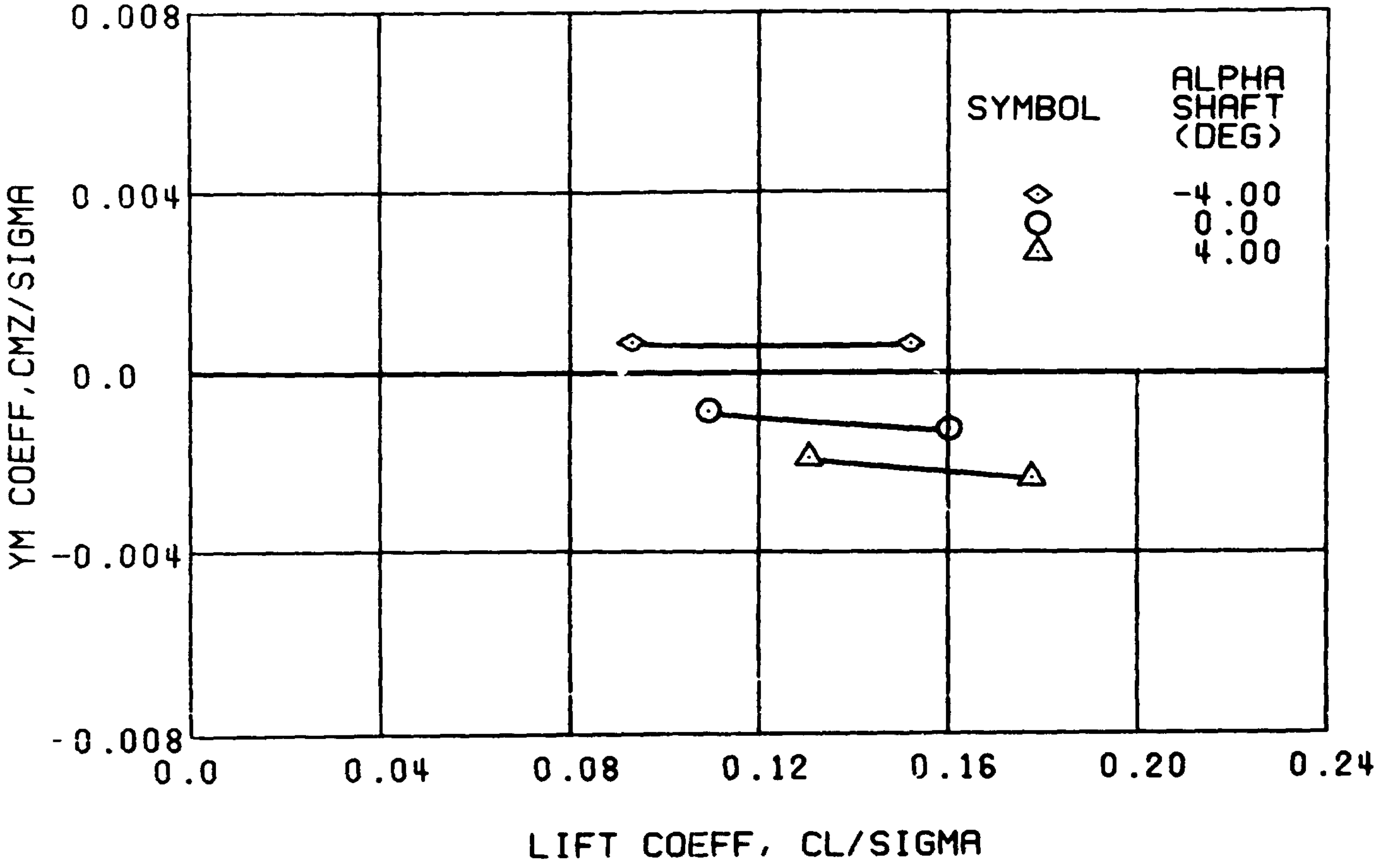

(i) YAW!NG MOMENT COEFFICIENT

Figure 31. Concluded.
$\mu = 0.70 \quad B'_{1s} = 2$ Deg

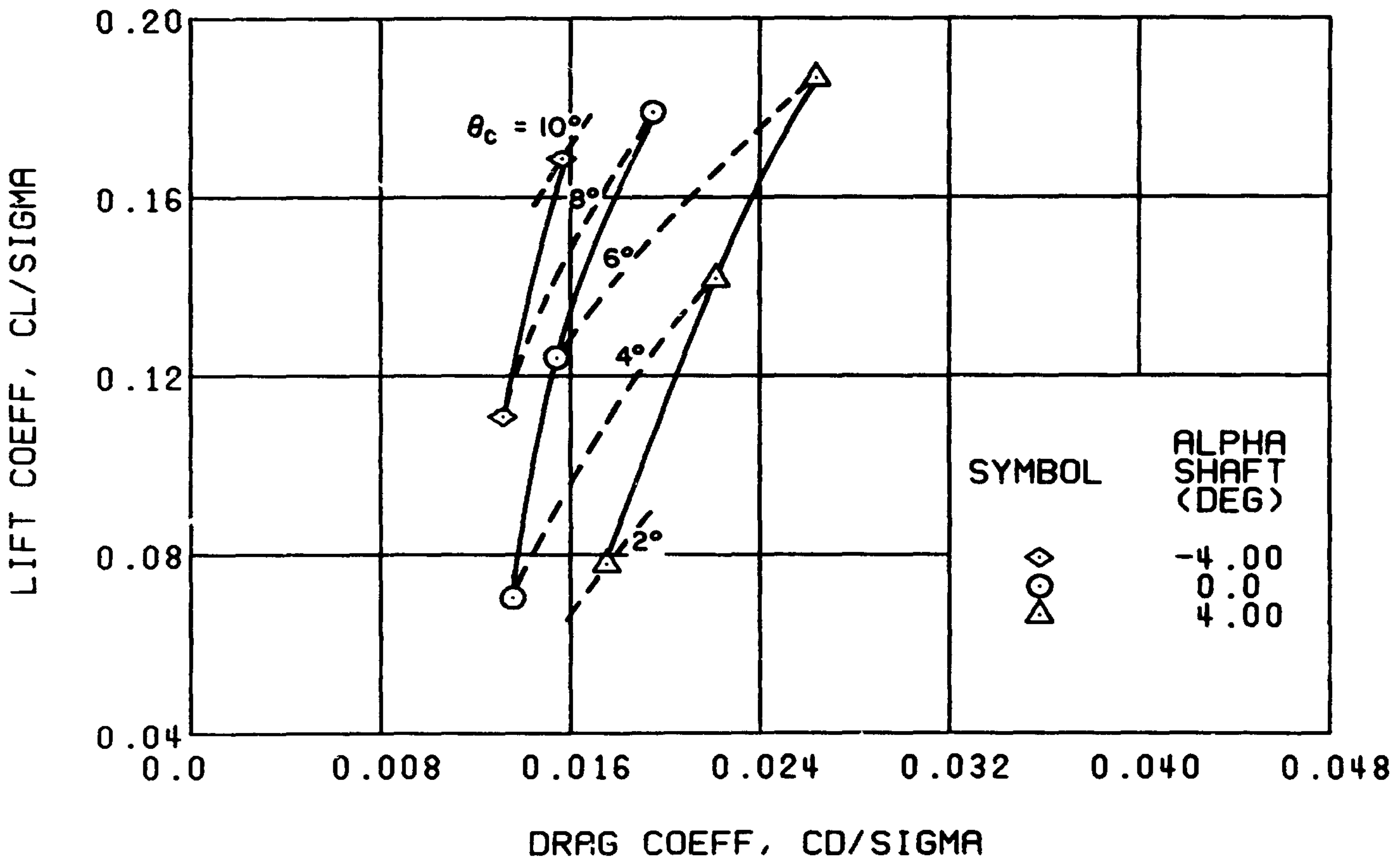

(a) DRAG COEFFICIENT

Figure 32. Performance Data at an Advance Ratio of 0.70 With the Lateral Displacement Control (B'_{1s}) Set at 4 Degrees.

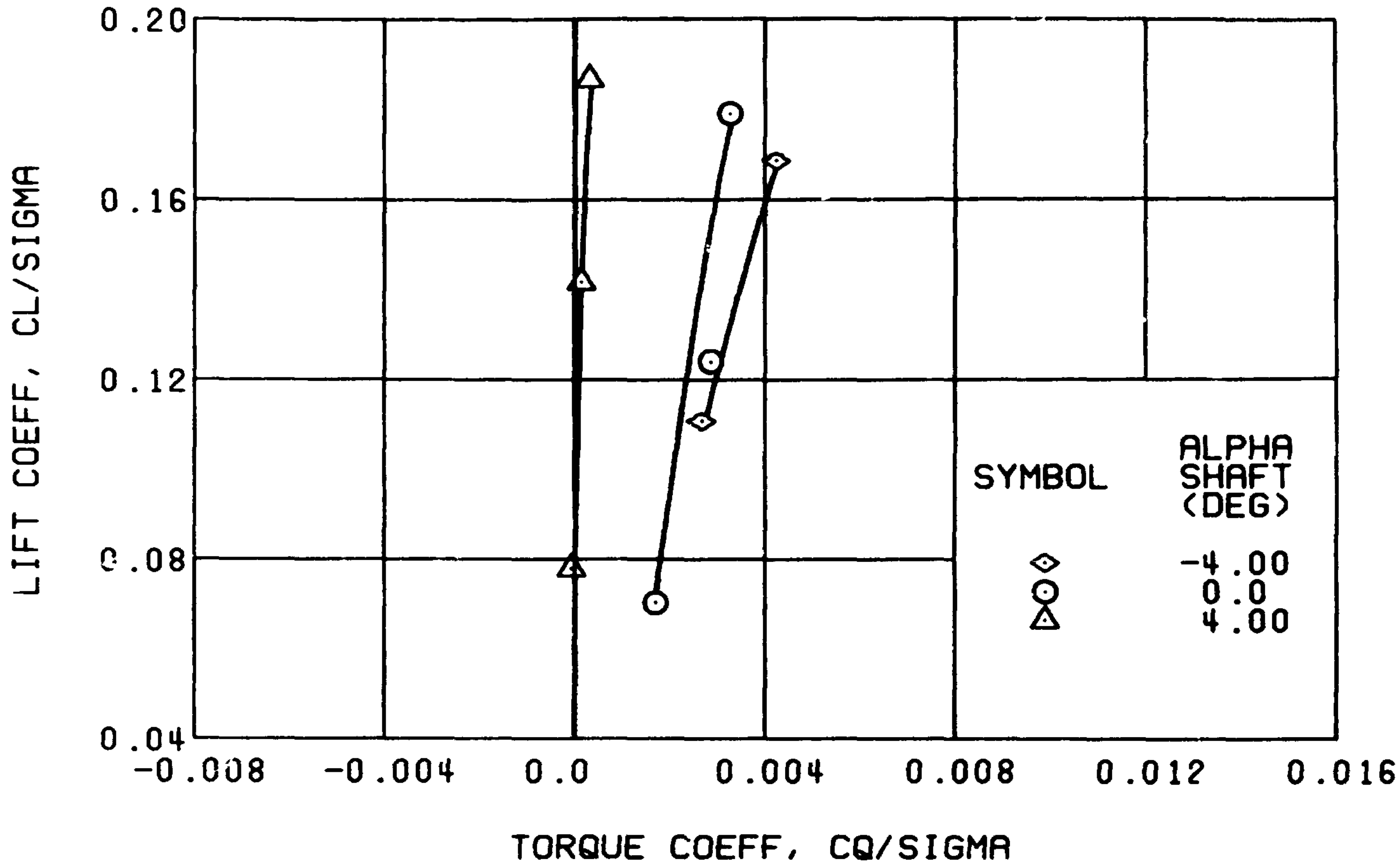

(b) TORQUE COEFFICIENT

Figure 32. Continued.
$\mu = 0.70 \quad B'_{1s} = 4$ Deg

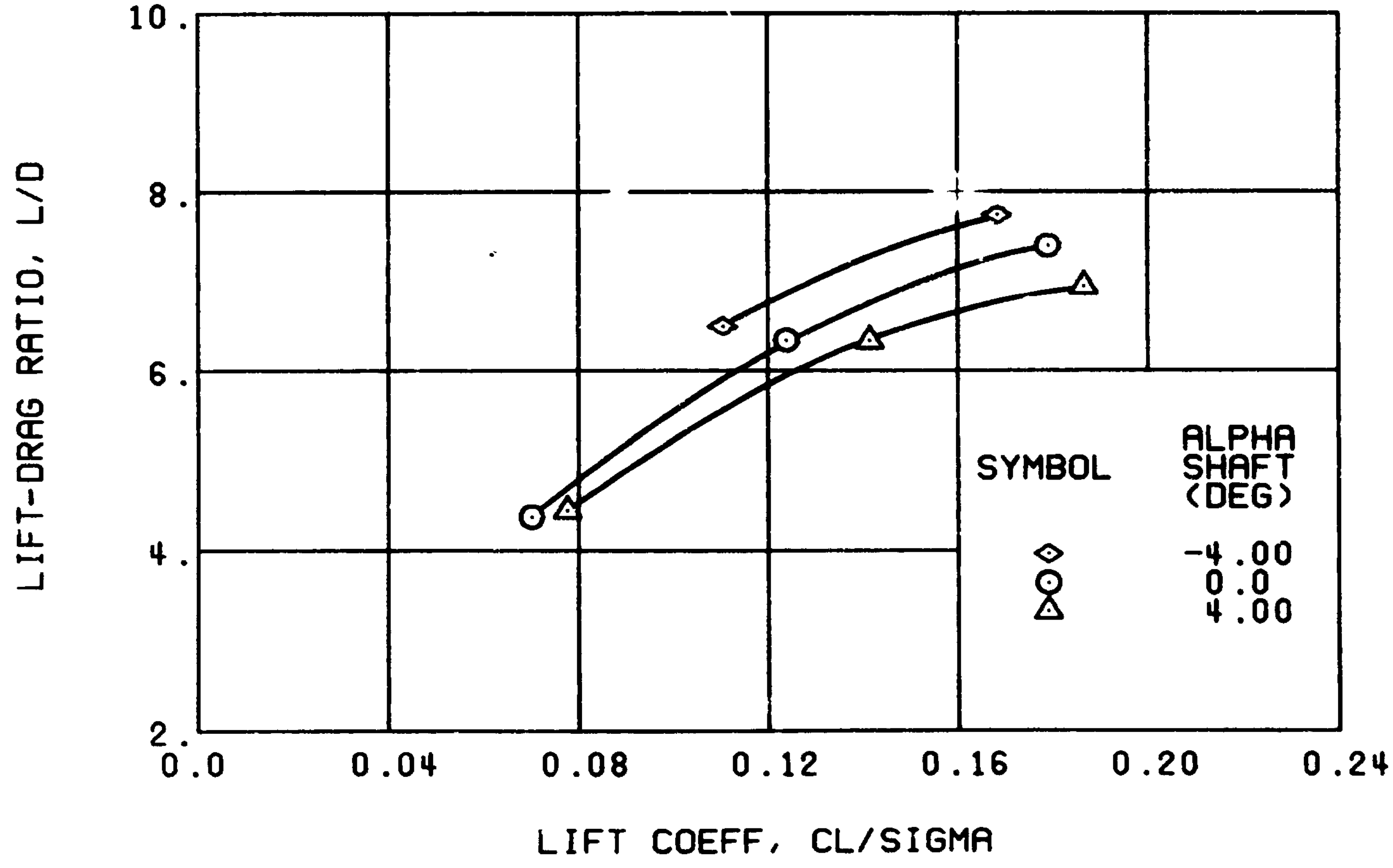

(c) LIFT-DRAG RATIO

Figure 32. Continued.
μ = 0.70 B'_{1s} = 4 Deg

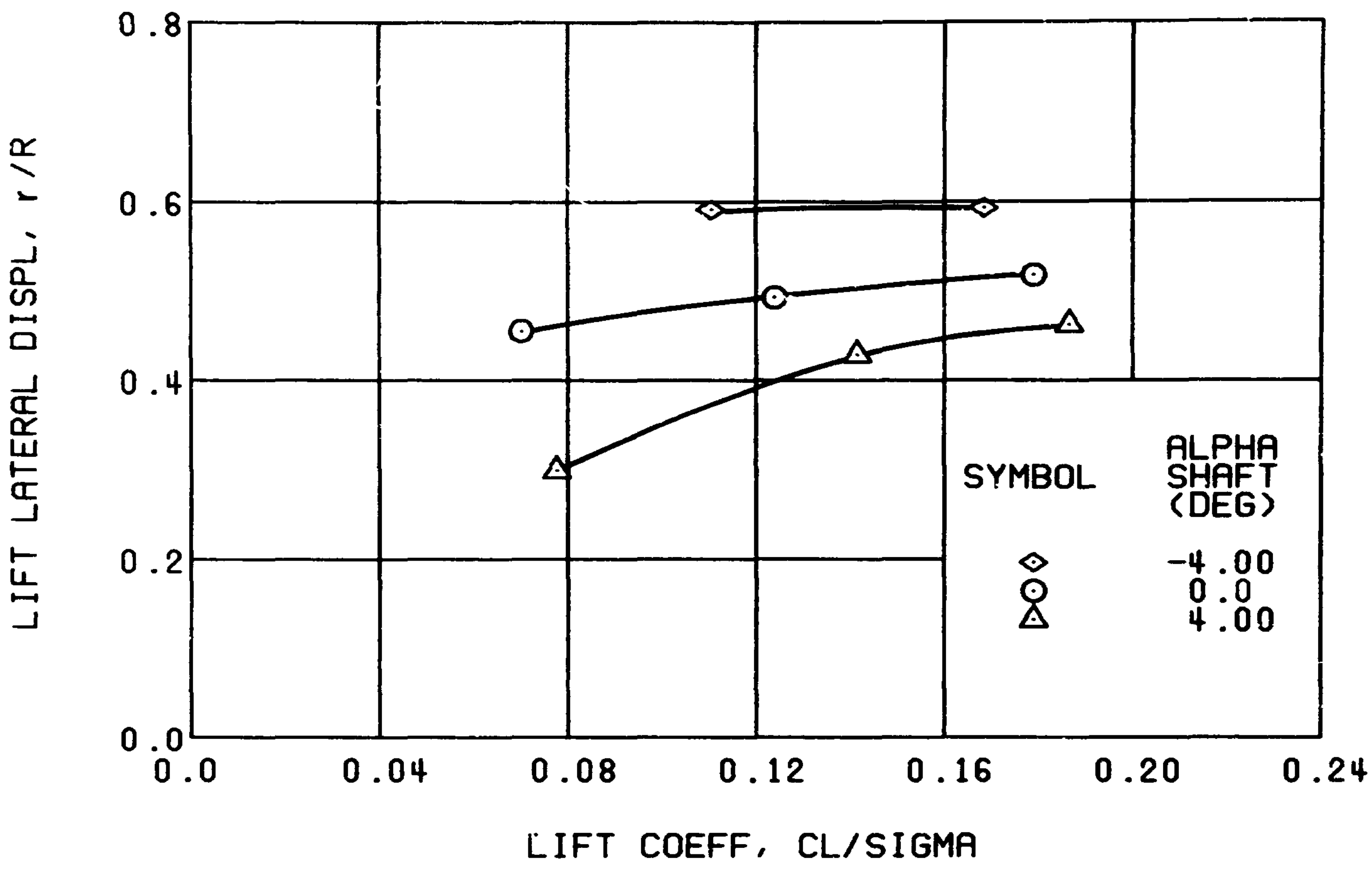

(d) LIFT LATERAL DISPLACEMENT

Figure 32. Continued.
$\mu = 0.70$ $B'_{1s} = 4$ Deg

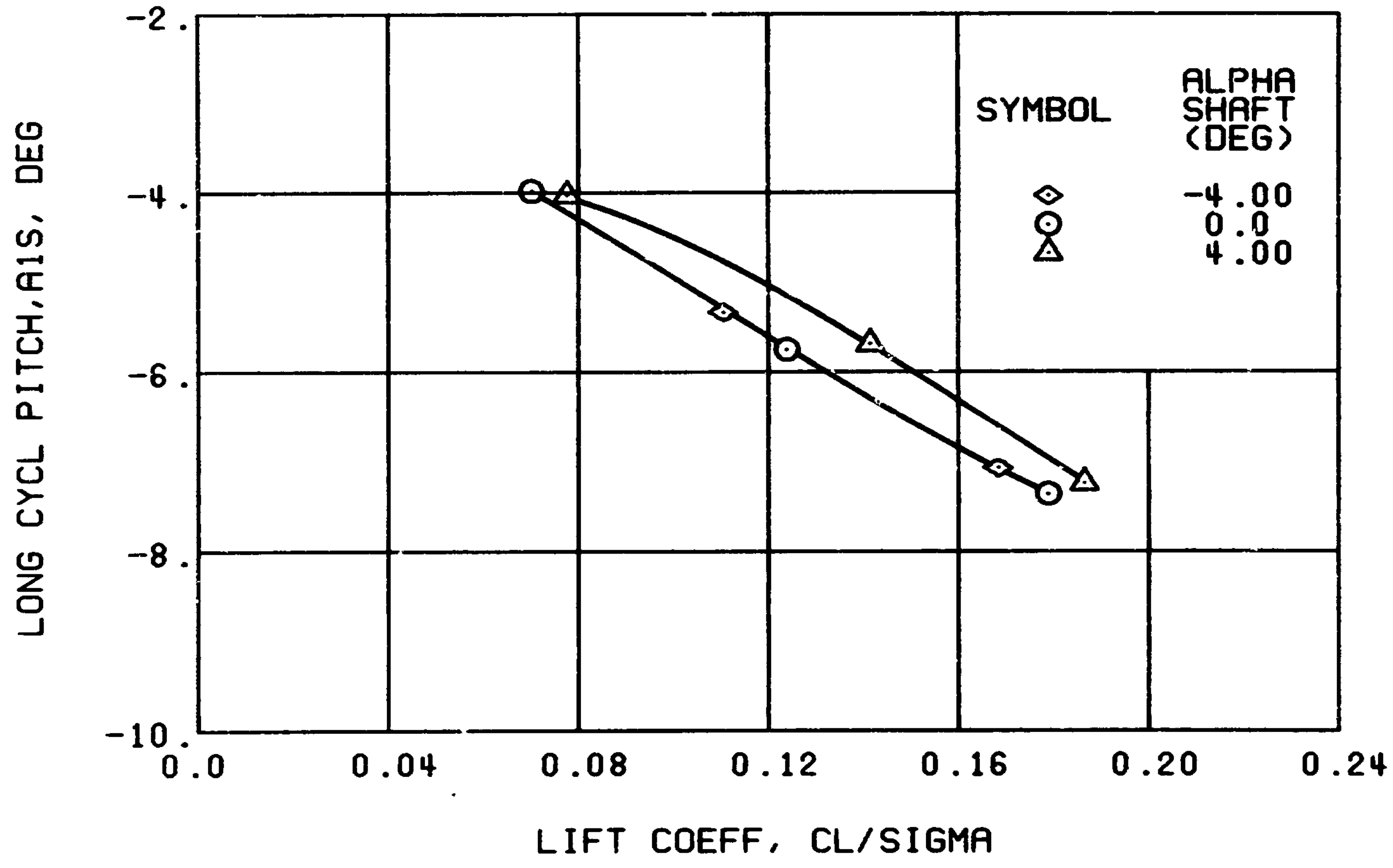

(e) LONGITUDINAL CYCLIC PITCH

Figure 32. Continued.
$\mu = 0.70 \quad B'_{1s} = 4$ Deg

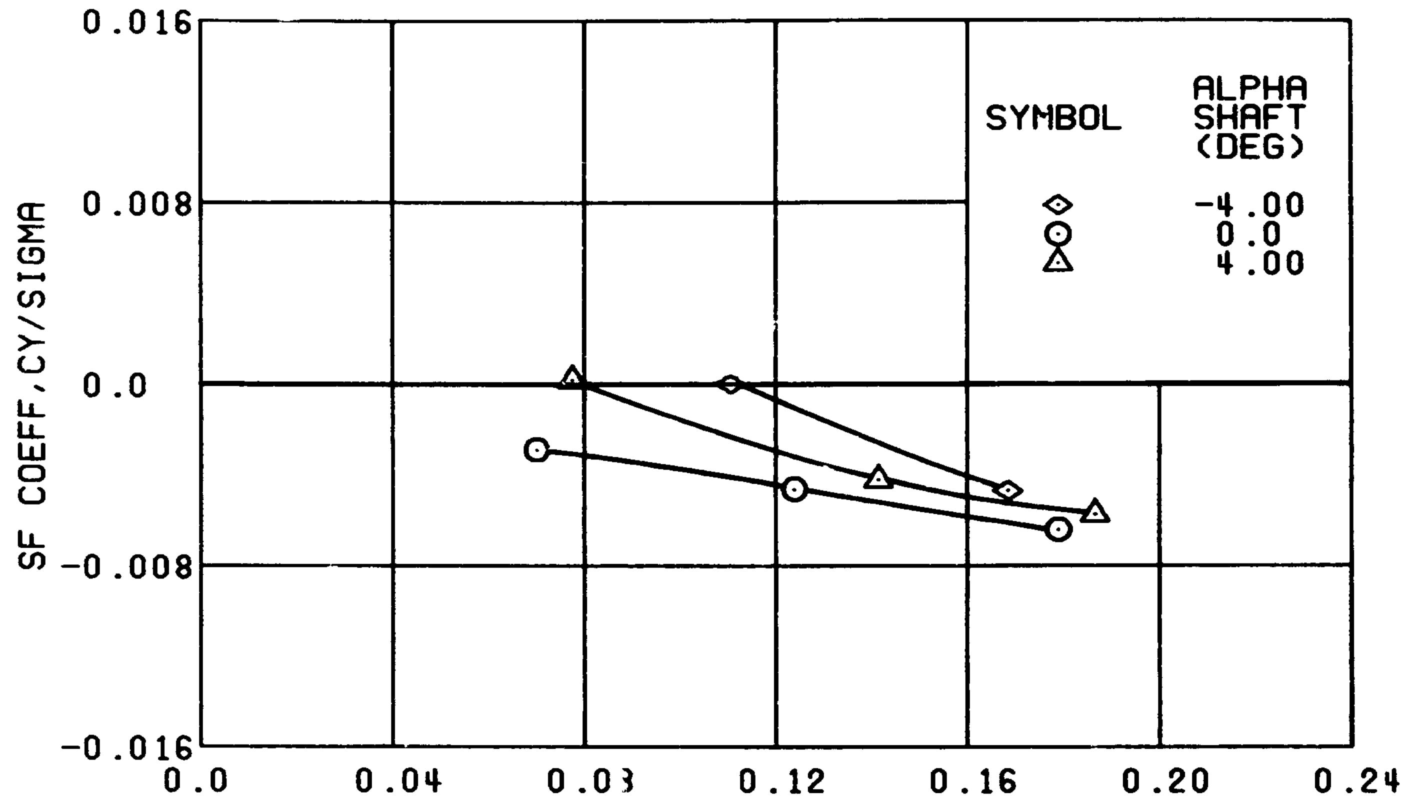

(f) SIDE FORCE COEFFICIENT

Figure 32. Continued.
$\mu = 0.70$ $B'_{1s} = 4$ Deg

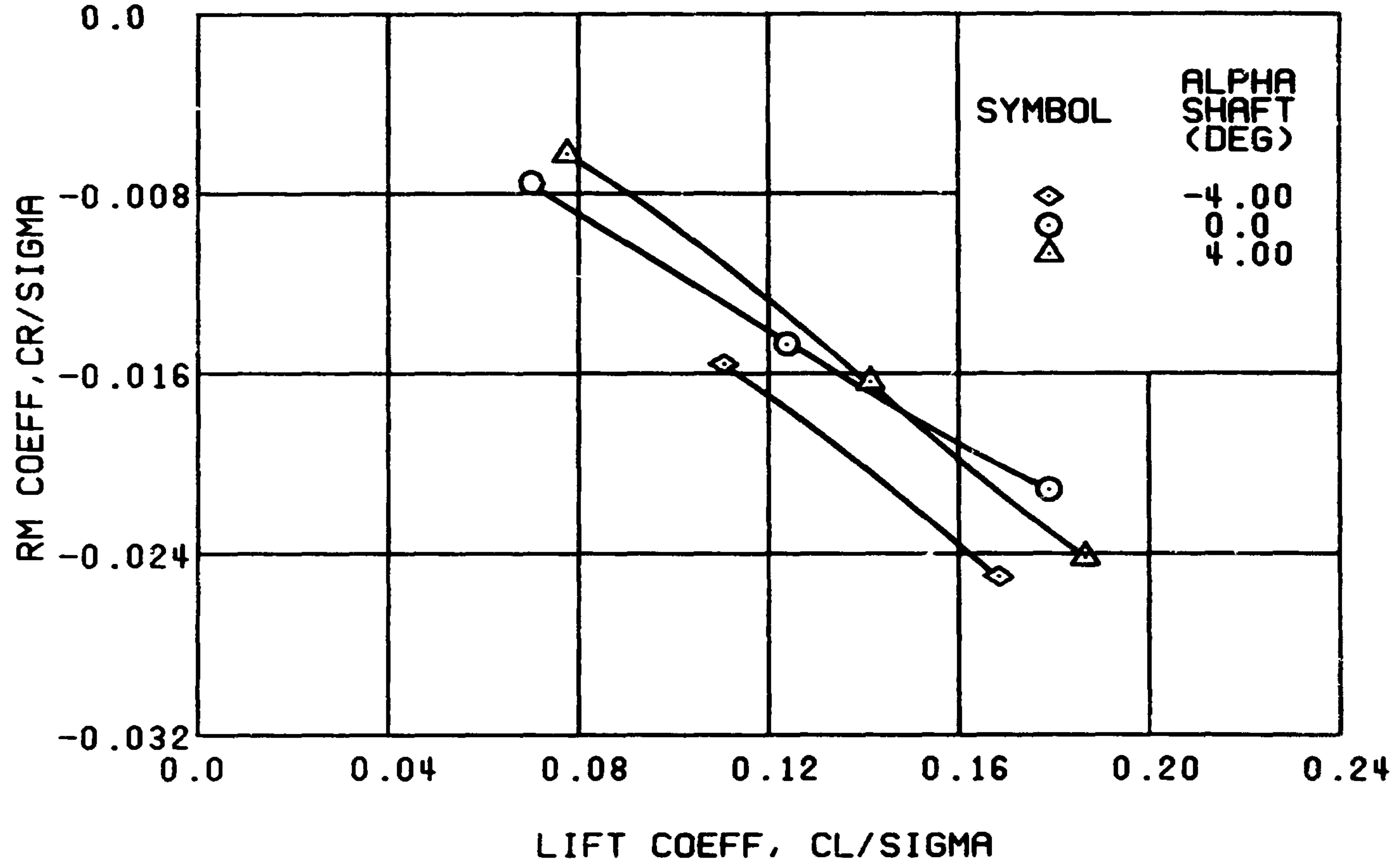

(g) ROLLING MOMENT COEFFICIENT

Figure 32. Continued.
μ = 0.70 B'_{1s} = 4 Deg

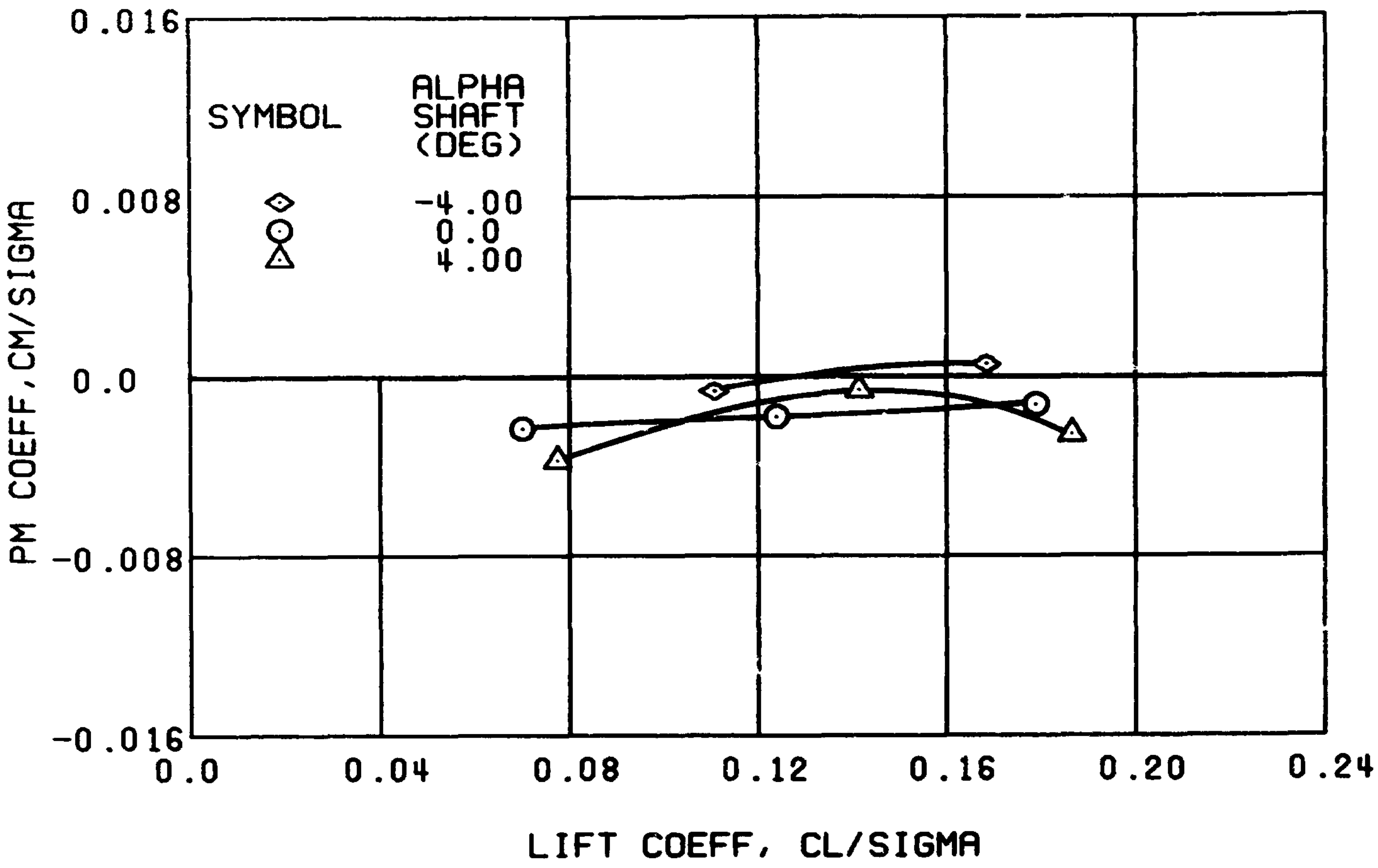

(h) PITCHING MOMENT COEFFICIENT

Figure 32. Continued.
μ = 0.70 B'_{1s} = 4 Deg

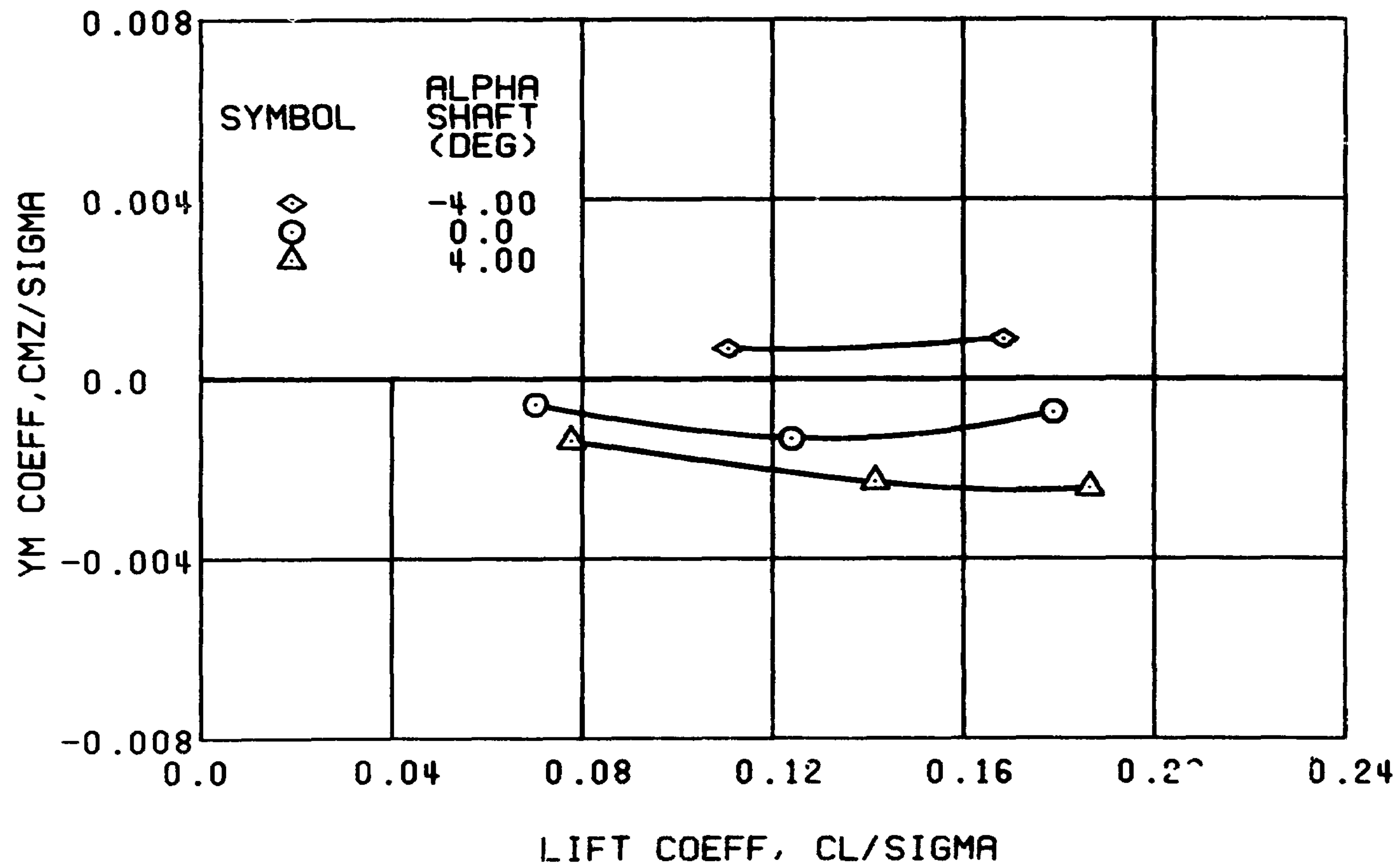

(i) YAWING MOMENT COEFFICIENT

Figure 32. Concluded.
$\mu = 0.70 \quad B'_{1s} = 4$ Deg

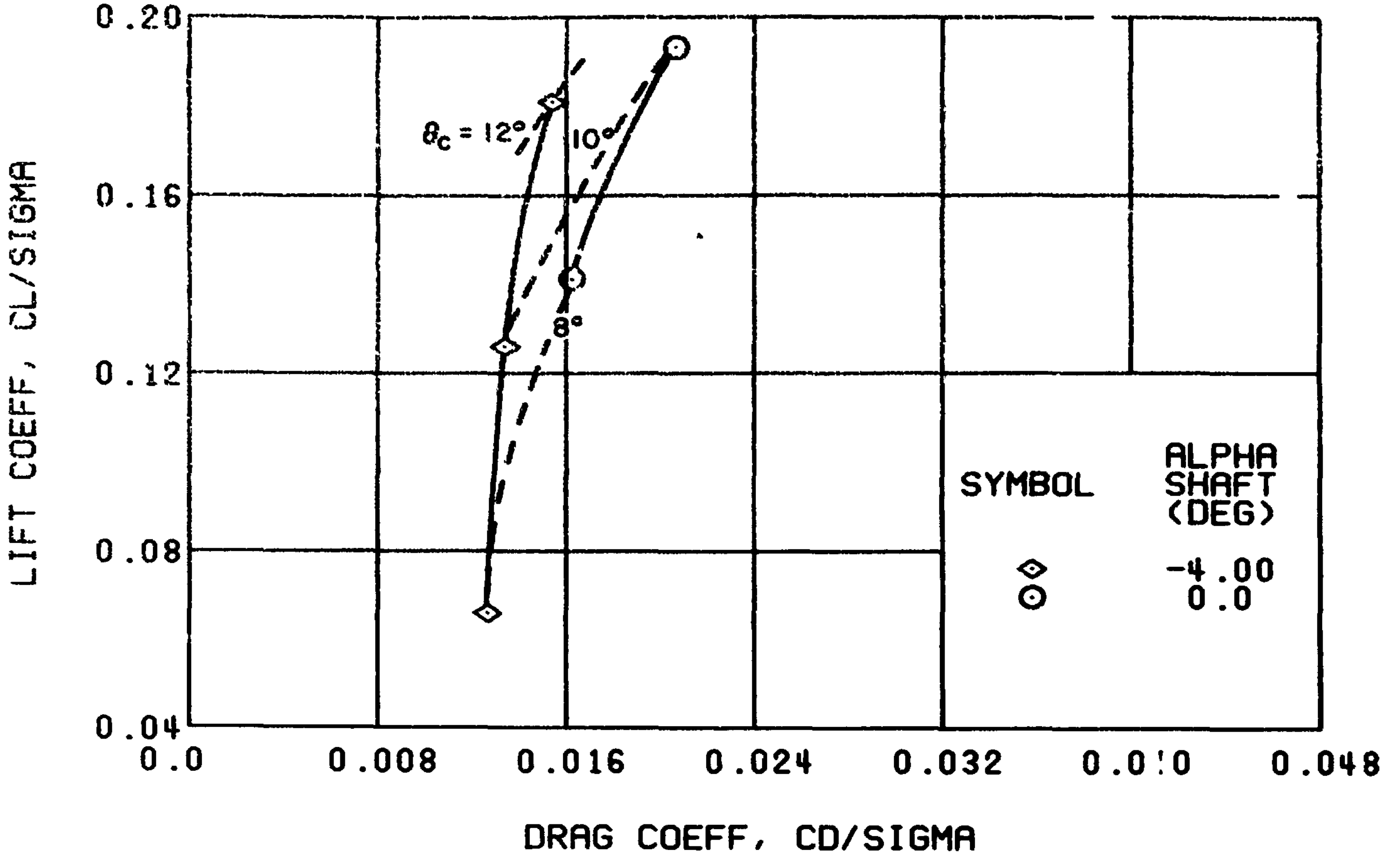

(a) DRAG COEFFICIENT

Figure 33. Performance Data at an Advance Ratio of 0.70 With the Lateral Displacement Control (B'_{1s}) Set at 6 Degrees.

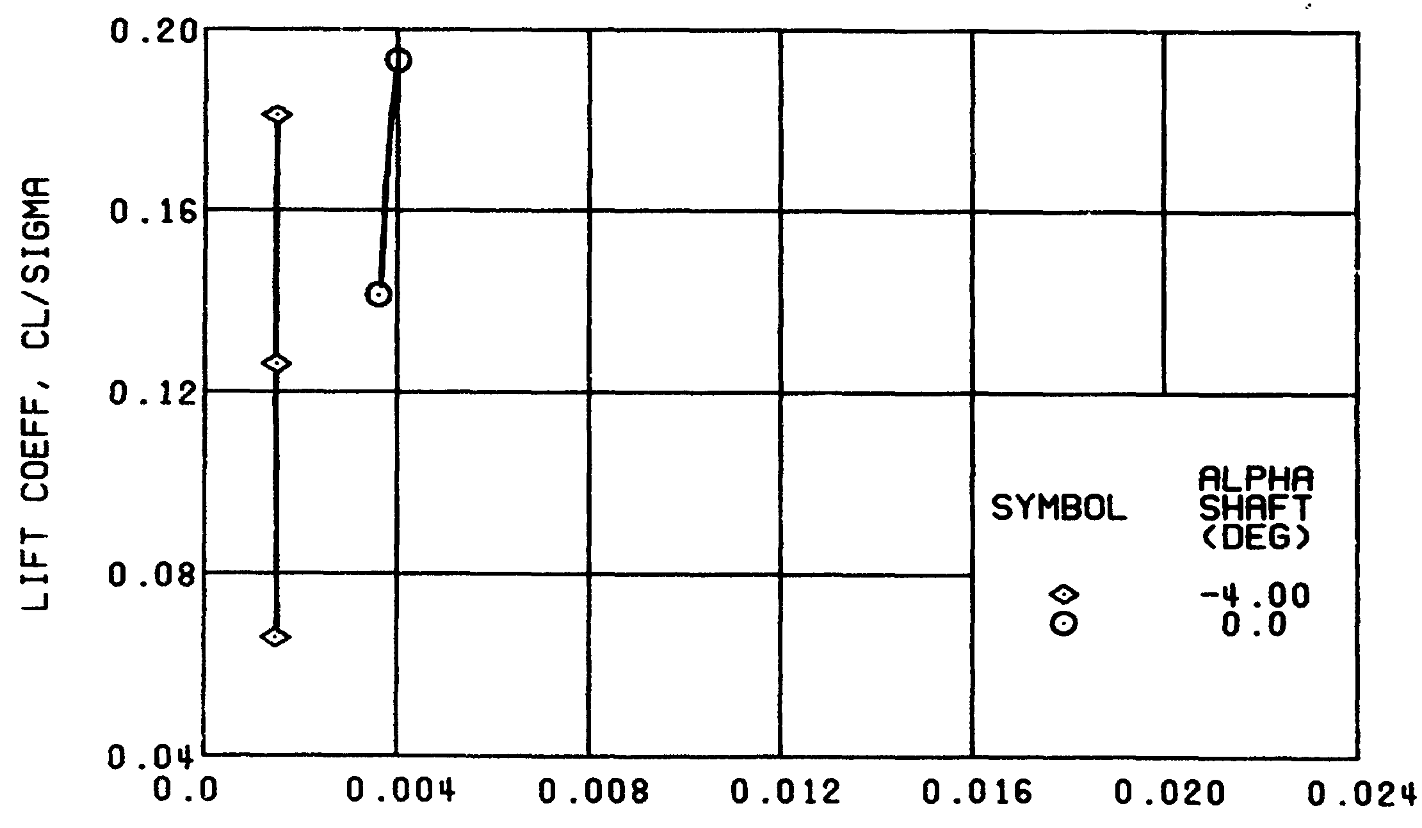

(b) TORQUE COEFFICIENT

Figure 33. Continued.
μ = 0.70 B'_{1s} = 6 Deg

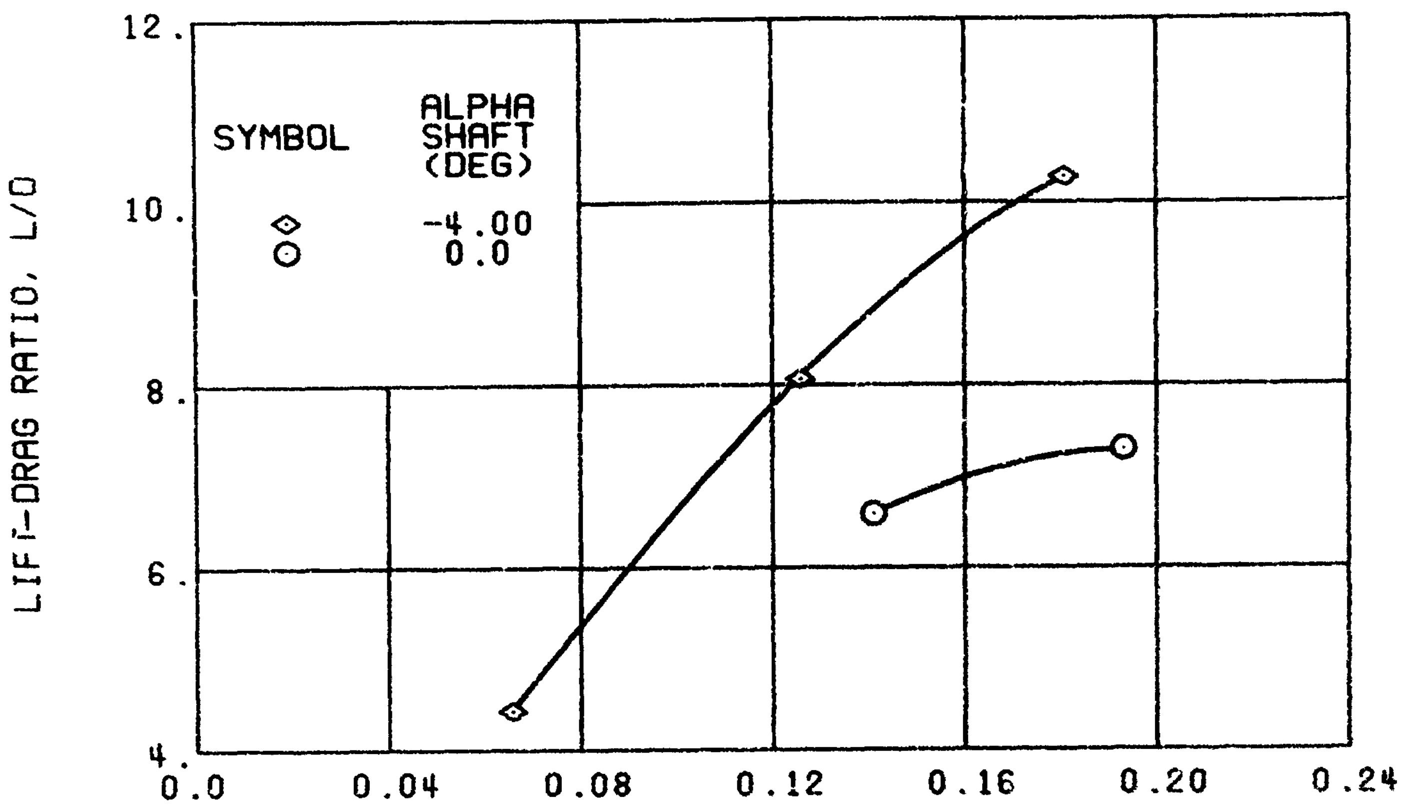

(c) LIFT-DRAG RATIO

Figure 33. Continued.
$\mu = 0.70$ $B'_{1s} = 6$ Deg

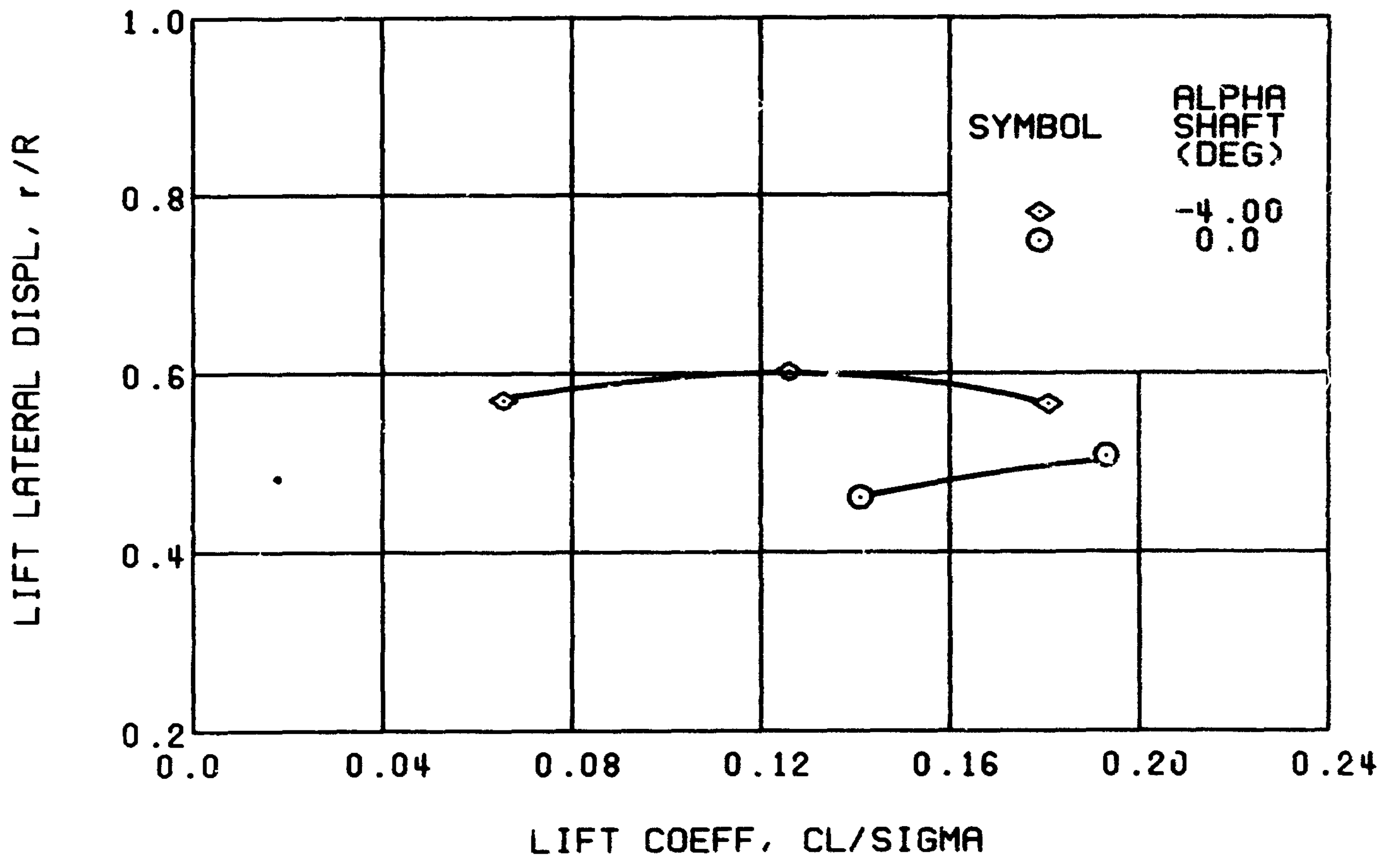

(d) LIFT LATERAL DISPLACEMENT

Figure 33. Continued.
$\mu = 0.70 \quad B'_{1s} = 6$ Deg

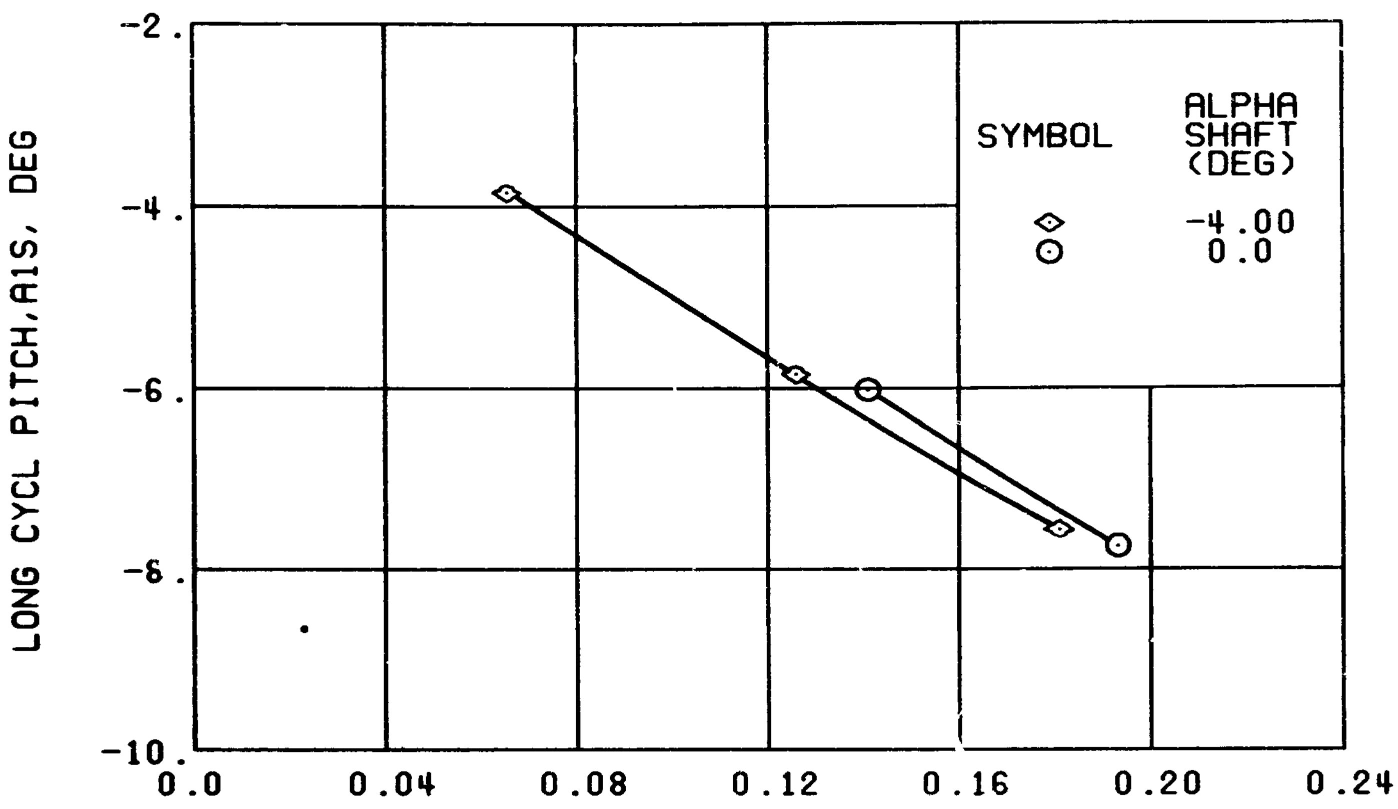

(e) LONGITUDINAL CYCLIC PITCH

Figure 33. Continued.
$\mu = 0.70$ $B'_{1s} = 6$ Deg

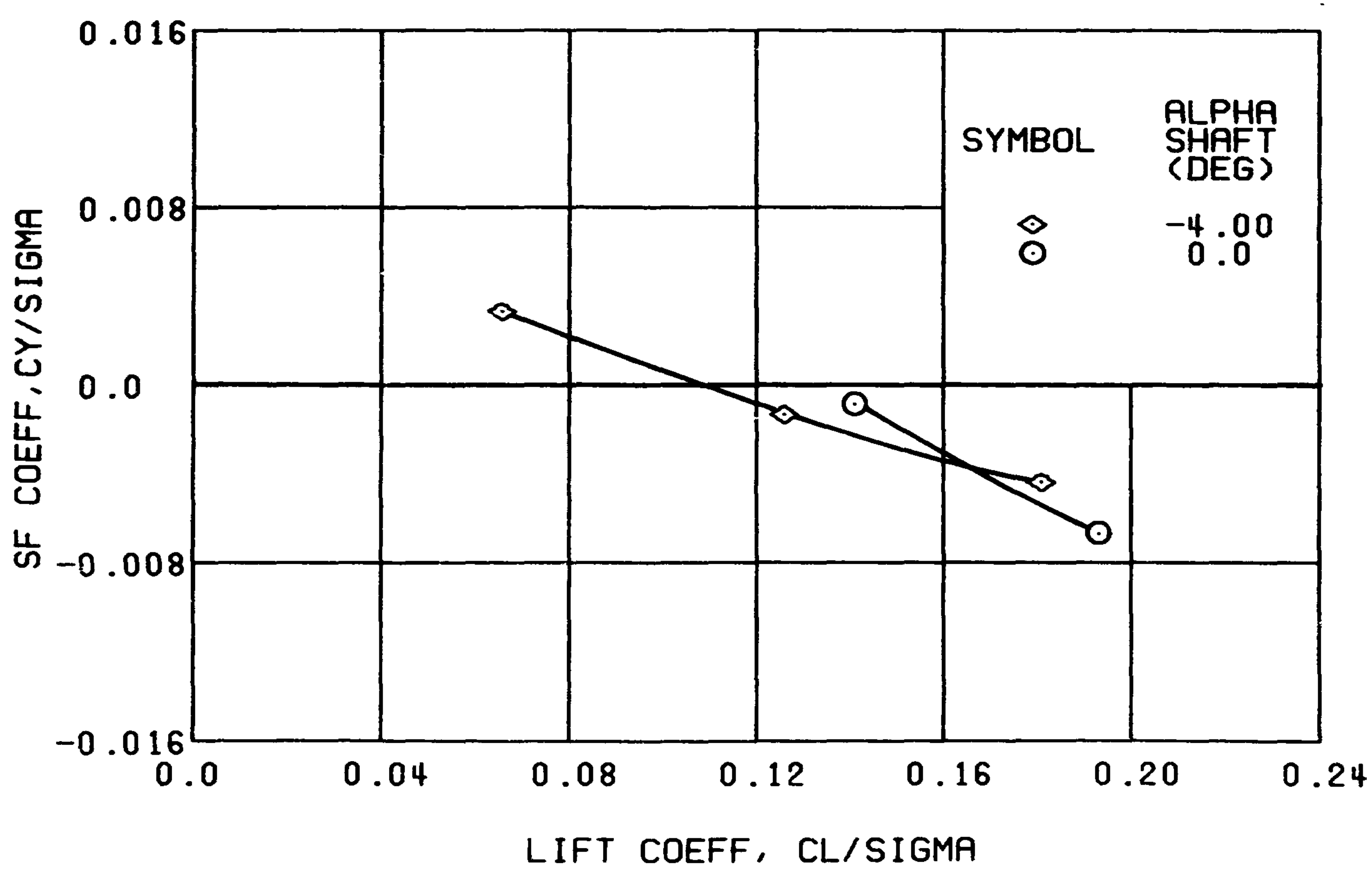

(f) SIDE FORCE COEFFICIENT

Figure 33. **Continued.**
$\mu = 0.70 \quad B'_{1s} = 6$ Deg

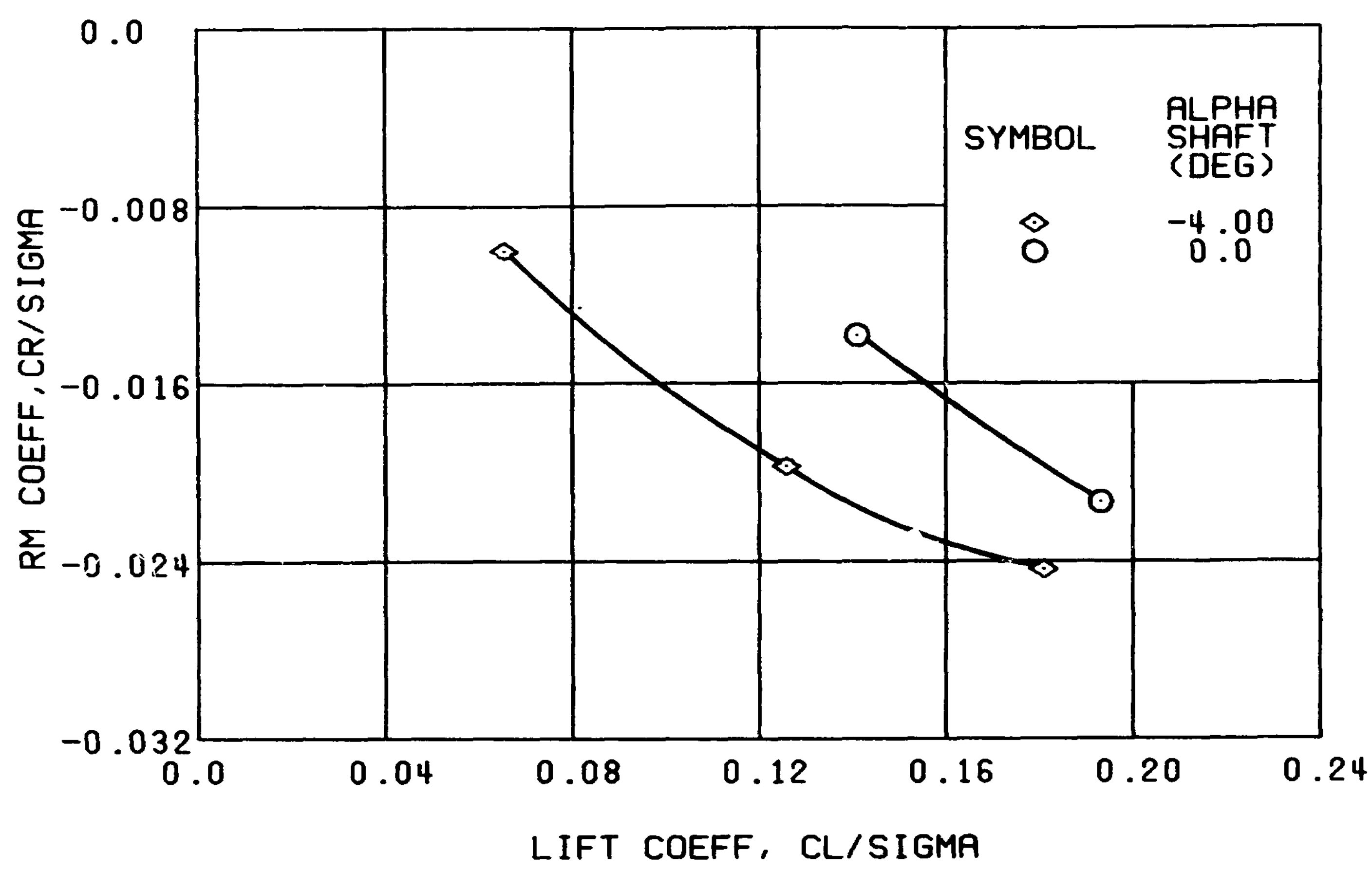

(g) ROLLING MOMENT COEFFICIENT

Figure 33. **Continued.**
$\mu = 0.70 \quad B'_{1s} = 6$ Deg

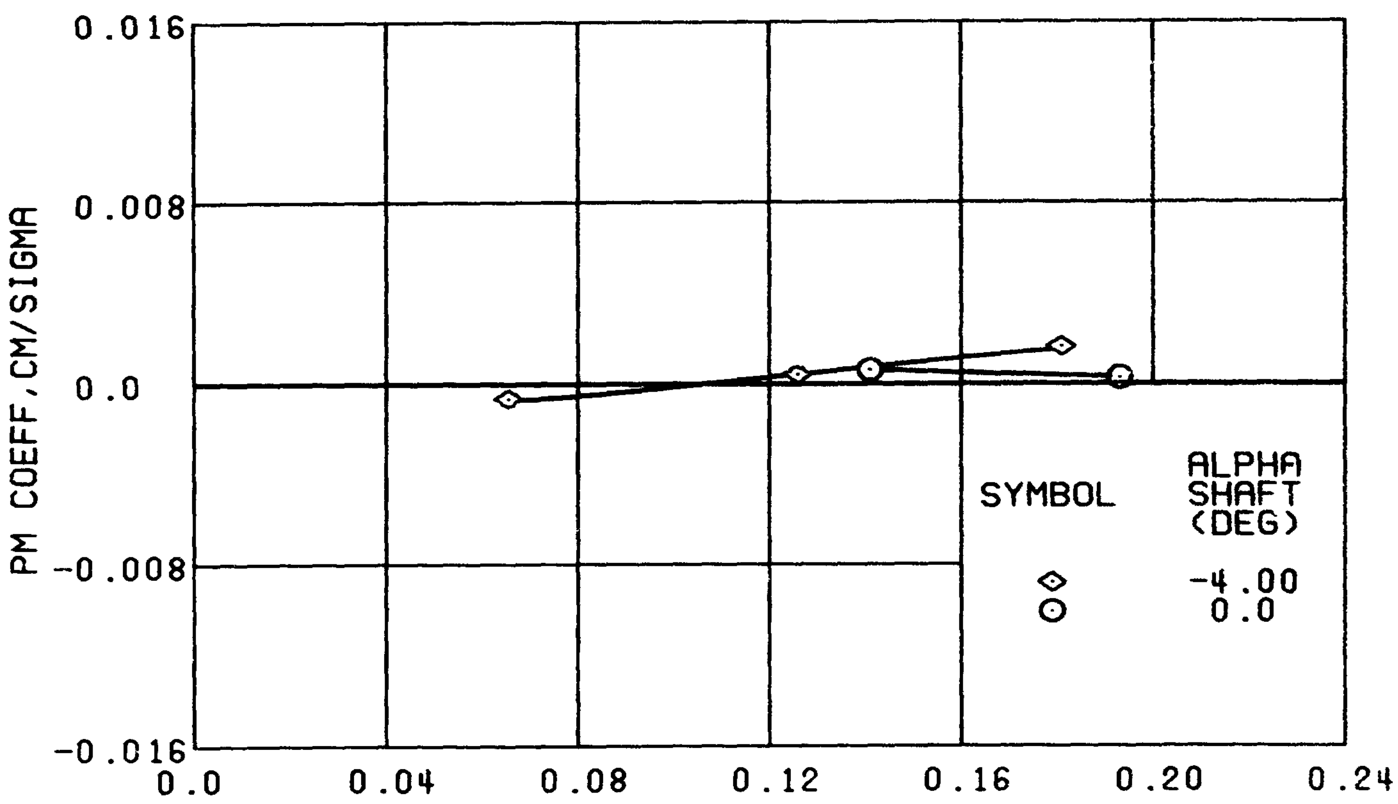

(h) PITCHING MOMENT COEFFICIENT

Figure 33. **Continued.**
μ = 0.70 B'_{1s} = 6 Deg

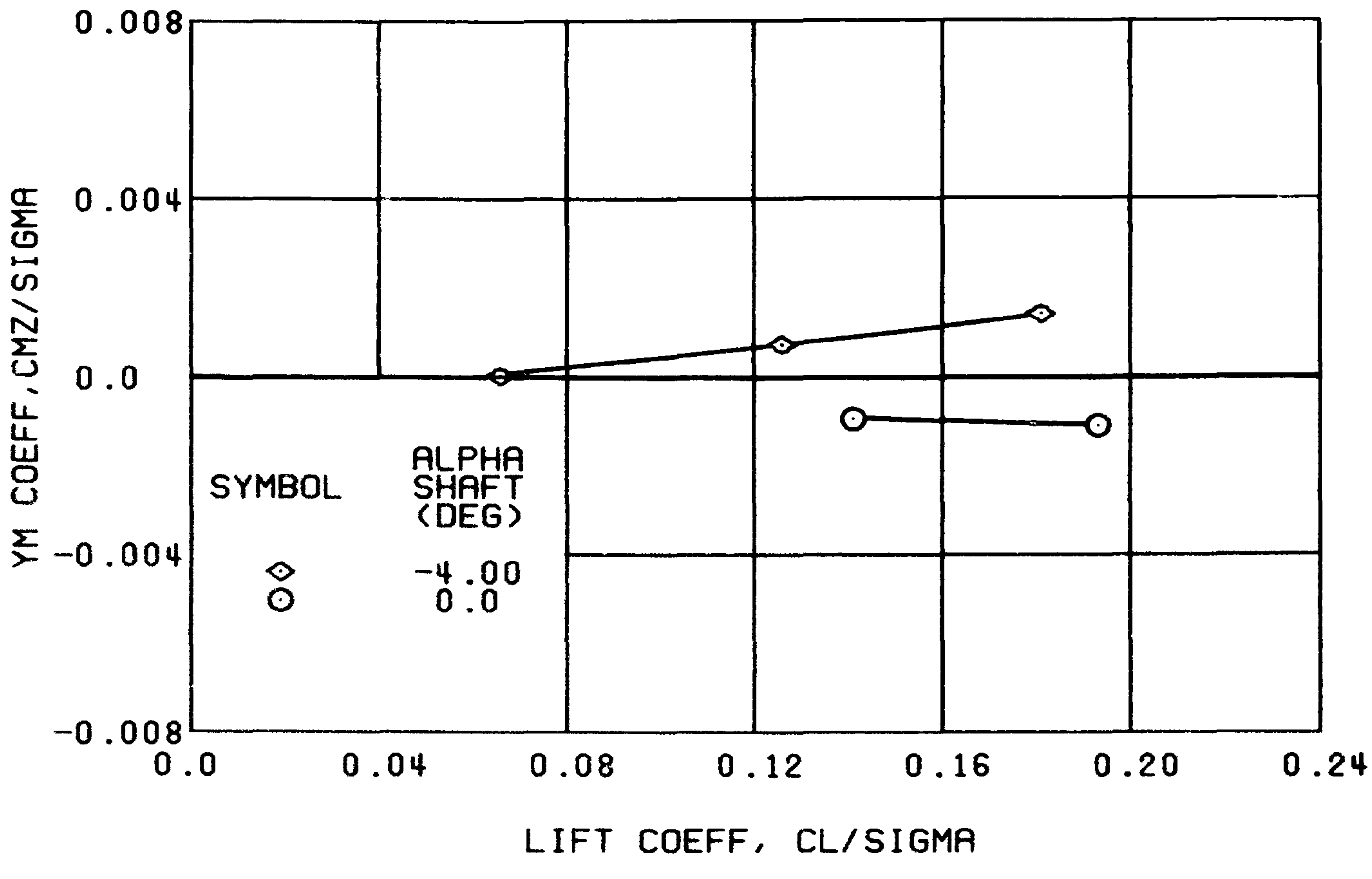

(i) YAWING MOMENT COEFFICIENT

Figure 33. Concluded.
$\mu = 0.70 \quad B'_{1s} = 6$ Deg

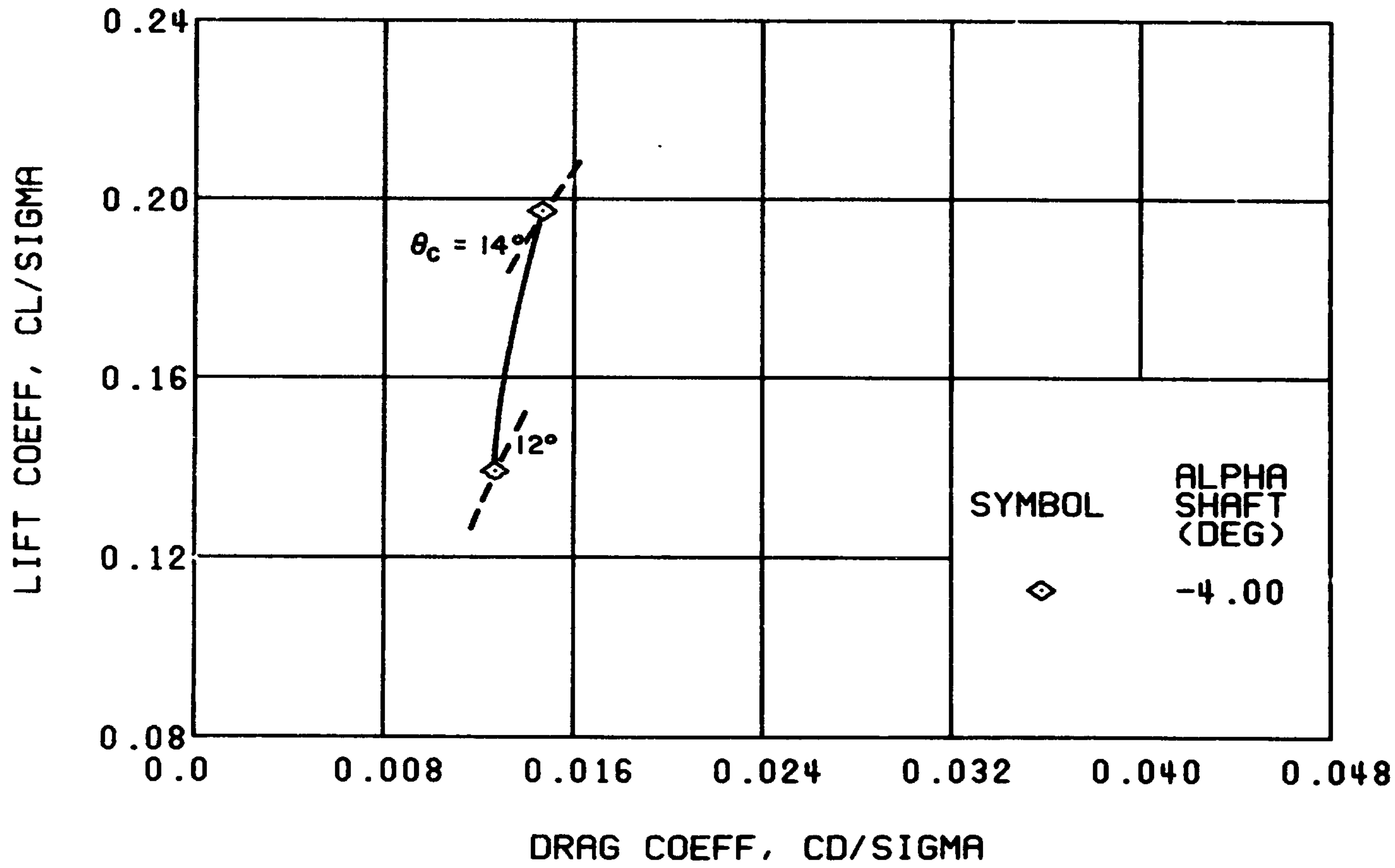

(a) DRAG COEFFICIENT

Figure 34. Performance Data at an Advance Ratio of 0.70 With the Lateral Displacement Control (B'_{1s}) Set at 8 Degrees.

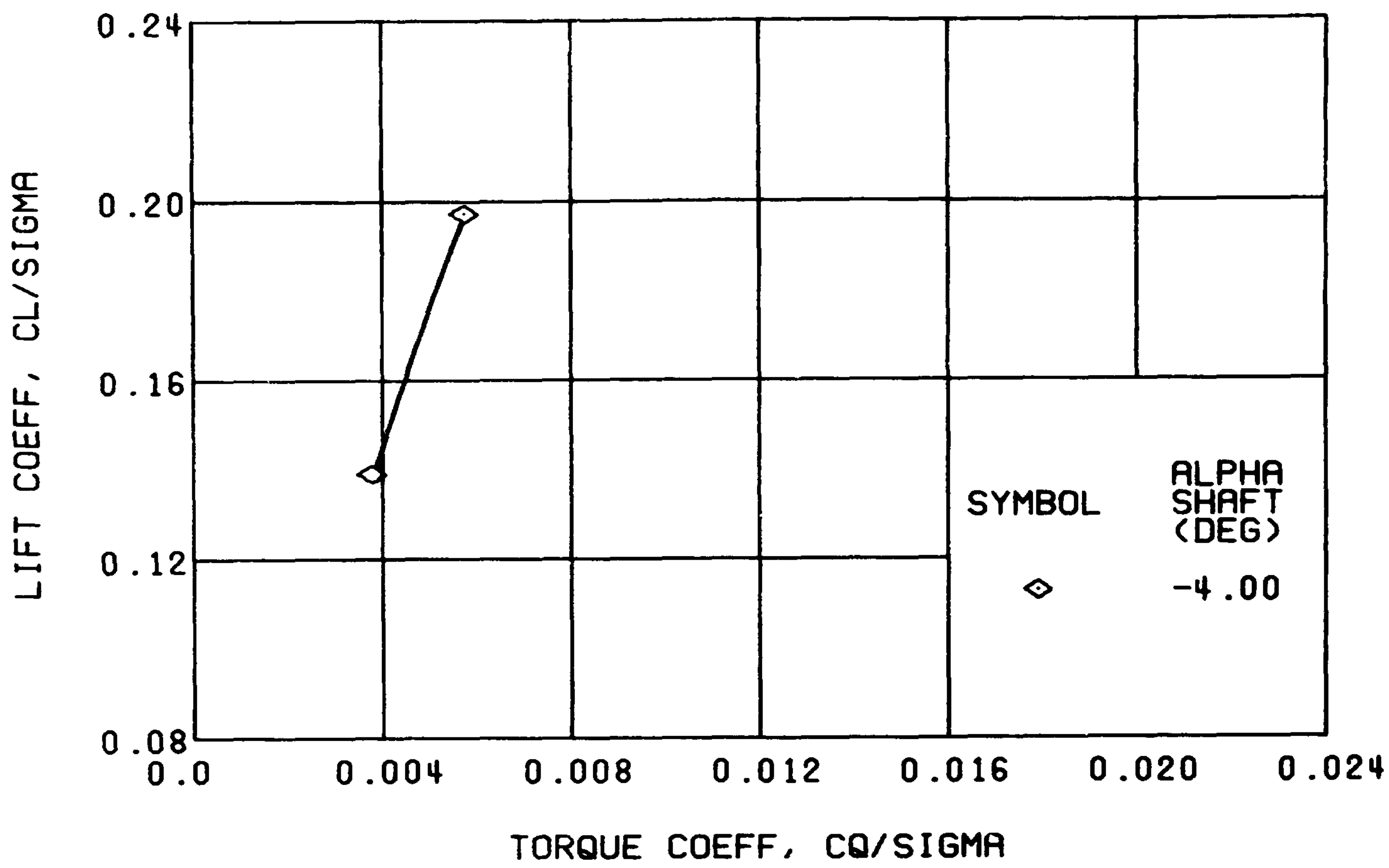

(b) TORQUE COEFFICIENT

Figure 34. Continued.
$\mu = 0.70$ $B'_{1s} = 8$ Deg

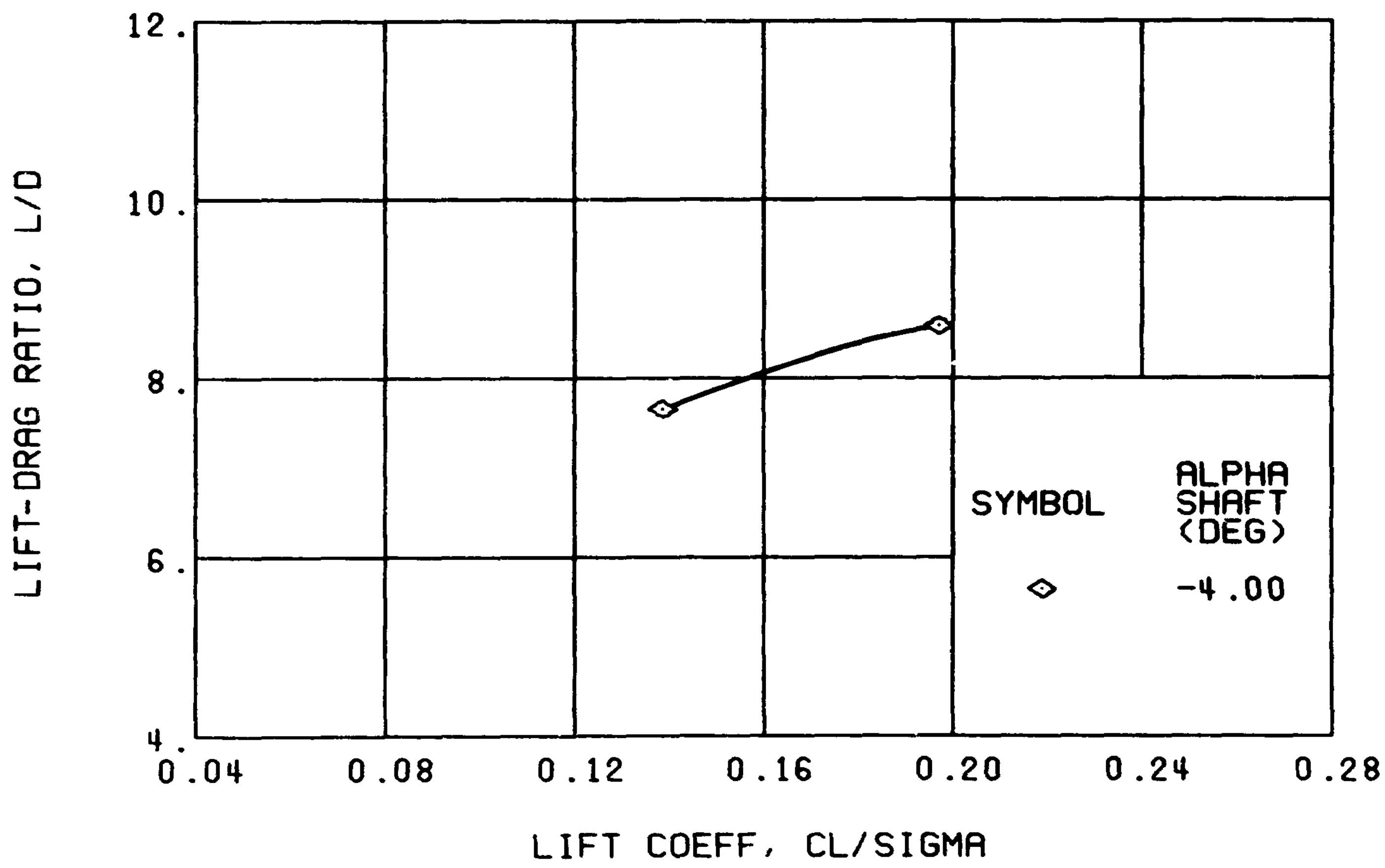

(c) LIFT-DRAG RATIO

Figure 34. Continued.
μ = 0.70 B'_{1s} = 8 Deg

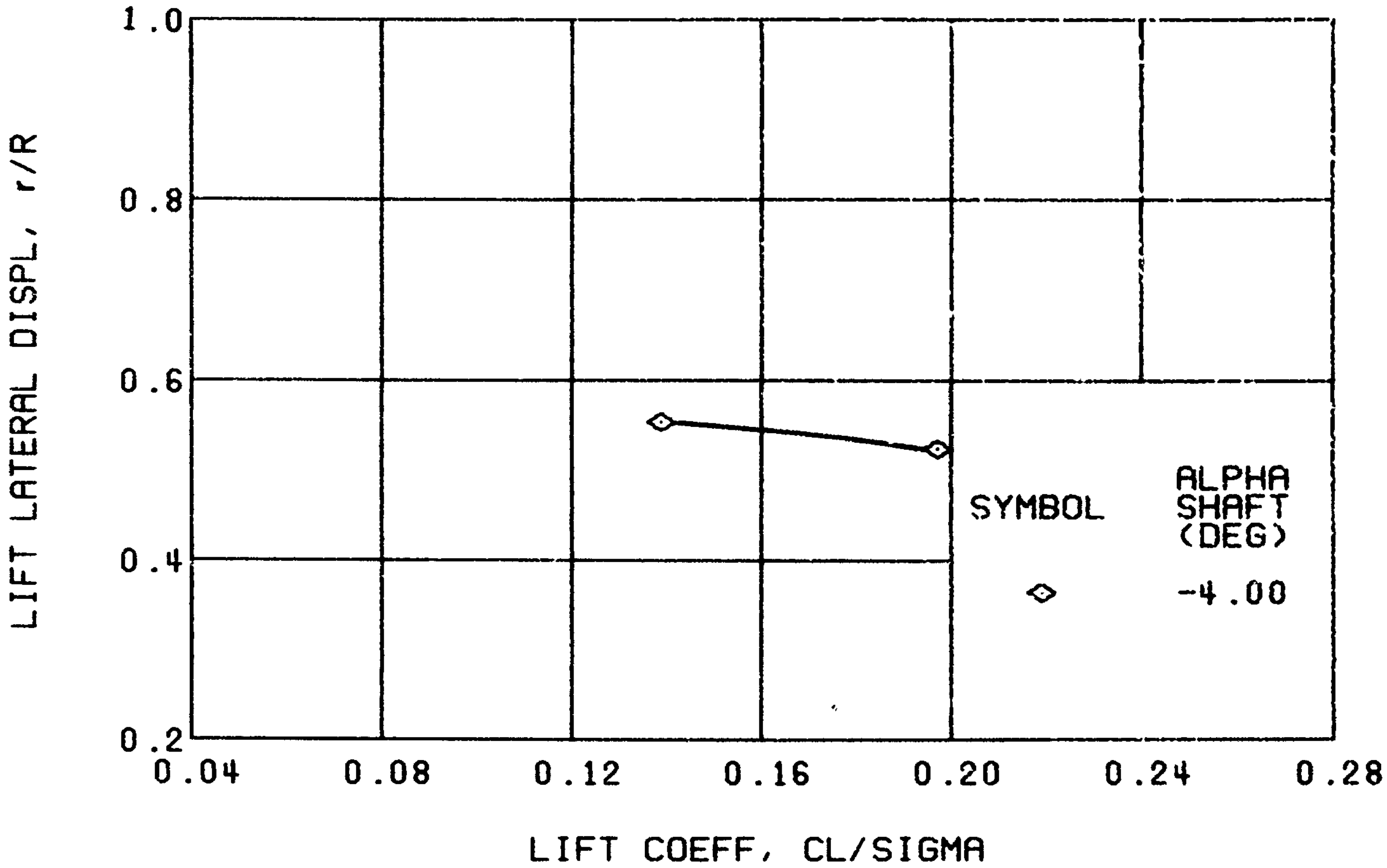

(d) LIFT LATERAL DISPLACEMENT

Figure 34. Continued.
$\mu = 0.70 \quad B'_{1s} = 8$ Deg

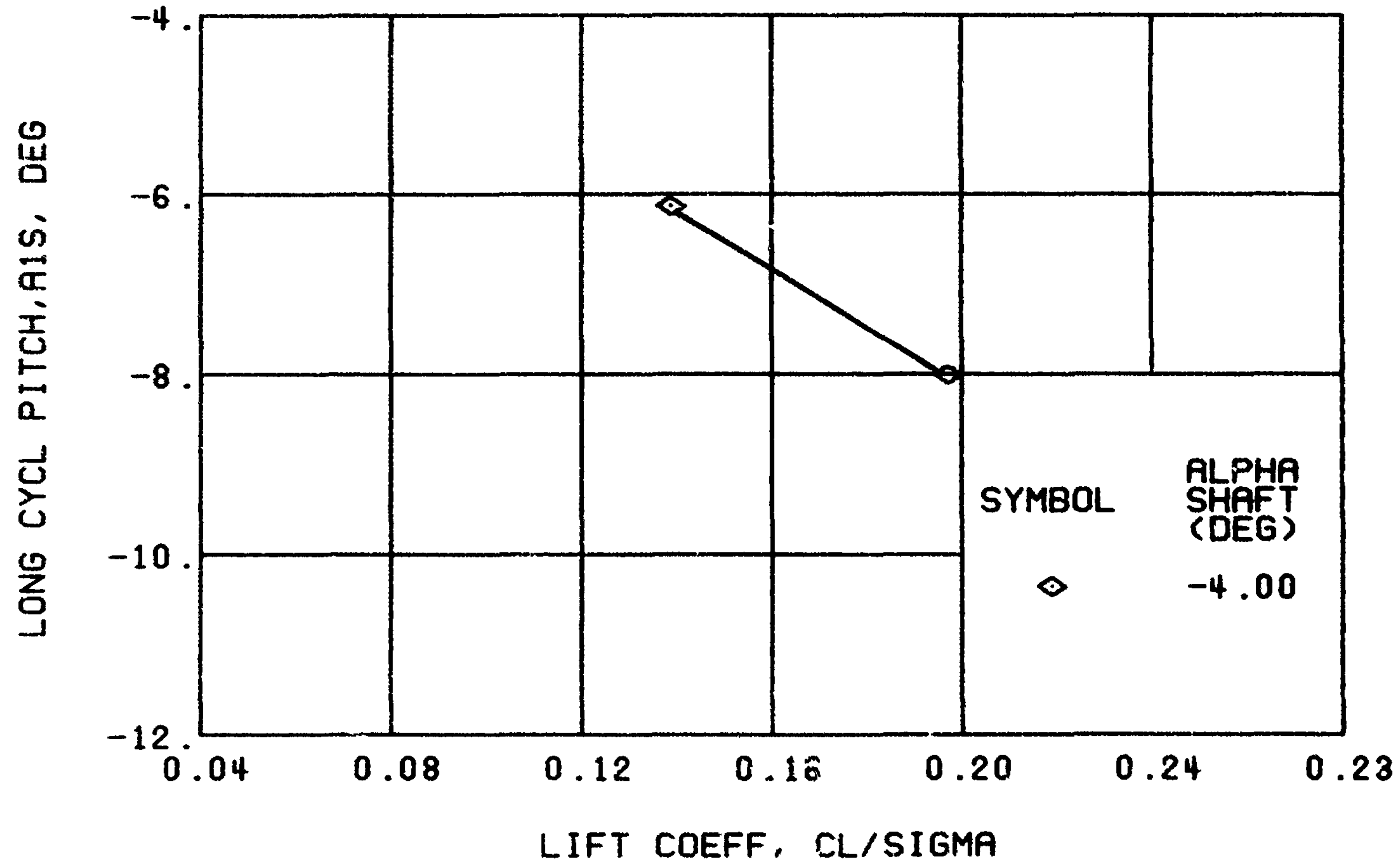

(e) LONGITUDINAL CYCLIC PITCH

Figure 34. Continued.
$\mu = 0.70 \quad B'_{1s} = 8$ **Deg**

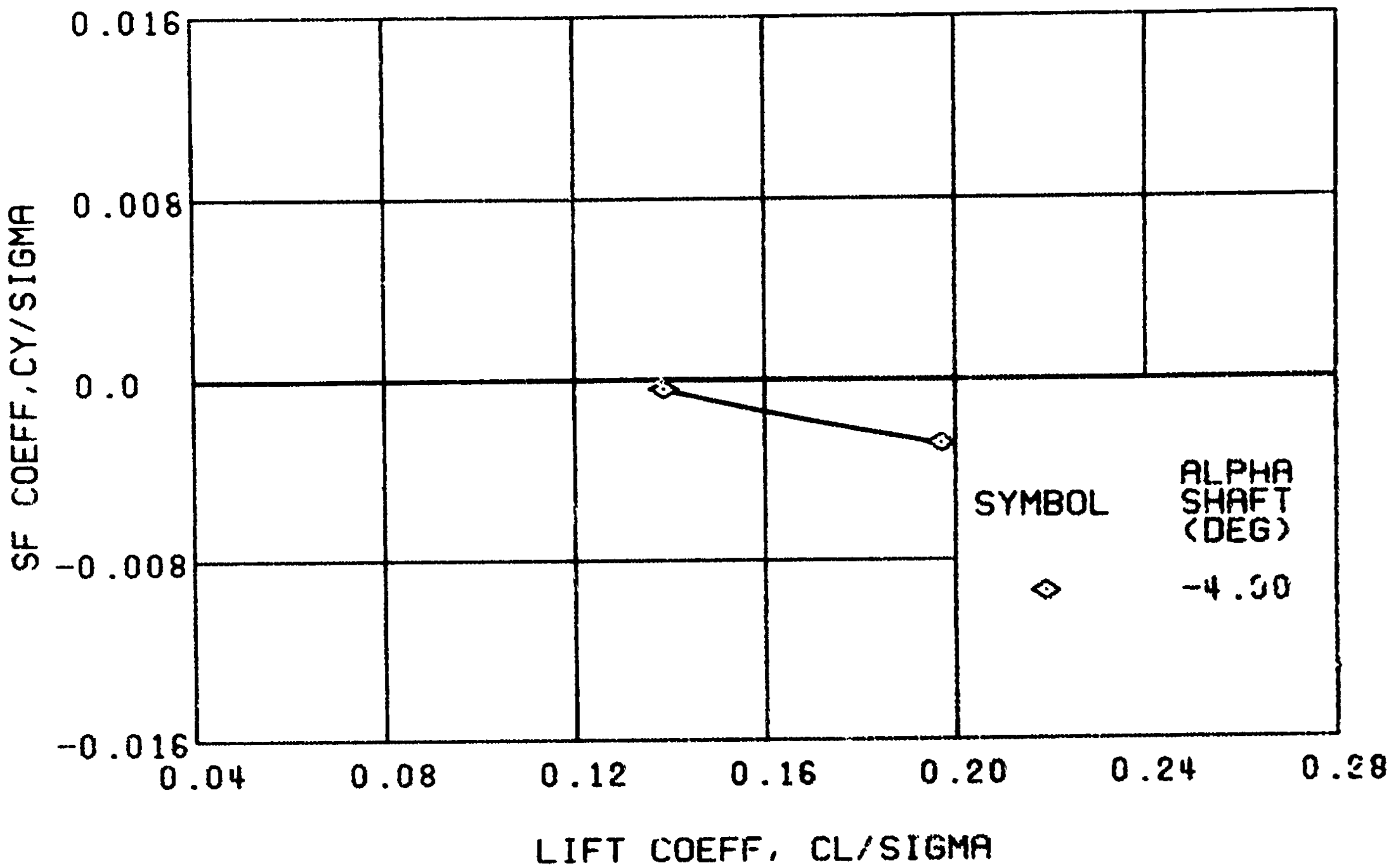

(f) SIDE FORCE COEFFICIENT

Figure 34. Continued.
$\mu = 0.70$ $B'_{1s} = 8$ Deg

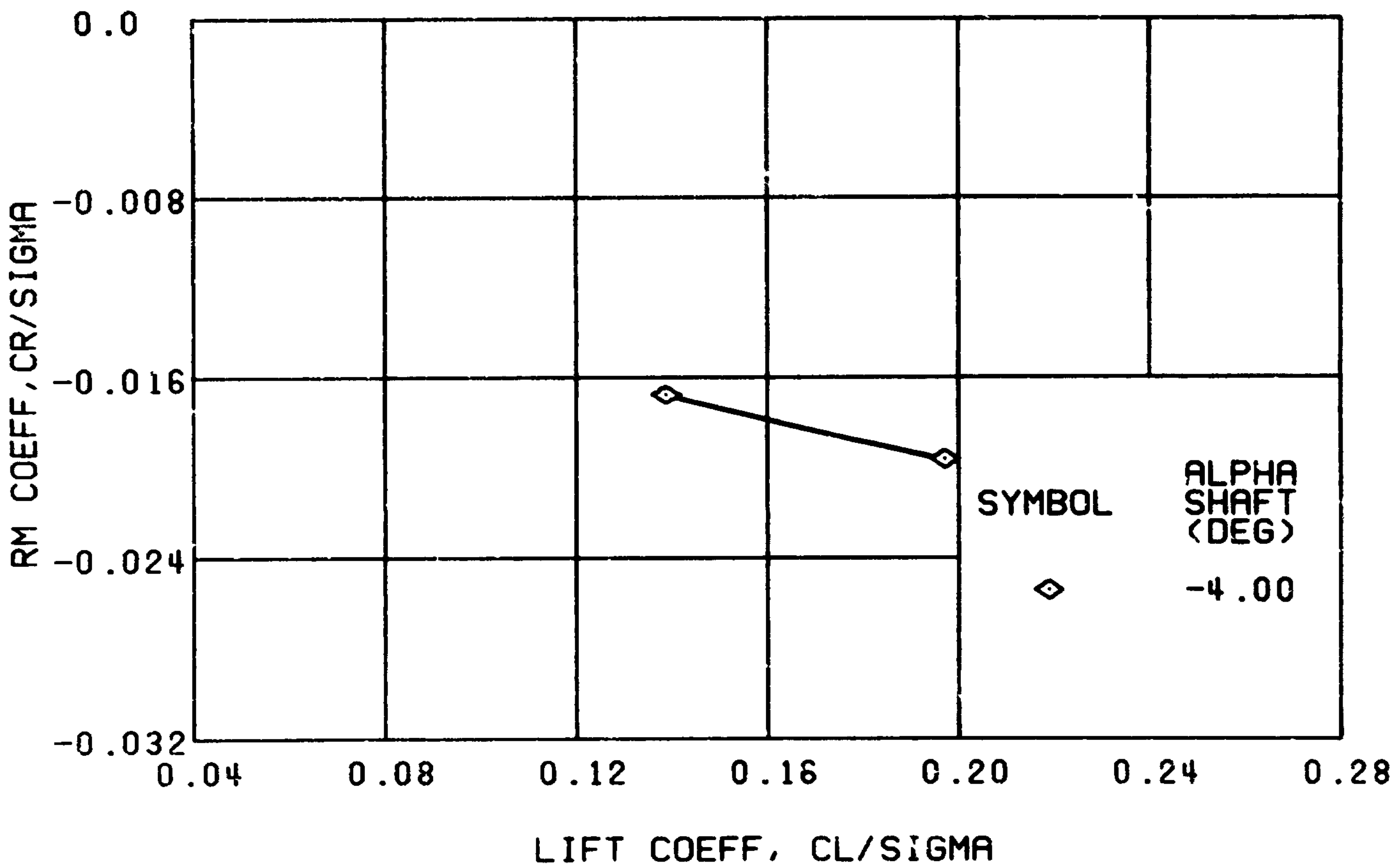

(g) ROLLING MOMENT COEFFICIENT

Figure 34. Continued.
μ = 0.70 B'_{1s} = 8 Deg

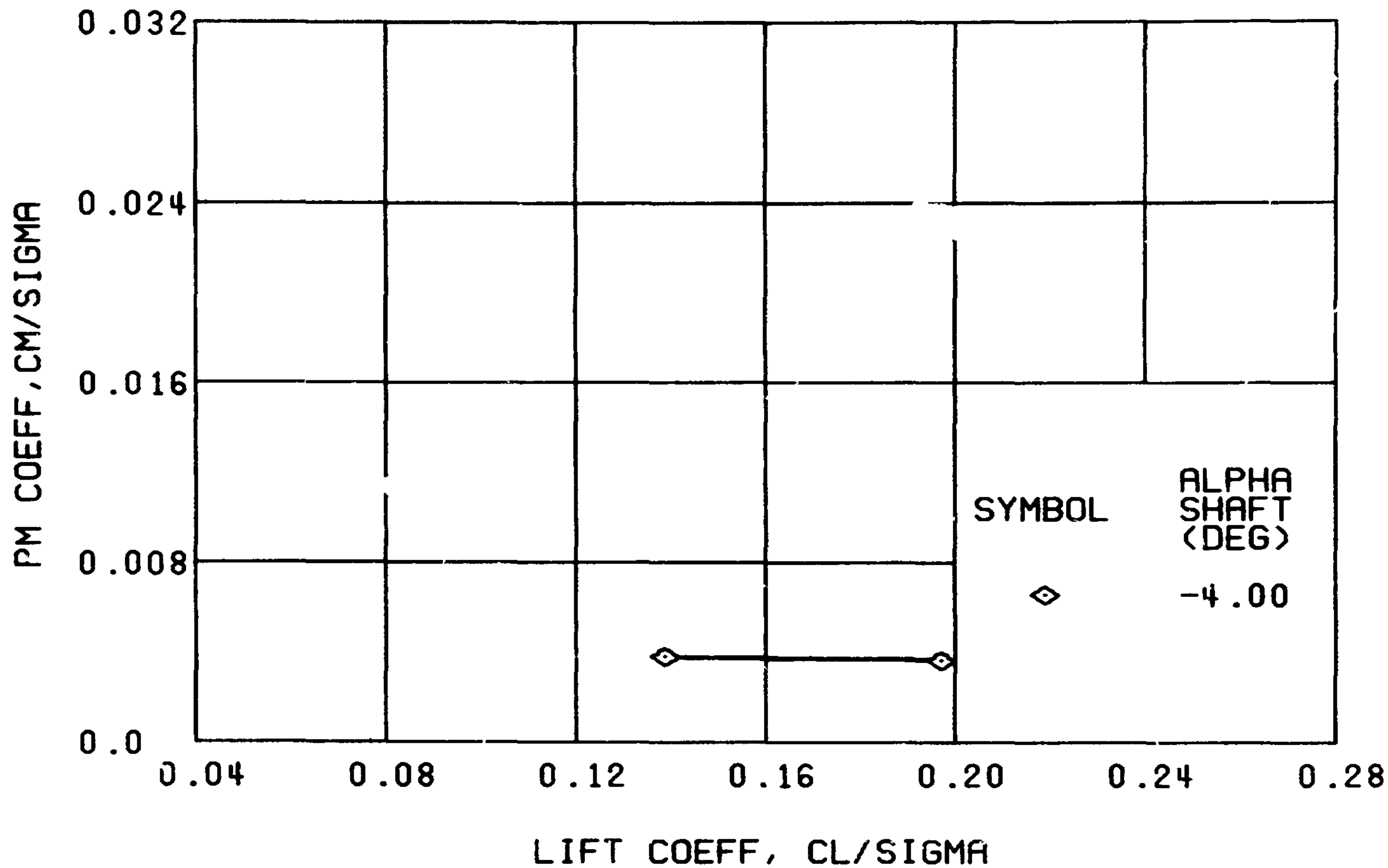

(h) PITCHING MOMENT COEFFICIENT

Figure 34. Continued.
$\mu = 0.70 \quad B'_{1s} = 8$ Deg

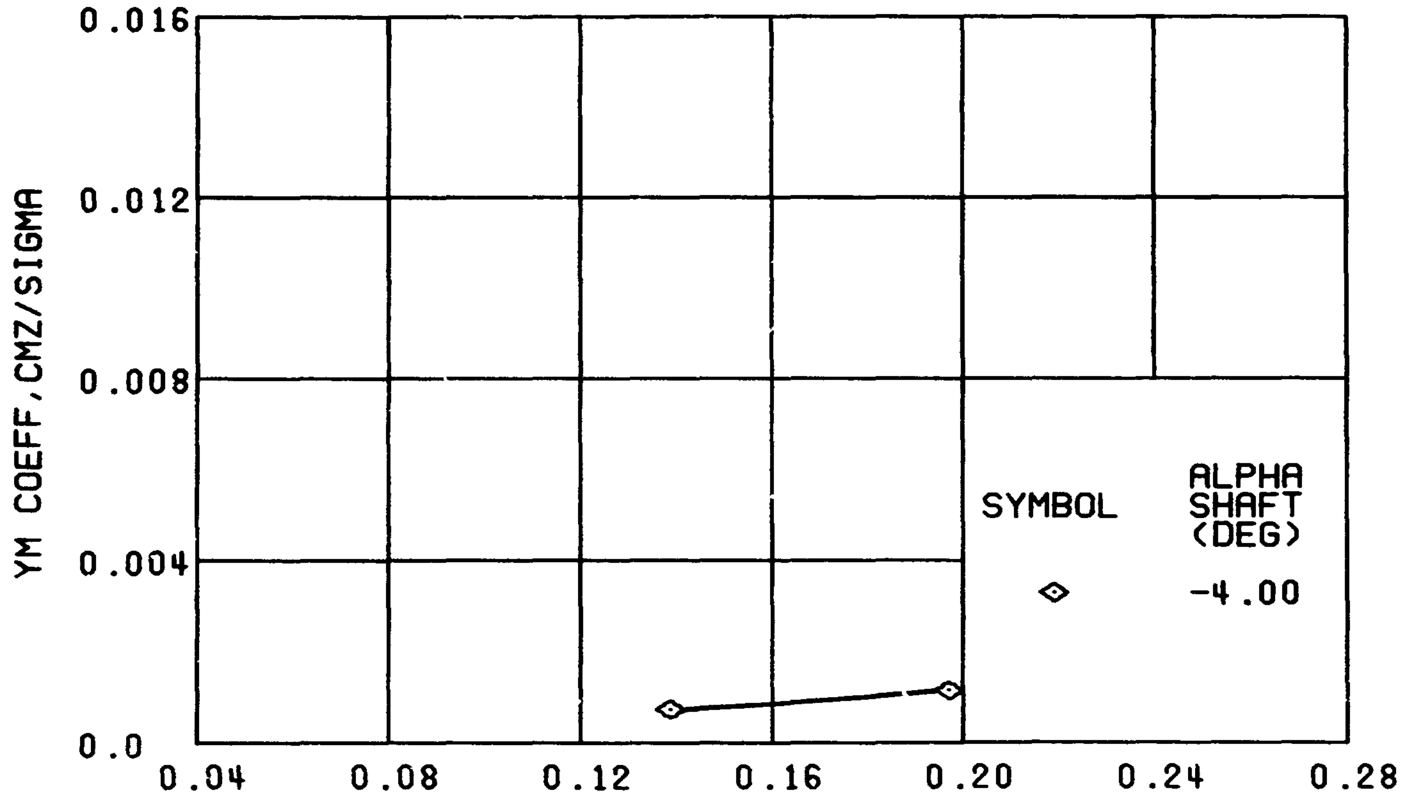

(i) YAWING MOMENT COEFFICIENT

Figure 34. Concluded.
$\mu = 0.70 \quad B'_{1s} = 8$ Deg

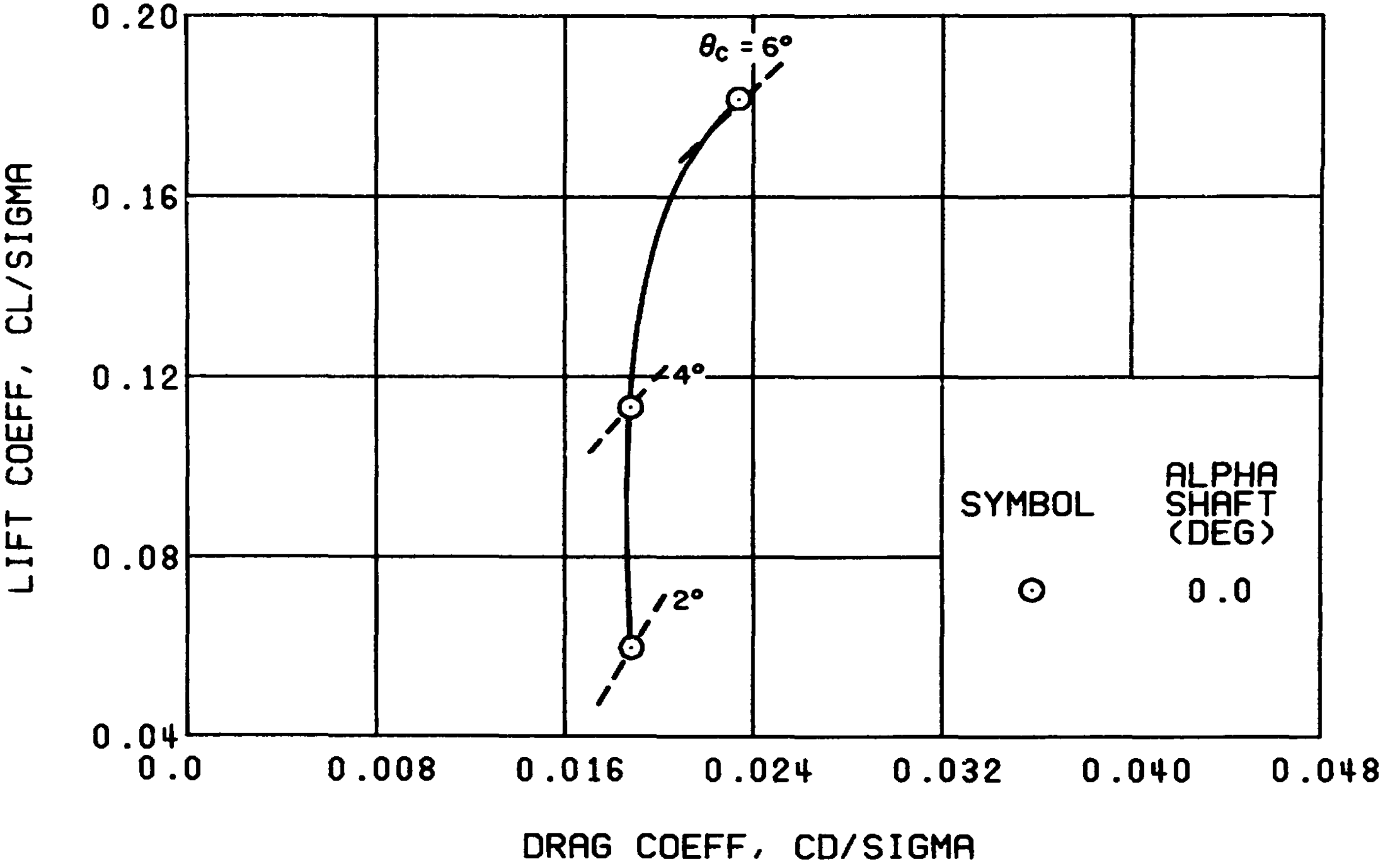

(a) DRAG COEFFICIENT

Figure 35. Performance Data at an Advance Ratio of 0.91 With the Lateral Displacement Control (B'_{1s}) Set at 2 Degrees.

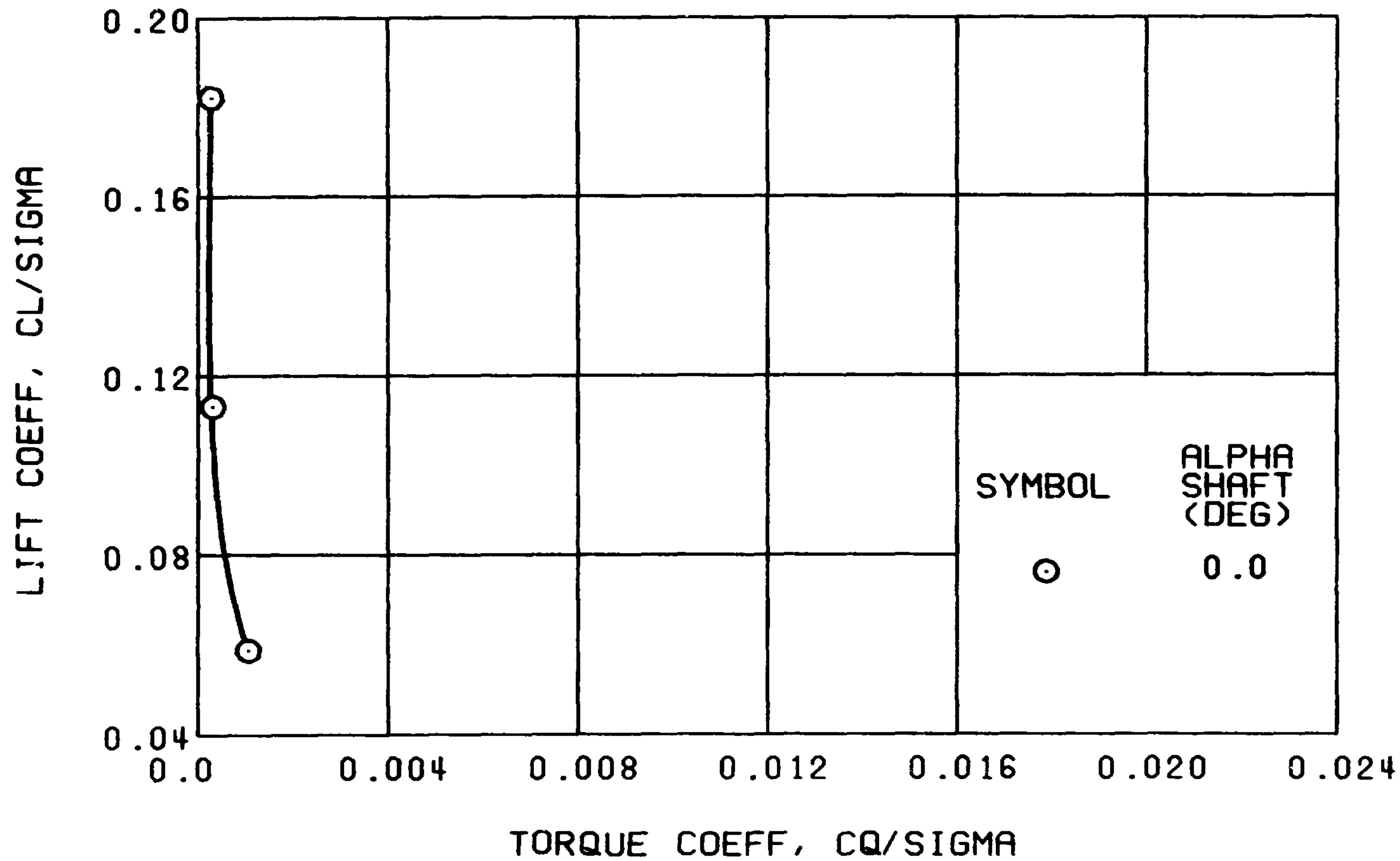

(b) TORQUE COEFFICIENT

Figure 35. **Continued.**
$\mu = 0.91 \quad B'_{1s} = 2$ **Deg**

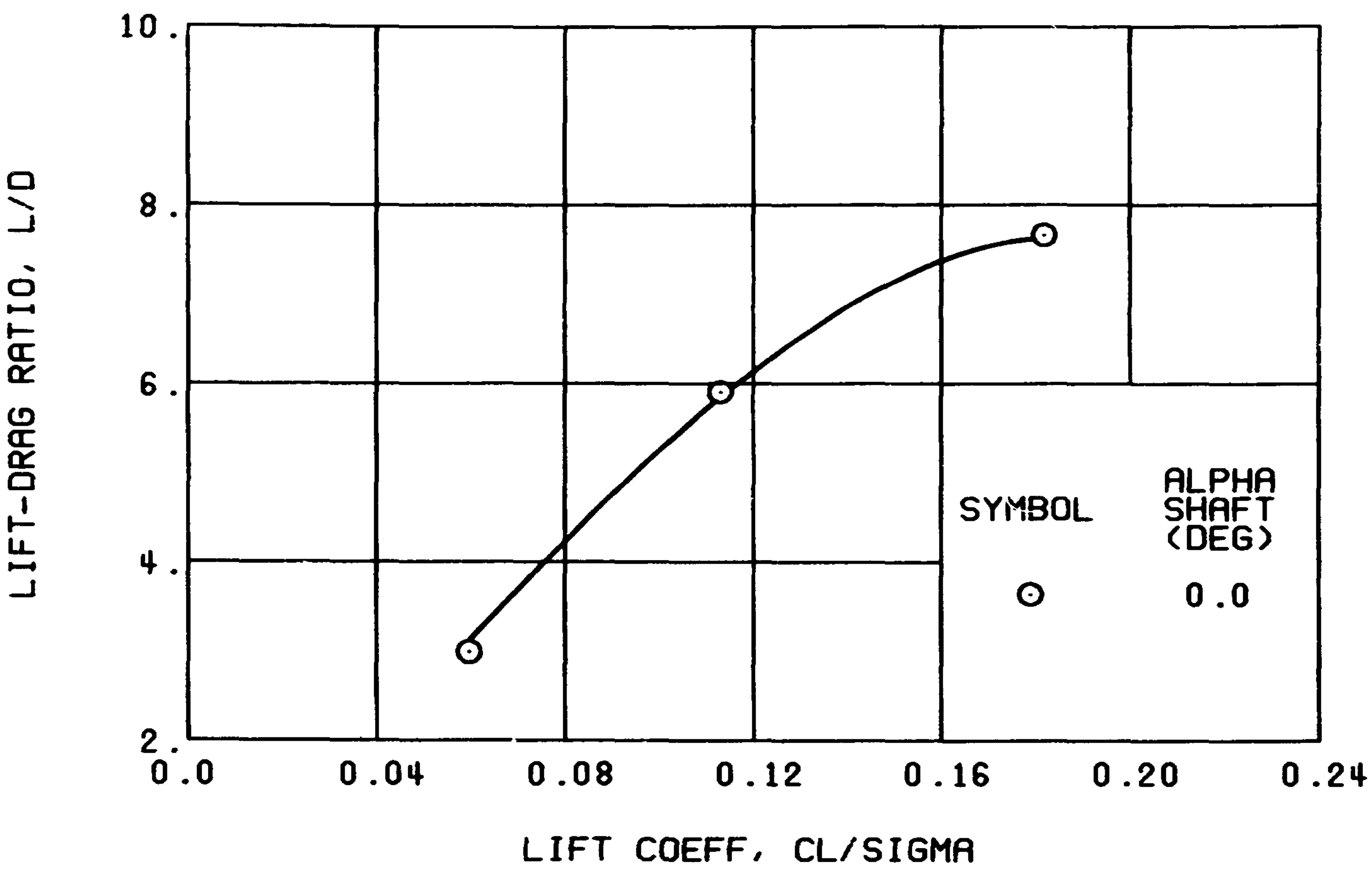

(c) LIFT-DRAG RATIO

Figure 35. Continued.
μ = 0.91 B'_{1s} = 2 Deg

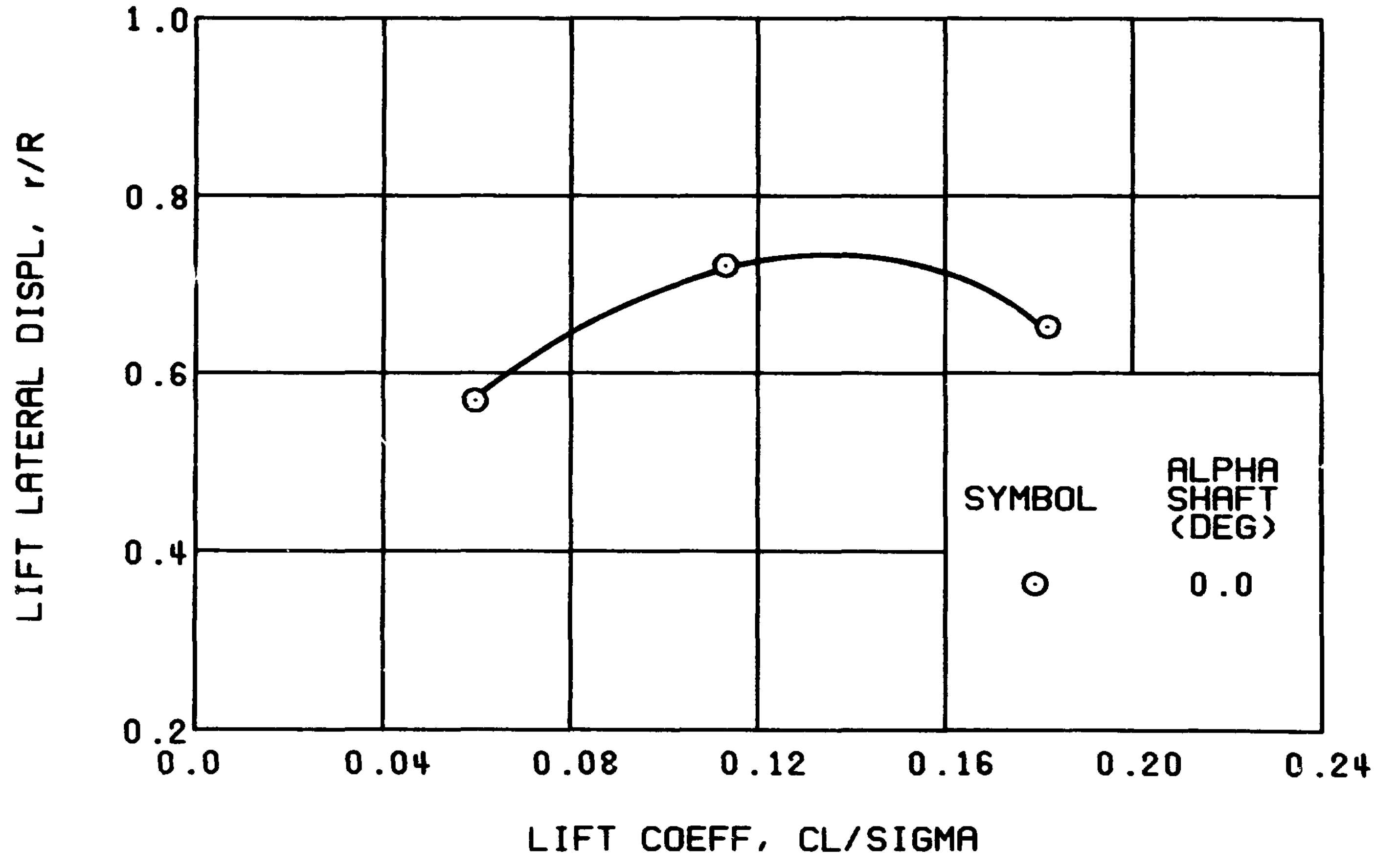

(d) LIFT LATERAL DISPLACEMENT

Figure 35. Continued.
$\mu = 0.91$ $B'_{1s} = 2$ Deg

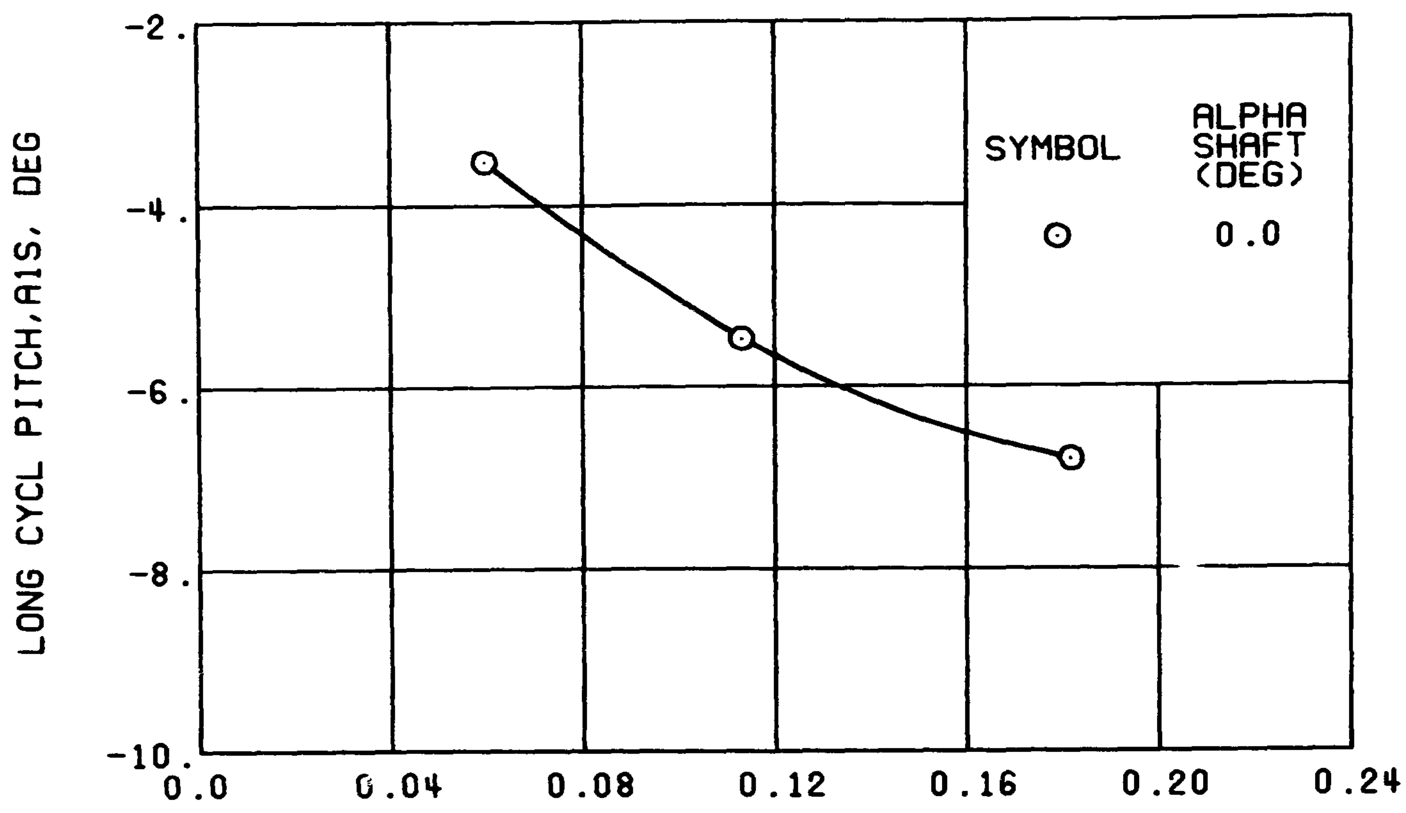

(e) LONGITUDINAL CYCLIC PITCH

Figure 35. Continued.
$\mu = 0.91 \quad B'_{1s} = 2$ Deg

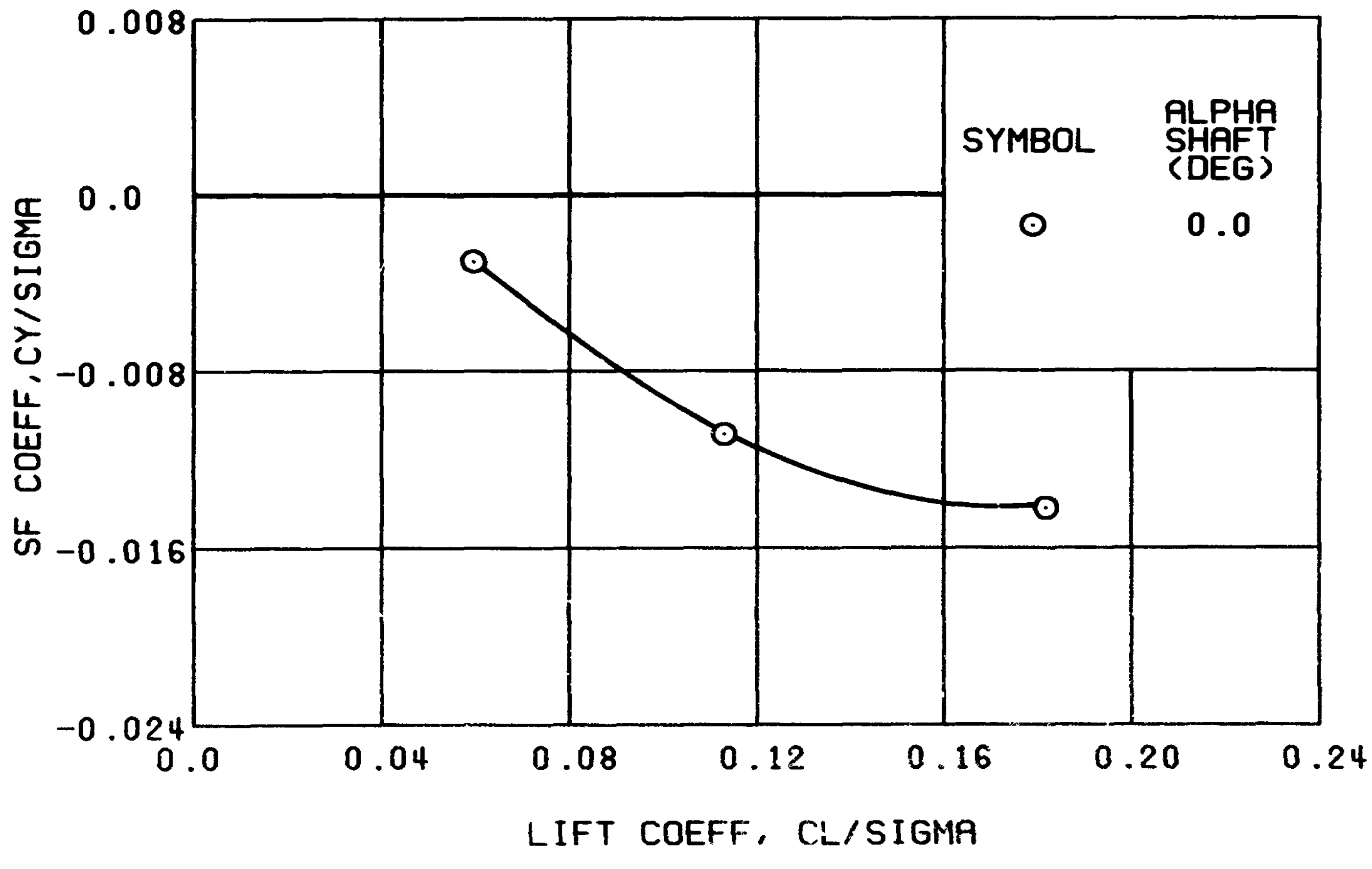

(f) SIDE FORCE COEFFICIENT

Figure 35. Continued.
$\mu = 0.91 \quad B'_{1s} = 2$ Deg

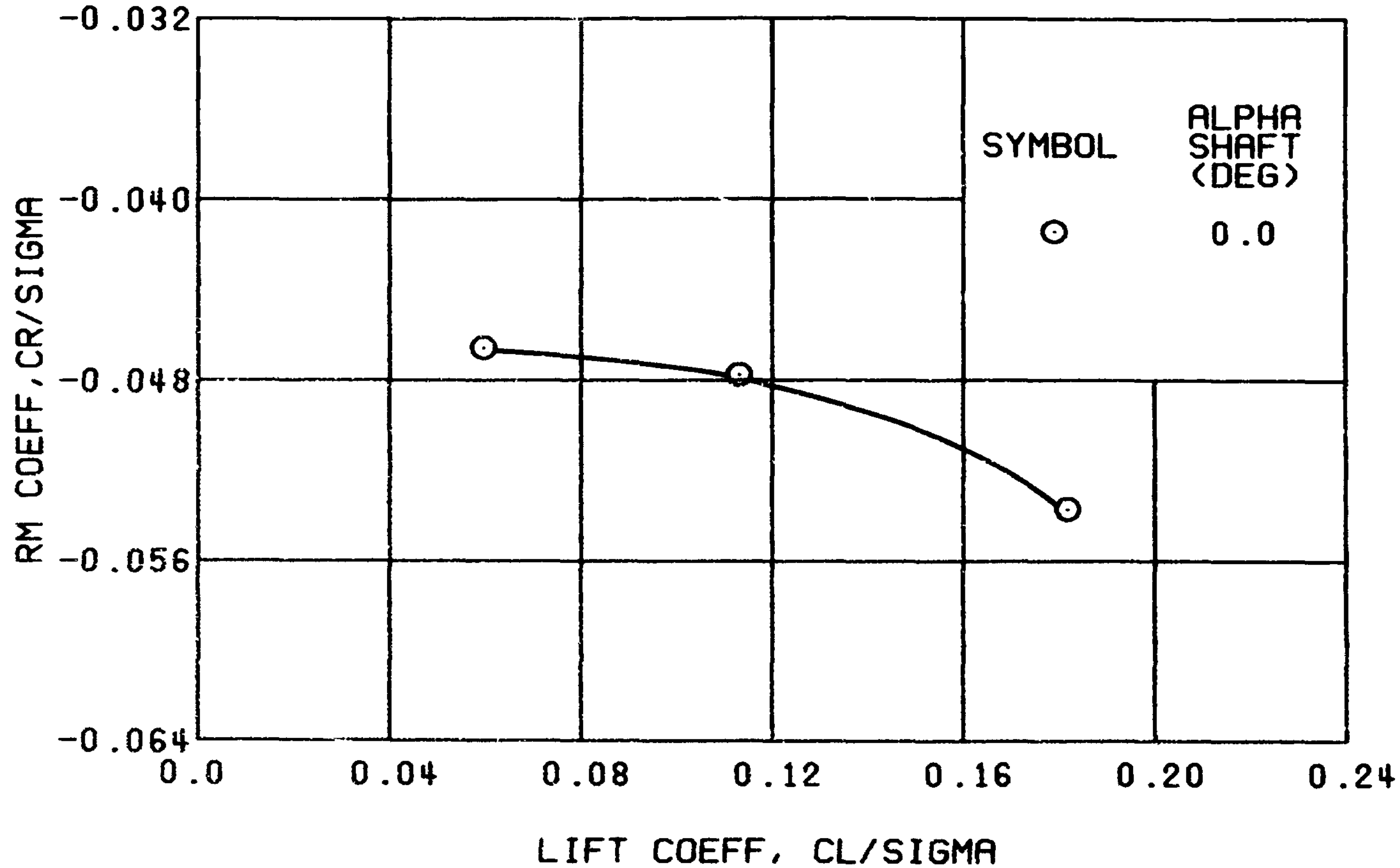

(g) ROLLING MOMENT COEFFICIENT

Figure 35. Continued.
$\mu = 0.91$ $B'_{1s} = 2$ Deg

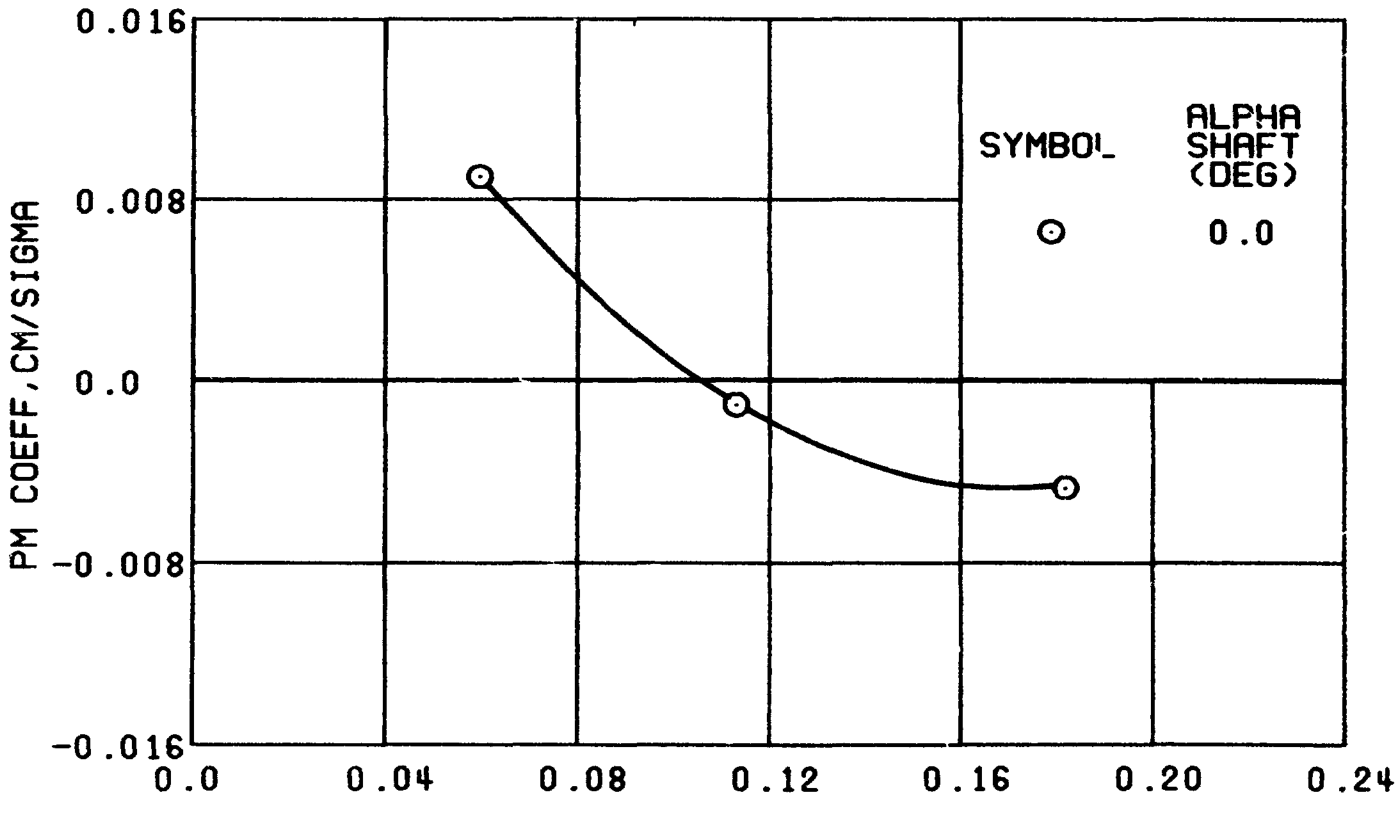

(h) PITCHING MOMENT COEFFICIENT

Figure 35. Continued.
μ = 0.91 B'_{1s} = 2 Deg

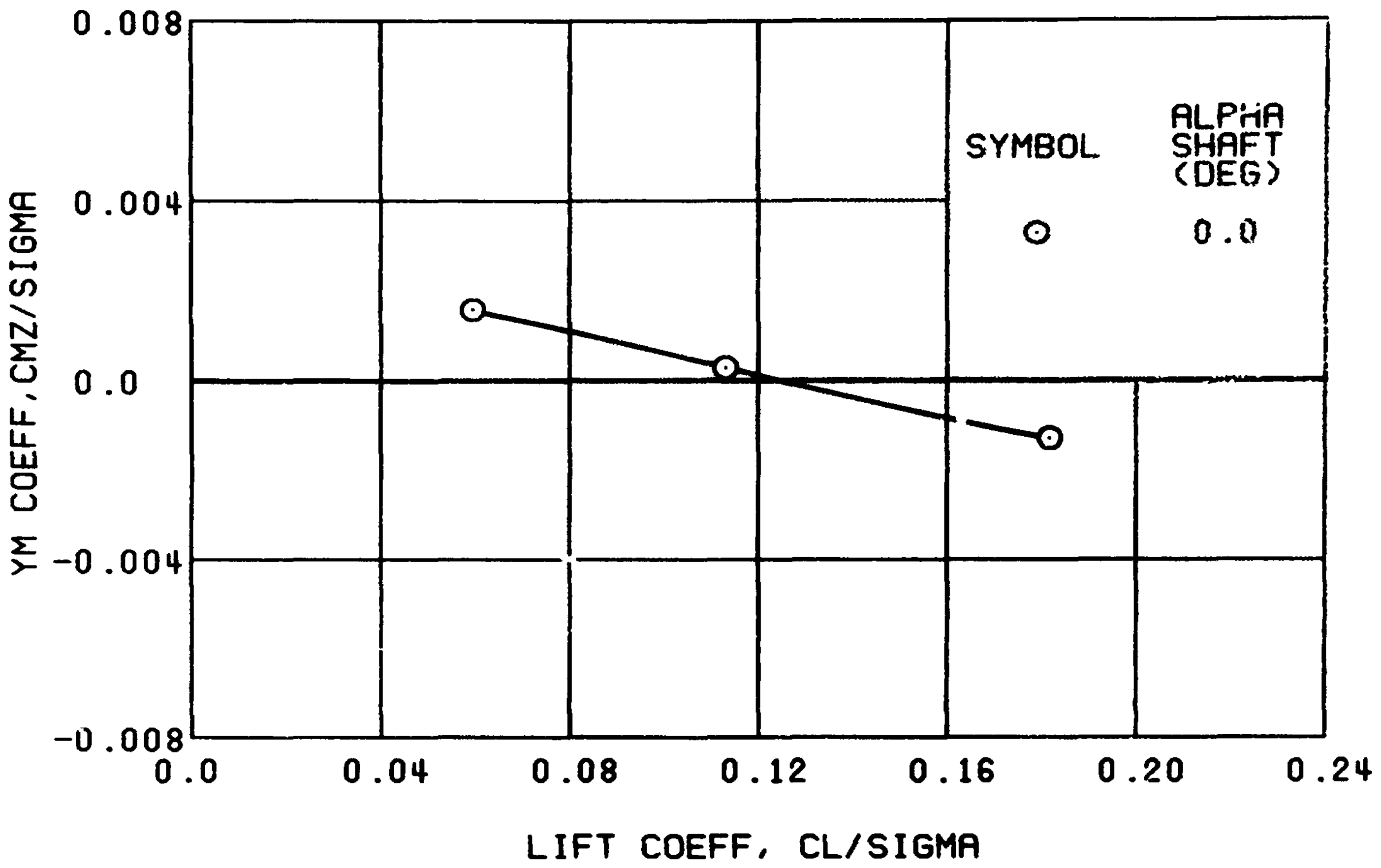

(i) YAWING MOMENT COEFFICIENT

Figure 35. Concluded.
$\mu = 0.91 \quad B'_{1s} = 2$ Deg

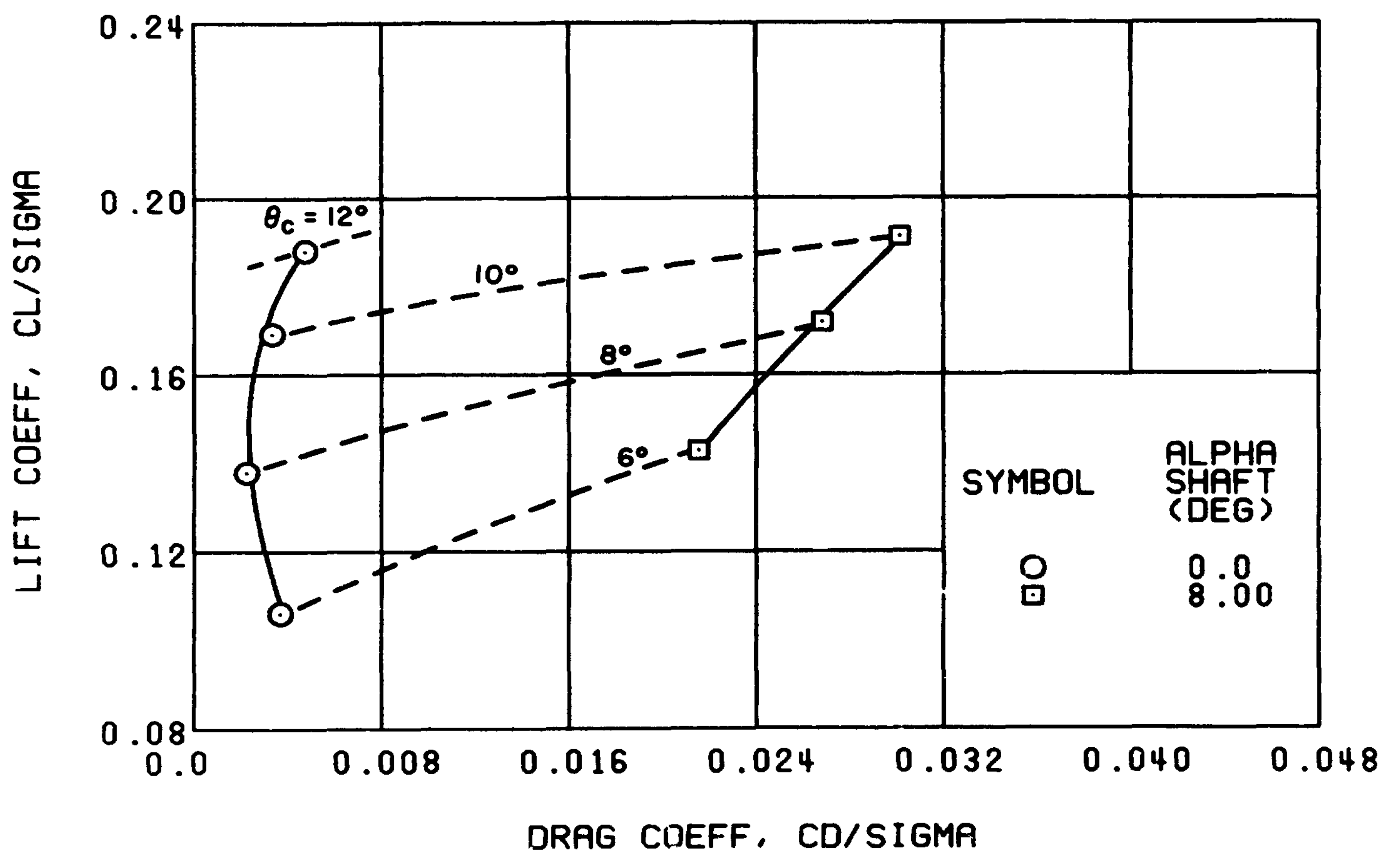

(a) DRAG COEFFICIENT

Figure 36. Performance Data at an Advance Ratio of 0.21 With the Lateral Displacement Control (B'_{1s}) Set at 2 Deg (Single-Rotor Configuration).

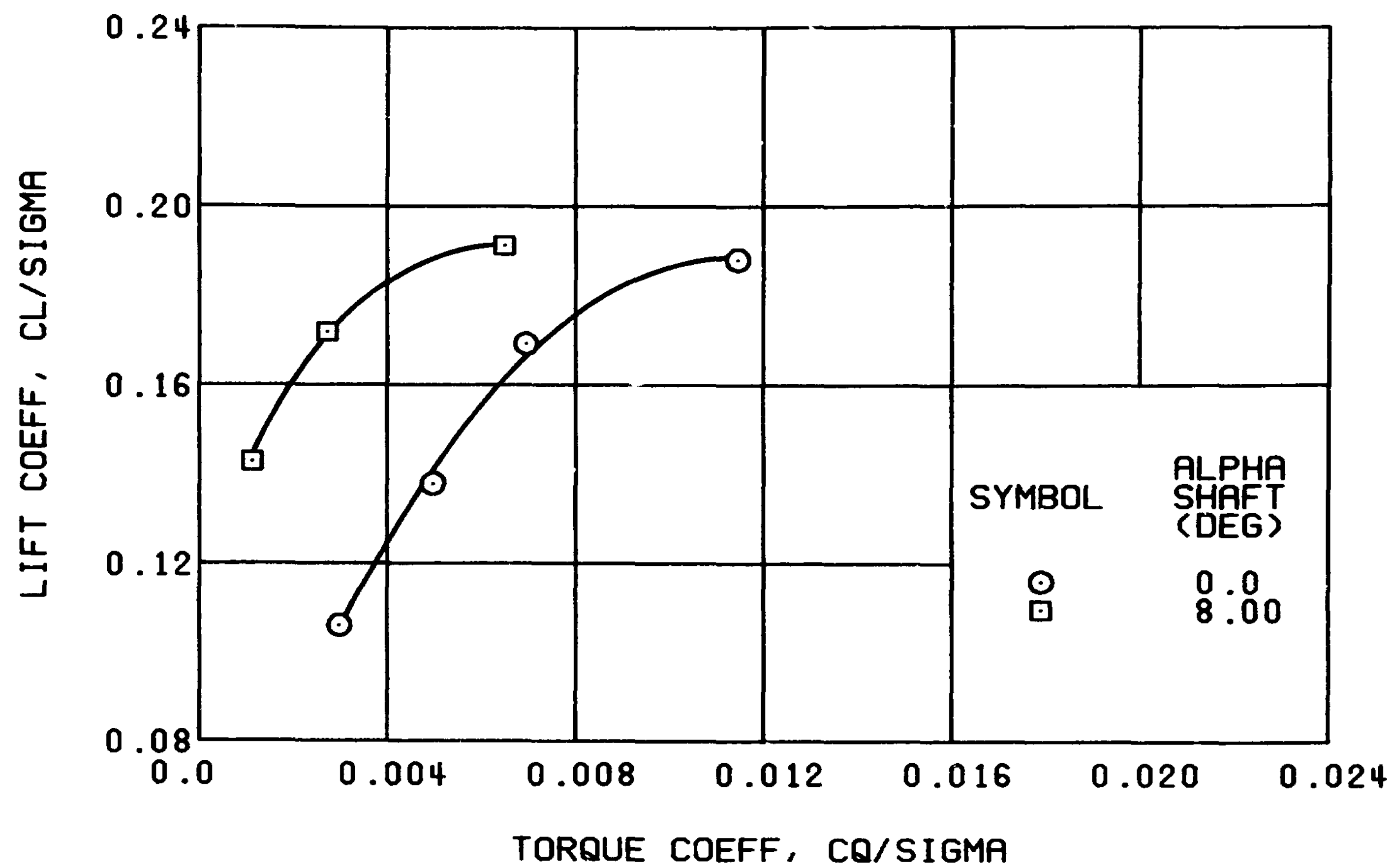

(b) TORQUE COEFFICIENT

Figure 36. Continued.
μ = 0.21 B'_{1s} = 2 Deg (Single-Rotor Configuration)

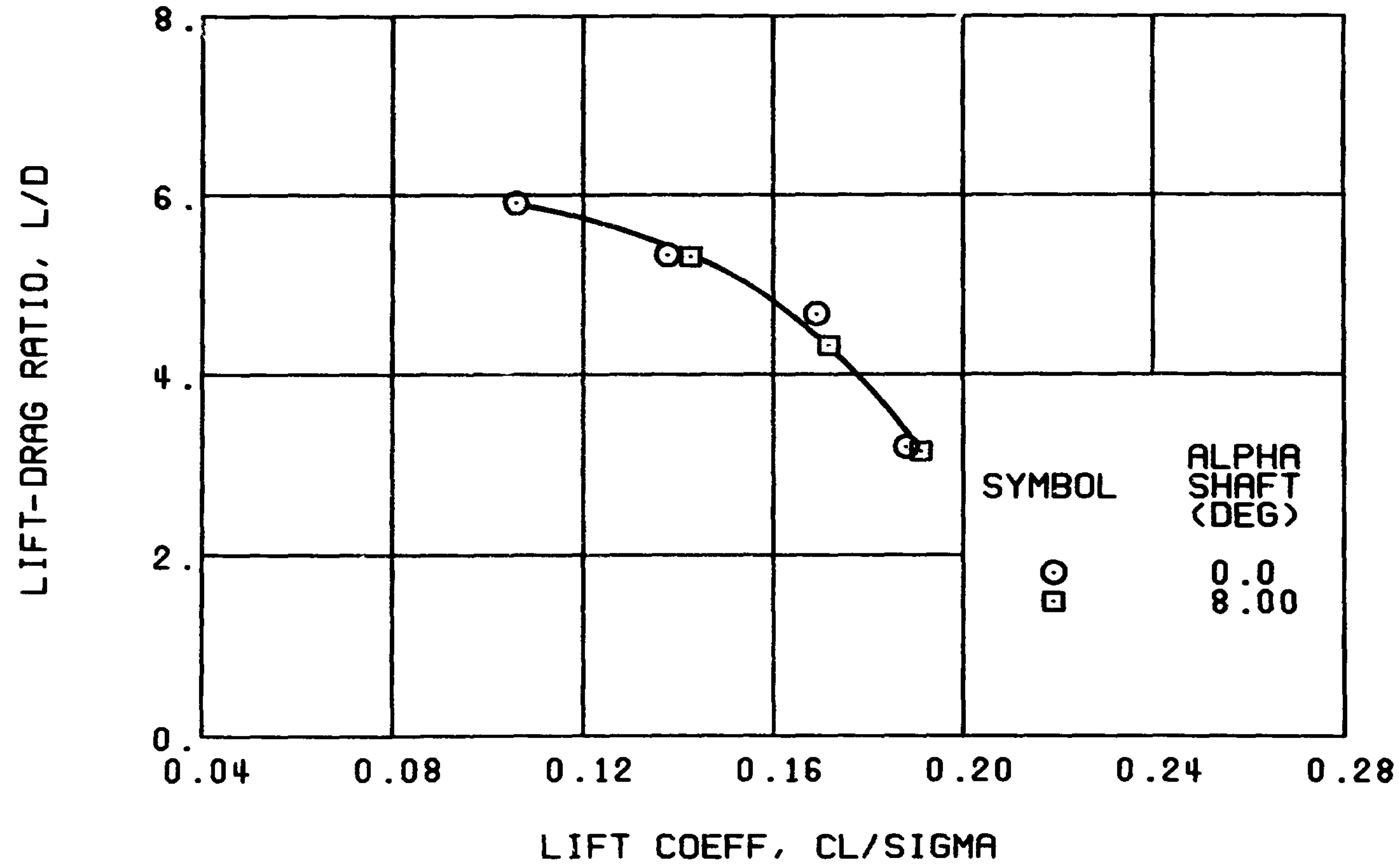

(c) LIFT-DRAG RATIO

Figure 36. Continued.
$\mu = 0.21$ $B'_{1s} = 2$ Deg (Single-Rotor Configuration)

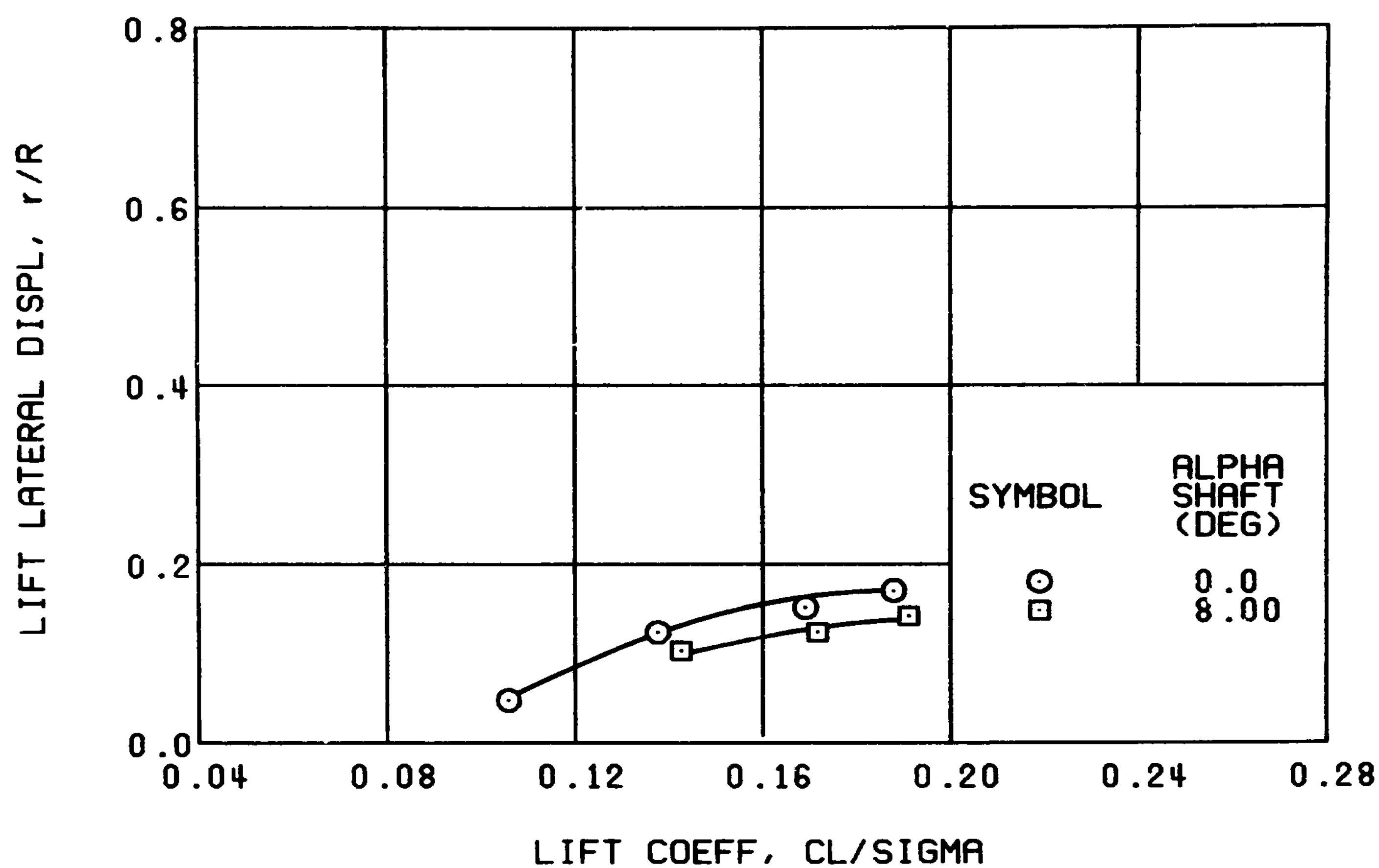

(d) LIFT LATERAL DISPLACEMENT

Figure 36. Continued.
$\mu = 0.21$ $B'_{1s} = 2$ Deg (Single-Rotor Configuration)

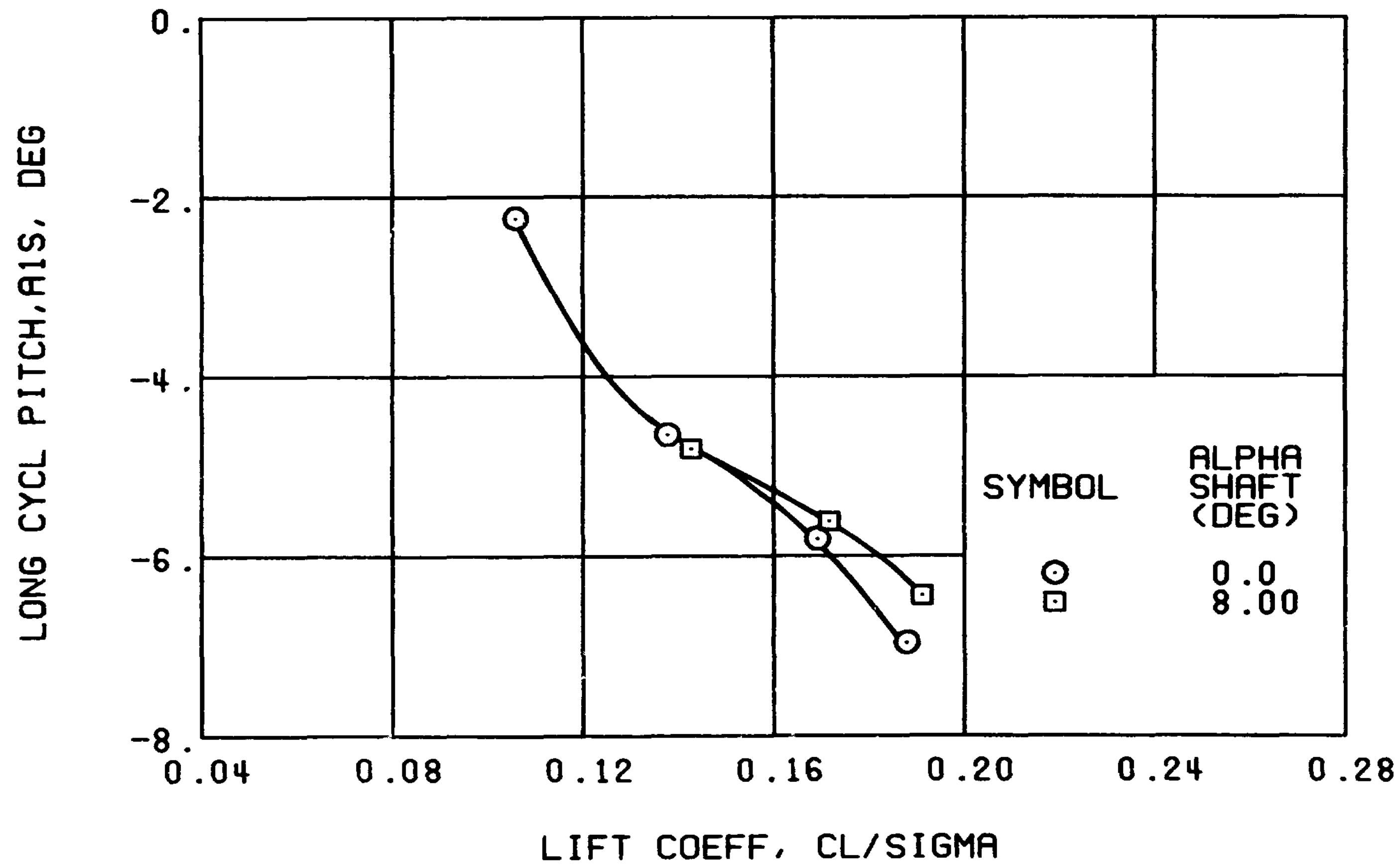

(e) LONGITUDINAL CYCLIC PITCH

Figure 36. **Continued.**
μ = 0.21 B'_{1s} = 2 Deg (Single-Rotor Configuration)

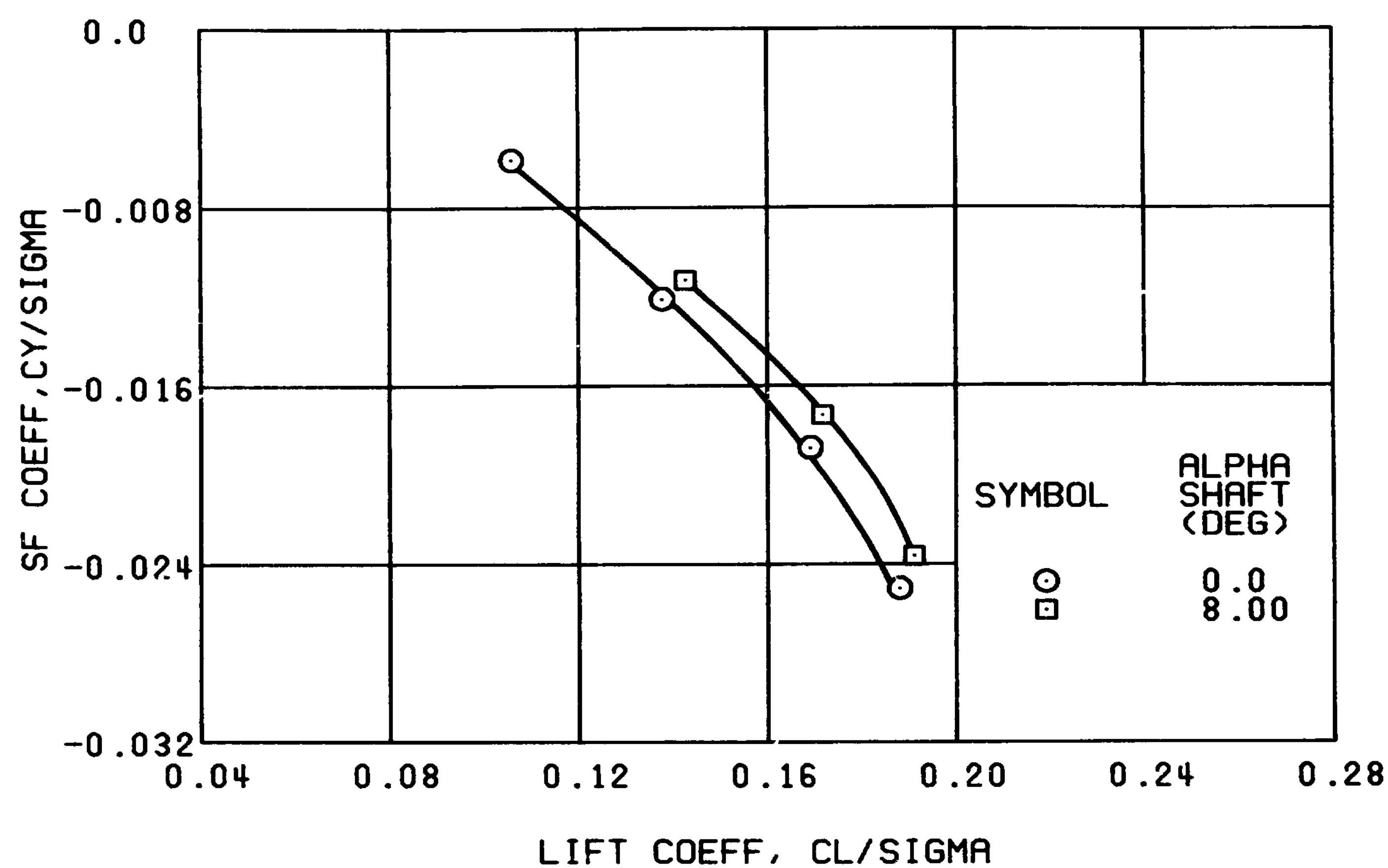

(f) SIDE FORCE COEFFICIENT

Figure 36. Continued.
μ = 0.21 B'_{1s} = 2 Deg (Single-Rotor Configuration)

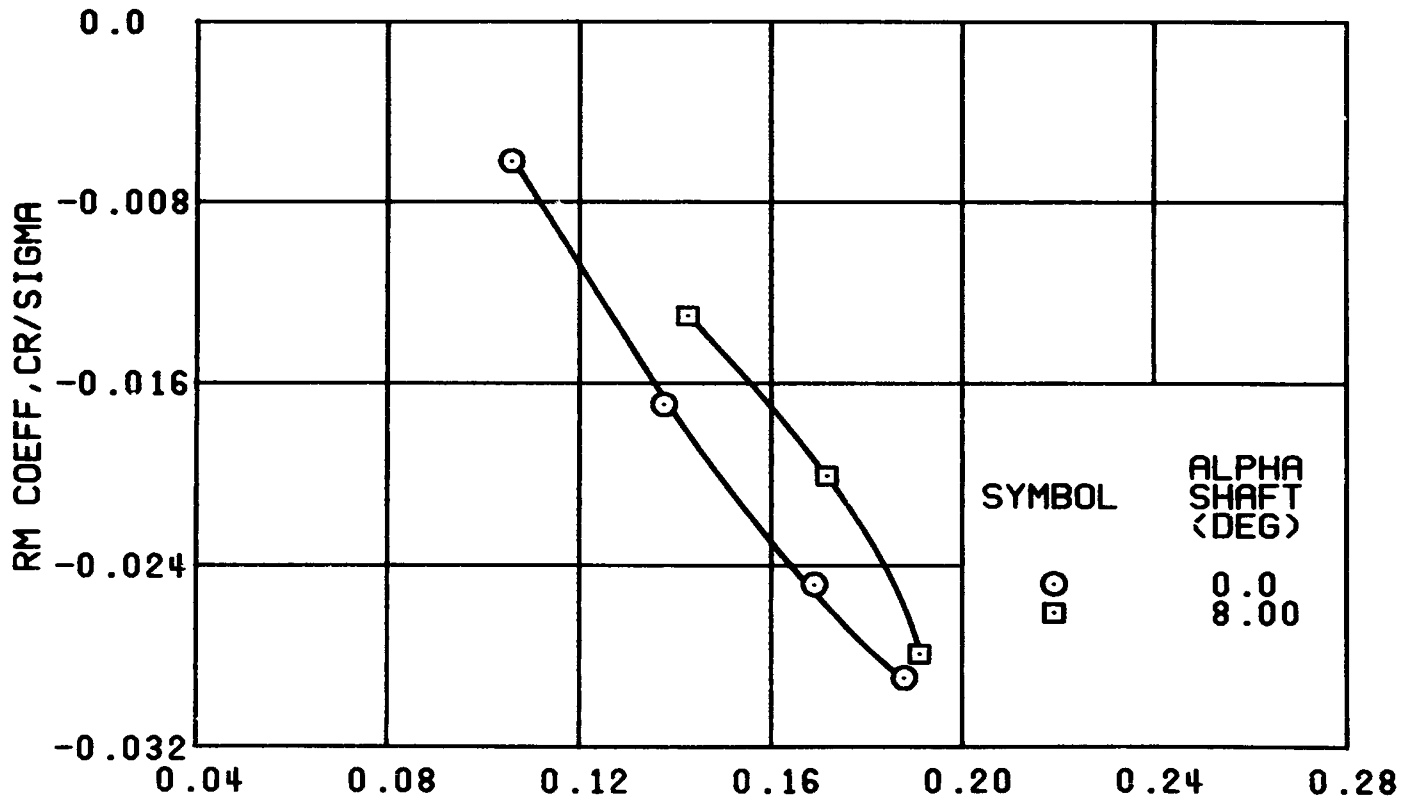

(g) ROLLING MOMENT COEFFICIENT

Figure 36. **Continued.**
$\bar{\mu}$ = 0.21 B'_{1s} = 2 Deg (Single-Rotor Configuration)

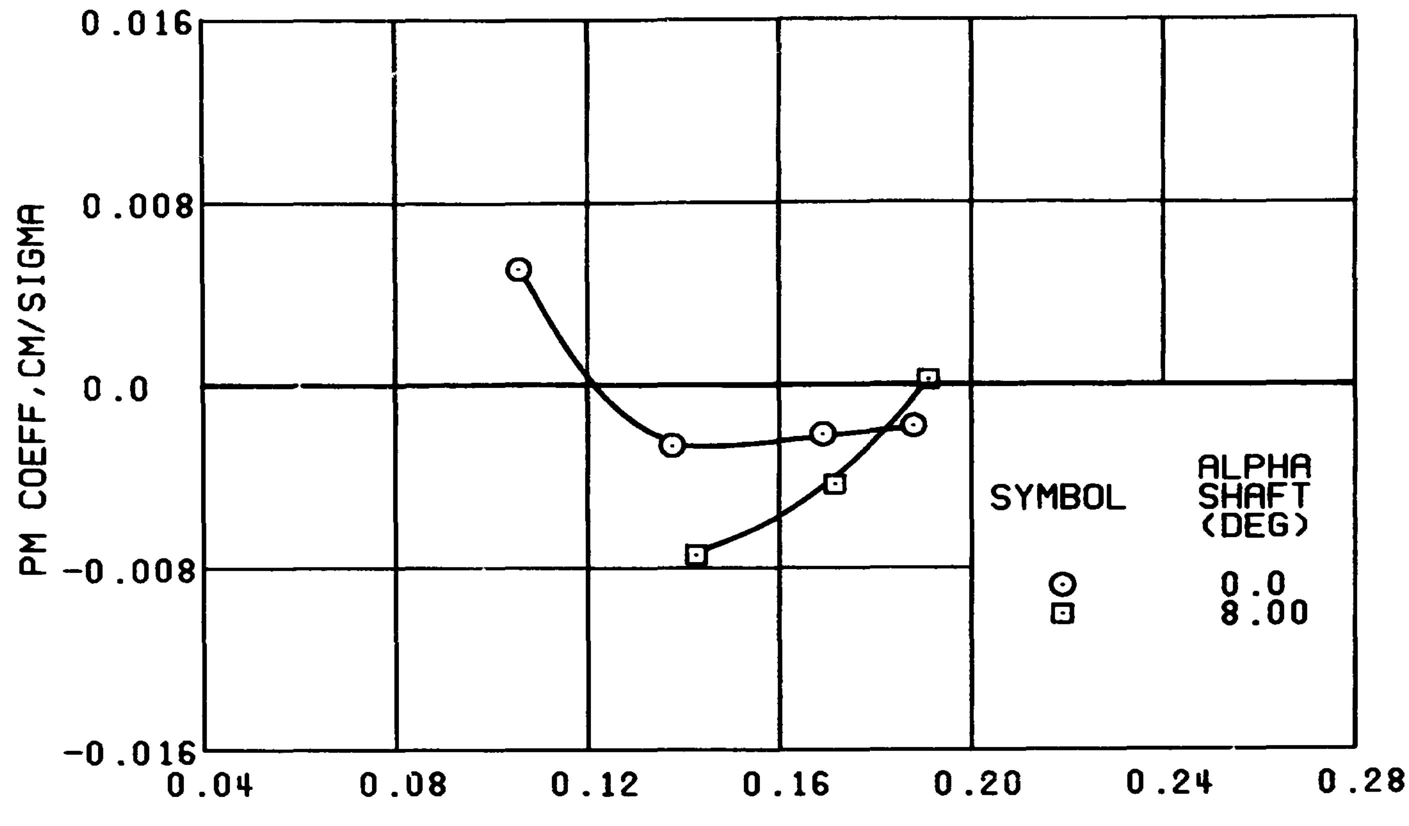

(h) PITCHING MOMENT COEFFICIENT

Figure 36. Continued.
$\mu = 0.21$ $B'_{1s} = 2$ Deg (Single-Rotor Configuration)

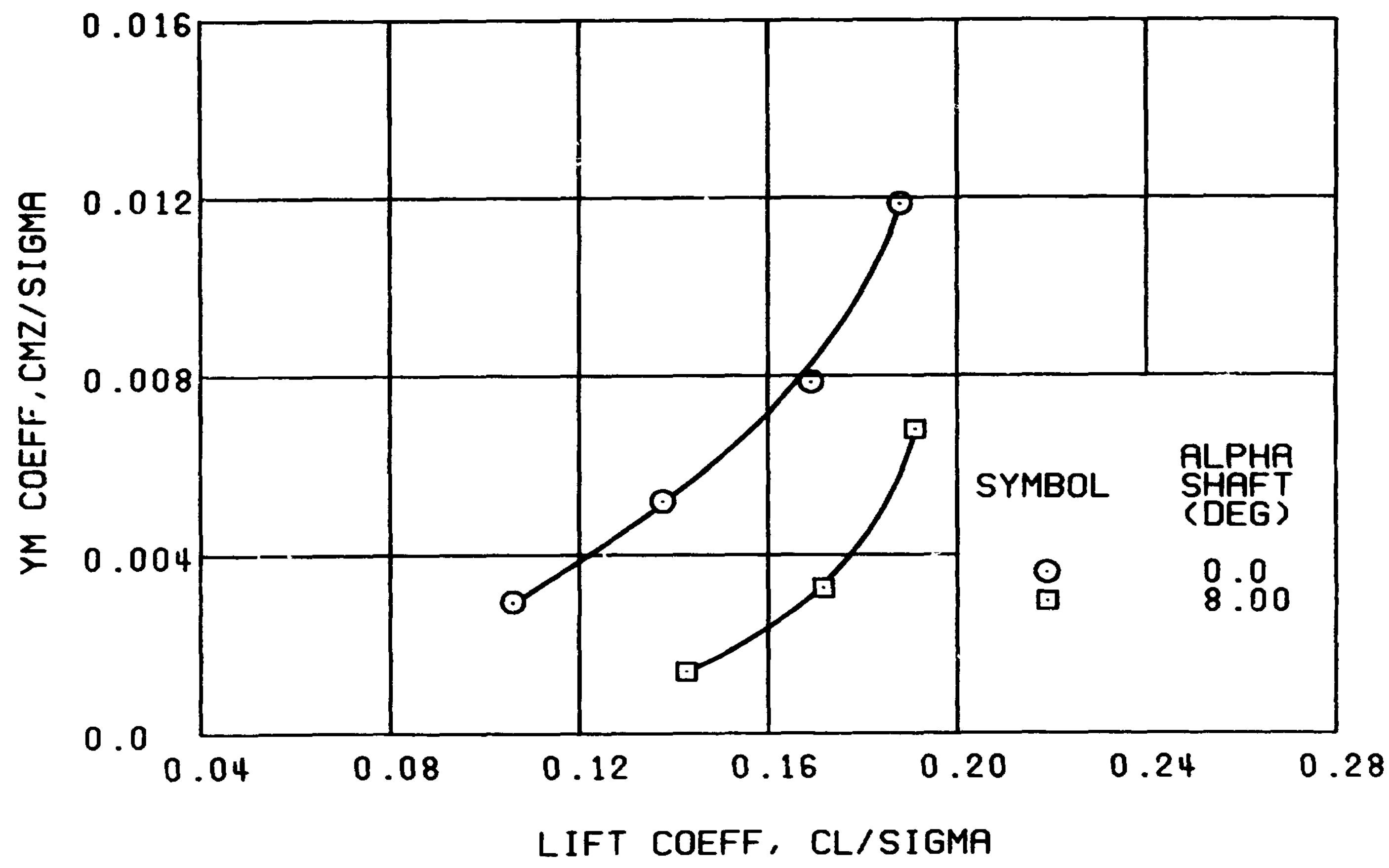

(i) YAWING MOMENT COEFFICIENT

Figure 36. **Continued.**
$\mu = 0.21$ $B'_{1s} = 2$ Deg (Single-Rotor Configuration)

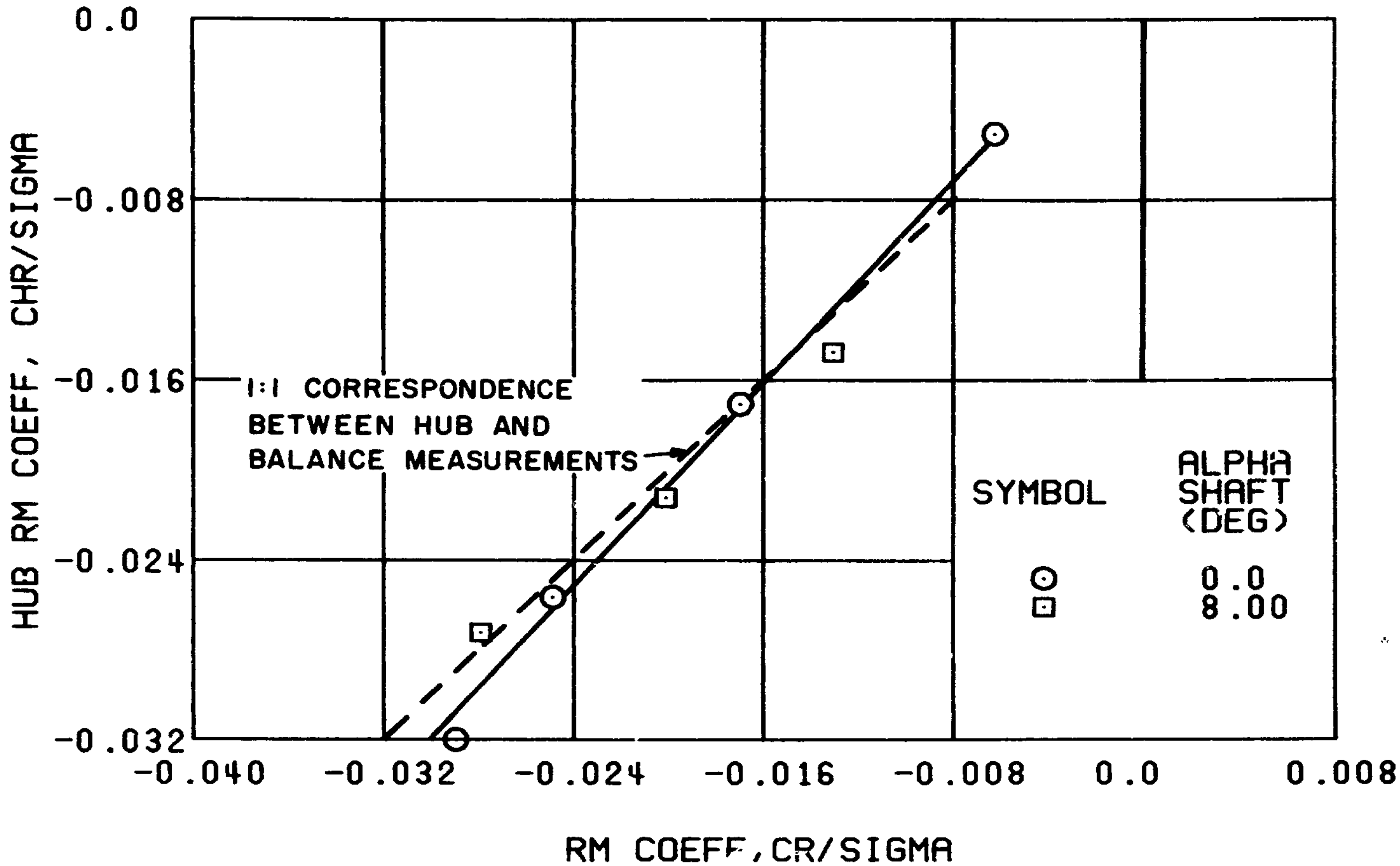

(j) HUB VERSUS BALANCE ROLLING MOMENT COEFFICIENT

Figure 36. Continued.
μ = 0.21 B'_{1s} = 2 Deg (Single-Rotor Configuration)

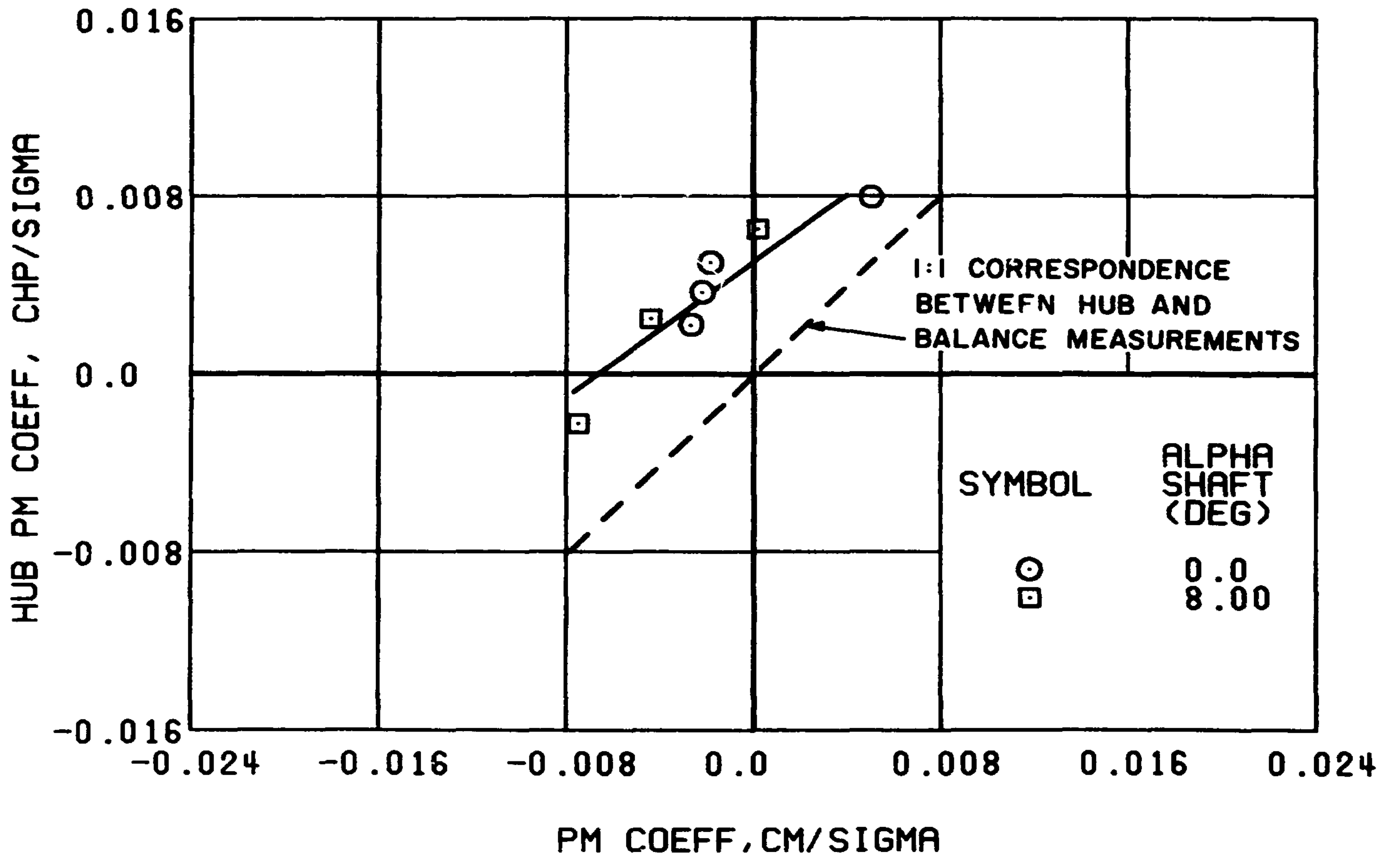

(k) HUB VERSUS BALANCE PITCHING MOMENT COEFFICIENT

Figure 36. Continued.
$\mu = 0.21$ $B'_{1s} = 2$ Deg (Single-Rotor Configuration)

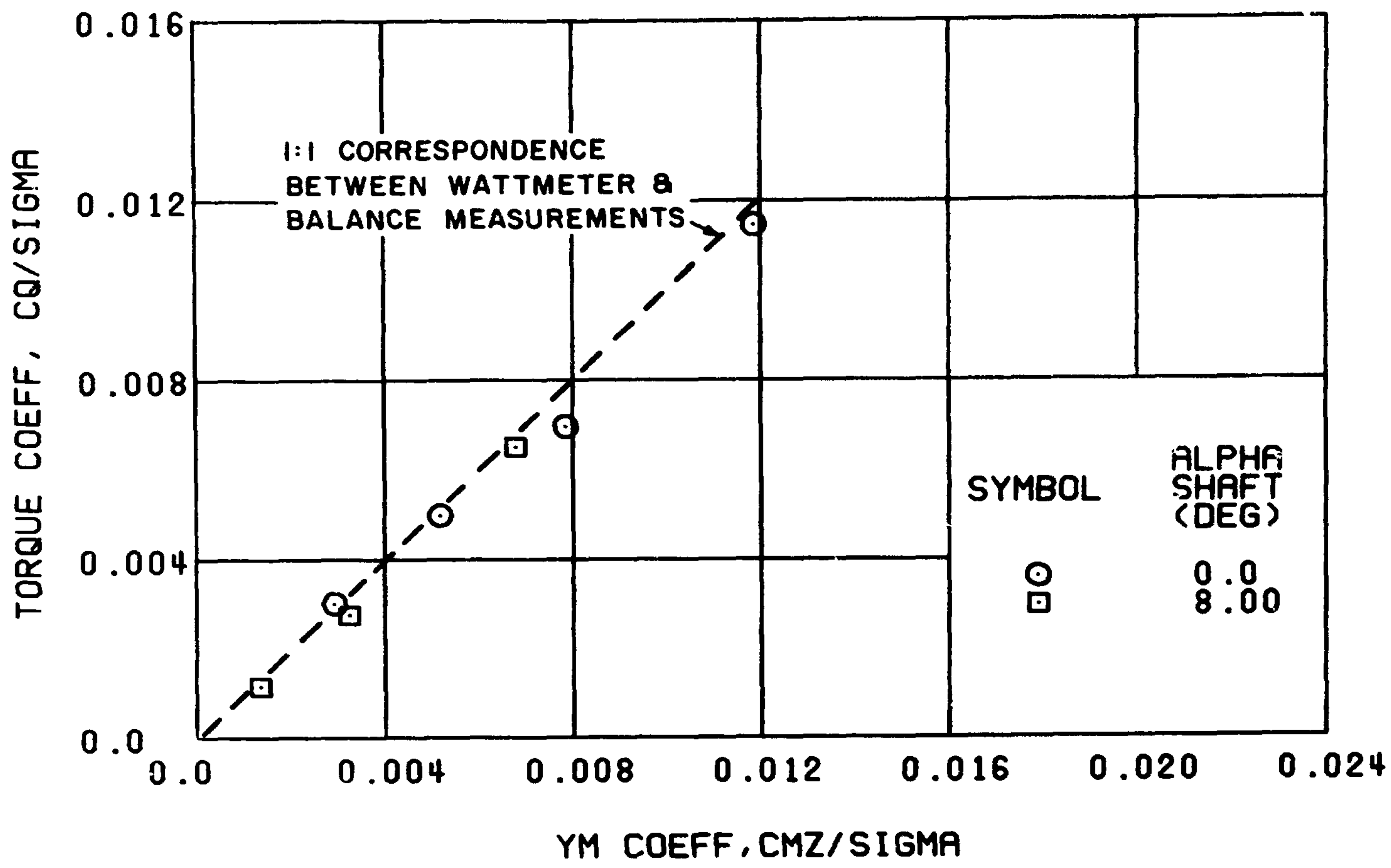

(I) WATTMETER VERSUS BALANCE YAWING MOMENT COEFFICIENT

Figure 36. Concluded.

$\mu = 0.21$ $B'_{1s} = 2$ Deg (Single-Rotor Configuration)

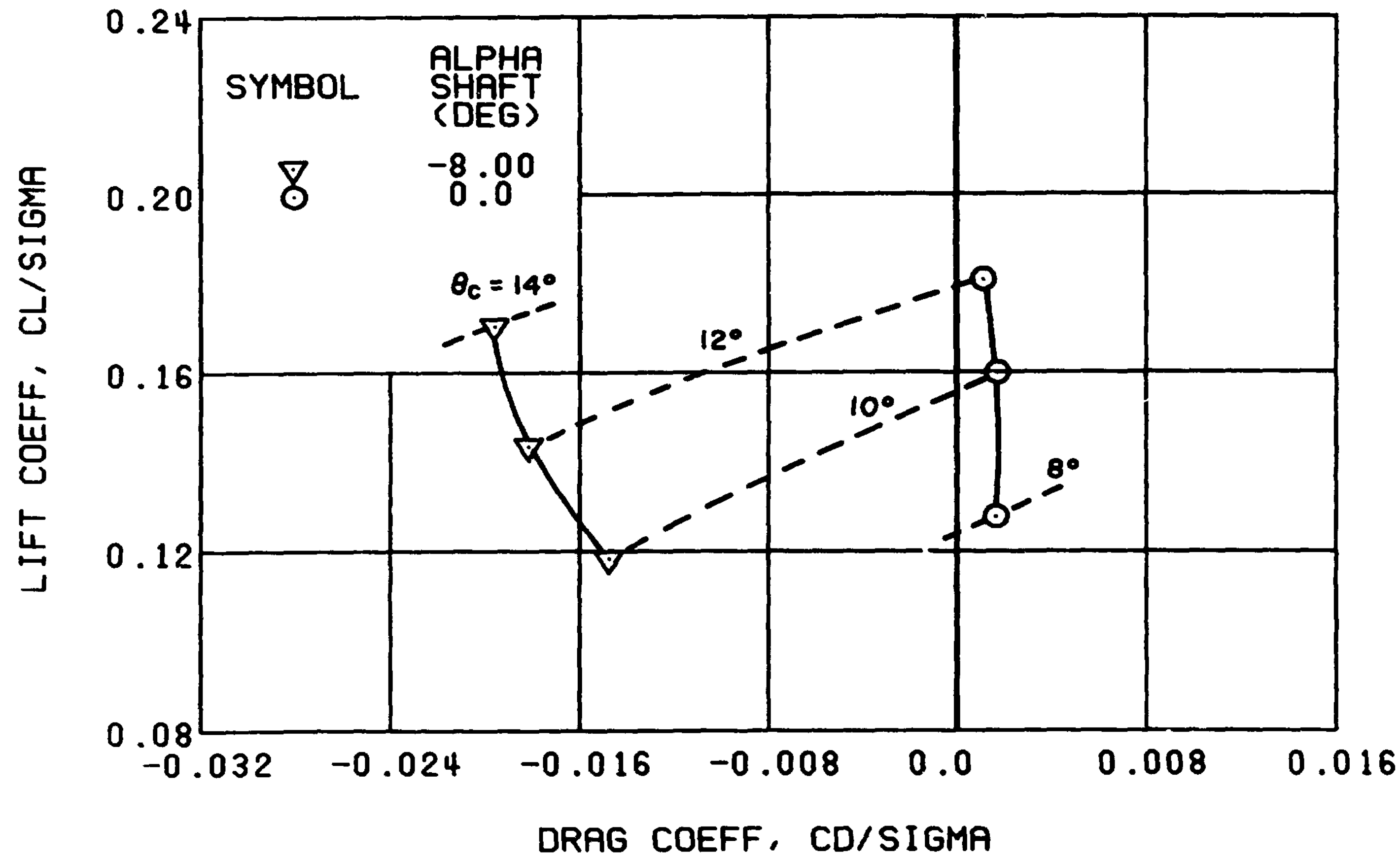

(a) DRAG COEFFICIENT

Figure 37. Performance Data at an Advance Ratio of 0.21 With the Lateral Displacement Control (B'_{1s}) Set at 4 Degrees (Single-Rotor Configuration).

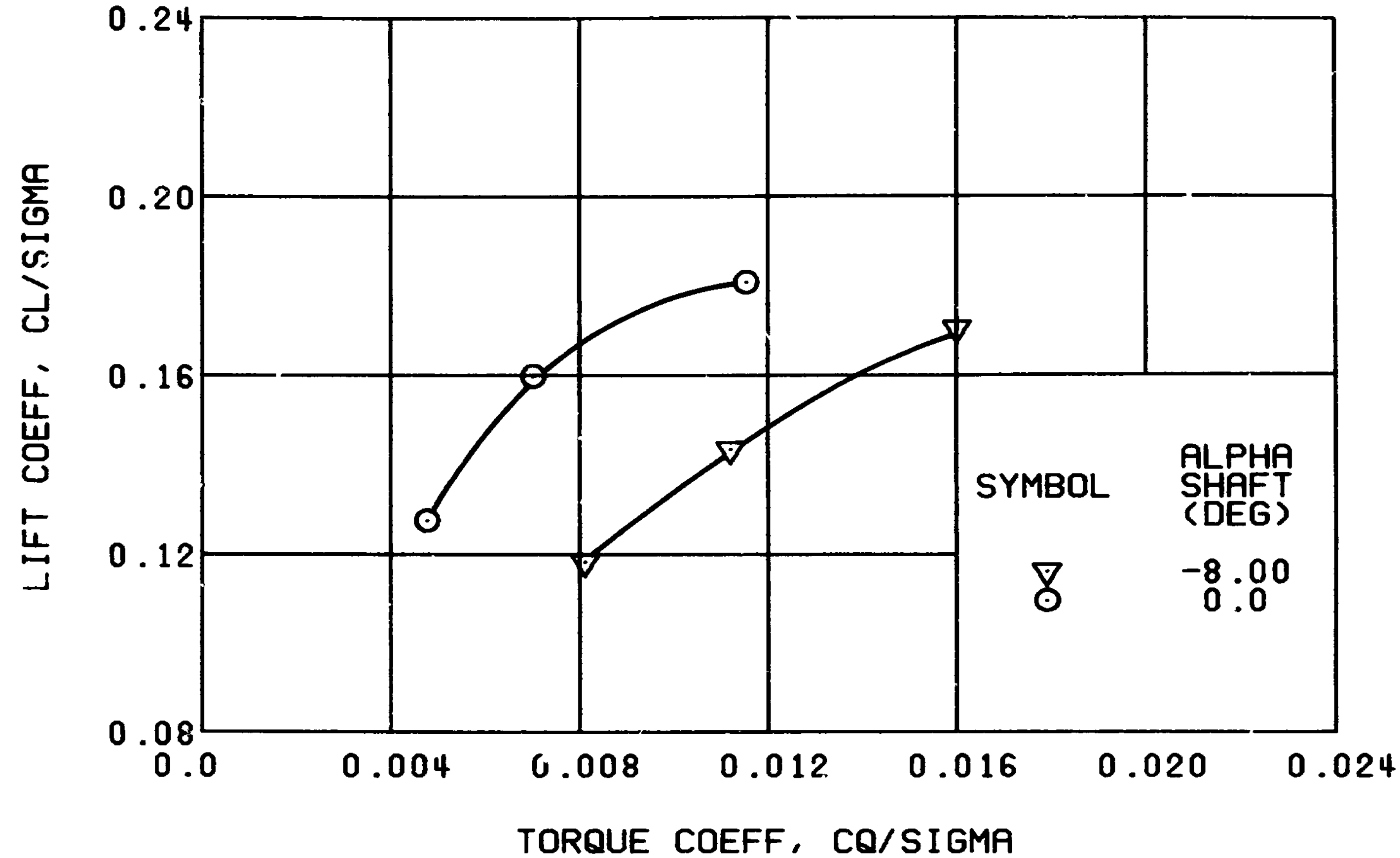

(b) TORQUE COEFFICIENT

Figure 37. **Continued.**
μ = 0.21 B'_{1s} = 4 Deg (Single-Rotor Configuration)

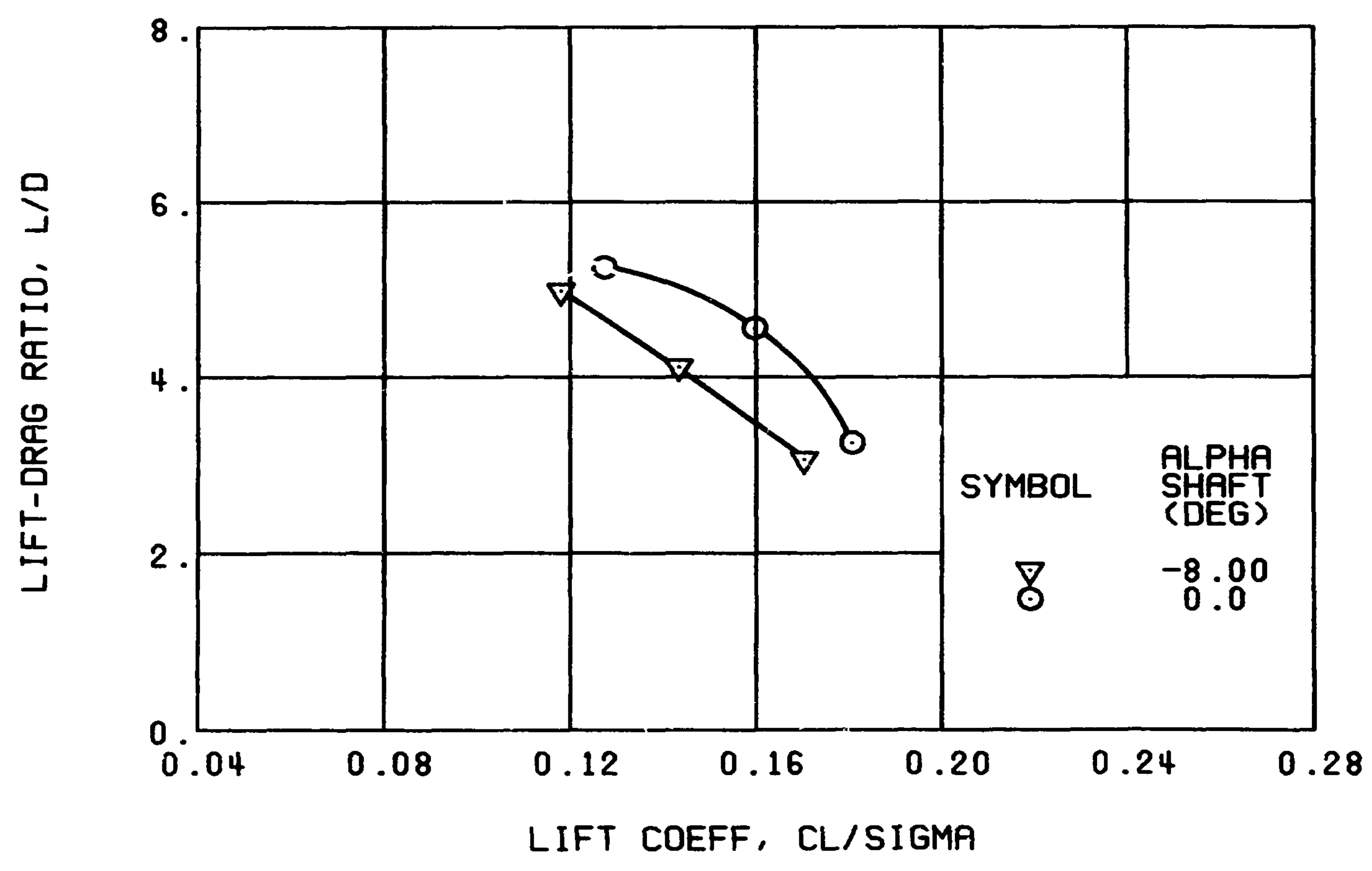

(c) LIFT-DRAG RATIO

Figure 37. Continued.
μ = 0.21 B'_{1s} = 4 Deg (Single-Rotor Configuration)

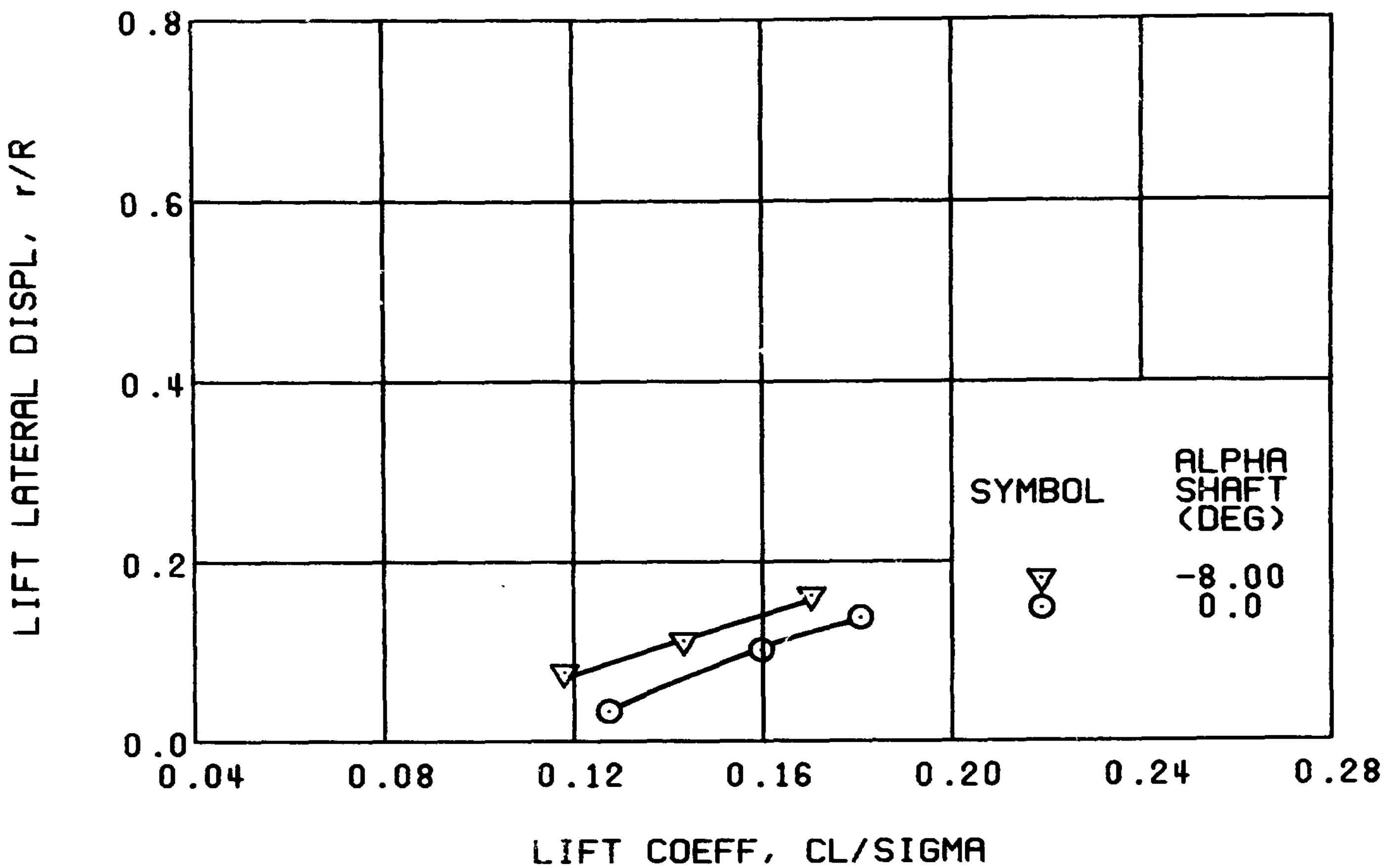

(d) LIFT LATERAL DISPLACEMENT

Figure 37. Continued.
$\mu = 0.21 \quad B'_{1s} = 4$ Deg (Single-Rotor Configuration)

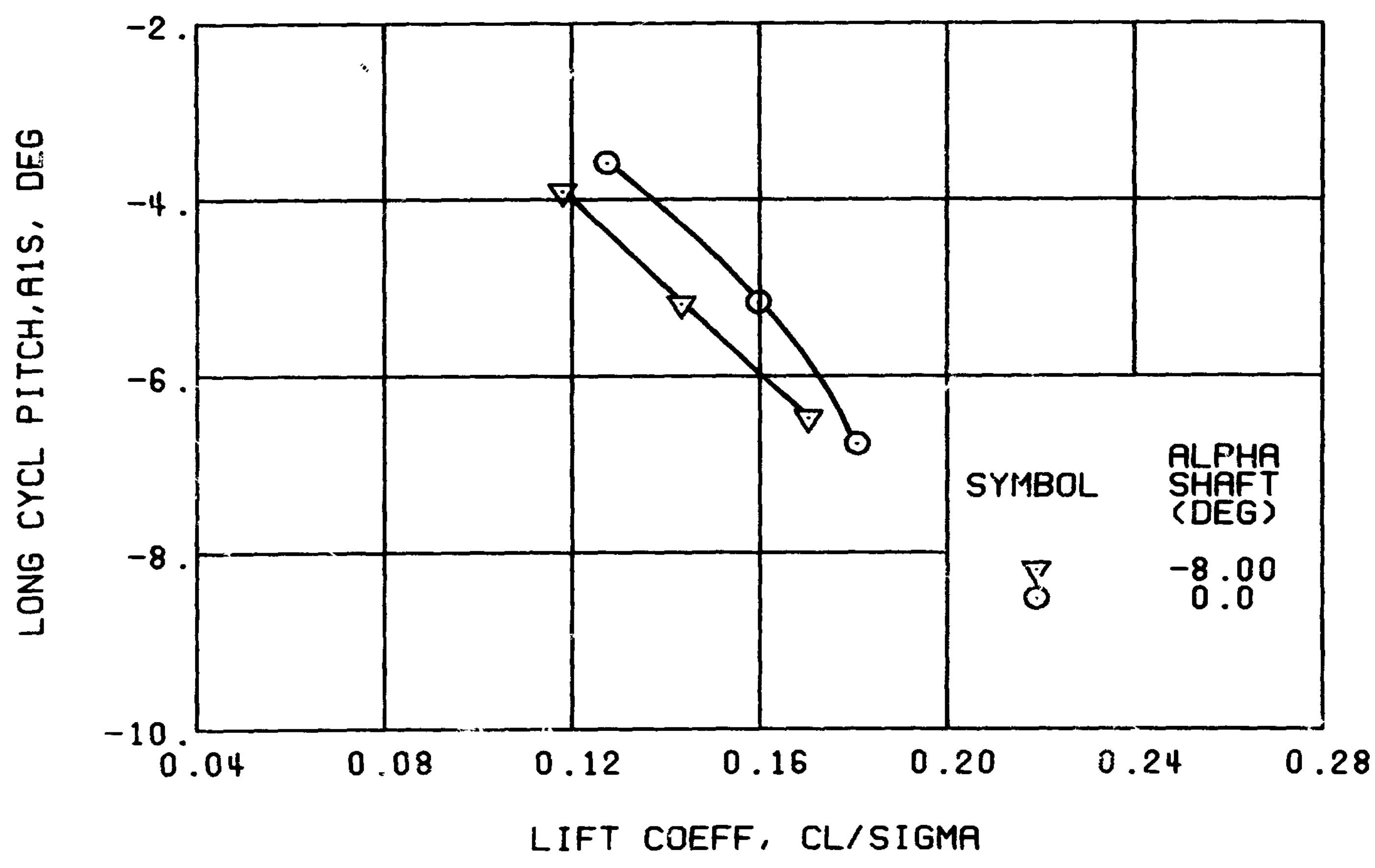

(e) LONGITUDINAL CYCLIC PITCH

Figure 37. Continued.
$\mu = 0.21$ $B'_{1s} = 4$ Deg (Single-Rotor Configuratio-)

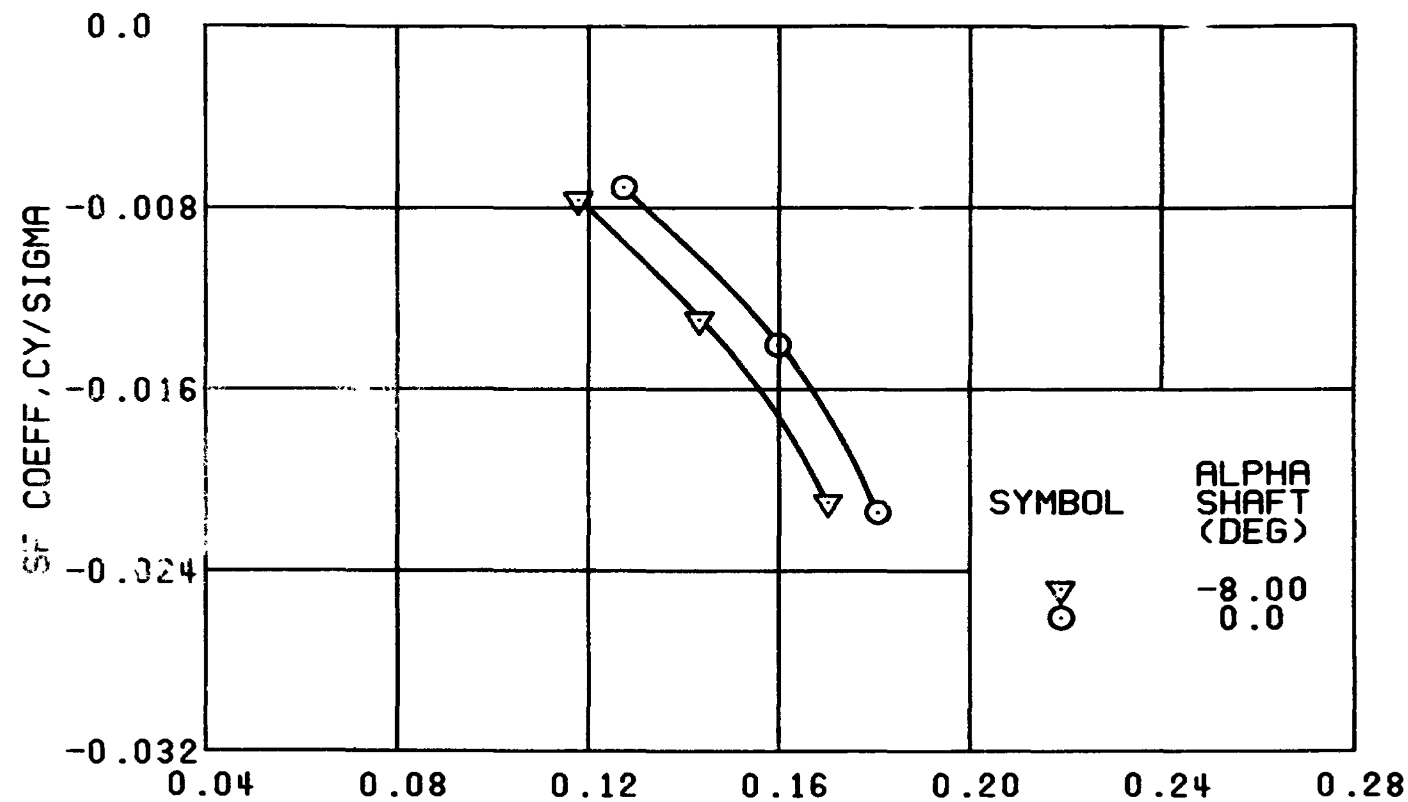

(f) SIDE FORCE COEFFICIENT

Figure 37. Continued.
μ = 0.21 B'_{1s} = 4 Deg (Single-Rotor Configuration)

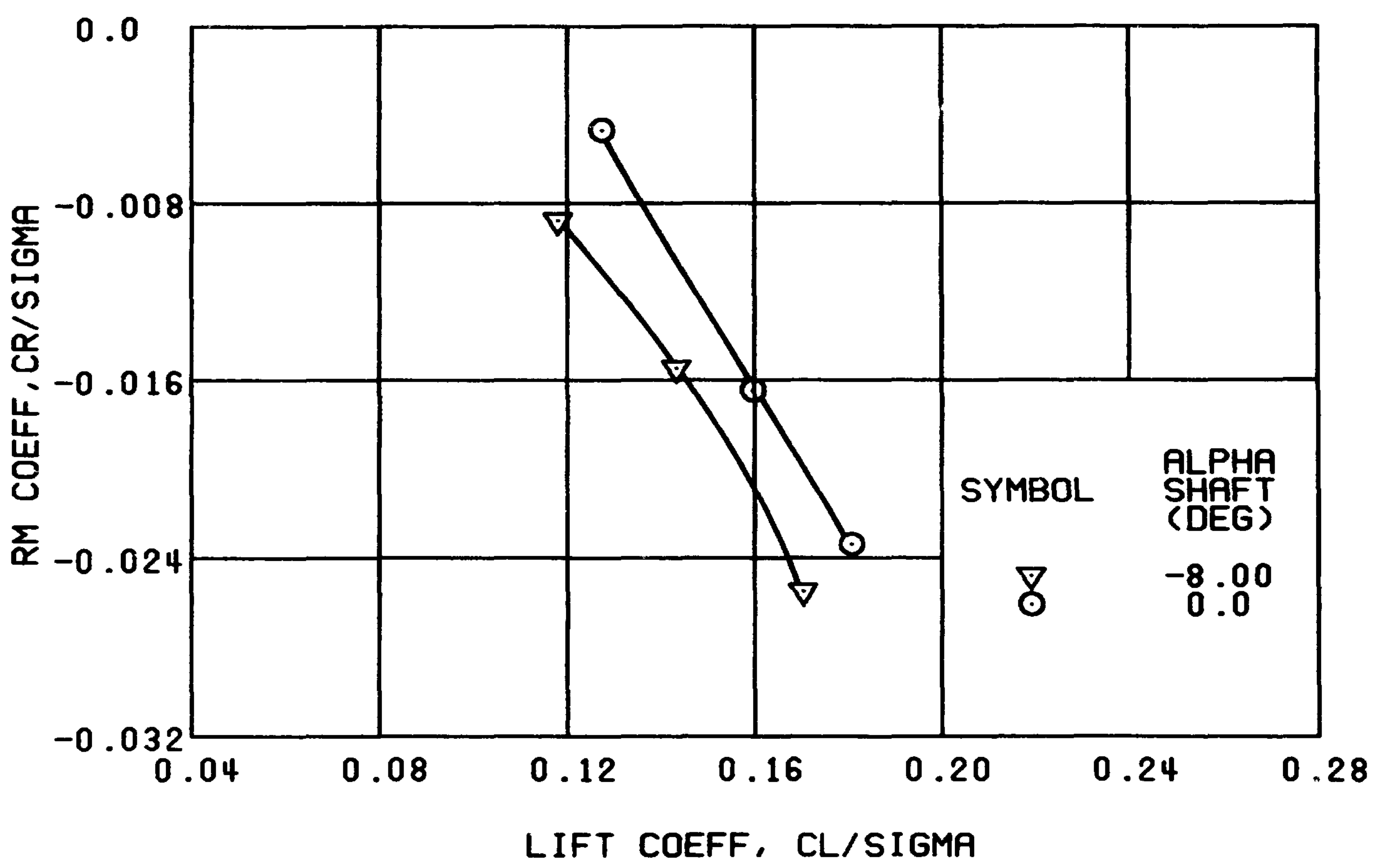

(g) ROLLING MOMENT COEFFICIENT

Figure 37. Continued.
$\mu = 0.21$ $B'_{1s} = 4$ Deg (Single-Rotor Configuration)

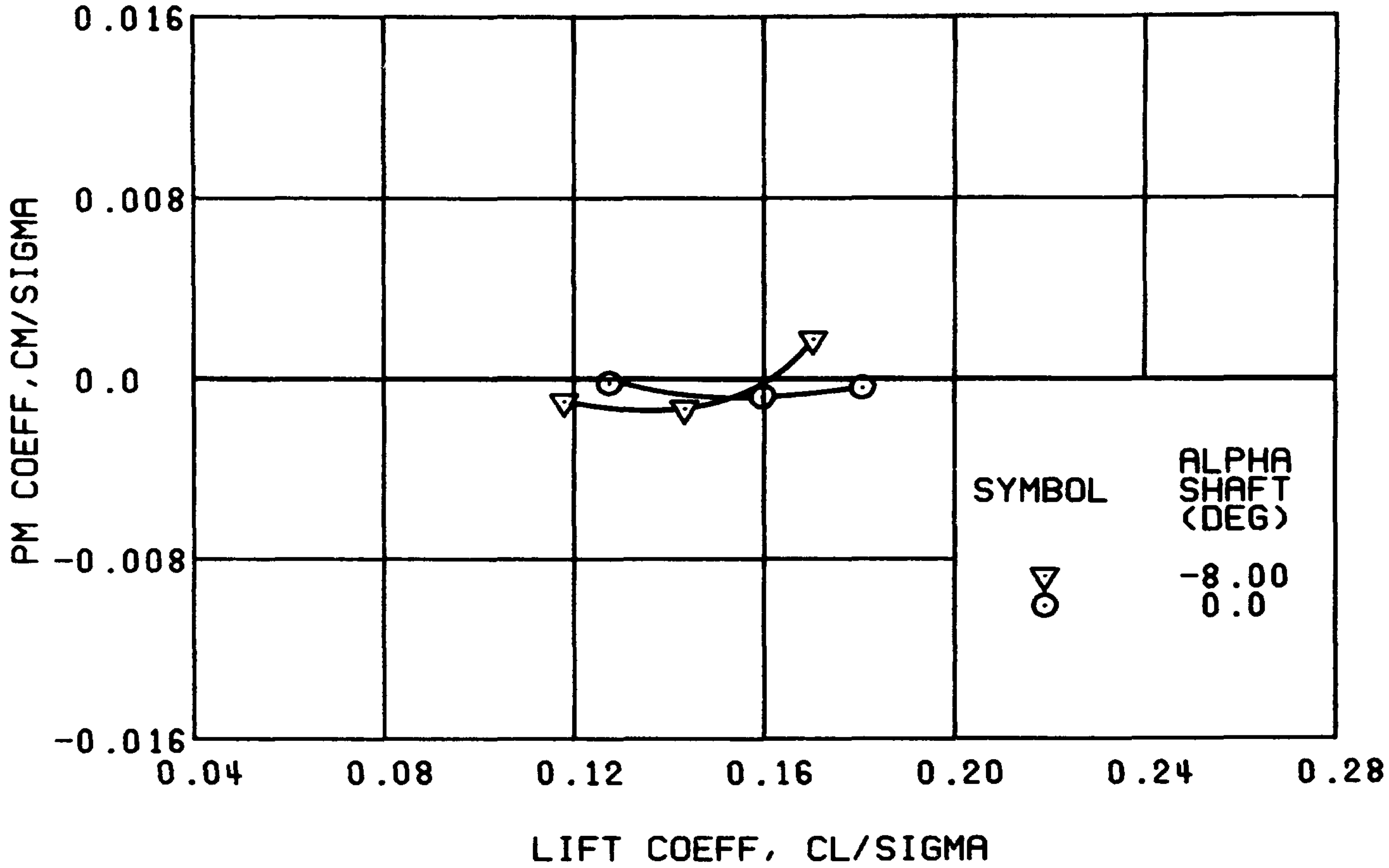

(h) PITCHING MOMENT COEFFICIENT

Figure 37. Continued.
$\mu = 0.21$ $B'_{1s} = 4$ Deg (Single-Rotor Configuration)

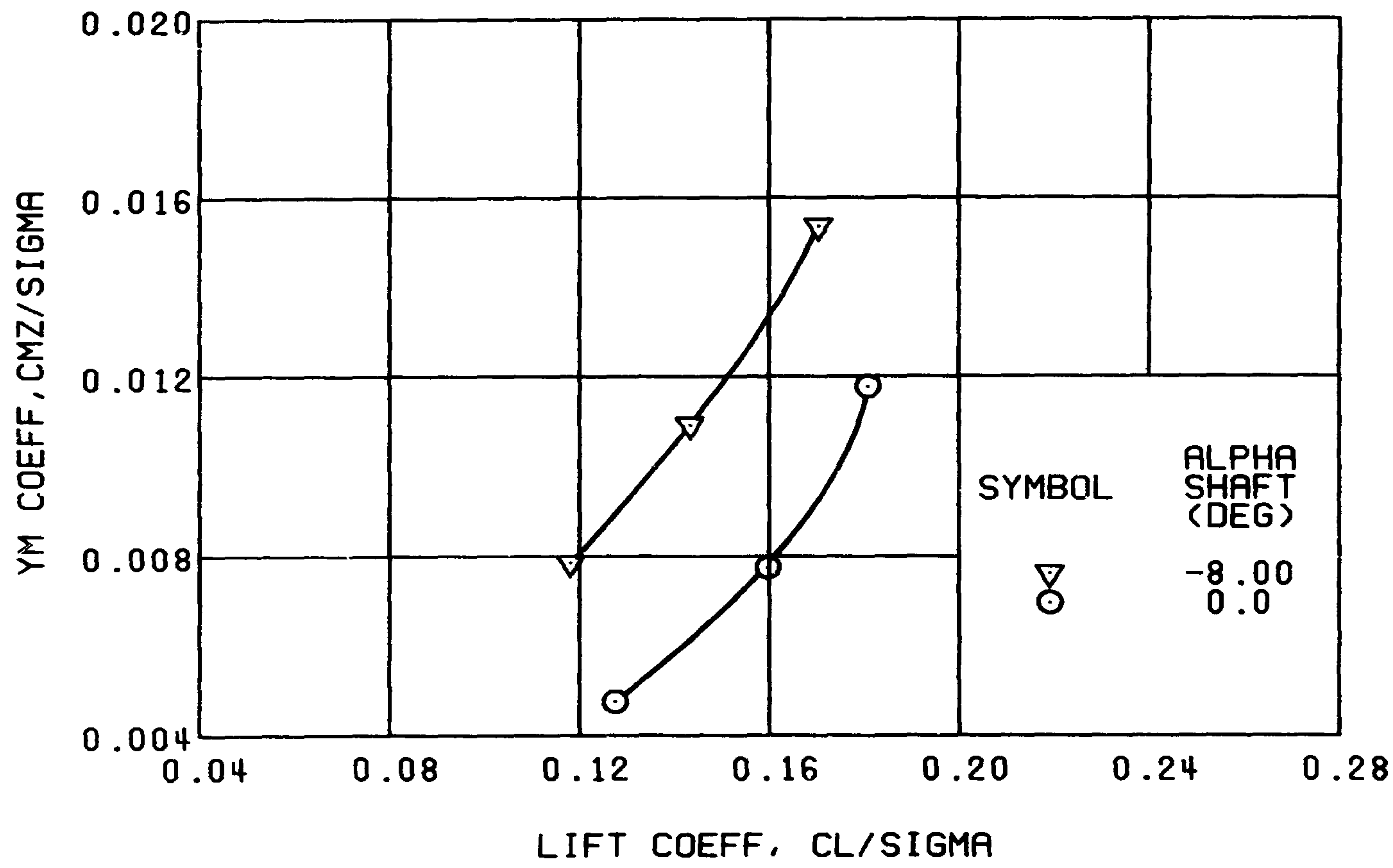

(i) YAWING MOMENT COEFFICIENT

Figure 37. **Continued.**
$\mu = 0.21$ $B'_{1s} = 4$ Deg (Single-Rotor Configuration)

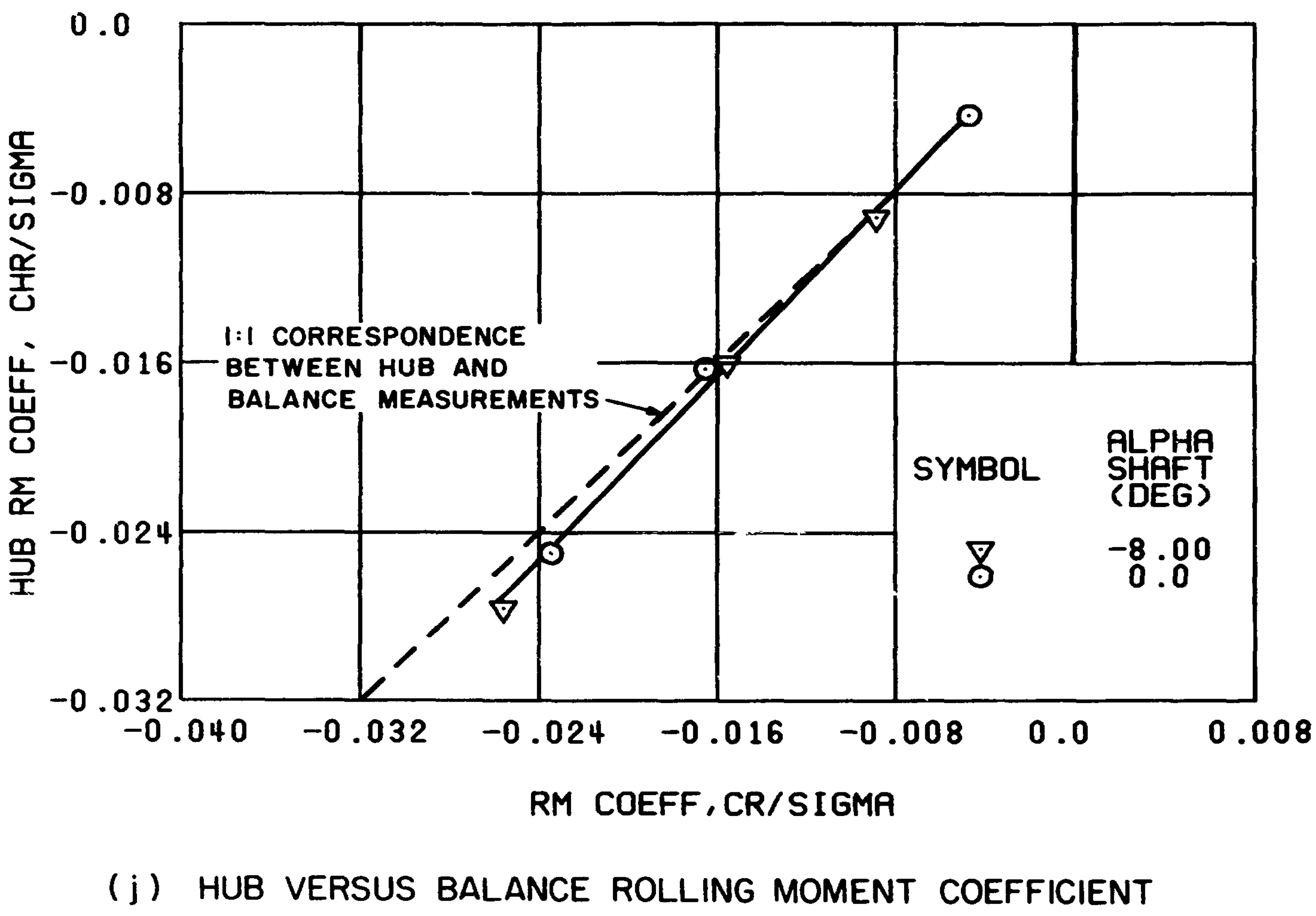

Figure 37. Continued.
$\mu = 0.21$ $B'_{1s} = 4$ Deg (Single-Rotor Configuration)

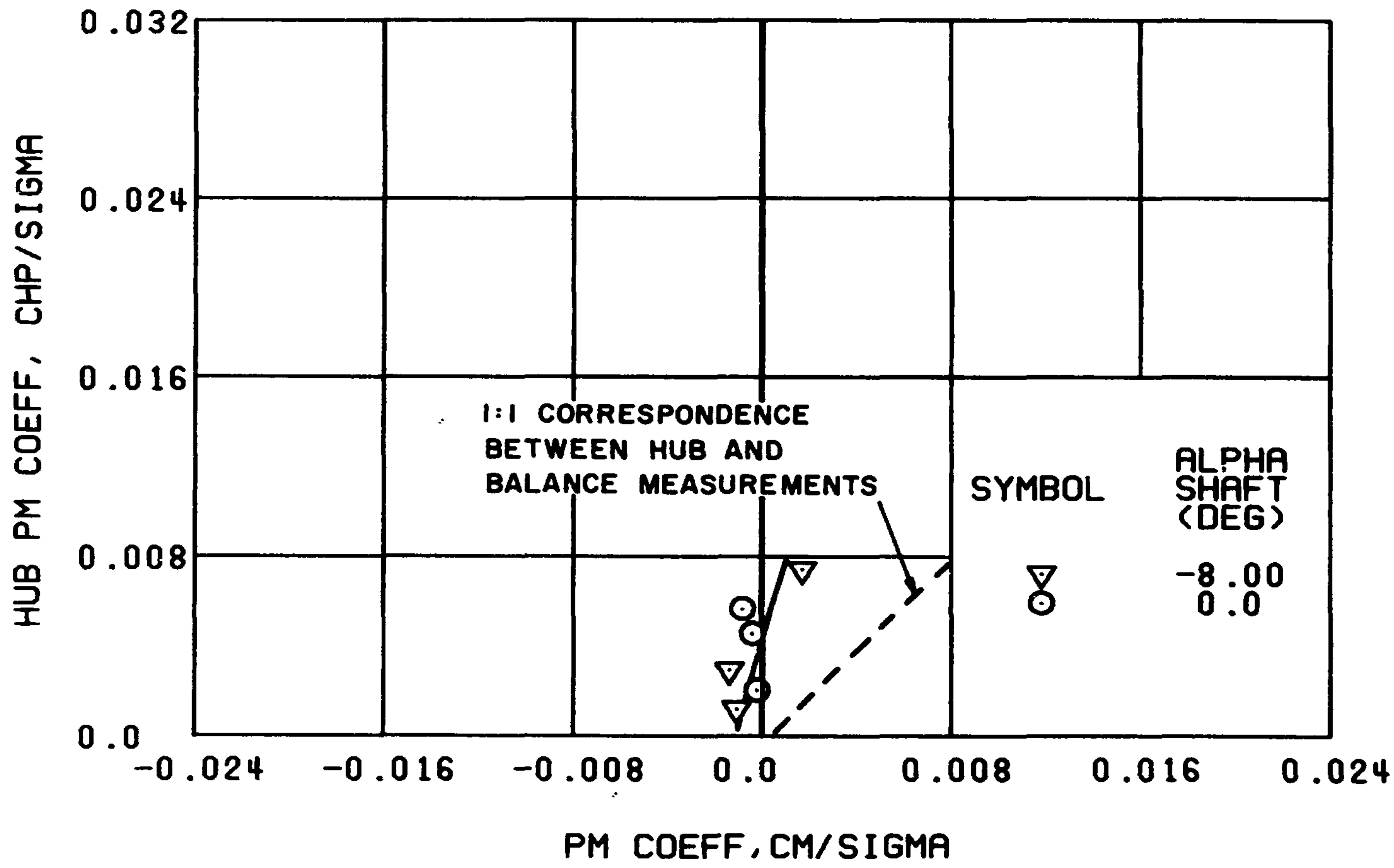

(k) HUB VERSUS BALANCE PITCHING MOMENT COEFFICIENT

Figure 37. Continued.
μ = 0.21 B'_{1s} = 4 Deg (Single-Rotor Configuration)

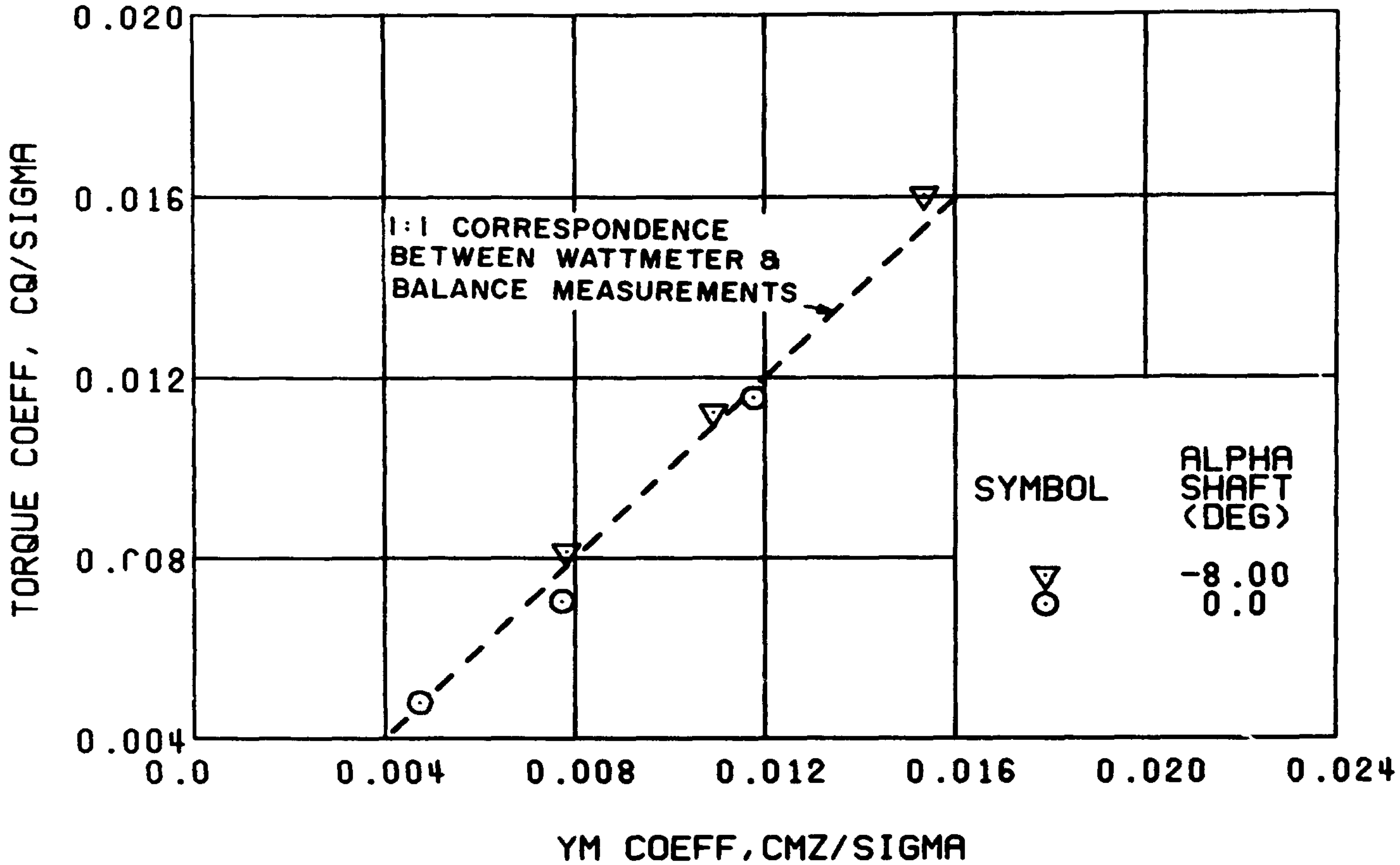

(I) WATTMETER VERSUS BALANCE YAWING MOMENT COEFFICIENT

Figure 37. Concluded.

$\mu = 0.21$ $B'_{1s} = 4$ Deg (Single-Rotor Configuration)

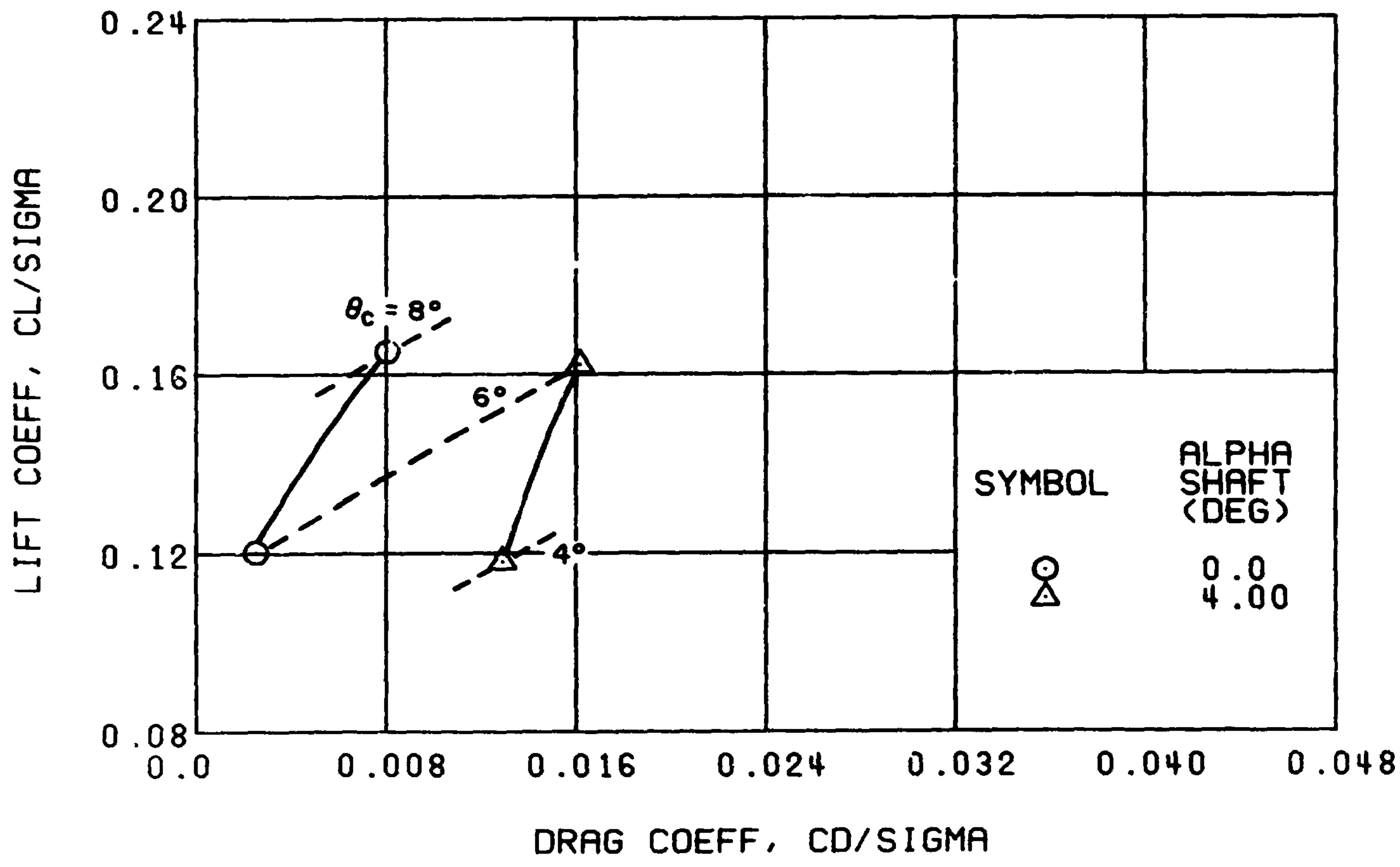

(a) DRAG COEFFICIENT

Figure 38. Performance Data at an Advance Ratio of 0.35 With the Lateral Displacement Control (B'_{1s}) Set at 2 Degrees (Single-Rotor Configuration).

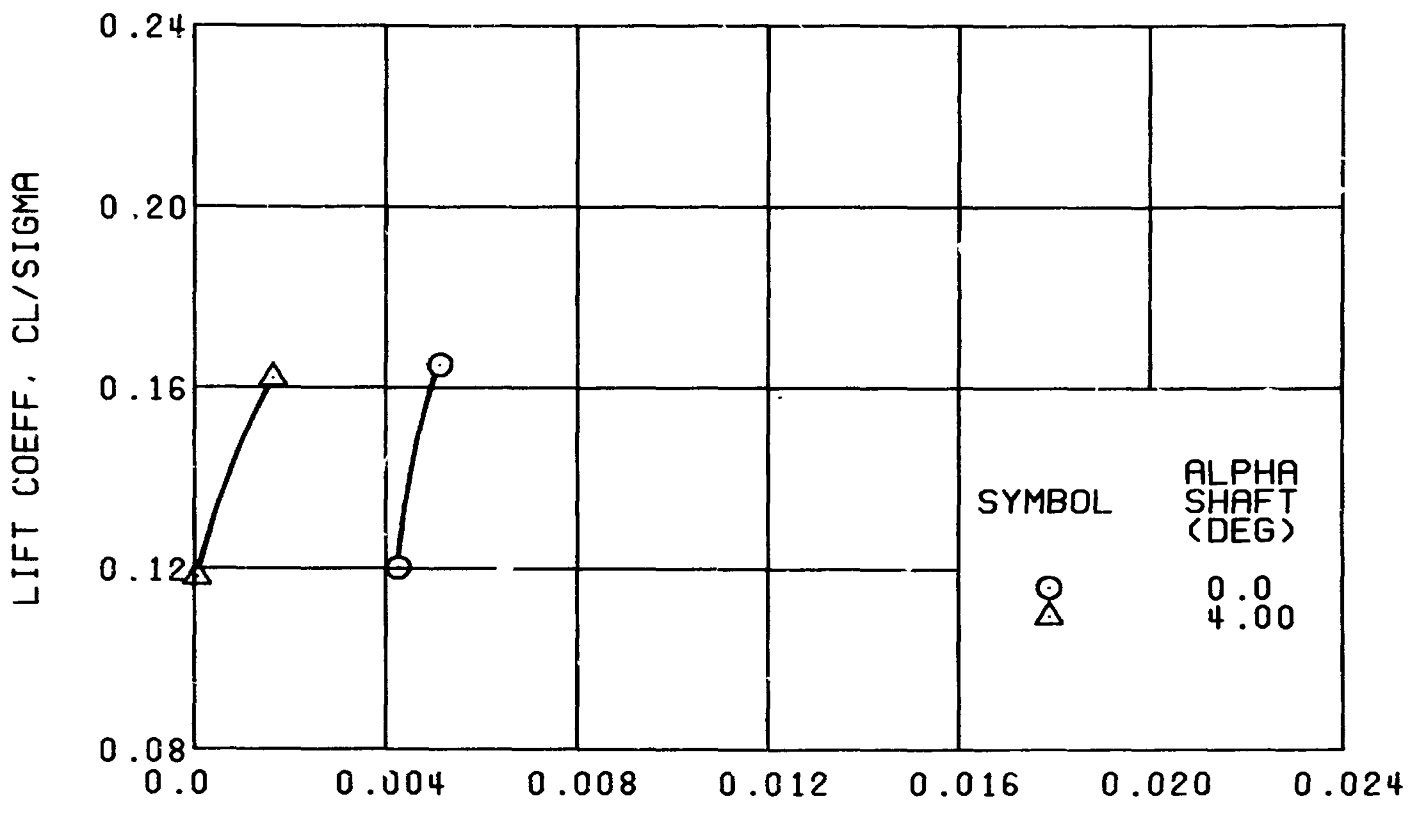

(b) TORQUE COEFFICIENT

Figure 38. Continued.
$\mu = 0.35$ $B'_{1s} = 2$ Deg (Single-Rotor Configuration)

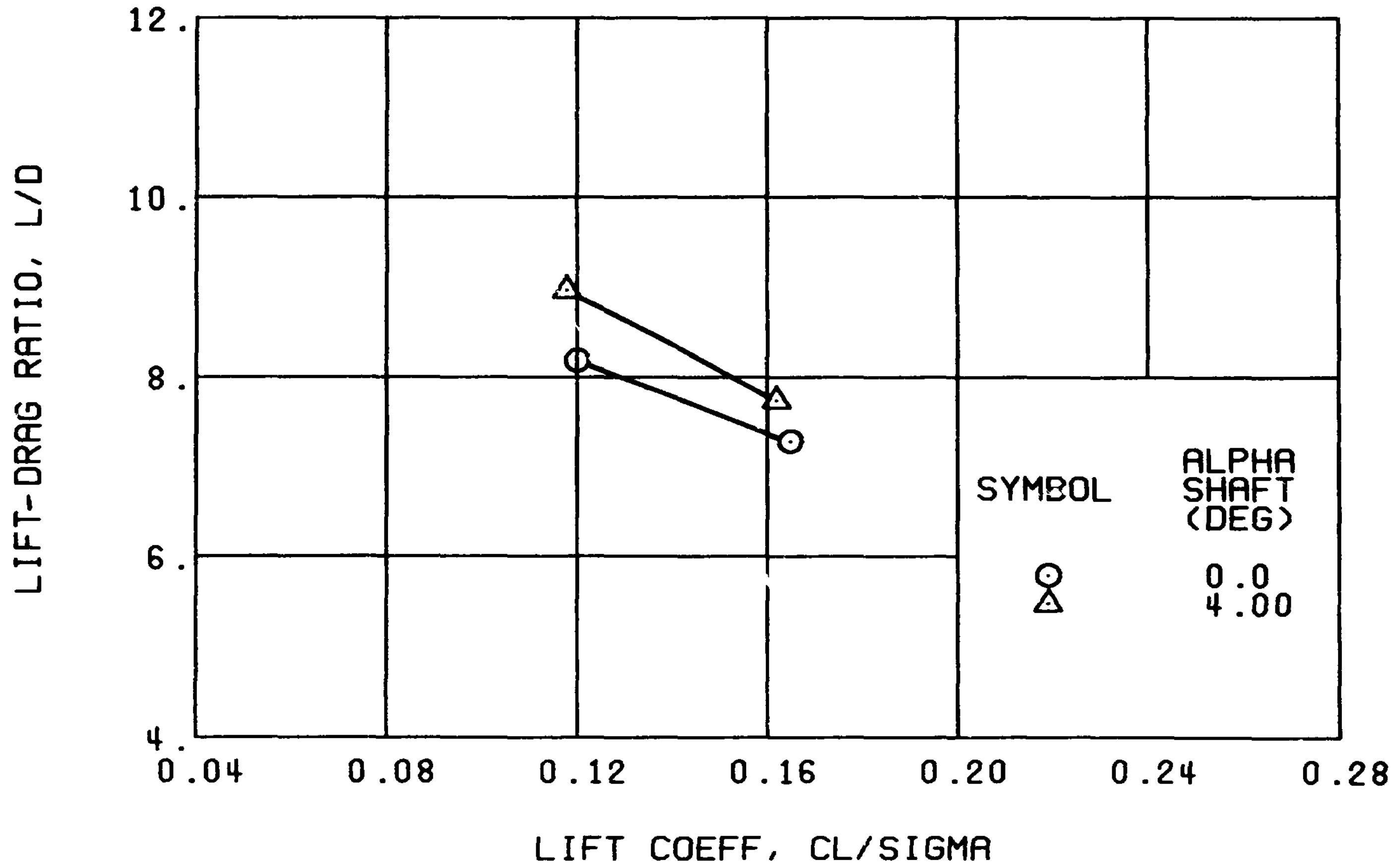

(c) LIFT-DRAG RATIO

Figure 38. Continued.
$\mu = 0.35 \quad B'_{1s} = 2$ Deg (Single-Rotor Configuration)

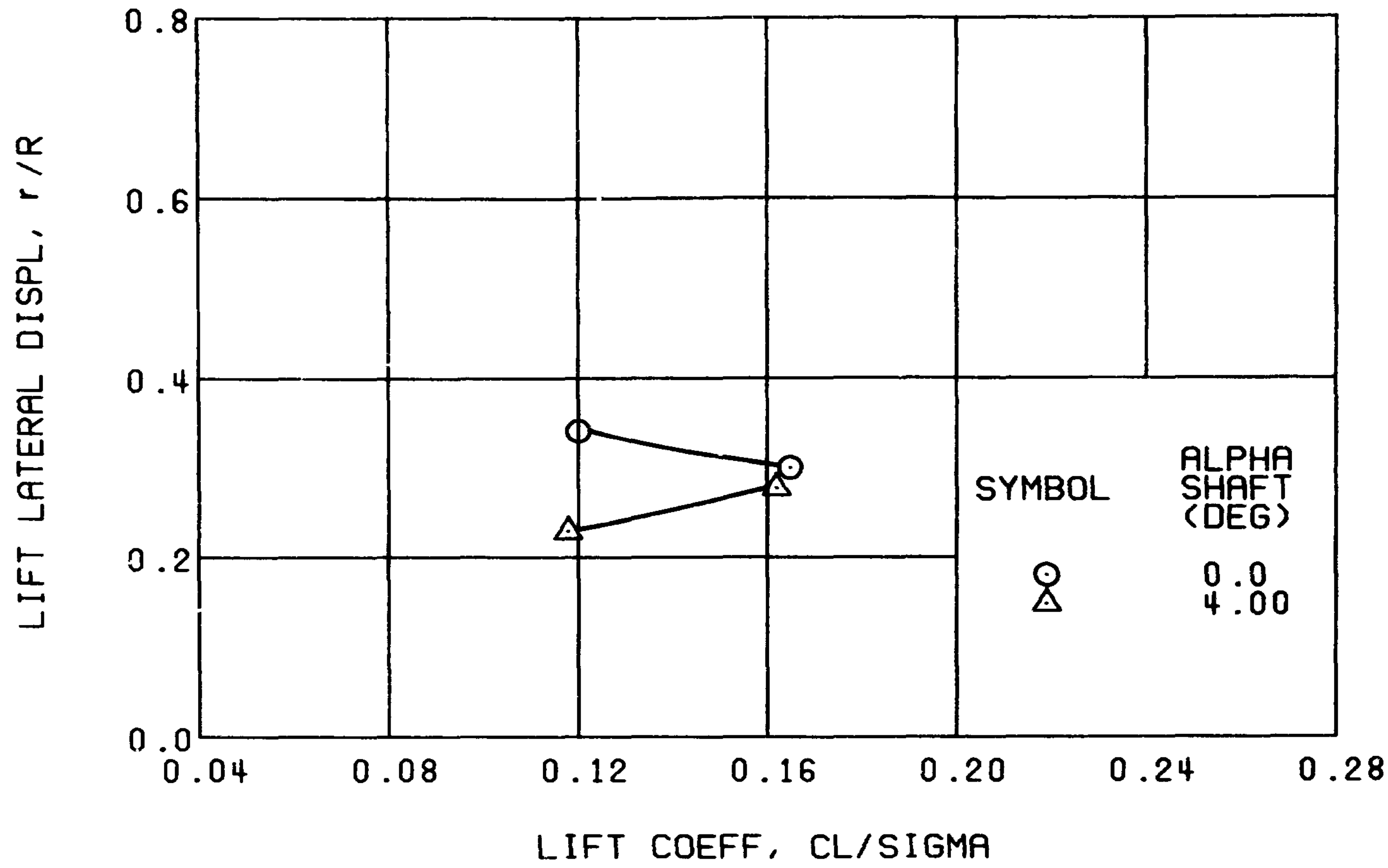

(d) LIFT LATERAL DISPLACEMENT

Figure 38. **Continued.**
$\mu = 0.35 \quad B'_{1s} = 2$ Deg (Single-Rotor Configuration)

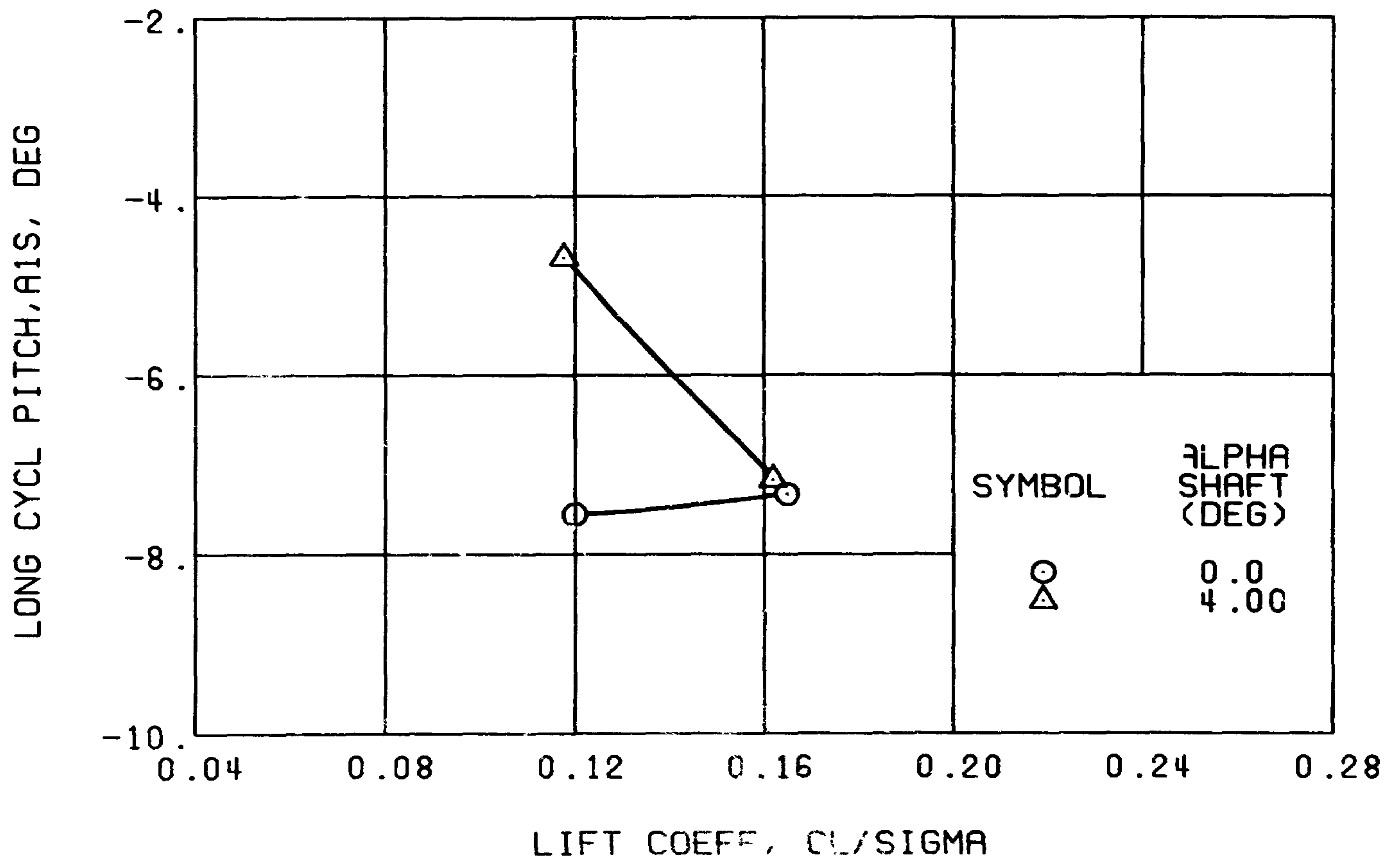

(e) LONGITUDINAL CYCLIC PITCH

Figure 38. Continued.
μ = 0.35 B'_{1s} = 2 Deg (Single-Rotor Configuration)

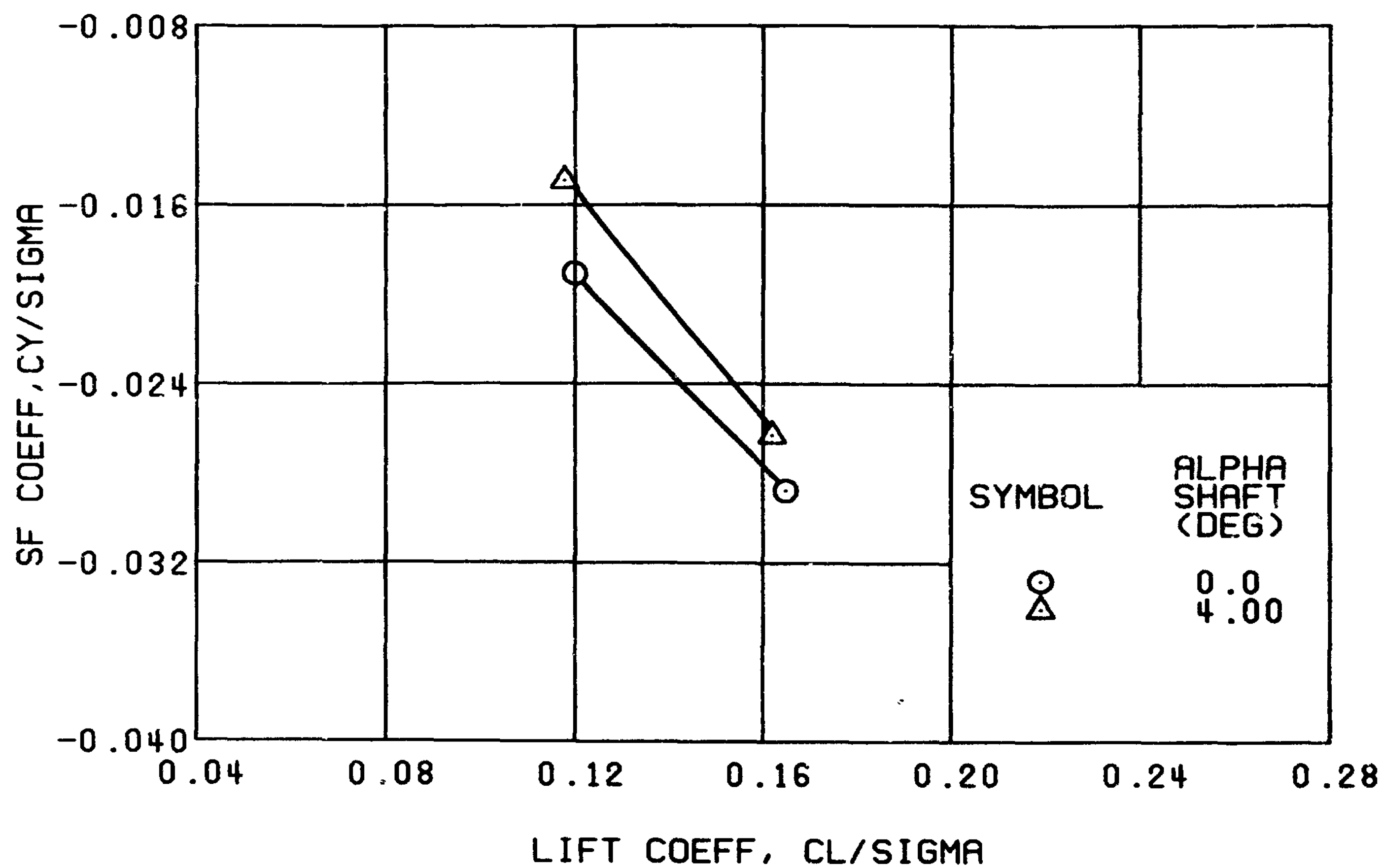

(f) SIDE FORCES COEFFICIENT

Figure 38. Continued.
μ = 0.35 B'_{1s} = 2 Deg (Single-Rotor Configuration)

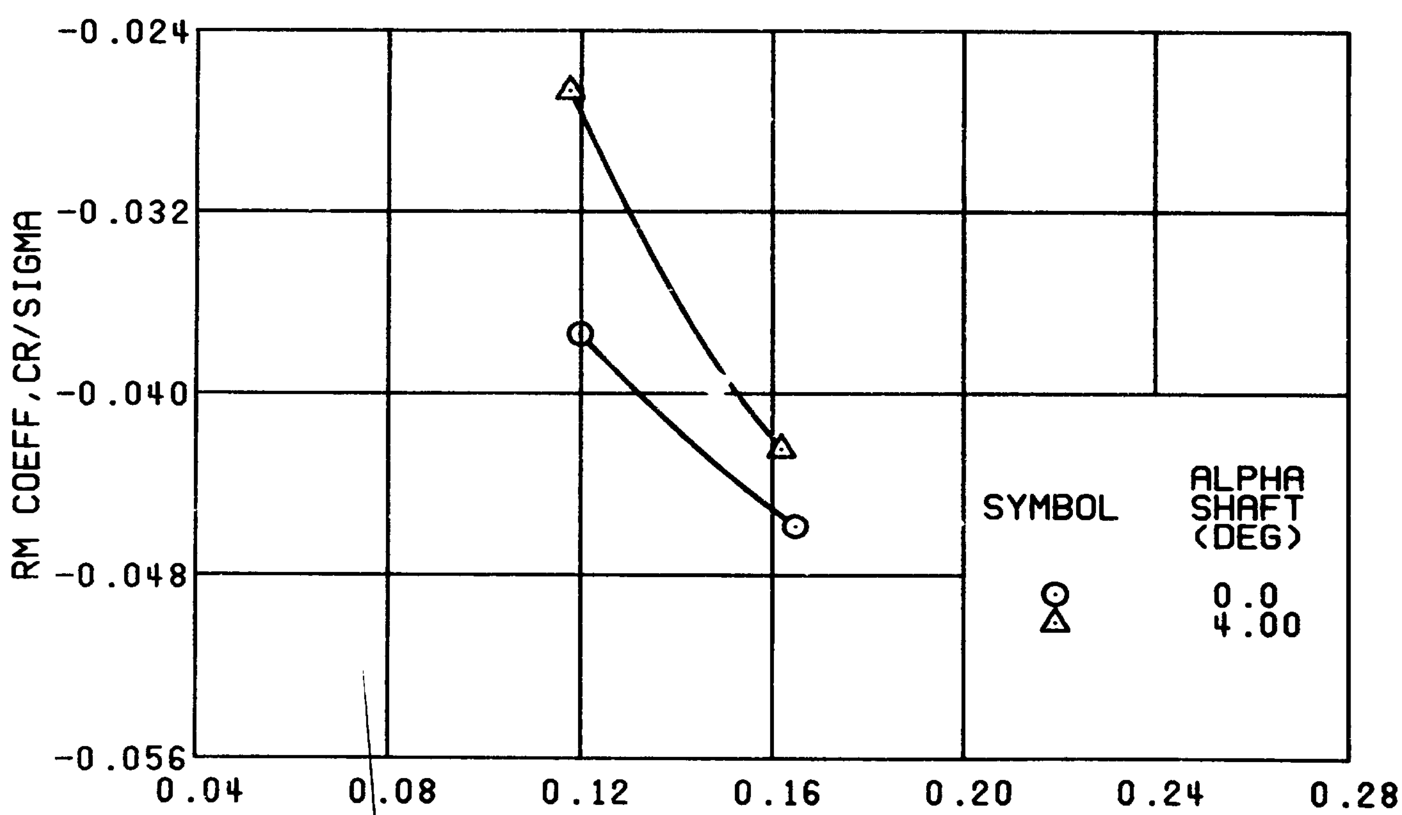

(g) ROLLING MOMENT COEFFICIENT

Figure 38. Continued.
$\mu = 0.35$ $B'_{1s} = 2$ Deg (Single-Rotor Configuration)

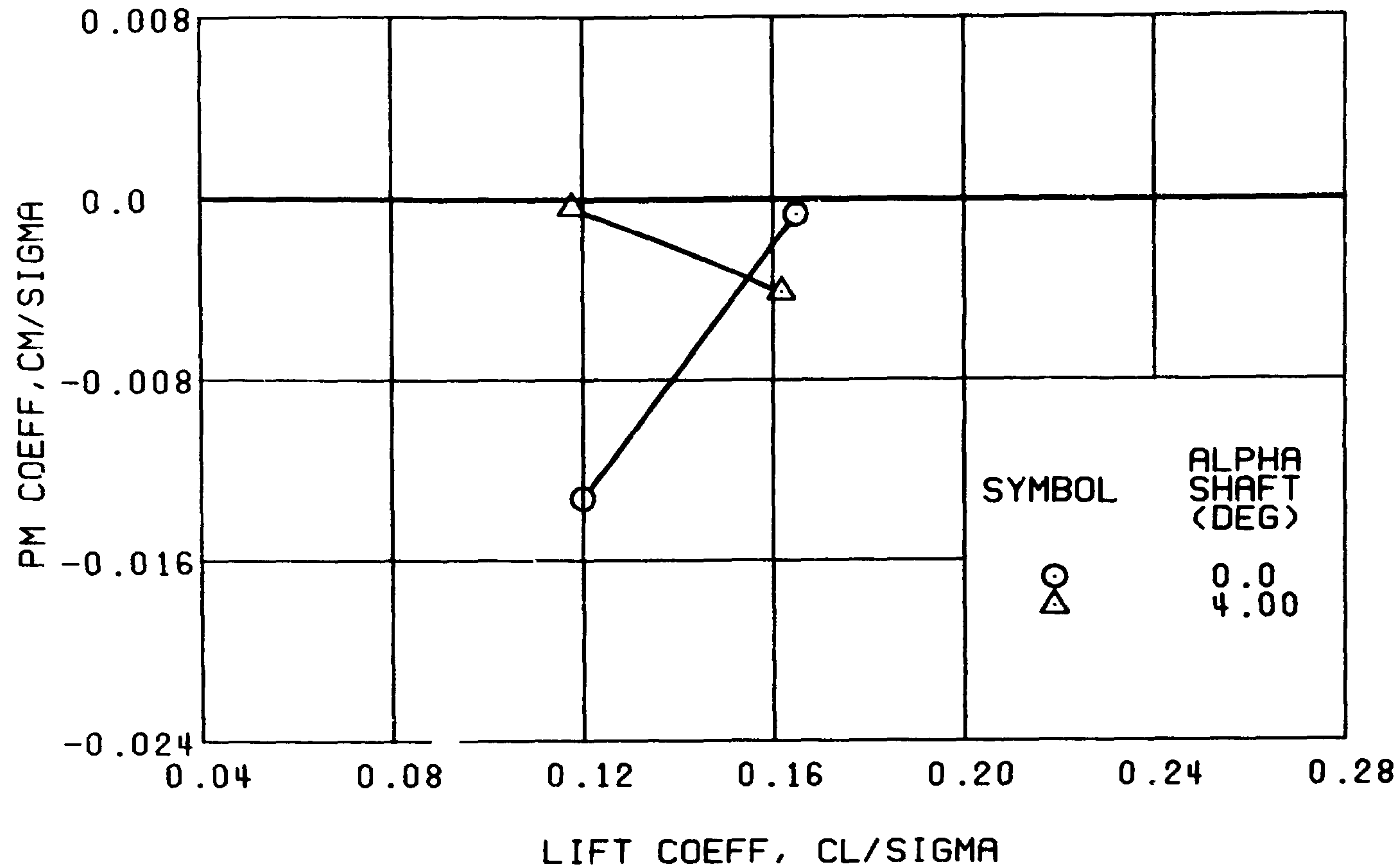

(h) PITCHING MOMENT COEFFICIENT

Figure 38. Continued.
$\mu = 0.35$ $B'_{1s} = 2$ Deg (Single-Rotor Configuration)

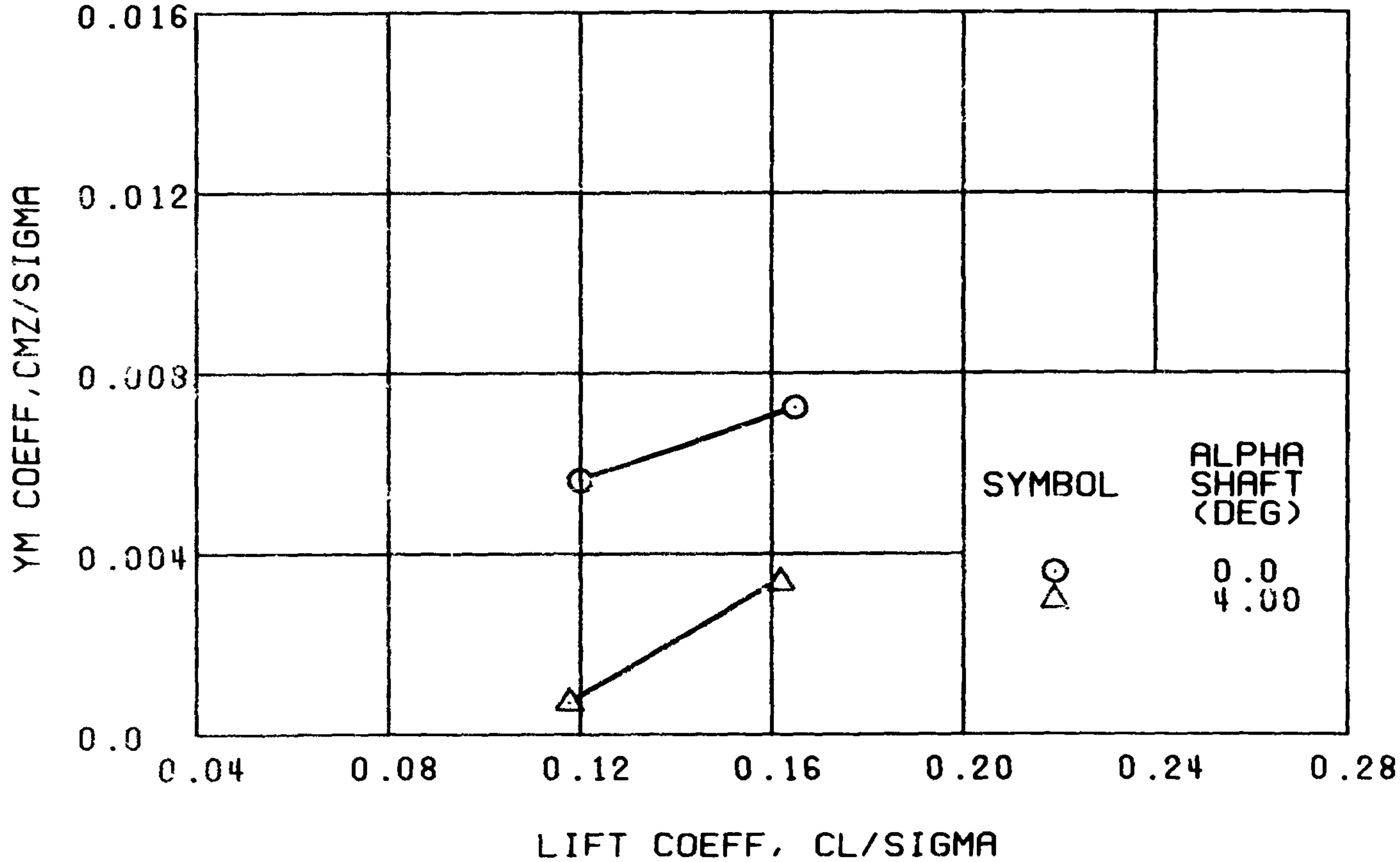

(i) YAWING MOMENT COEFFICIENT

Figure 38. Continued.
$\mu = 0.35$ $B'_{1s} = 2$ Deg (Single-Rotor Configuration)

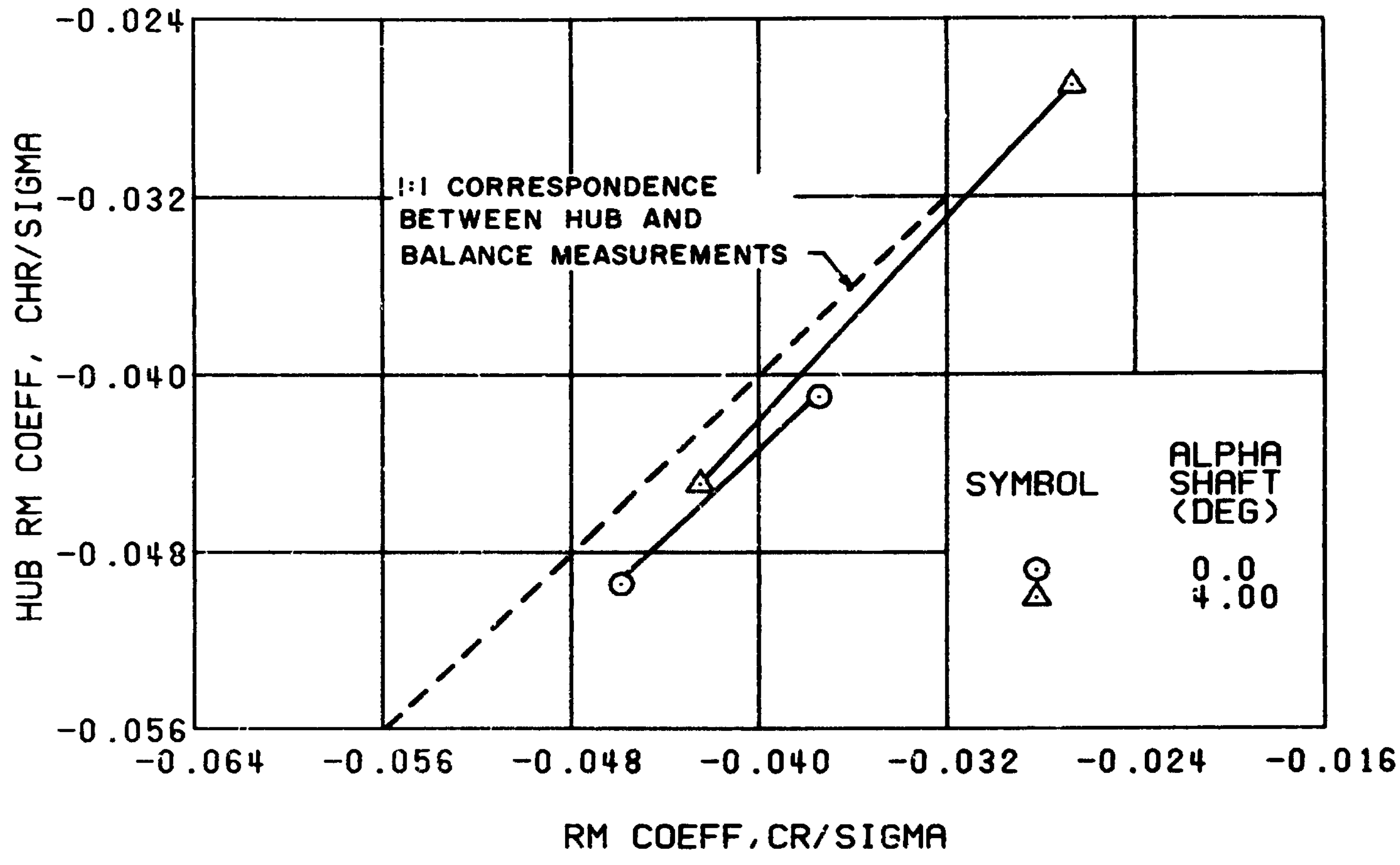

(j) HUB VERSUS BALANCE ROLLING MOMENT COEFFICIENT

Figure 38. Continued.
$\mu = 0.35$ $B'_{1s} = 2$ Deg (Single-Rotor Configuration)

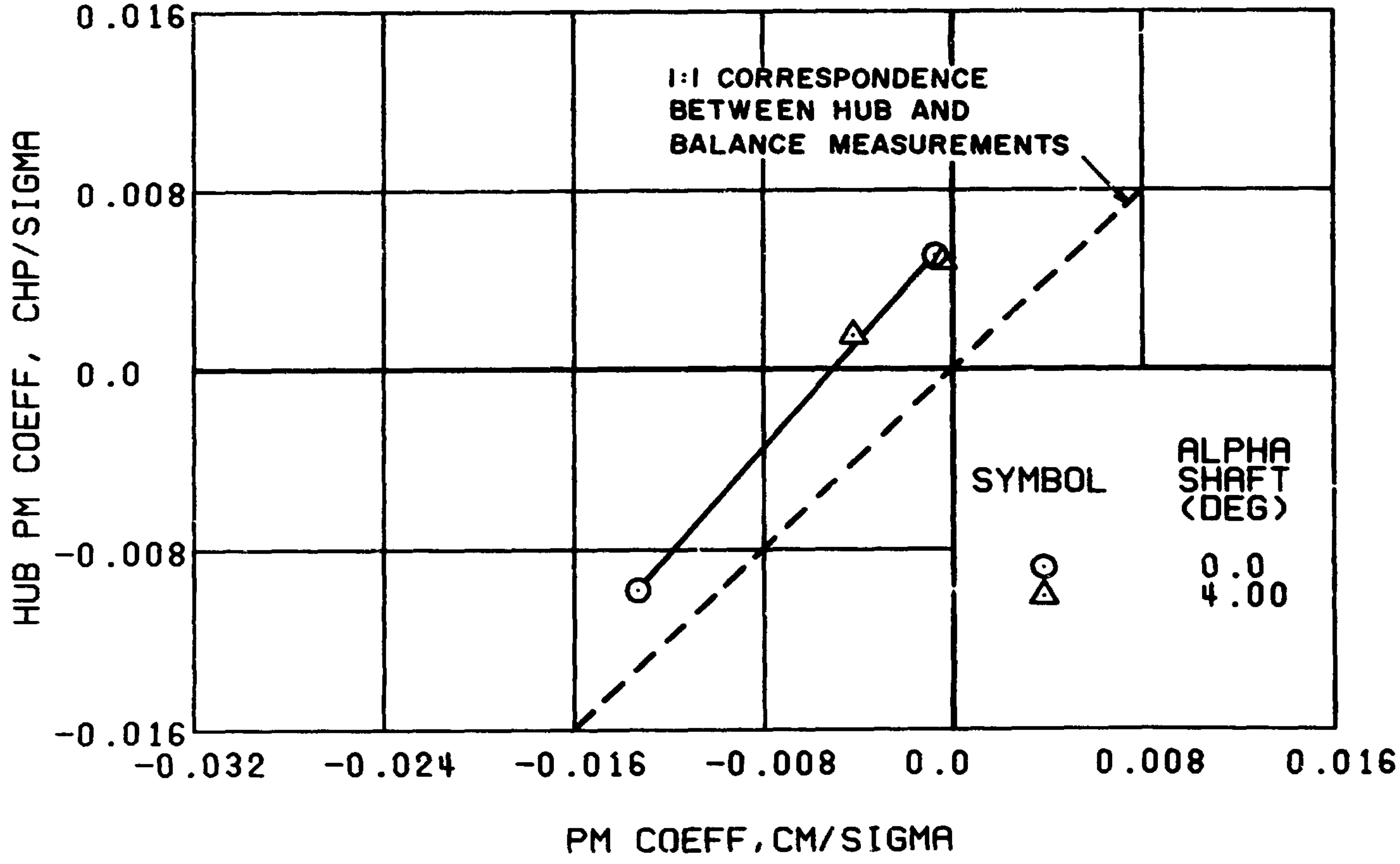

(k) HUB VERSUS BALANCE PITCHING MOMENT COEFFICIENT

Figure 38. Continued.
$\mu = 0.35$ $B'_{1s} = 2$ Deg (Single-Rotor Configuration)

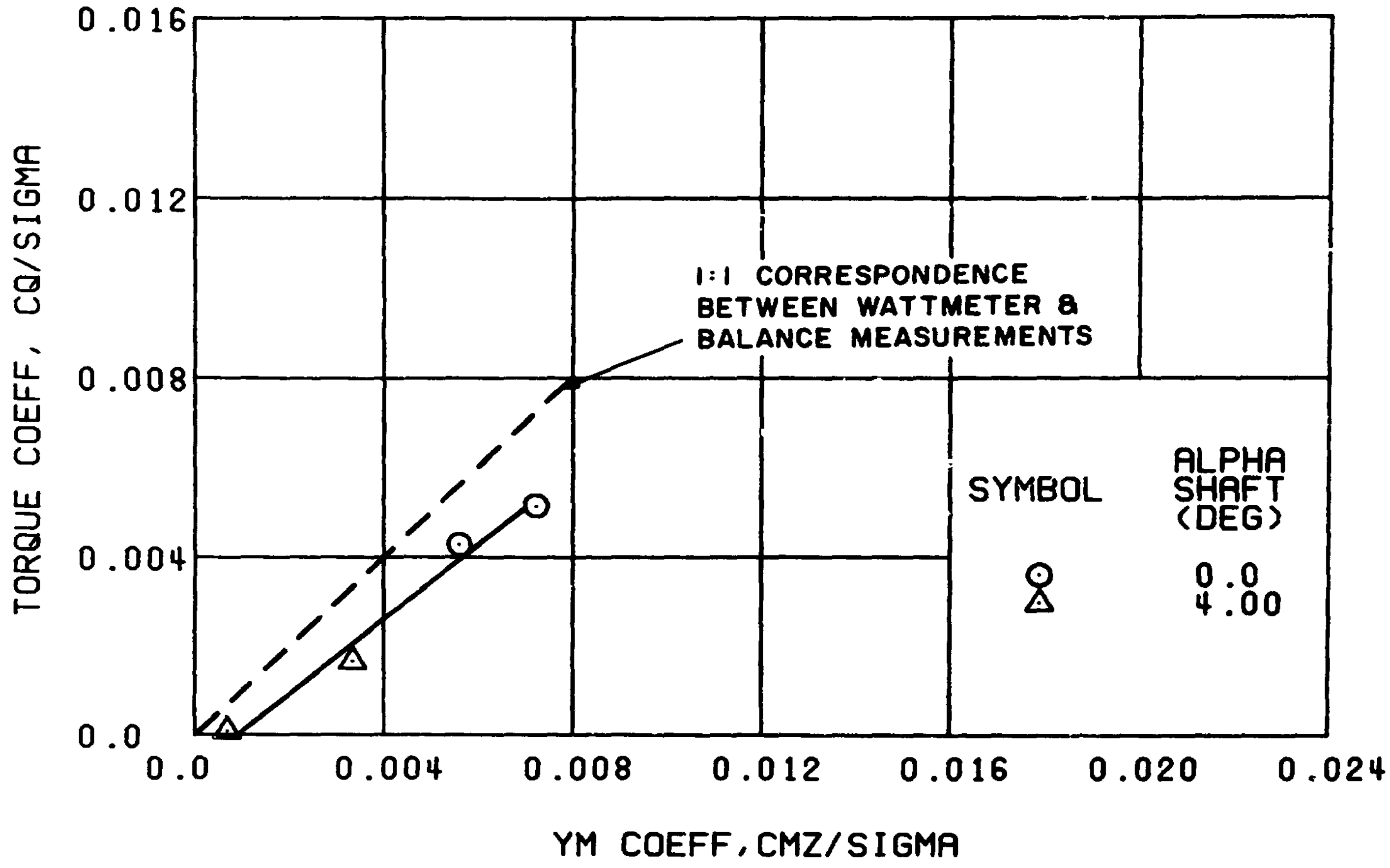

(I) WATTMETER VERSUS BALANCE YAWING MOMENT COEFFICIENT

Figure 38. **Concluded.**

$\mu = 0.35 \quad B'_{1s} = 2$ Deg (Single-Rotor Configuration)

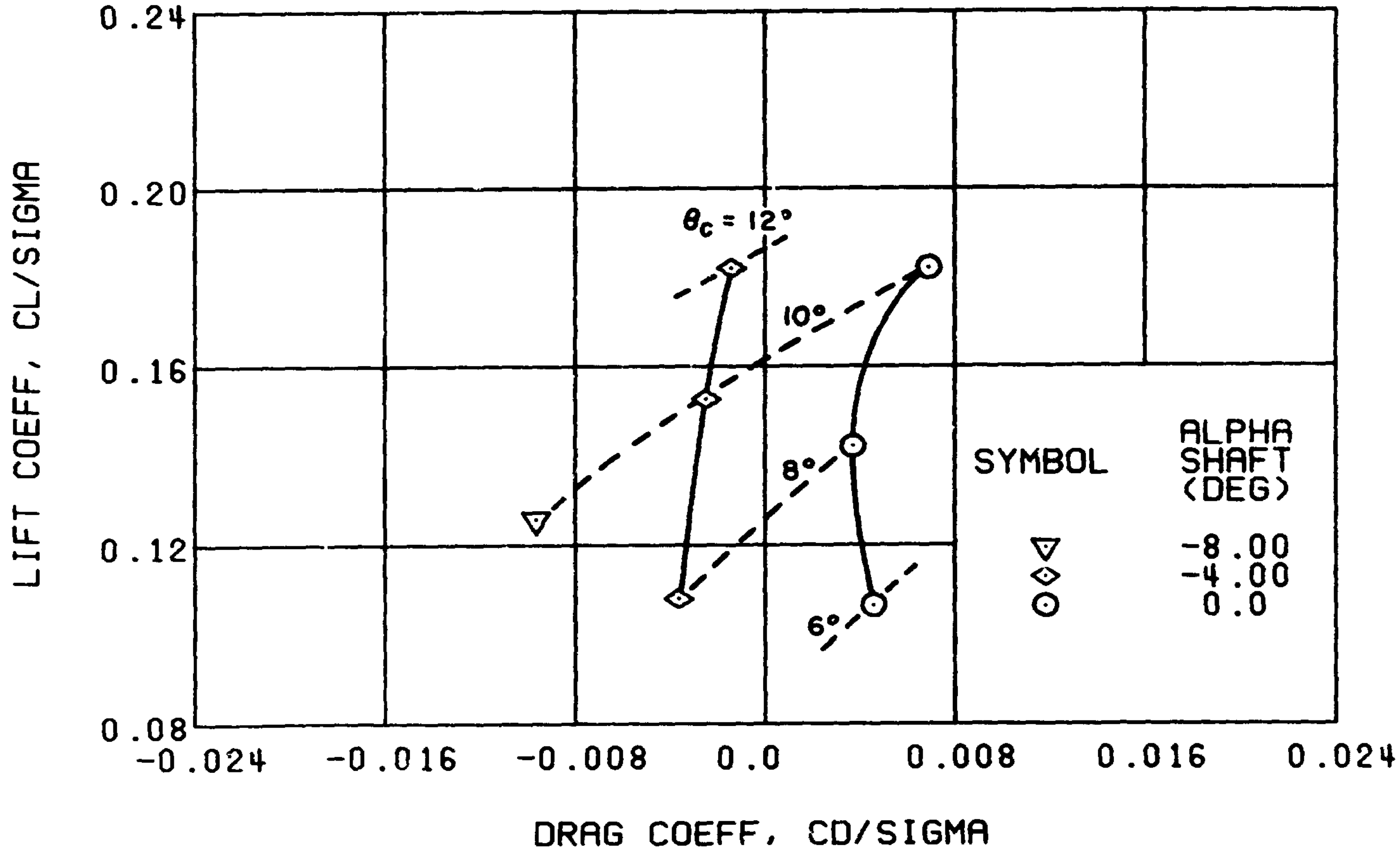

(a) DRAG COEFFICIENT

Figure 39. Performance Data at an Advance Ratio of 0.35 With the Lateral Displacement Control (B'_{1s}) Set at 4 Degrees (Single-Rotor Configuration).

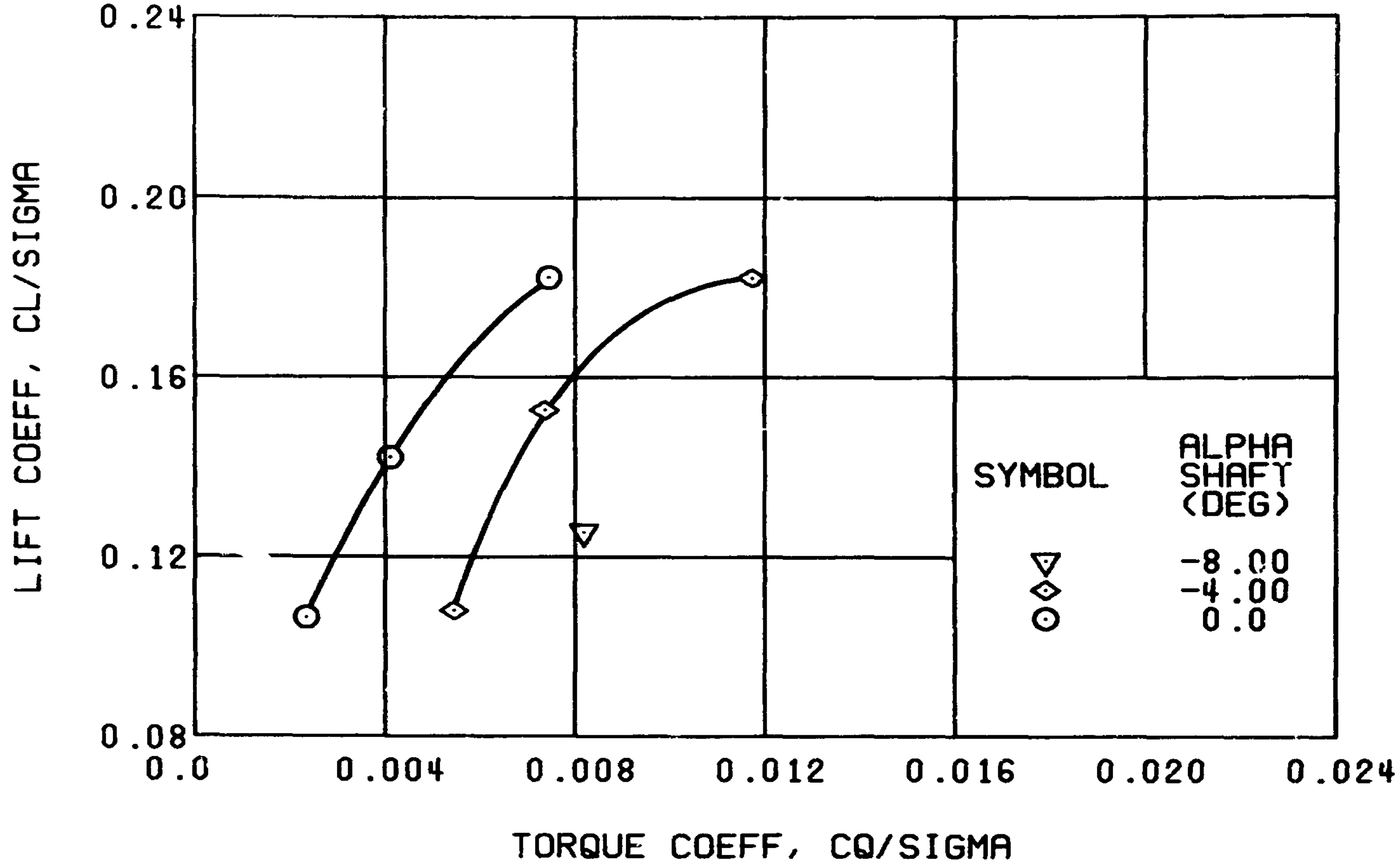

(b) TORQUE COEFFICIENT

Figure 39. Continued.
μ = 0.35 B'_{1s} = 4 Deg (Single-Rotor Configuration)

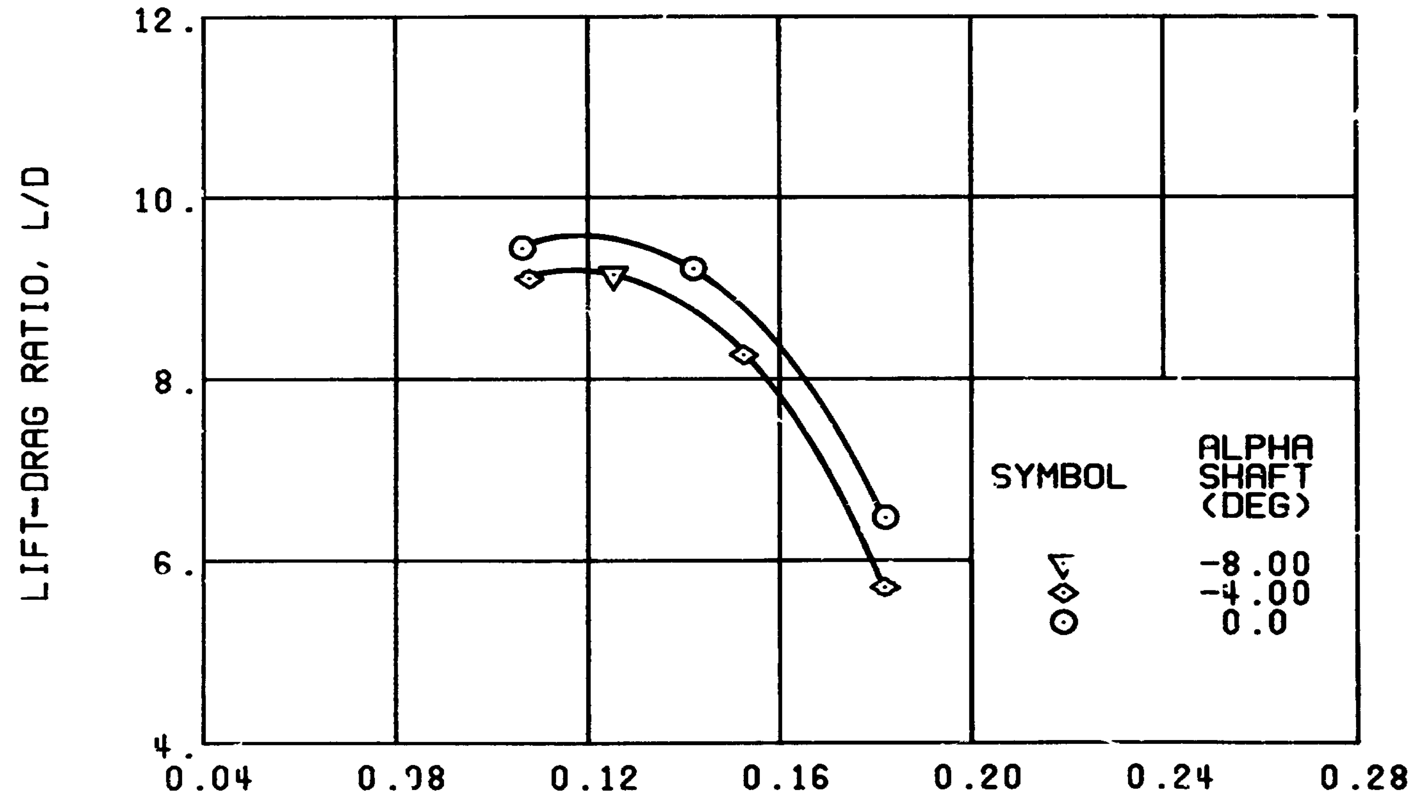

(c) LIFT-DRAG RATIO

Figure 39. Continued.
μ = 0.35 B'_{1s} = 4 Deg (Single-Rotor Configuration)

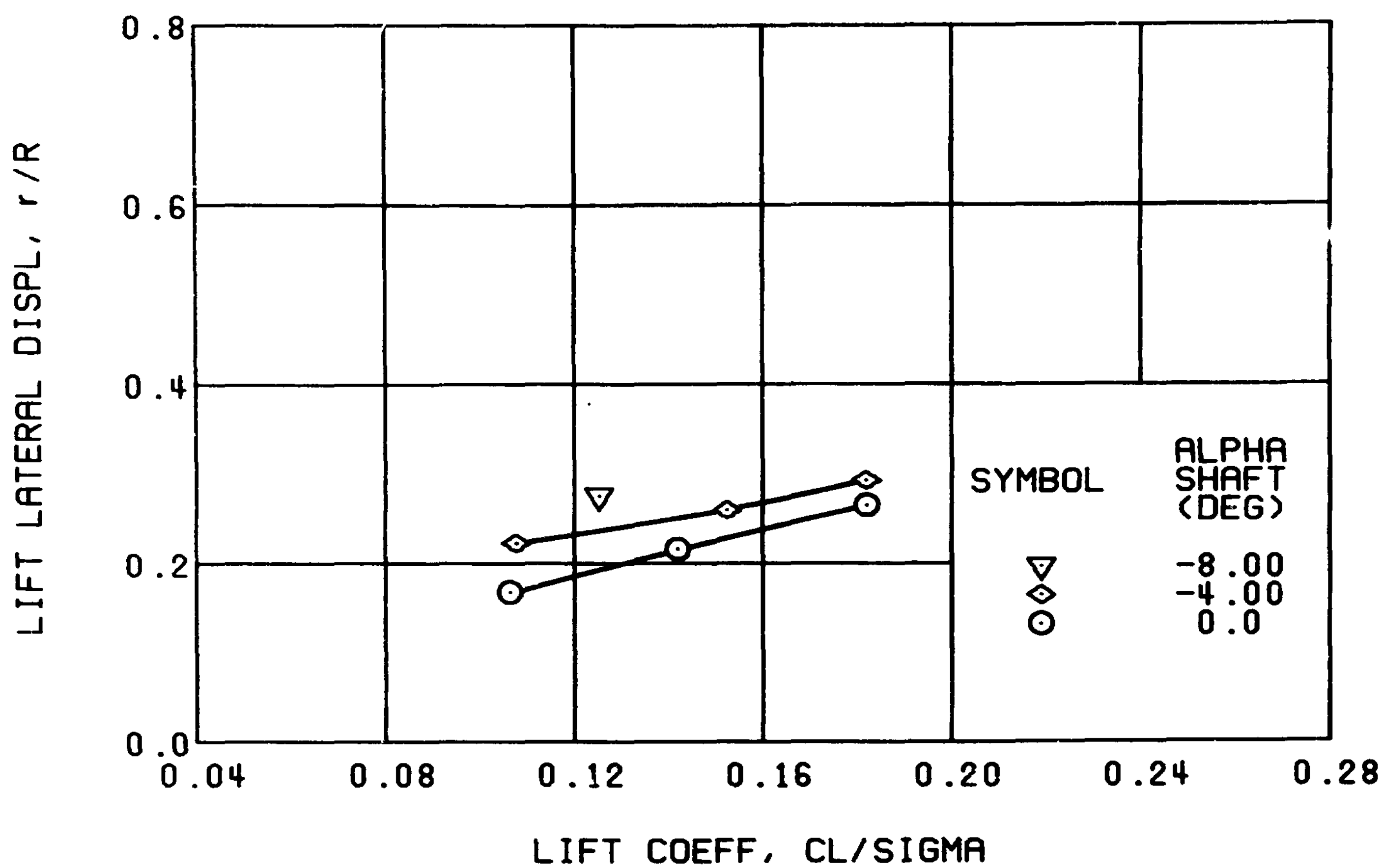

(d) LIFT LATERAL DISPLACEMENT

Figure 39. Continued.
$\mu = 0.35$ $B'_{1s} = 4$ Deg (Single-Rotor Configuration)

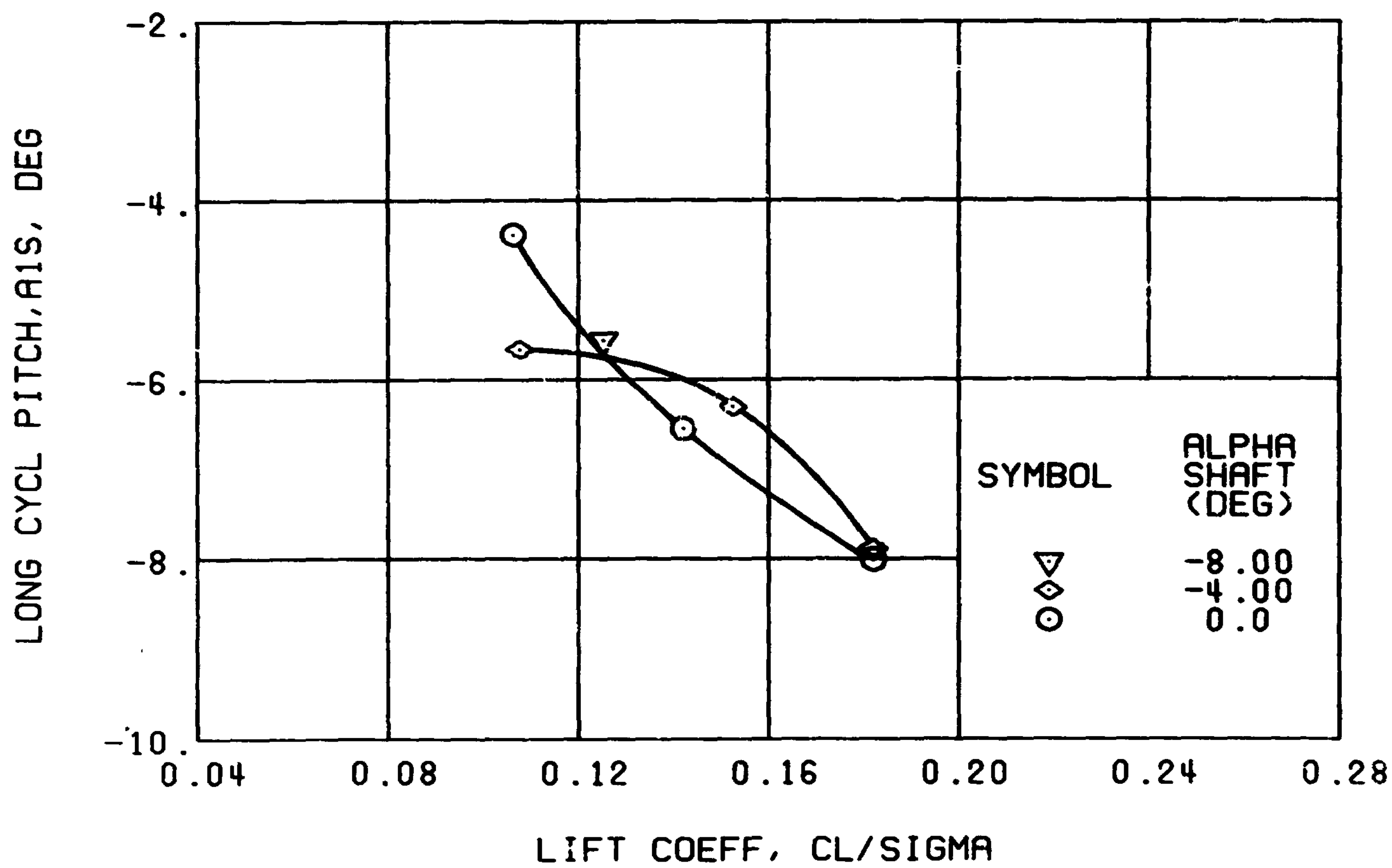

(e) LONGITUDINAL CYCLIC PITCH

Figure 39. Continued.
μ = 0.35 B'_{1s} = 4 Deg (Single-Rotor Configuration)

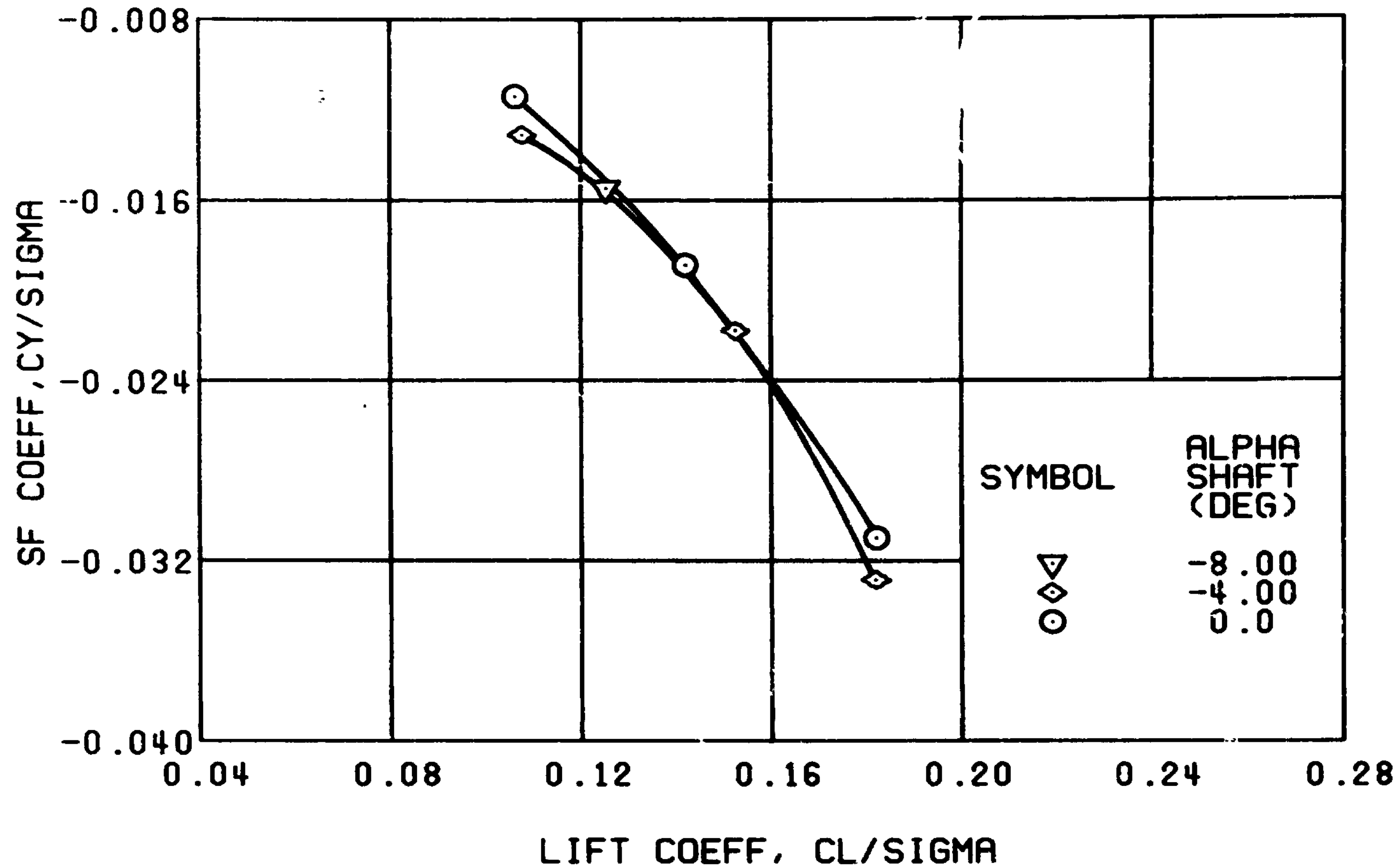

(f) SIDE FORCE COEFFICIENT

Figure 39. Continued.
$\mu = 0.35$ $B'_{1s} = 4$ Deg (Single-Rotor Configuration)

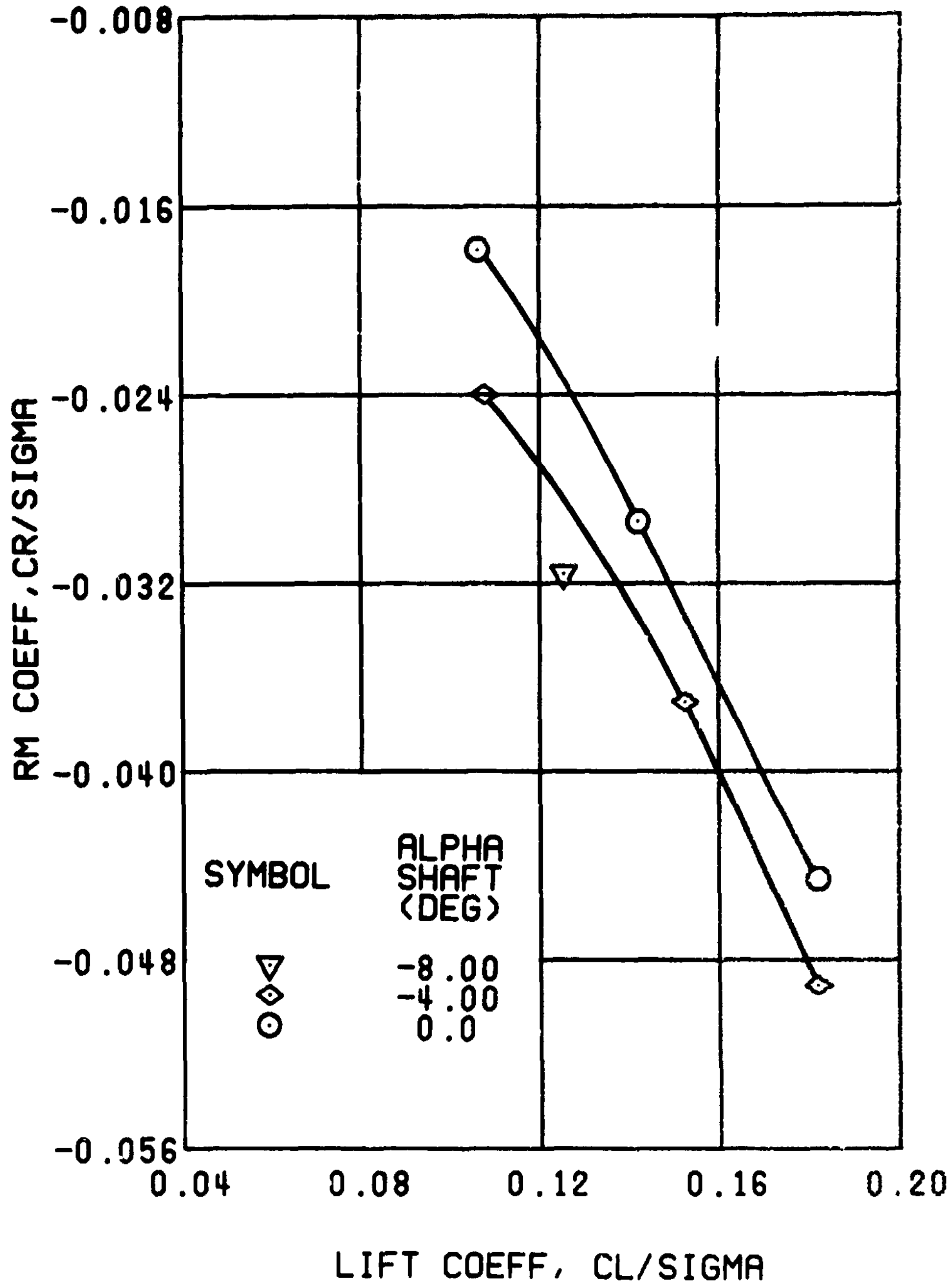

(g) ROLLING MOMENT COEFFICIENT

Figure 39. Continued.
$\mu = 0.35$ $B'_{1s} = 4$ Deg (Single-Rotor Configuration)

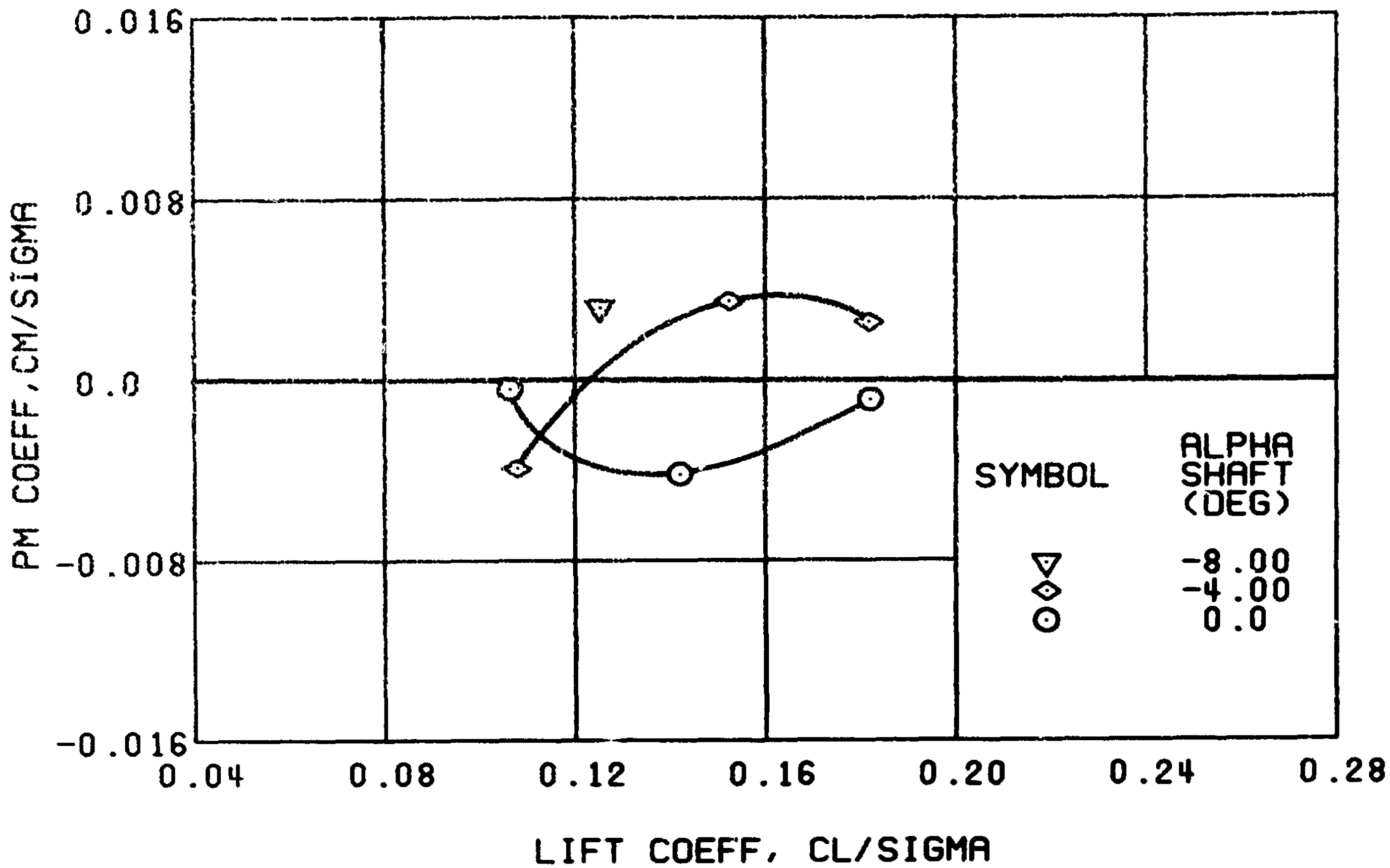

(h) PITCHING MOMENT COEFFICIENT

Figure 39. Continued.
μ = 0.35 B'_{1s} = 4 Deg (Single-Rotor Configuration)

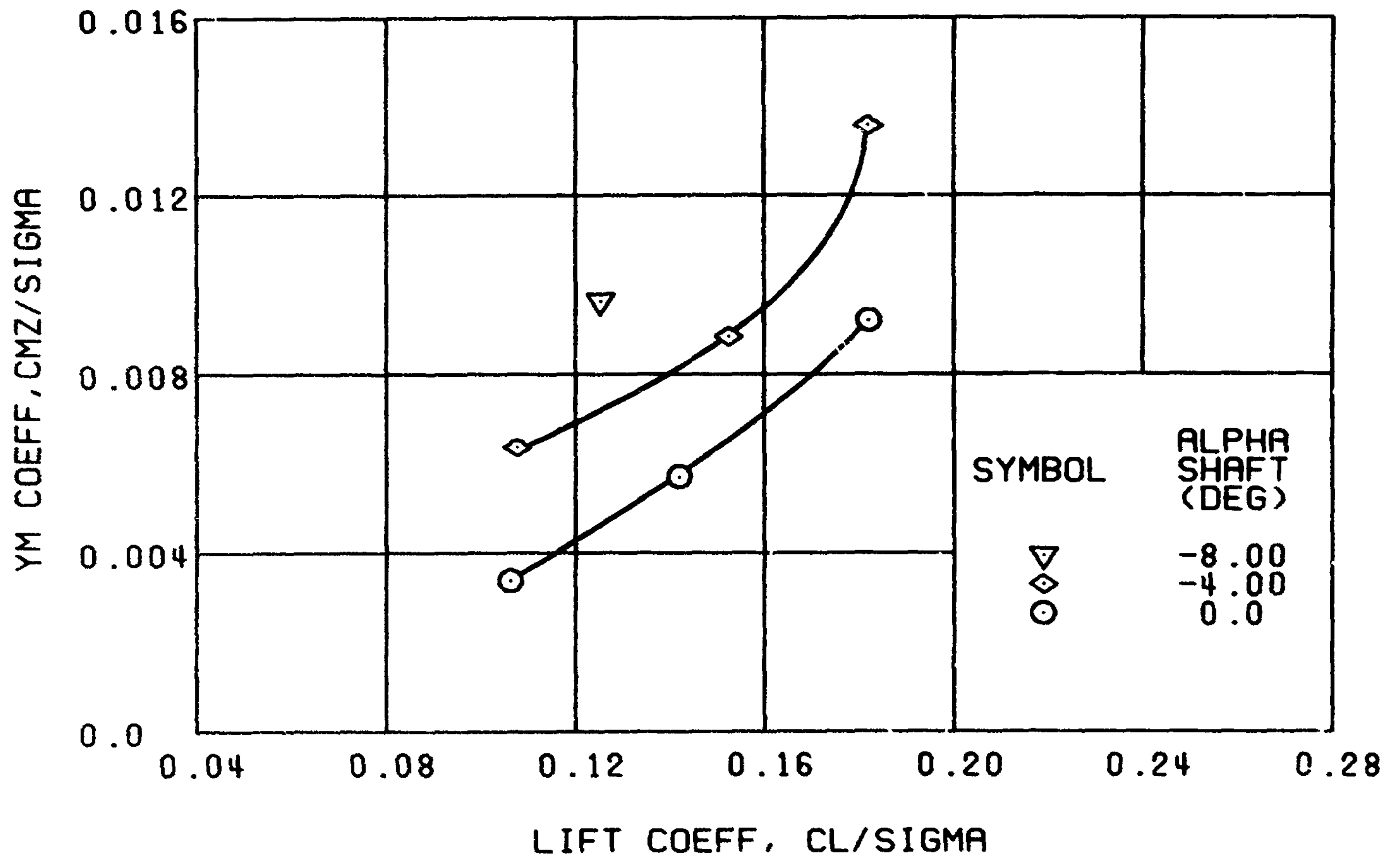

(i) YAWING MOMENT COEFFICIENT

Figure 39. Continued.
$\mu = 0.35$ $B'_{1s} = 4$ Deg (Single-Rotor Configuration)

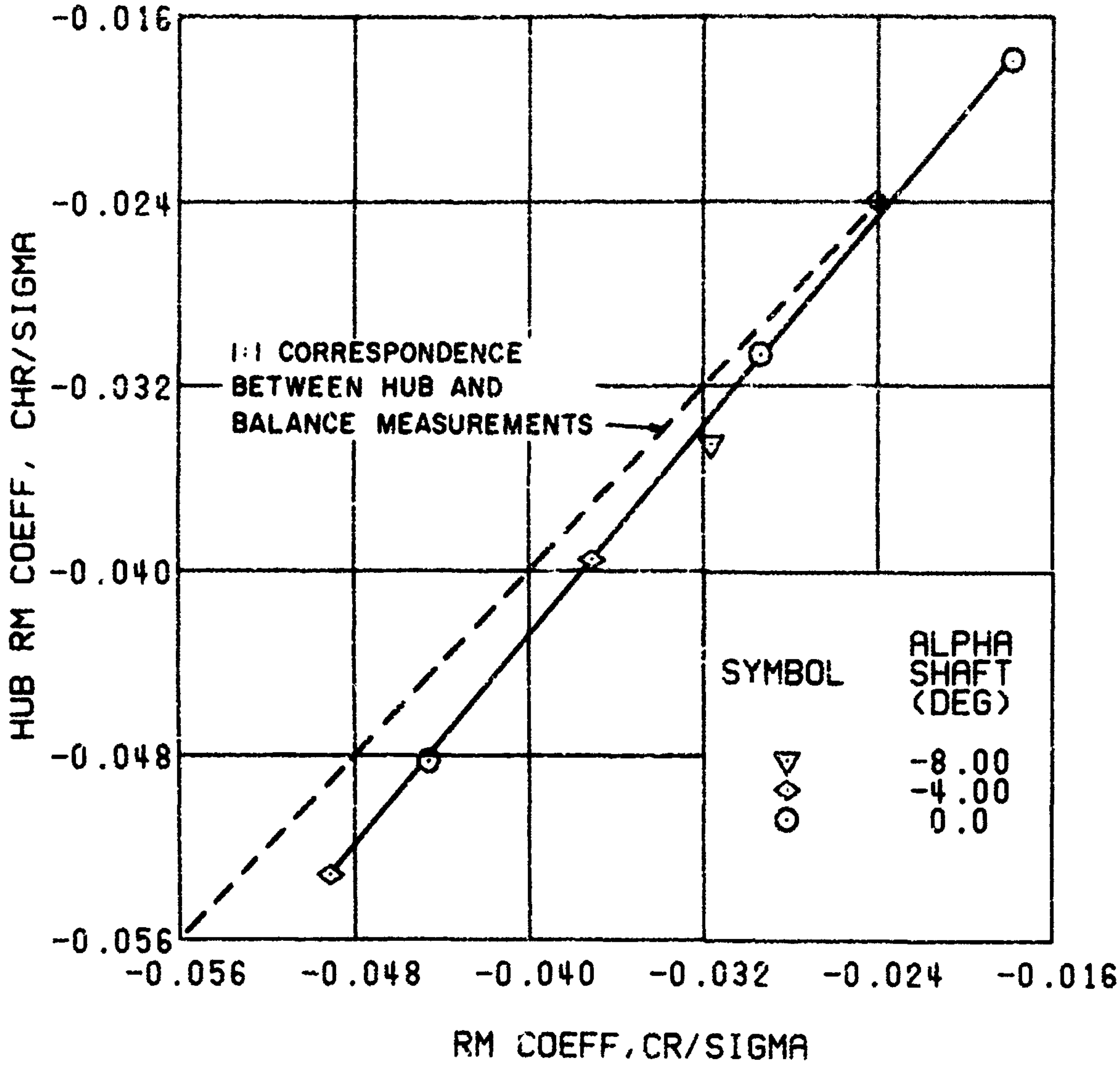

(j) HUB VERSUS BALANCE ROLLING MOMENT COEFFICIENT

Figure 39. Continued.
$\mu = 0.35$ $B'_{1s} = 4$ Deg (Single-Rotor Configuration)

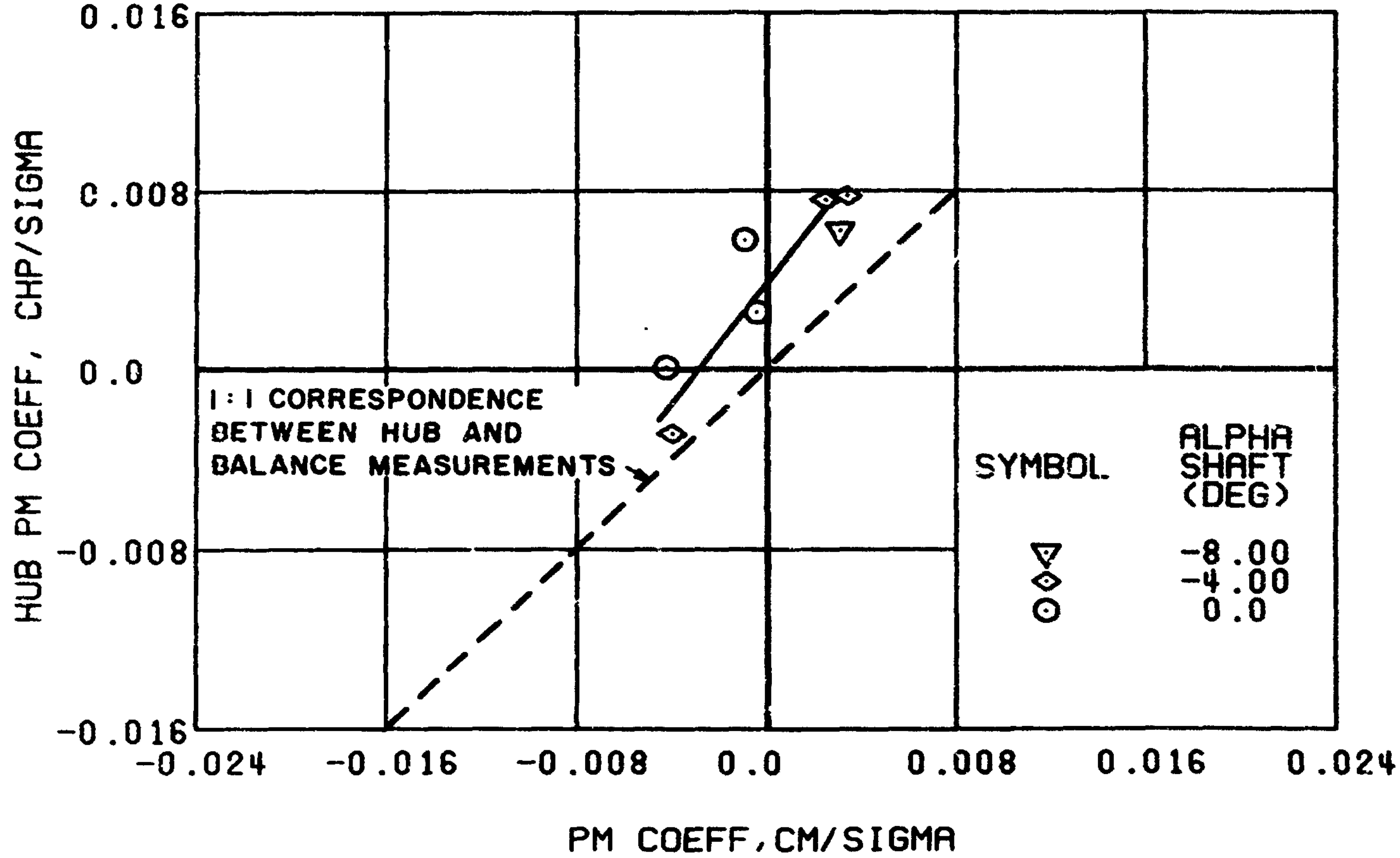

(k) HUB VERSUS BALANCE PITCHING MOMENT COEFFICIENT

Figure 39. Continued.
$\mu = 0.35$ $B'_{1s} = 4$ Deg (Single-Rotor Configuration)

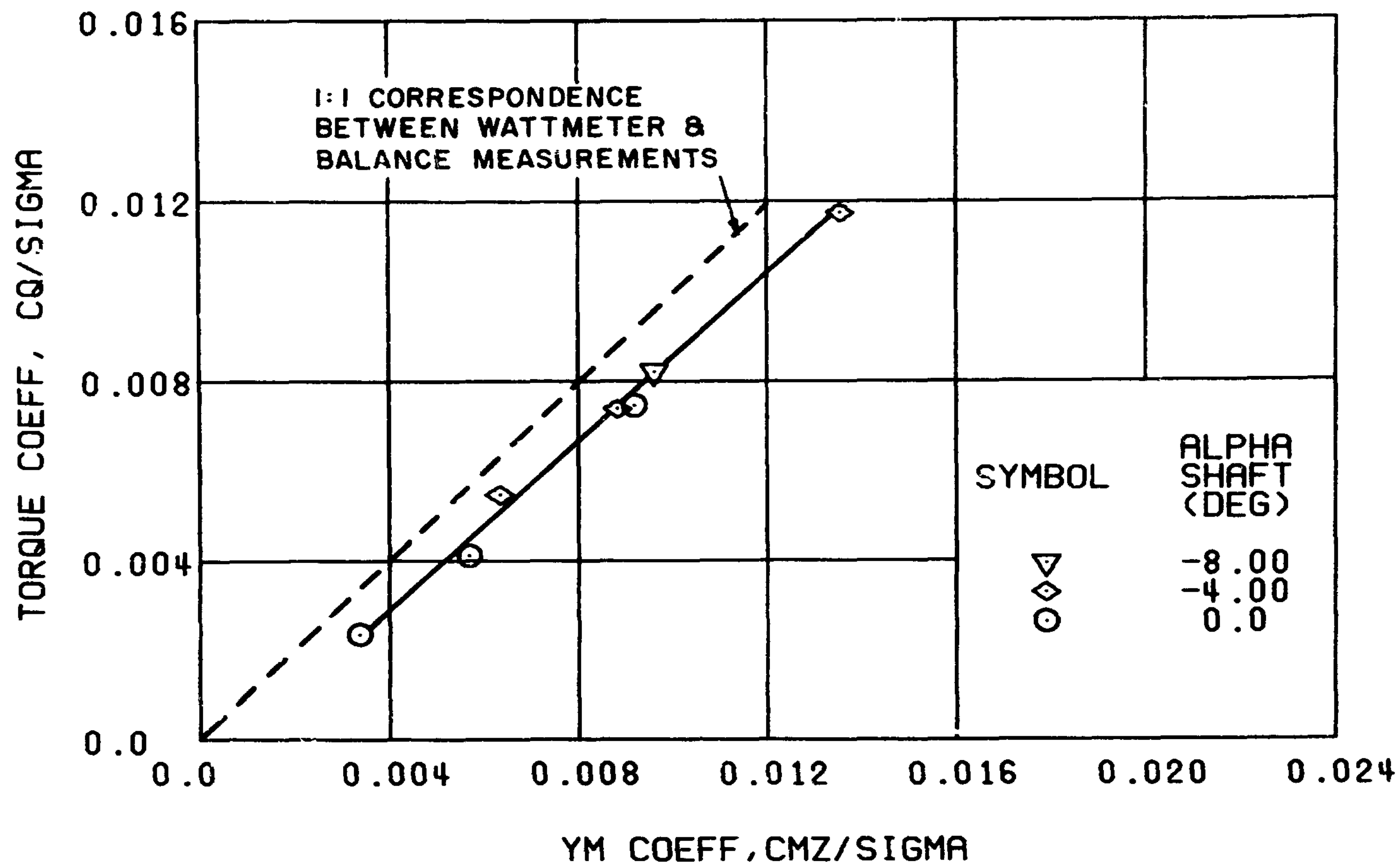

(I) WATTMETER VERSUS BALANCE YAWING MOMENT COEFFICIENT

Figure 39. Concluded.

$\mu = 0.35$ $B'_{1s} = 4$ Deg (Single-Rotor Configuration)

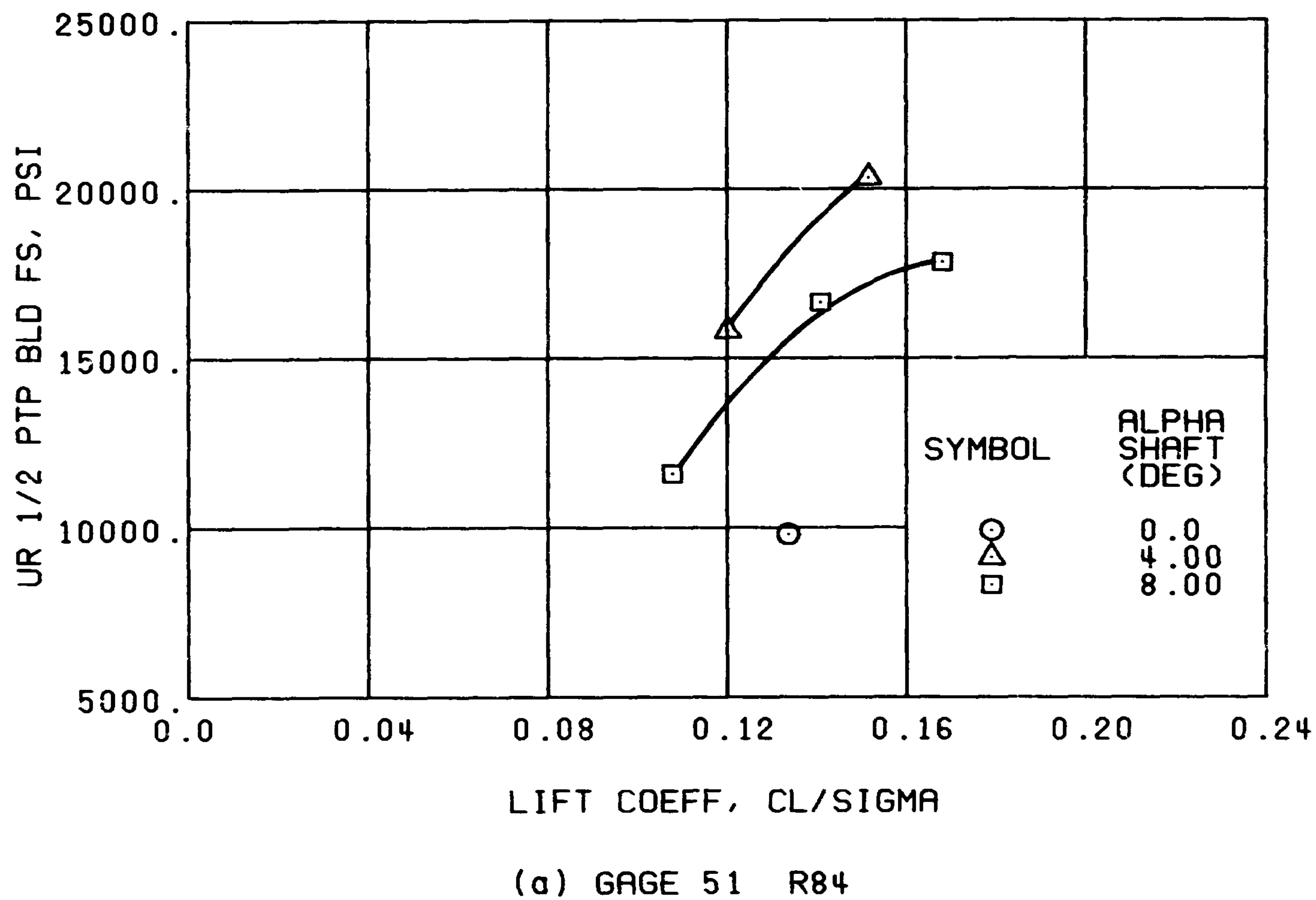

Figure 40. Stress, Load, and Vibration Data at an Advance Ratio of 0.21 With the Lateral Displacement Control (B'_{1s}) Set at 0 Degrees.

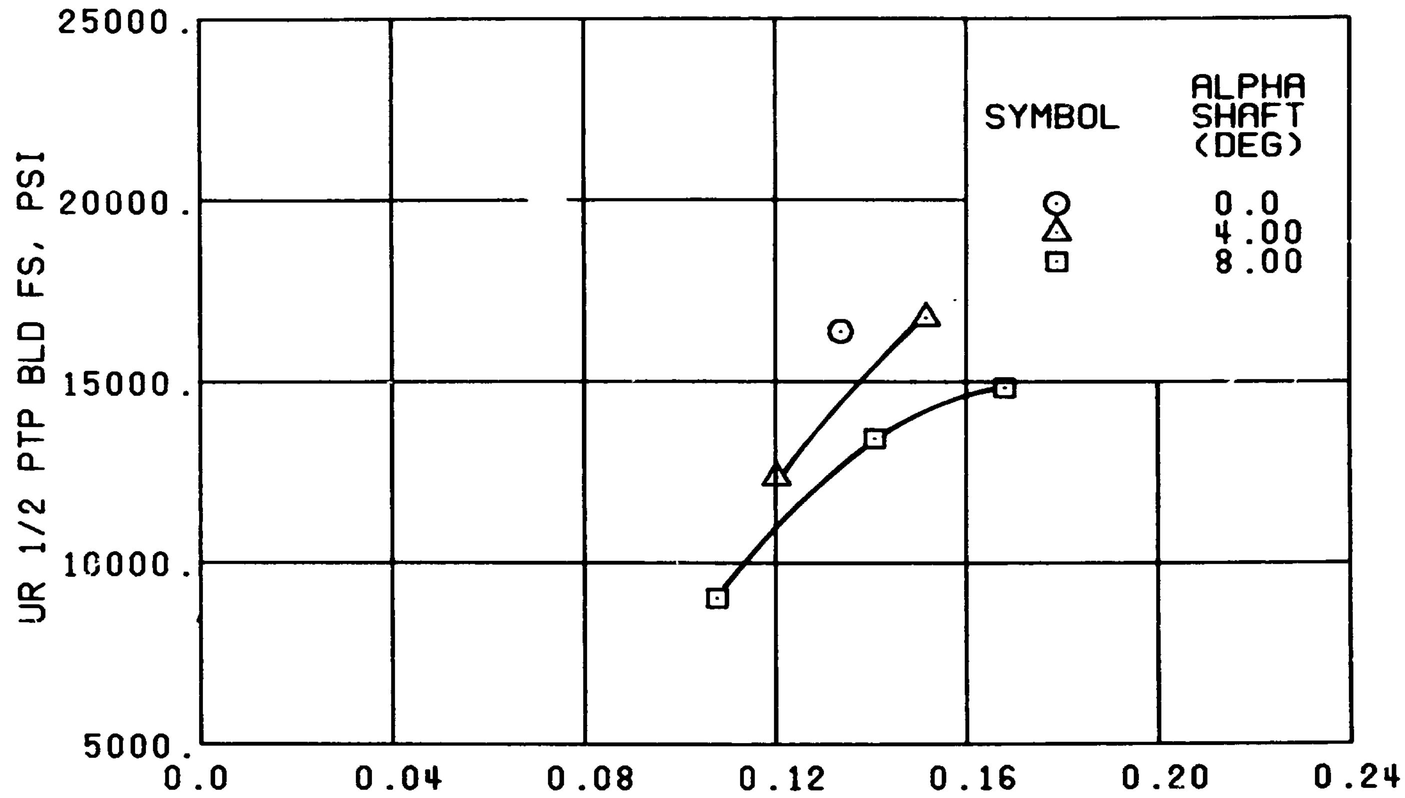

(c) GAGE 52 R108

Figure 40. Continued.
$\mu = 0.21 \quad B'_{1s} = 0$ Deg

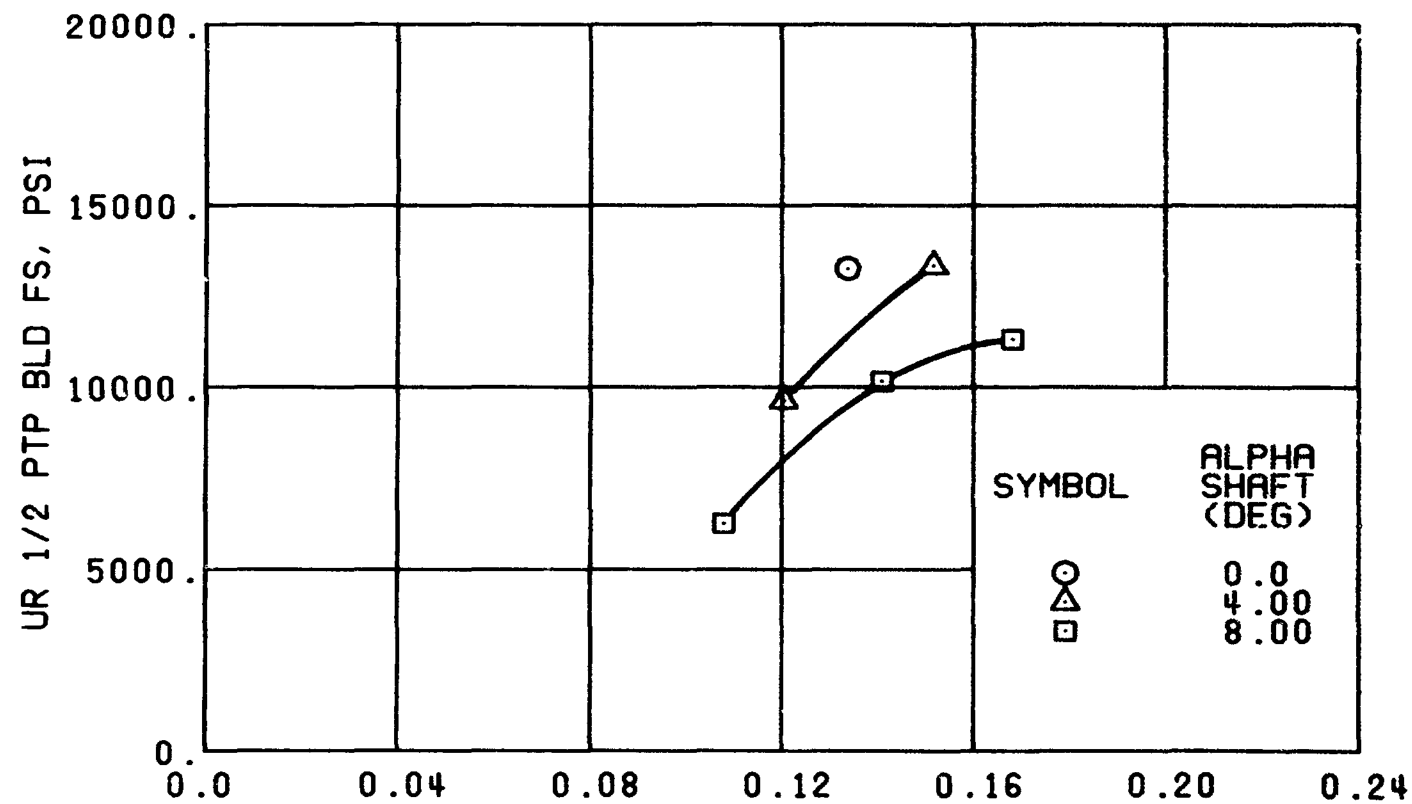

(d) GAGE 53 R132

Figure 40. Continued.
$\mu = 0.21$ $B'_{1s} = 0$ Deg

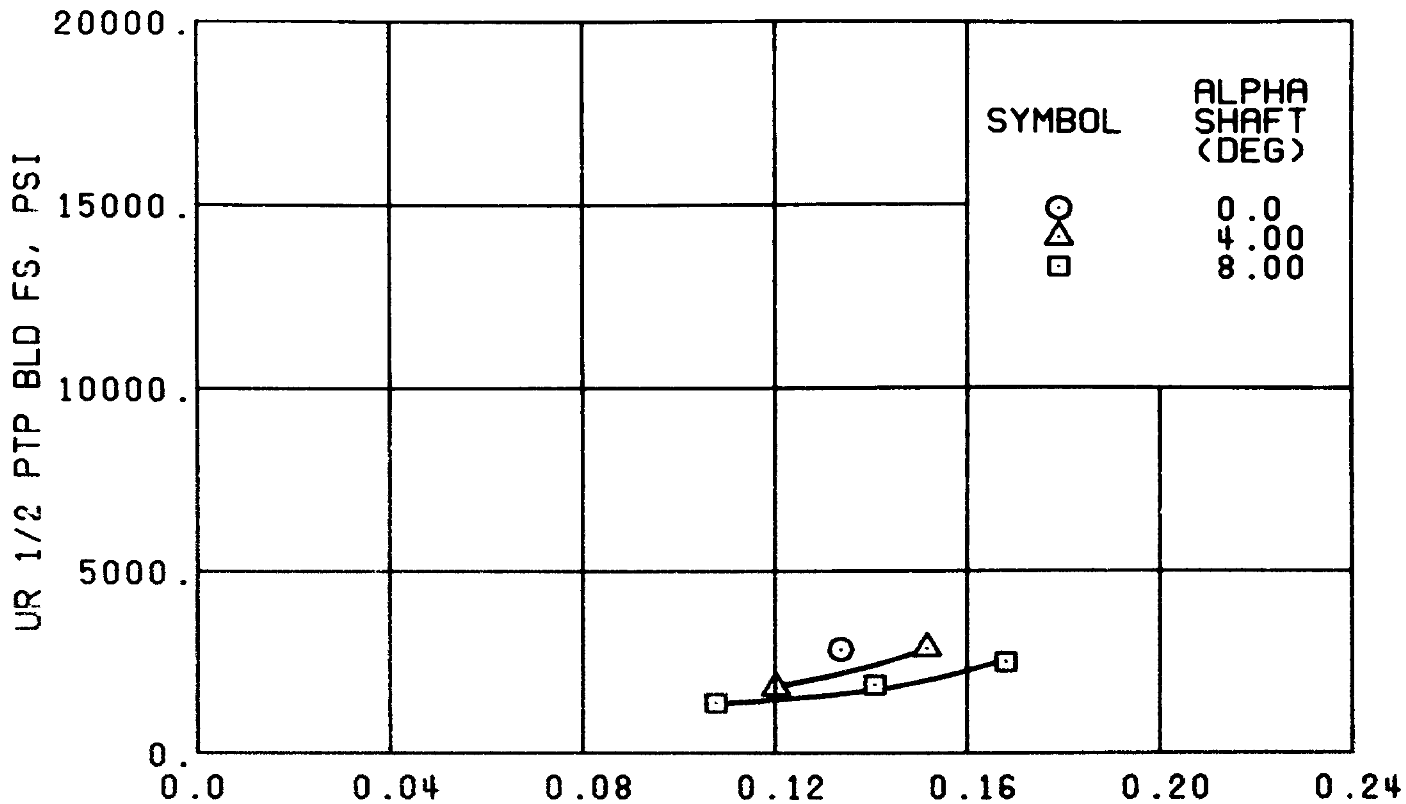

(f) GAGE 55 R204

Figure 40. Continued.
$\mu = 0.21 \quad B'_{1s} = 0$ Deg

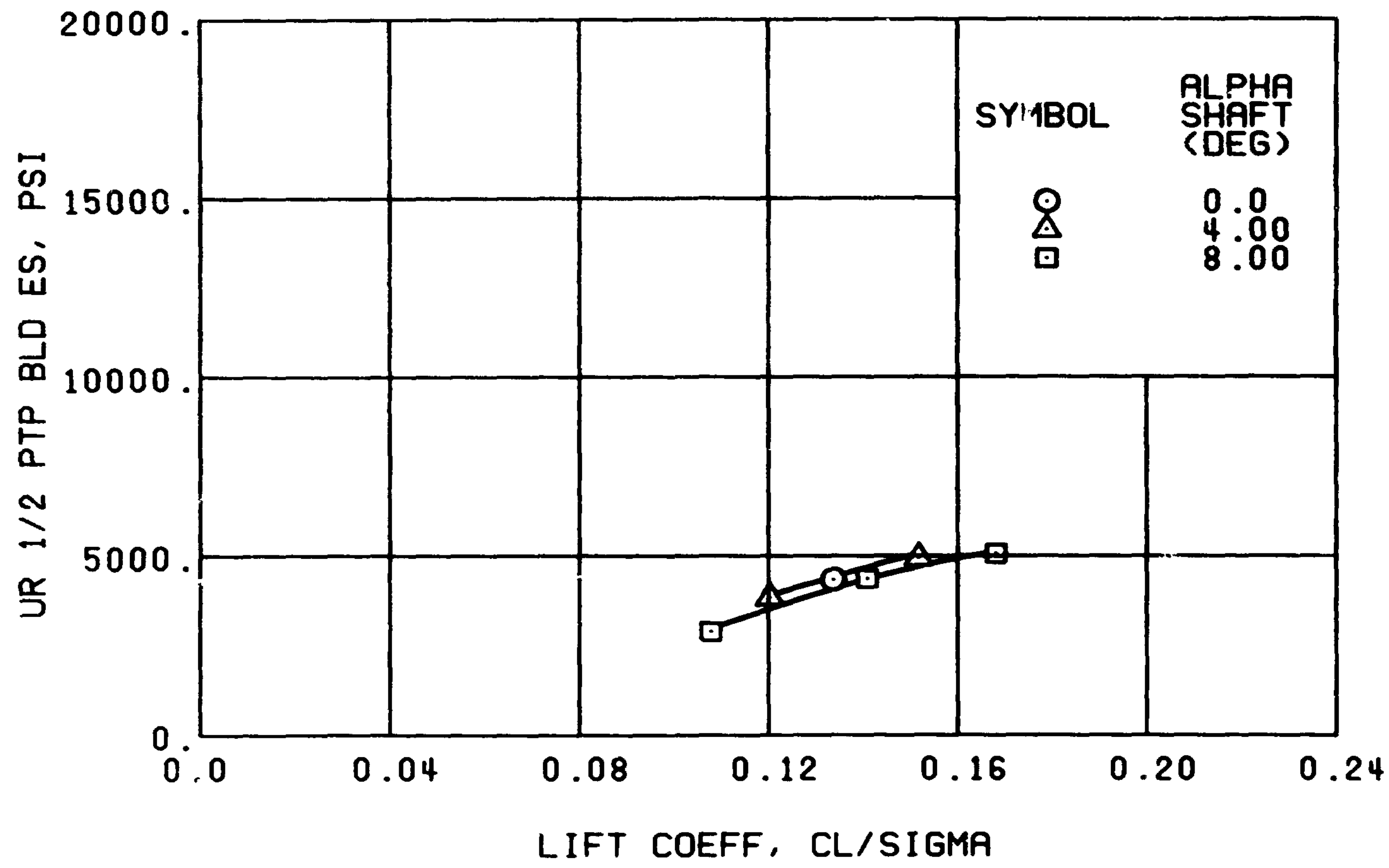

(g) GAGE 79 R60

Figure 40. Continued.
$\mu = 0.21$ $B'_{1s} = 0$ Deg

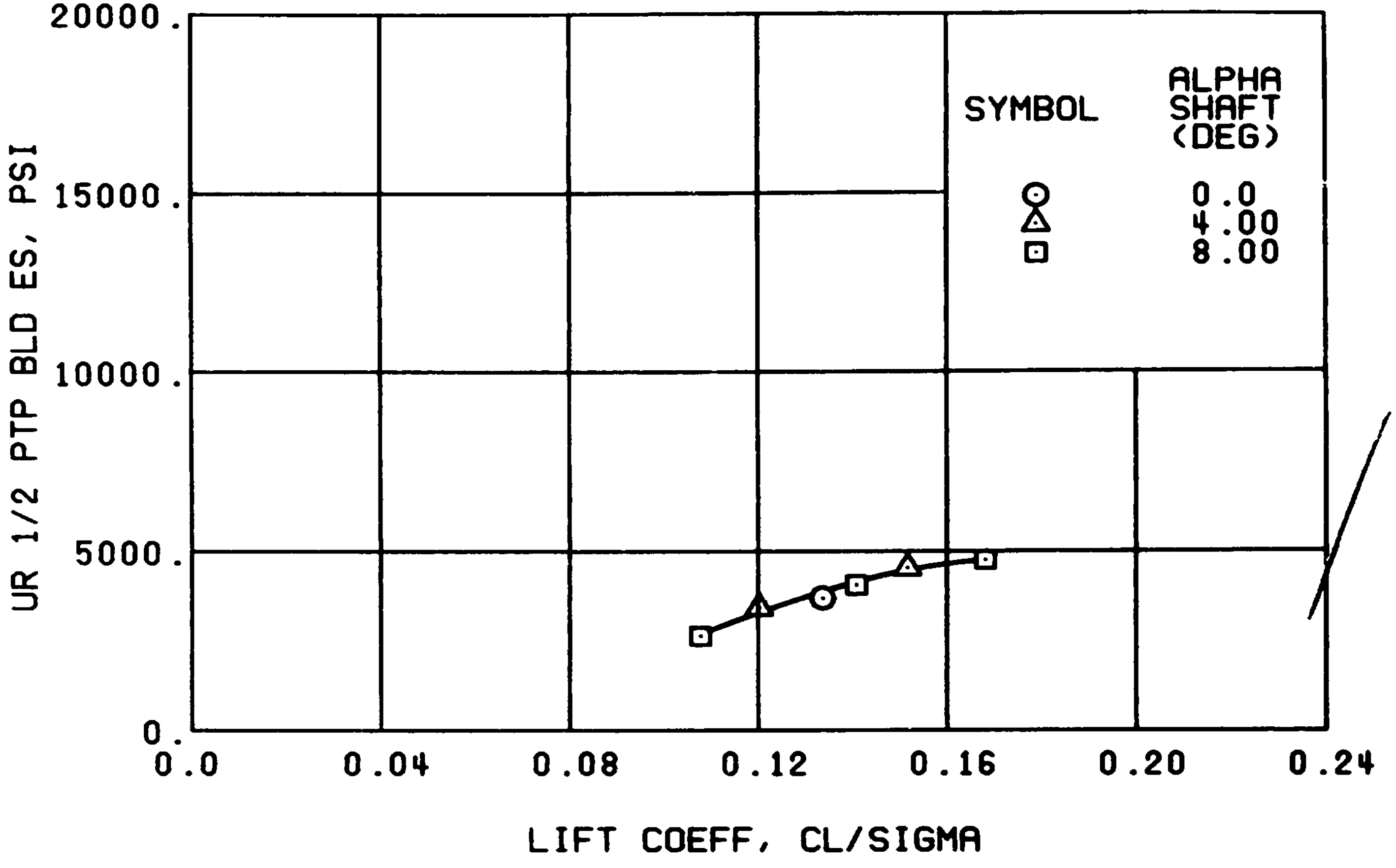

(h) GAGE 40 R84

Figure 40. Continued.
$\mu = 0.21$ $B'_{1s} = 0$ Deg

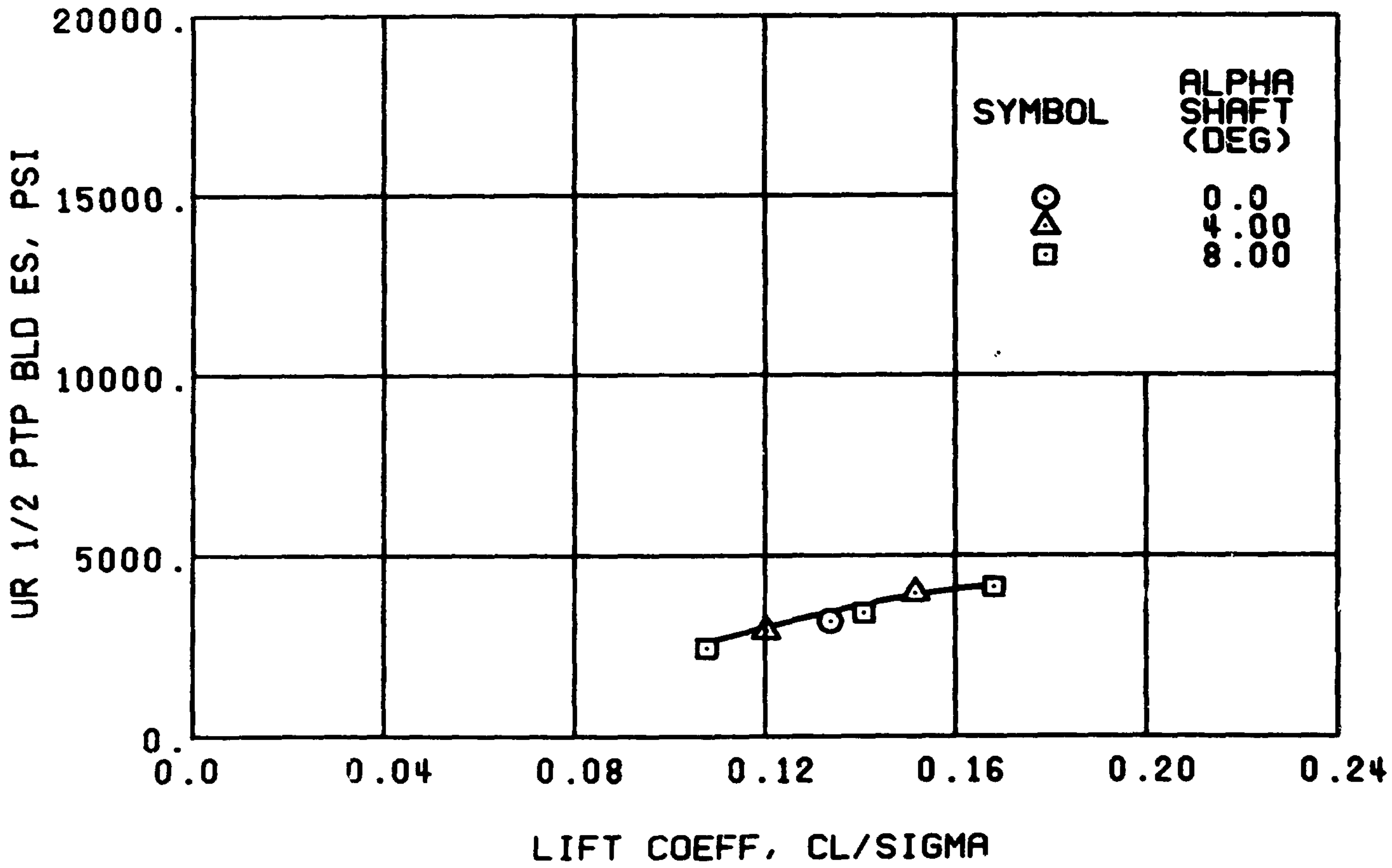

(j) GAGE 42 R132

Figure 40. Continued.
$\mu = 0.21$ $B'_{1s} = 0$ Deg

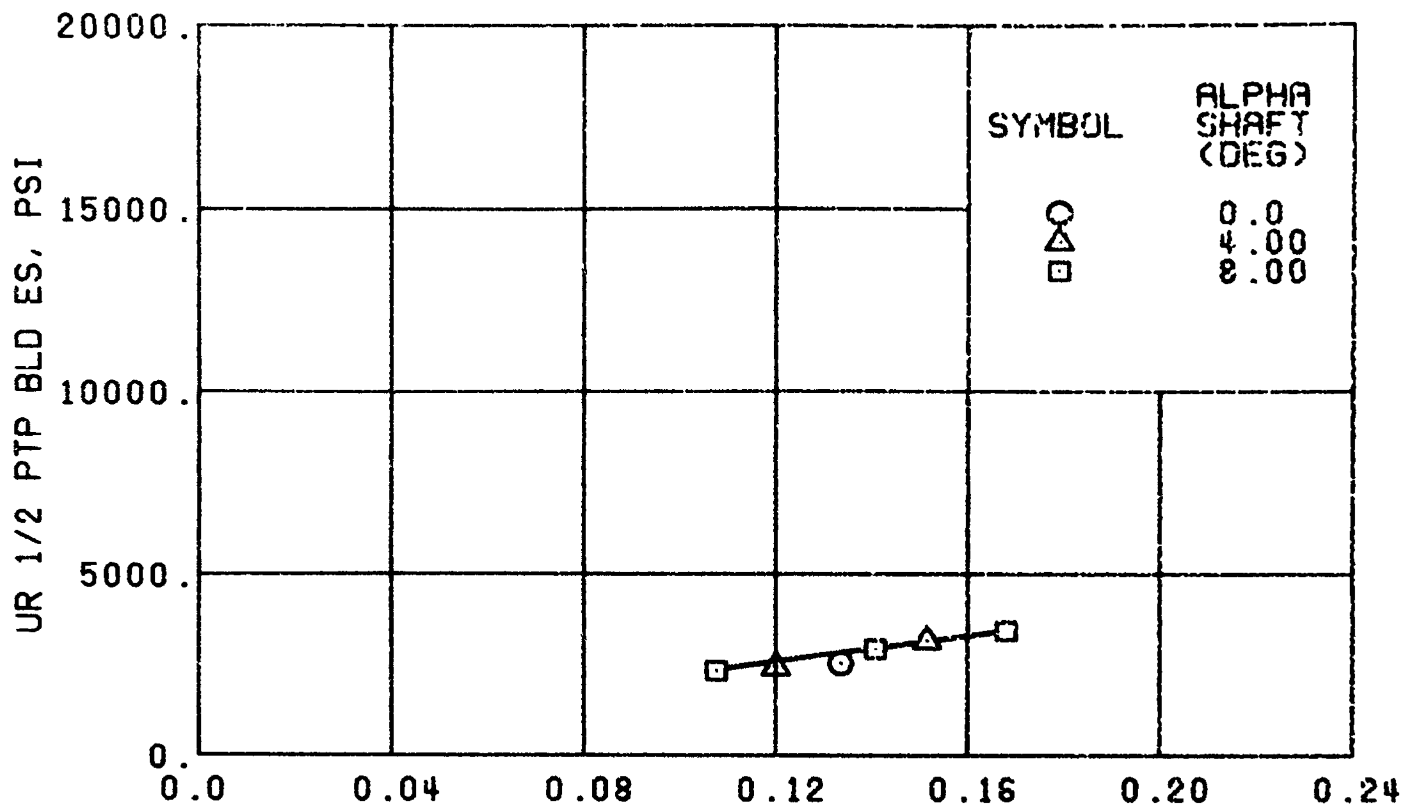

(k) GAGE 43 R168

Figure 40. Continued.
$\mu = 0.21$ $B'_{1s} = 0$ Deg

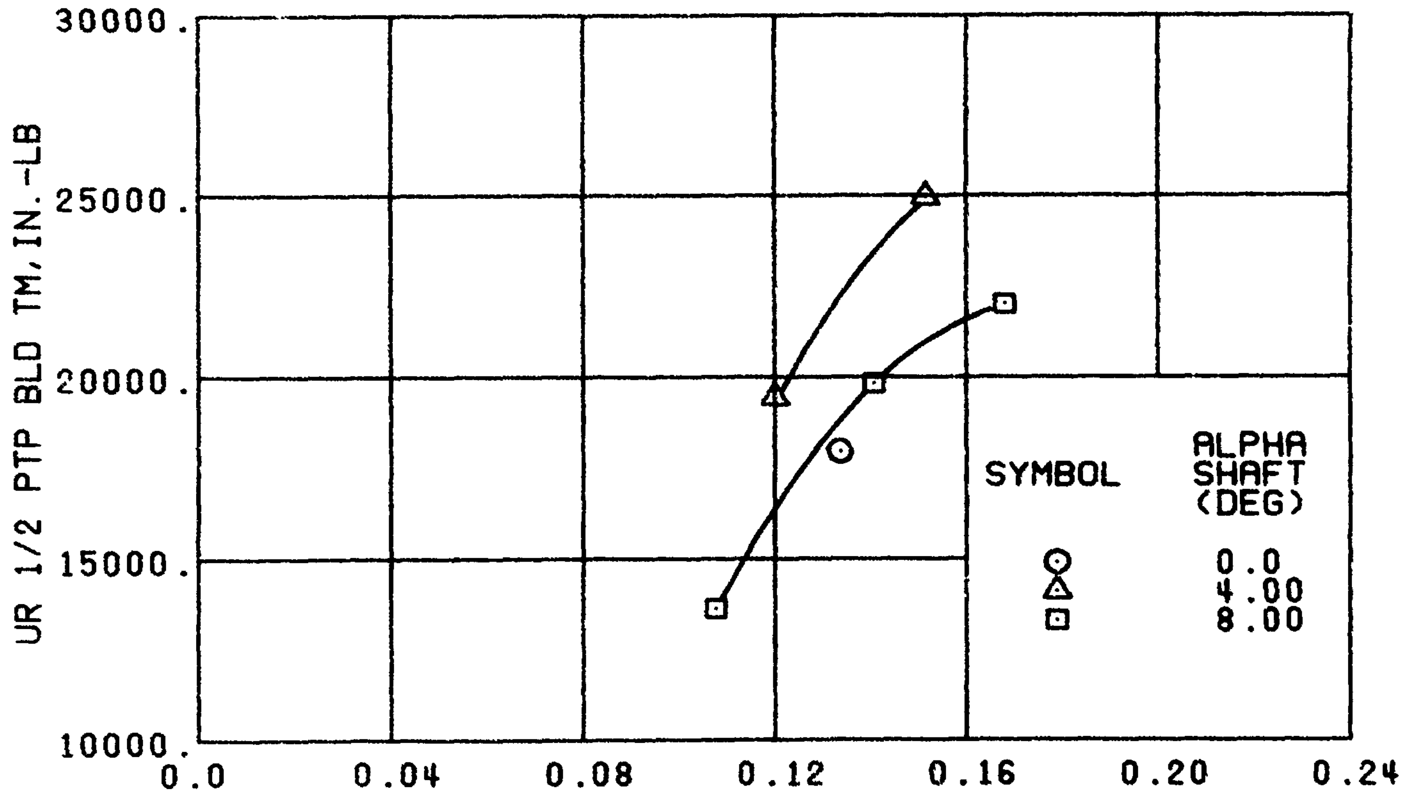

(I) GAGE 45 R82

Figure 40. Continued.
$\mu = 0.21$ $B'_{1s} = 0$ Deg

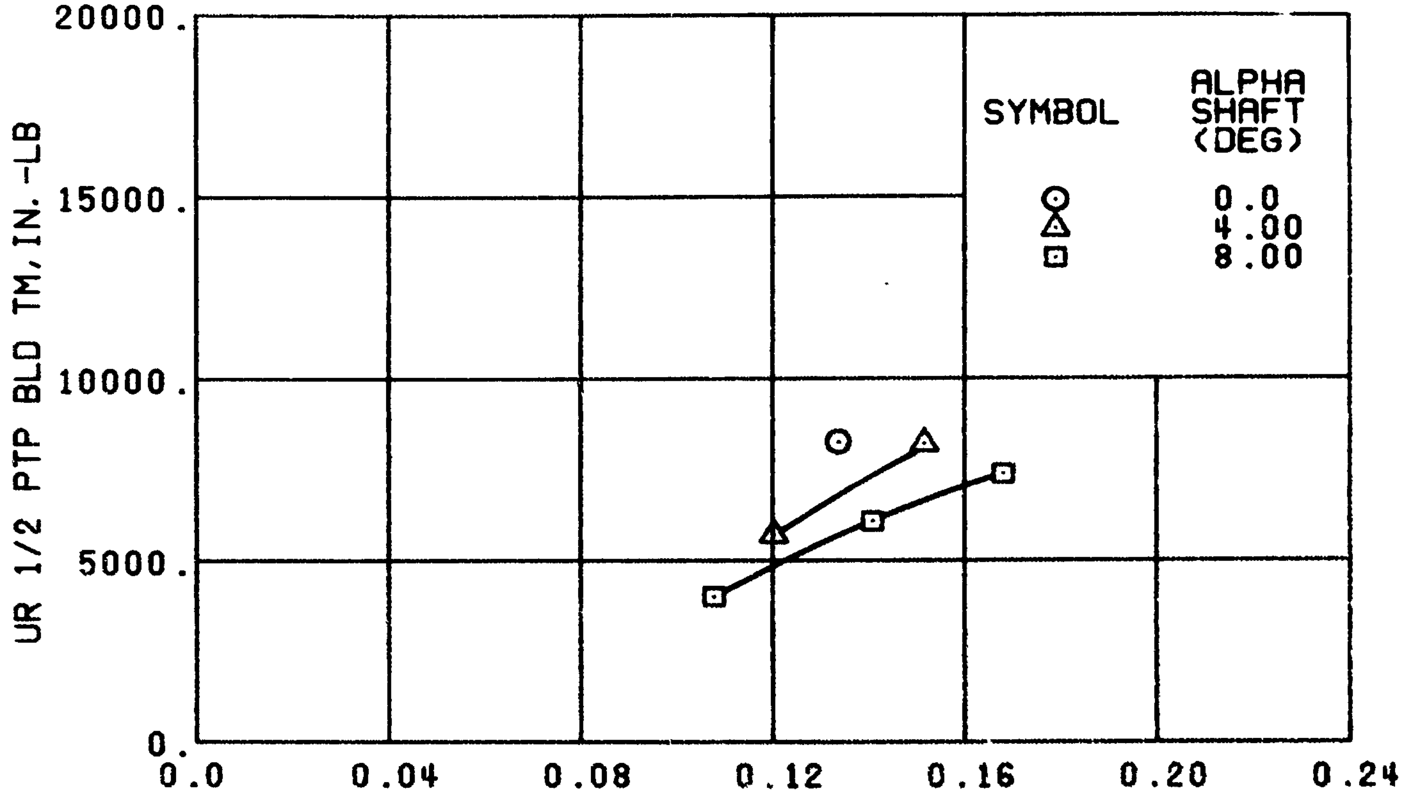

(m) GAGE 46 R130

Figure 40. Continued.
$\mu = 0.21$ $B'_{1s} = 0$ Deg

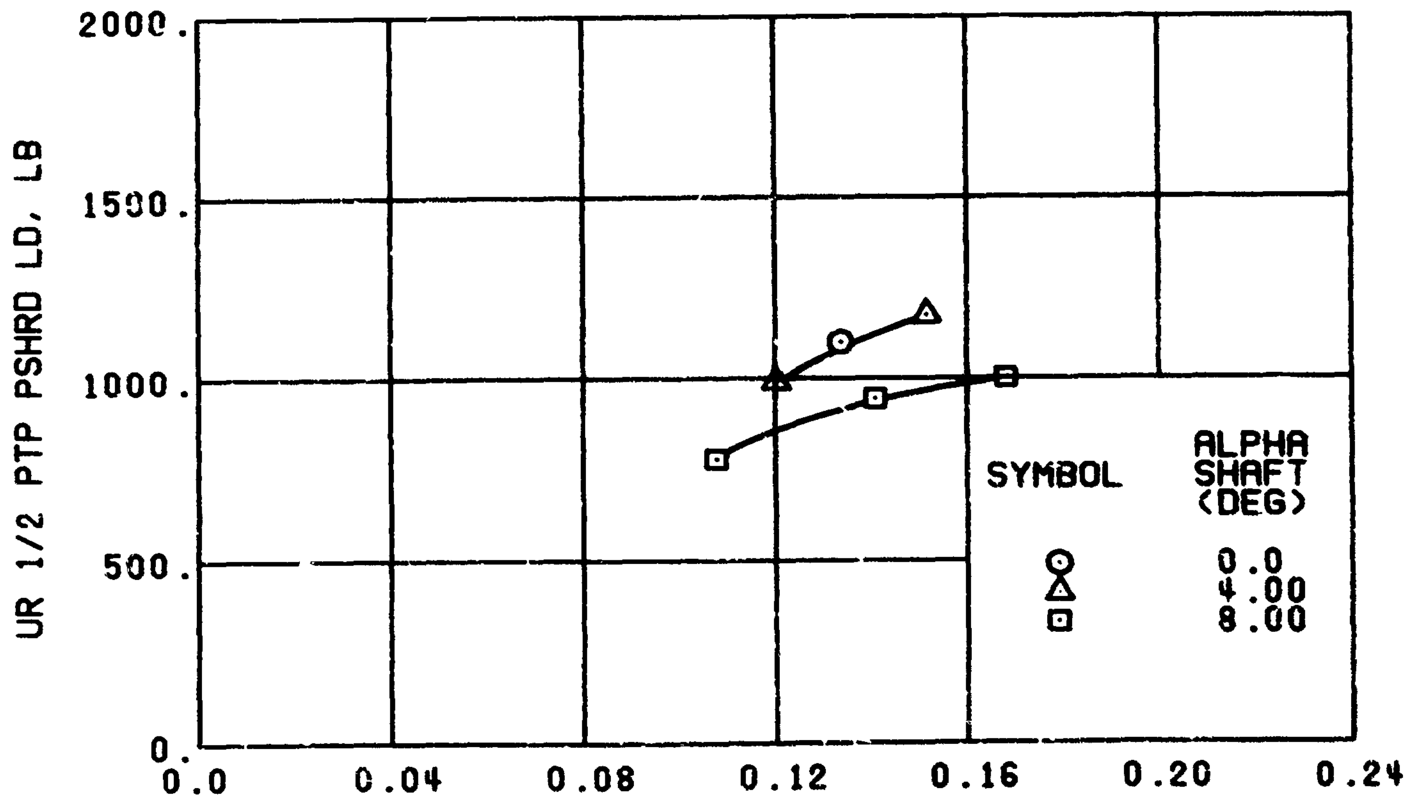

(n) GAGE 37

Figure 40. Continued.
$\mu = 0.21$ $B'_{1s} = 0$ Deg

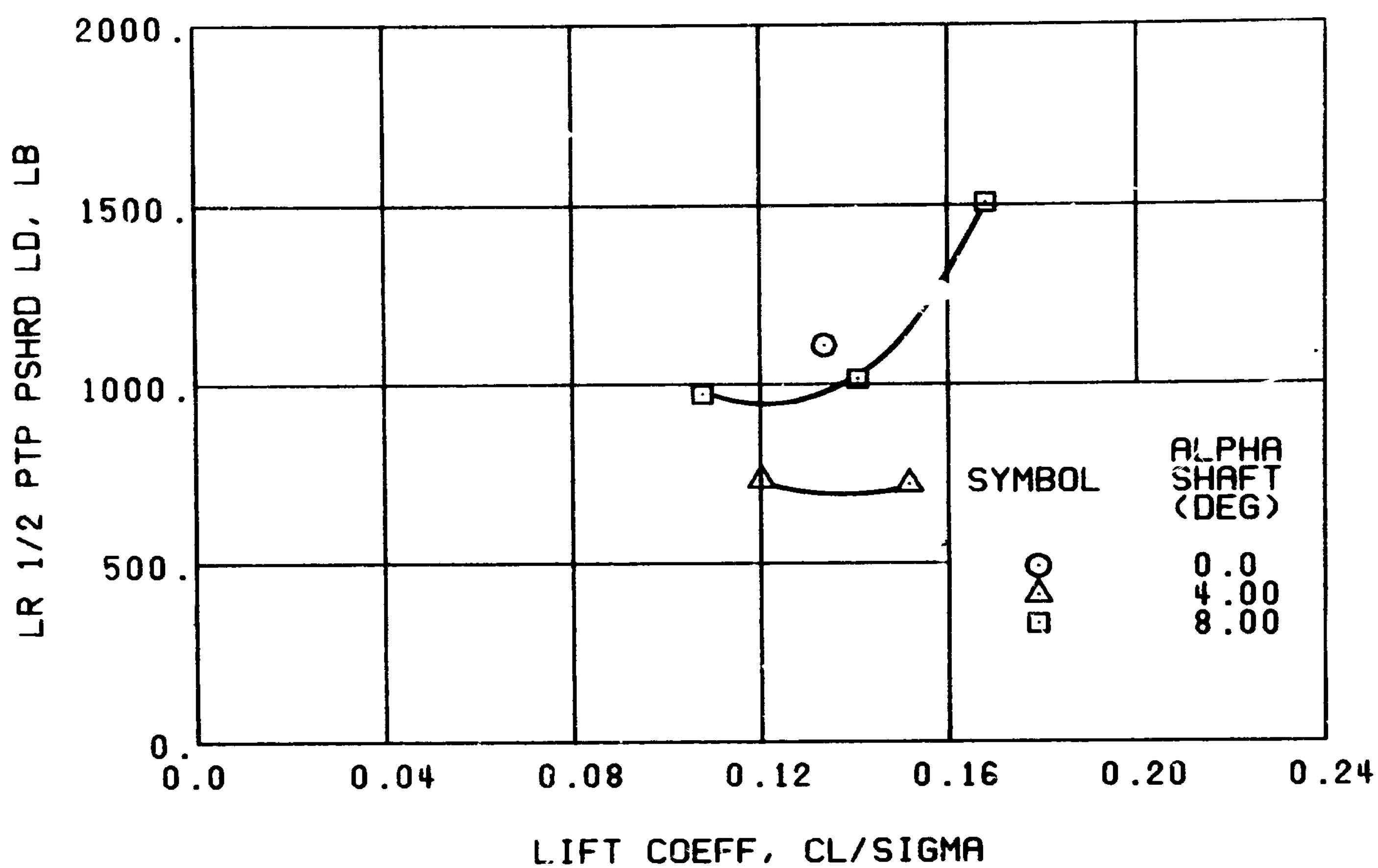

(o) GAGE 34

Figure 40. Continued.
μ = 0.21 B'_{1s} = 0 Deg

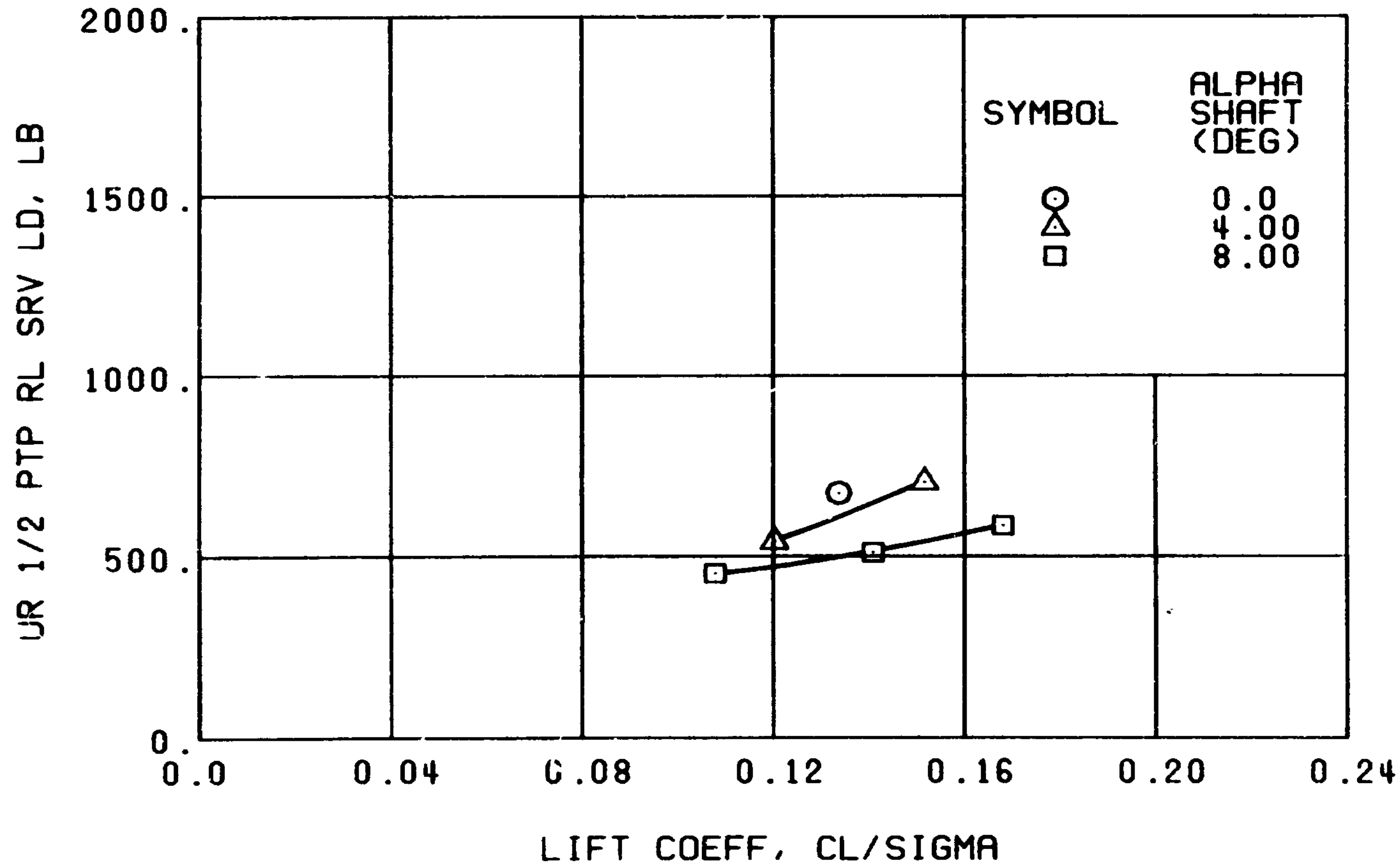

(p) GAGE 22

Figure 40. Continued.
$\mu = 0.21 \quad B_{1s}' = 0$ Deg

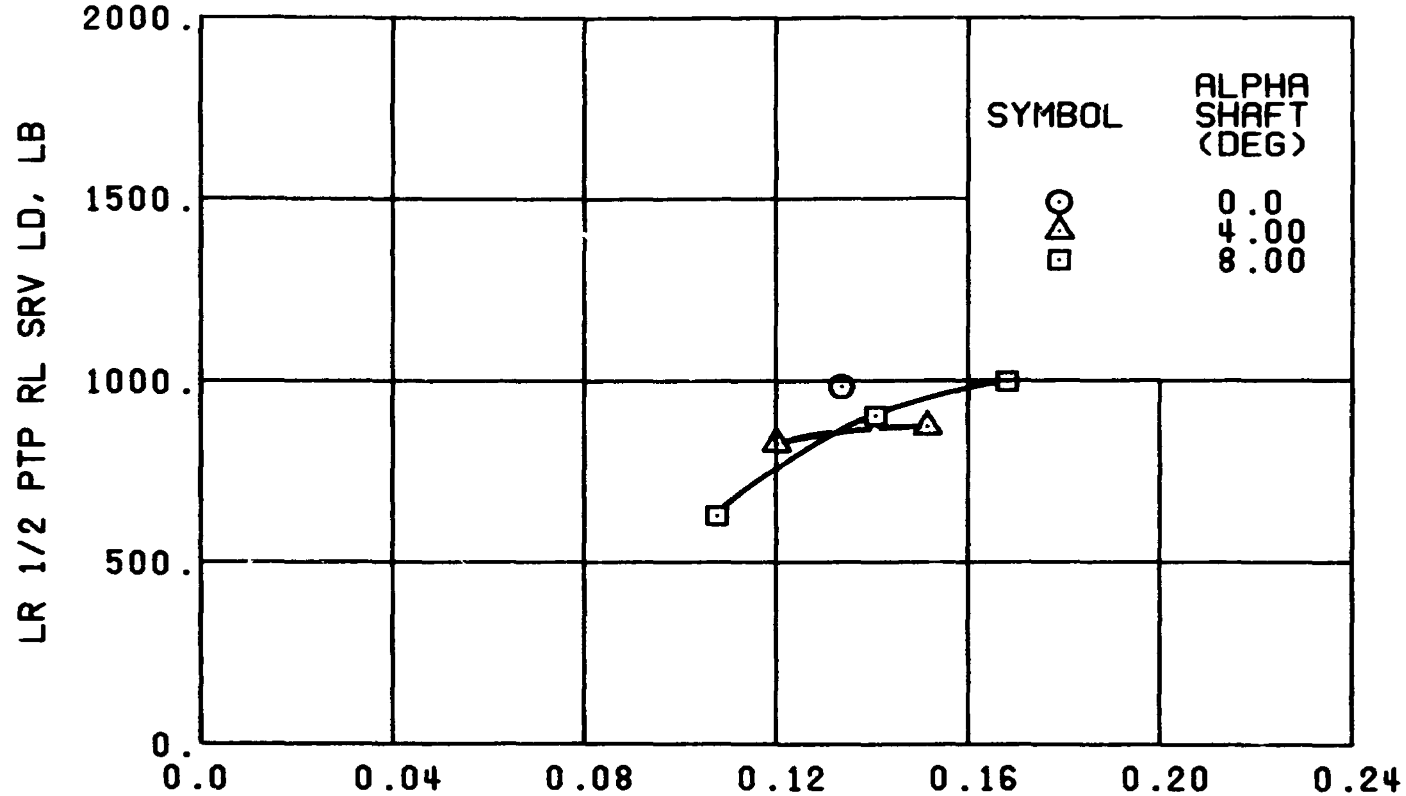

LIFT COEFF, CL/SIGMA

(q) GAGE 25

Figure 40. Continued.
μ = 0.21 B'_{1s} = 0 Deg

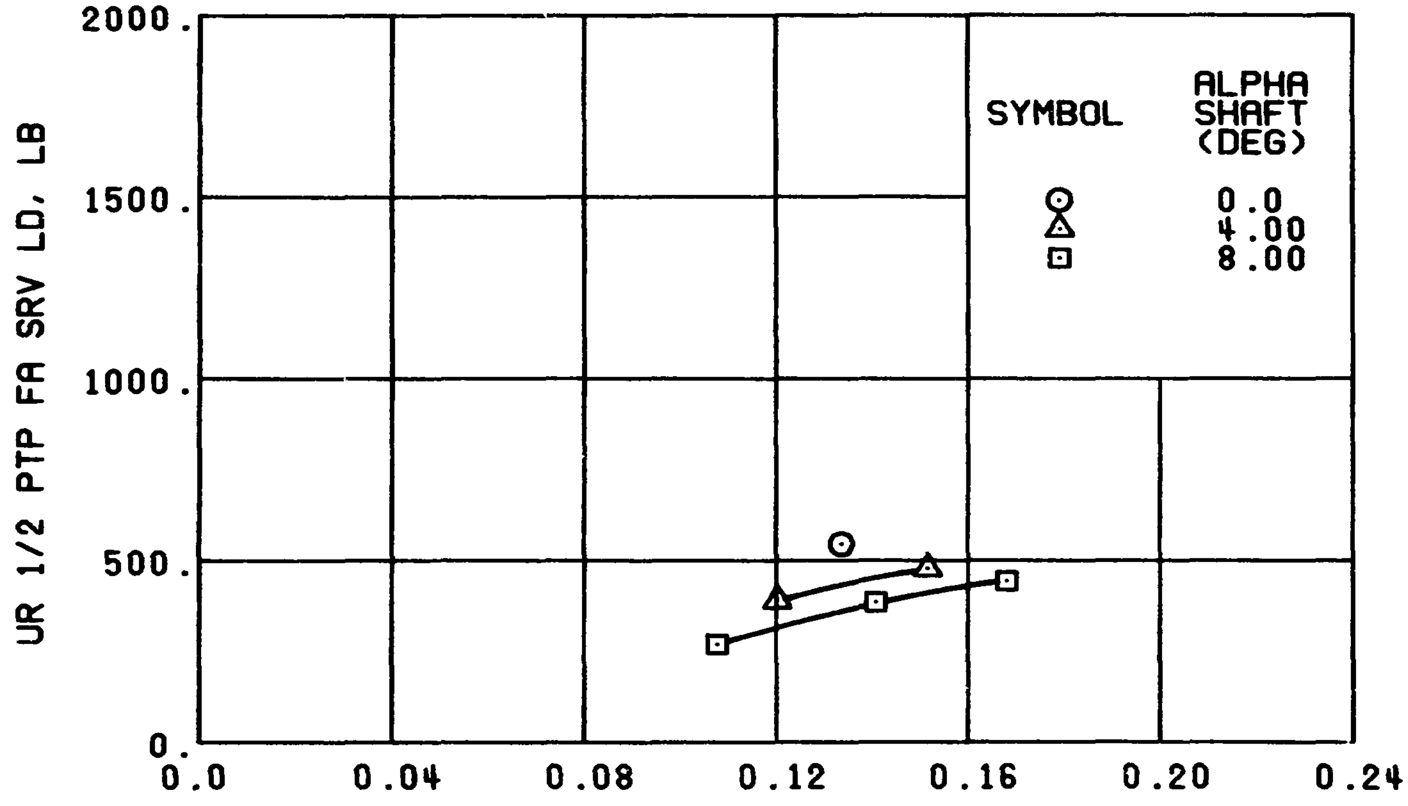

(r) GAGE 24

Figure 40. Continued.
μ = 0.21 B'_{1s} = 0 Deg

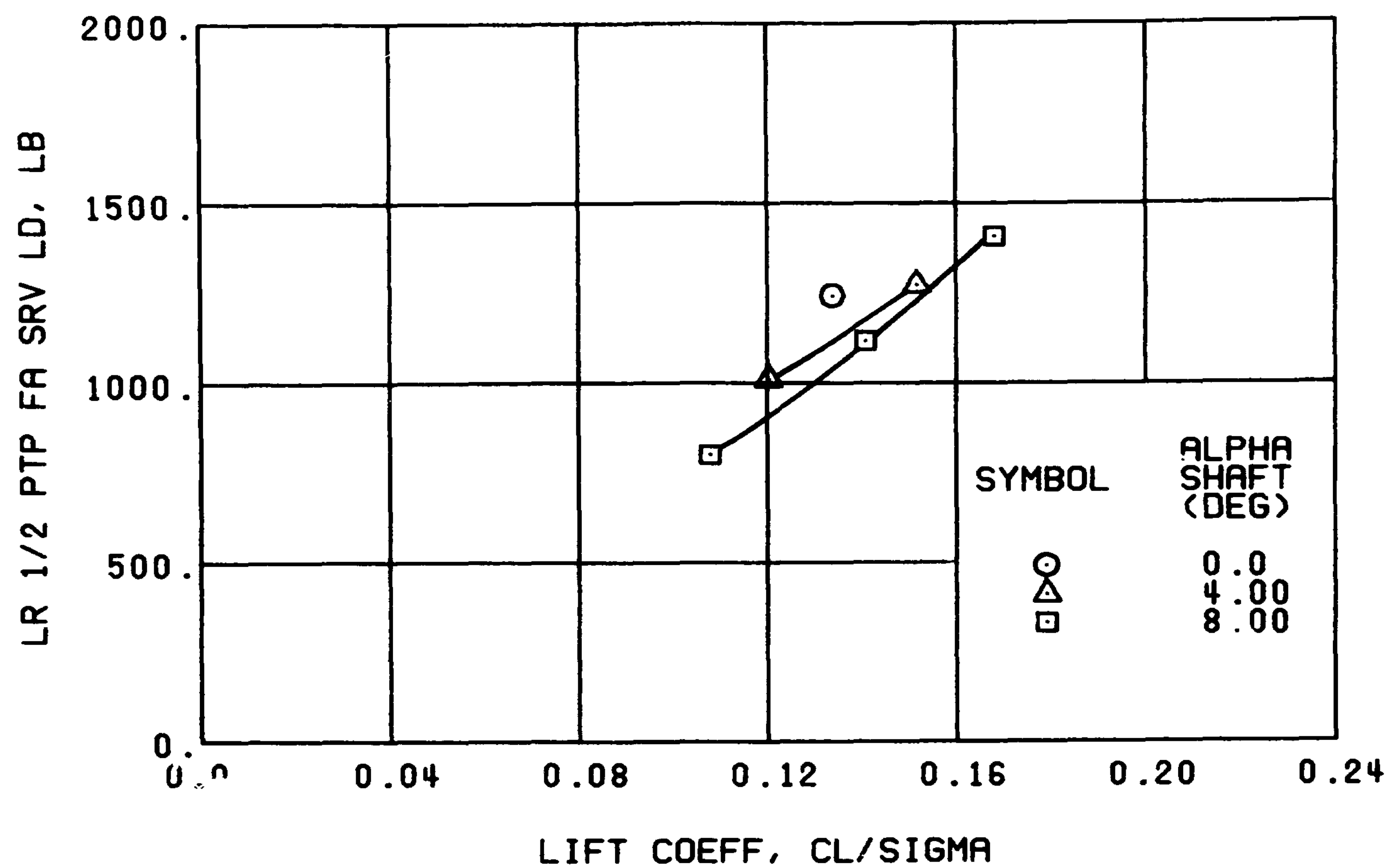

(s) GAGE 27

Figure 40. Continued.
$\mu = 0.21 \quad B'_{1s} = 0$ Deg

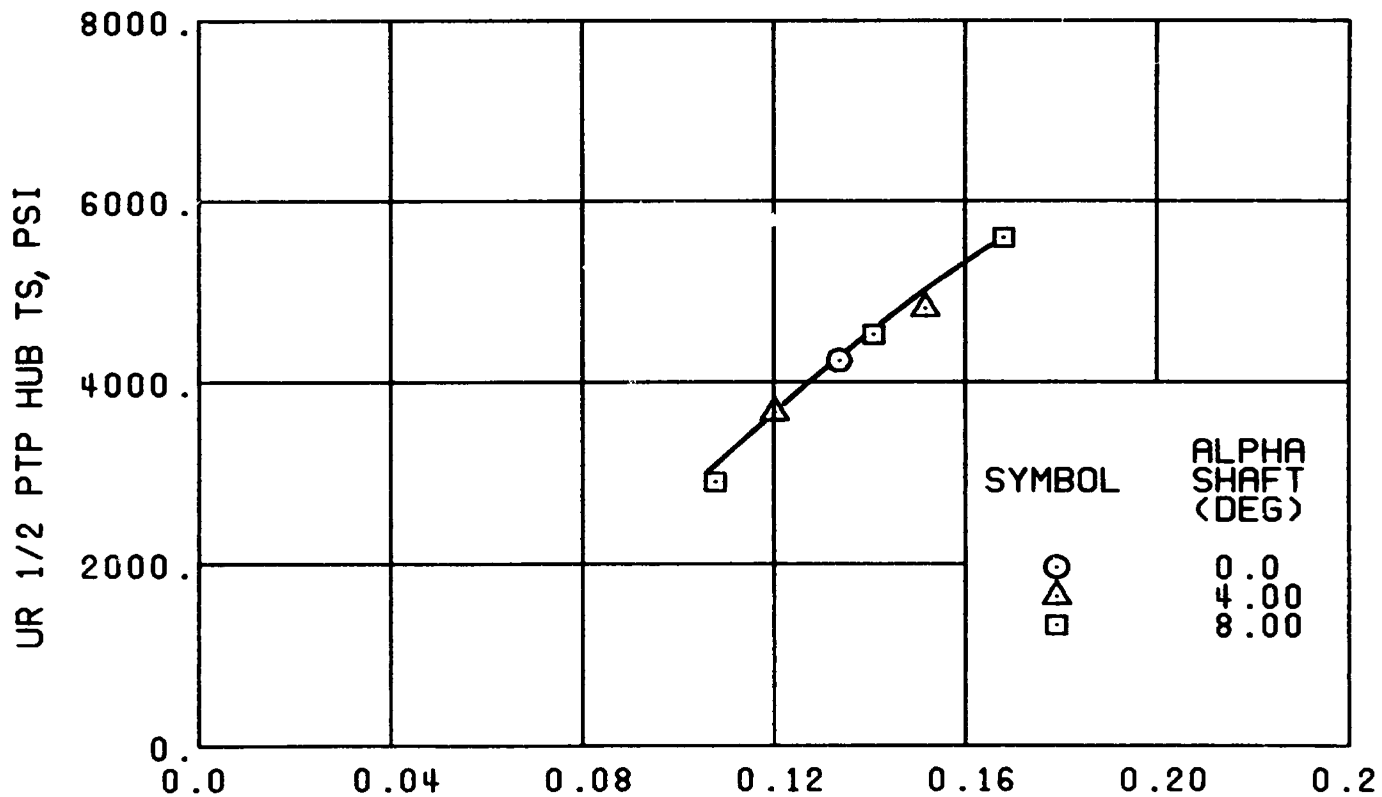

(t) GAGE 65

Figure 40. Continued.
$\mu = 0.21 \quad B'_{1s} = 0$ Deg

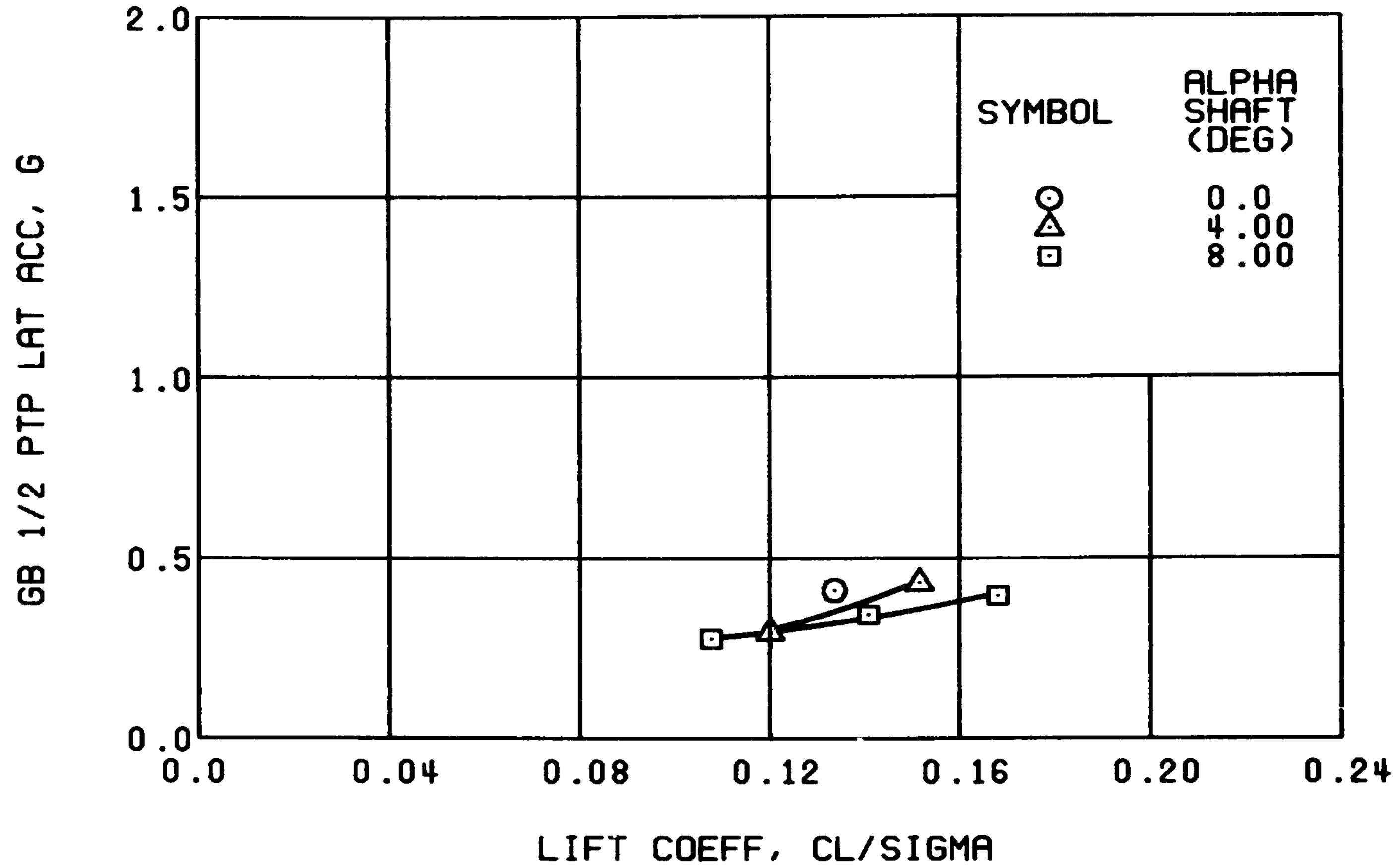

(u) GAGE 15 STA 76, BL 30

Figure 40. Continued.
$\mu = 0.21$ $B'_{1s} = 0 \text{ Deg}$

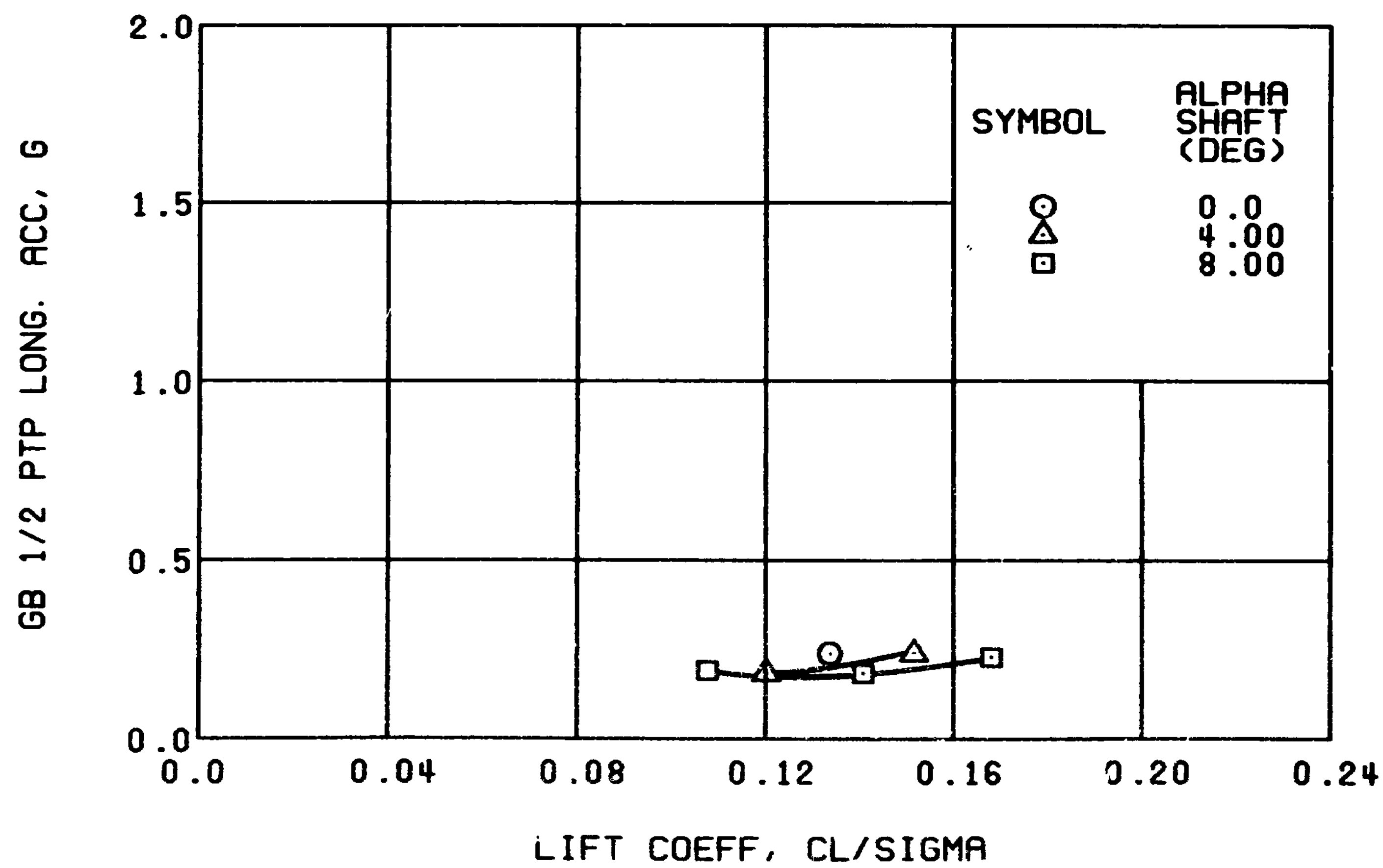

(v) GAGE 14 STA 61, BL 0

Figure 40. Continued.
$\mu = 0.21$ $B'_{1s} = 0$ Deg

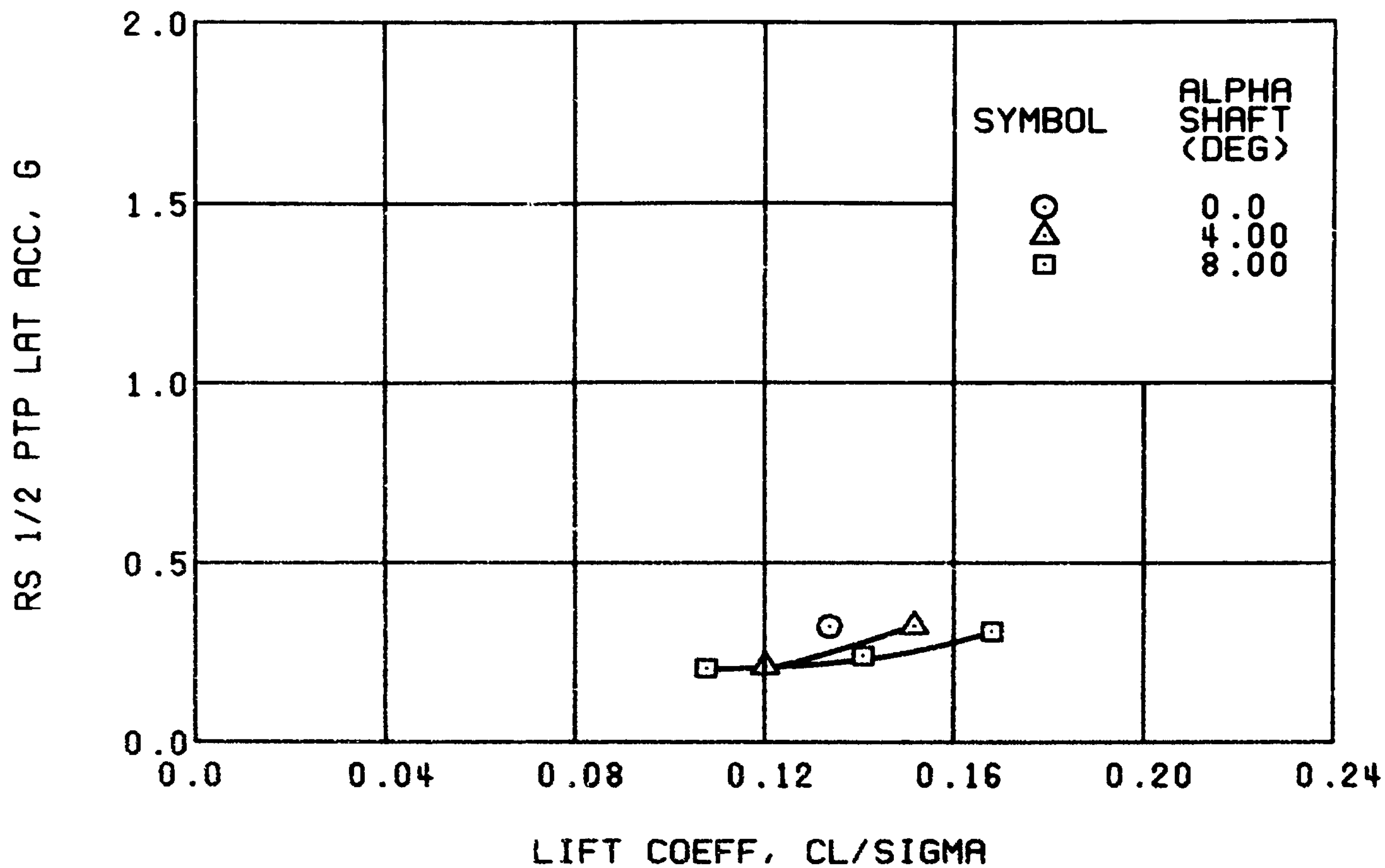

(w) GAGE 16 ROVER 3

Figure 40. Continued.
$\mu = 0.21 \quad B'_{1s} = 0$ Deg

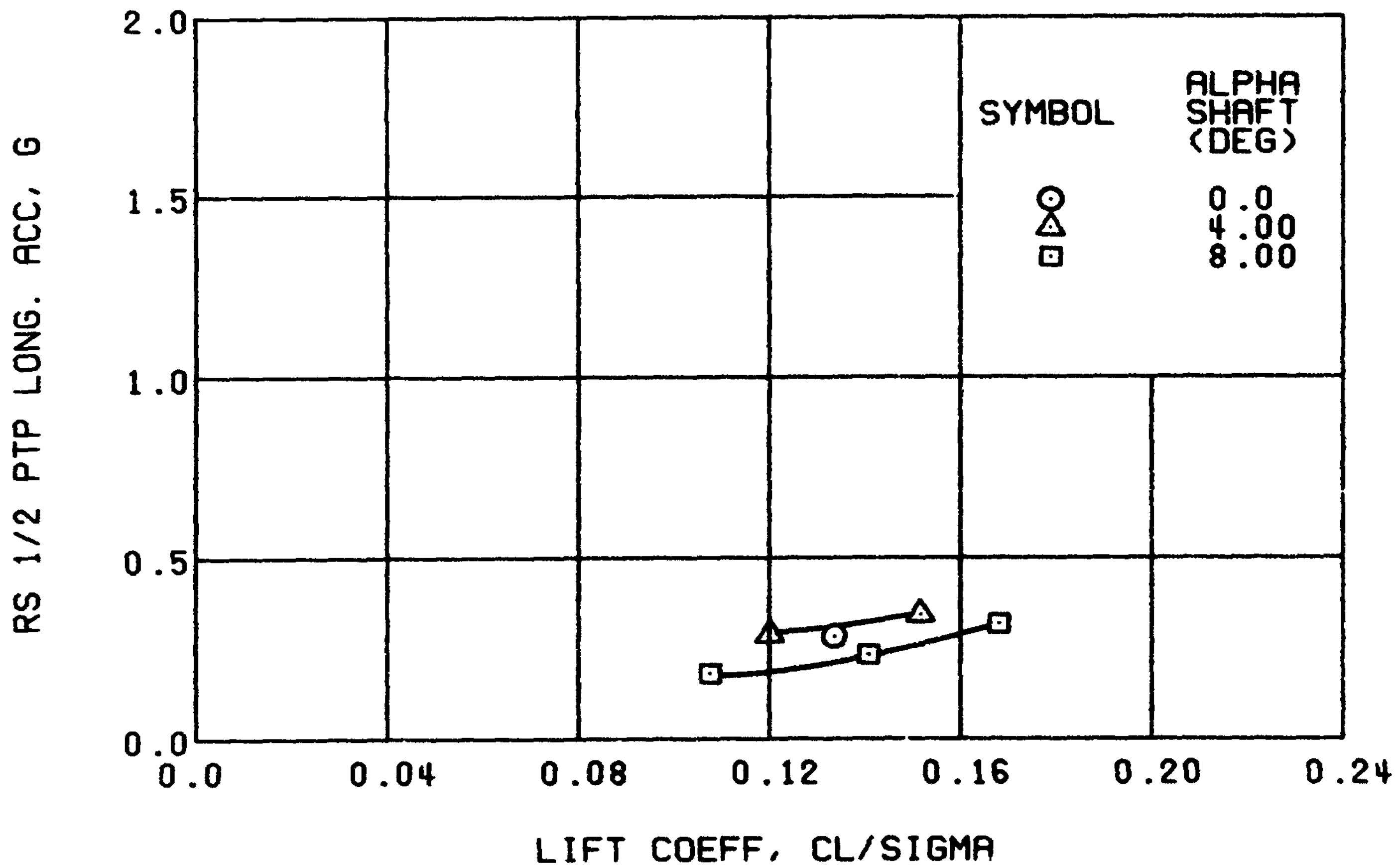

(x) GAGE 17 ROVER 4

Figure 40. Concluded.
$\mu = 0.21$ $B'_{1s} = 0$ Deg

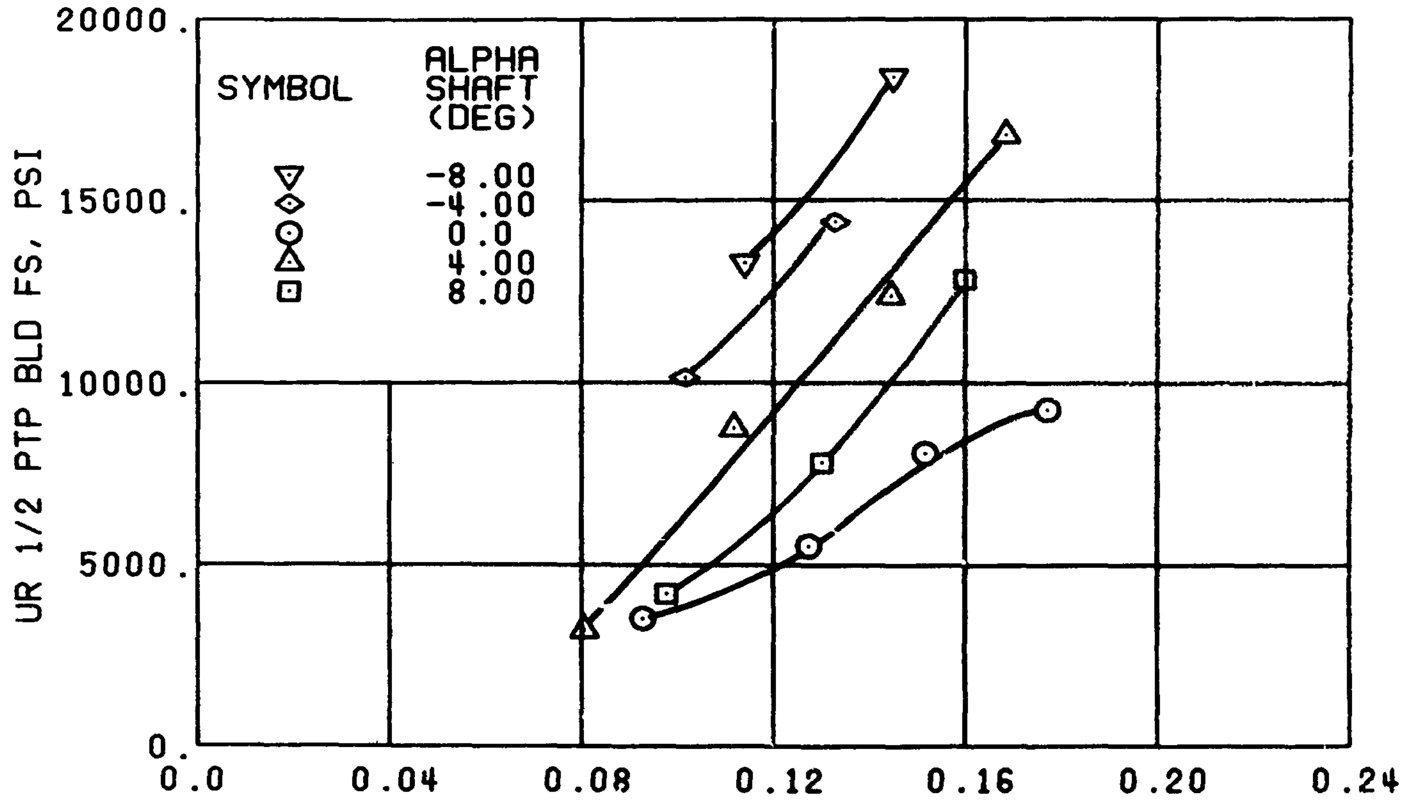

(a) GAGE 51 R84

Figure 41. Stress, Load, and Vibration Data at an Advance Ratio of 0.21 With the Lateral Displacement Control (B'_{1s}) Set at 2 Degrees.

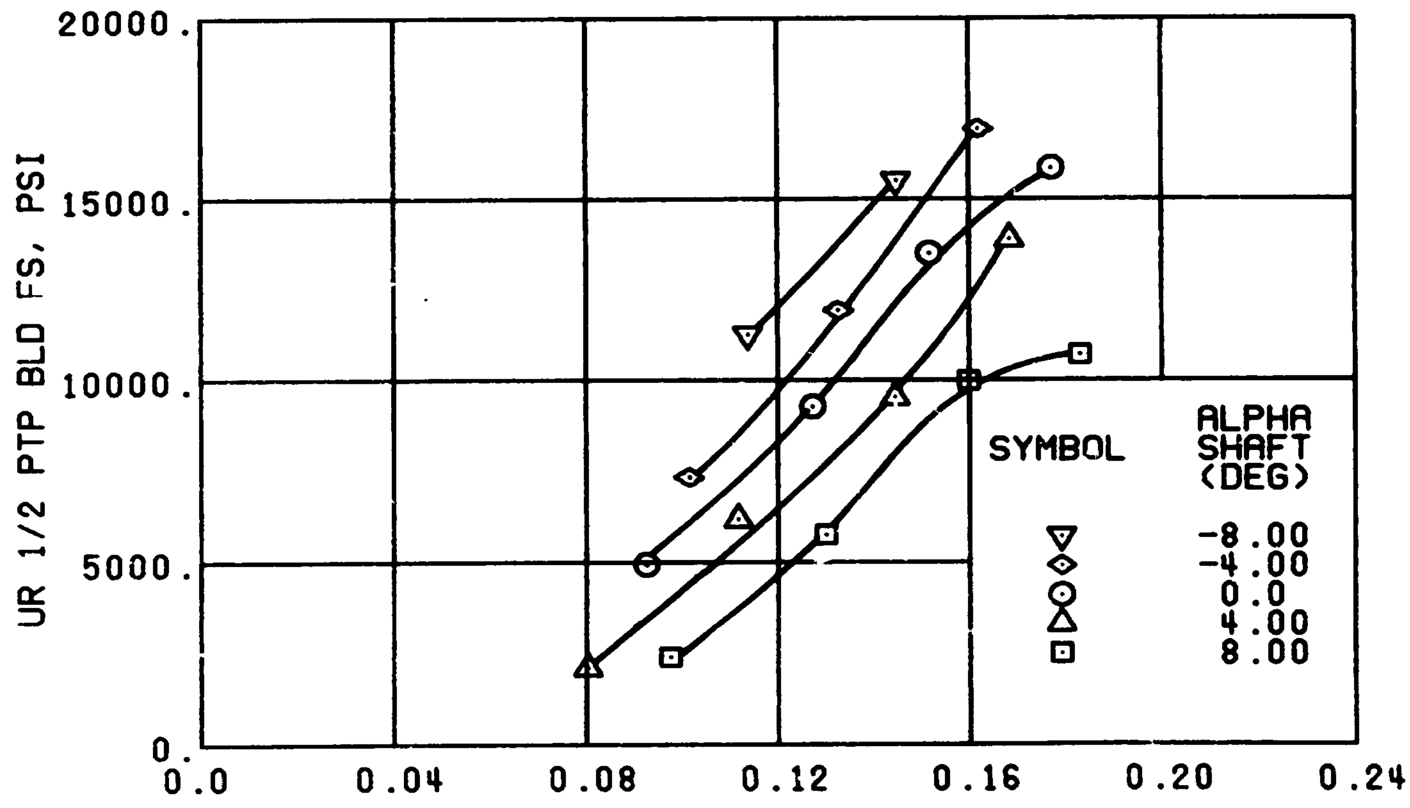

(c) GAGE 52 R108

Figure 41. Continued.
$\mu = 0.21$ $B_{1s}' = 2$ Deg

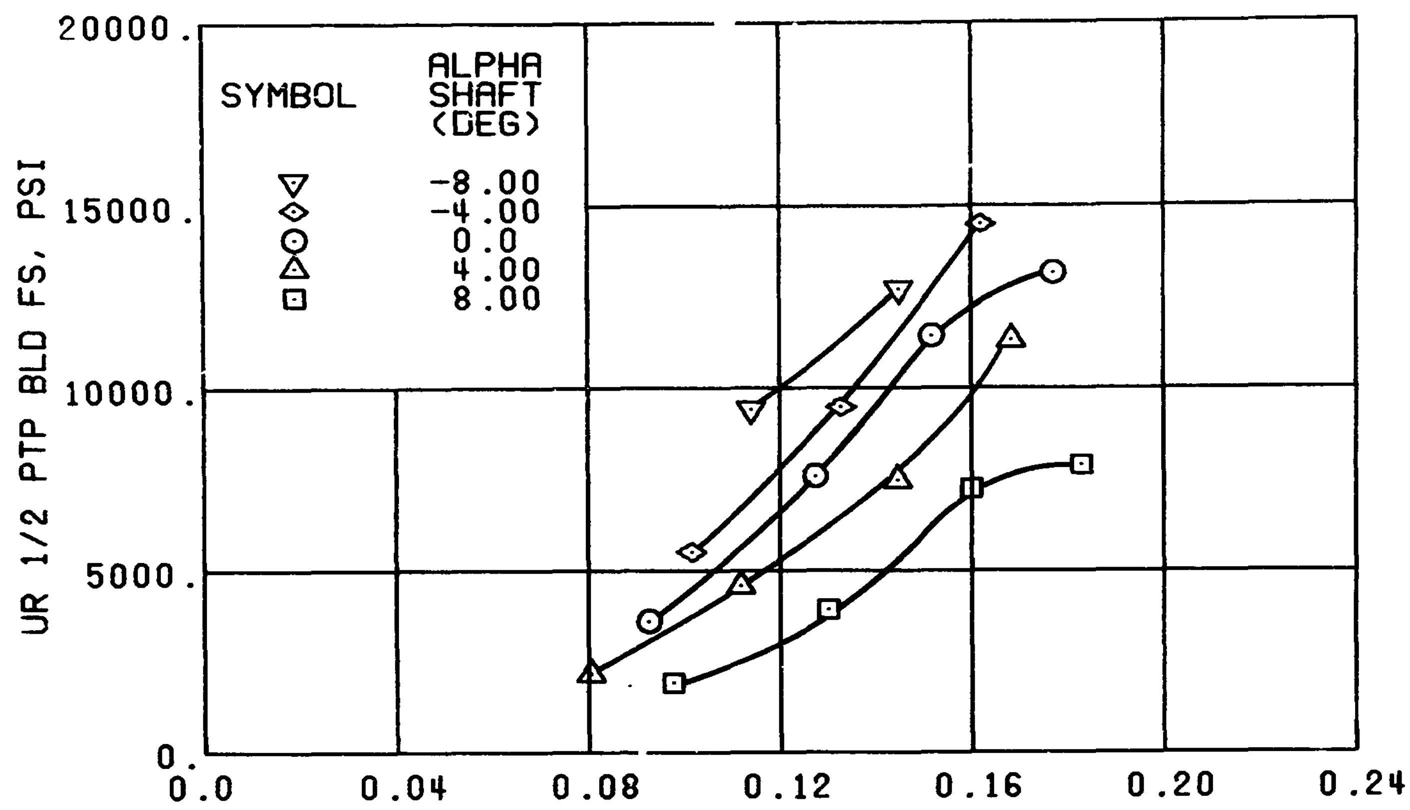

(d) GAGE 53 R132

Figure 41. Continued.
$\mu = 0.21 \quad B'_{1s} = 2$ Deg

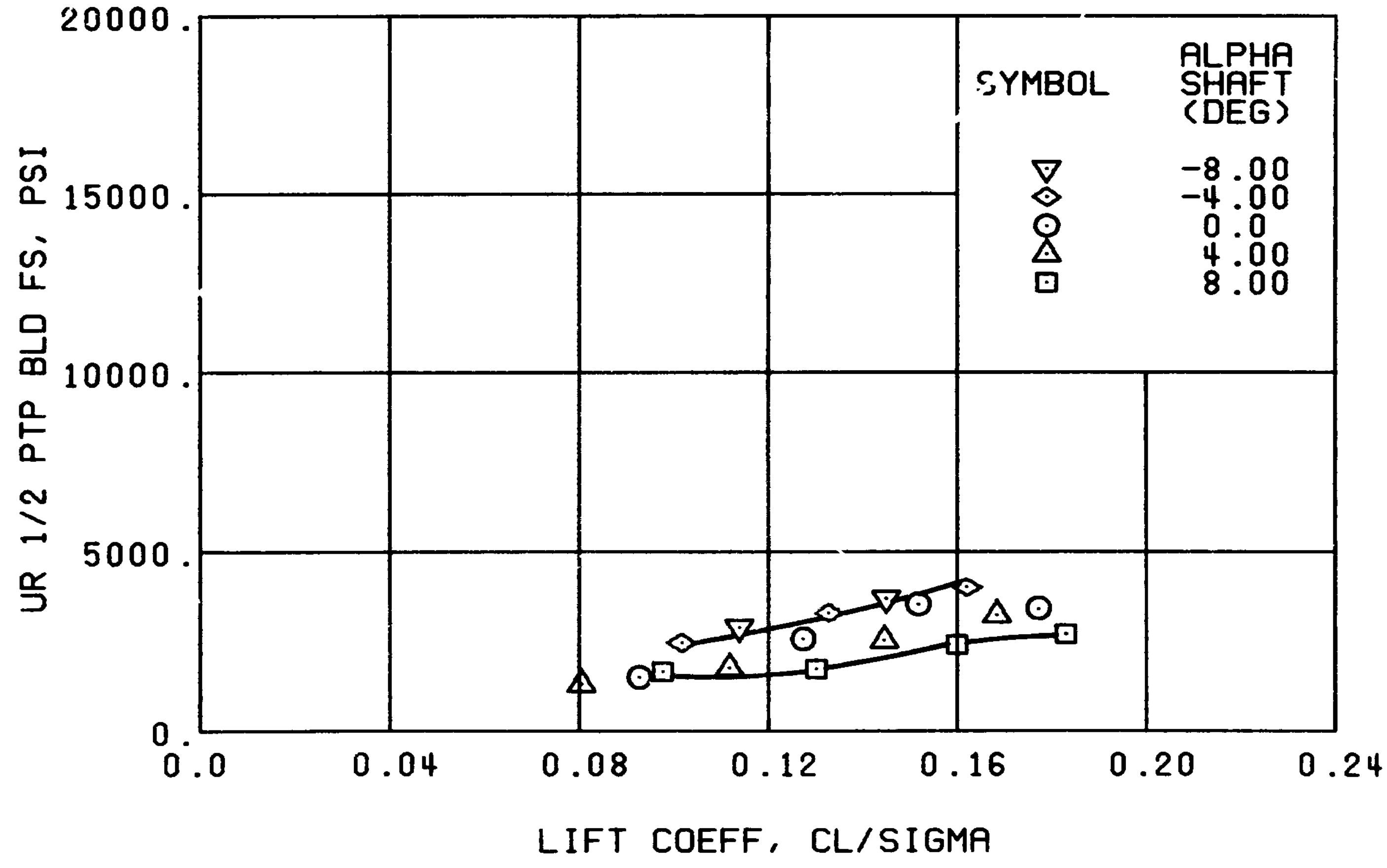

(f) GAGE 55 R204

Figure 41. Continued.
$\mu = 0.21$ $B'_{1s} = 2$ Deg

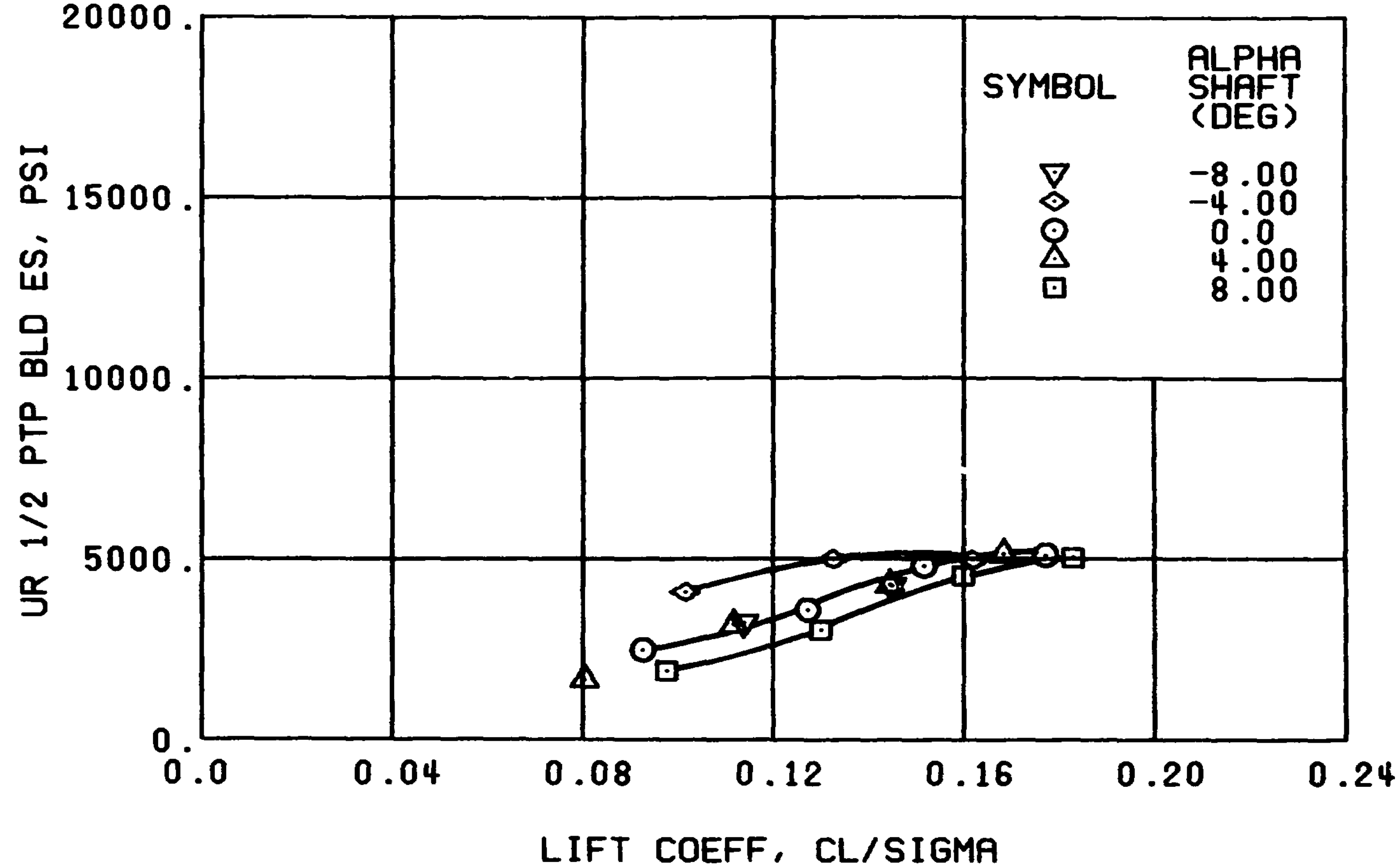

(g) GAGE 79 R60

Figure 41. Continued.
$\mu = 0.21$ $B'_{1s} = 2$ Deg

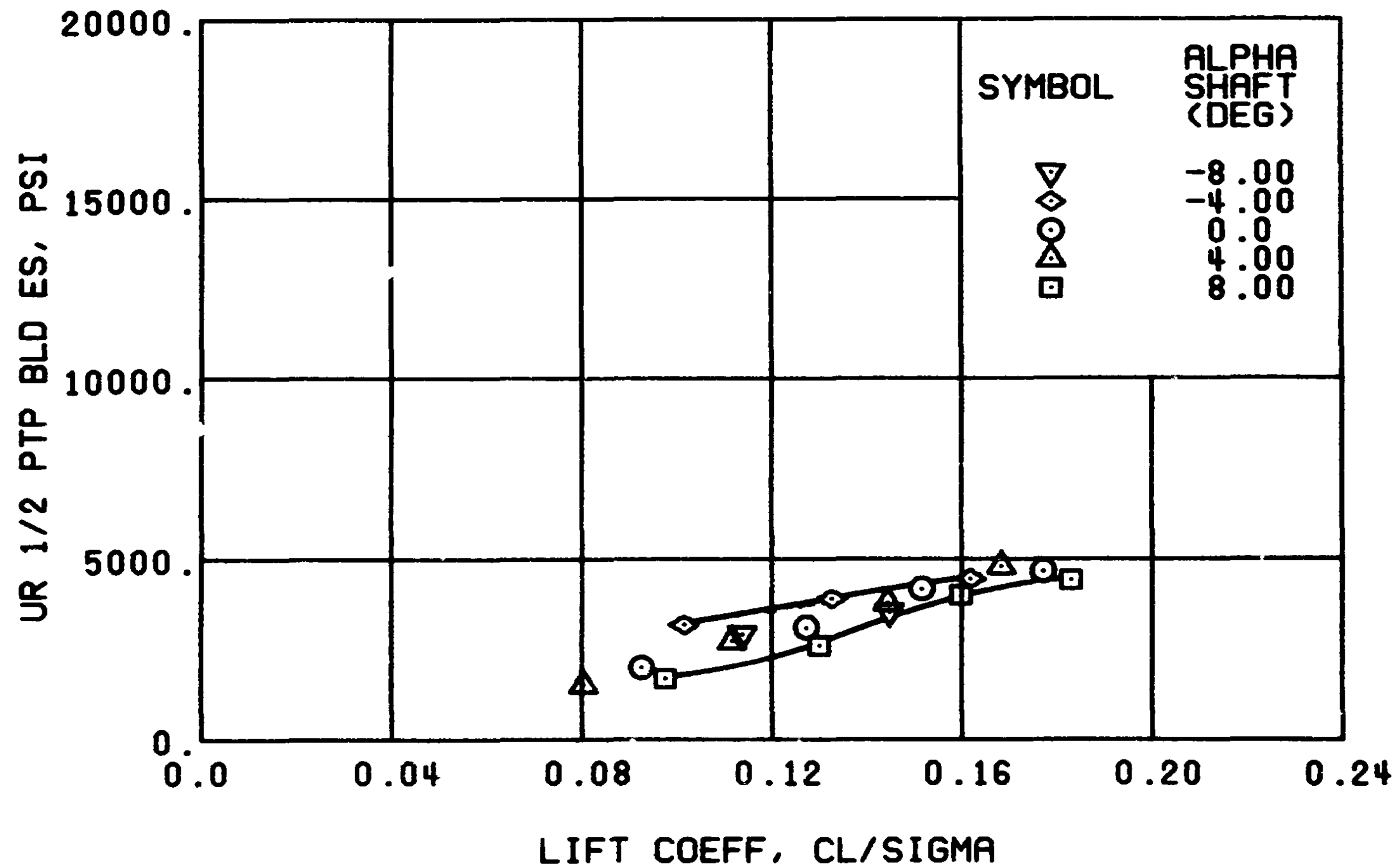

(h) GAGE 40 R84

Figure 41. Continued.
$\mu = 0.21$ $B'_{1s} = 2$ Deg

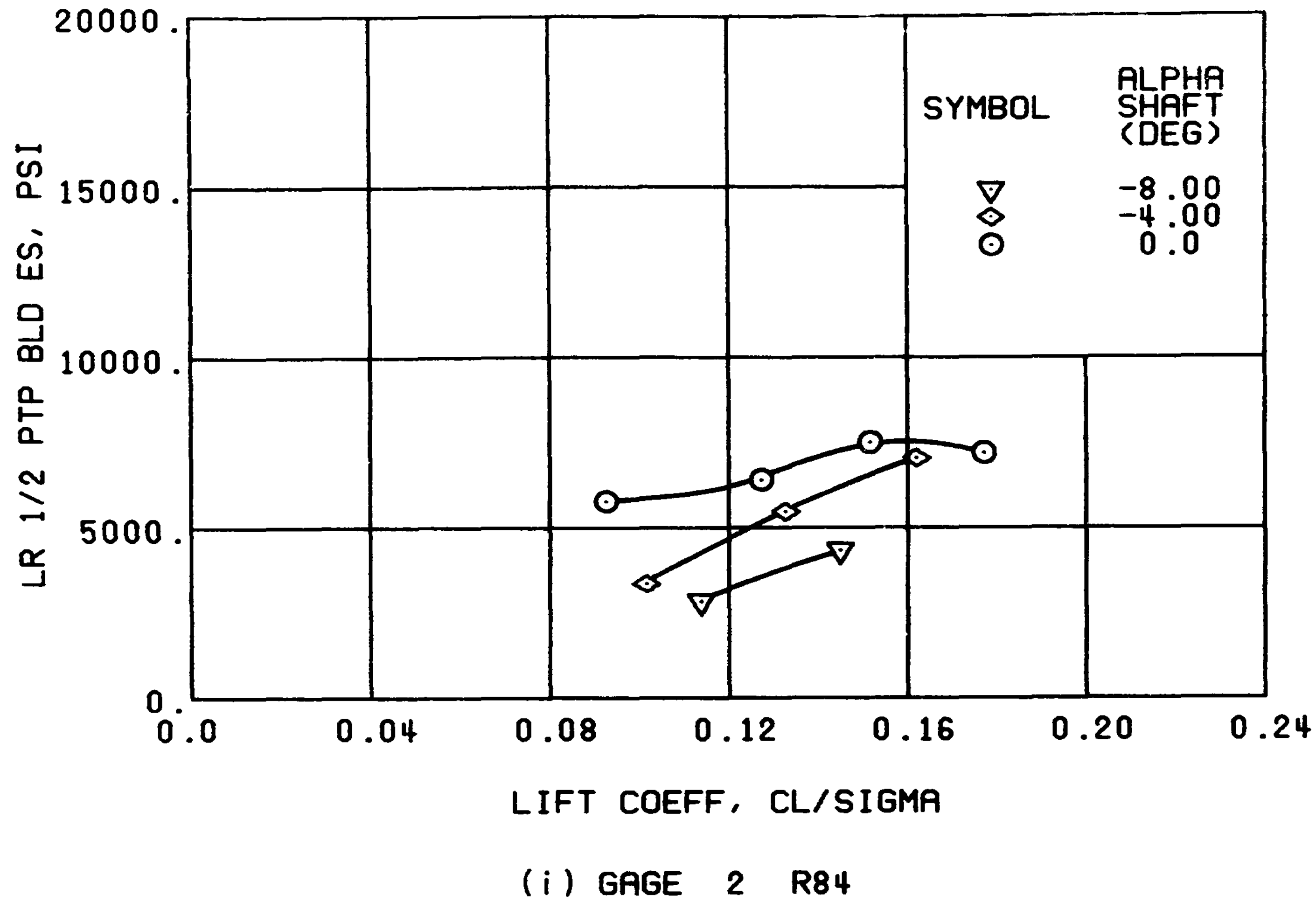

Figure 41. Continued.
μ = 0.21 B'_{1s} = 2 Deg

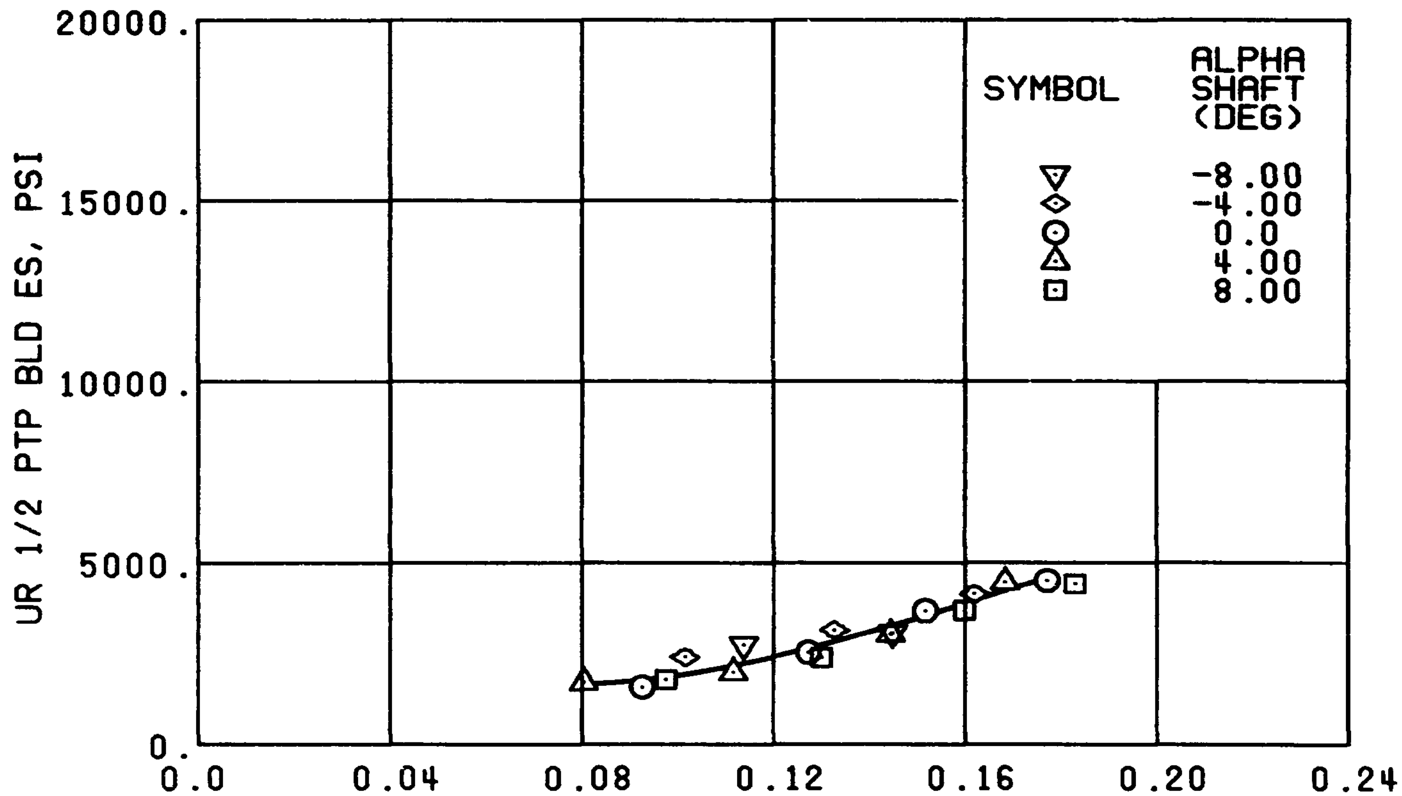

(j) GAGE 42 R132

Figure 41. Continued.
$\mu = 0.21 \quad B'_{1s} = 2$ Deg

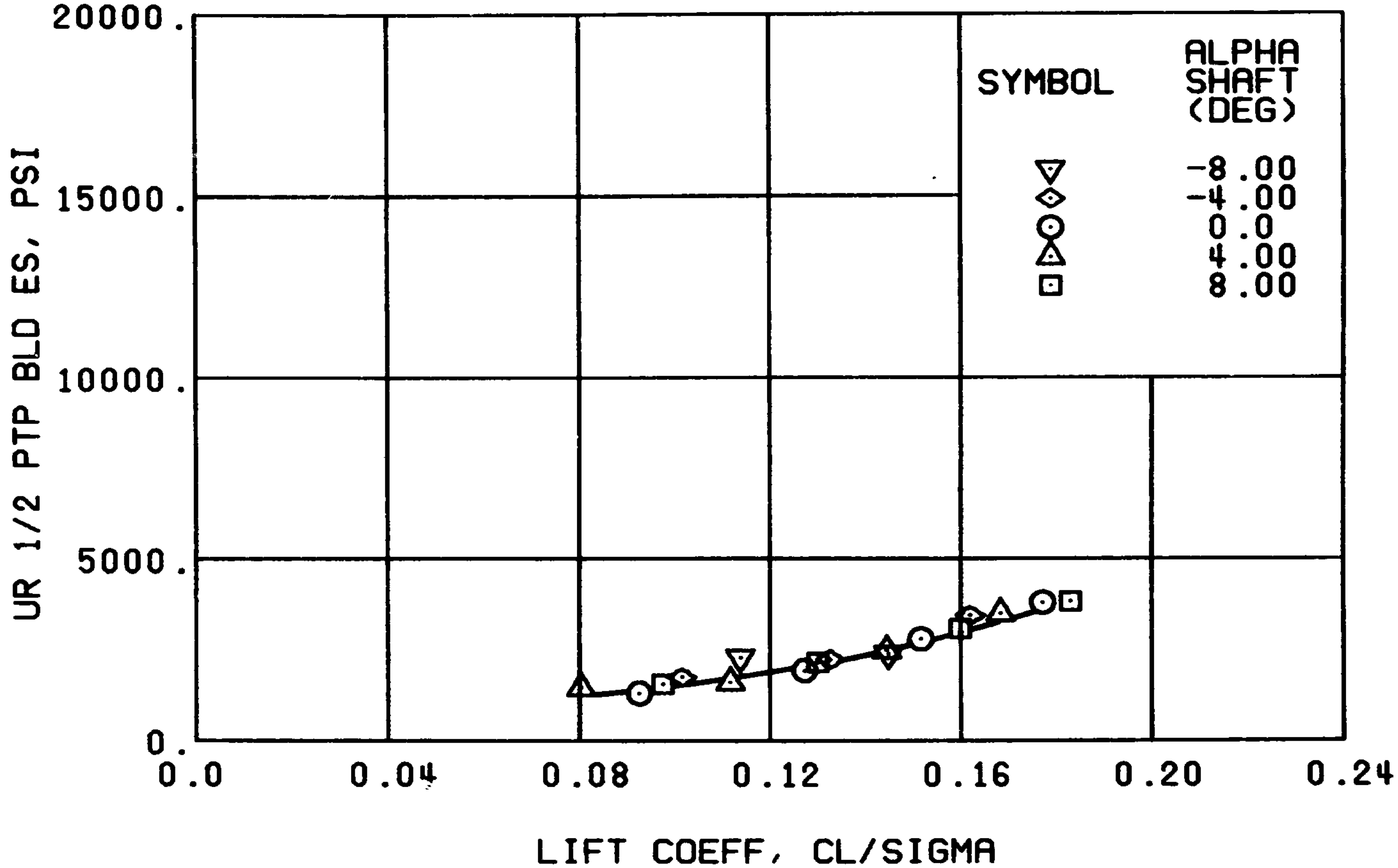

(k) GAGE 43 R168

Figure 41. Continued.
$\mu = 0.21$ $B'_{1s} = 2$ Deg

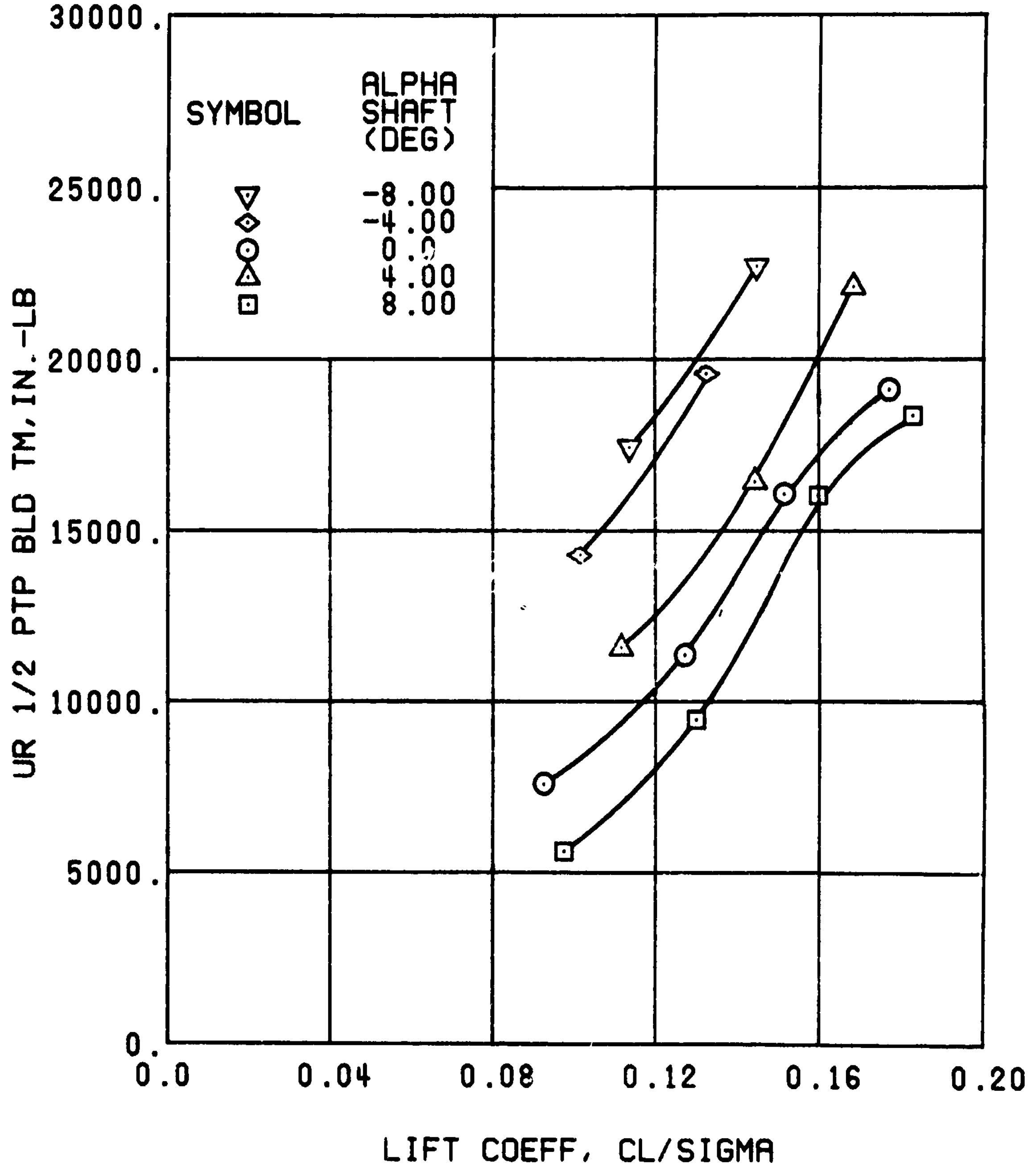

(I) GAGE 45 R82

Figure 41. Continued.
$\mu = 0.21 \quad B'_{1s} = 2$ Deg

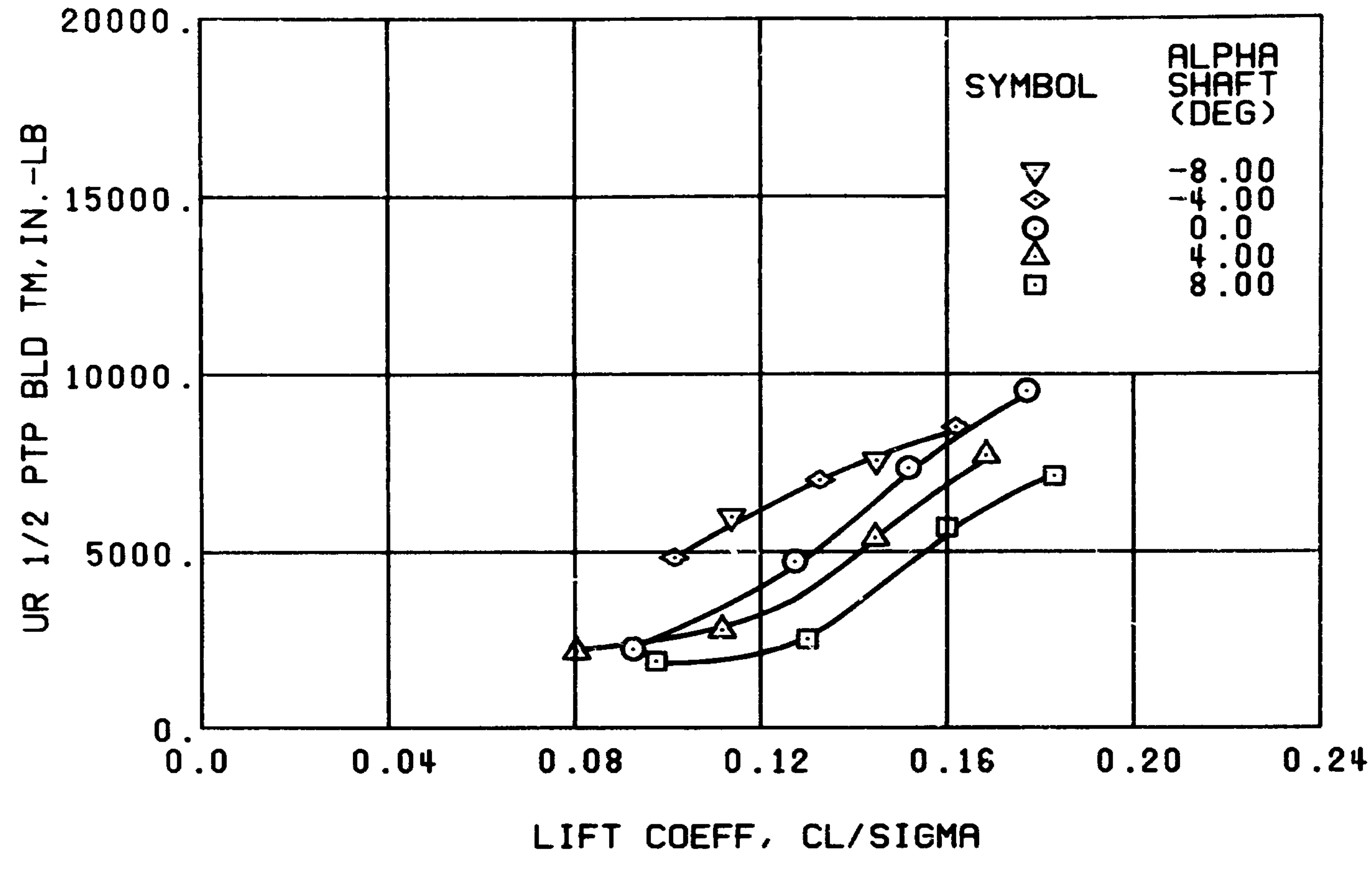

(m) GAGE 46 R130

Figure 41. Continued.
$\mu = 0.21$ $B'_{1s} = 2$ Deg

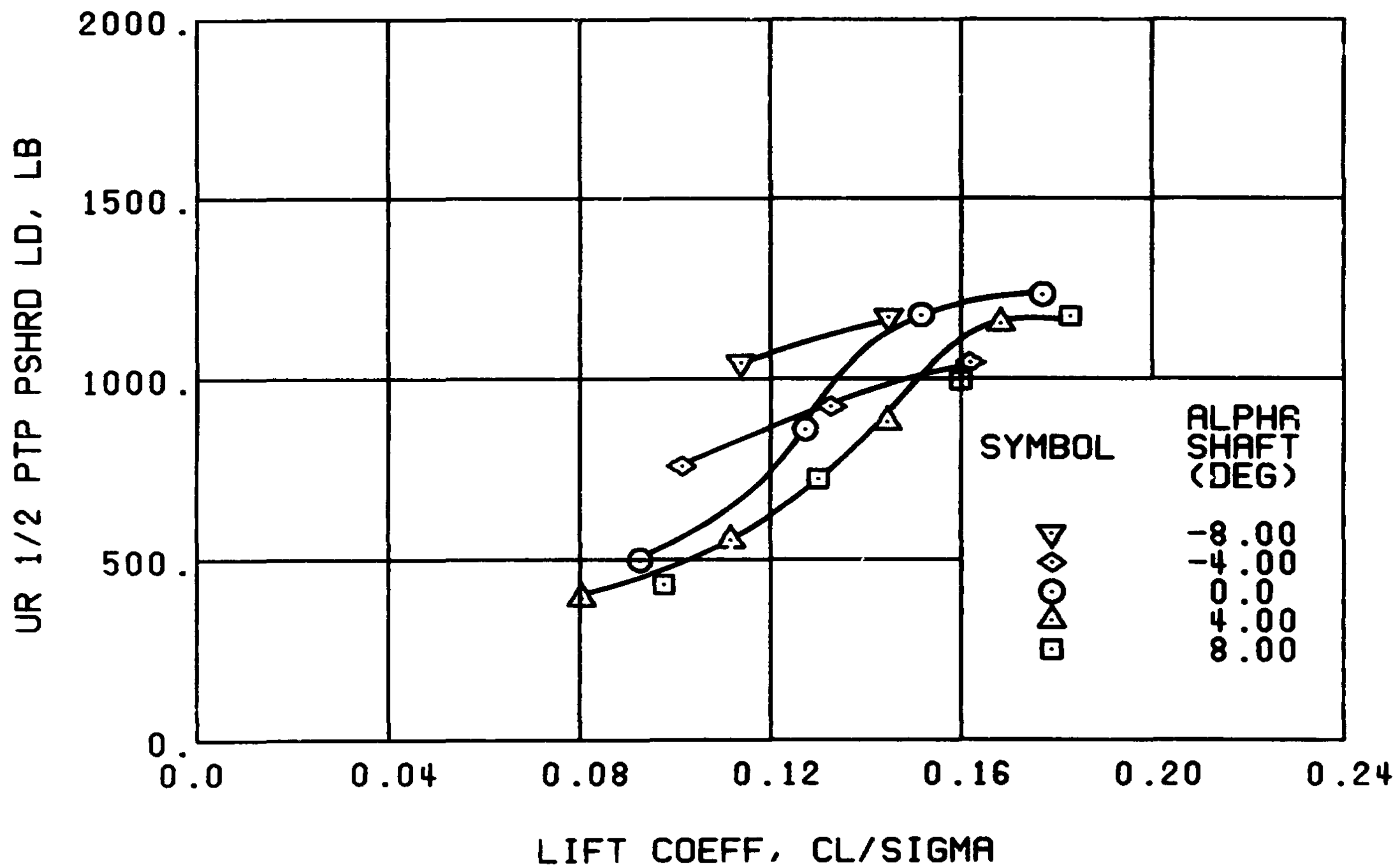

(n) GAGE 37

Figure 41. Continued.
$\mu = 0.21 \quad B'_{1s} = 2$ Deg

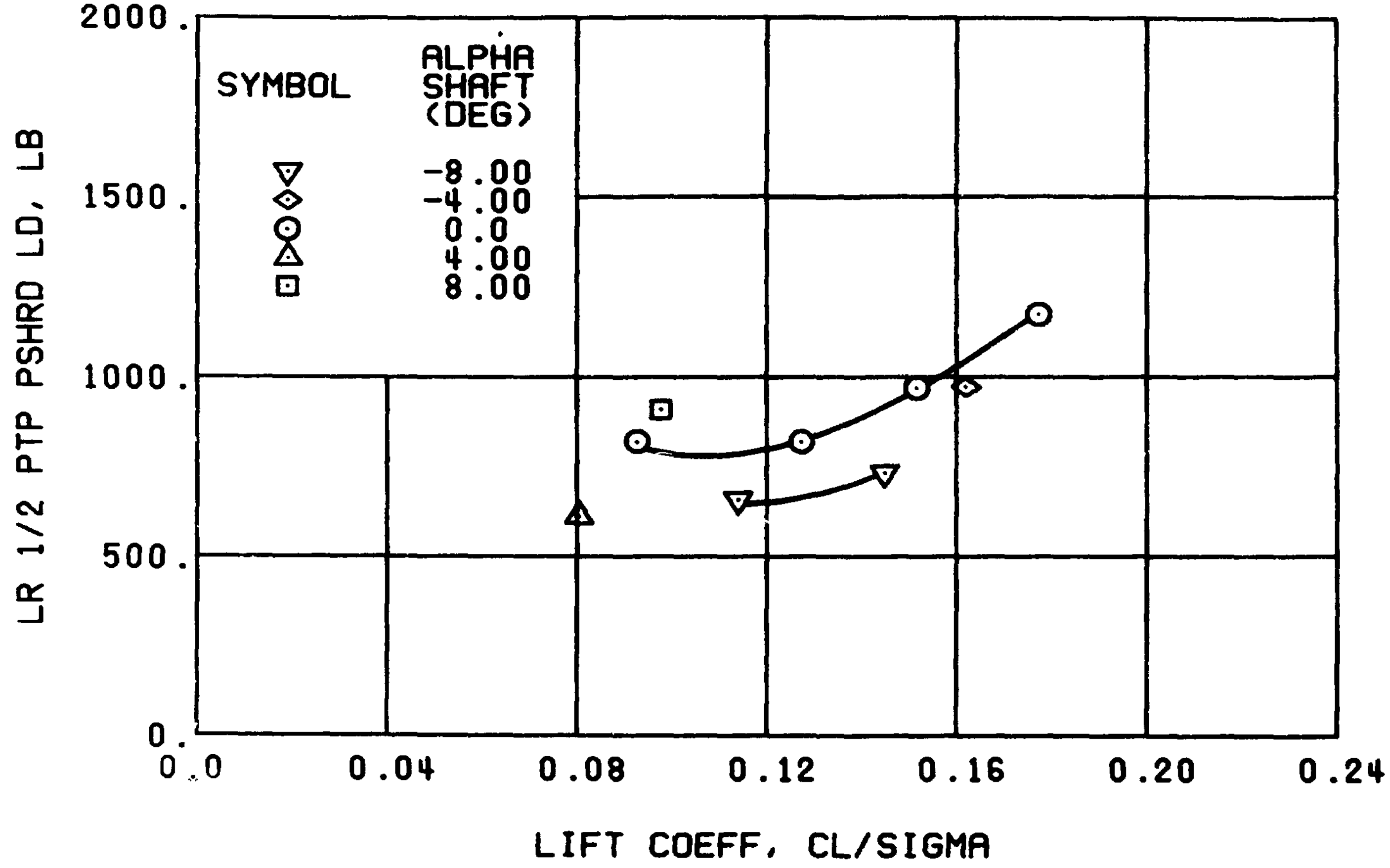

(o) GAGE 34

Figure 41. Continued.
$\mu = 0.21 \quad B'_{1s} = 2$ Deg

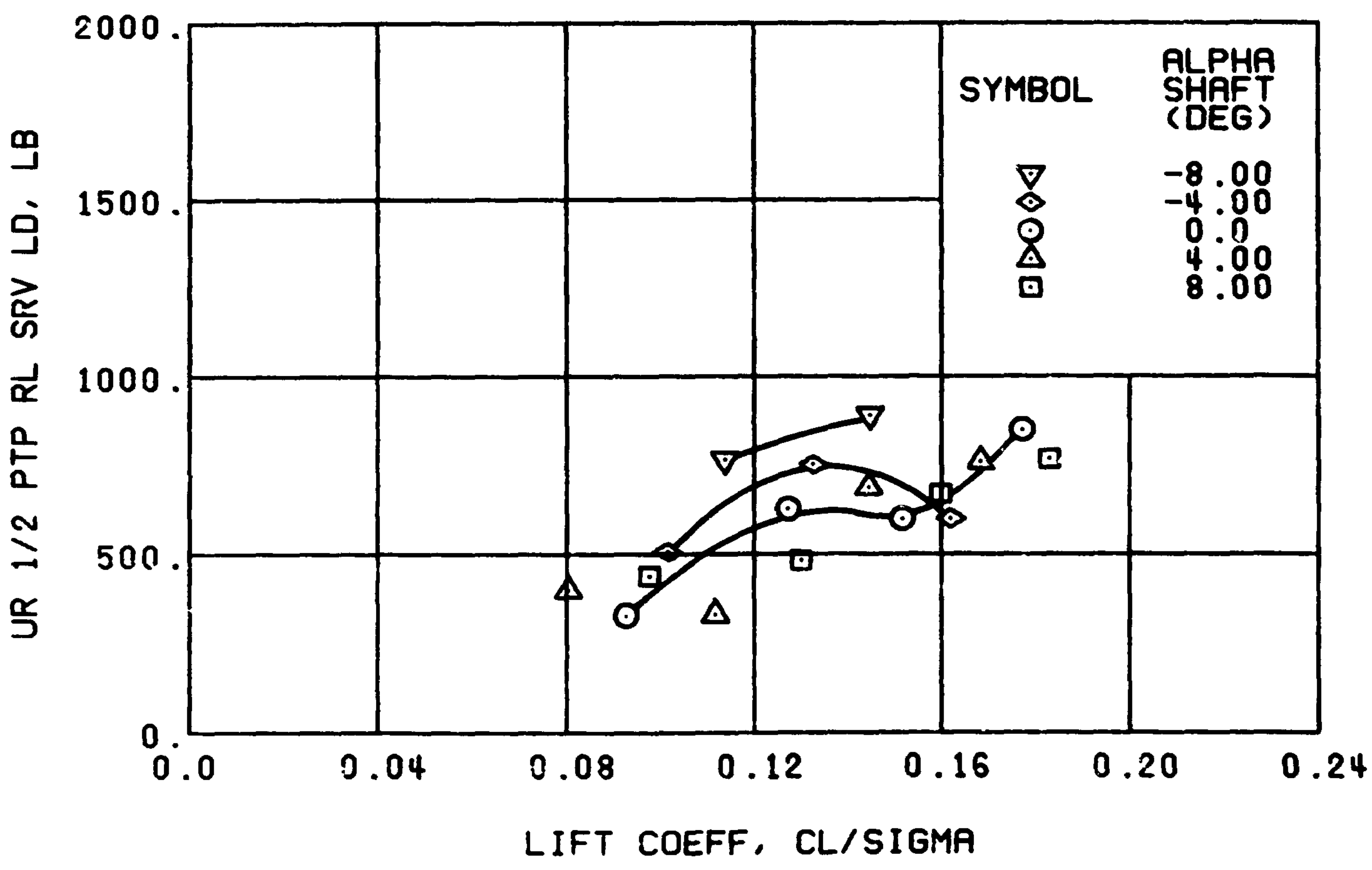

(p) GAGE 22

Figure 41. Continued.
$\mu = 0.21$ $B'_{1s} = 2$ Deg

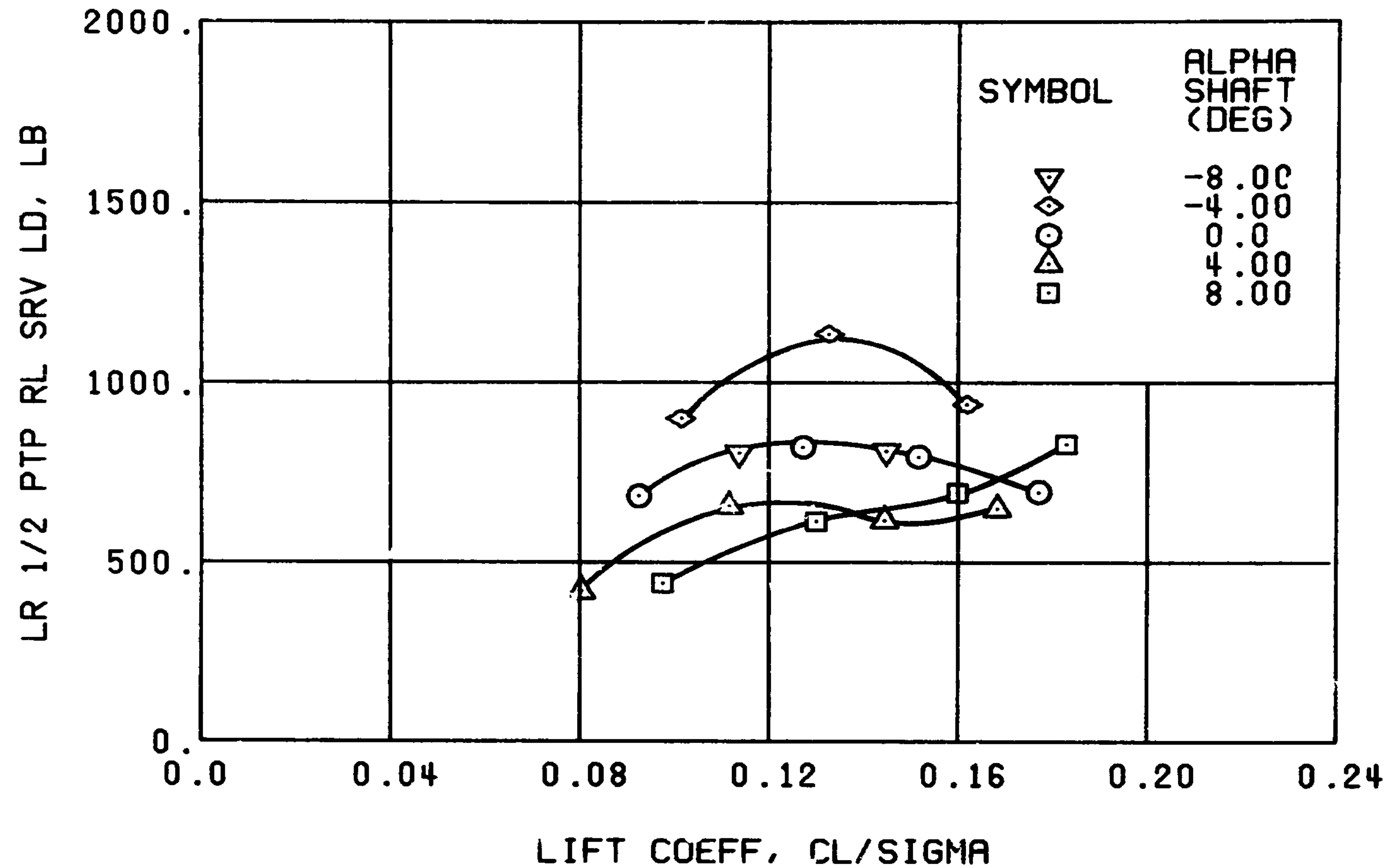

(q) GAGE 25

Figure 41. Continued.
μ = 0.21 B'_{1s} = 2 Deg

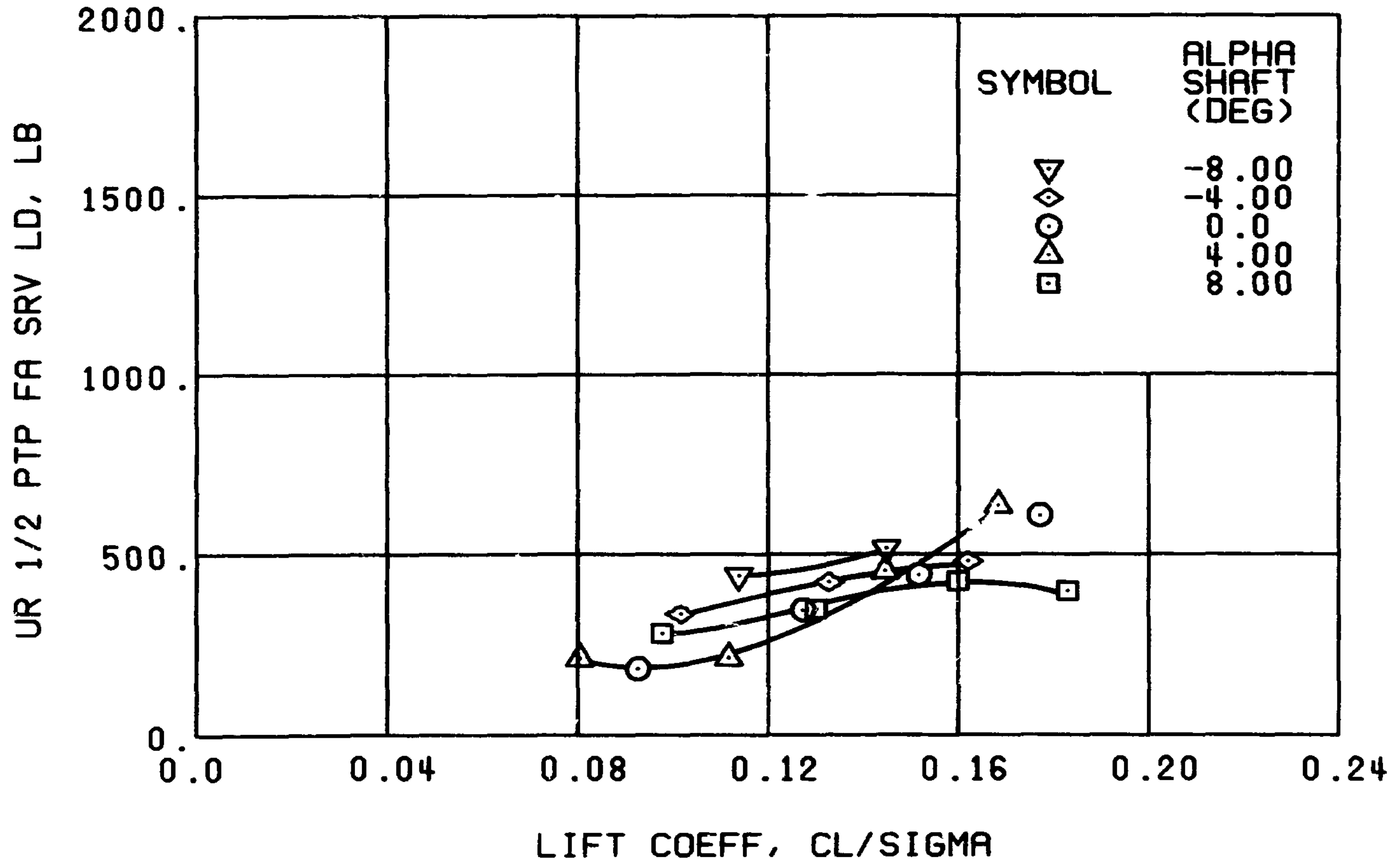

(r) GAGE 24

Figure 41. Continued.
$\mu = 0.21 \quad B'_{1s} = 2$ Deg

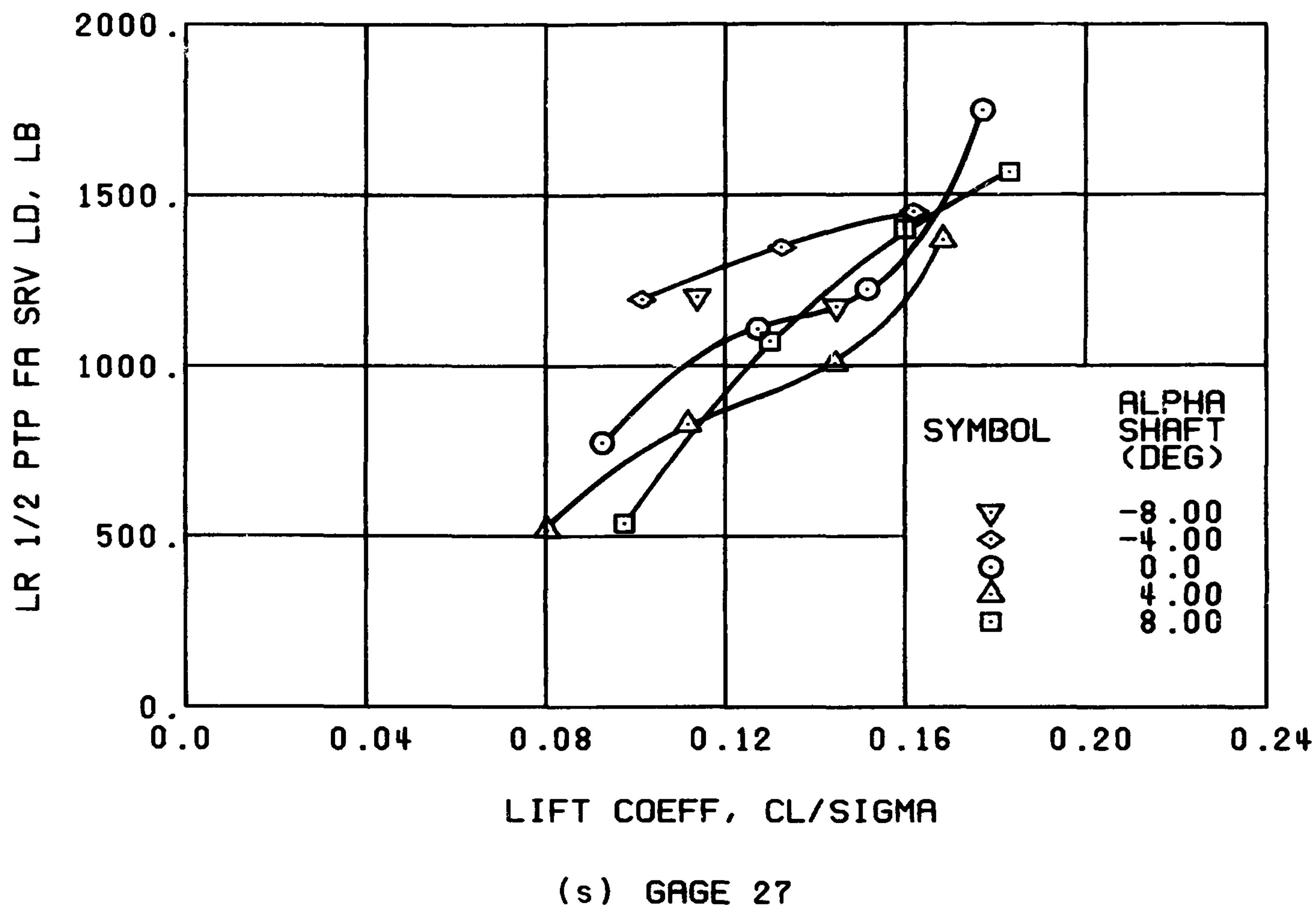

Figure 41. Continued.
$\mu = 0.21$ $B'_{1s} = 2$ Deg

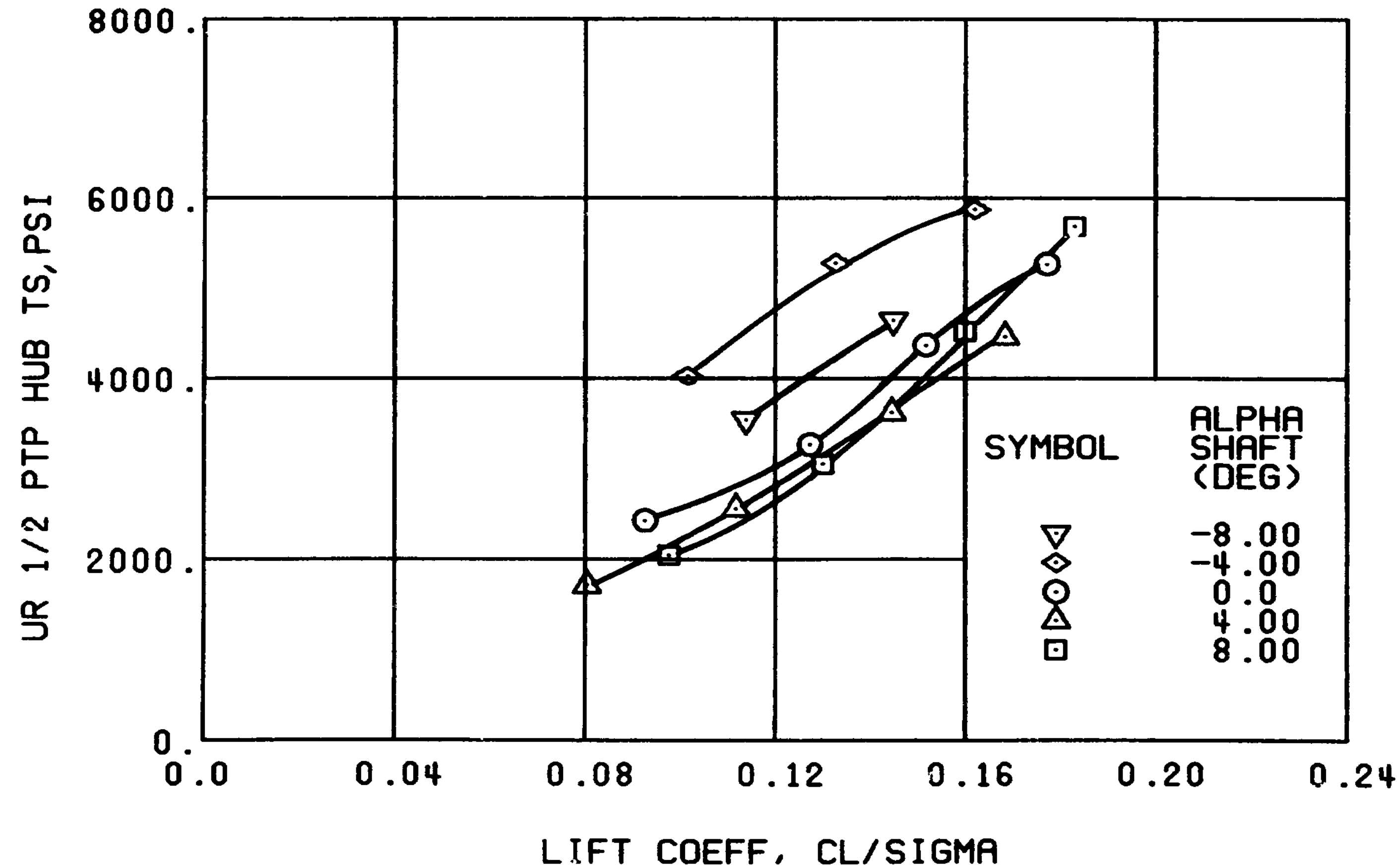

(t) GAGE 65

Figure 41. Continued.
$\mu = 0.21$ $B'_{1s} = 2$ Deg

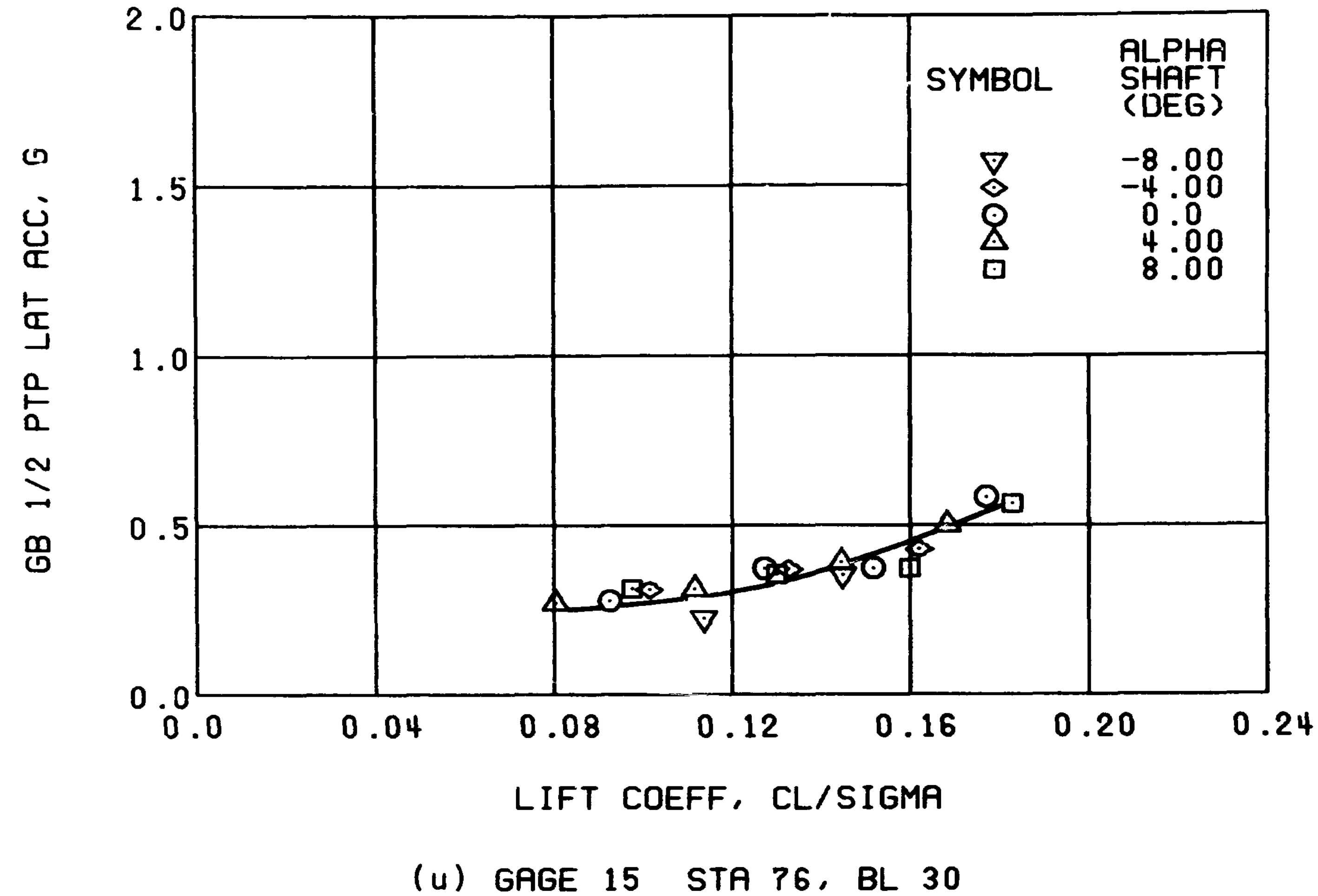

Figure 41. Continued.
$\mu = 0.21$ $B'_{1s} = 2$ Deg

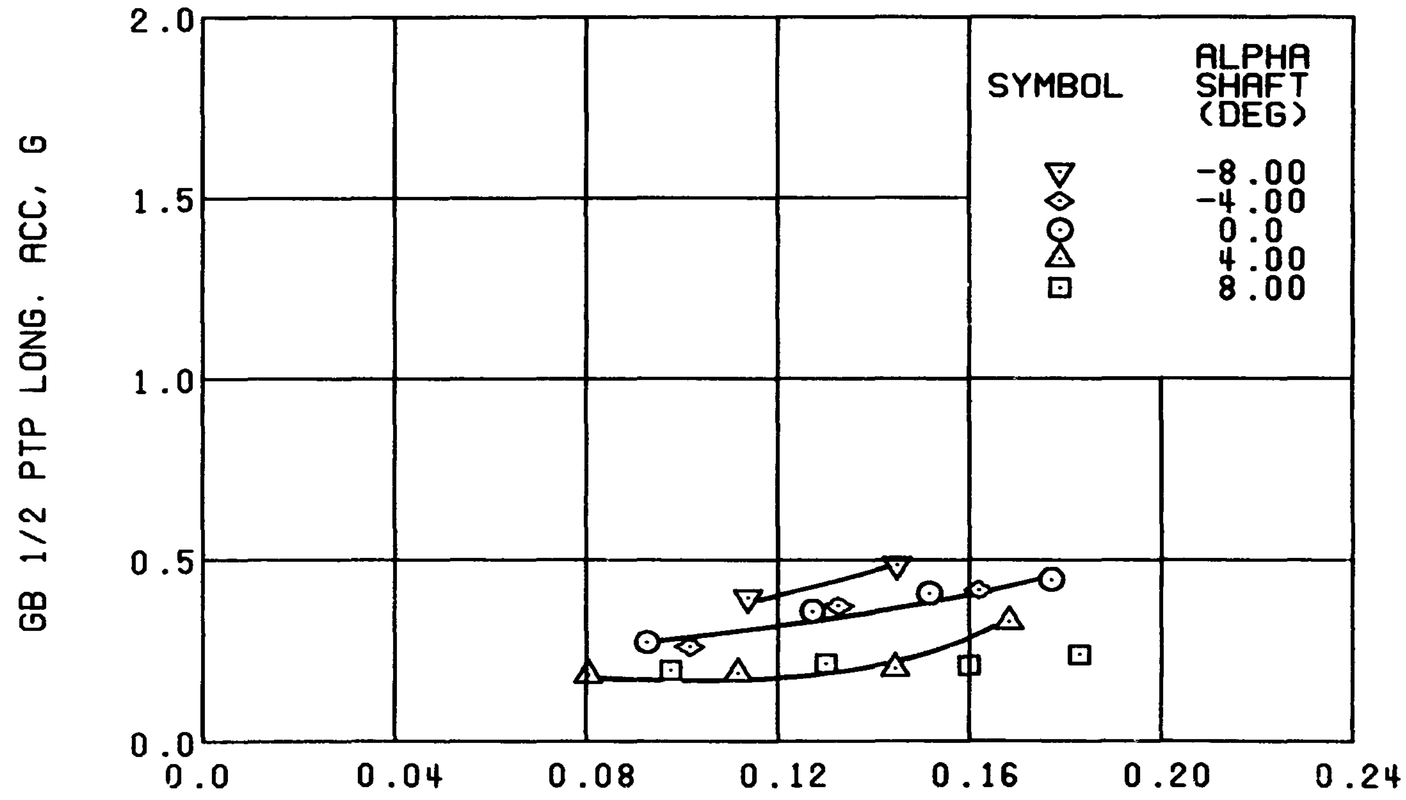

(v) GAGE 14 STA 61, BL 0

Figure 41. Continued.
$\mu = 0.21 \quad B'_{1s} = 2$ Deg

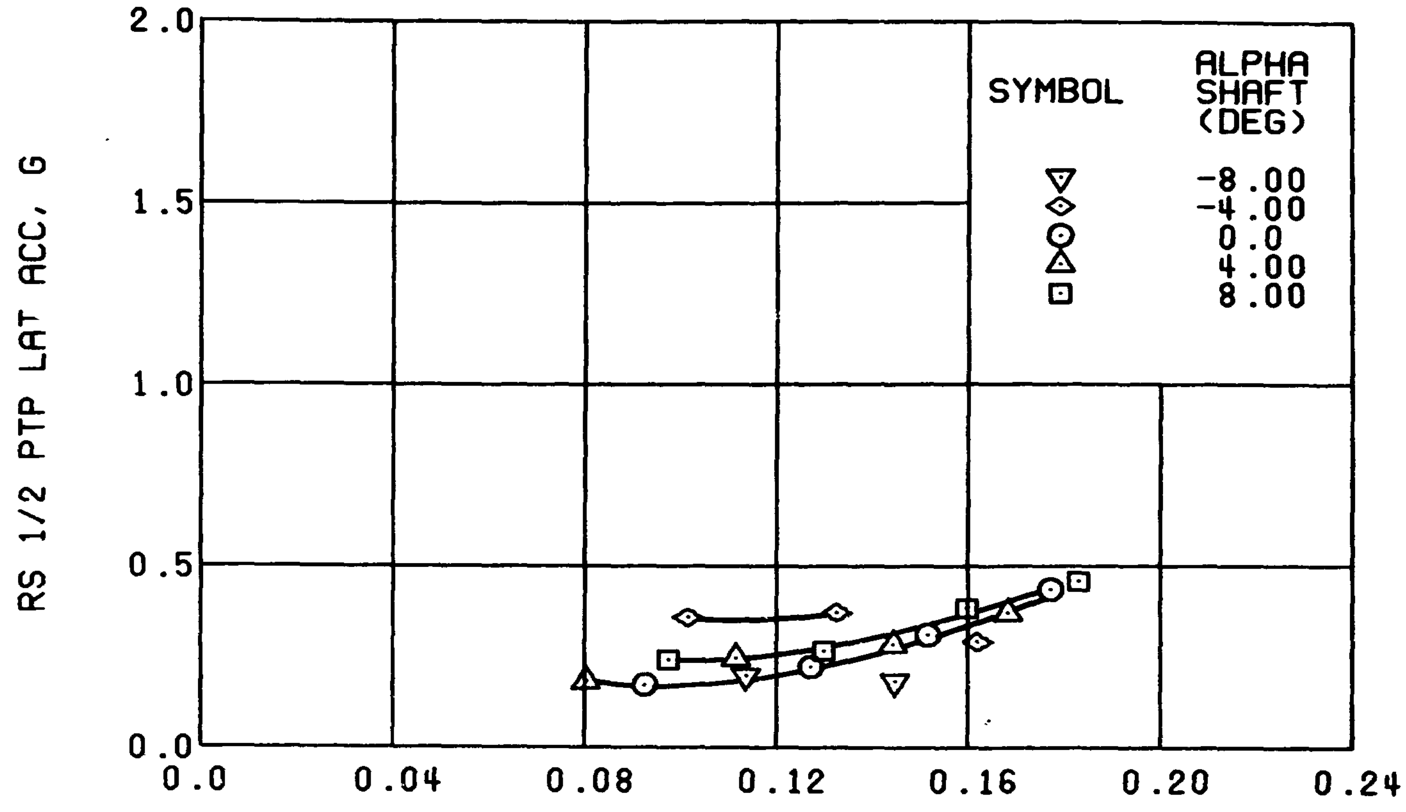

(w) GAGE 16 ROVER 3

Figure 41. Continued.
$\mu = 0.21$ $B'_{1s} = 2$ Deg

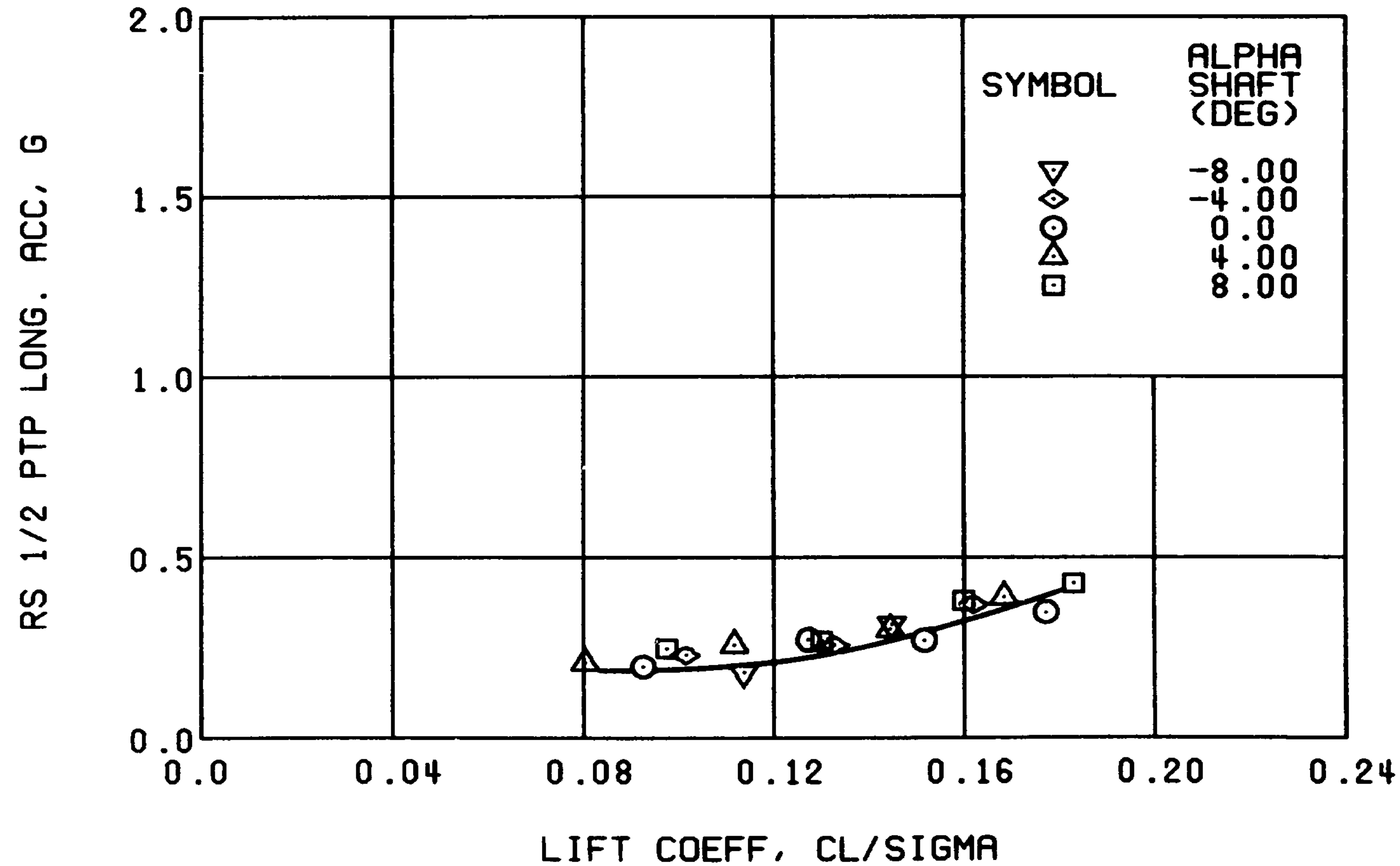

(x) GAGE 17 ROVER 4

Figure 41. Concluded.
$\mu = 0.21$ $B'_{1s} = 2$ Deg

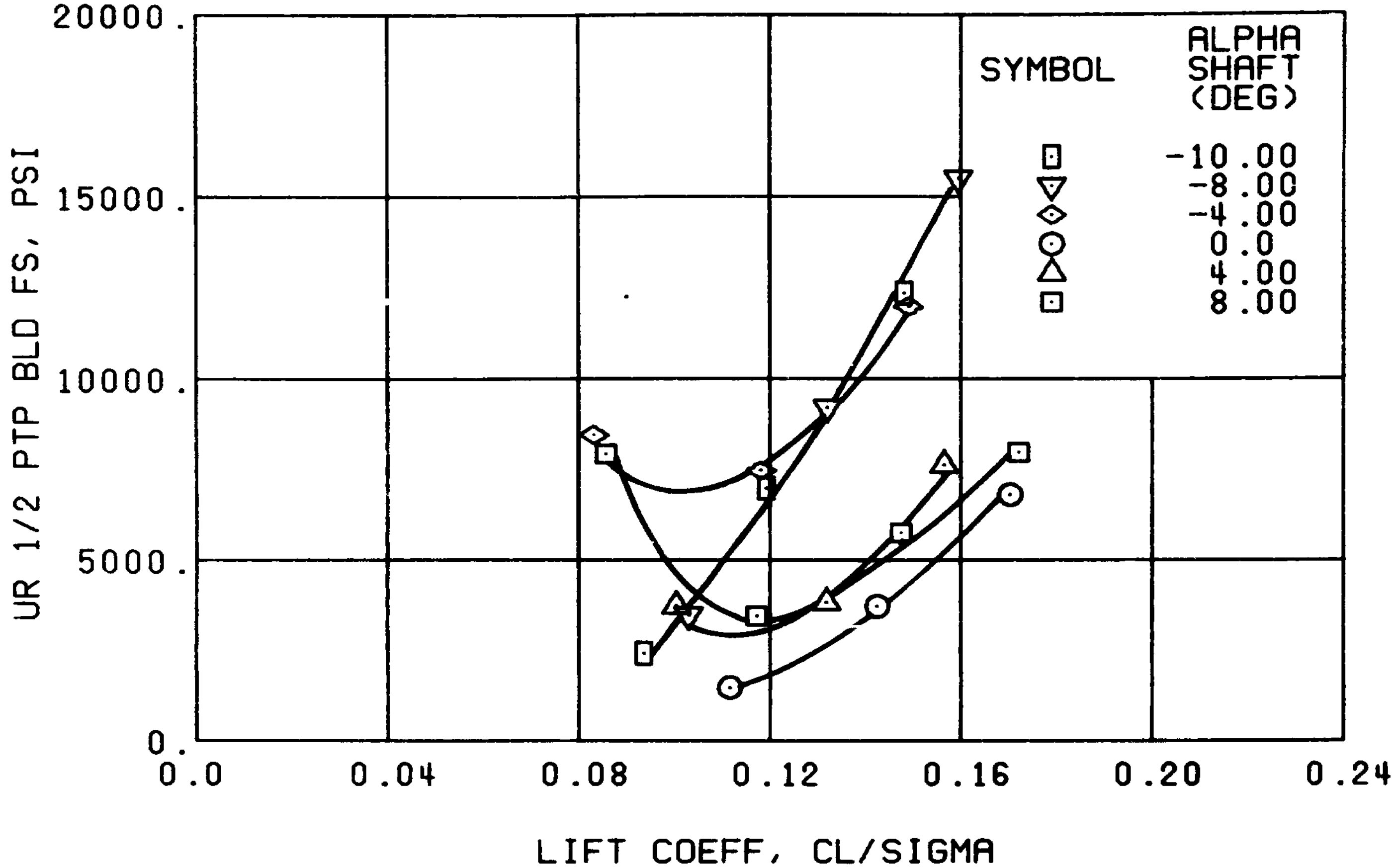

(a) GAGE 51 R84

Figure 42. Stress, Load, and Vibration Data at an Advance Ratio of 0.21 With the Lateral Displacement Control (B'_{1s}) Set at 4 Degrees.

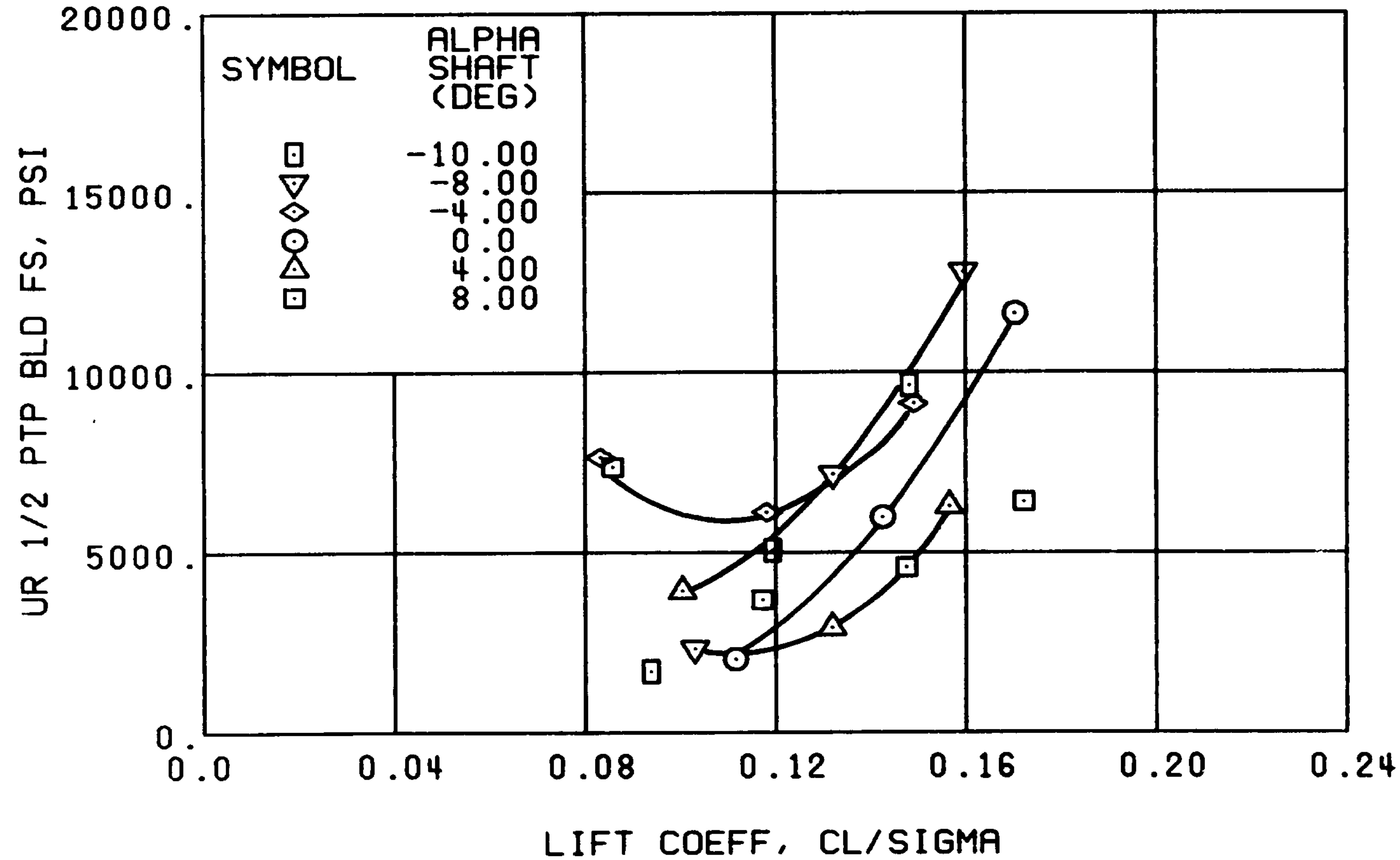

(c) GAGE 52 R108

Figure 42. Continued.
μ = 0.21 B'_{1s} = 4 Deg

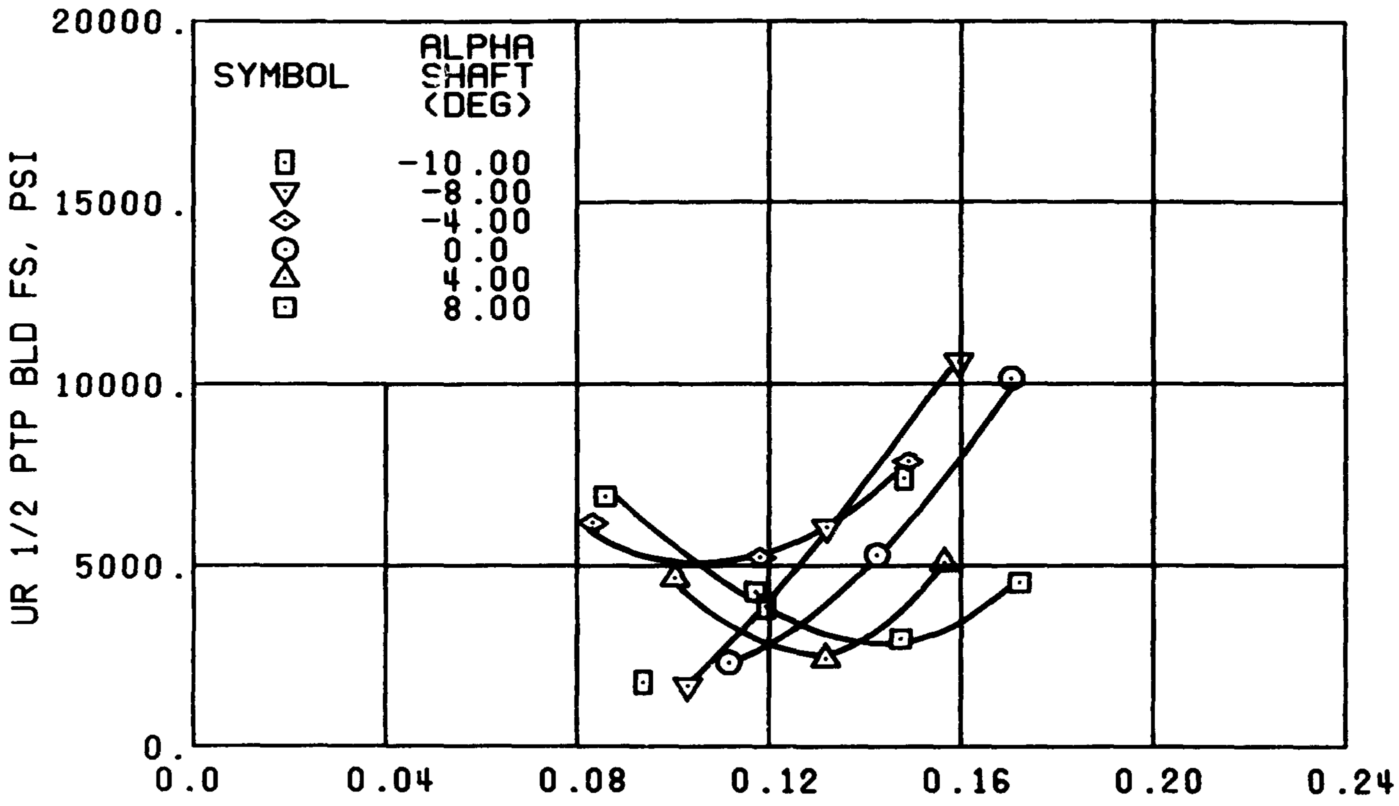

(d) GAGE 53 R132

Figure 42. Continued.
$\mu = 0.21 \quad B'_{1s} = 4$ Deg

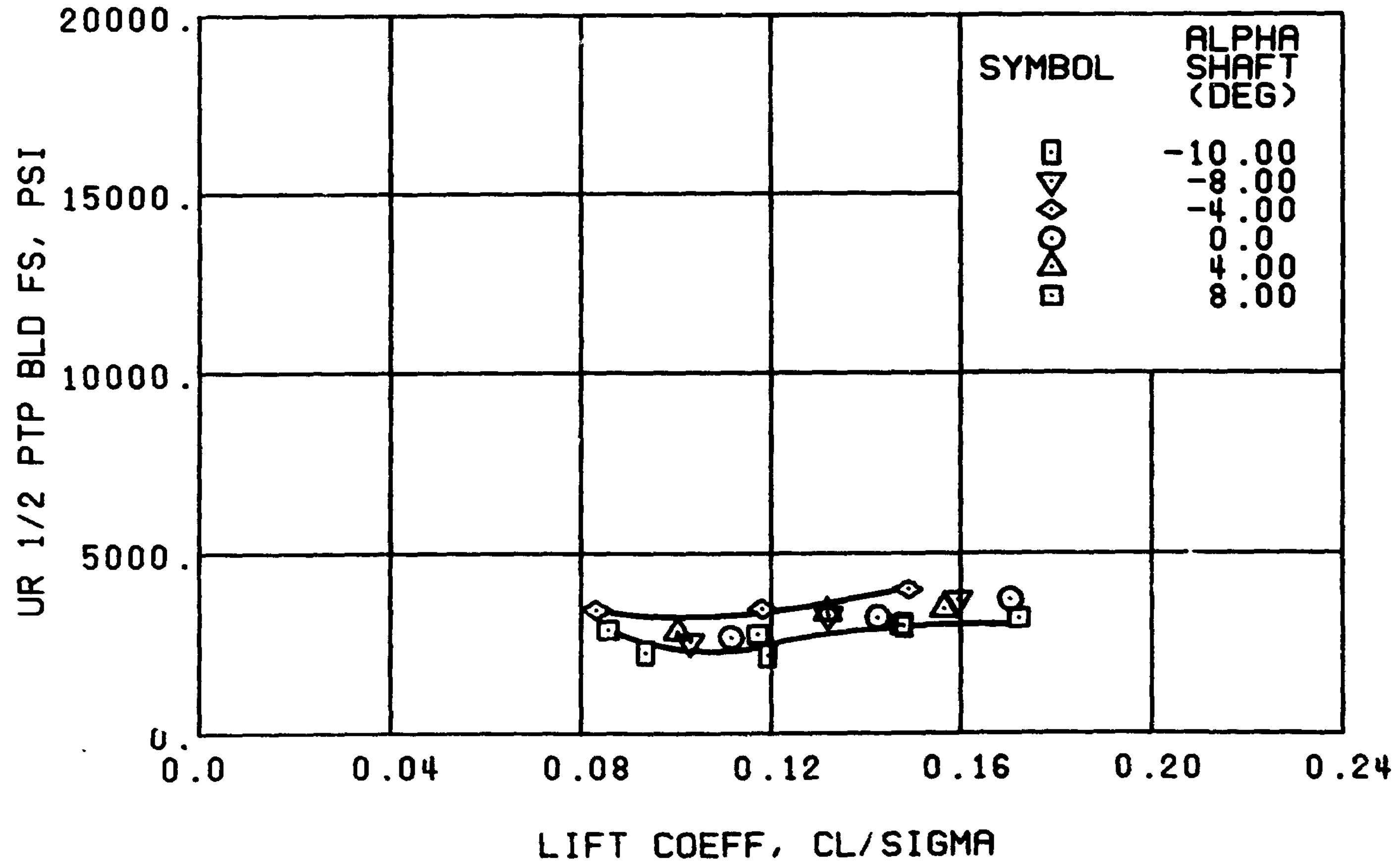

(f) GAGE 55 R204

Figure 42. Continued.
$\mu = 0.21 \quad B'_{1s} = 4$ Deg

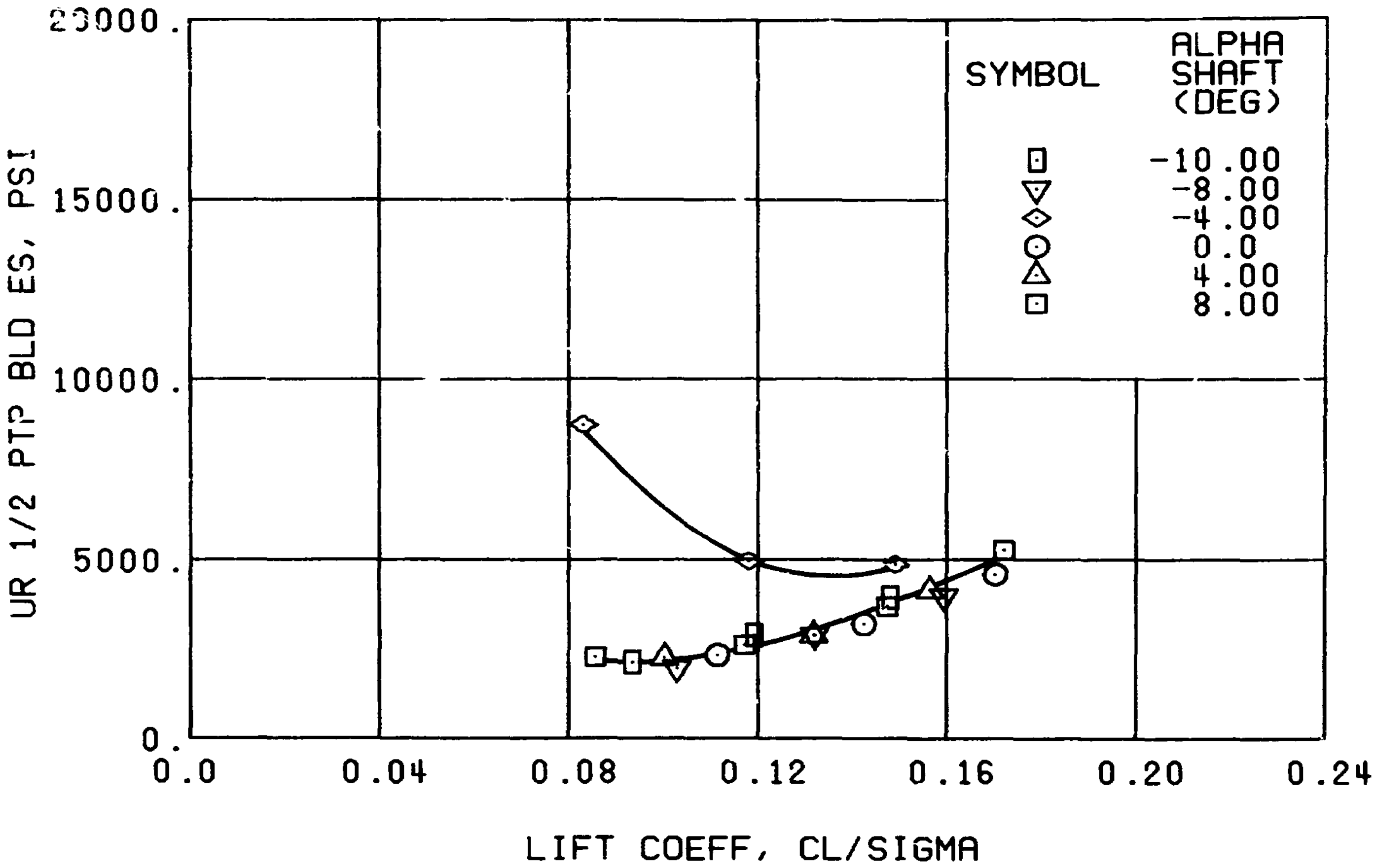

(g) GAGE 79 R60

Figure 42. Continued.
$\mu = 0.21$ $B'_{1s} = 4$ Deg

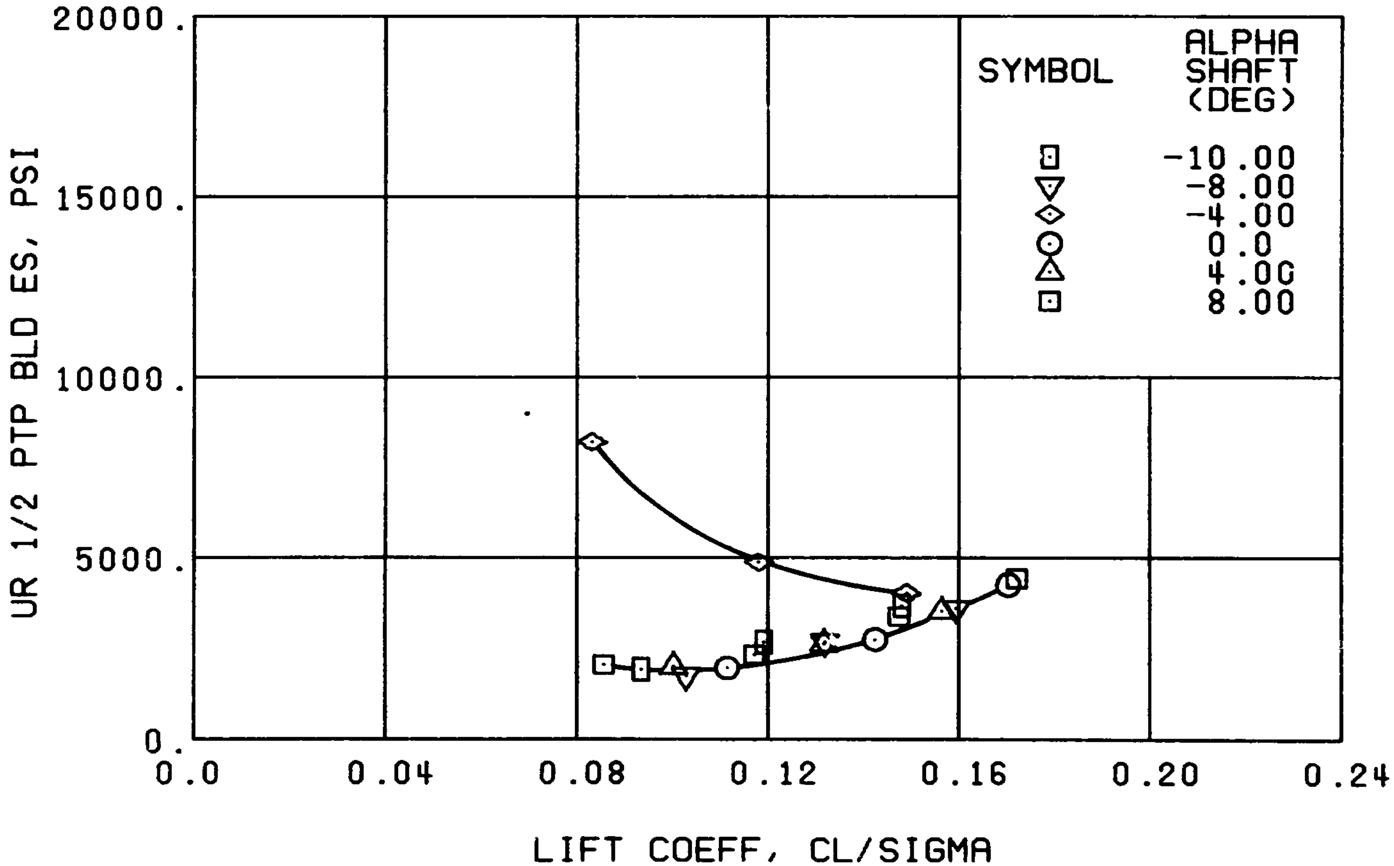

(h) GAGE 40 R84

Figure 42. Continued.
$\mu = 0.21$ $B'_{1s} = 4$ Deg

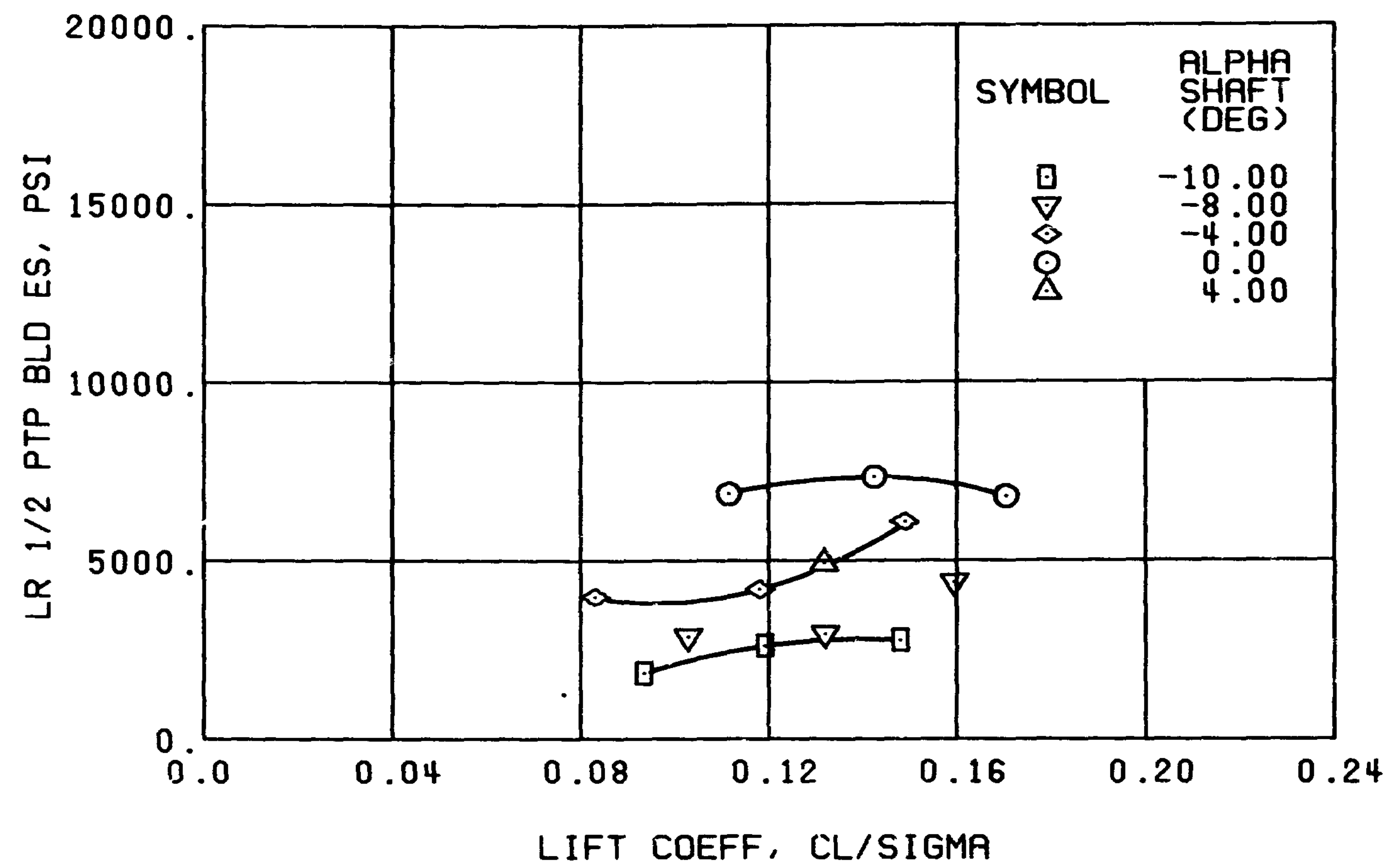

(i) GAGE 2 R84

Figure 42. Continued.
$\mu = 0.21 \quad B'_{1s} = 4$ Deg

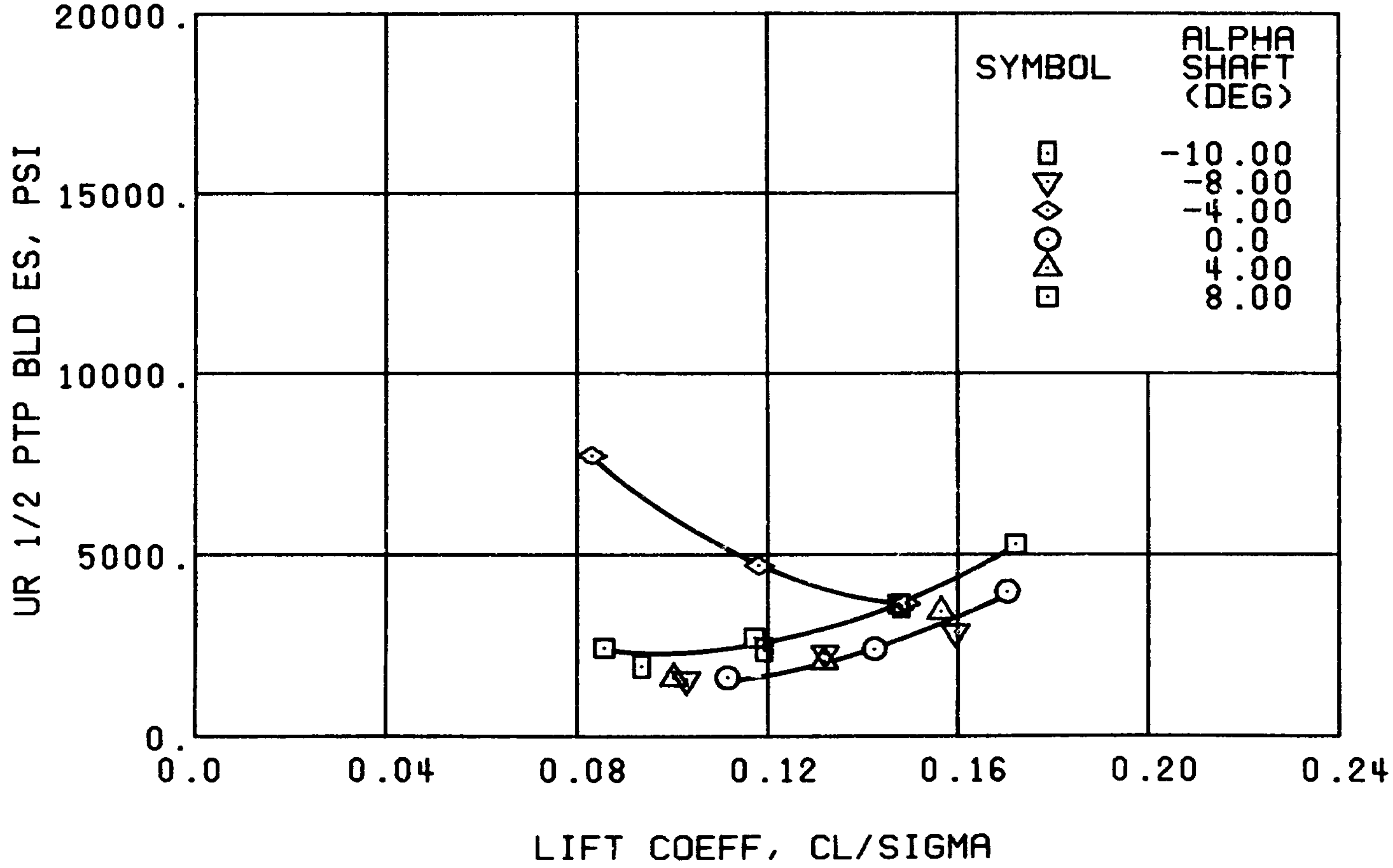

(j) GAGE 42 R132

Figure 42. Continued.
μ = 0.21 B'_{1s} = 4 Deg

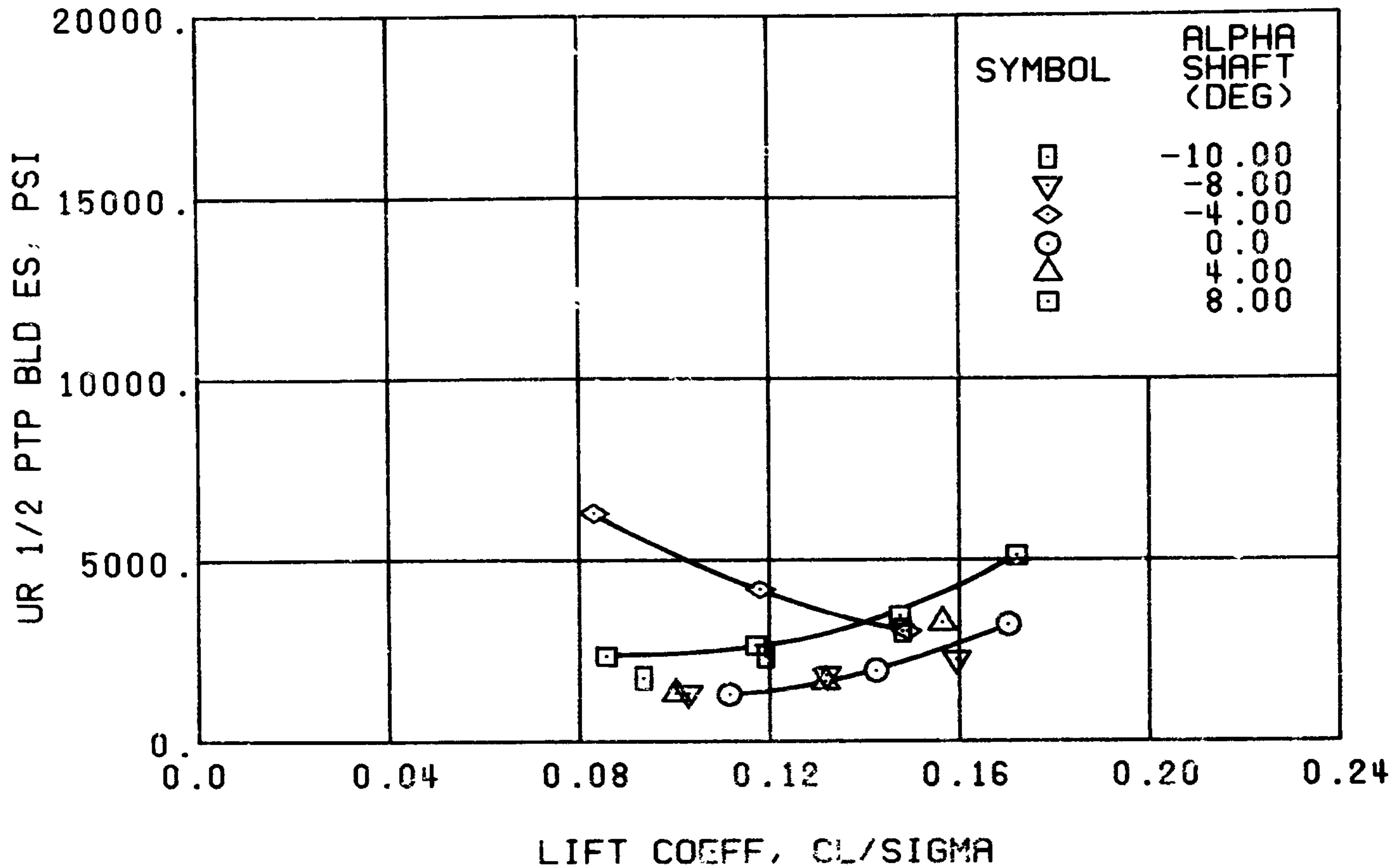

(k) GAGE 43 R168

Figure 42. Continued.
$\mu = 0.21 \quad B'_{1s} = 4$ Deg

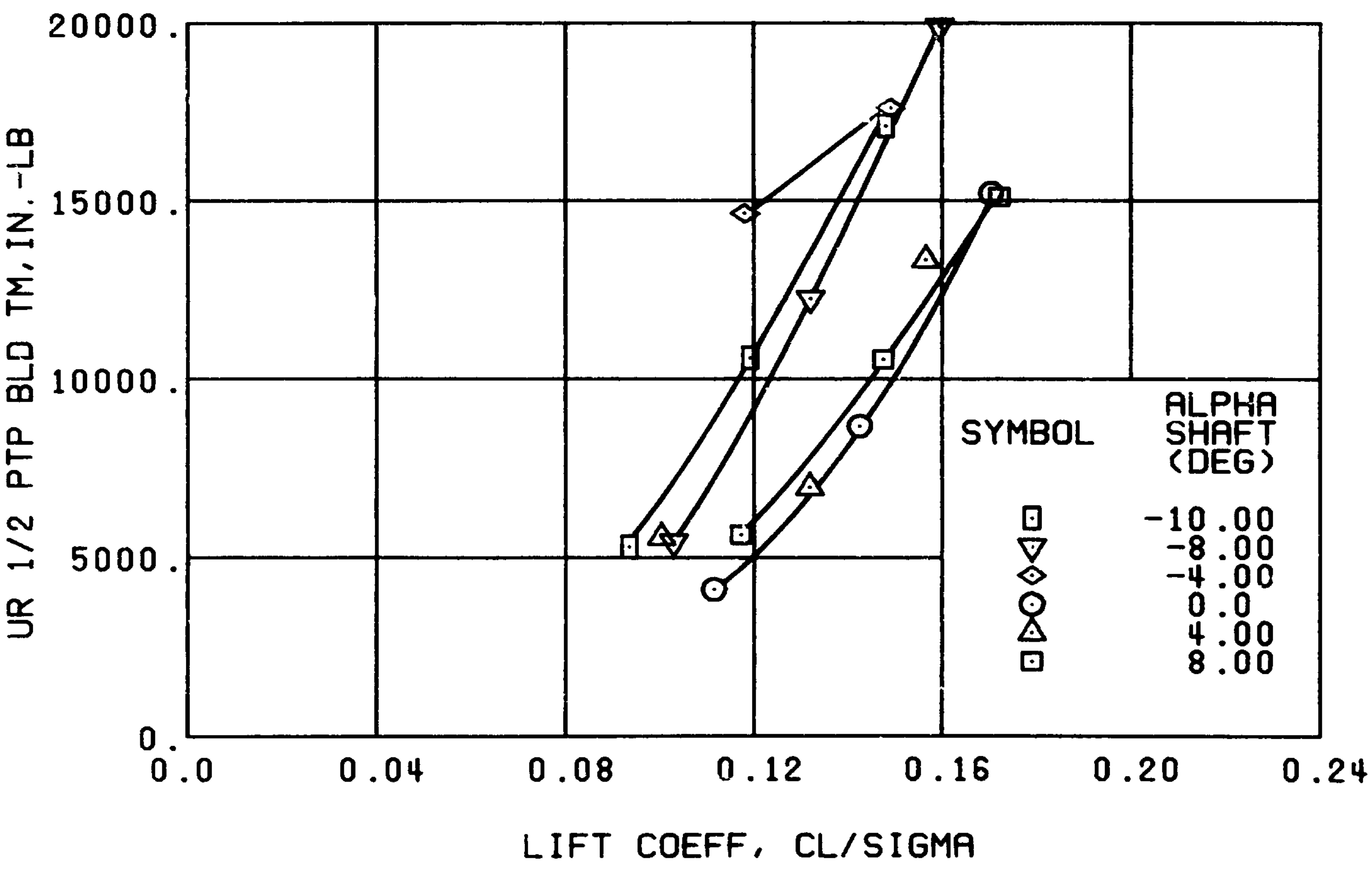

(I) GAGE 45 R82

Figure 42. Continued.
$\mu = 0.21$ $B'_{1s} = 4$ Deg

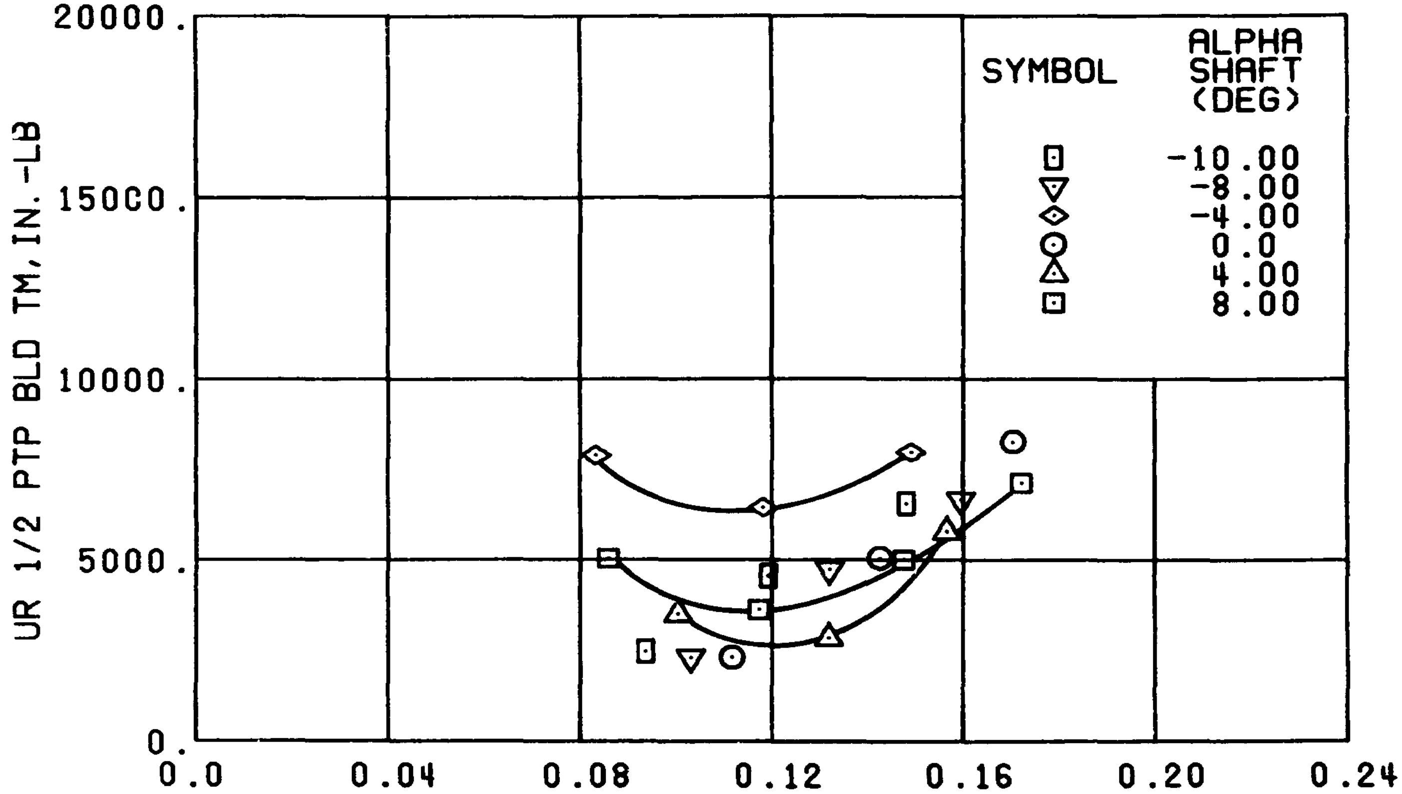

(m) GAGE 46 R130

Figure 42. Continued.
$\mu = 0.21$ $B'_{1s} = 4$ Deg

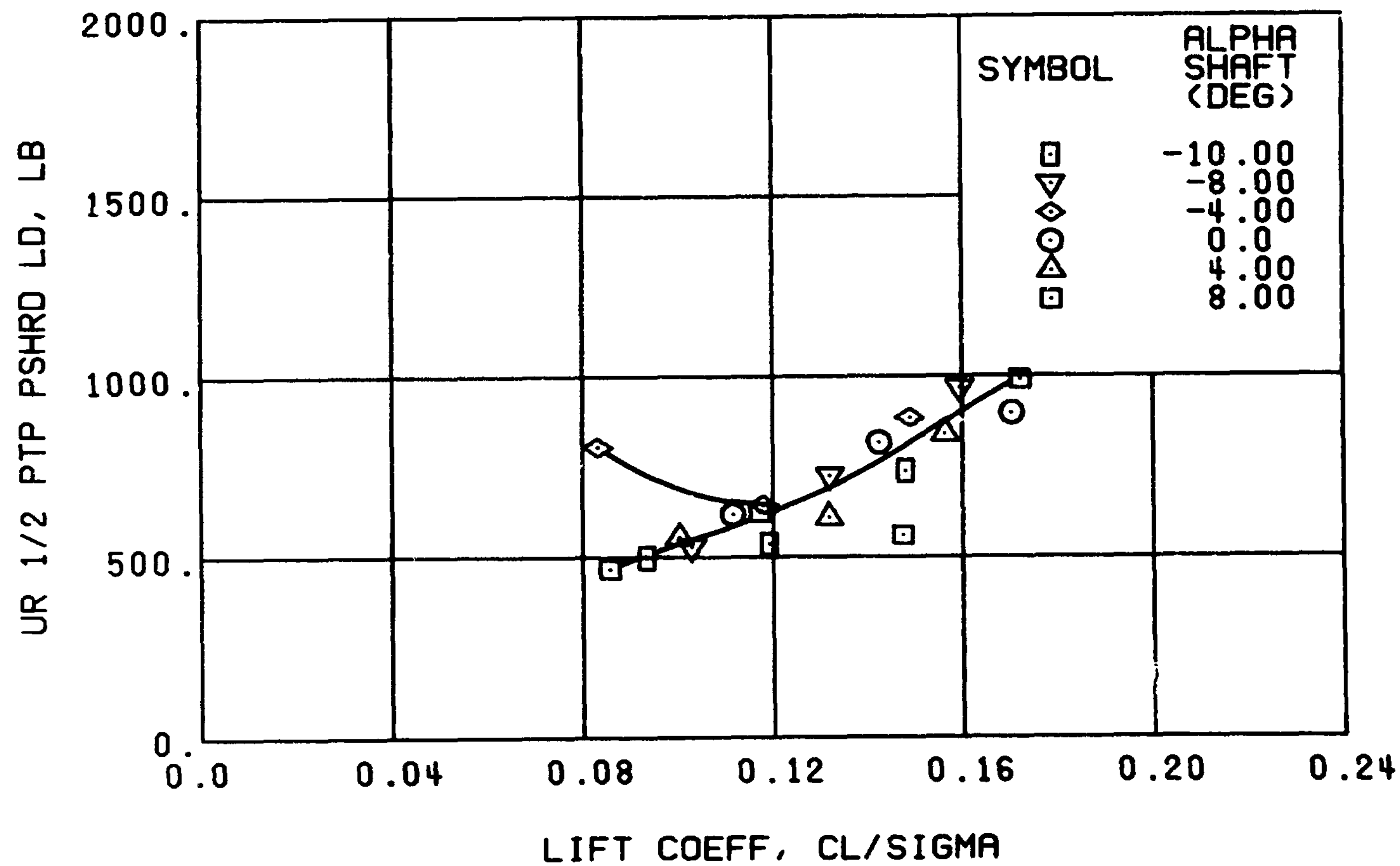

(n) GAGE 37

Figure 42. Continued.
μ = 0.21 B'_{1s} = 4 Deg

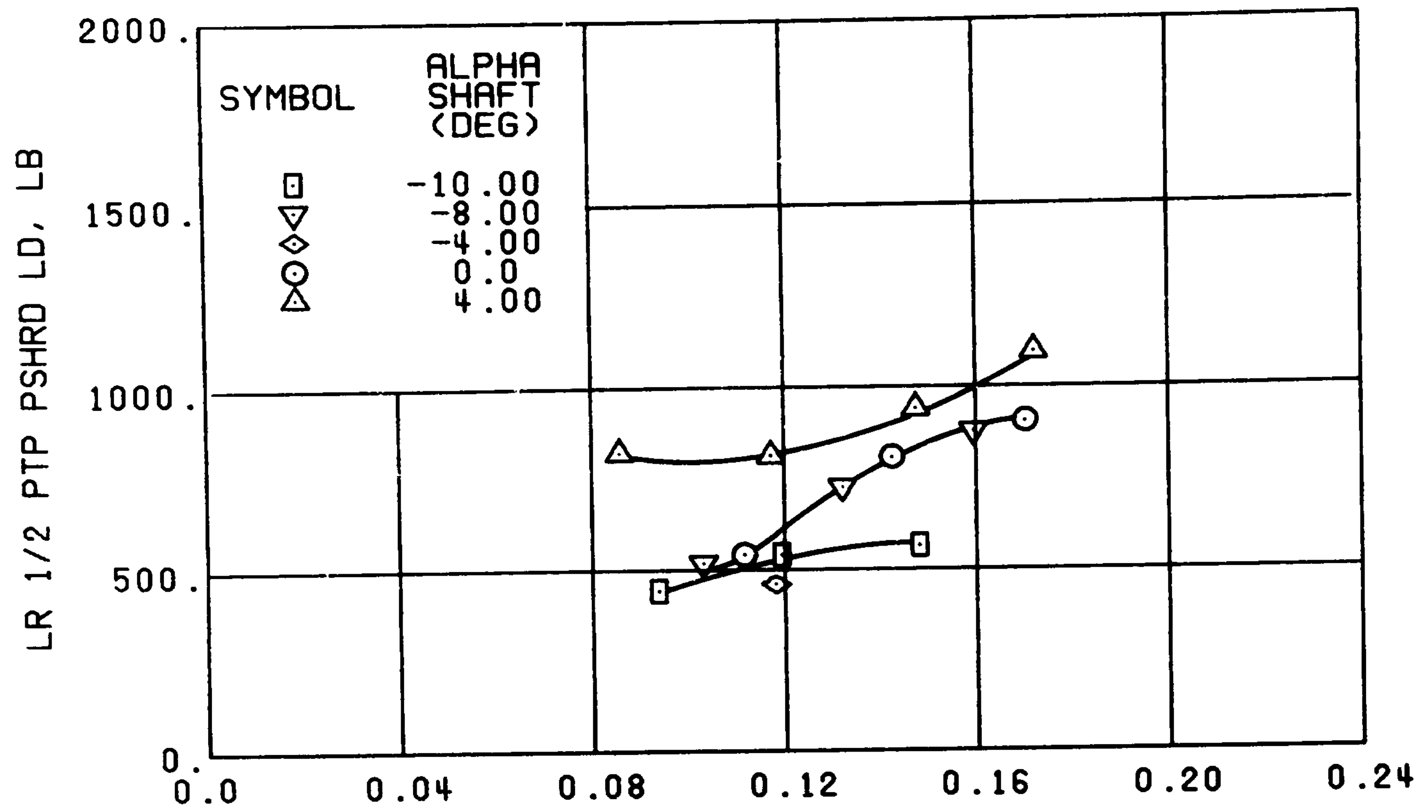

(o) GAGE 34

Figure 42. Continued.
$\mu = 0.21$ $B'_{1s} = 4$ Deg

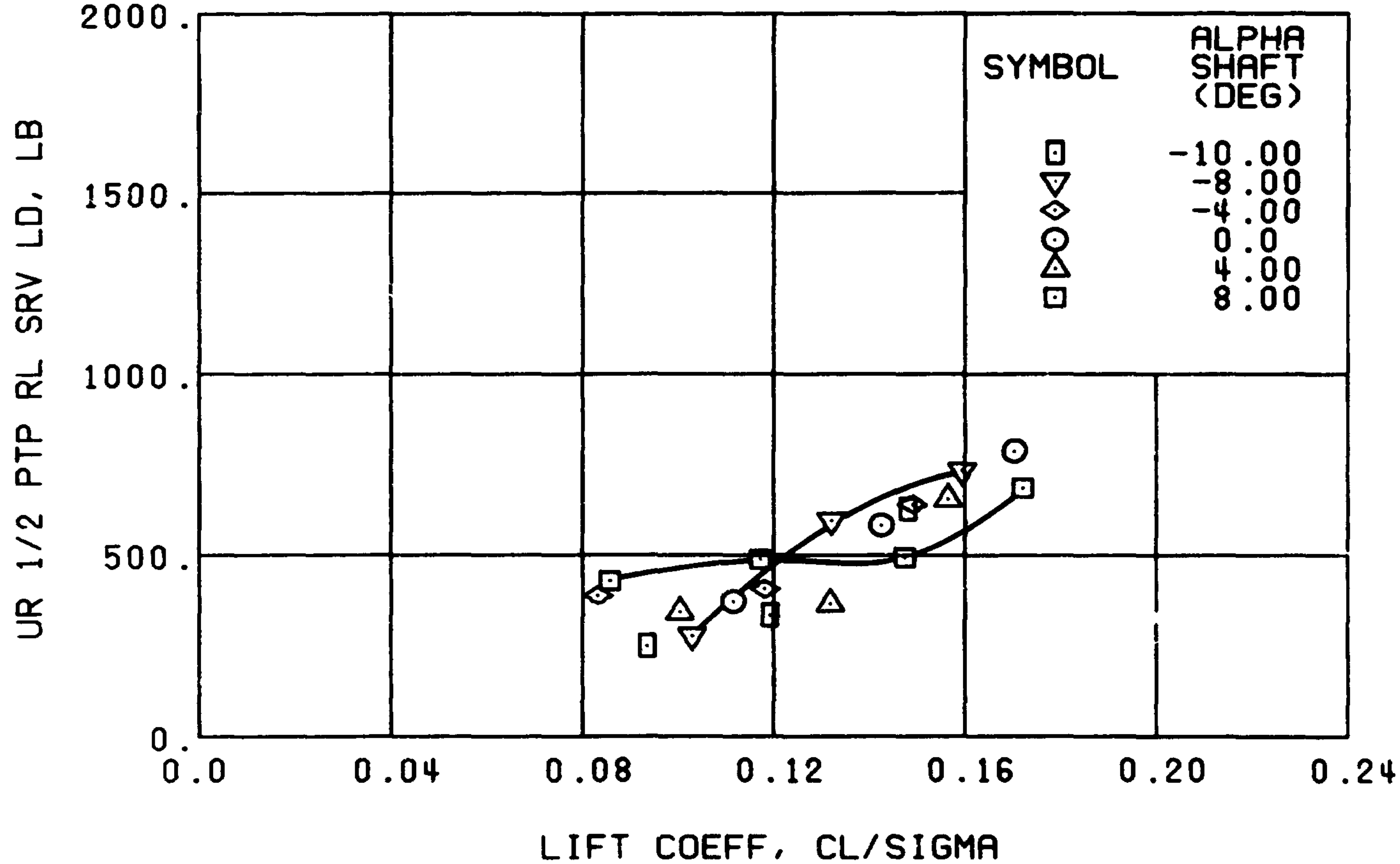

(p) GAGE 22

Figure 42. Continued.
$\mu = 0.21 \quad B'_{1s} = 4$ Deg

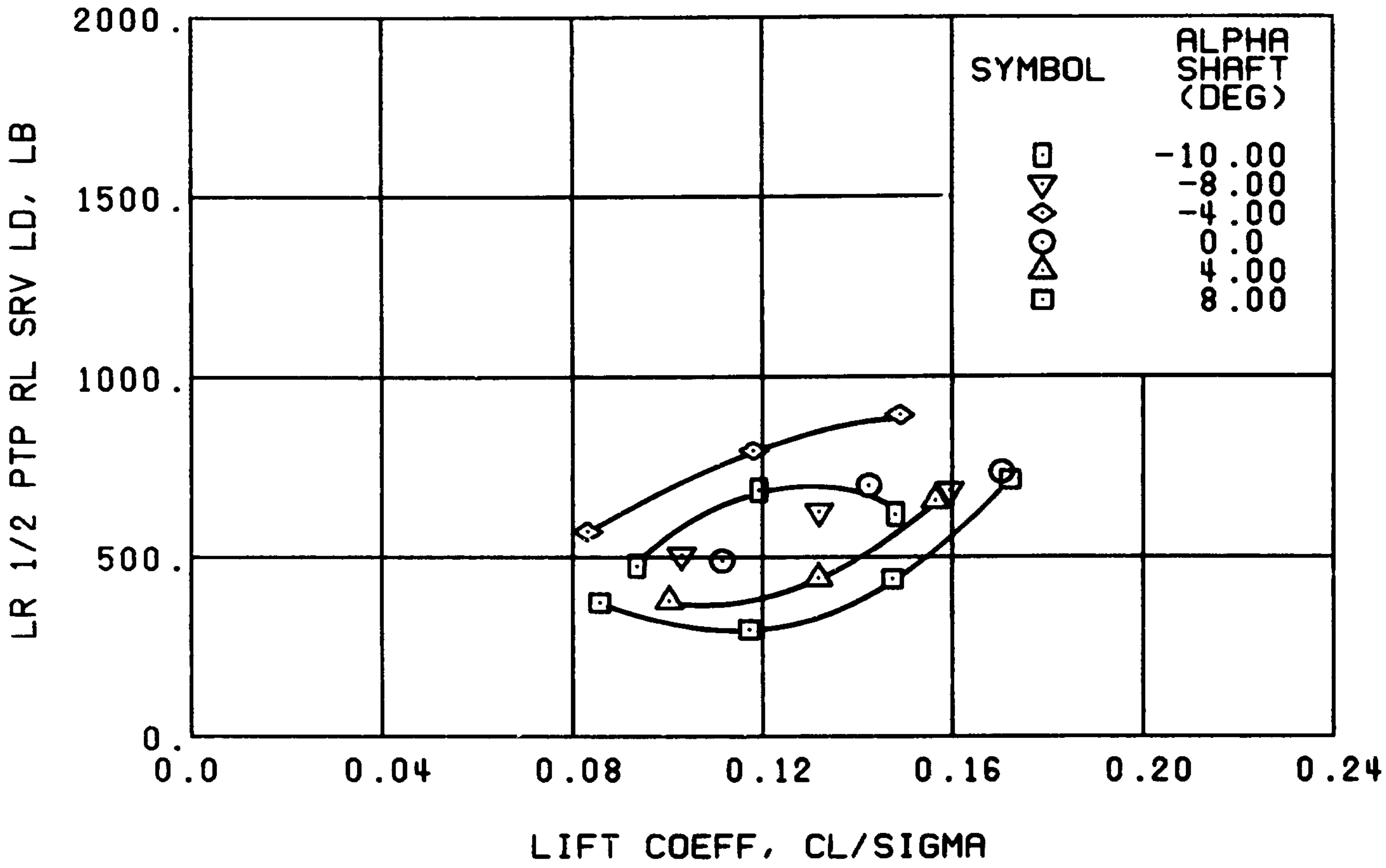

(q) GAGE 25

Figure 42. Continued.
$\mu = 0.21$ $B'_{1s} = 4$ Deg

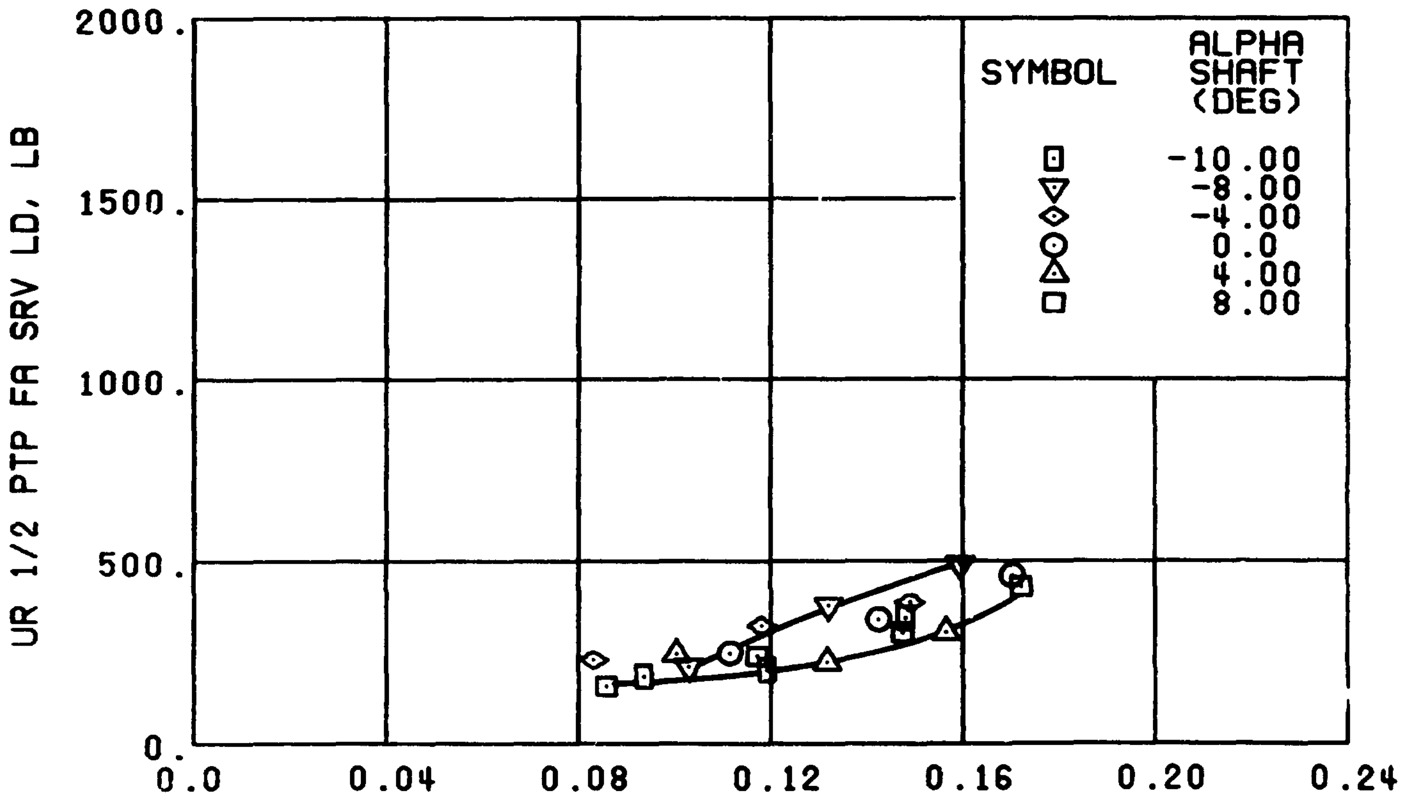

(r) GAGE 24

Figure 42. Continued.
$\mu = 0.21$ $B'_{1s} = 4$ Deg

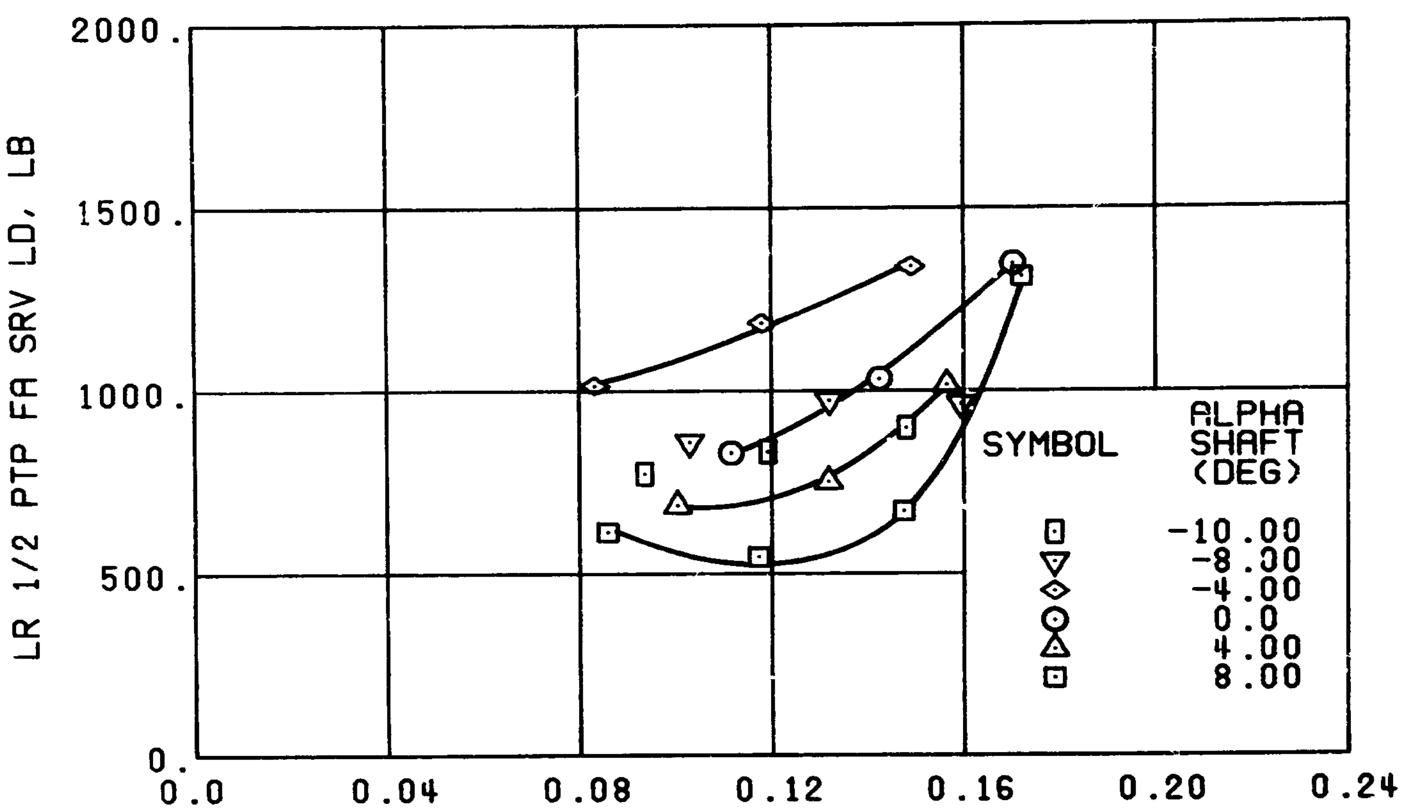

(s) GAGE 27

Figure 42. Continued.
$\mu = 0.21 \quad B'_{1s} = 4$ Deg

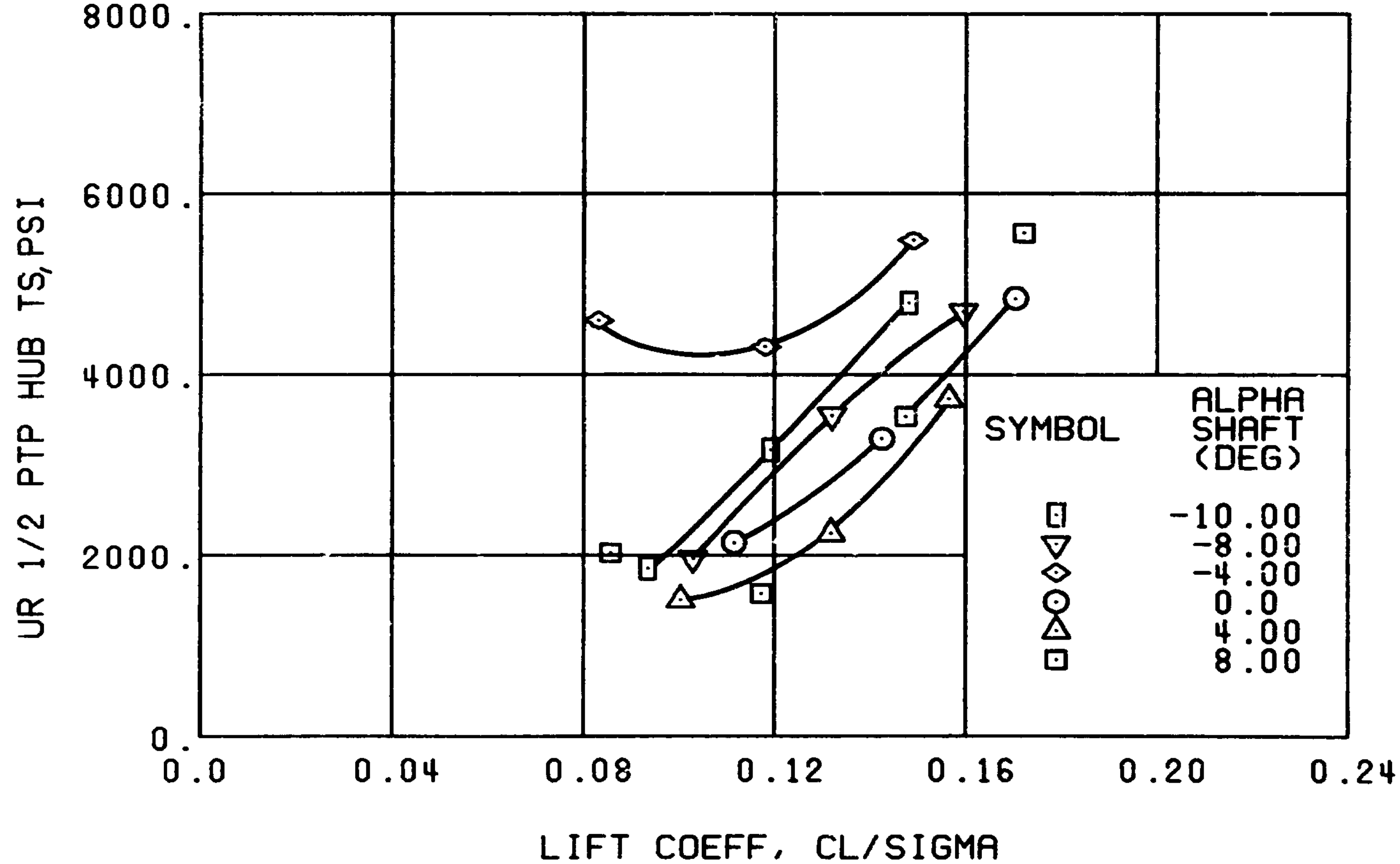

(f) GAGE 65

Figure 42. Continued.
$\mu = 0.21 \quad B'_{1s} = 4$ Deg

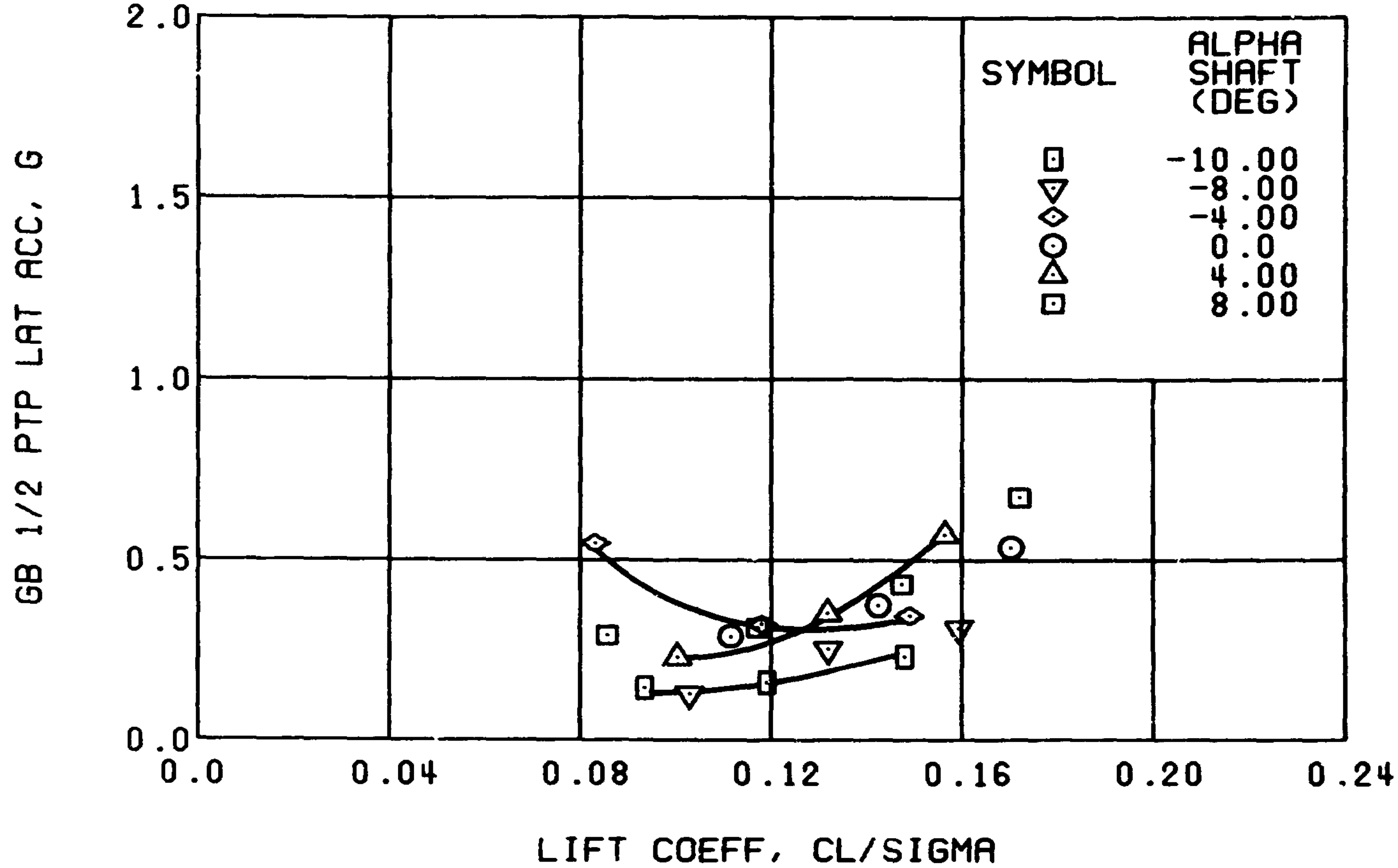

(u) GAGE 15 STA 76, BL 30

Figure 42. Continued.
$\mu = 0.21 \quad B'_{1s} = 4$ Deg

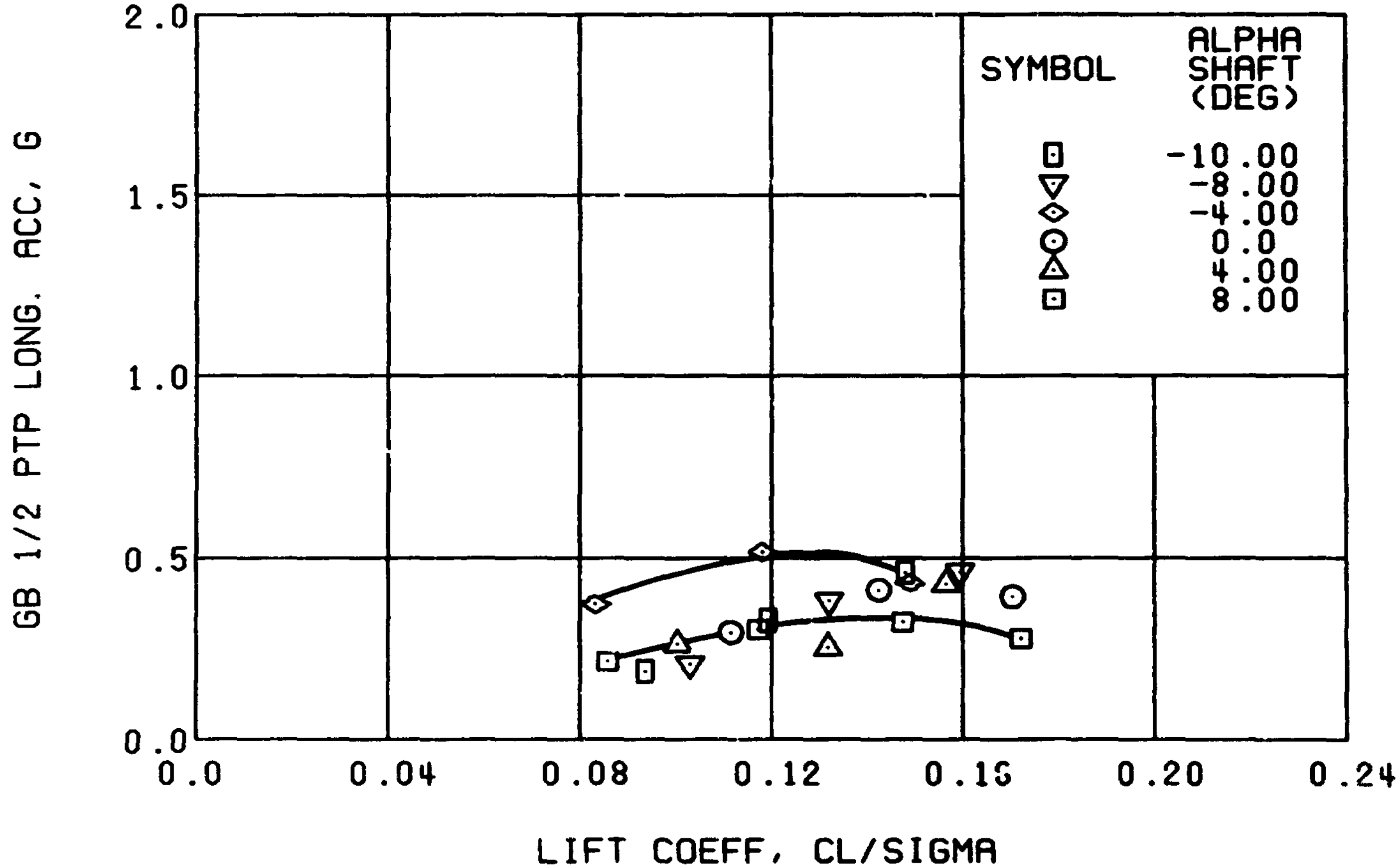

(v) GAGE 14 STA 61, BL 0

Figure 42. Continued.
$\mu = 0.21 \quad B_{1s}' = 4$ Deg

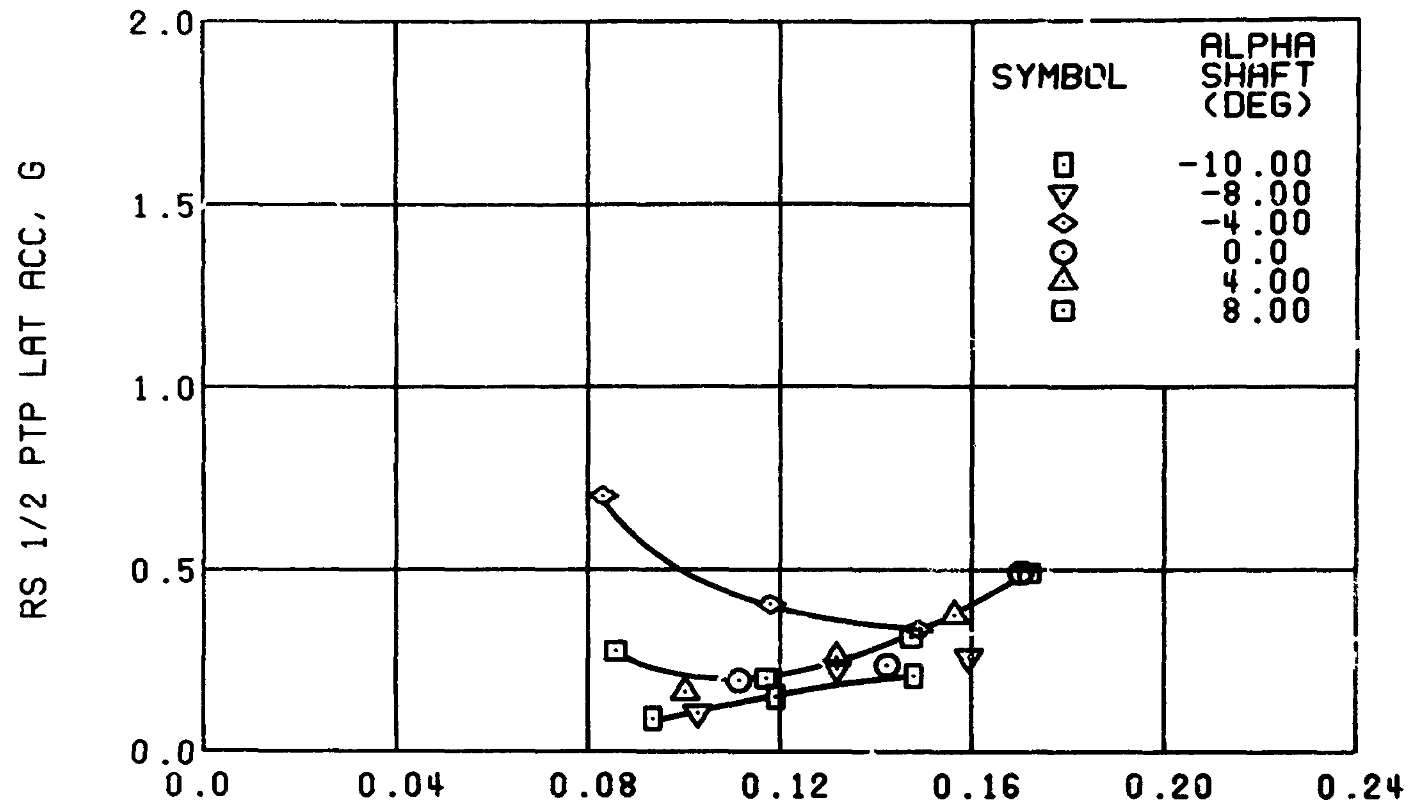

(w) GAGE 16 ROVER 3

Figure 42. Continued.
$\mu = 0.21$ $B_{1s}' = 4$ Deg

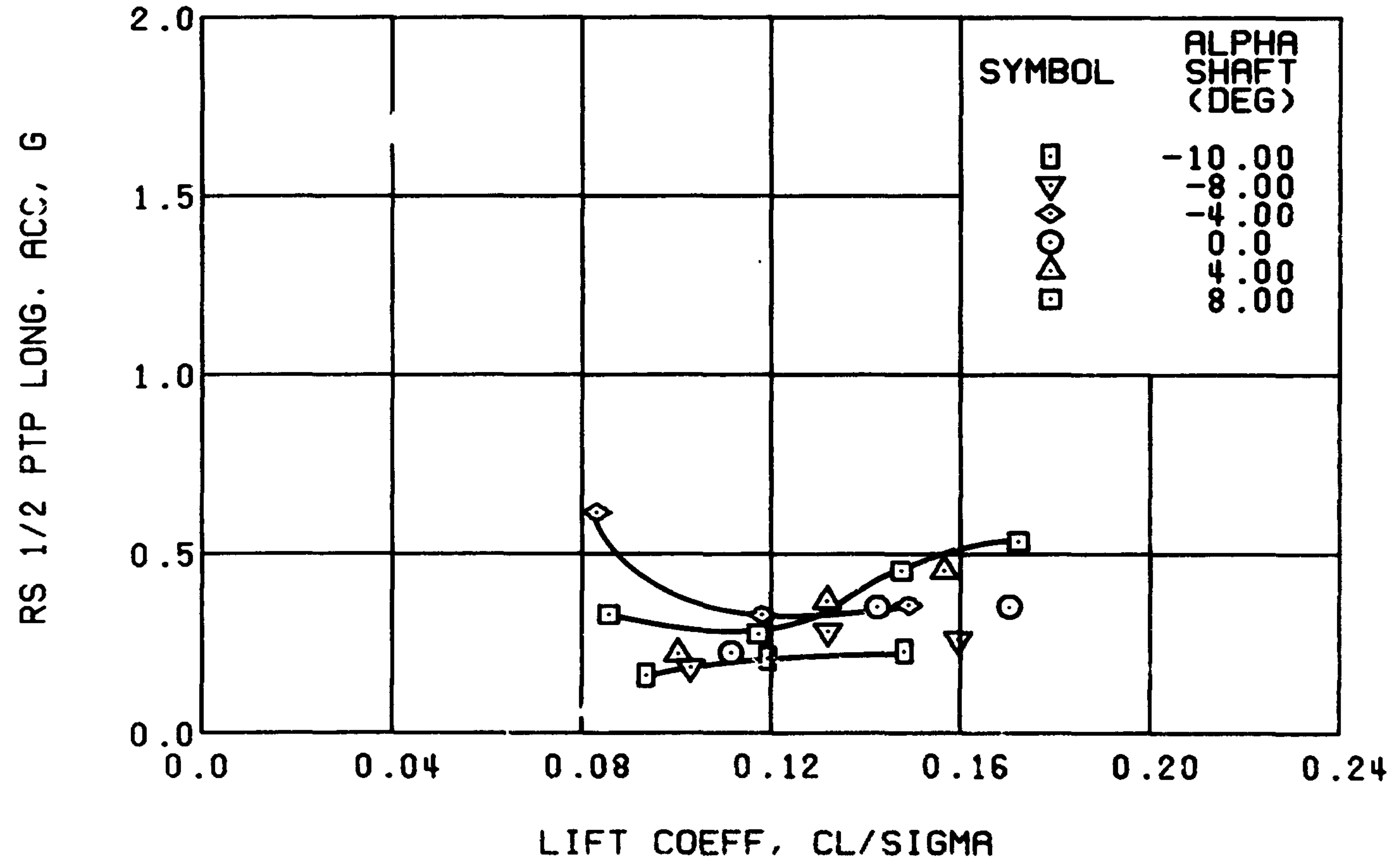

(x) GAGE 17 ROVER 4

Figure 42. Concluded.
$\mu = 0.21 \quad B'_{1s} = 4$ Deg

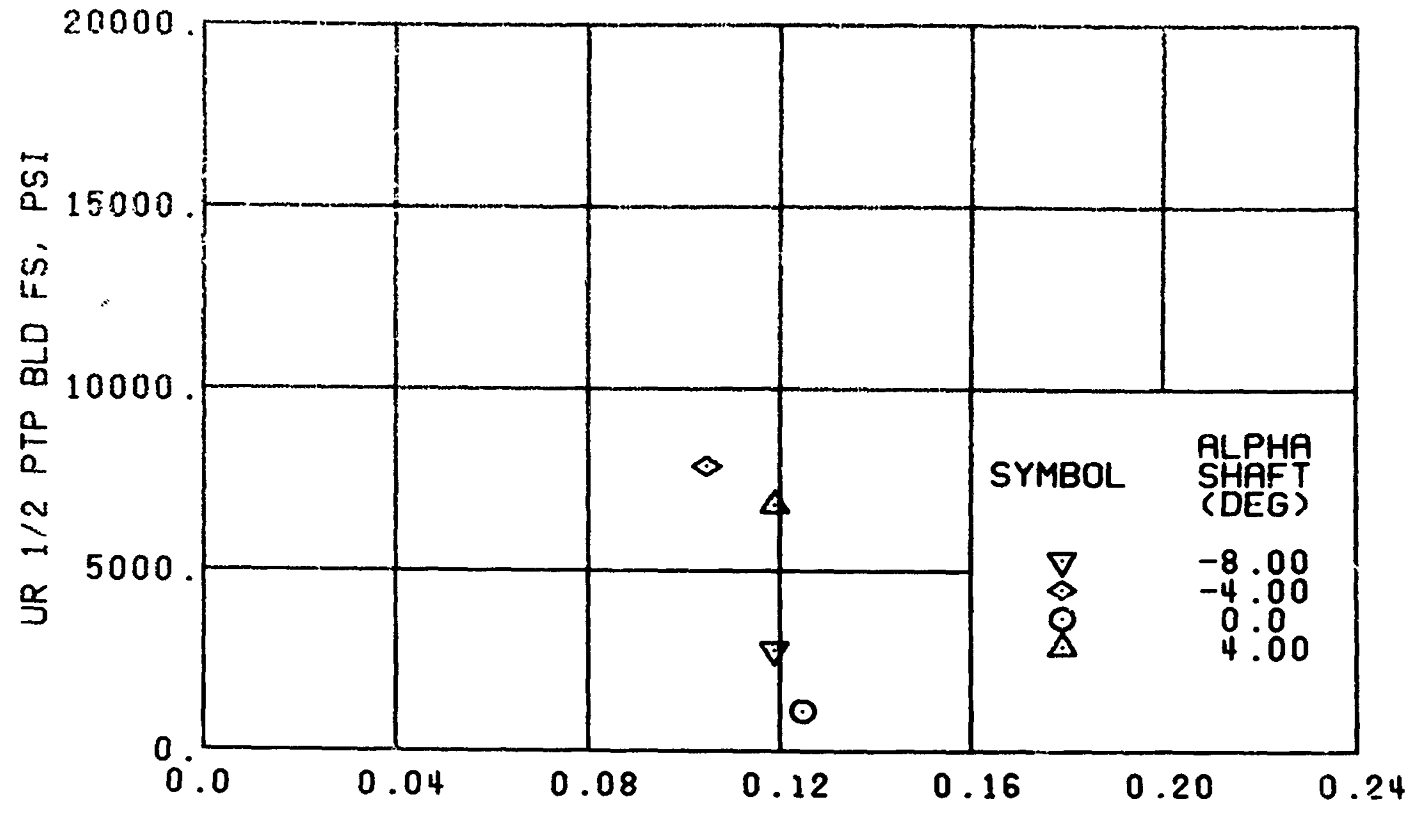

(a) GAGE 51 R84

Figure 43. Stress, Load, and Vibration Data at an Advance Ratio of 0.21 Witn the Lateral Displacement Control (B'_{1s}) Set at 6 Degrees.

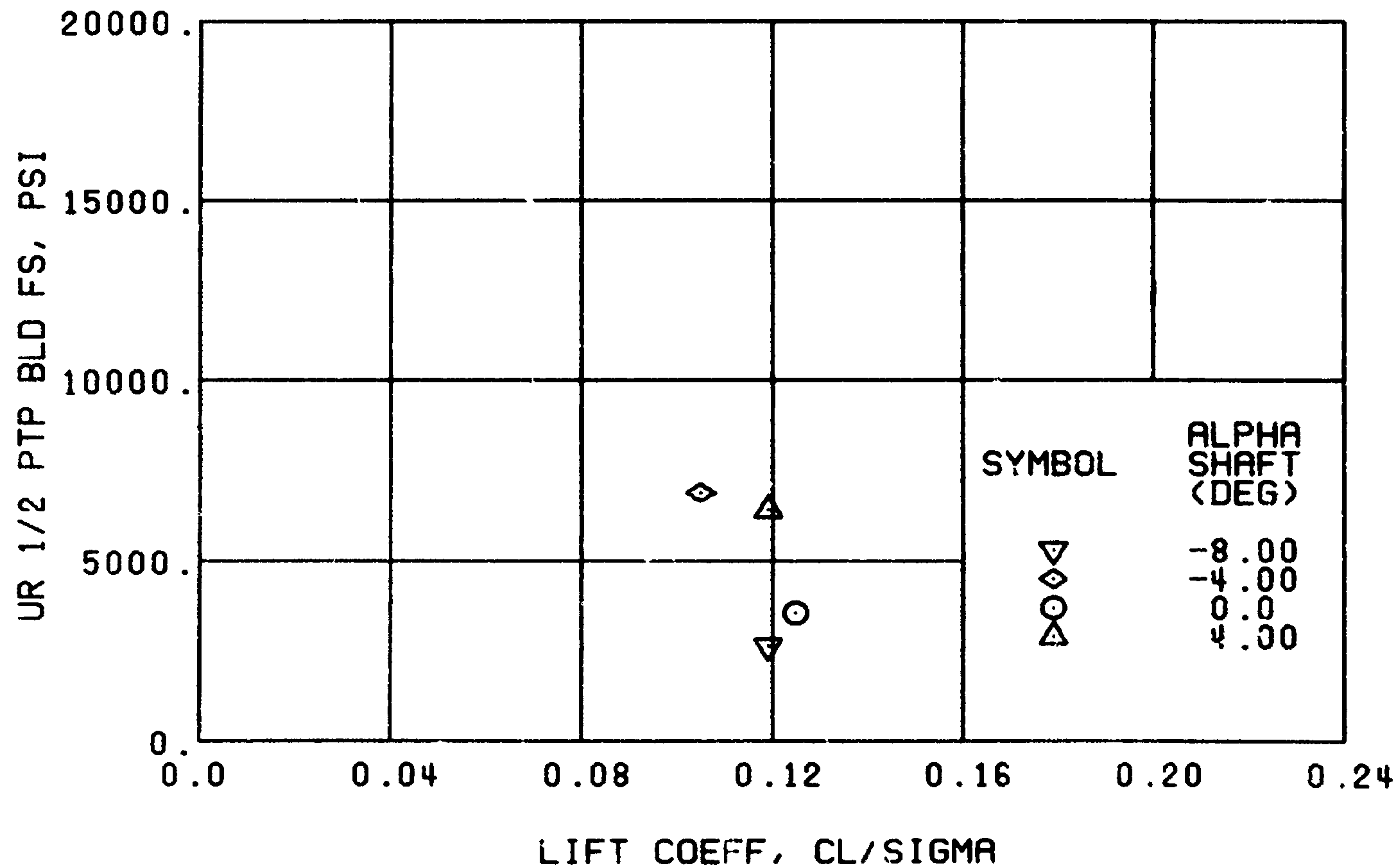

(c) GAGE 52 R108

Figure 43. Continued.
μ = 0.21 B'_{1s} = 6 Deg

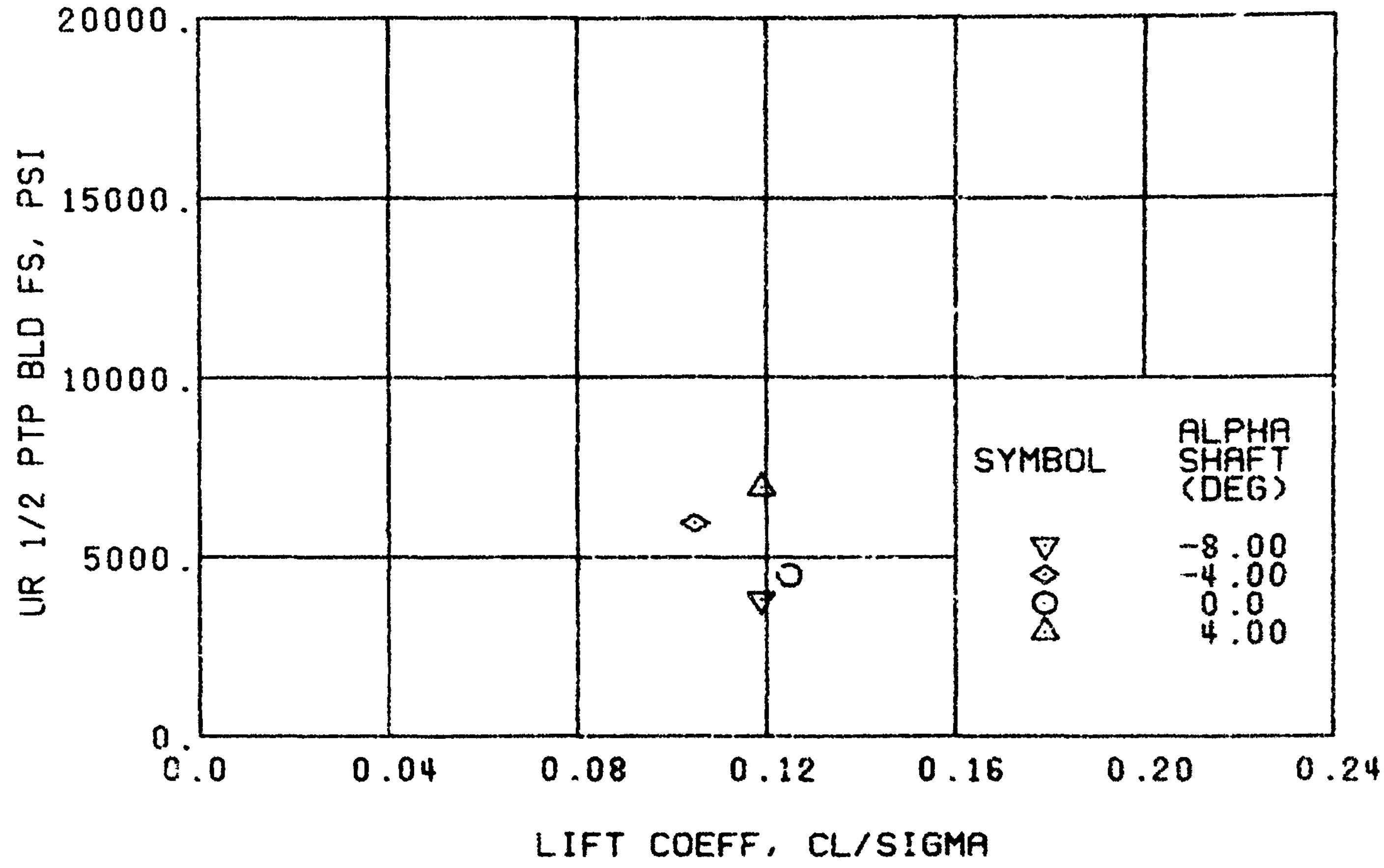

(d) GAGE 53 R132

Figure 43. Continued.
μ = 0.21 B'_{1s} = 6 Deg

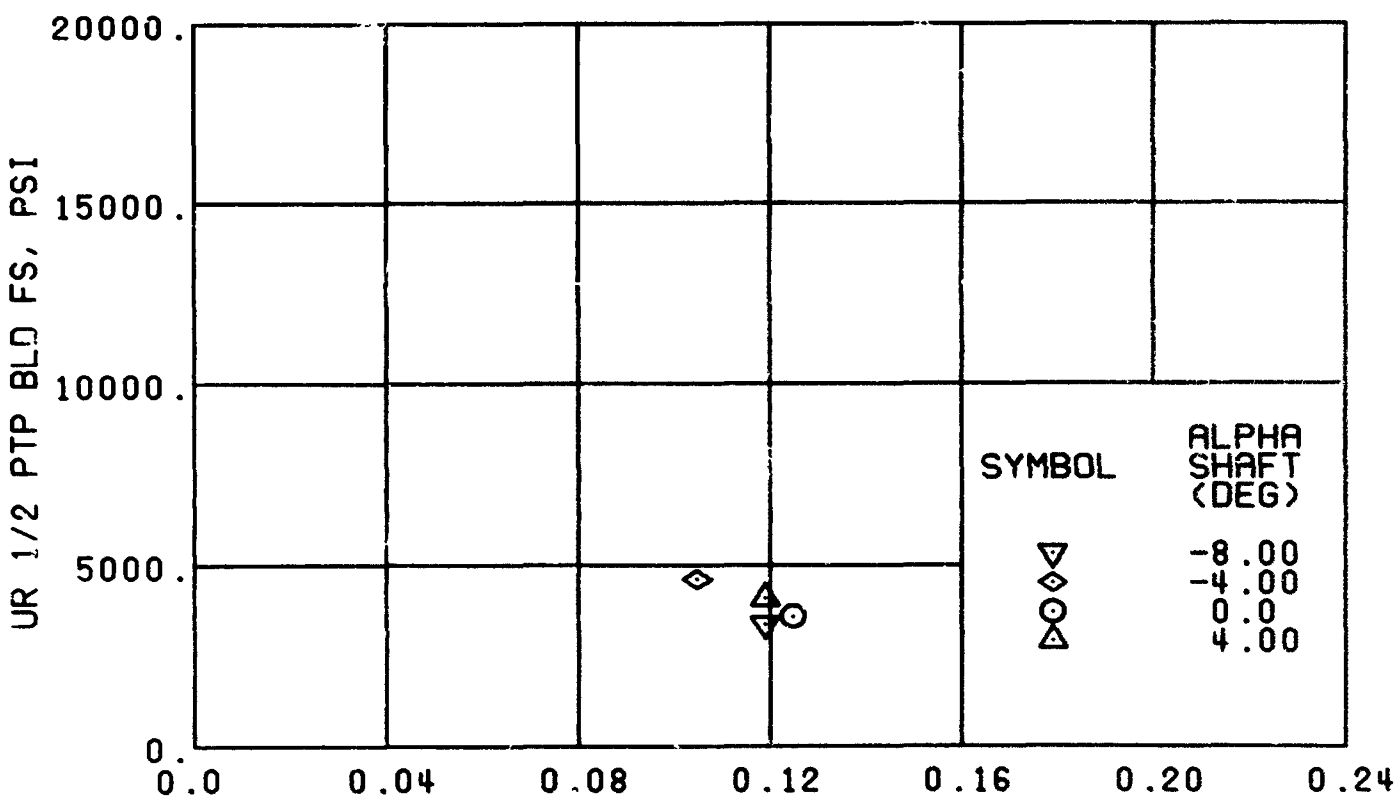

(f) GAGE 55 R204

Figure 43. Continued.
μ = 0.21 B'_{1s} = 6 Deg

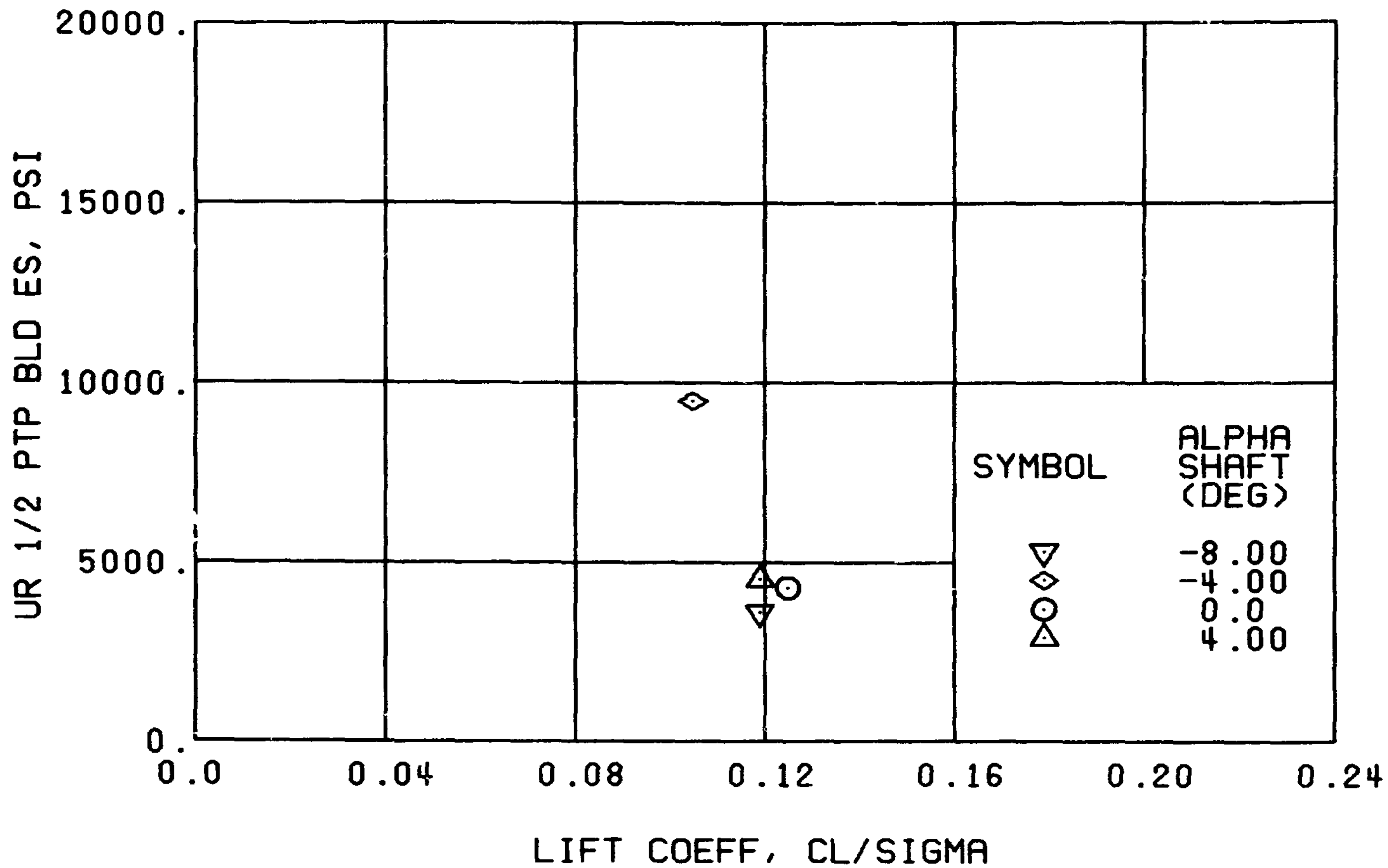

(g) GAGE 79 R60

Figure 43. Continued.
$\mu = 0.21 \quad B'_{1s} = 6$ Deg

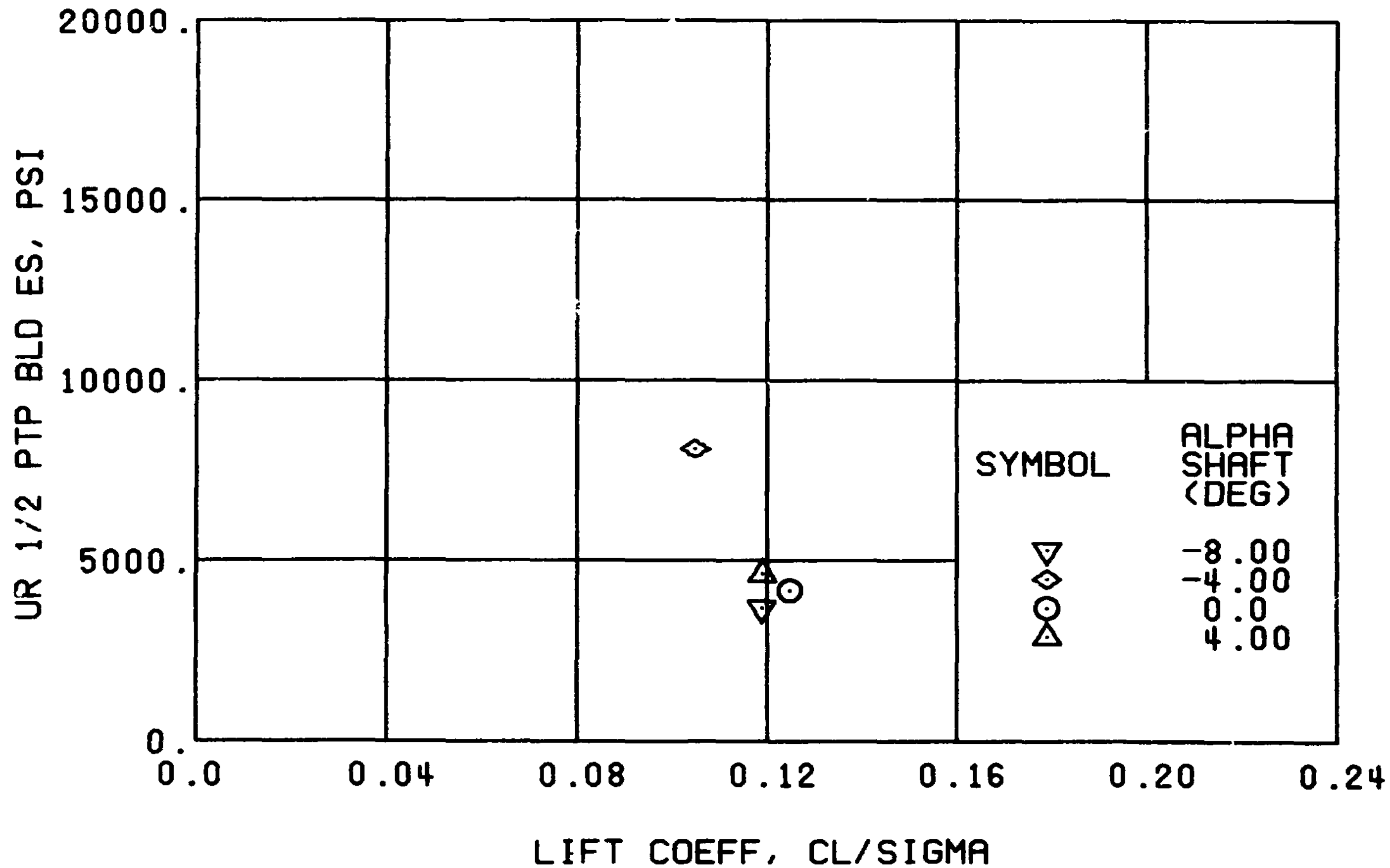

(h) GAGE 40 R84

Figure 43. Continued.
$\mu = 0.21$ $B'_{1s} = 6$ Deg

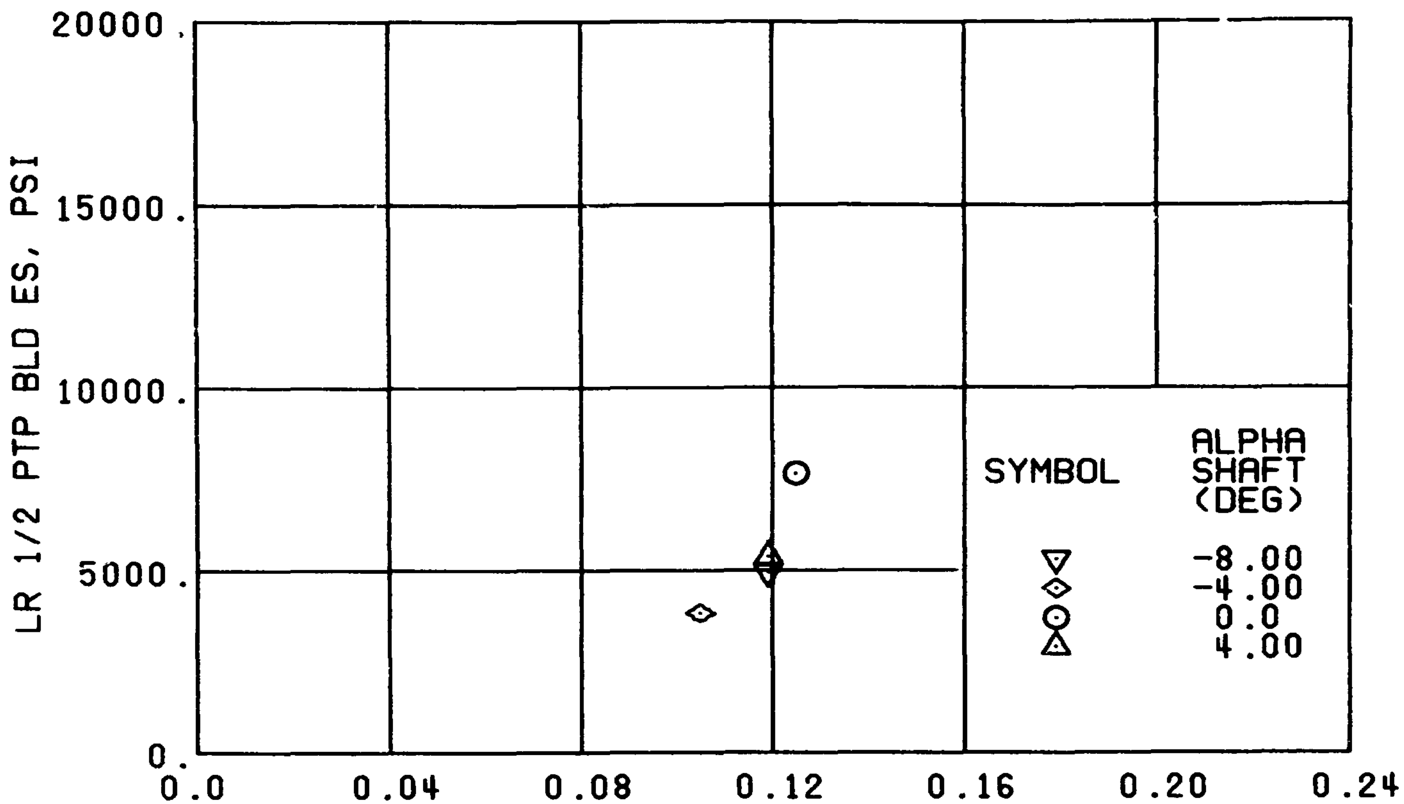

(i) GAGE 2 R84

Figure 43. Continued.
$\mu = 0.21$ $B'_{1s} = 6$ Deg

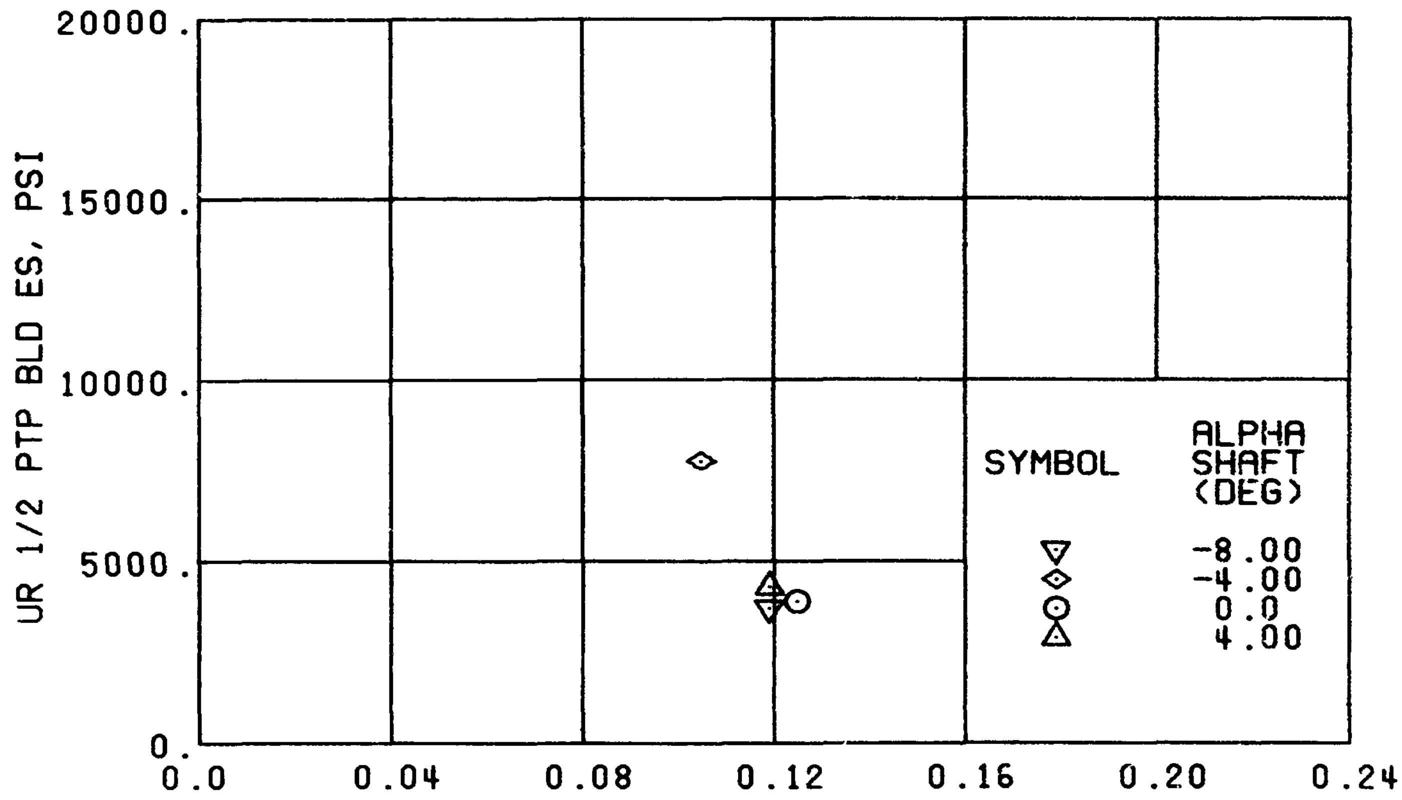

(j) GAGE 42 R132

Figure 43. Continued.
$\mu = 0.21$ $B'_{1s} = 6$ Deg

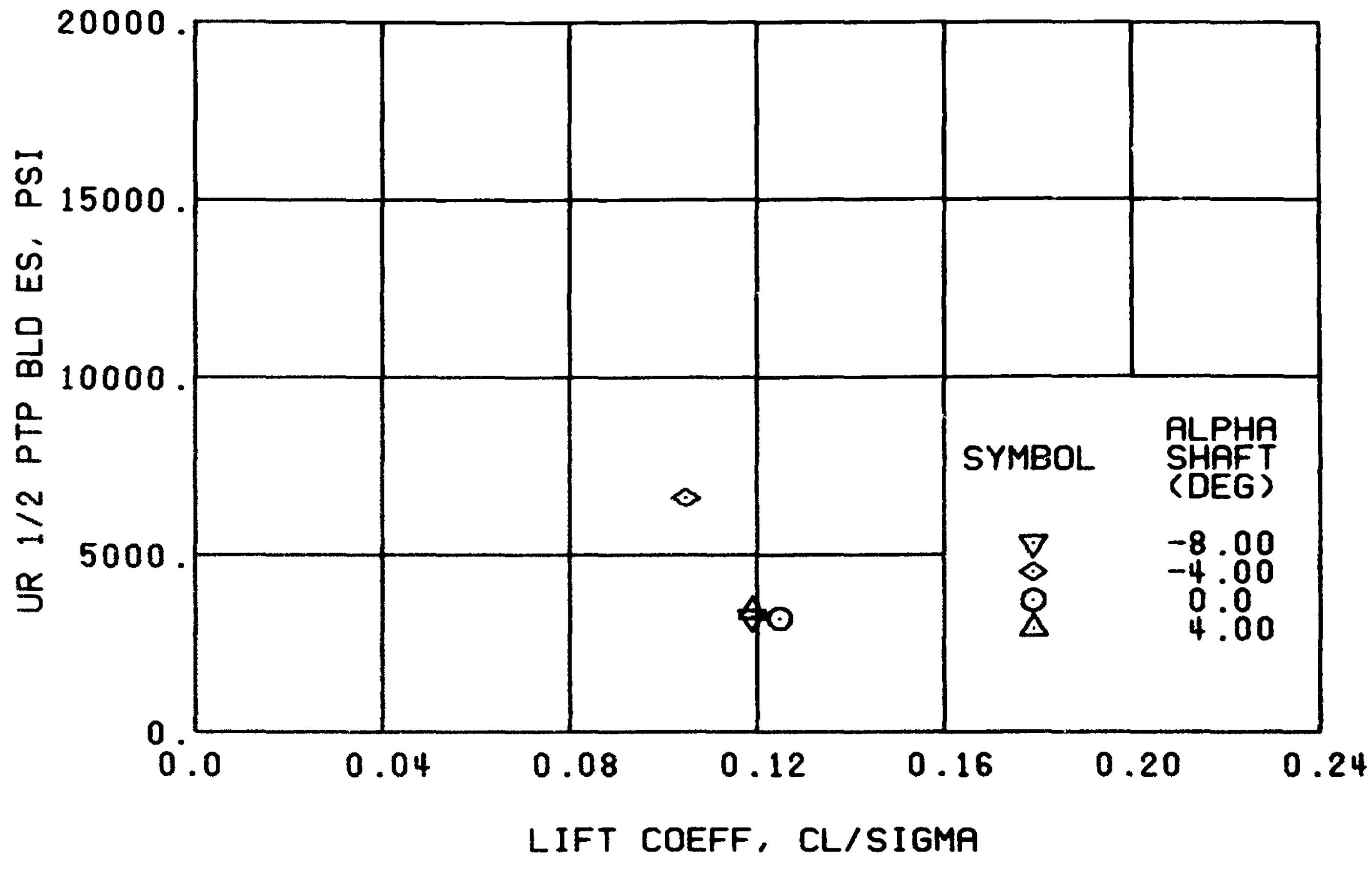

(k) GAGE 43 R168

Figure 43. Continued.
$\mu = 0.21$ $B'_{1s} = 6$ Deg

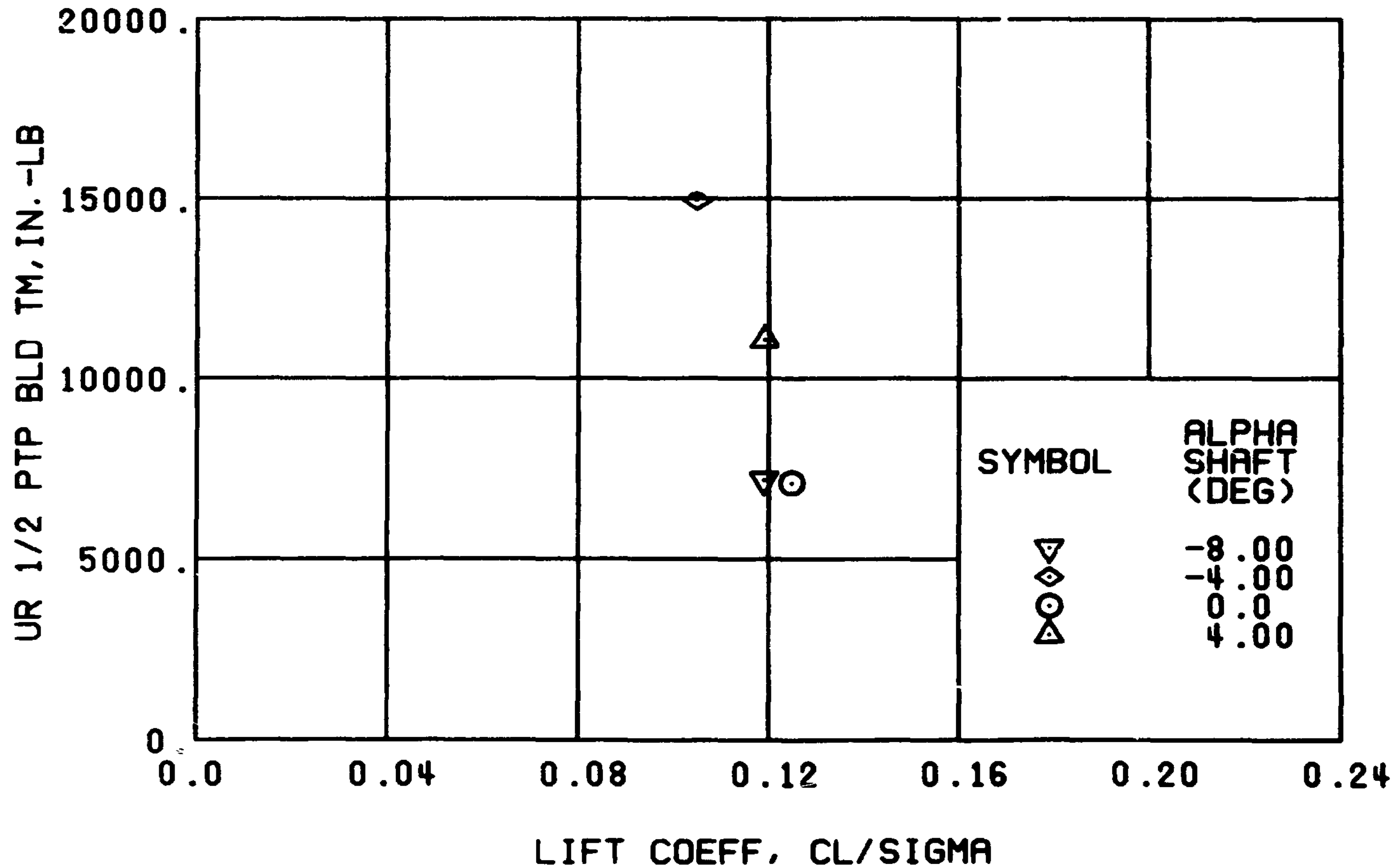

(I) GAGE 45 R82

Figure 43. Continued.
$\mu = 0.21 \quad B'_{1s} = 6$ Deg

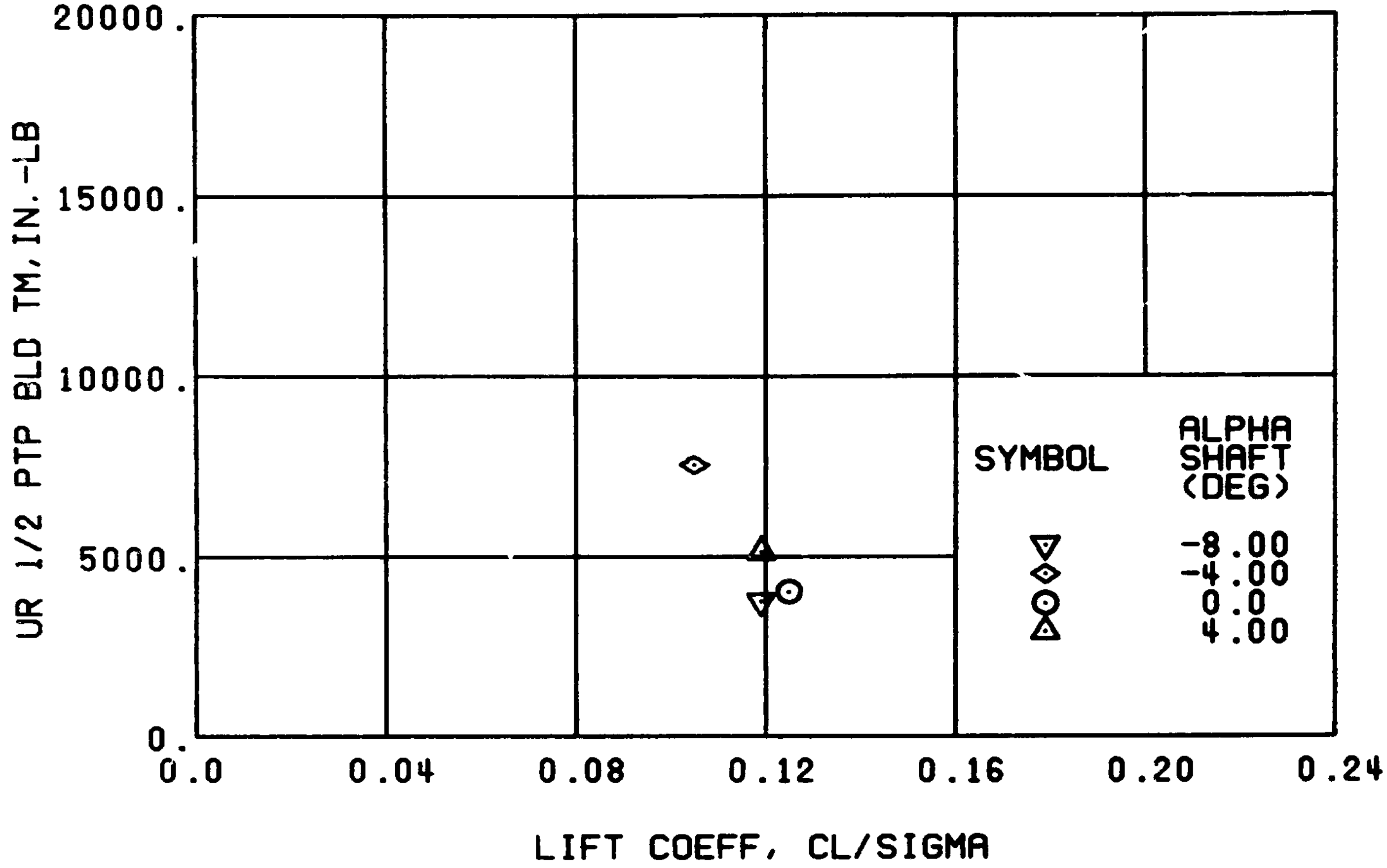

(m) GAGE 46 R130

Figure 43. Continued.
$\mu = 0.21$ $B'_{1s} = 6$ Deg

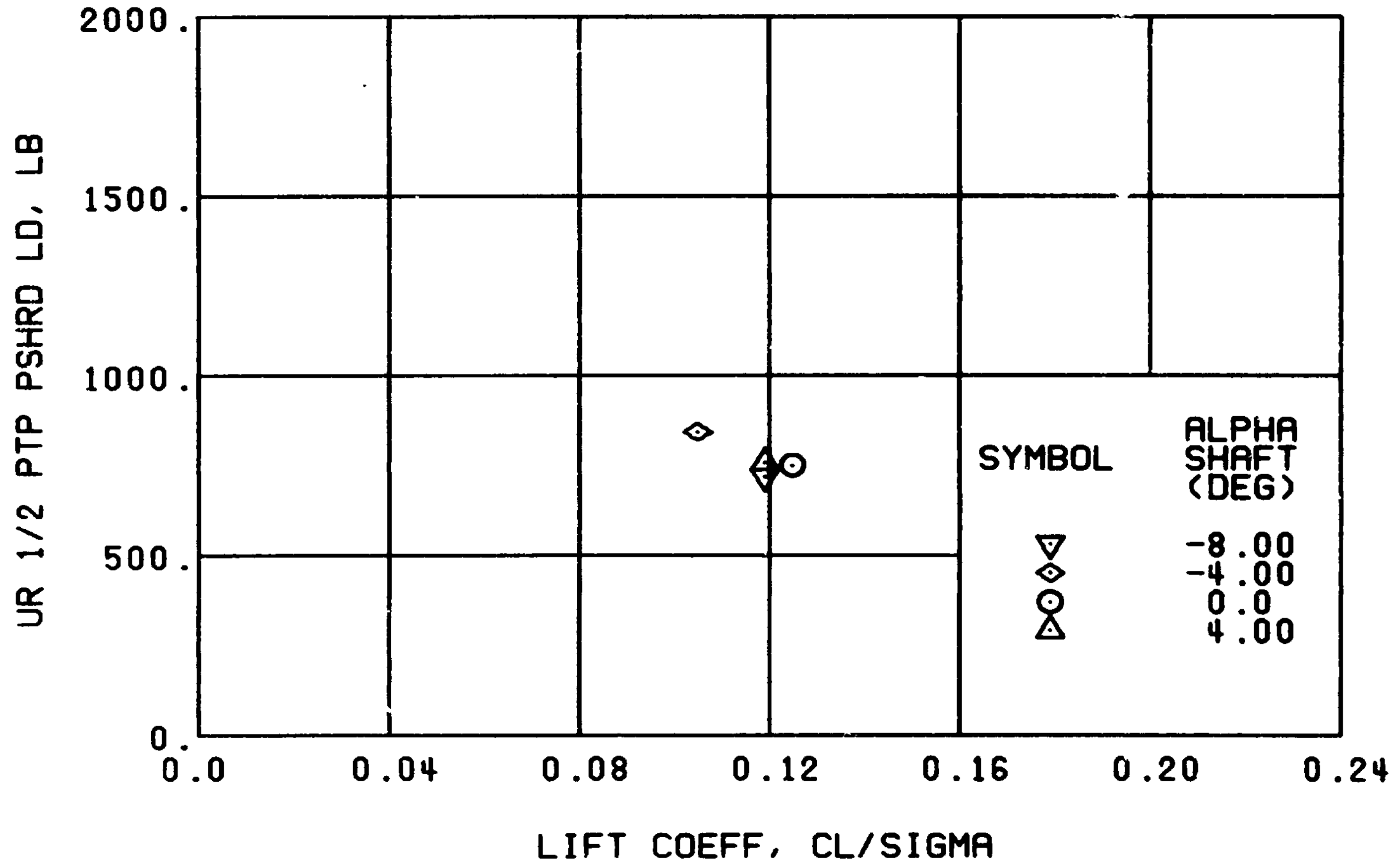

(n) GAGE 37

Figure 43. Continued.
$\mu = 0.21 \quad B'_{1s} = 6$ Deg

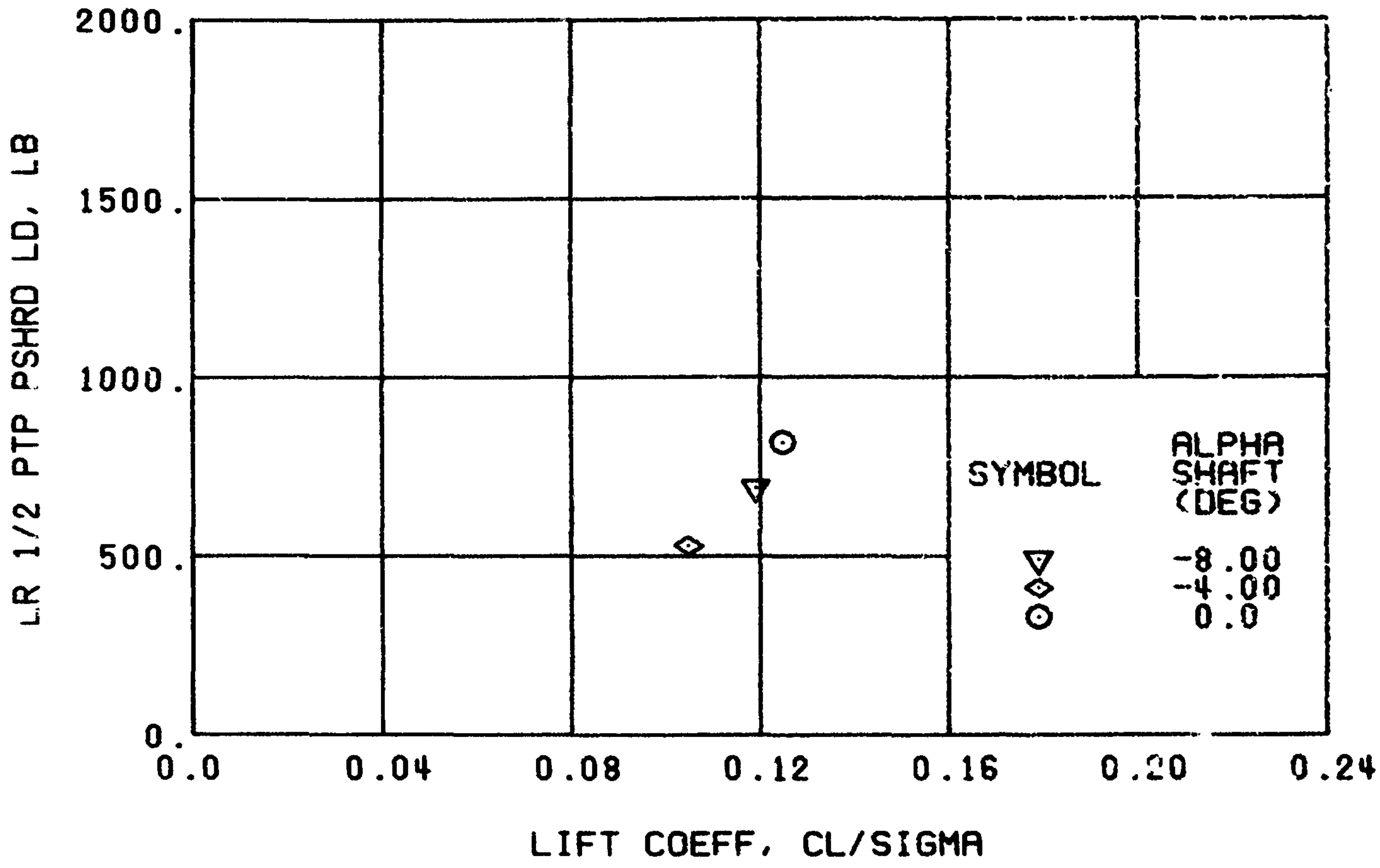

(o) GAGE 34

Figure 43. Continued.
$\mu = 0.21$ $B'_{1s} = 6$ Deg

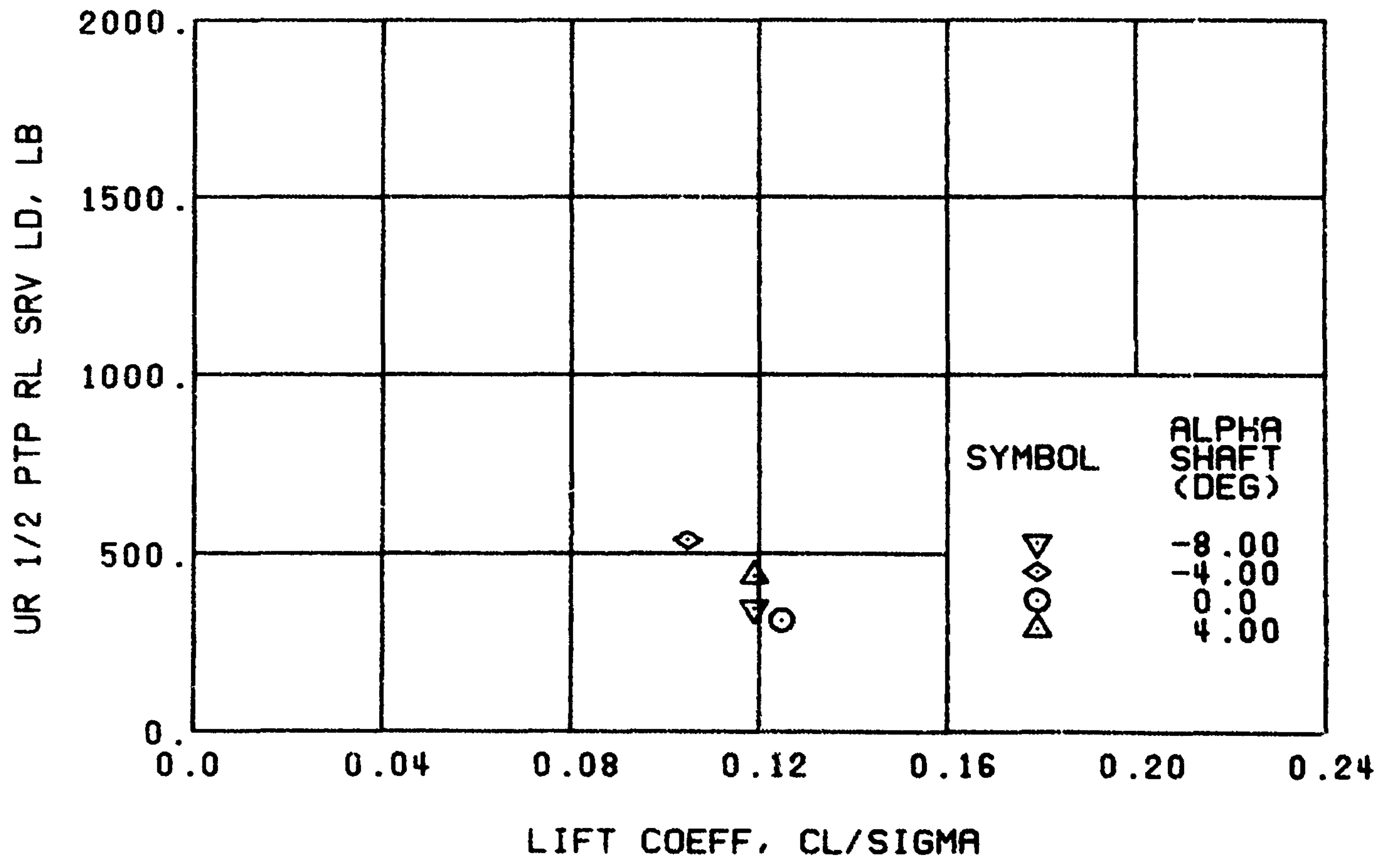

(p) GAGE 22

Figure 43. Continued.
$\mu = 0.21$ $B'_{1s} = 5$ Deg

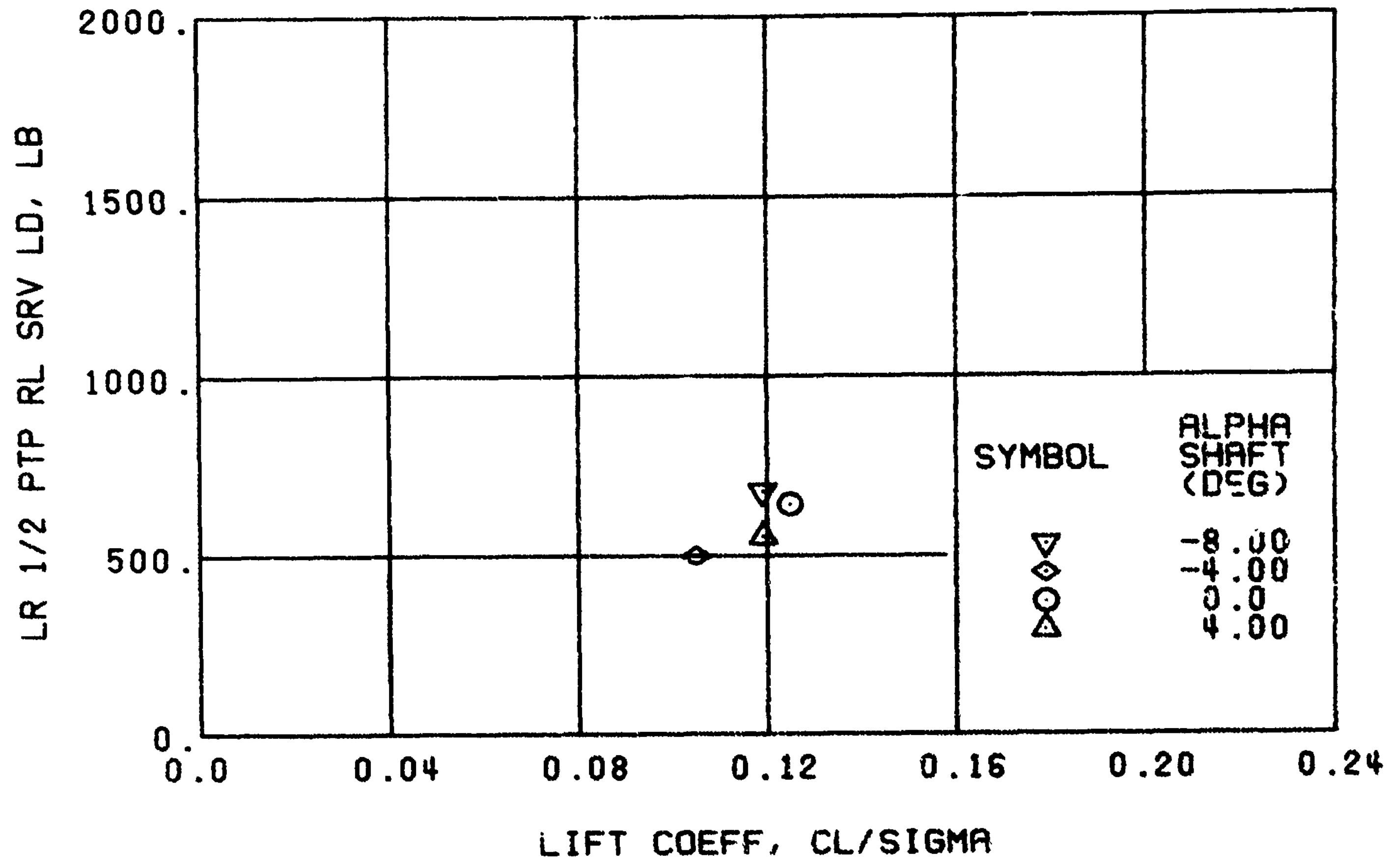

(q) GAGE 25

Figure 43. Continued.
μ = 0.21 B'_{1s} = 6 Deg

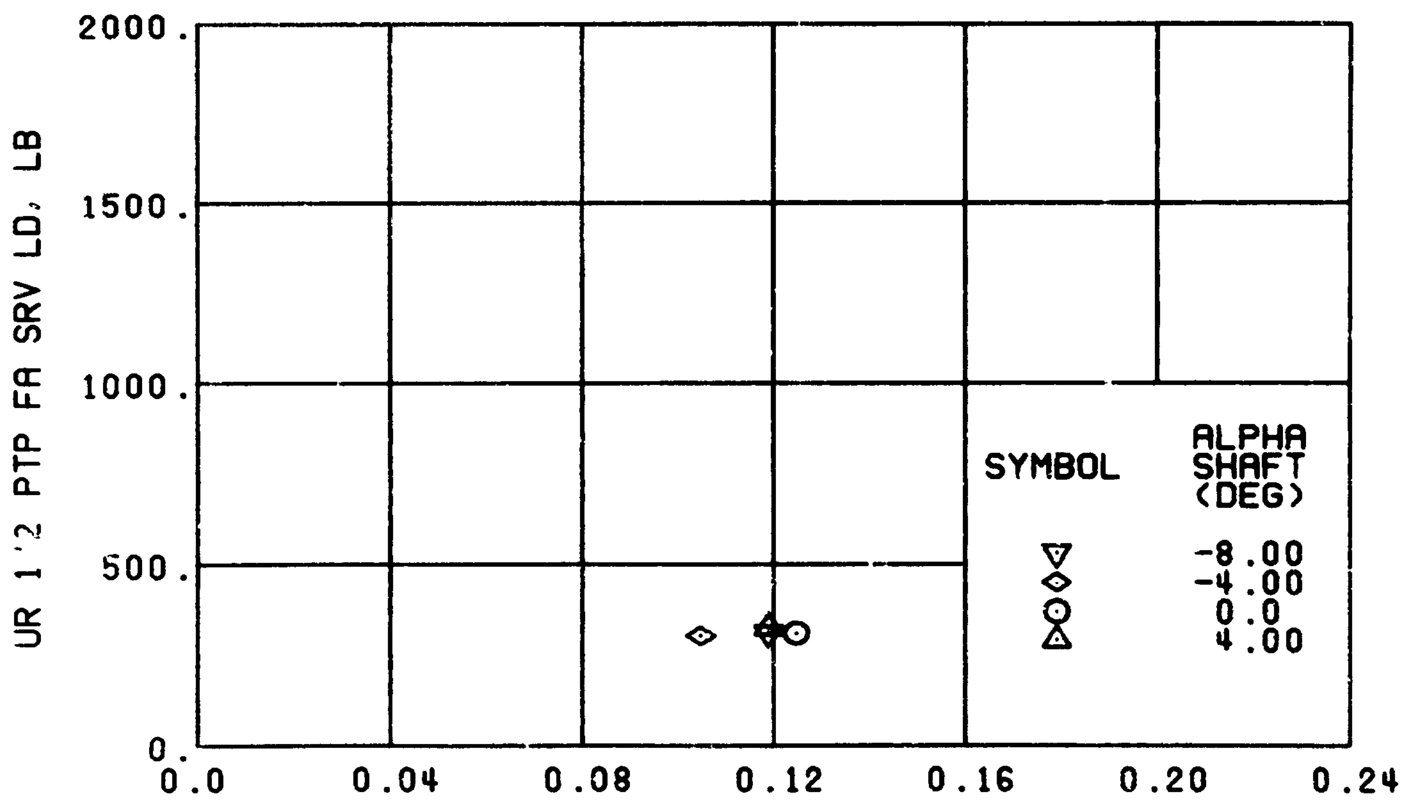

(r) GAGE 24

Figure 43. Continued.
$\mu = 0.21 \quad B'_{1s} = 6$ Deg

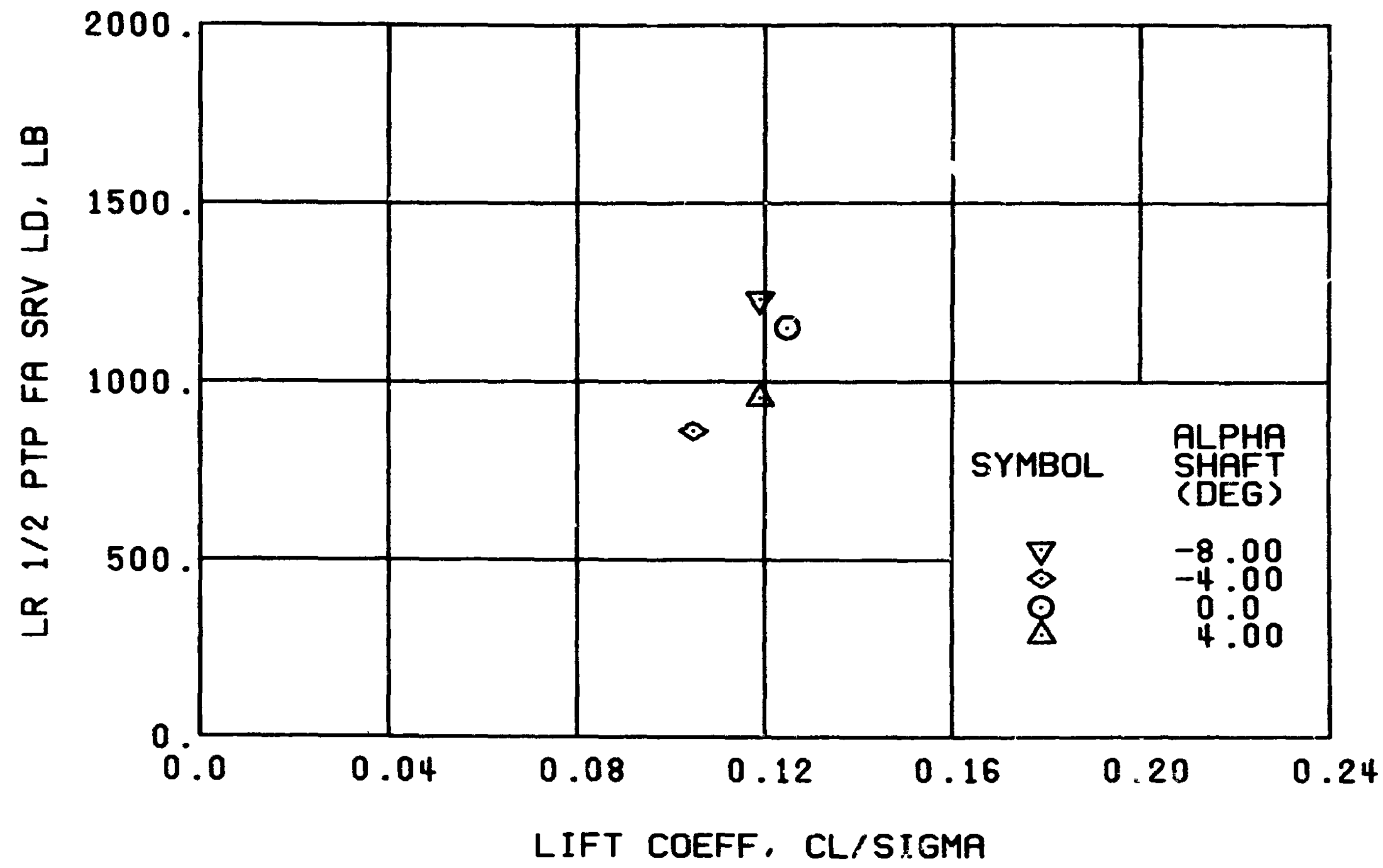

(s) GAGE 27

Figure 43. Continued.
$\mu = 0.21 \quad B'_{1s} = 6$ Deg

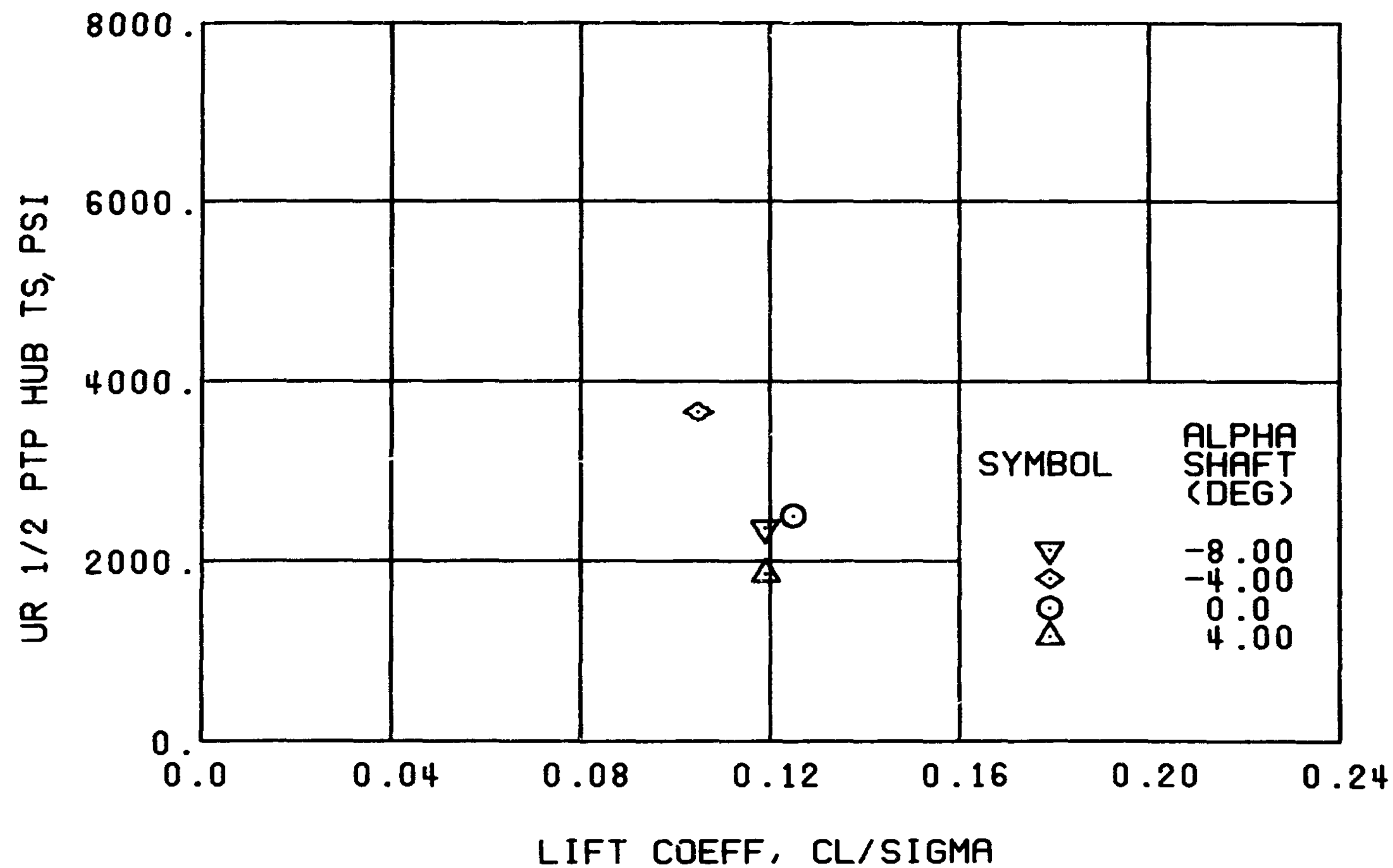

(f) GAGE 65

Figure 43. Continued.
$\mu = 0.21$ $B'_{1s} = 6$ Deg

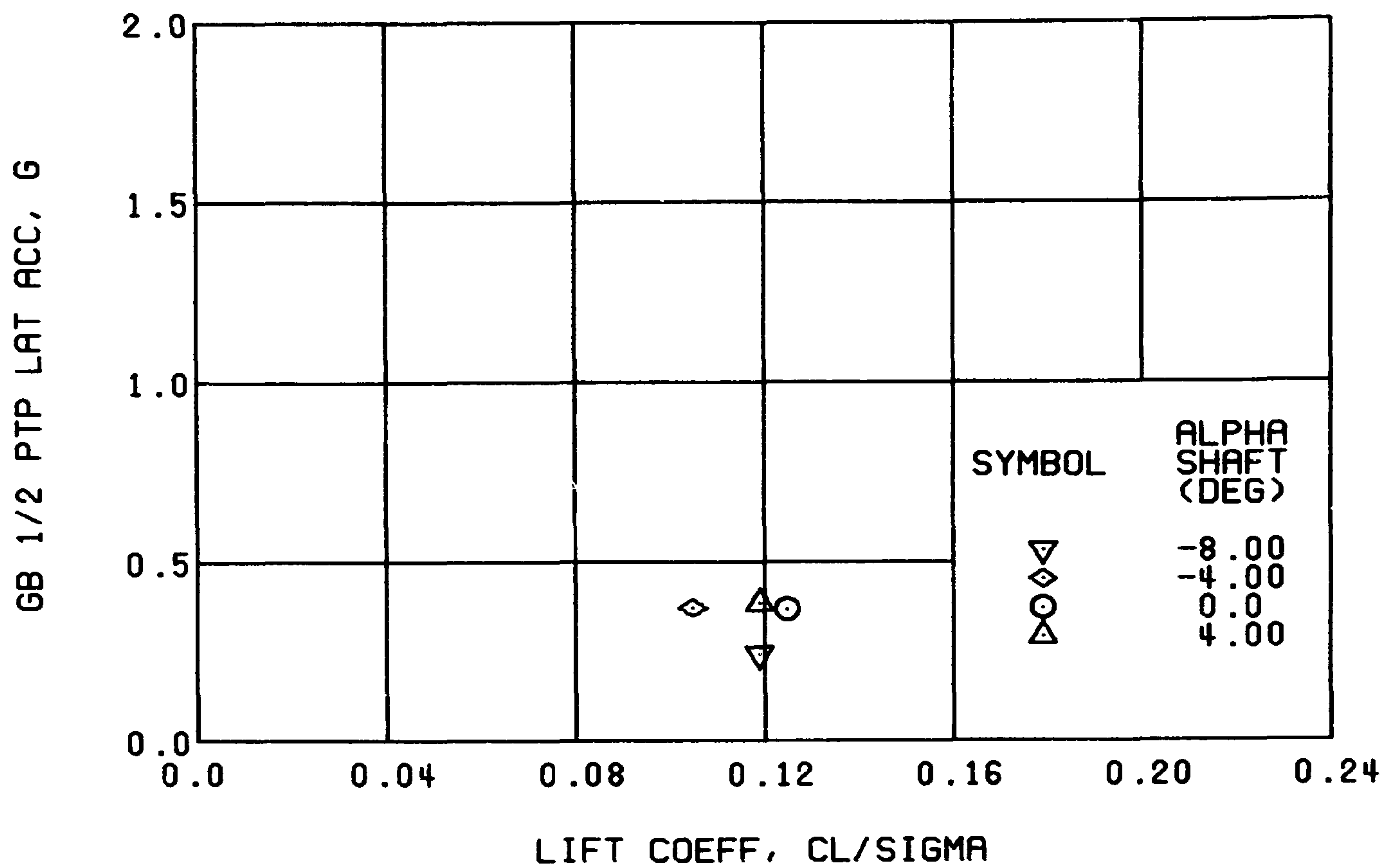

(u) GAGE 15 STA 76, BL 30

Figure 43. Continued.
$\mu = 0.21$ $B'_{1s} = 6$ Deg

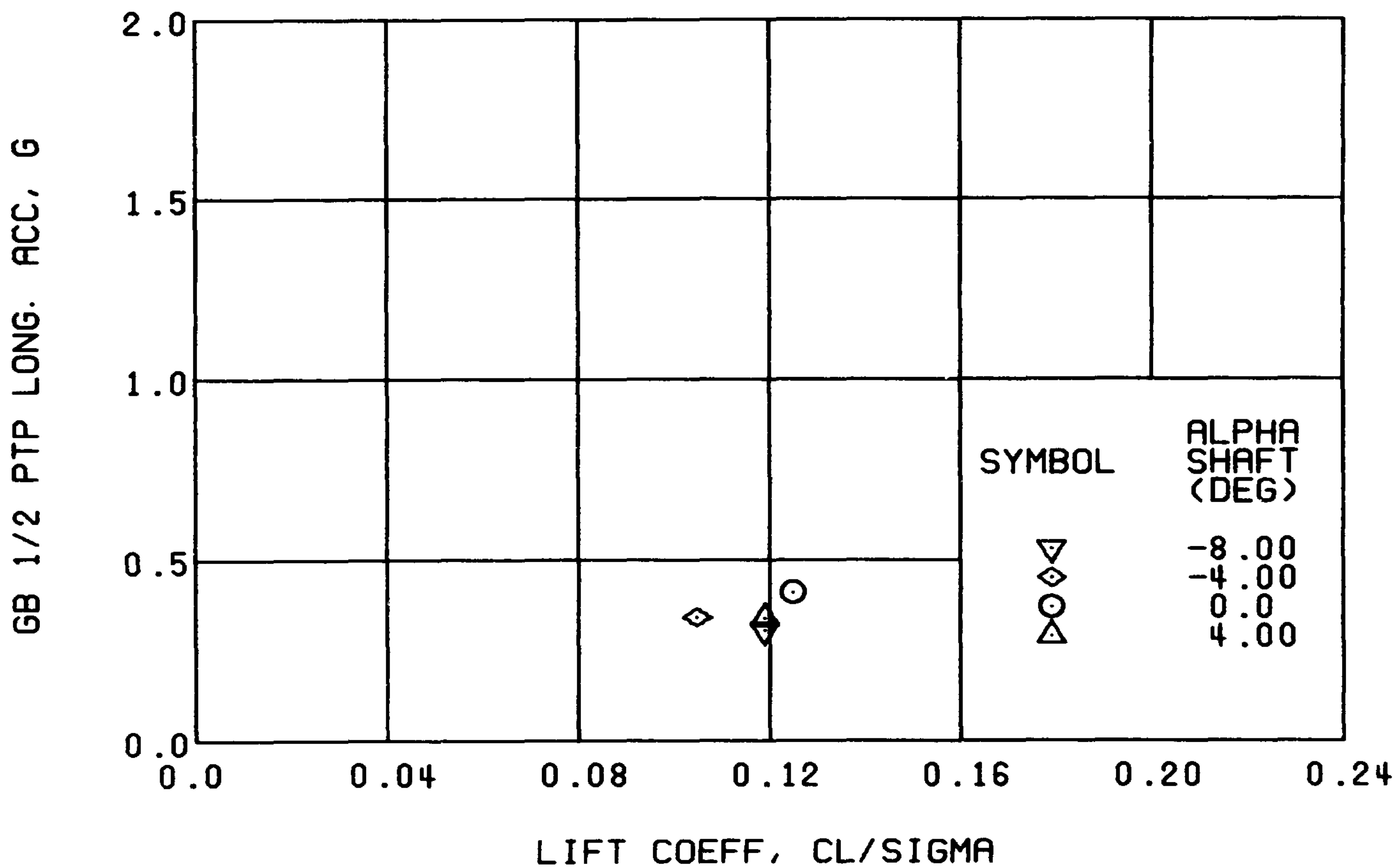

(v) GAGE 14 STA 61, BL 0

Figure 43. Continued.
$\mu = 0.21 \quad B'_{1s} = 6$ Deg

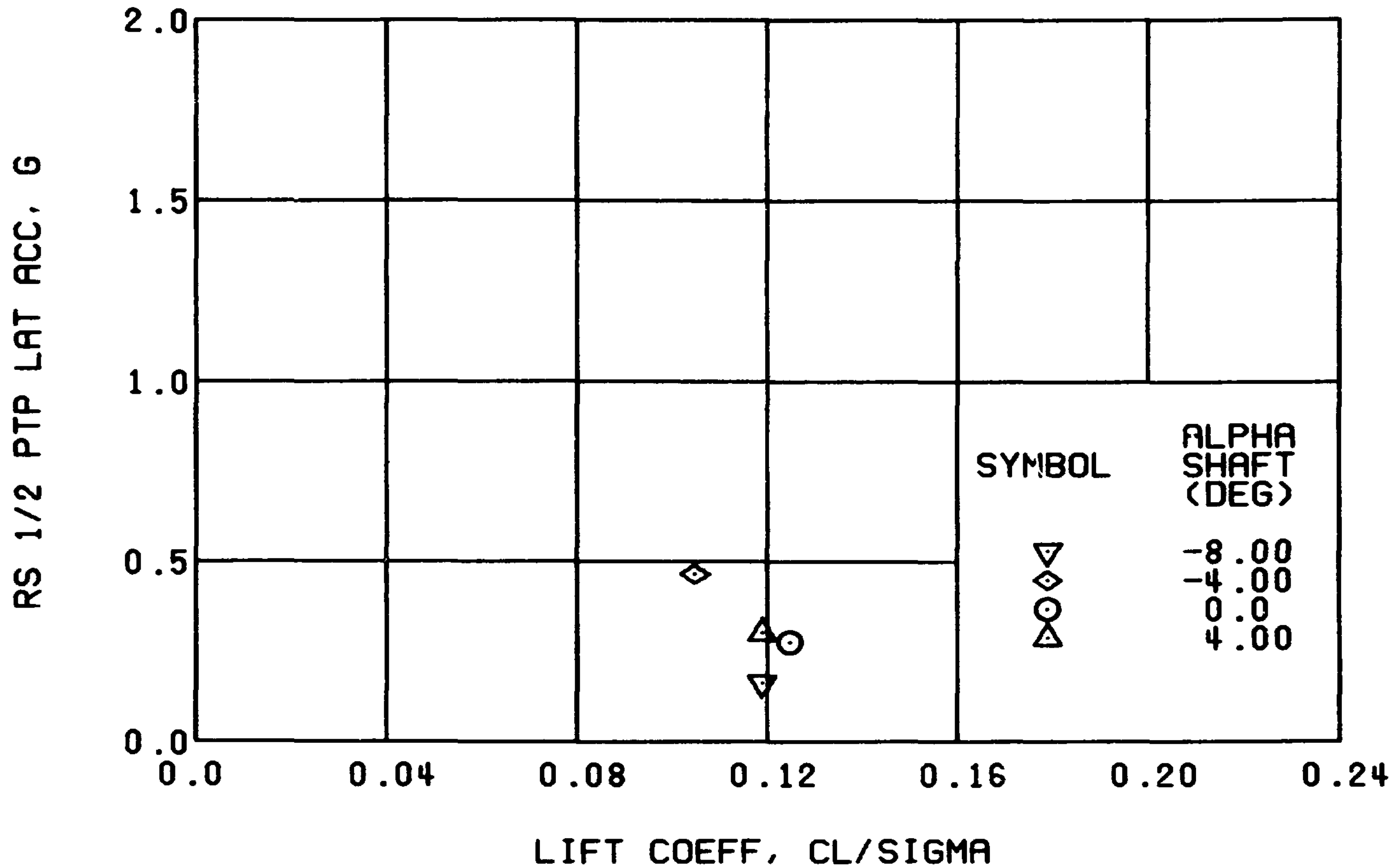

(w) GAGE 16 ROVER 3

Figure 43. Continued.
$\mu = 0.21 \quad B'_{1s} = 6$ Deg

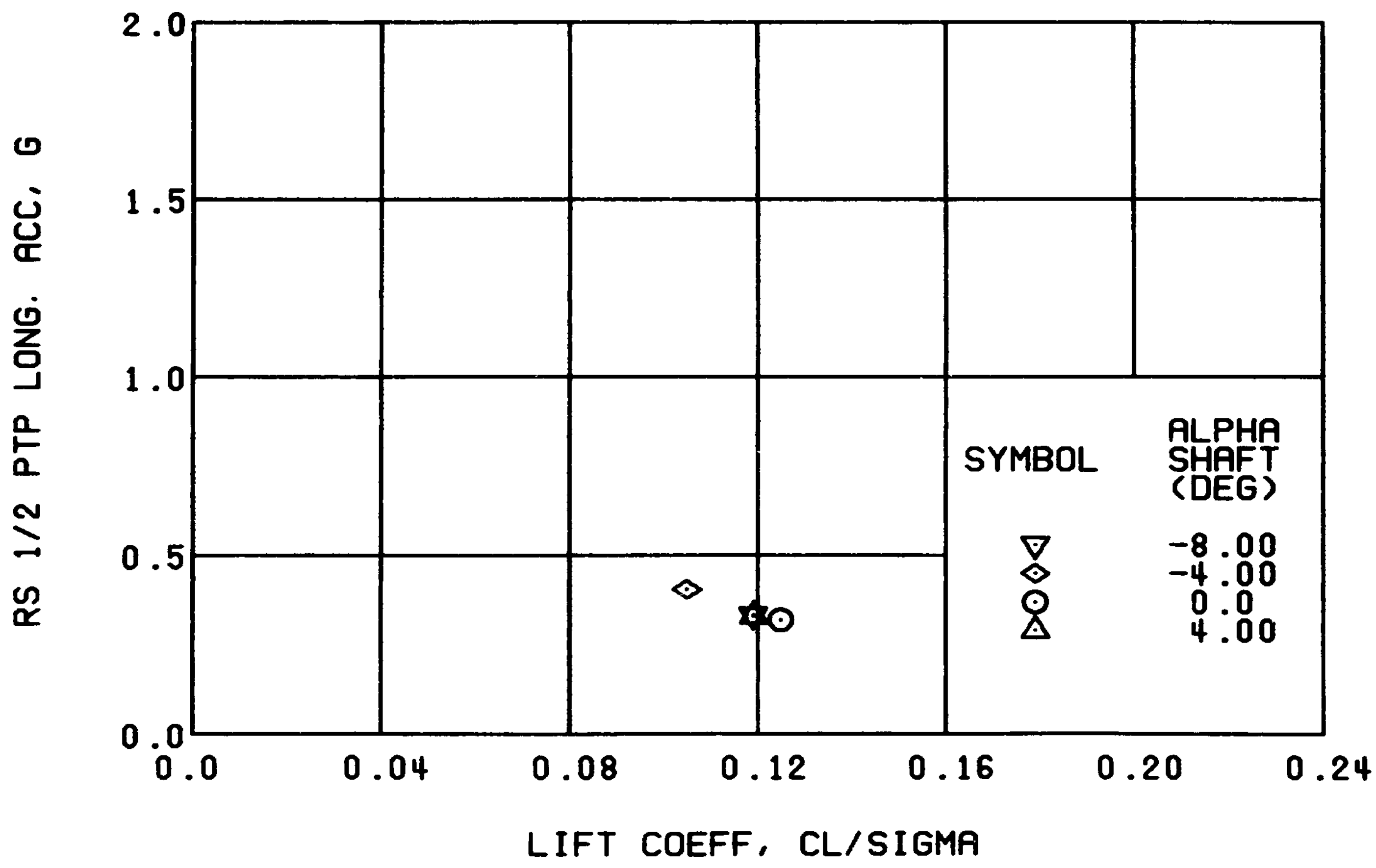

(x) GAGE 17 ROVER 4

Figure 43. Concluded.
$\mu = 0.21$ $B'_{1s} = 6$ Deg

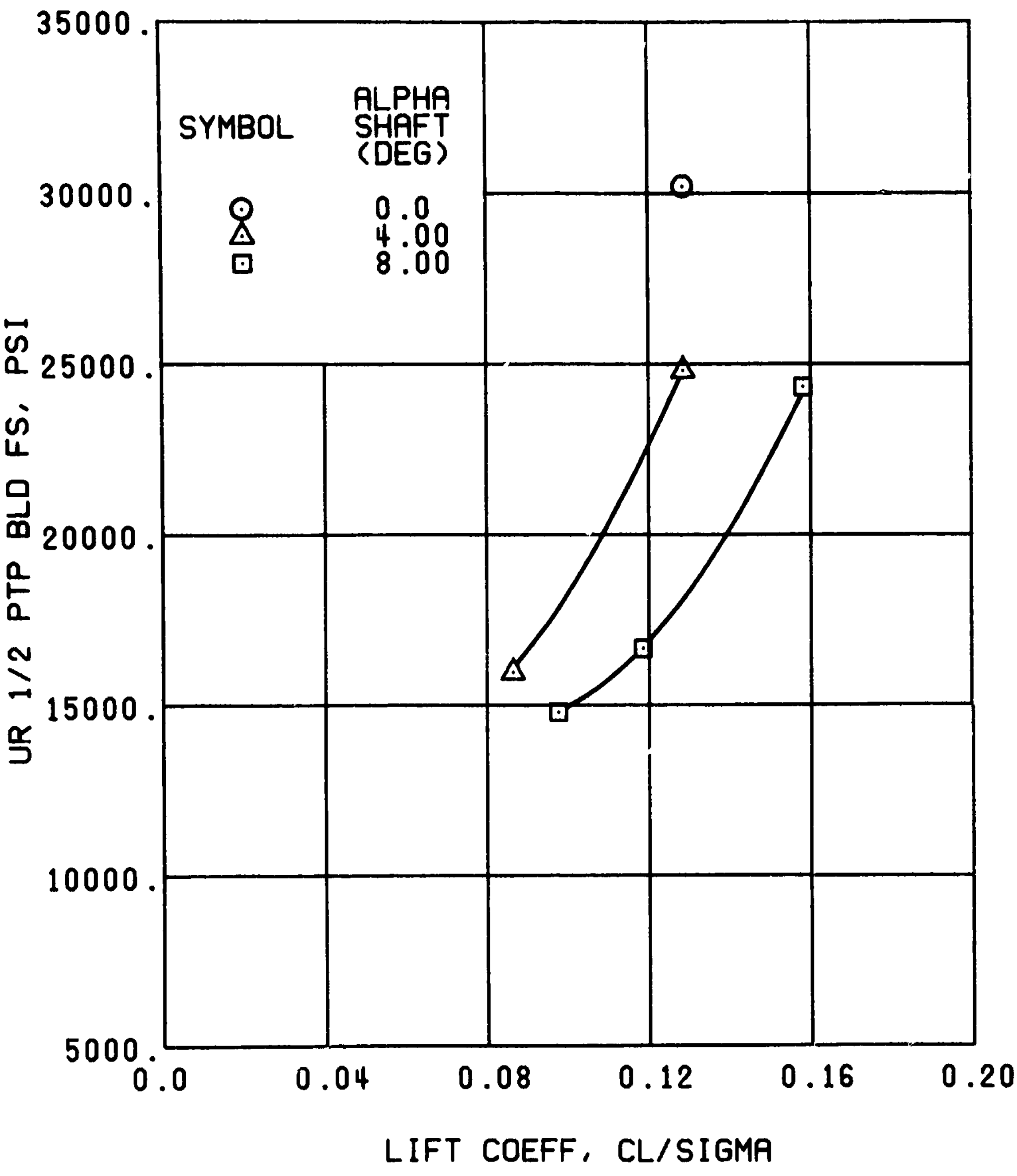

(a) GAGE 51 R84

Figure 44. Stress, Load, and Vibration Data at an Advance Ratio of 0.35 With the Lateral Displacement Control (B'_{1s}) Set at 0 Degrees.

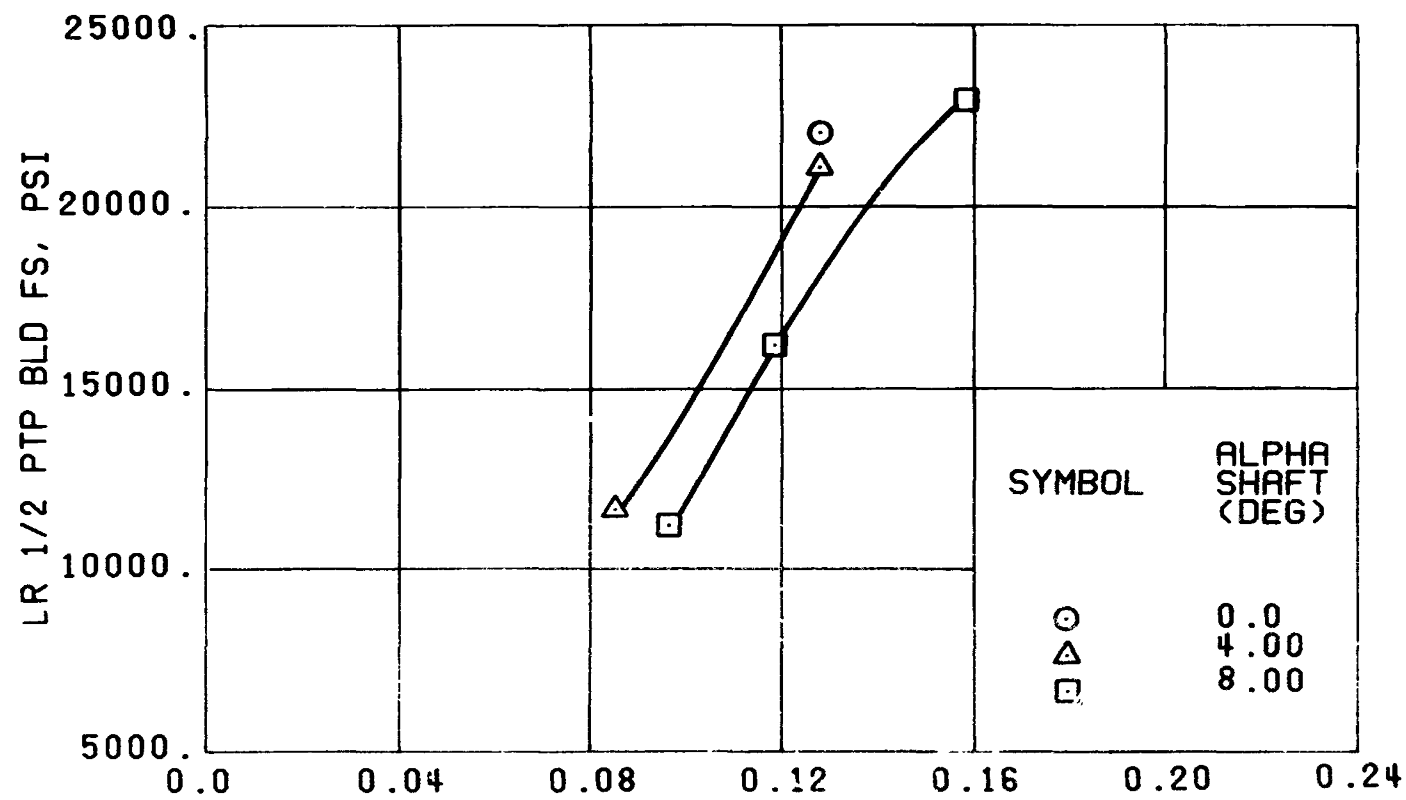

(b) GAGE 1 R84

Figure 44. Continued.
$\mu = 0.35$ $B'_{1s} = 0$ Deg

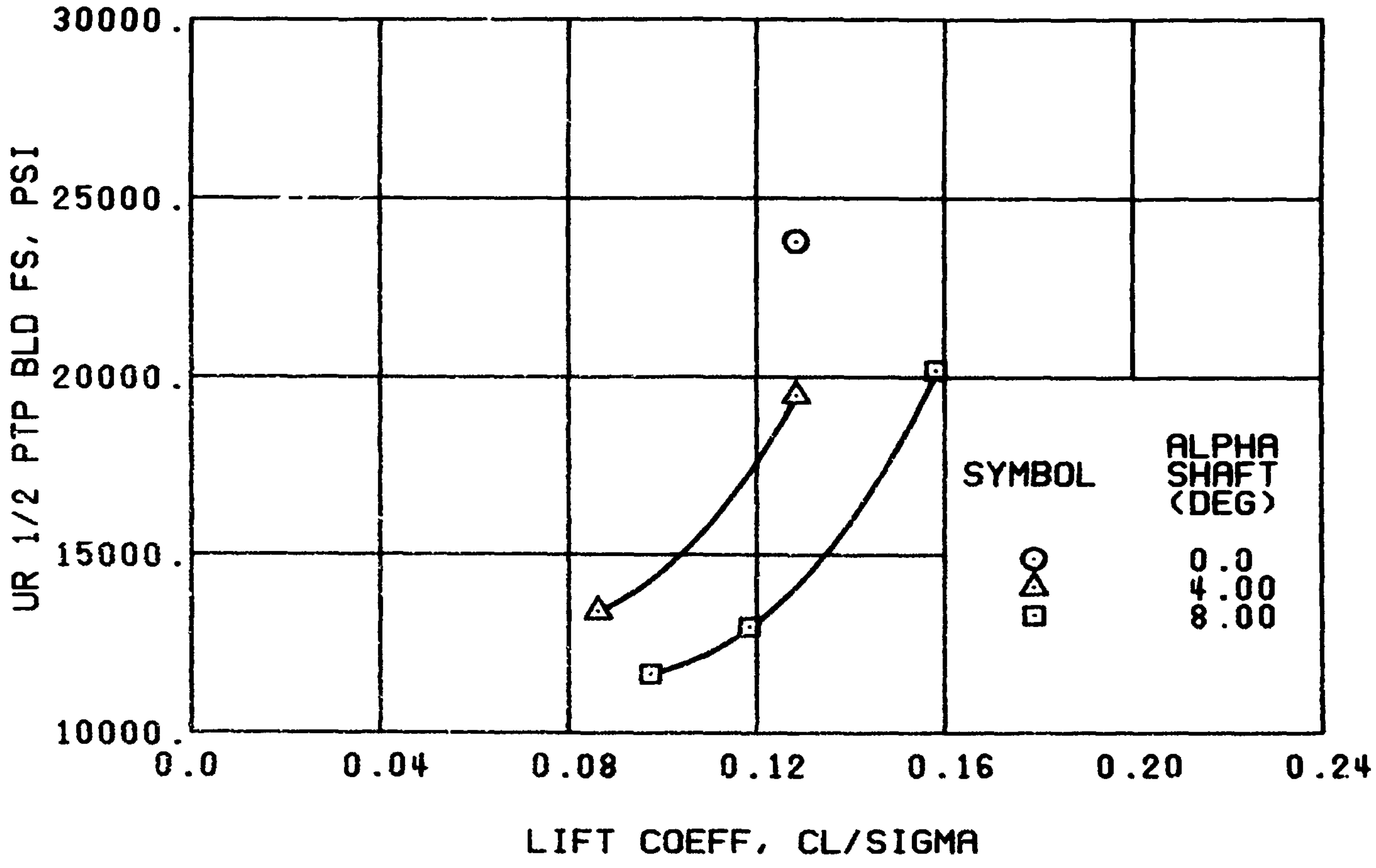

(c) GAGE 52 R108

Figure 44. Continued.
$\mu = 0.35$ $B_{1s}' = 0$ Deg

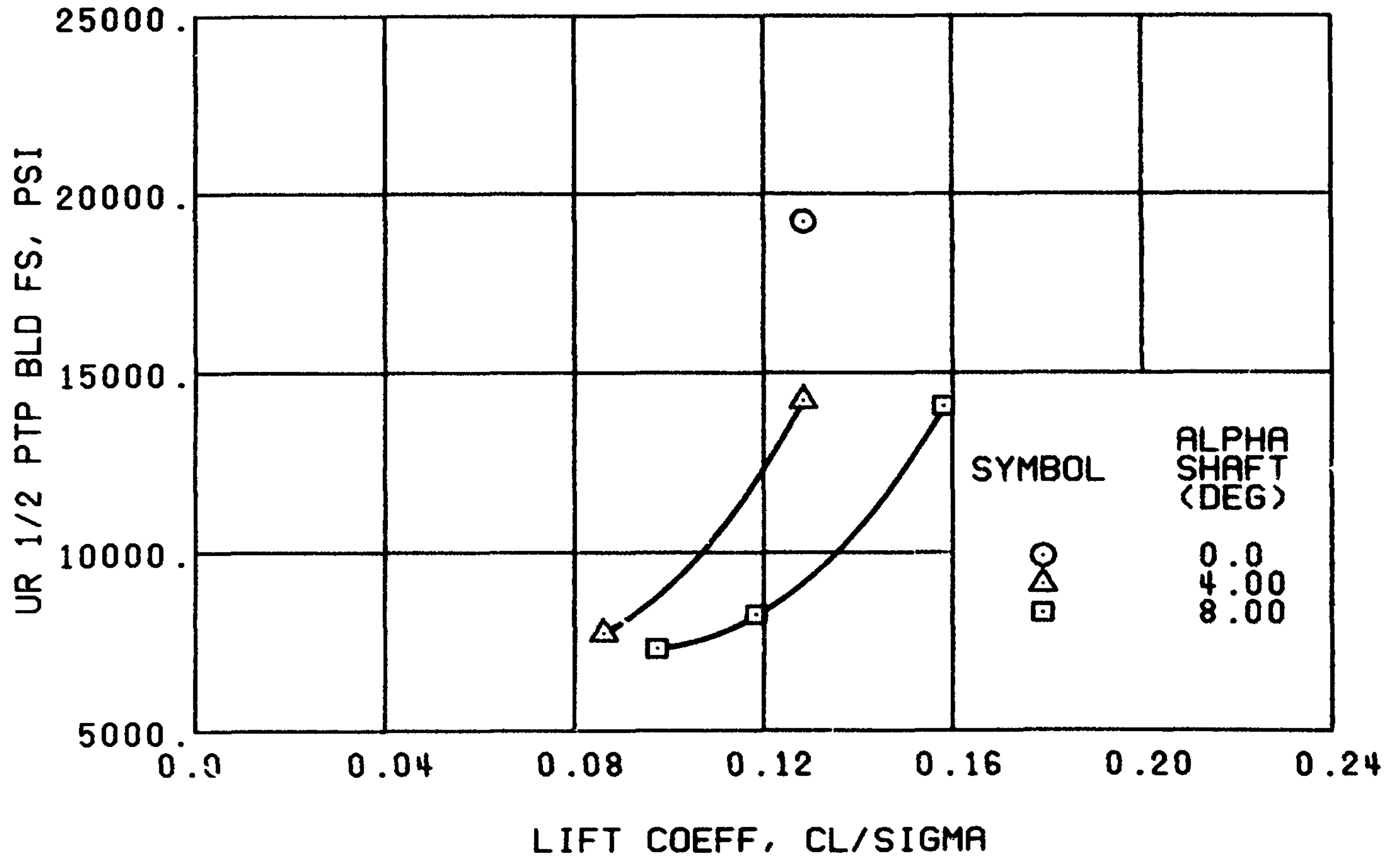

(d) GAGE 53 R132

Figure 44. Continued.
$\mu = 0.35$ $B'_{1s} = 0$ Deg

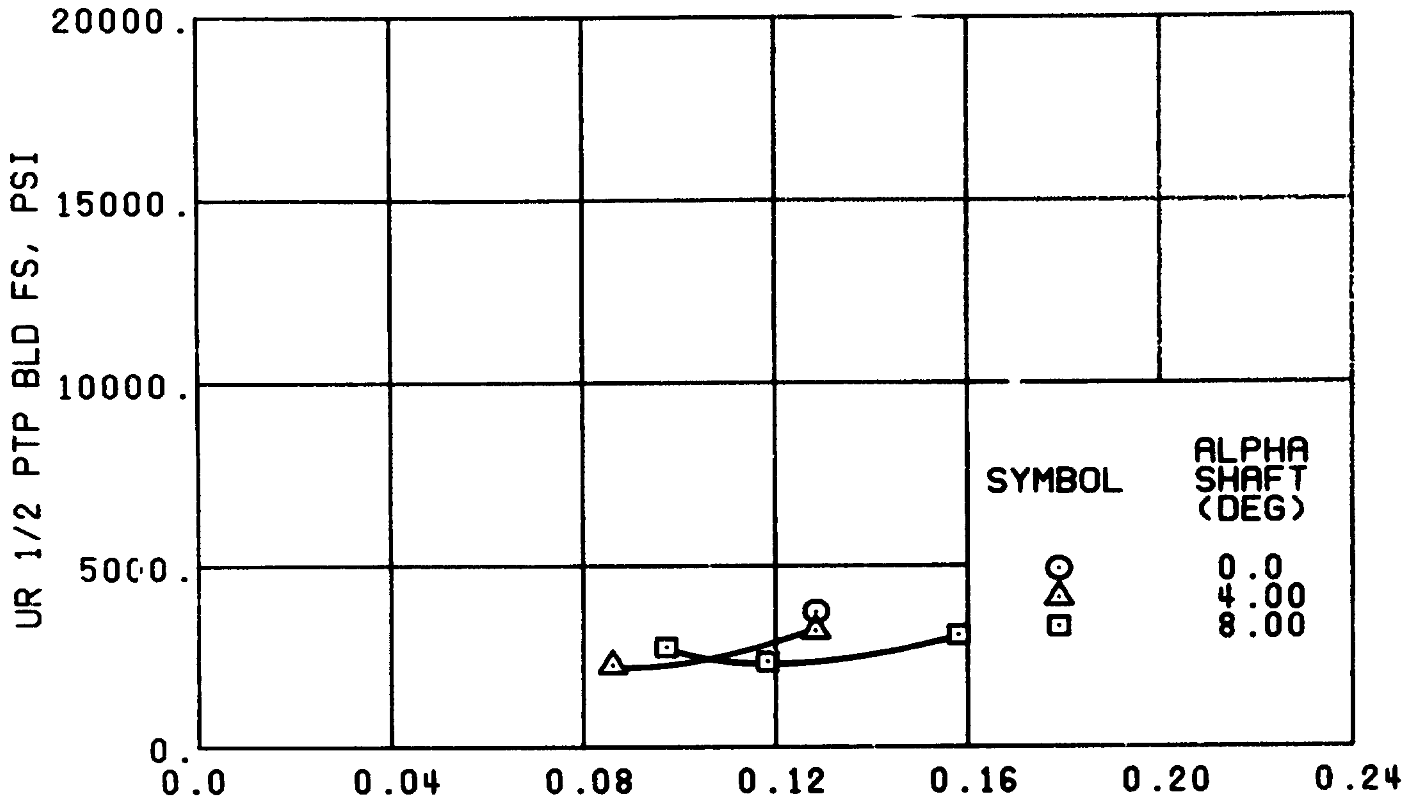

(f) GAGE 55 R204

Figure 44. Continued.
$\mu = 0.35$ $B'_{1s} = 0$ Deg

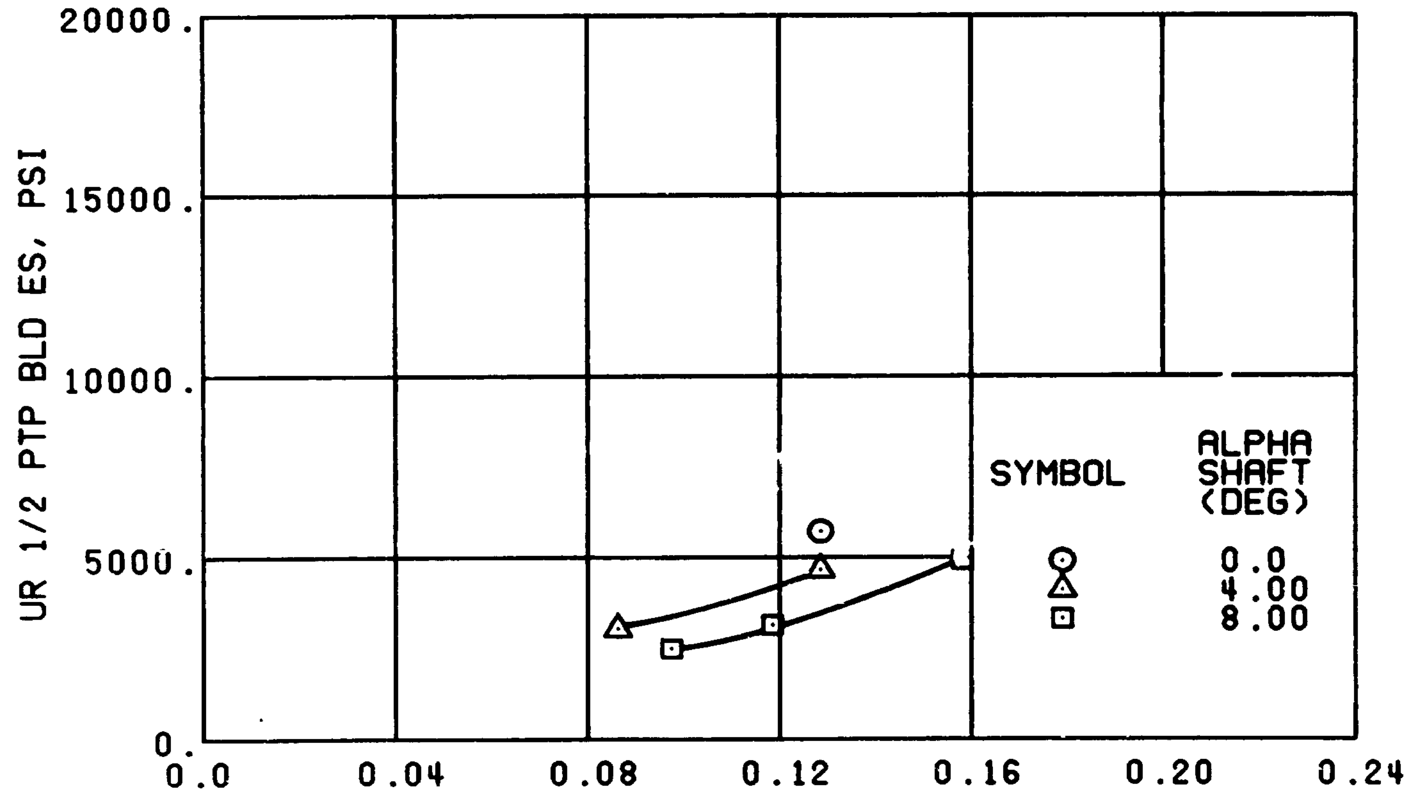

(h) GAGE 40 R84

Figure 44. Continued.
μ = 0.35 B'_{1s} = 0 Deg

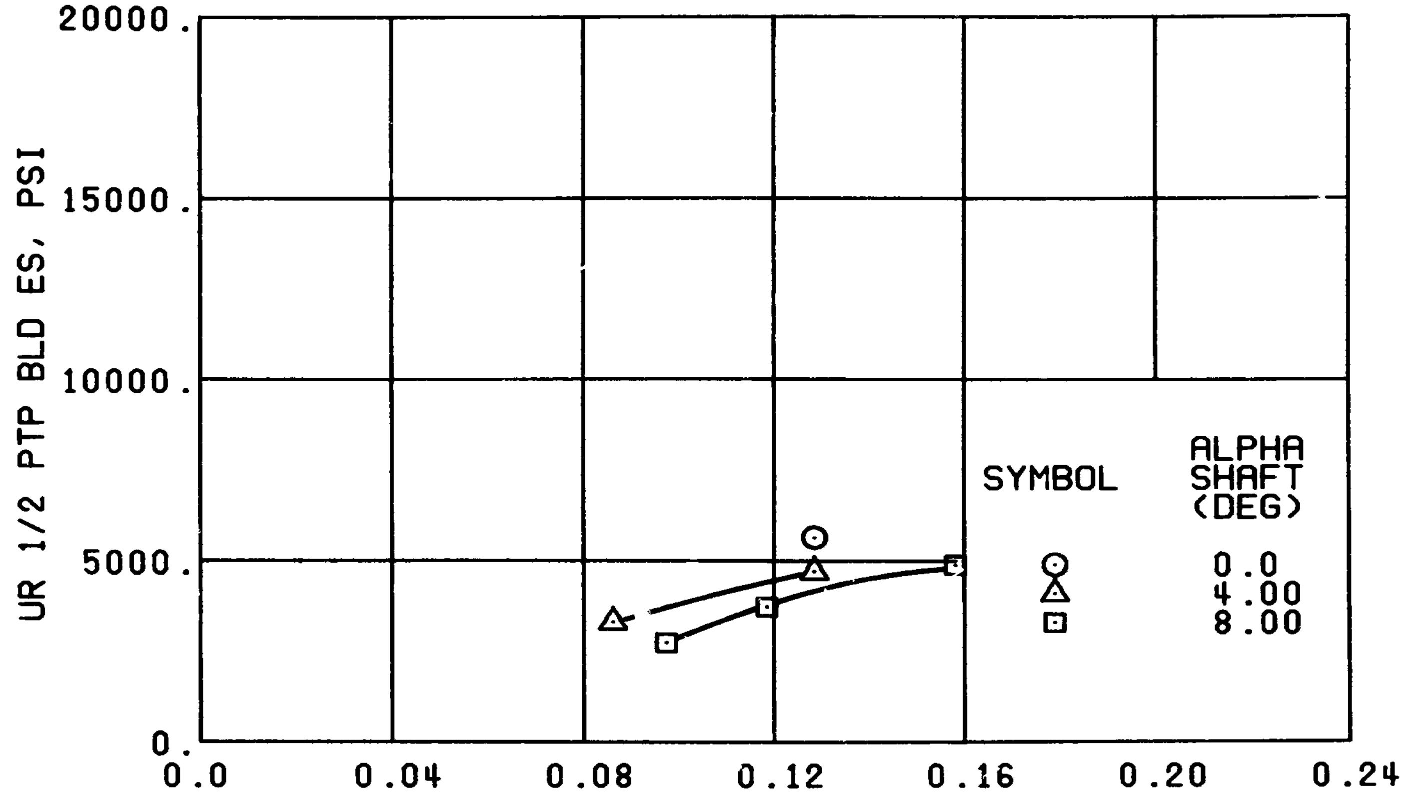

(j) GAGE 42 R132

Figure 44. Continued.
$\mu = 0.35$ $B'_{1s} = 0$ Deg

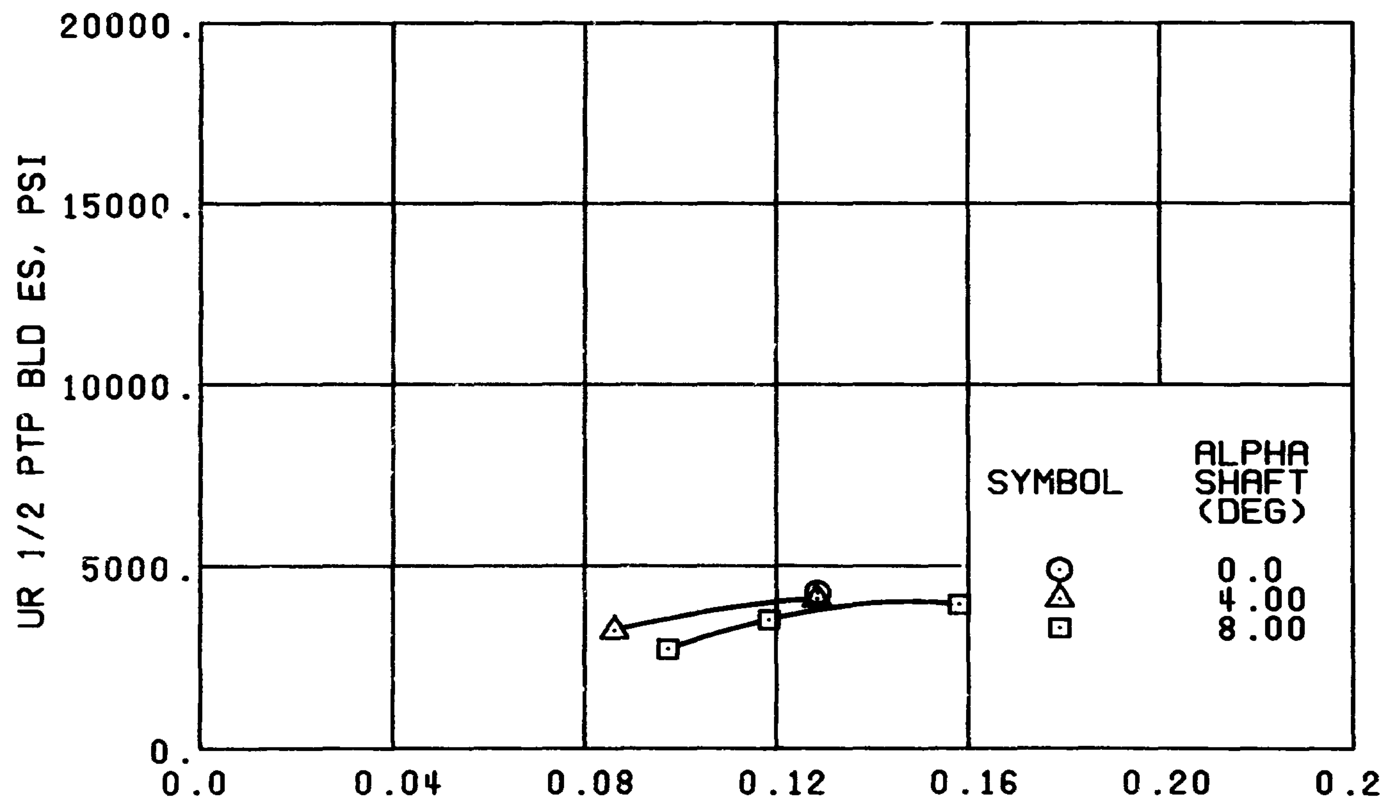

(k) GAGE 43 R168

Figure 44. Continued.
μ = 0.35 B'_{1s} = 0 Deg

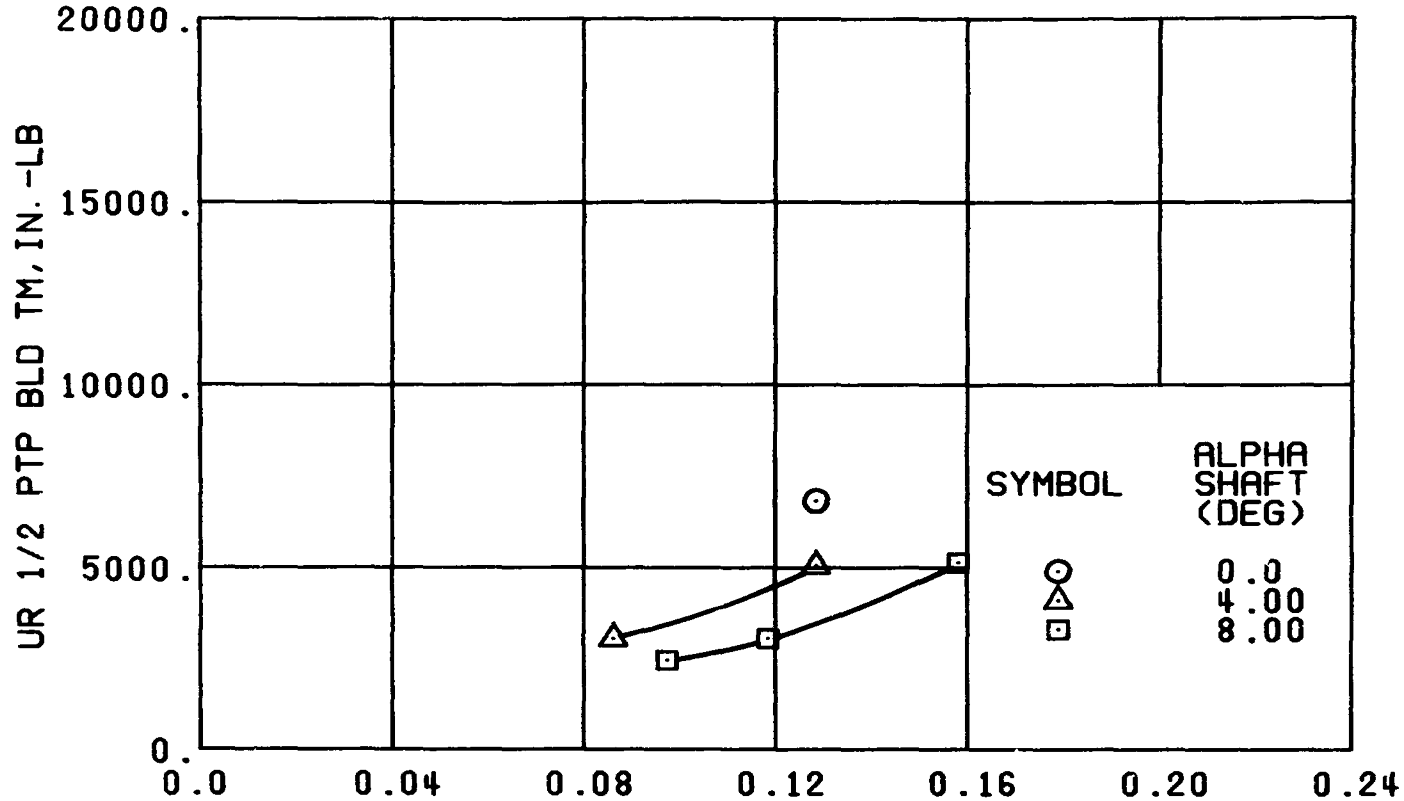

(m) GAGE 46 R130

Figure 44. Continued.
$\mu = 0.35$ $B'_{1s} = 0$ Deg

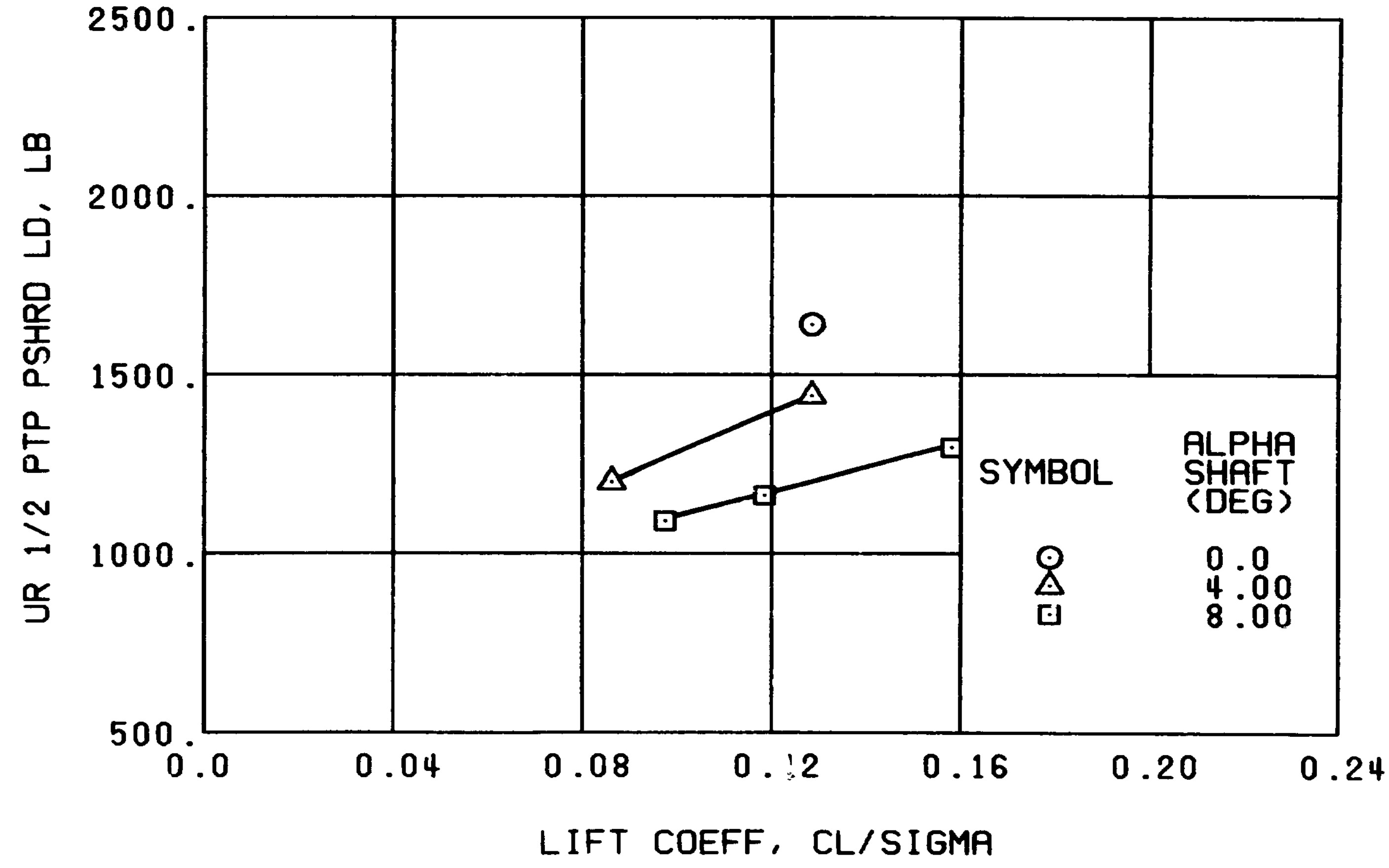

(n) GAGE 37

Figure 44. Continued.
$\mu = 0.35$ $B'_{1s} = 0$ Deg

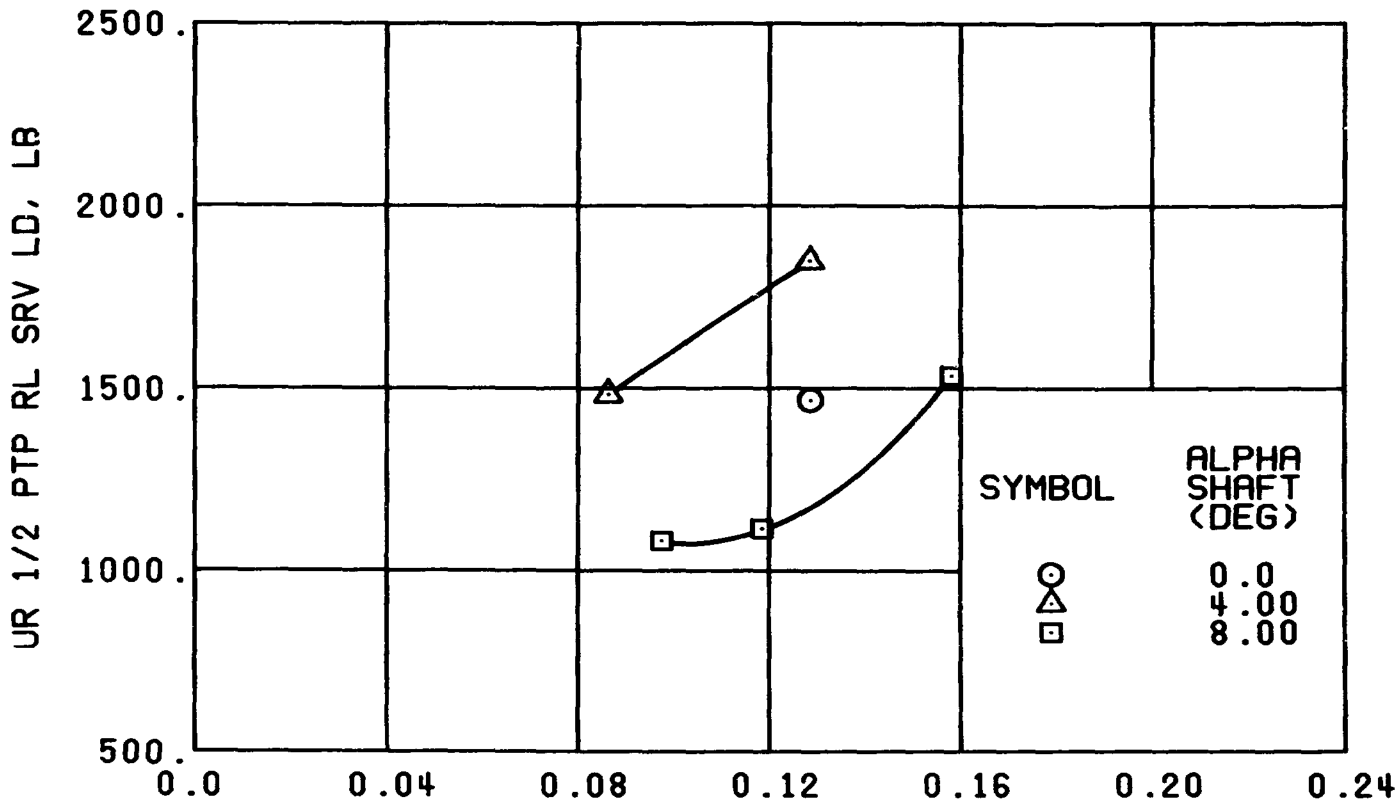

(p) GAGE 22

Figure 44. Continued.
$\mu = 0.35$ $B'_{1s} = 0$ Deg

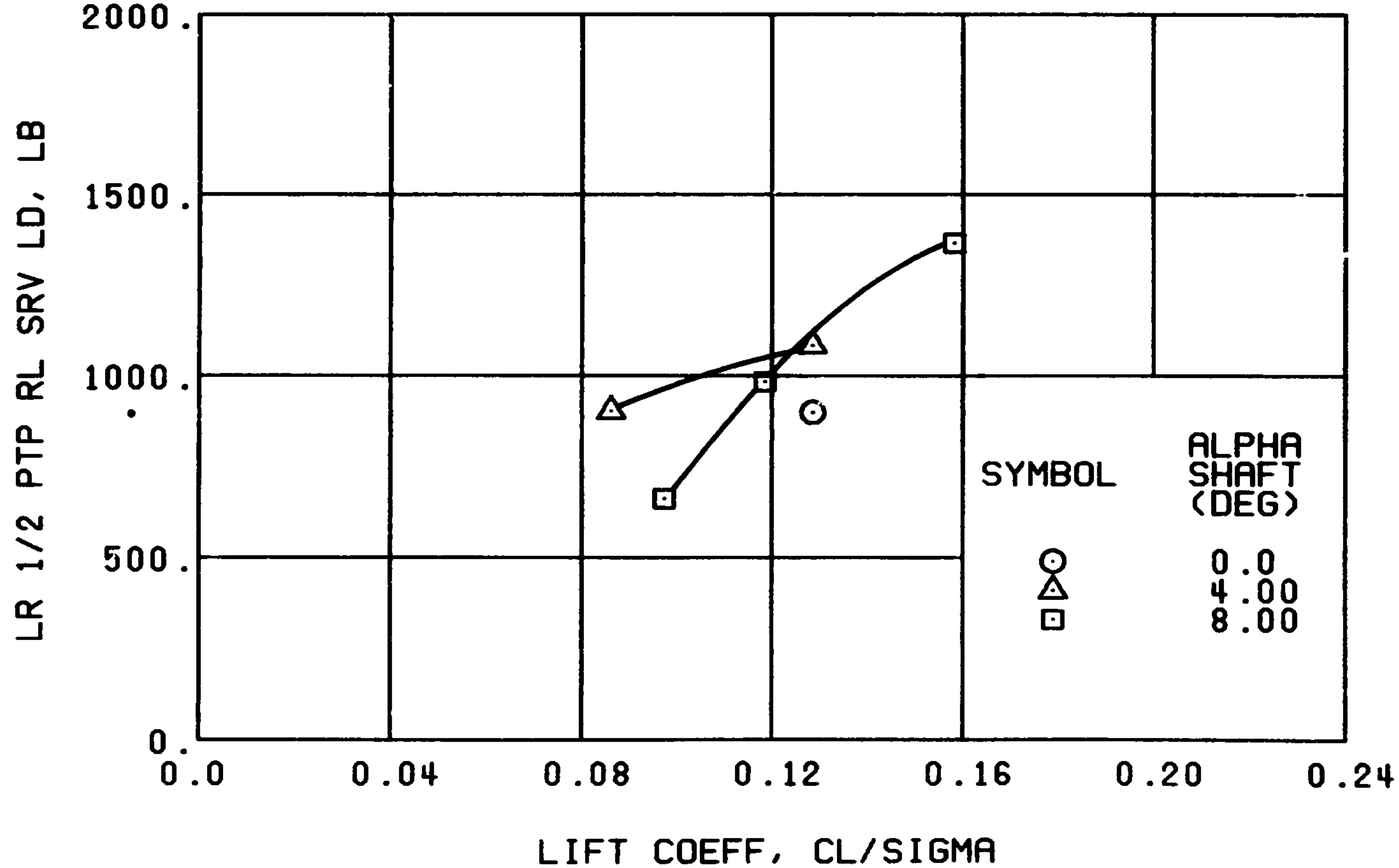

(q) GAGE 25

Figure 44. Continued.
$\mu = 0.35$ $B'_{1s} = 0$ Deg

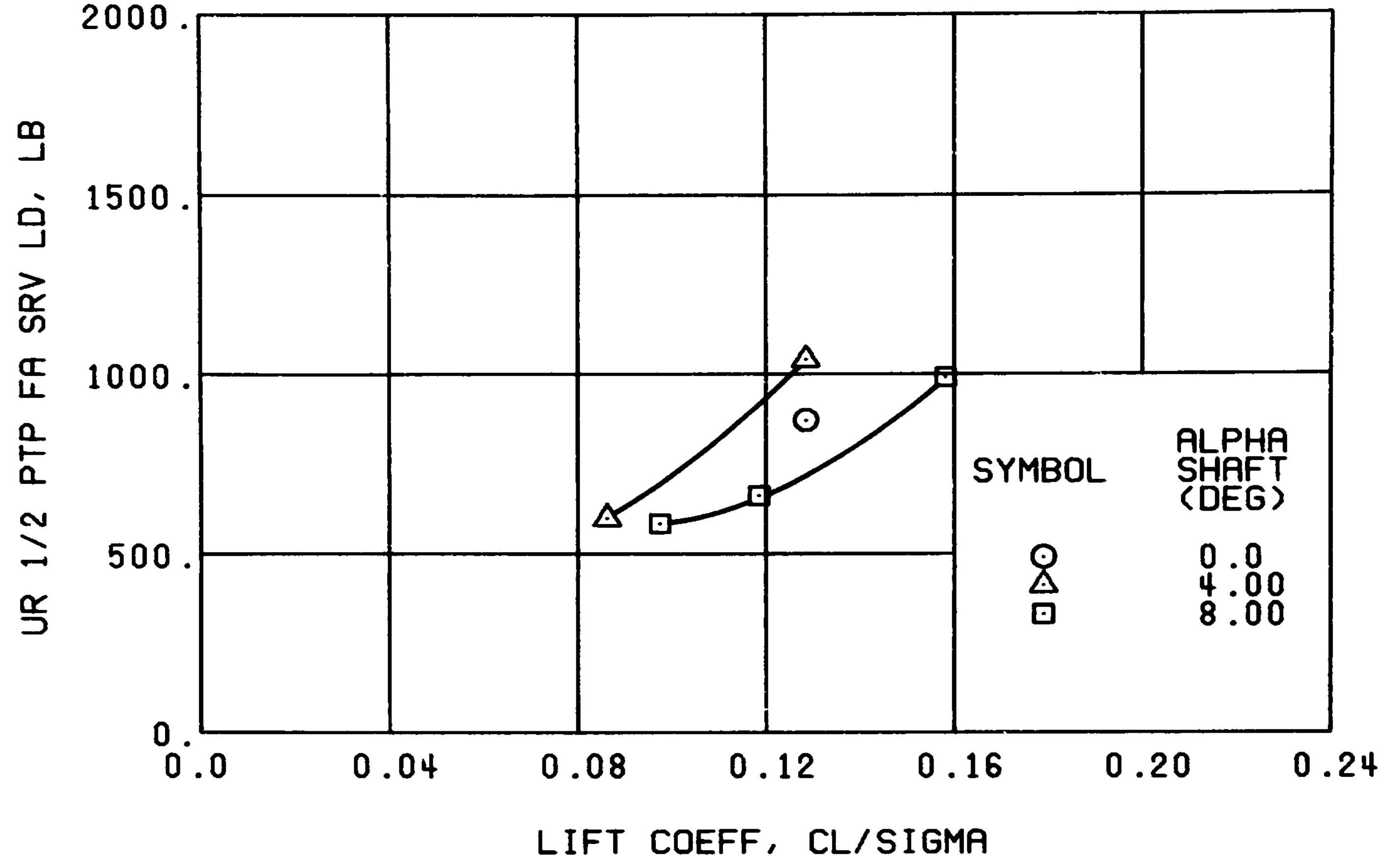

(r) GAGE 24

Figure 44. Continued.
$\mu = 0.35$ $B'_{1s} = 0$ Deg

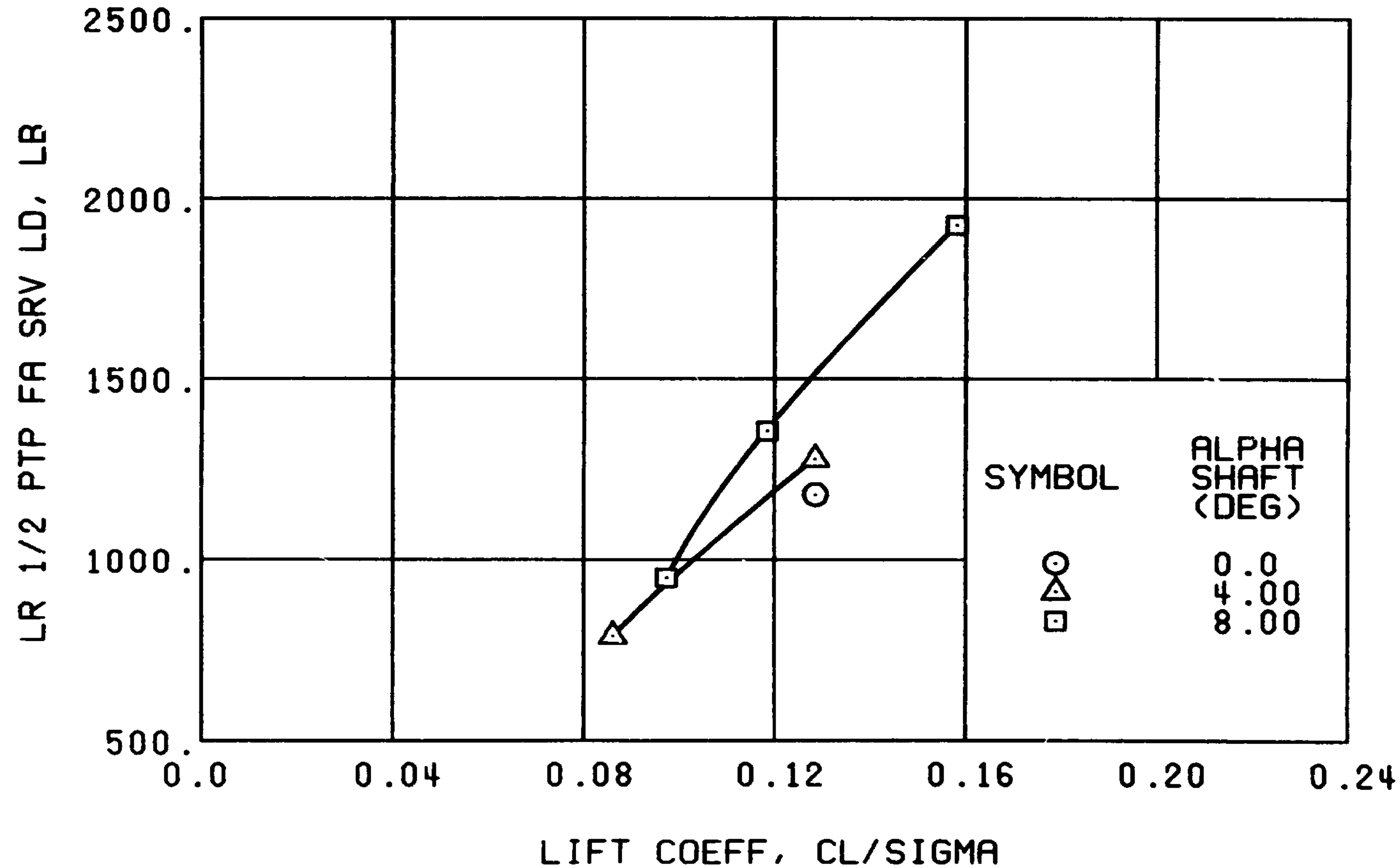

(s) GAGE 27

Figure 44. Continued.
$\mu = 0.35$ $B'_{1s} = 0$ Deg

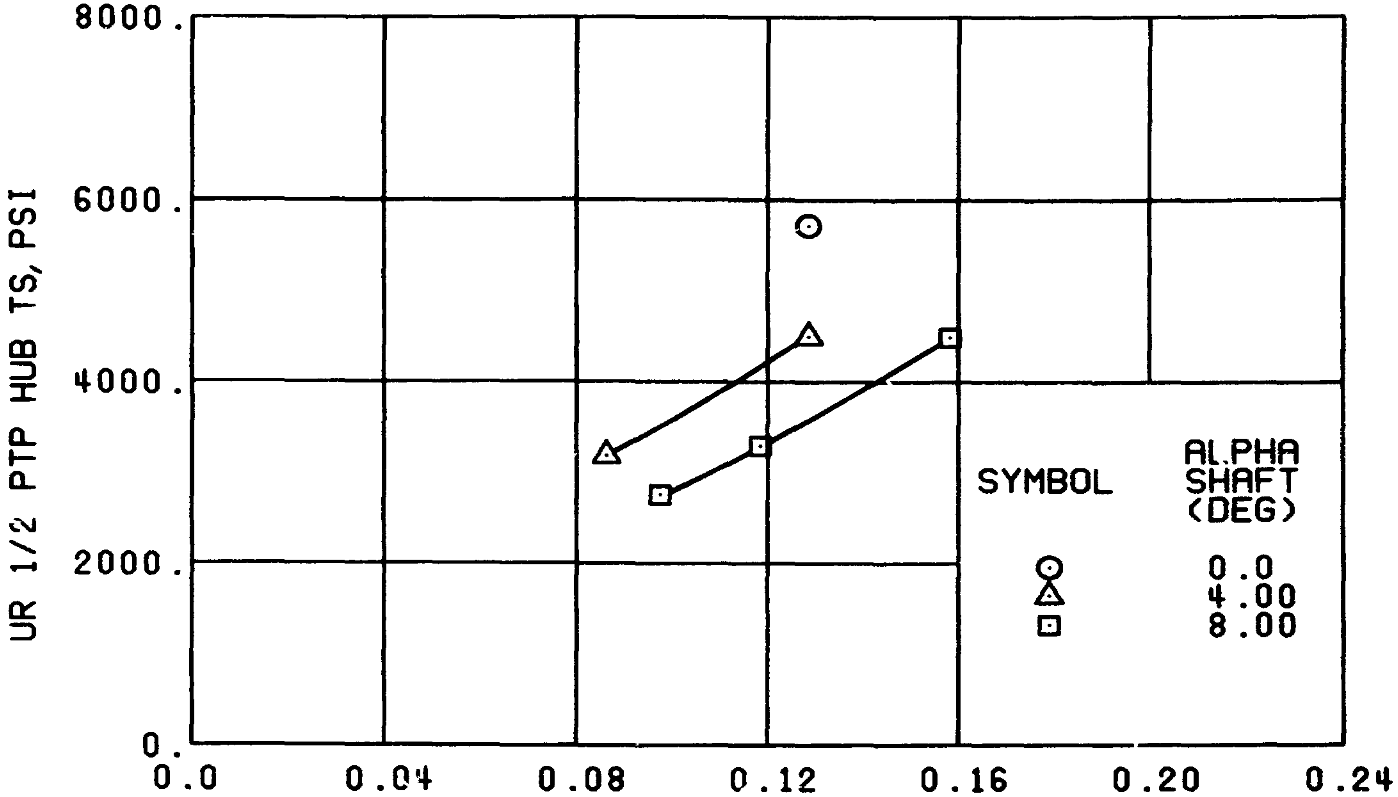

(†) GAGE 65

Figure 44. Continued.
$\mu = 0.35$ $B'_{1s} = 0$ Deg

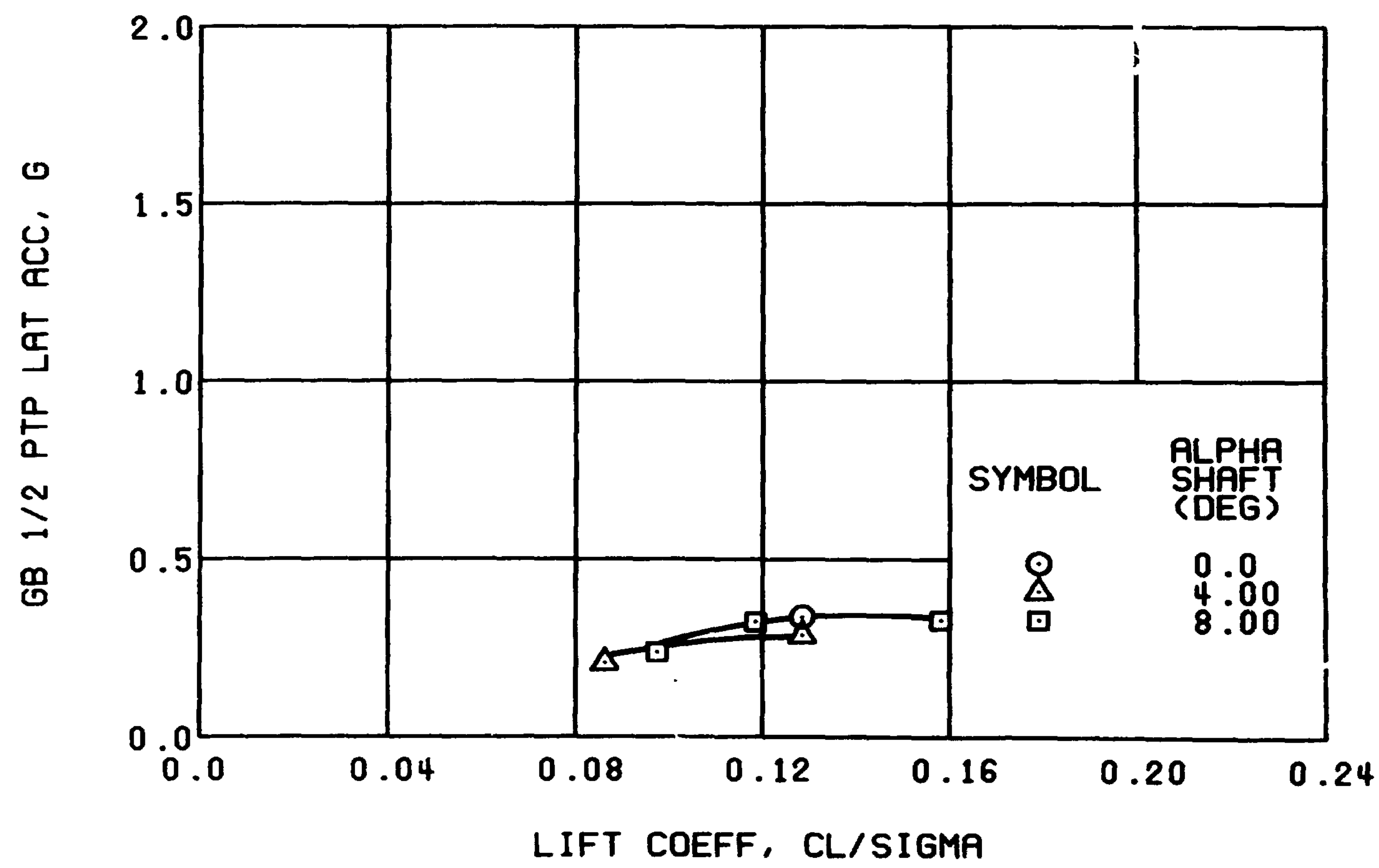

(u) GAGE 15 STA 76, BL 30

Figure 44. Continued.
μ = 0.35 B'_{1s} = 0 Deg

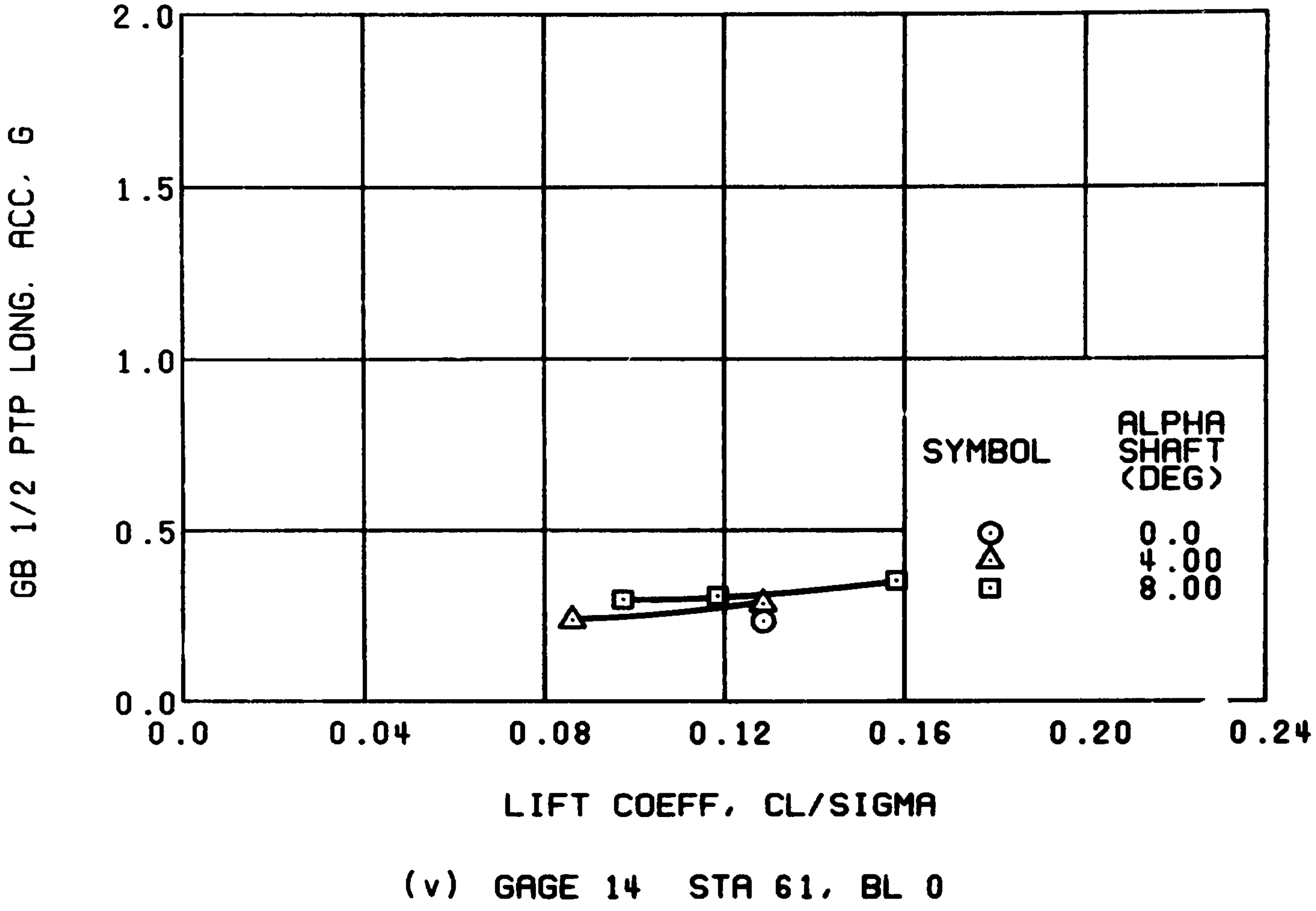

Figure 44. Continued.
$\mu = 0.35$ $B'_{1s} = 0$ Deg

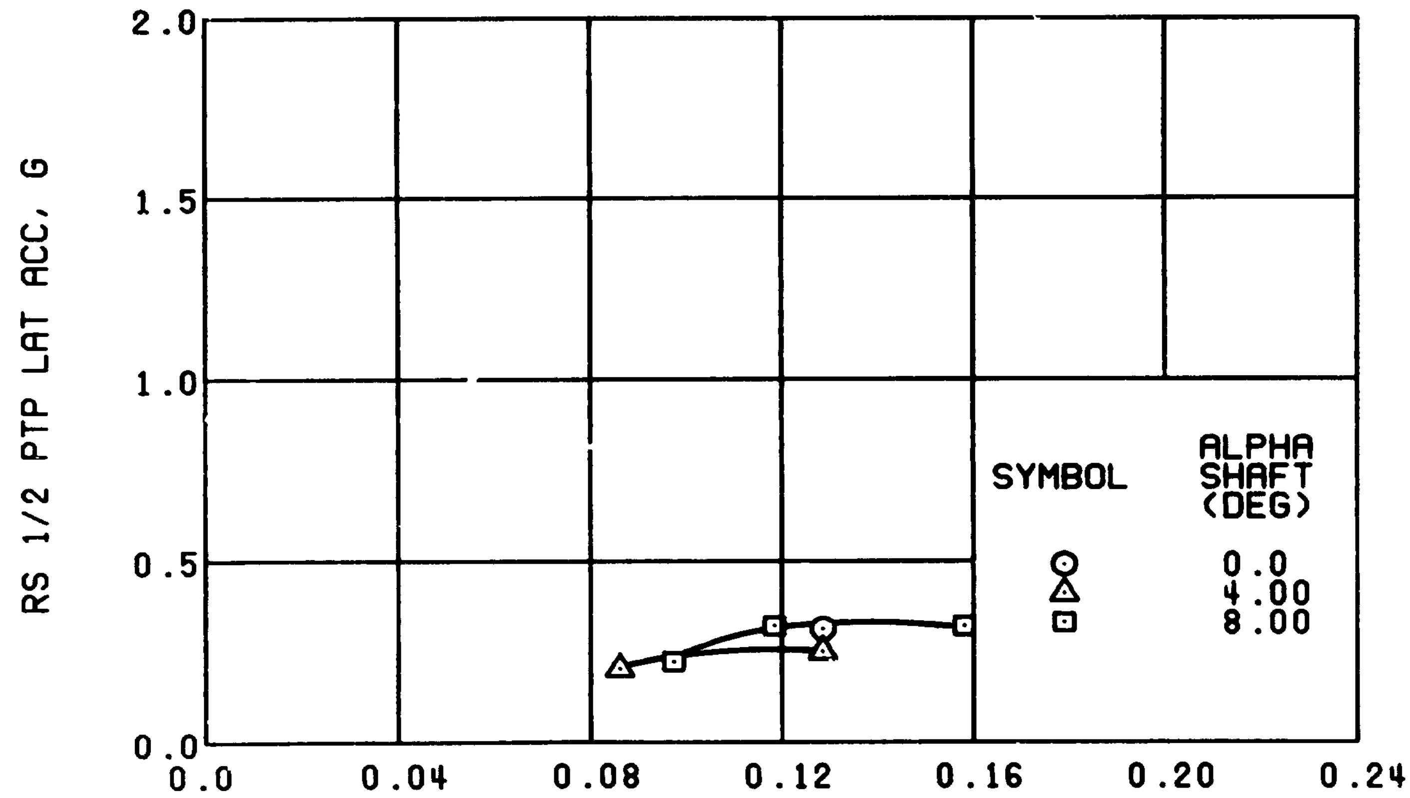

(w) GAGE 16 ROVER 3

Figure 44. Continued.
$\mu = 0.35 \quad B'_{1s} = 0 \text{ Deg}$

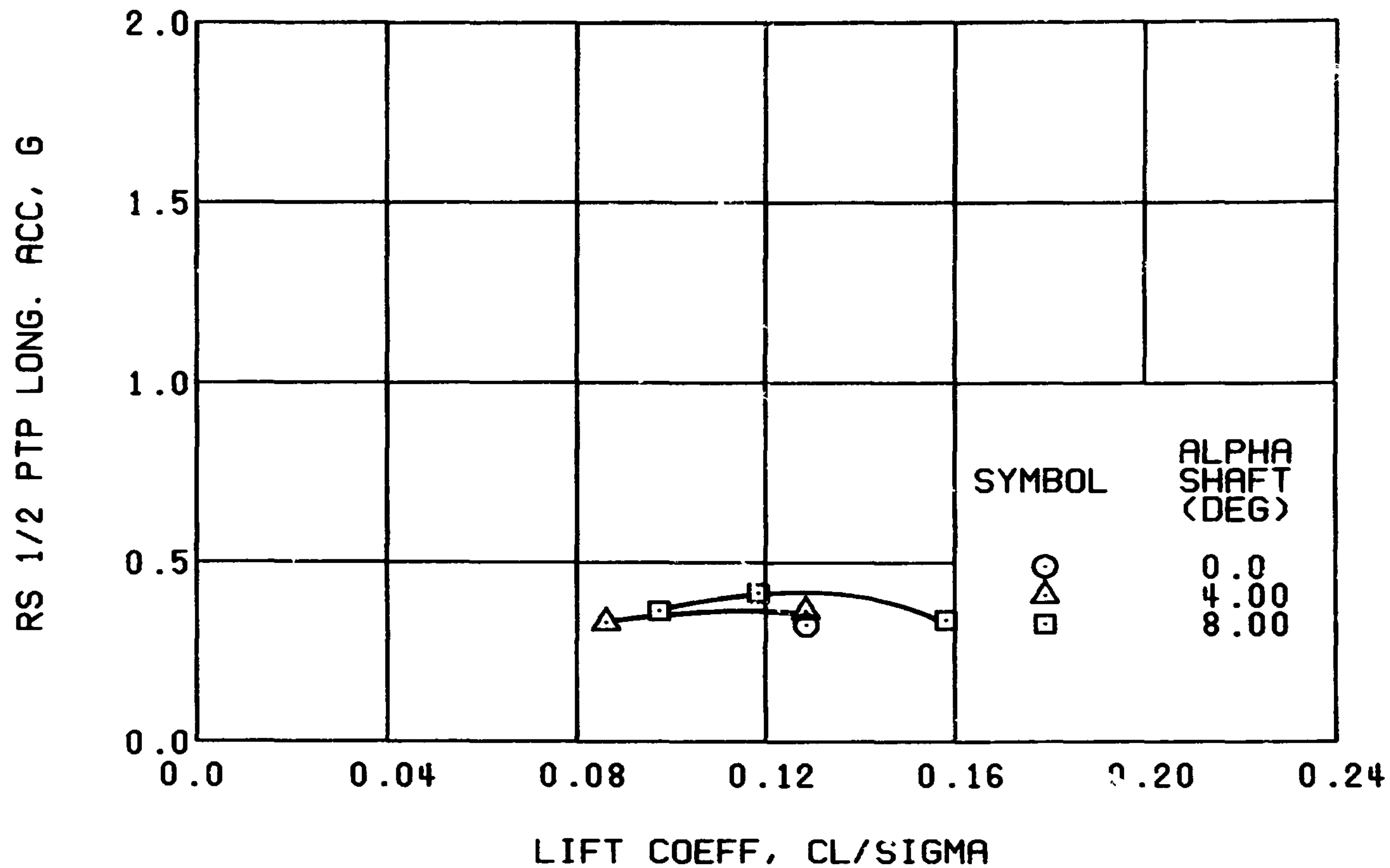

(x) GAGE 17 ROVER 4

Figure 44. Concluded.
$\mu = 0.35$ $B'_{1s} = 0$ Deg

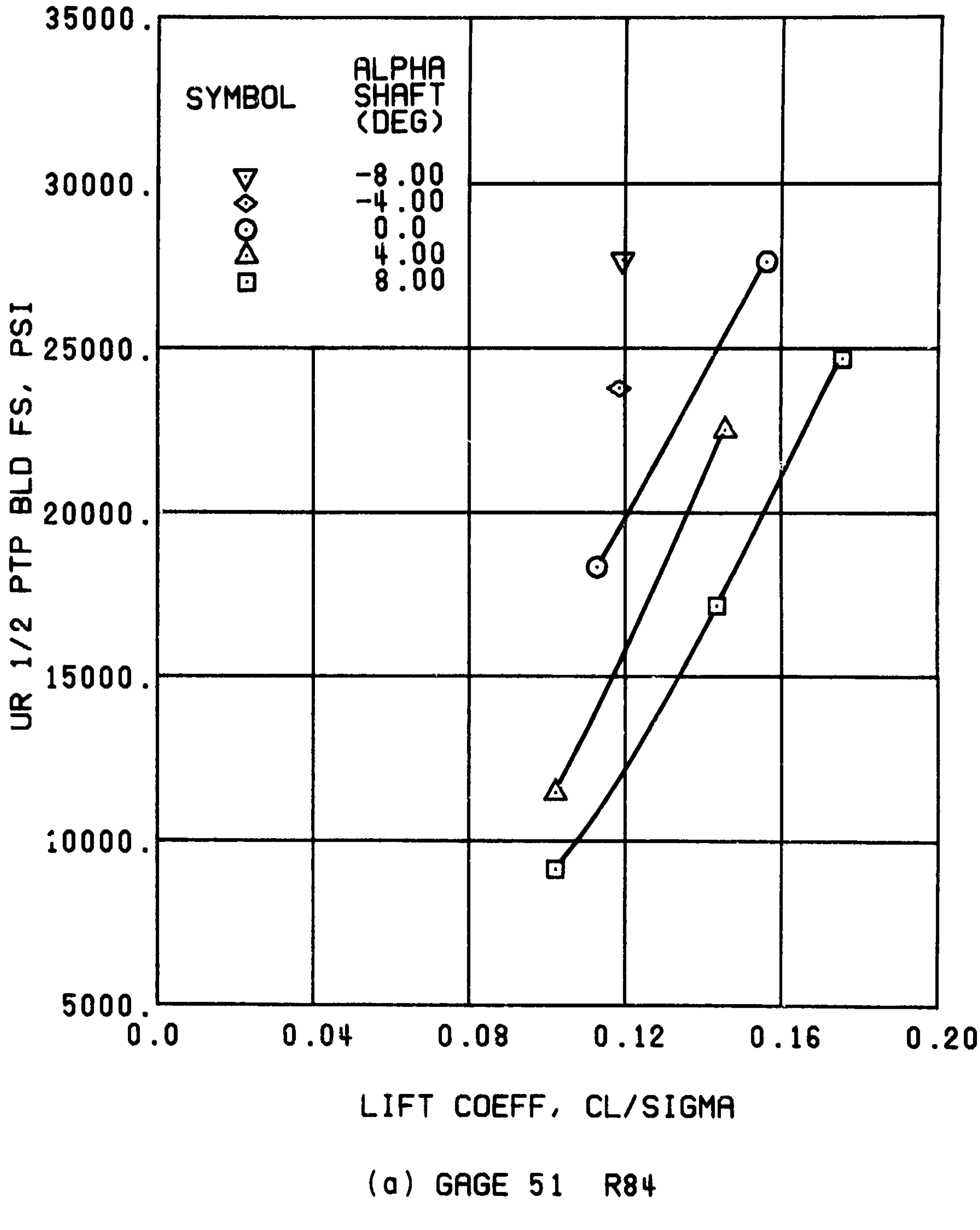

Figure 45. Stress, Load, and Vibration Data at an Aavance Ratio of 0.35 With the Lateral Displacement Control (B'_{1s}) Set at 2 Degrees.

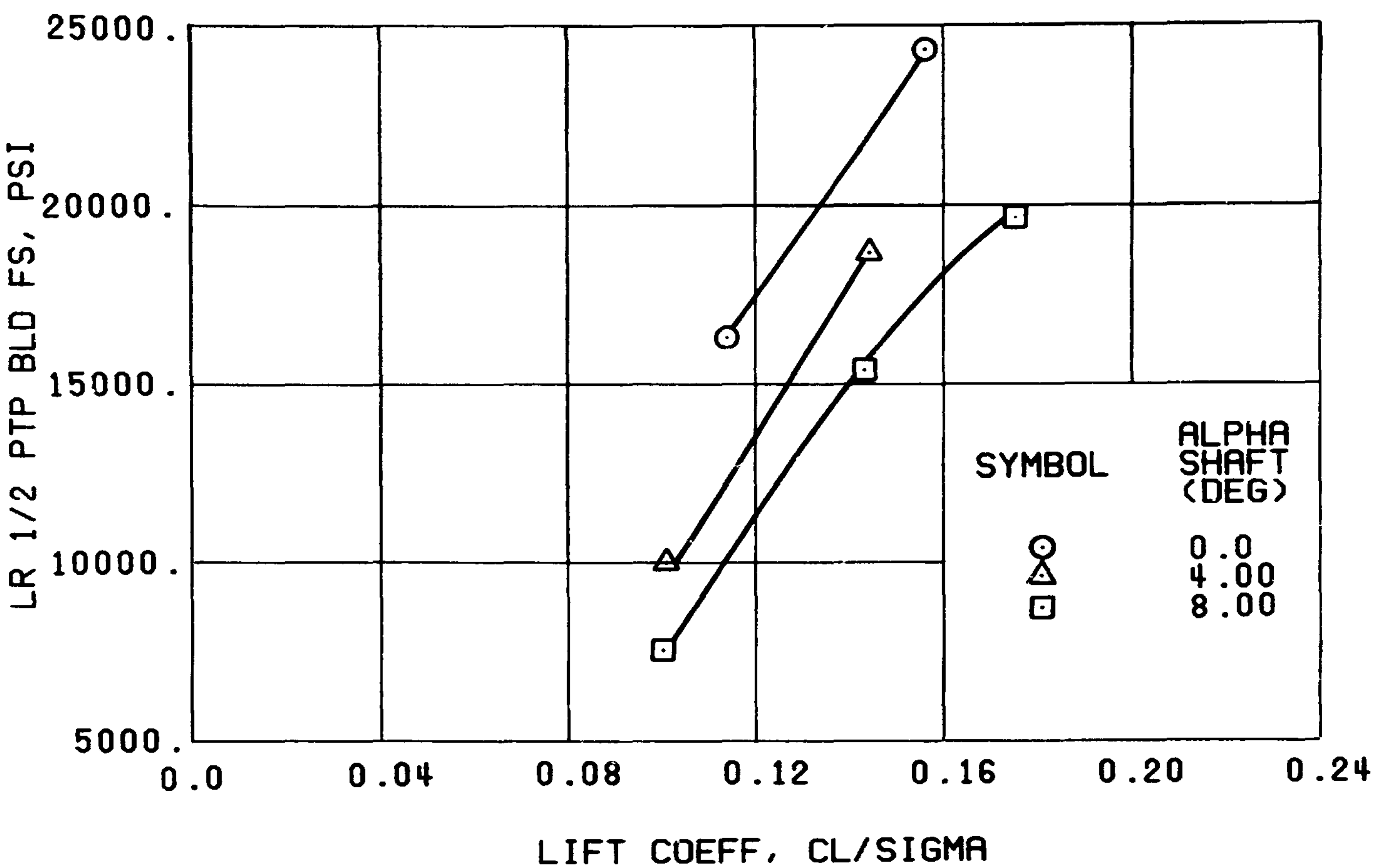

(b) GAGE 1 R84

Figure 45. Continued.
$\mu = 0.35$ $B'_{1s} = 2$ Deg

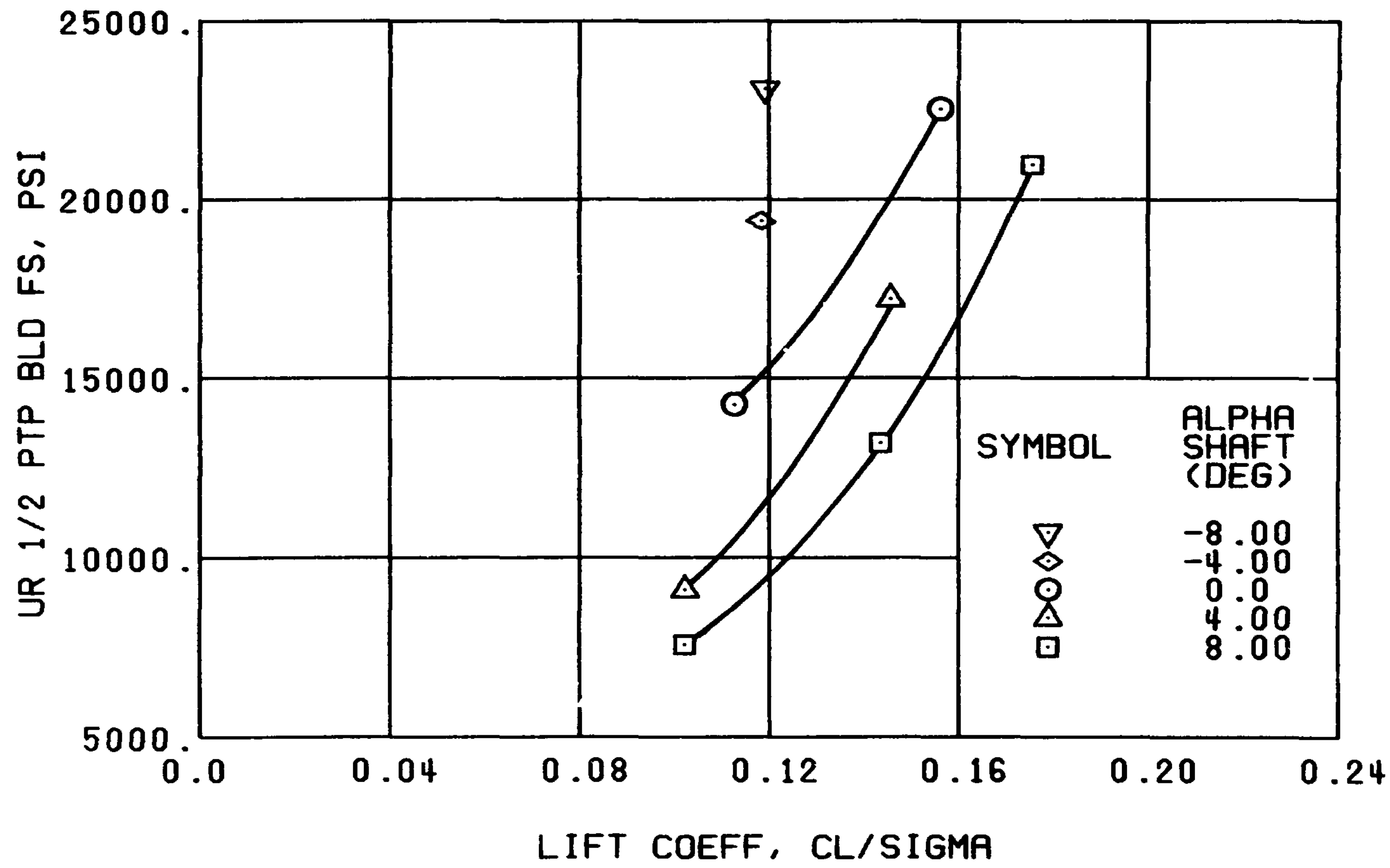

(c) GAGE 52 R108

Figure 45. Continued.
$\mu = 0.35$ $B'_{1s} = 2$ Deg

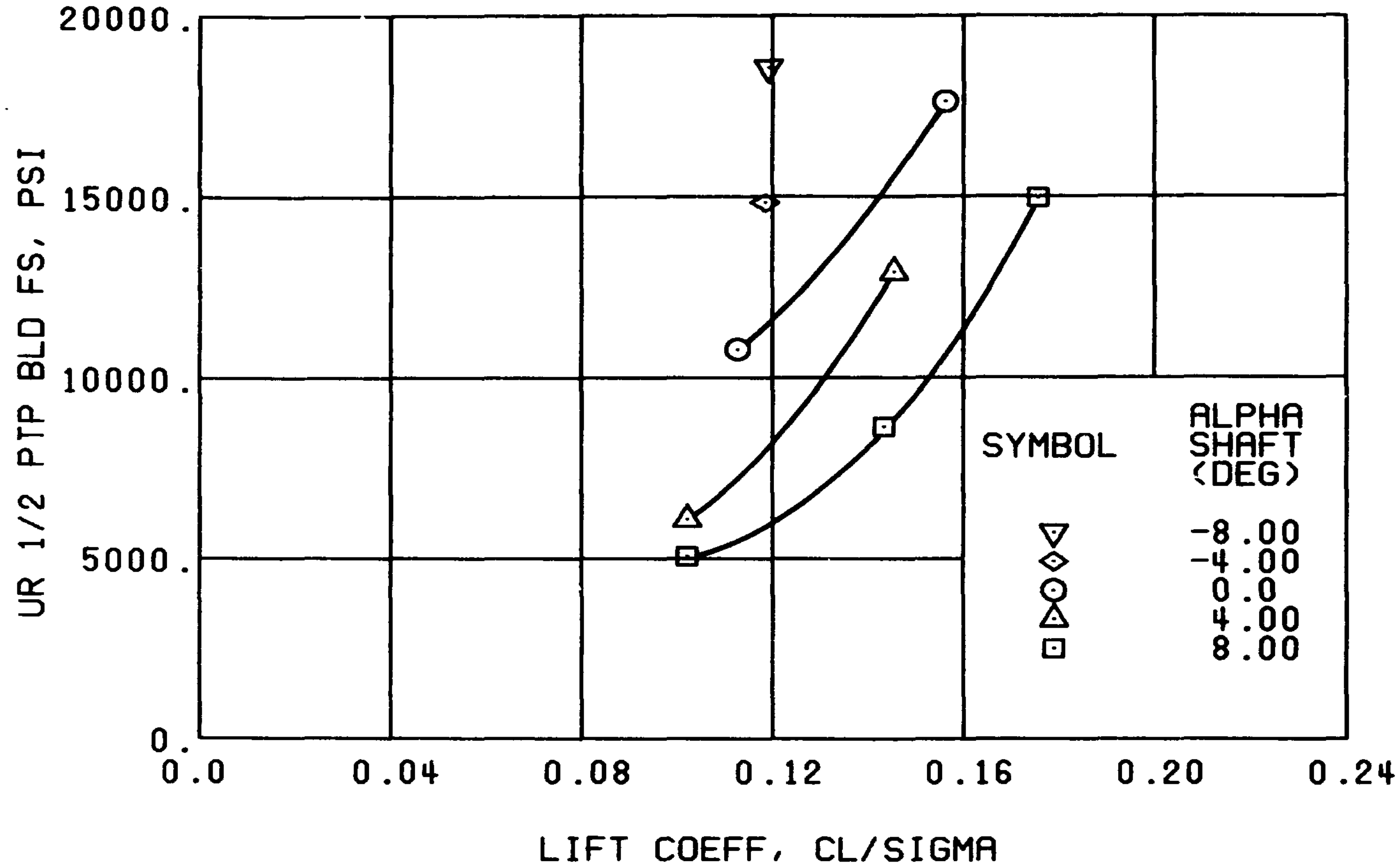

(d) GAGE 53 R132

Figure 45. Continued.
$\mu = 0.35$ $B'_{1s} = 2$ Deg

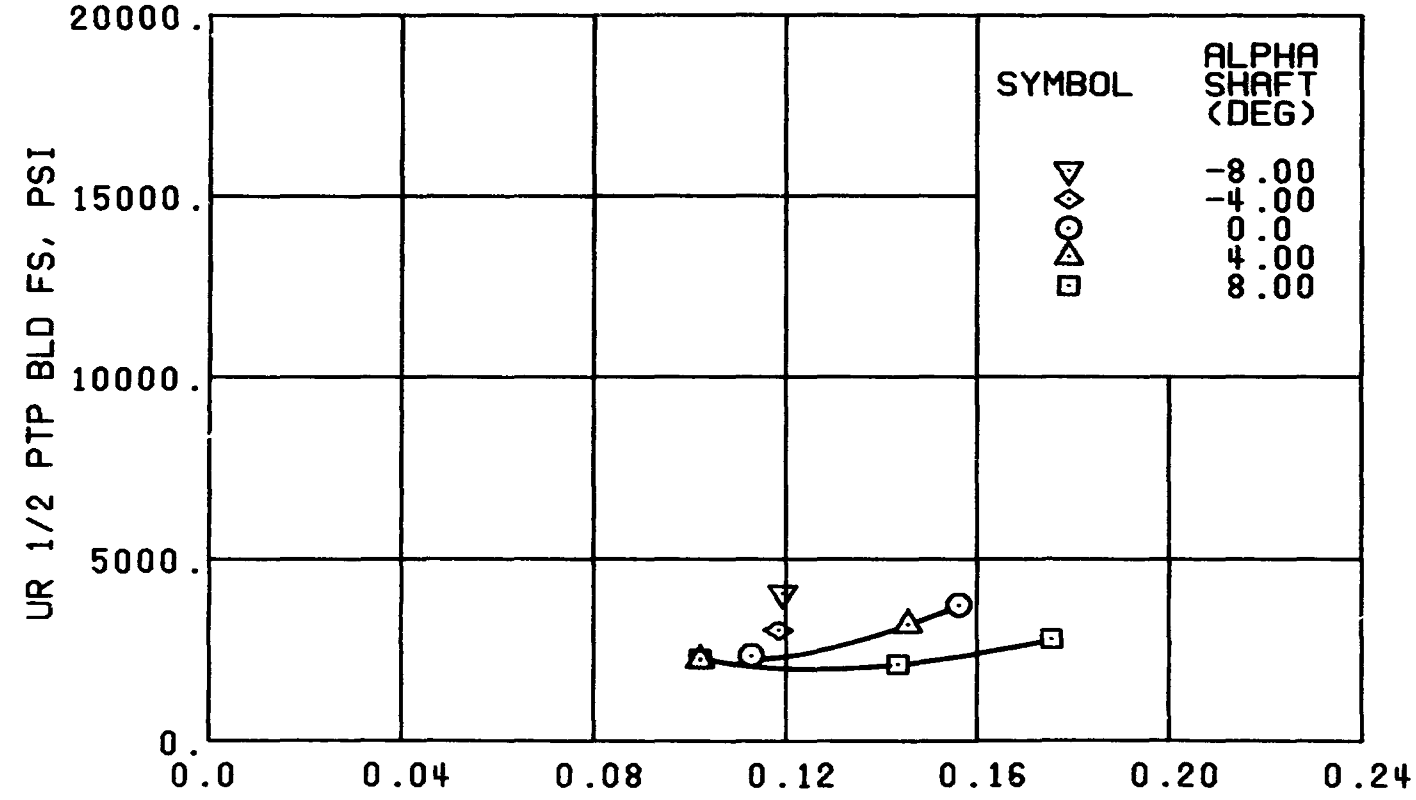

(f) GAGE 55 R204

Figure 45. Continued.
$\mu = 0.35$ $B'_{1s} = 2$ Deg

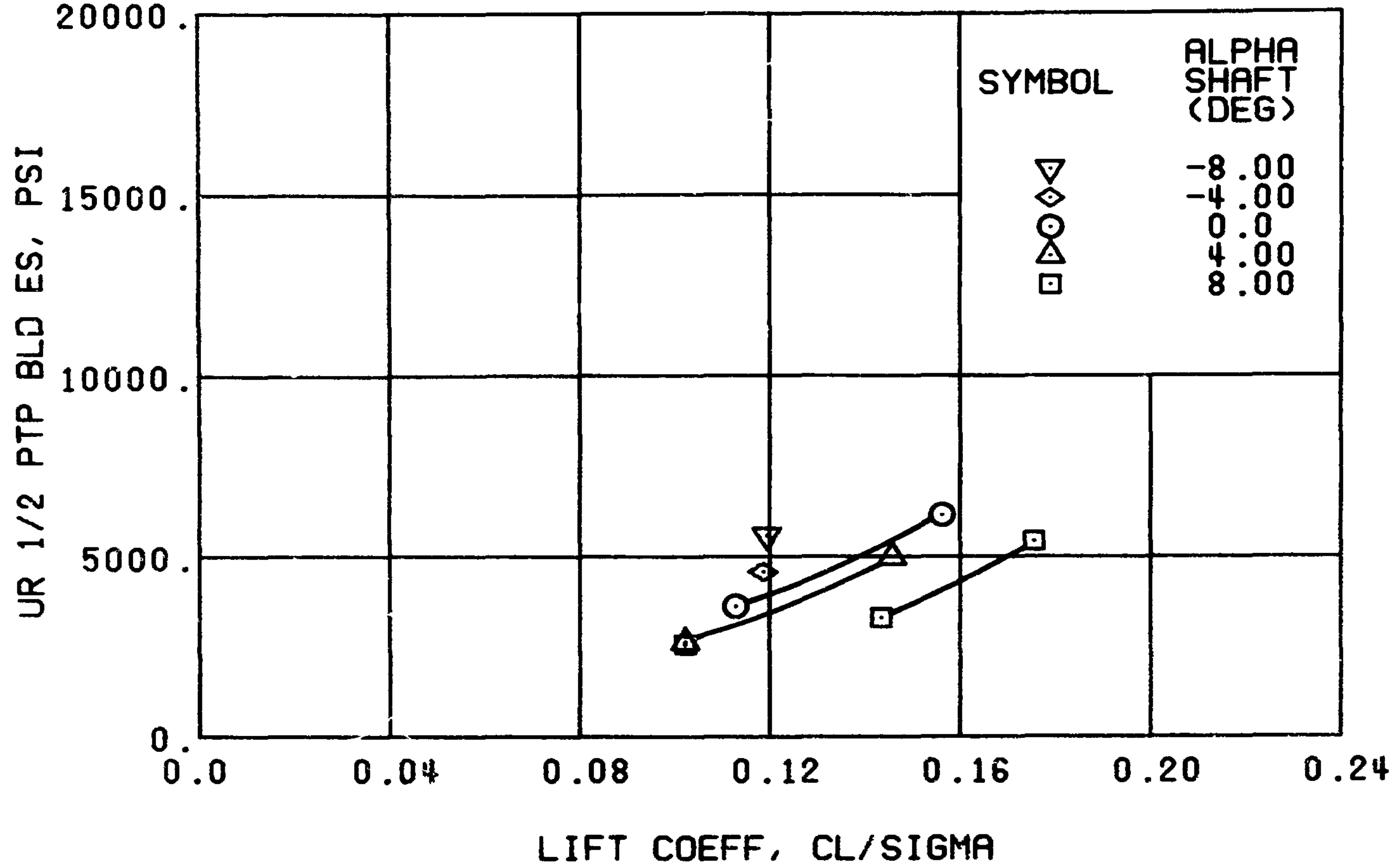

(h) GAGE 40 R84

Figure 45. Continued.
$\mu = 0.35 \quad B'_{1s} = 2$ Deg

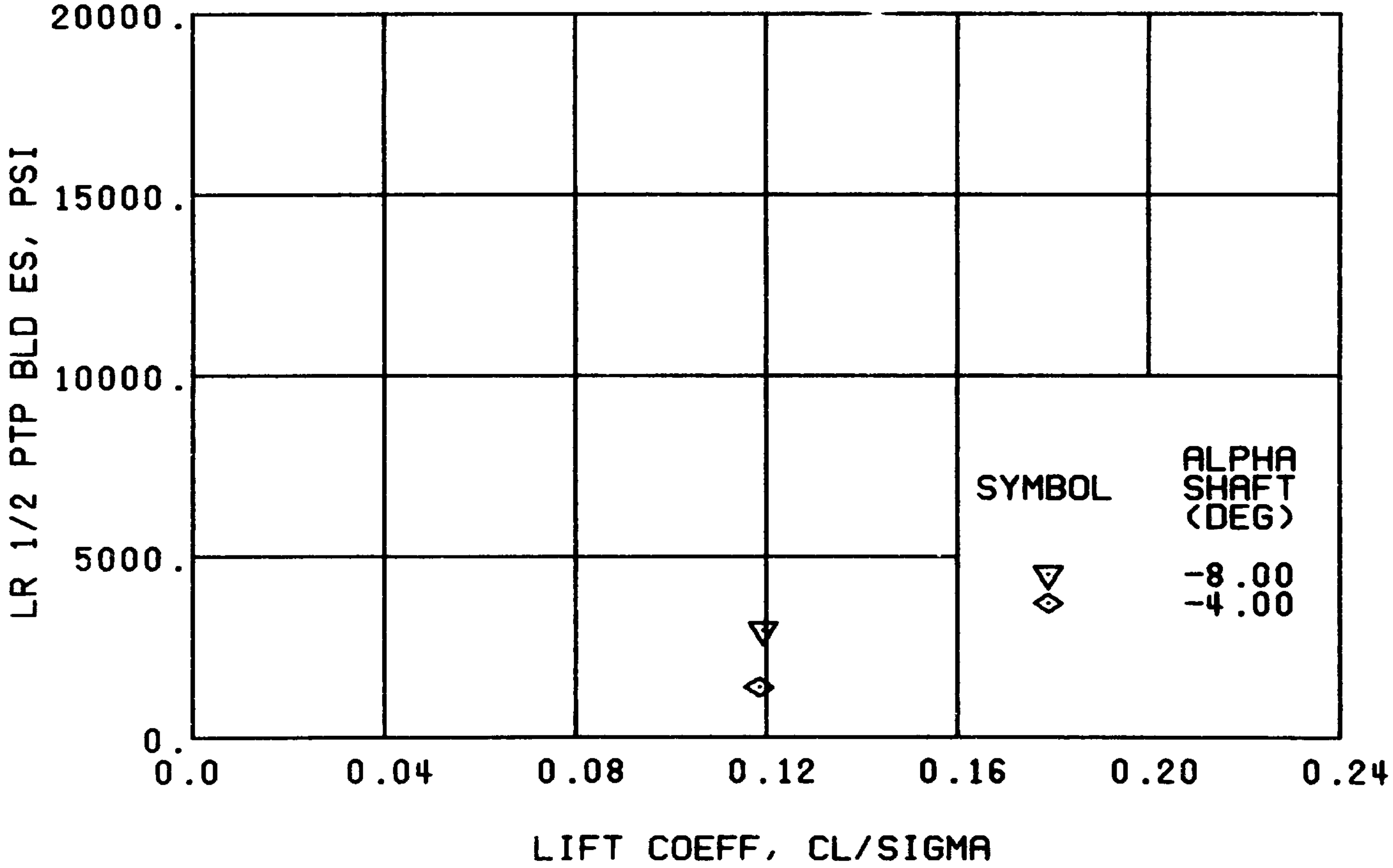

(i) GAGE 2 R84

Figure 45. Continued.
$\mu = 0.35 \quad B'_{1s} = 2$ Deg

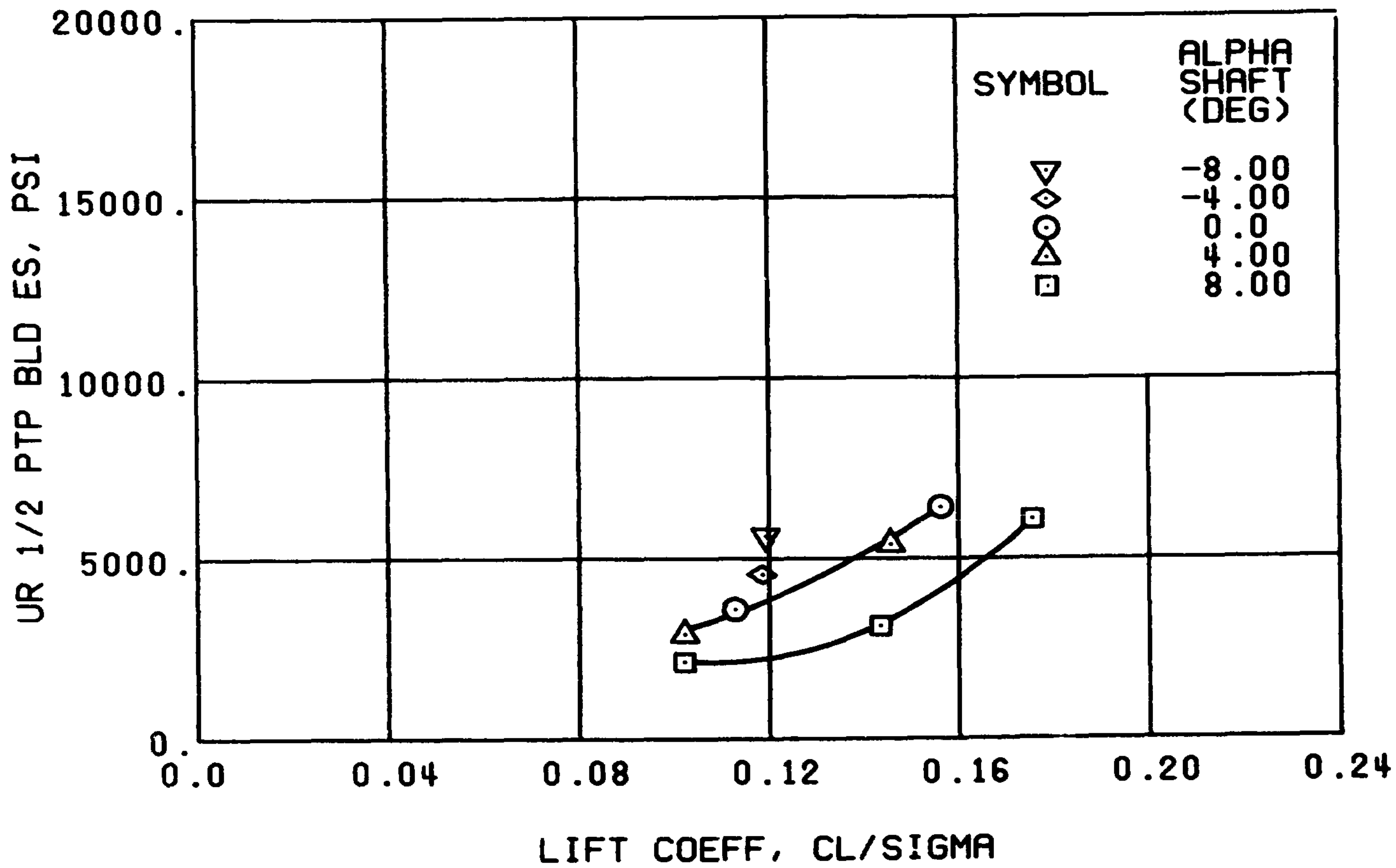

(j) GAGE 42 R132

Figure 45. Continued.
$\mu = 0.35$ $B_{1s}' = 2$ Deg

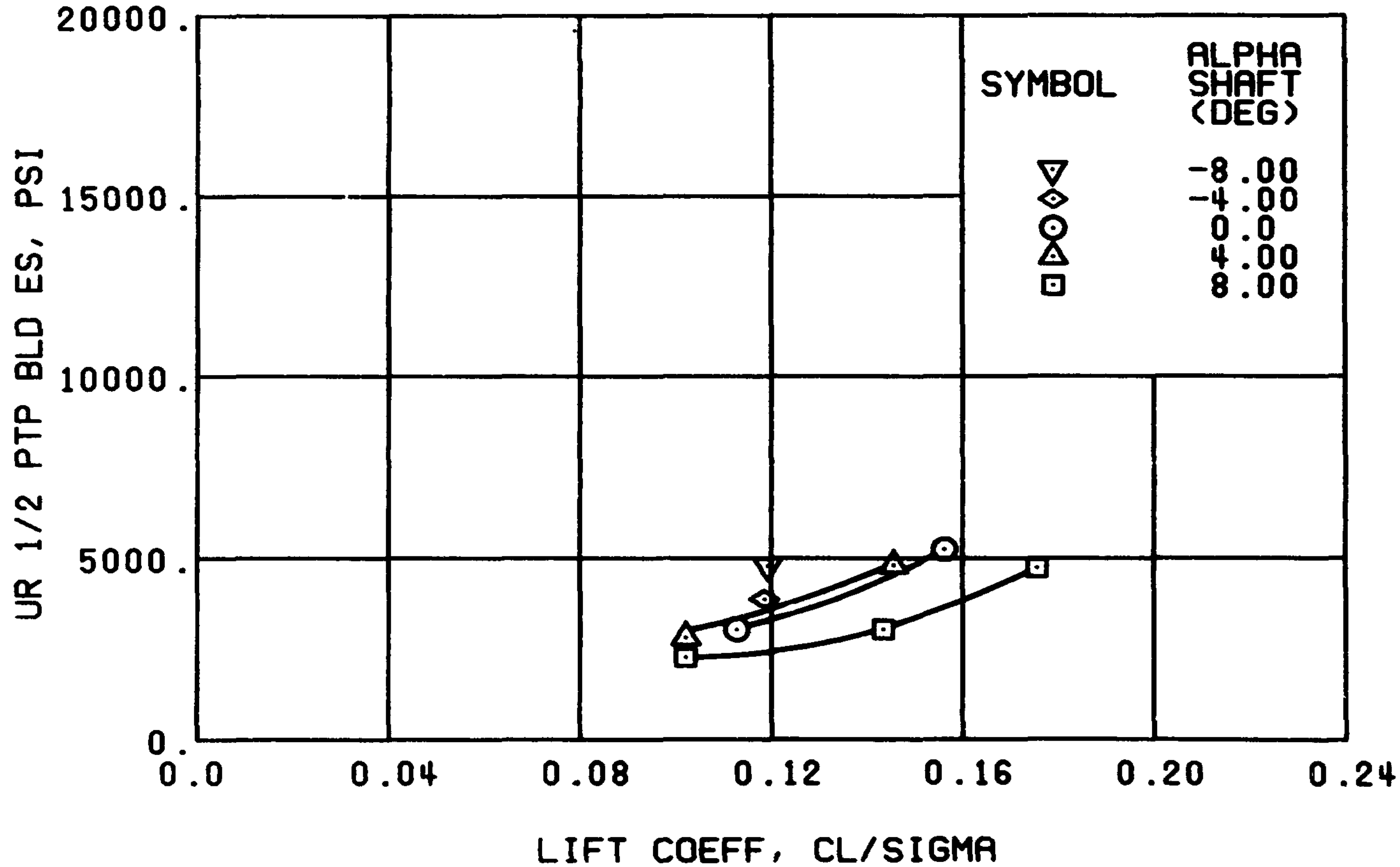

(k) GAGE 43 R168

Figure 45. Continued.
μ = 0.35 B'_{1s} = 2 Deg

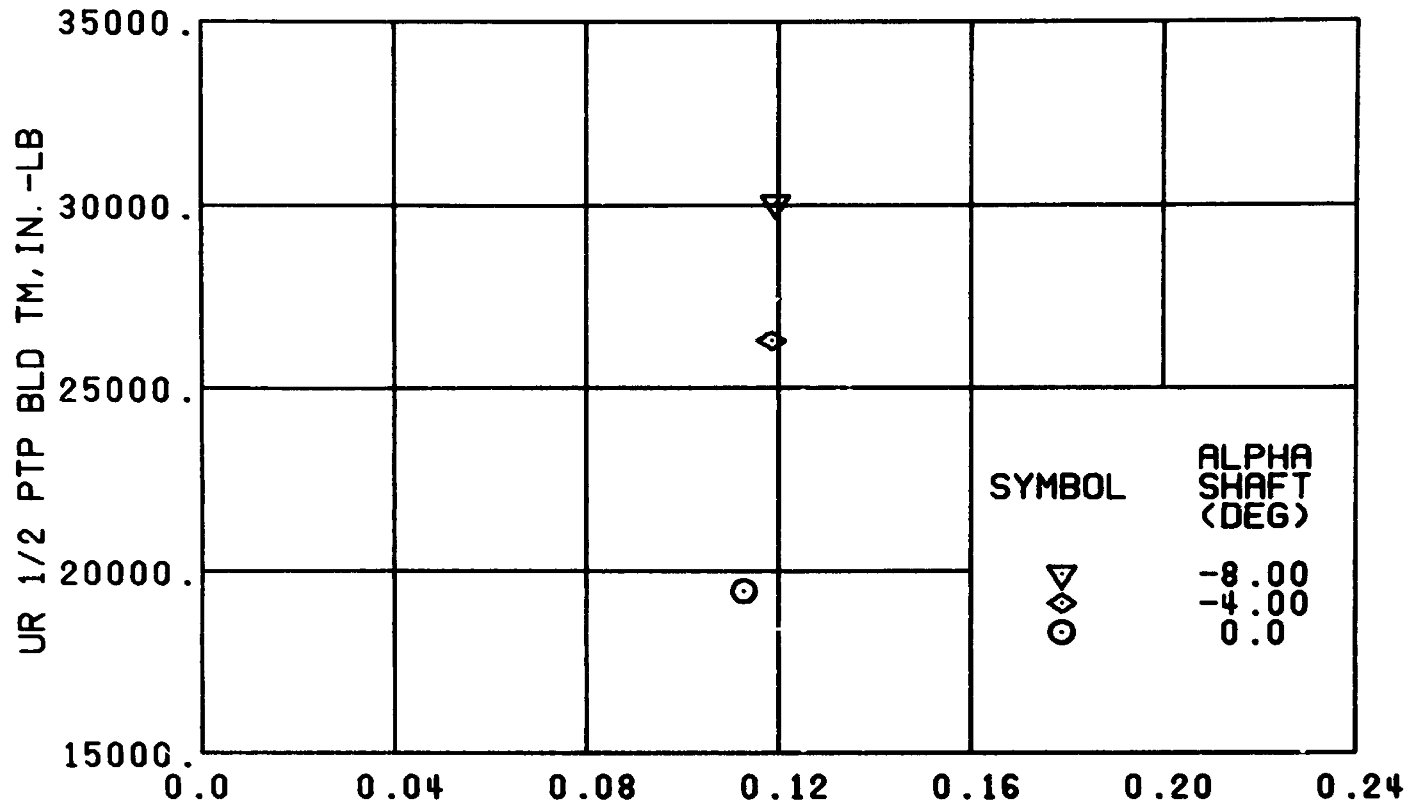

(I) GAGE 45 R82

Figure 45. Continued.
$\mu = 0.35$ $B'_{1s} = 2$ Deg

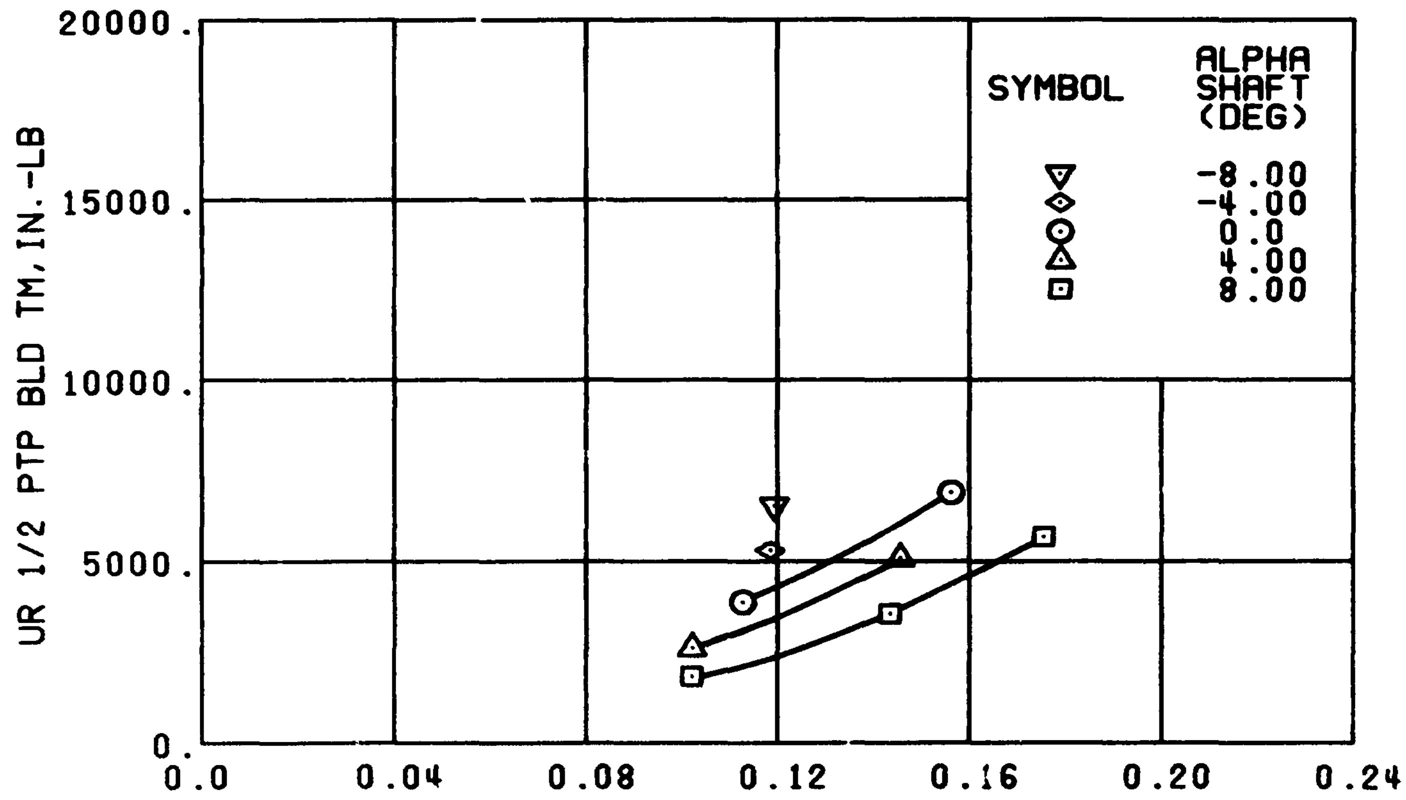

(m) GAGE 46 R130

Figure 45. Continued.
$\mu = 0.35$ $B'_{1s} = 2$ Deg

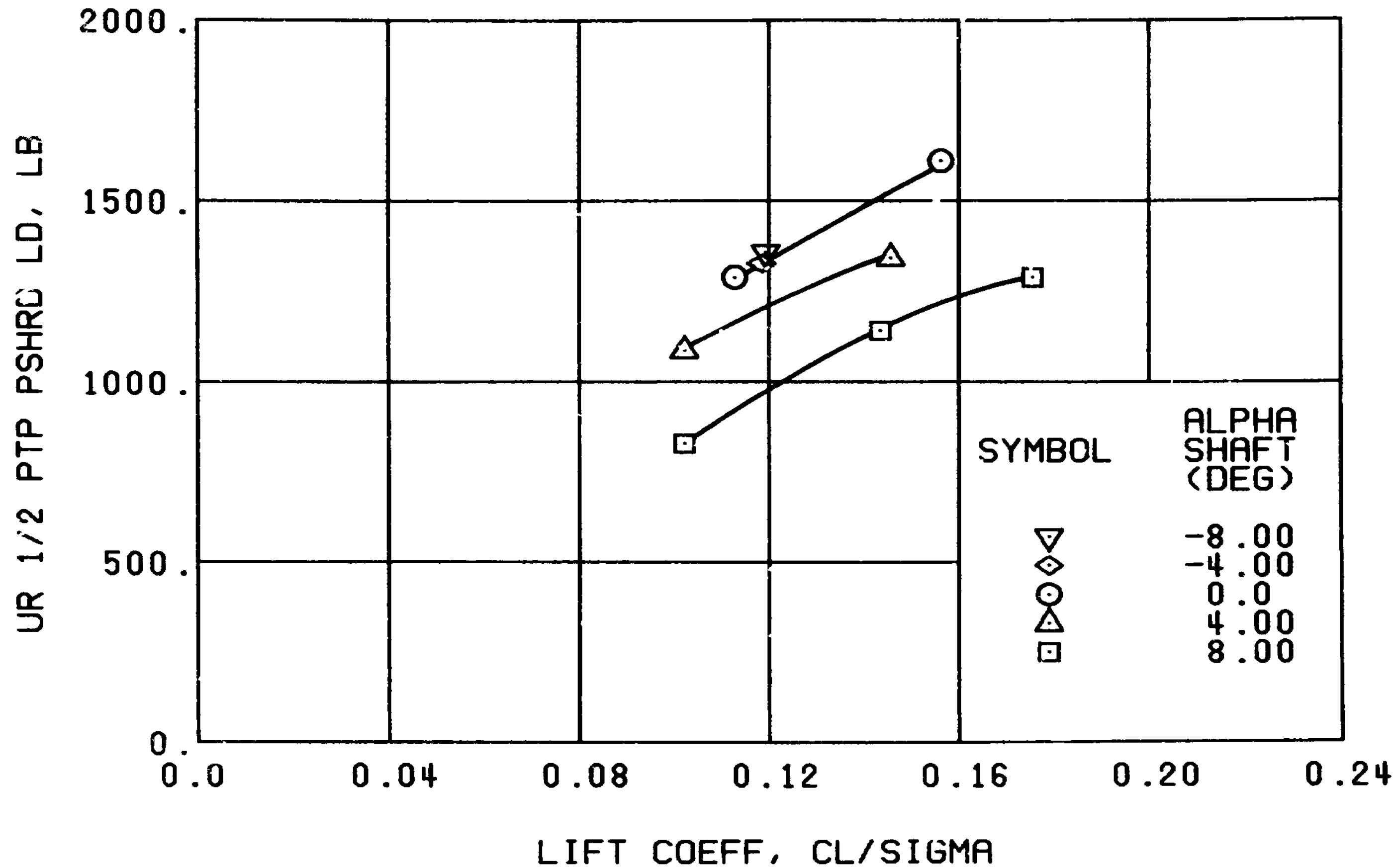

(n) GAGE 37

Figure 45. Continued.
$\mu = 0.35$ $B'_{1s} = 2$ Deg

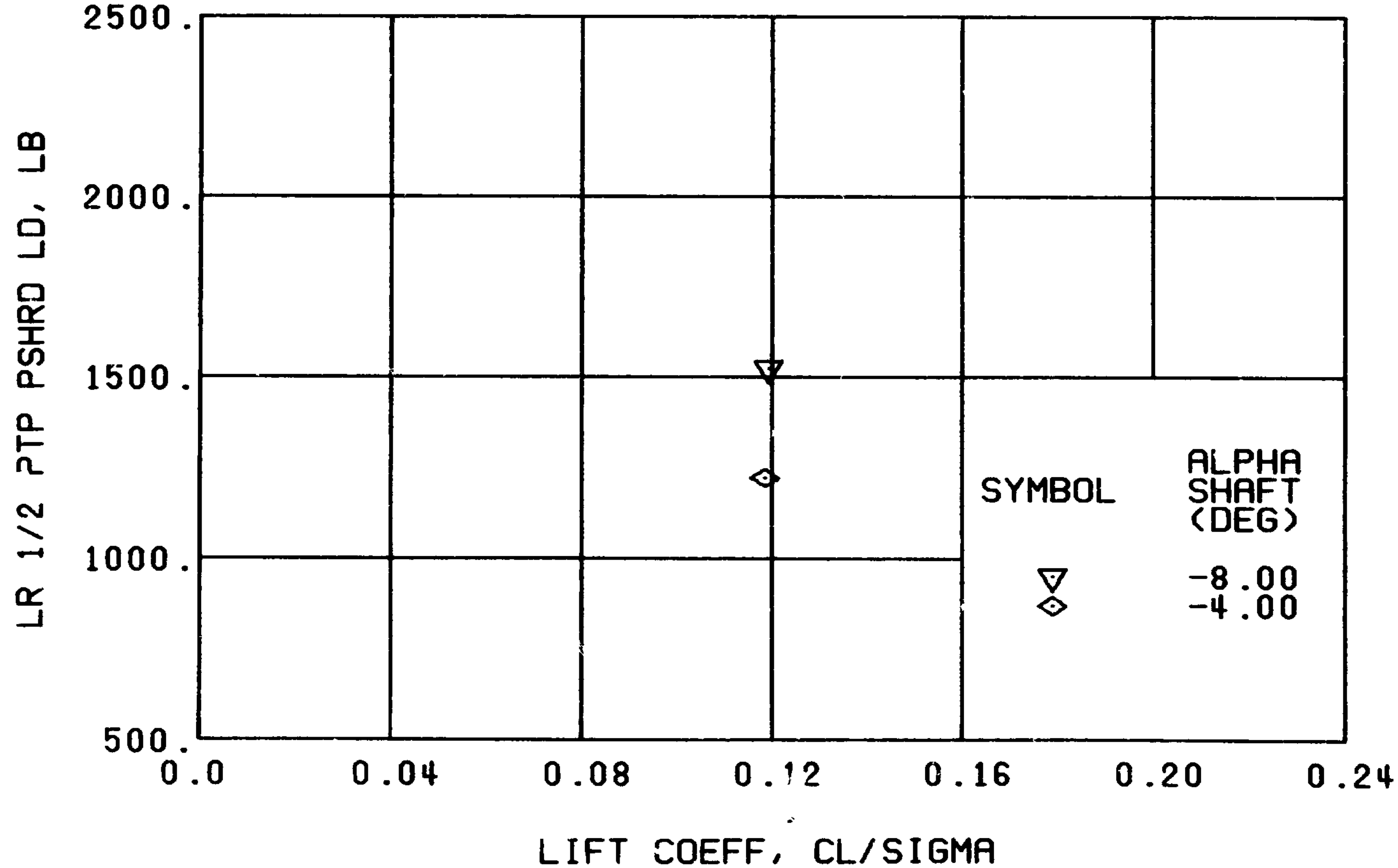

(o) GAGE 34

Figure 45. Continued.
$\mu = 0.35 \quad B'_{1s} = 2$ Deg

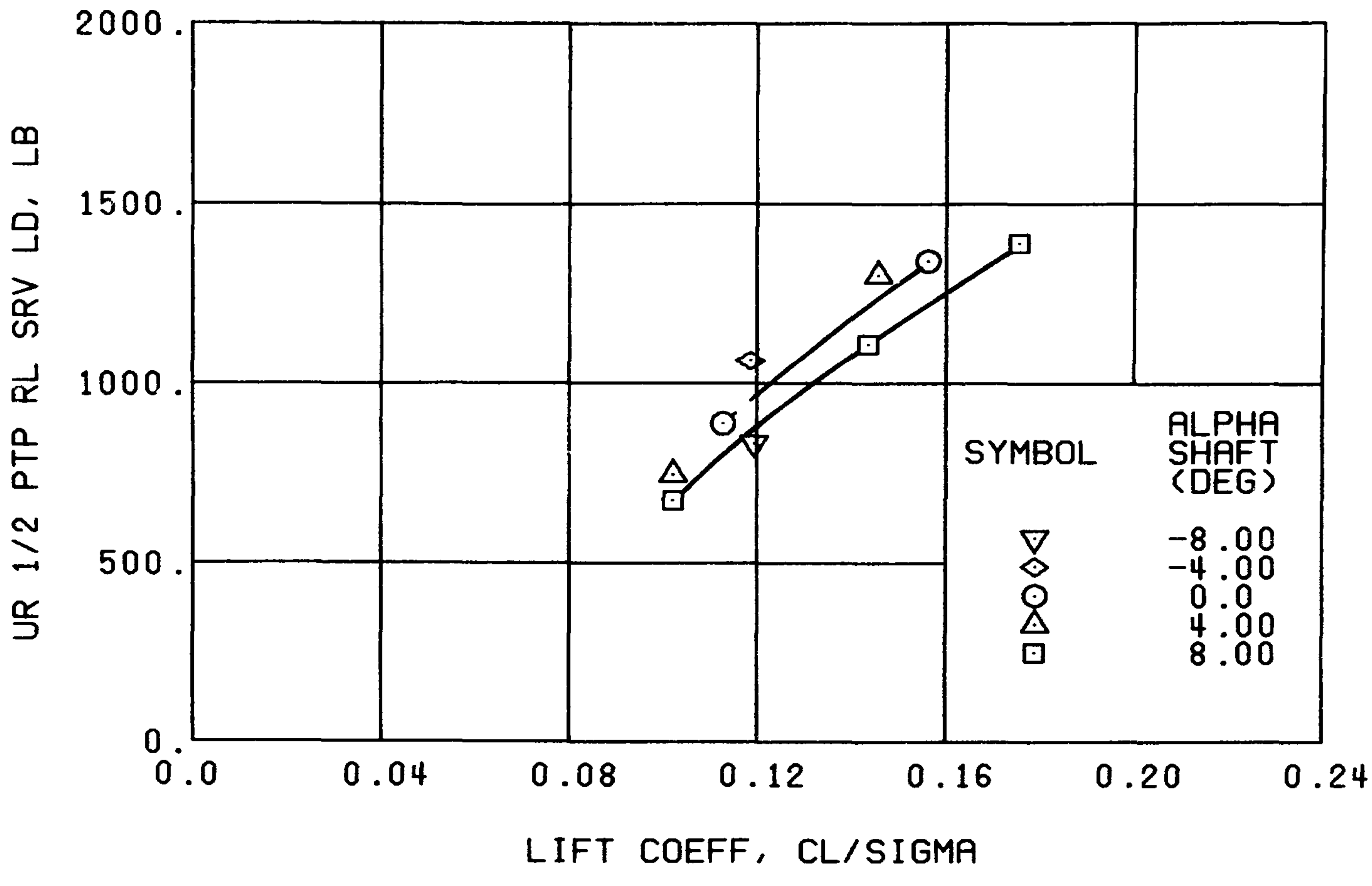

(p) GAGE 22

Figure 45. Continued.
$\mu = 0.35$ $B'_{1s} = 2$ Deg

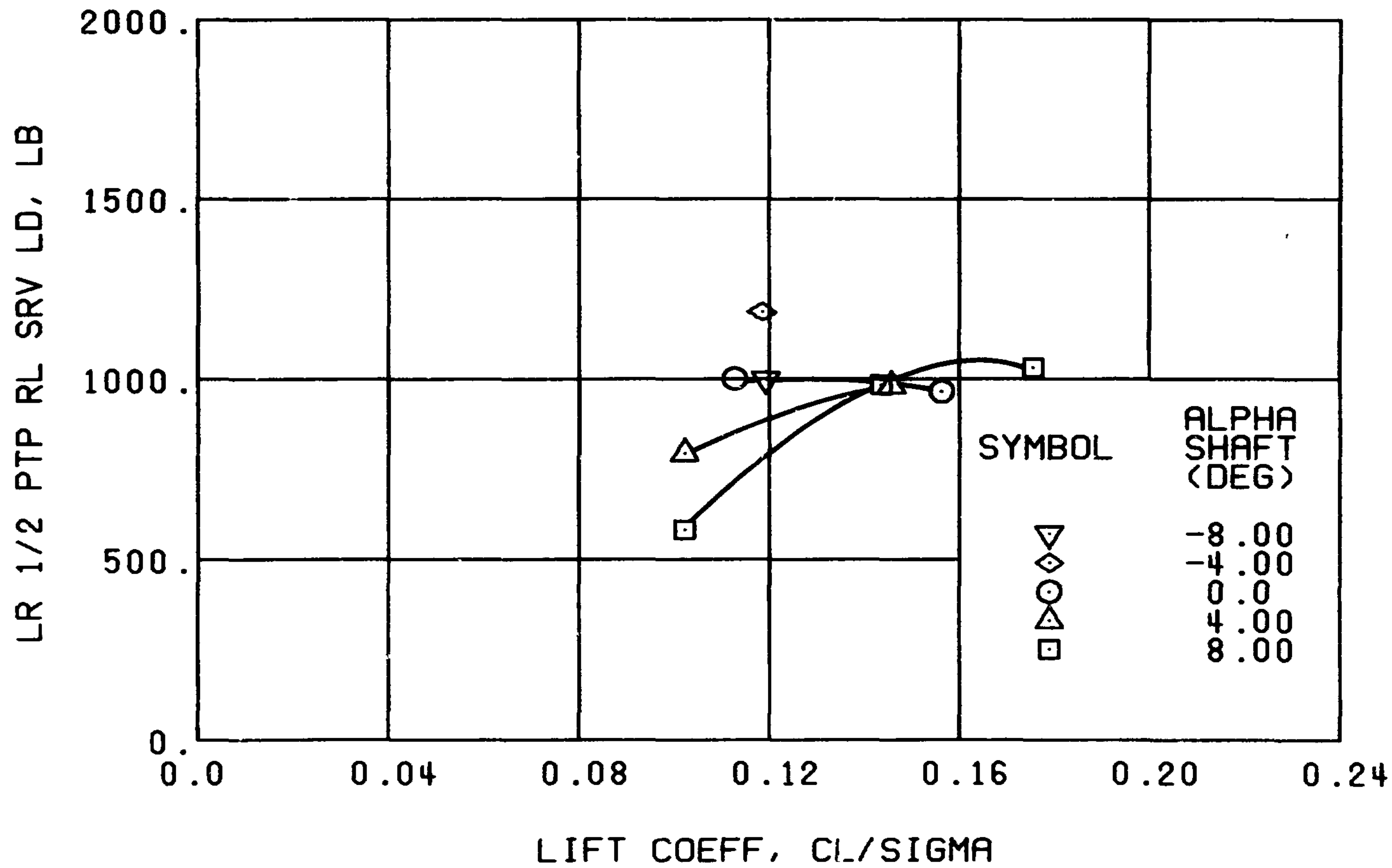

(q) GAGE 25

Figure 45. Continued.
$\mu = 0.35$ $B'_{1s} = 2$ Deg

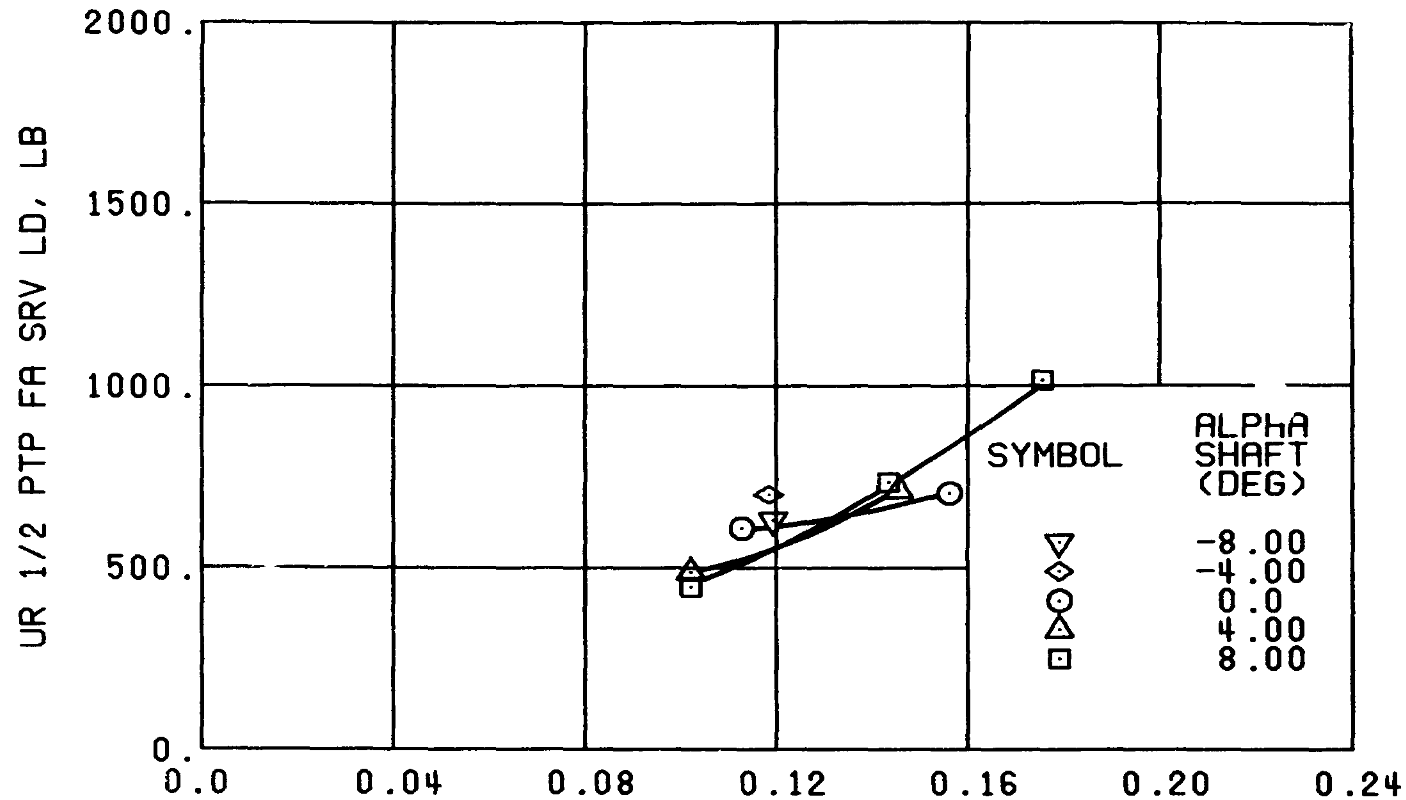

(r) GAGE 24

Figure 45. Continued.
$\mu = 0.35 \quad B'_{1s} = 2$ Deg

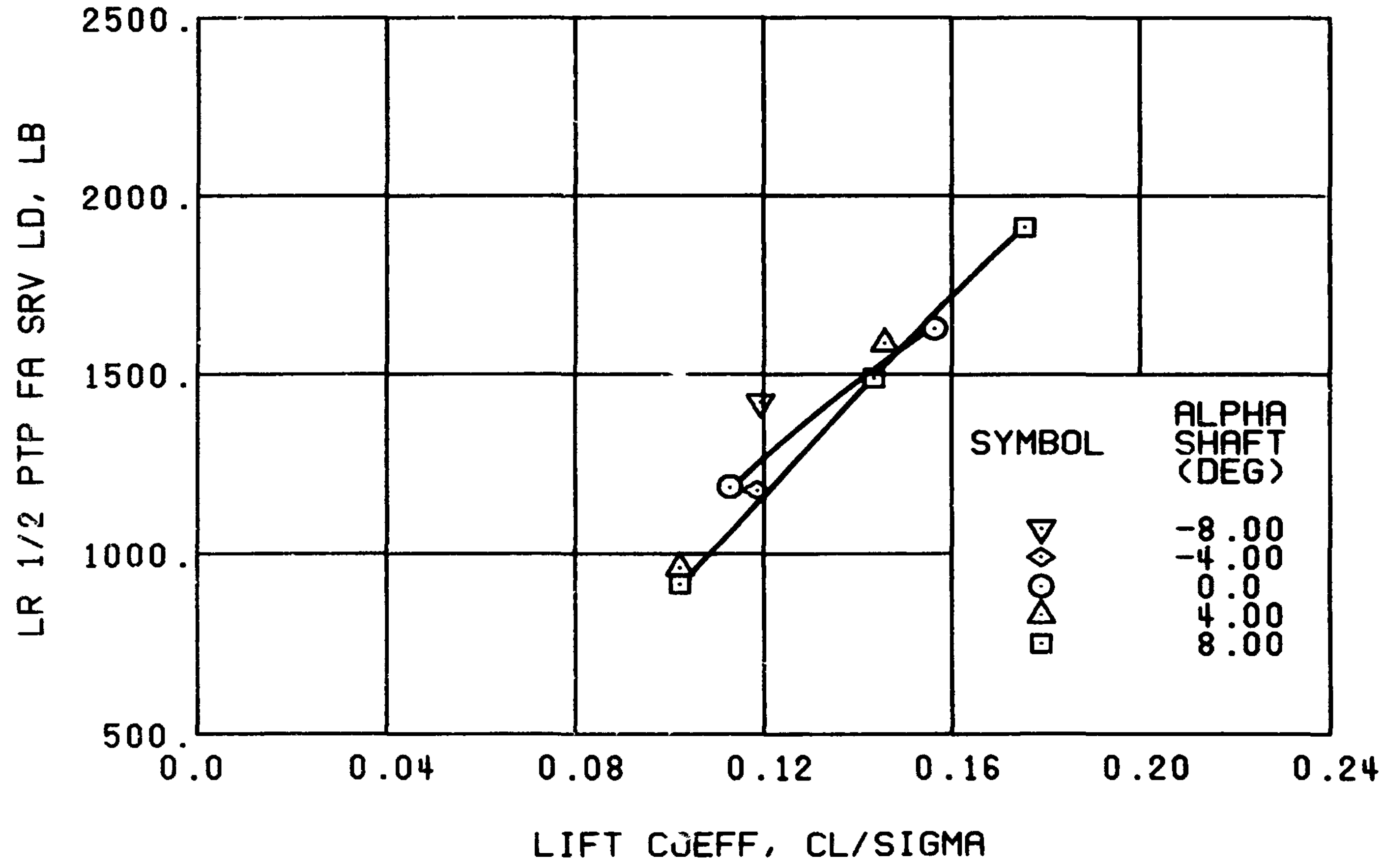

(s) GAGE 27

Figure 45. Continued.
μ = 0.35 B'_{1s} = 2 Deg

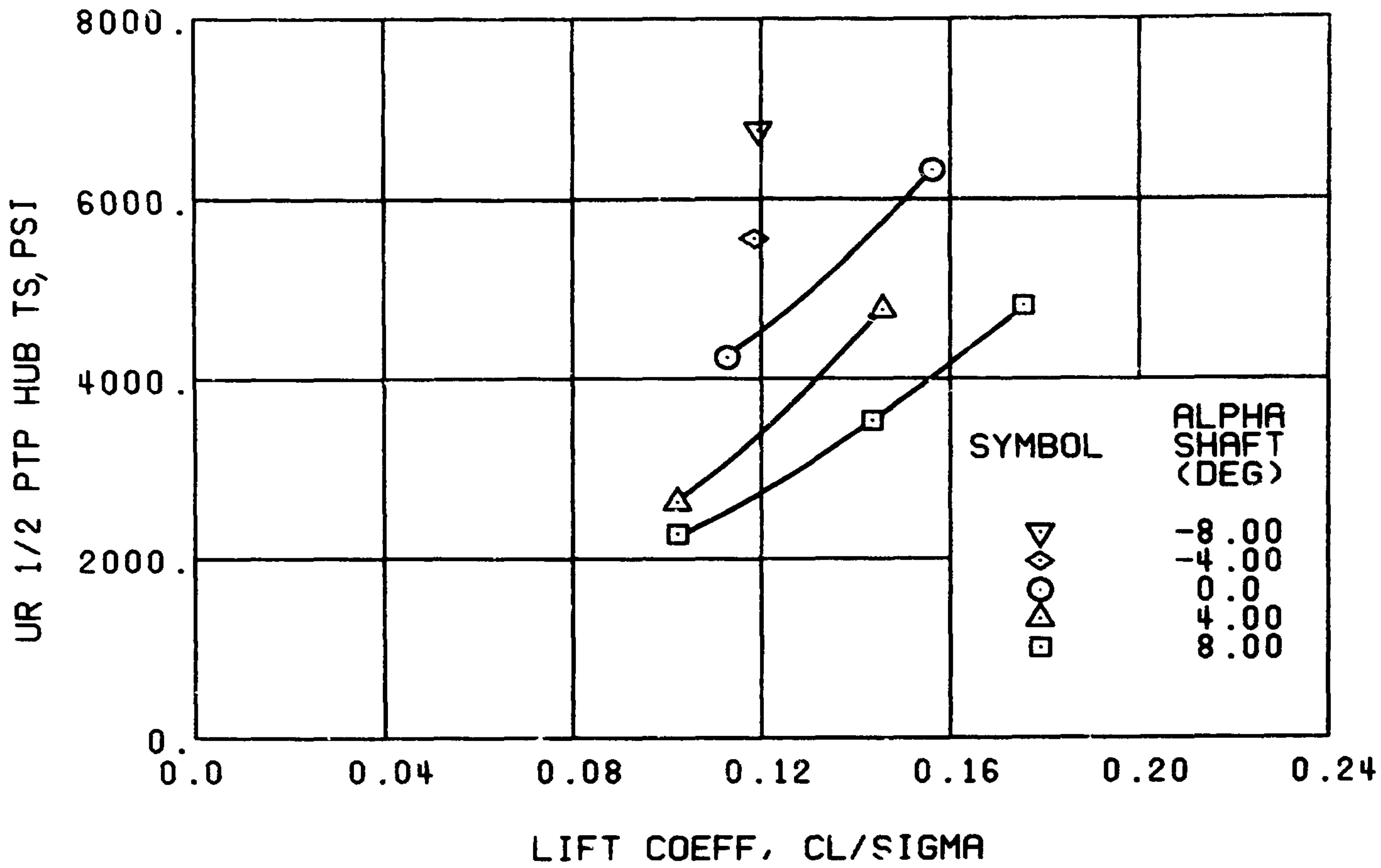

(f) GAGE 65

Figure 45. Continued.
$\mu = 0.35$ $B'_{1s} = 2$ Deg

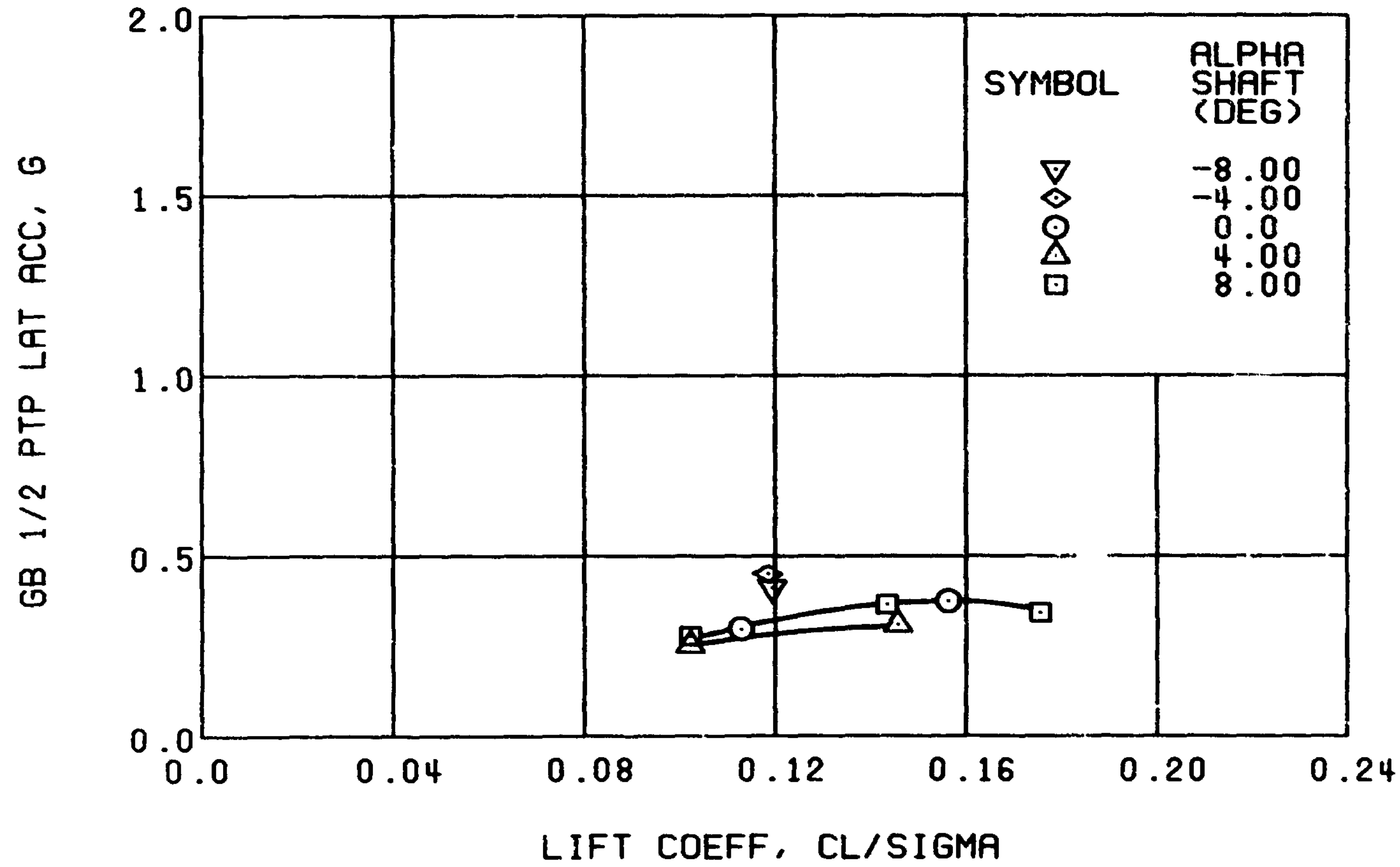

(u) GAGE 15   STA 76, BL 30

Figure 45. Continued.
μ = 0.35 B'_{1s} = 2 Deg

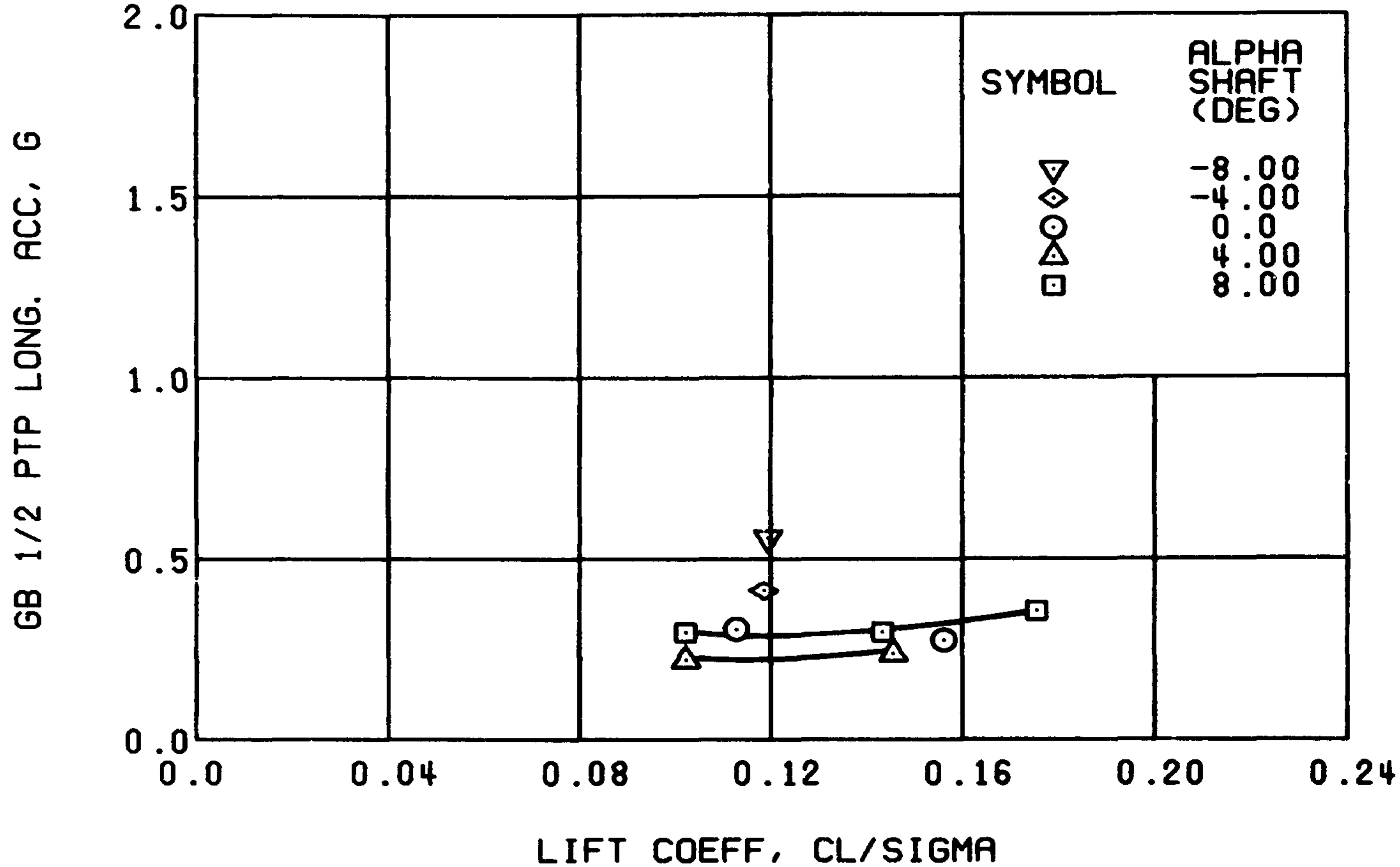

(v) GAGE 14 STA 61, BL 0

Figure 45. Continued.
μ = 0.35 B'_{1s} = 2 Deg

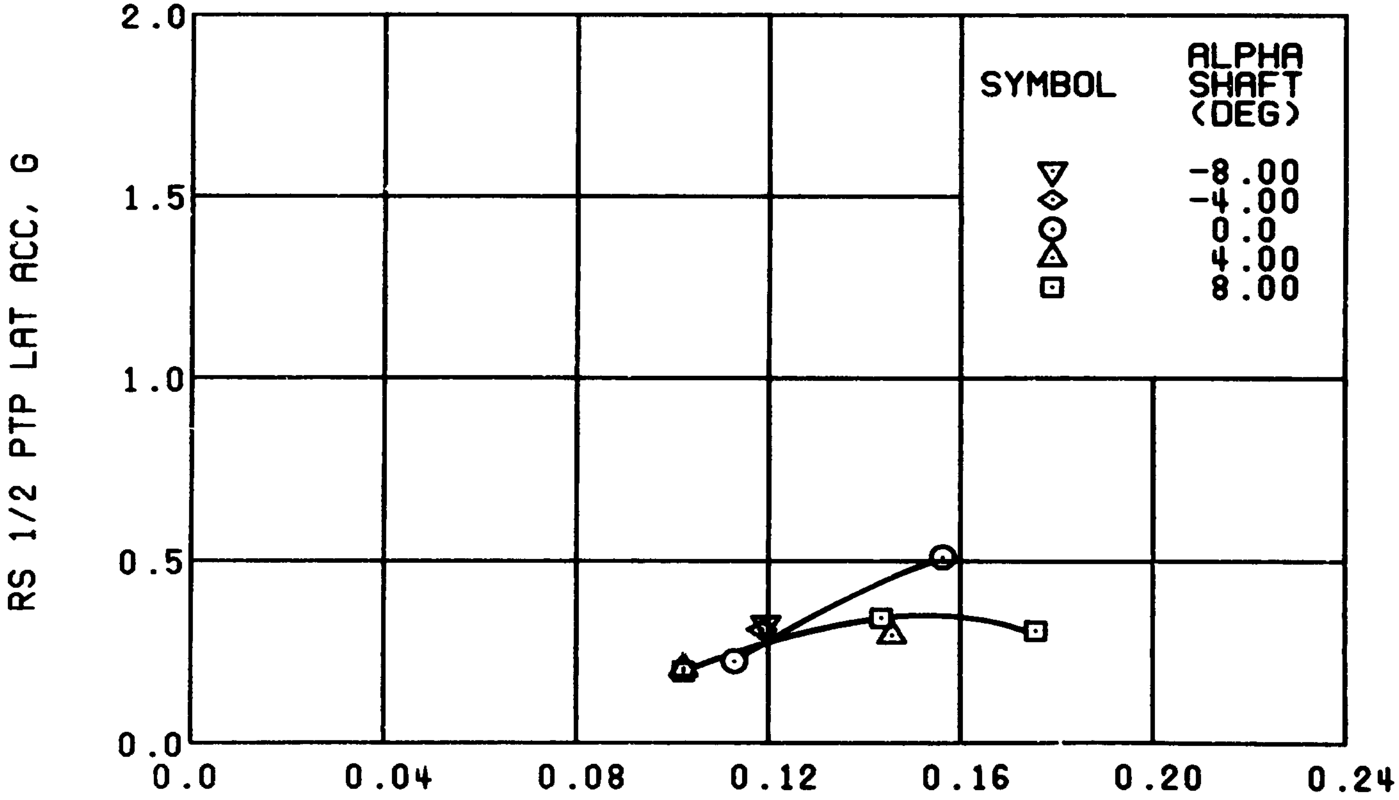

(w) GAGE 16 ROVER 3

Figure 45. Continued.
$\mu = 0.35$ $B'_{1s} = 2$ Deg

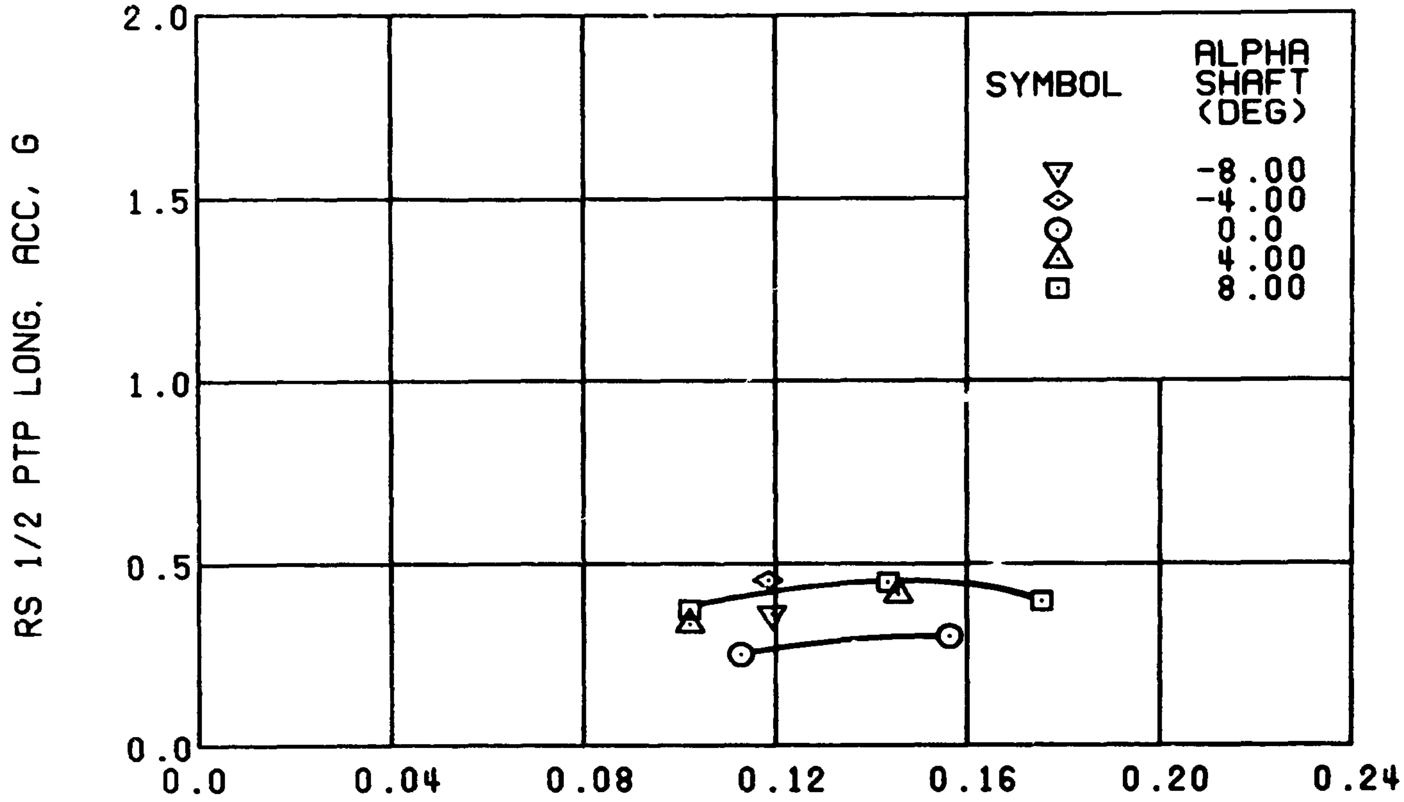

(x) GAGE 17 ROVER 4

Figure 45. Concluded.
$\mu = 0.35$ $B'_{1s} = 2$ Deg

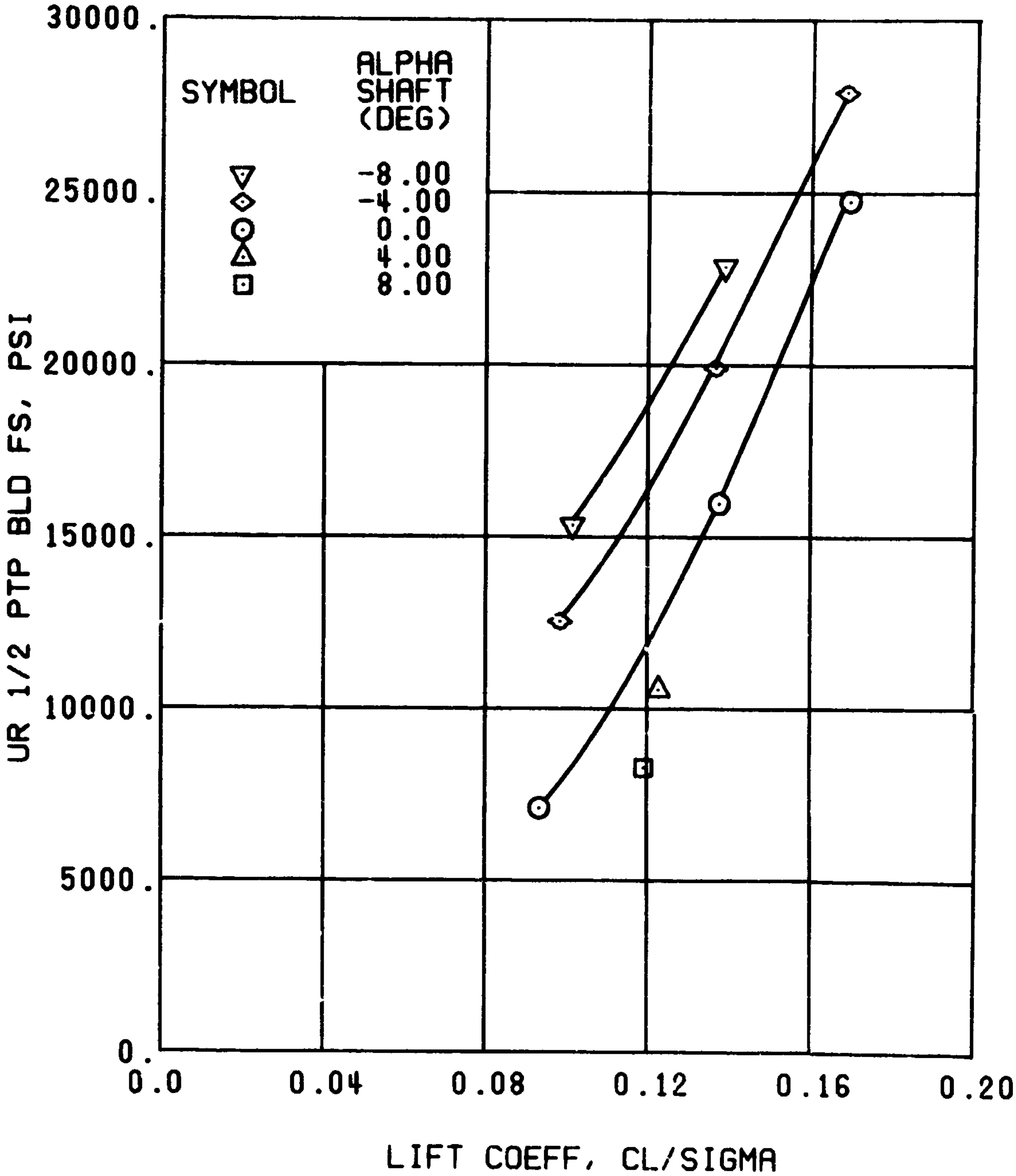

(a) GAGE 51 R84

Figure 46. Stress, Load, and Vibration Data at an Advance Ratio of 0.35 With the Lateral Displacement Control (B'_{1s}) Set at 4 Degrees.

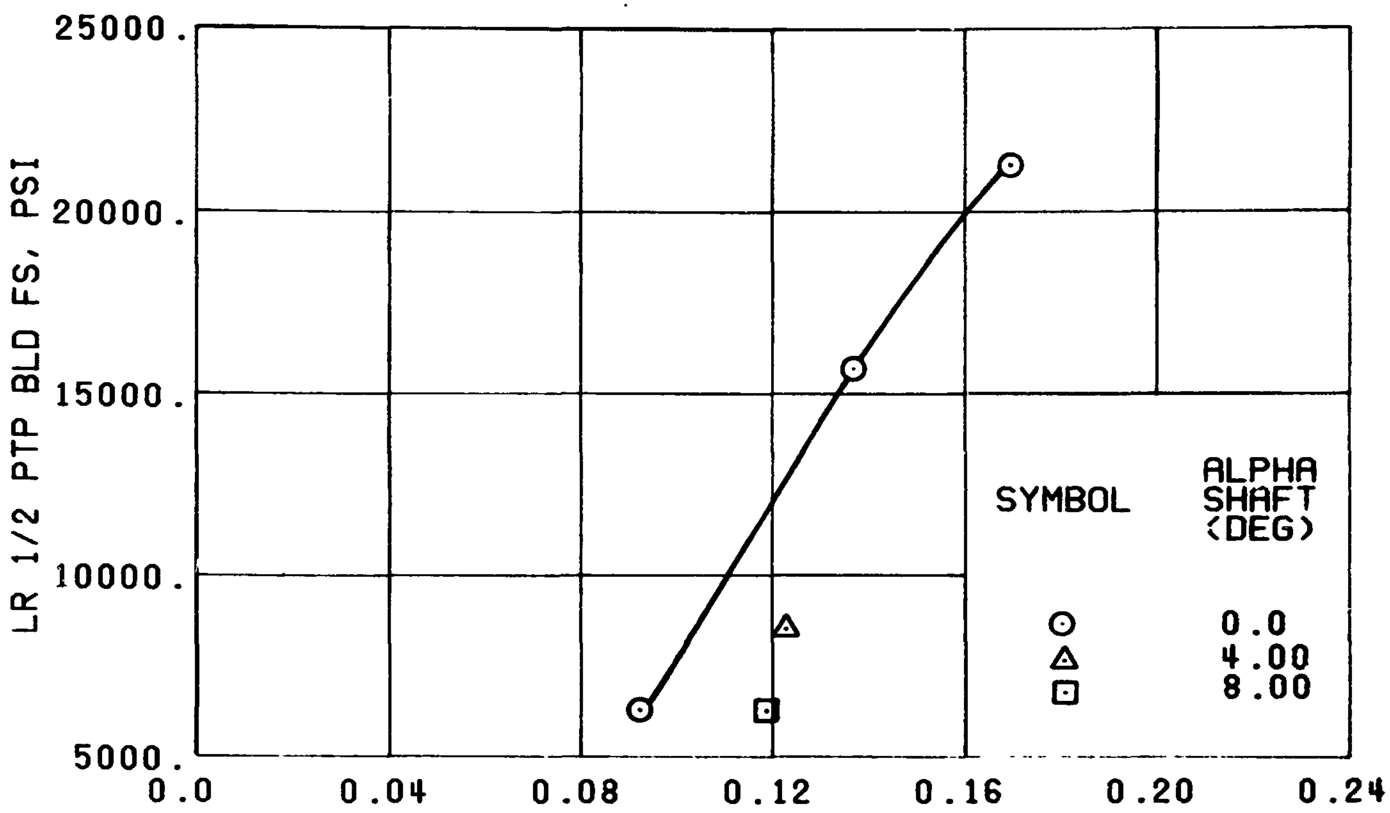

(b) GAGE 1 R84

Figure 46. Continued.
$\mu = 0.35 \quad B'_{1s} = 4$ Deg

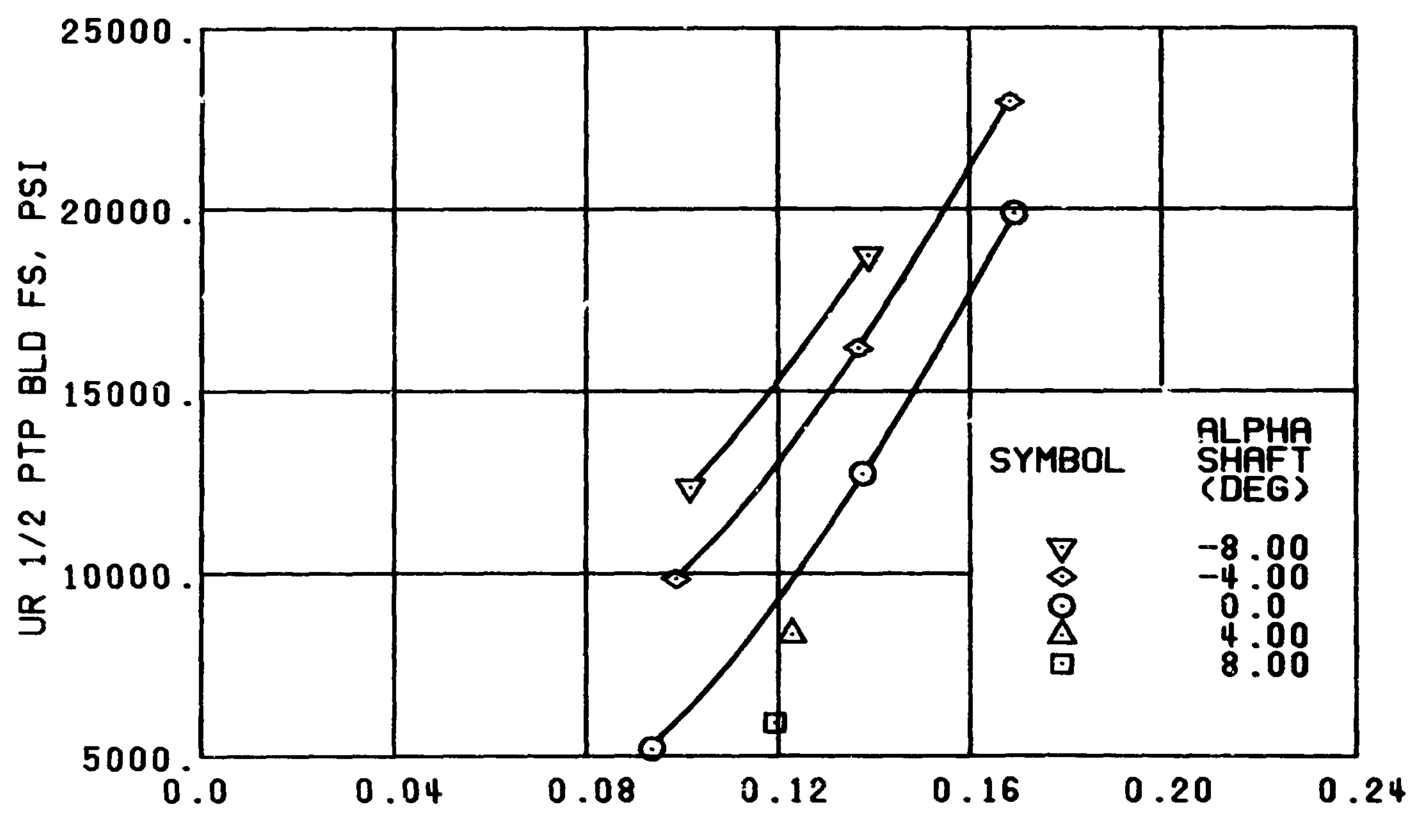

(c) GAGE 52 R108

Figure 46. Continued.
$\mu = 0.35$ $B'_{1s} = 4$ Deg

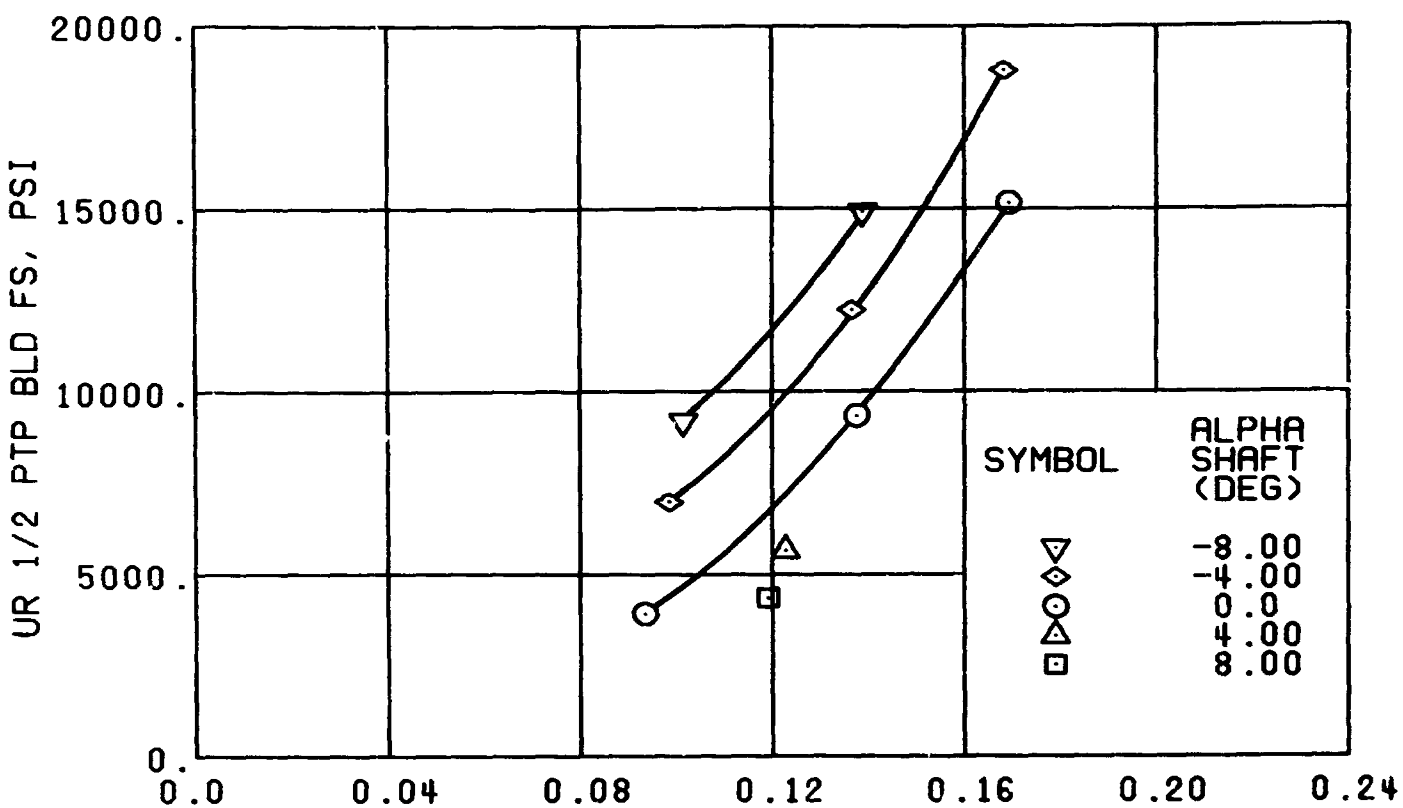

(d) GAGE 53 R132

Figure 46. Continued.
$\mu = 0.35$ $B'_{1s} = 4$ Deg

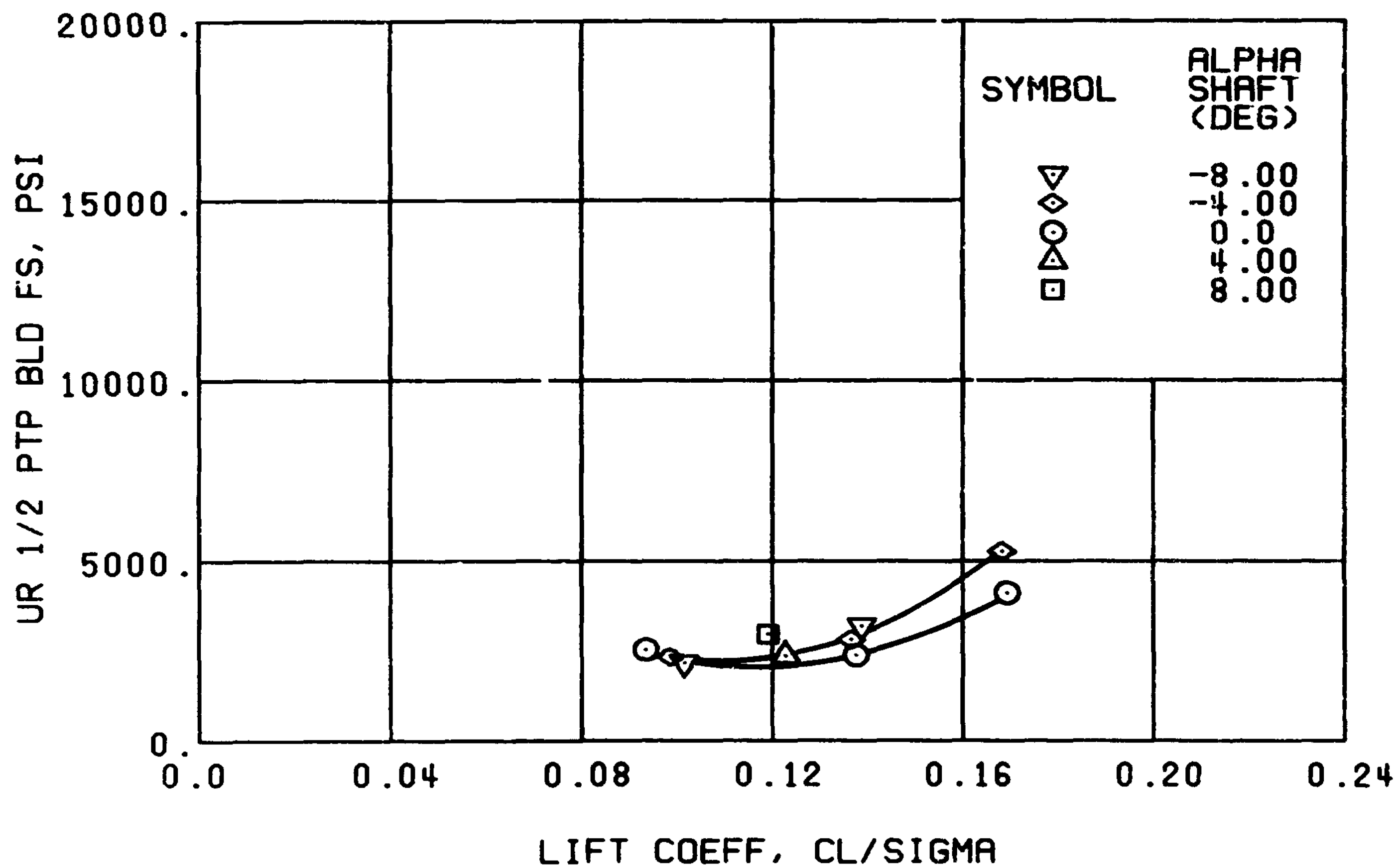

(f) GAGE 55 R204

Figure 46. Continued.
$\mu = 0.35$ $B'_{1s} = 4$ Deg

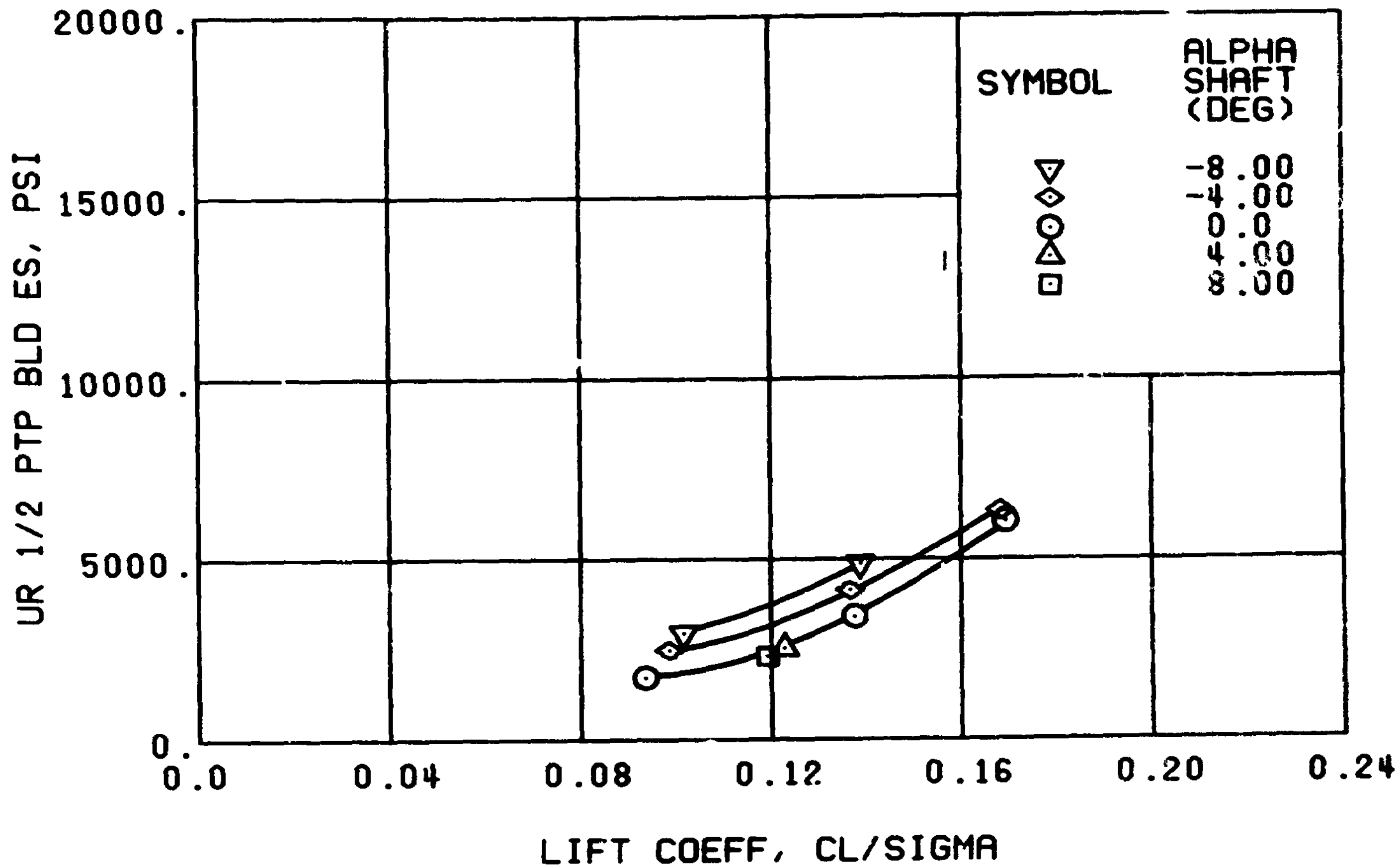

(h) GAGE 40 R84

Figure 46. Continued.
$\mu = 0.35$ $B'_{1s} = 4$ Deg

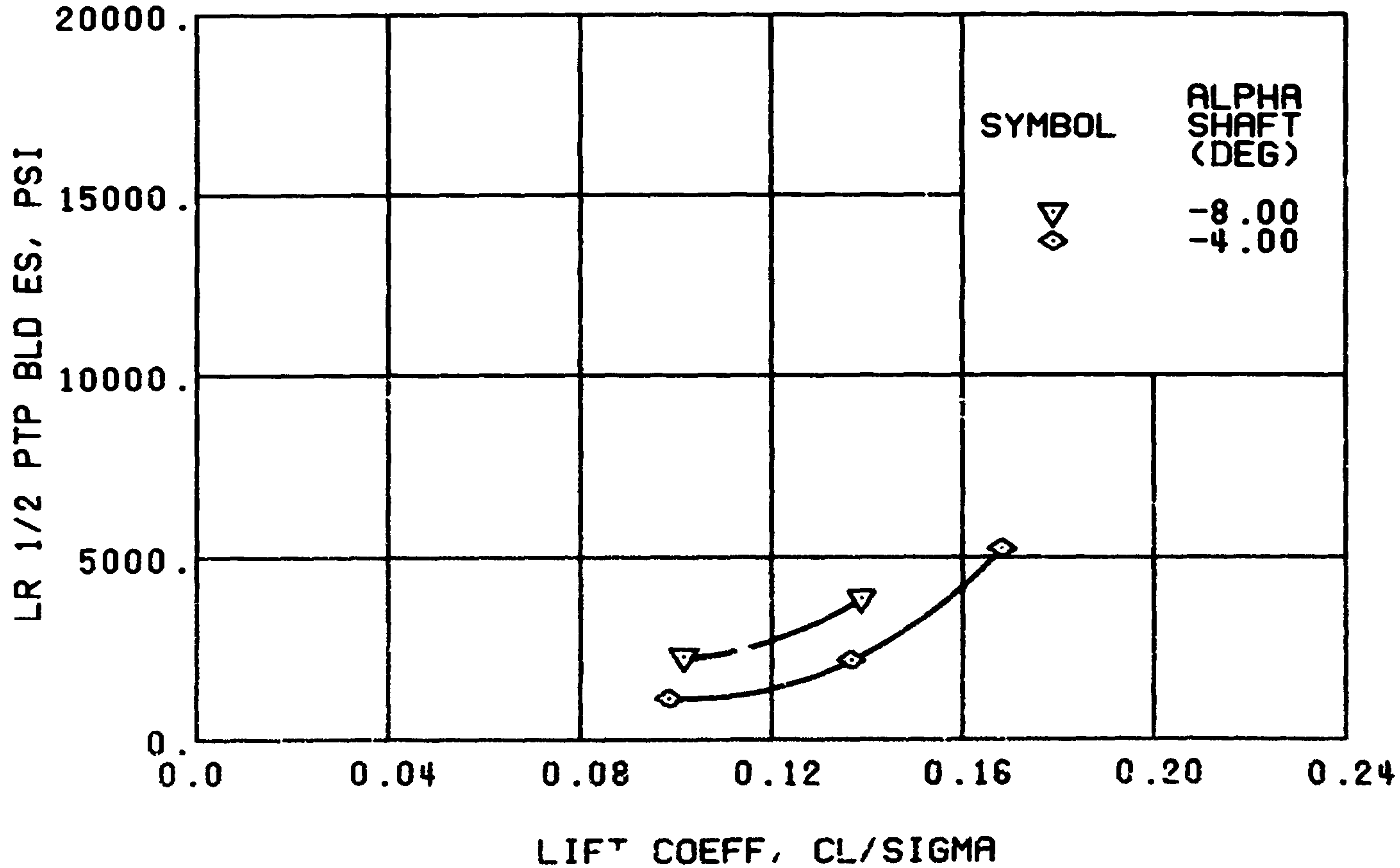

(i) GAGE 2 R84

Figure 46. Continued.
$\mu = 0.35$ $B'_{1s} = 4$ Deg

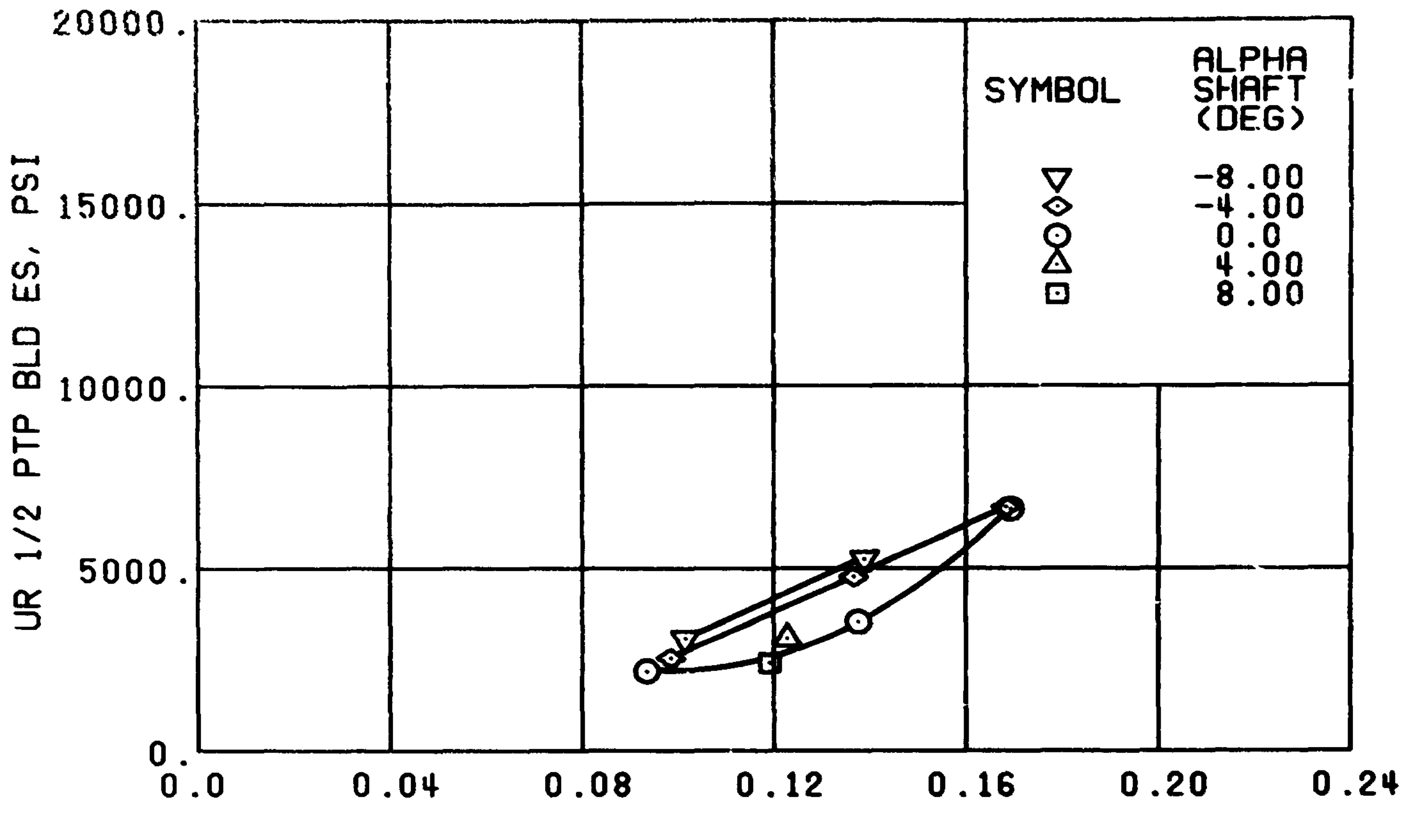

(j) GAGE 42 R132

Figure 46. Continued.
$\mu = 0.35 \quad B'_{1s} = 4$ Deg

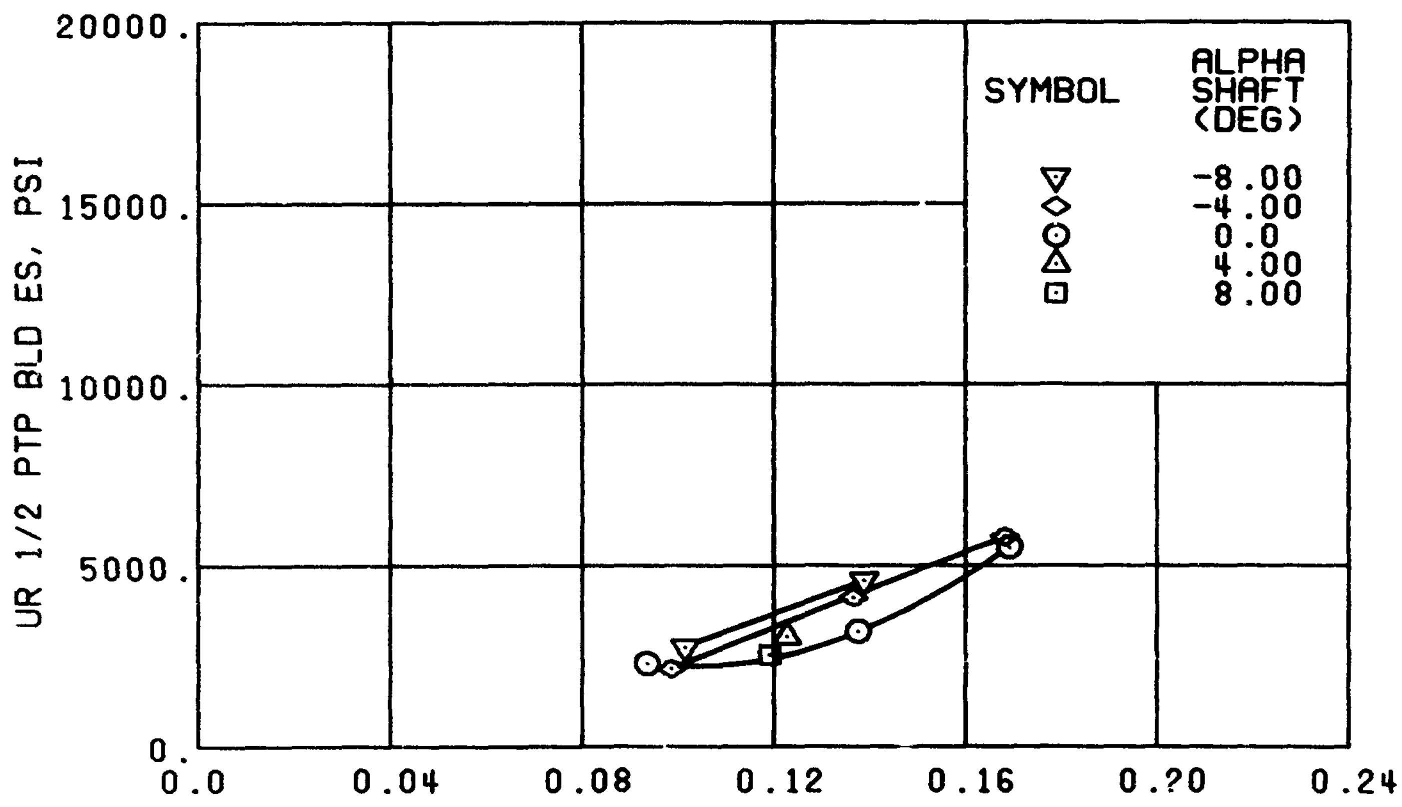

(k) GAGE 43 R168

Figure 46. Continued.
$\mu = 0.35$ $B'_{1s} = 4$ Deg

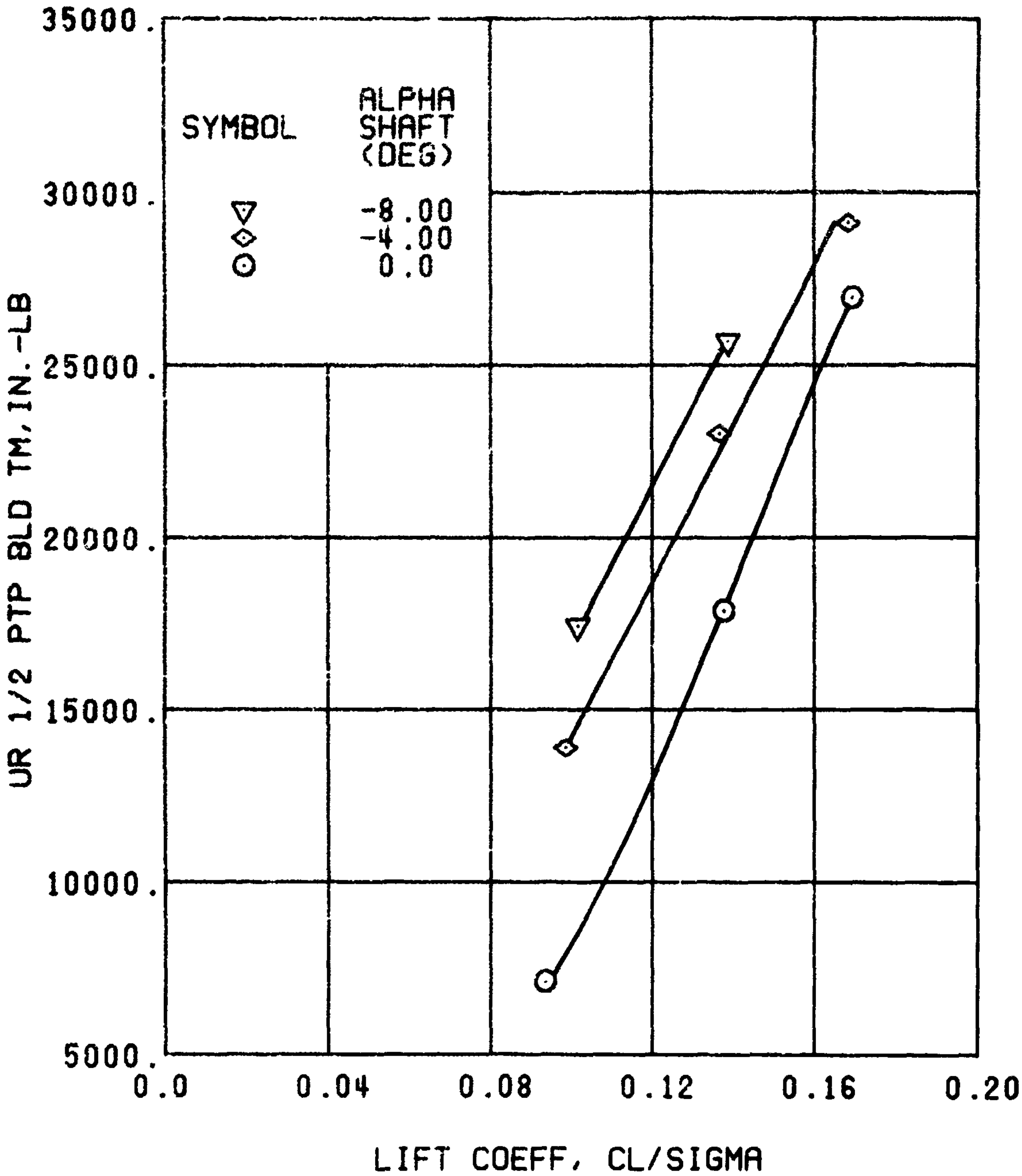

(I) GAGE 45 R82

Figure 46. Continued.
$\mu = 0.35$ $B'_{1s} = 4$ Deg

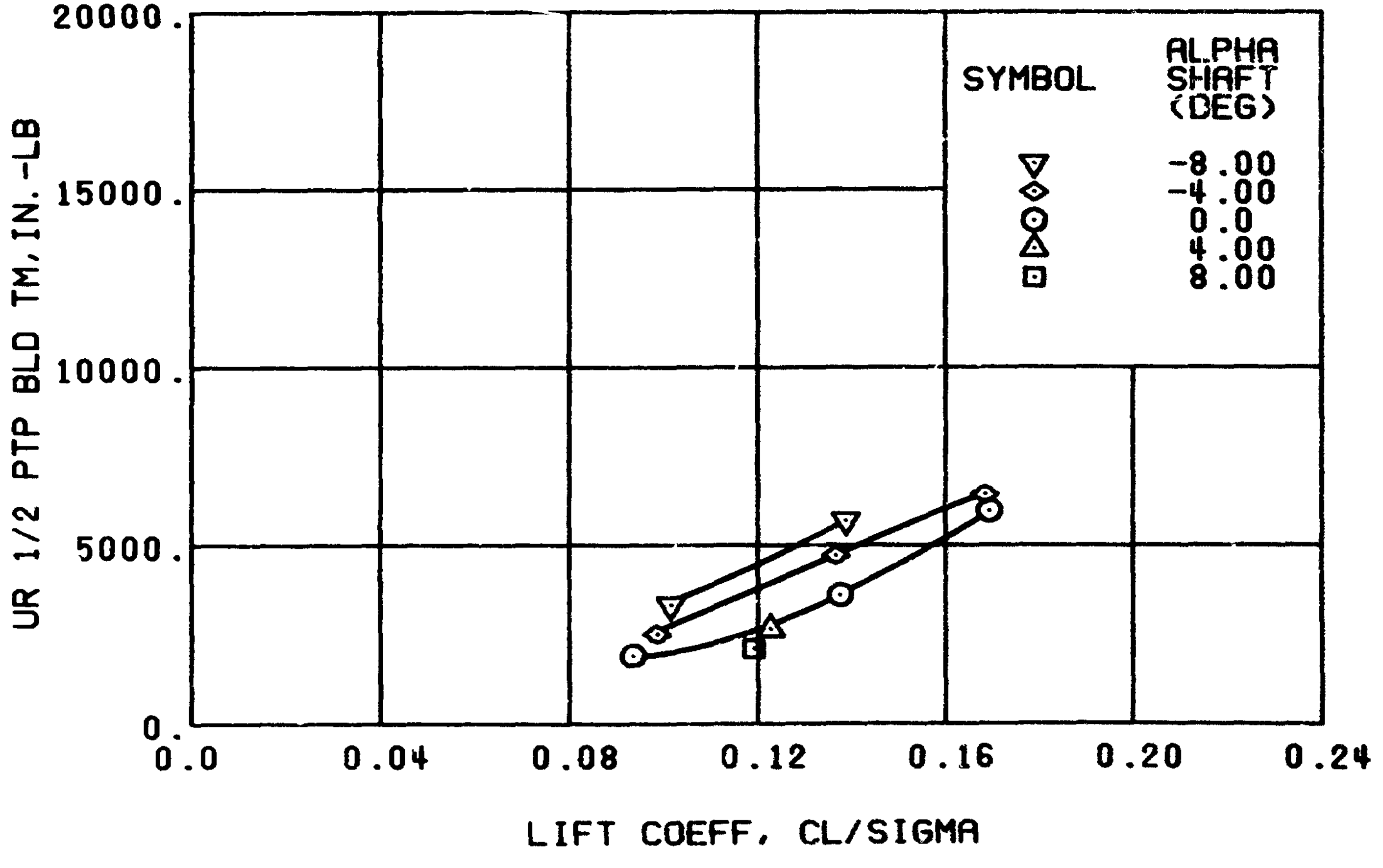

(m) GAGE 46 R130

Figure 46. Continued.
$\mu = 0.35$ $B'_{1s} = 4$ Deg

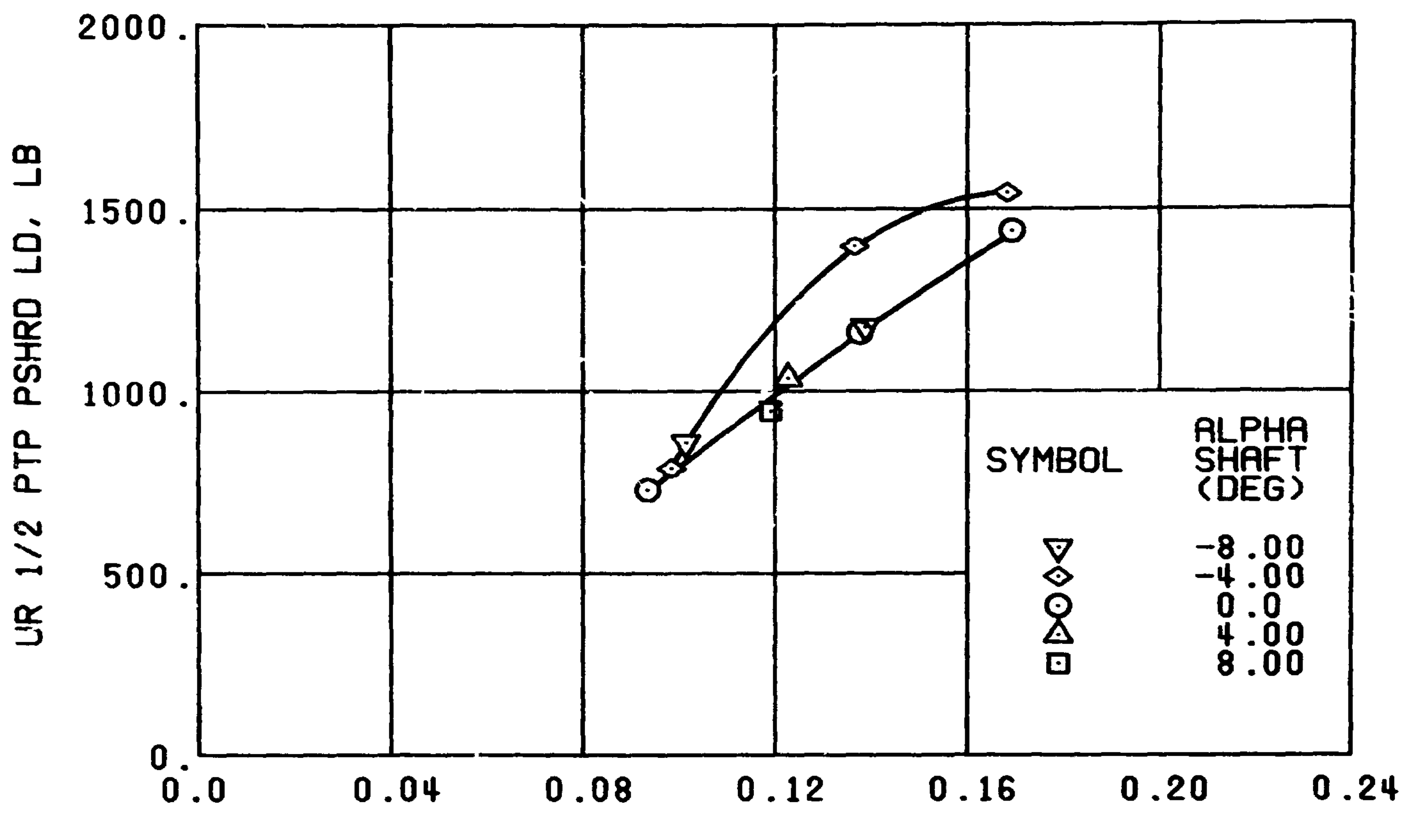

(n) GAGE 37

Figure 46. Continued.
$\mu = 0.35 \quad B'_{1s} = 4$ Deg

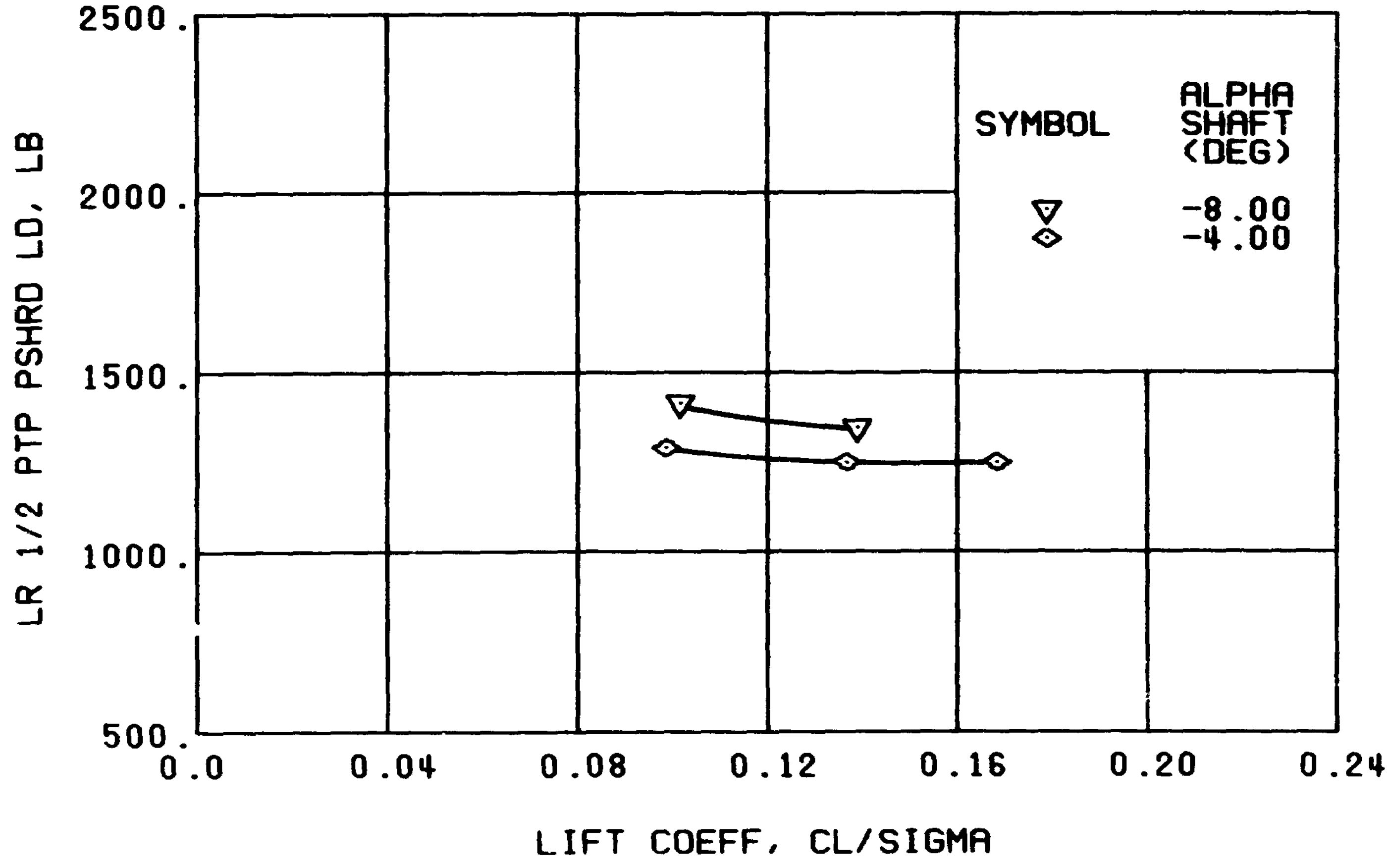

(o) GAGE 34

Figure 46. Continued.
$\mu = 0.35$ $B'_{1s} = 4$ Deg

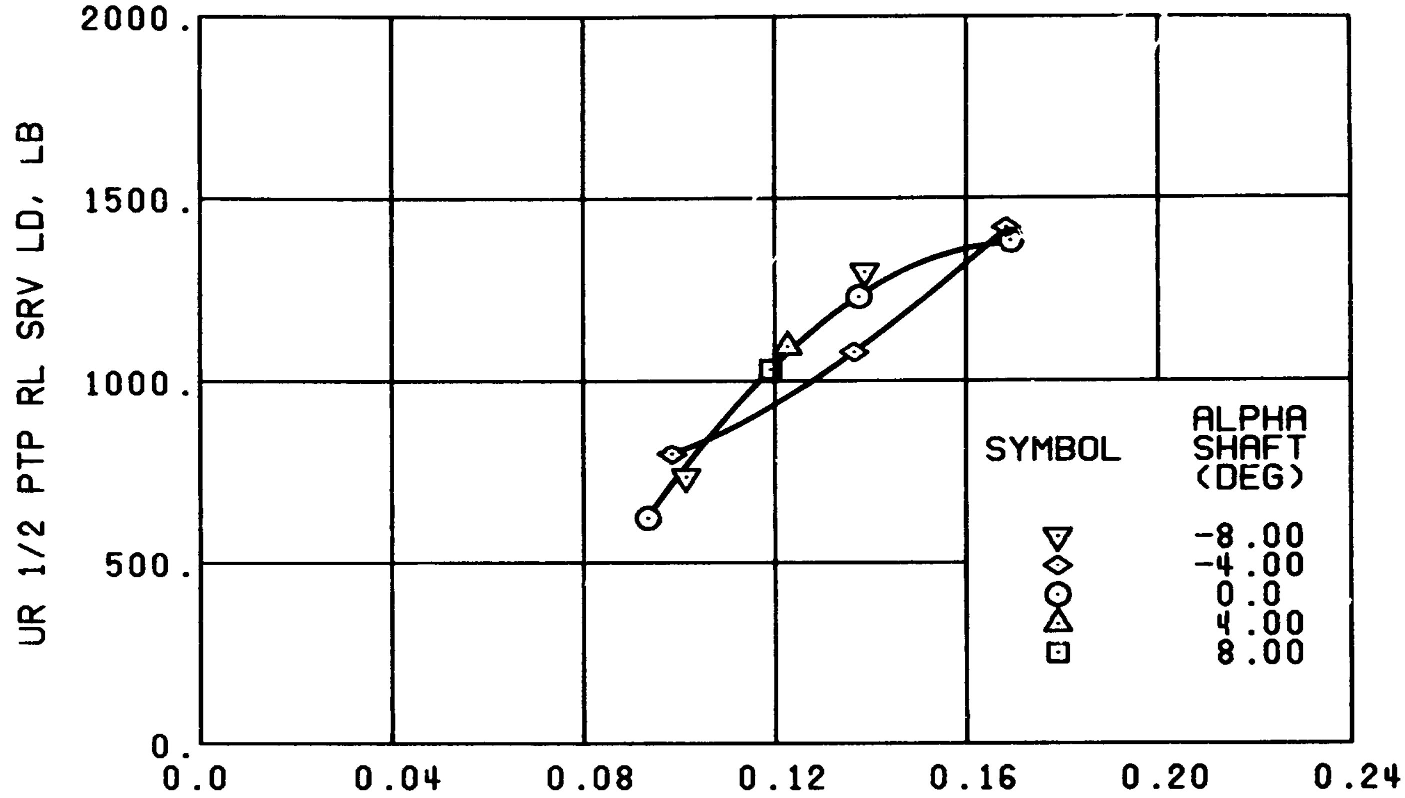

(p) GAGE 22

Figure 46. Continued.
$\mu = 0.35$ $B'_{1s} = 4$ Deg

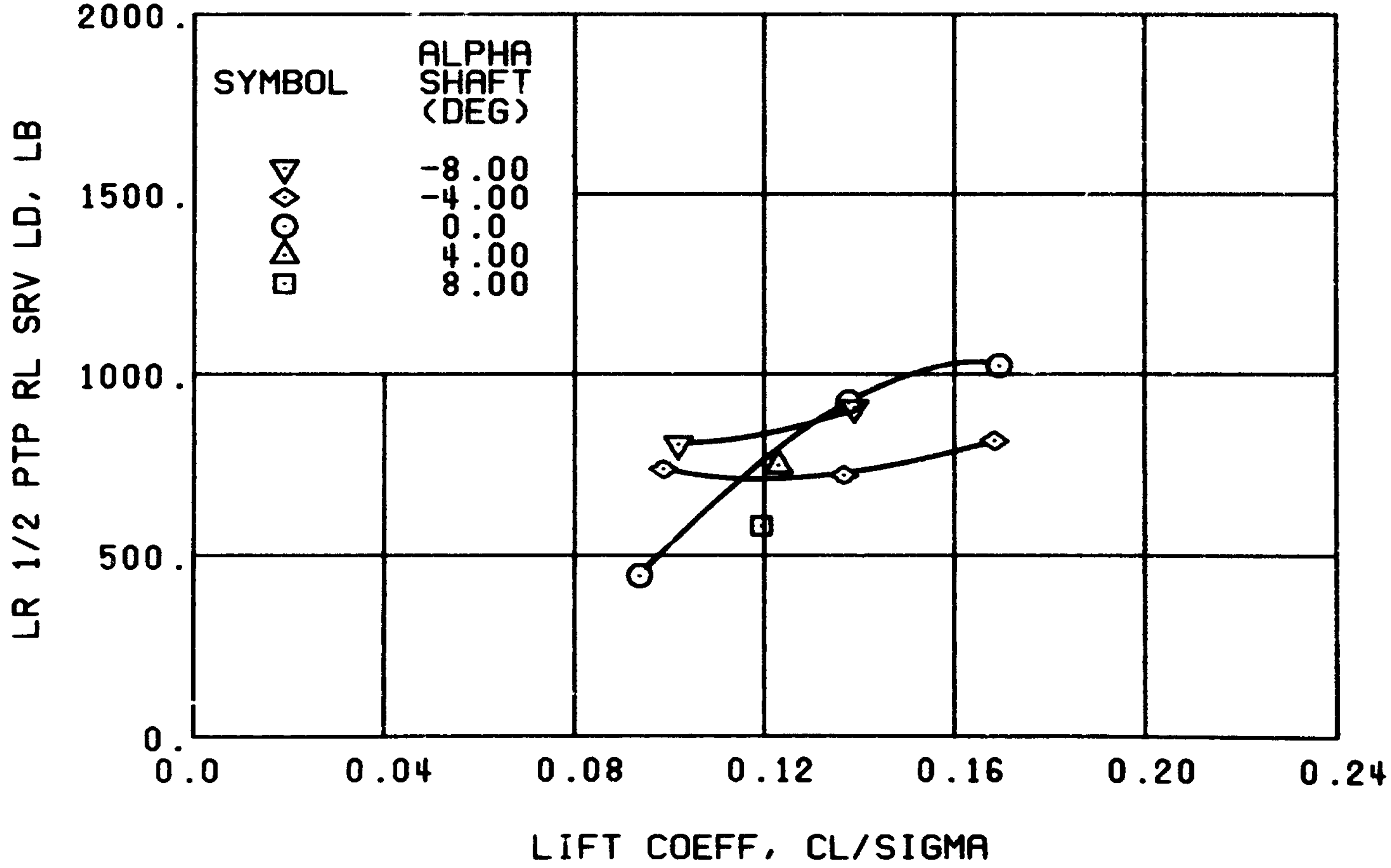

(q) GAGE 25

Figure 46. Continued.
$\mu = 0.35 \quad B'_{1s} = 4$ Deg

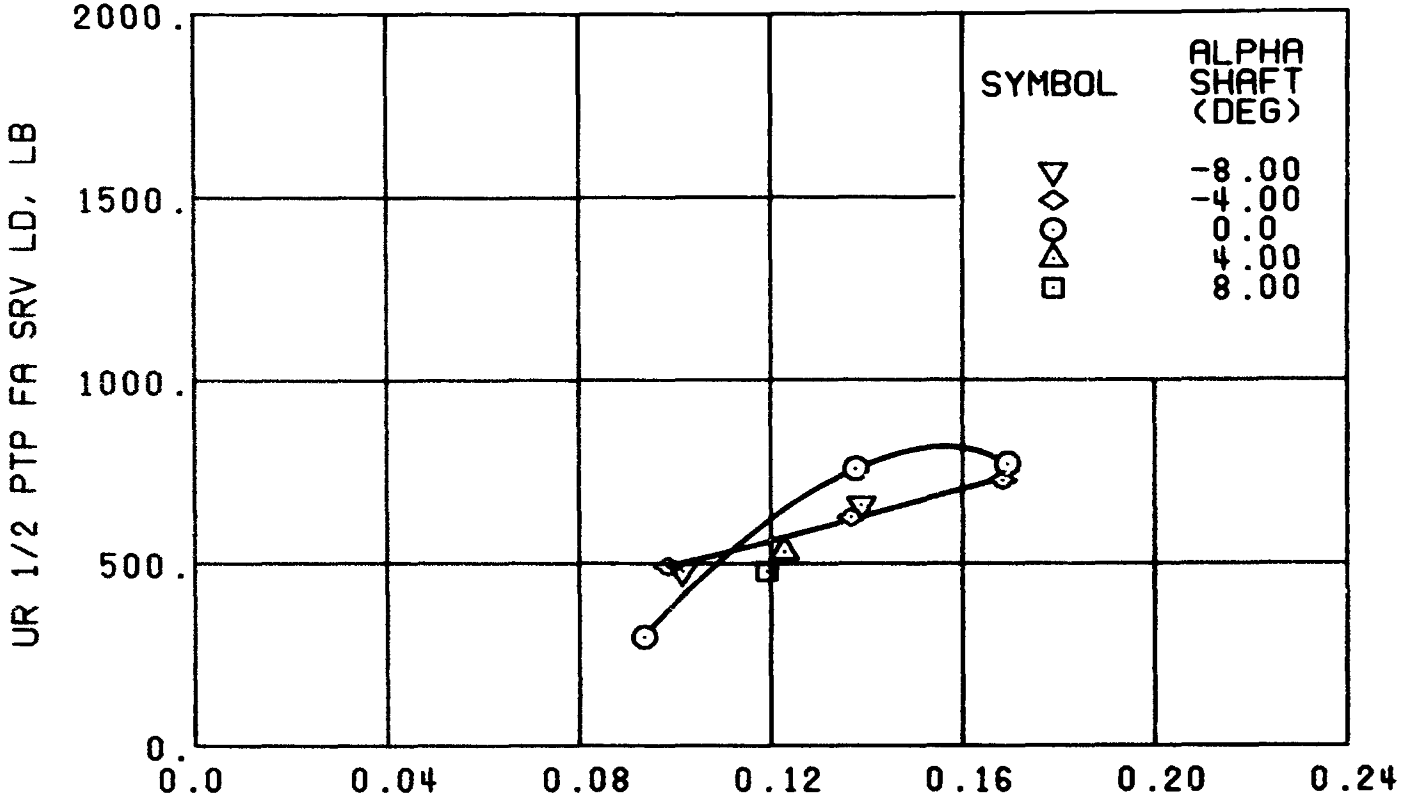

(r) GAGE 24

Figure 46. Continued.
$\mu = 0.35 \quad B'_{1s} = 4$ Deg

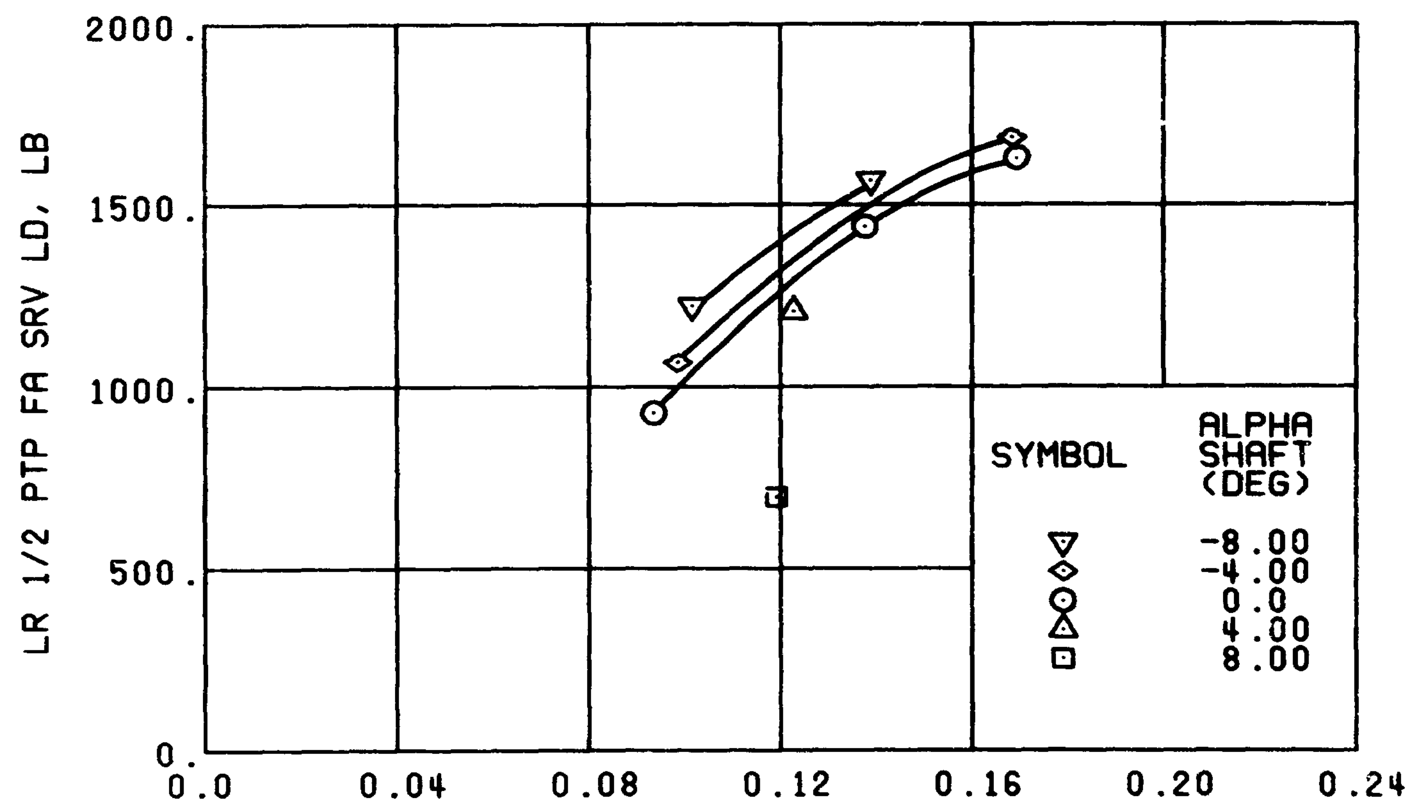

LIFT COEFF, CL/SIGMA

(s) GAGE 27

Figure 46. Continued.
$\mu = 0.35 \quad B'_{1s} = 4$ Deg

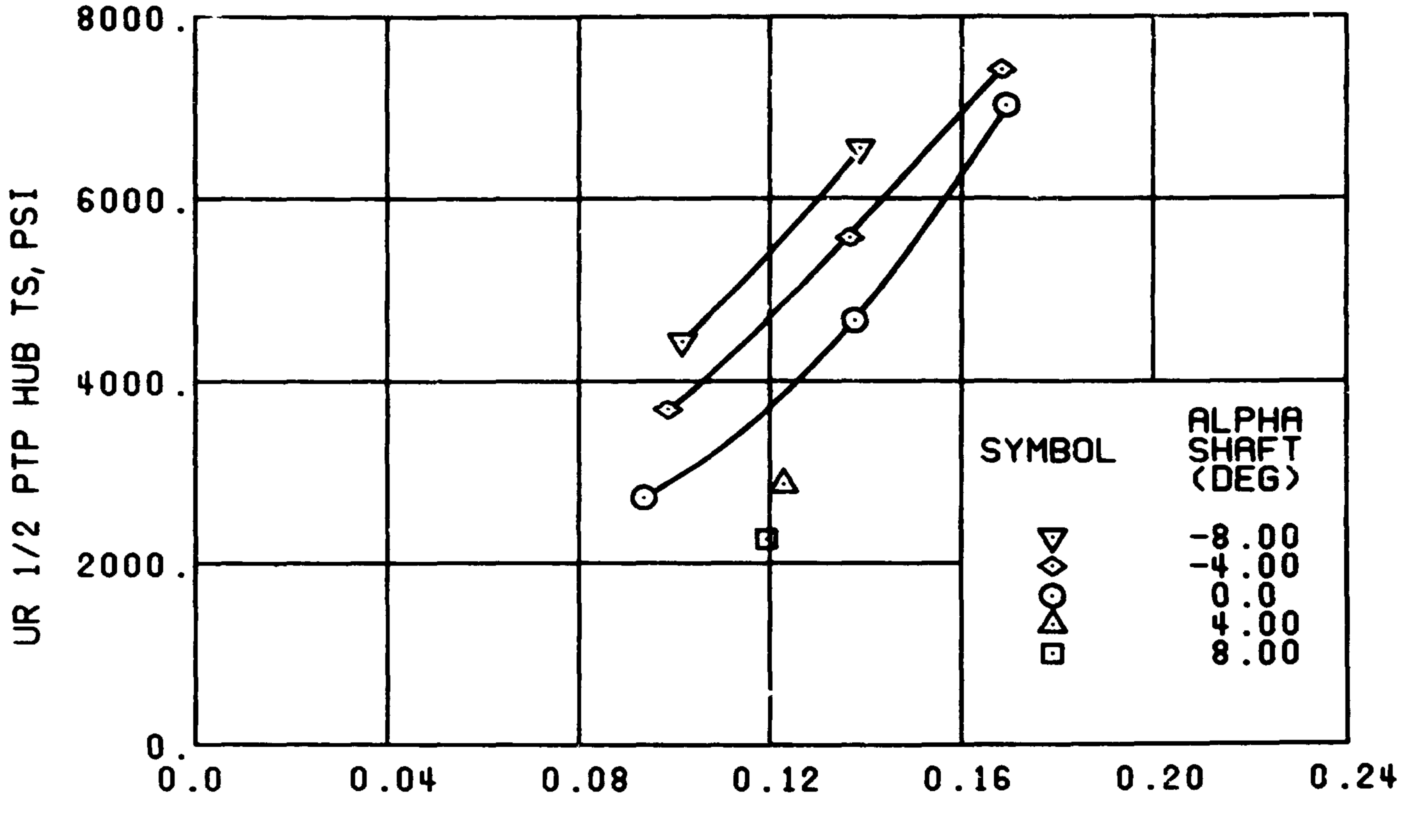

(t) GAGE 65

Figure 46. Continued.
$\mu = 0.35 \quad B'_{1s} = 4$ Deg

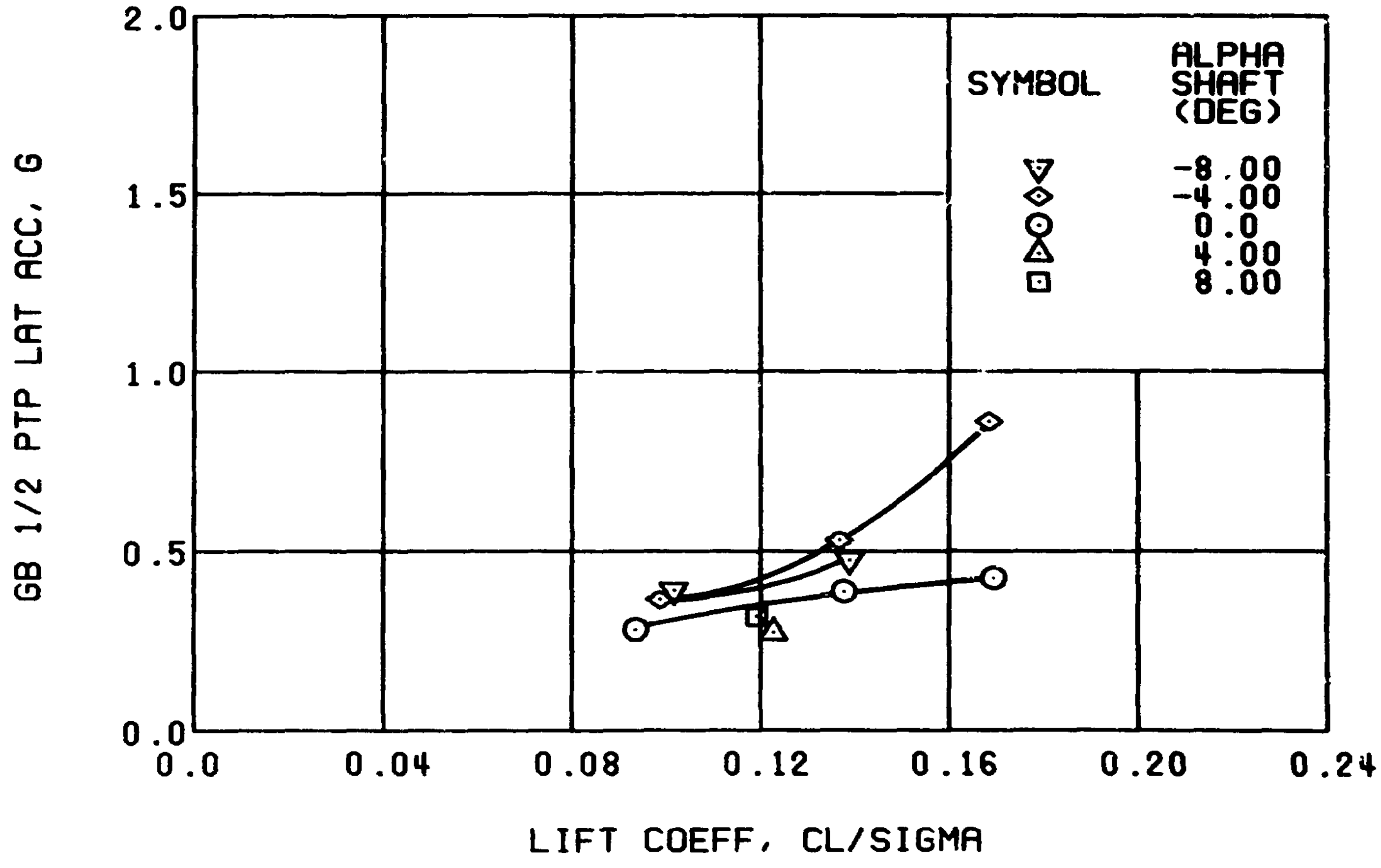

(u) GAGE 15 STA 76, BL 30

Figure 46. Continued.
$\mu = 0.35$ $B'_{1s} = 4$ Deg

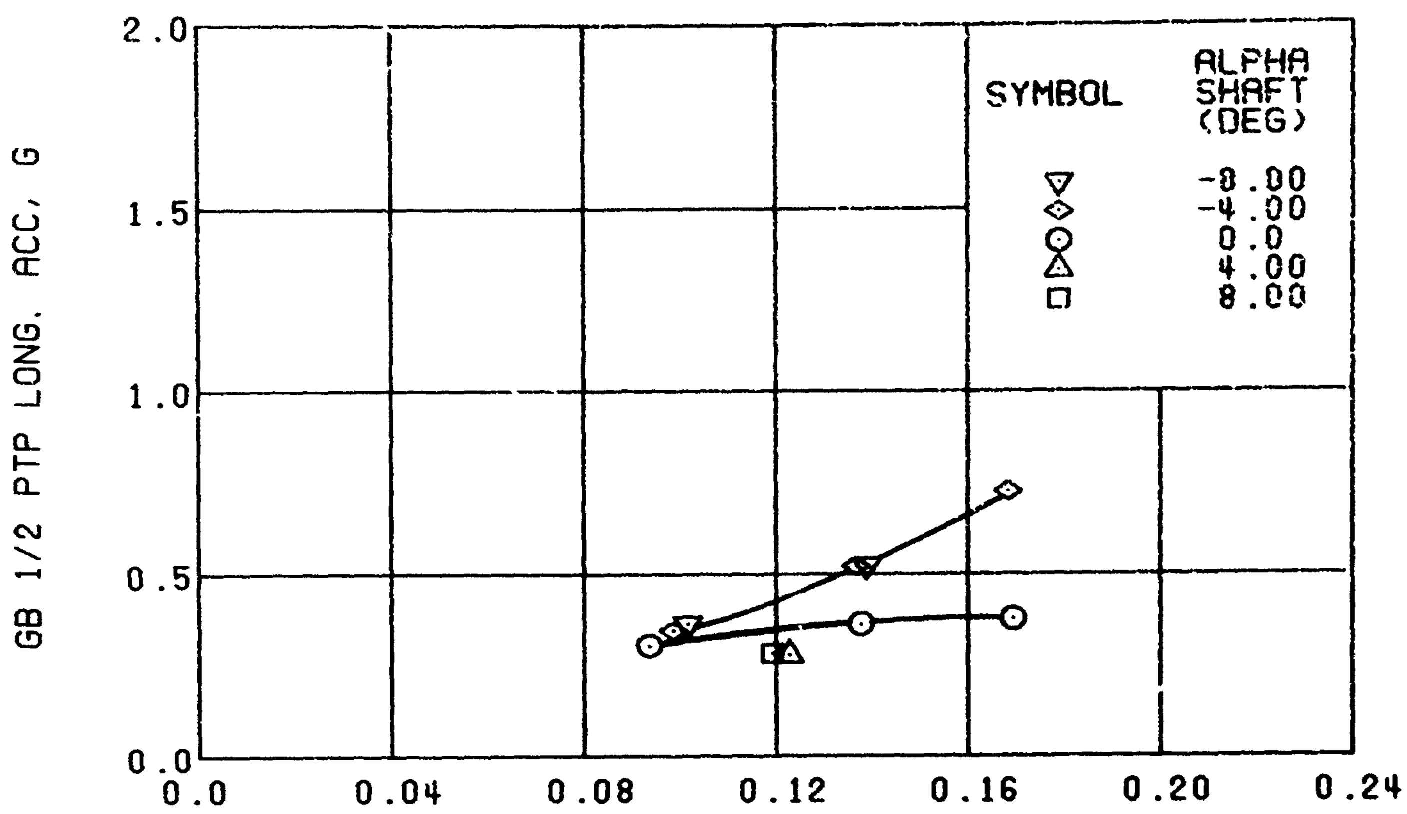

(v) GAGE 14 STA 61, BL 0

Figure 46. Continued.
$\mu = 0.35 \quad B'_{1s} = 4$ Deg

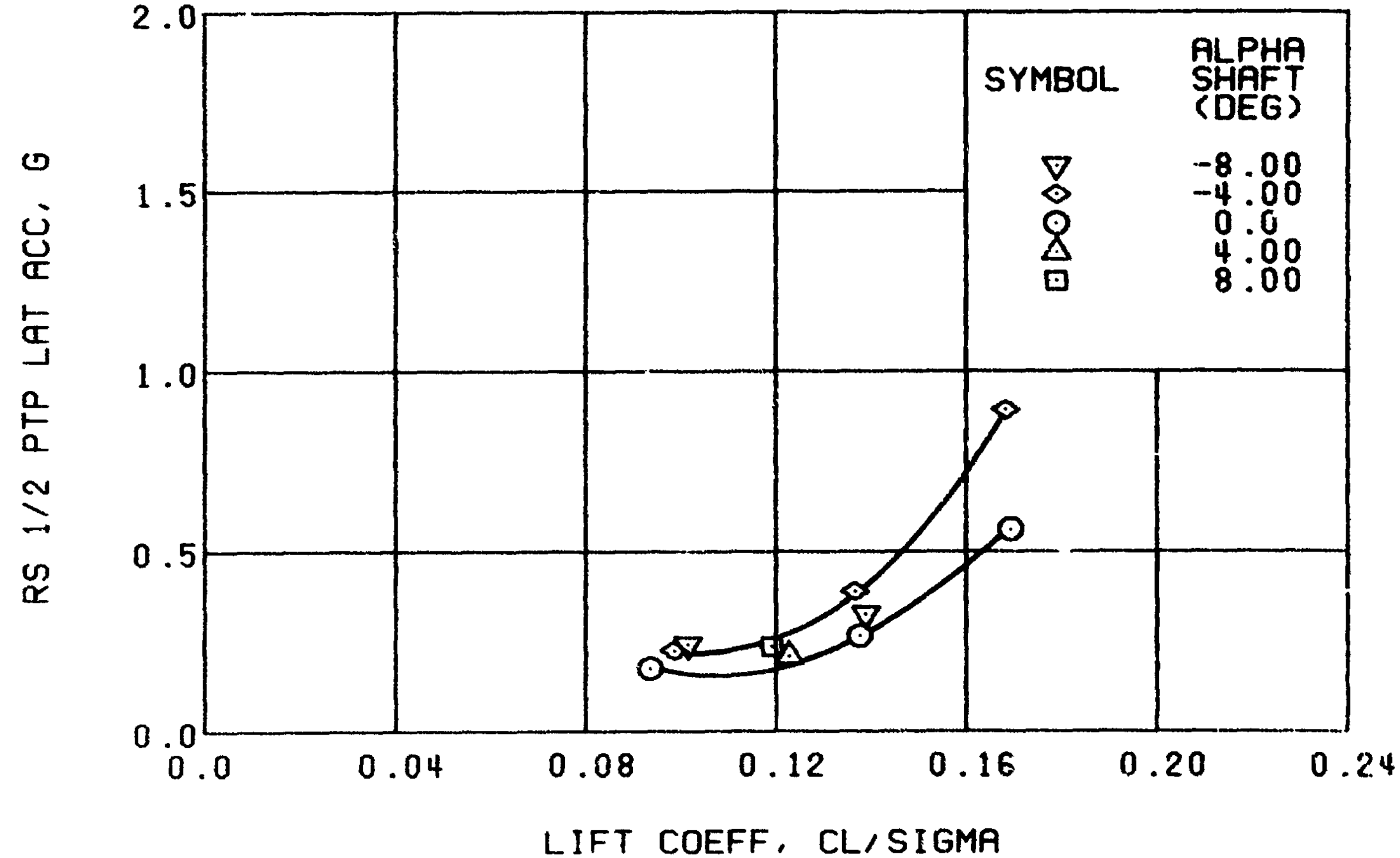

(w) GAGE 16 ROVER 3

Figure 46. Continued.
$\mu = 0.35$ $B'_{1s} = 4$ Deg

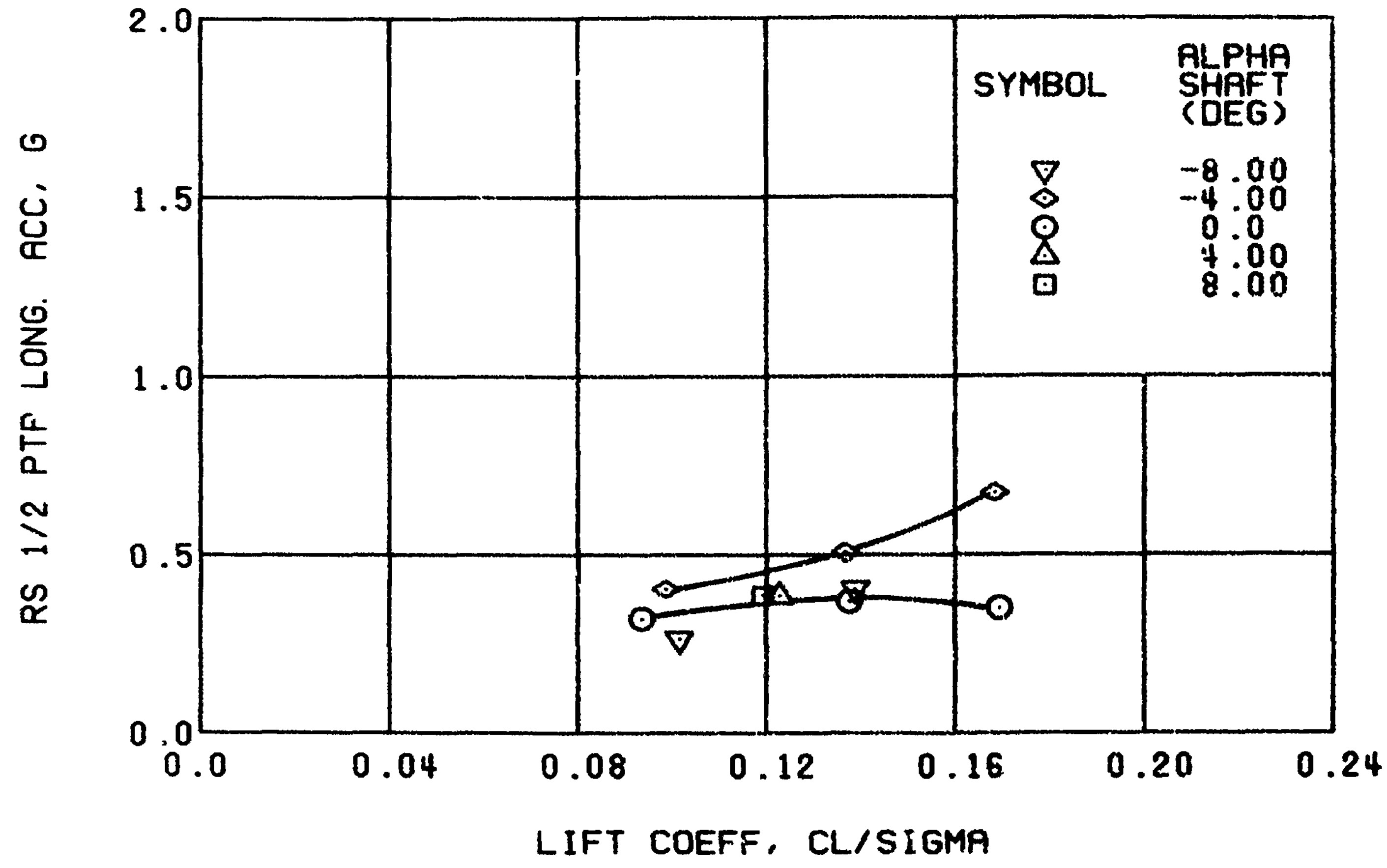

(x) GAGE 17 ROVER 4

Figure 46. Concluded.
$\mu = 0.35 \quad B'_{1s} = 4$ Deg

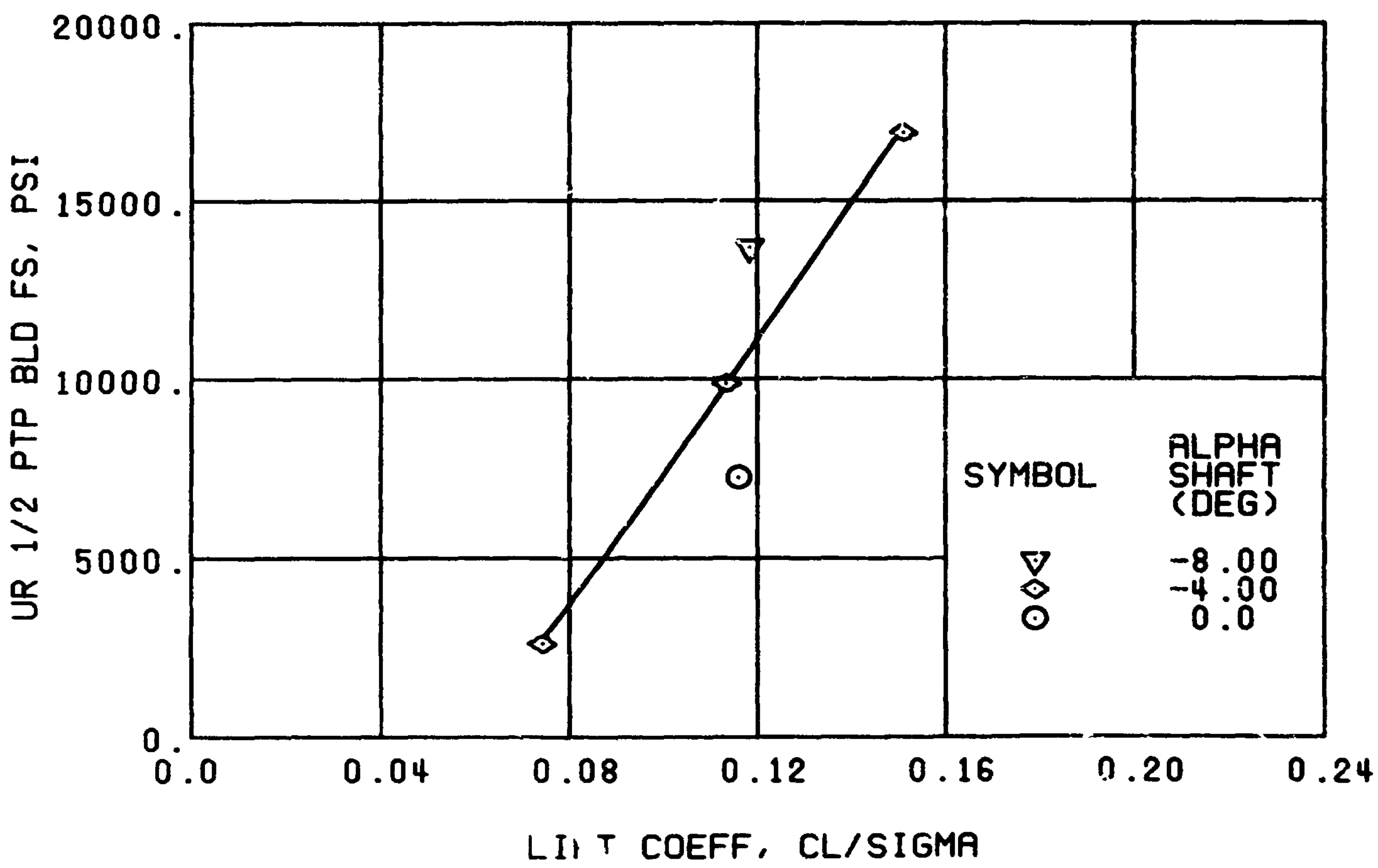

(a) GAGE 51 R84

Figure 47. Stress, Load, and Vibration Data at an Advance Ratio of 0.35 With the Lateral Displacement Control (B'_{1s}) Set at 6 Degrees.

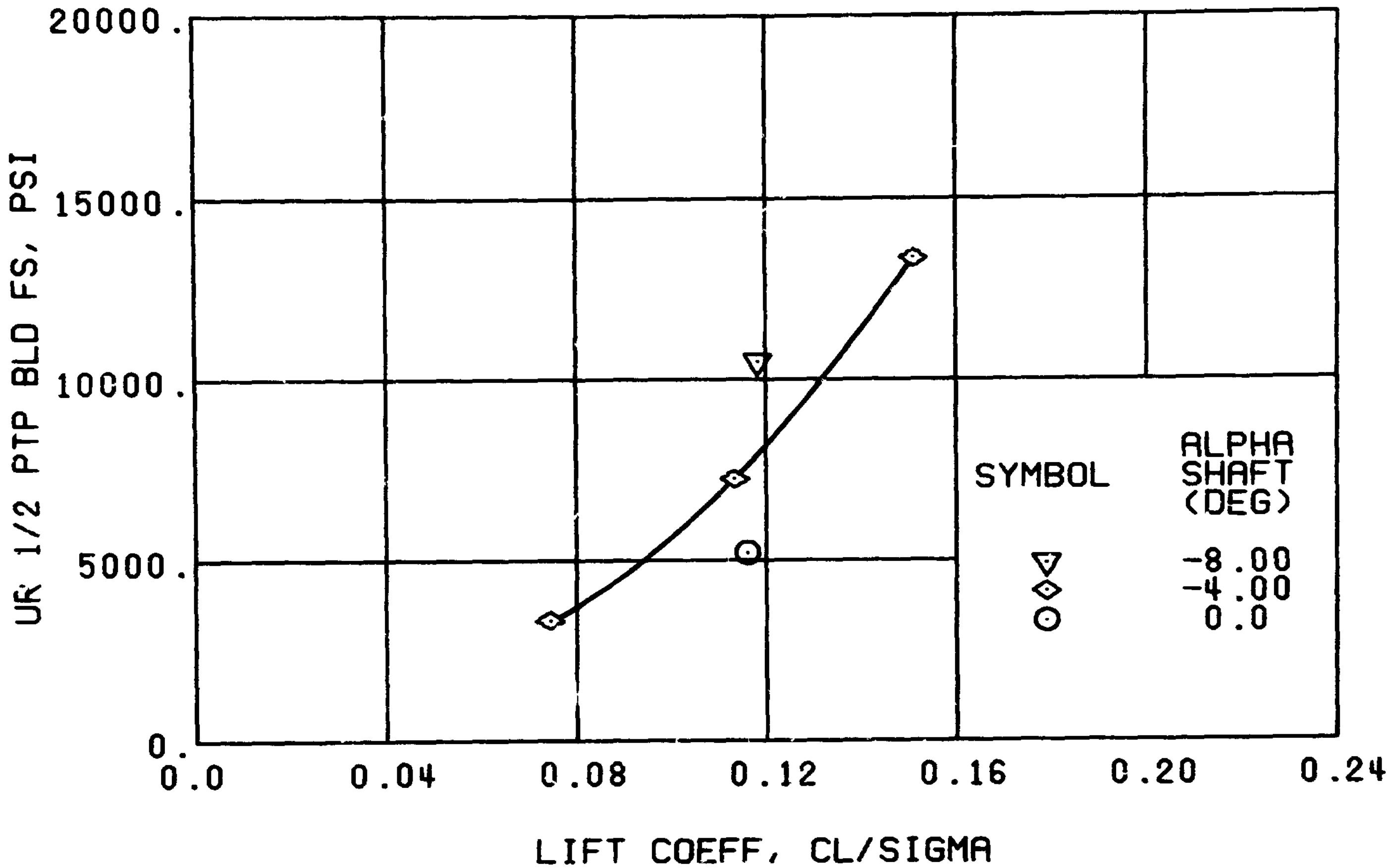

(c) GAGE 52 R108

Figure 47. Continued.
$\mu = 0.35$ $B'_{1s} = 6$ Deg

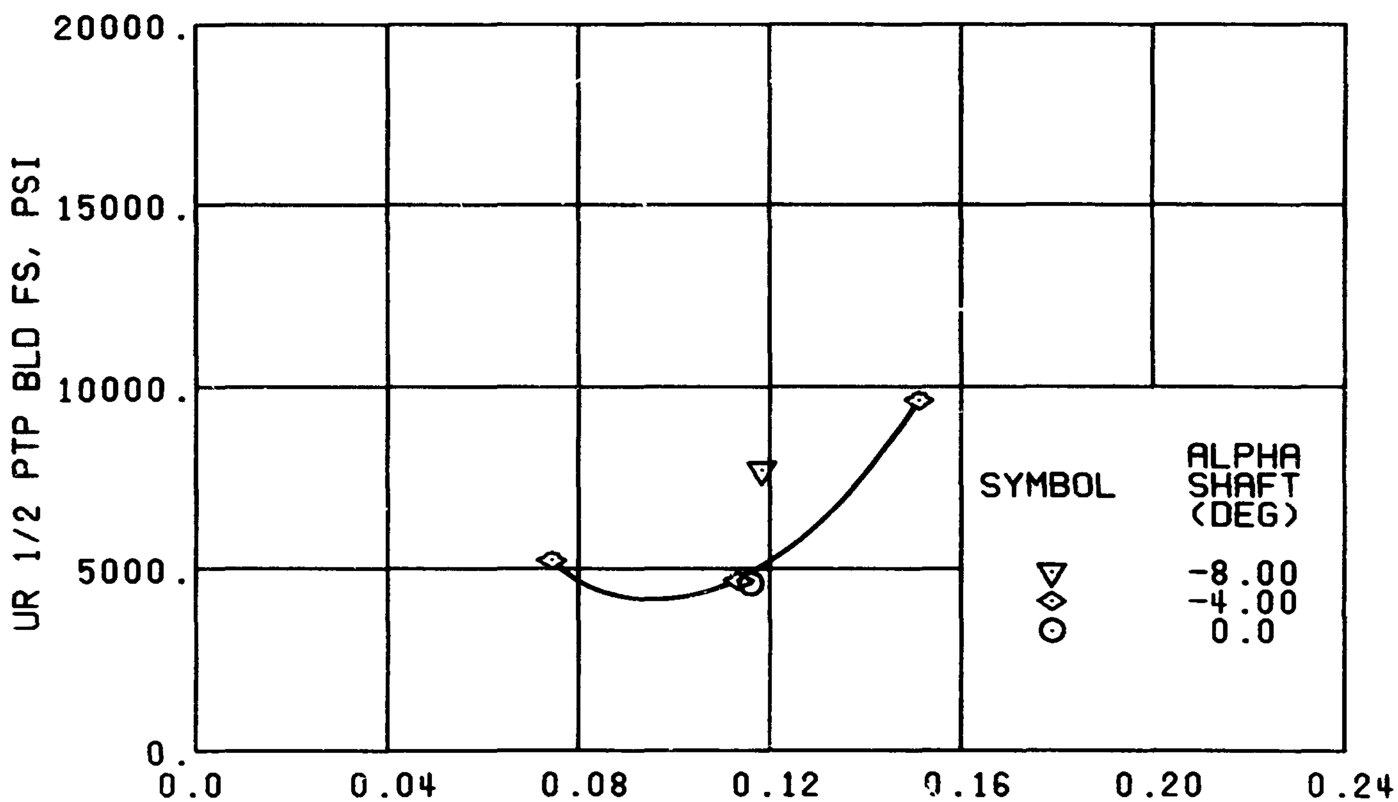

(d) GAGE 53 R132

Figure 47. Continued.
$\mu = 0.35$ $B'_{1s} = 6$ Deg

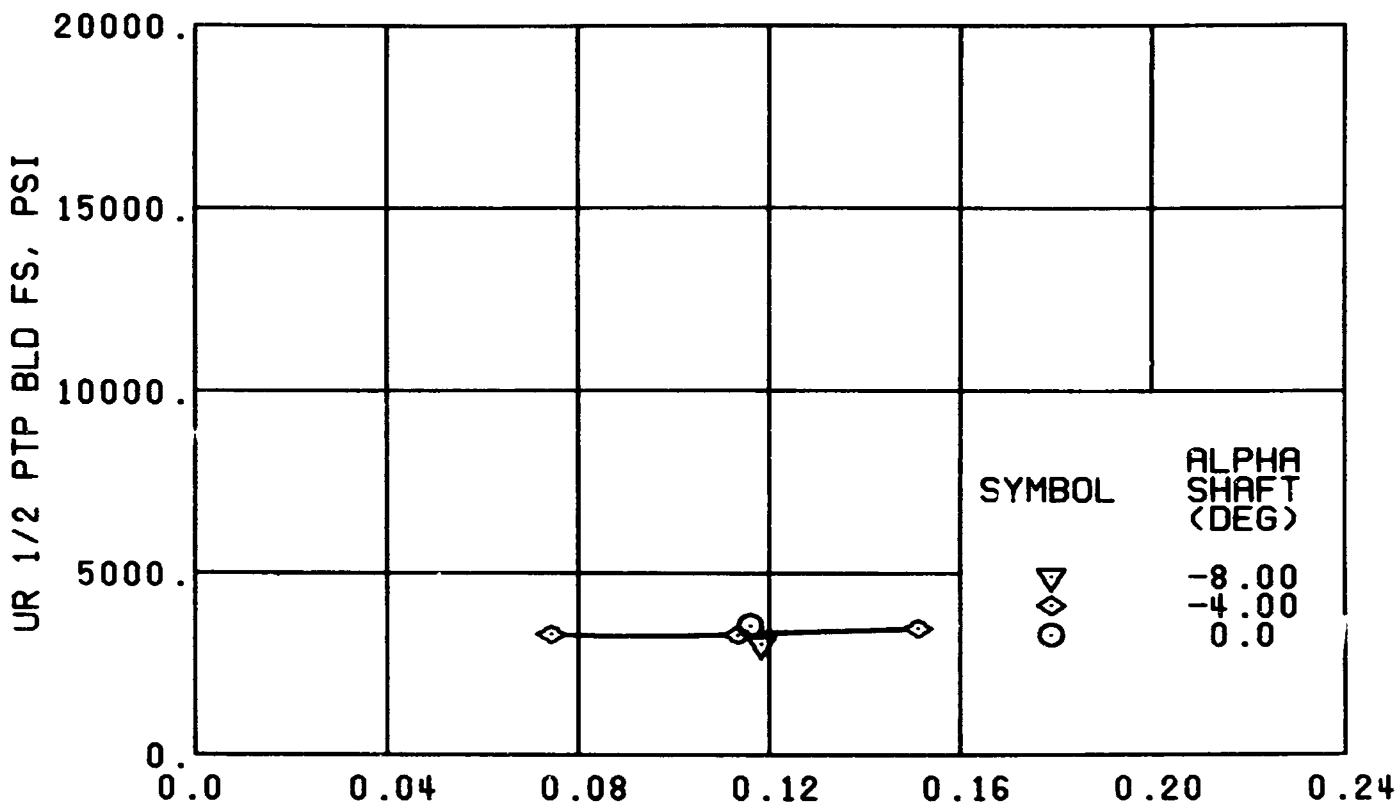

(f) GAGE 55 R204

Figure 47. Continued.
$\mu = 0.35$ $B'_{1s} = 6$ Deg

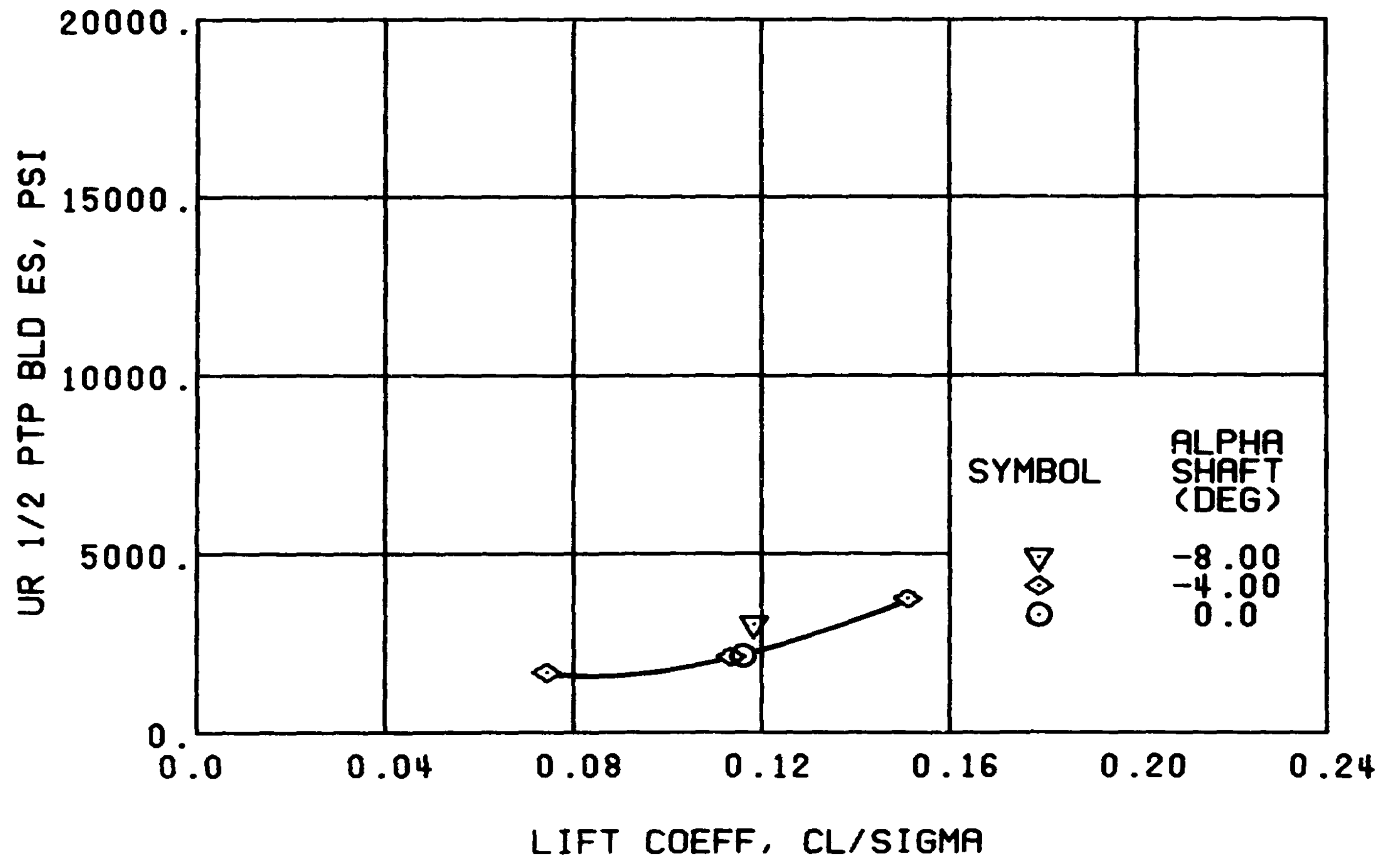

(h) GAGE 40 R84

Figure 47. Continued.
$\mu = 0.35$ $B'_{1s} = 6$ Deg

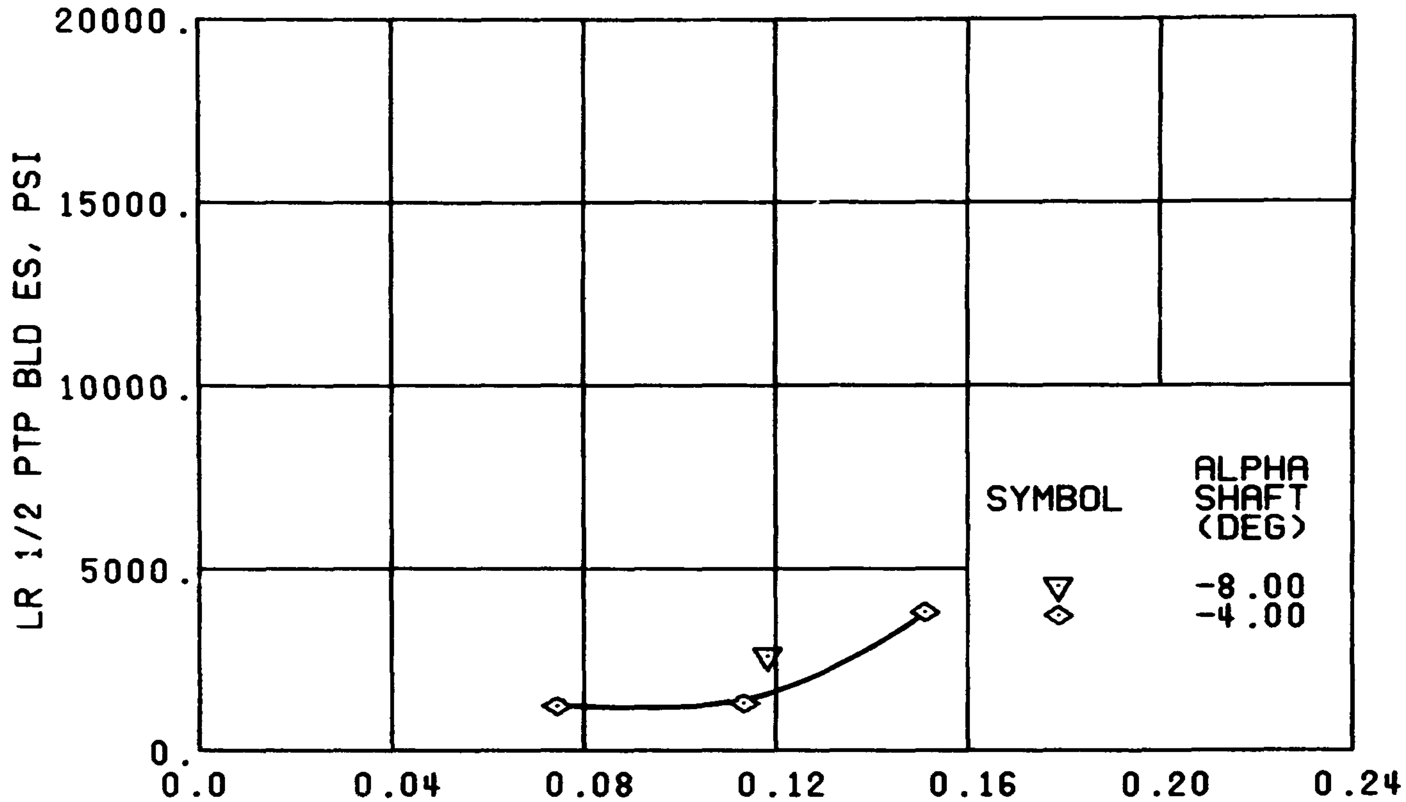

(i) GAGE 2 R84

Figure 47. Continued.
$\mu = 0.35$ $B'_{1s} = 6$ Deg

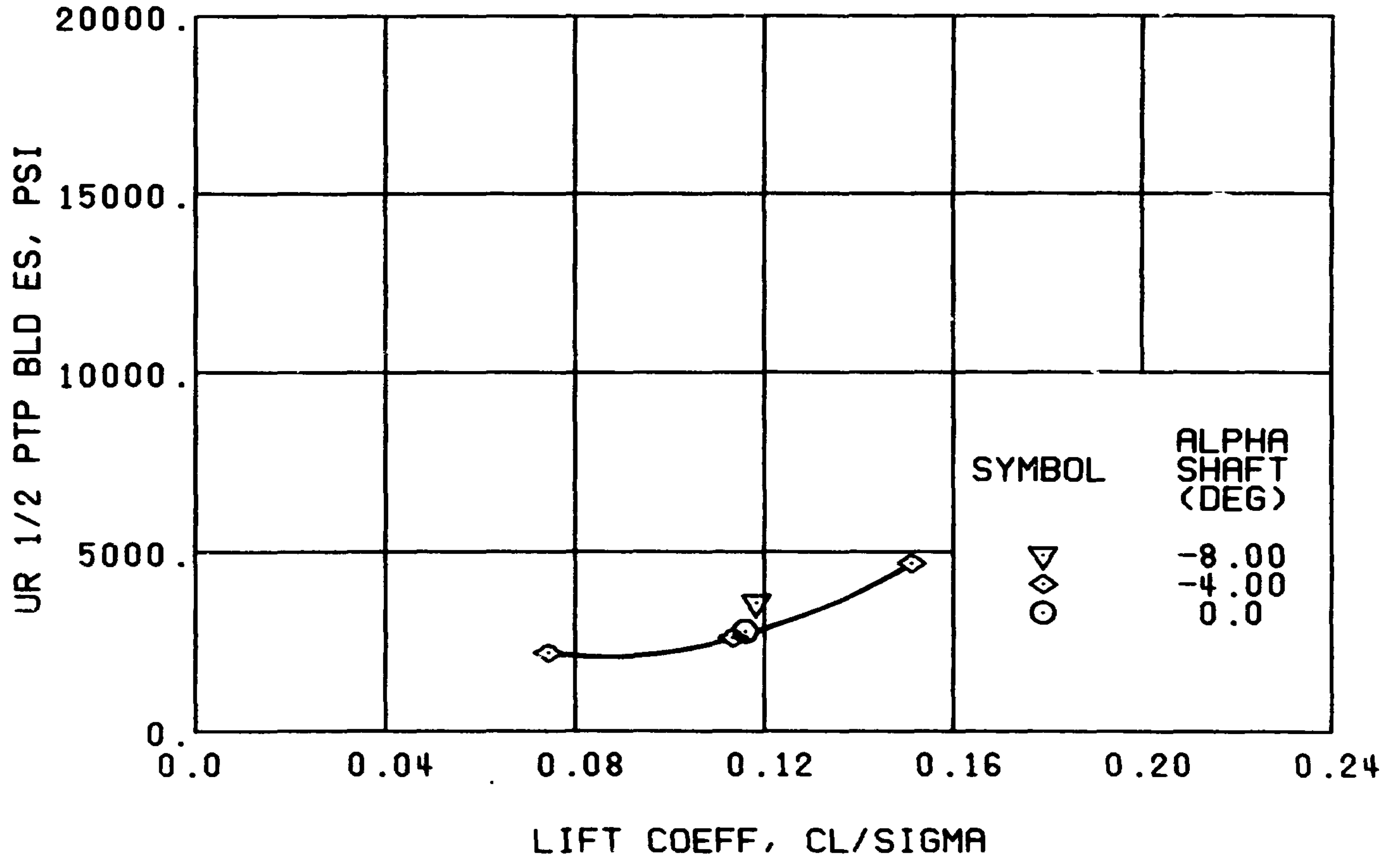

(j) GAGE 42 R132

Figure 47. Continued.
$\mu = 0.35 \quad B'_{1s} = 6$ Deg

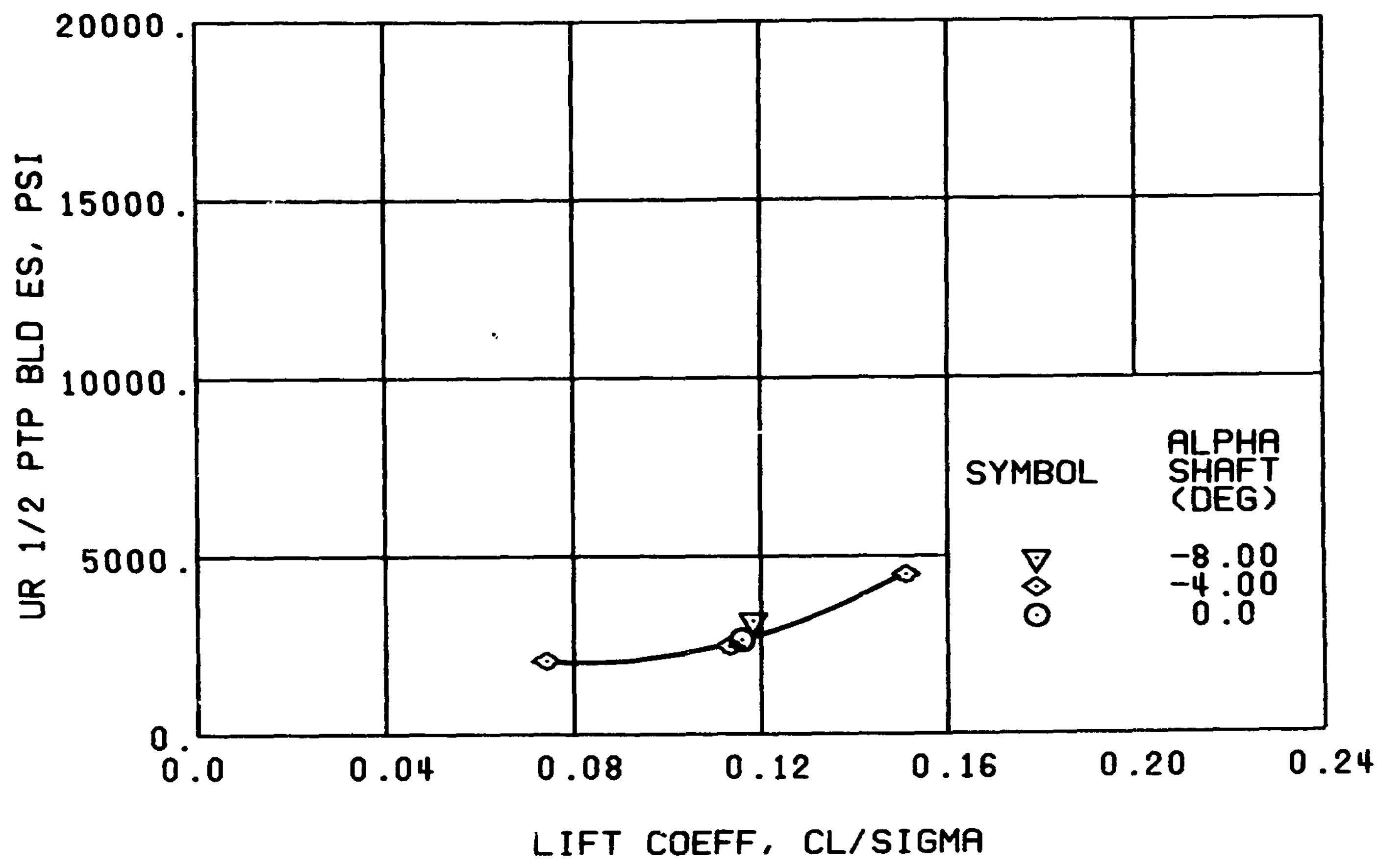

(k) GAGE 43 R168

Figure 47. Continued.
$\mu = 0.35$ $B'_{1s} = 6$ Deg

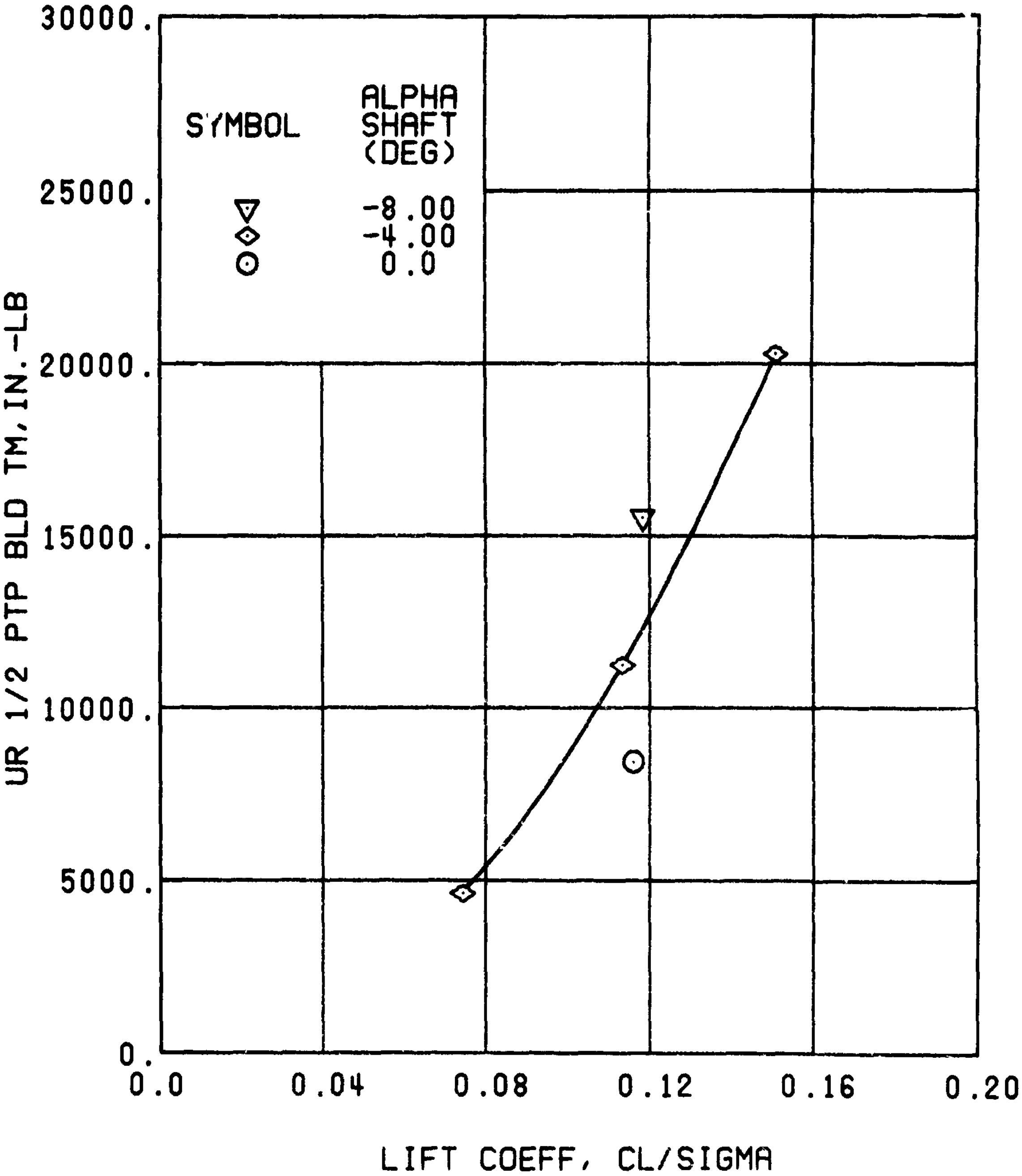

(I) GAGE 45 R82

Figure 47. Continued.
$\mu = 0.35$ $B'_{1s} = 6$ Deg

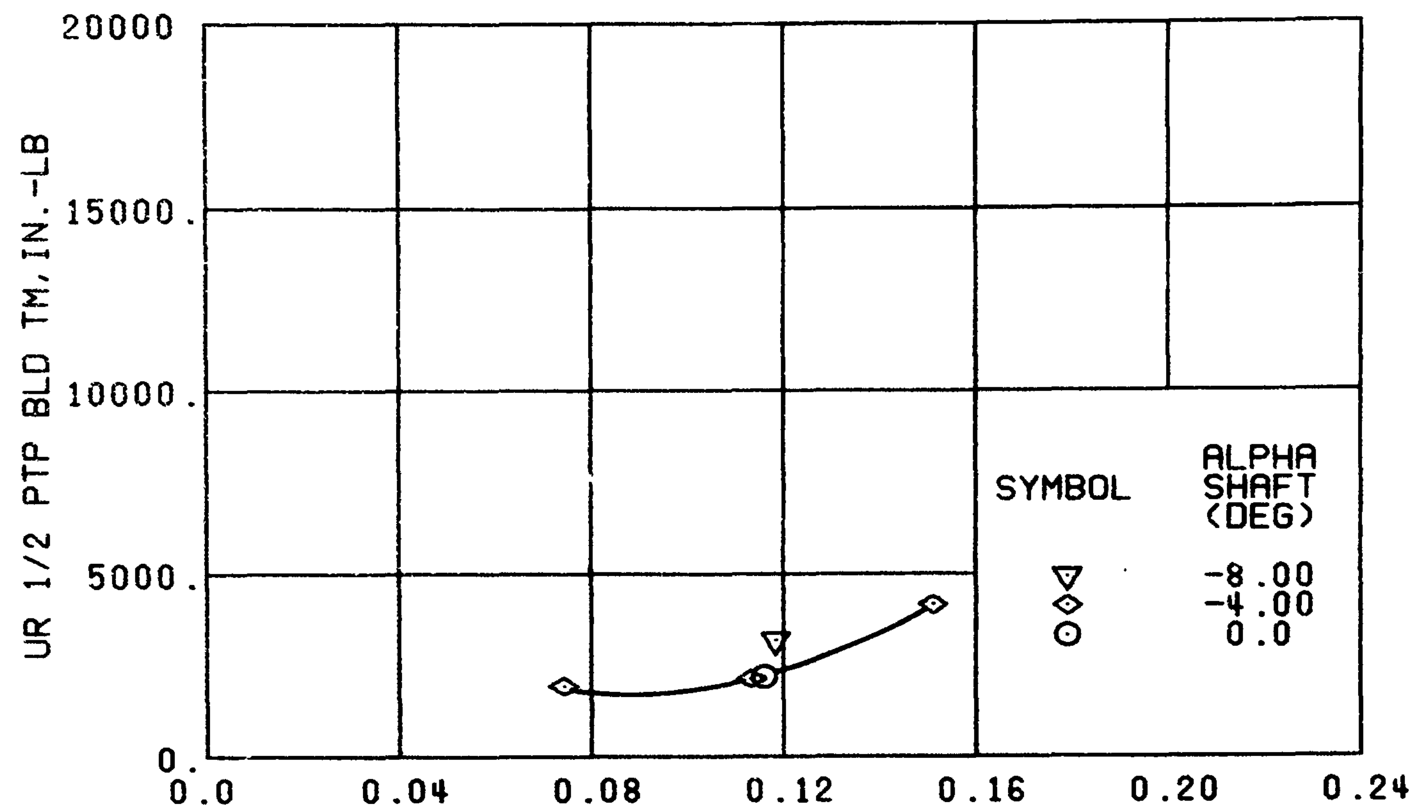

(m) GAGE 46 R130

Figure 47. Continued.
$\mu = 0.35$ $B'_{1s} = 6$ Deg

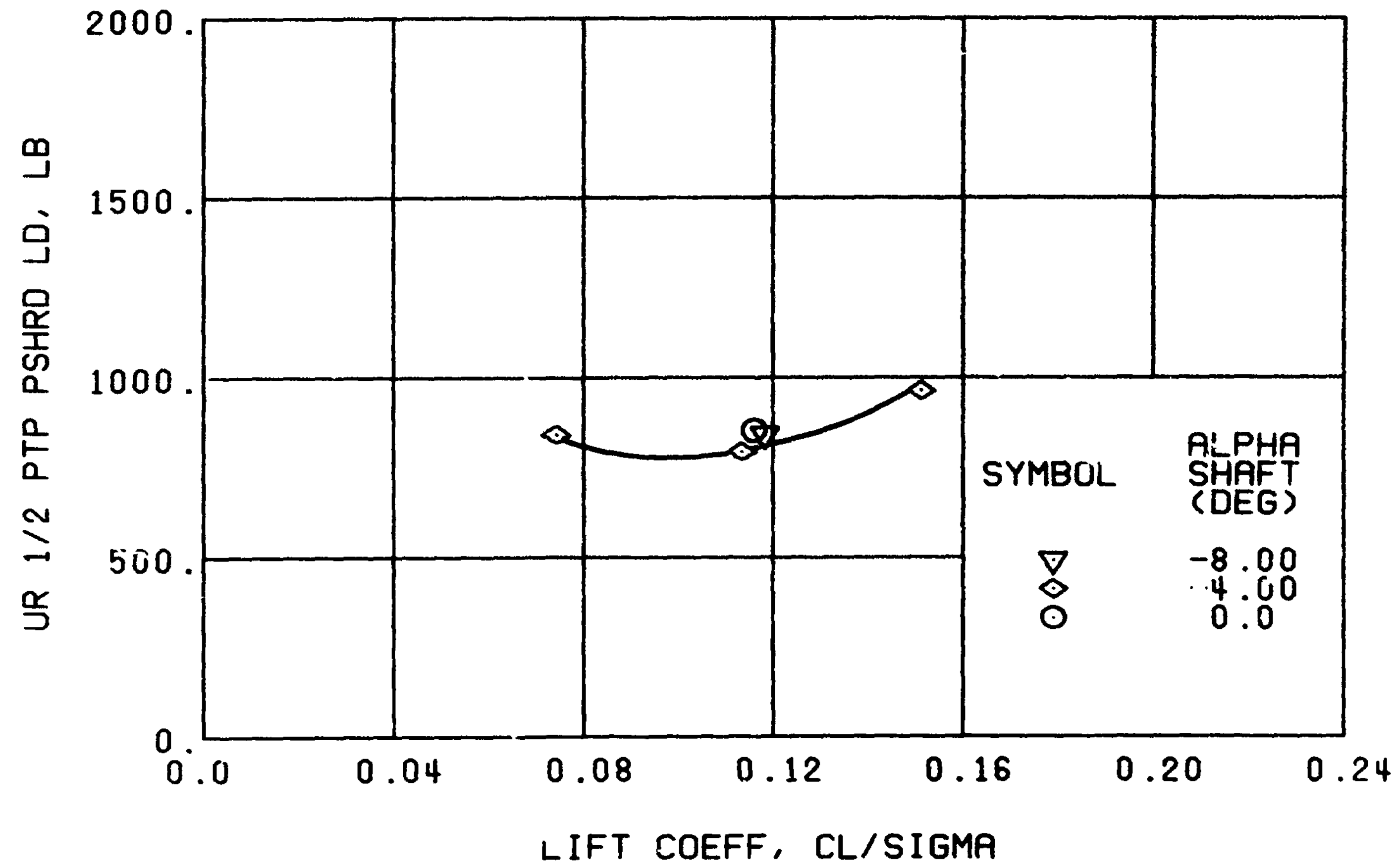

(n) GAGE 37

Figure 47. Continued.
$\mu = 0.35$ $B'_{1s} = 6$ Deg

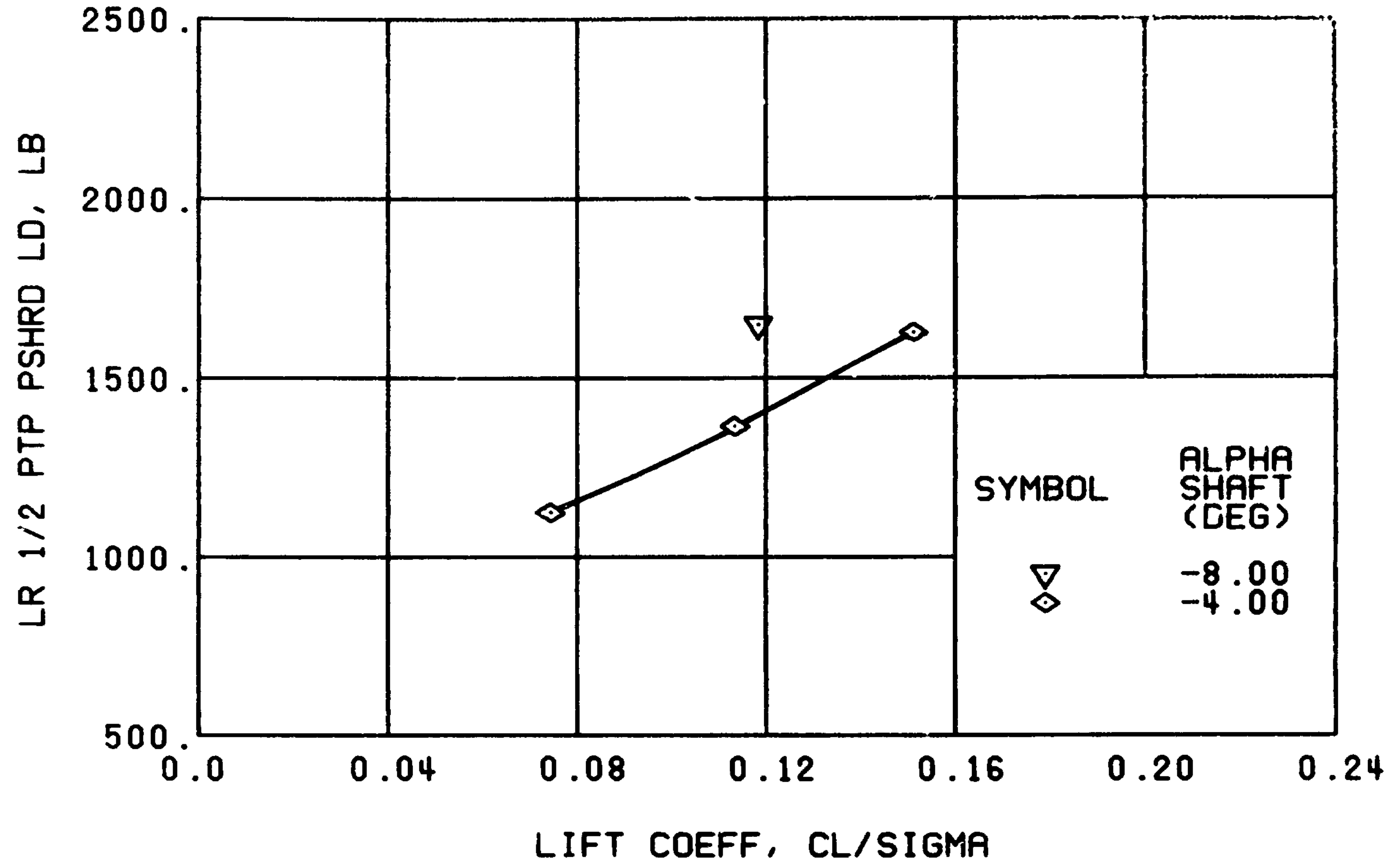

(o) GAGE 34

Figure 47. Continued.
$\mu = 0.35$ $B'_{1s} = 6$ Deg

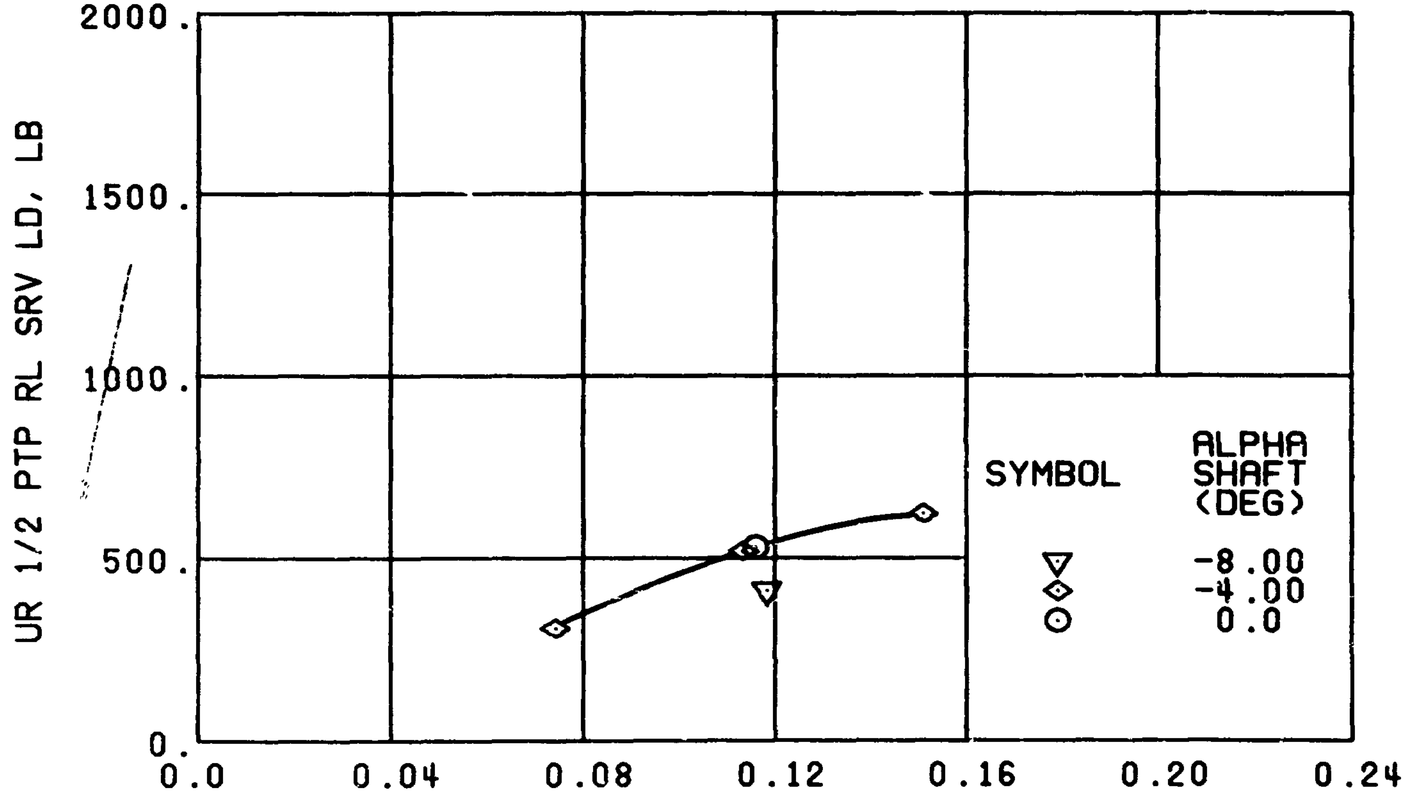

(p) GAGE 22

Figure 47. Continued.
$\mu = 0.35$ $B'_{1s} = 6$ Deg

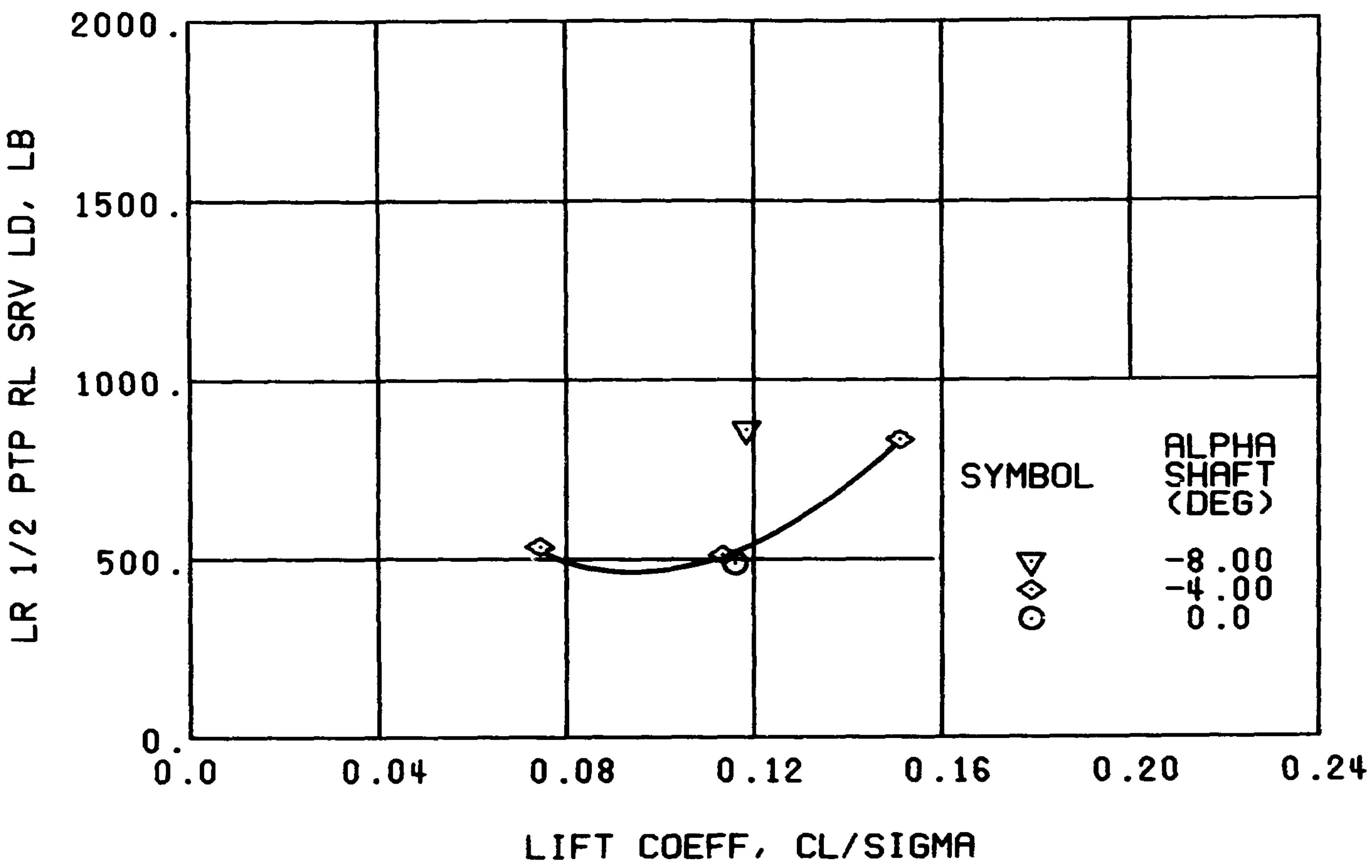

(q) GAGE 25

Figure 47. Continued.
$\mu = 0.35$ $B'_{1s} = 6$ Deg

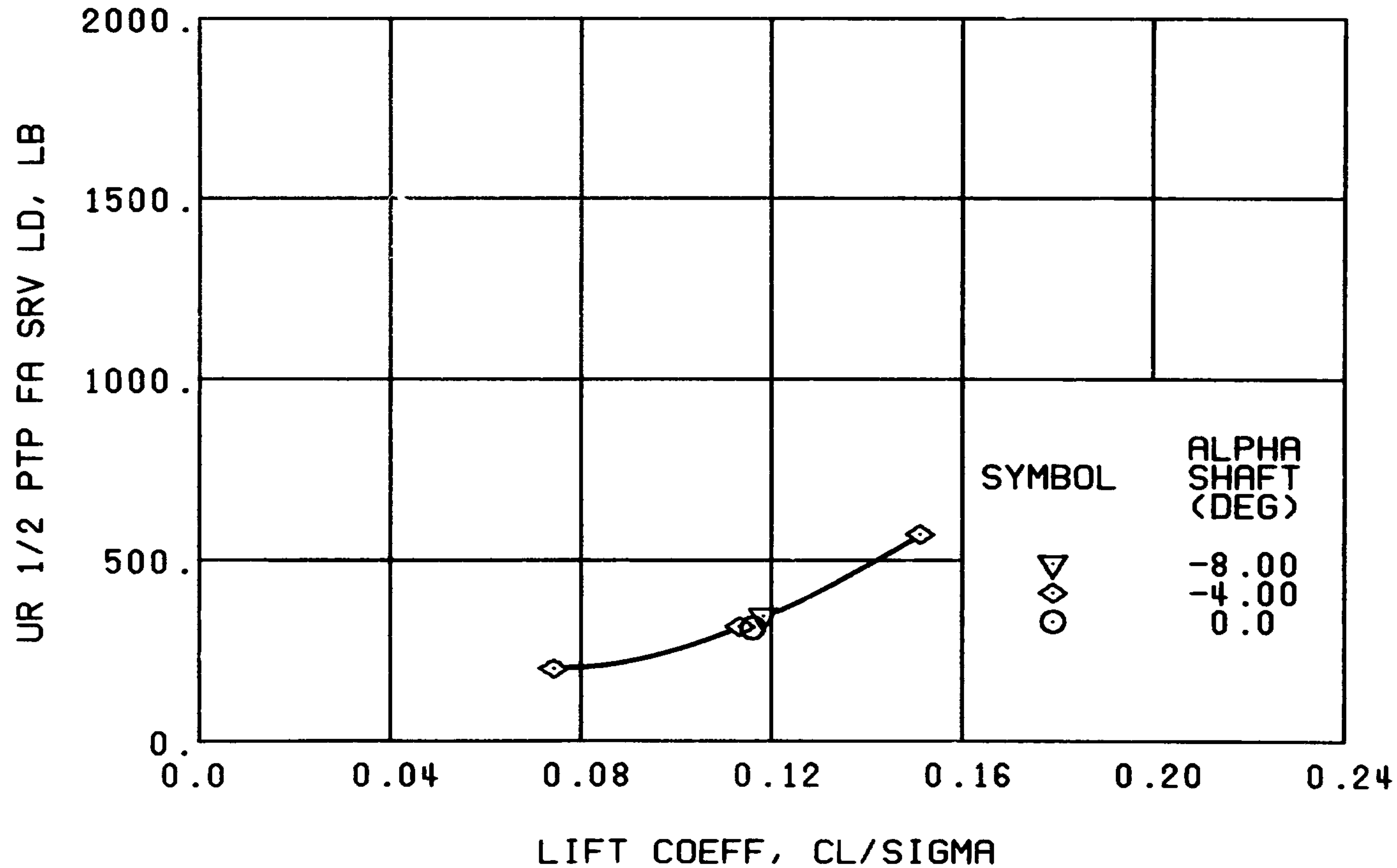

(r) GAGE 24

Figure 47. Continued.
$\mu = 0.35 \quad B'_{1s} = 6$ Deg

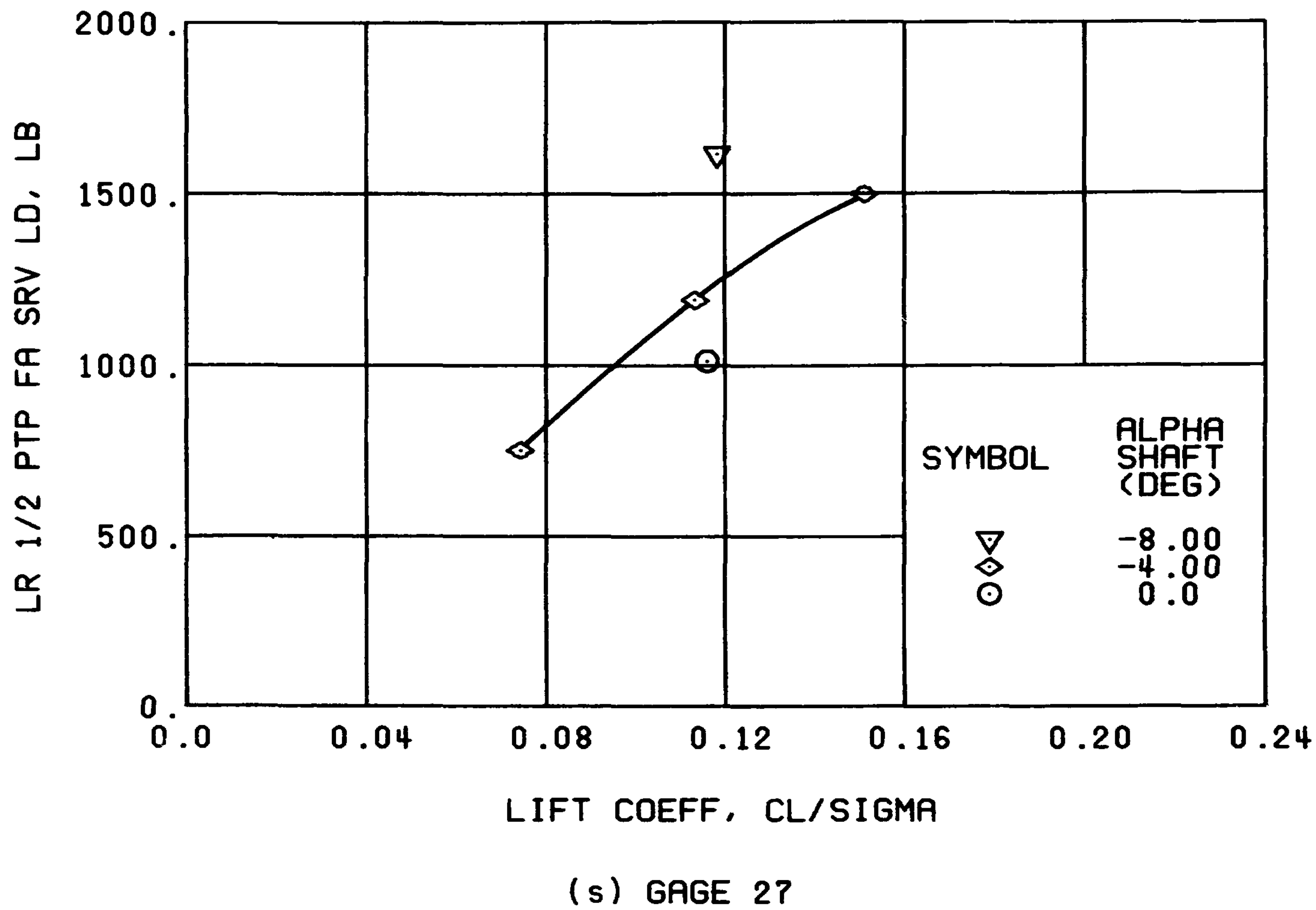

Figure 47. Continued.
$\mu = 0.35$ $B'_{1s} = 6$ Deg

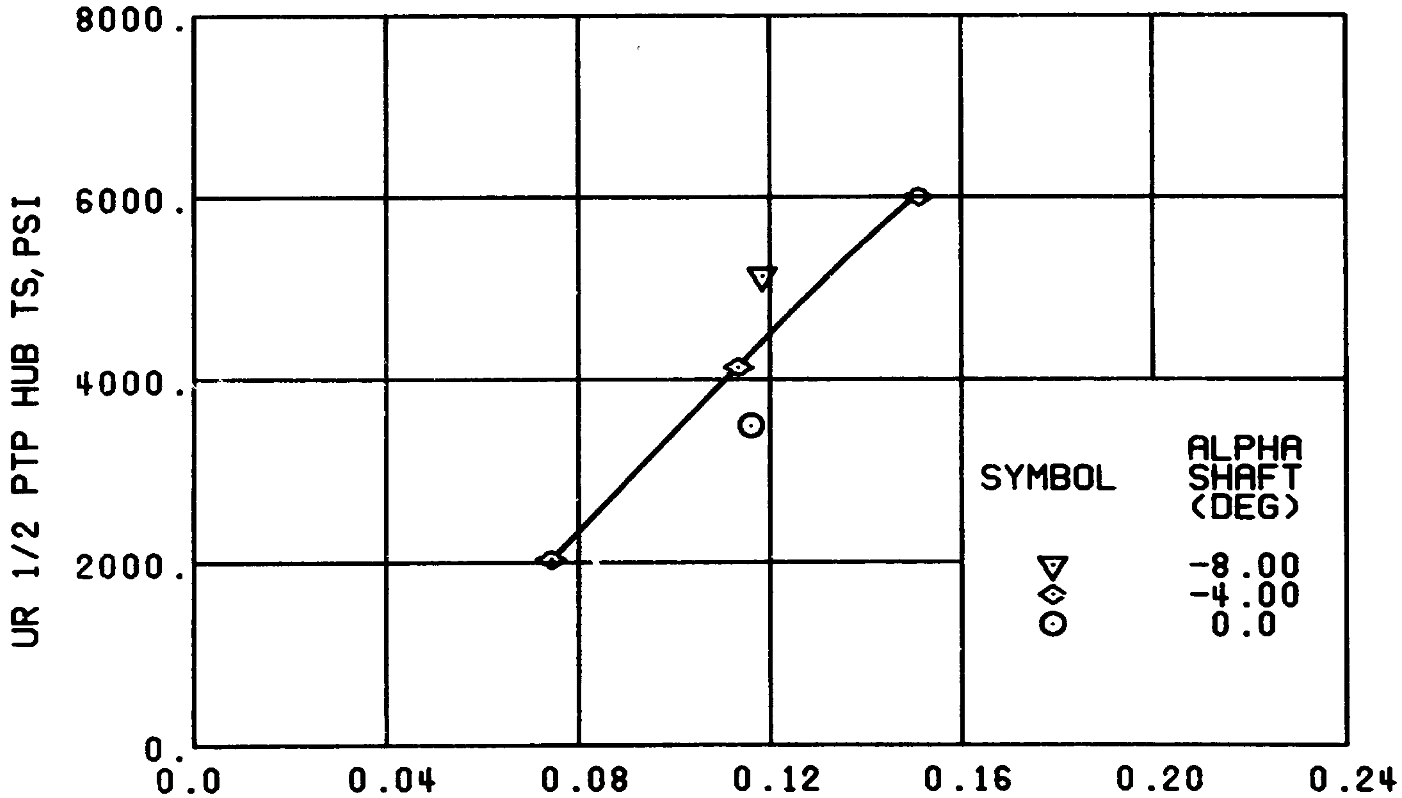

(f) GAGE 65

Figure 47. Continued.
$\mu = 0.35 \quad B'_{1s} = 6$ Deg

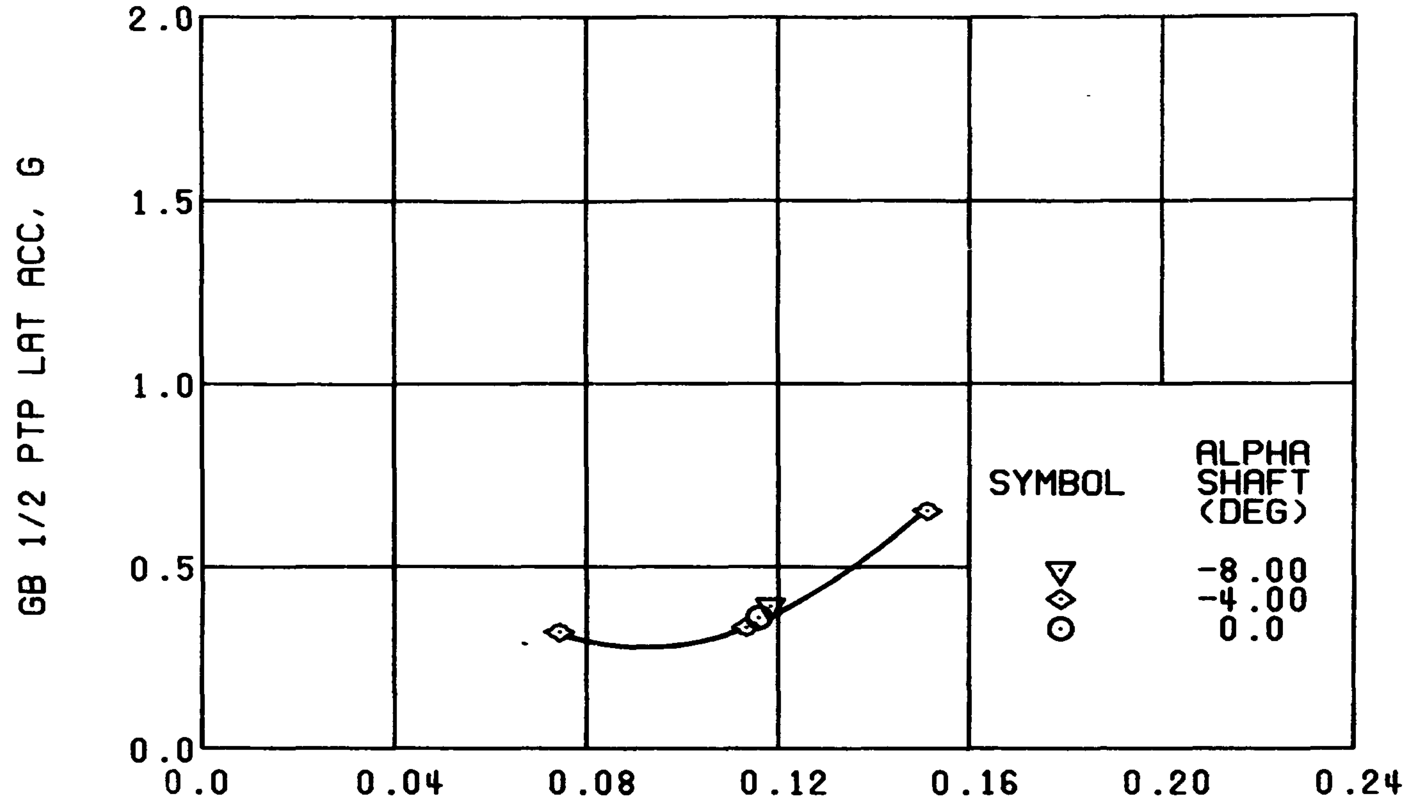

(u) GAGE 15 STA 76, BL 30

Figure 47. Continued.
$\mu = 0.35$ $B_{1s}' = 6$ Deg

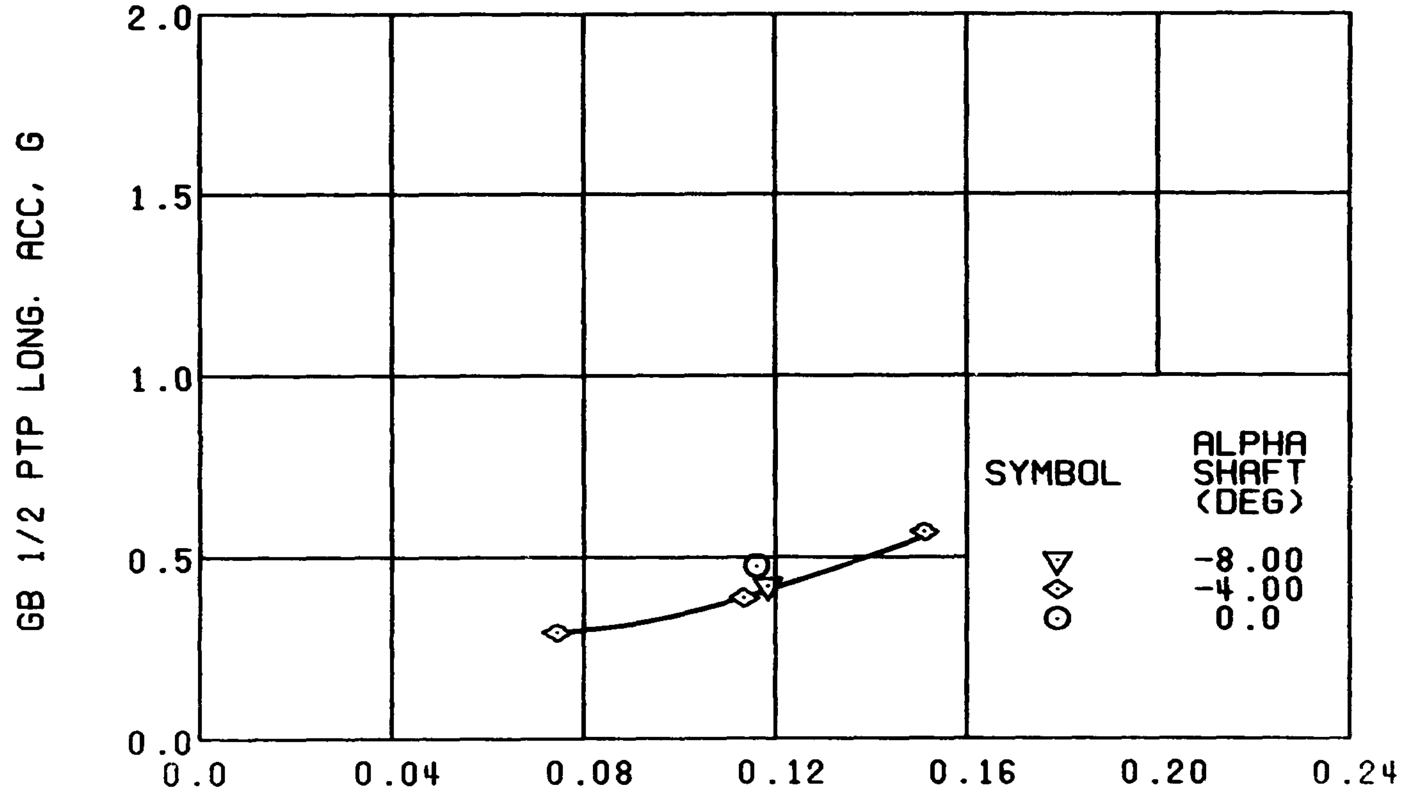

(v) GAGE 14 STA 61, BL 0

Figure 47. Continued.
$\mu = 0.35$ $B'_{1s} = 6$ Deg

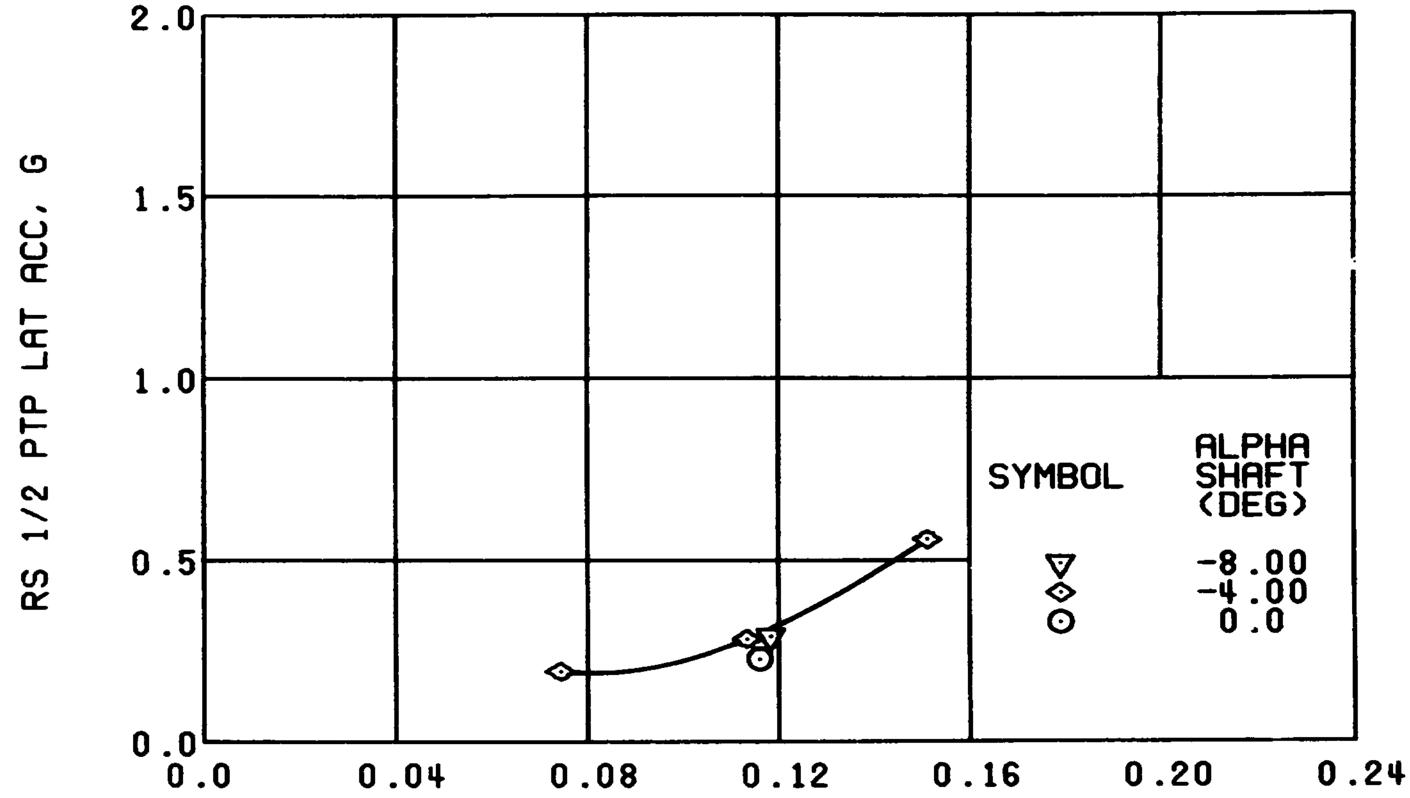

(w) GAGE 16 ROVER 3

Figure 47. Continued.
$\mu = 0.35 \quad B'_{1s} = 6$ Deg

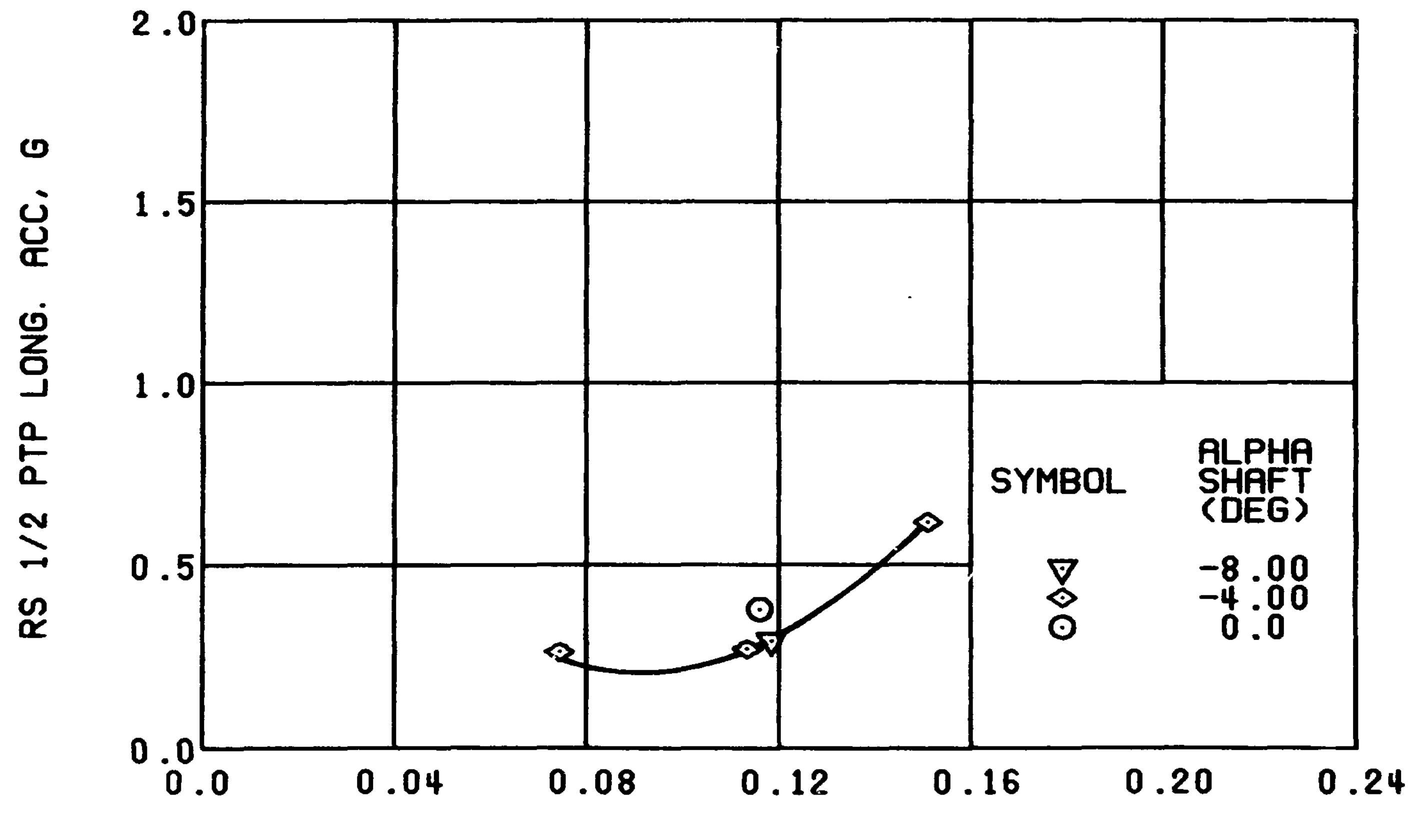

(x) GAGE 17 ROVER 4

Figure 47. Concluded.
$\mu = 0.35$ $B'_{1s} = 6$ Deg

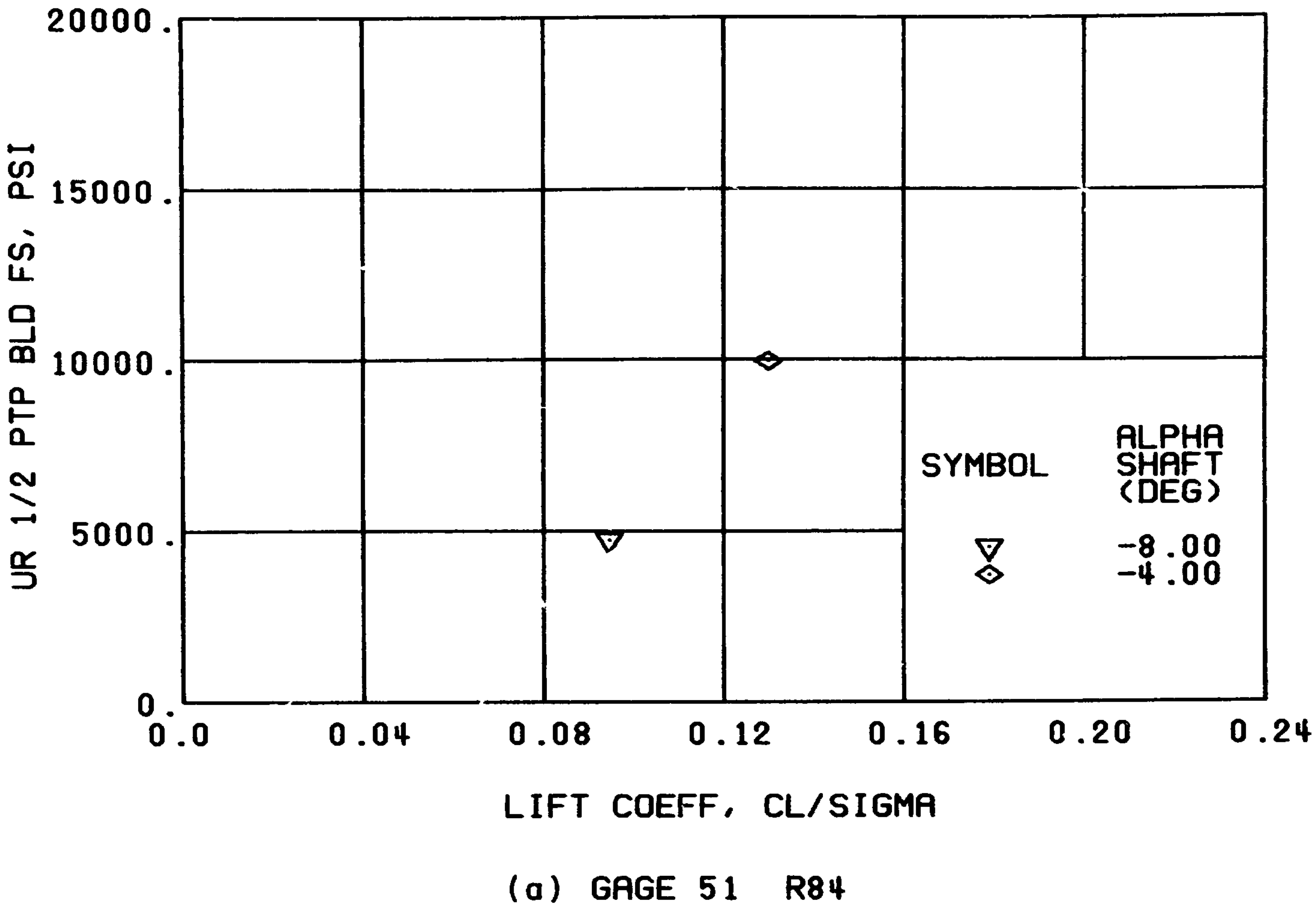

Figure 48. Stress, Load, and Vibration Data at an Advance Ratio of 0.35 With the Lateral Displacement Control (B'_{1s}) Set at 8 Degrees.

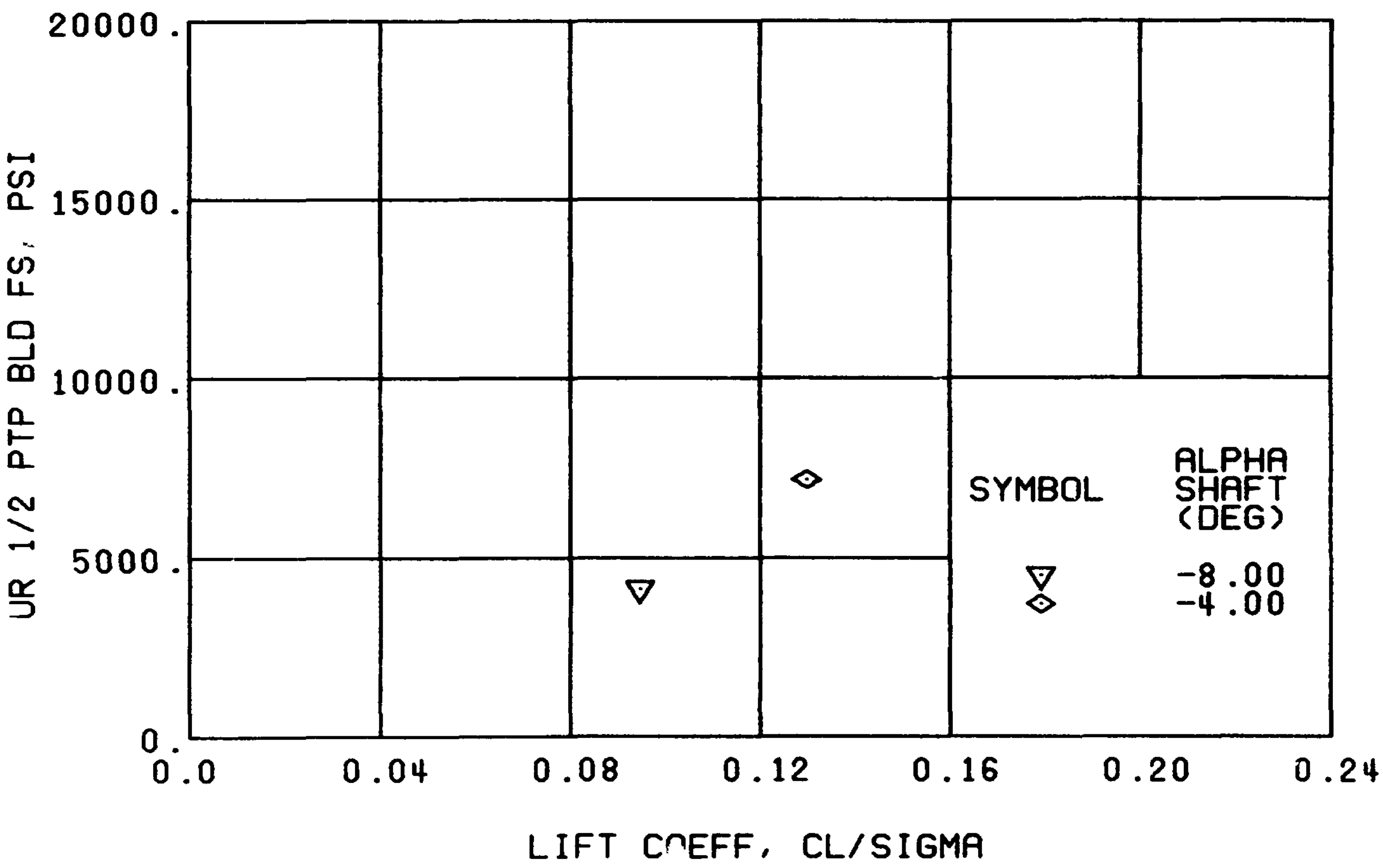

(c) GAGE 52 R108

Figure 48. Continued.
$\mu = 0.35$ $B'_{1s} = 8$ Deg

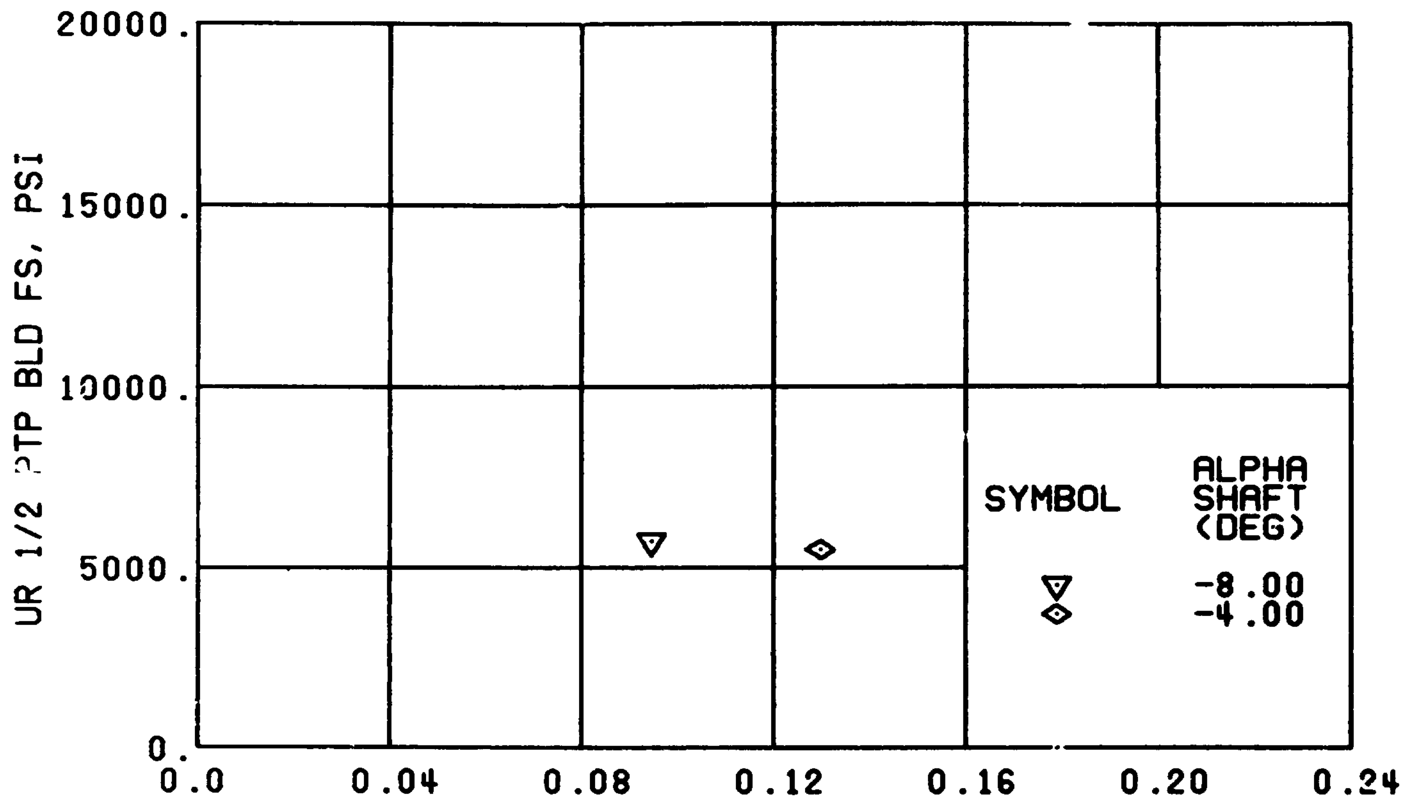

(d) GAGE 53 R132

Figure 48. Continued.
$\mu = 0.35$ $B'_{1s} = 8$ Deg

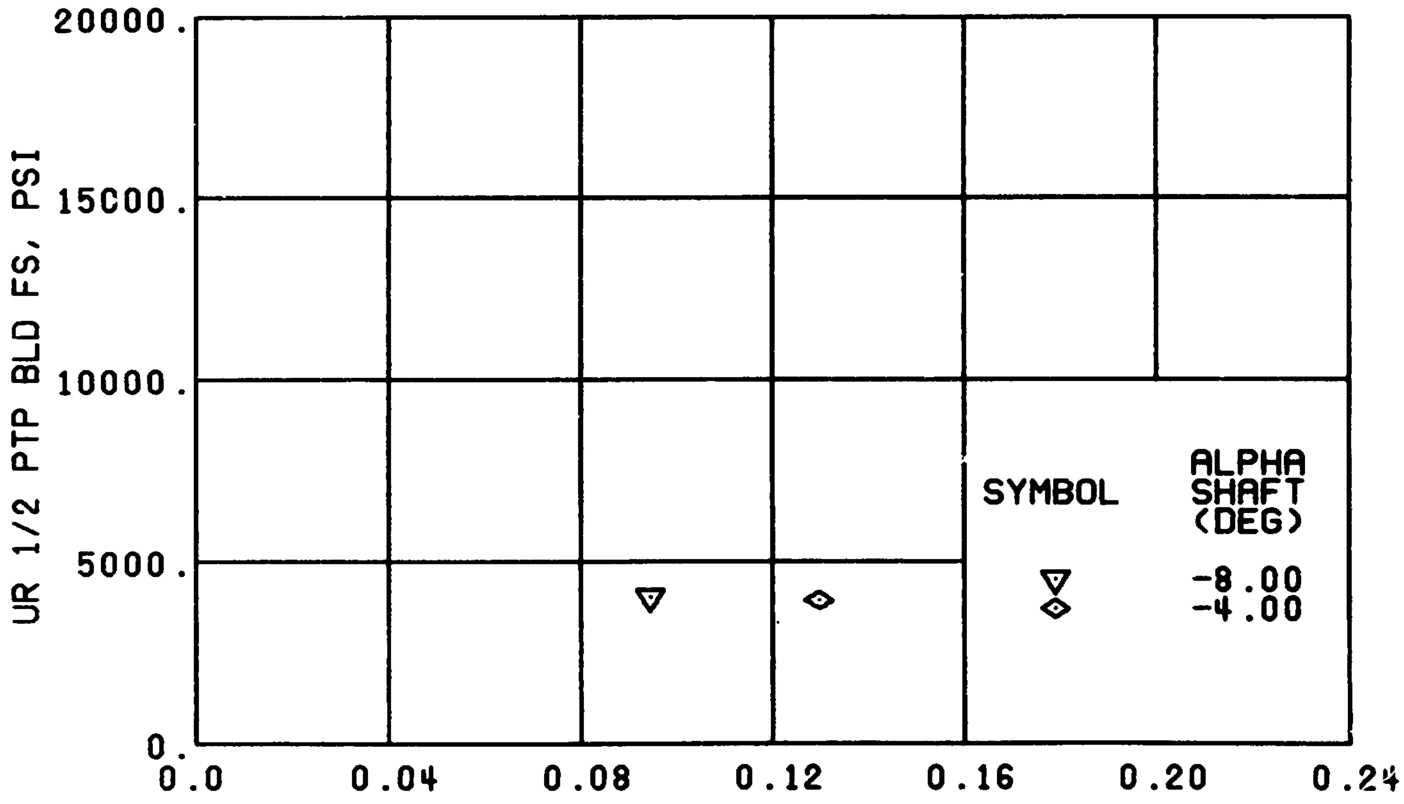

(f) GAGE 55 R204

Figure 48. Continued.
$\mu = 0.35$ $B'_{1s} = 8$ Deg

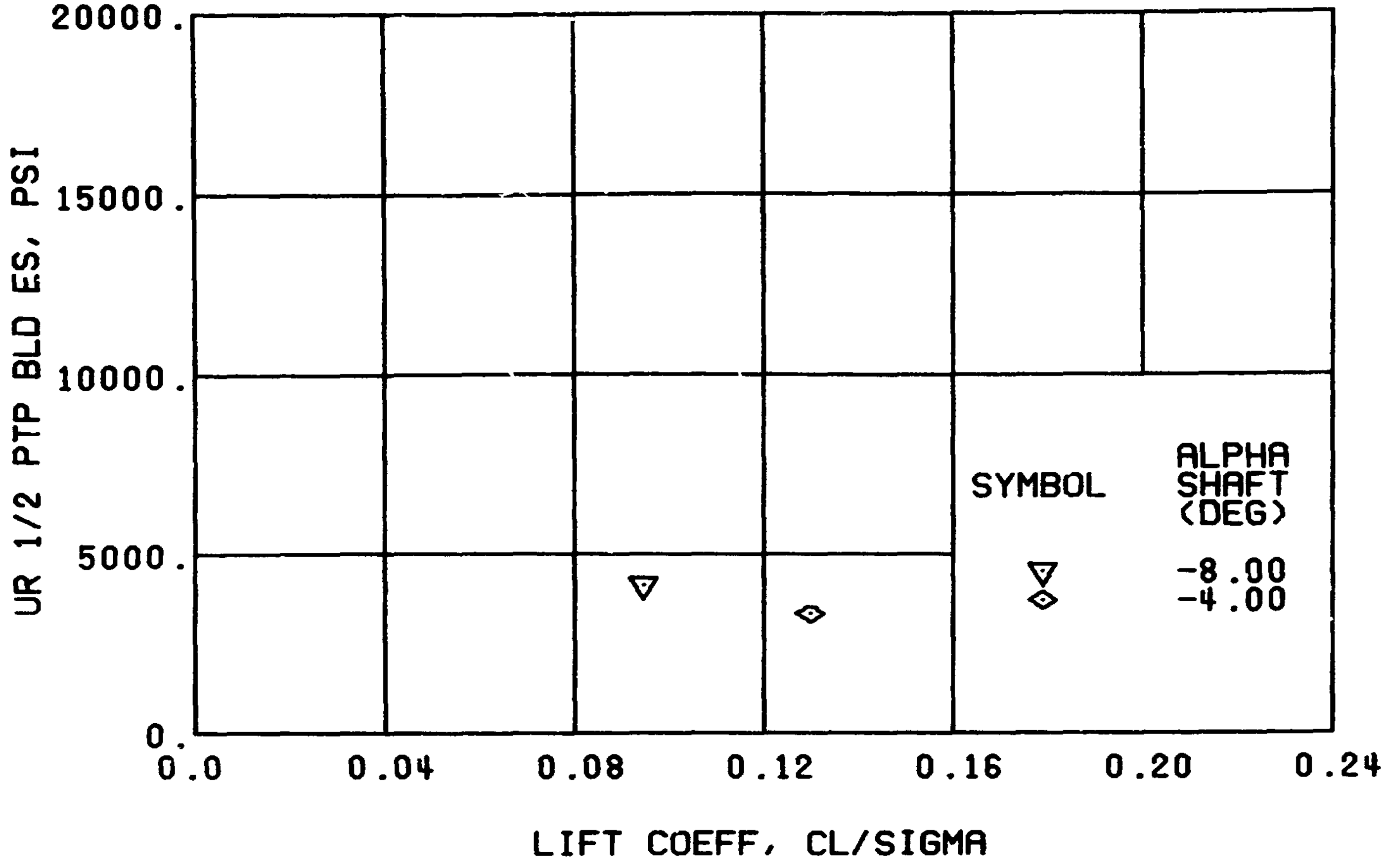

(h) GAGE 40 R84

Figure 48. Continued.
$\mu = 0.35$ $B'_{1s} = 8$ Deg

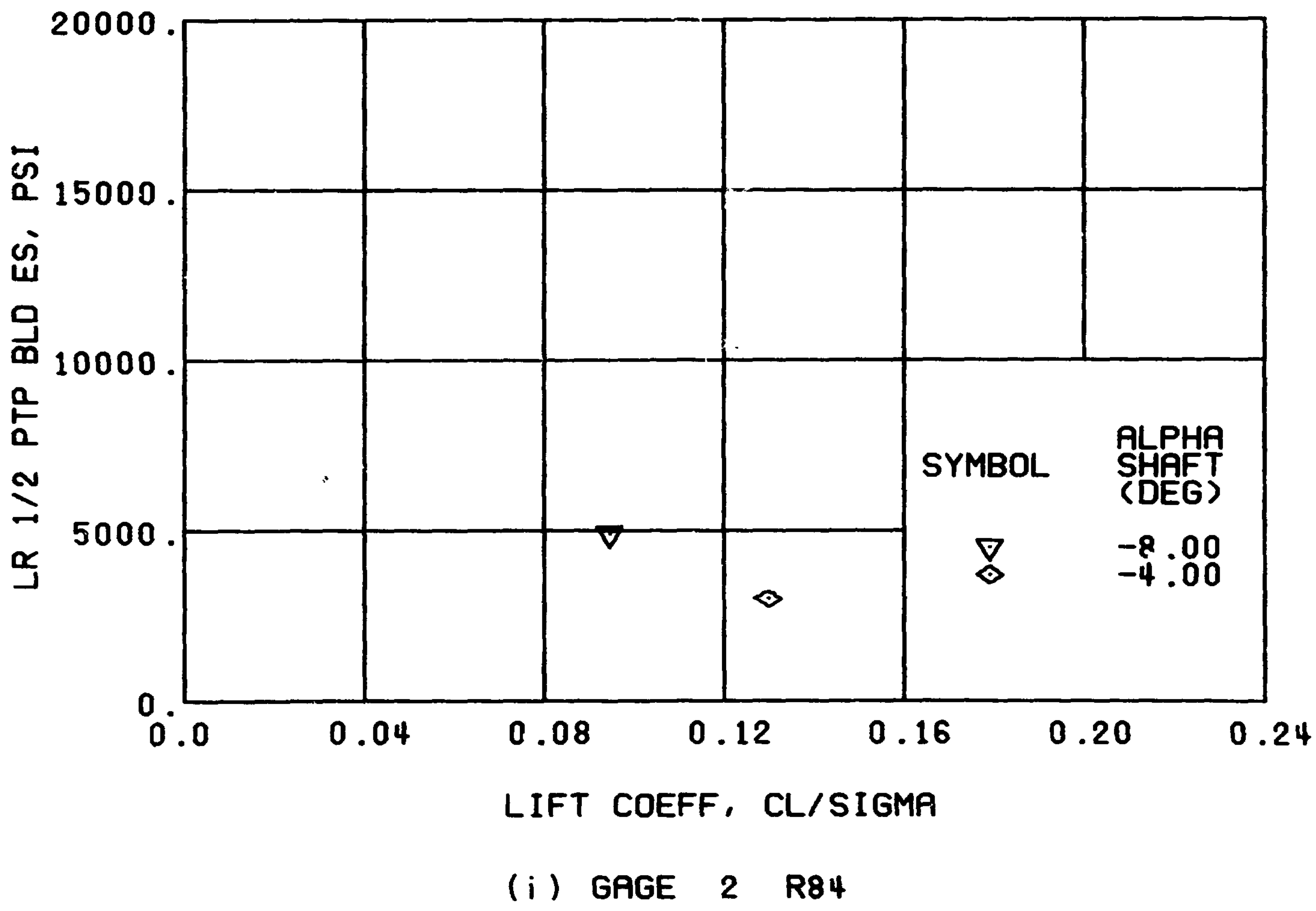

Figure 48. Continued.
$\mu = 0.35 \quad B'_{1s} = 8$ Deg

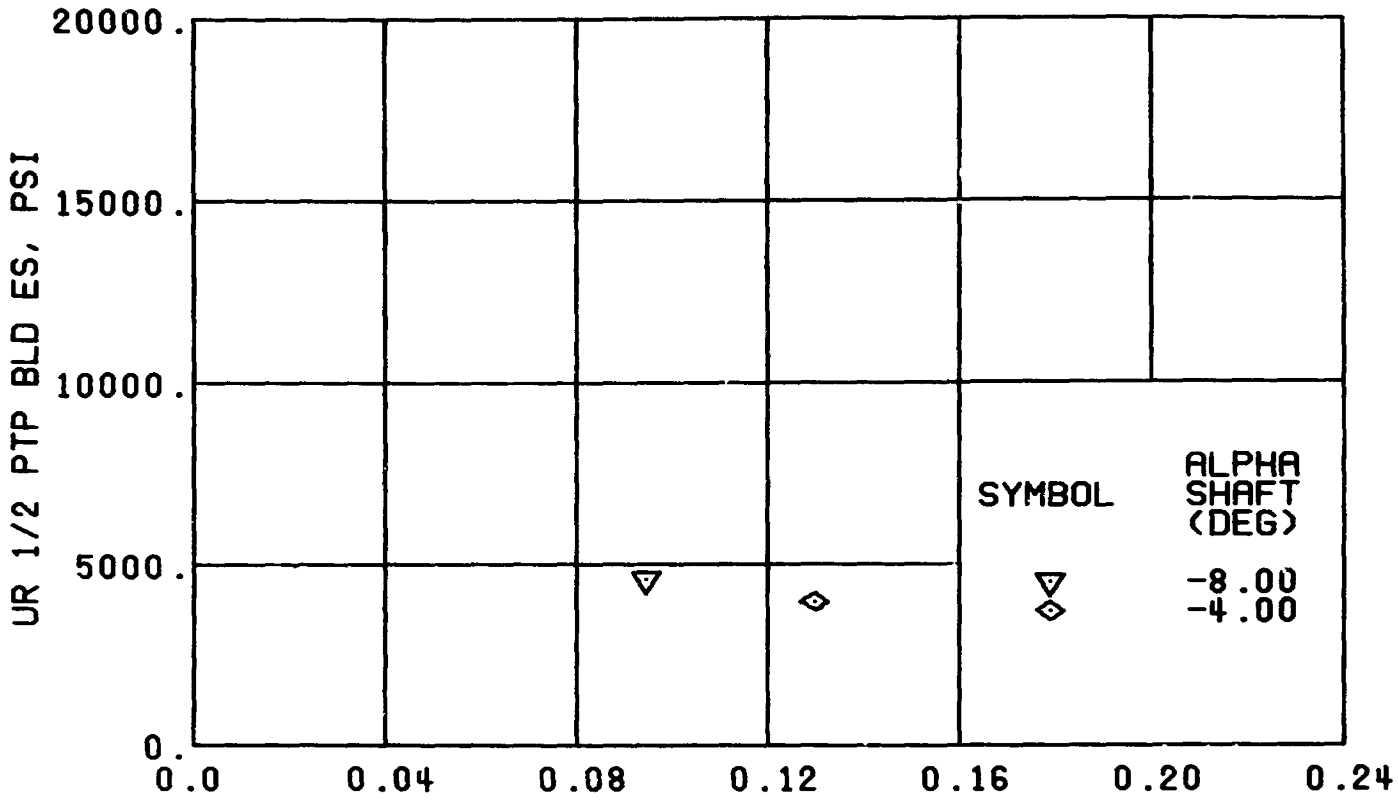

(j) GAGE 42 R132

Figure 48. Continued.
$\mu = 0.35$ $B'_{1s} = 8$ Deg

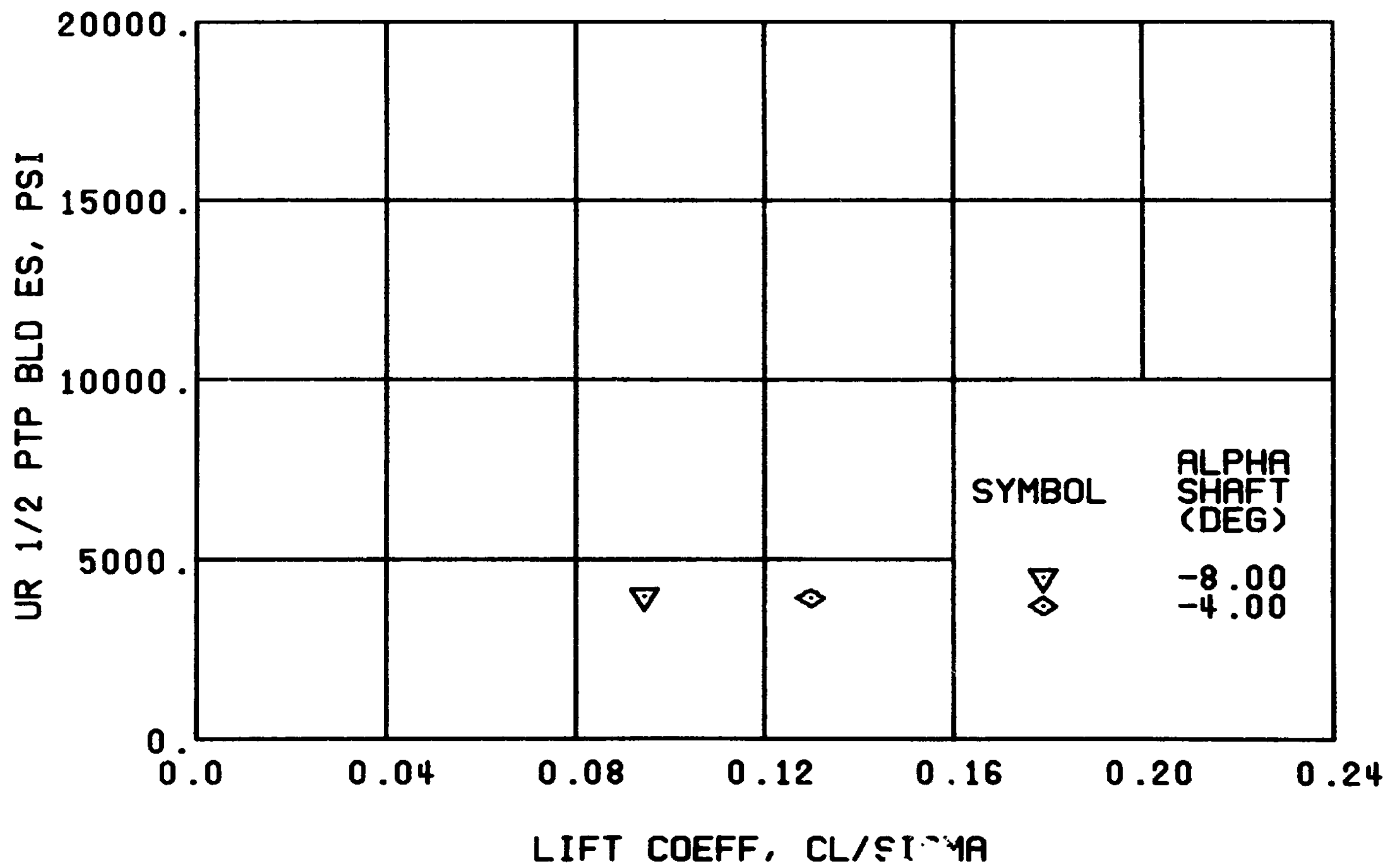

(k) GAGE 43 R168

Figure 48. Continued.
$\mu = 0.35 \quad B'_{1s} = 8$ Deg

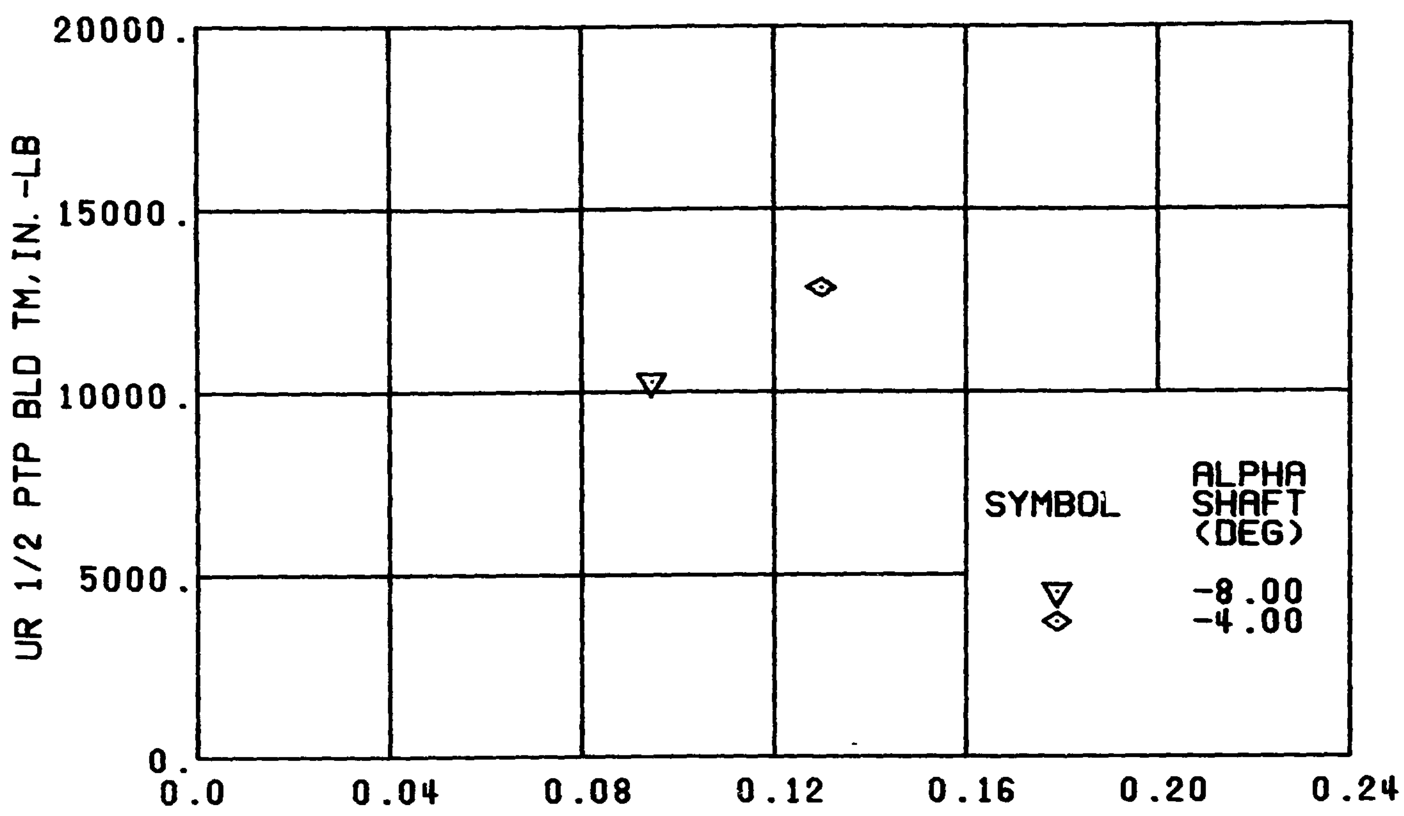

(I) GAGE 45 R82

Figure 48. Continued.
$\mu = 0.35 \quad B'_{1s} = 8$ Deg

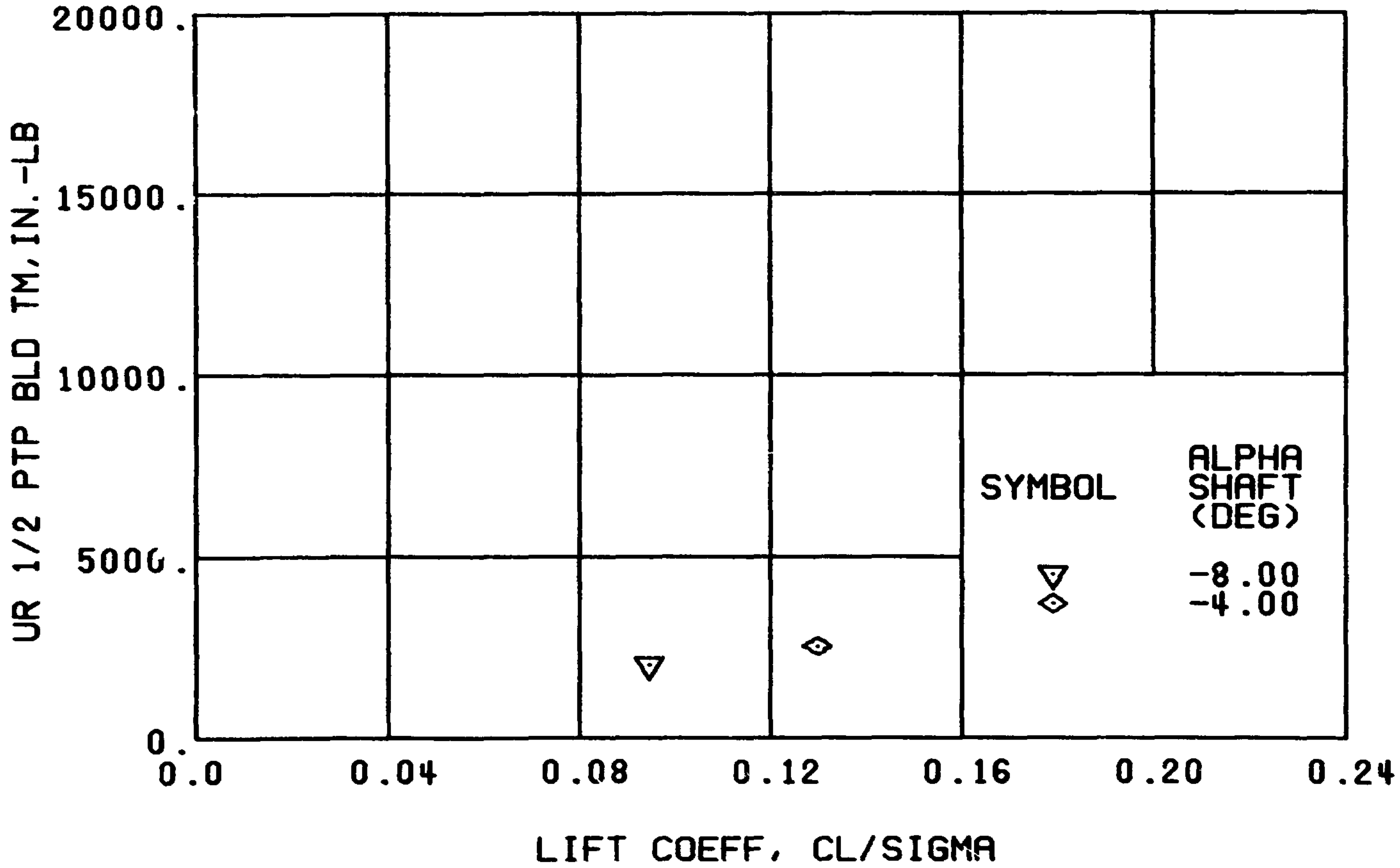

(m) GAGE 46 R130

Figure 48. Continued.
$\mu = 0.35$ $B'_{1s} = 8$ Deg

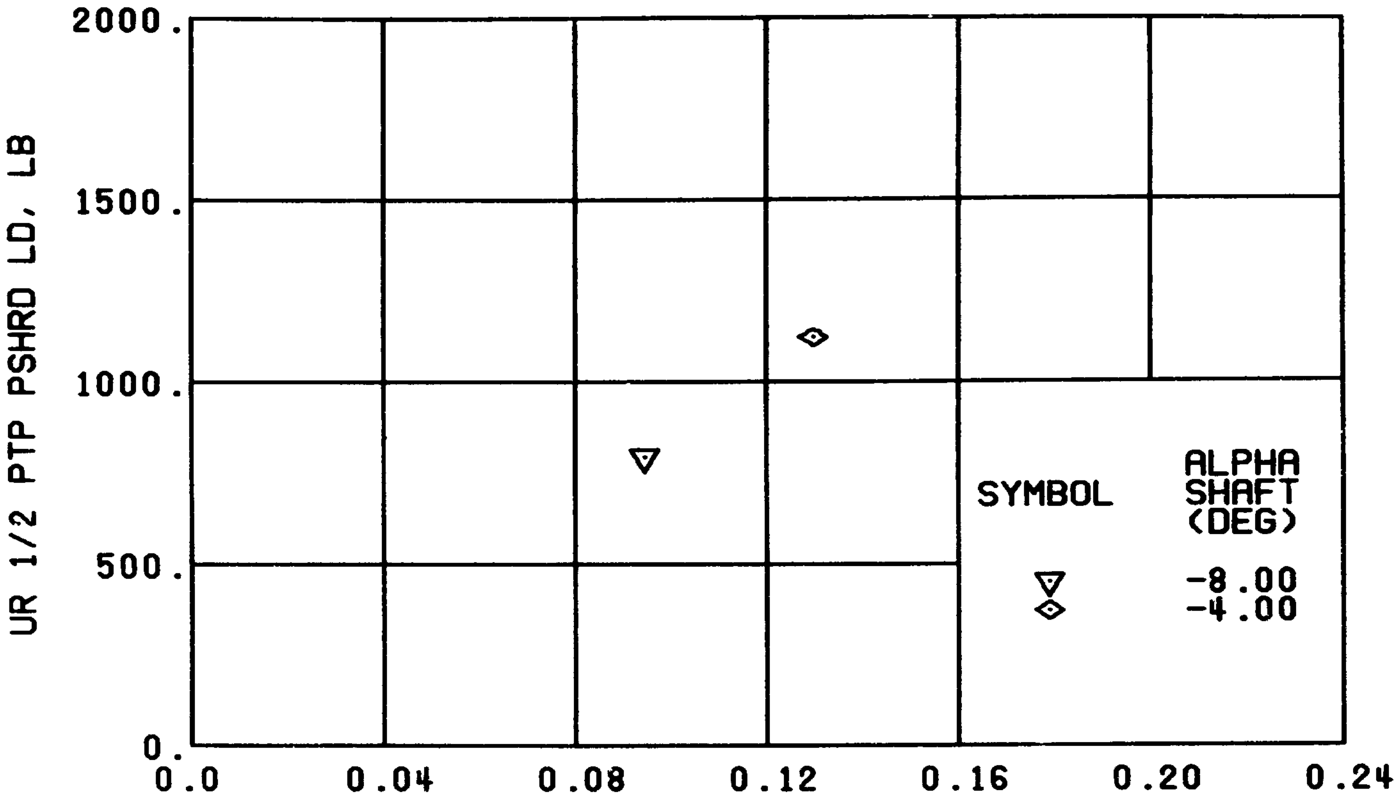

(n) GAGE 37

Figure 48. Continued.
$\mu = 0.35$ $B'_{1s} = 8$ Deg

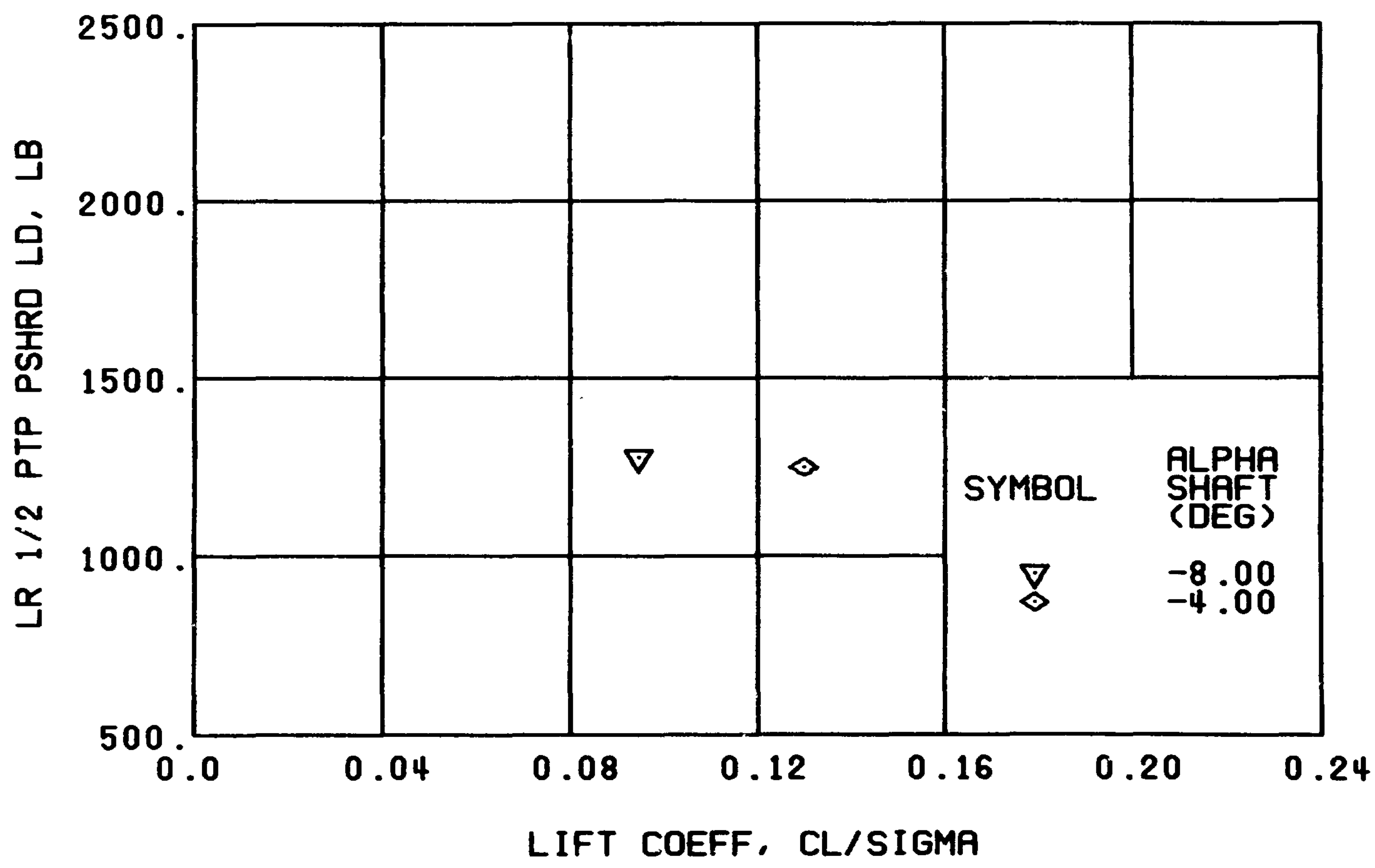

(o) GAGE 34

Figure 48. Continued.
$\mu = 0.35 \quad B'_{1s} = 8$ Deg

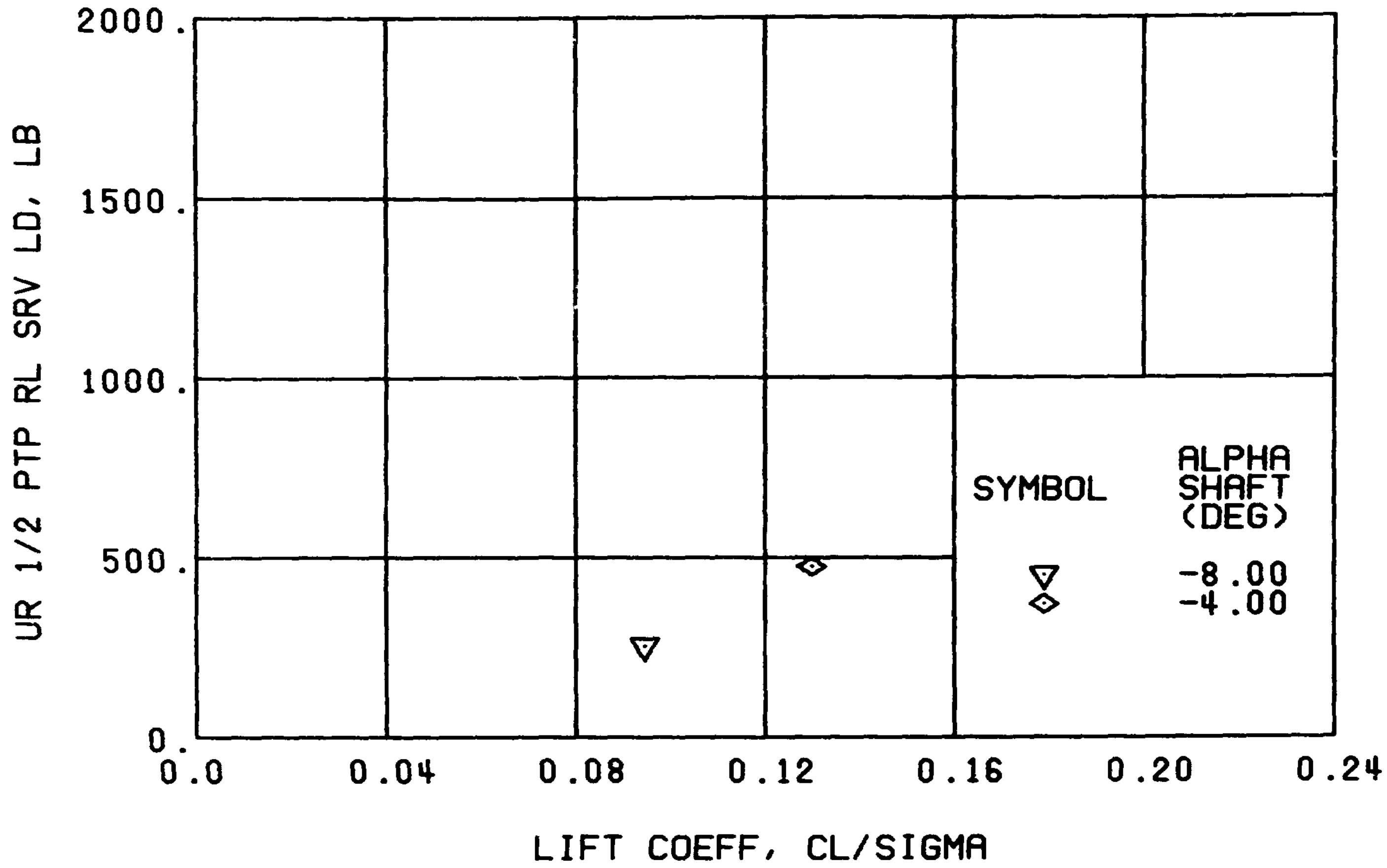

(p) GAGE 22

Figure 48. Continued.
$\mu = 0.35$ $B'_{1s} = 8$ Deg

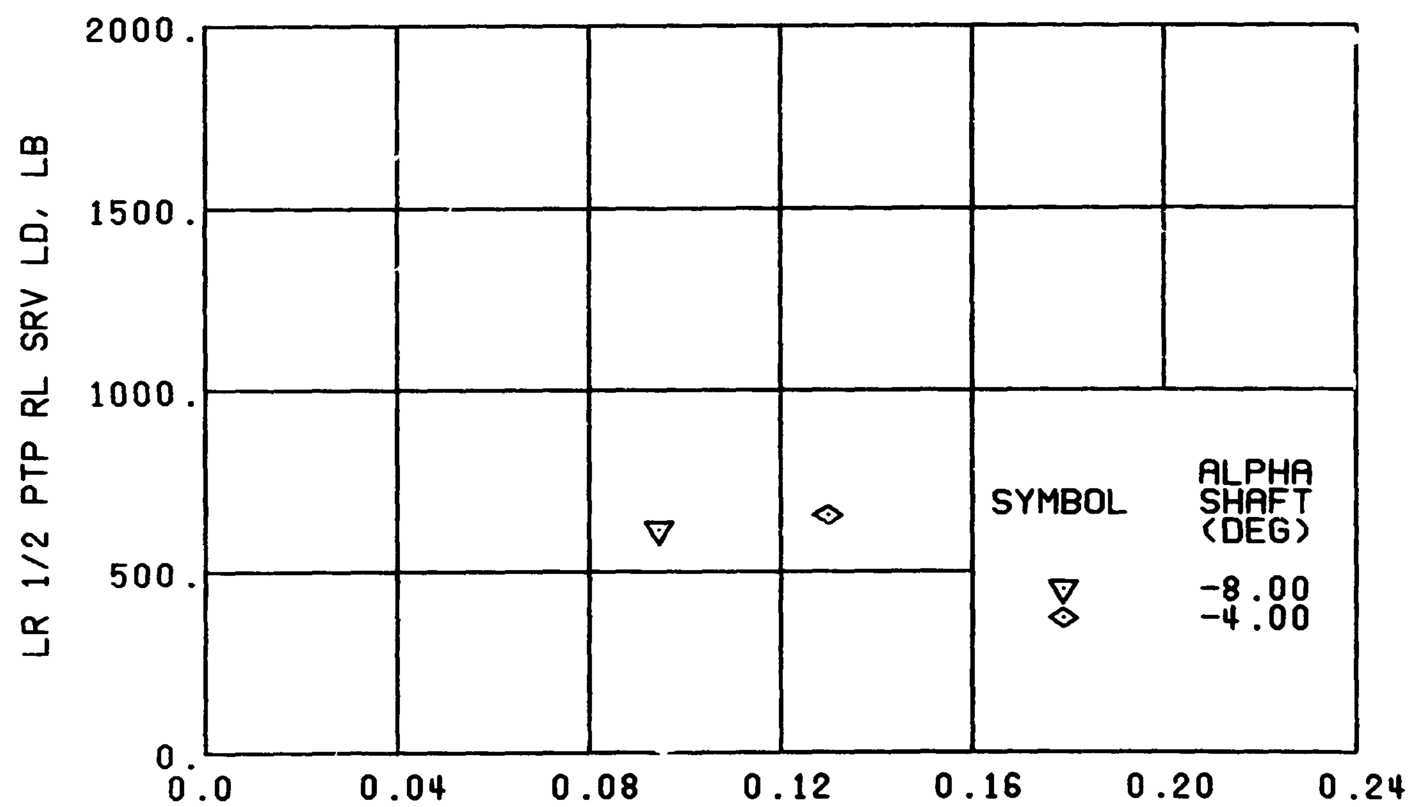

(q) GAGE 25

Figure 48. Continued.
μ = 0.35 B'_{1s} = 8 Deg

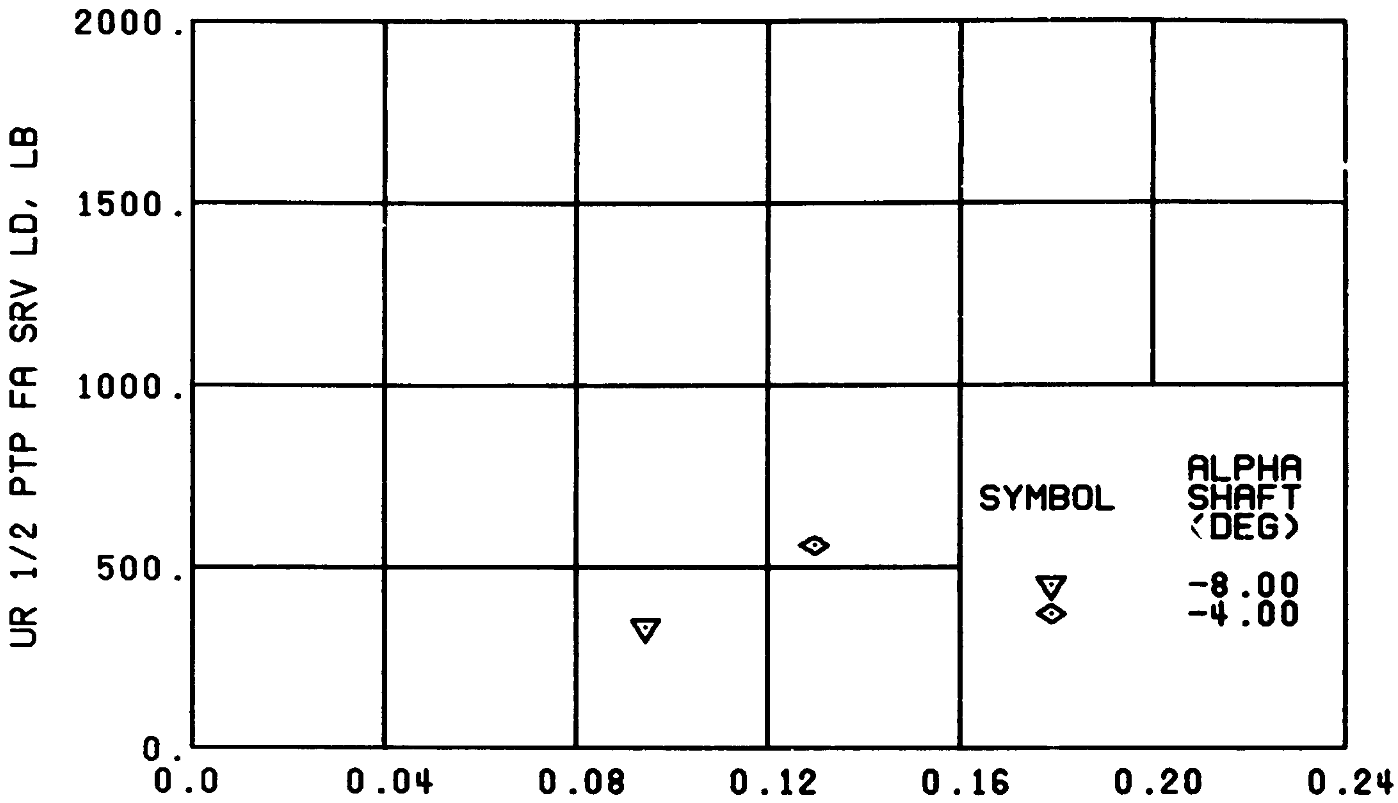

(r) GAGE 24

Figure 48. Continued.
$\mu = 0.35 \quad B'_{1s} = 8$ Deg

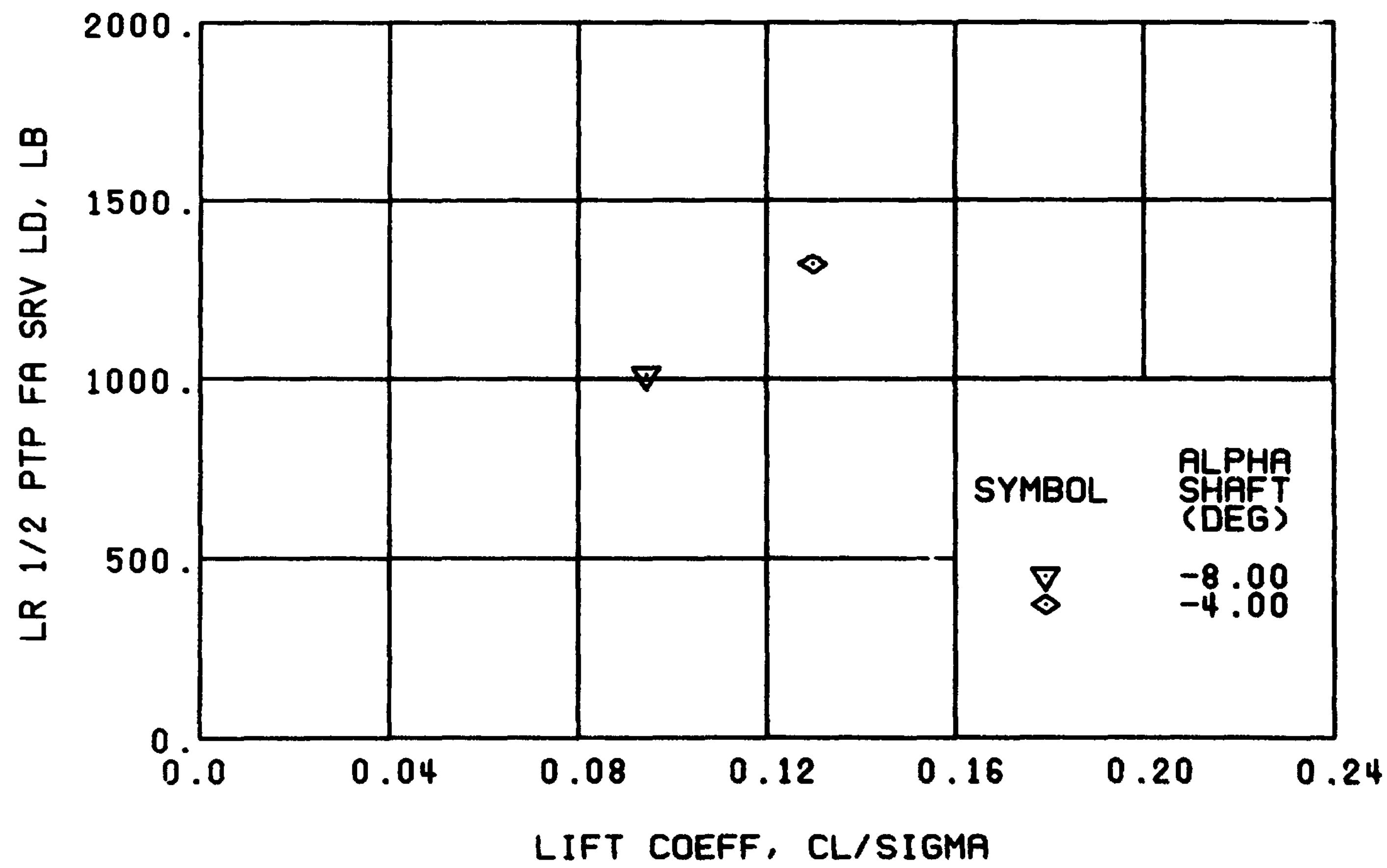

(s) GAGE 27

Figure 48. Continued.
$\mu = 0.35 \quad B'_{1s} = 8$ Deg

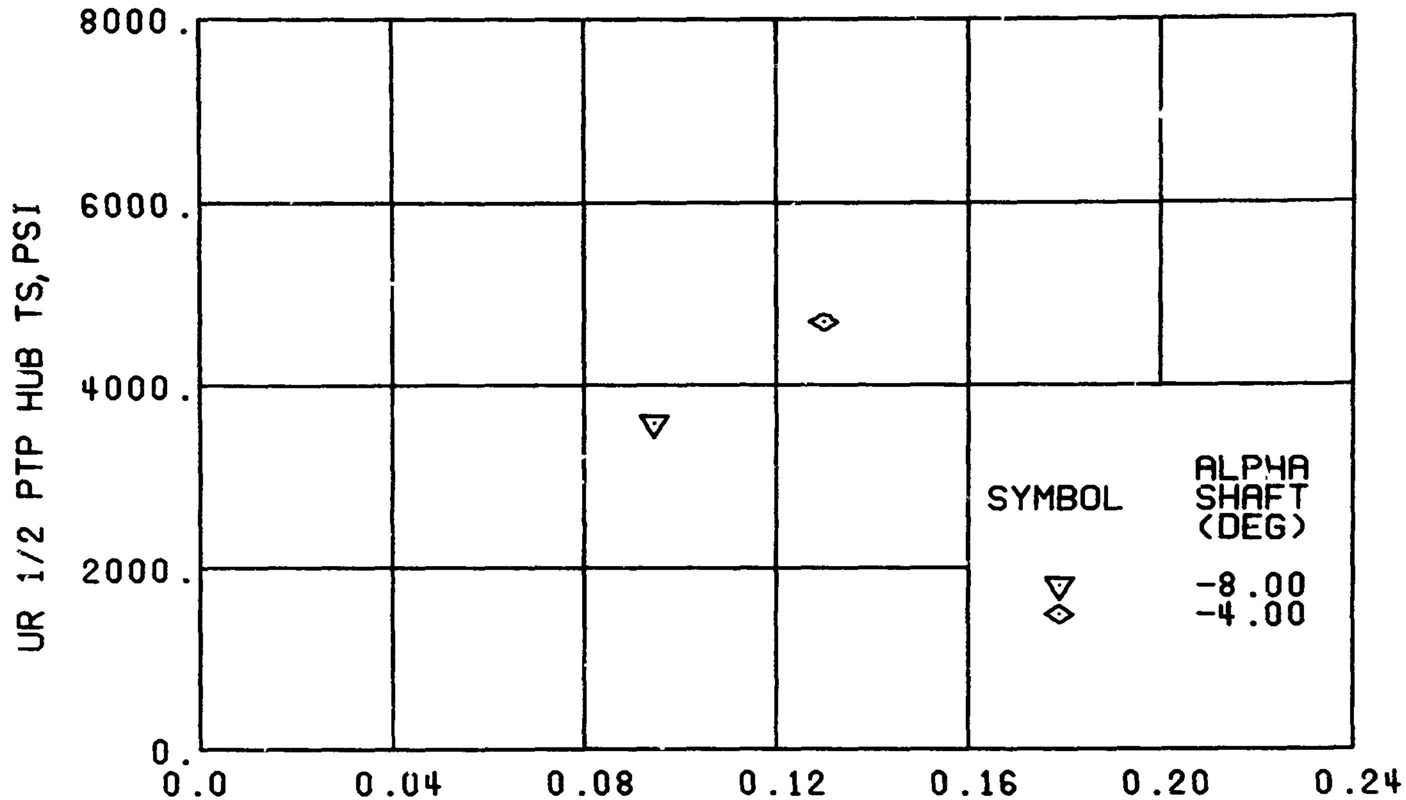

(f) GAGE 65

Figure 48. Continued.
$\mu = 0.35$ $B'_{1s} = 8$ Deg

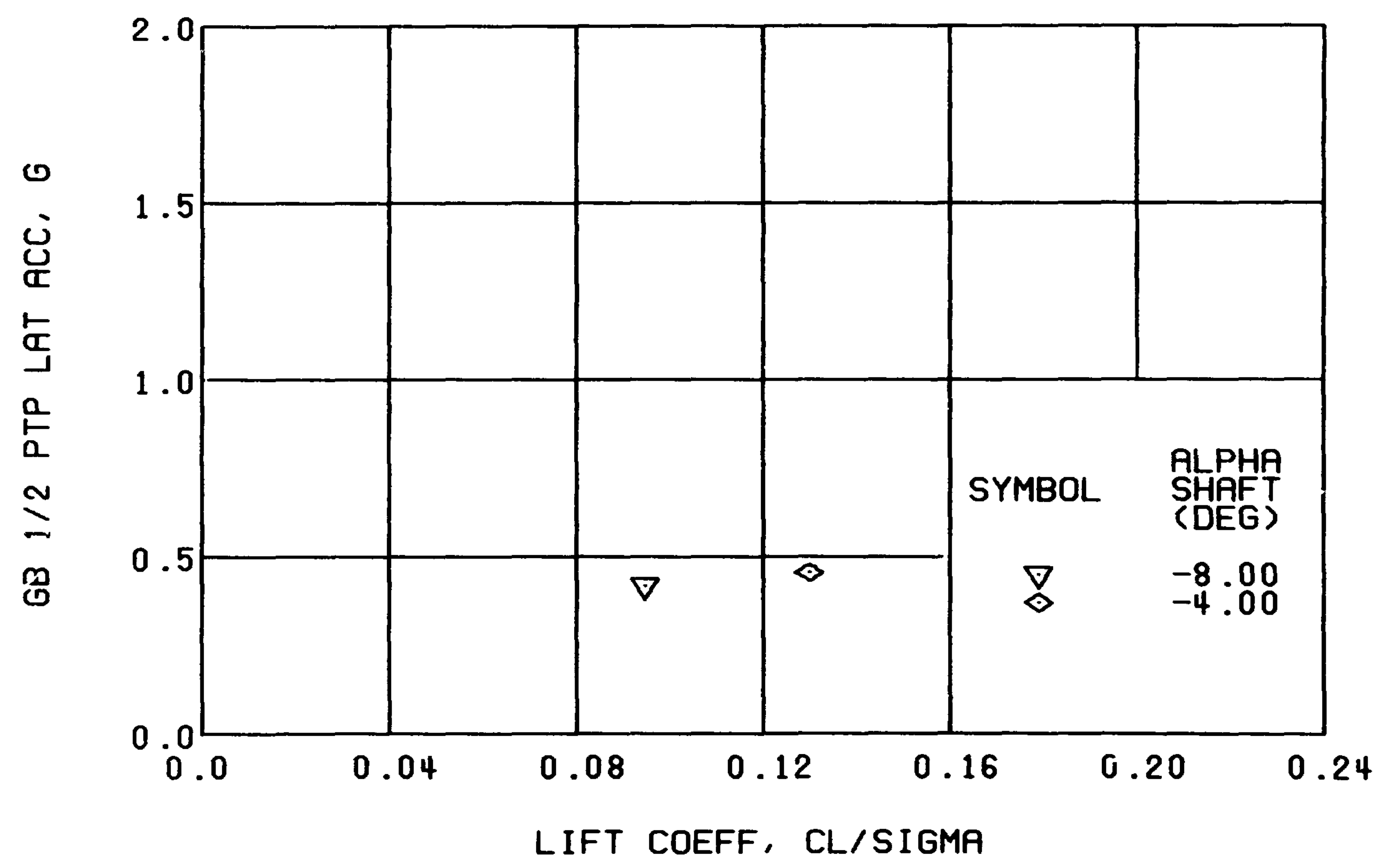

(u) GAGE 15 STA 76, BL 30

Figure 48. Continued.
$\mu = 0.35$ $B'_{1s} = 8$ Deg

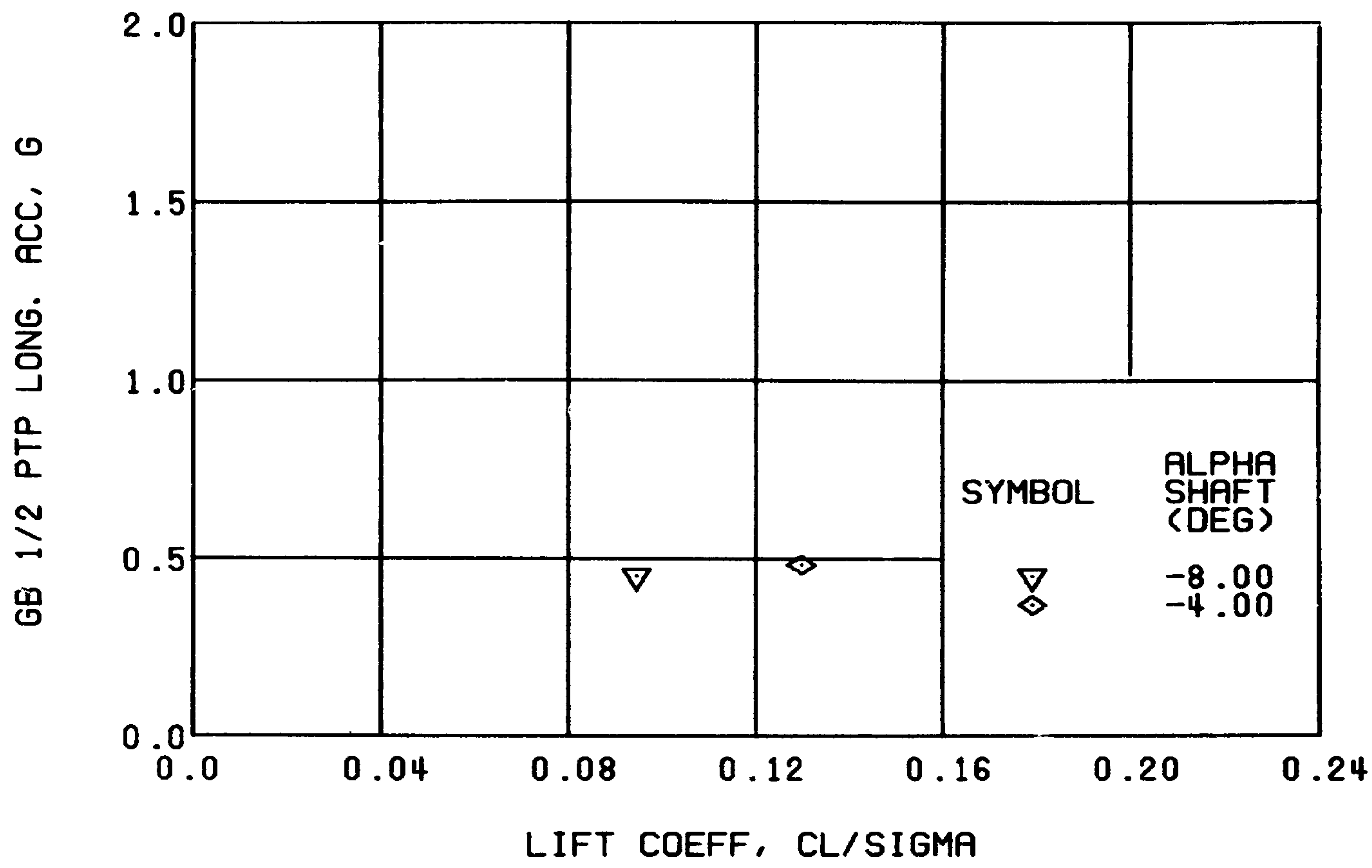

(v) GAGE 14 STA 61, BL 0

Figure 48. Continued.
$\mu = 0.35$ $B'_{1s} = 8$ Deg

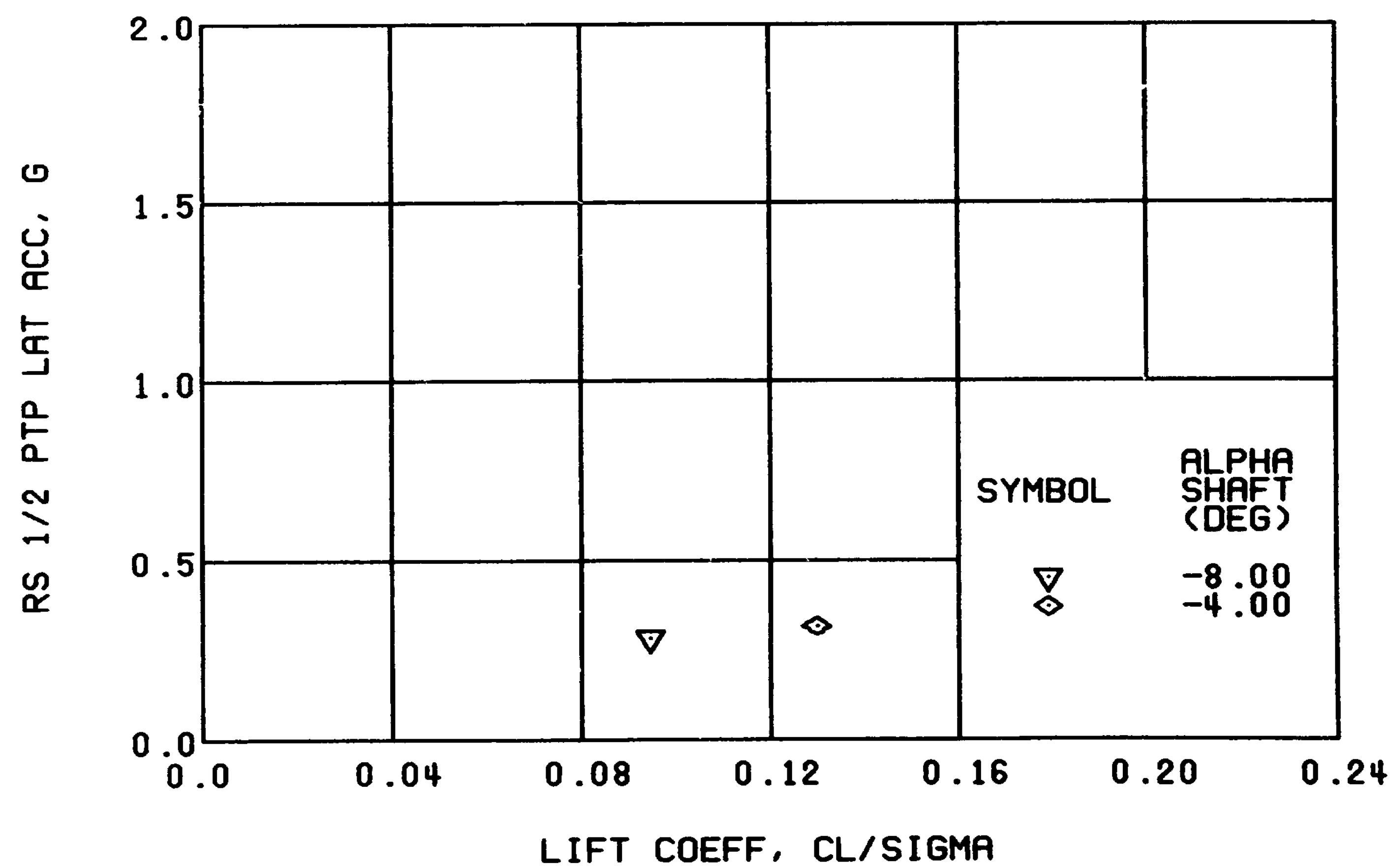

(w) GAGE 16 ROVER 3

Figure 48. Continued.
$\mu = 0.35 \quad B'_{1s} = 8$ Deg

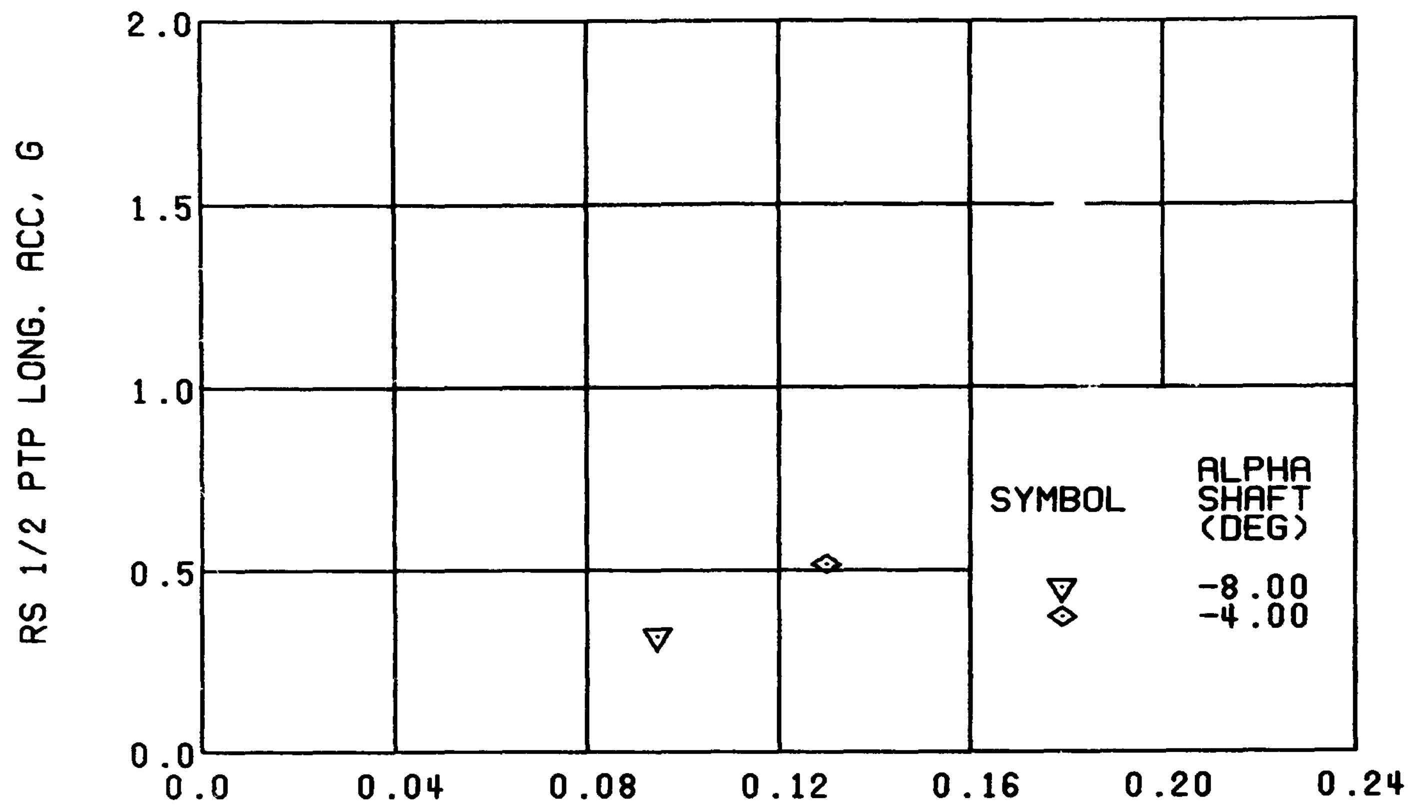

(x) GAGE 17 ROVER 4

Figure 48. Concluded.
$\mu = 0.35 \quad B'_{1s} = 8$ Deg

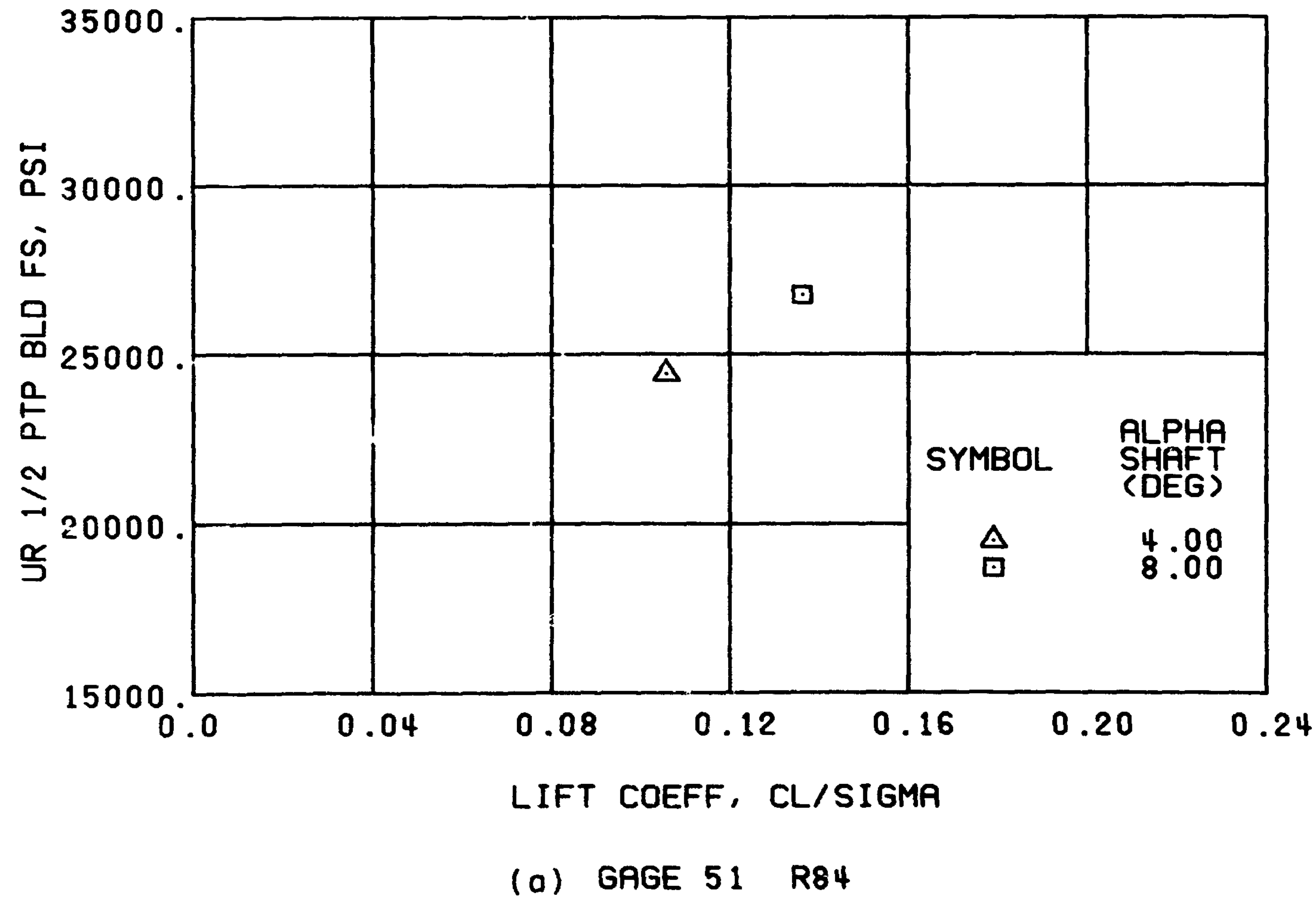

Figure 49. Stress, Load, and Vibration Data at an Advance Ratio of 0.47 With the Lateral Displacement Control (B'_{1s}) Set at 0 Degrees.

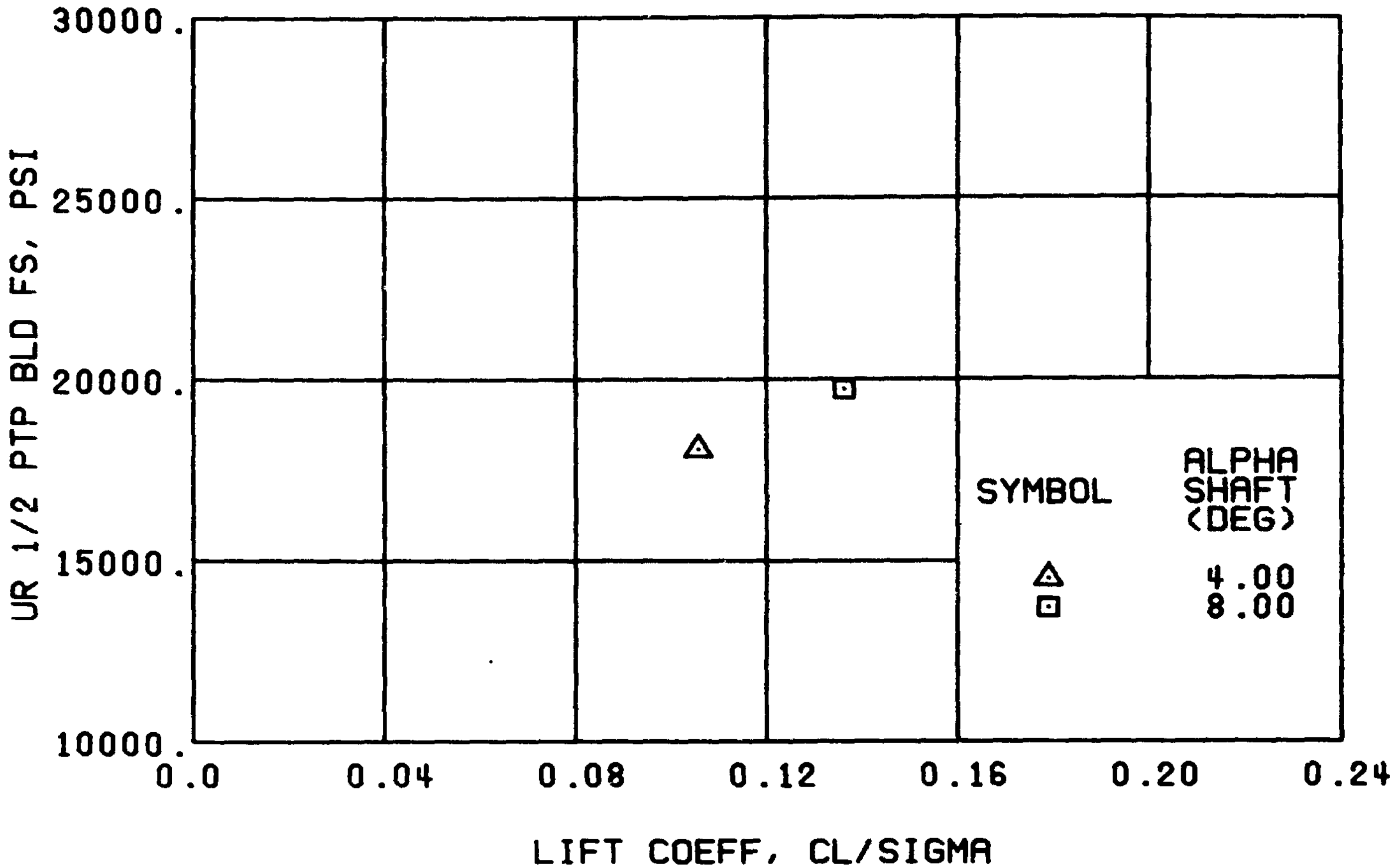

(c) GAGE 52 R108

Figure 49. Continued.
$\mu = 0.47$ $B'_{1s} = 0$ Deg

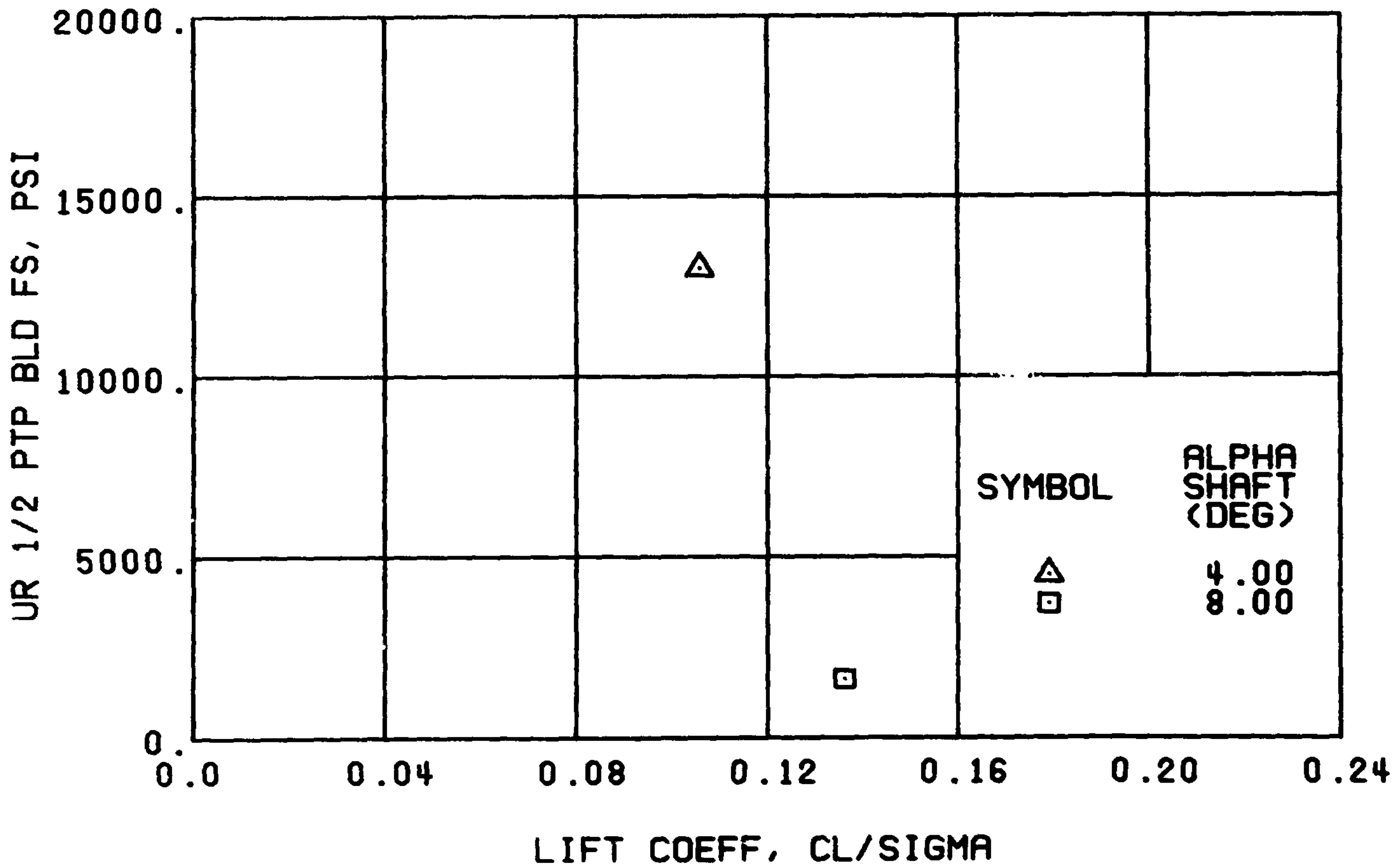

(d) GAGE 53 R132

Figure 49. Continued.
$\mu = 0.47$ $B'_{1s} = 0$ Deg

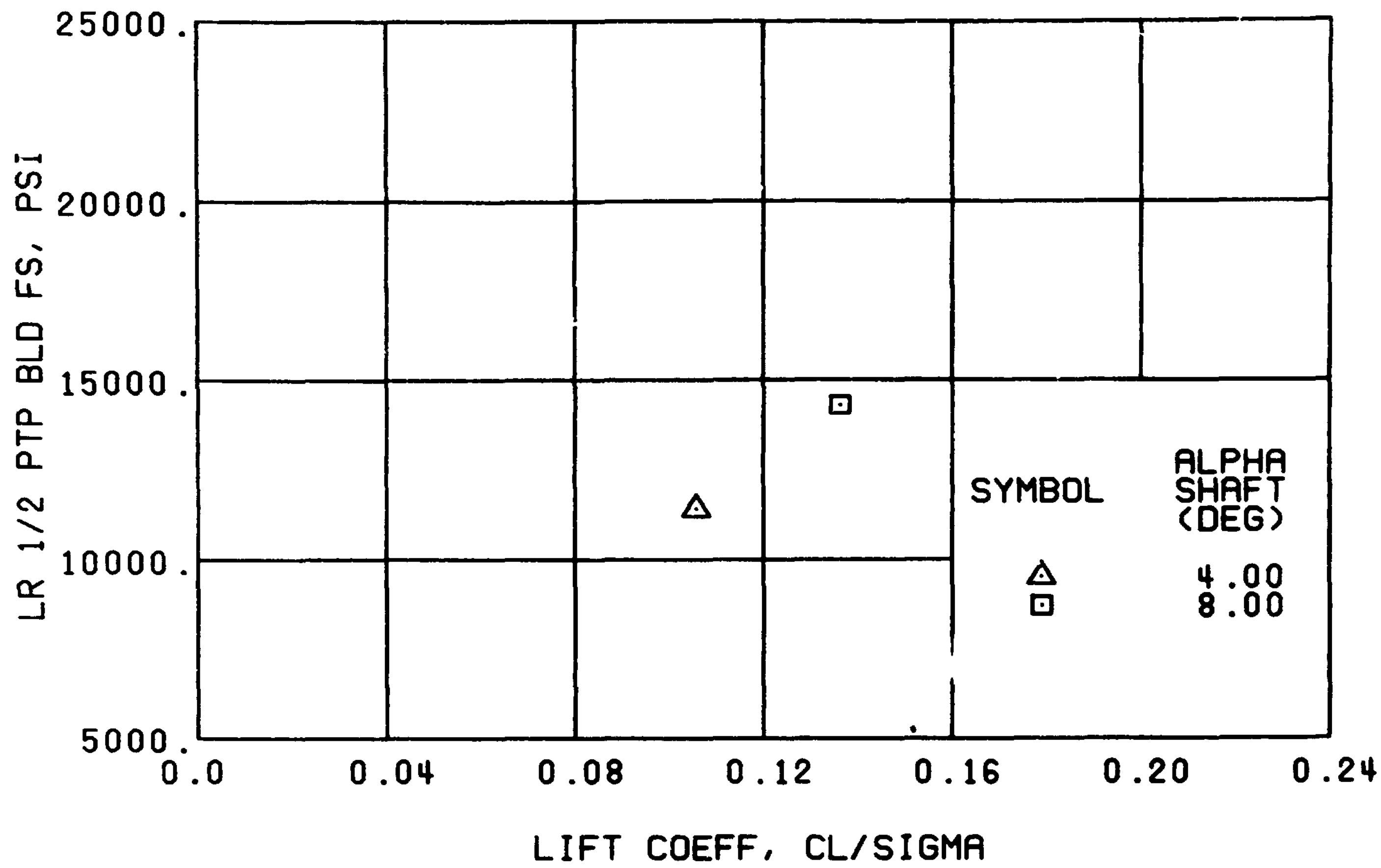

(e) GAGE 93 R132

Figure 49. Continued.
$\mu = 0.47$ $B'_{1s} = 0$ Deg

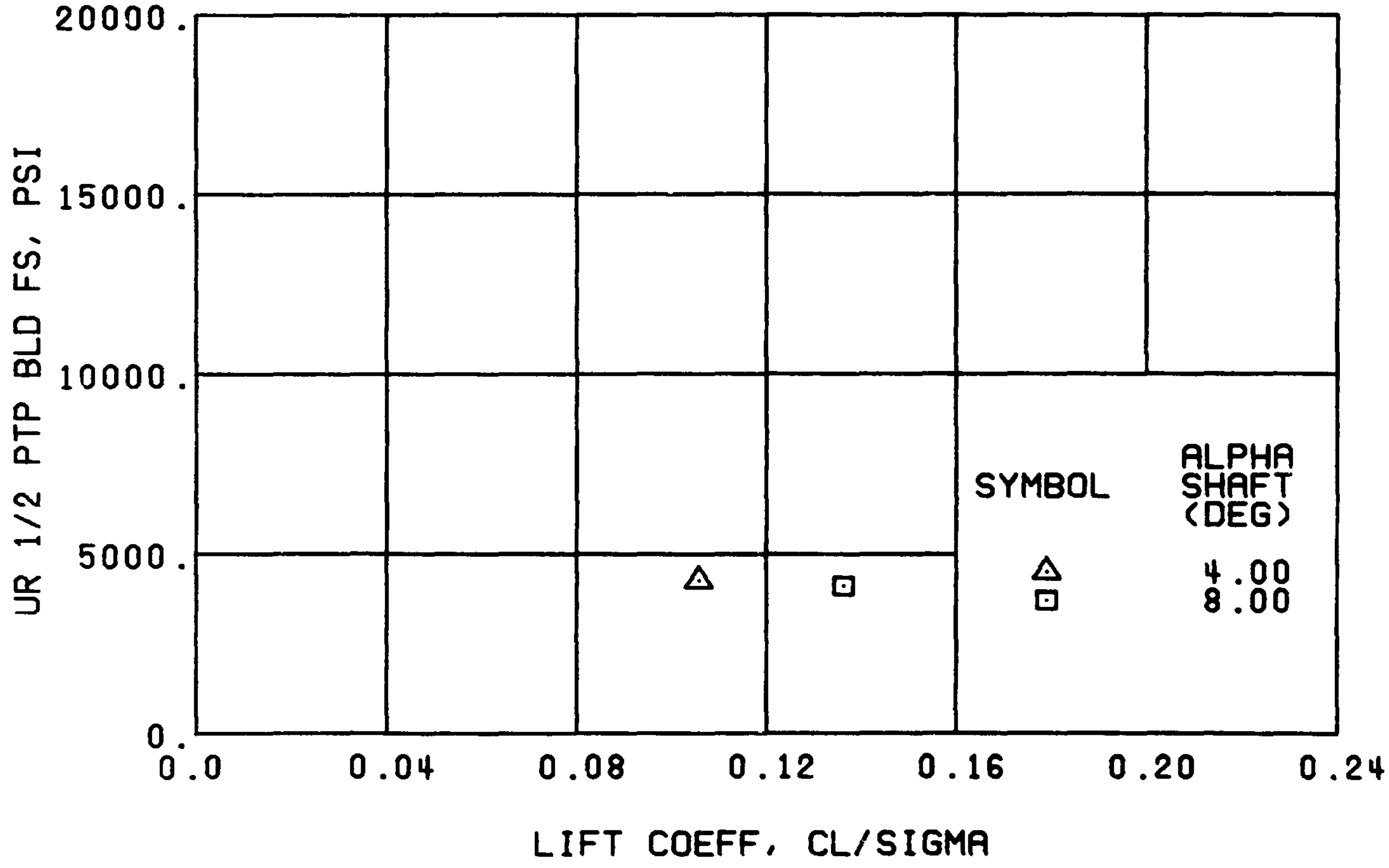

(f) GAGE 55 R204

Figure 49. Continued.
$\mu = 0.47$ $B'_{1s} = 0$ Deg

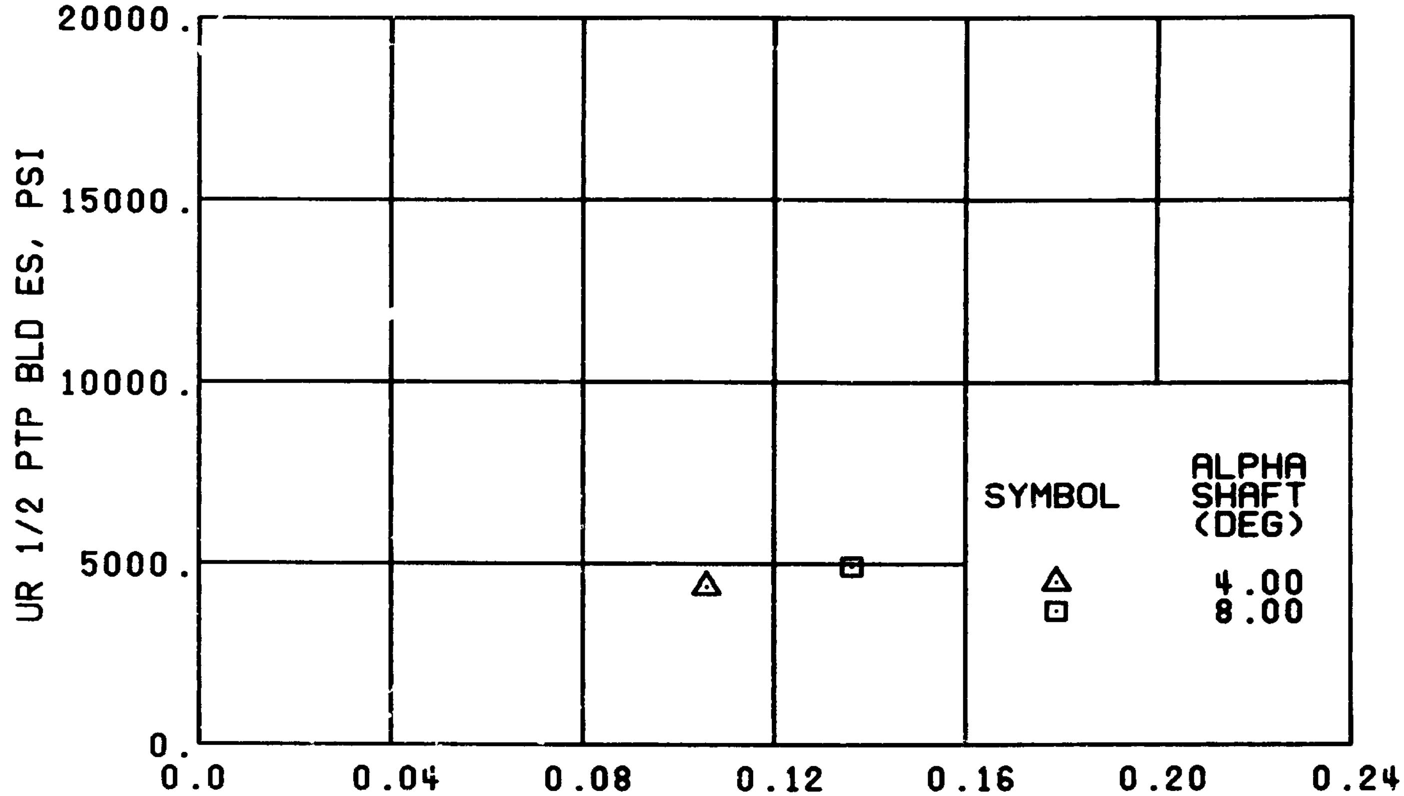

(h) GAGE 40 R84

Figure 49. Continued.
$\mu = 0.47$ $B'_{1s} = 0$ Deg

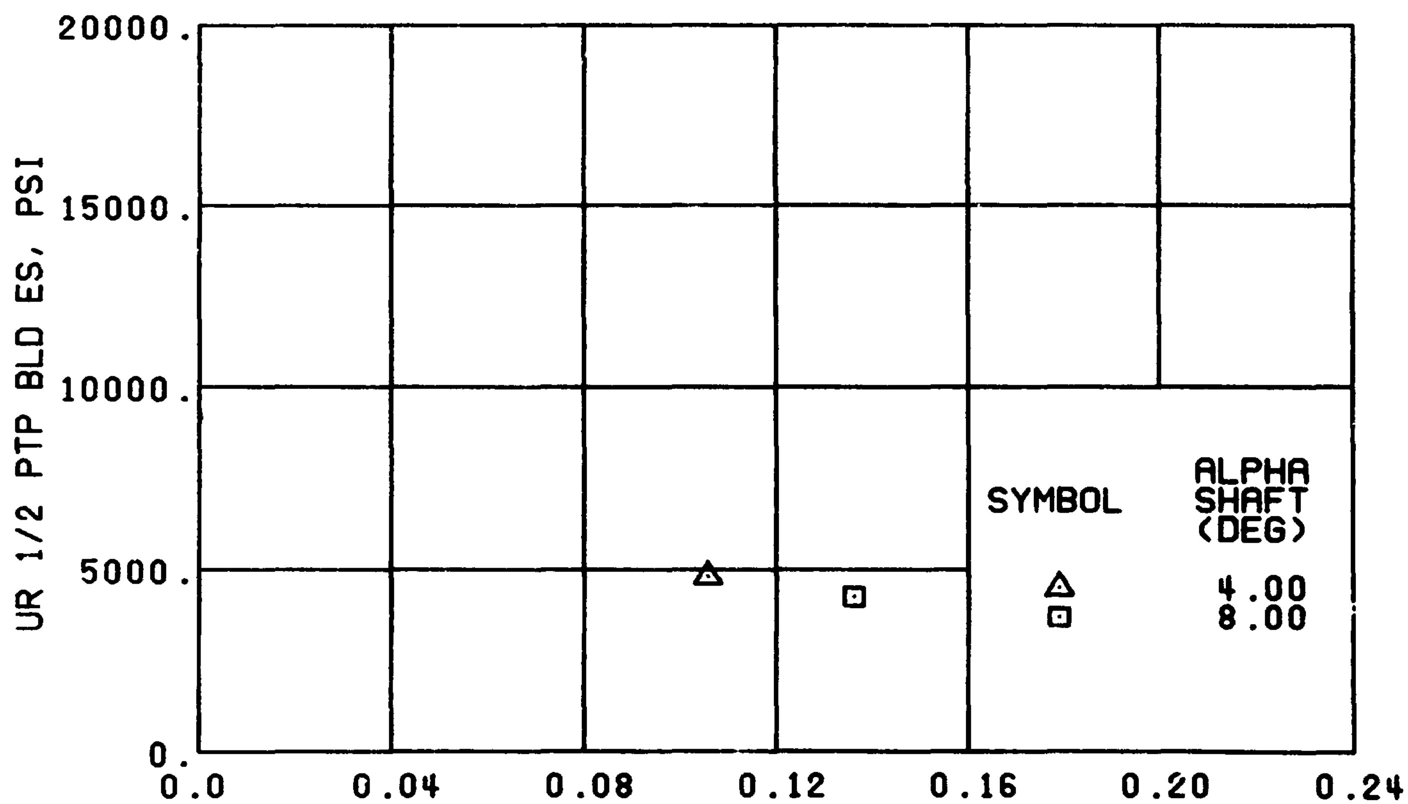

LIFT COEFF, CL/SIGMA

(j) GAGE 42 R132

Figure 49. Continued.
$\mu = 0.47 \quad B'_{1s} = 0 \text{ Deg}$

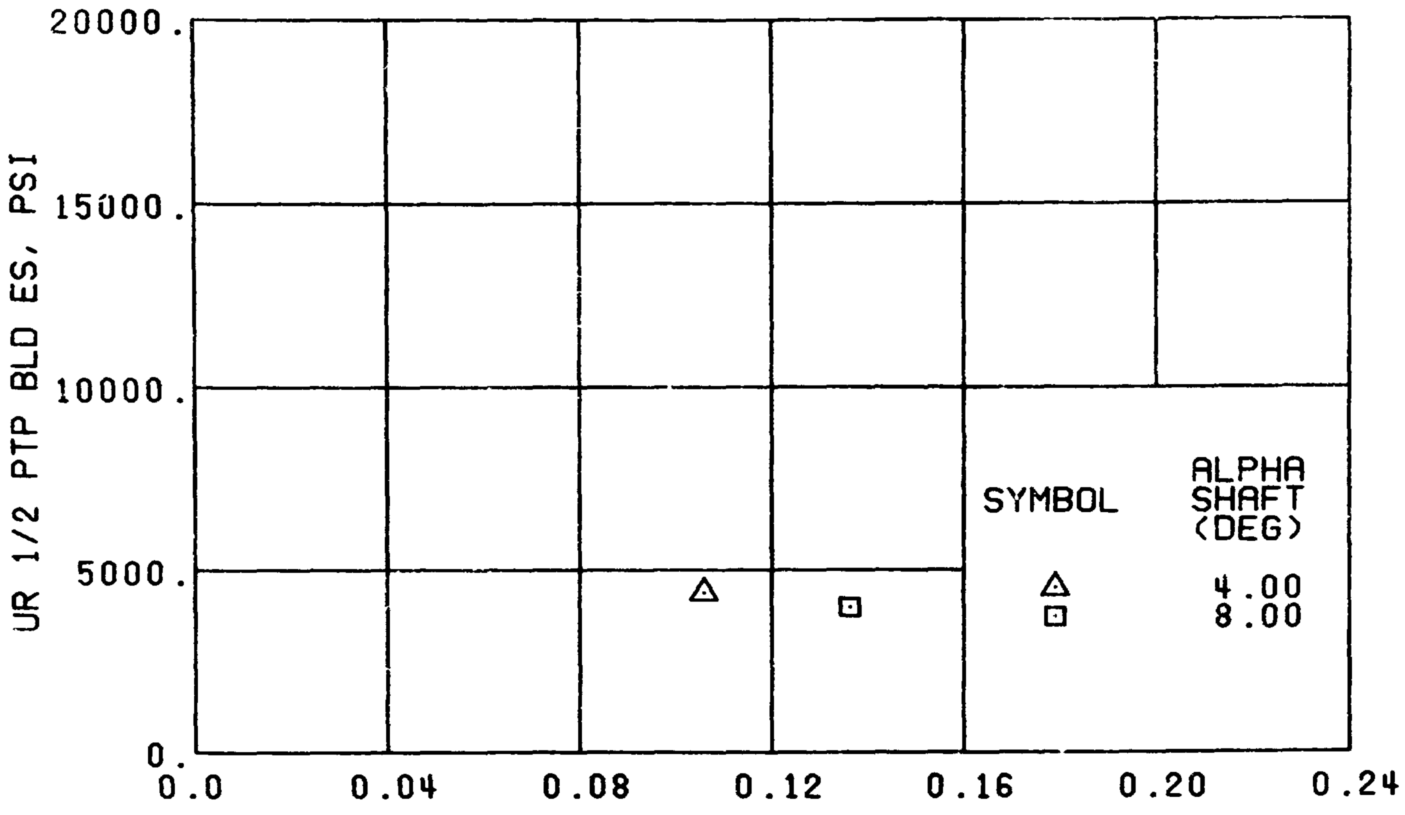

(k) GAGE 43 R168

Figure 49. Continued.
$\mu = 0.47$ $B'_{1s} = 0$ Deg

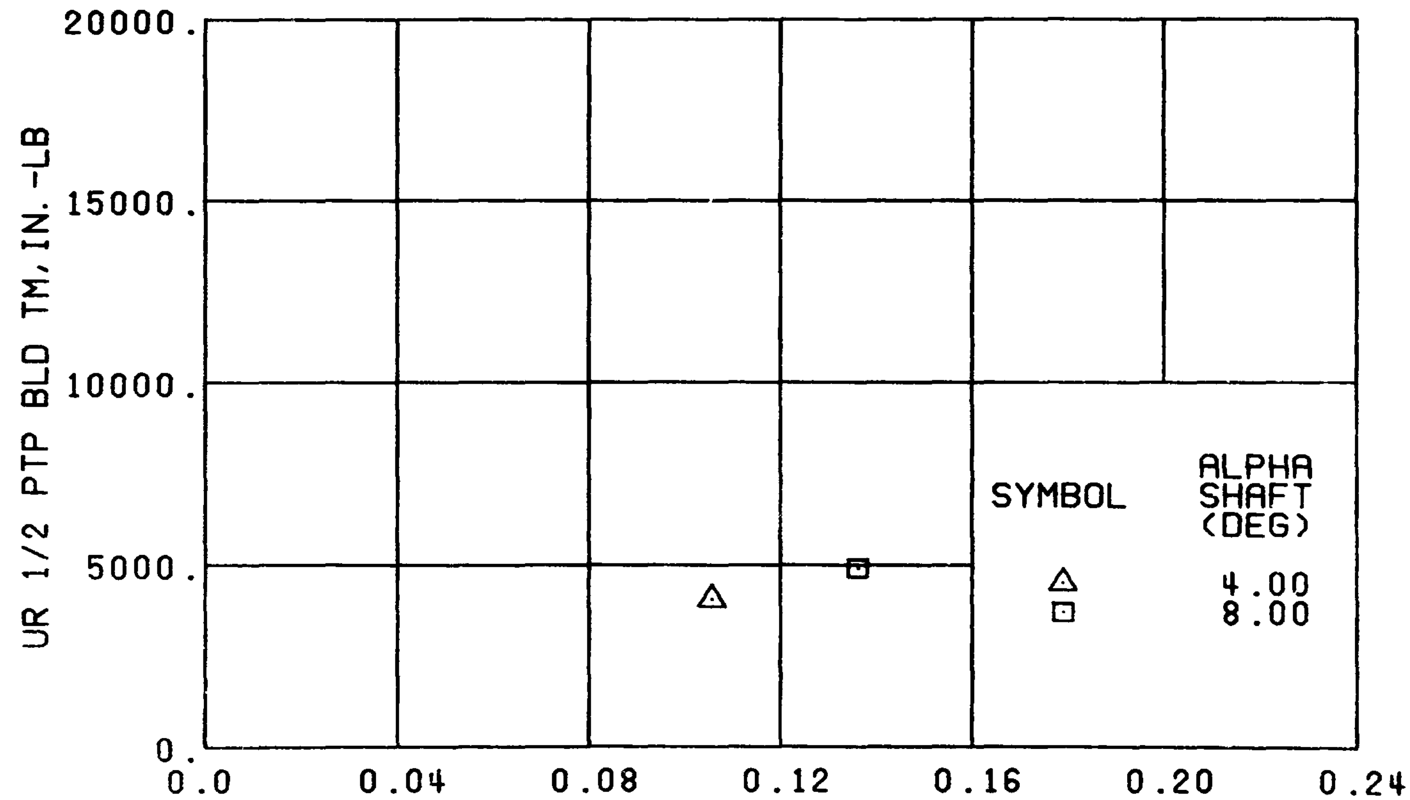

(m) GAGE 46 R130

Figure 49. Continued.
$\mu = 0.47$ $B'_{1s} = 0$ Deg

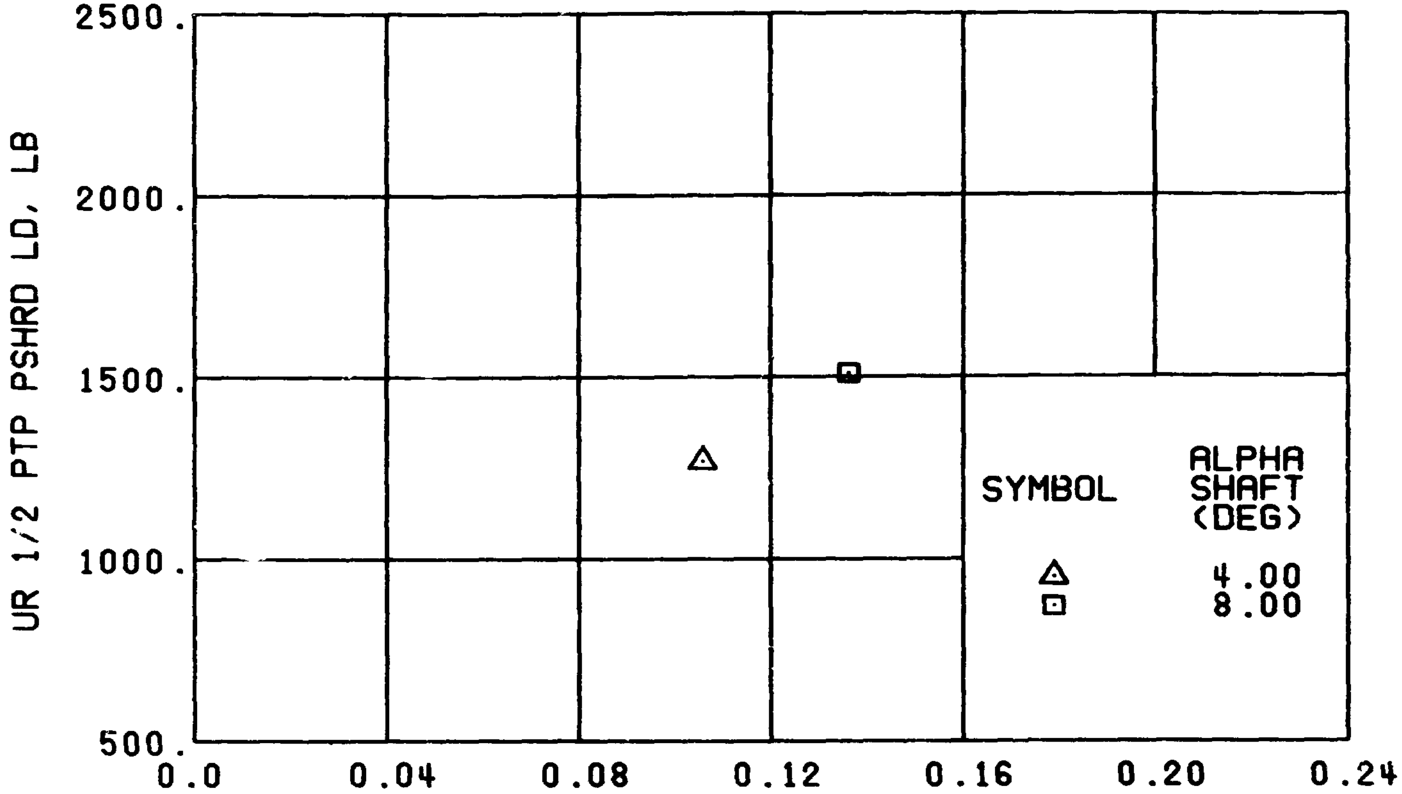

(n) GAGE 37

Figure 49. Continued.
$\mu = 0.47$ $B'_{1s} = 0$ Deg

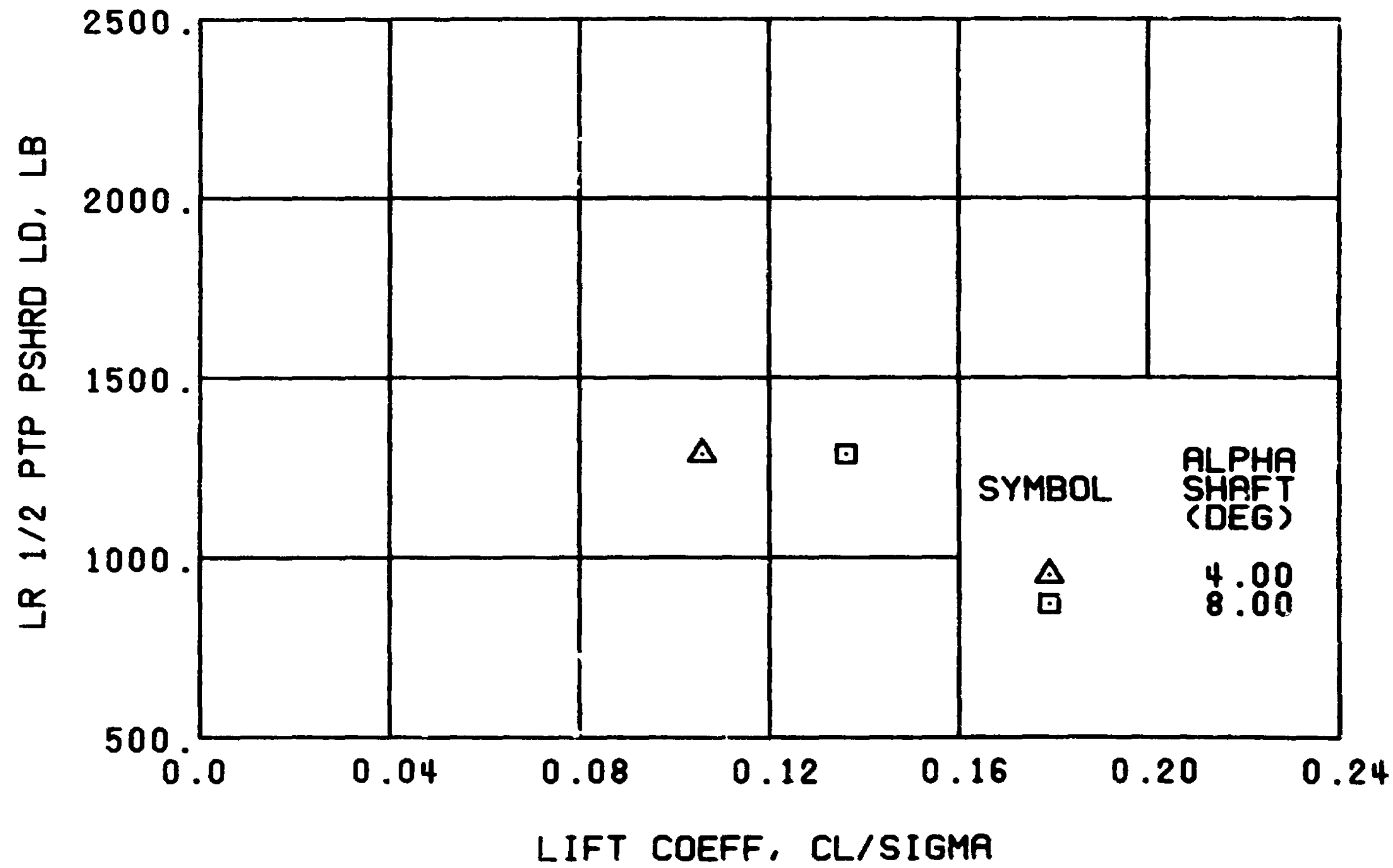

(o) GAGE 34

Figure 49. Continued.
$\mu = 0.47$ $B'_{1s} = 0$ Deg

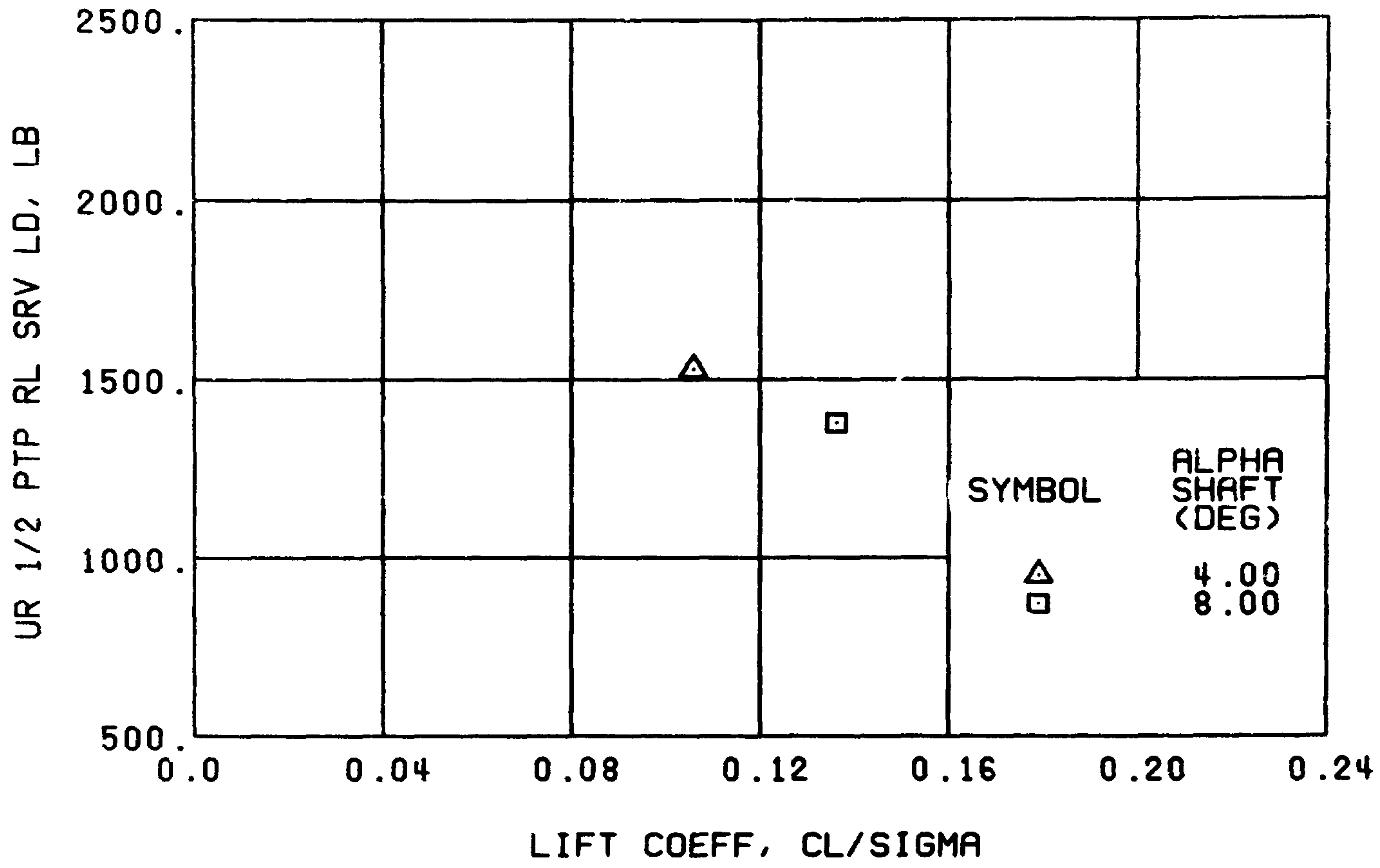

(p) GAGE 22

Figure 49. Continued.
$\mu = 0.47 \quad B'_{1s} = 0$ Deg

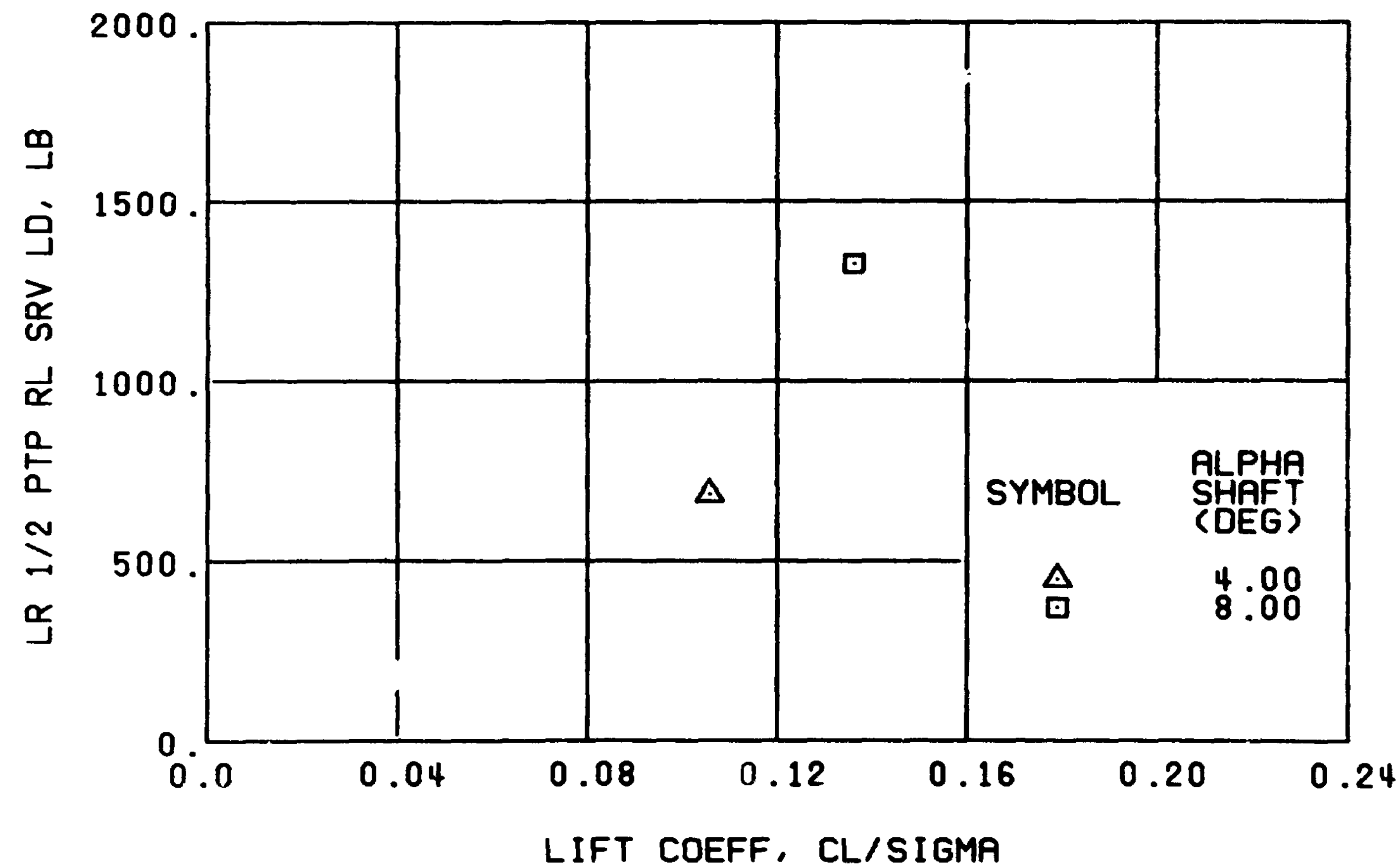

(q) GAGE 25

Figure 49. Continued.
$\mu = 0.47 \quad B'_{1s} = 0$ Deg

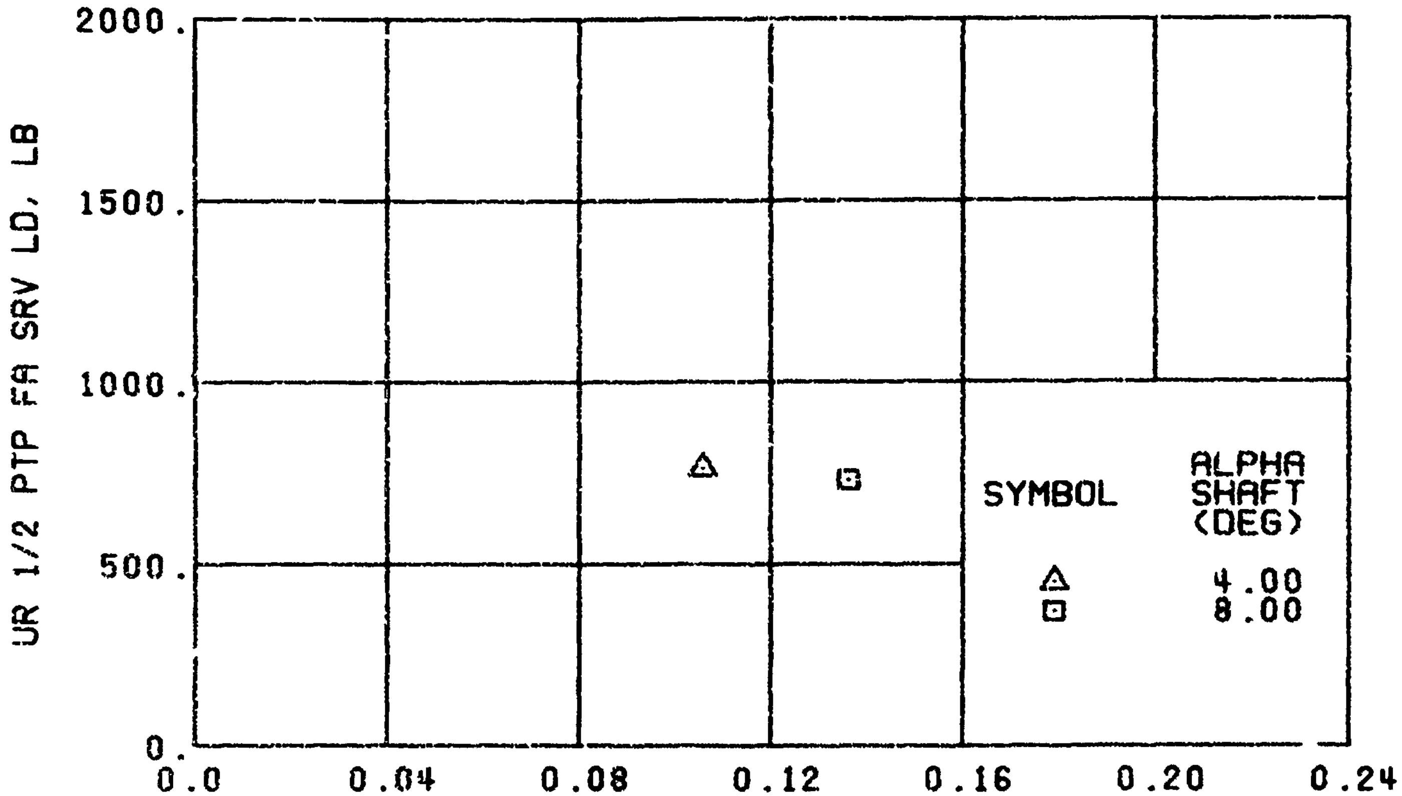

(r) GAGE 24

Figure 49. Continued.
μ = 0.47 B'_{1s} = 0 Deg

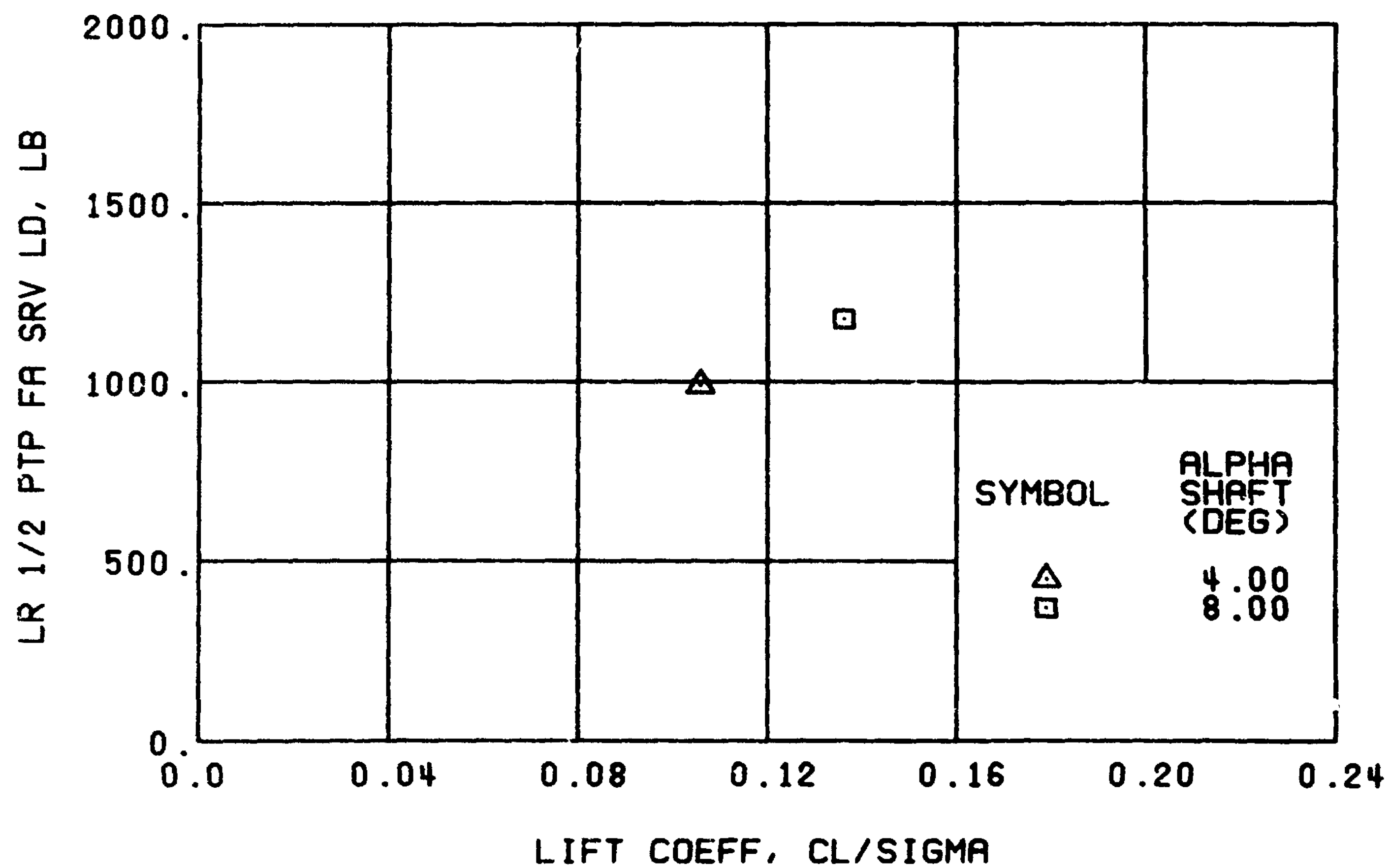

(s) GAGE 27

Figure 49. Continued.
$\mu = 0.47$ $B'_{1s} = 0$ Deg

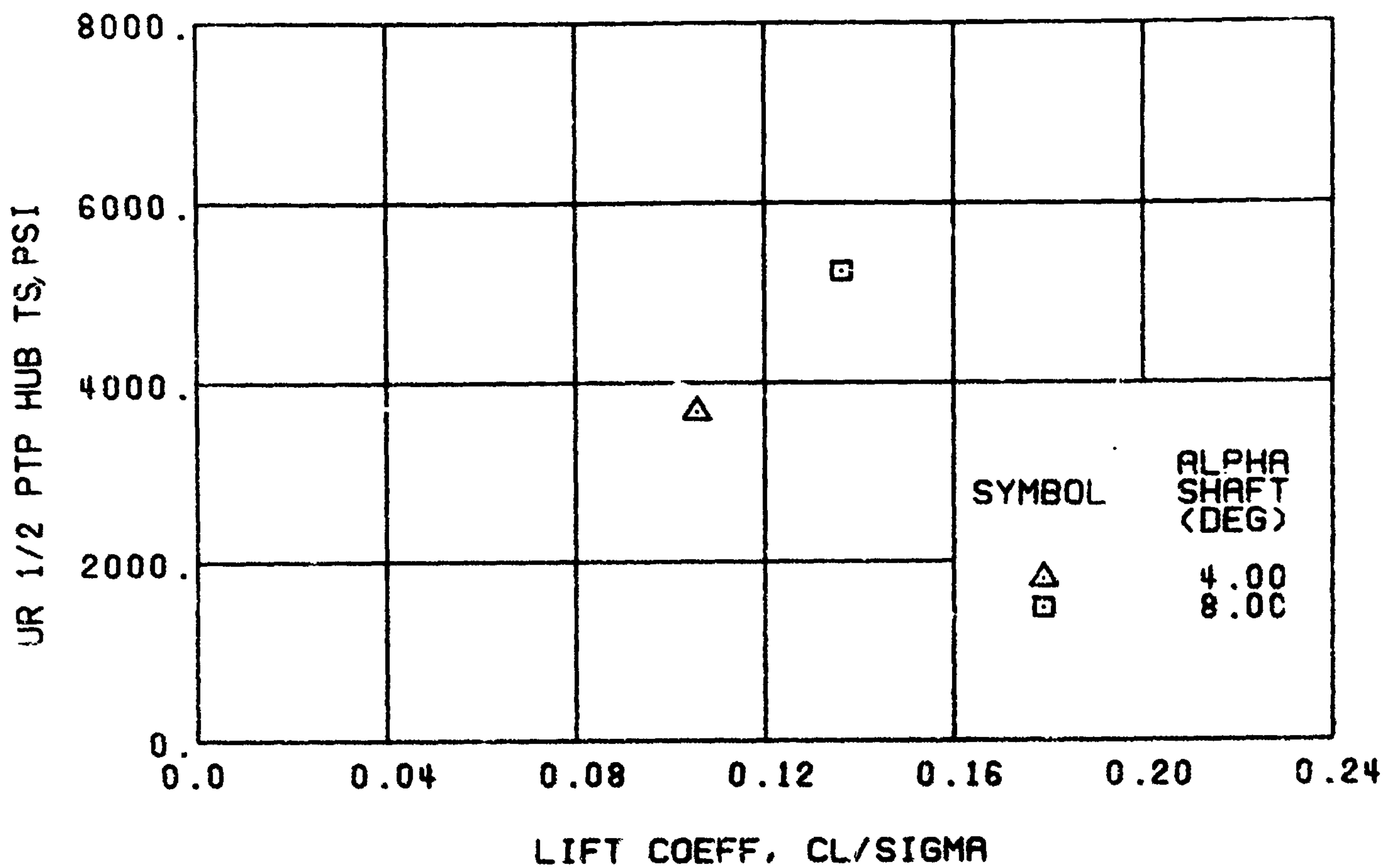

(f) GAGE 65

Figure 49. Continued.
$\mu = 0.47$ $B'_{1s} = 0$ Deg

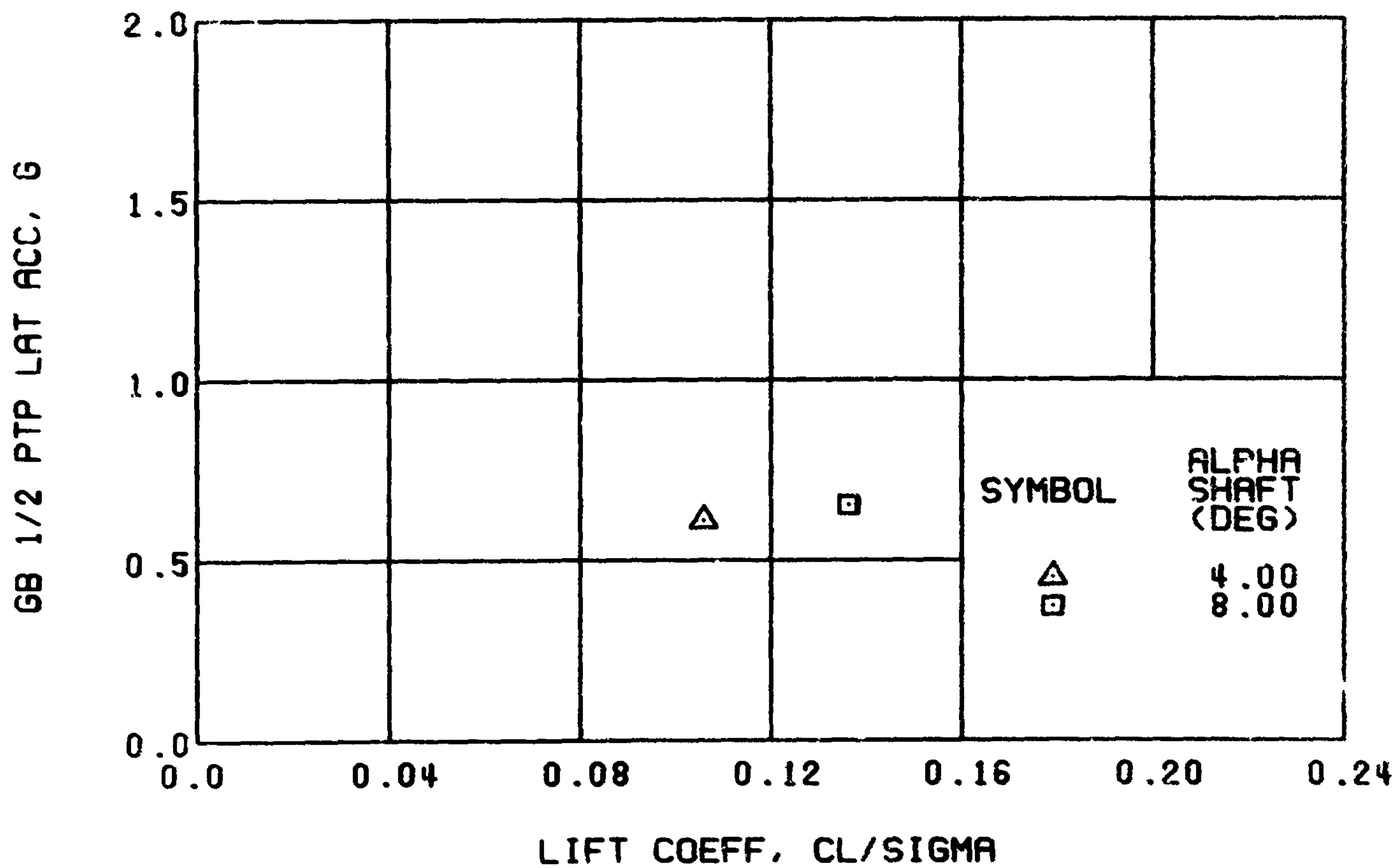

(u) GAGE 15 STA 76, BL 30

Figure 49. Continued.
$\mu = 0.47 \quad B'_{1s} = 0$ Deg

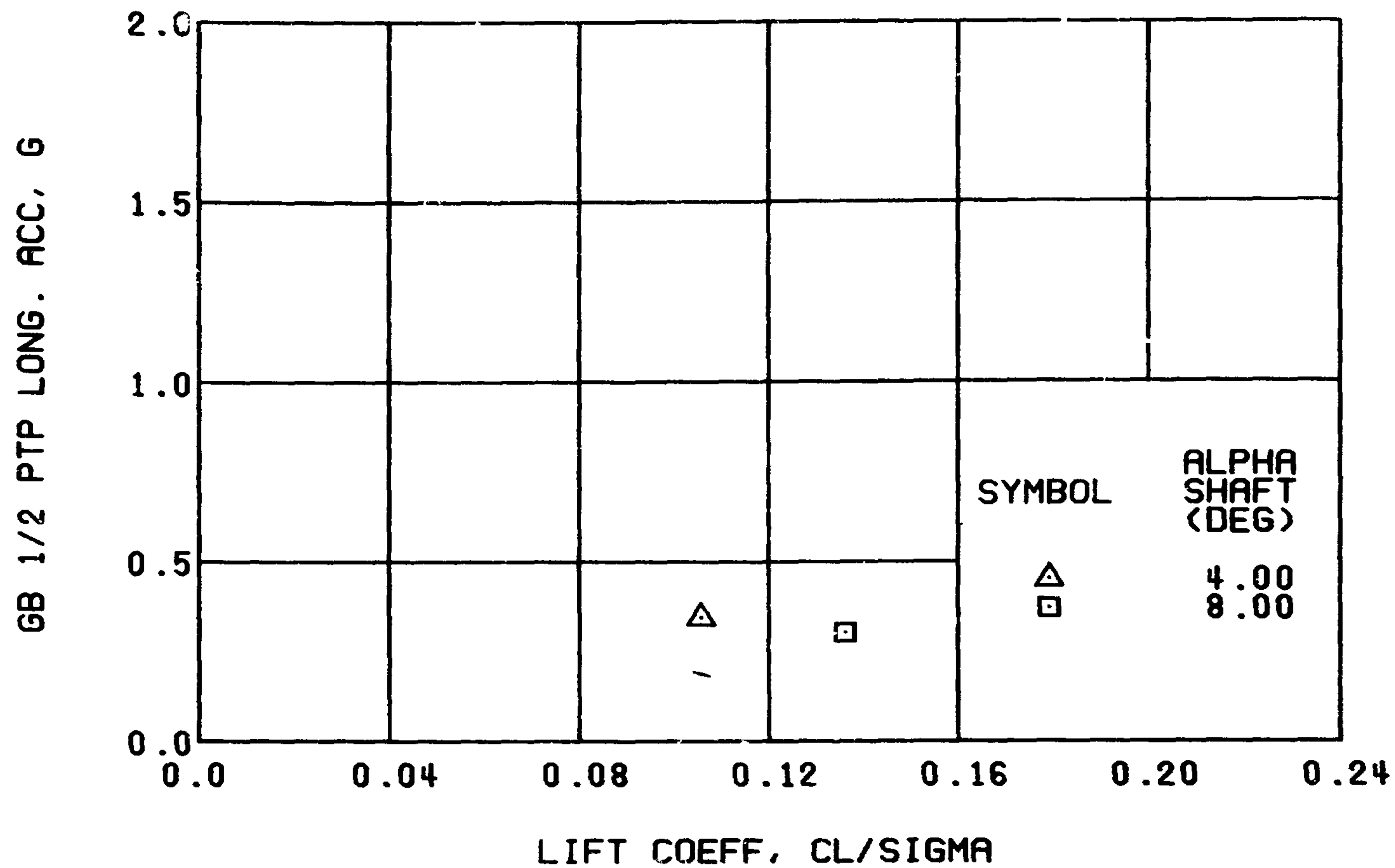

(v) GAGE 14 STA 61, BL 0

Figure 49. Continued.
$\mu = 0.47$ $B'_{1s} = 0$ Deg

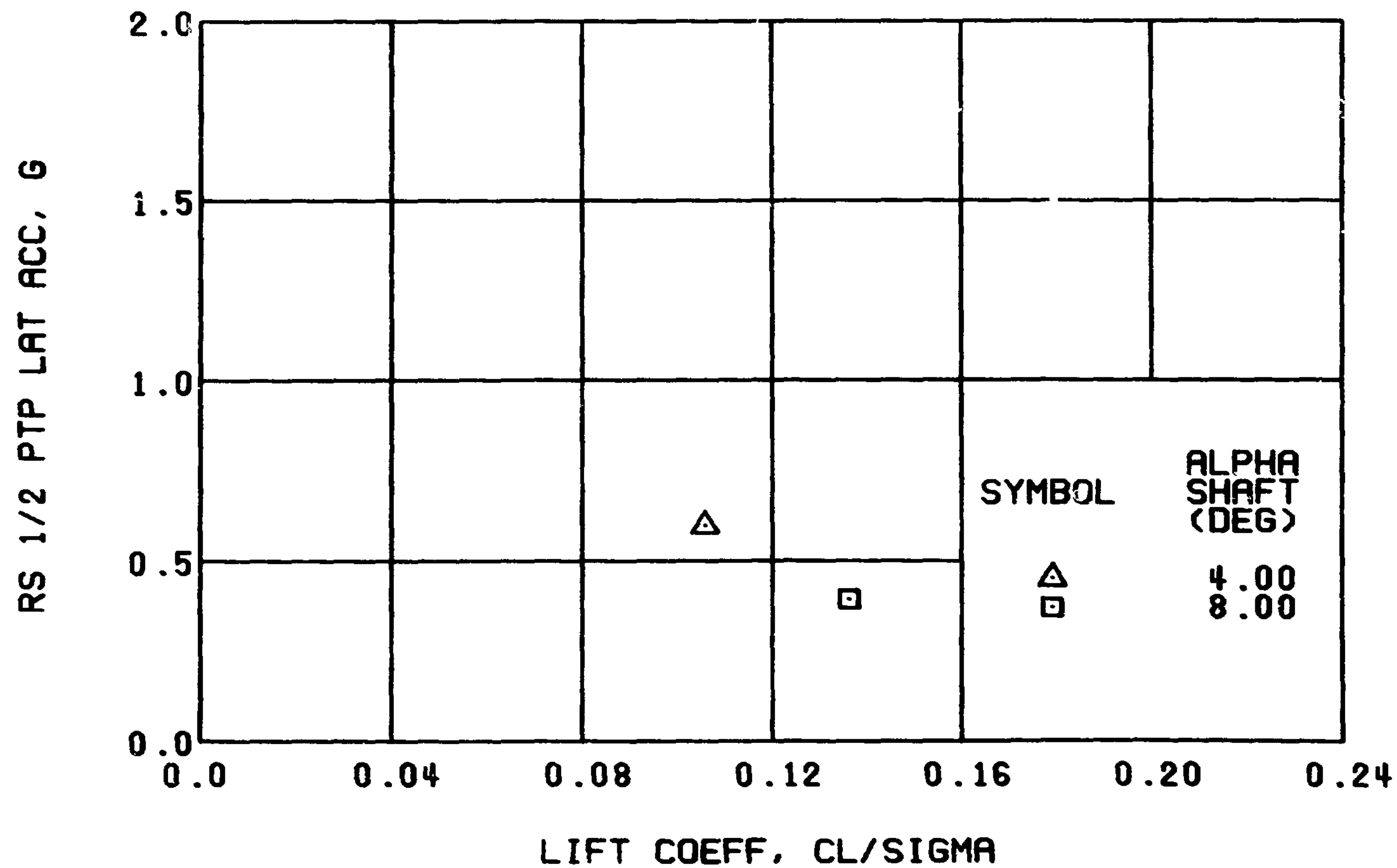

(w) GAGE 16 ROVER 3

Figure 49. Continued.
μ = 0.47 B'_{1s} = 0 Deg

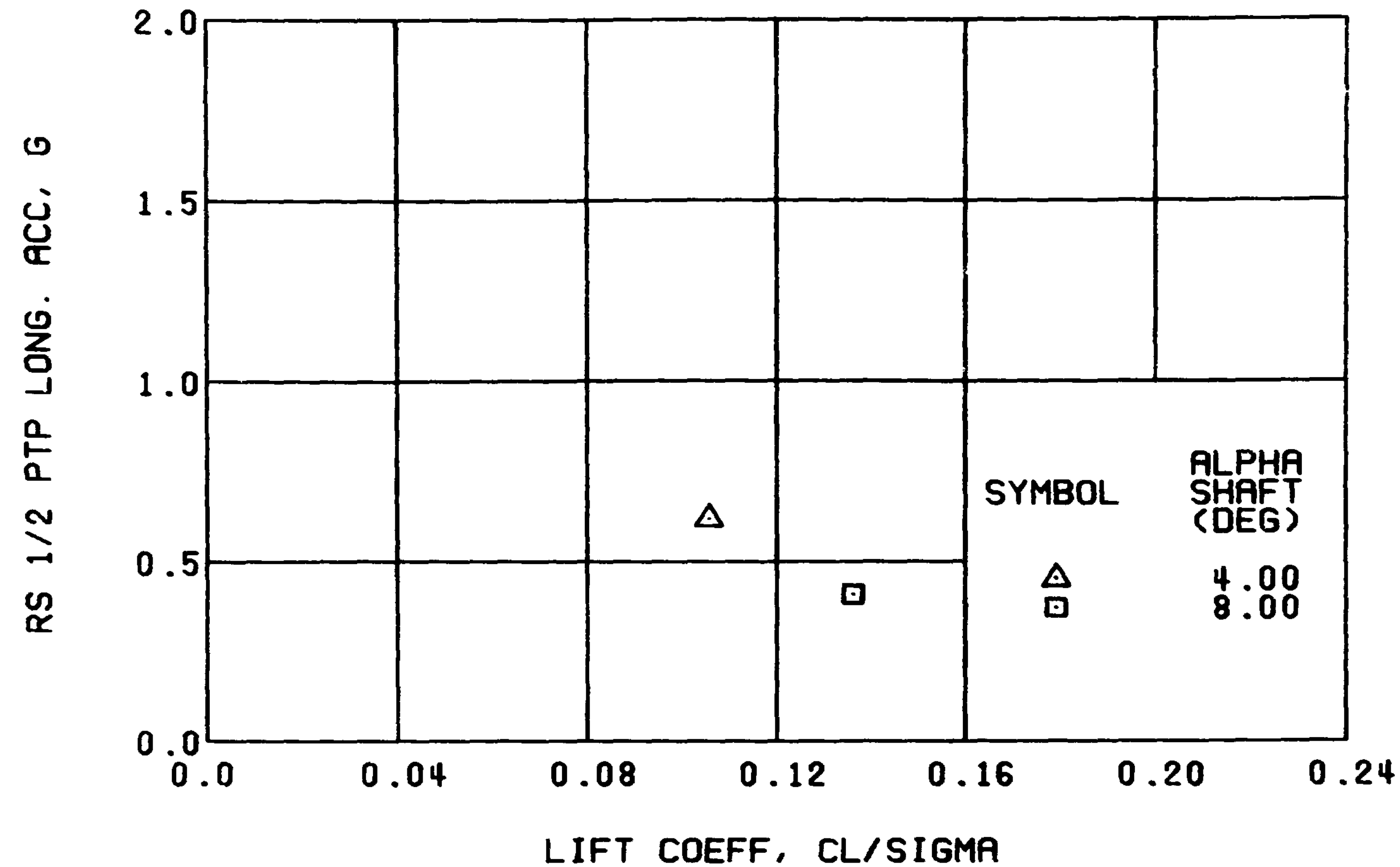

(x) GAGE 17 ROVER 4

Figure 49. Concluded.
$\mu = 0.47 \quad B_{1s}' = 0$ Deg

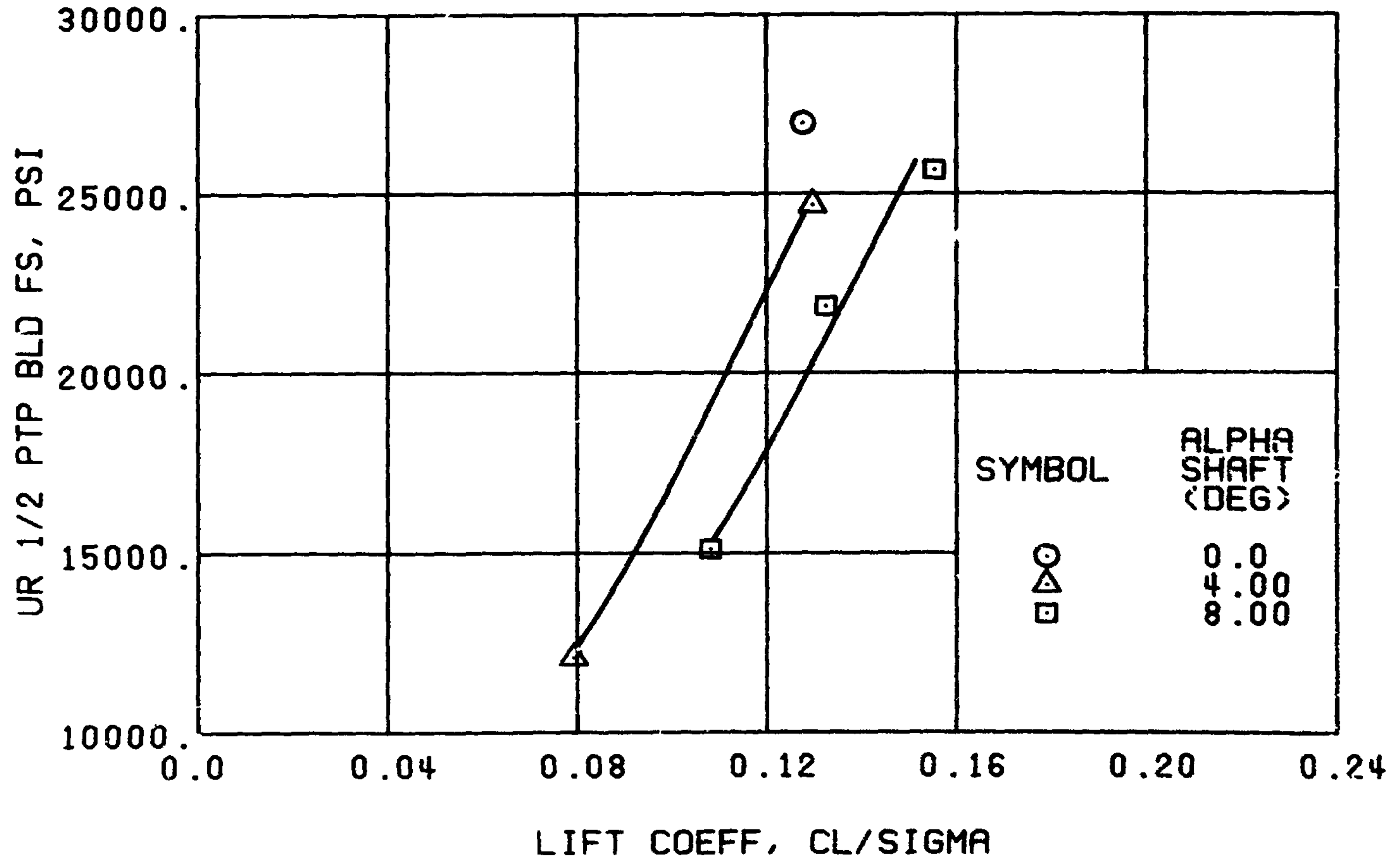

(a) GAGE 51 R84

Figure 50. Stress, Load, and Vibration Data at an Advance Ratio of 0.47 With the Lateral Displacement Control (B'_{1s}) Set at 2 Degrees.

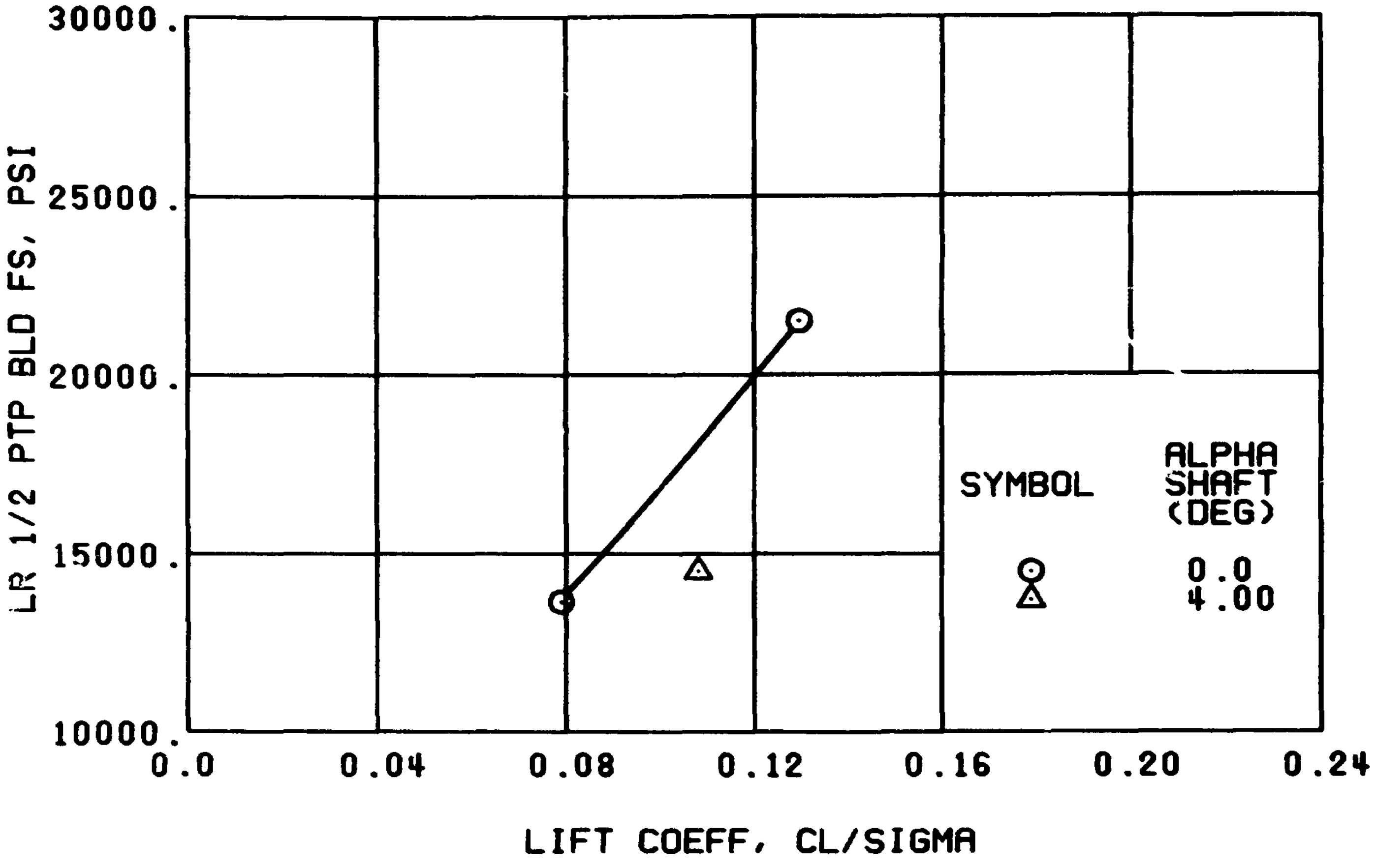

(b) GAGE 1 R84

Figure 50. Continued.
$\mu = 0.47 \quad B'_{1s} = 2$ Deg

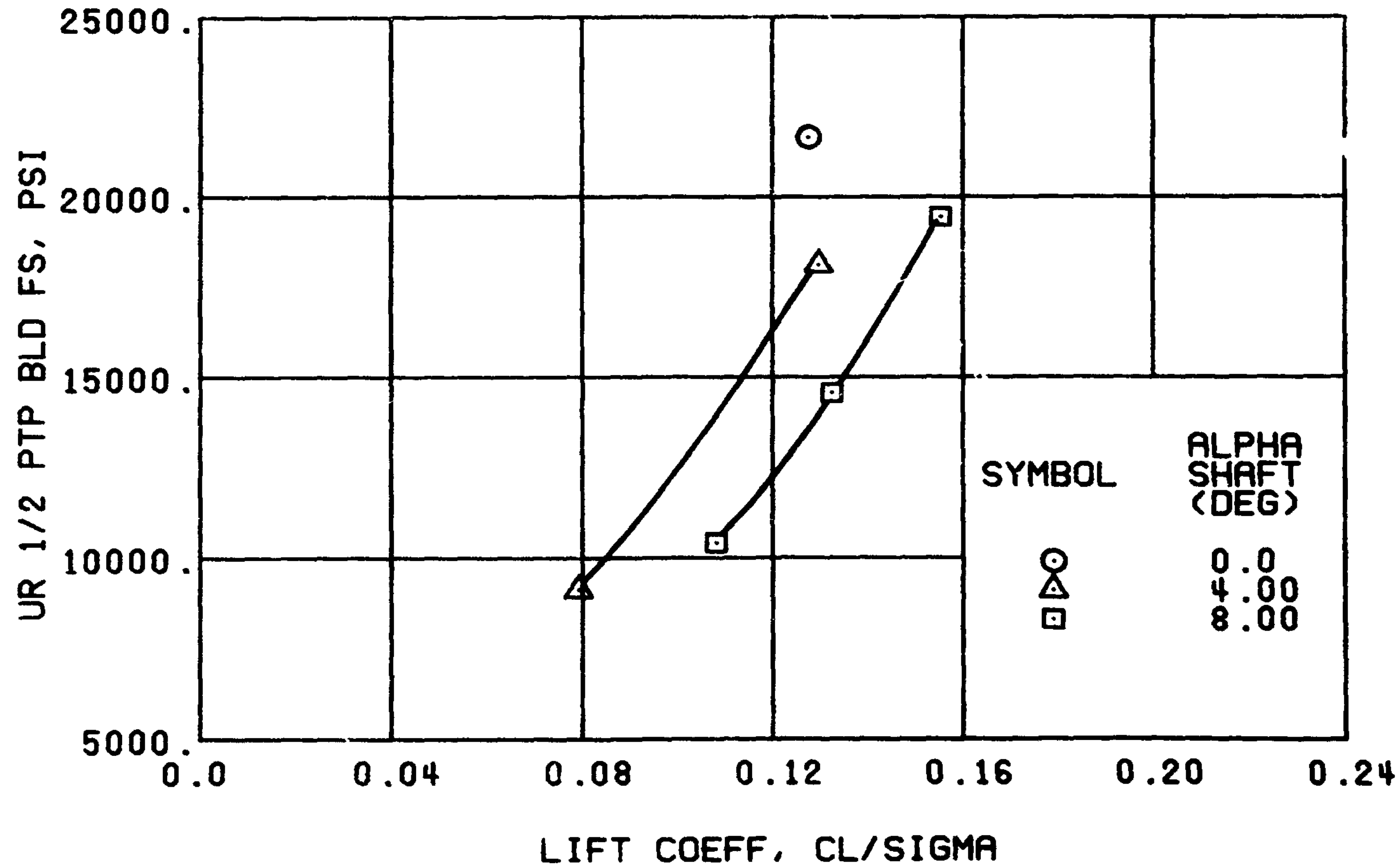

(c) GAGE 52 R108

Figure 50. **Continued.**
$\mu = 0.47$ $B'_{1s} = 2$ Deg

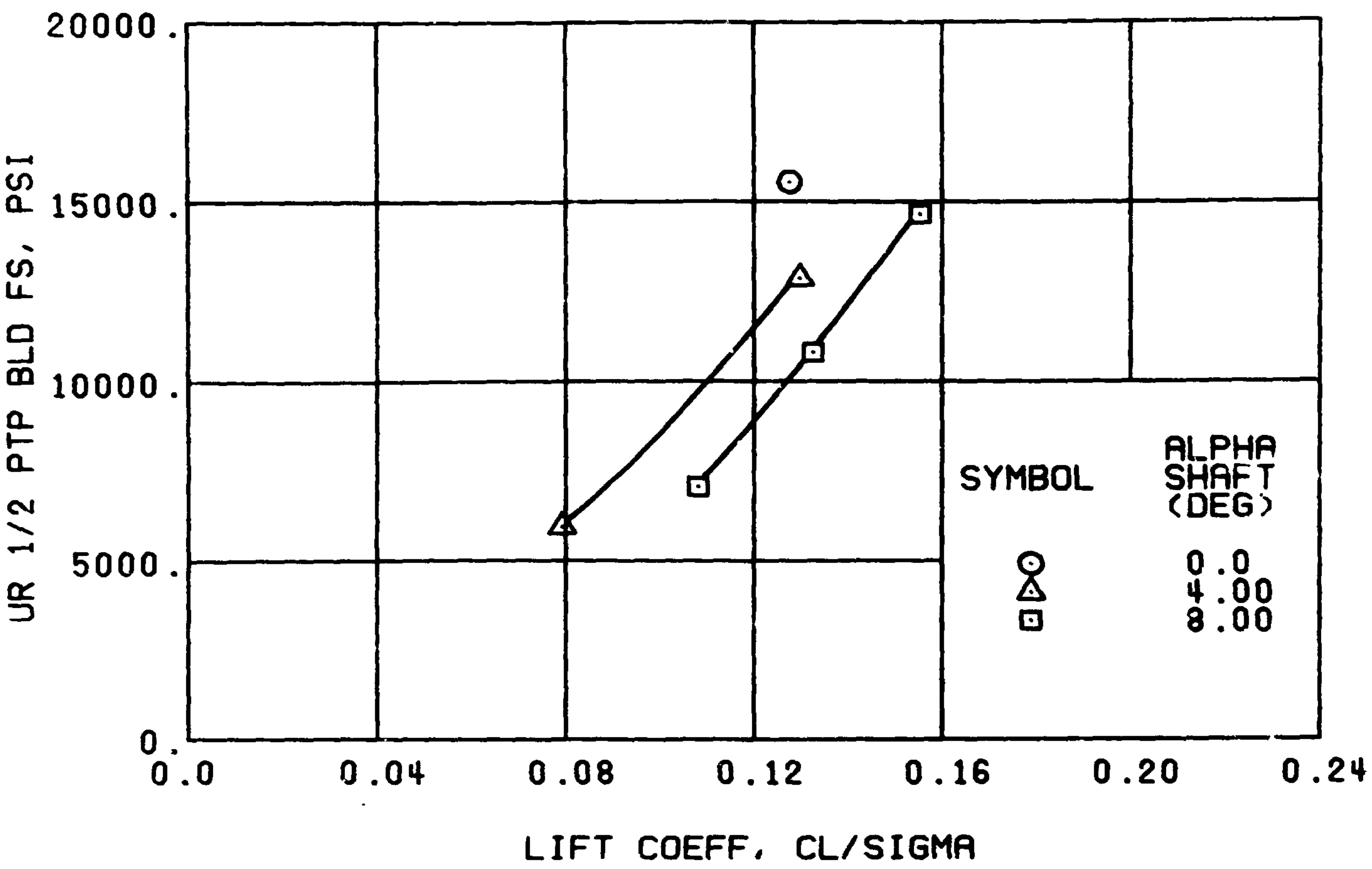

(d) GAGE 53 R132

Figure 50. Continued.
$\mu = 0.47 \quad B'_{1s} = 2$ Deg

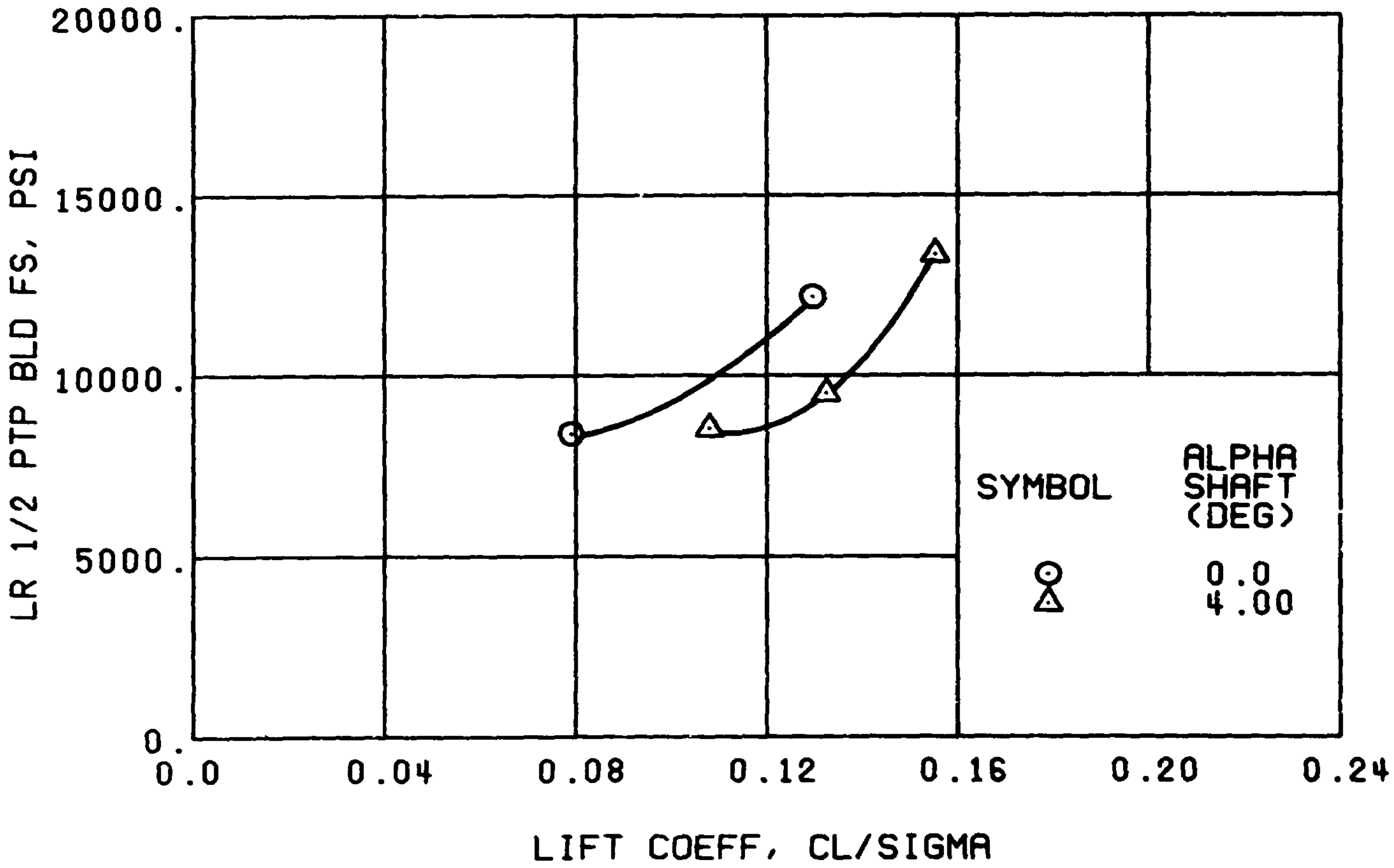

(e) GAGE 93 R132

Figure 50. **Continued.**
$\mu = 0.47$ $B'_{1s} = 2$ Deg

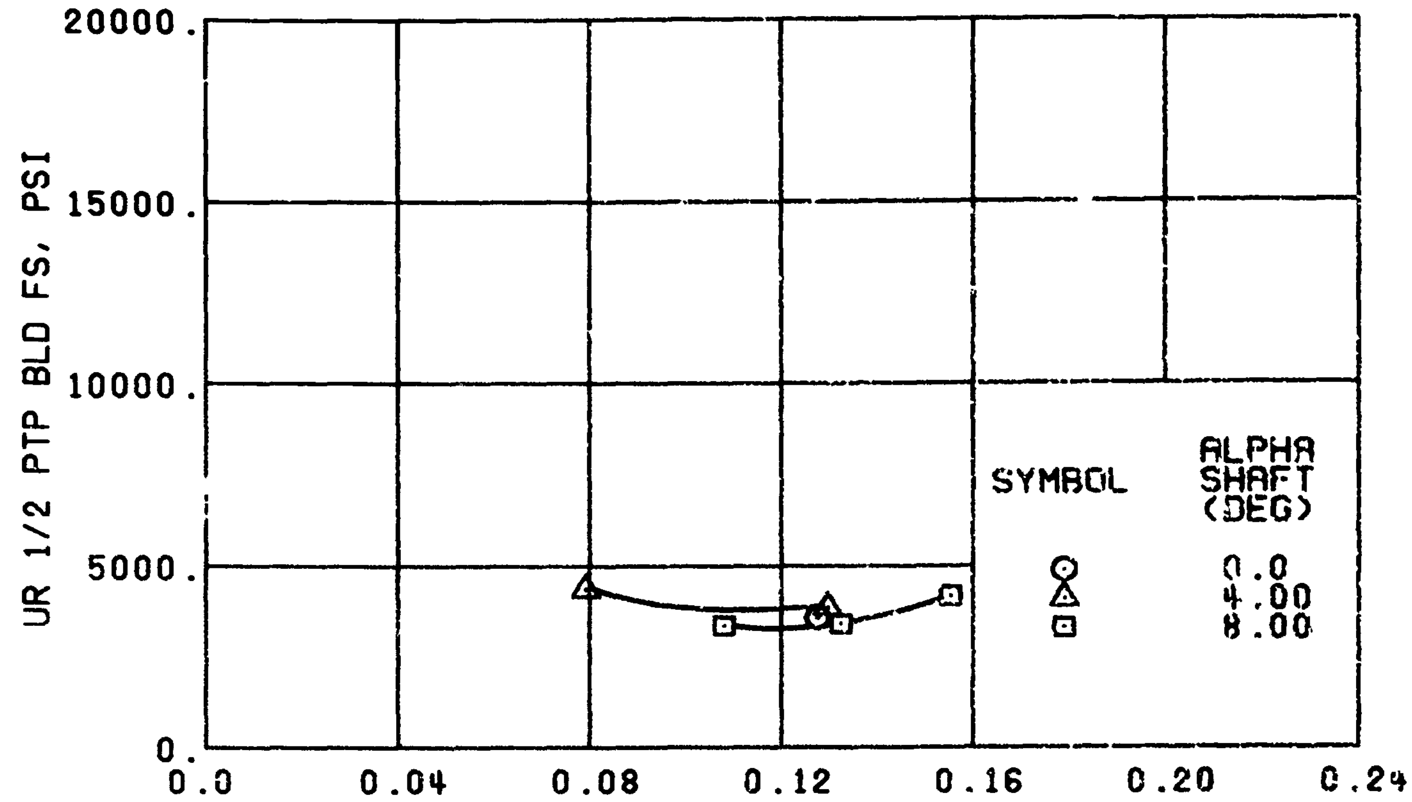

(f) GAGE 55 R204

Figure 50. Continued.
$\mu = 0.47$ $B_{1s}' = 2$ Deg

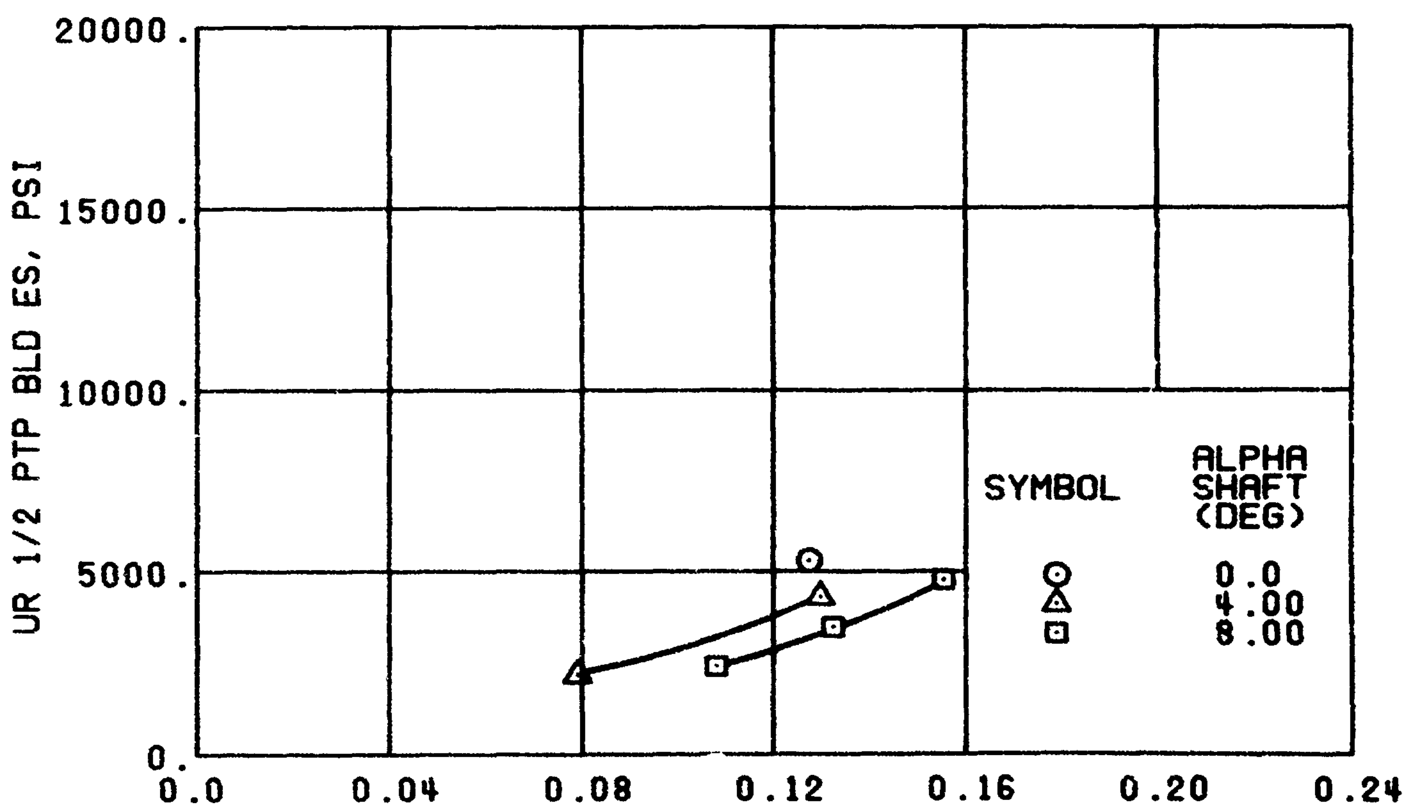

(h) GAGE 40 R84

Figure 50. Continued.
$\mu = 0.47$ $B'_{1s} = 2$ Deg

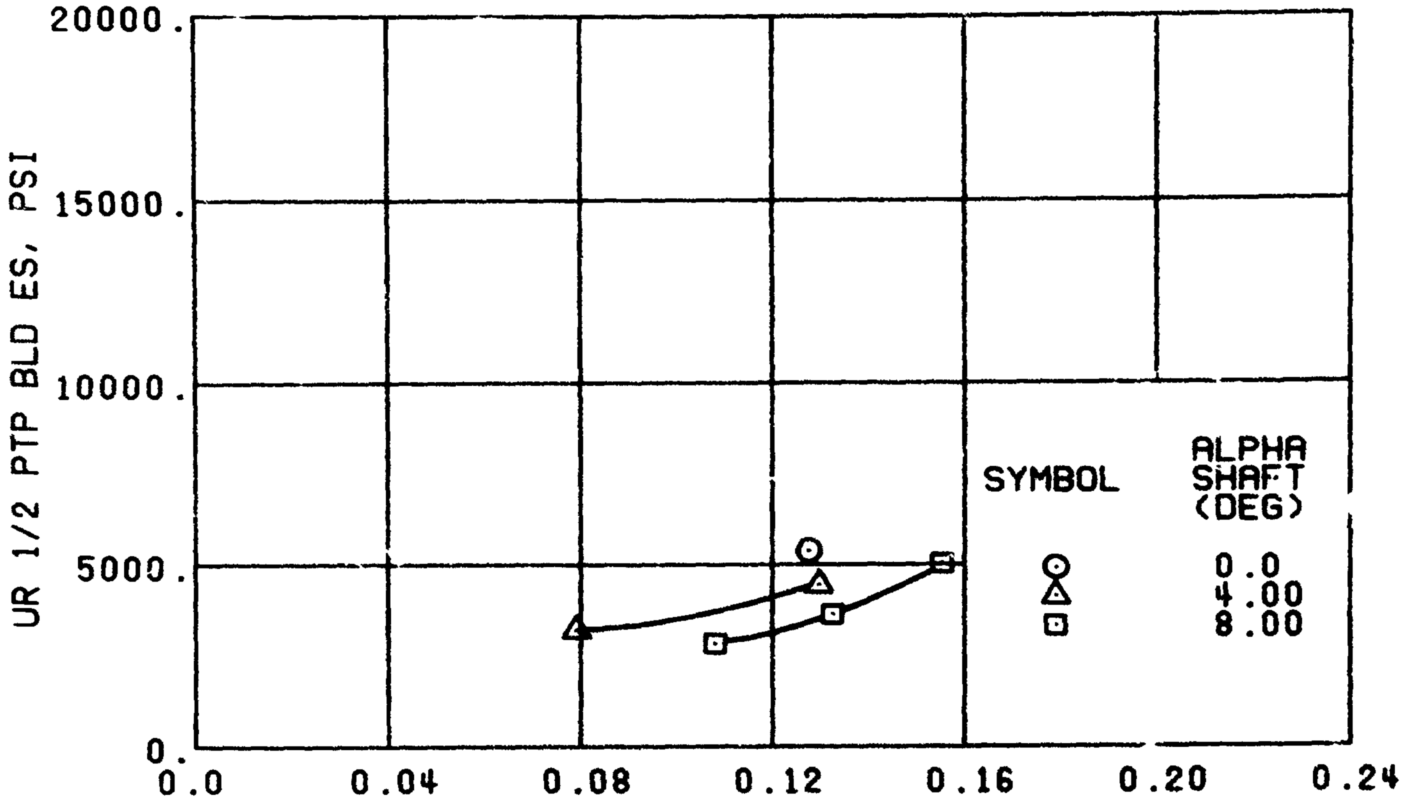

(j) GAGE 42 R132

Figure 50. Continued.
$\mu = 0.47$ $B'_{1s} = 2$ Deg

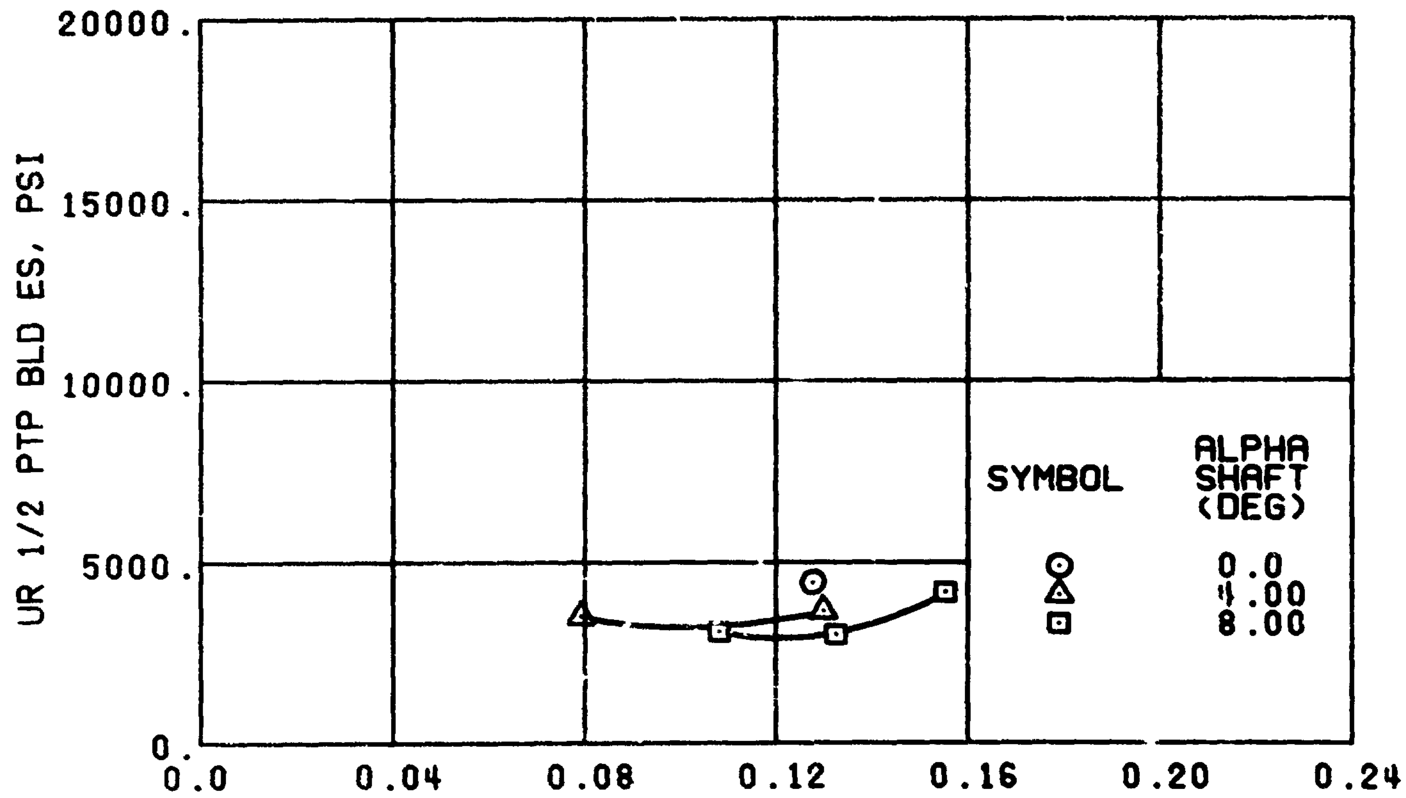

(k) GAGE 43 R166

Figure 50. Continued.
$\mu = 0.47$ $B'_{1s} = 2$ Deg

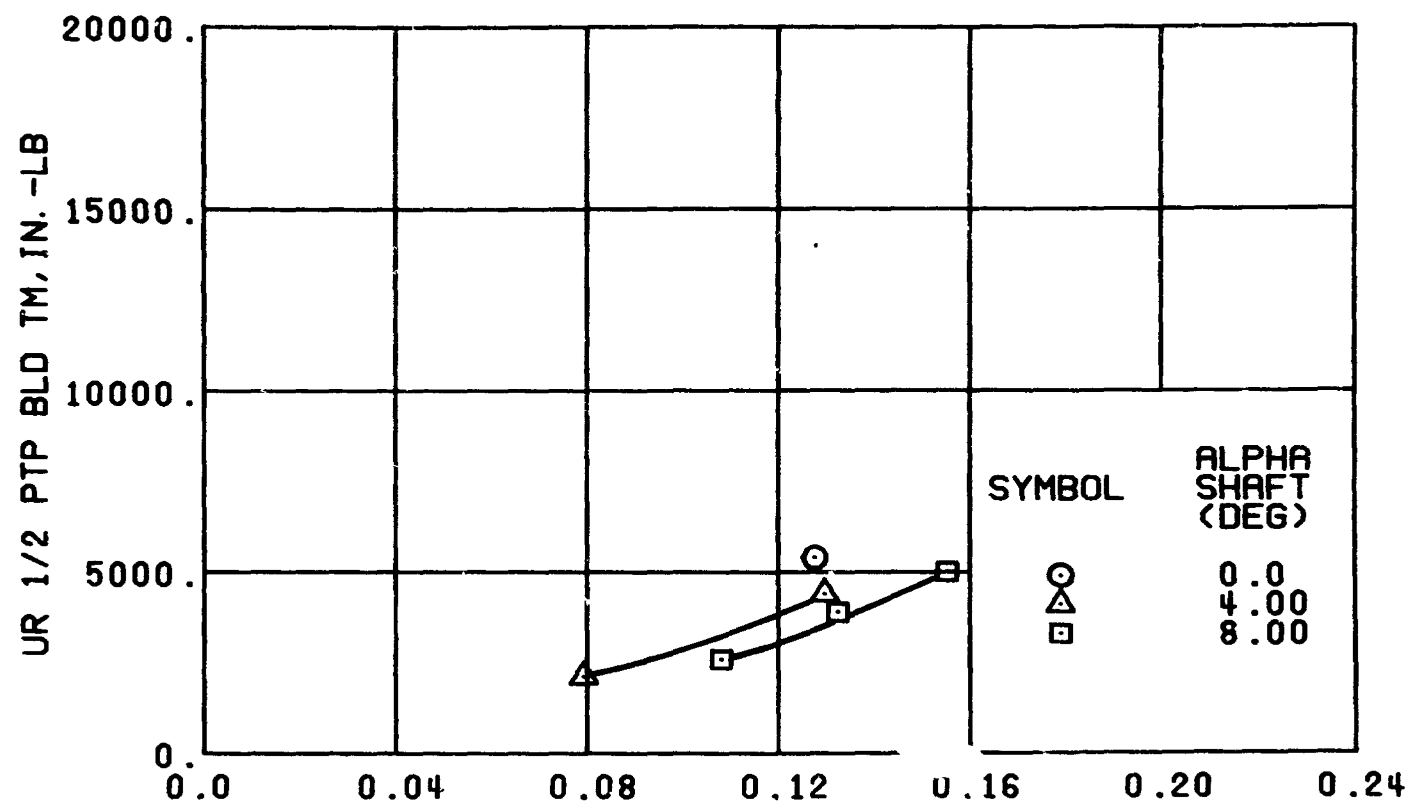

(m) GAGE 46 R130

Figure 50. Continued.
$\mu = 0.47 \quad B'_{1s} = 2$ Deg

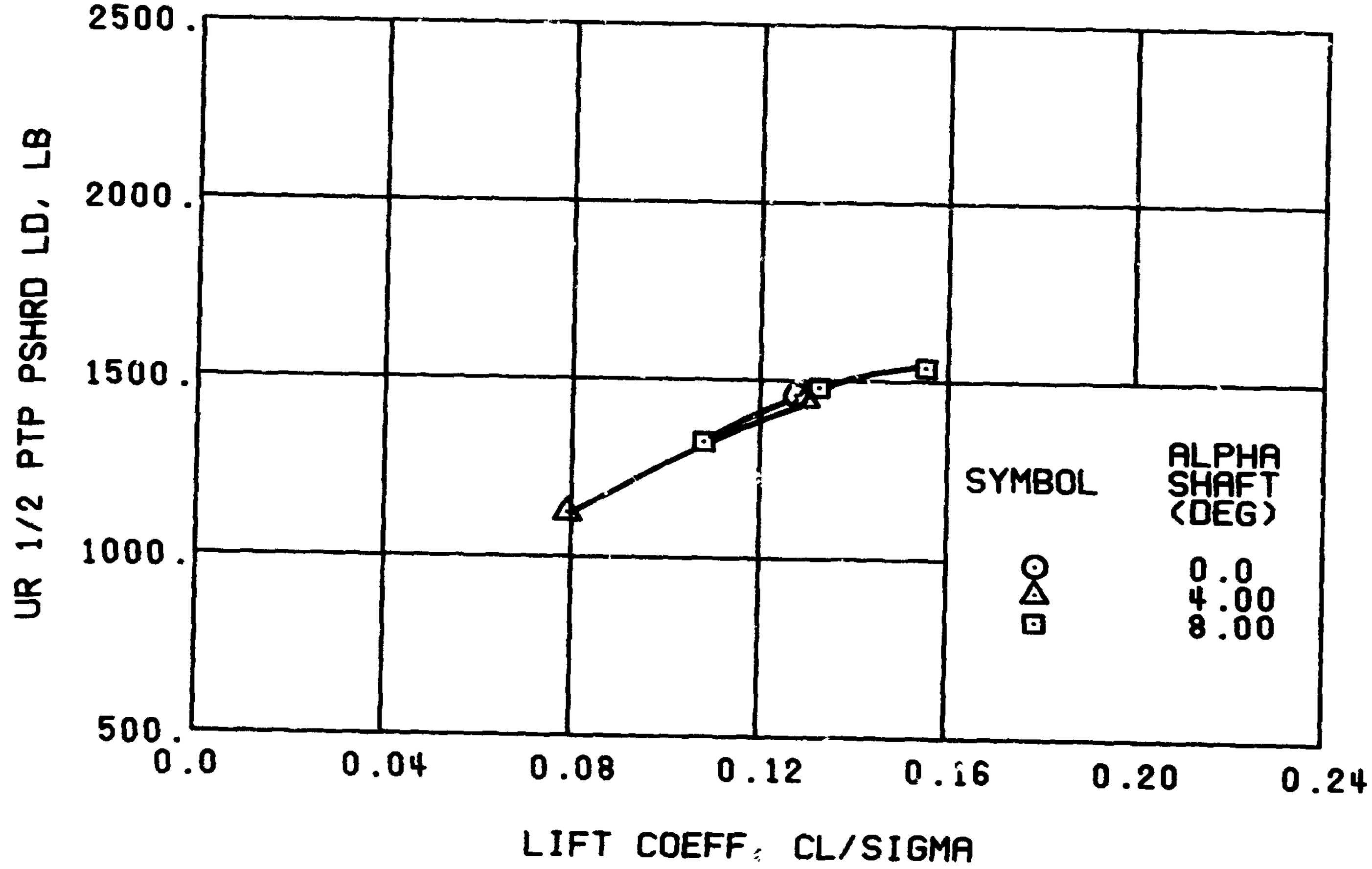

(n) GAGE 37

Figure 50. Continued.
$\mu = 0.47$ $B'_{1s} = 2$ Deg

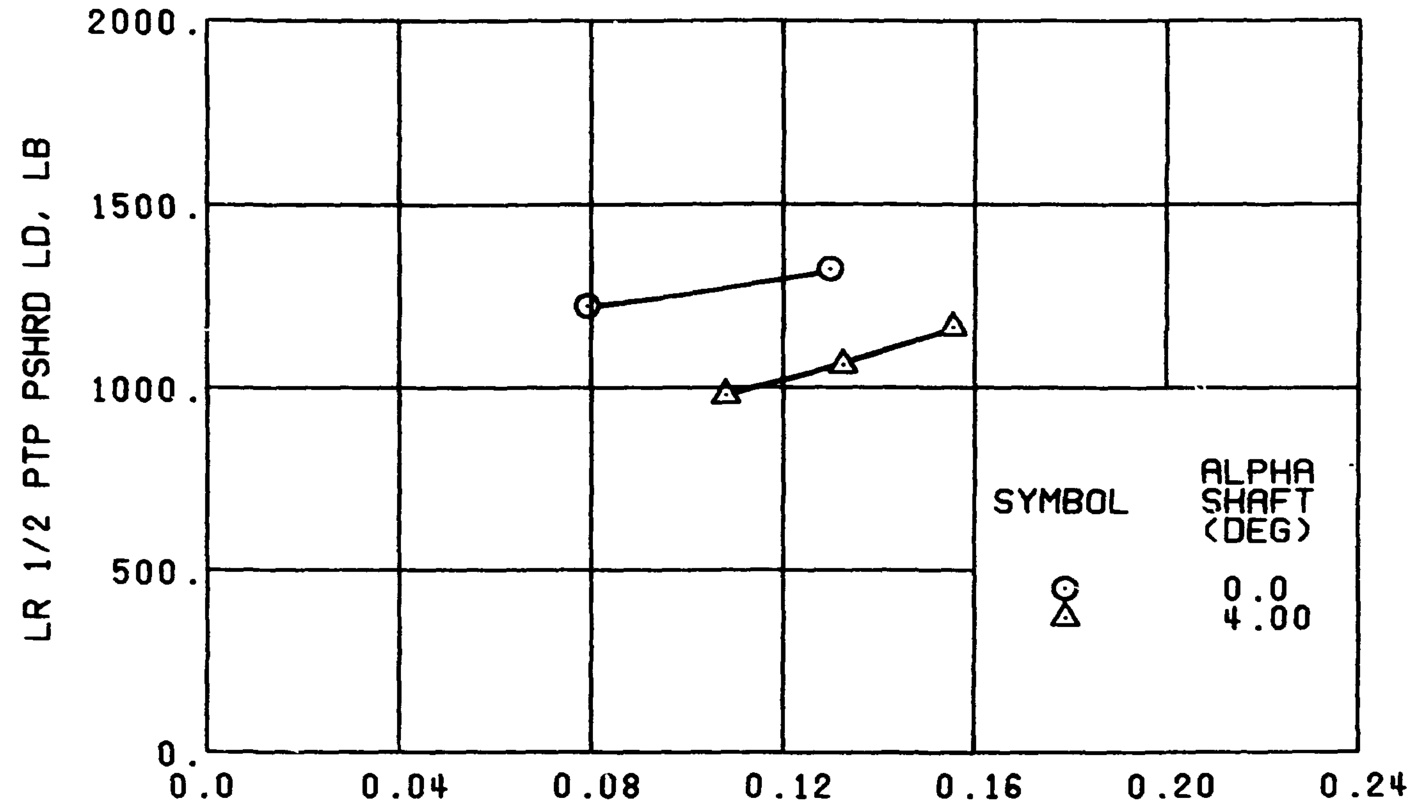

(o) GAGE 34

Figure 50. Continued.
$\mu = 0.47 \quad B'_{1s} = 2$ Deg

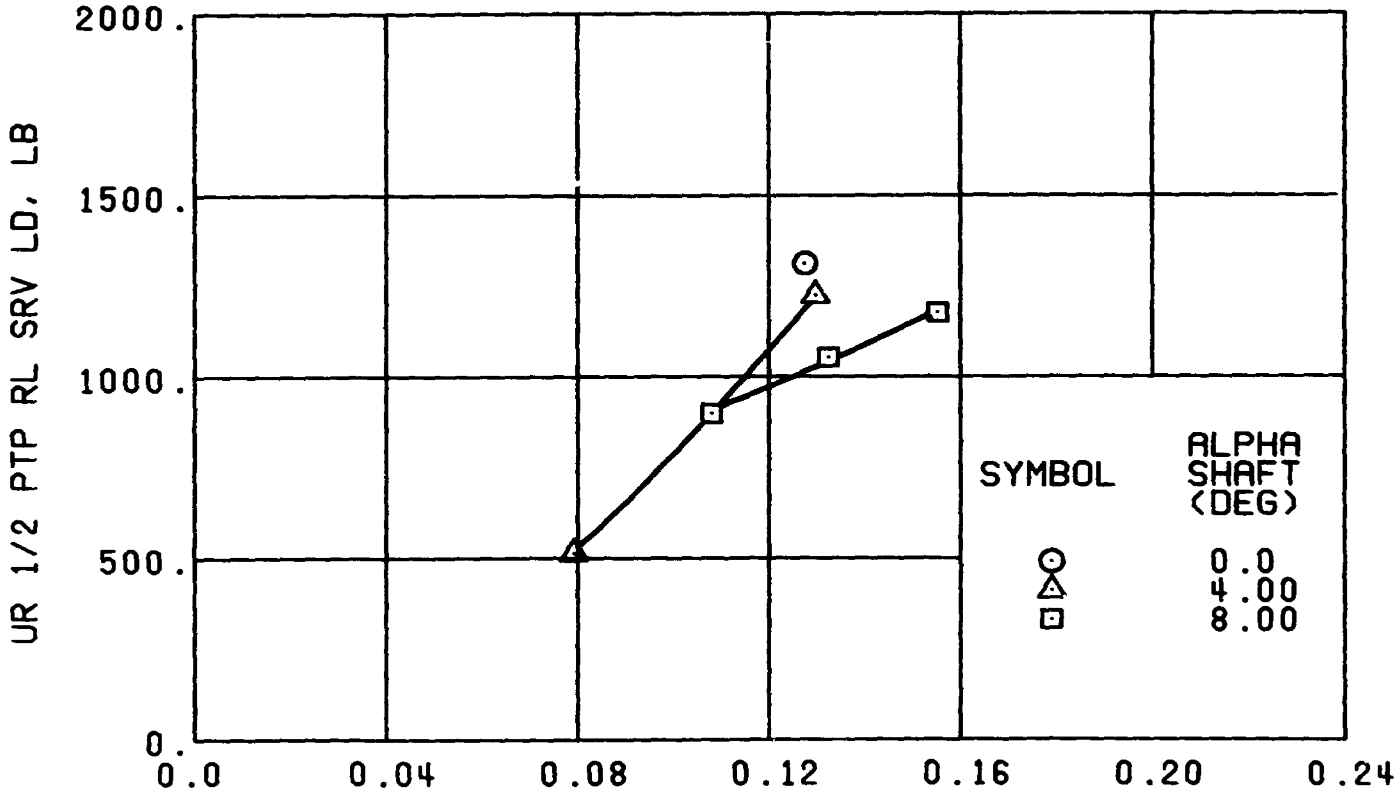

(p) GAGE 22

Figure 50. Continued.
$\mu = 0.47$ $B'_{1s} = 2$ Deg

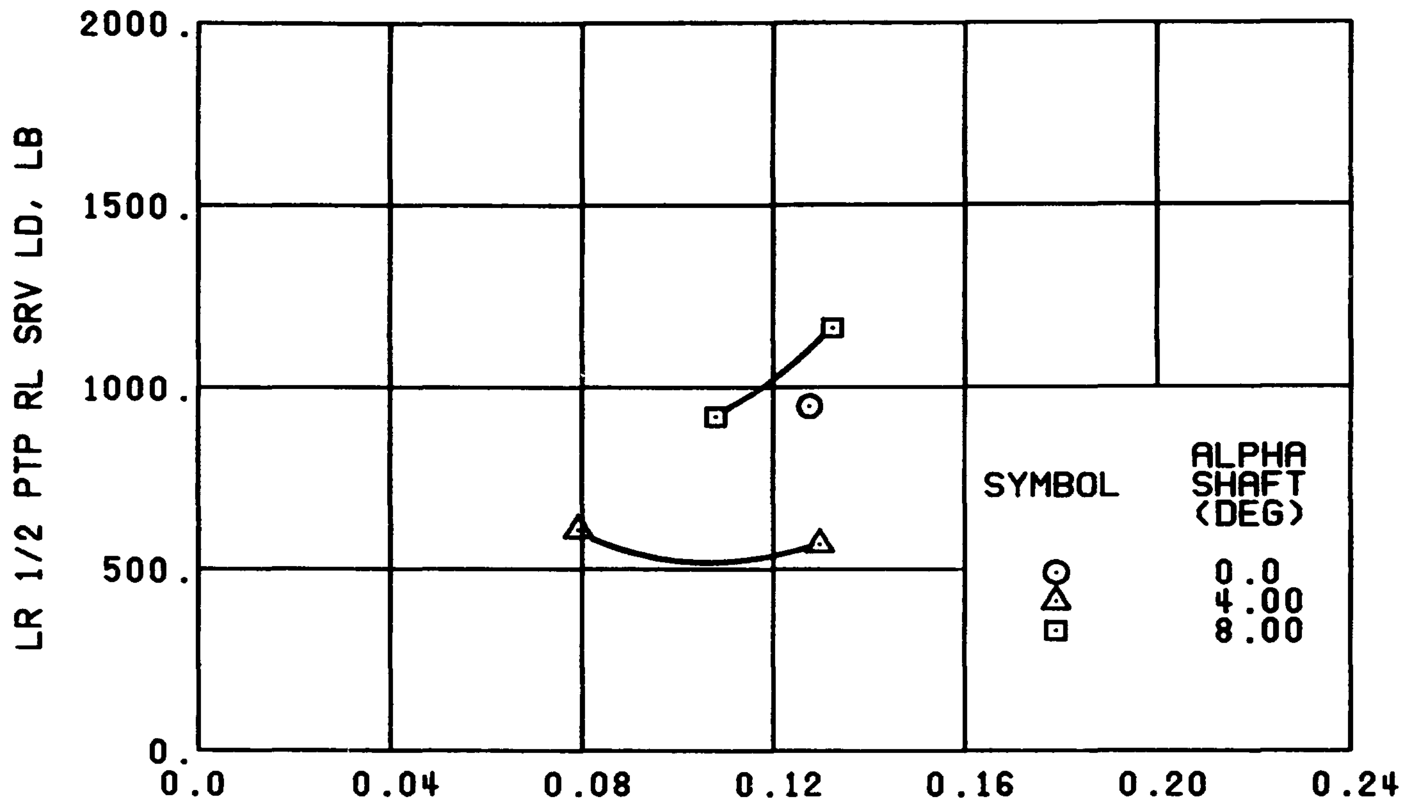

(q) GAGE 25

Figure 50. **Continued.**
$\mu = 0.47$ $B'_{1s} = 2$ Deg

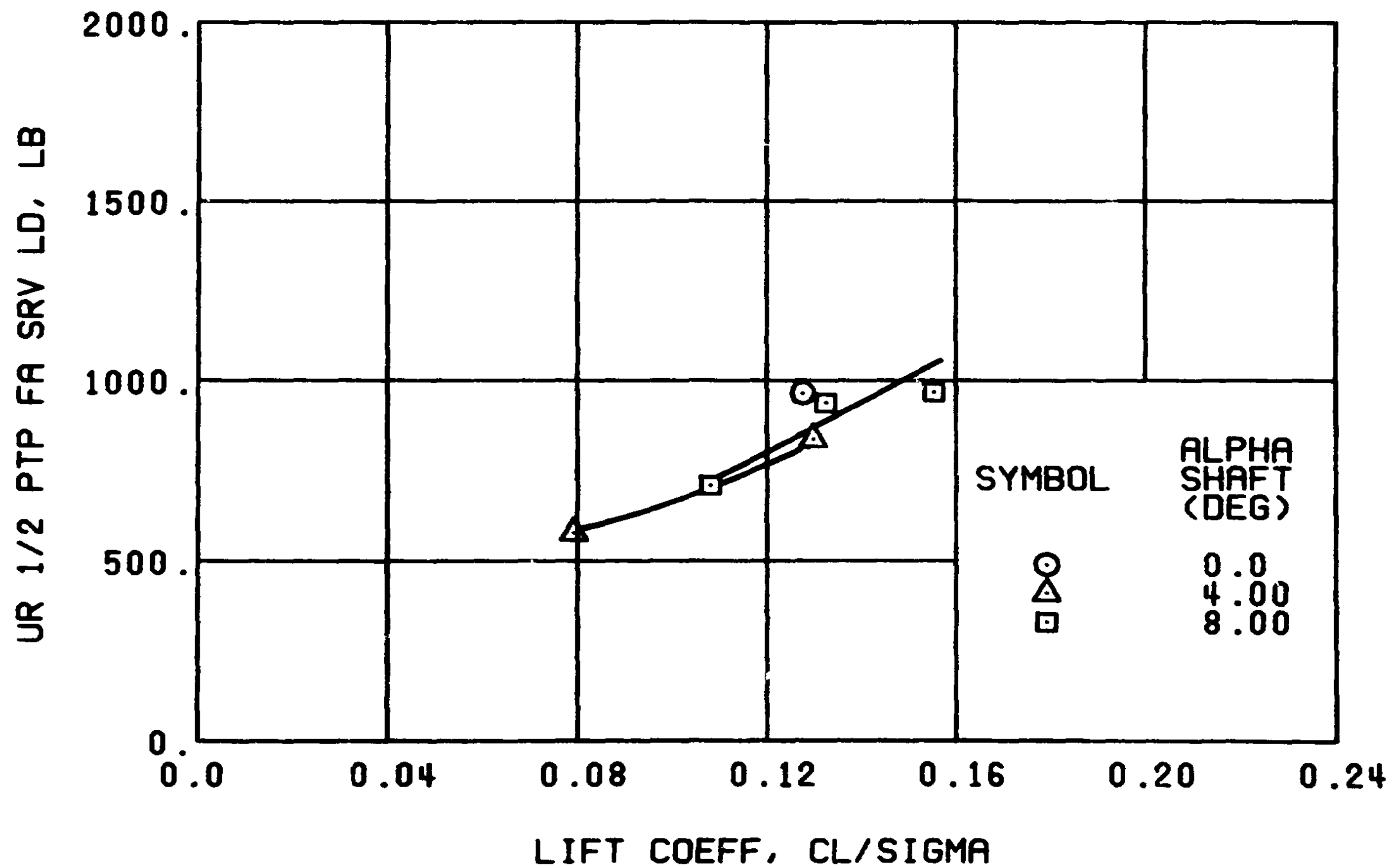

(r) GAGE 24

Figure 50. Continued.
$\mu = 0.47 \quad B'_{1s} = 2$ Deg

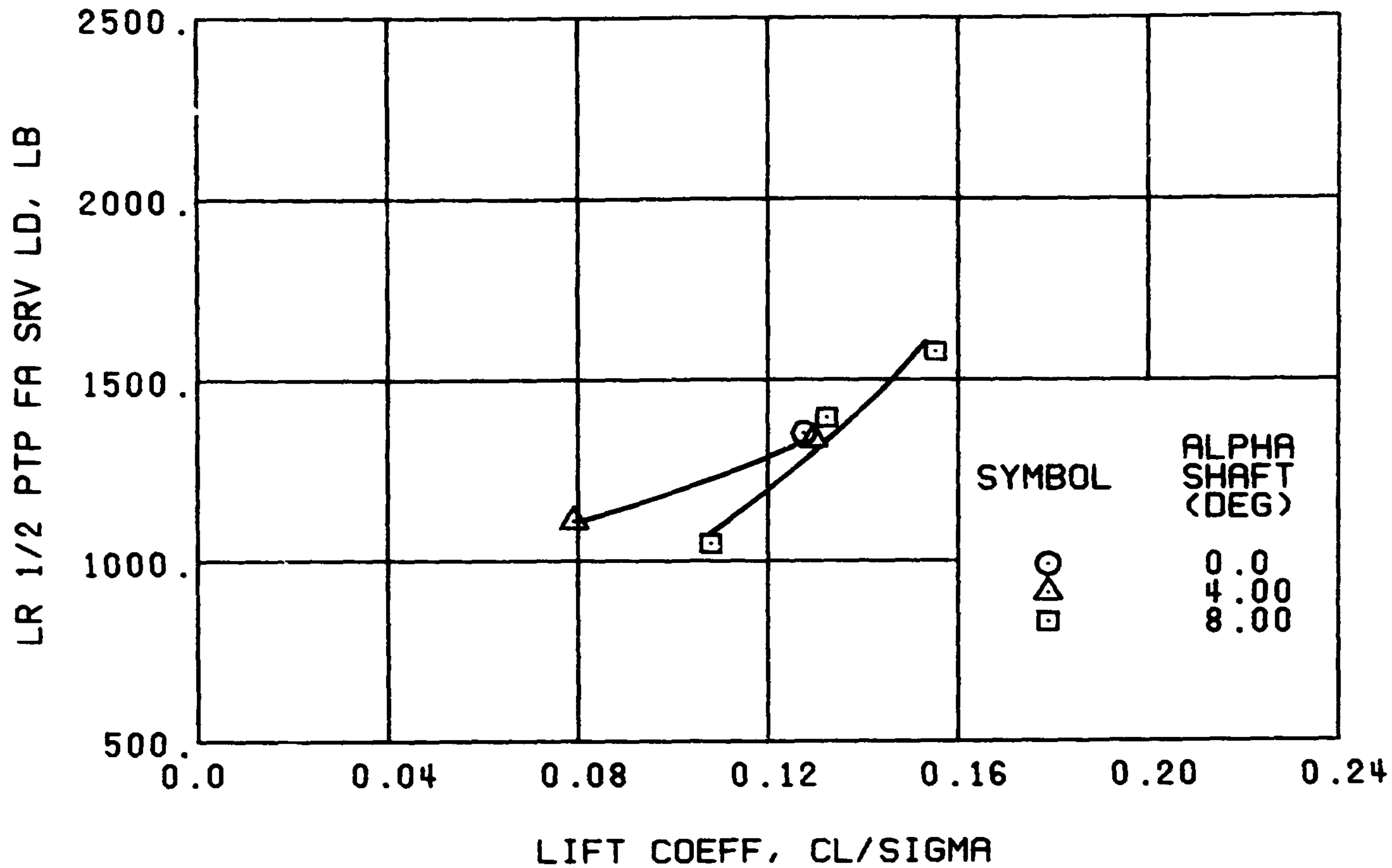

(s) GAGE 27

Figure 50. Continued.
$\mu = 0.47$ $B'_{1s} = 2$ Deg

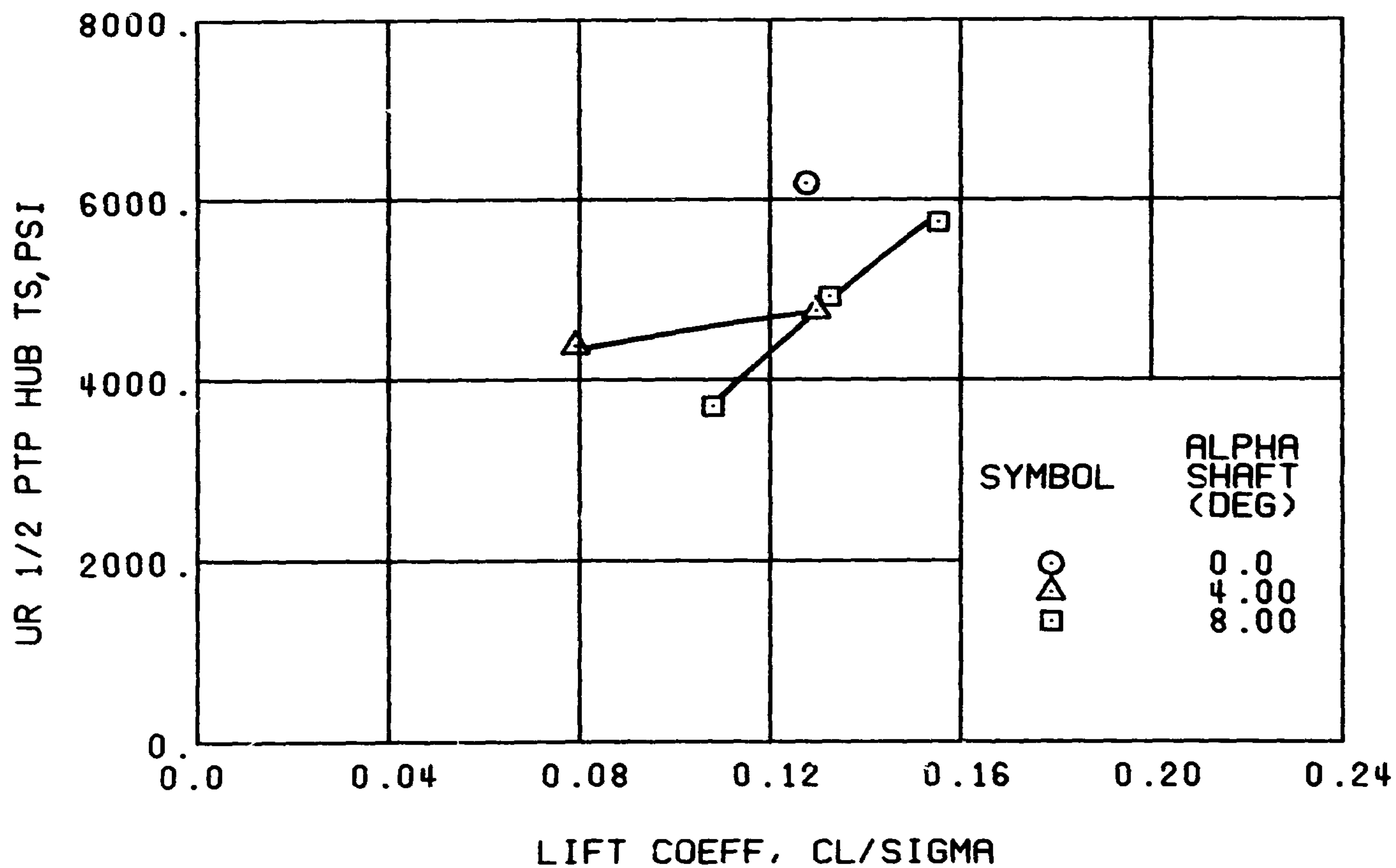

(f) GAGE 65

Figure 50. Continued.
$\mu = 0.47 \quad B_{1s}' = 2$ Deg

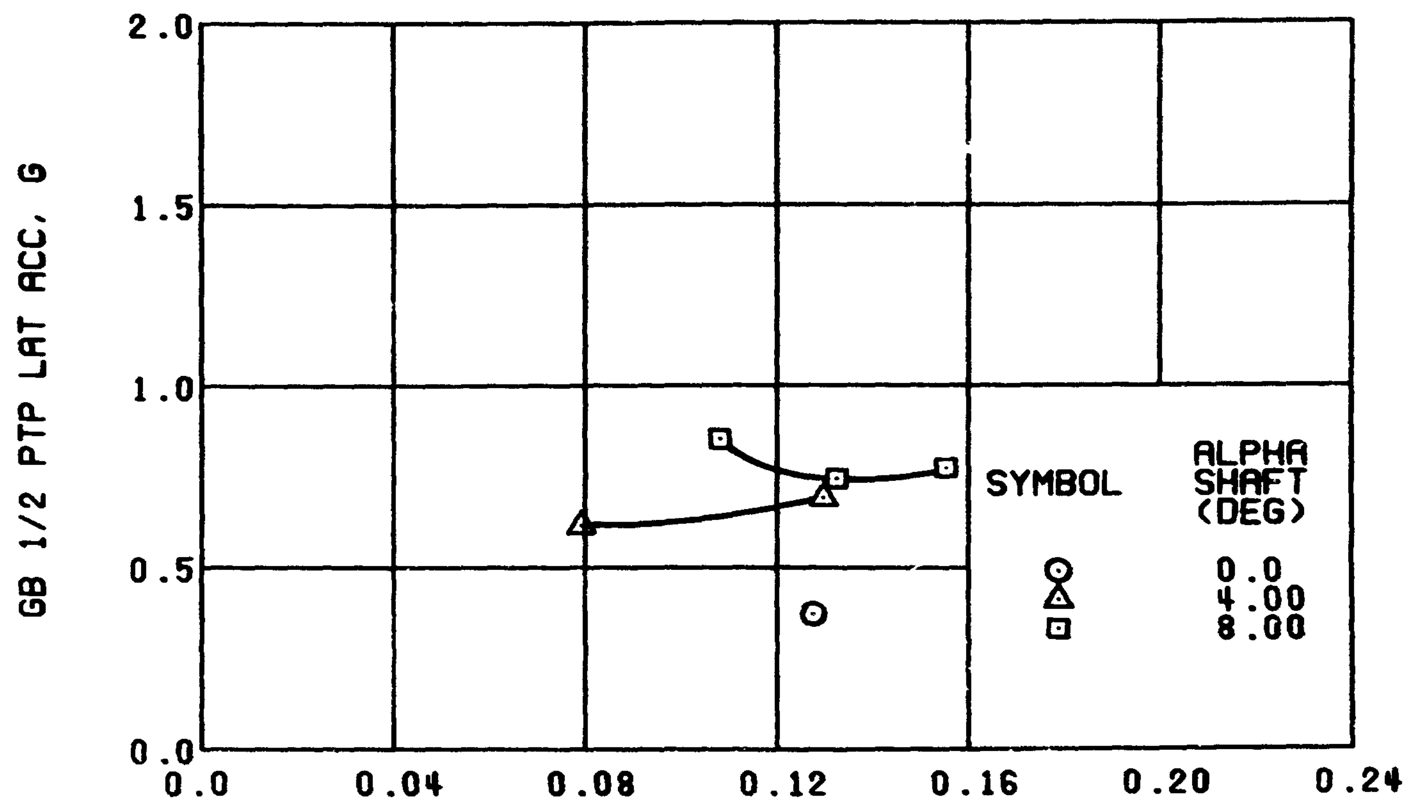

(u) GAGE 15 STA 76, BL 30

Figure 50. **Continued.**
μ = 0.47 B'_{1s} = 2 Deg

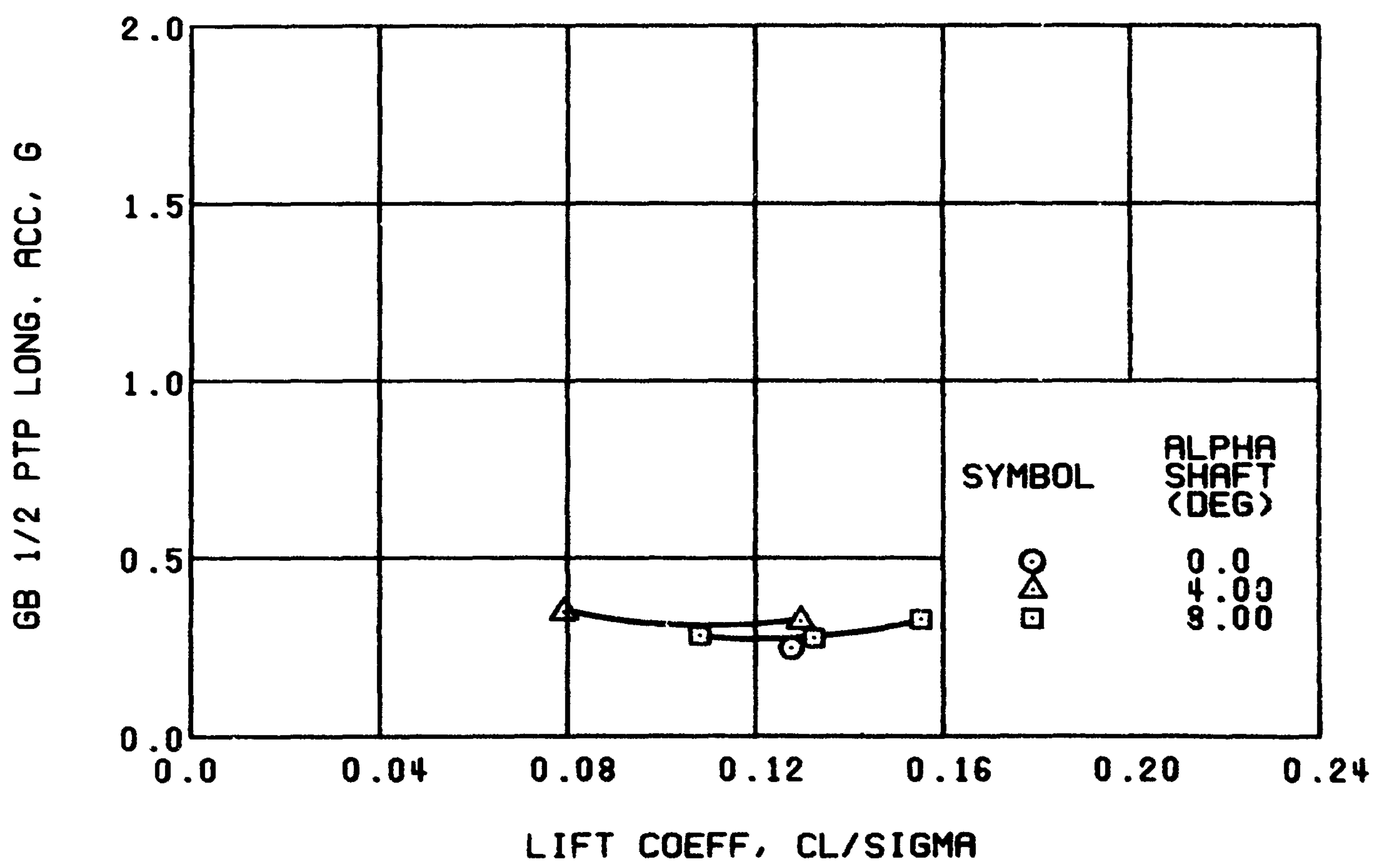

(v) GAGE 14 STA 61, BL 0

Figure 50. **Continued.**
$\mu = 0.47$ $B'_{1s} = 2$ Deg

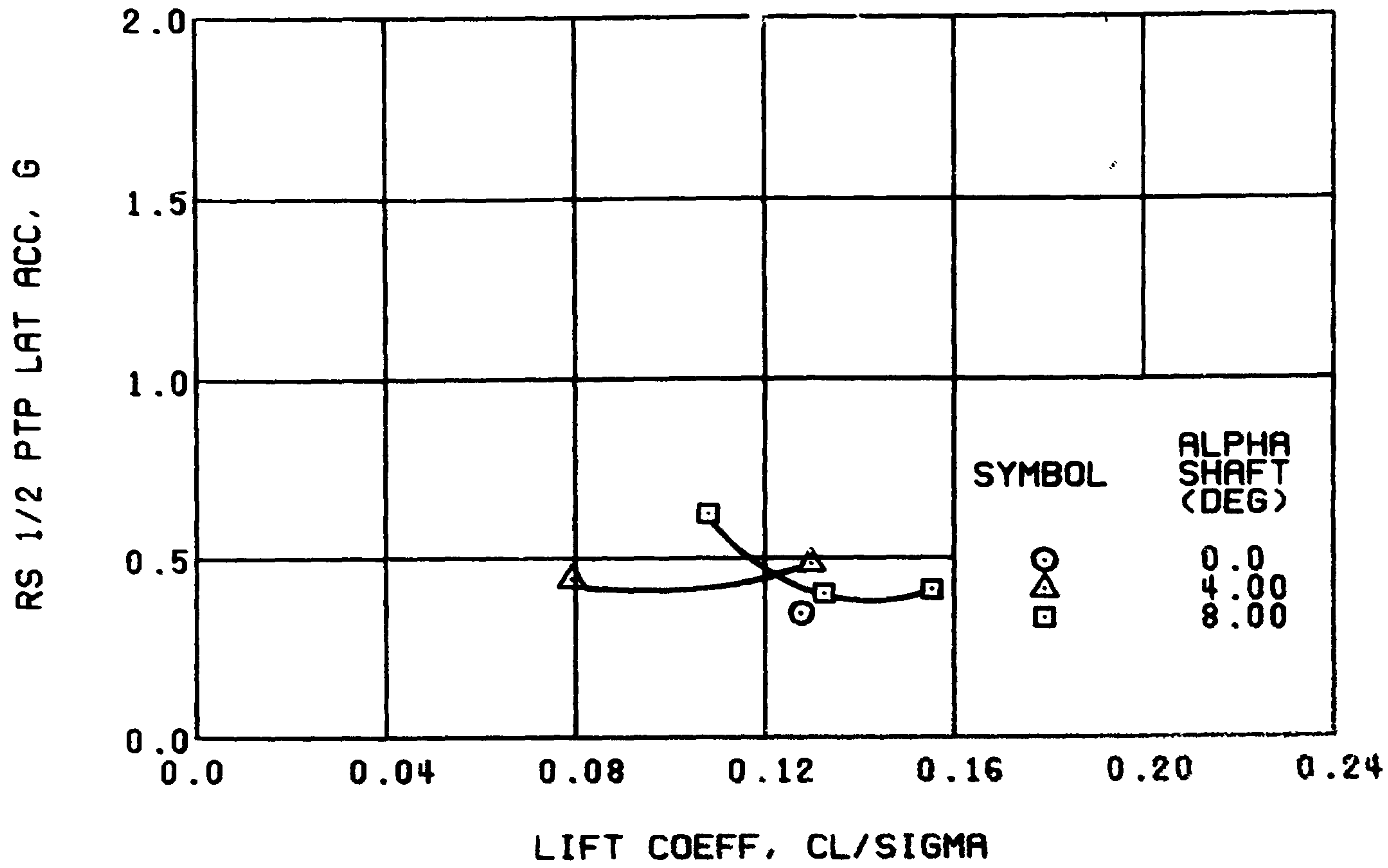

(w) GAGE 16 ROVER 3

Figure 50. Continued.
$\mu = 0.47$ $B'_{1s} = 2$ Deg

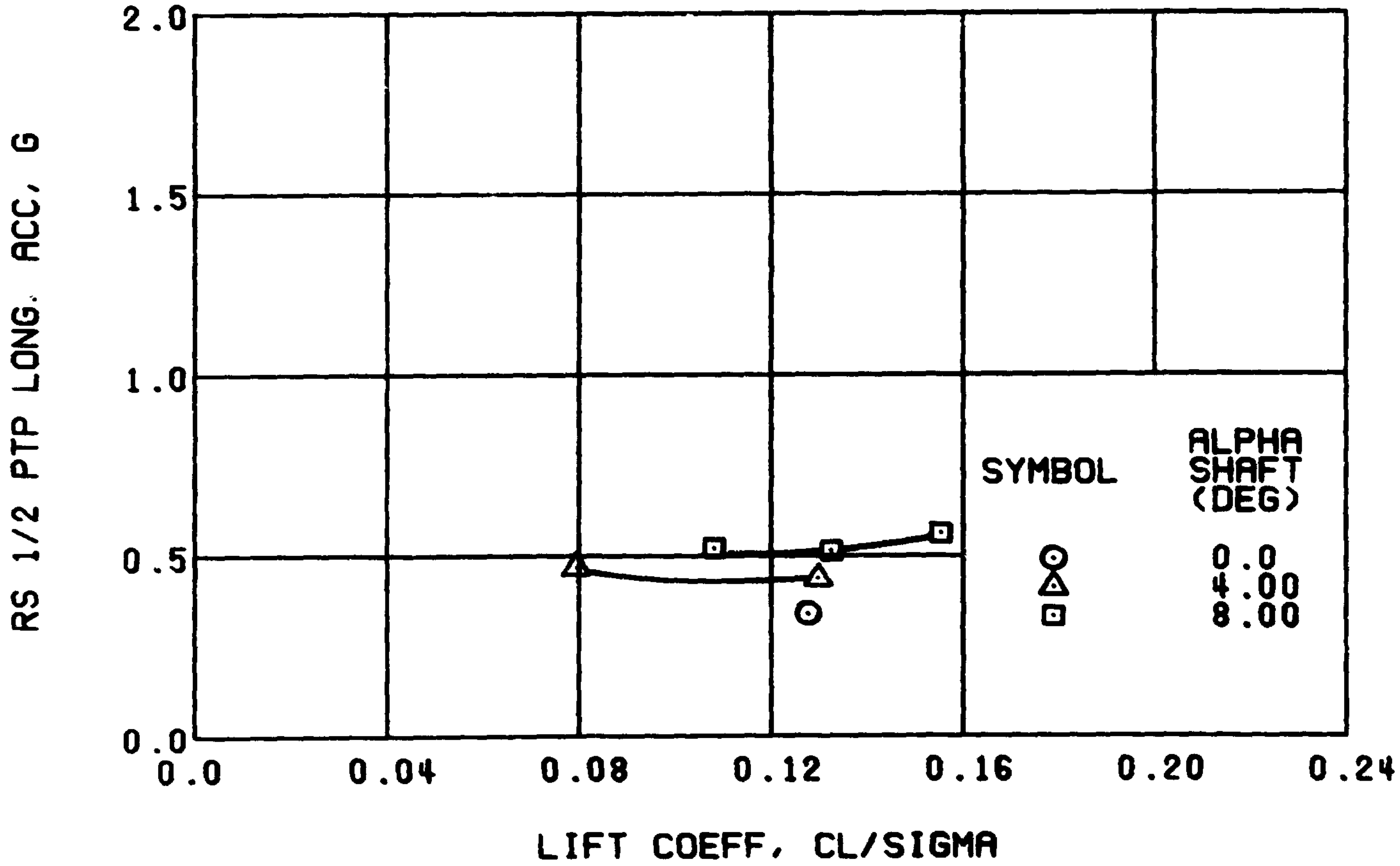

(x) GAGE 17 ROVER 4

Figure 50. Concluded.
$\mu = 0.47 \quad B'_{1s} = 2$ Deg

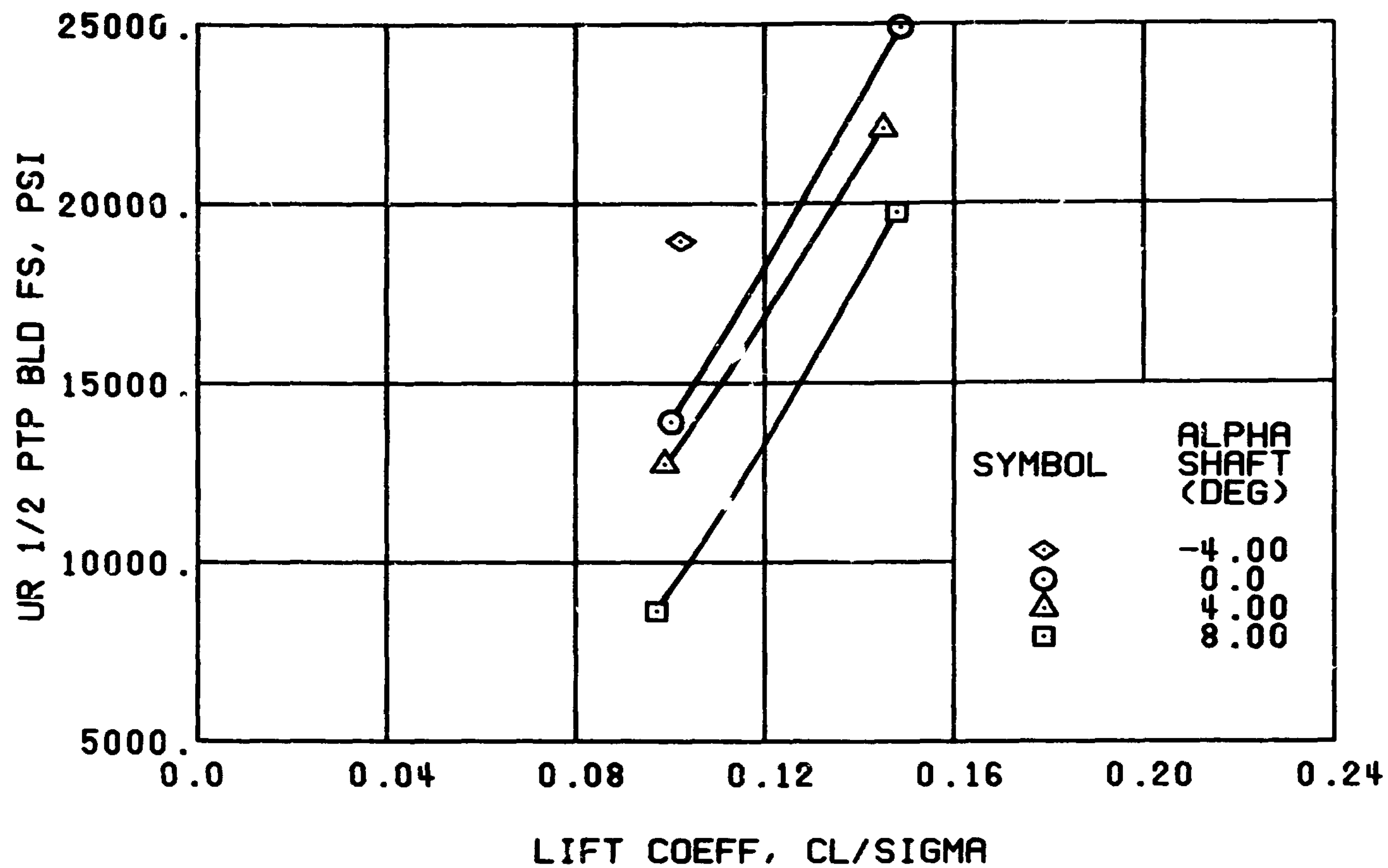

(a) GAGE 51 R84

Figure 51.: Stress, Load, and Vibration Data at an Advance Ratio of 0.47 With the Lateral Displacement Control (B'_{1s}) Set at 4 Degrees.

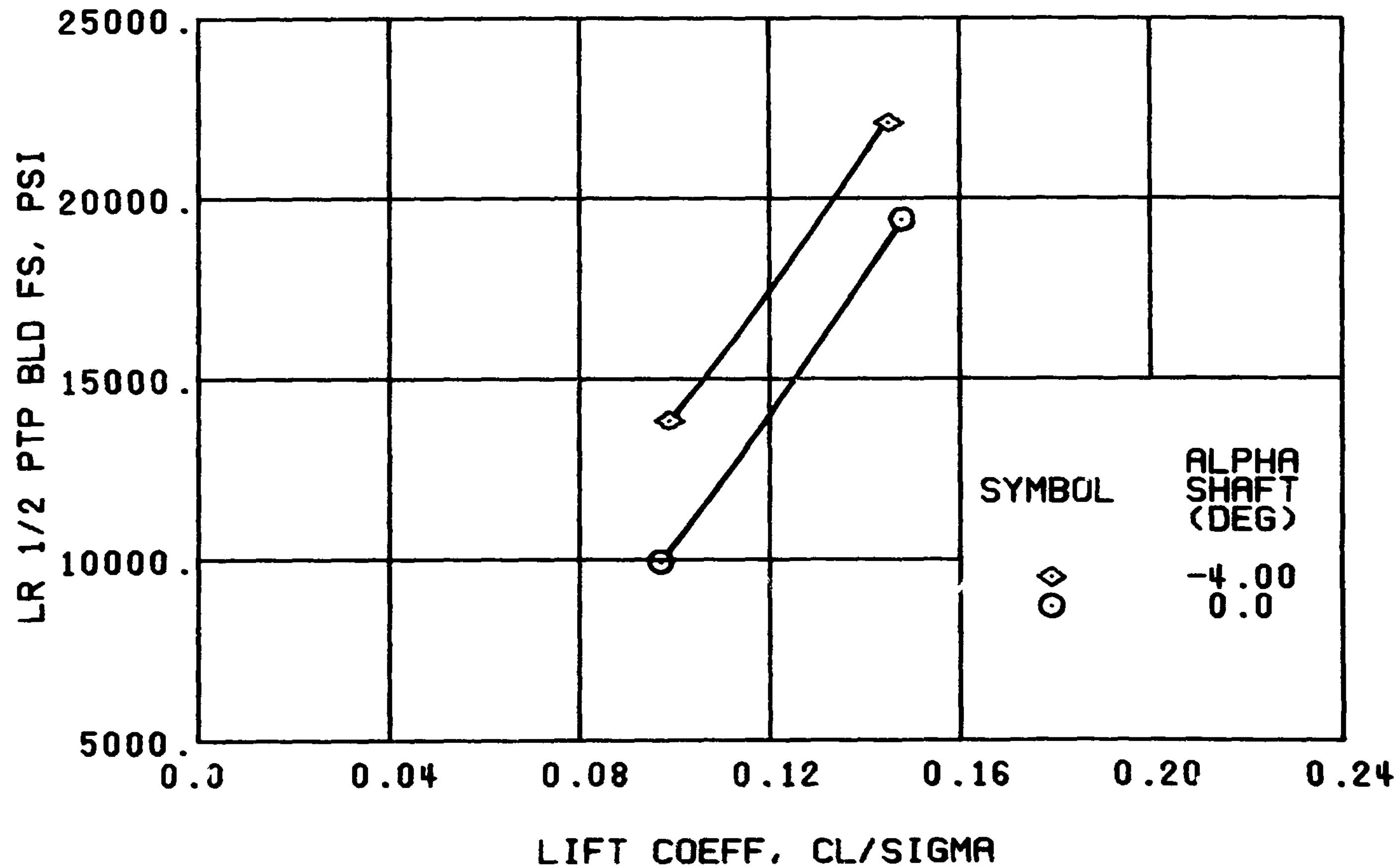

(b) GAGE 1 R84

Figure 51. Continued.
$\mu = 0.47$ $B'_{1s} = 4$ **Deg**

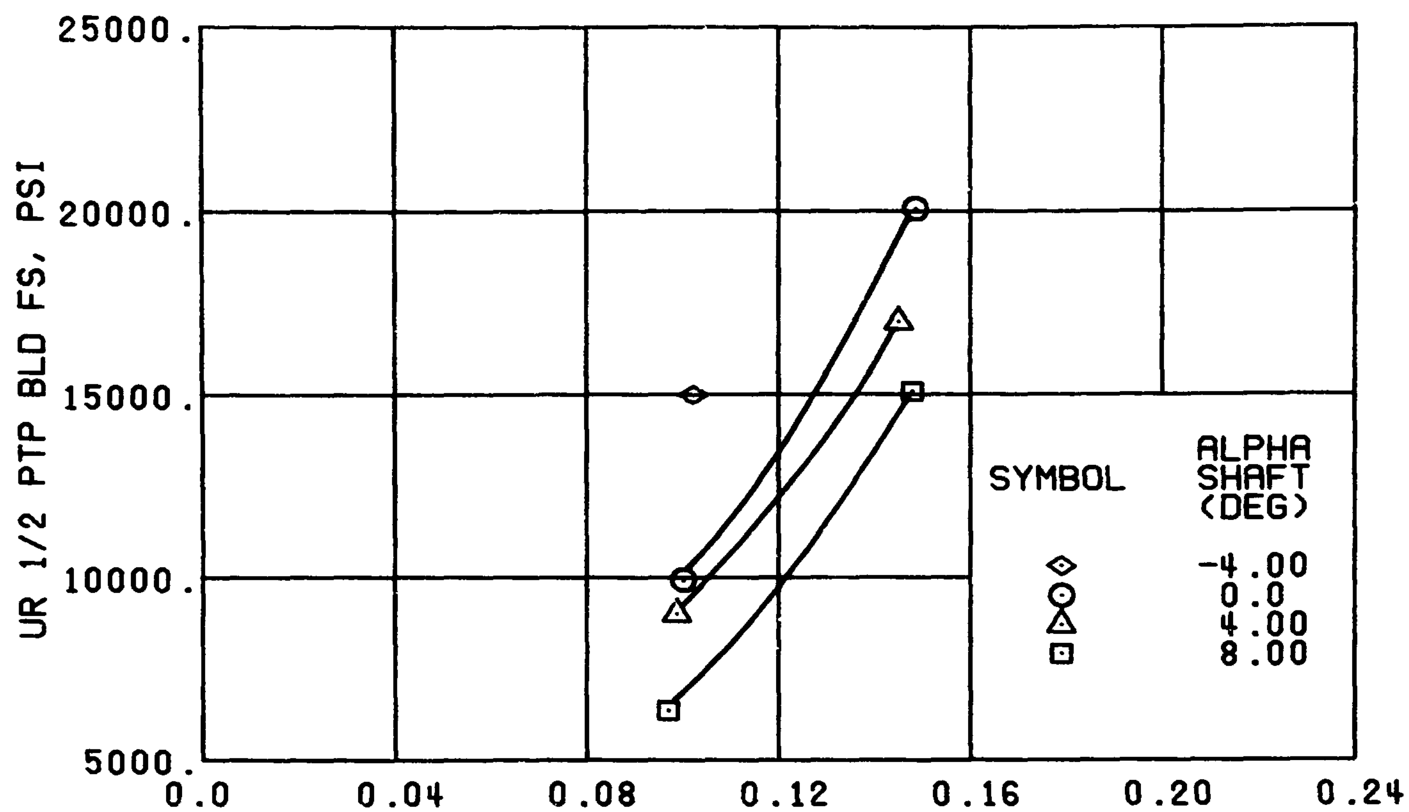

(c) GAGE 52 R108

Figure 51. Continued.
$\mu = 0.47$ $B'_{1s} = 4$ Deg

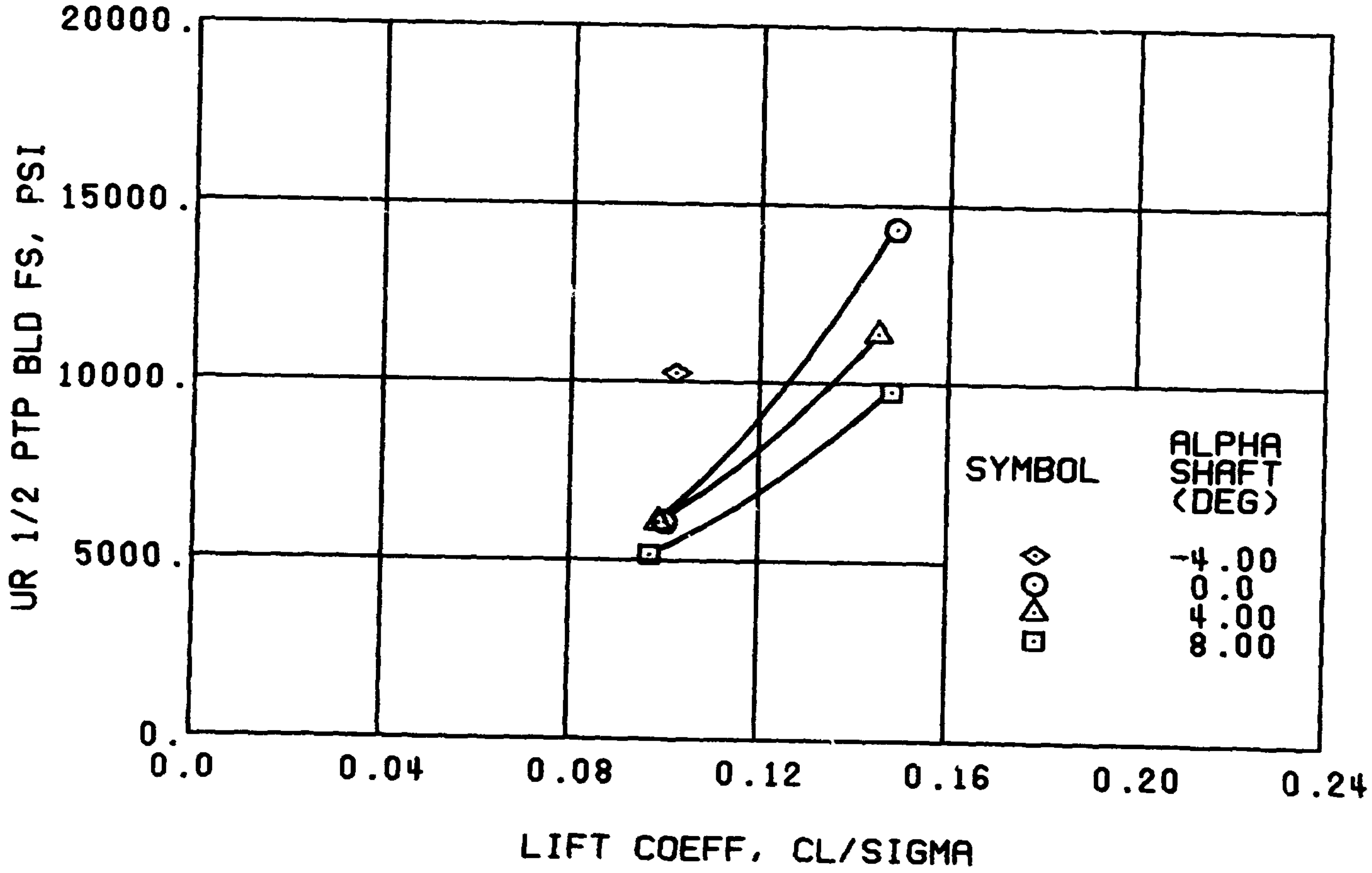

(d) GAGE 53 R132

Figure 51. Continued.
$\mu = 0.47$ $B'_{1s} = 4$ Deg

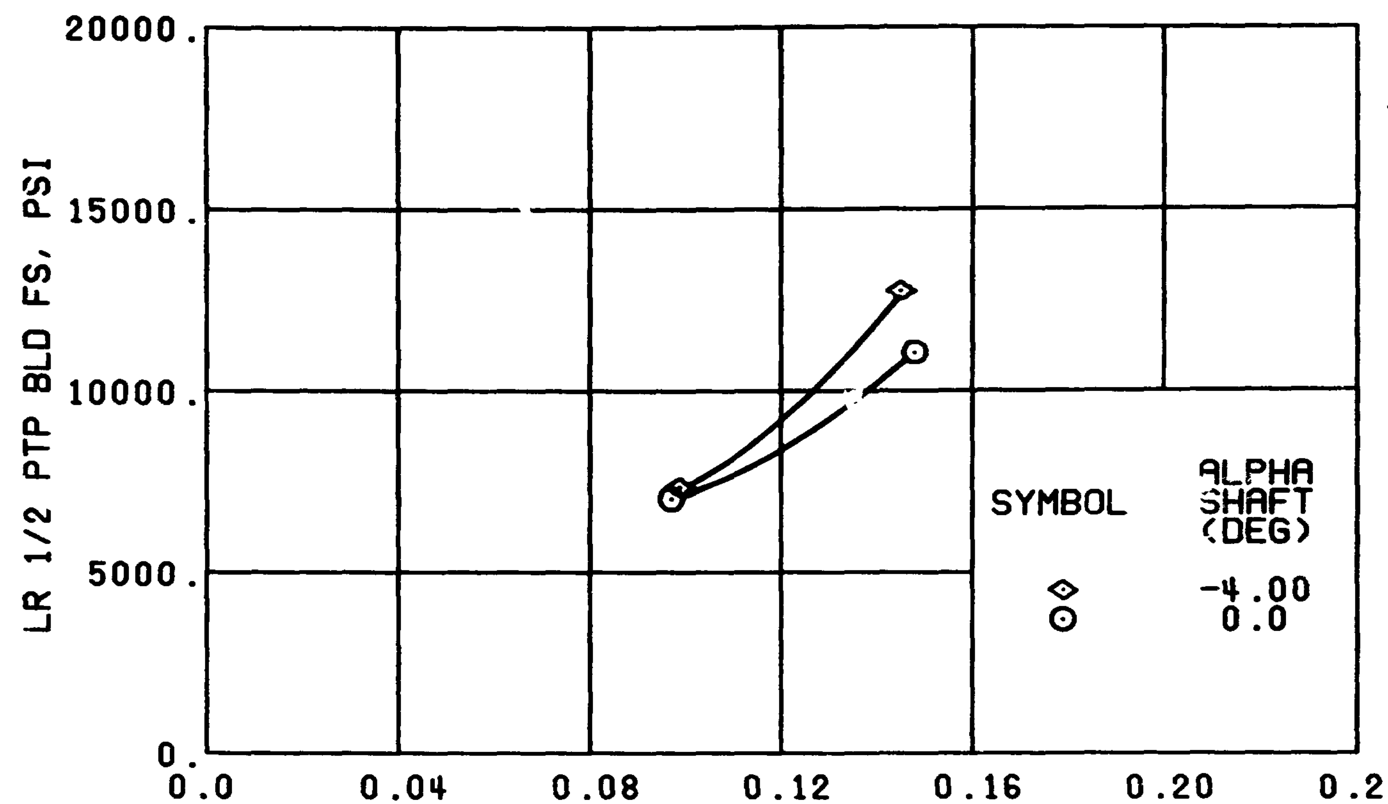

(e) GAGE 93 R132

Figure 51. Continued.
$\mu = 0.47$ $B'_{1s} = 4$ Deg

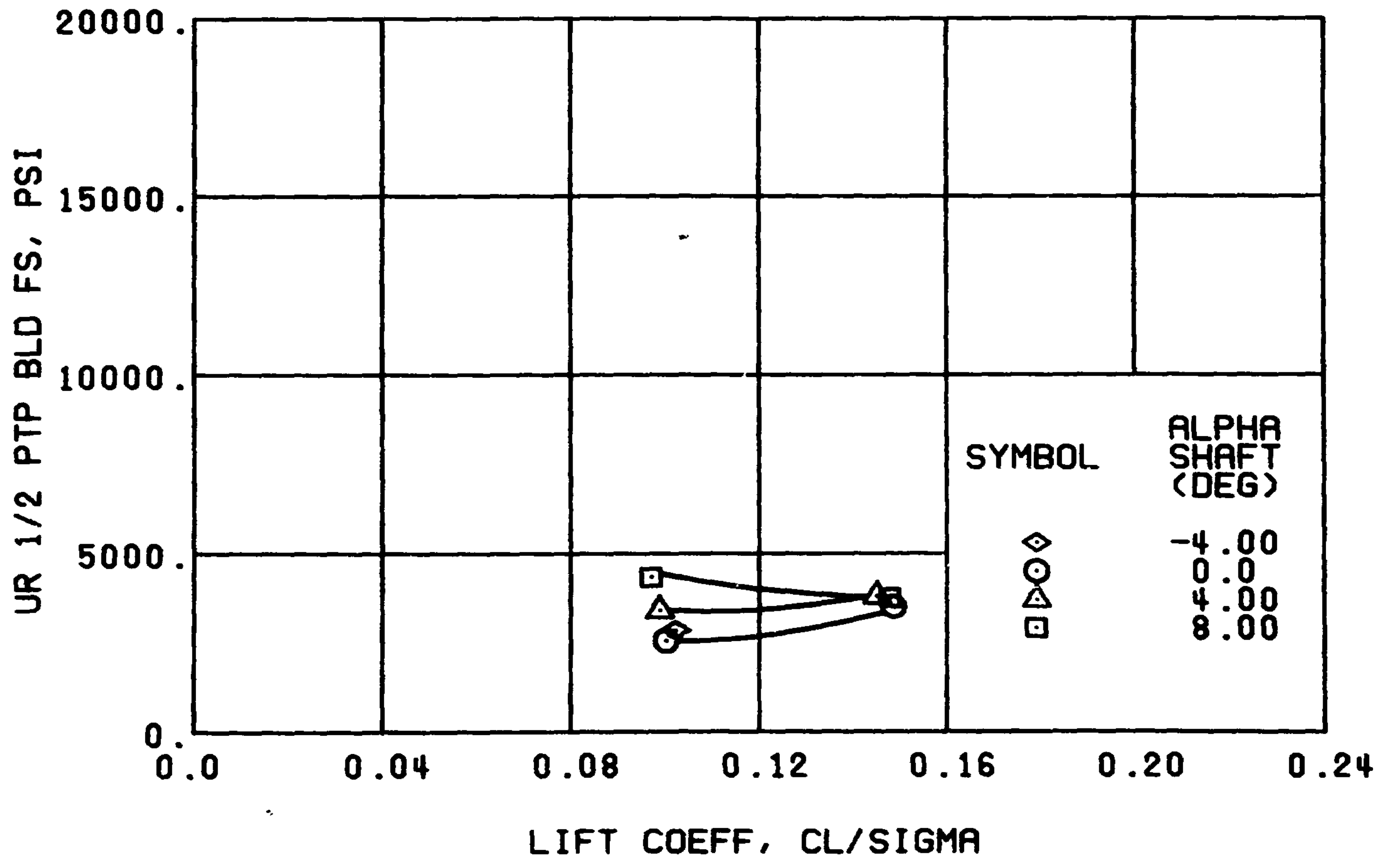

(f) GAGE 55 R204

Figure 51. Continued.
$\mu = 0.47$ $B'_{1s} = 4$ Deg

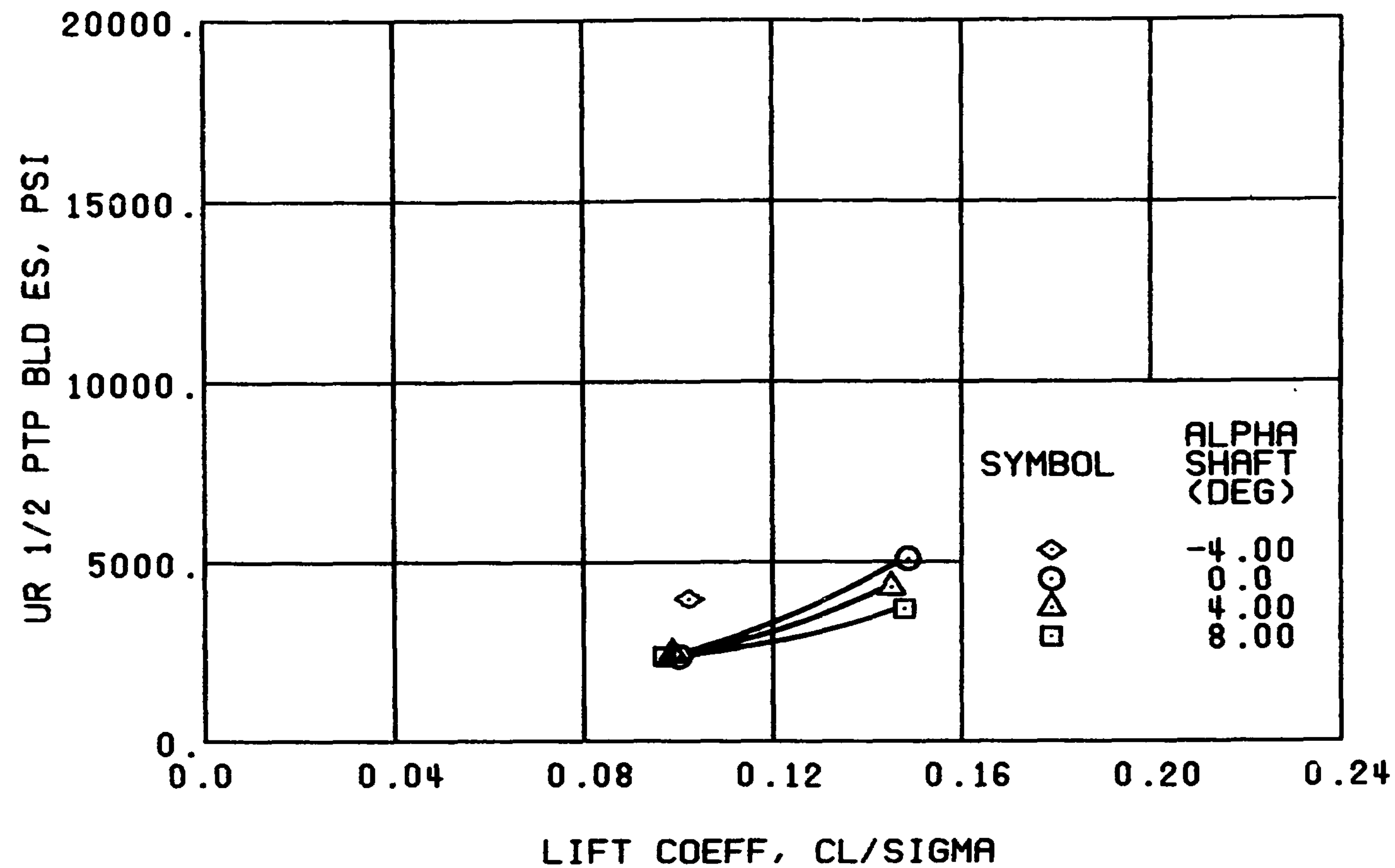

(h) GAGE 40 R84

Figure 51. Continued.
$\mu = 0.47$ $B'_{1s} = 4$ Deg

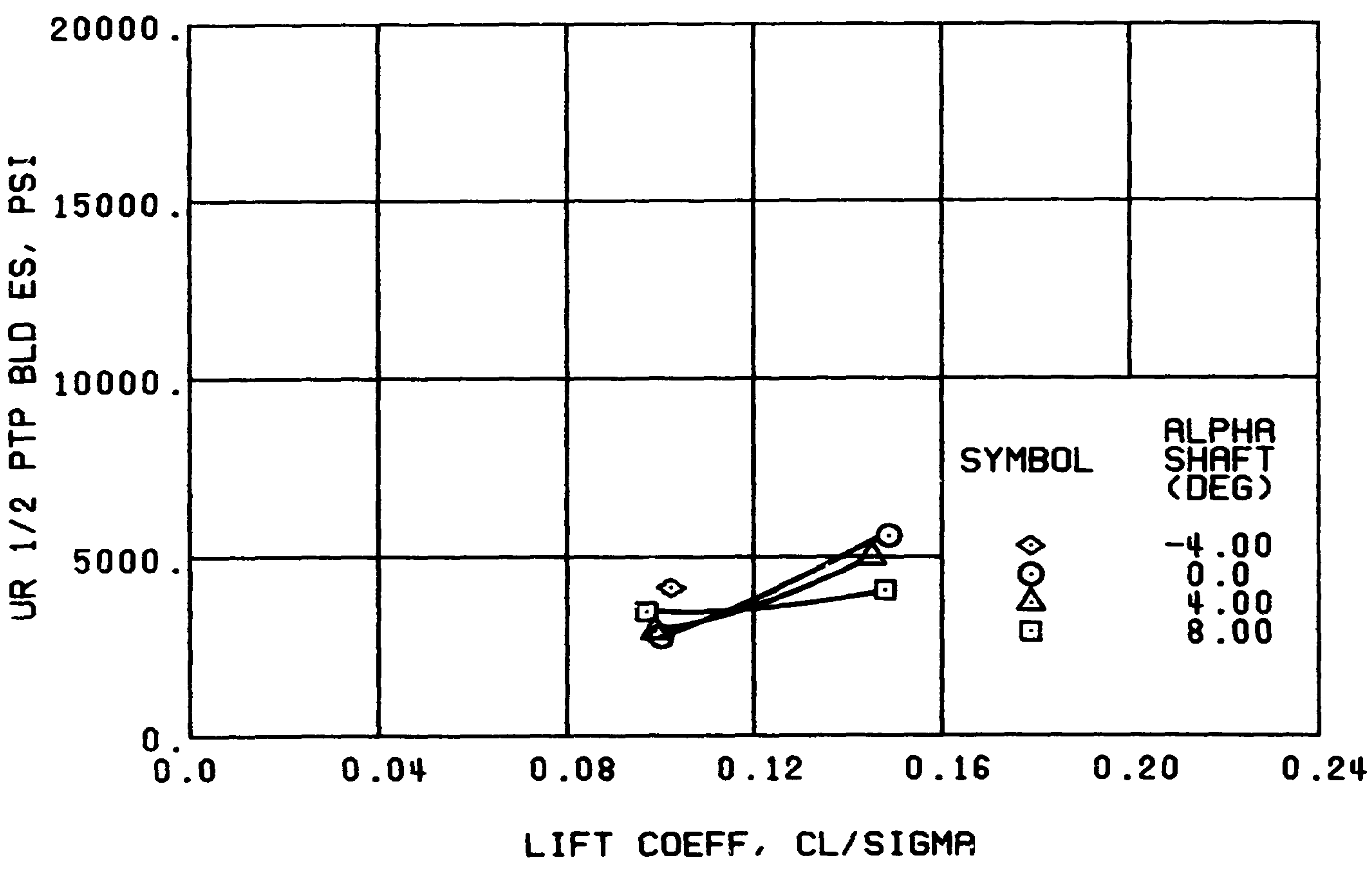

(j) GAGE 42 R132

Figure 51. Continued.
$\mu = 0.47$ $B'_{1s} = 4$ Deg

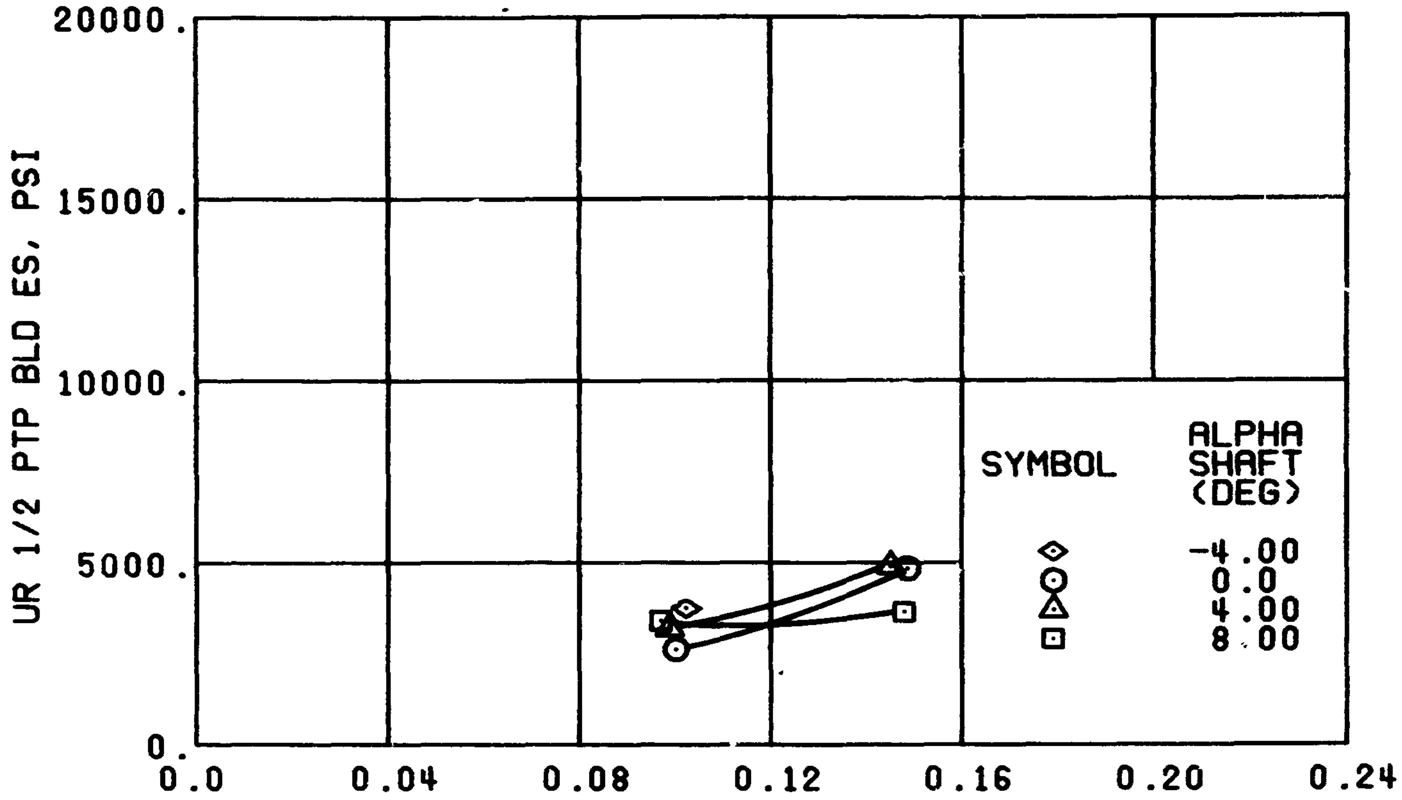

(k) GAGE 43 R168

Figure 51. Continued.
$\mu = 0.47$ $B'_{1s} = 4$ Deg

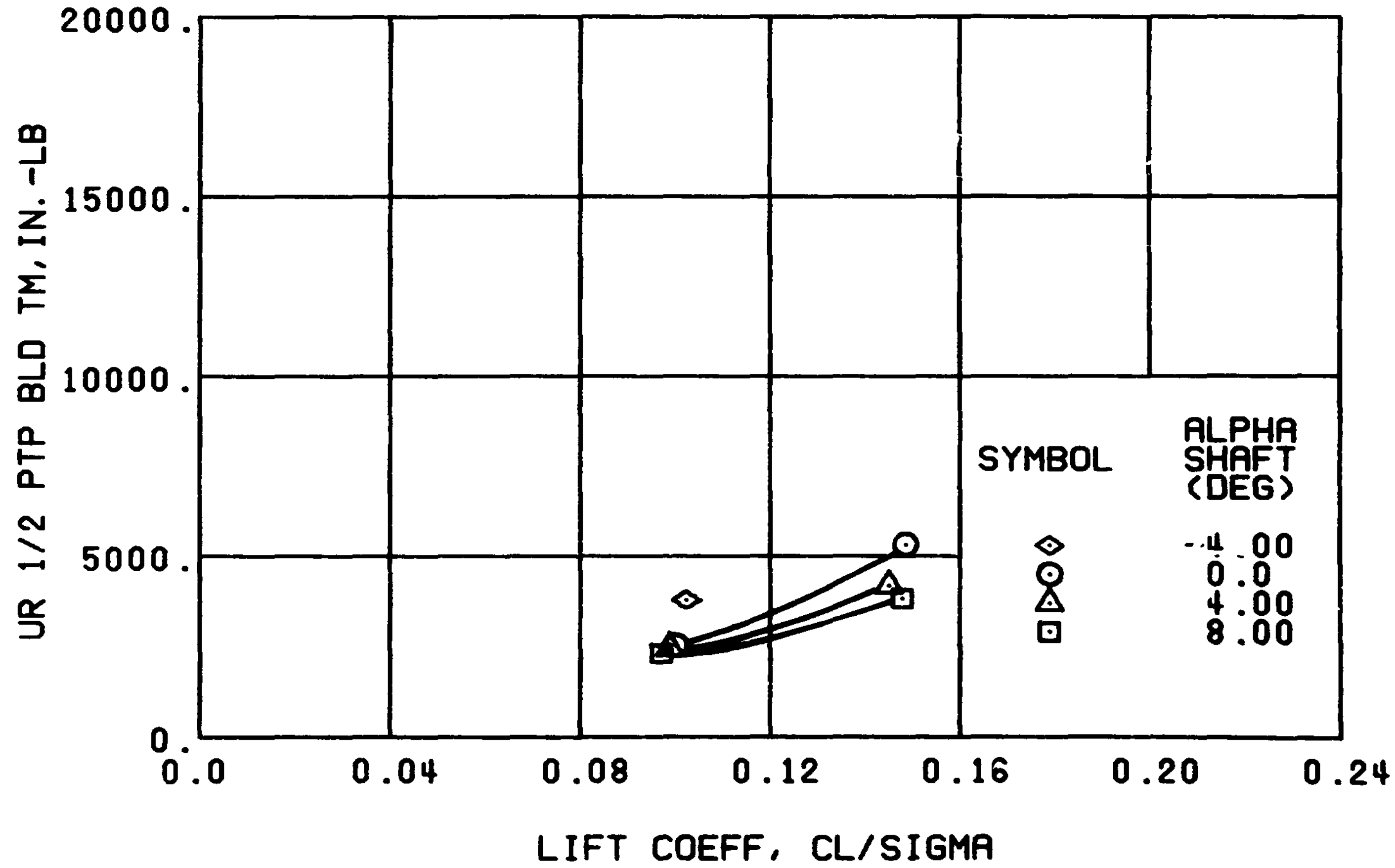

(m) GAGE 46 R130

Figure 51. Continued.
μ = 0.47 B'_{1s} = 4 Deg

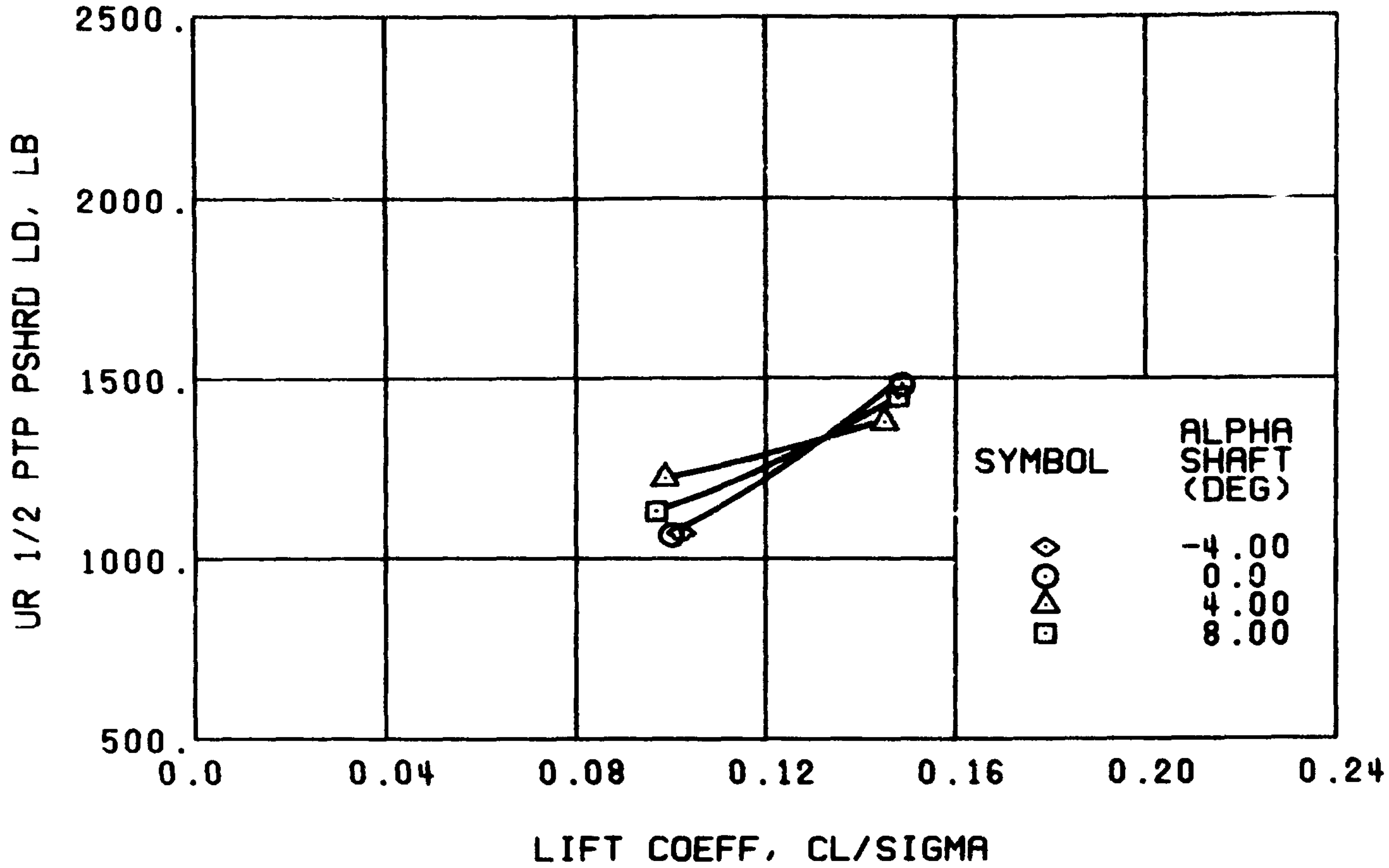

(n) GAGE 37

Figure 51. Continued.
$\mu = 0.47$ $B'_{1s} = 4$ Deg

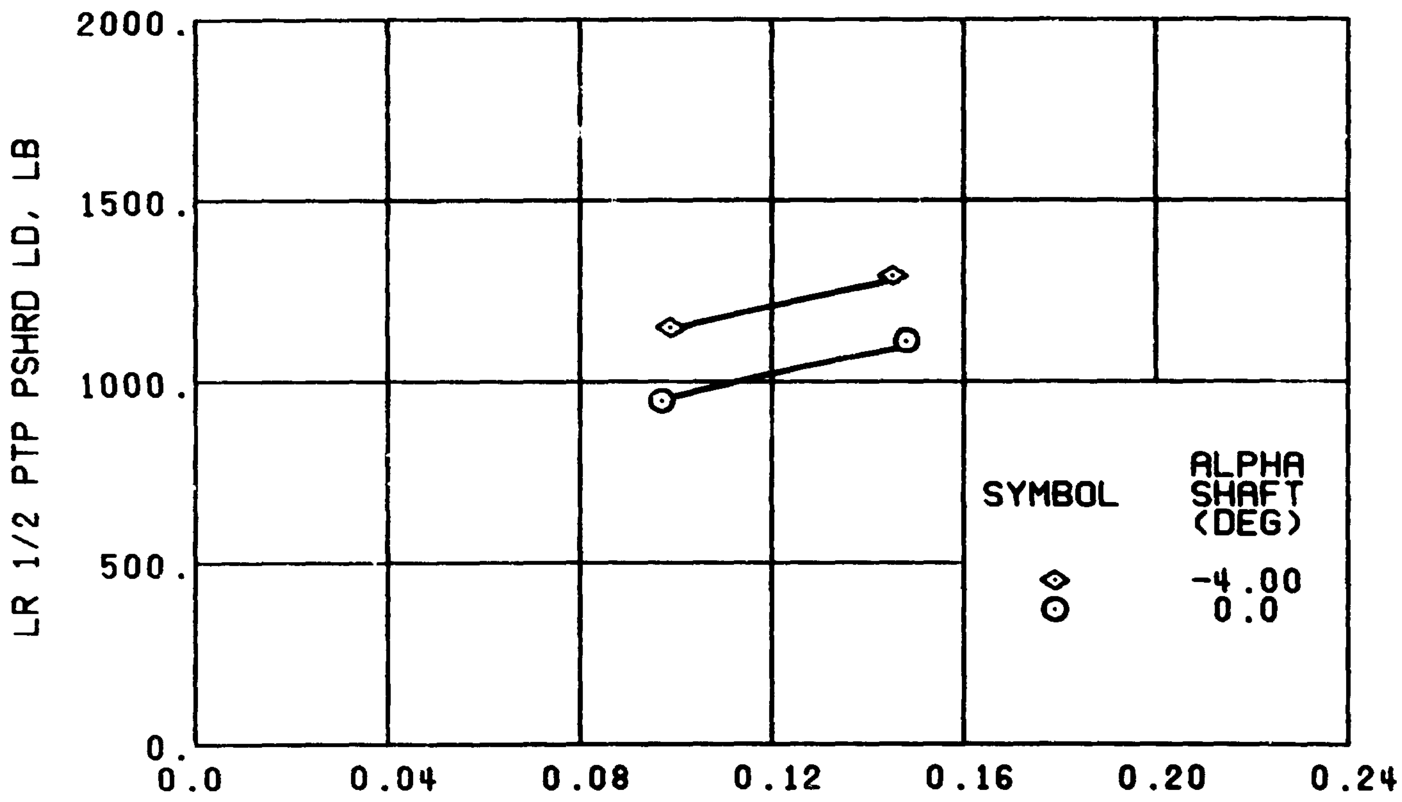

LIFT COEFF, CL/SIGMA

(o) GAGE 34

Figure 51. Continued.
$\mu = 0.47$ $B'_{1s} = 4$ Deg

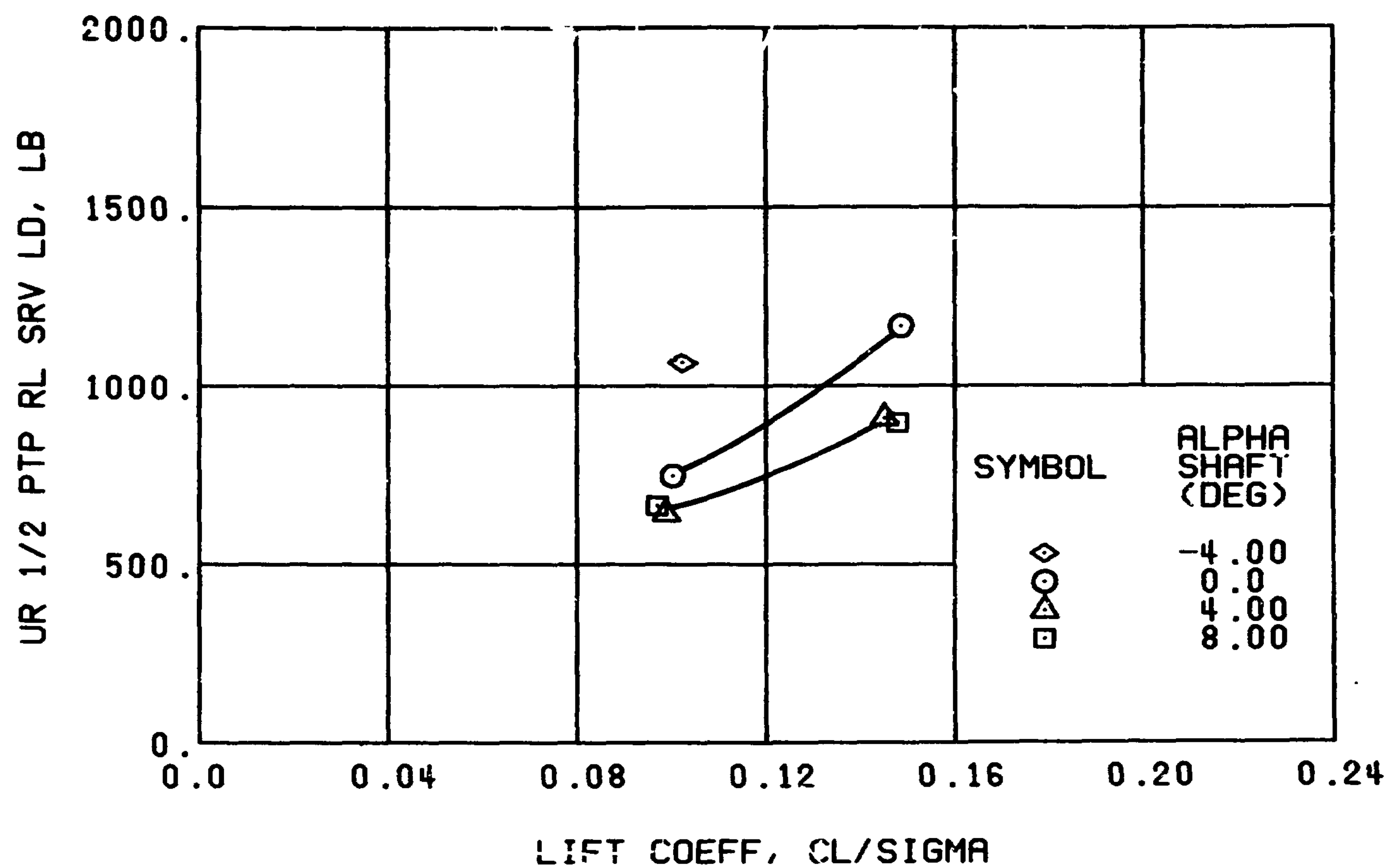

(p) GAGE 22

Figure 51. Continued.
$\mu = 0.47 \quad B'_{1s} = 4$ Deg

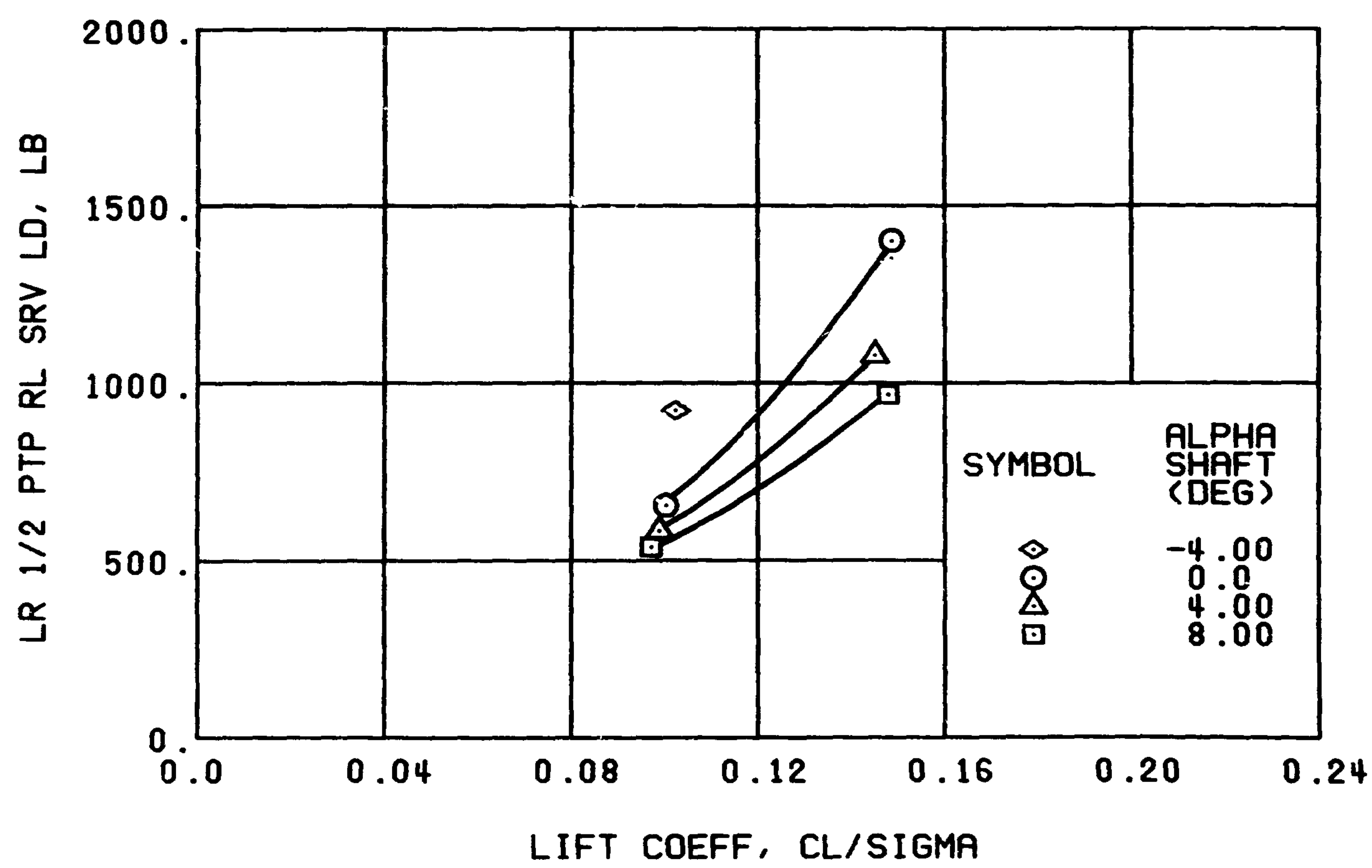

(q) GAGE 25

Figure 51. Continued.
$\mu = 0.47 \quad B'_{1s} = 4$ **Deg**

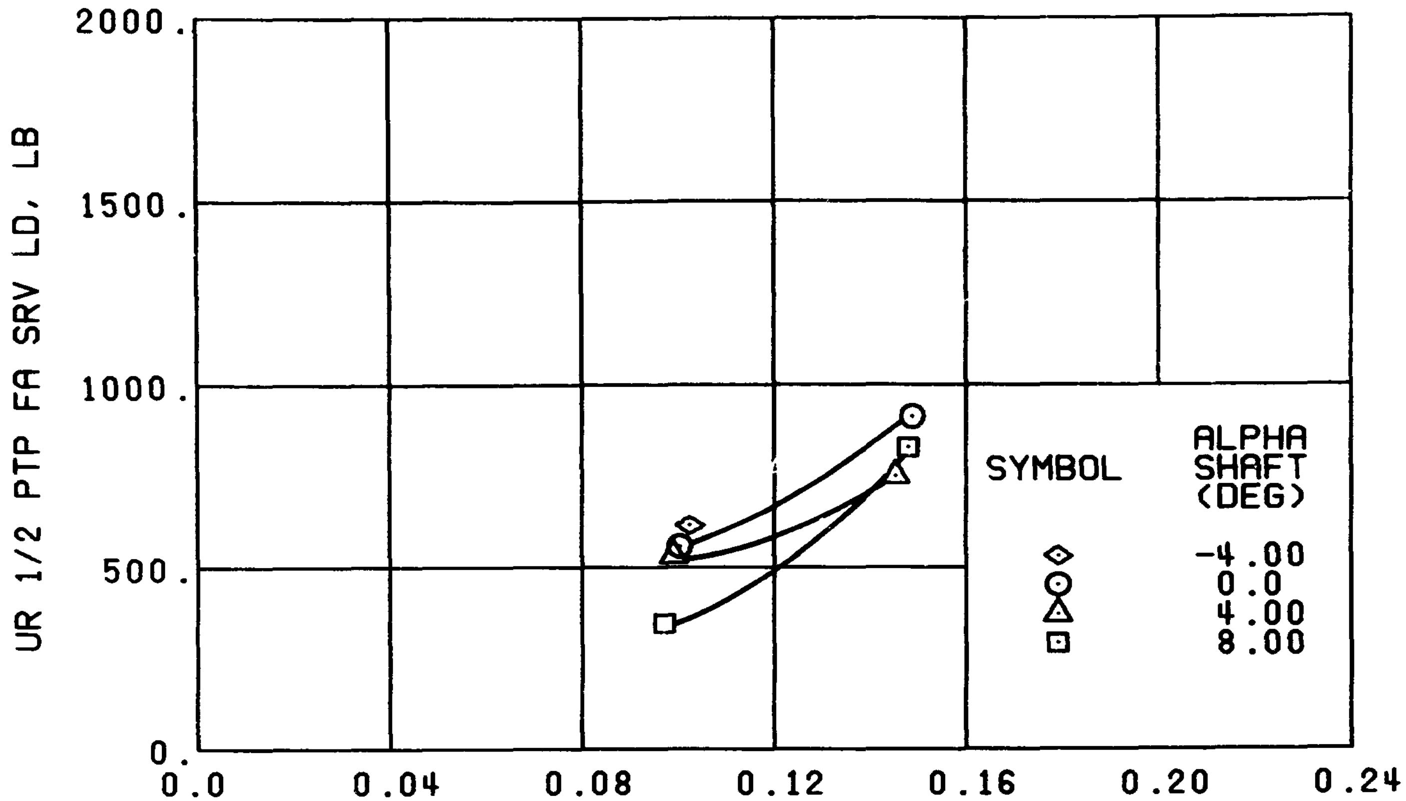

(r) GAGE 24

Figure 51. Continued.
$\mu = 0.47$ $B'_{1s} = 4$ Deg

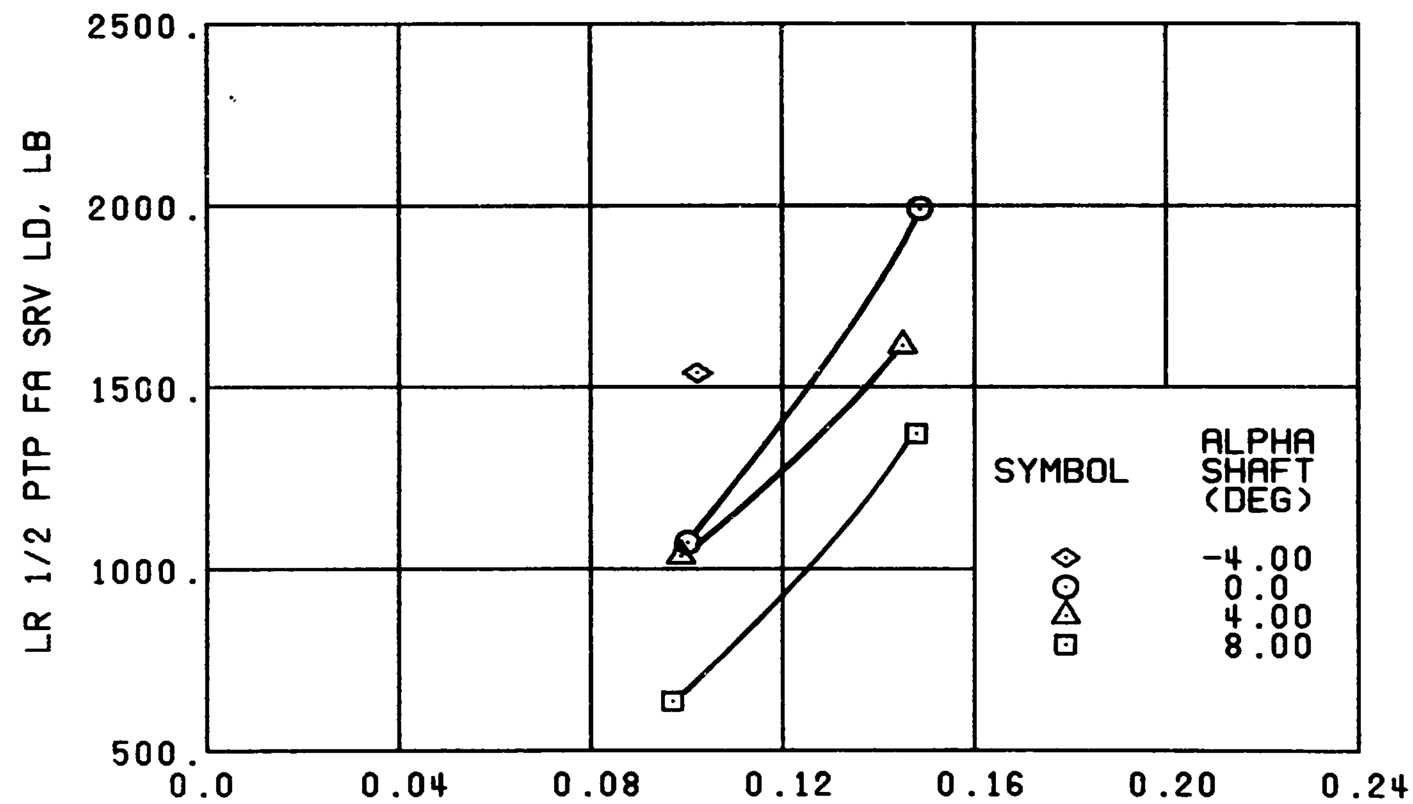

(s) GAGE 27

Figure 51. Continued.
$\mu = 0.47 \quad B'_{1s} = 4$ Deg

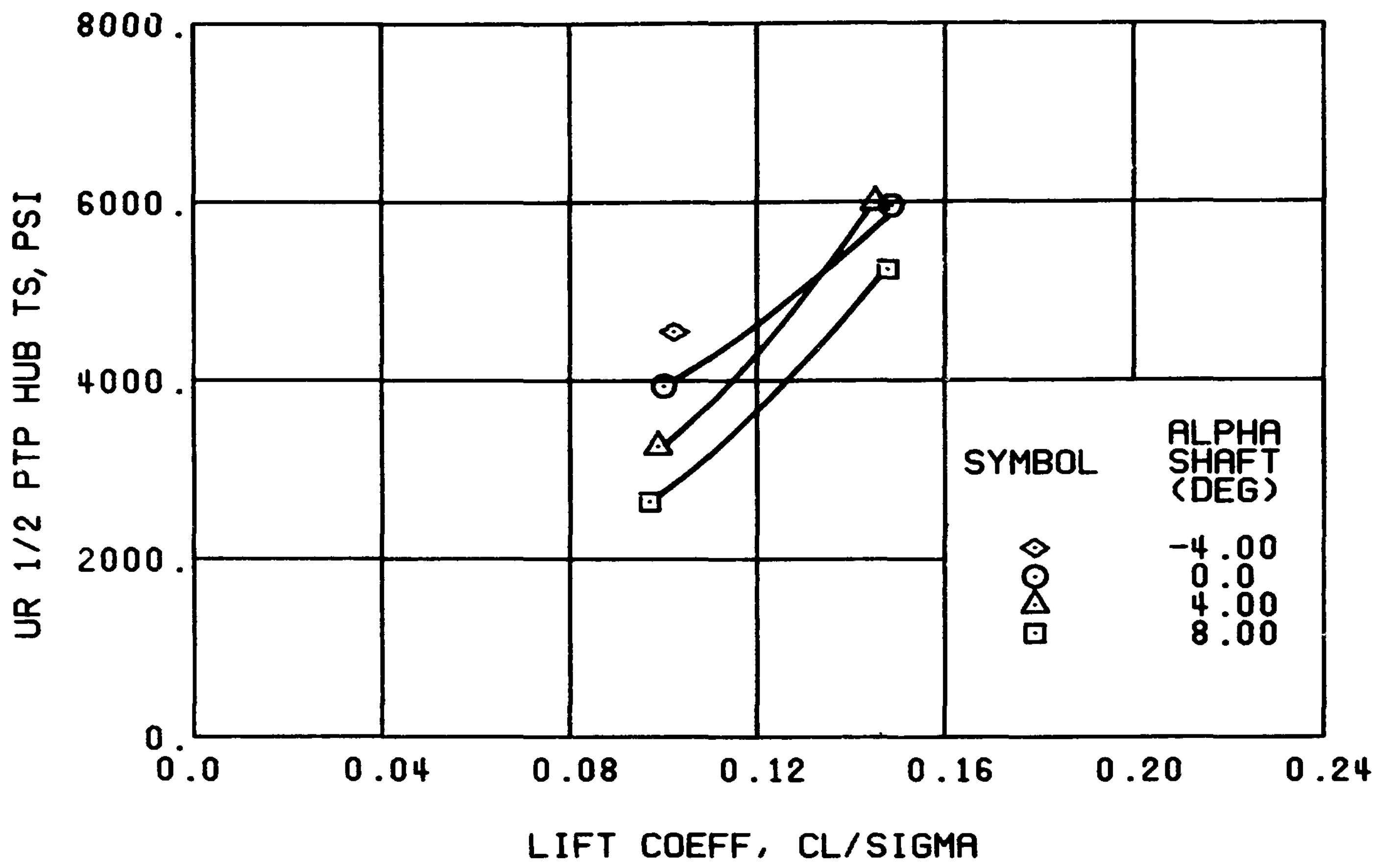

(f) GAGE 65

Figure 51. Continued.
μ = 0.47 B'_{1s} = 4 Deg

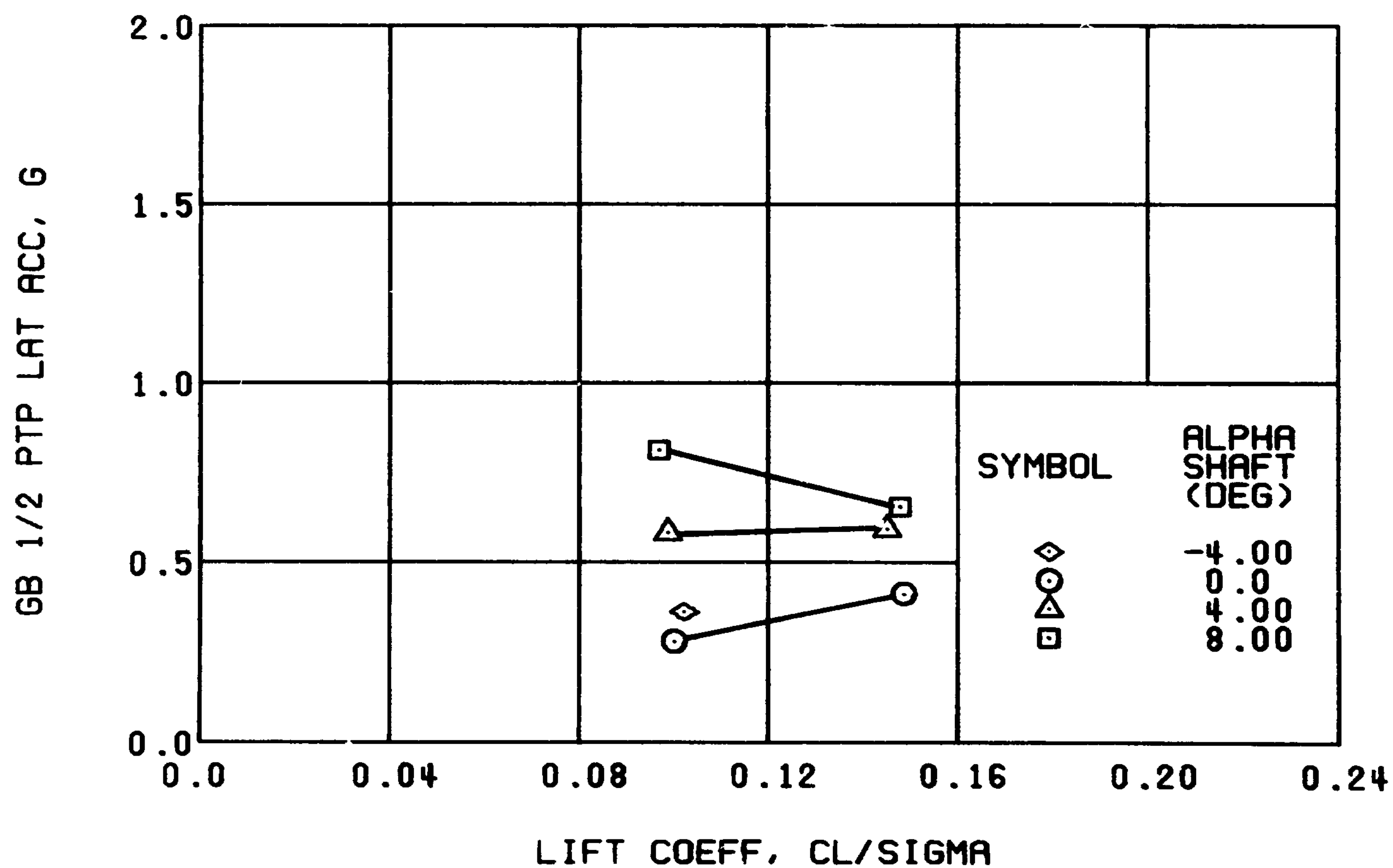

(u) GAGE 15 STA 76, BL 30

Figure 51. Continued.
$\mu = 0.47$ $B'_{1s} = 4$ Deg

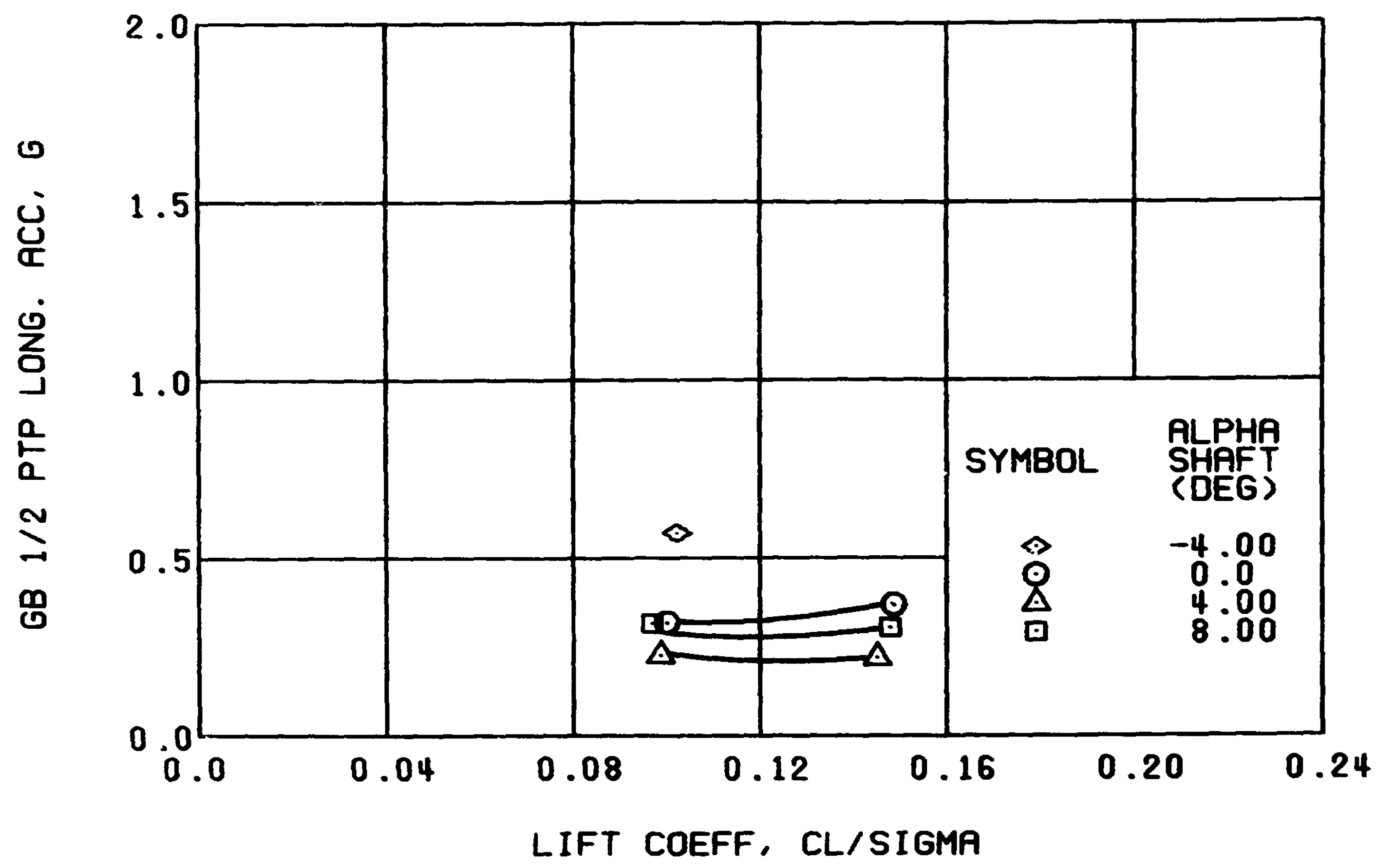

(v) GAGE 14 STA 61, BL 0

Figure 51. Continued.
$\mu = 0.47$ $B'_{1s} = 4$ Deg

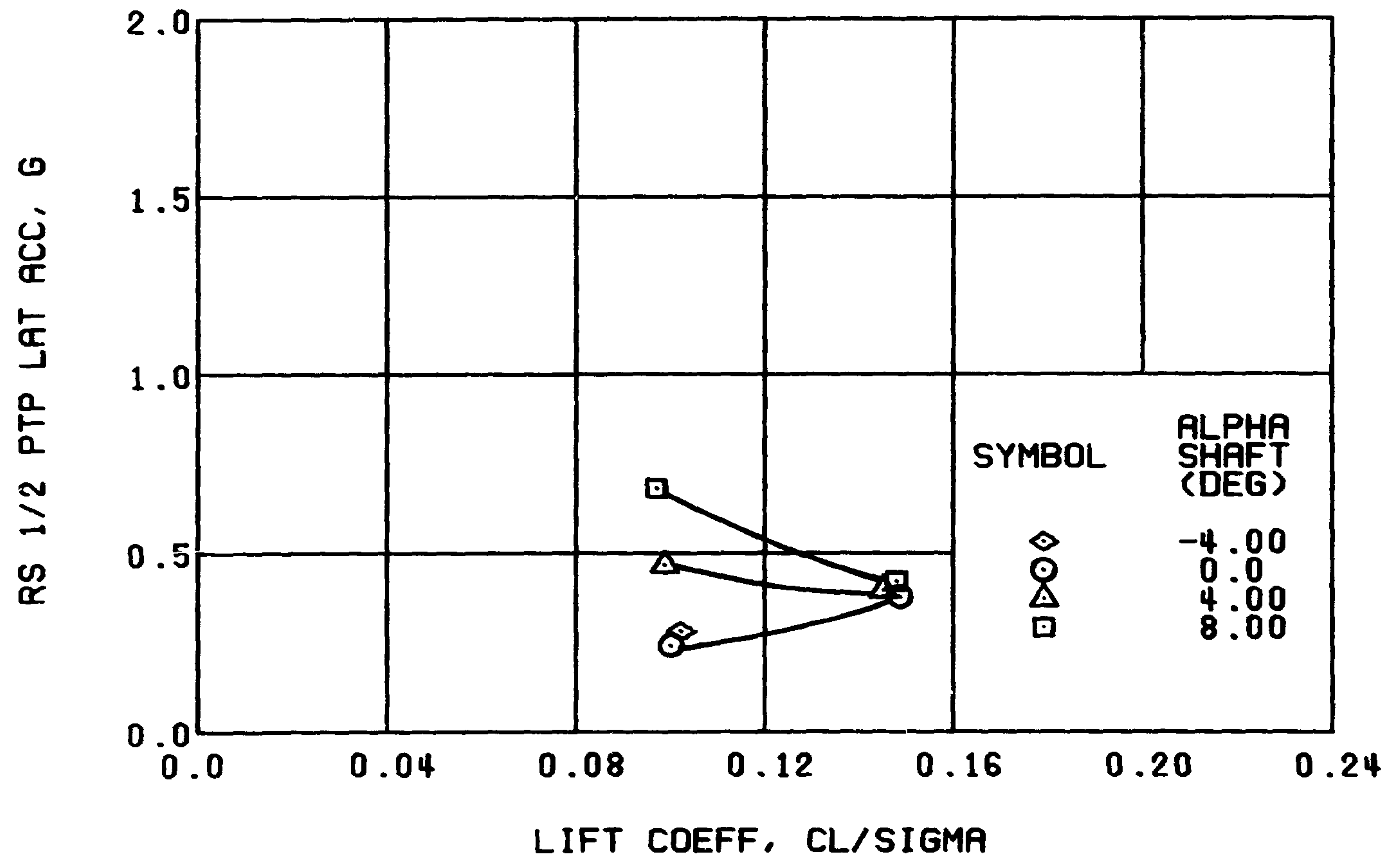

(w) GAGE 16 ROVER 3

Figure 51. Continued.
$\mu = 0.47$ $B'_{1s} = 4$ Deg

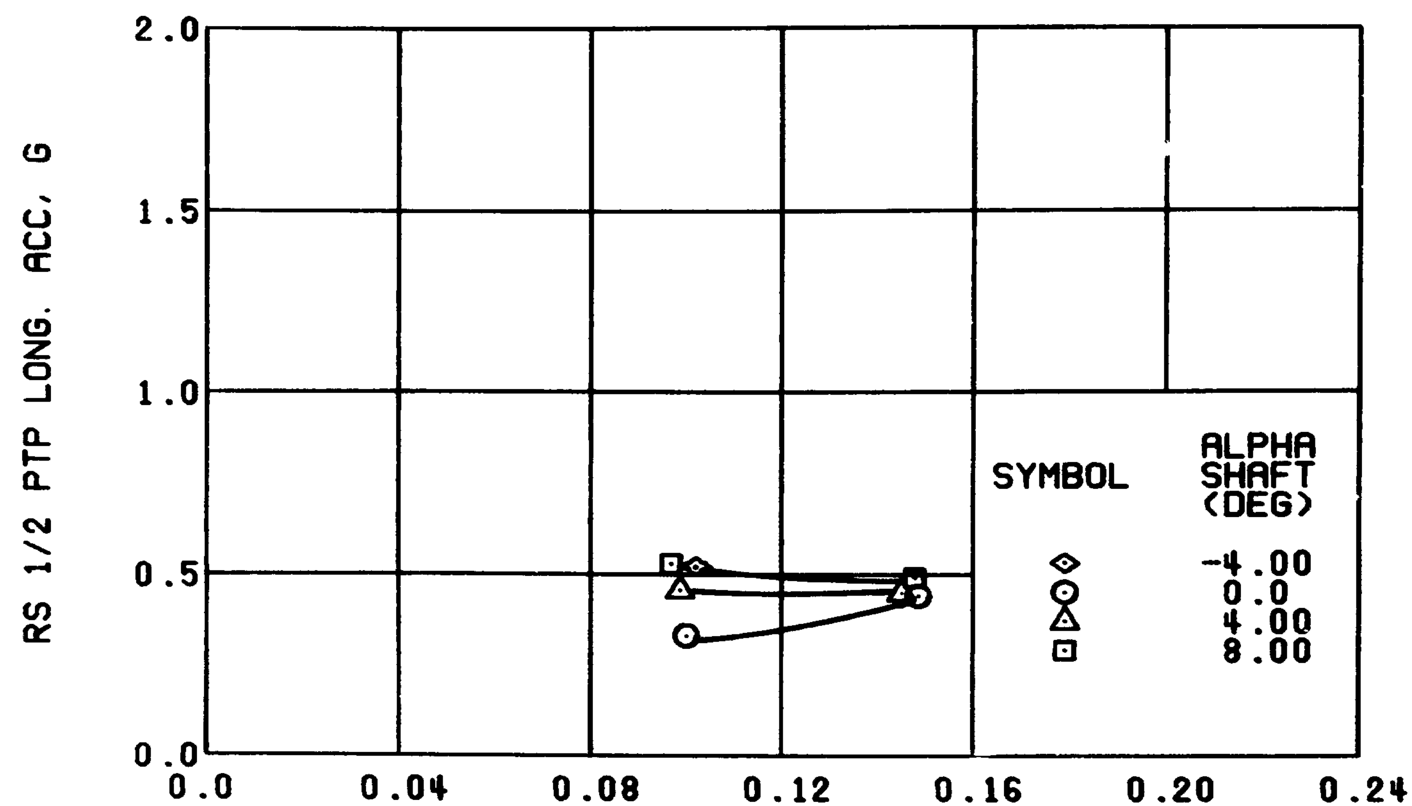

(x) GAGE 17 ROVER 4

Figure 51. Concluded.
$\mu = 0.47$ $B'_{1s} = 4$ Deg

Note: Stress, load, and vibration data at an advance ratio of 0.47 with the lateral displacement control (B_{1_s}) set at 6 degrees is contained in Figure 12, page 61.

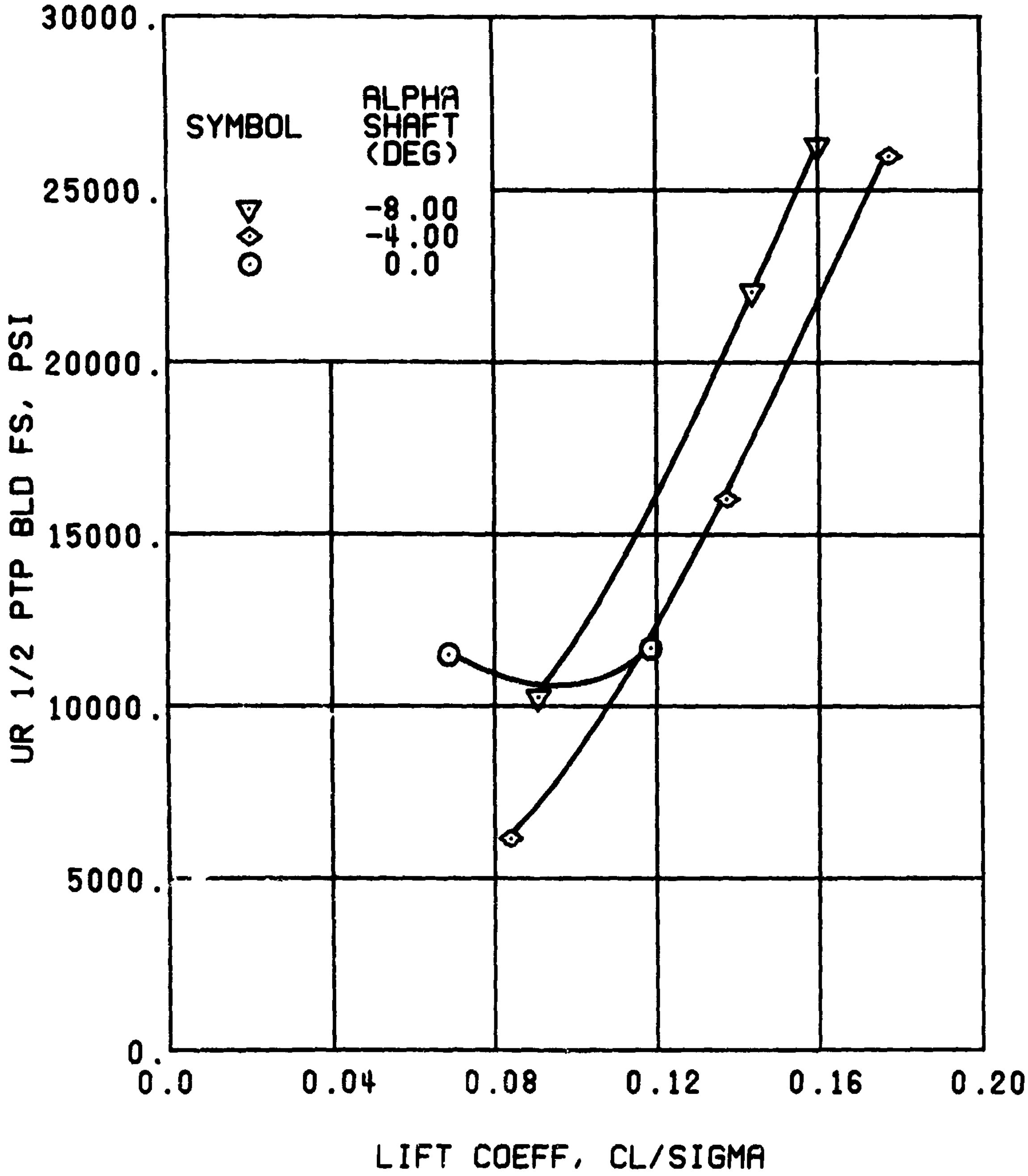

(a) GAGE 51 R84

Figure 52. Stress, Load, and Vibration Data at an Advance Ratio of 0.47 With the Lateral Displacement Control (B'_{1s}) Set at 8 Degrees.

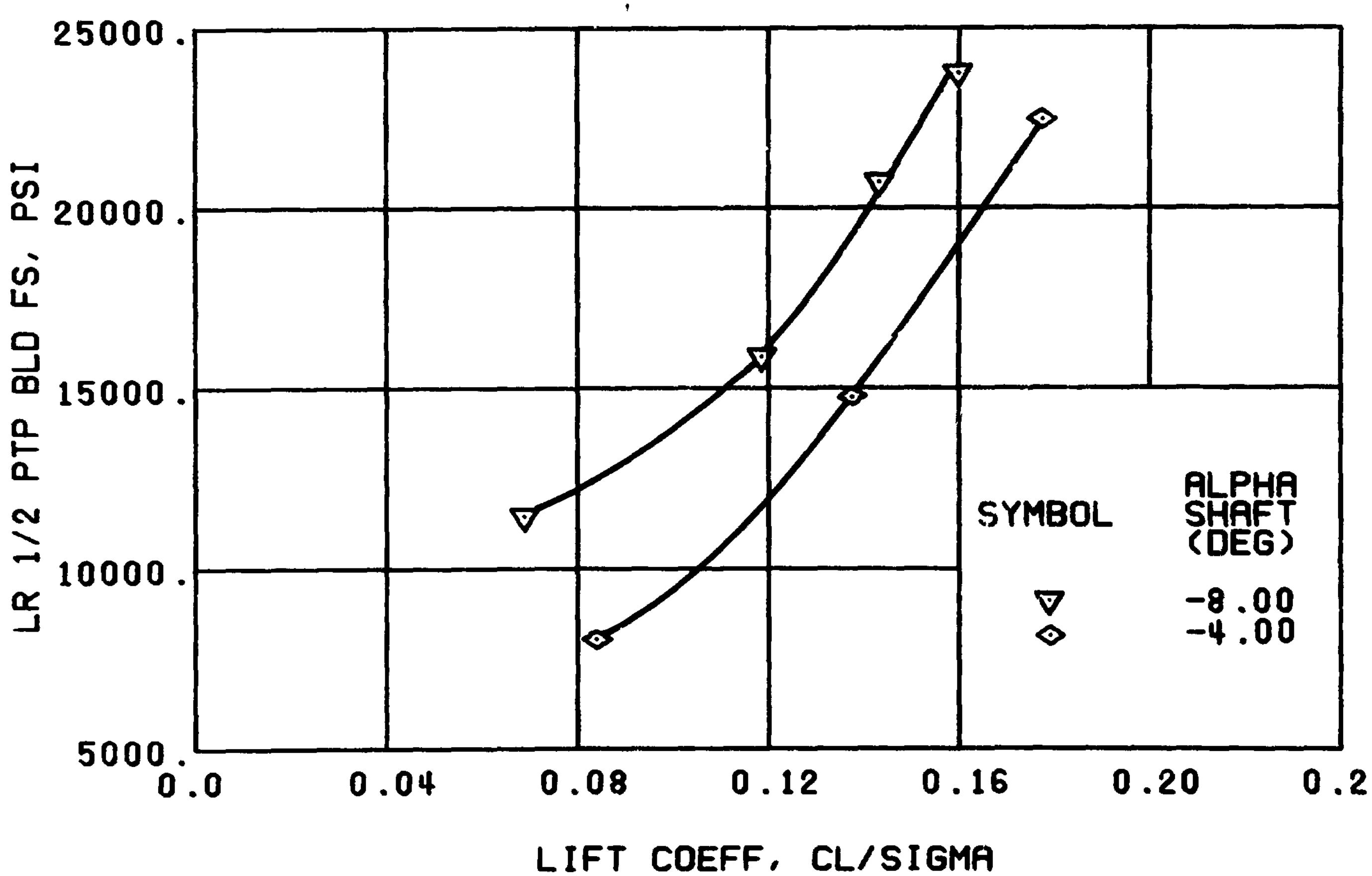

(b) GAGE 1 R84

Figure 52. Continued.
$\mu = 0.47 \quad B'_{1s} = 8$ Deg

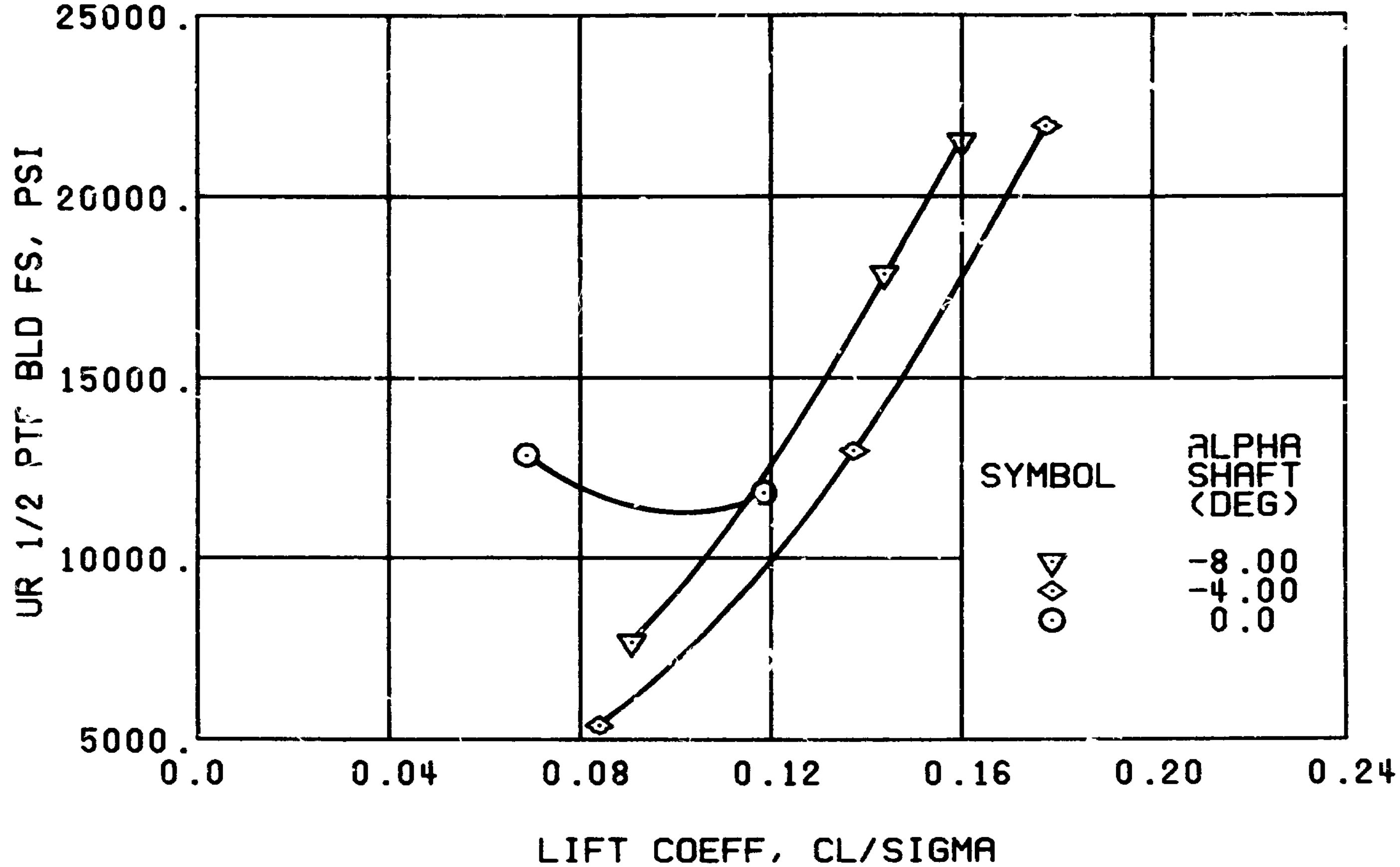

(c) GAGE 52 R108

Figure 52. Continued.
$\mu = 0.47 \quad B'_{1s} = 8$ Deg

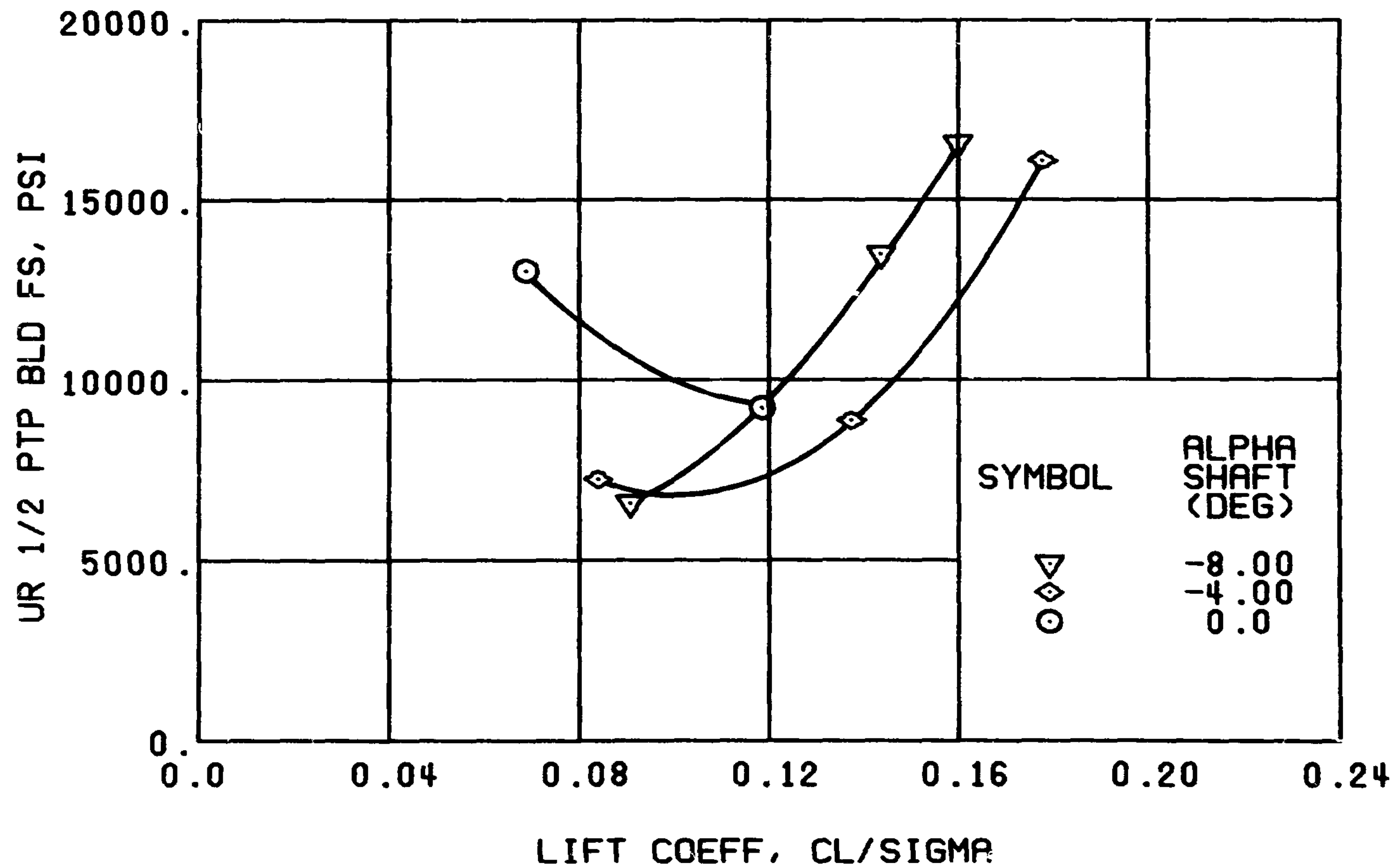

(d) GAGE 53 R132

Figure 52. Continued.
$\mu = 0.47$ $B'_{1s} = 8$ Deg

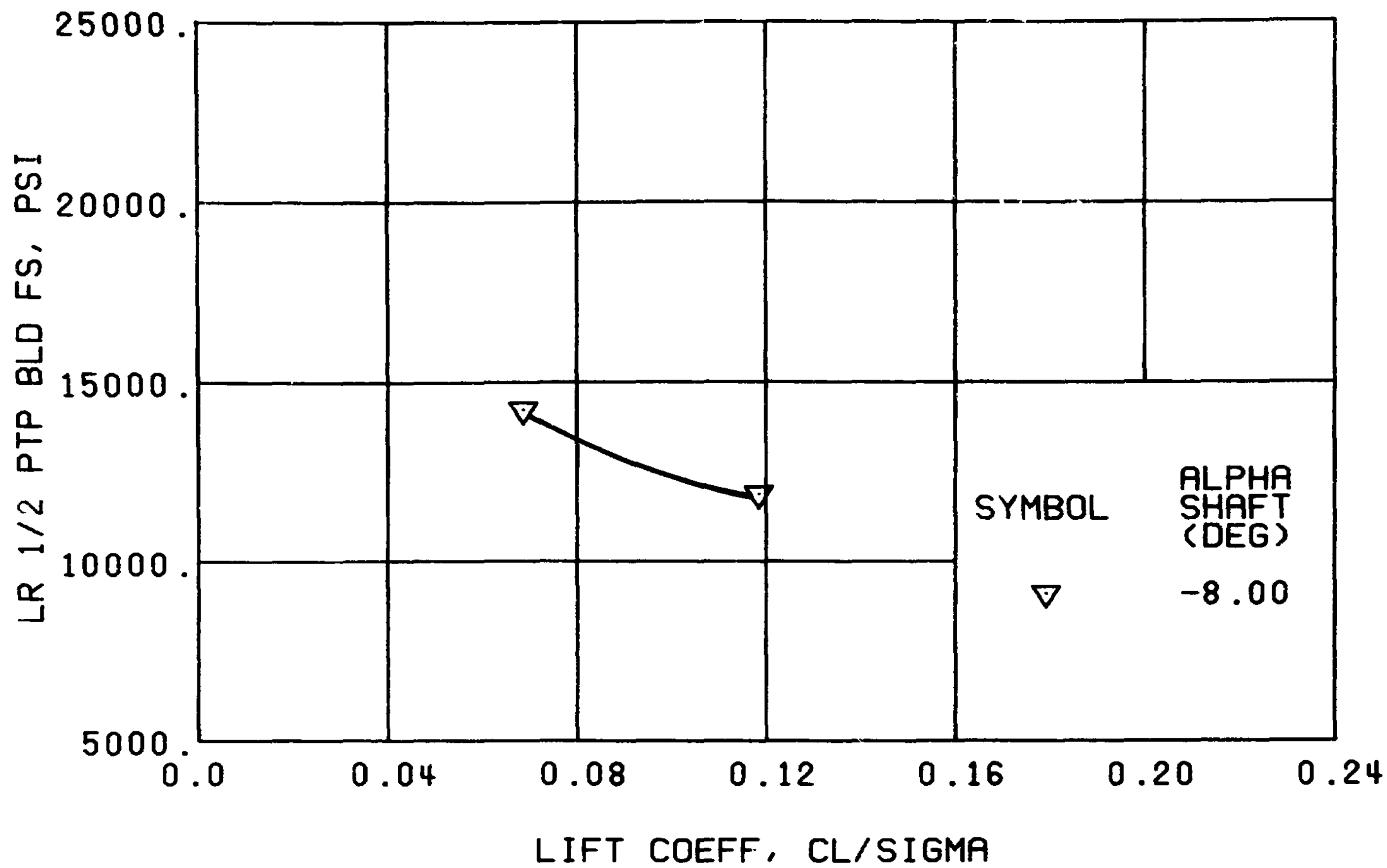

(e) GAGE 93 R132

Figure 52. Continued.
$\mu = 0.47$ $B'_{1s} = 8$ Deg

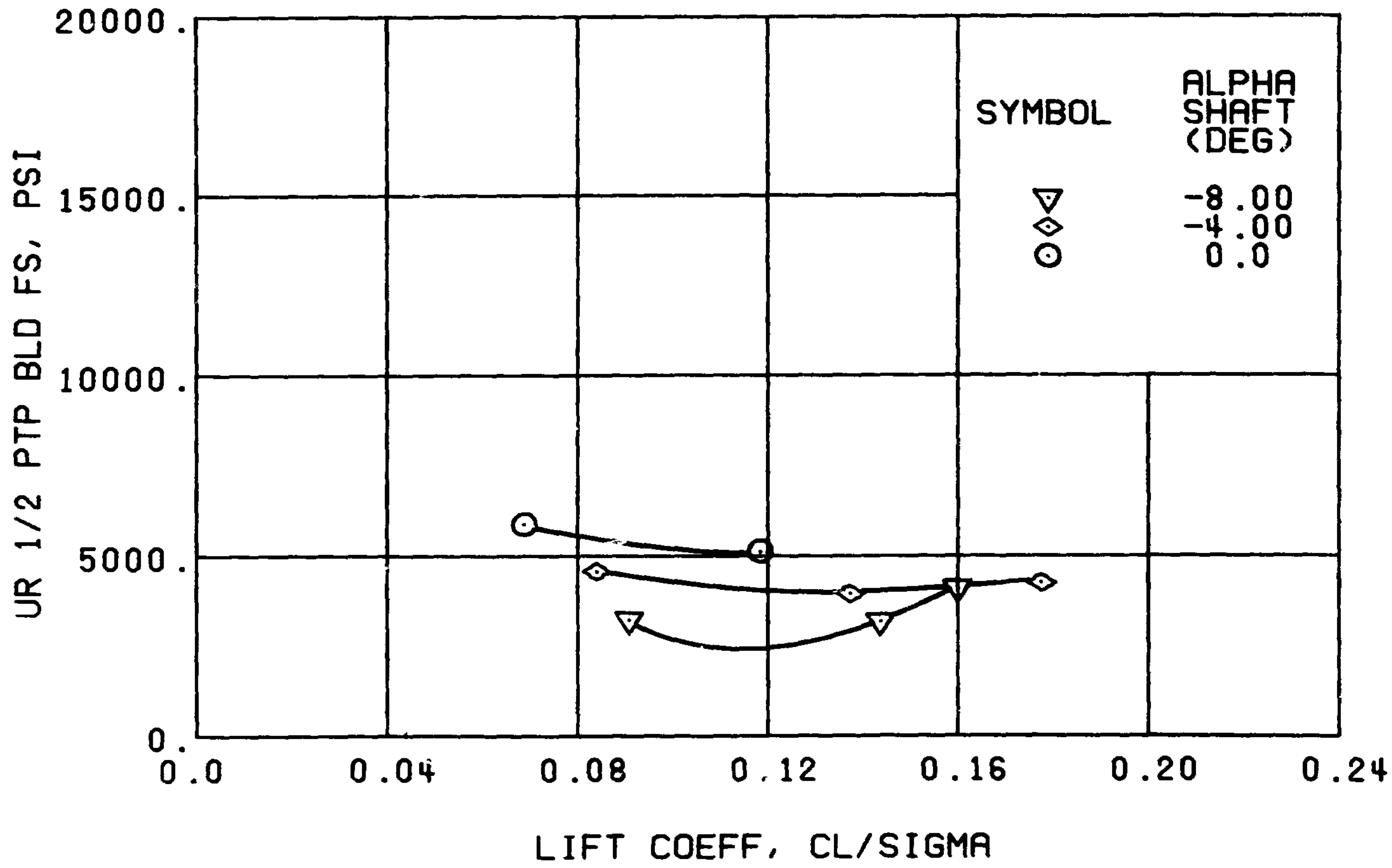

(f) GAGE 55 R204

Figure 52. Continued.
$\mu = 0.47$ $B'_{1s} = 8$ Deg

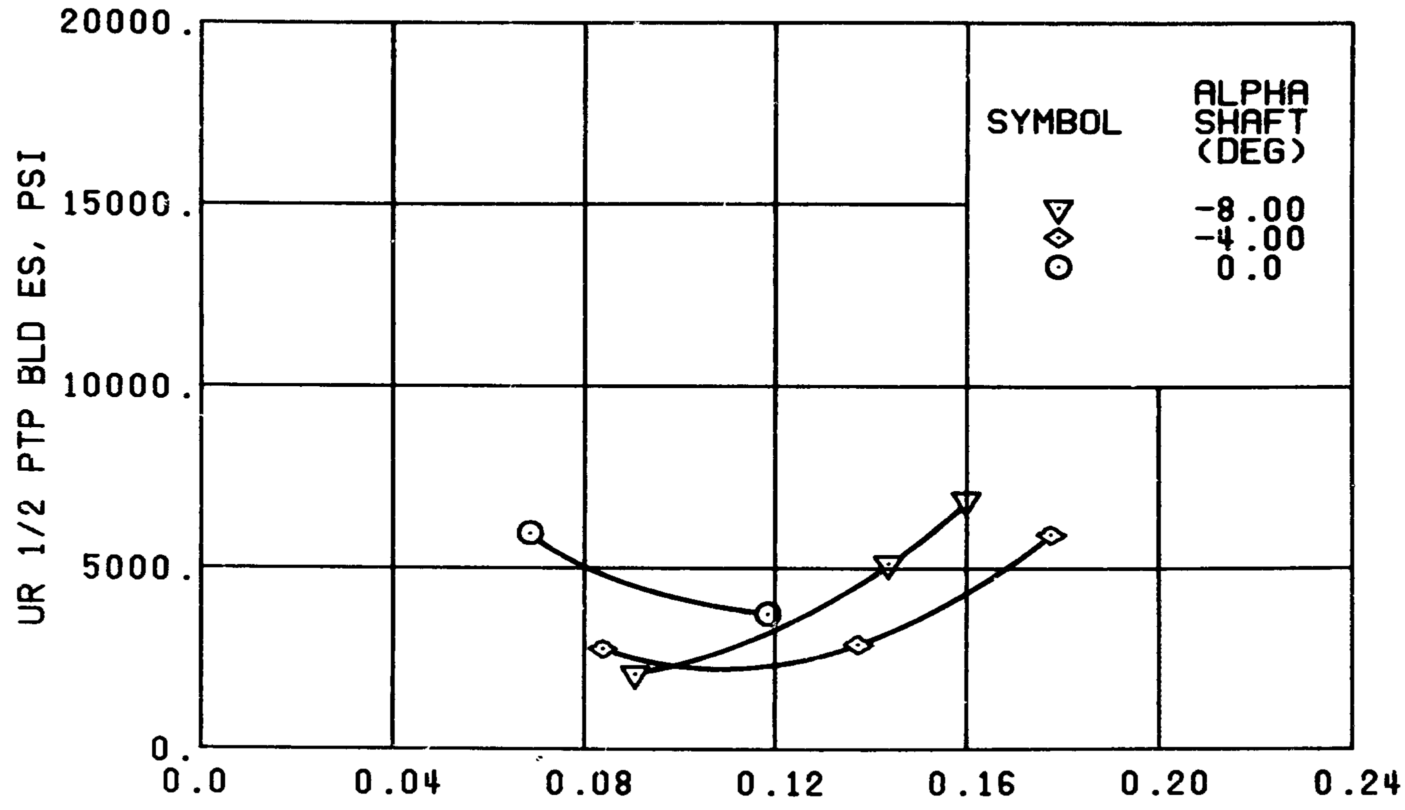

(h) GAGE 40 R84

Figure 52. Continued.
$\mu = 0.47 \quad B'_{1s} = 8$ Deg

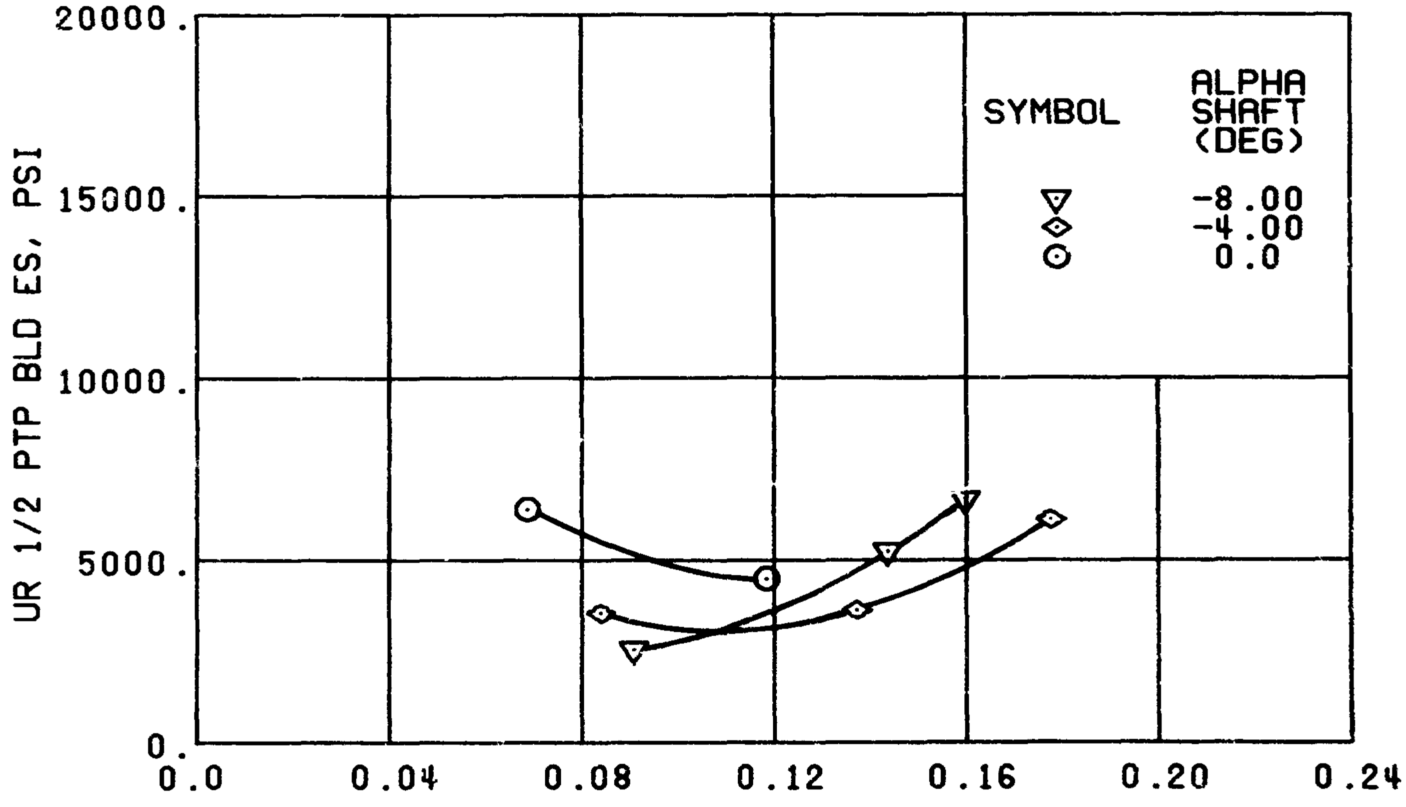

(j) GAGE 42 R132

Figure 52. Continued.
$\mu = 0.47$ $B'_{1s} = 8$ Deg

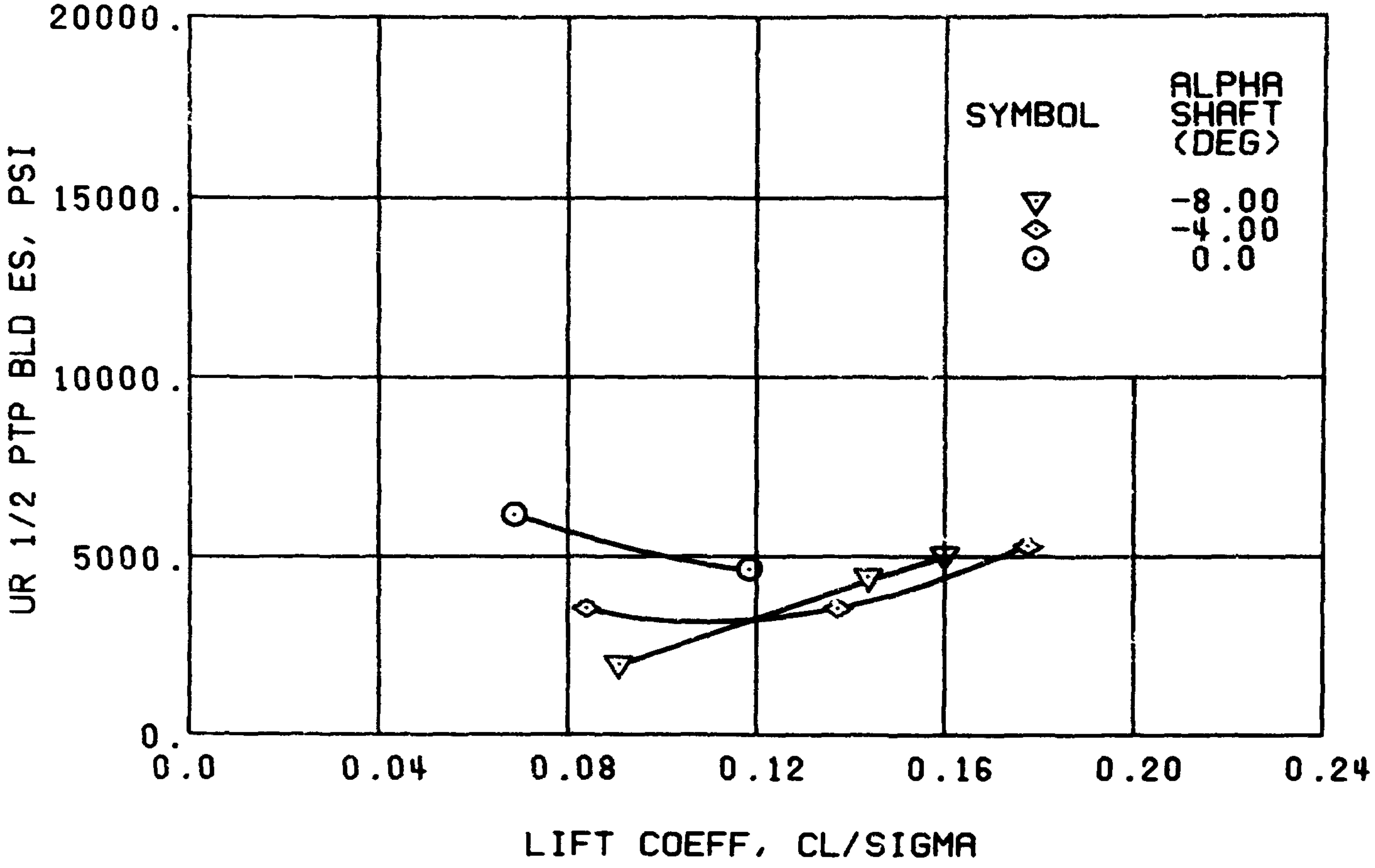

(k) GAGE 43 R168

Figure 52. Continued.
$\mu = 0.47 \quad B'_{1s} = 8$ Deg

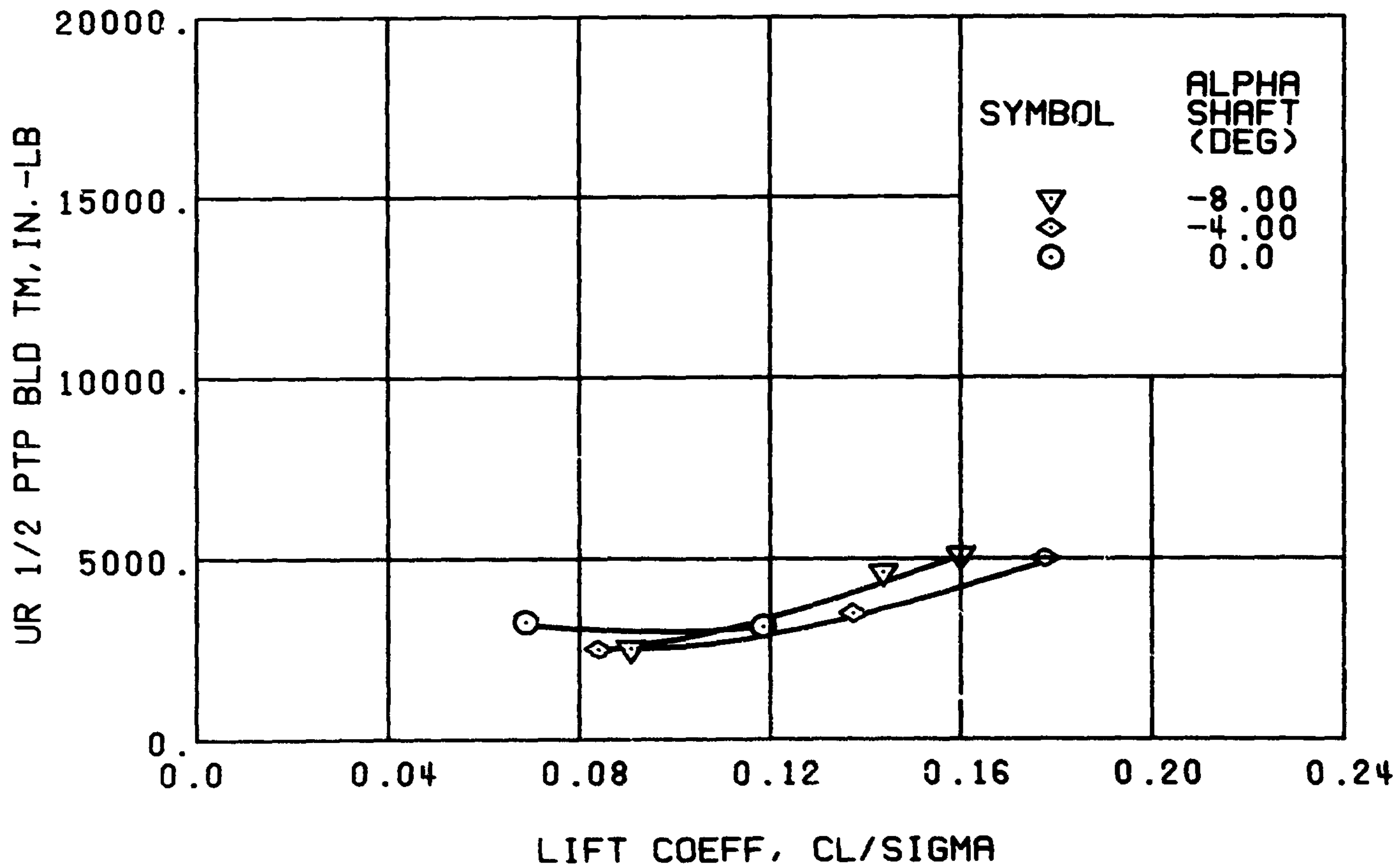

(m) GAGE 46 R130

Figure 52. Continued.
$\mu = 0.47$ $B'_{1s} = 8$ Deg

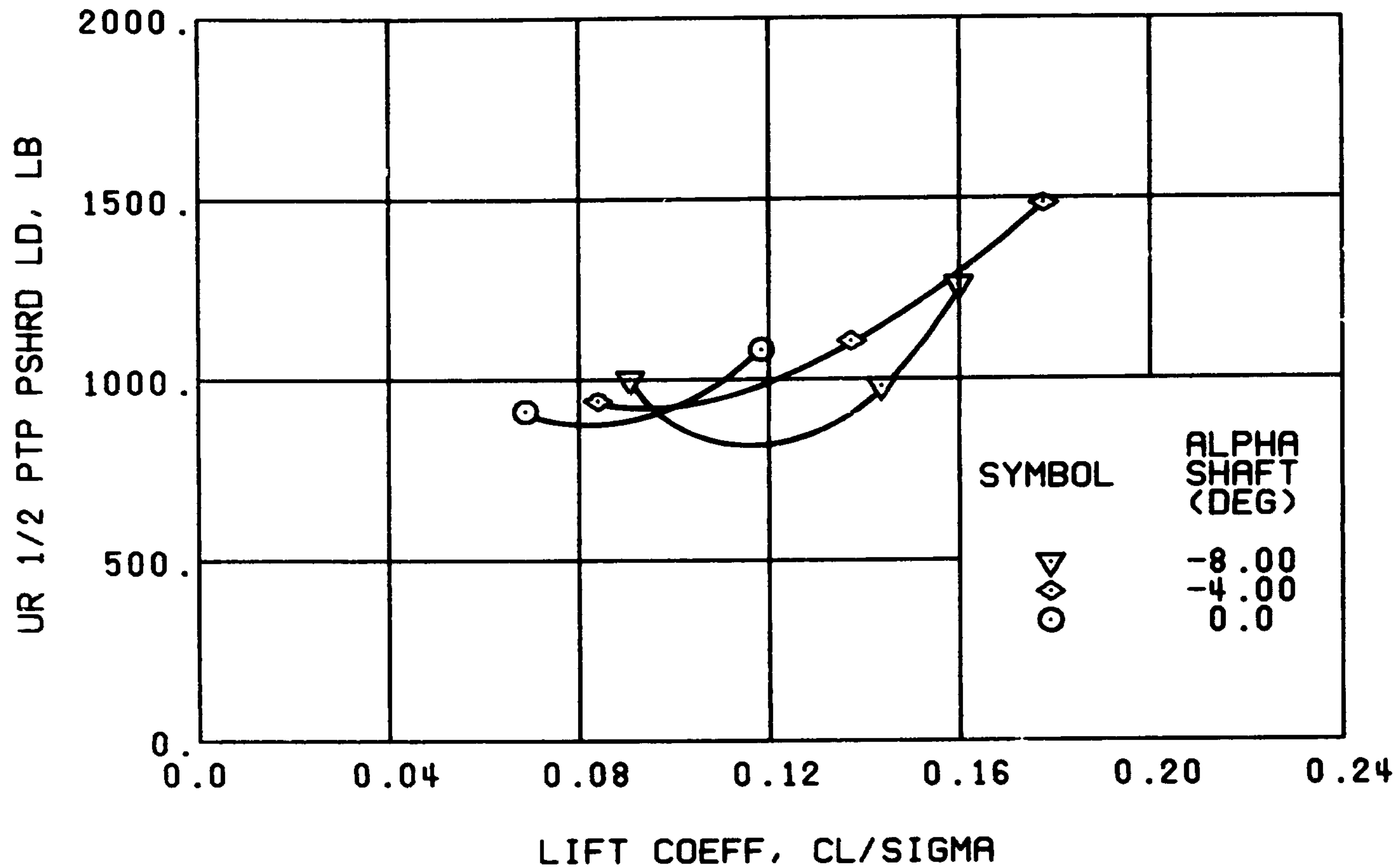

(n) GAGE 37

Figure 52 Continued.
$\mu = 0.47 \quad B'_{1s} = 8$ Deg

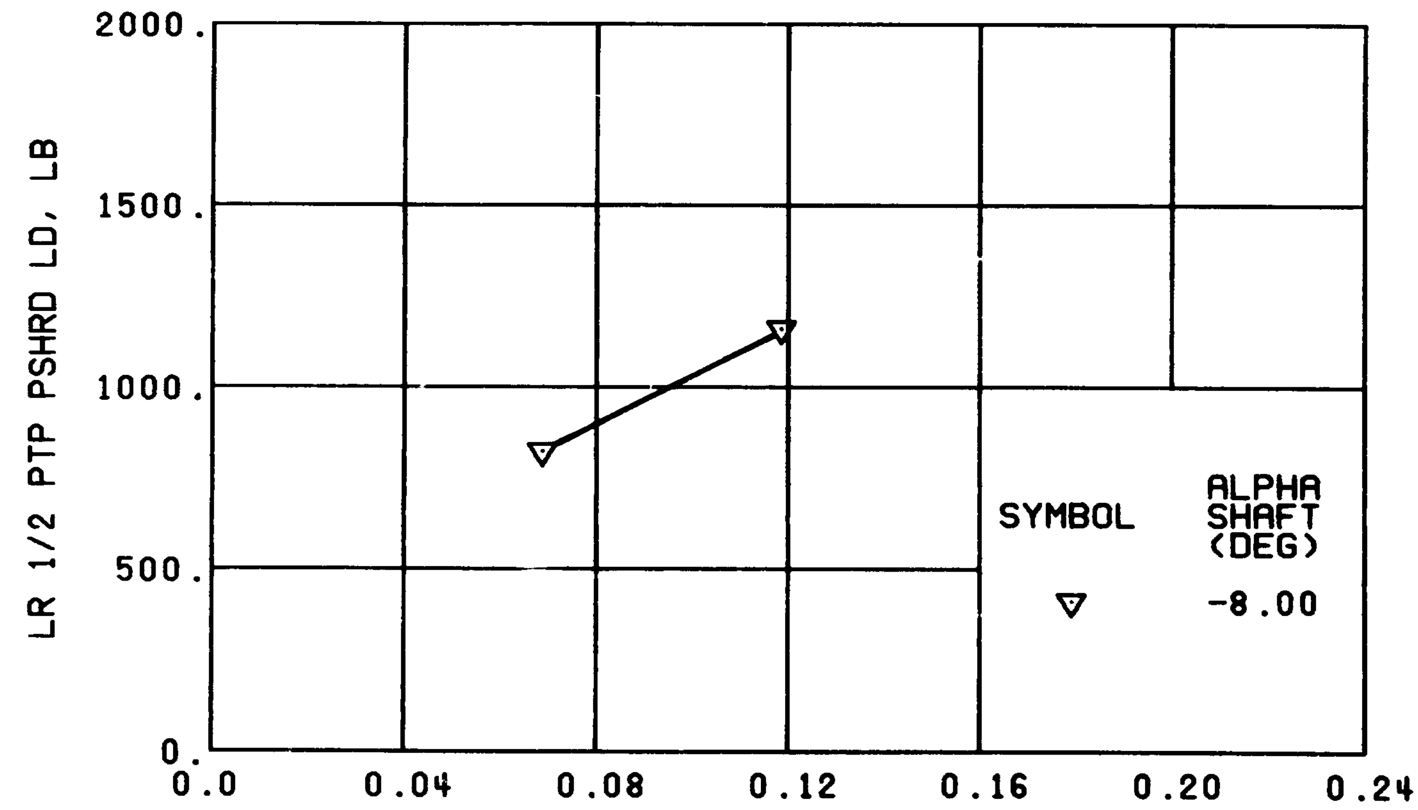

(o) GAGE 34

Figure 52. Continued.
$\mu = 0.47$ $B'_{1s} = 8$ Deg

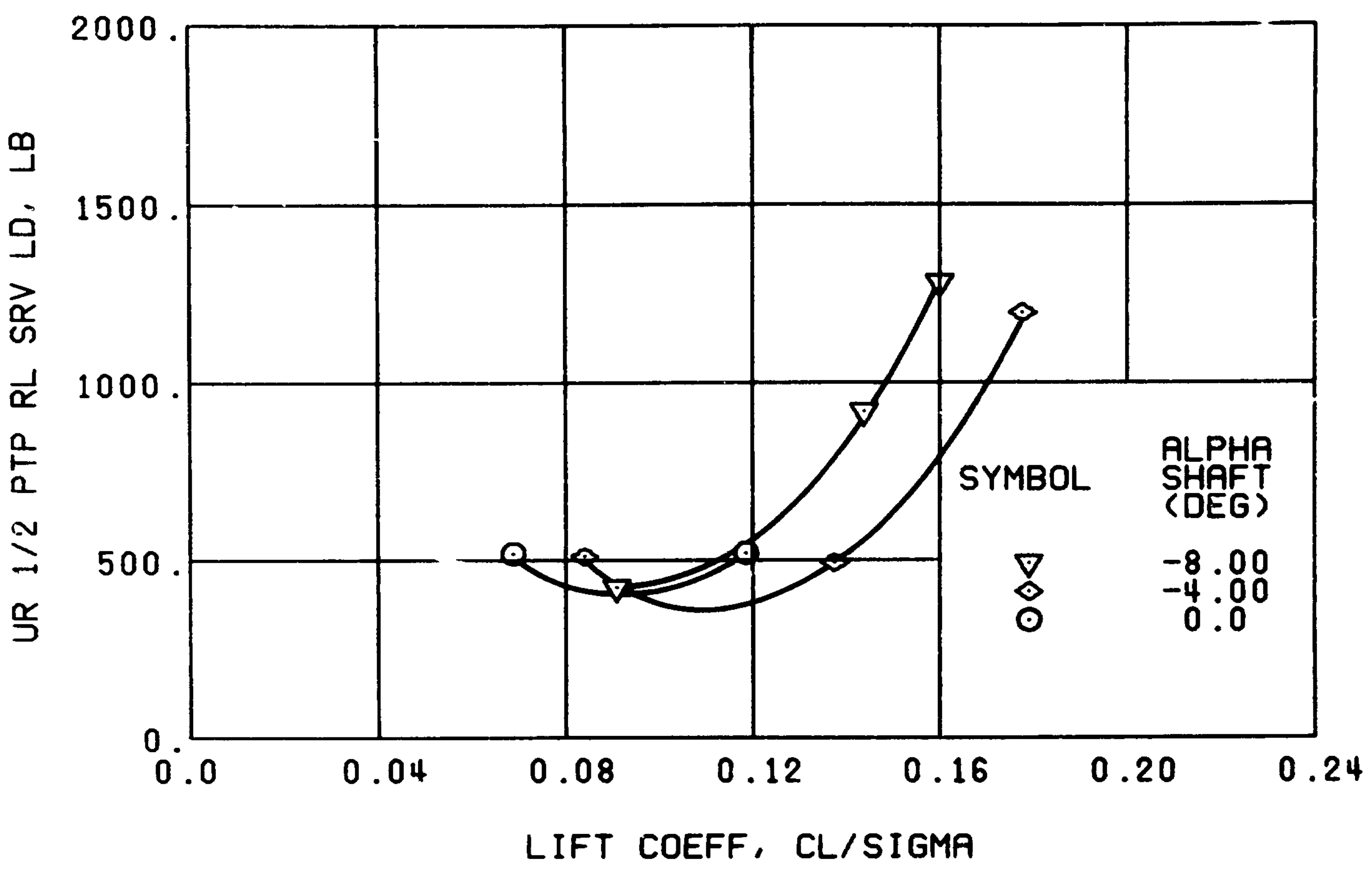

(p) GAGE 22

Figure 52. Continued.
$\mu = 0.47 \quad B'_{1s} = 8$ Deg

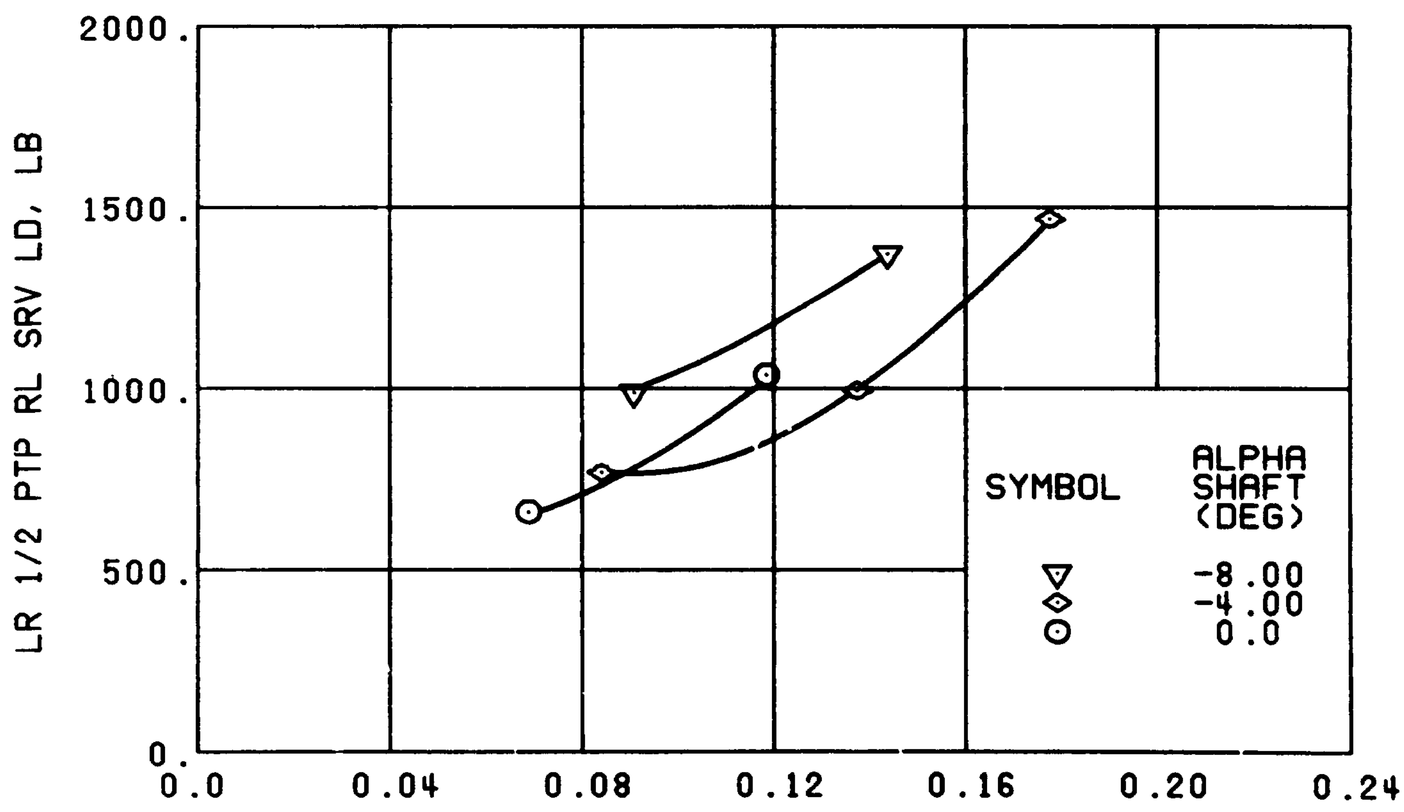

(q) GAGE 25

Figure 52. Continued.
$\mu = 0.47 \quad B'_{1s} = 8$ Deg

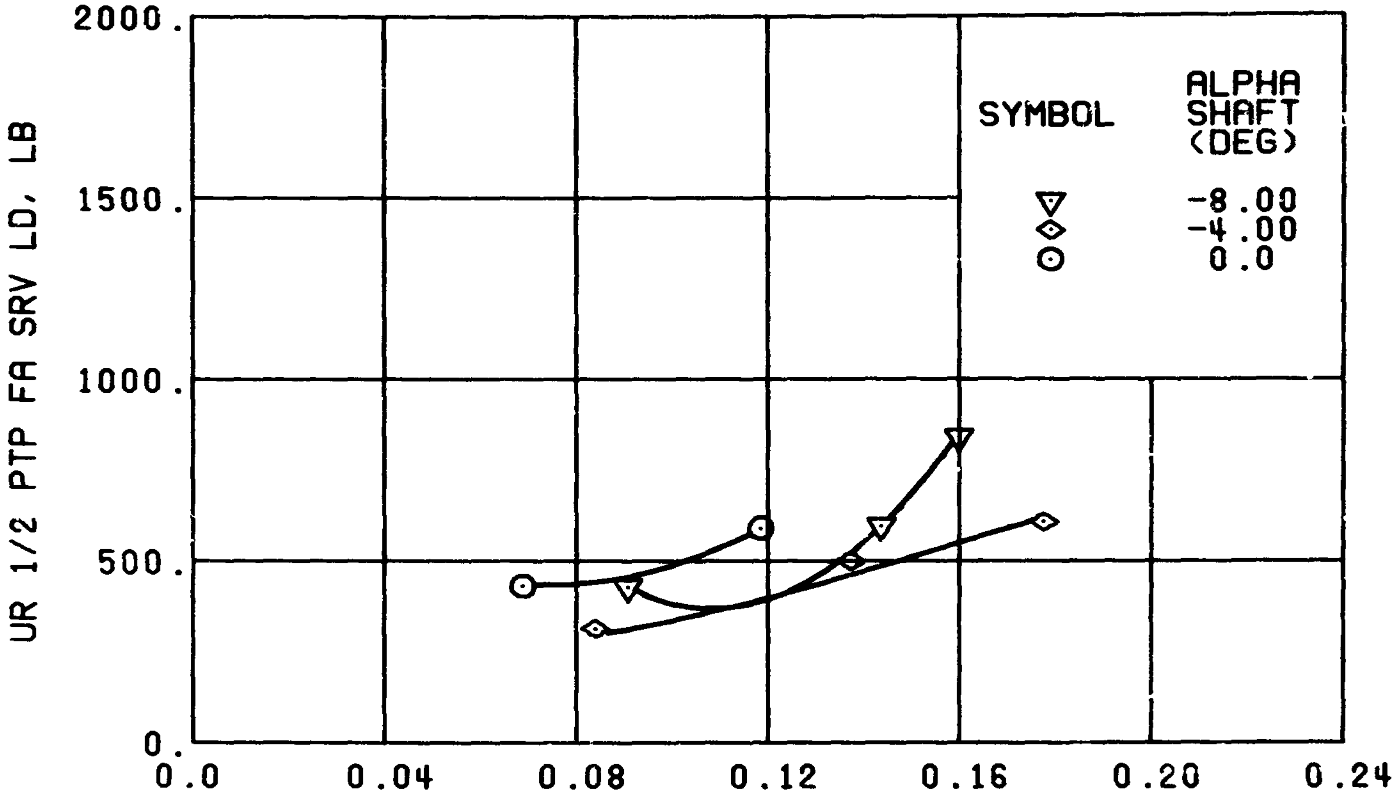

(r) GAGE 24

Figure 52. Continued.
$\mu = 0.47 \quad B'_{1s} = 8$ Deg

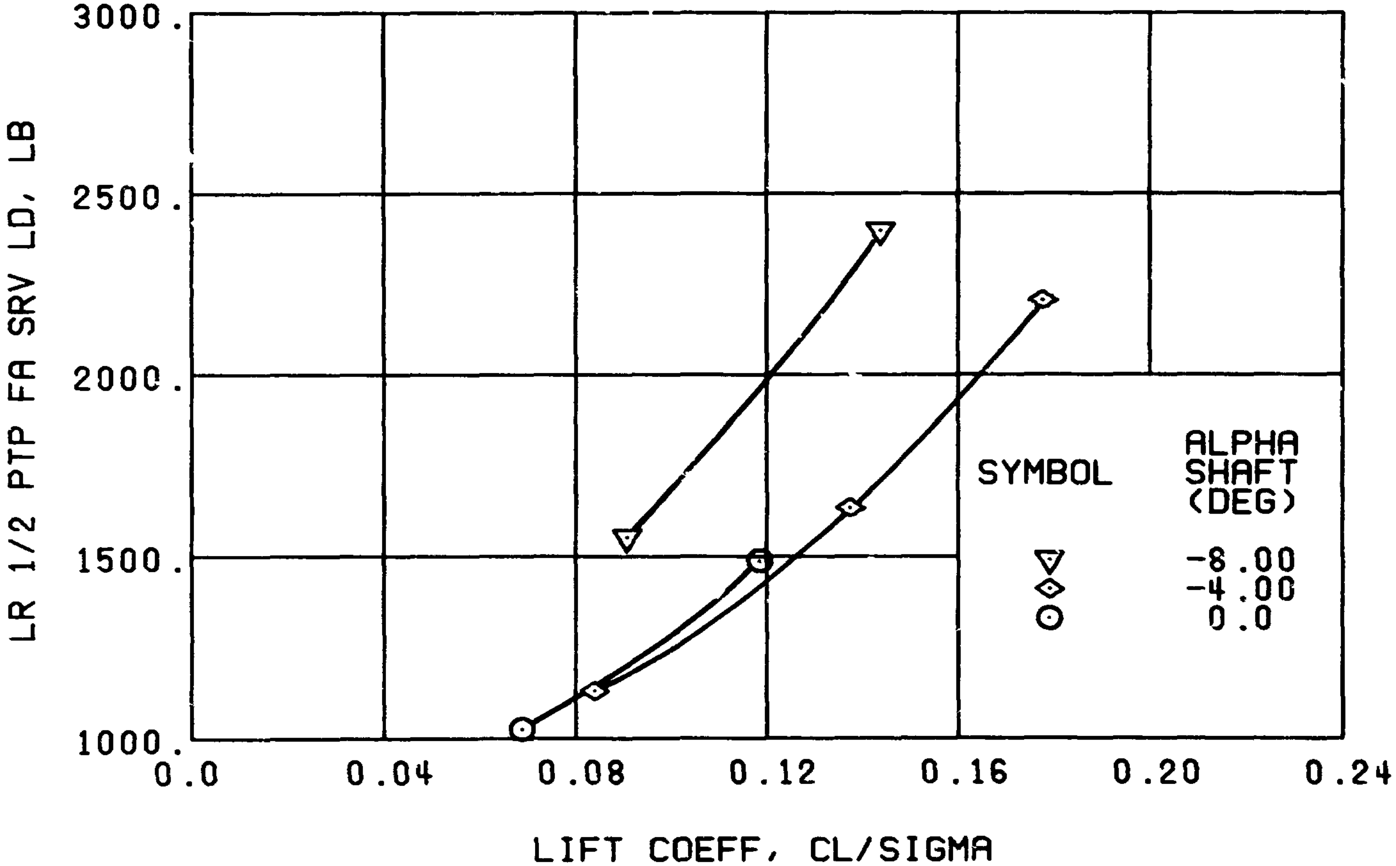

(s) GAGE 27

Figure 52. Continued.
$\mu = 0.47$ $B'_{1s} = 8$ Deg

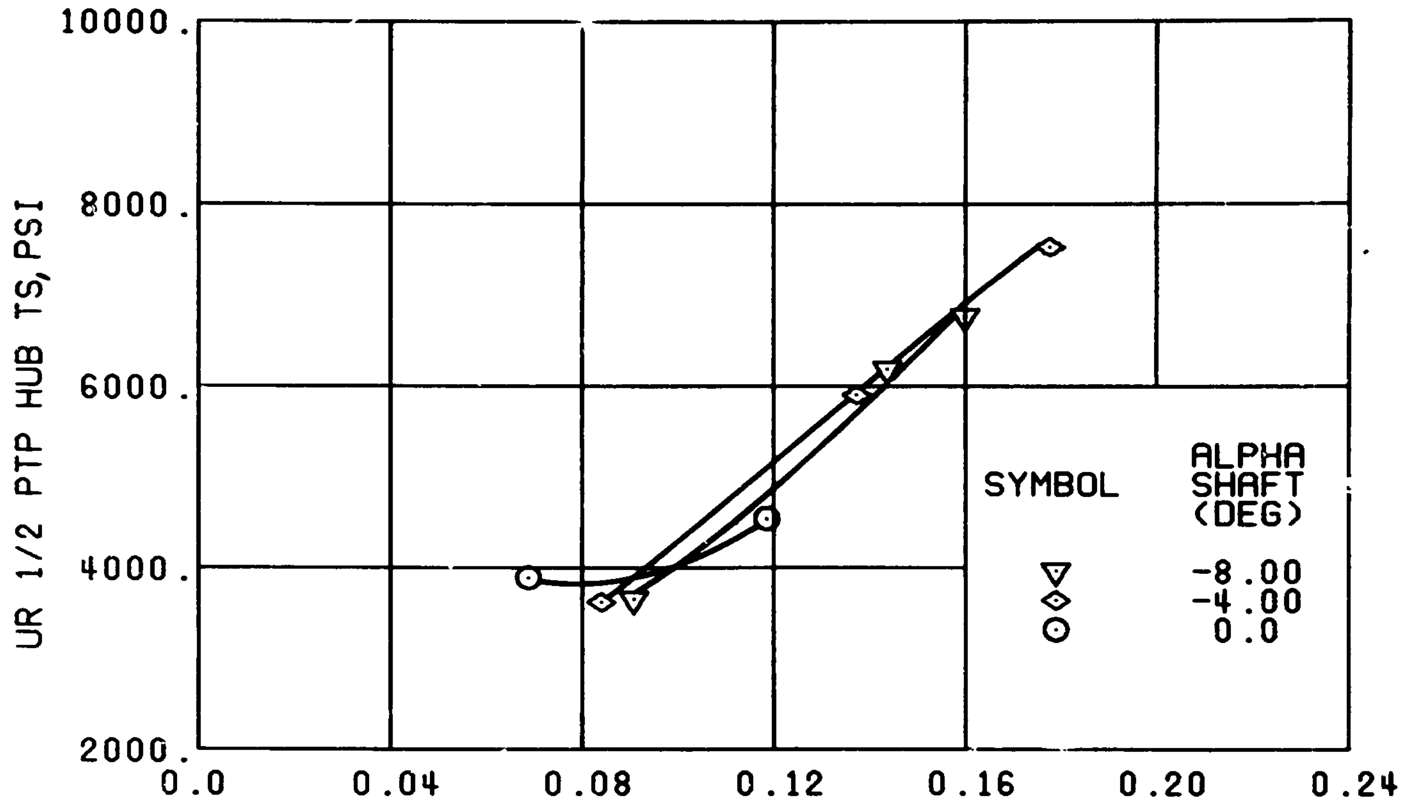

(†) GAGE 65

Figure 52. Continued.
$\mu = 0.47$ $B'_{1s} = 8$ Deg

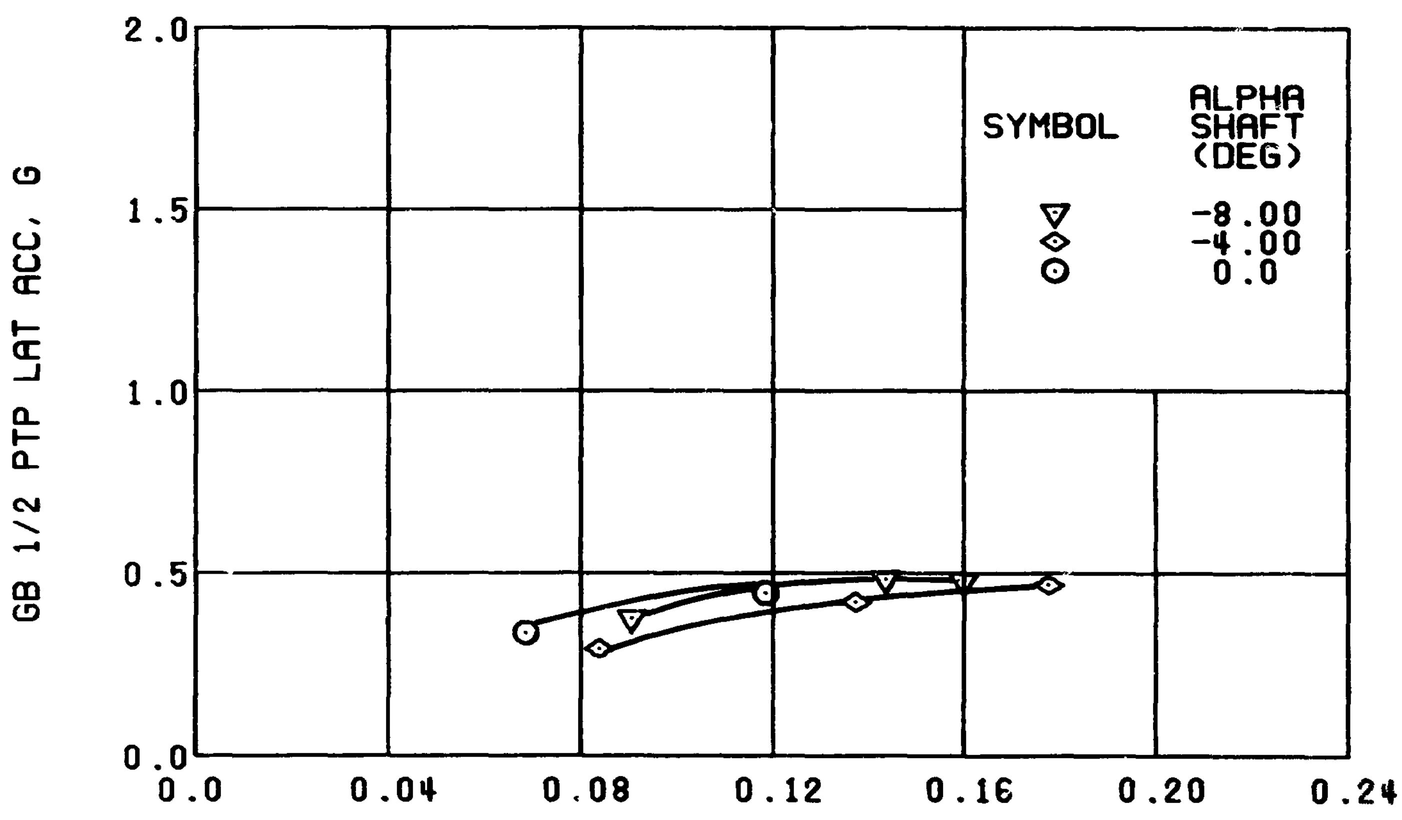

(u) GAGE 15 STA 76, BL 30

Figure 52. Continued.
$\mu = 0.47$ $B'_{1s} = 8$ Deg

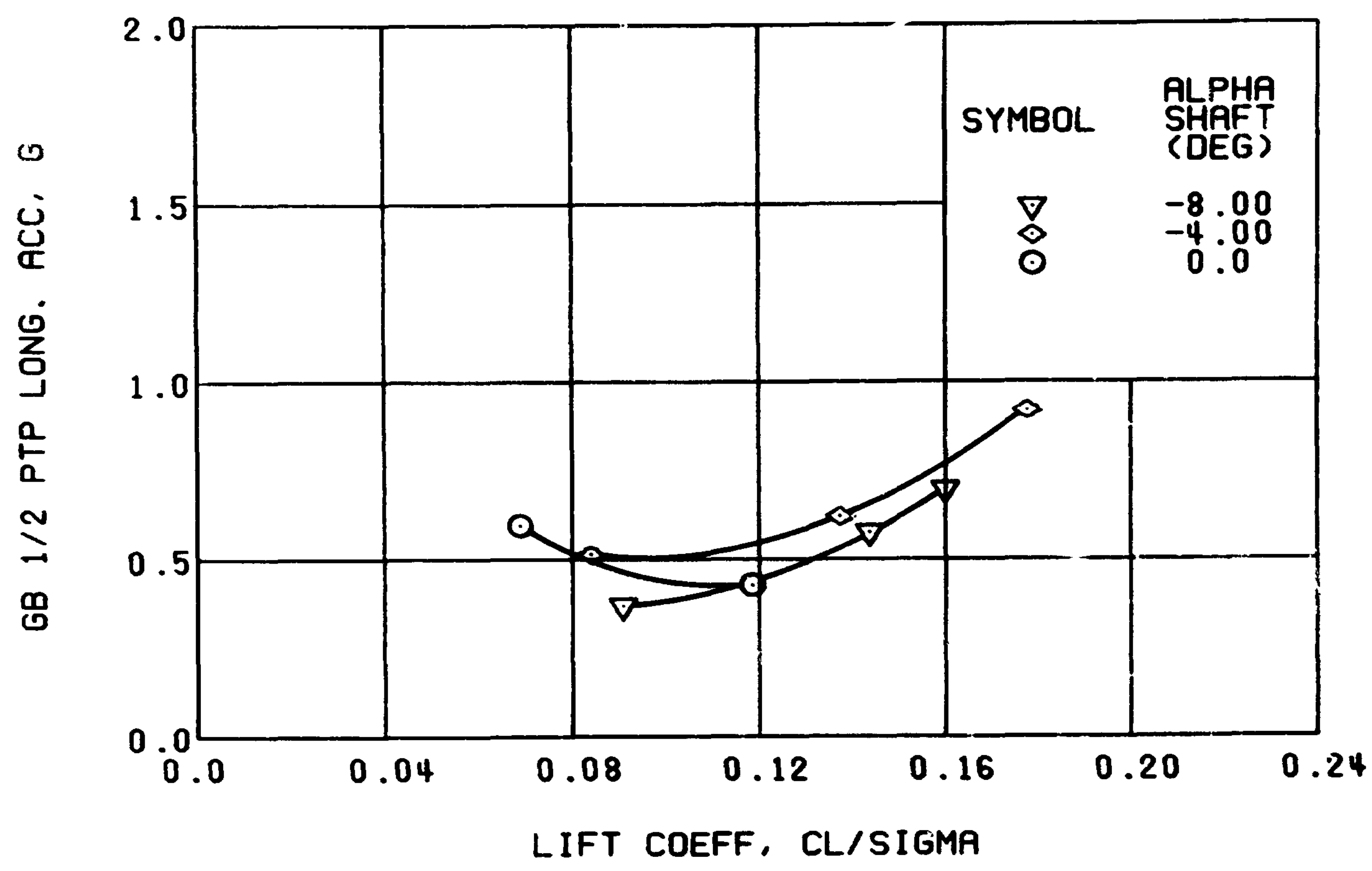

(v) GAGE 14 STA 61, BL 0

Figure 52. Continued.
$\mu = 0.47 \quad B'_{1s} = 8$ Deg

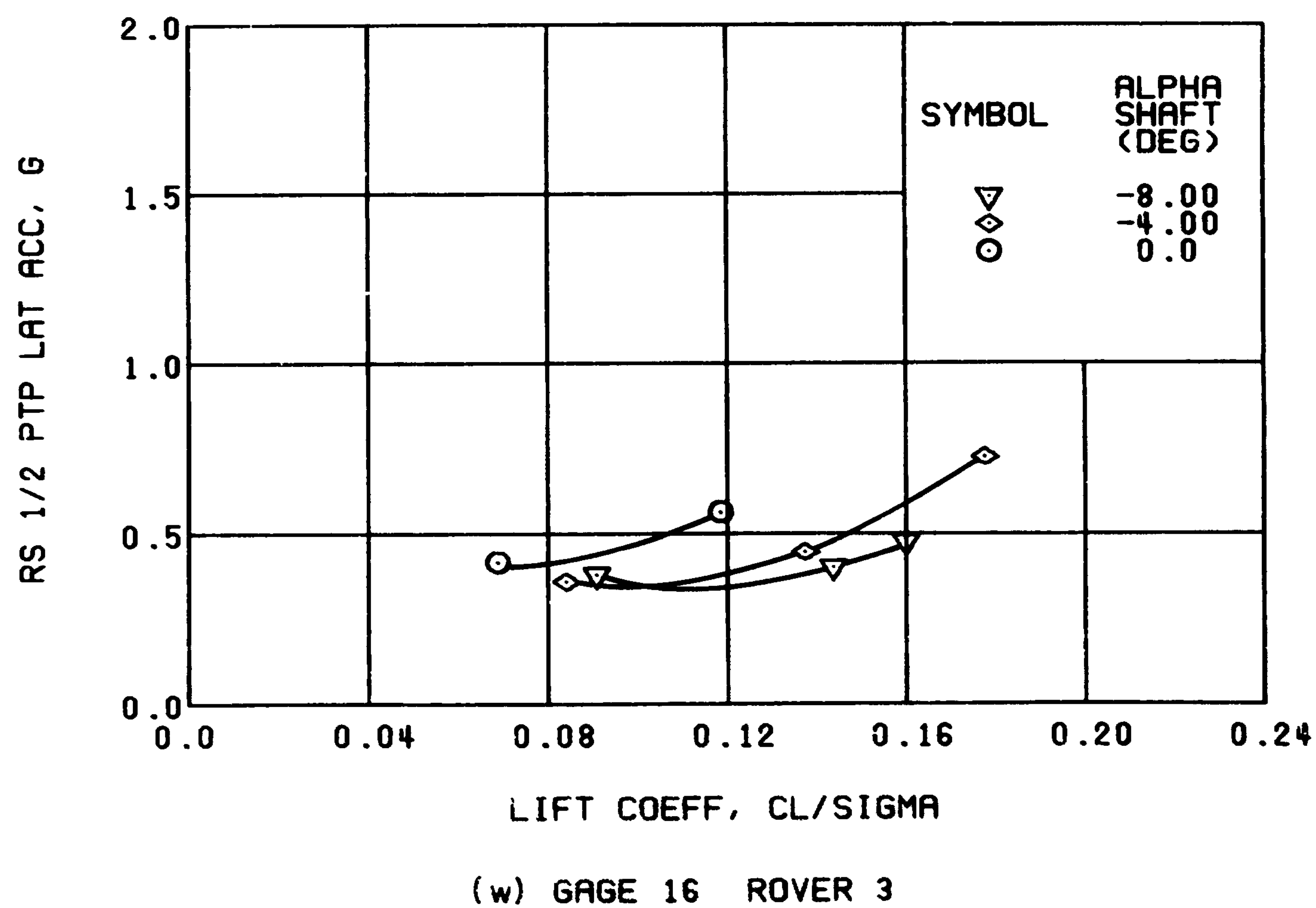

Figure 52. Continued.
$\mu = 0.47 \quad B'_{1s} = 8$ Deg

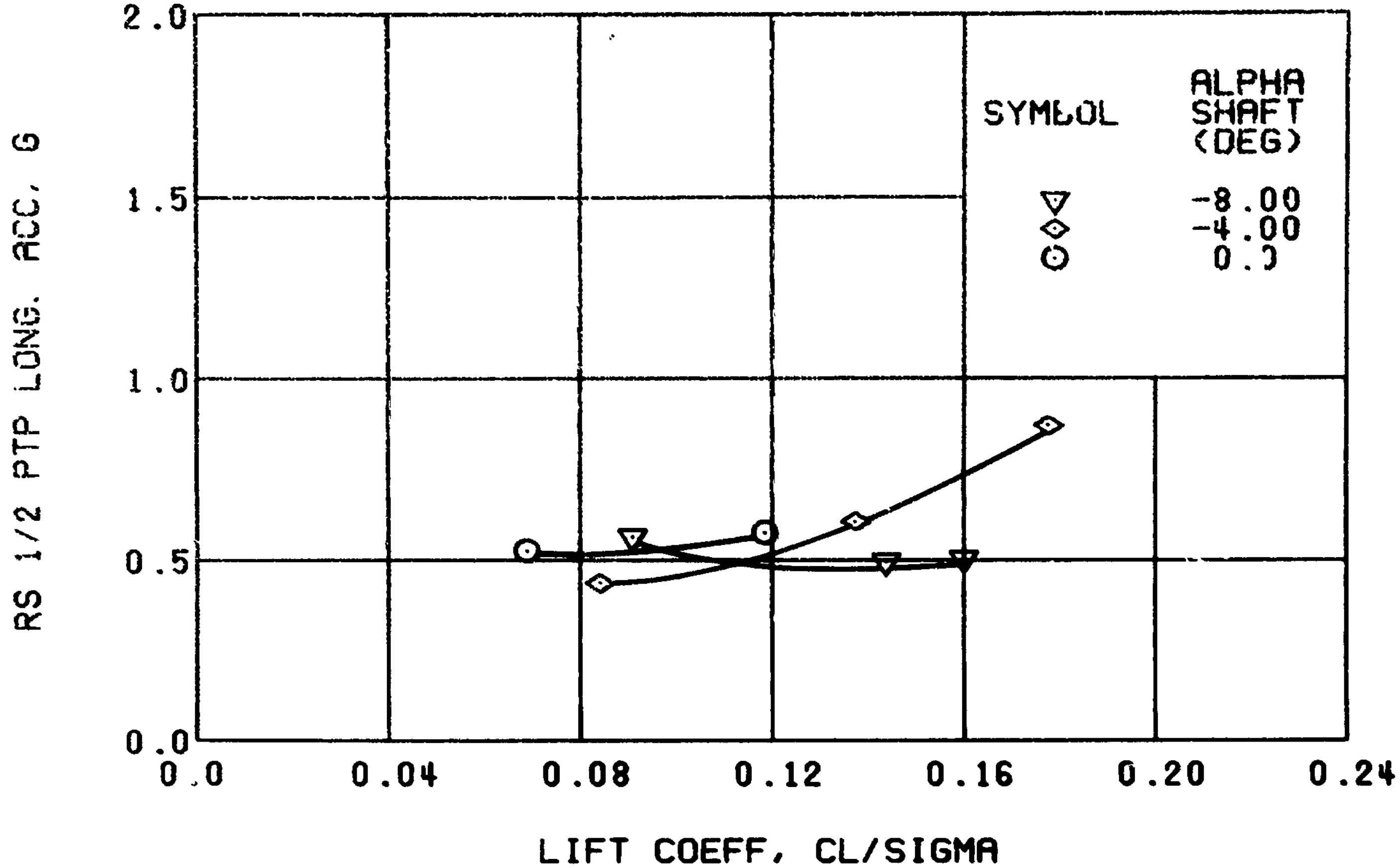

(x) GAGE 17 ROVER 4

Figure 52. Concluded.
$\mu = 0.47 \quad B'_{1s} = 8$ Deg

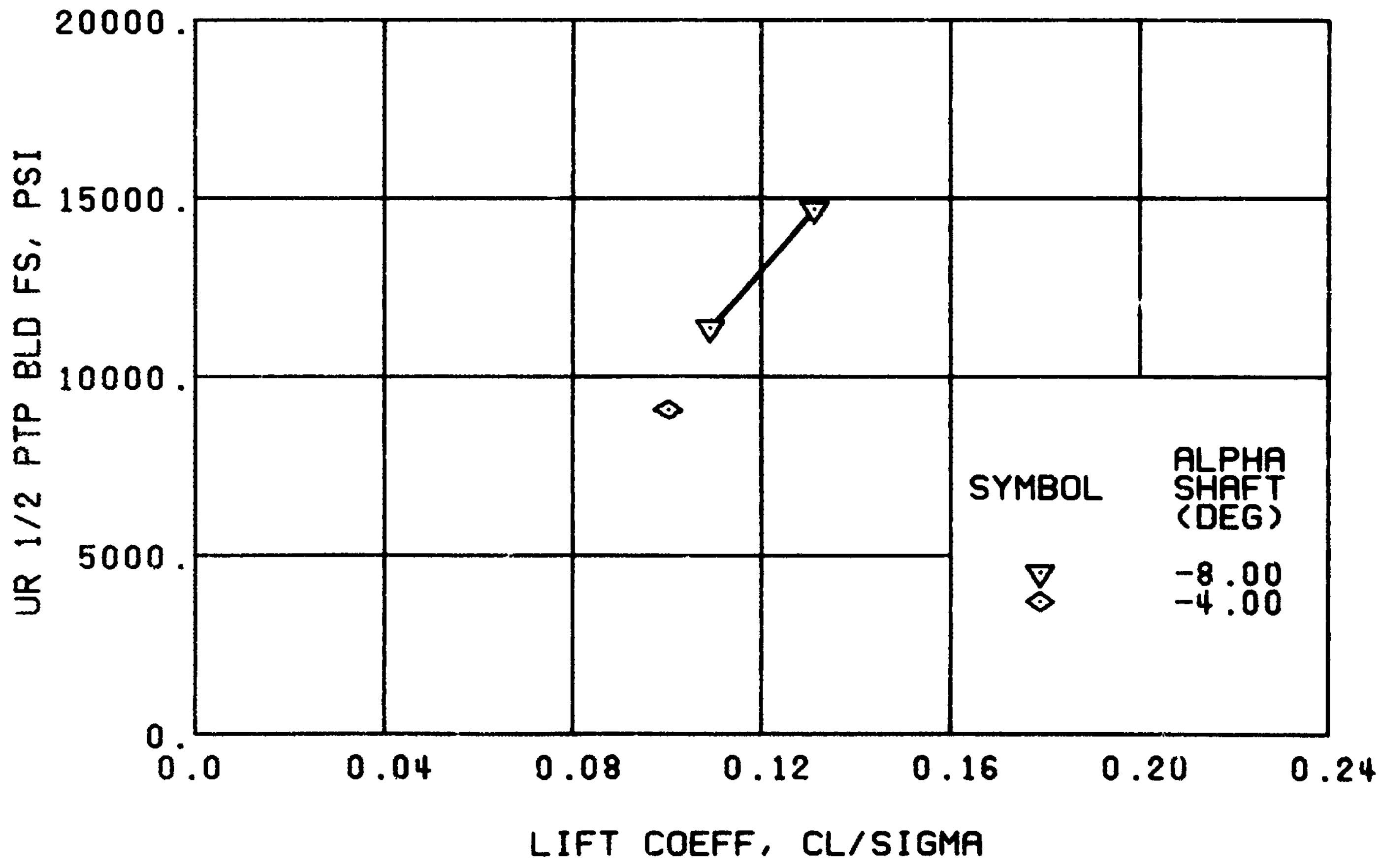

(a) GAGE 51 R84

Figure 53. Stress, Load, and Vibration Data at an Advance Ratio of 0.47 With the Lateral Displacement Control (B'_{1s}) Set at 10 Degrees.

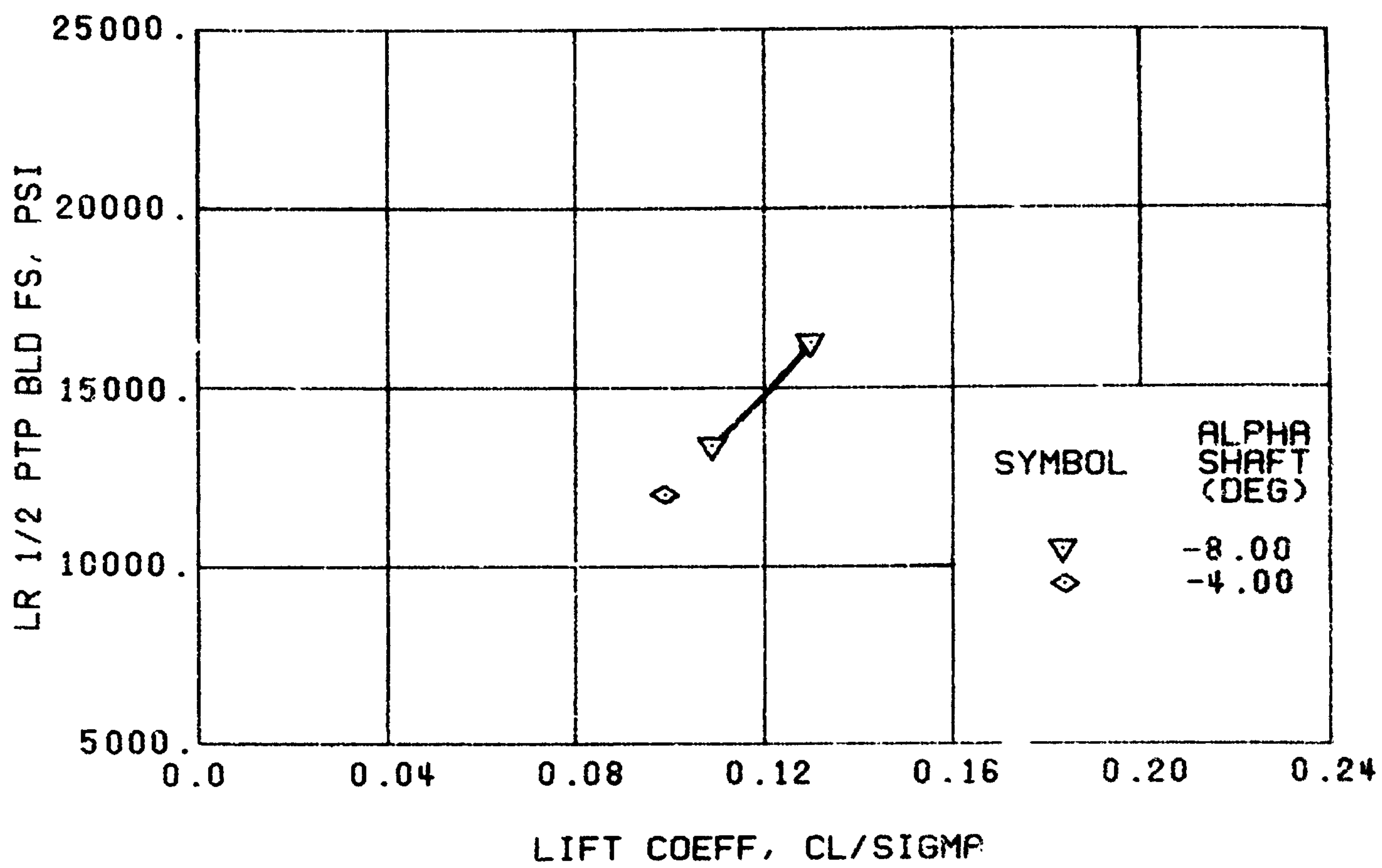

(b) GAGE 1 R84

Figure 53. Continued.
$\mu = 0.47$ $B'_{1s} = 10$ Deg

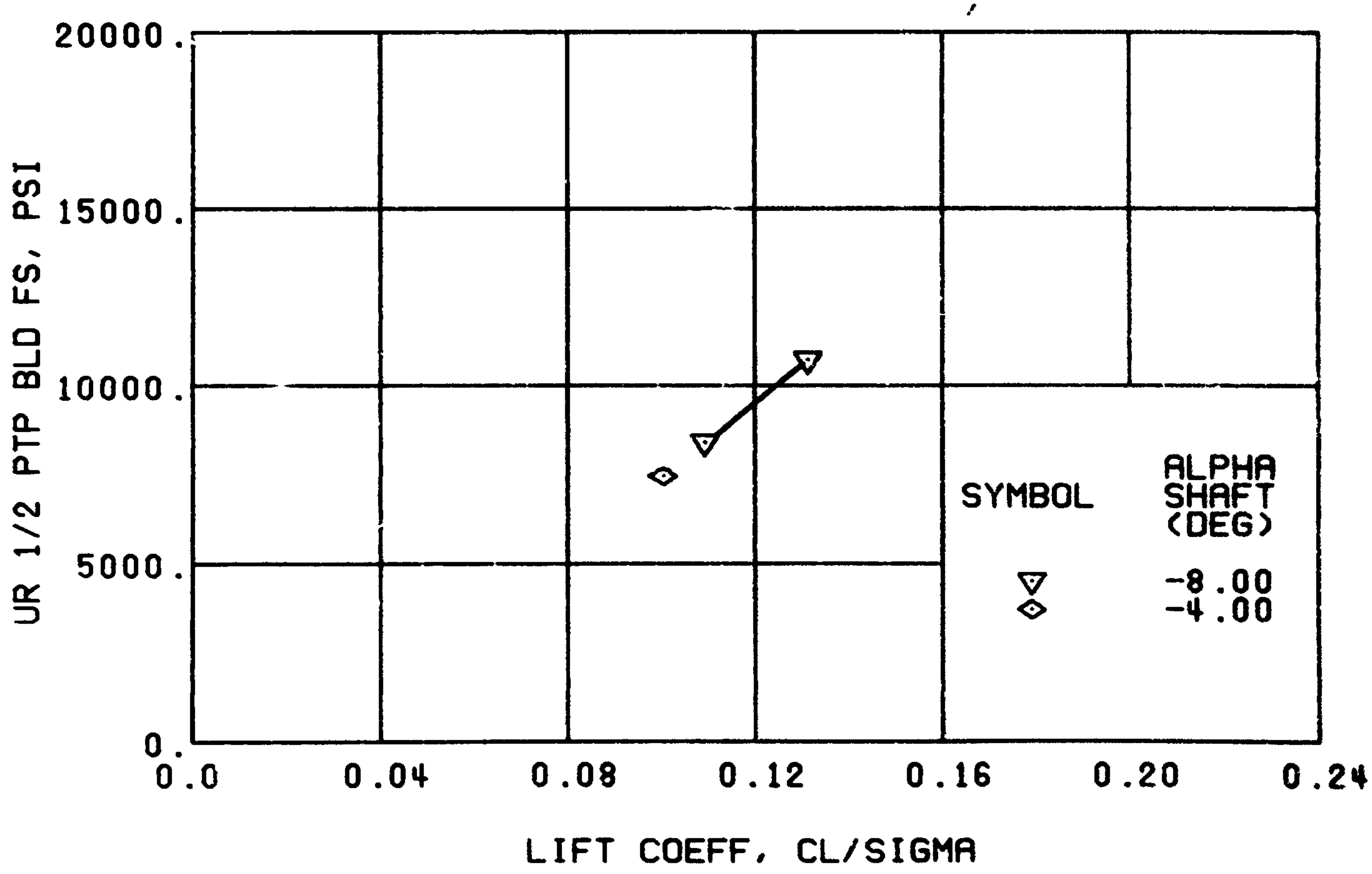

(c) GAGE 52 R108

Figure 53. Continued.
$\mu = 0.47$ $B'_{1s} = 10$ Deg

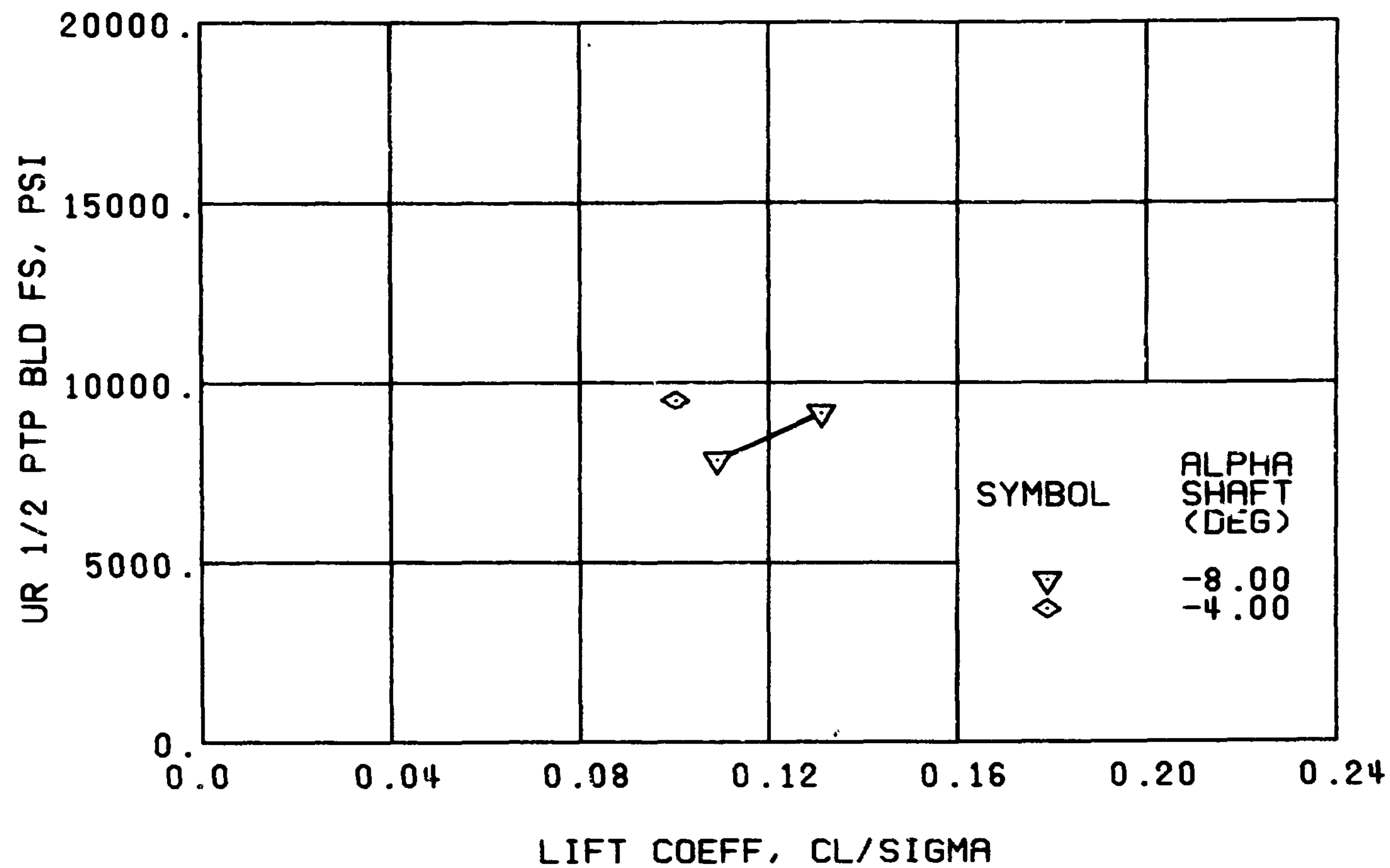

(d) GAGE 53 R132

Figure 53. Continued.
$\mu = 0.47$ $B'_{1s} = 10$ Deg

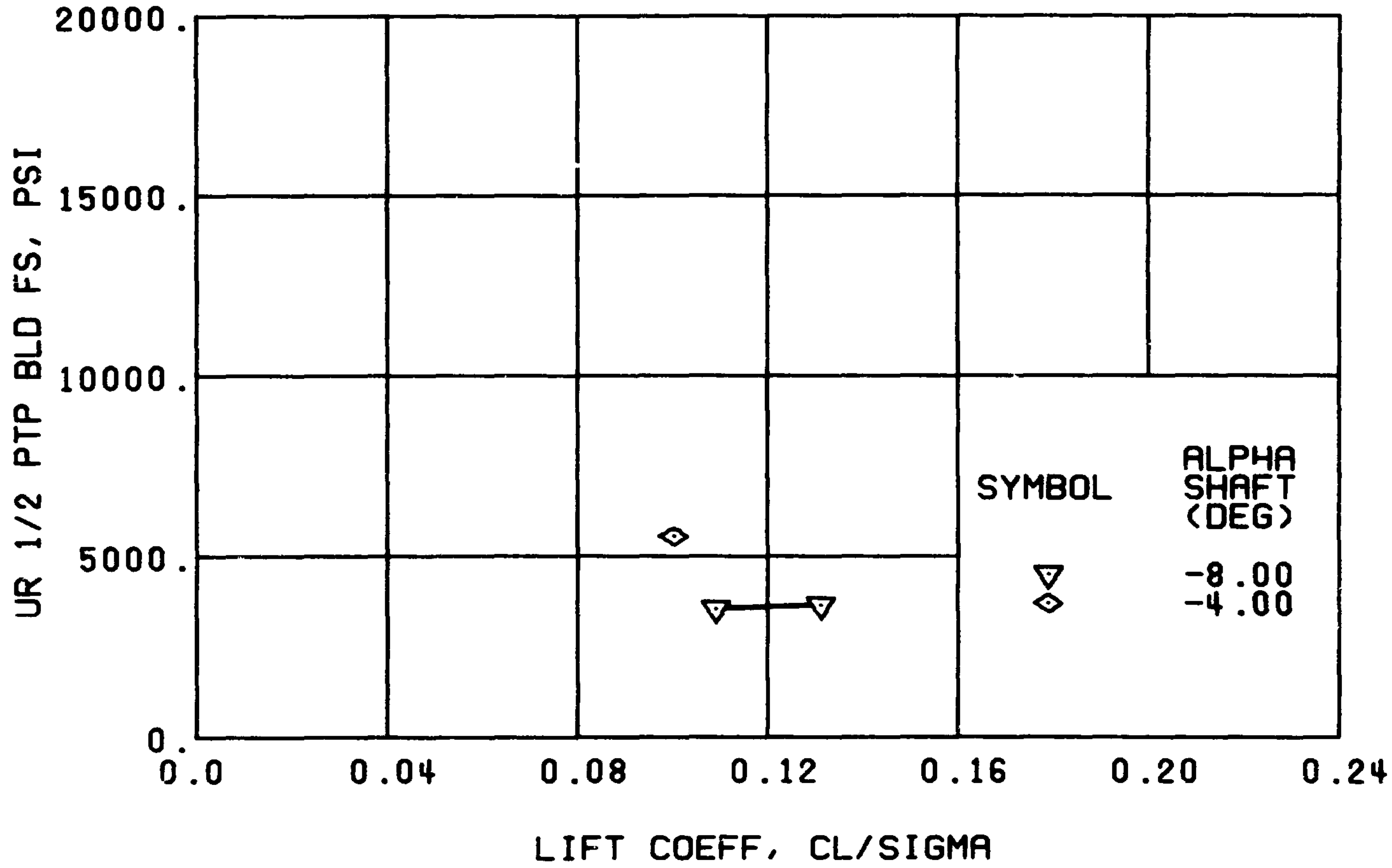

(f) GAGE 55 R204

Figure 53. Continued.
$\mu = 0.47$ $B'_{1s} = 10$ Deg

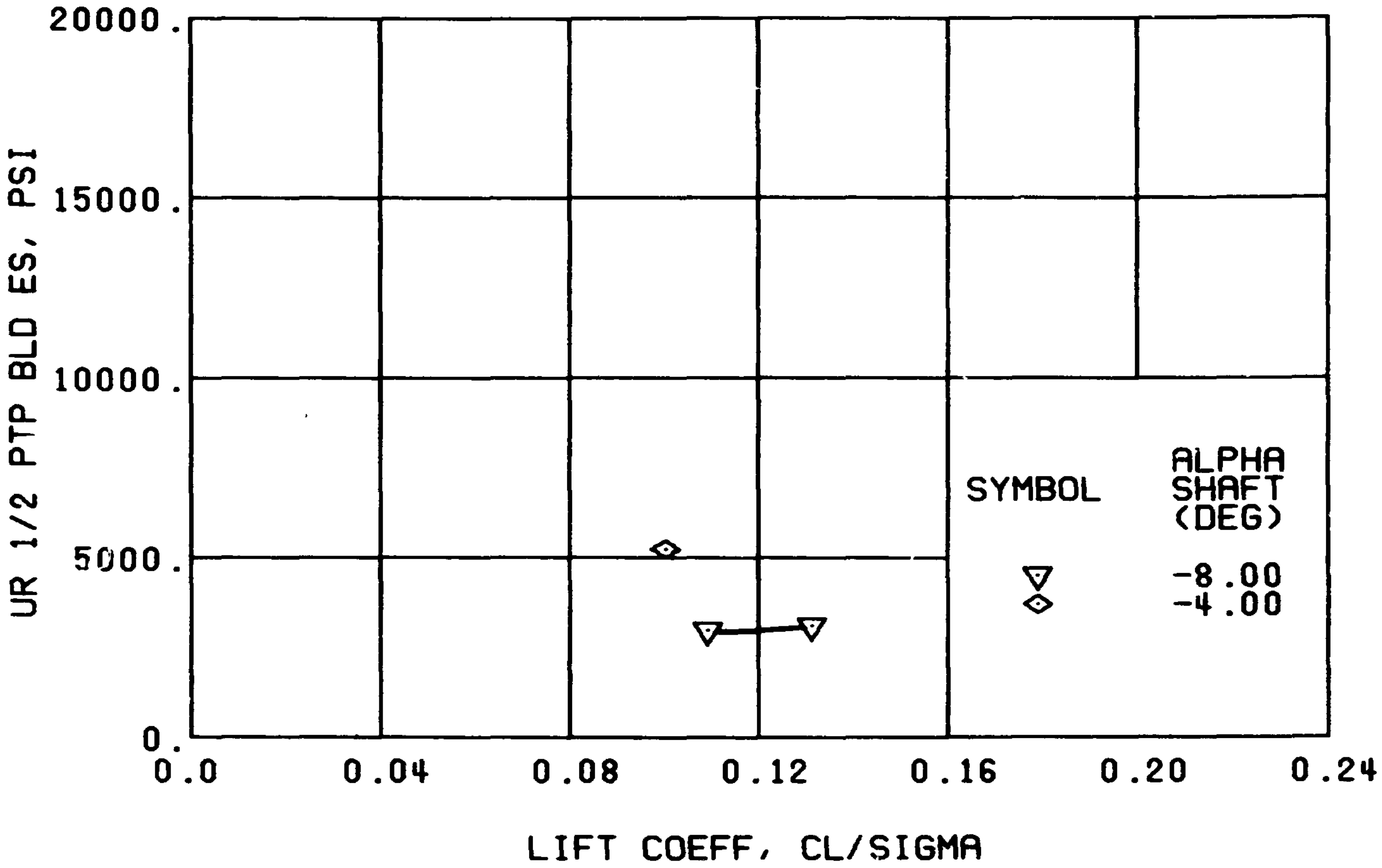

(h) GAGE 40 R84

Figure 53. Continued.
$\mu = 0.47 \quad B'_{1s} = 10$ Deg

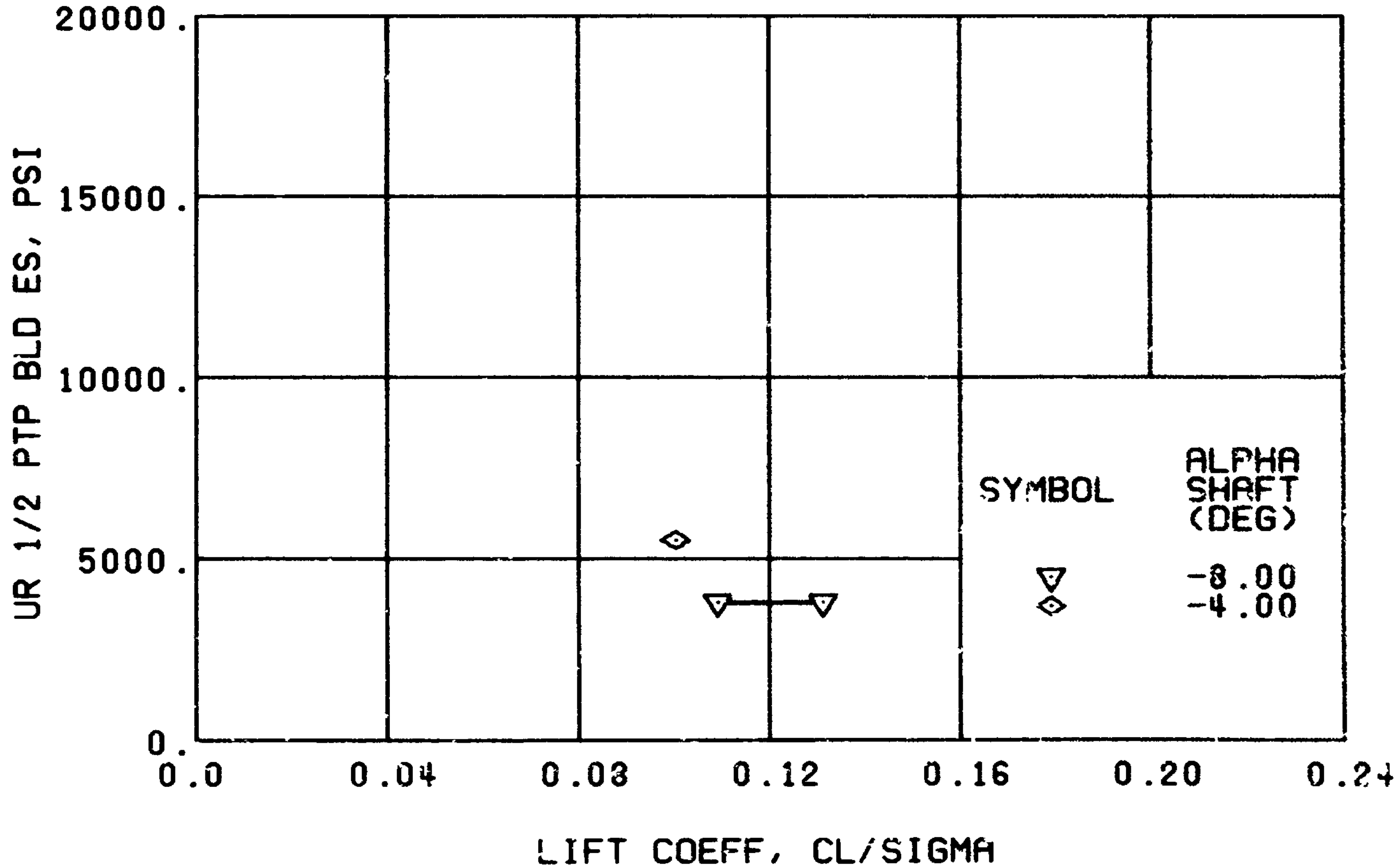

(j) GAGE 42 R132

Figure 53. Continued.
$\mu = 0.47$ $B'_{1s} = 10$ Deg

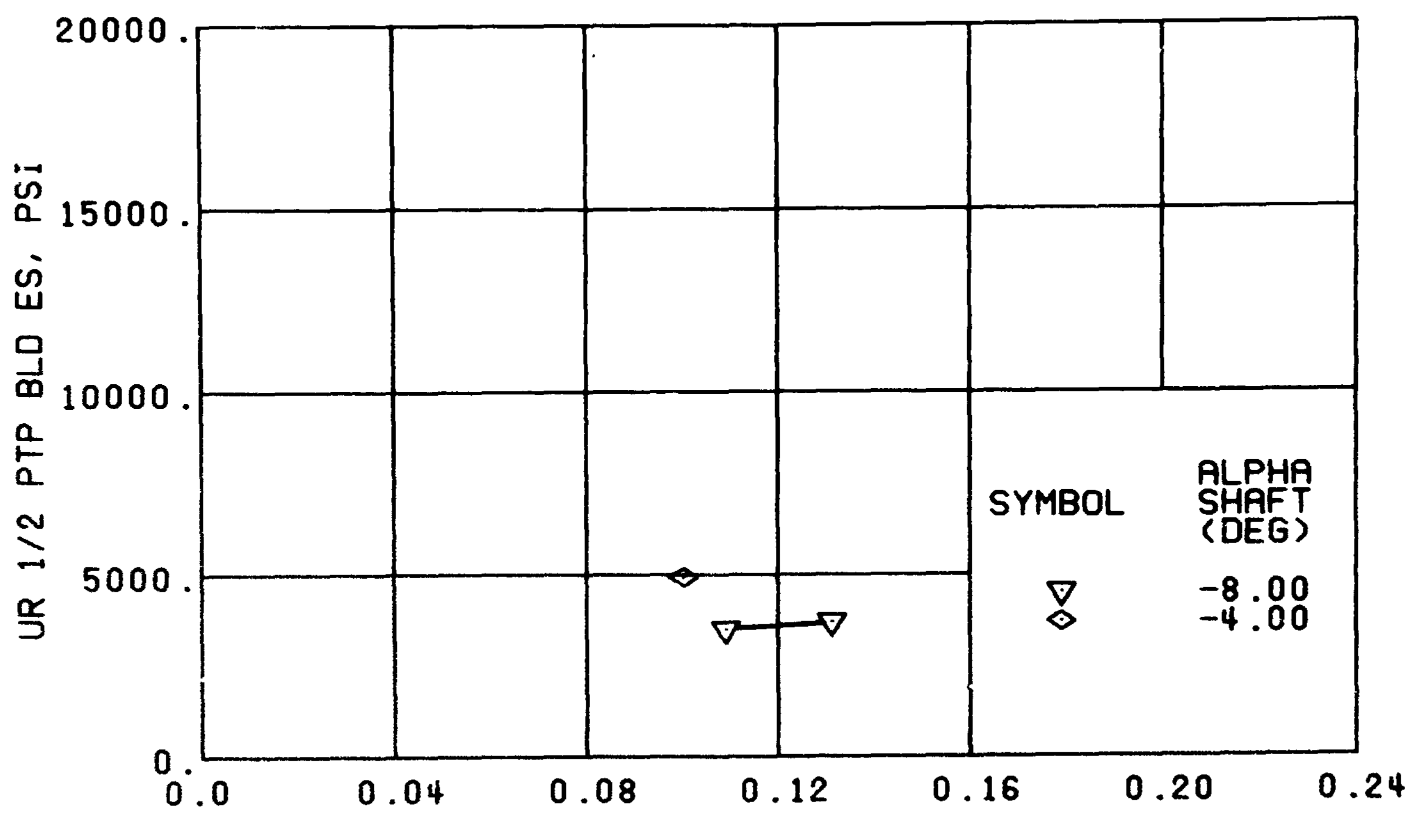

(k) GAGE 43 R168

Figure 53. Continued.
$\mu = 0.47 \quad B'_{1s} = 10$ Deg

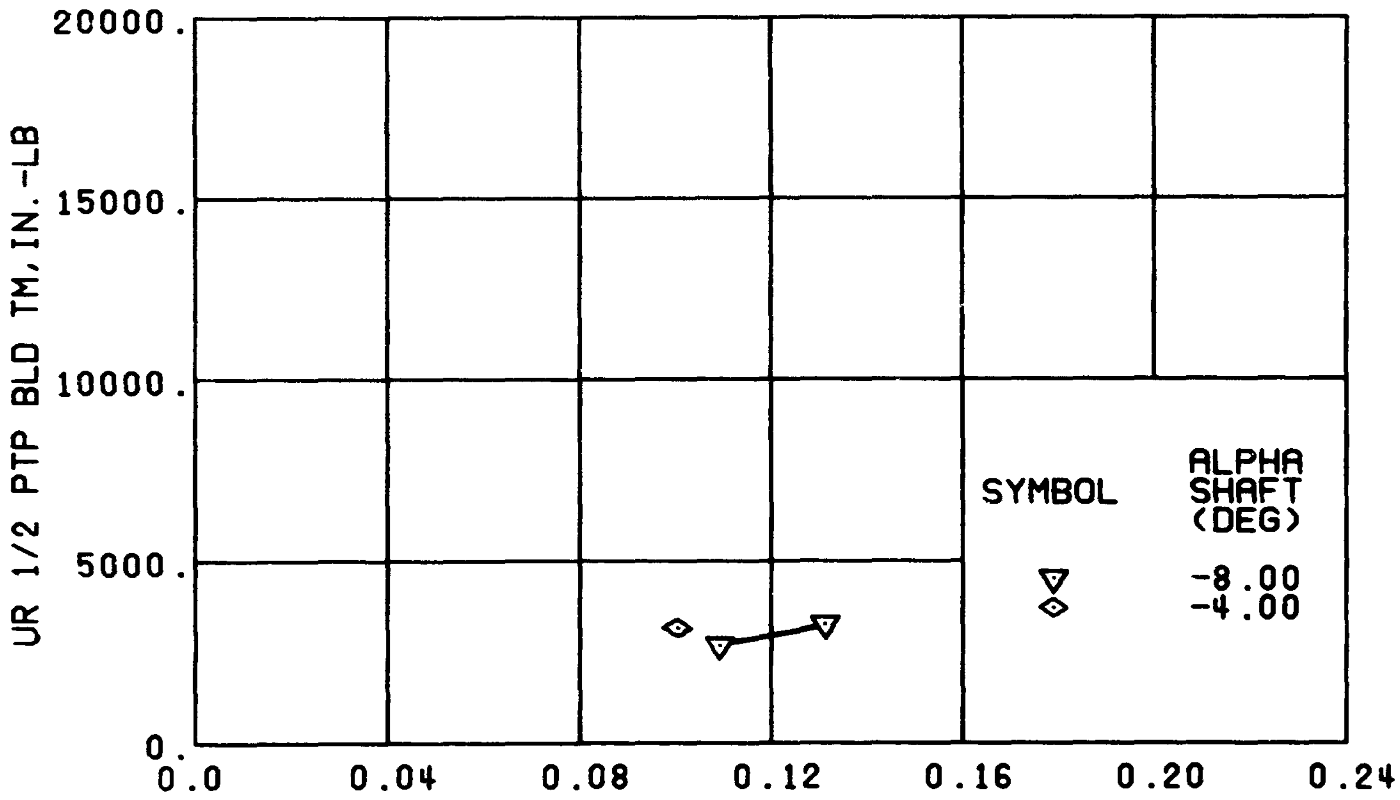

(m) GAGE 46 R130

Figure 53. Continued.
$\mu = 0.47$ $B'_{1s} = 10$ Deg

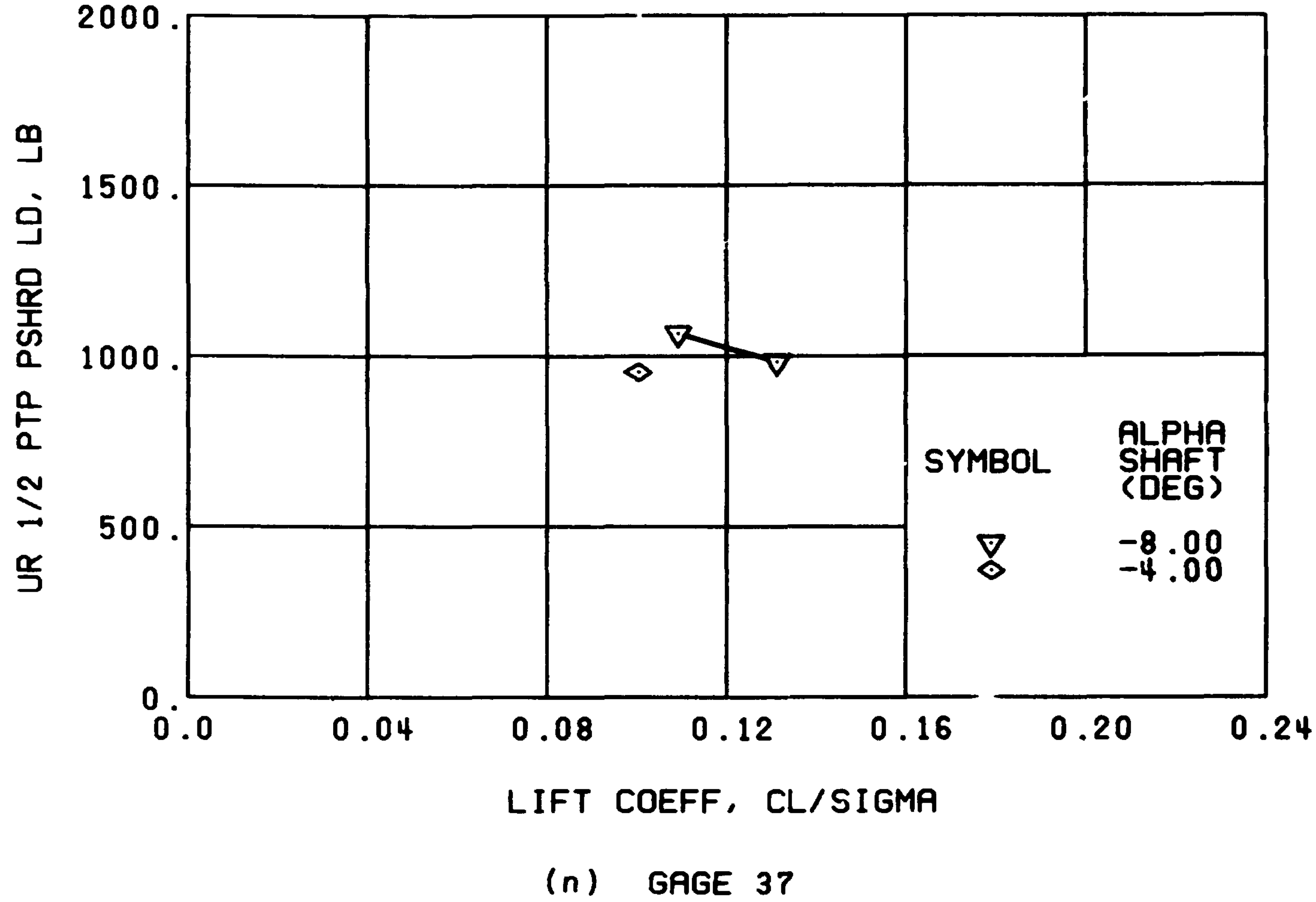

Figure 53. Continued.
$\mu = 0.47$ $B'_{1s} = 10$ Deg

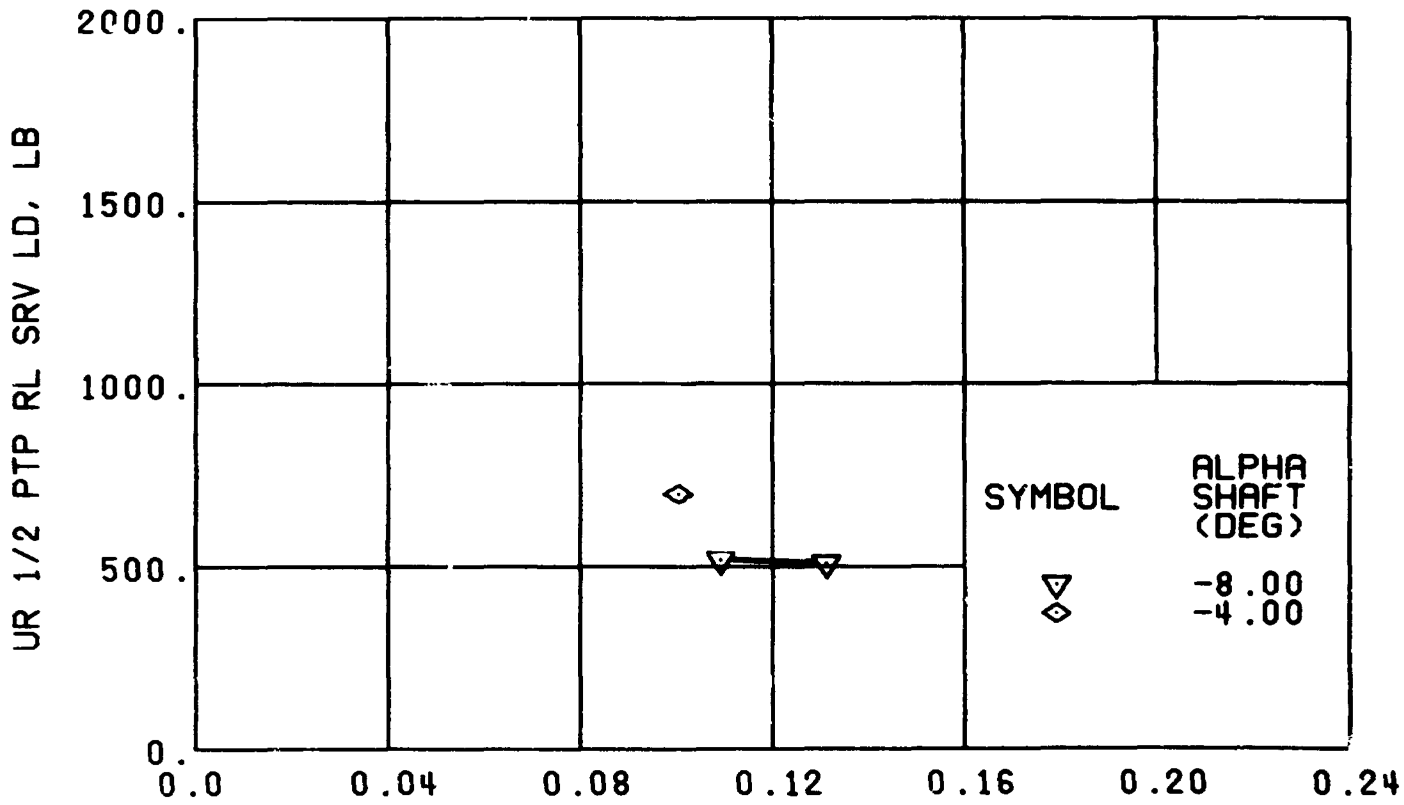

(p) GAGE 22

Figure 53. Continued.
$\mu = 0.47 \quad B'_{1s} = 10$ Deg

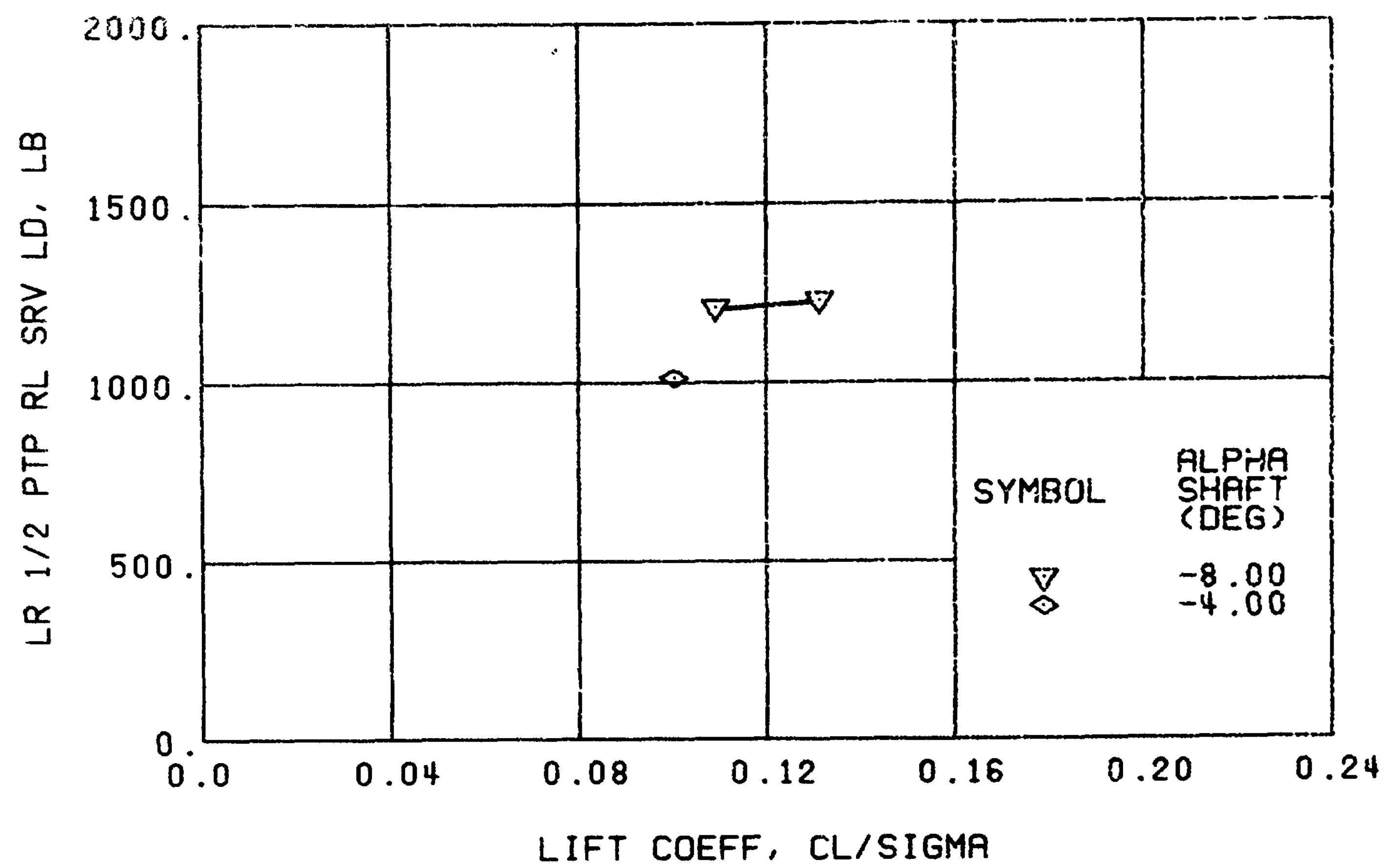

(q) GAGE 25

Figure 53. Continued.
$\mu = 0.47 \quad B'_{1s} = 10$ Deg

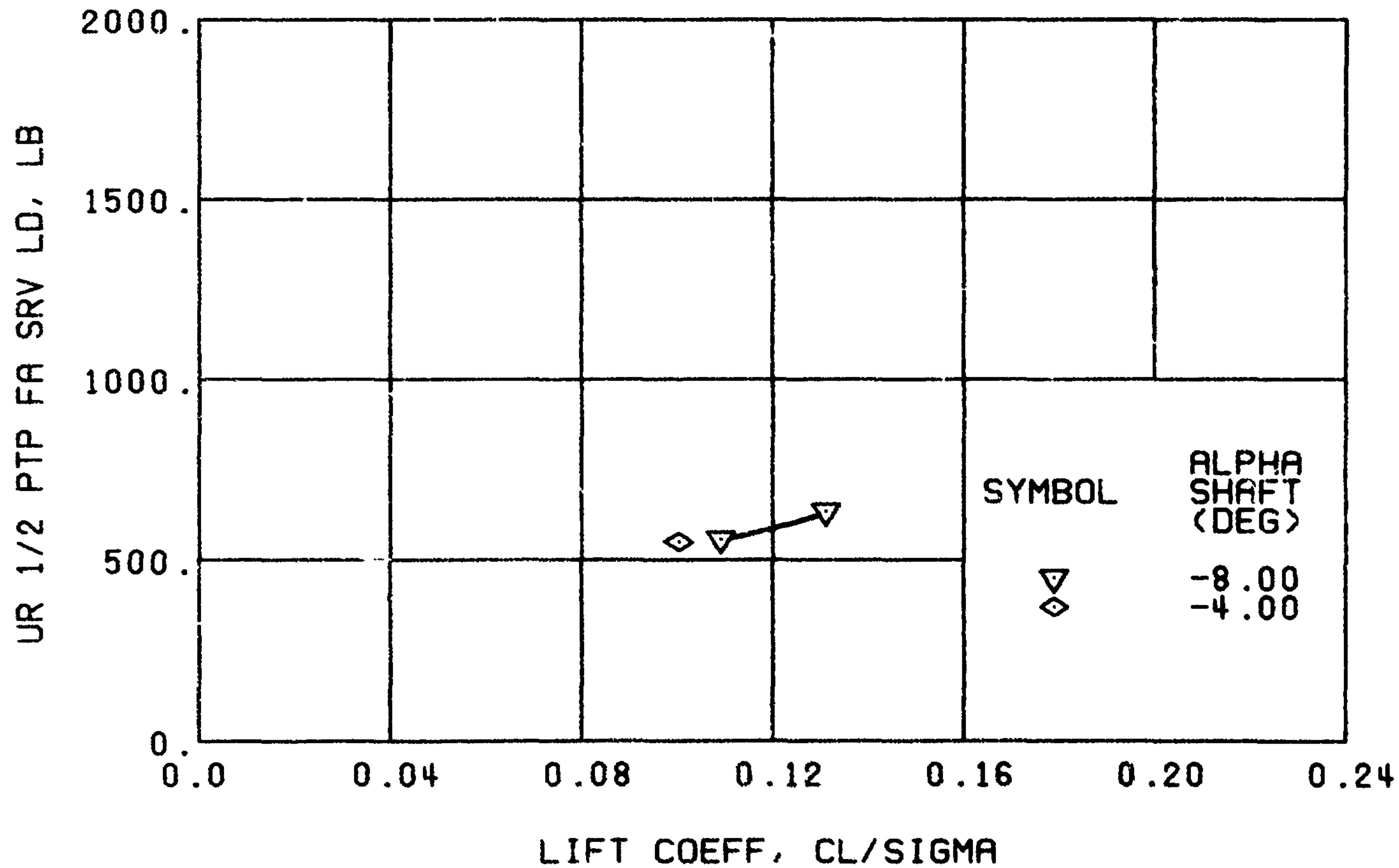

(r) GAGE 24

Figure 53. Continued.
$\mu = 0.47 \quad B'_{1s} = 10$ Deg

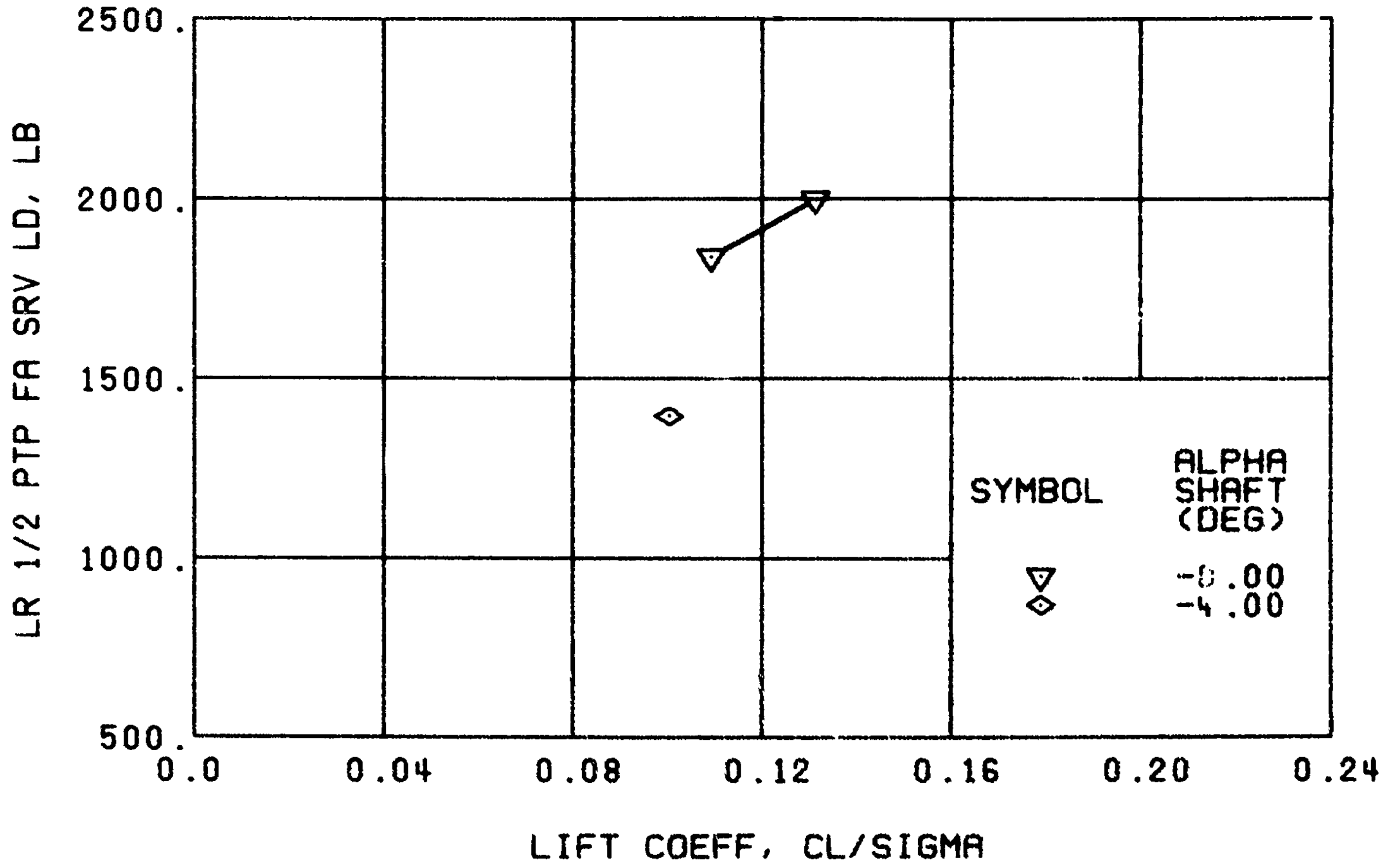

(s) GAGE 27

Figure 53. Continued.
μ = 0.47 B'_{1s} = 10 Deg

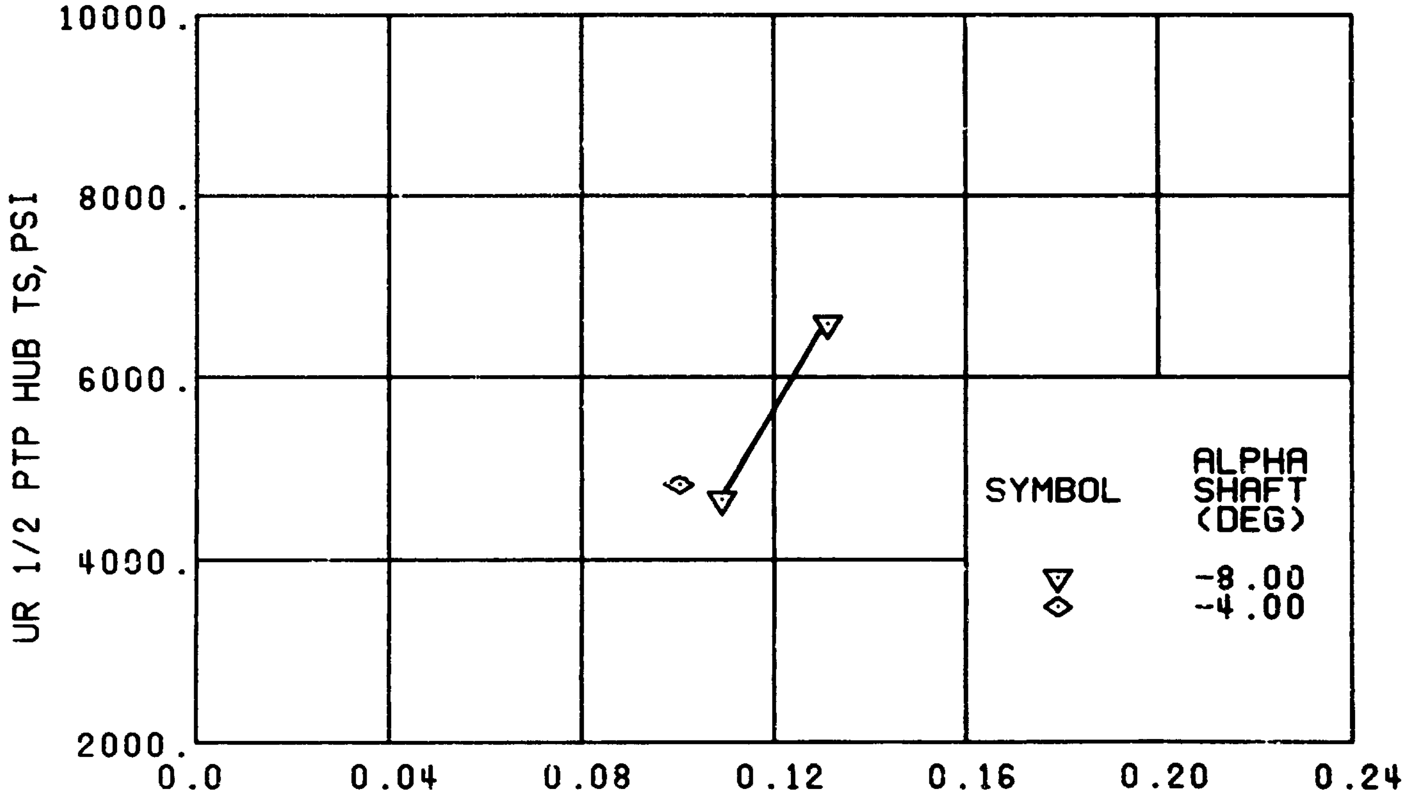

(f) GAGE 65

Figure 53. Continued.
$\mu = 0.47$ $B'_{1s} = 10$ Deg

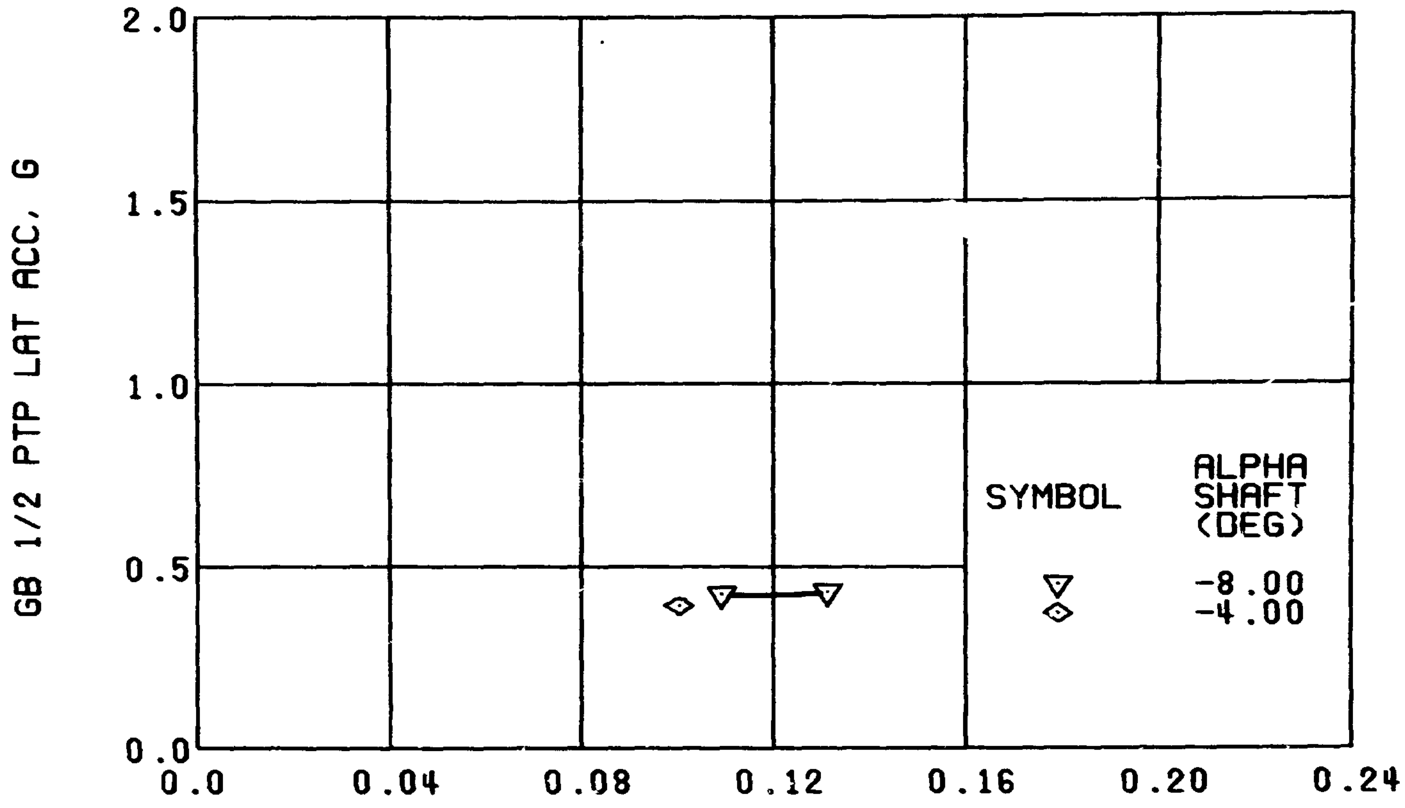

(u) GAGE 15 STA 76, BL 30

Figure 53. Continued.
$\mu = 0.47$ $B'_{1s} = 10$ Deg

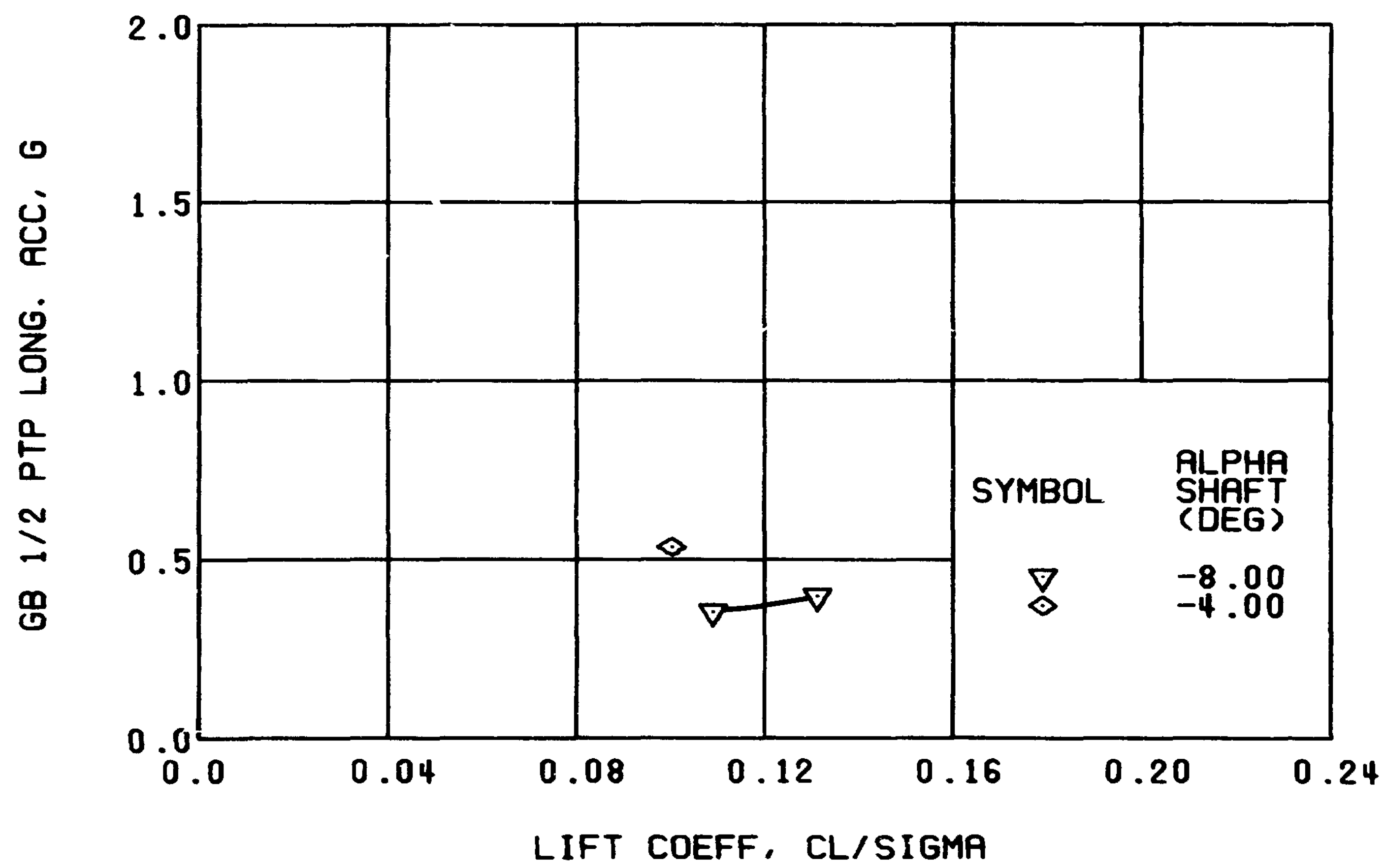

(v) GAGE 14 STA 61, BL 0

Figure 53. Continued.
$\mu = 0.47 \quad B'_{1s} = 10$ Deg

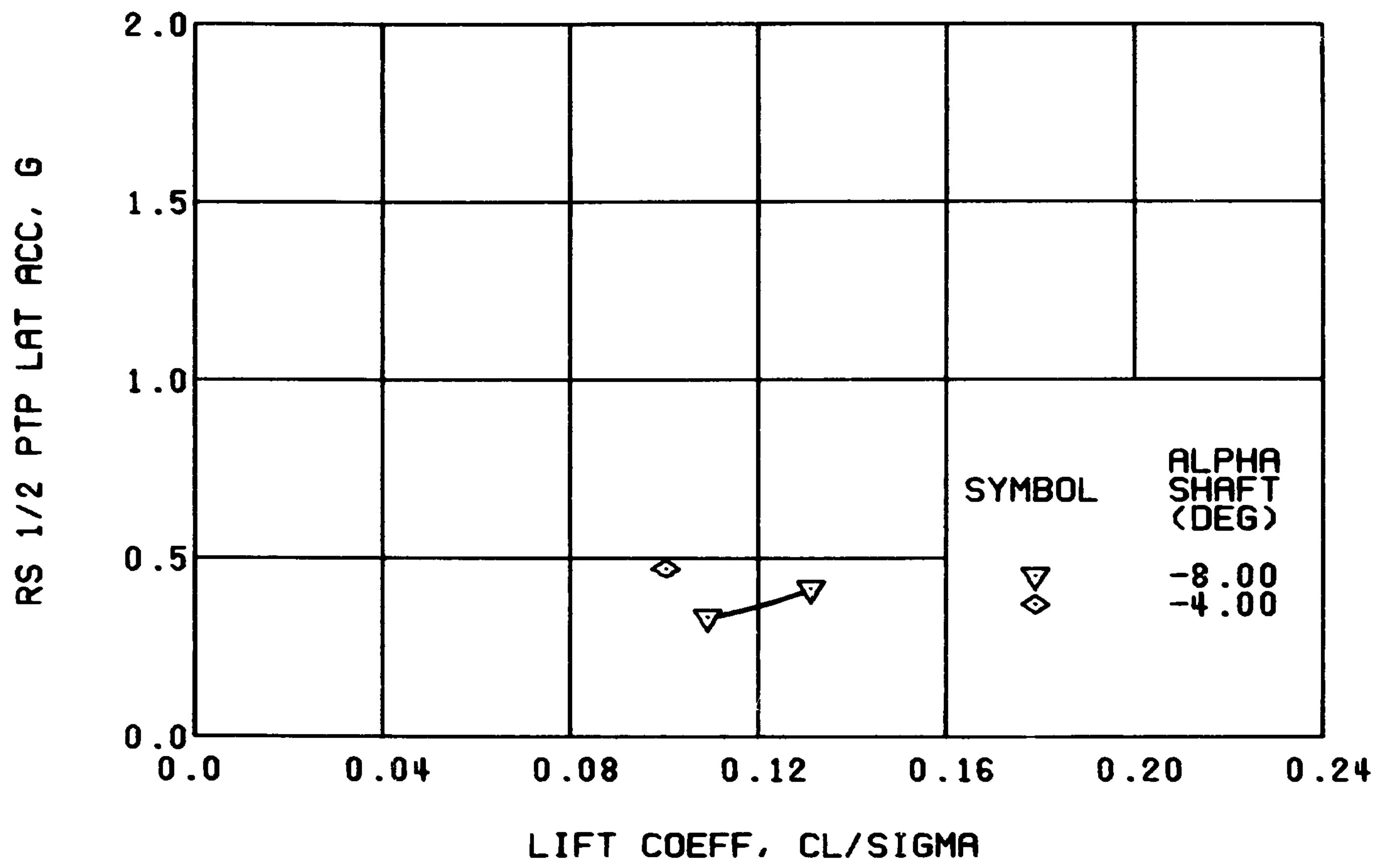

(w) GAGE 16 ROVER 3

Figure 53. Continued.
$\mu = 0.47$ $B'_{1s} = 10$ Deg

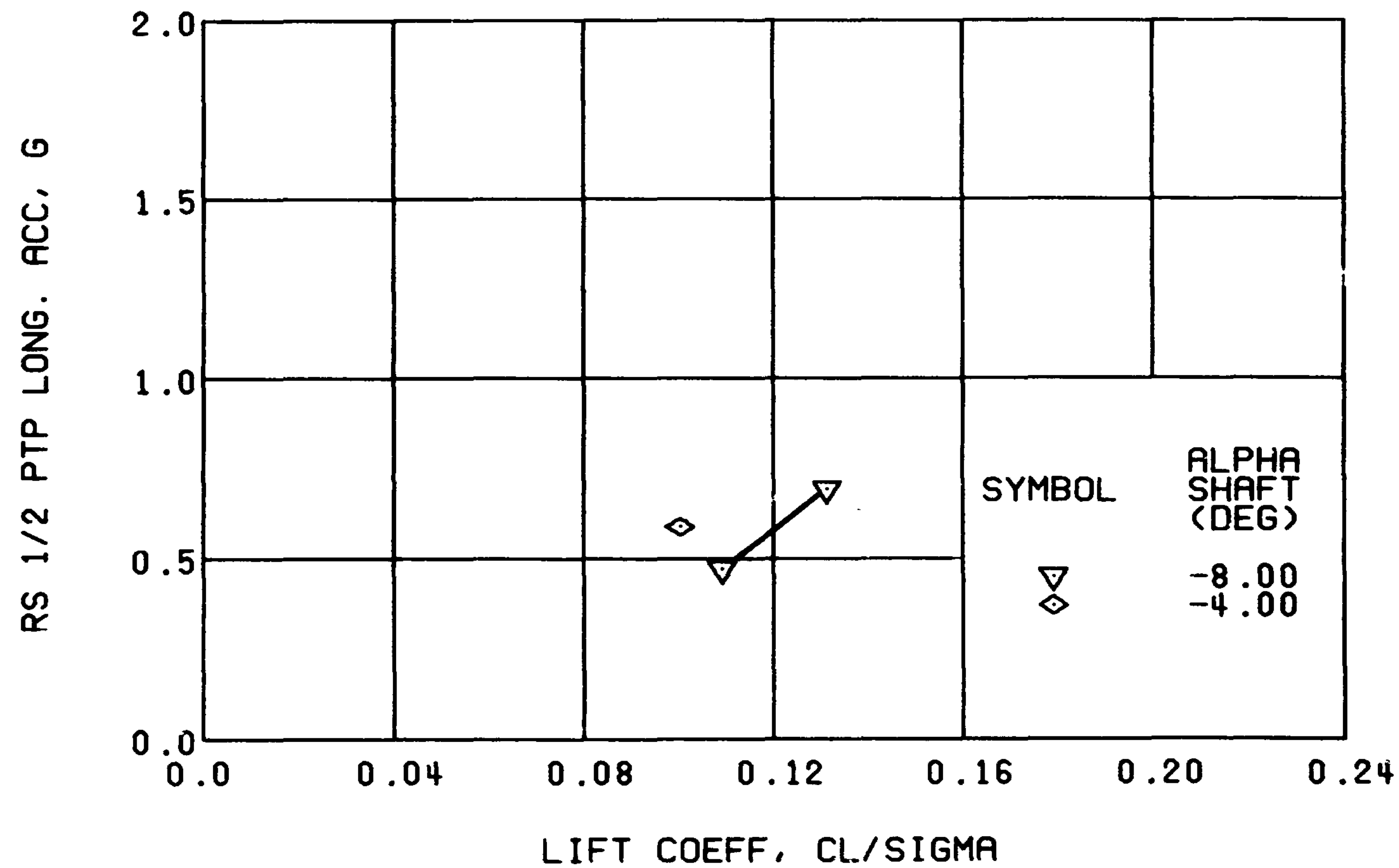

(x) GAGE 17 ROVER 4

Figure 53. Concluded.
$\mu = 0.47$ $B'_{1s} = 10$ Deg

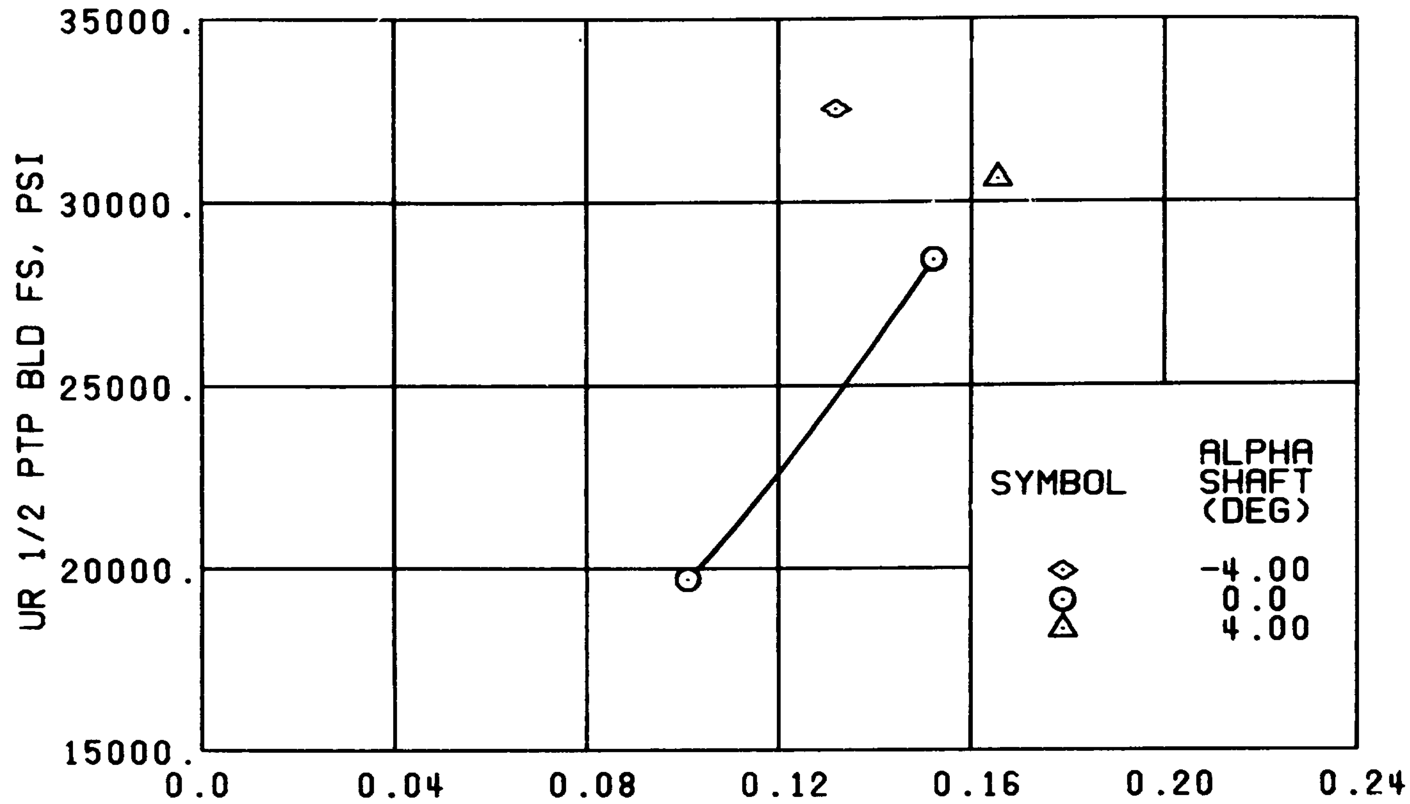

(a) GAGE 51 R84

Figure 54. Stress, Load, and Vibration Data at an Advance Ratio of 0.70 With the Lateral Displacement Control (B'_{1s}) Set at 0 Degrees.

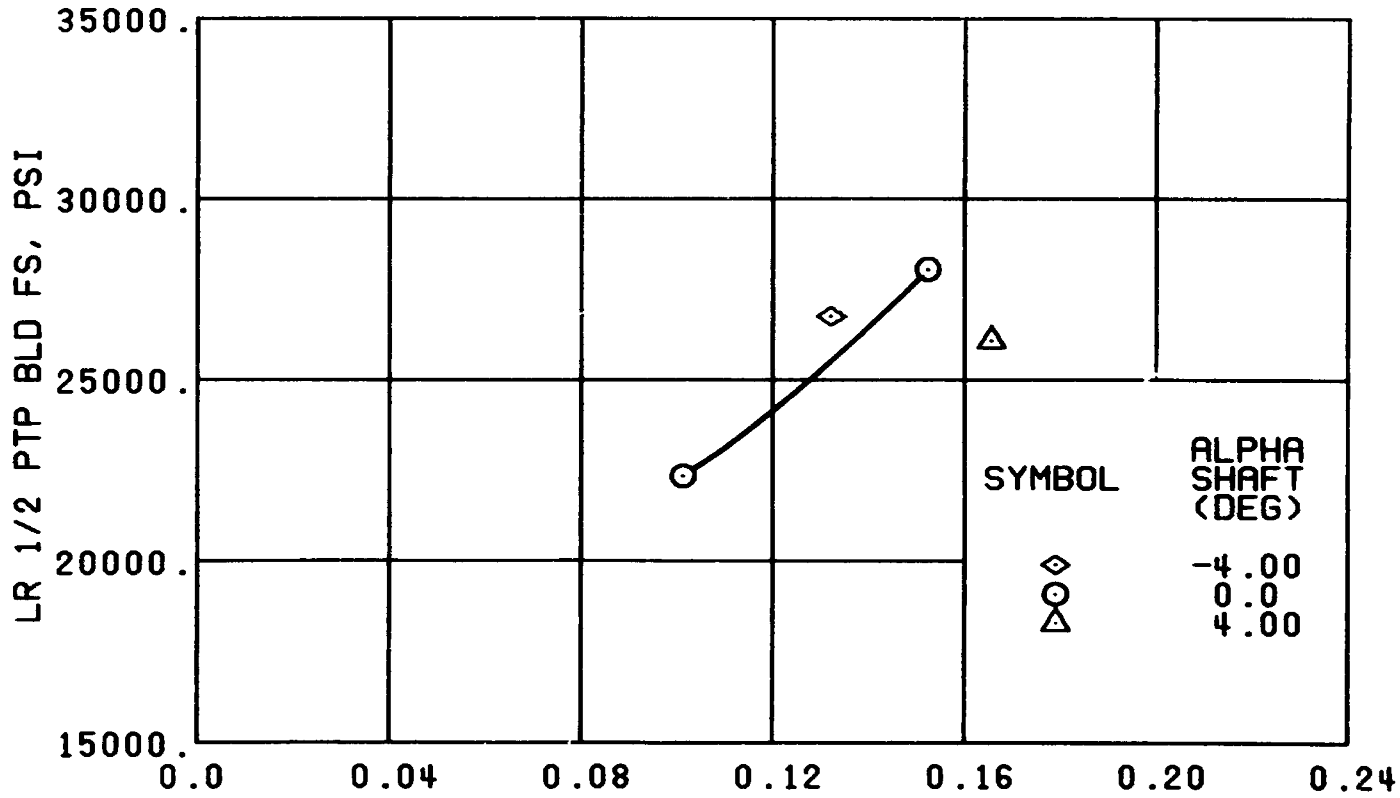

(b) GAGE 1 R84

Figure 54. Continued.
$\mu = 0.70 \quad B'_{1s} = 0$ Deg

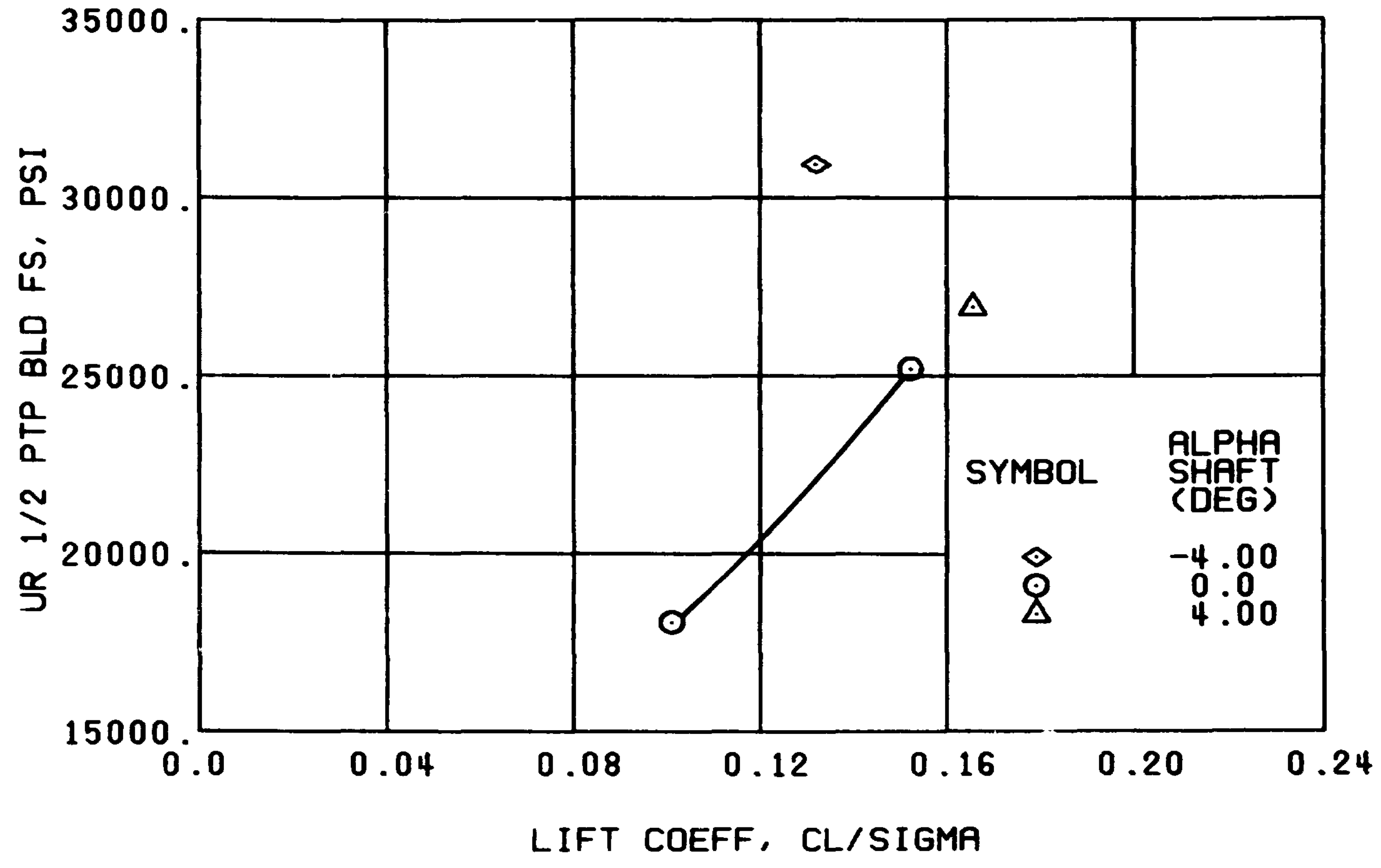

(c) GAGE 52 R108

Figure 54. Continued.
μ = 0.70 B_{1s}' = 0 Deg

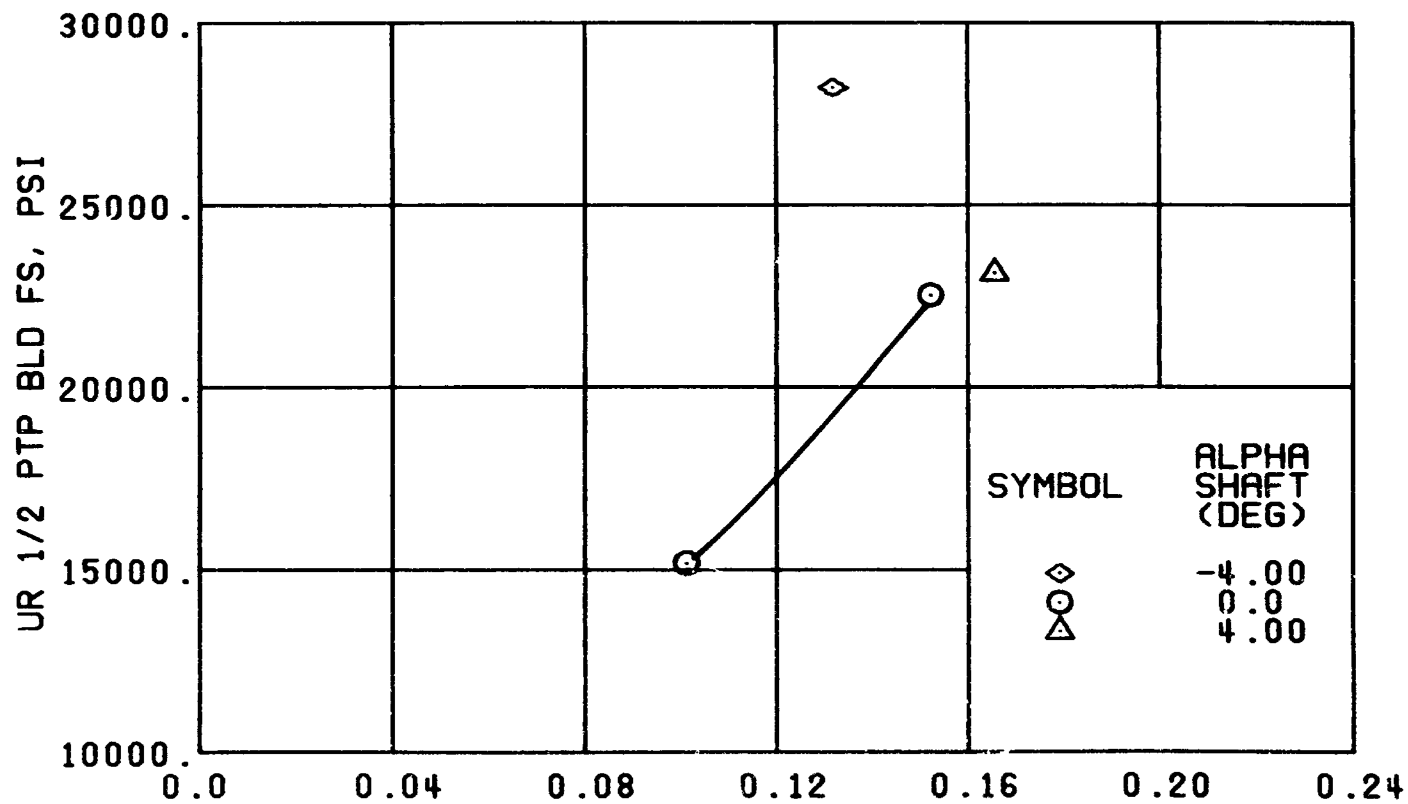

(d) GAGE 53 R132

Figure 54. Continued.
$\mu = 0.70$ $B'_{1s} = 0$ Deg

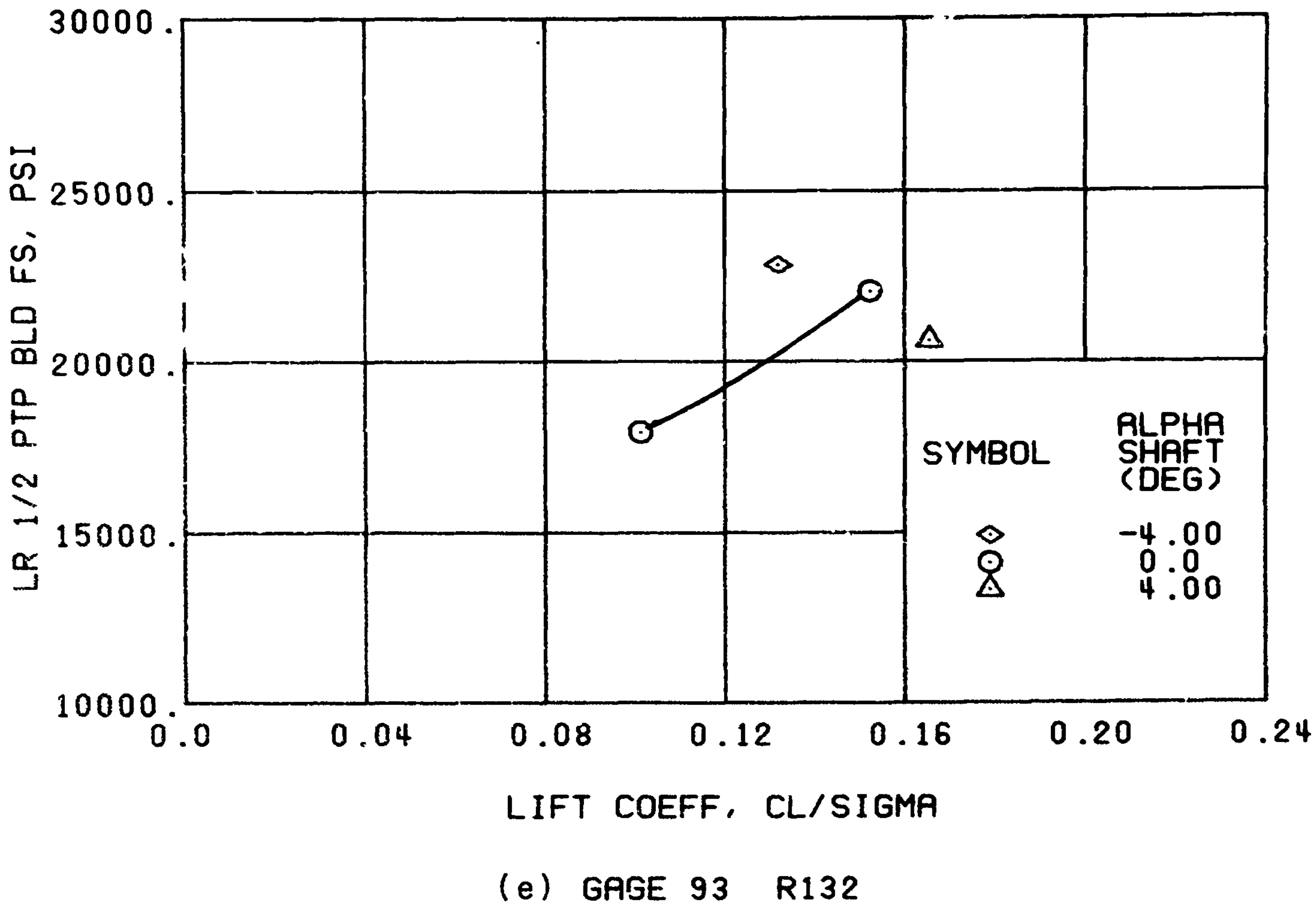

Figure 54. Continued.
$\mu = 0.70$ $B'_{1s} = 0$ Deg

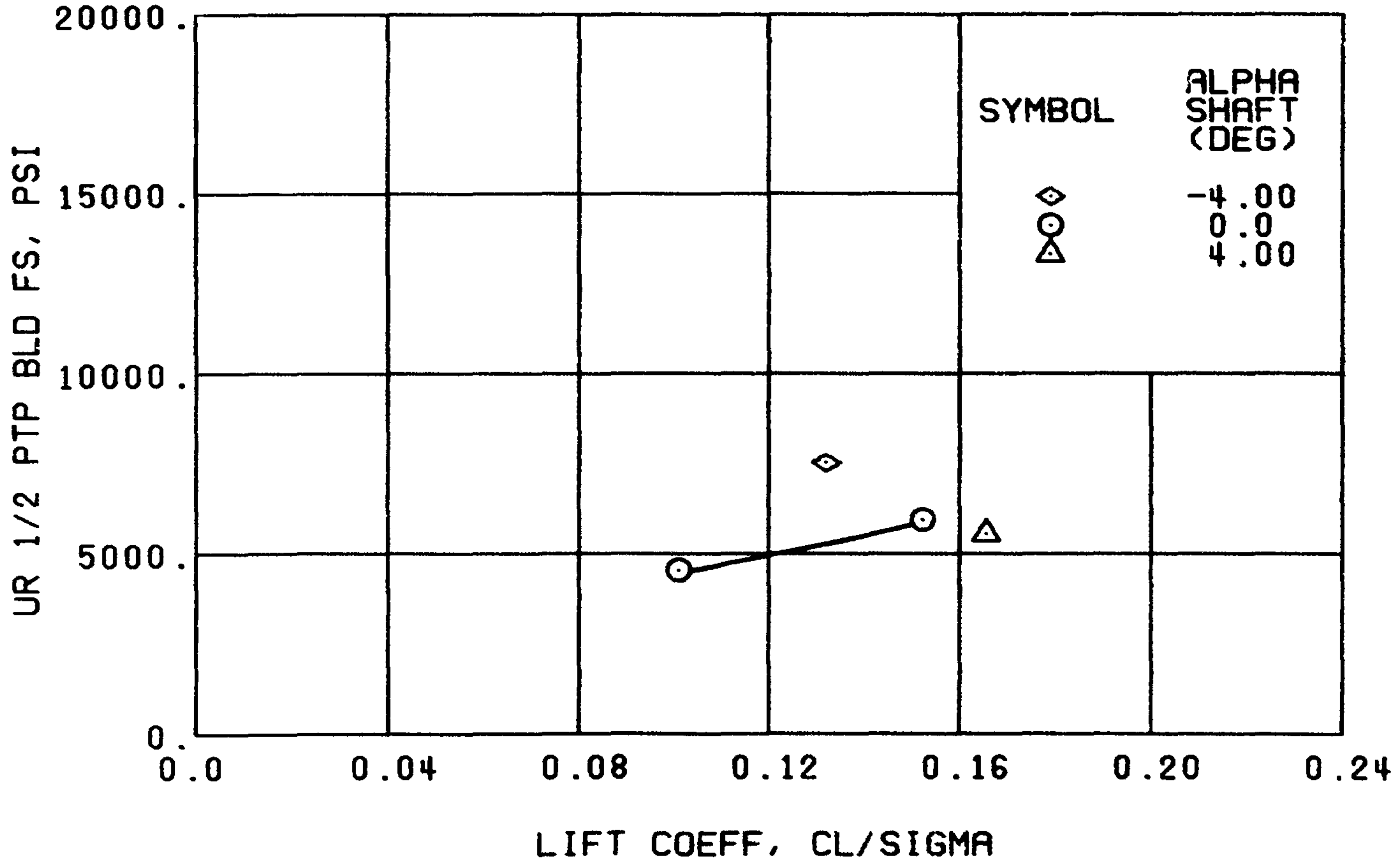

(f) GAGE 55 R204

Figure 54. Continued.
μ = 0.70 B'_{1s} = 0 Deg

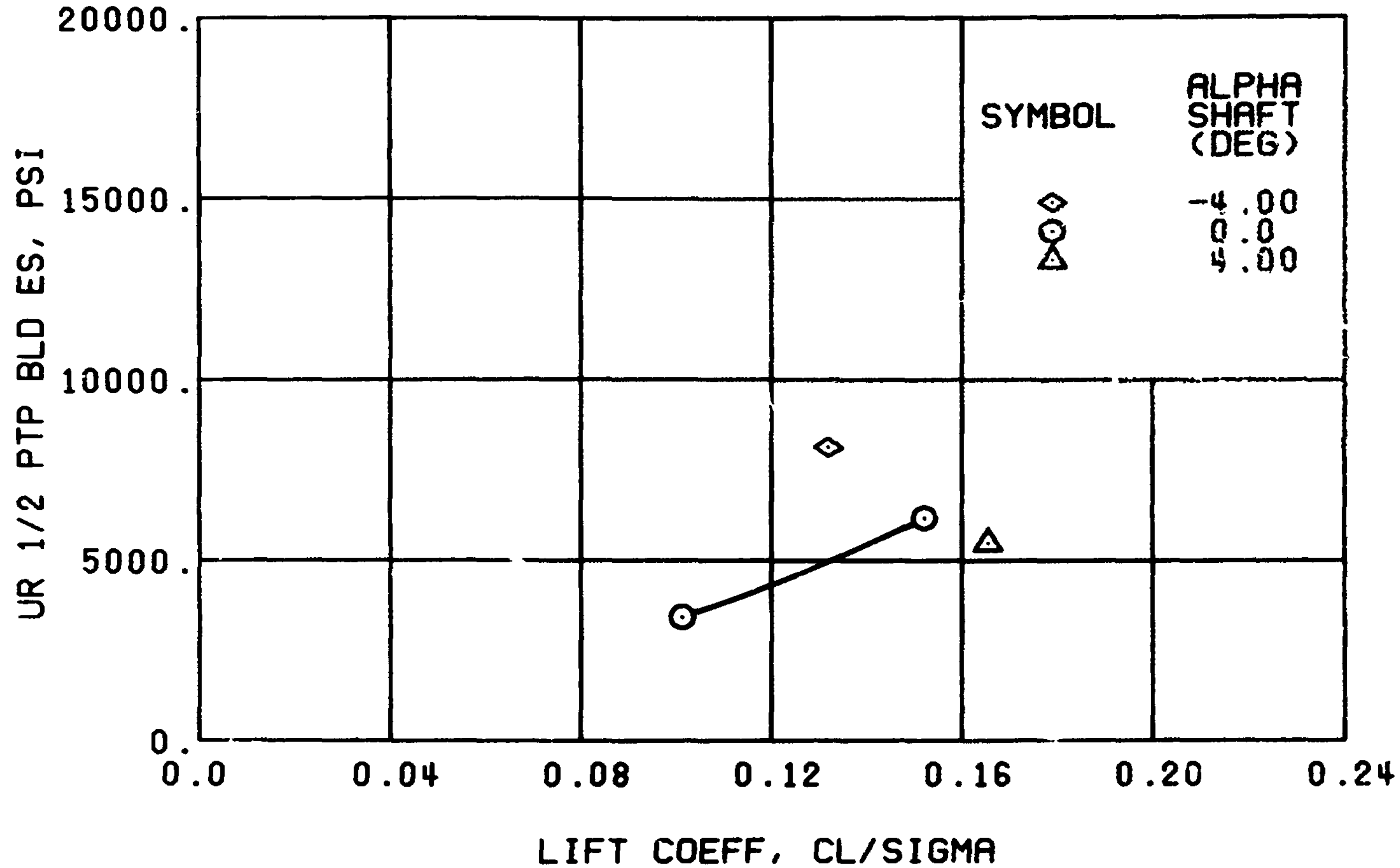

(h) GAGE 40 R84

Figure 54. Continued.
μ = 0.70 B'_{1s} = 0 Deg

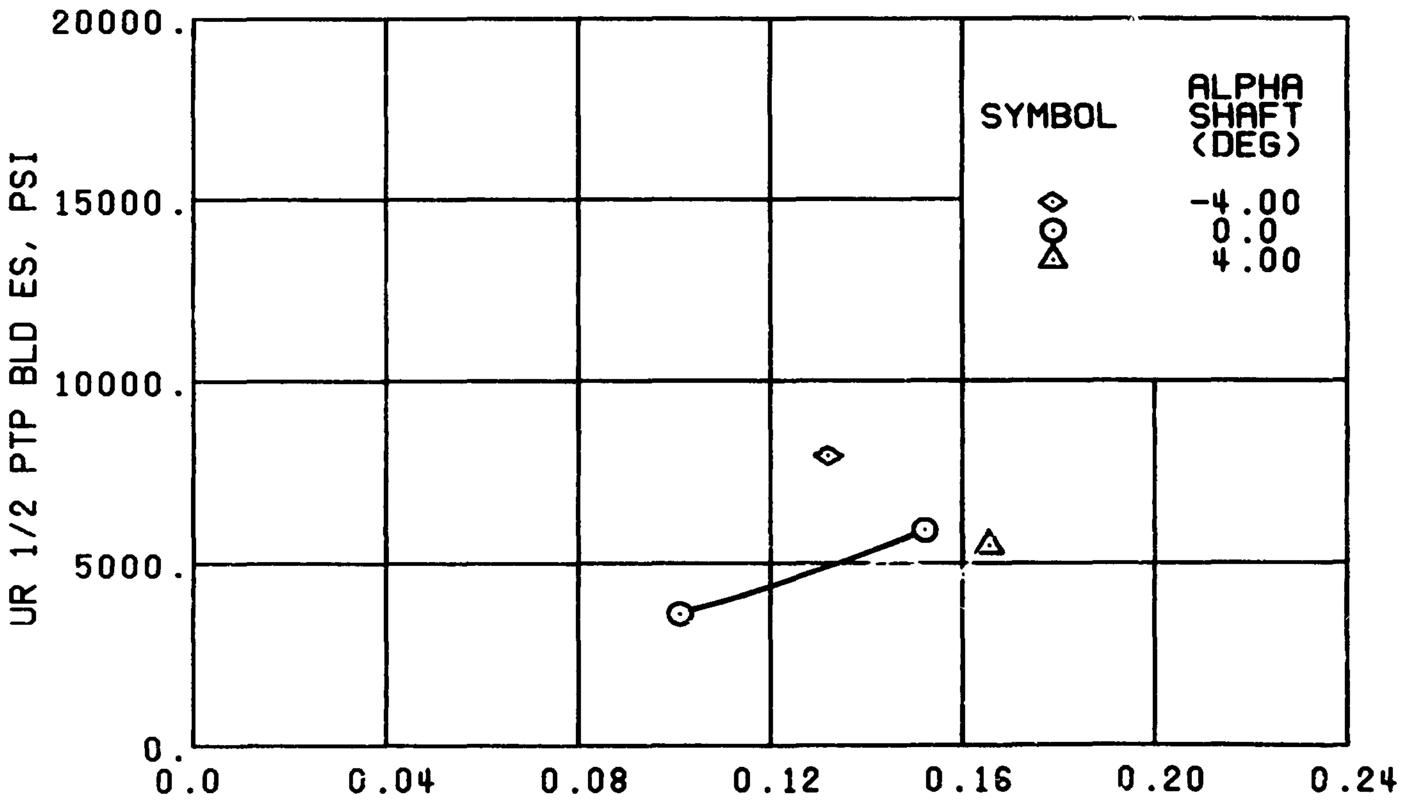

(j) GAGE 42 R132

Figure 54. Continued.
$\mu = 0.70 \quad B_{1s}' = 0 \text{ Deg}$

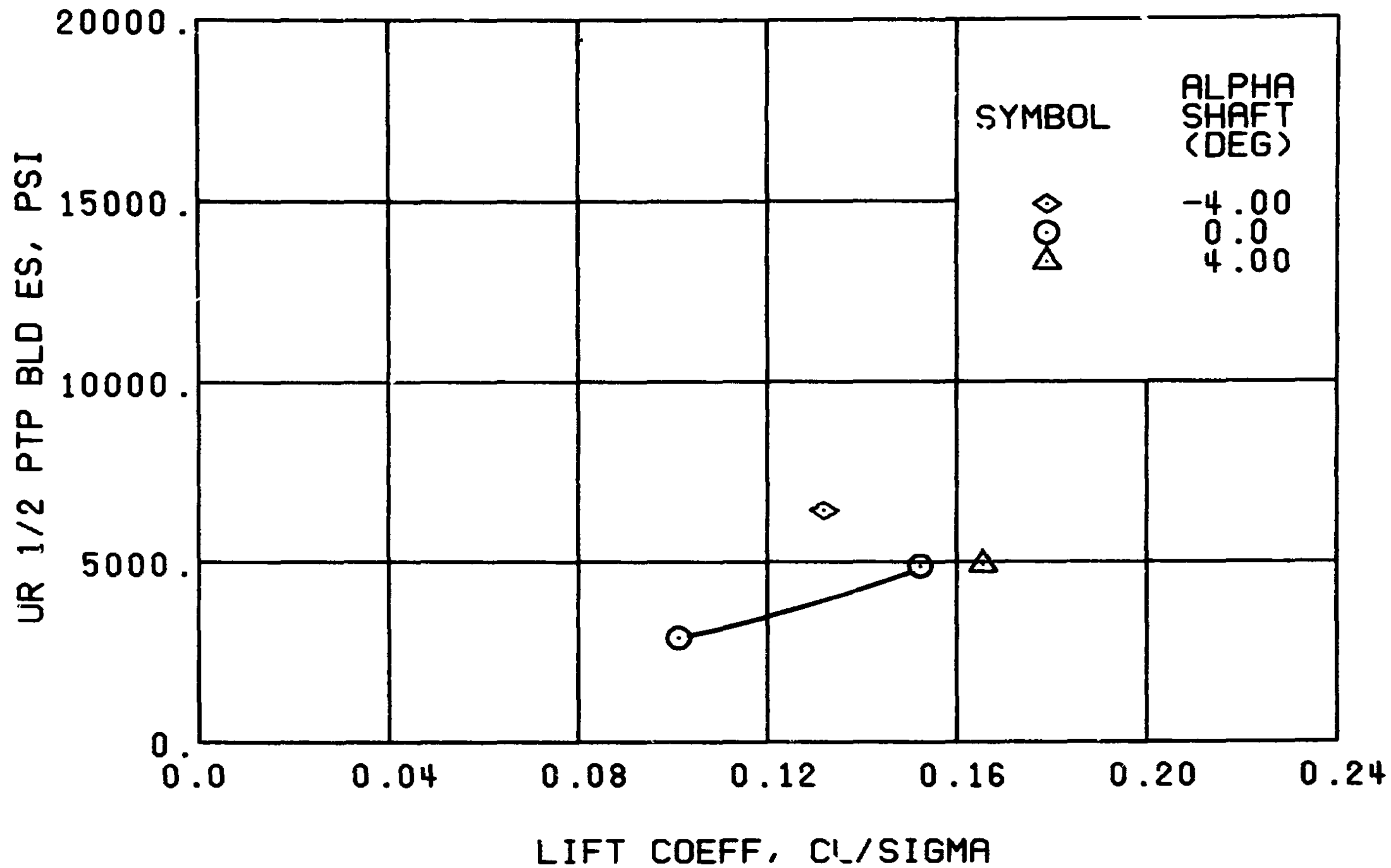

(k) GAGE 43 R168

Figure 54. Continued.
$\mu = 0.70 \quad B'_{1s} = 0$ Deg

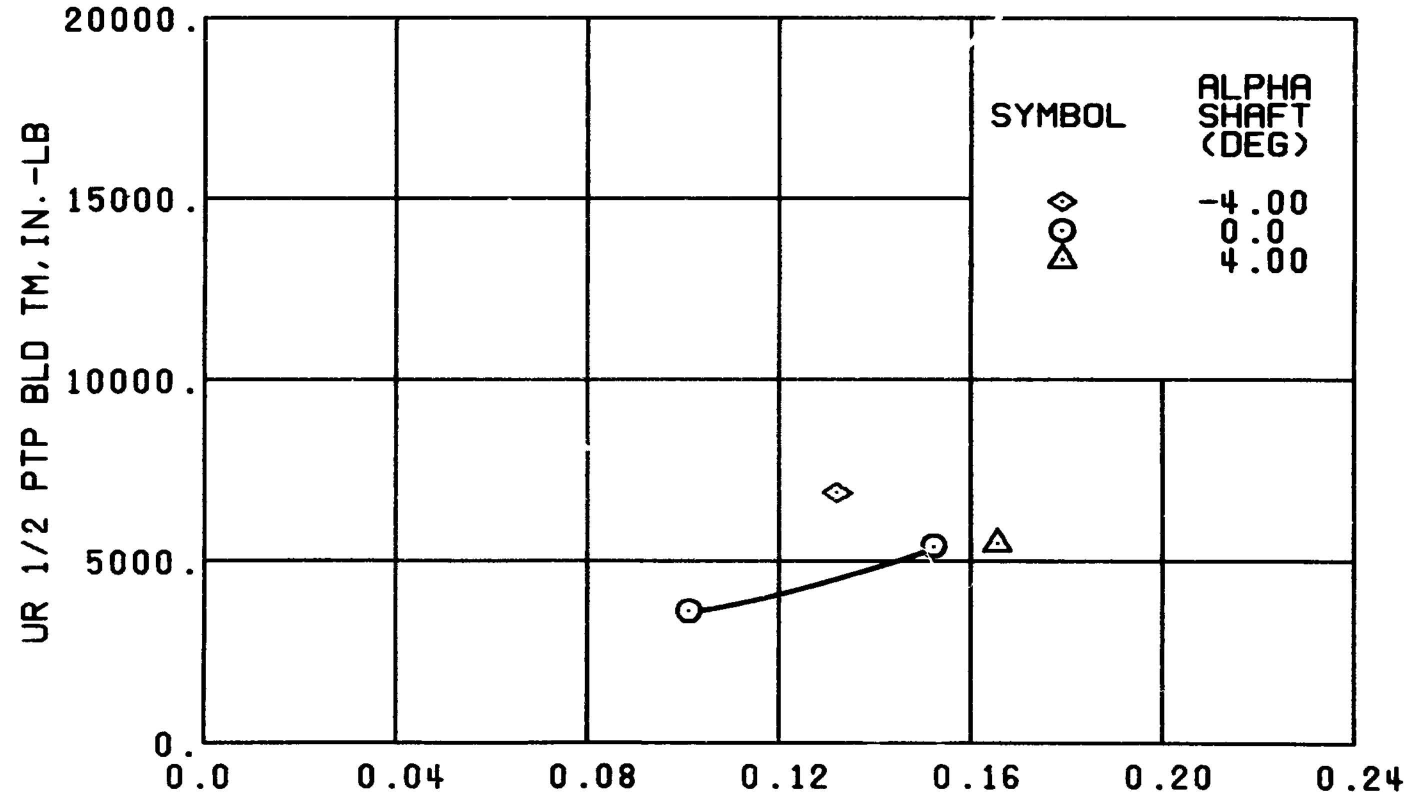

(m) GAGE 46 R130

Figure 54. Continued.
$\mu = 0.70$ $B'_{1s} = 0$ Deg

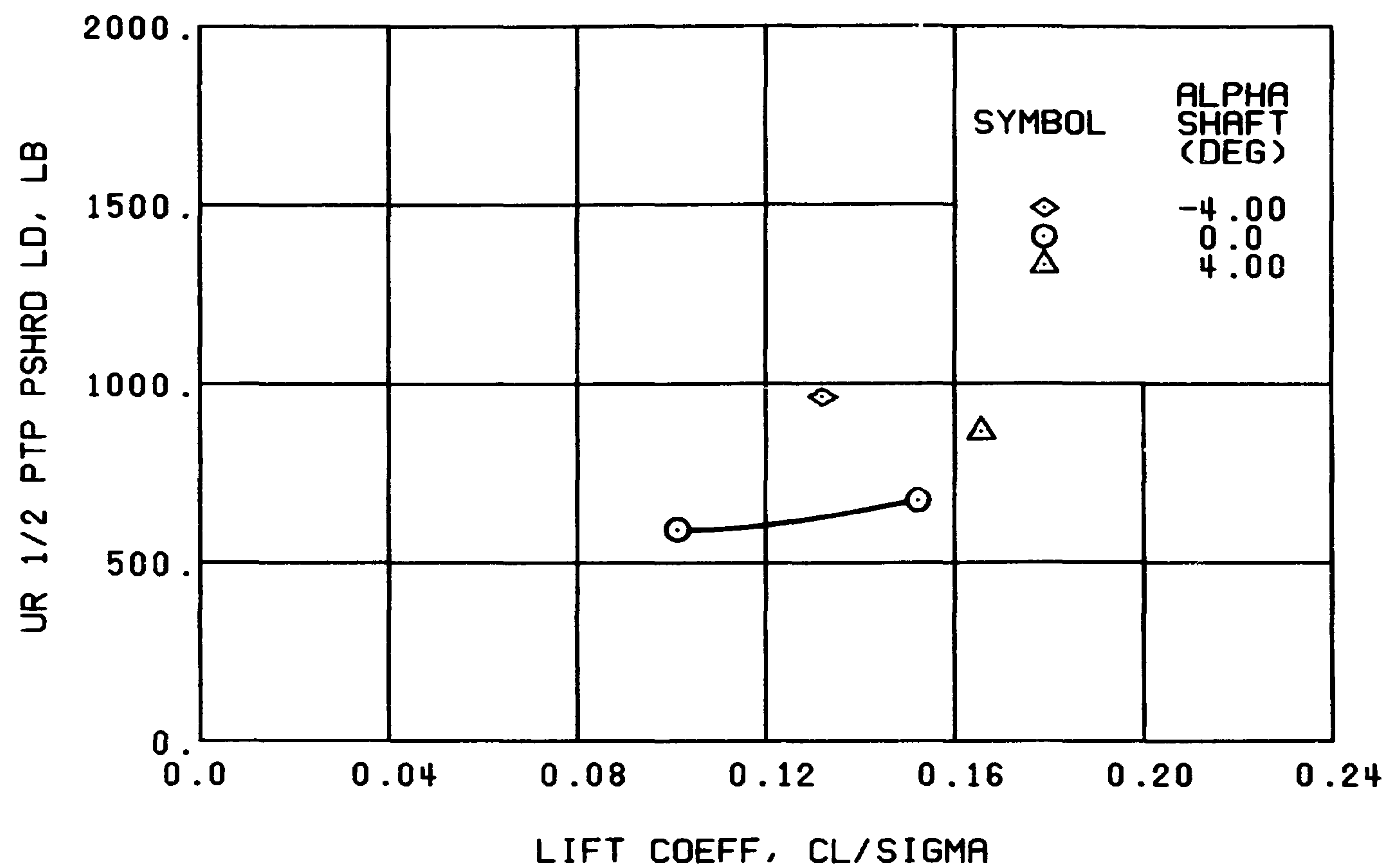

(n) GAGE 37

Figure 54. Continued.
$\mu = 0.70 \quad B'_{1s} = 0$ Deg

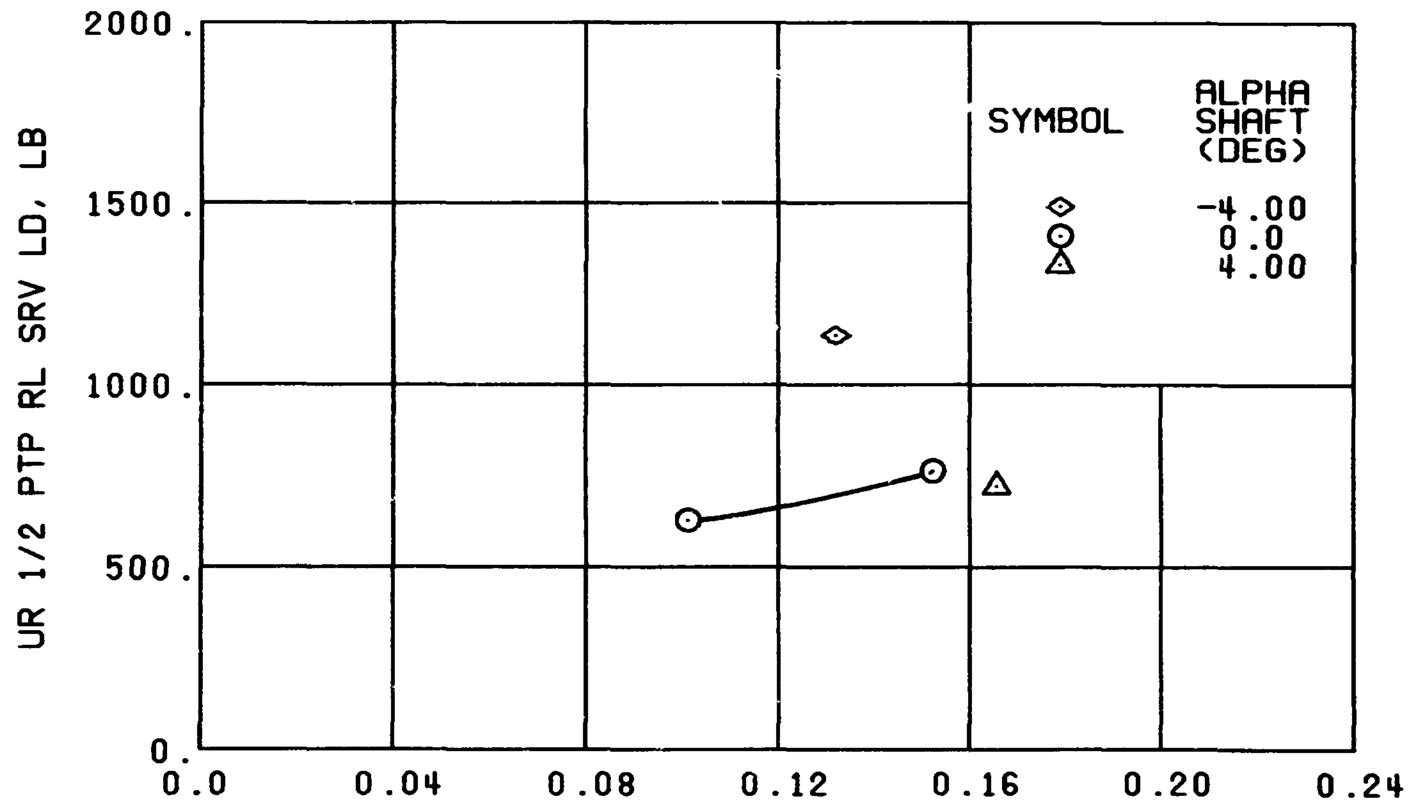

(p) GAGE 22

Figure 54. Continued.
μ = 0.70 B'_{1s} = 0 Deg

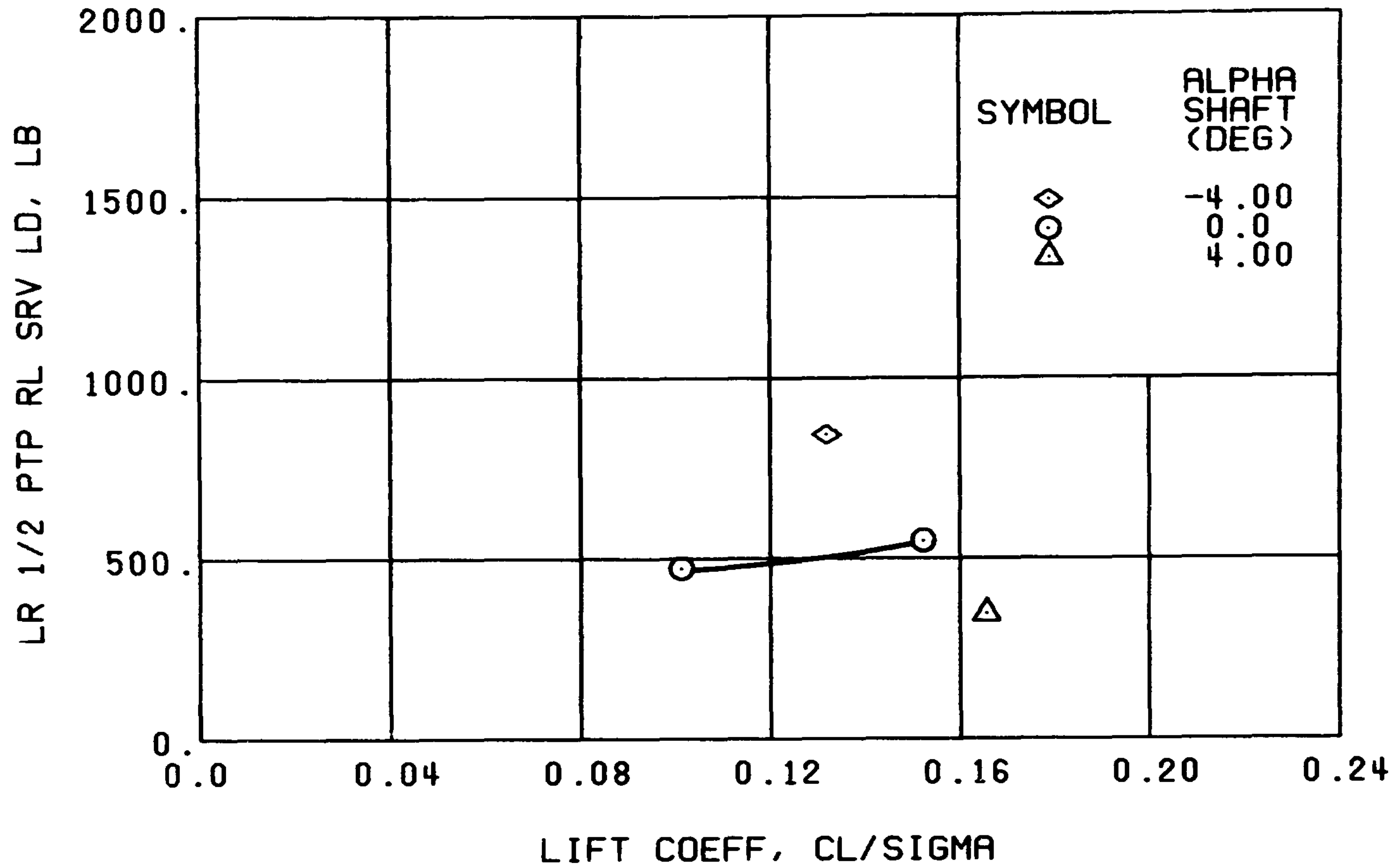

(q) GAGE 25

Figure 54. Continued.
$\mu = 0.70 \quad B'_{1s} = 0$ Deg

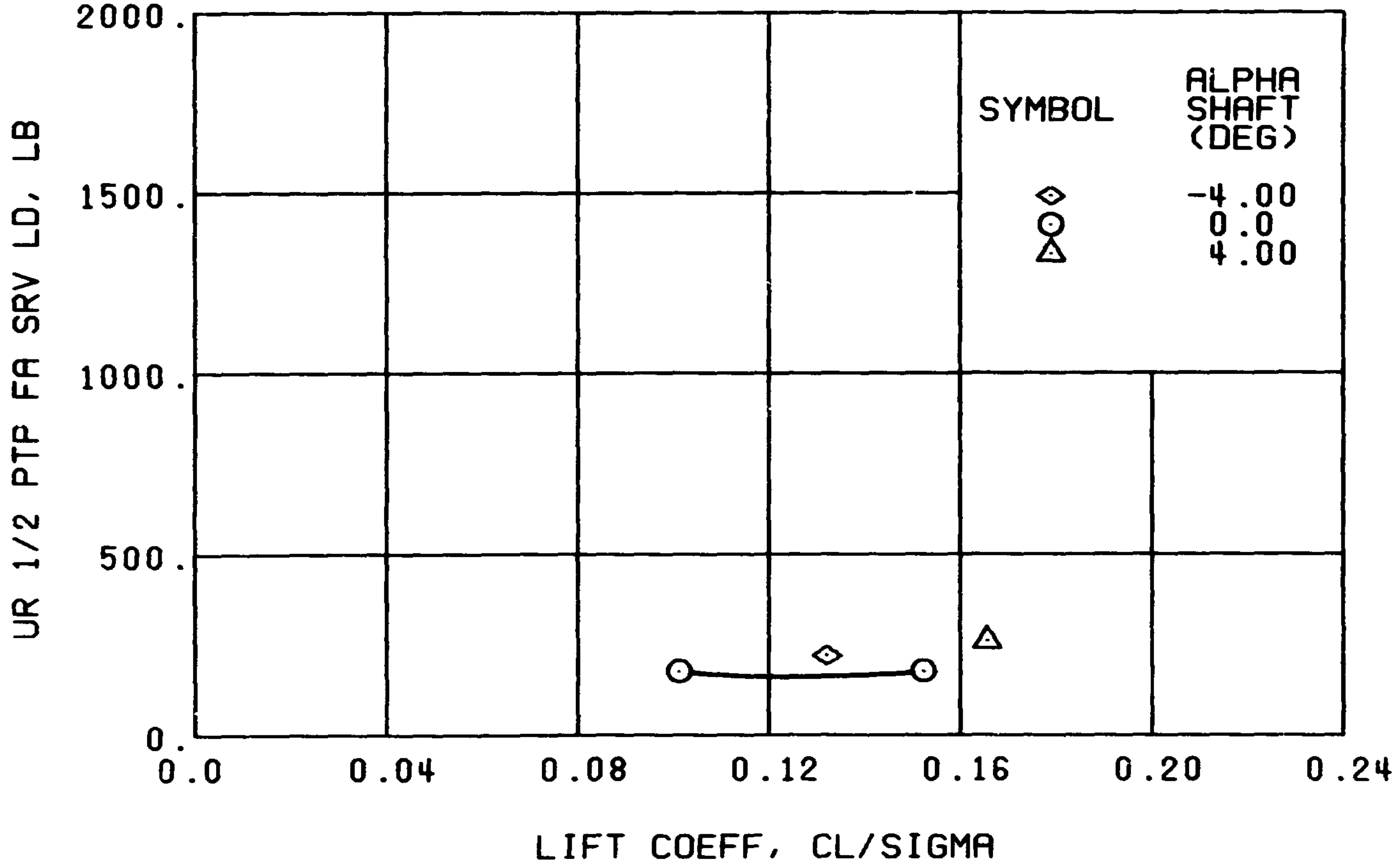

(r) GAGE 24

Figure 54. Continued.
$\mu = 0.70 \quad B'_{1s} = 0$ Deg

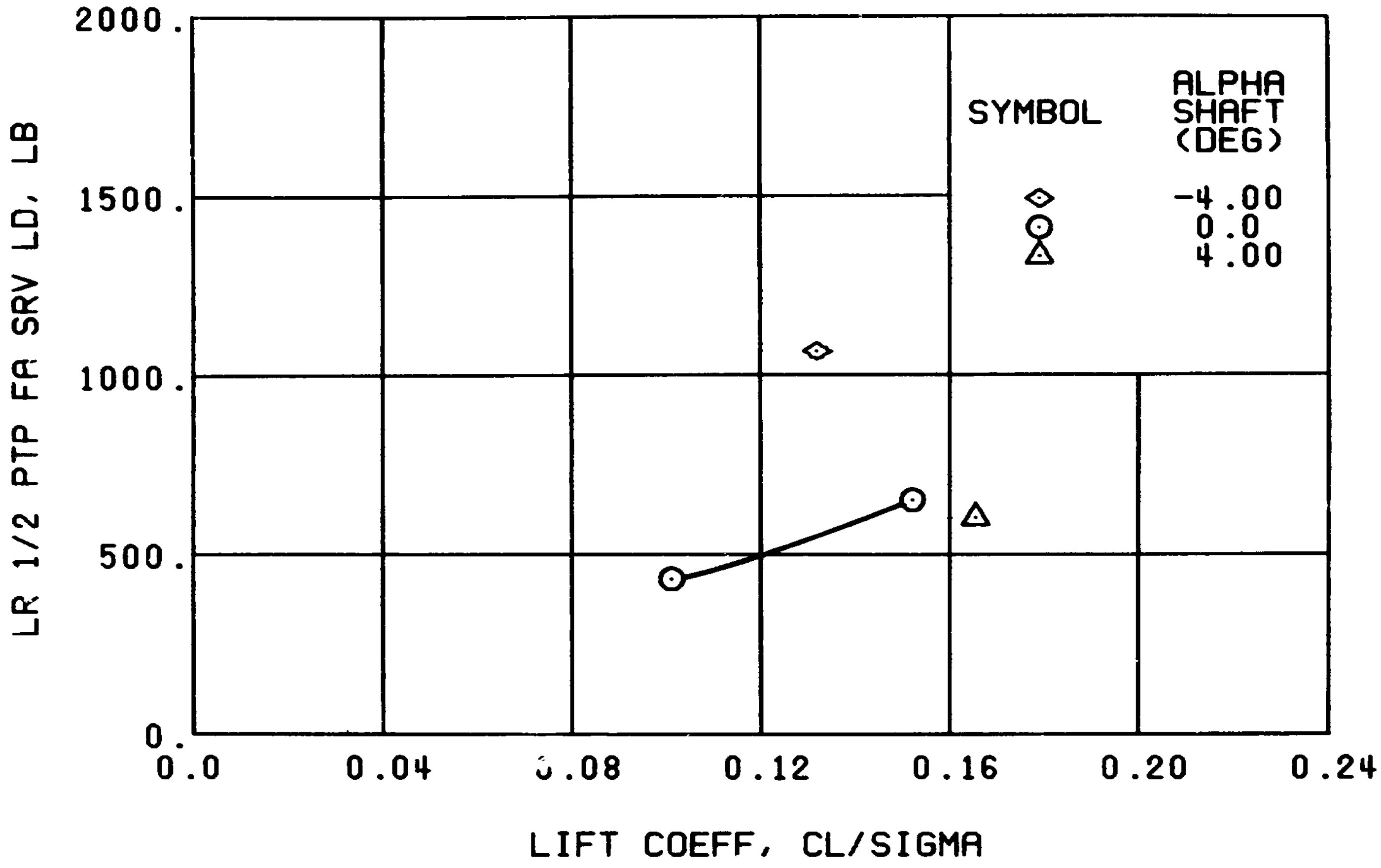

(s) GAGE 27

Figure 54. Continued.
μ = 0.70 B'_{1s} = 0 Deg

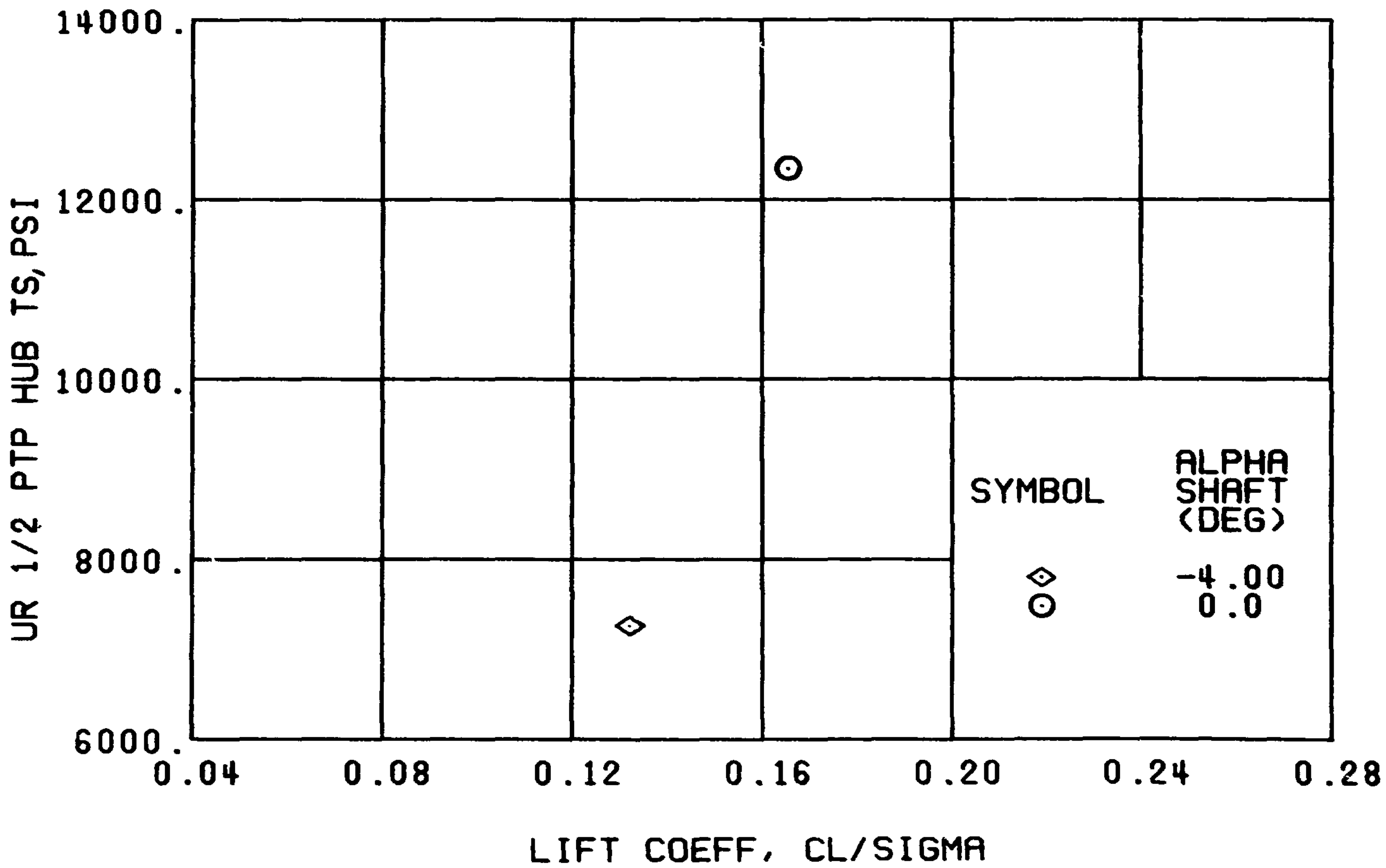

(t) GAGE 65

Figure 54. Continued.
μ = 0.70 B'_{1s} = 0 Deg

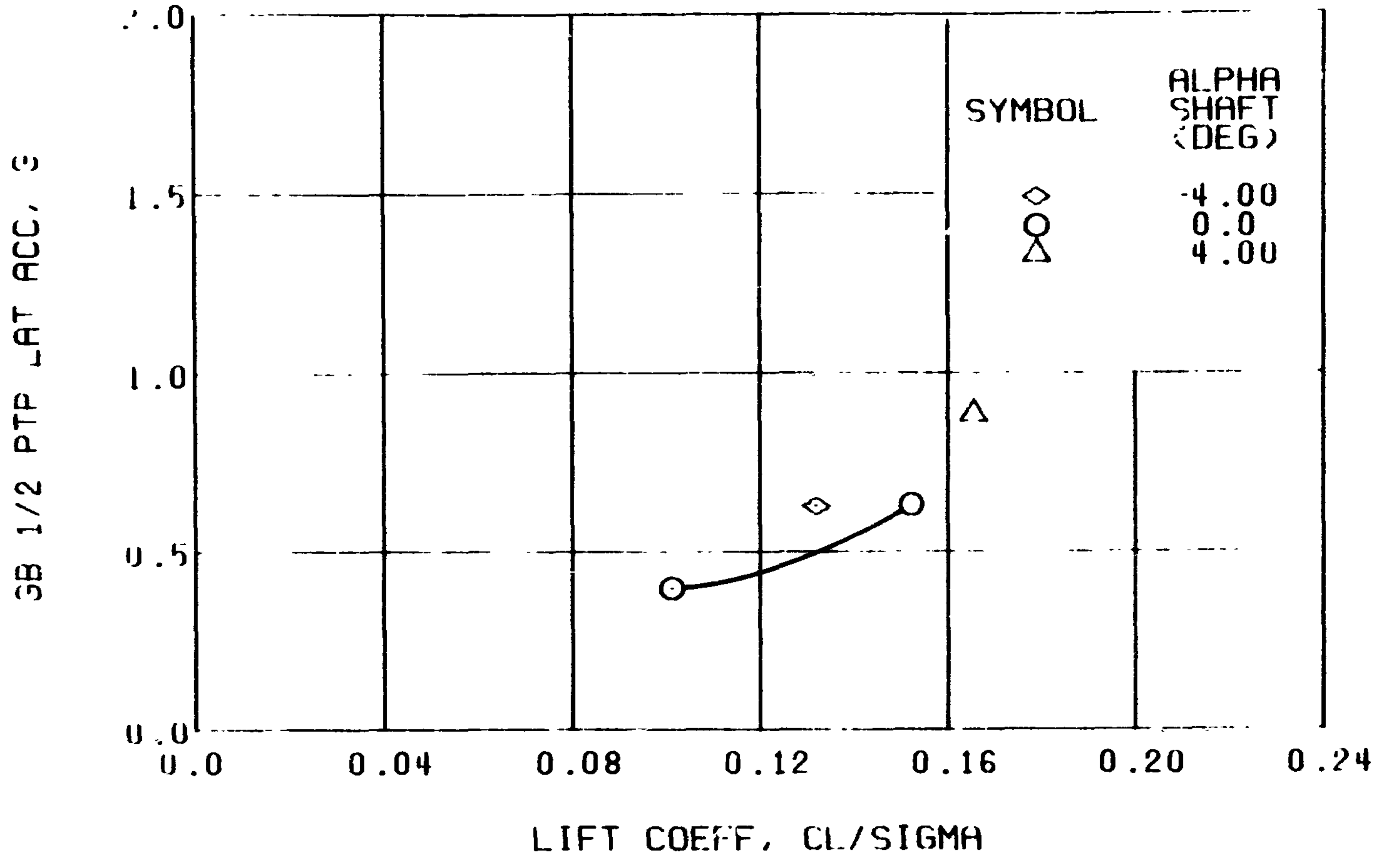

(u) GAGE 15 STA 76, BL 30

Figure 54. Continued.
$\mu = 0.70 \quad B'_{1s} = 0$ Deg

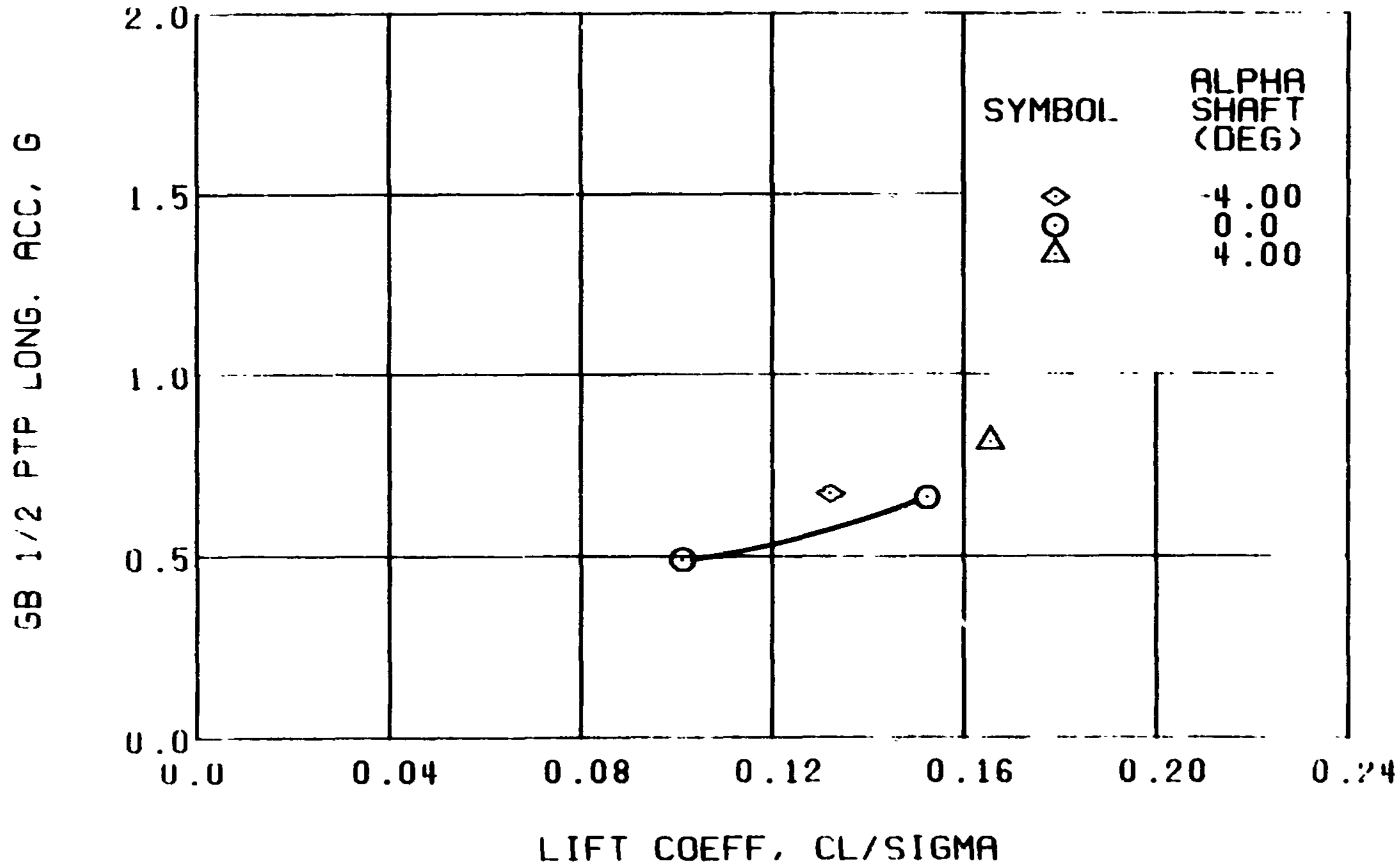

(v) GAGE 14 STA 61, BL 0

Figure 54. Continued.
$\mu = 0.70 \quad B'_{1s} = 0$ Deg

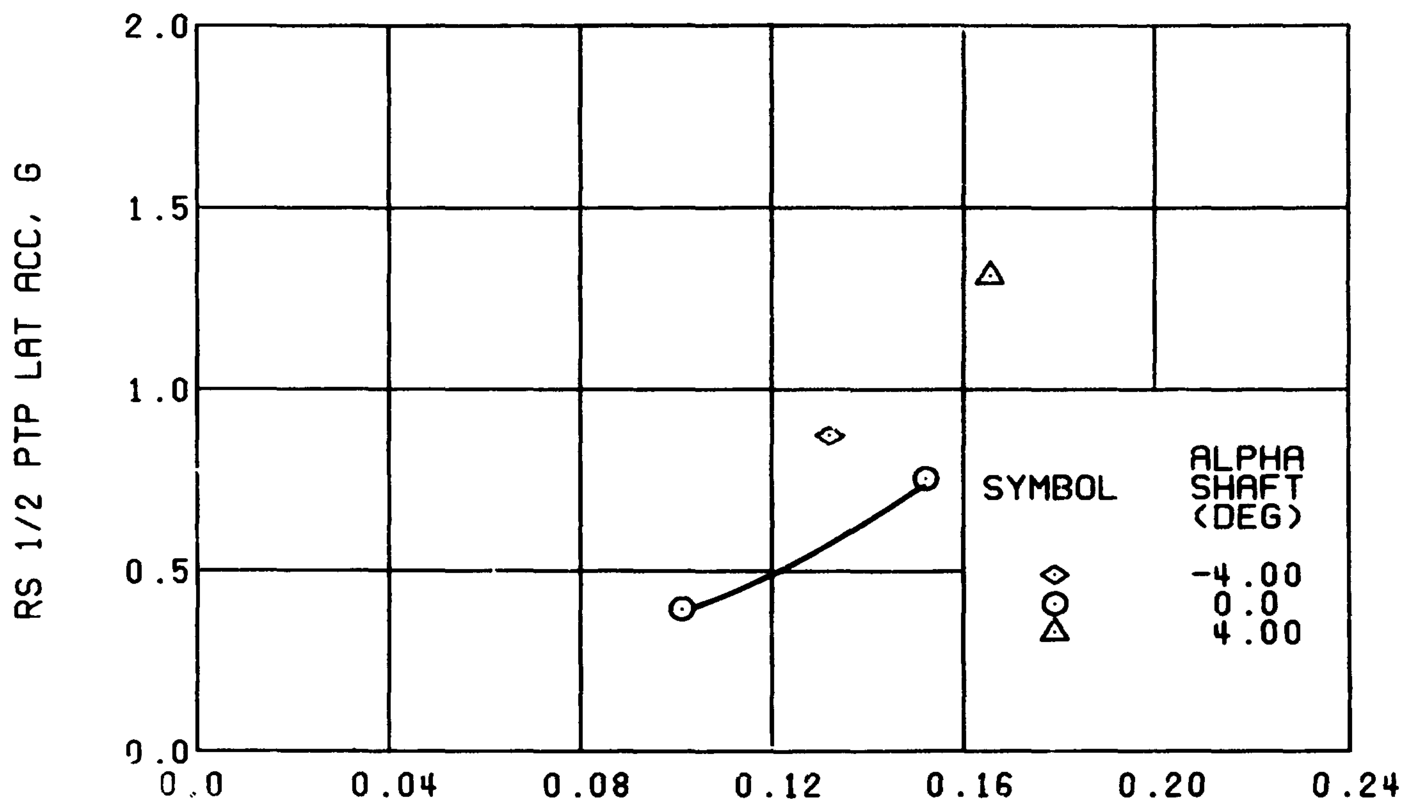

(w) GAGE 16 ROVER 3

Figure 54. Continued.
μ = 0.70 B'_{1s} = 0 Deg

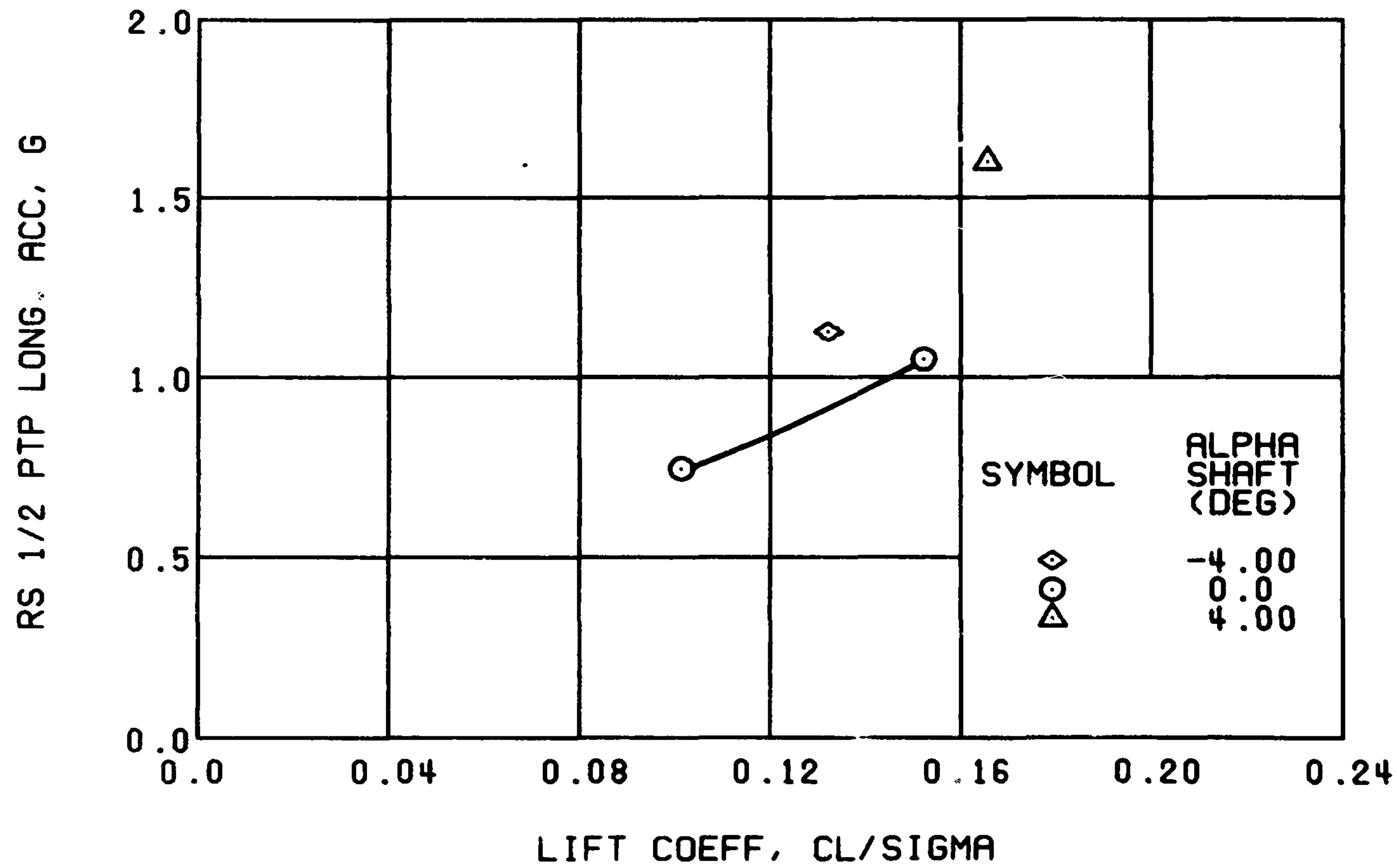

(x) GAGE 17 ROVER 4

Figure 54. Concluded.
$\mu = 0.70$ $B'_{1s} = 0$ Deg

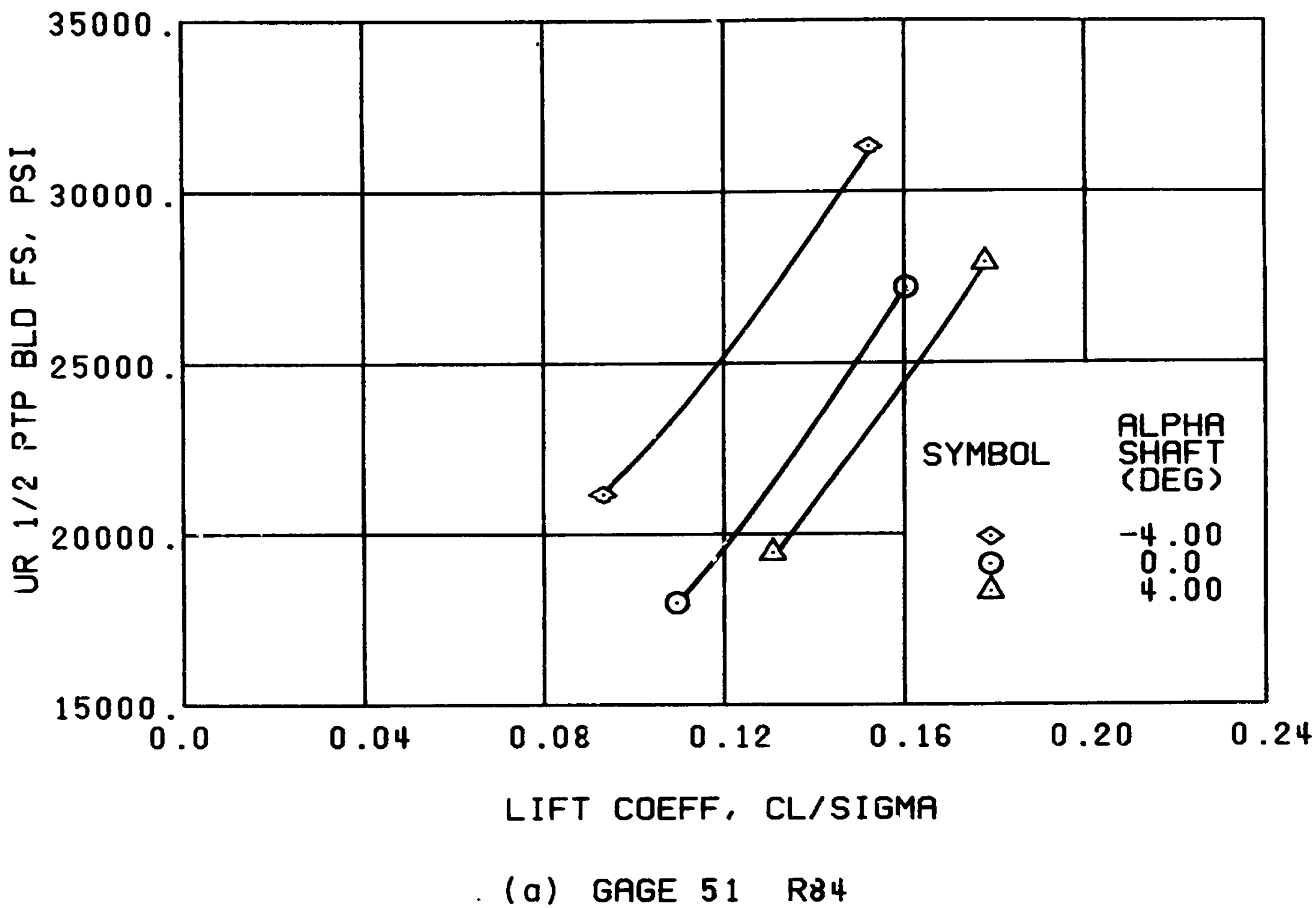

Figure 55. Stress, Load, and Vibration Data at an Advance Ratio of 0.70 With the Lateral Displacement Control (B'_{1s}) Set at 2 Degrees.

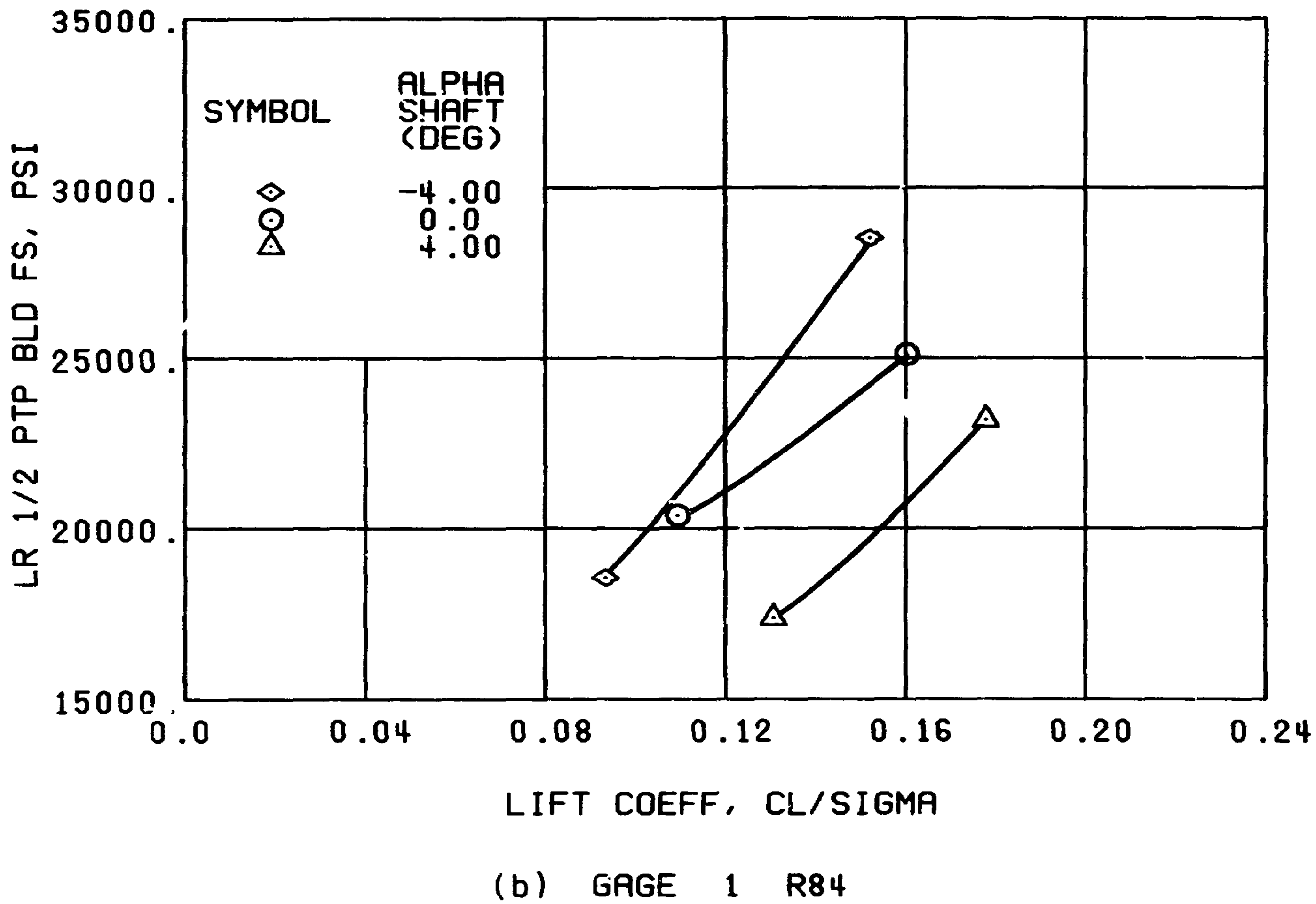

Figure 55. Continued.
$\mu = 0.70$ $B'_{1s} = 2$ Deg

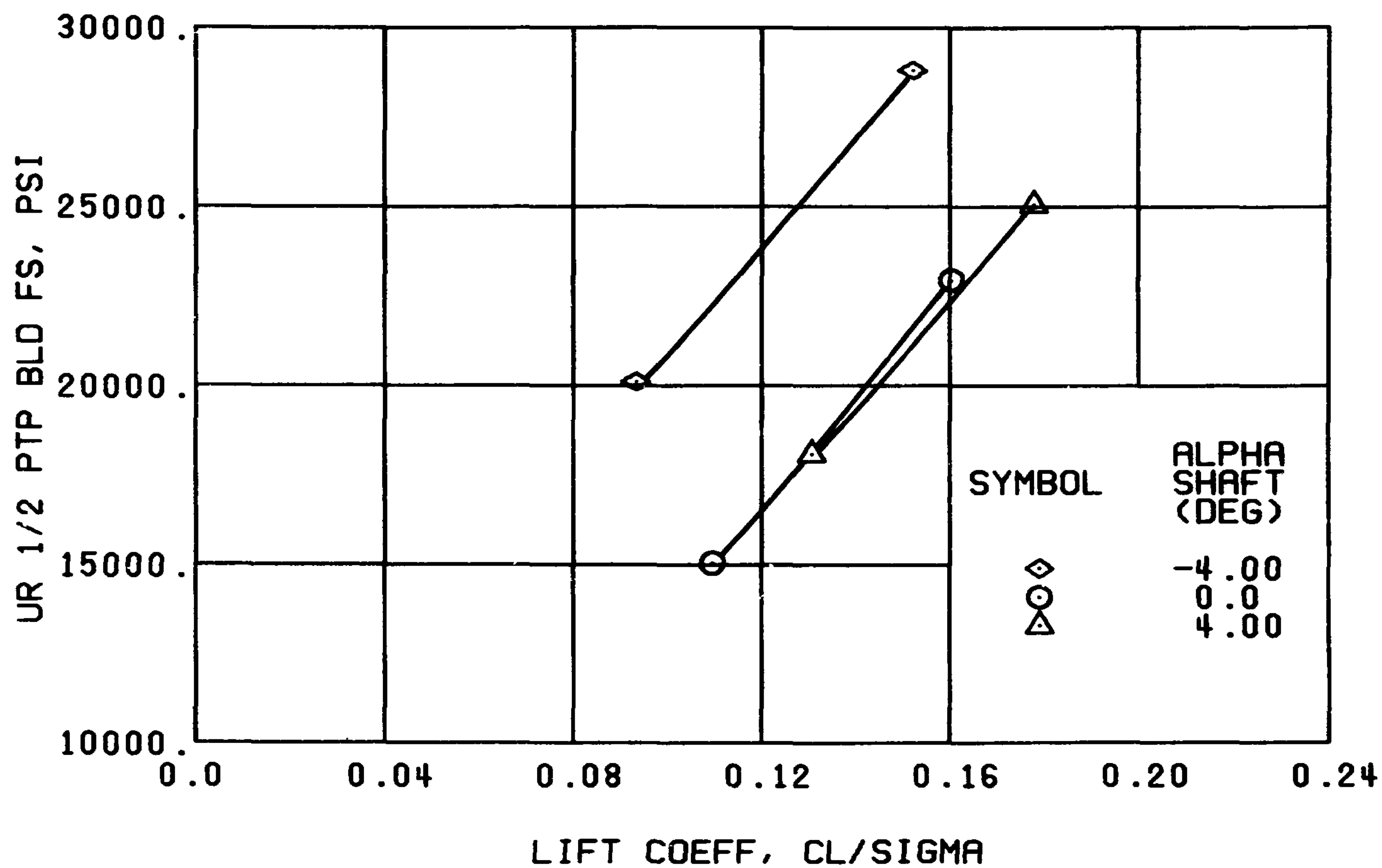

(c) GAGE 52 R108

Figure 55. Continued.
$\mu = 0.70 \quad B'_{1s} = 2$ Deg

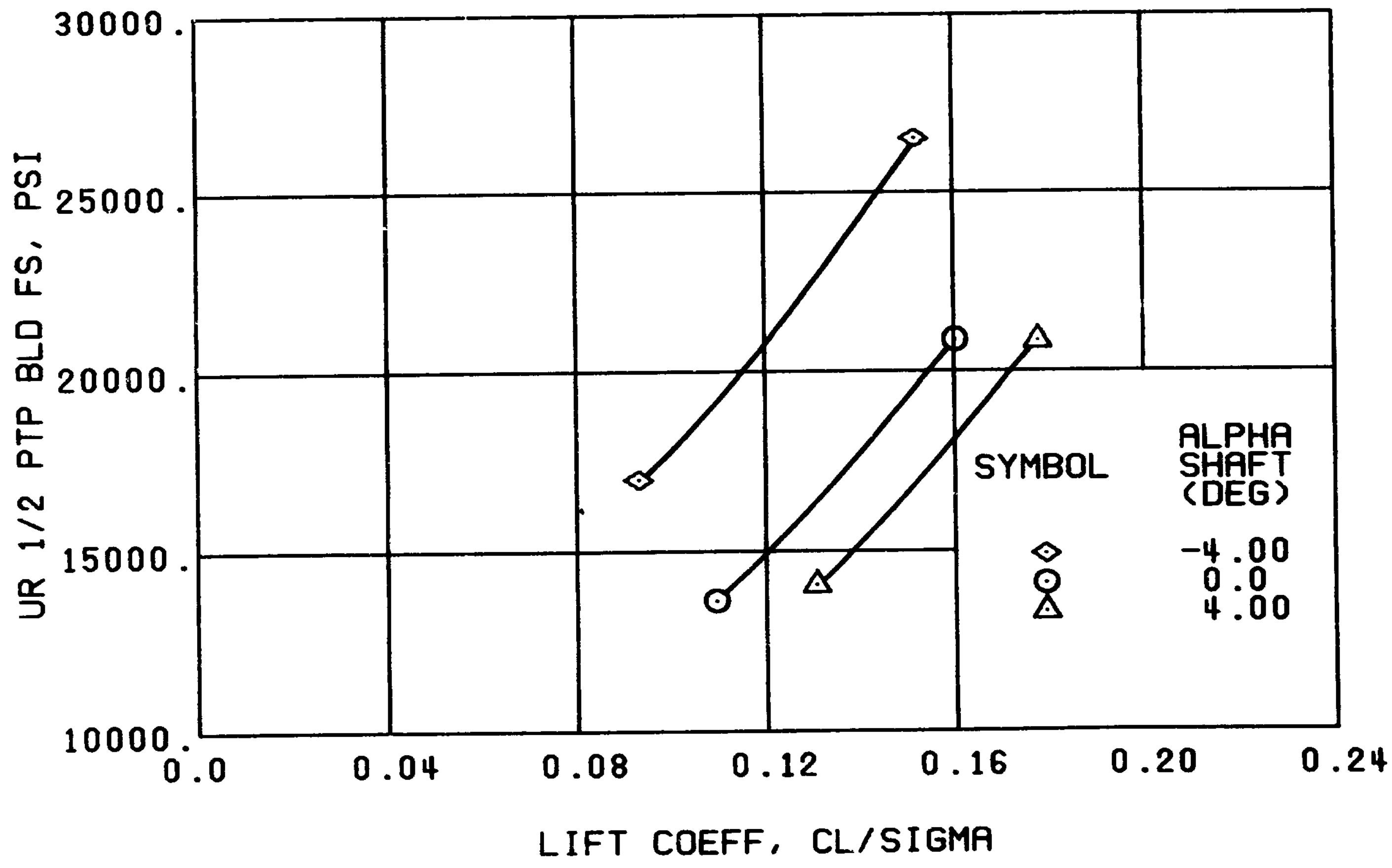

(d) GAGE 53 R132

Figure 55. Continued.
$\mu = 0.70 \quad B'_{1s} = 2$ Deg

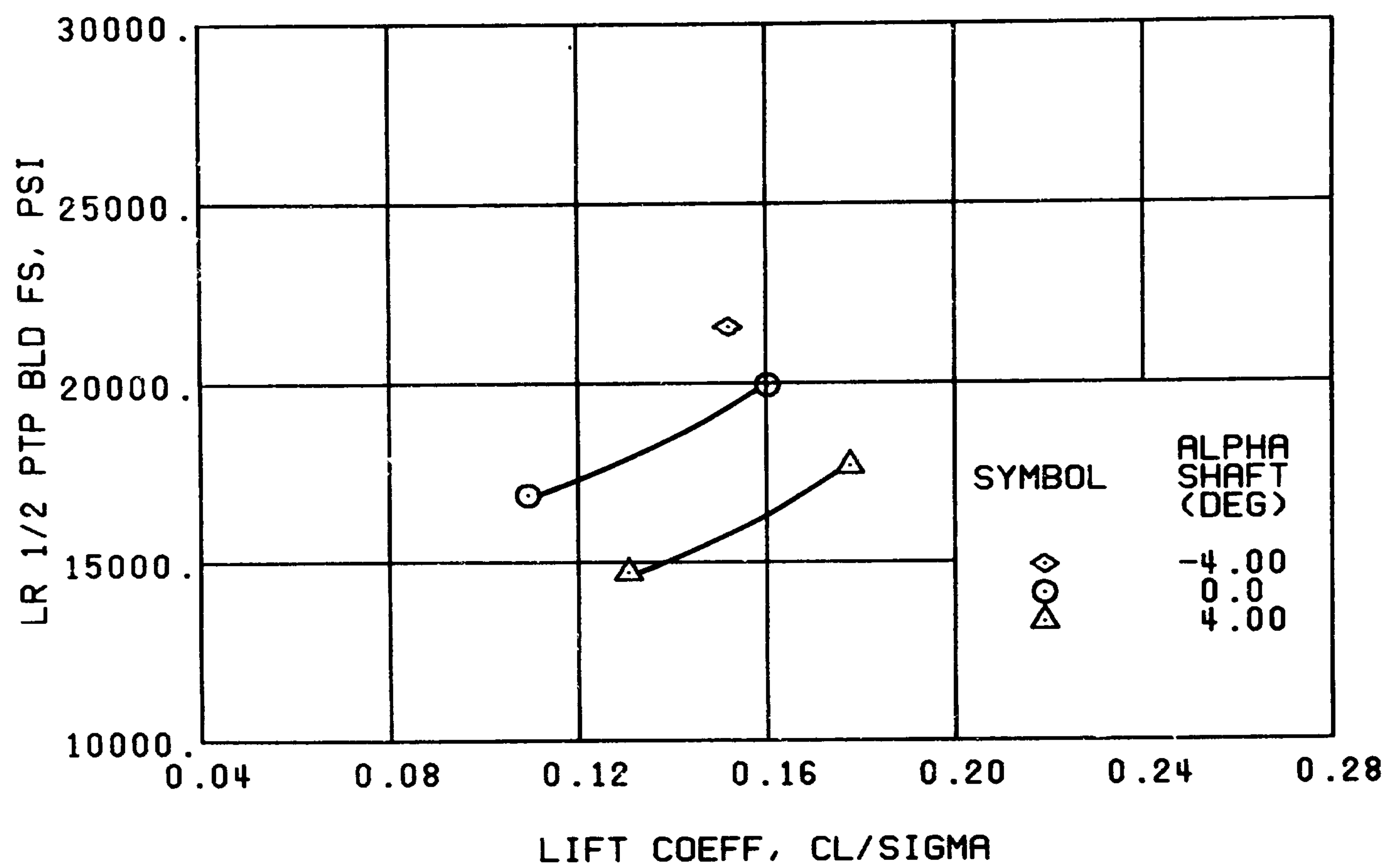

(e) GAGE 93 R132

Figure 55. Continued.
$\mu = 0.70$ $B'_{1s} = 2$ Deg

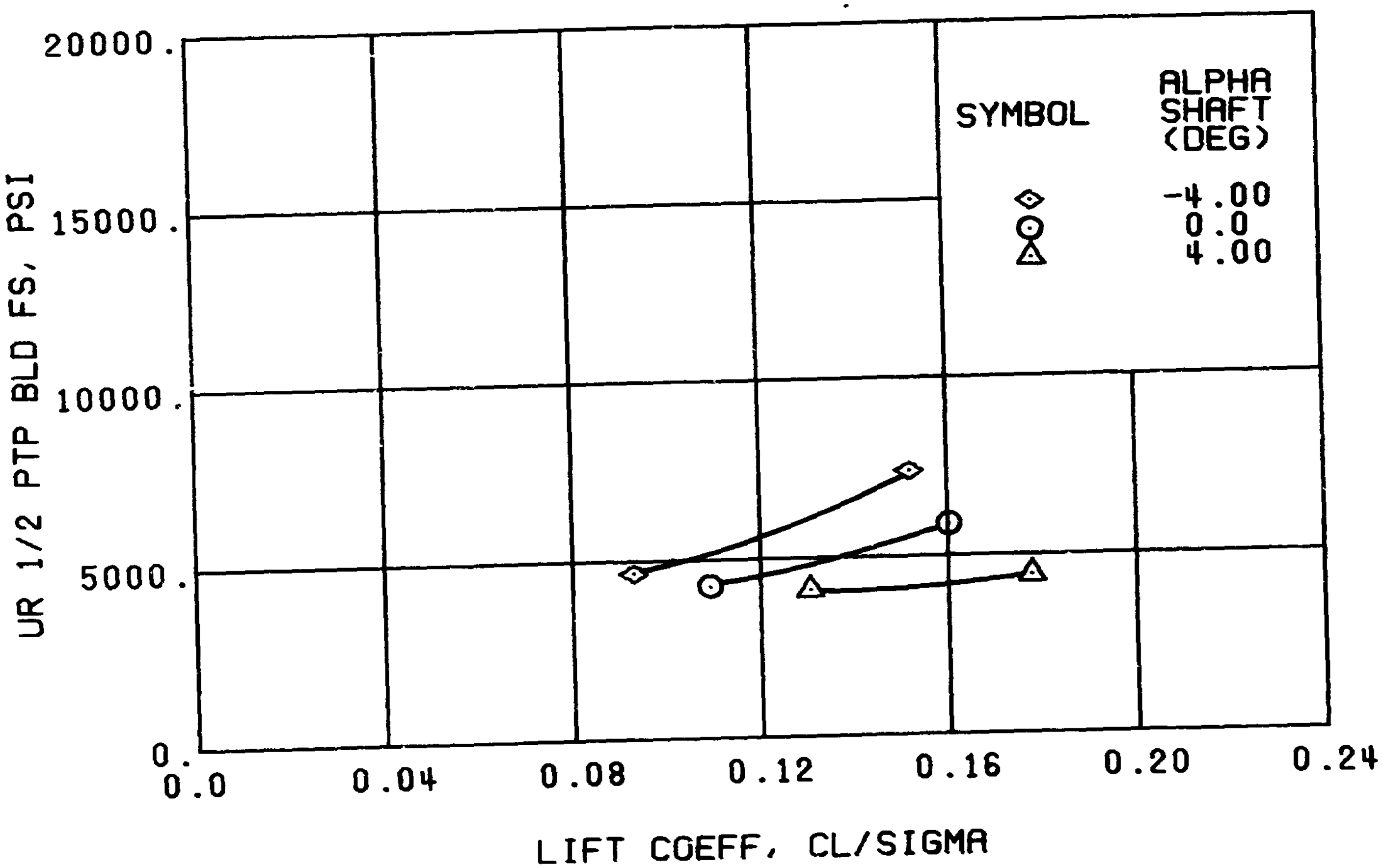

(f) GAGE 55 R204

Figure 55. Continued.
$\mu = 0.70$ $B'_{1s} = 2$ Deg

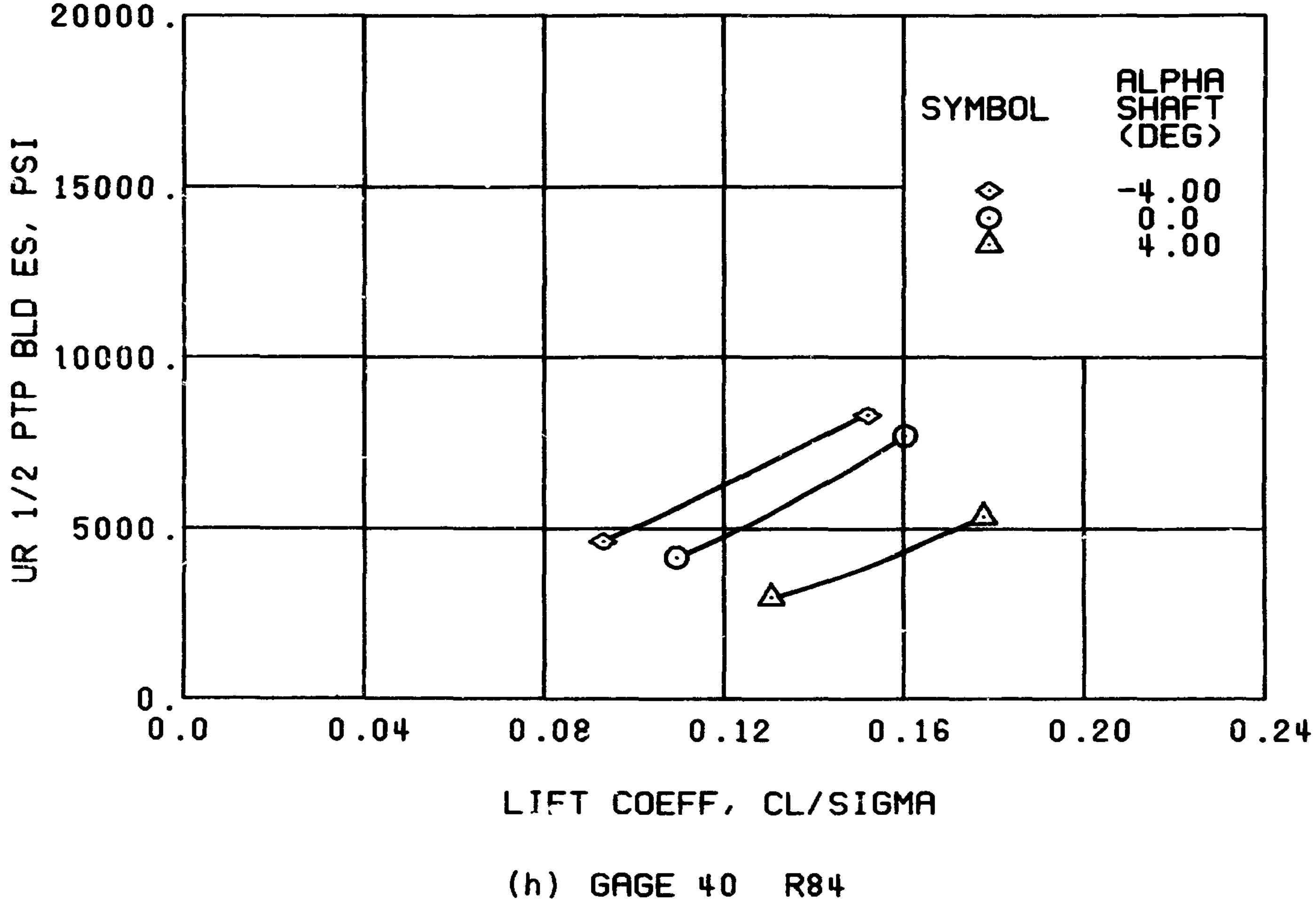

Figure 55. Continued.
$\mu = 0.70$ $B'_{1s} = 2$ Deg

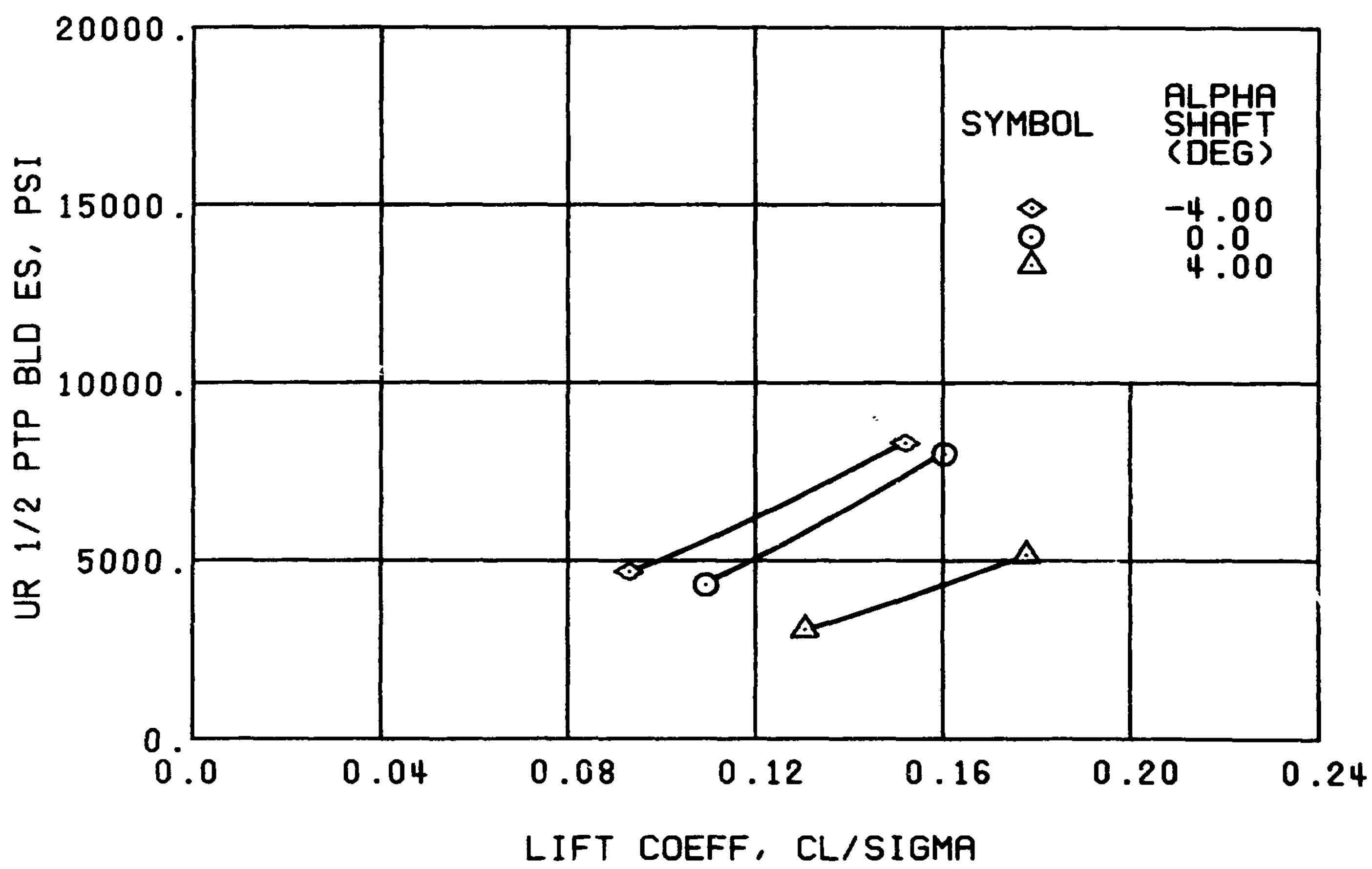

(j) GAGE 42 R132

Figure 55. Continued.
$\mu = 0.70 \quad B'_{1s} = 2$ Deg

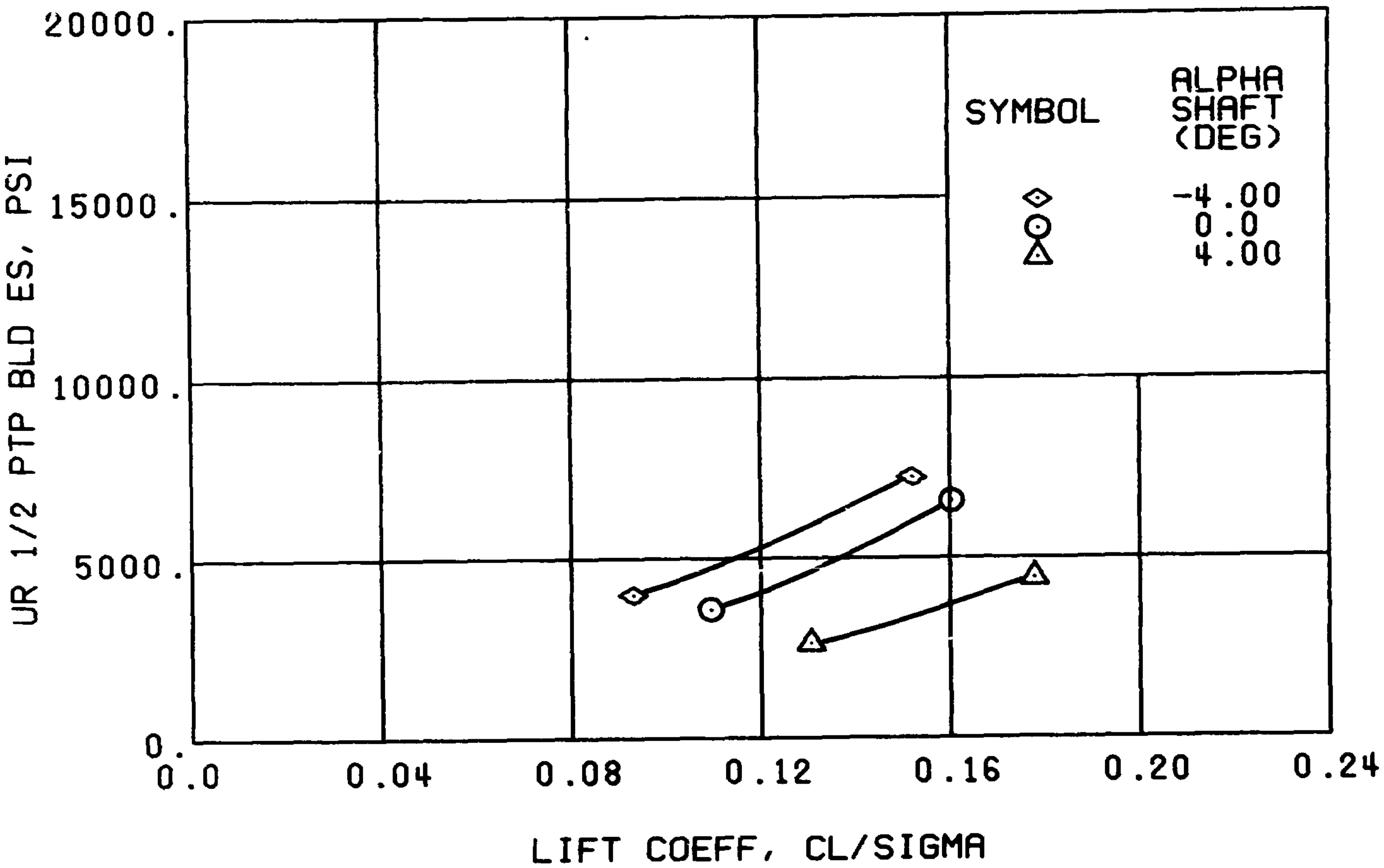

(k) GAGE 43 R168

Figure 55. Continued.
$\mu = 0.70$ $B'_{1s} = 2$ Deg

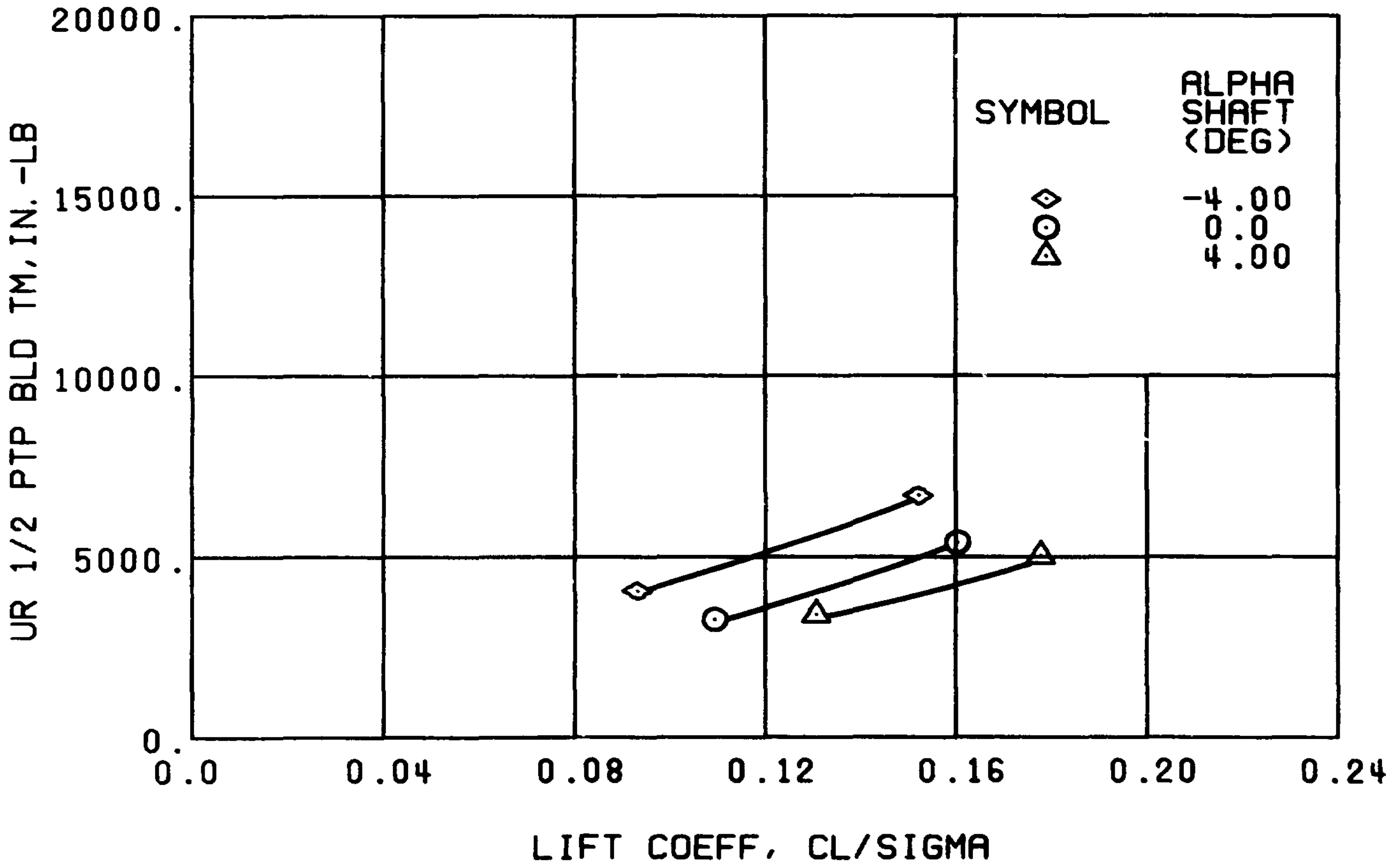

(m) GAGE 46 R130

Figure 55. Continued.
μ = 0.70 B'_{1s} = 2 Deg

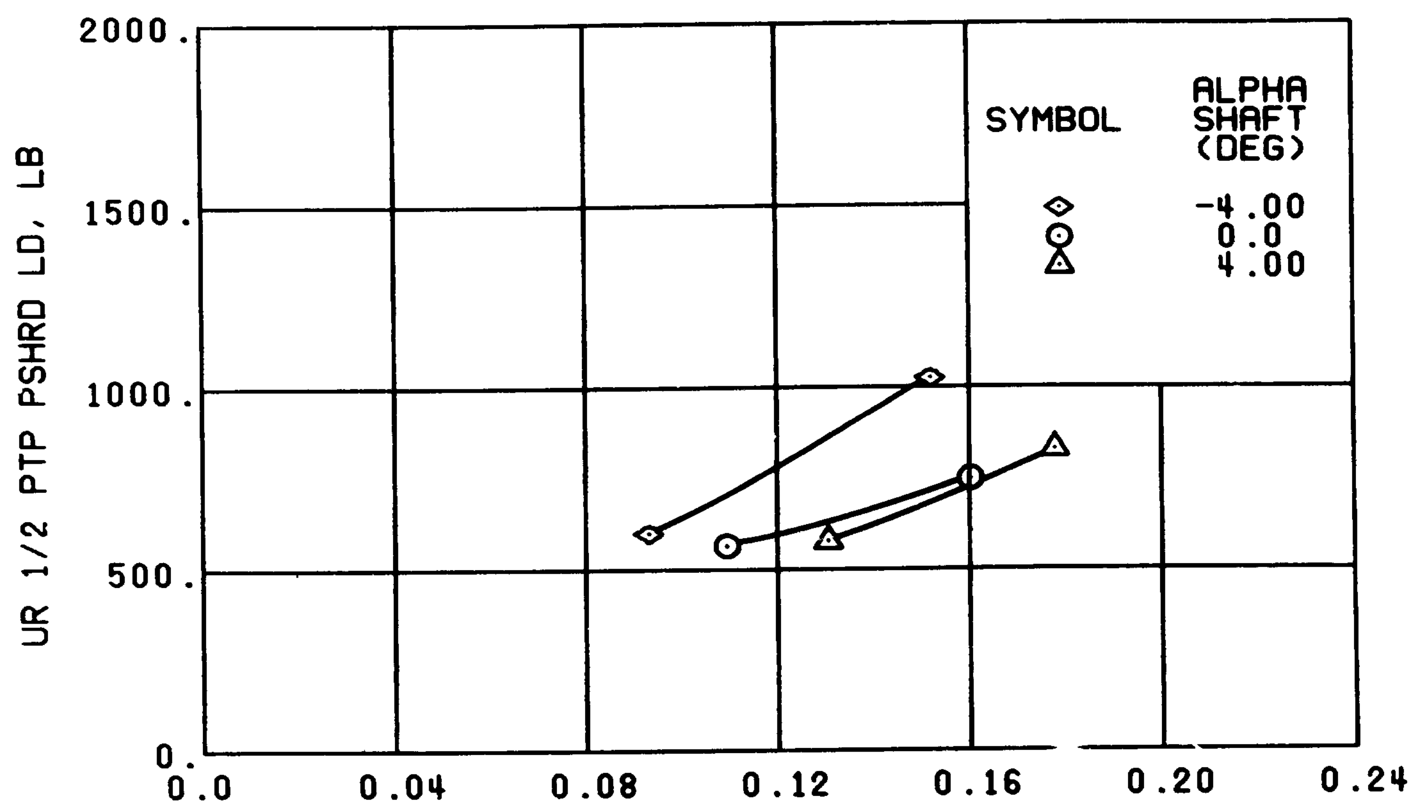

(n) GAGE 37

Figure 55. Continued.
$\mu = 0.70$ $B'_{1s} = 2$ Deg

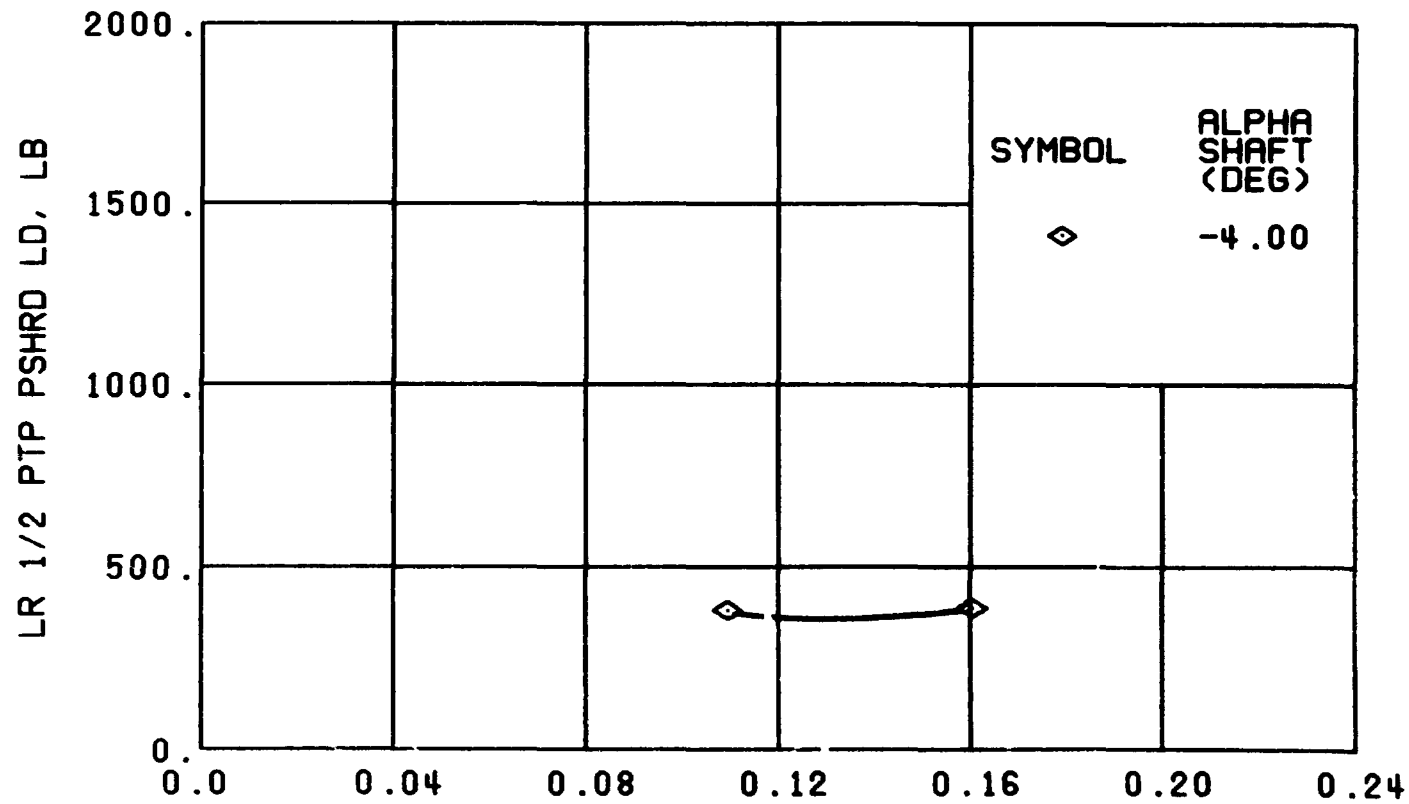

(o) GAGE 34

Figure 55. Continued.
$\mu = 0.70$ $B'_{1s} = 2$ Deg

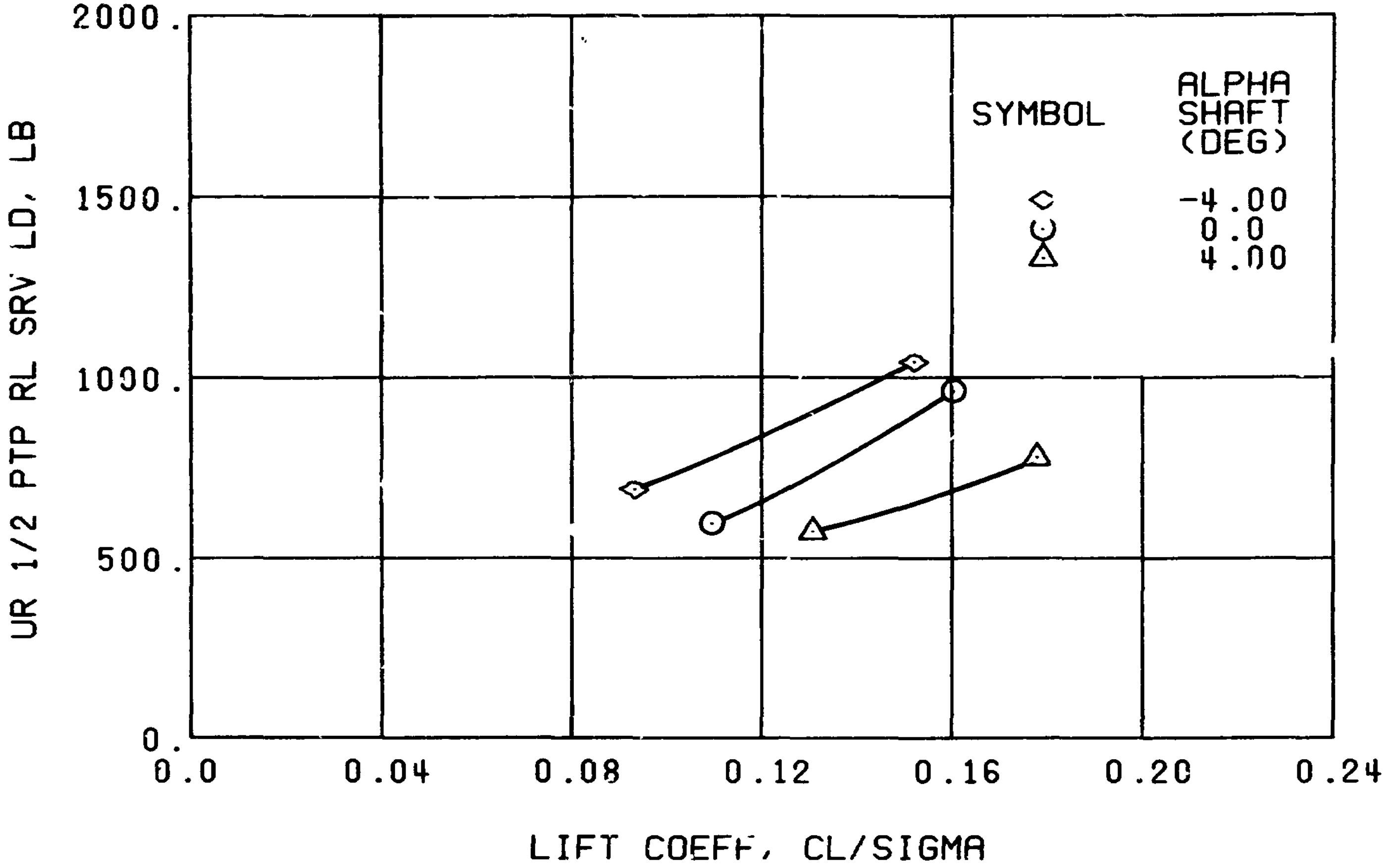

(p) GAGE 22

Figure 55. Continued.
$\mu = 0.70 \quad B'_{1s} = 2$ Deg

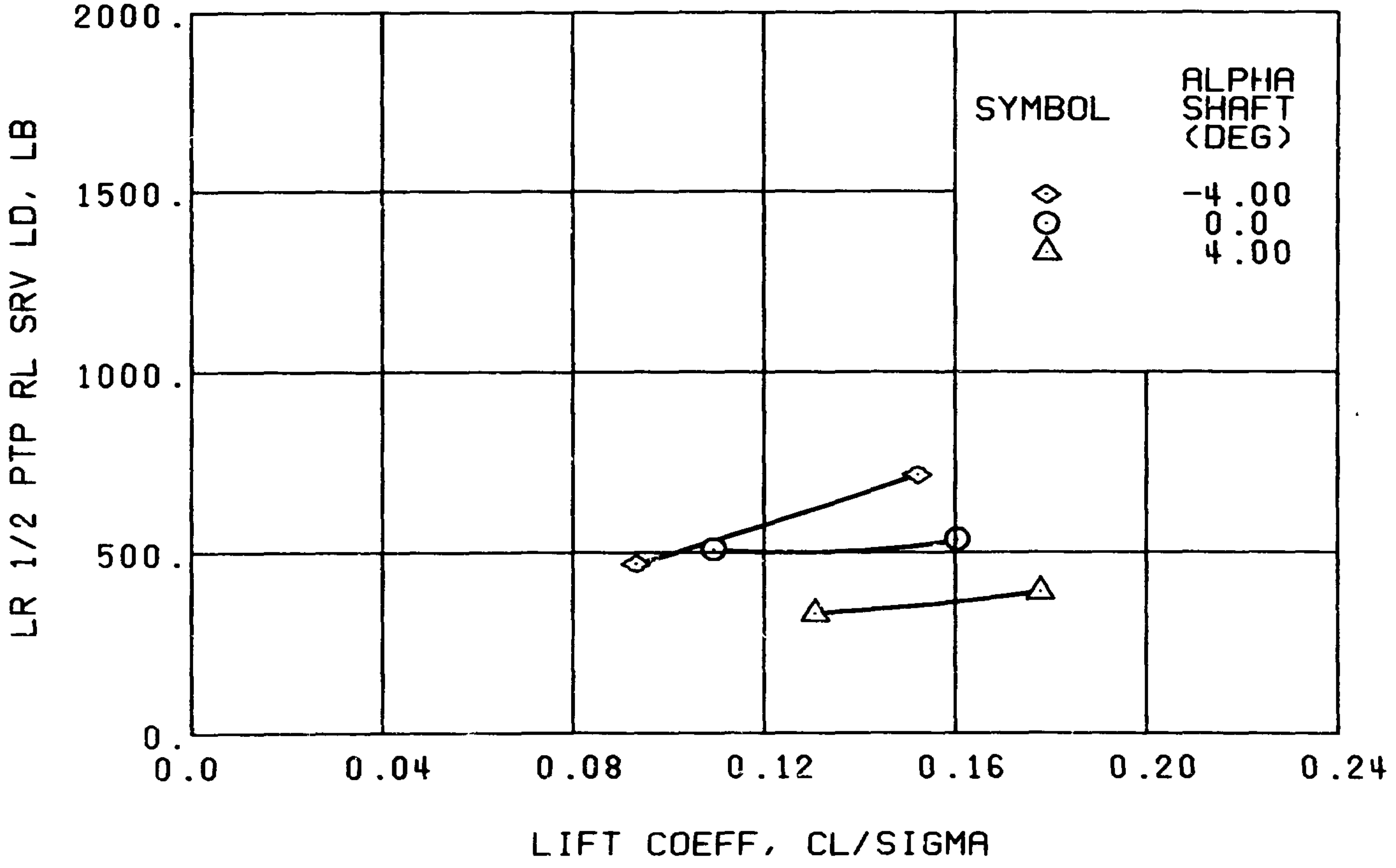

(q) GAGE 25

Figure 55. Continued.
μ = 0.70 B'_{1s} = 2 Deg

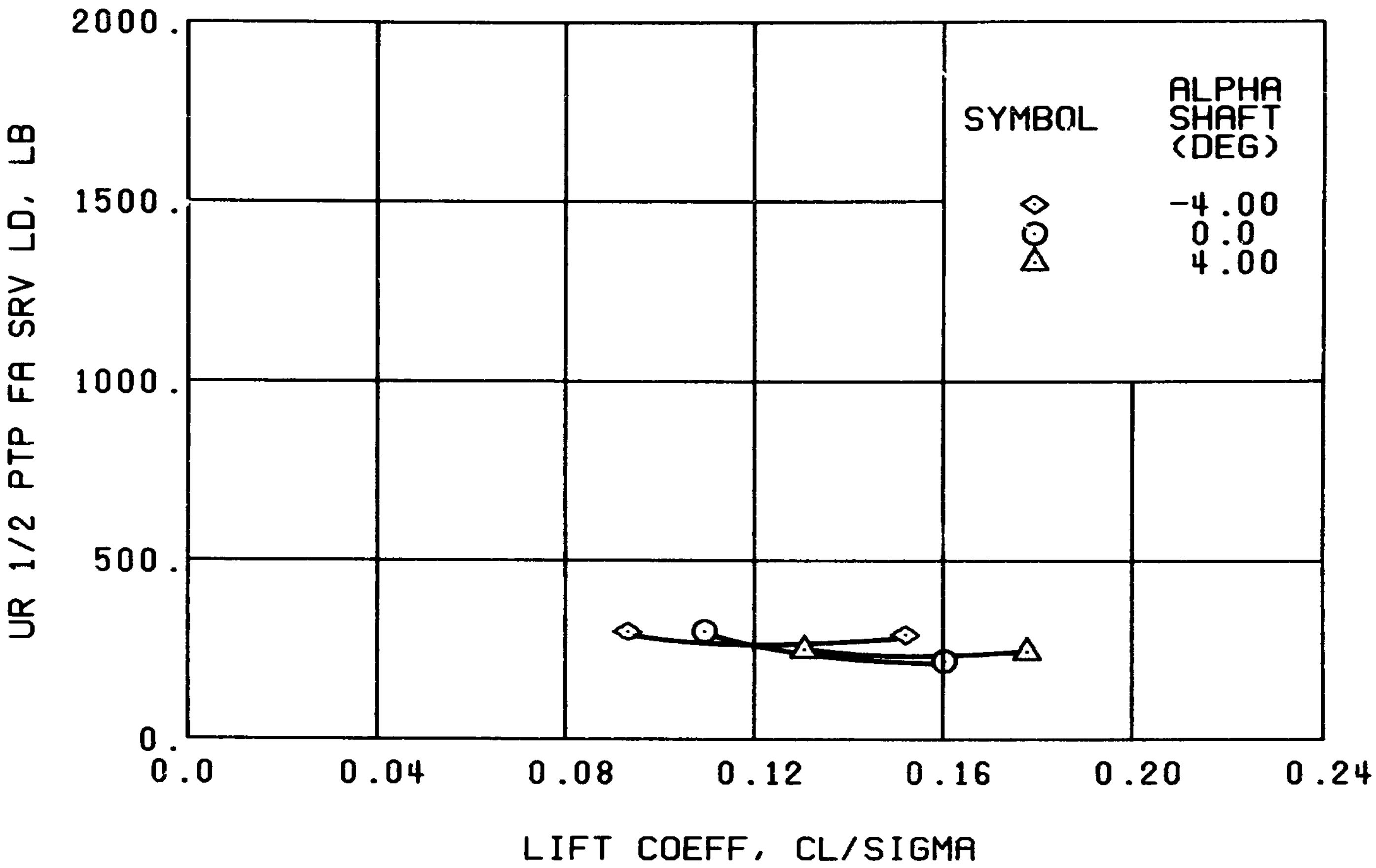

(r) GAGE 24

Figure 55. Continued.
$\mu = 0.70 \quad B'_{1s} = 2$ Deg

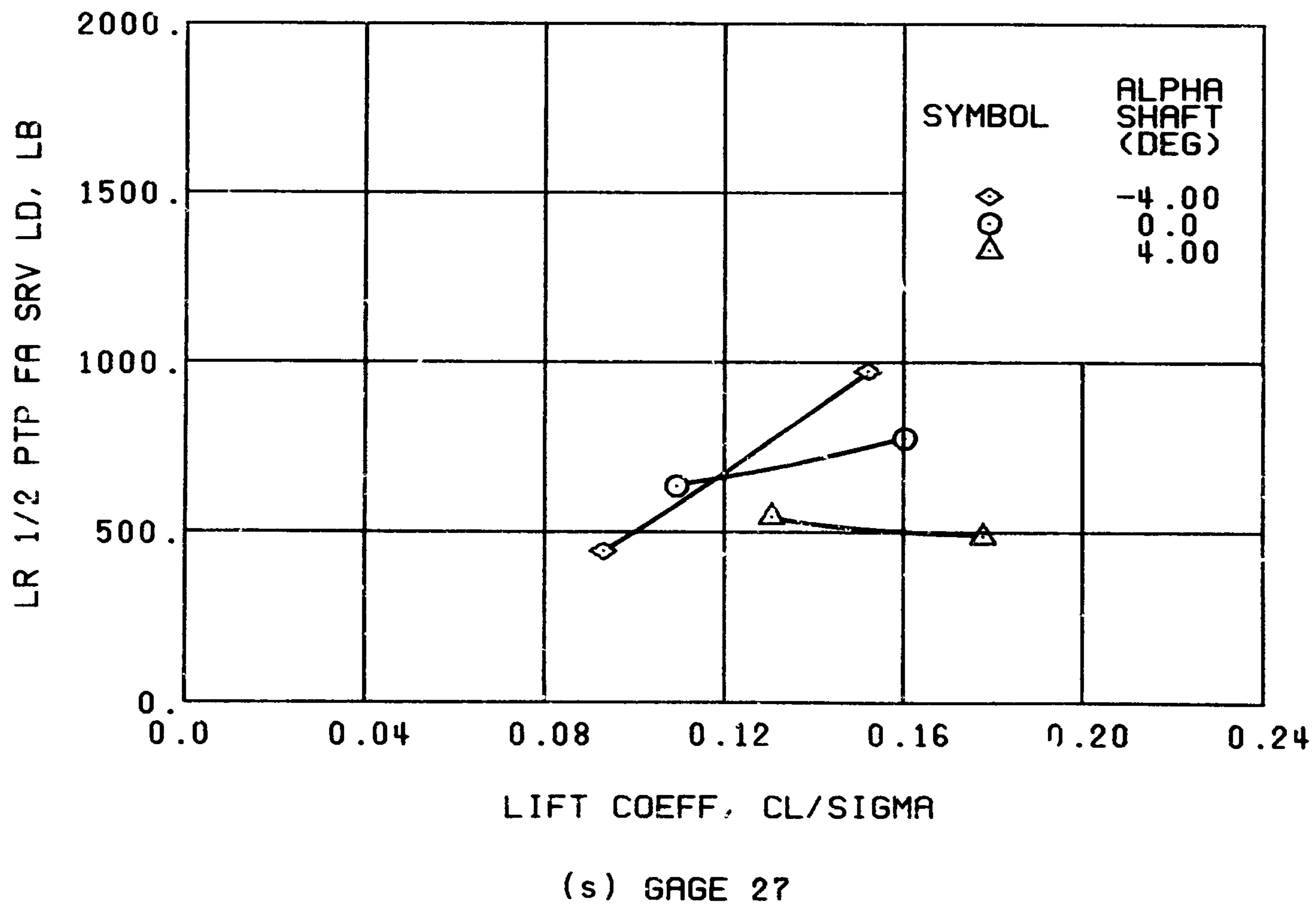

Figure 55. Continued.
$\mu = 0.70 \quad B'_{1s} = 2$ Deg

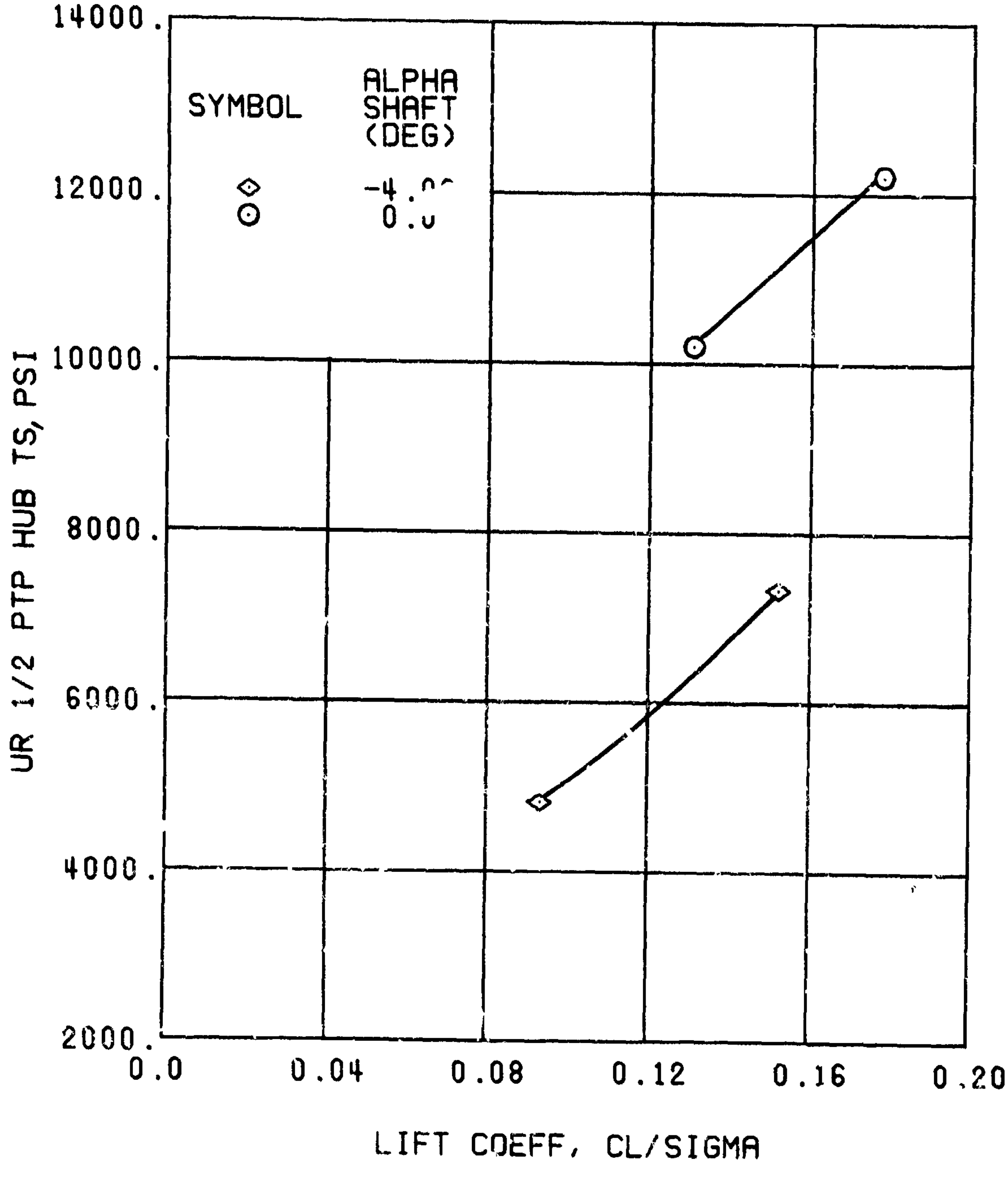

(f) GAGE 65

Figure 55. Continued.
$\mu = 0.70 \quad B'_{1s} = 2$ Deg

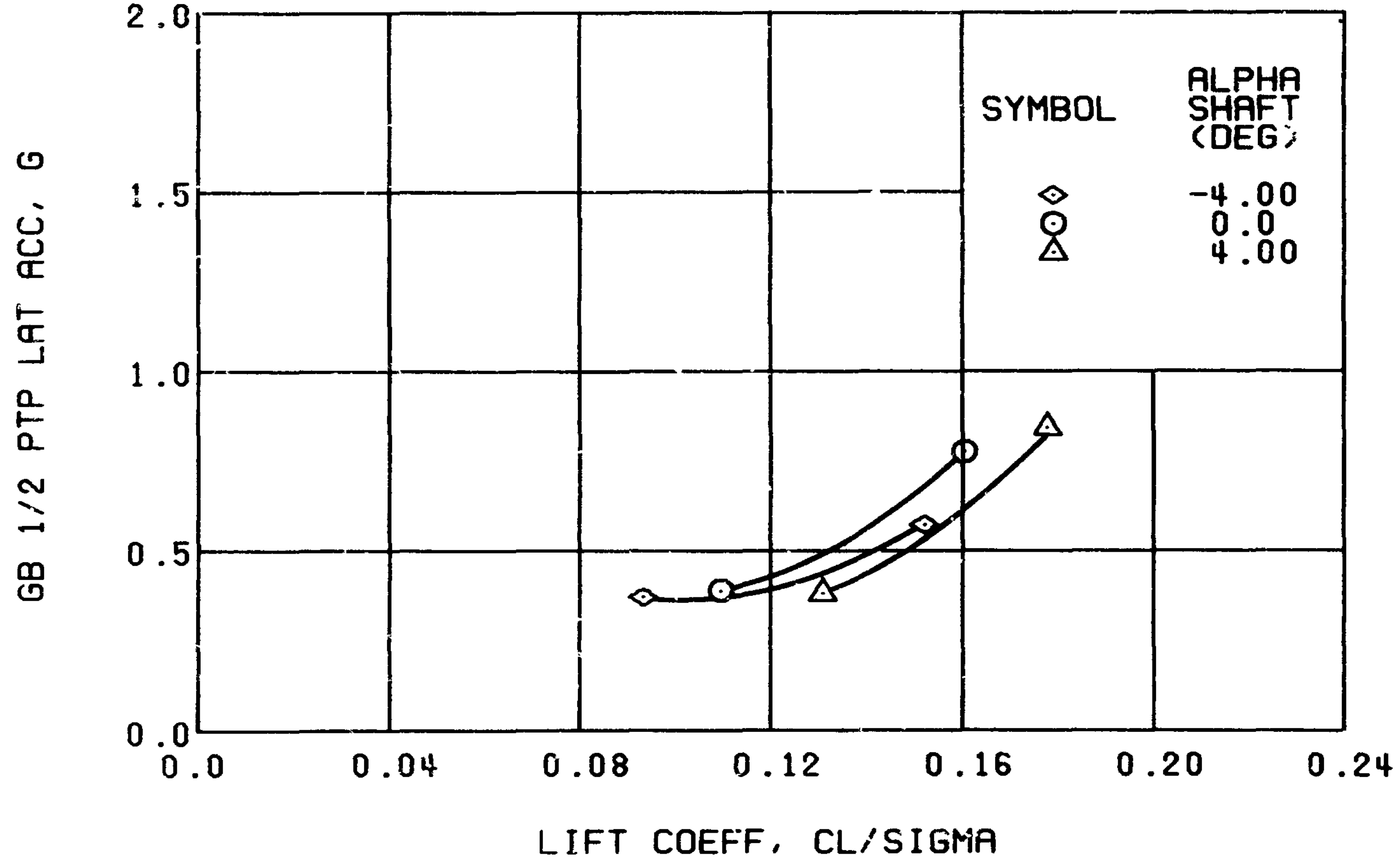

(u) GAGE 15 STA 76, BL 30

Figure 55. Continued.
$\mu = 0.70$ $B'_{1s} = 2$ Deg

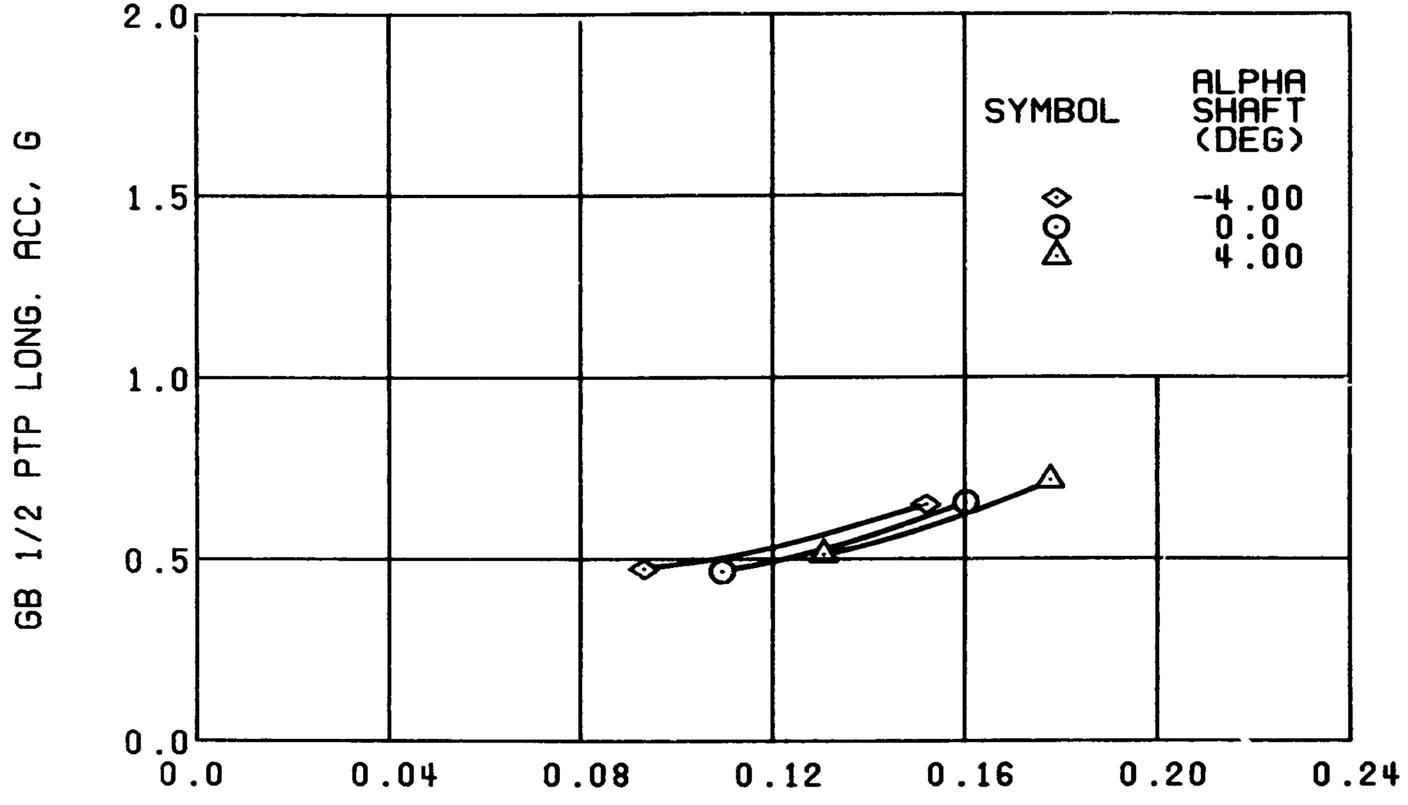

(v) GAGE 14 STA 61, BL 0

Figure 55. Continued.
$\mu = 0.70$ $B'_{1s} = 2$ Deg

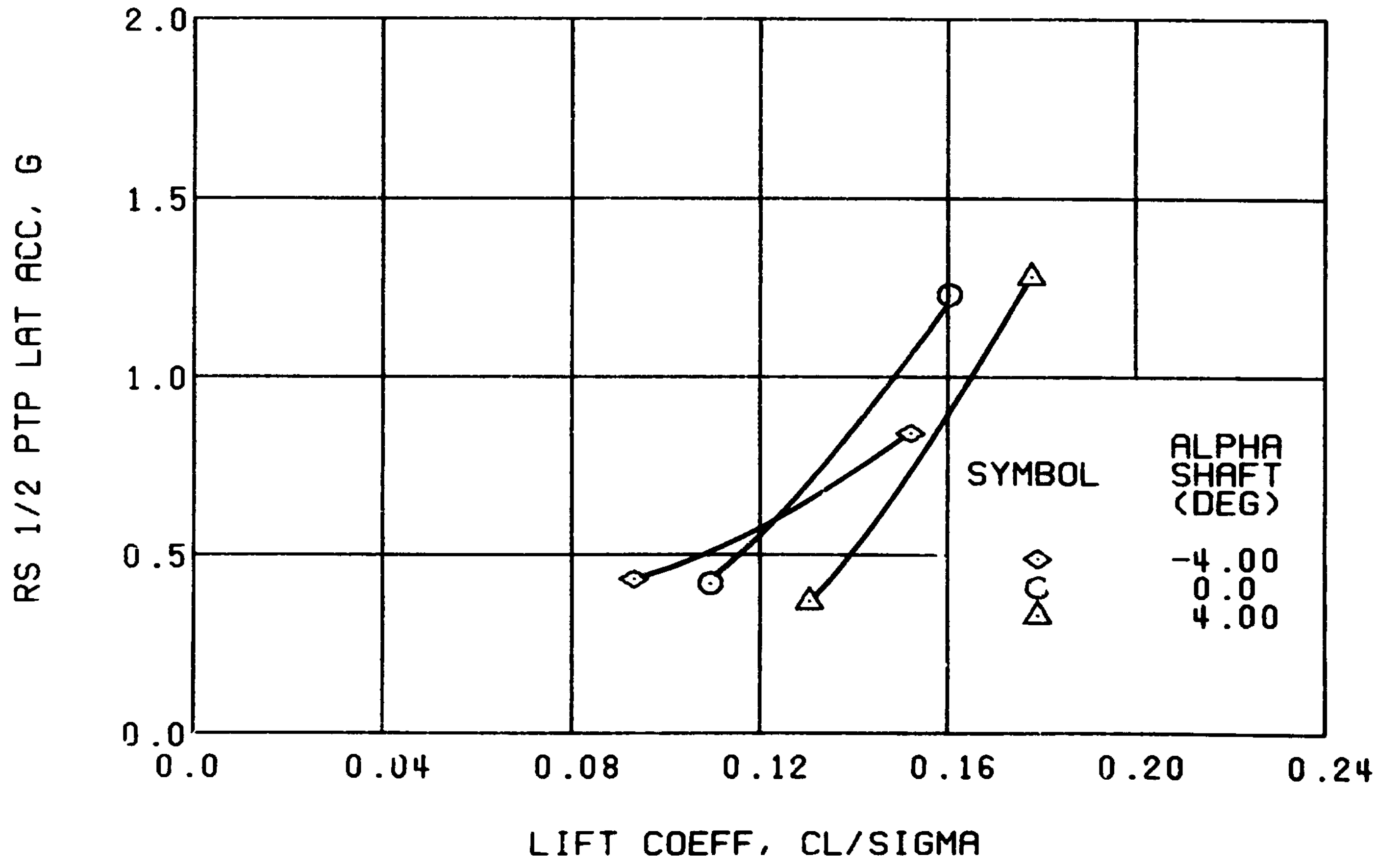

(w) GAGE 16 ROVER 3

Figure 55. Continued.
$\mu = 0.70$ $B'_{1s} = 2$ Deg

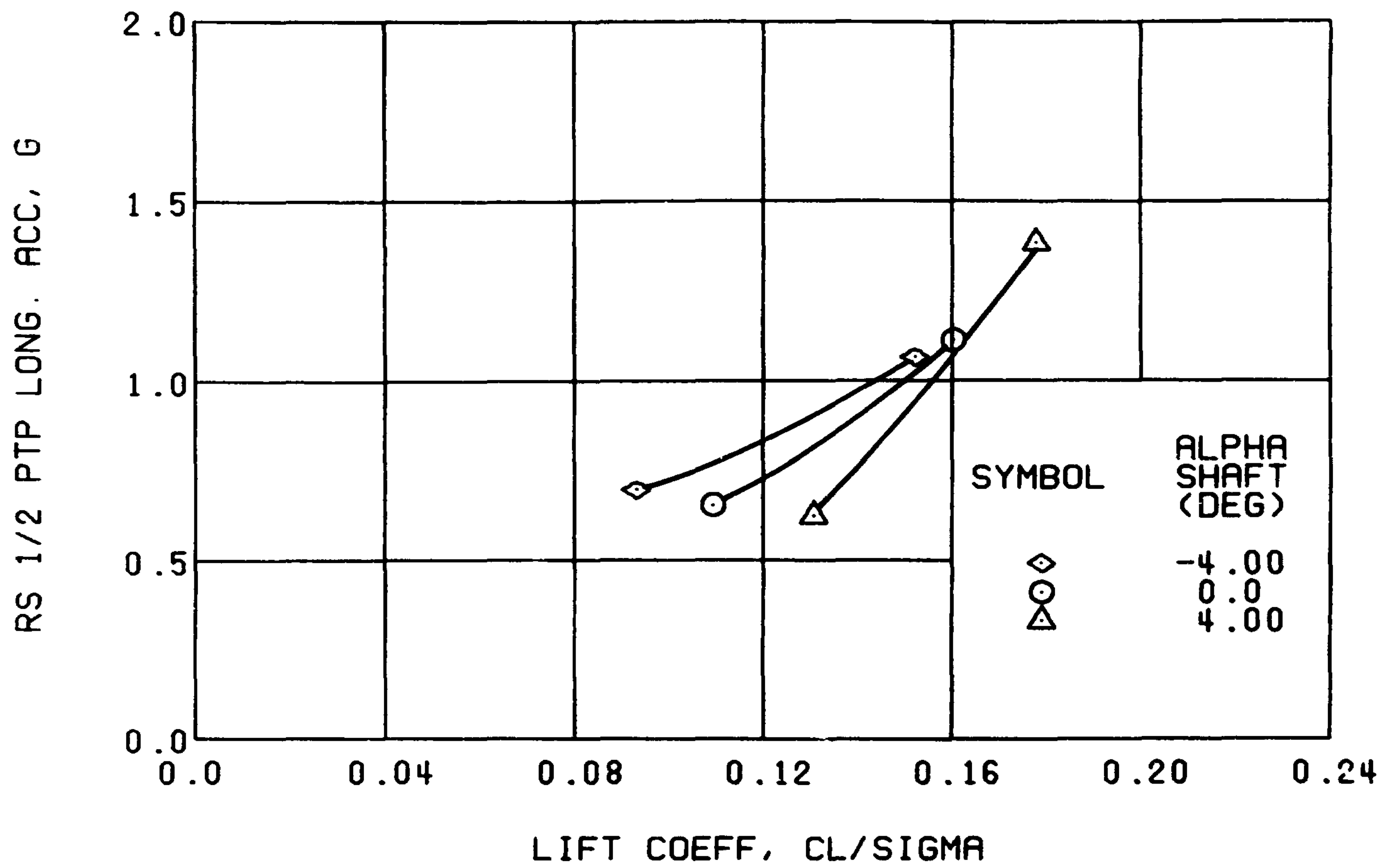

(x) GAGE 17 ROVER 4

Figure 55. Concluded.
$\mu = 0.70$ $B'_{1s} = 2$ Deg

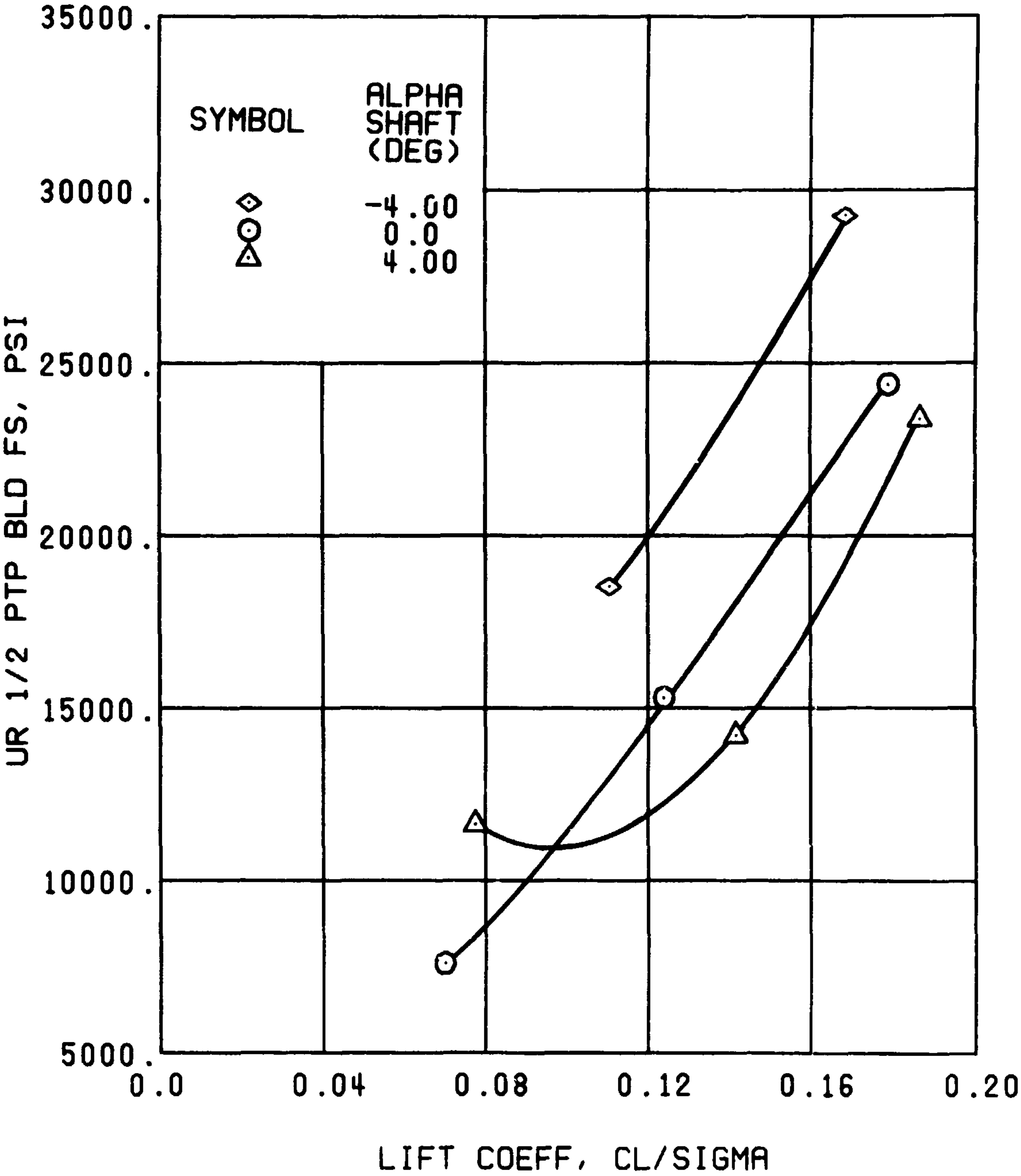

(a) GAGE 51 R84

Figure 56. Stress, Load, and Vibration Data at an Advance Ratio of 0.70 With the Lateral Displacement Control (B'_{1s}) Set at 4 Degrees.

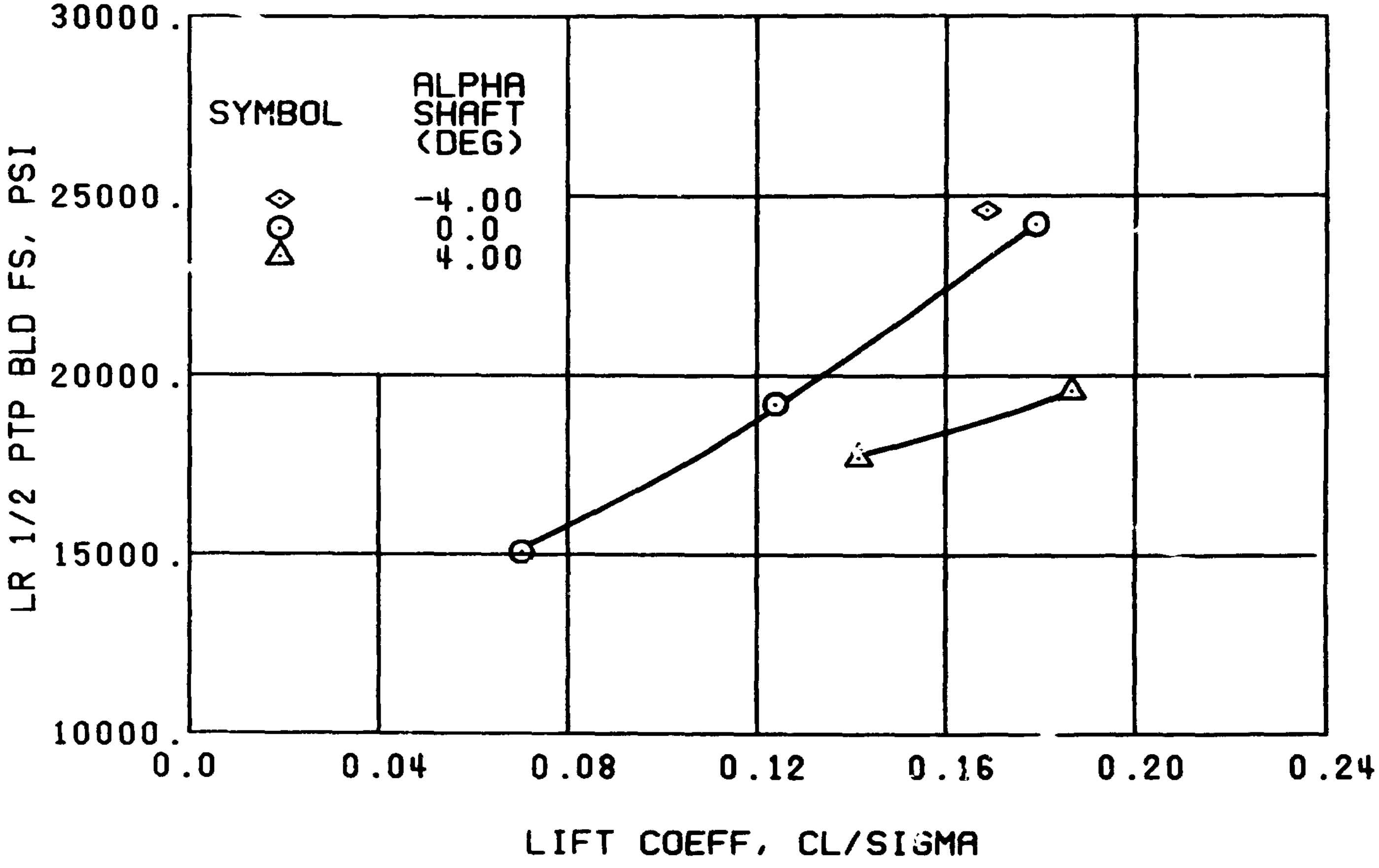

(b) GAGE 1 R84

Figure 56. Continued.
$\mu = 0.70 \quad B'_{1s} = 4$ Deg

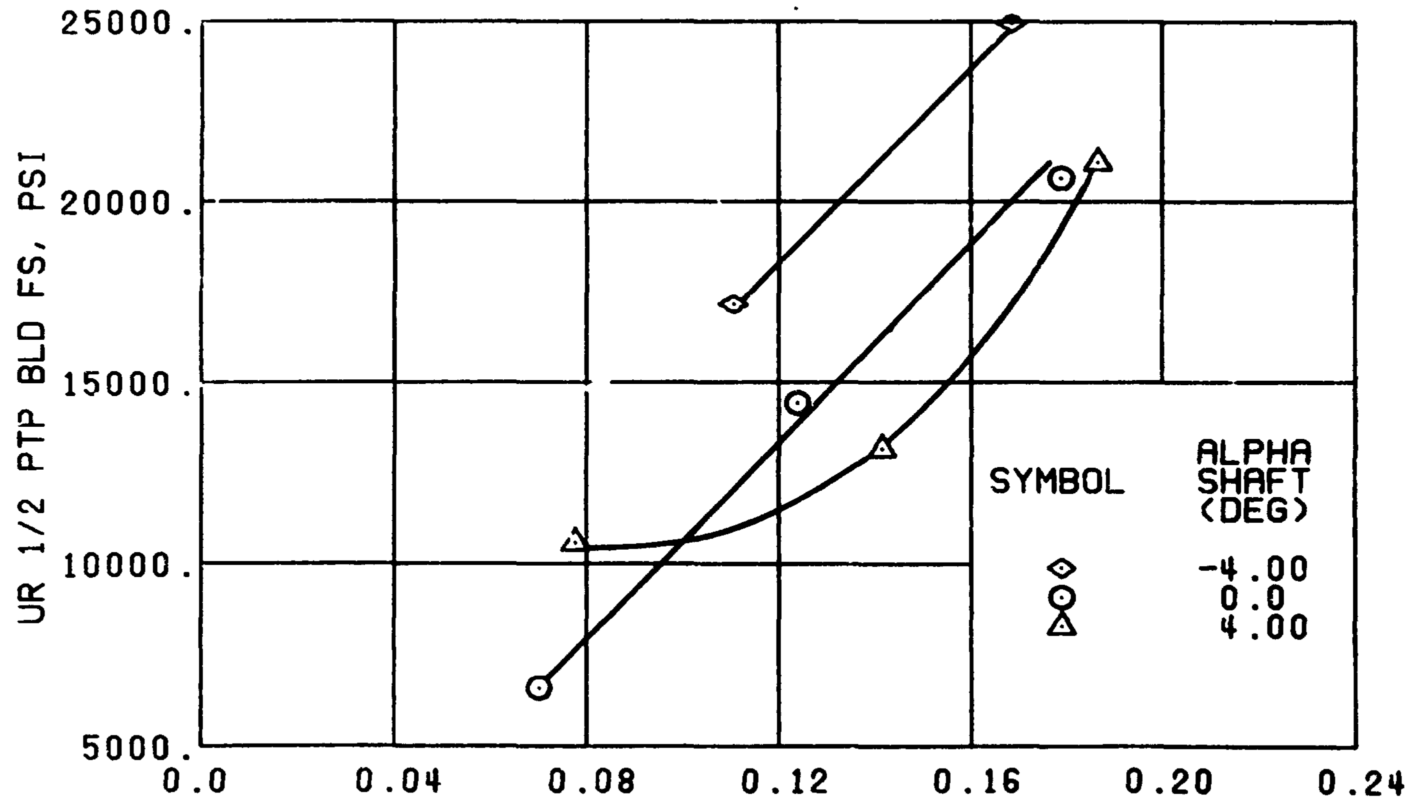

(c) GAGE 52 R108

Figure 56. Continued.
$\mu = 0.70 \quad B'_{1s} = 4$ Deg

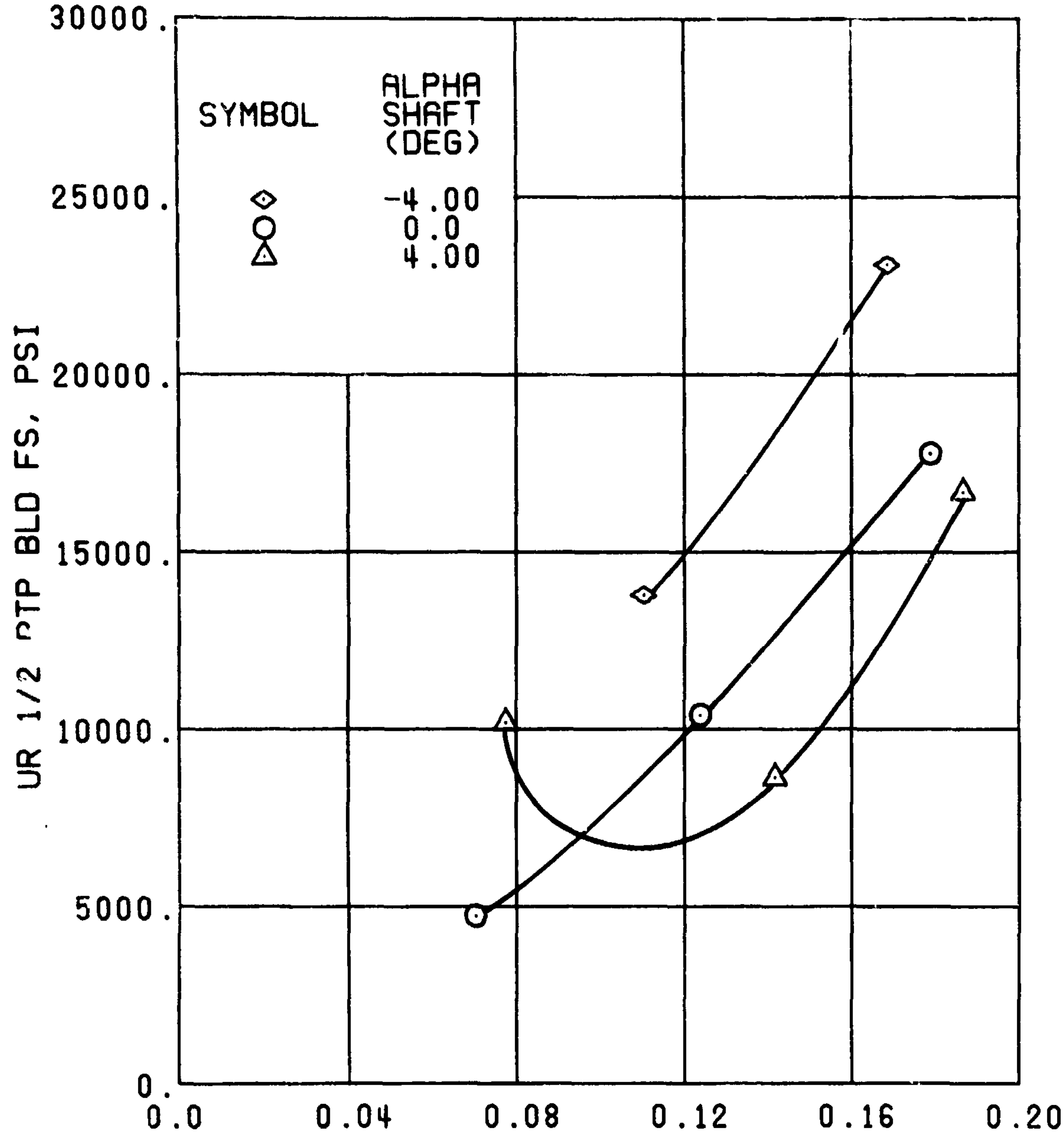

(d) GAGE 53 R132

Figure 56. Continued.
$\mu = 0.70$ $B'_{1s} = 4$ Deg

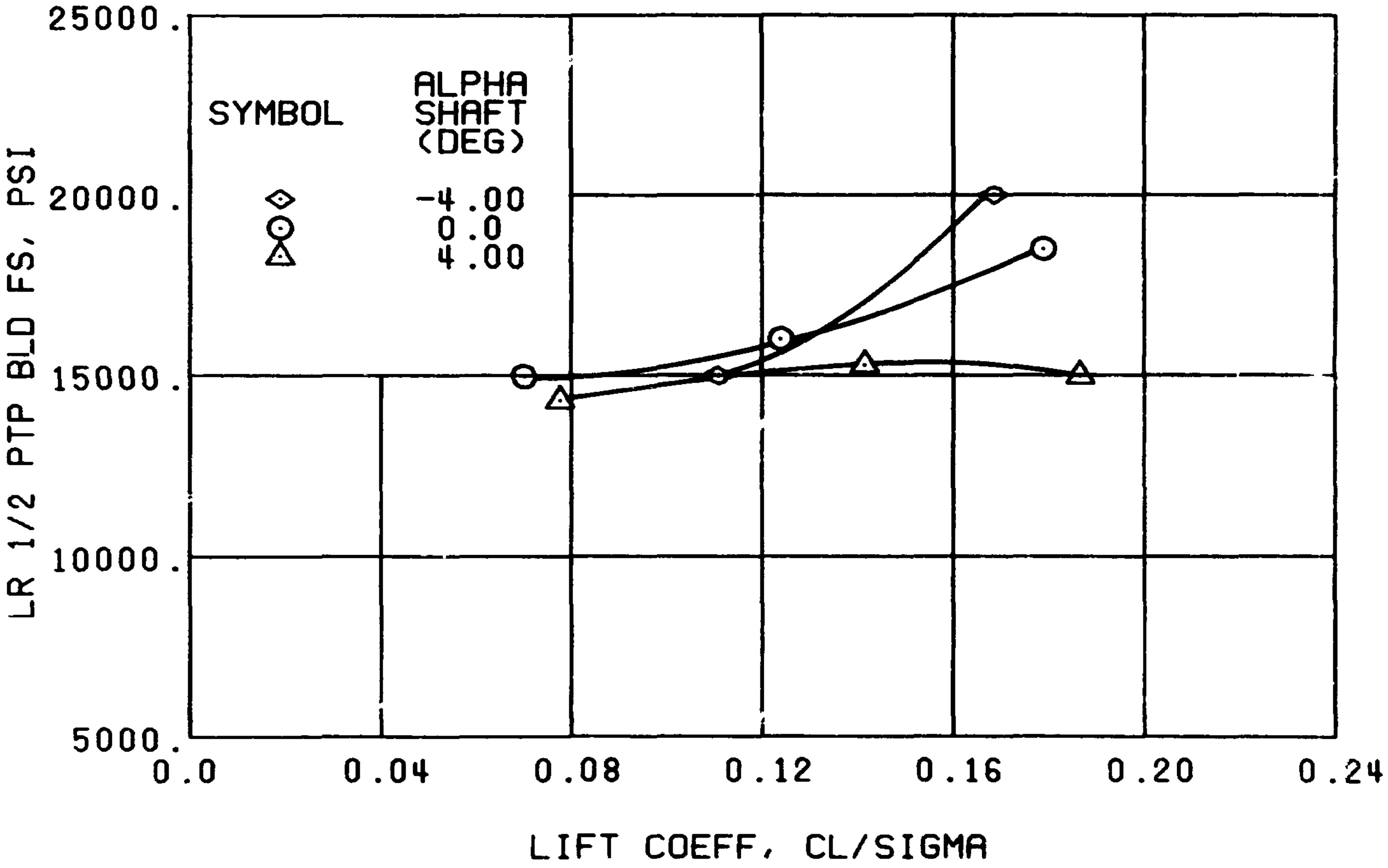

(e) GAGE 93 R132

Figure 56. Continued.
$\mu = 0.70 \quad B'_{1s} = 4$ Deg

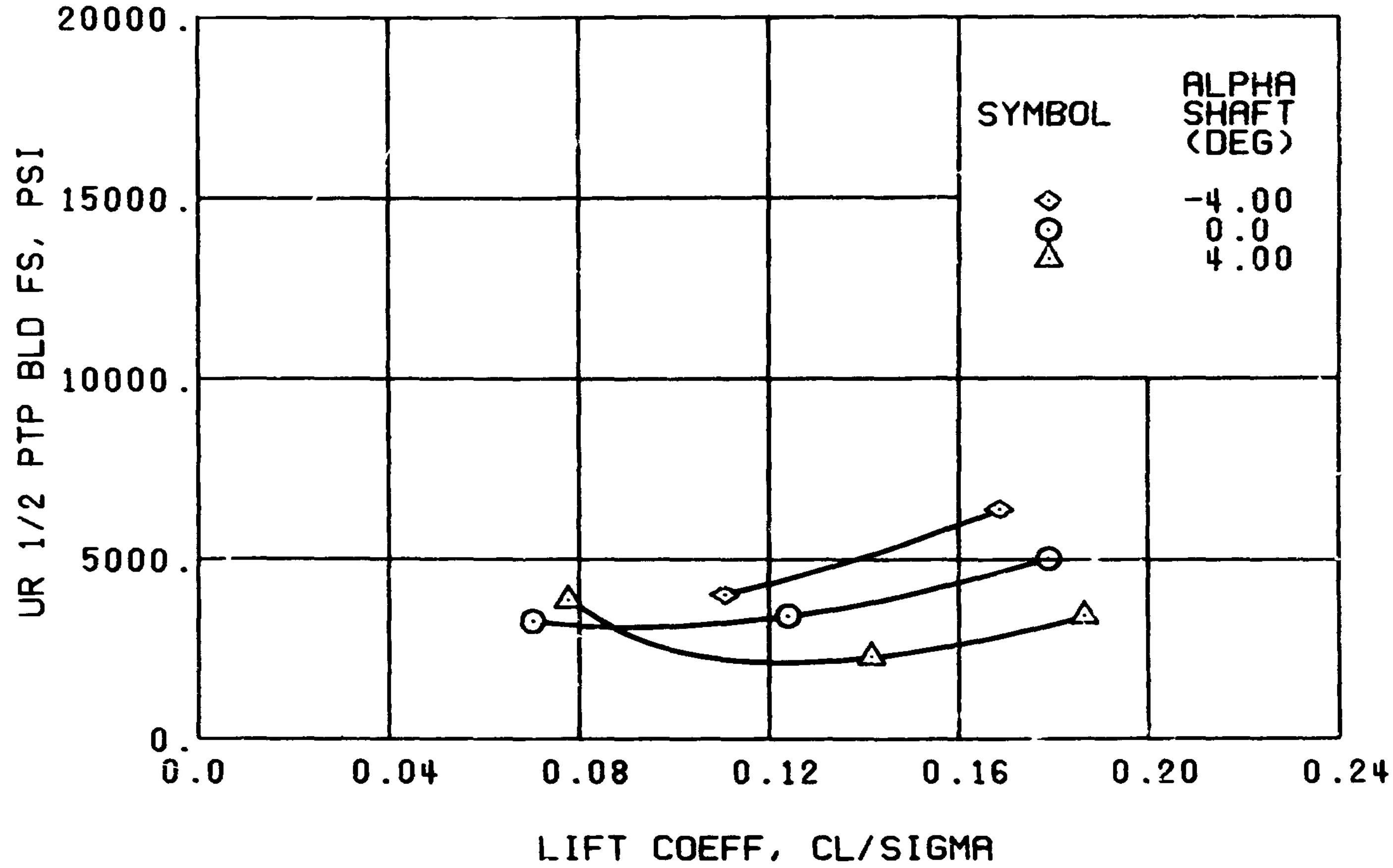

(f) GAGE 55 R204

Figure 56. Continued.
$\mu = 0.70$ $B'_{1s} = 4$ Deg

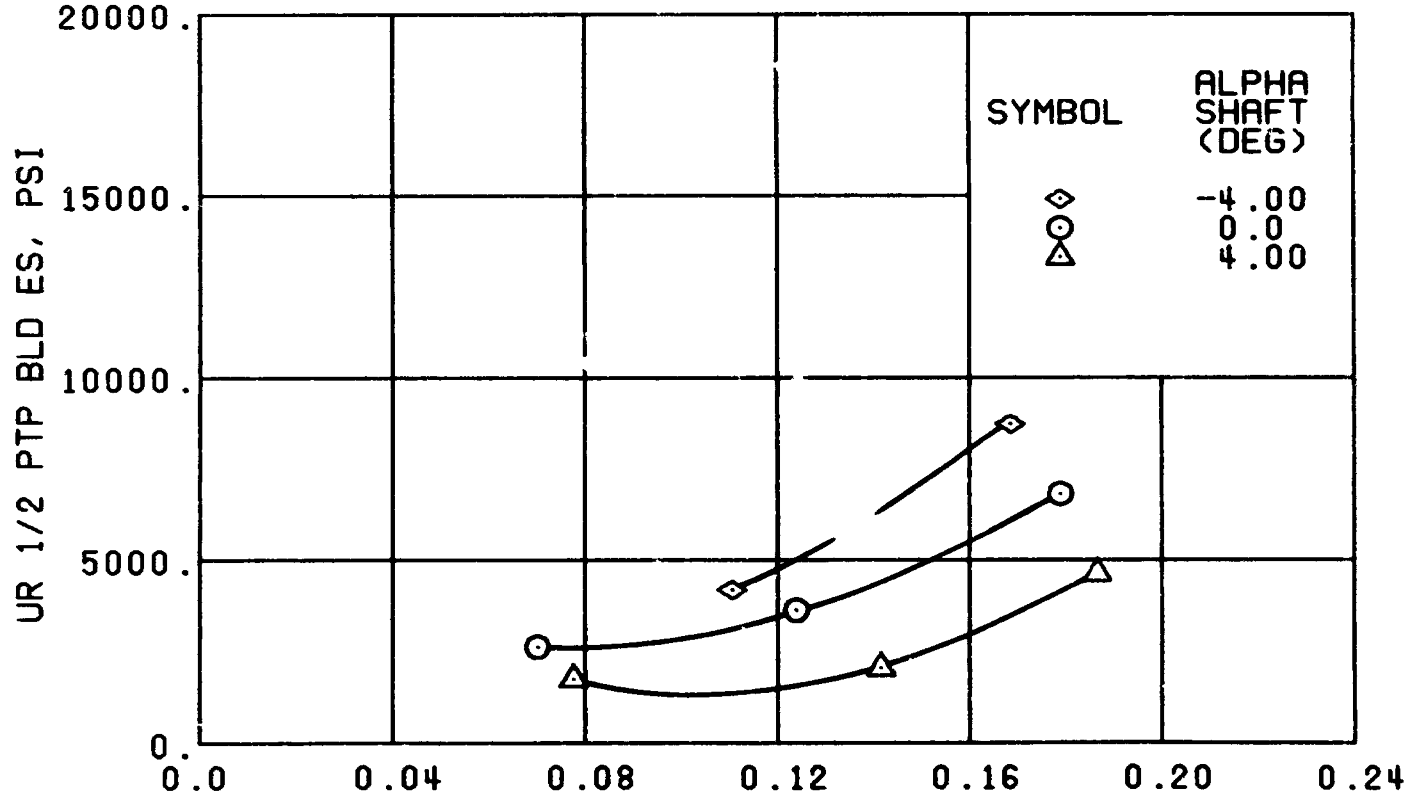

(h) GAGE 40 R84

Figure 56. Continued.
$\mu = 0.70$ $B'_{1s} = 4$ Deg

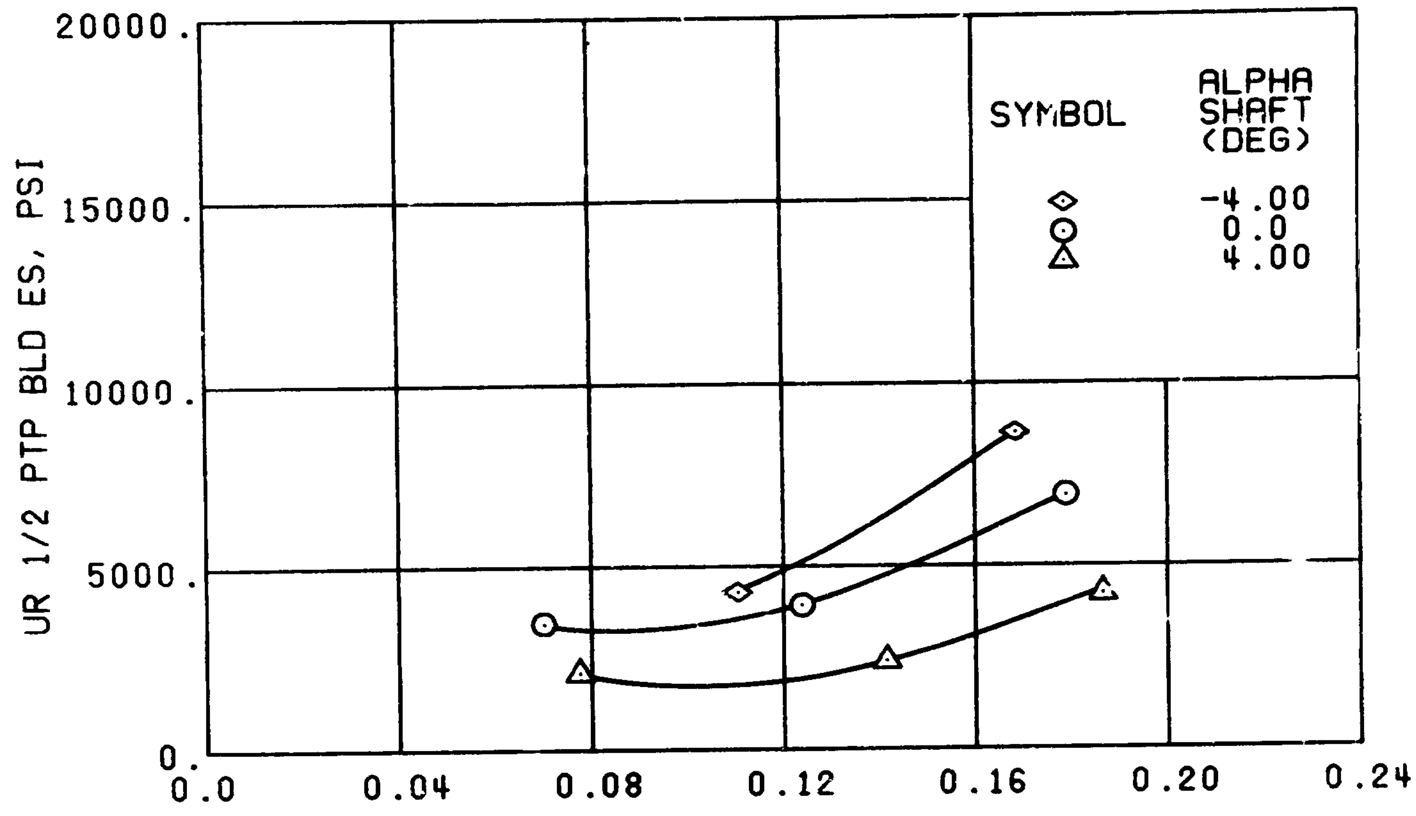

(j) GAGE 42 R132

Figure 56. Continued.
$\mu = 0.70$ $B'_{1s} = 4$ Deg

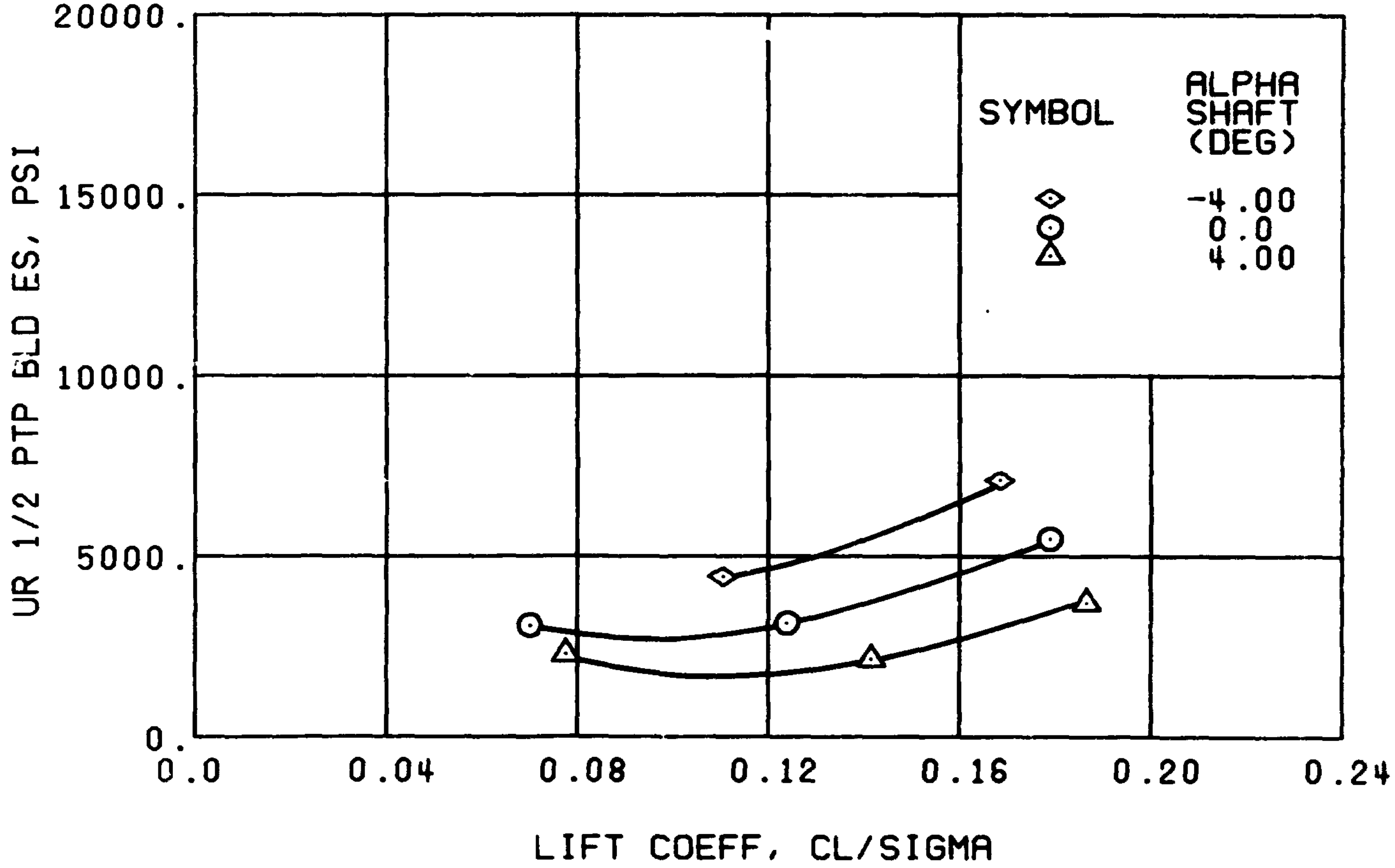

(k) GAGE 43 R168

Figure 56. Continued.
$\mu = 0.70 \quad B'_{1s} = 4$ Deg

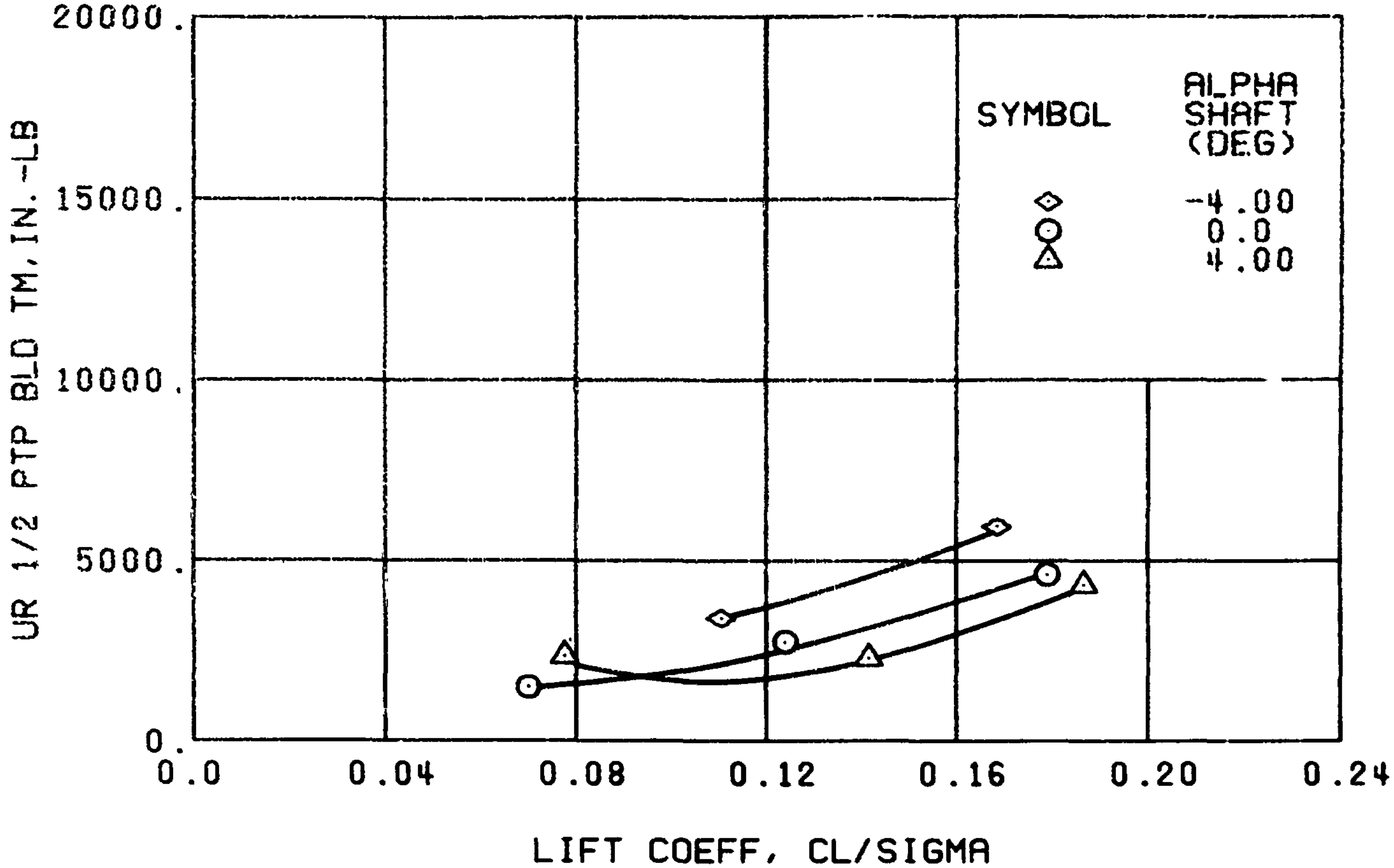

(m) GAGE 46 R130

Figure 56. Continued.
$\mu = 0.70 \quad B'_{1s} = 4$ Deg

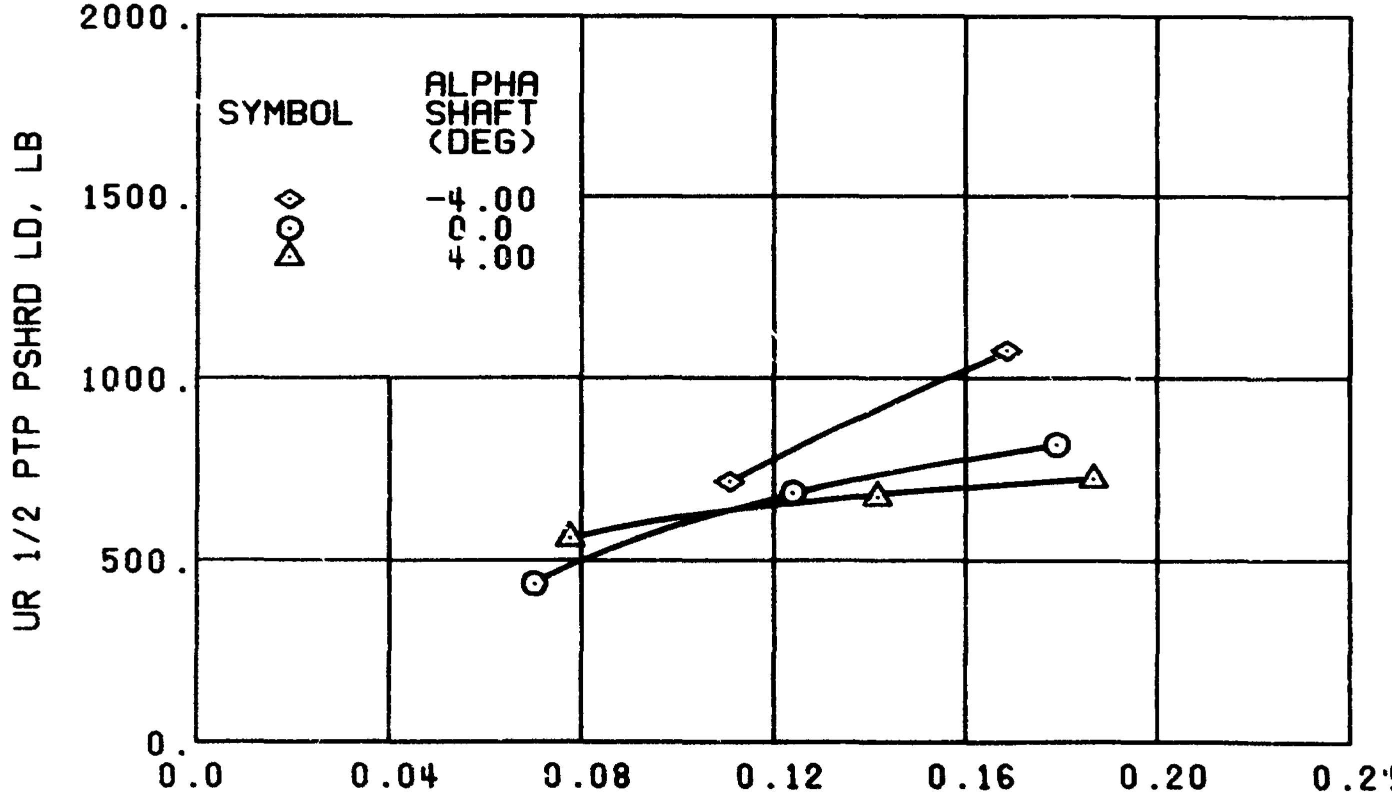

(n) GAGE 37

Figure 56. Continued.
$\mu = 0.70 \quad B'_{1s} = 4$ Deg

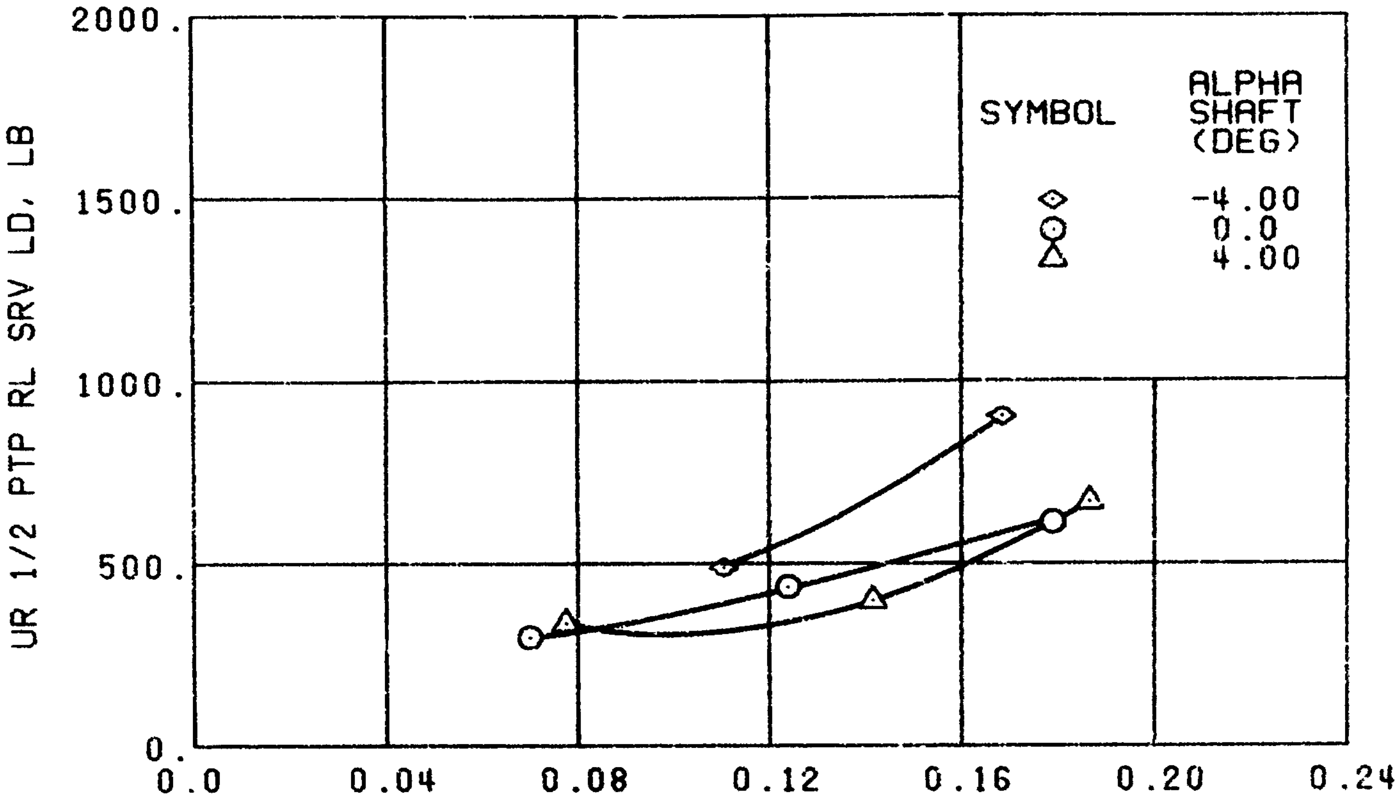

(p) GAGE 22

Figure 56. Continued.
$\mu = 0.70 \quad B'_{1s} = 4$ Deg

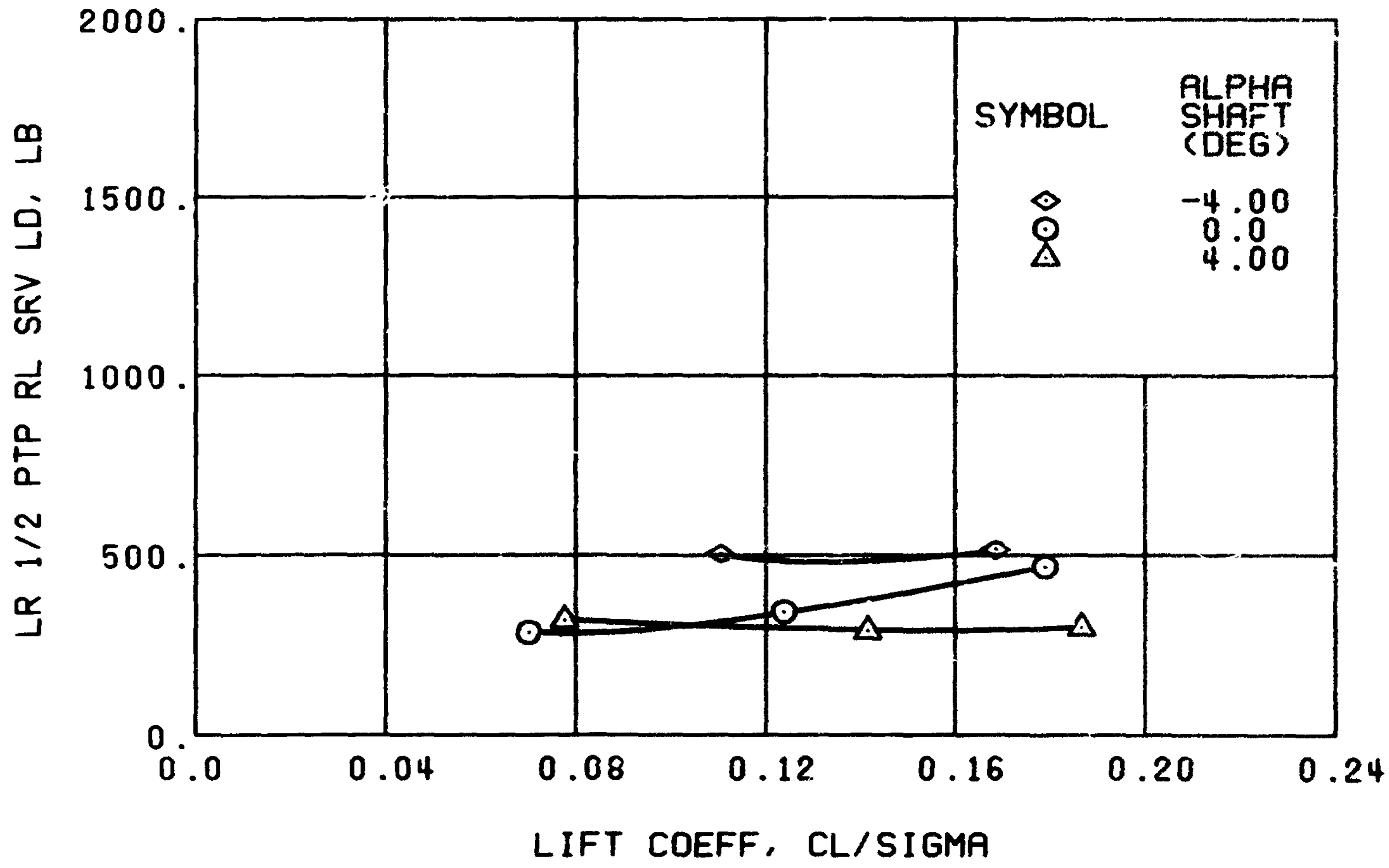

(q) GAGE 25

Figure 56. Continued.
$\mu = 0.70$ $B'_{1s} = 4$ Deg

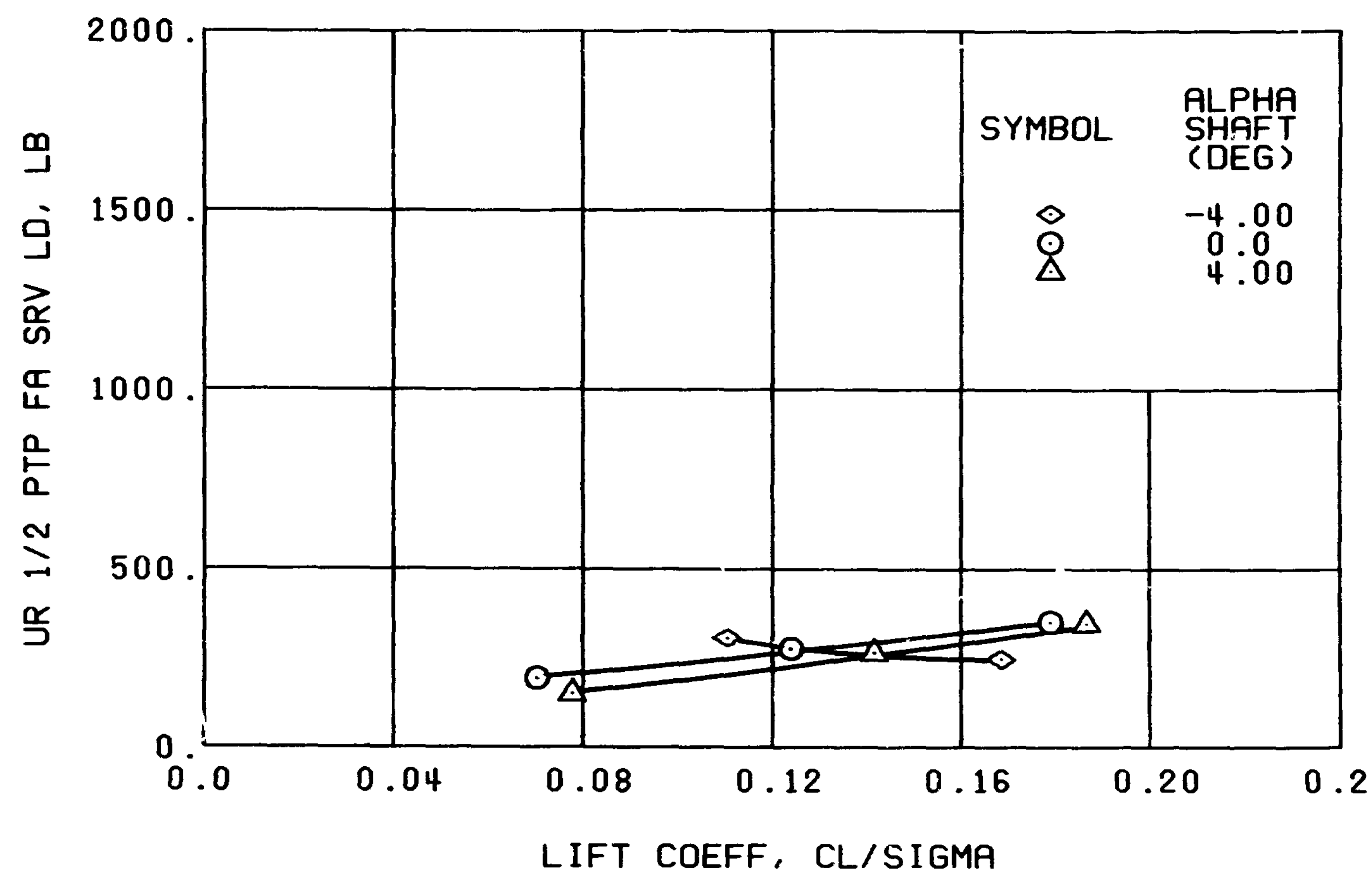

(r) GAGE 24

Figure 56. Continued.
$\mu = 0.70 \quad B'_{1s} = 4$ Deg

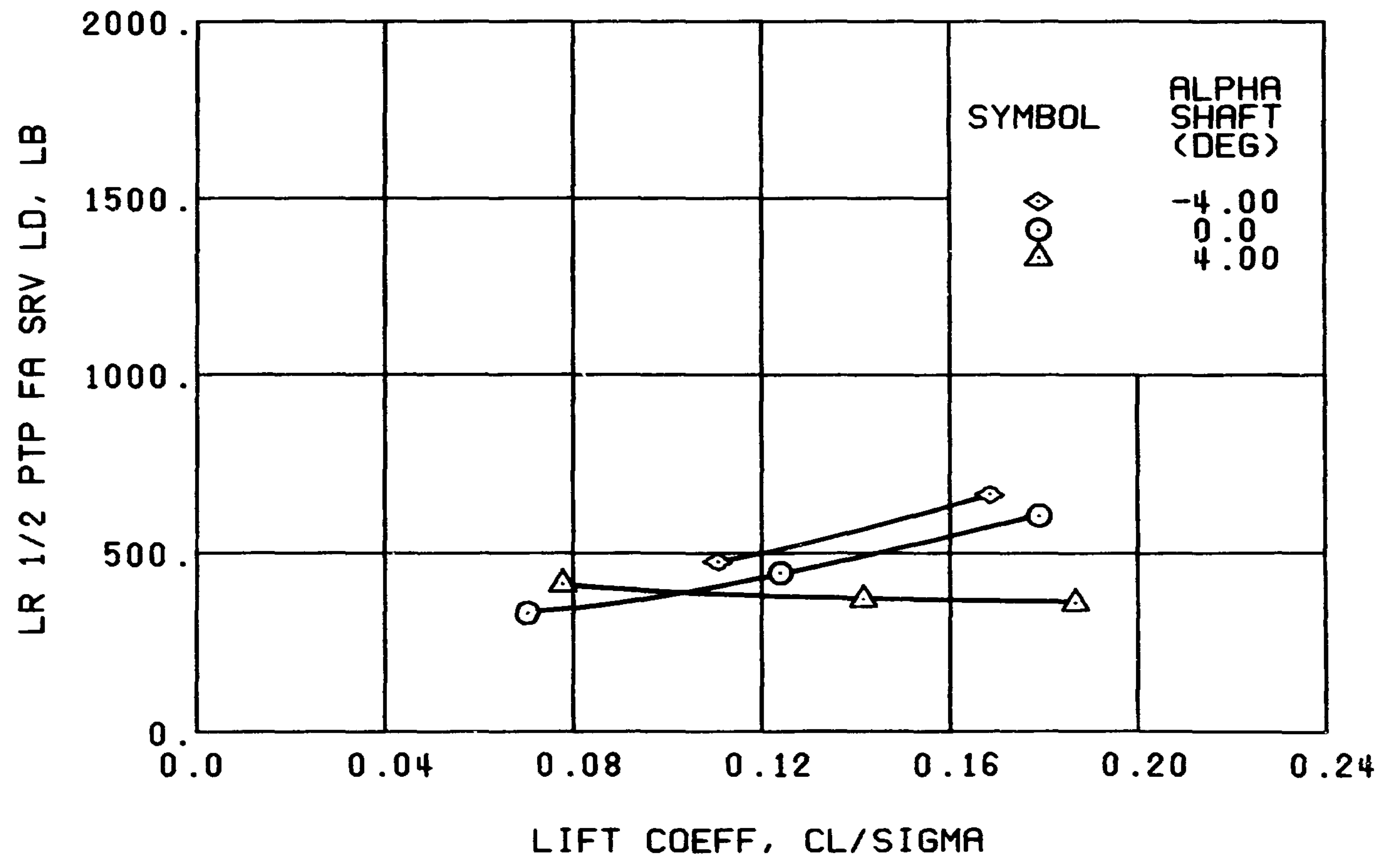

(s) GAGE 27

Figure 56. Continued.
$\mu = 0.70$ $B'_{1s} = 4$ Deg

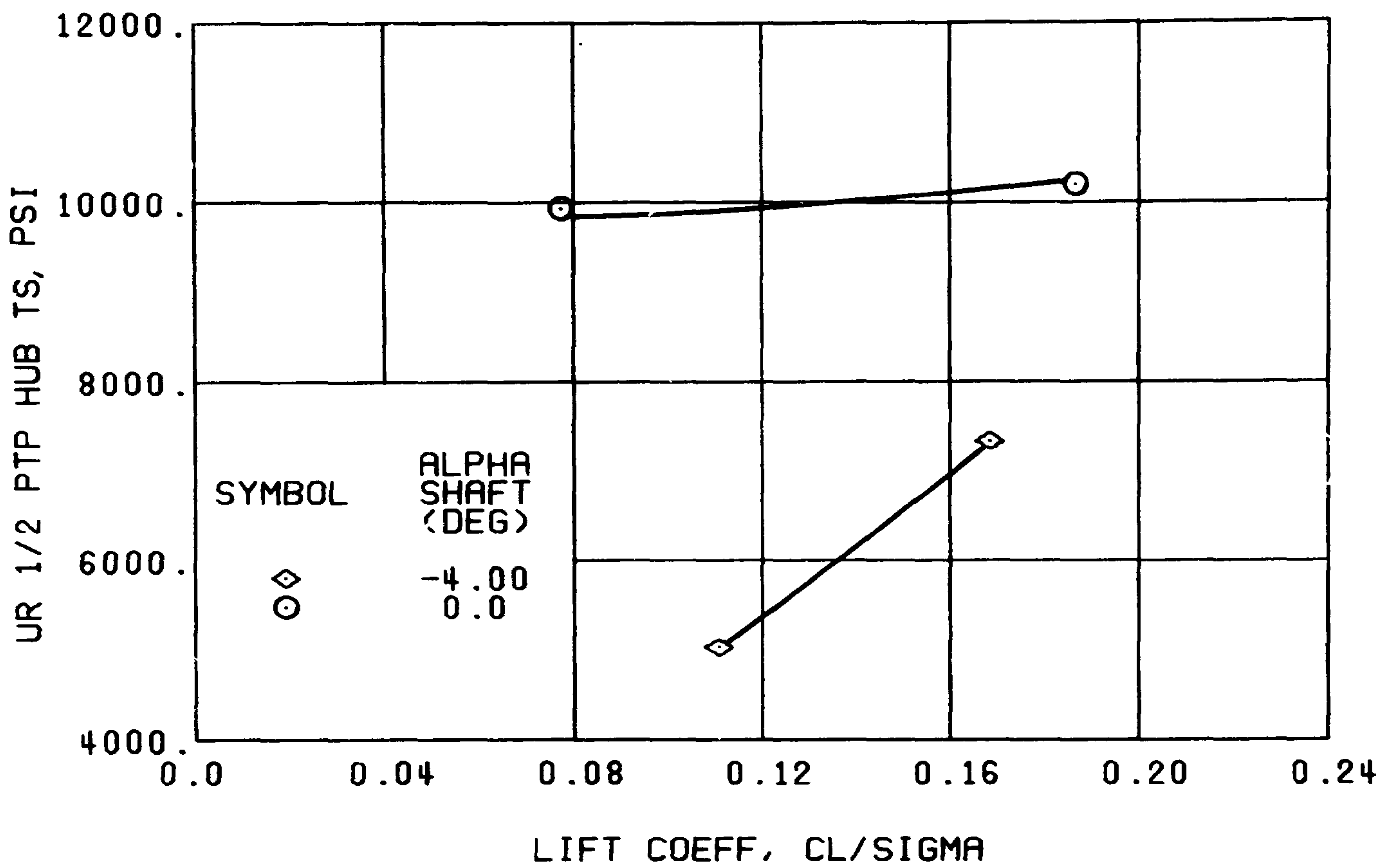

(f) GAGE 65

Figure 56. Continued.
$\mu = 0.70 \quad B'_{1s} = 4$ Deg

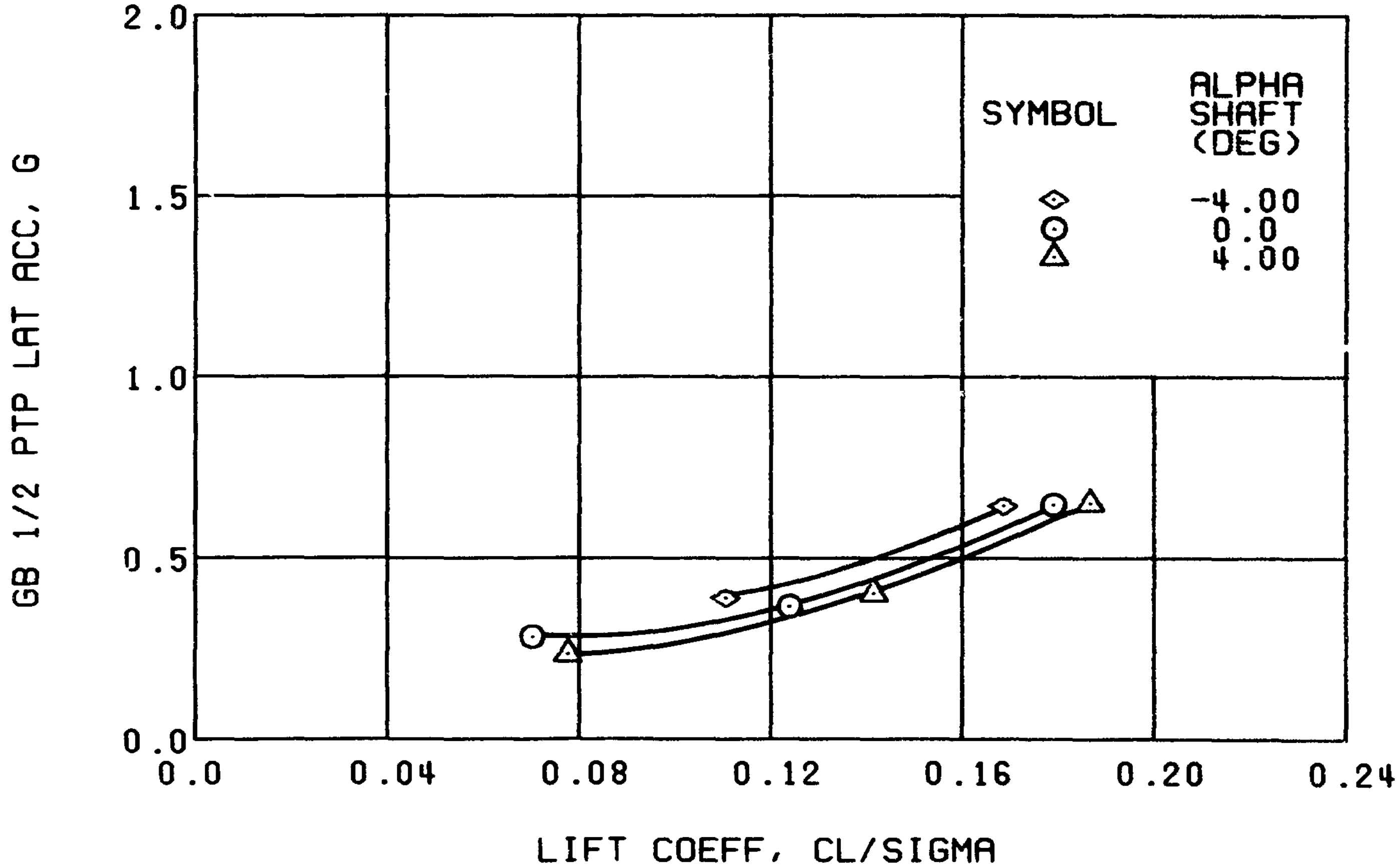

(u) GAGE 15 STA 76, BL 3C

Figure 56. Continued.
$\mu = 0.70$ $B'_{1s} = 4$ Deg

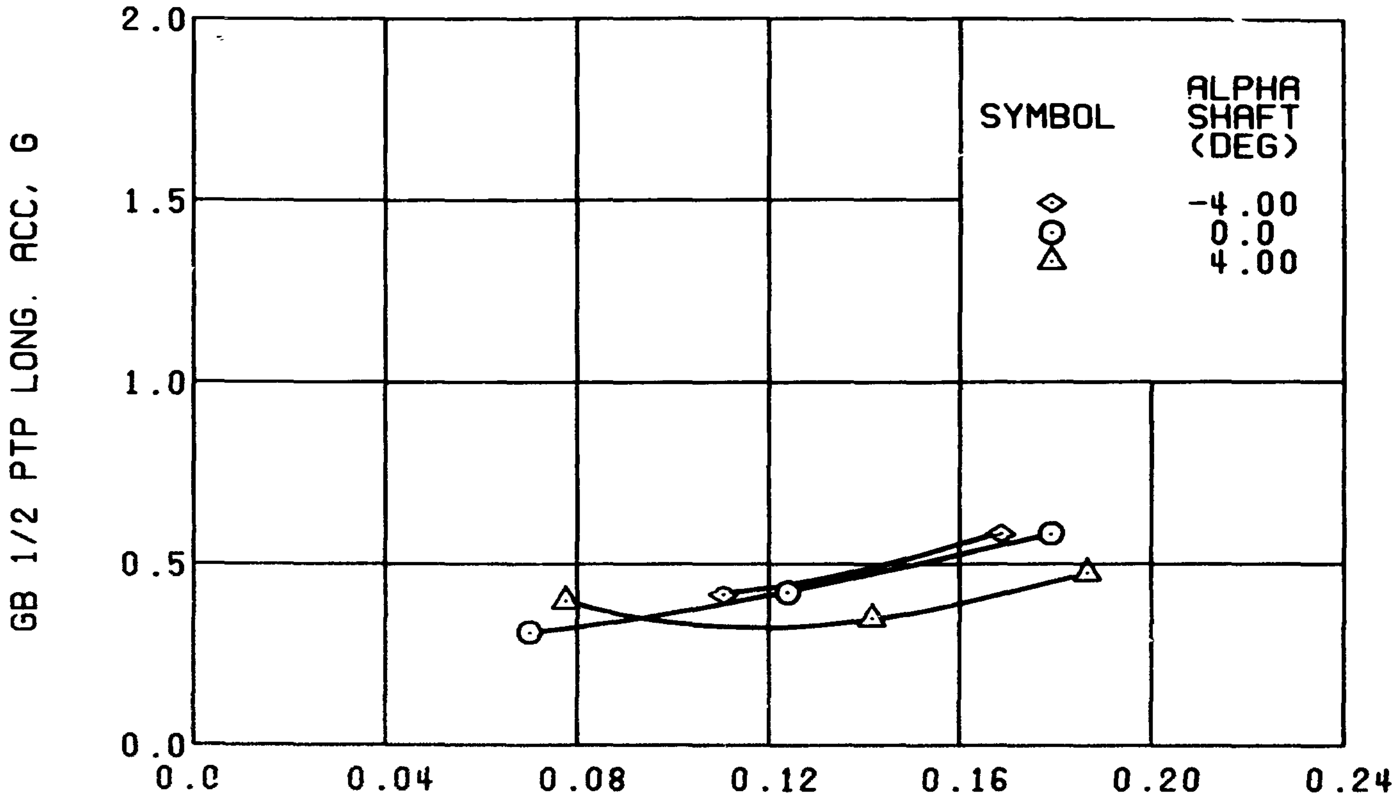

(v) GAGE 14 STA 61, BL 0

Figure 56. Continued.
$\mu = 0.70 \quad B'_{1s} = 4$ Deg

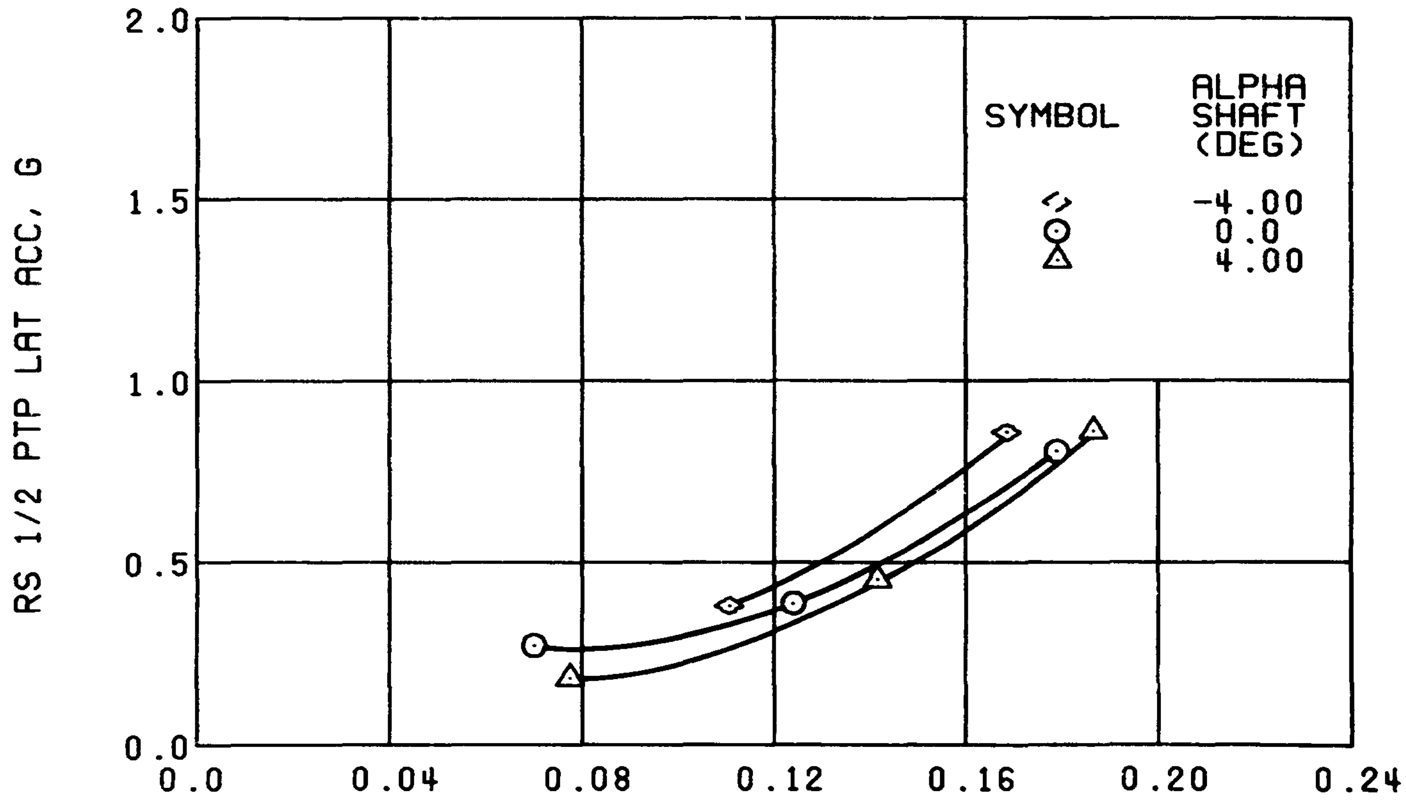

(w) GAGE 16 ROVER 3

Figure 56. Continued.
$\mu = 0.70$ $B'_{1s} = 4$ Deg

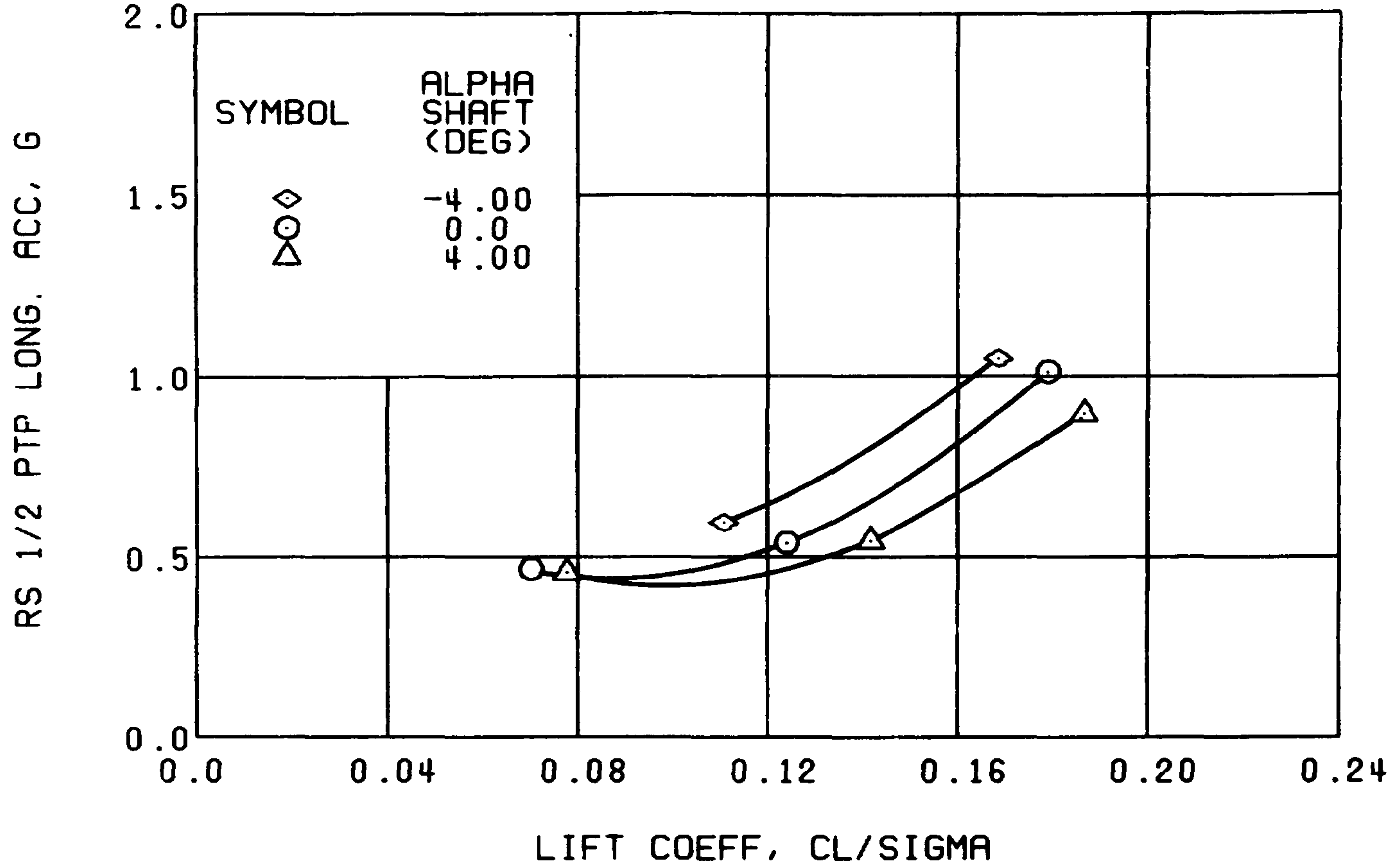

(x) GAGE 17 ROVER 4

Figure 56. Concluded.
$\mu = 0.70 \quad B'_{1s} = 4$ Deg

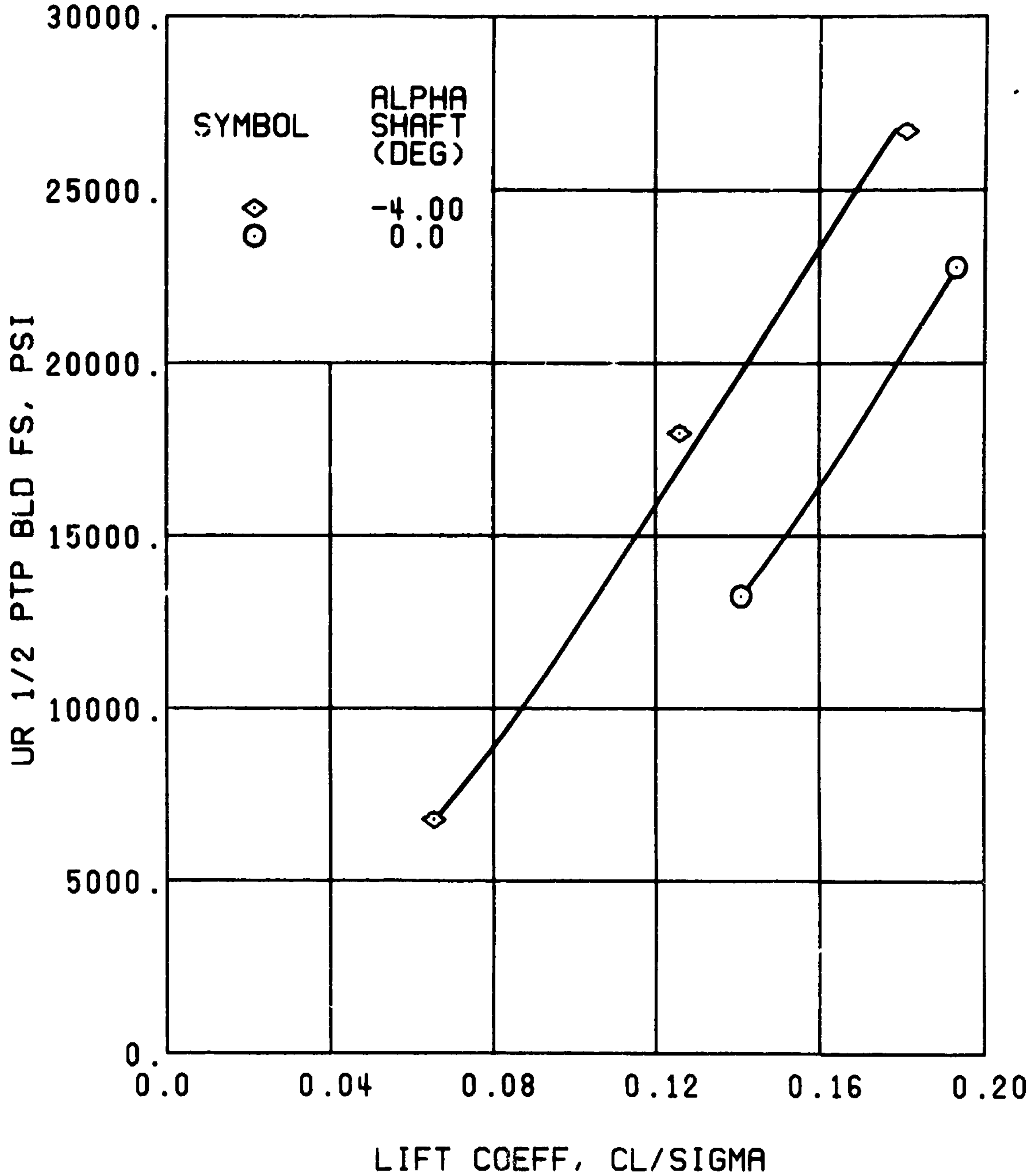

(a) GAGE 51 R84

Figure 57. Stress, Load, and Vibration Data at an Advance Ratio of 0.70 With the Lateral Displacement Control (B'_{1s}) Set at 6 Degrees.

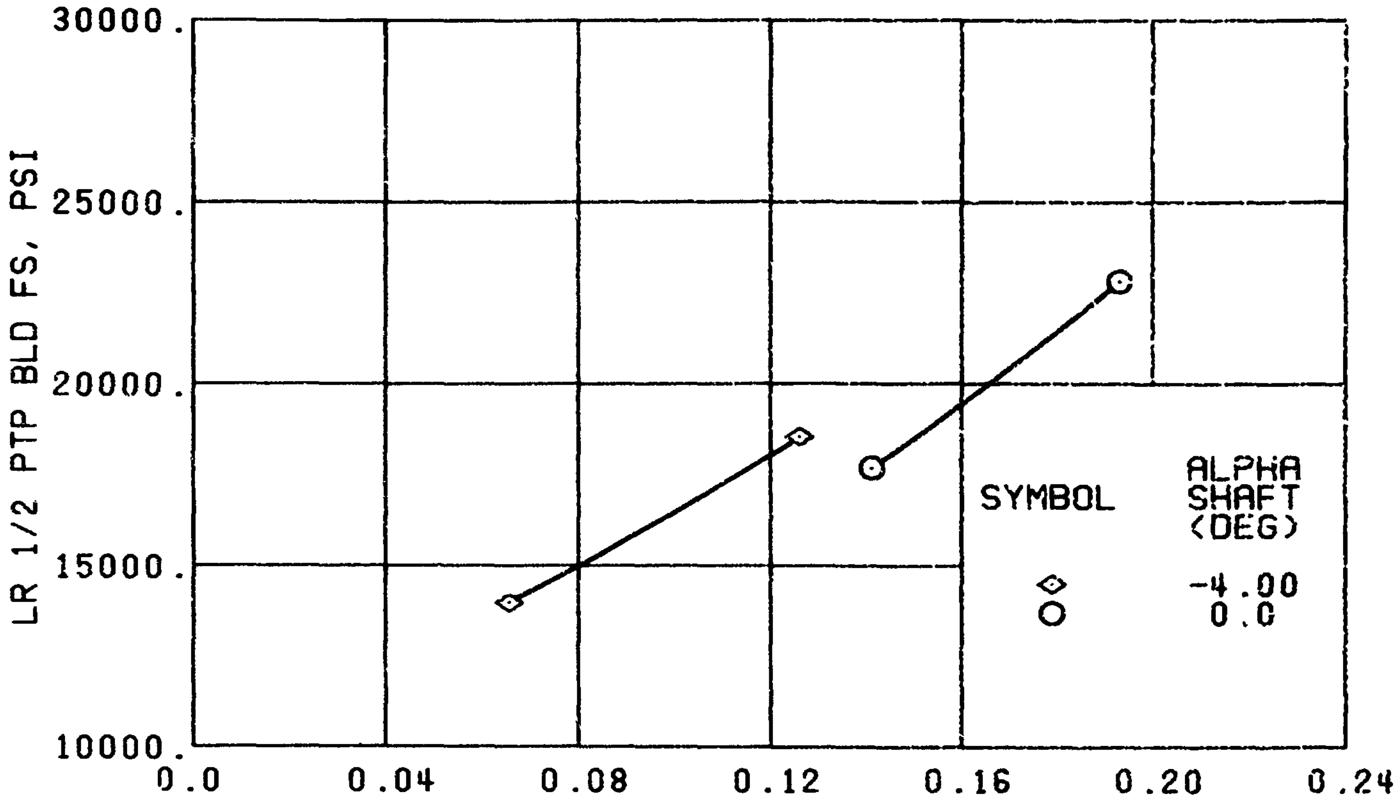

(b) GAGE 1 R84

Figure 57. Continued.
$\mu = 0.70 \quad B'_{1s} = 6$ Deg

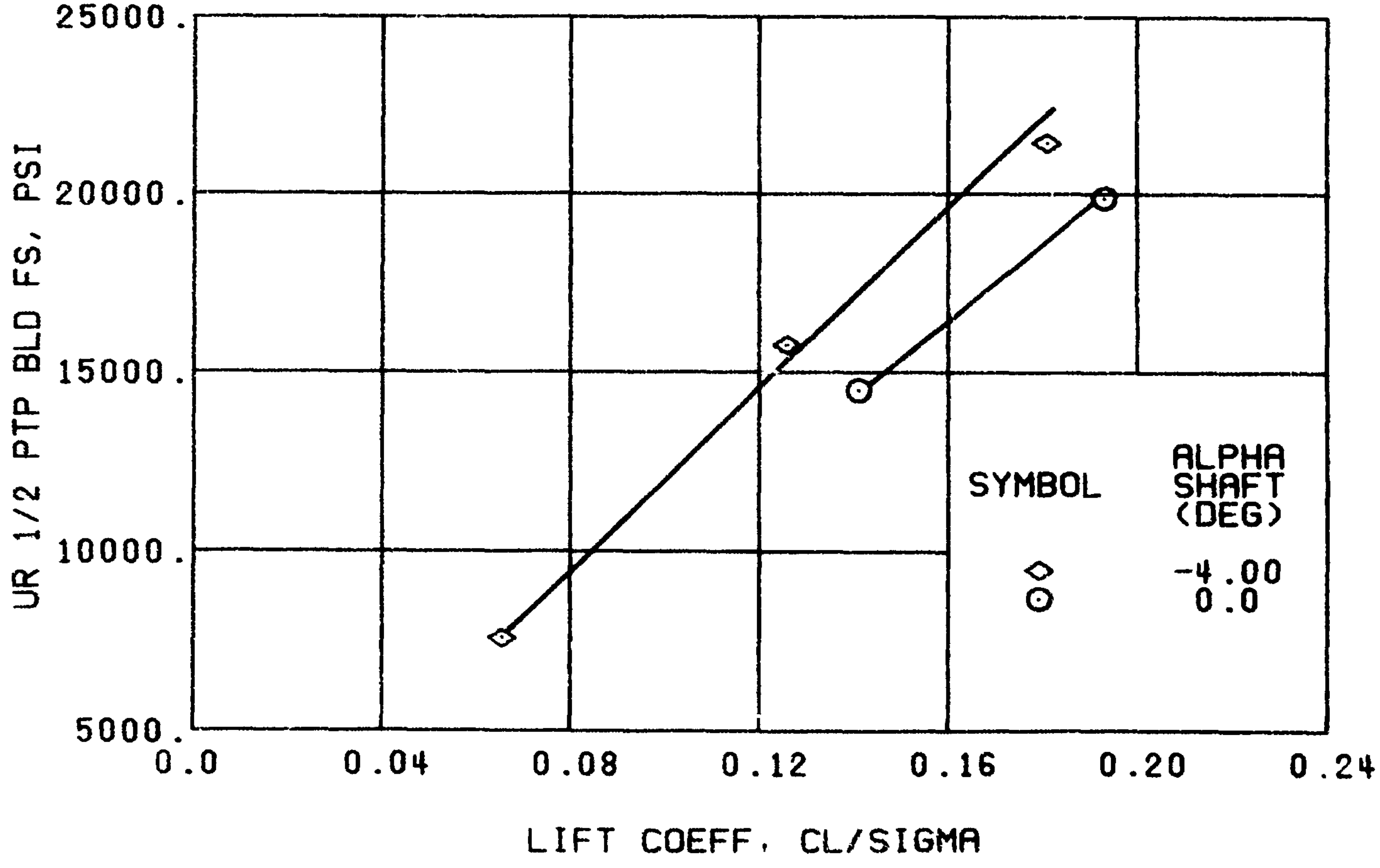

(c) GAGE 52 R108

Figure 57. Continued.
$\mu = 0.70$ $B'_{1s} = 6$ Deg

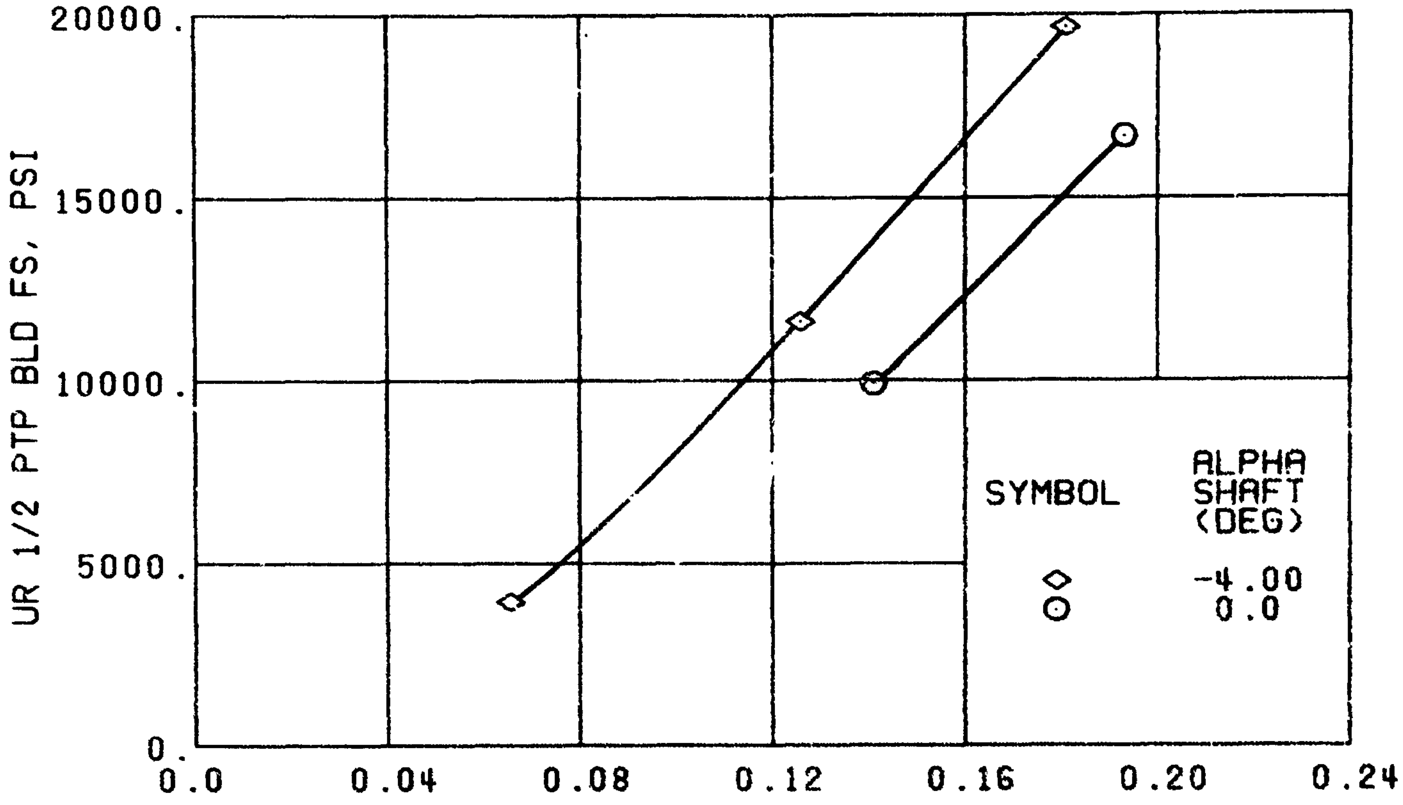

(d) GAGE 53 R132

Figure 57. Continued.
$\mu = 0.70$ $B'_{1s} = 6$ Deg

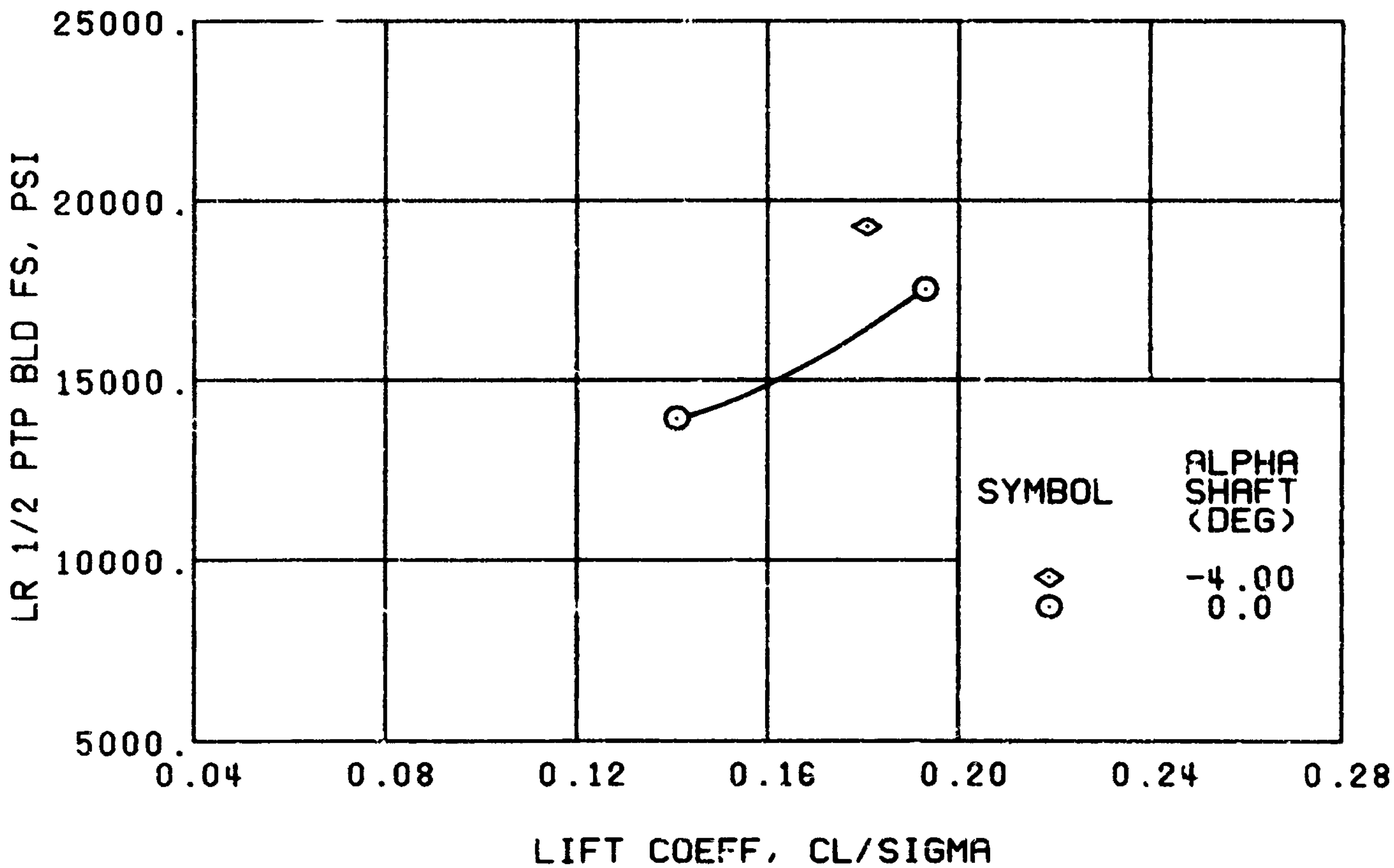

(e) GAGE 93 R132

Figure 57. Continued.
μ = 0.70 B'_{1s} = 6 Deg

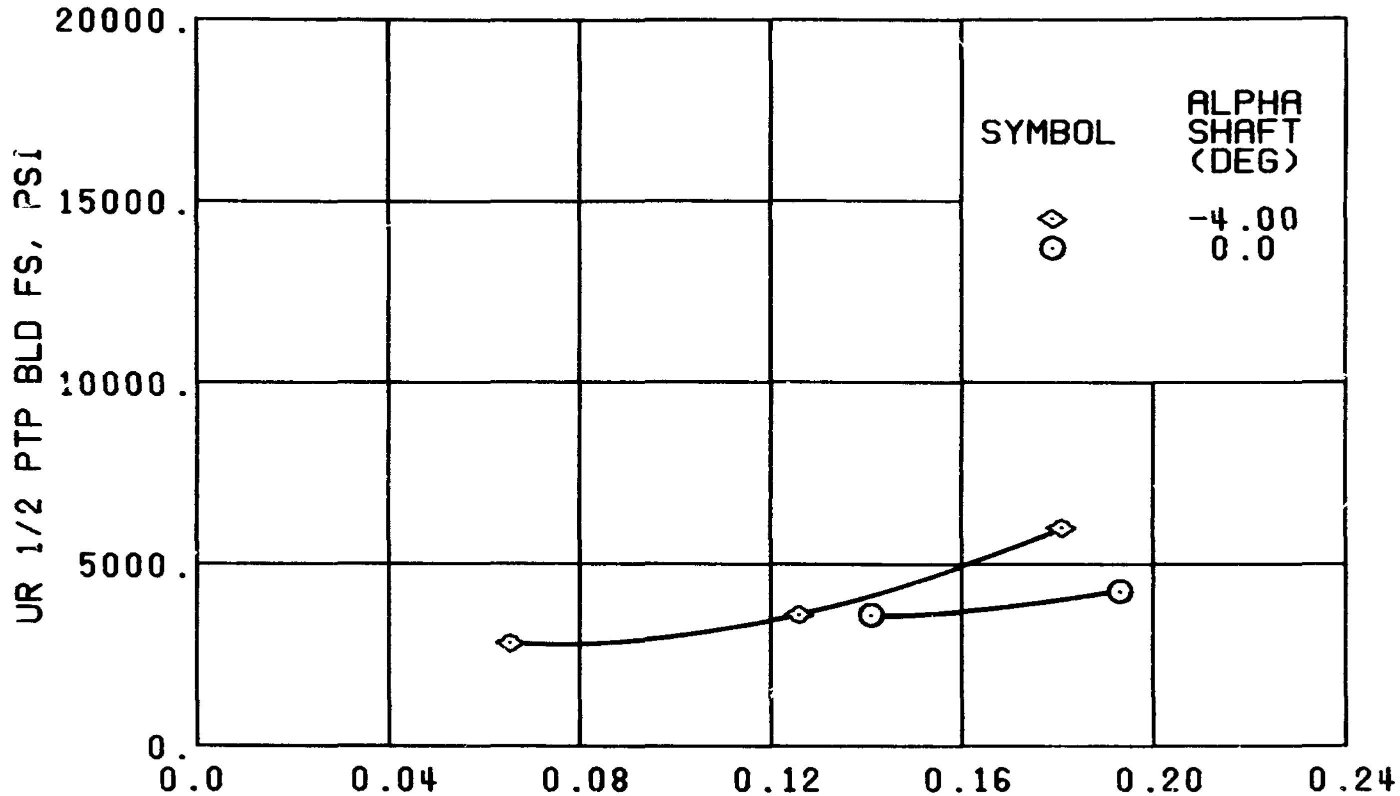

(f) GAGE 55 R204

Figure 57. Continued.
$\mu = 0.70 \quad B'_{1s} = 6$ Deg

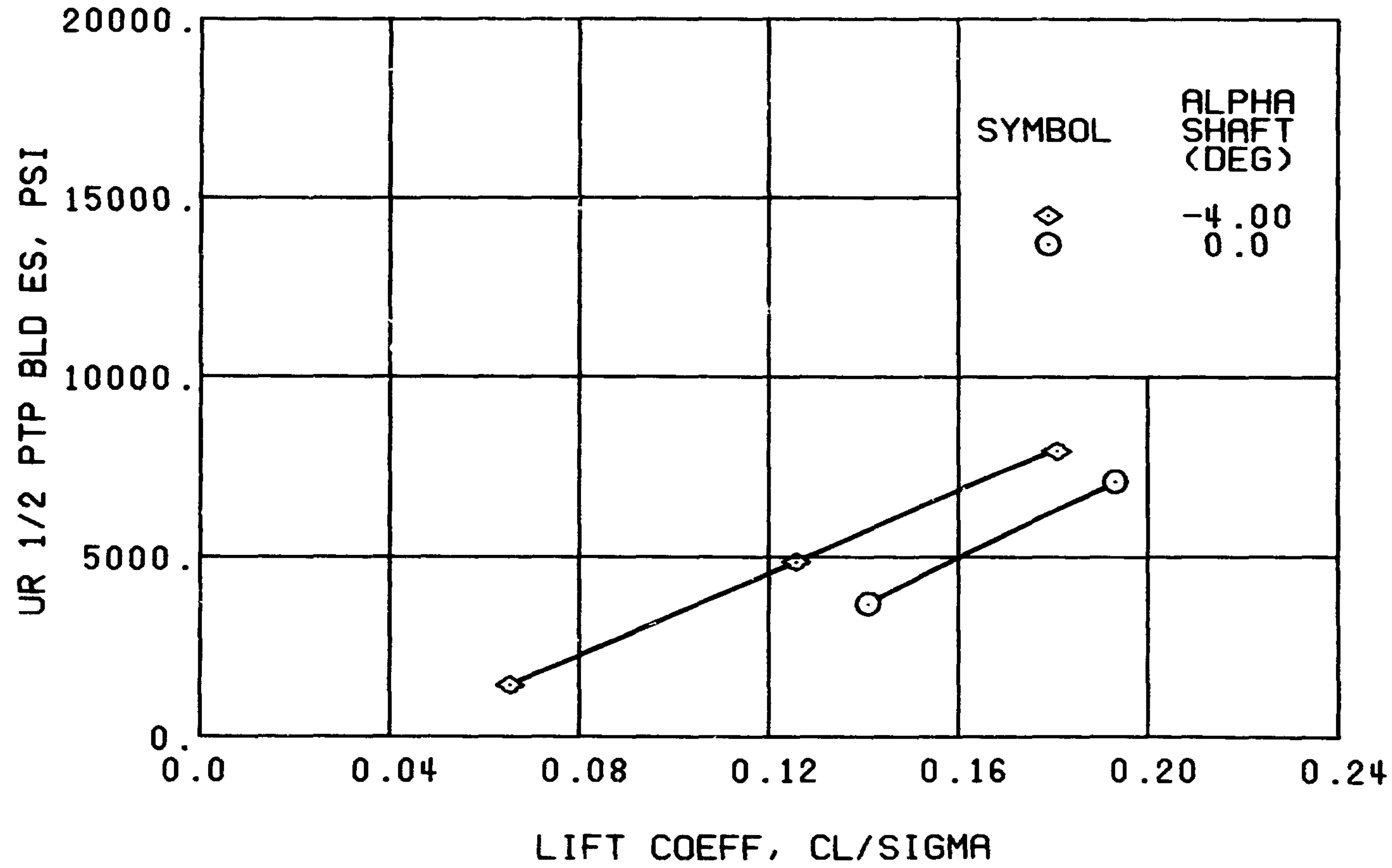

(h) GAGE 40 R84

Figure 57. Continued.
$\mu = 0.70 \quad B'_{1s} = 6$ Deg

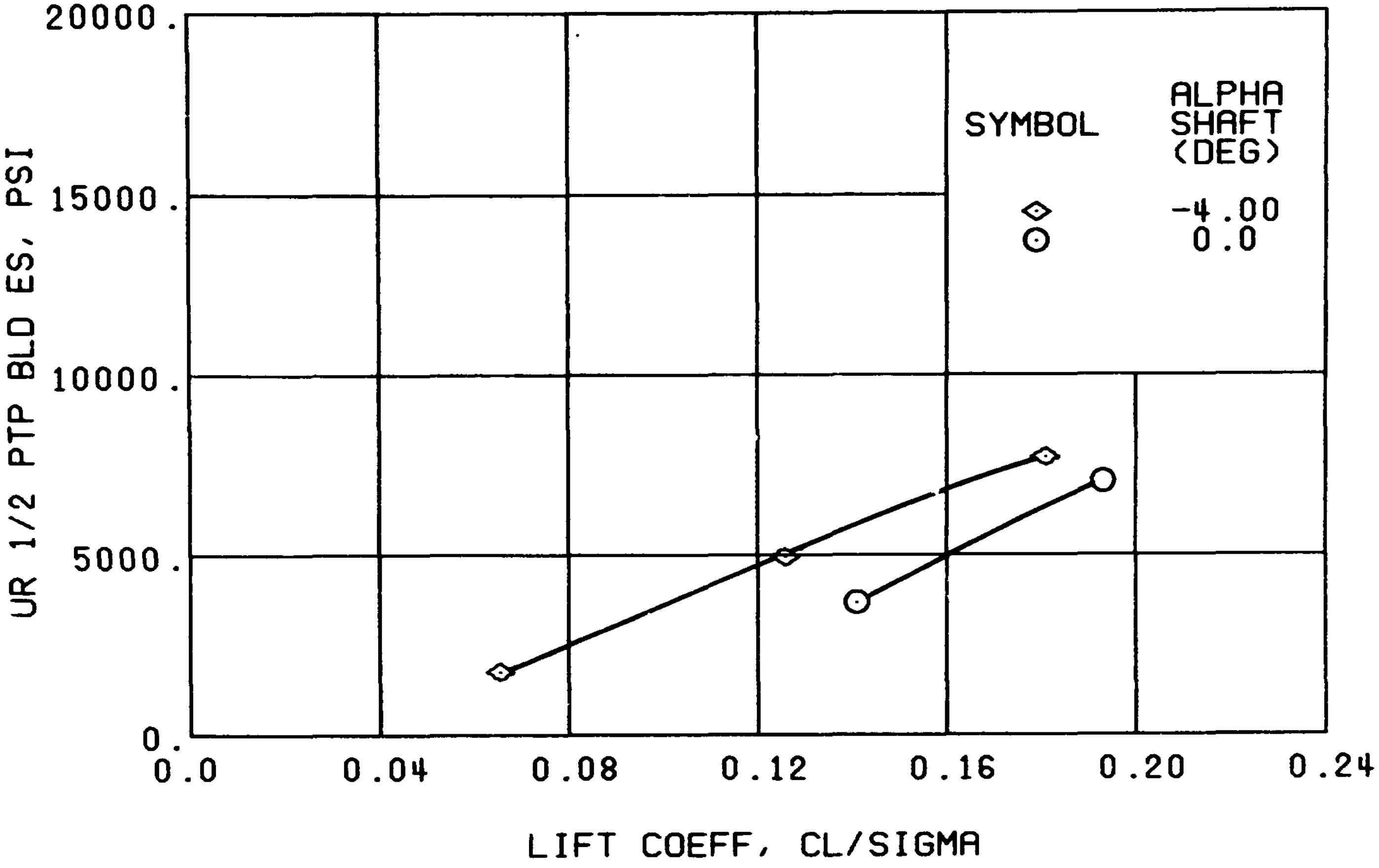

(j) GAGE 42 R132

Figure 57. Continued.
μ = 0.70 B'_{1s} = 6 Deg

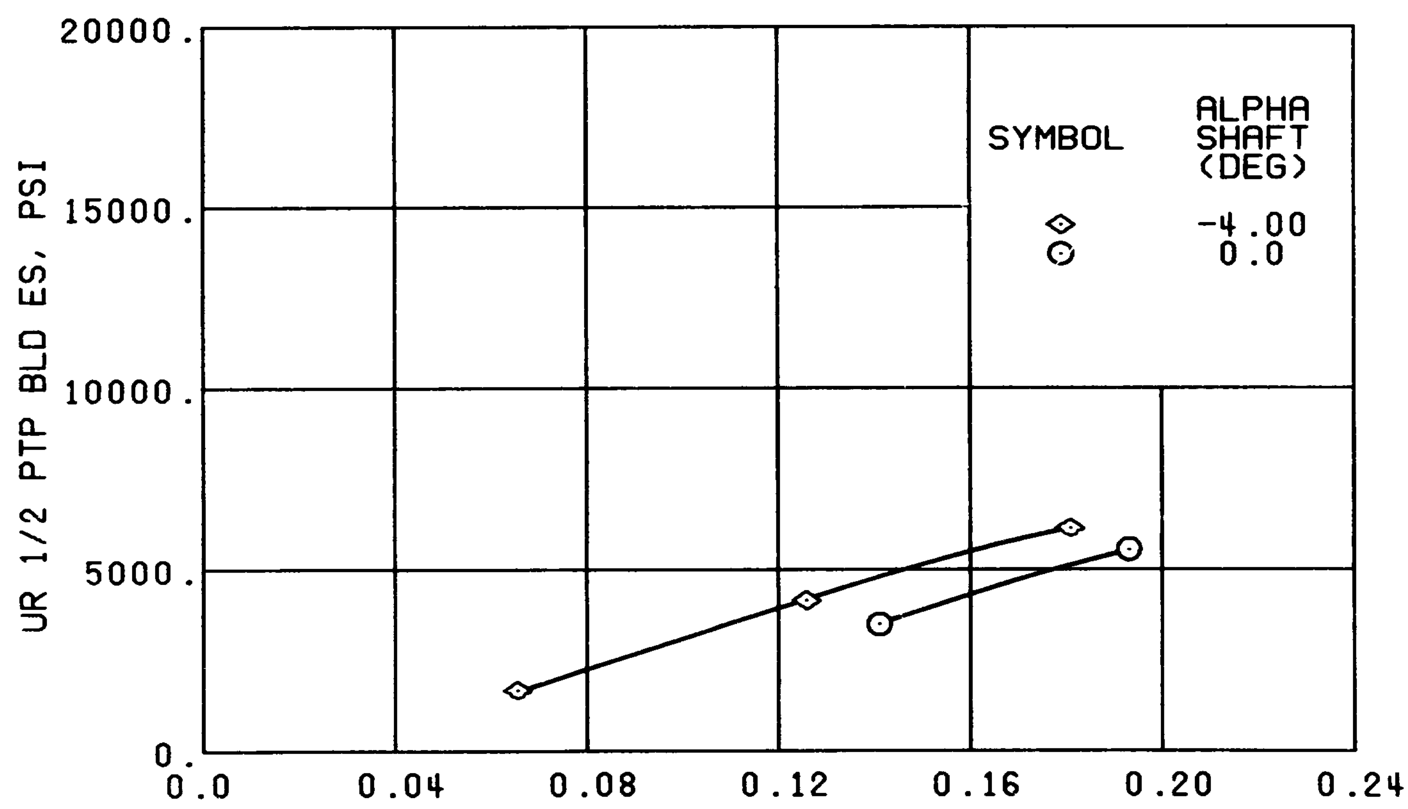

(k) GAGE 43 R168

Figure 57. Continued.
$\mu = 0.70$ $B'_{1s} = 6$ Deg

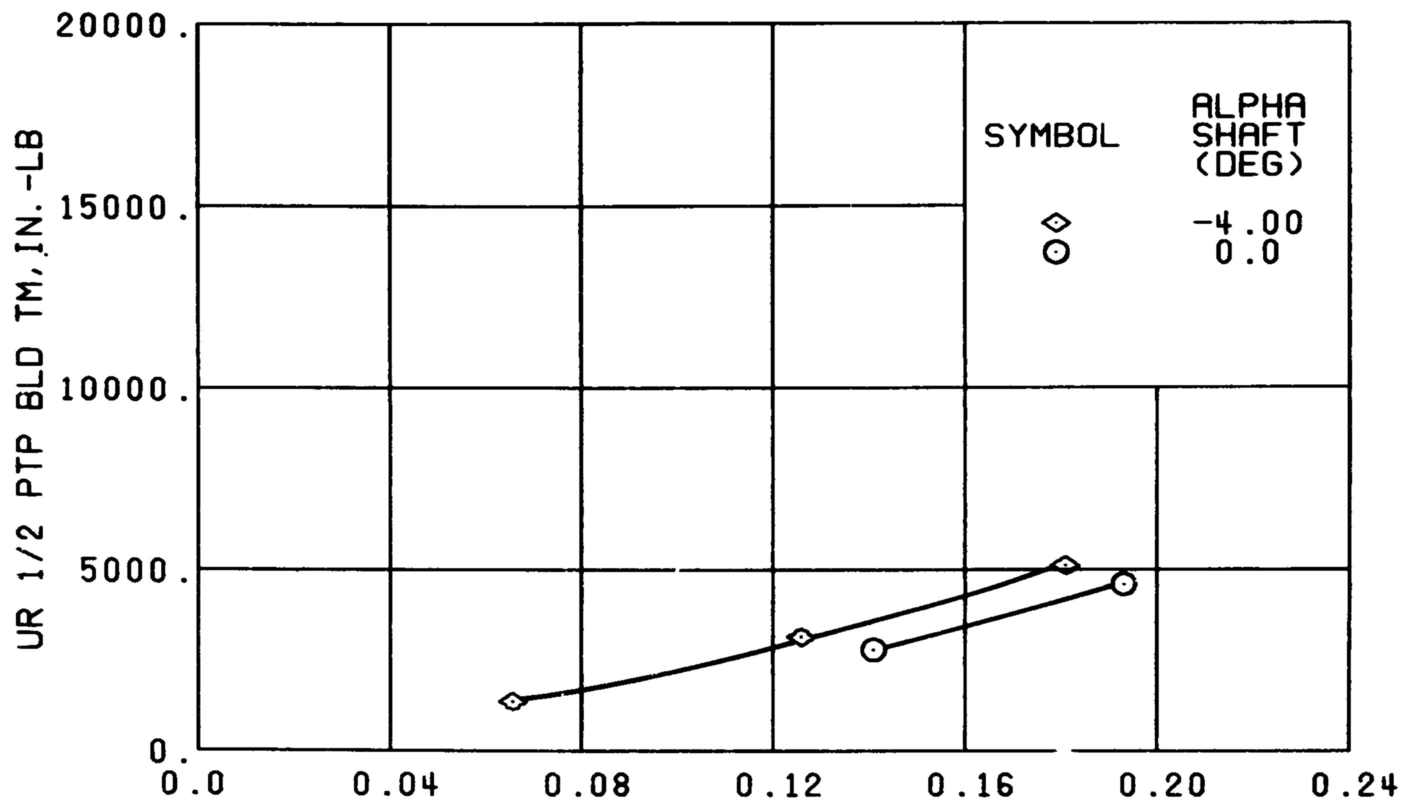

(m) GAGE 46 R130

Figure 57. Continued.
$\mu = 0.70 \quad B'_{1s} = 6$ Deg

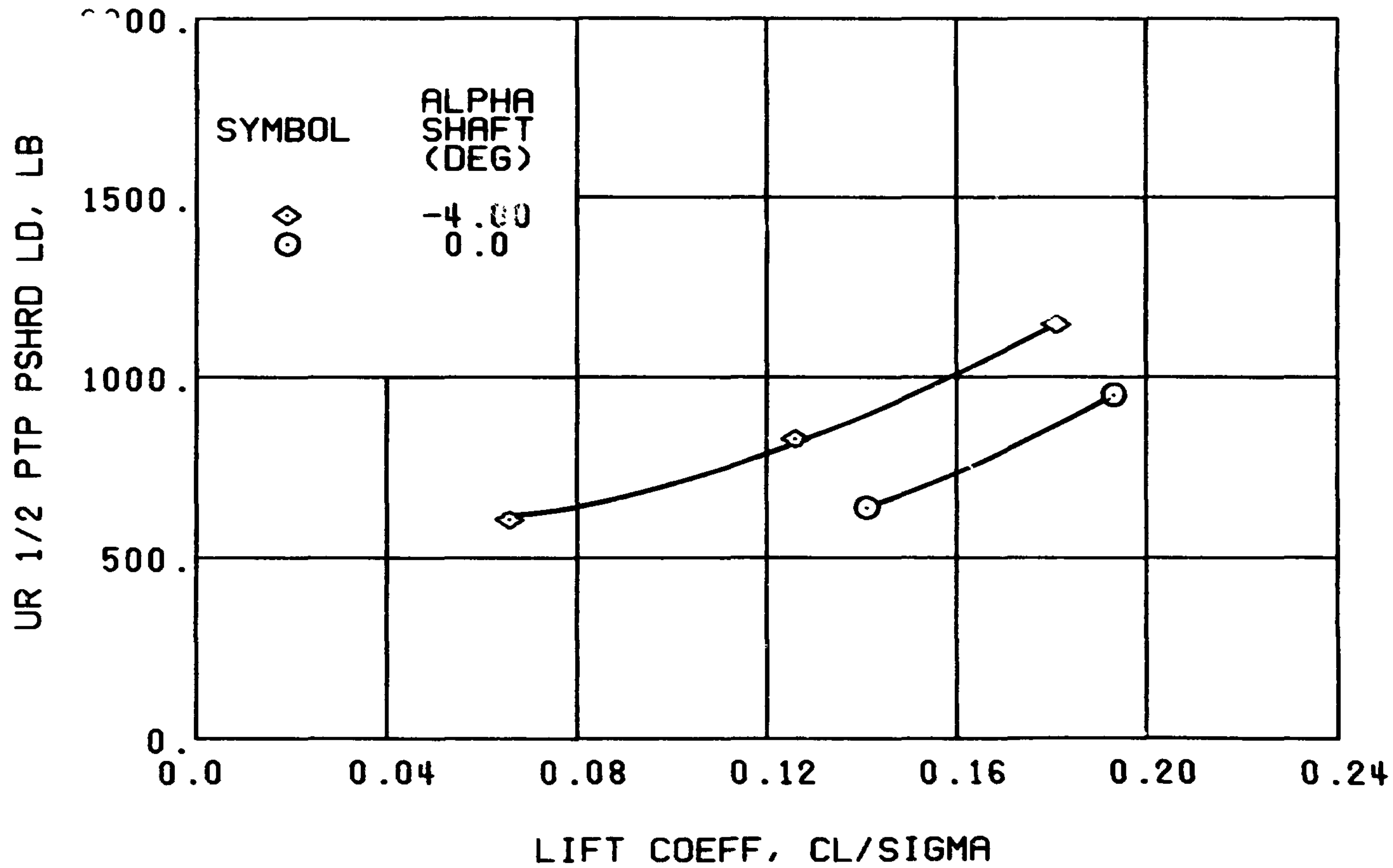

(n) GAGE 37

Figure 57. Continued.
$\mu = 0.70$ $B'_{1s} = 6$ Deg

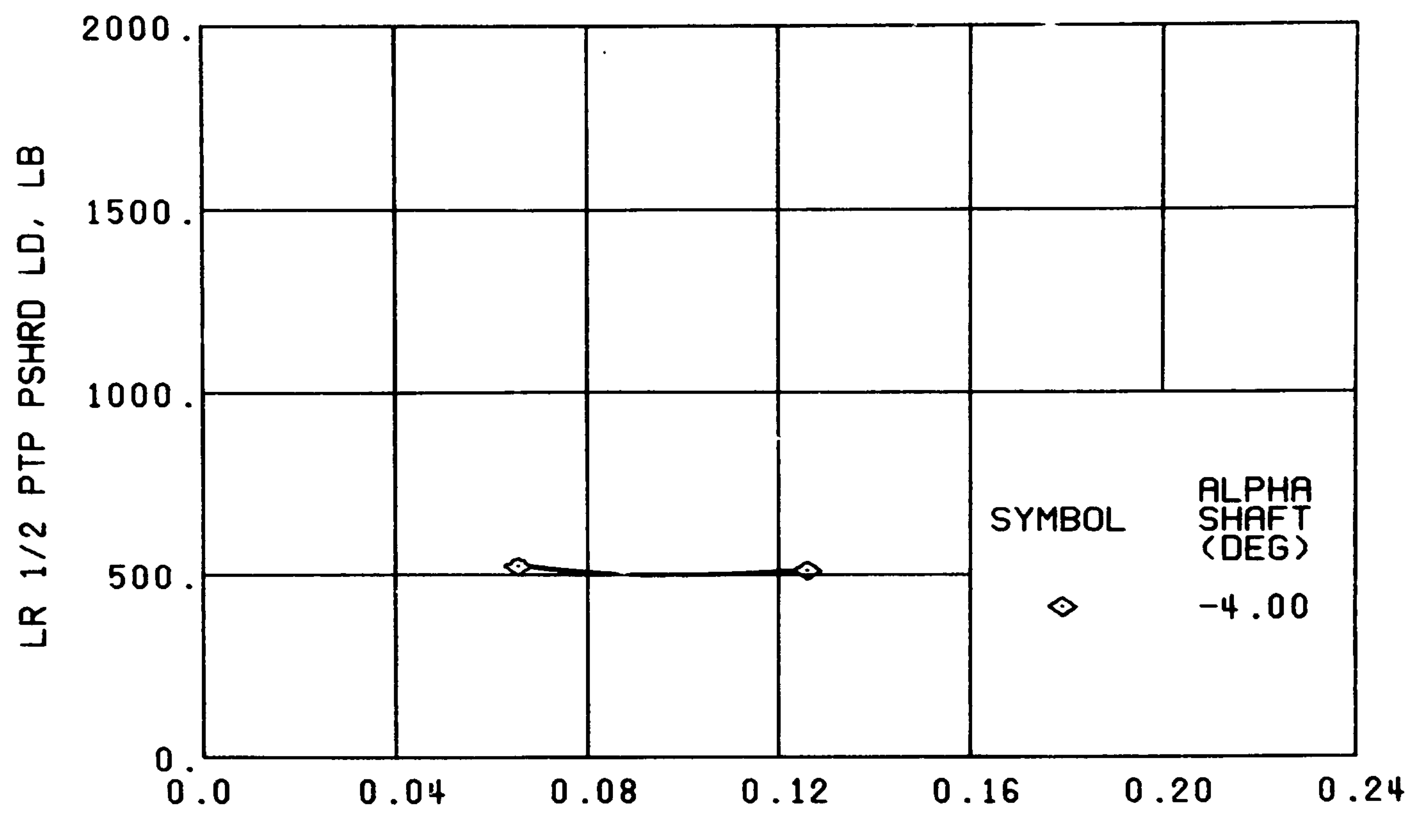

(o) GAGE 34

Figure 57. Continued.
$\mu = 0.70$ $B'_{1s} = 6$ Deg

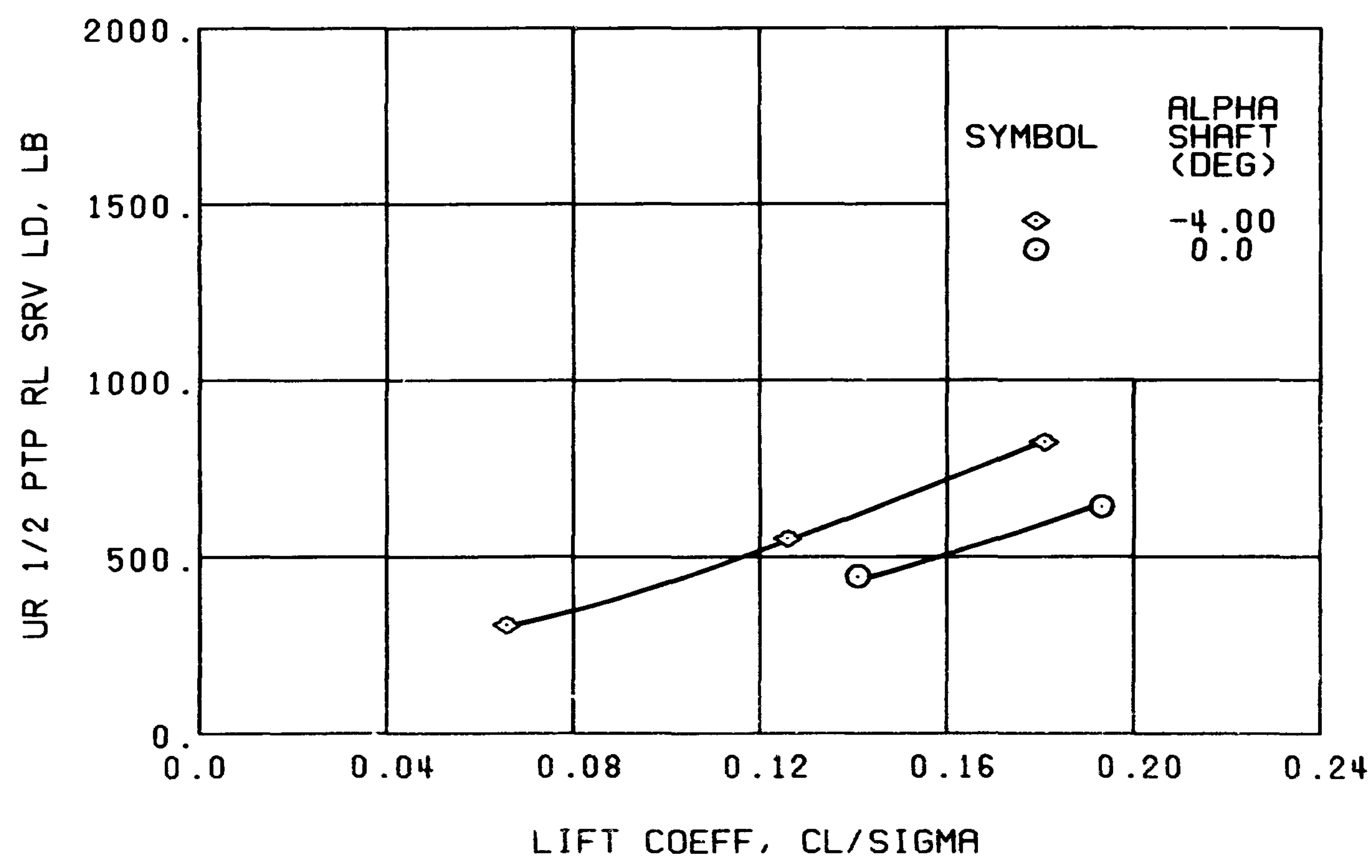

(p) GAGE 22

Figure 57. Continued.
μ = 0.70 B'_{1s} = 6 Deg

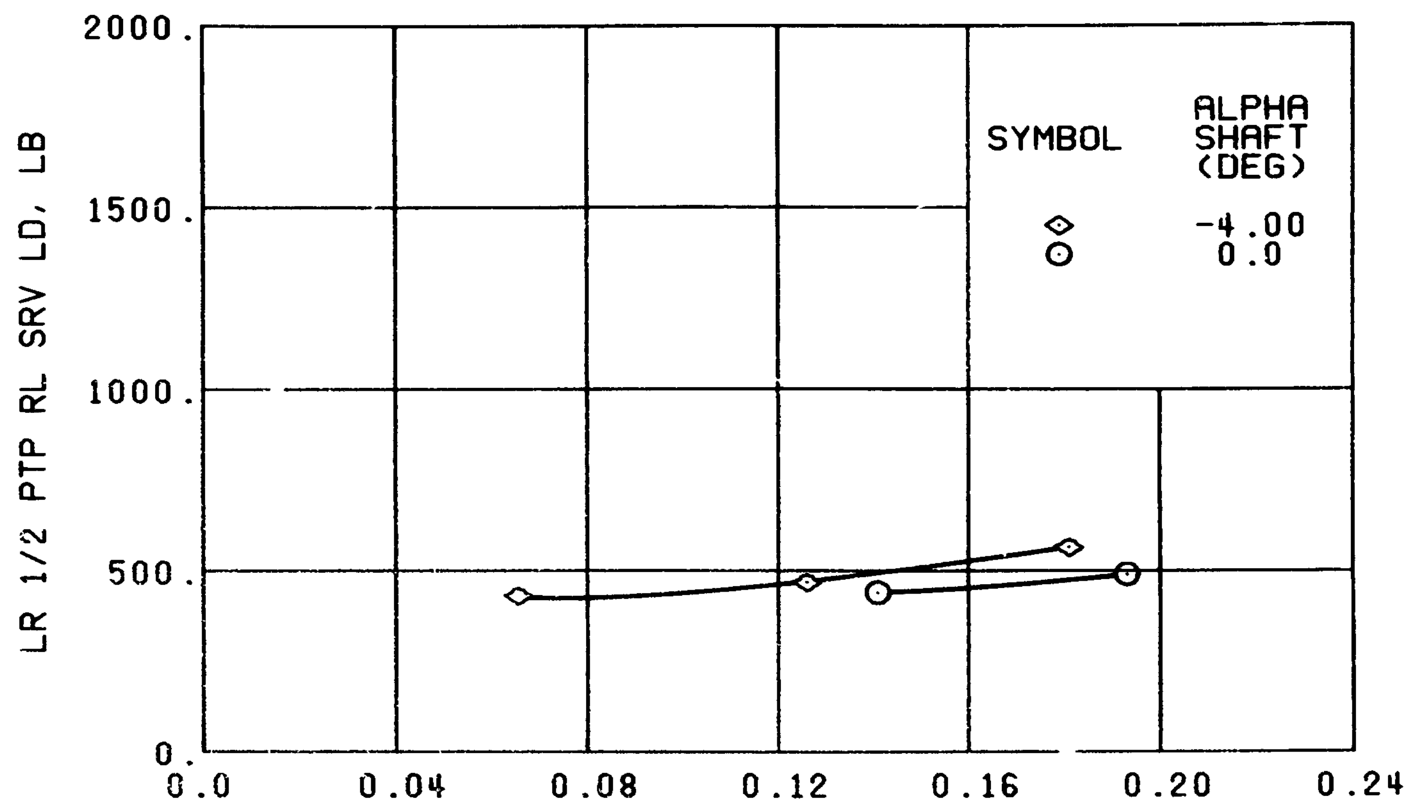

(q) GAGE 25

Figure 57. Continued.
$\mu = 0.70 \quad B'_{1s} = 6$ Deg

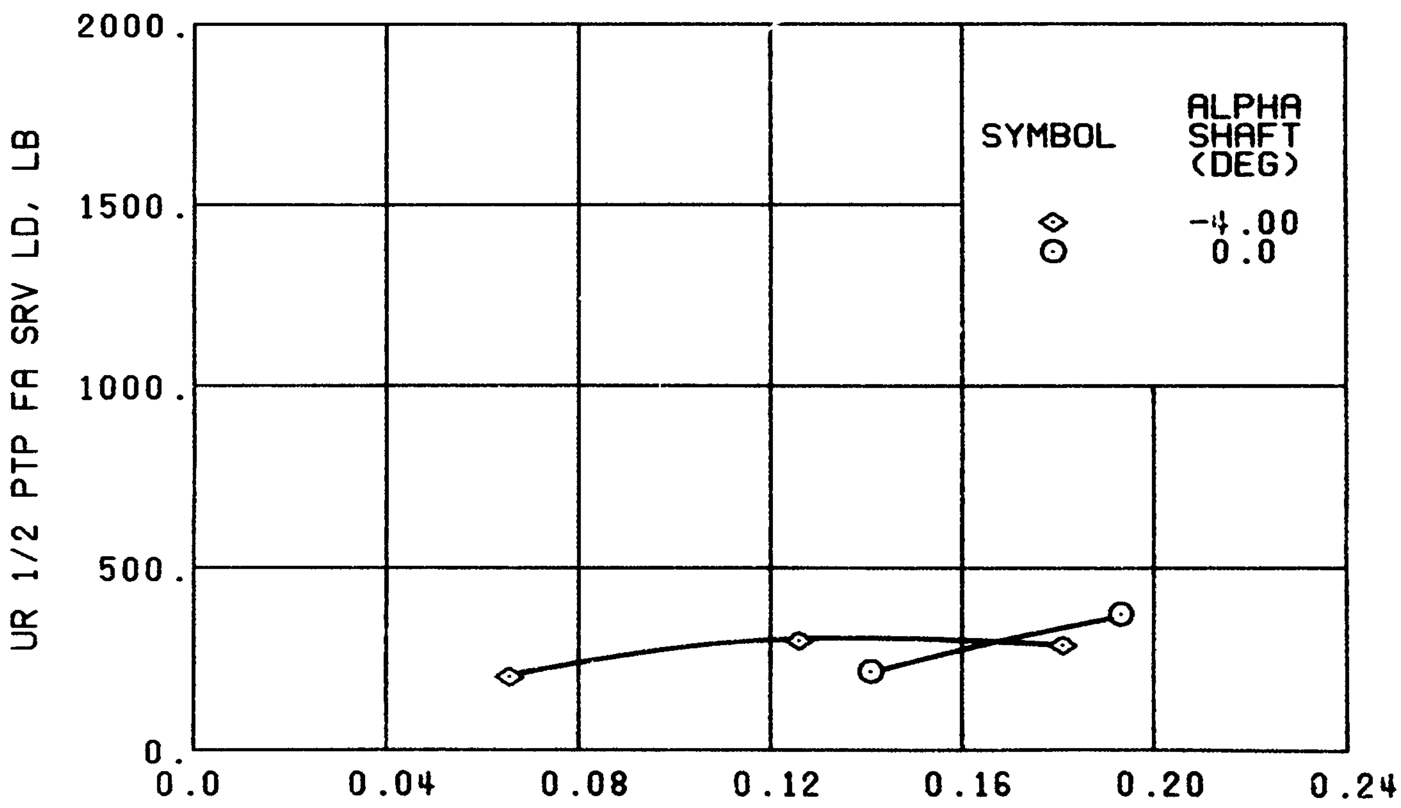

(r) GAGE 24

Figure 57. Continued.
$\mu = 0.70 \quad B'_{1s} = 6$ Deg

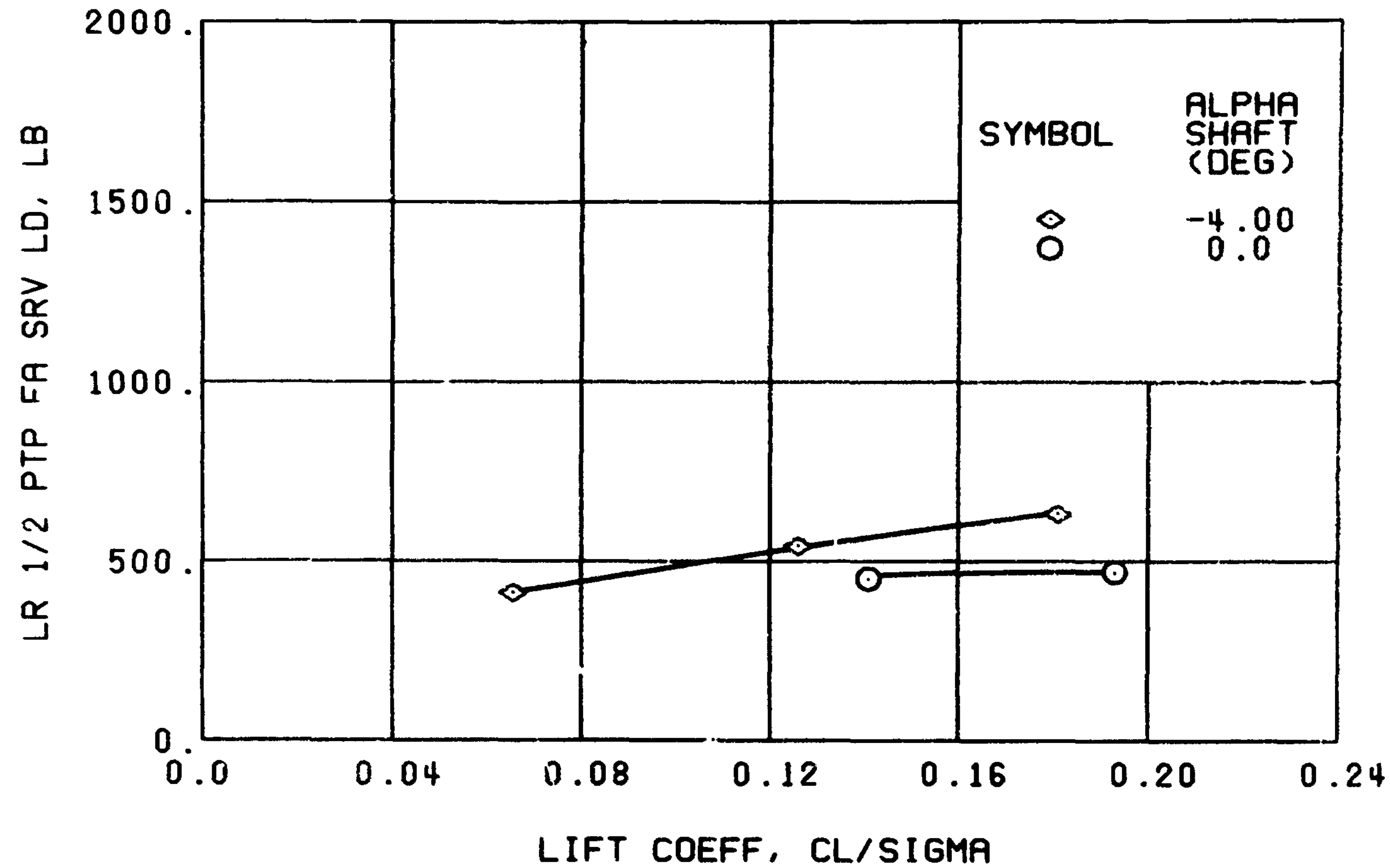

(s) GAGE 27

Figure 57. Continued.
$\mu = 0.70$ $B'_{1s} = 6$ Deg

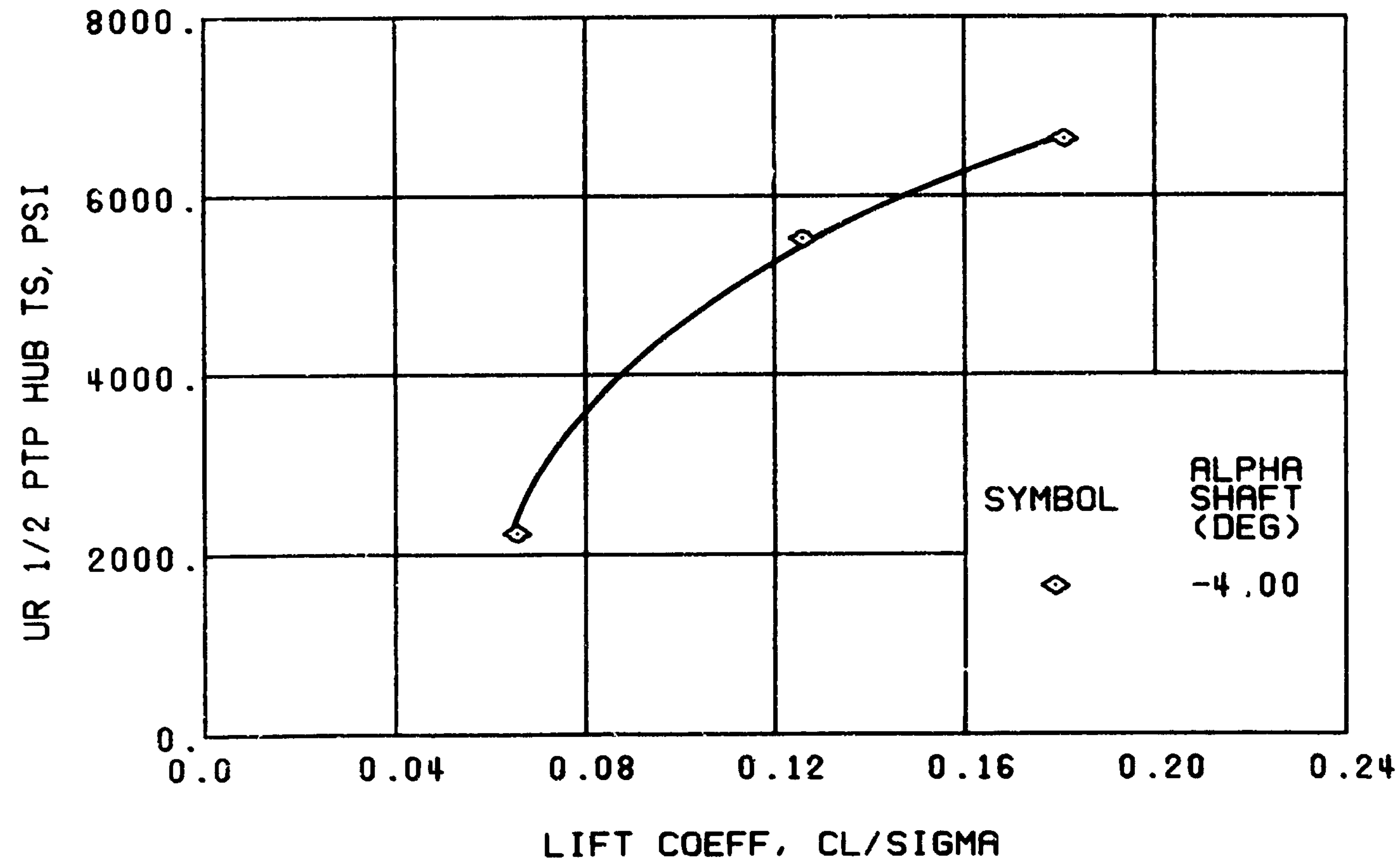

(f) GAGE 65

Figure 57. Continued.
$\mu = 0.70 \quad B'_{1s} = 6$ Deg

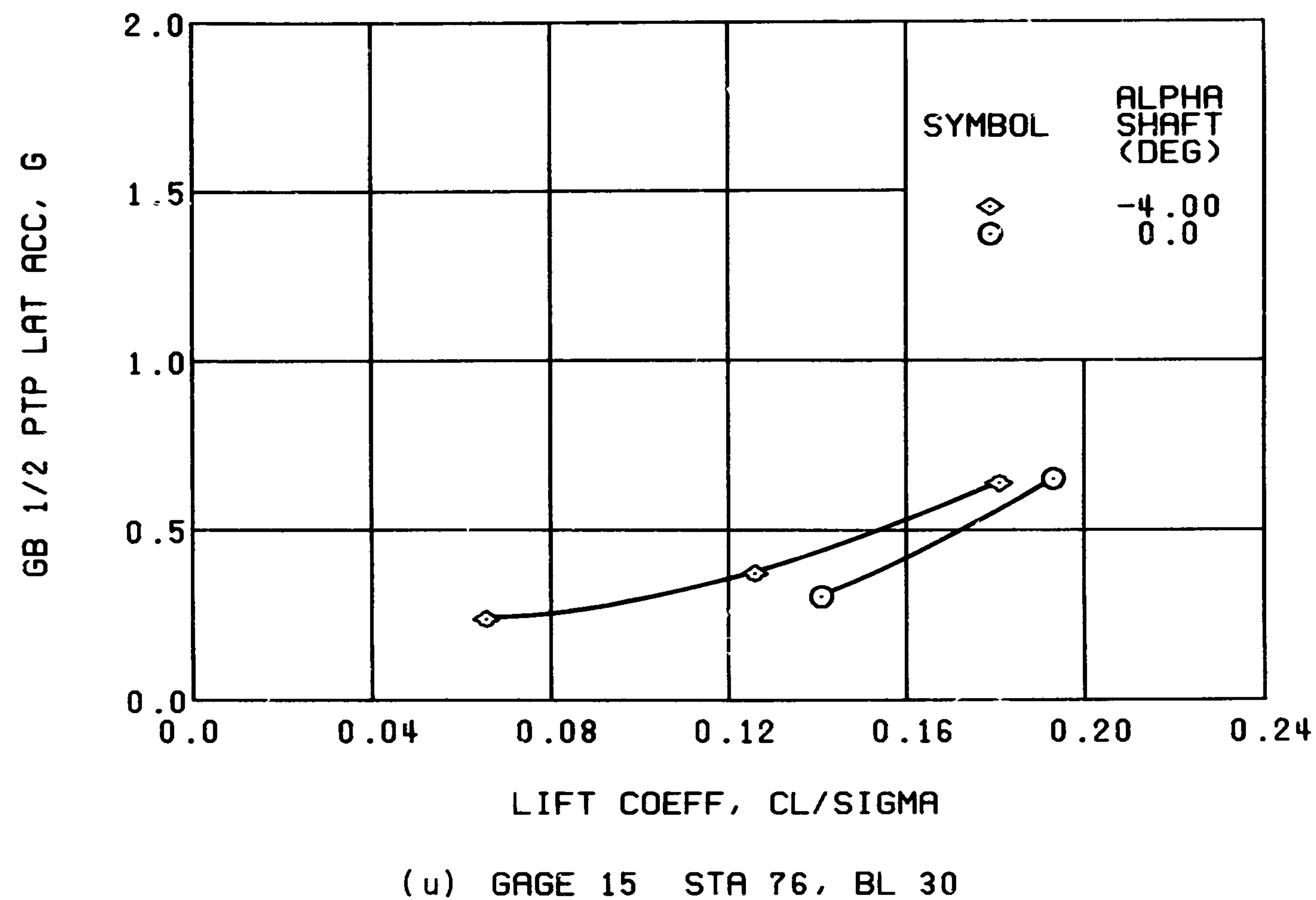

Figure 57. Continued.
$\mu = 0.70 \quad B'_{1s} = 6$ Deg

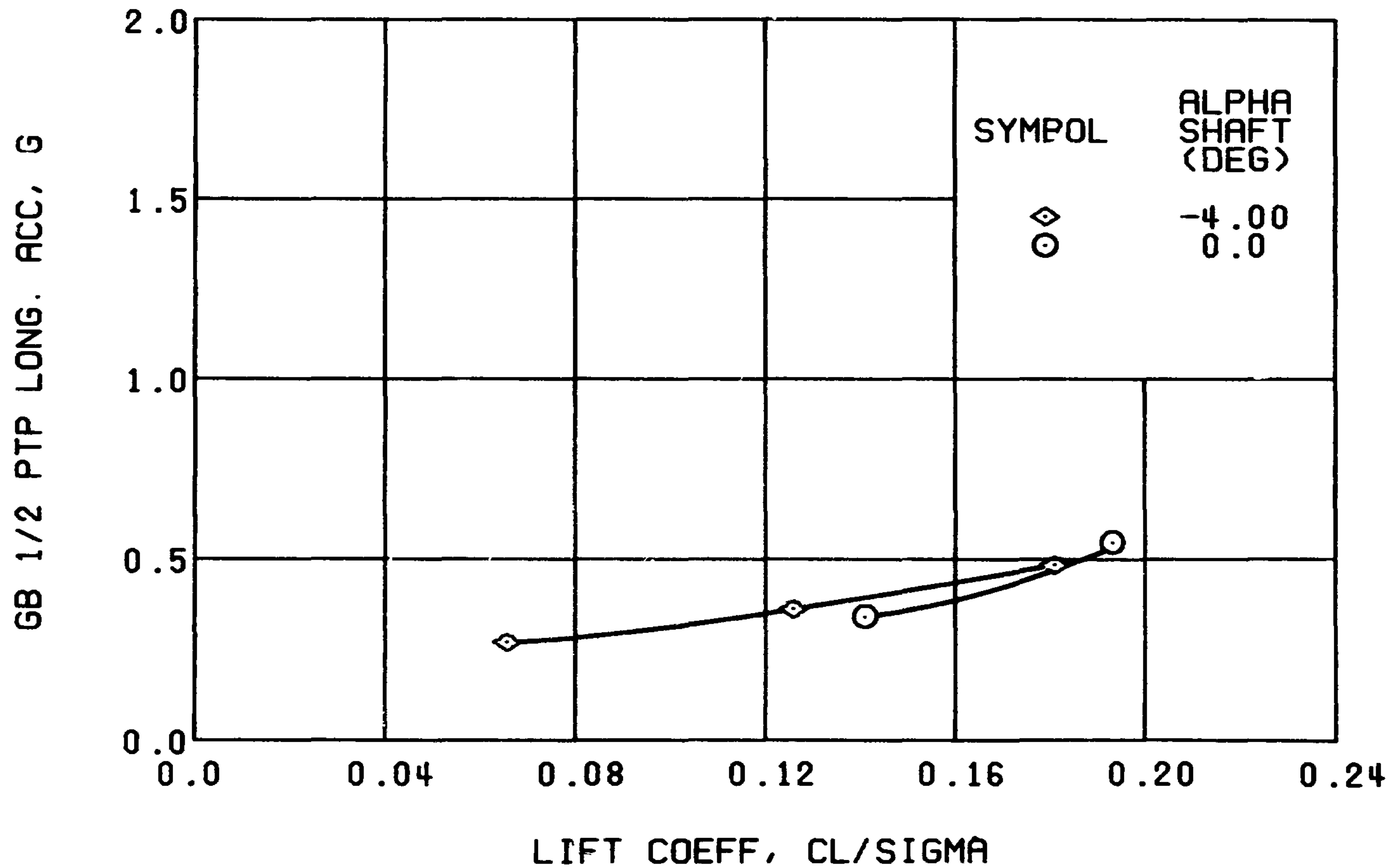

(v) GAGE 14 STA 61, BL 0

Figure 57. Continued.
$\mu = 0.70$ $B'_{1s} = 6$ Deg

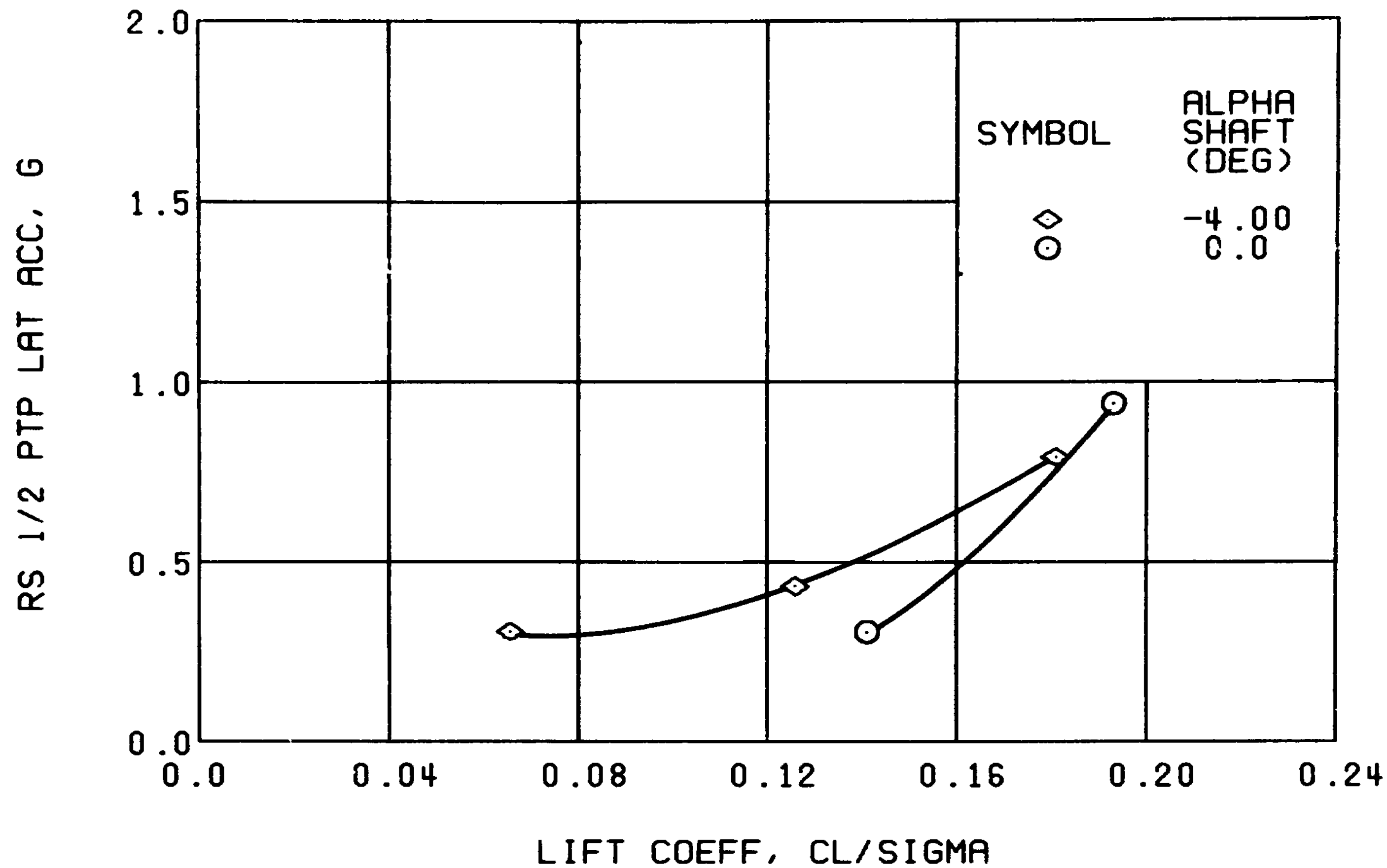

(w) GAGE 16 ROVER 3

Figure 57. Continued.
$\mu = 0.70$ $B'_{1s} = 6$ Deg

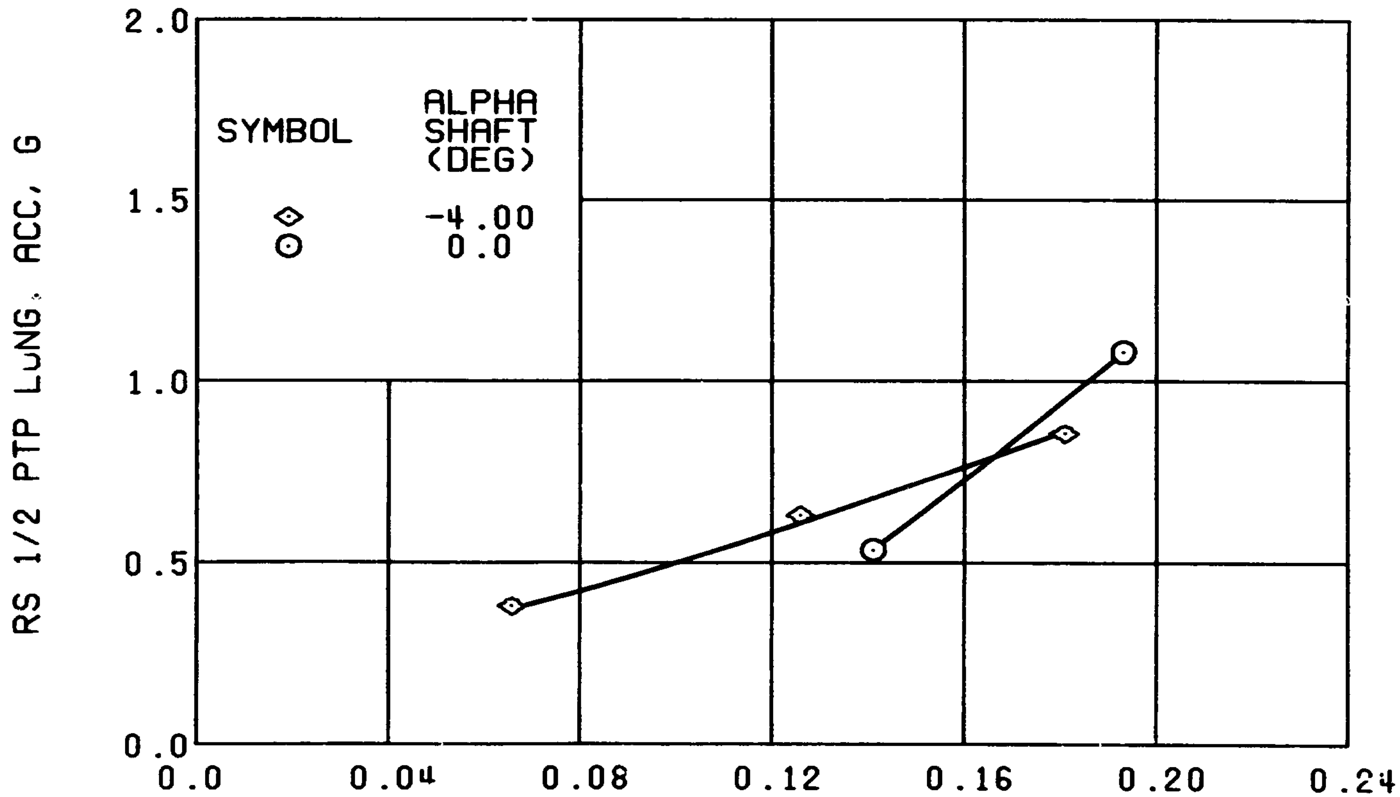

(x) GAGE 17 ROVER 4

Figure 57. Concluded.
$\mu = 0.70$ $B'_{1s} = 6$ Deg

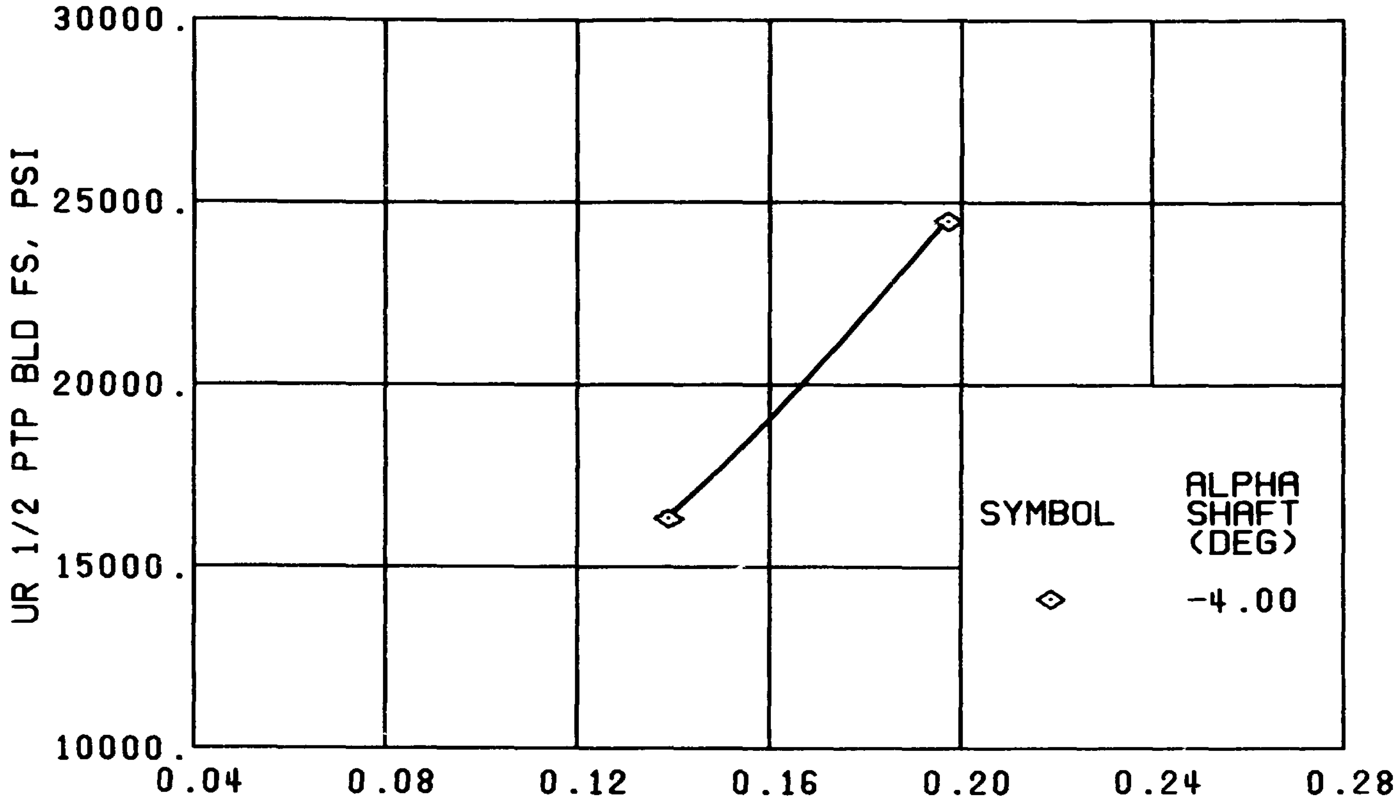

(a) GAGE 51 R84

Figure 58. Stress, Load, and Vibration Data at an Advance Ratio of 0.70 With the Lateral Displacement Control (B'_{1s}) Set at 8 Degrees.

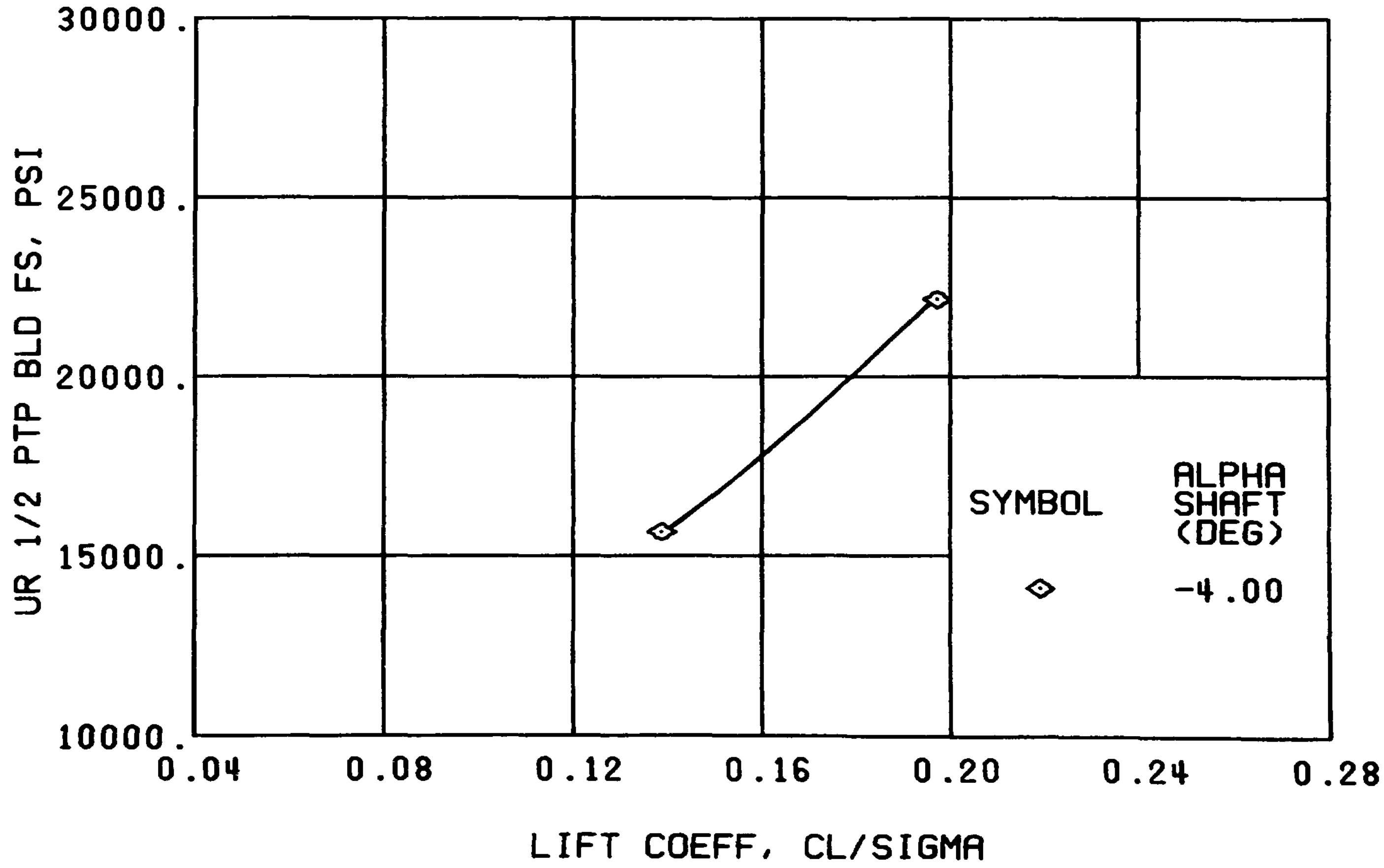

(c) GAGE 52 R108

Figure 58. Continued.
$\mu = 0.70$ $B'_{1s} = 8$ Deg

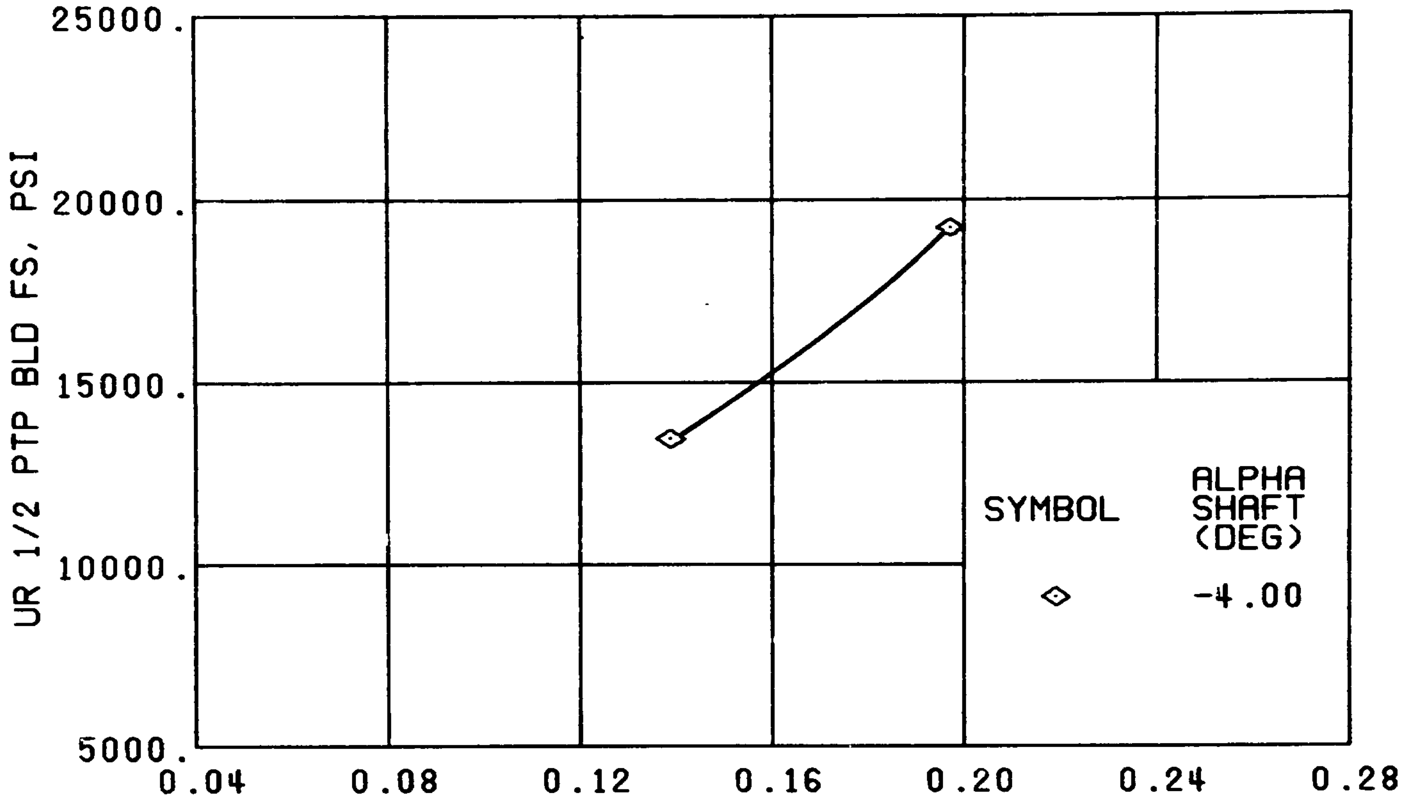

(d) GAGE 53 R132

Figure 58. Continued.
$\mu = 0.70$ $B'_{1s} = 8$ Deg

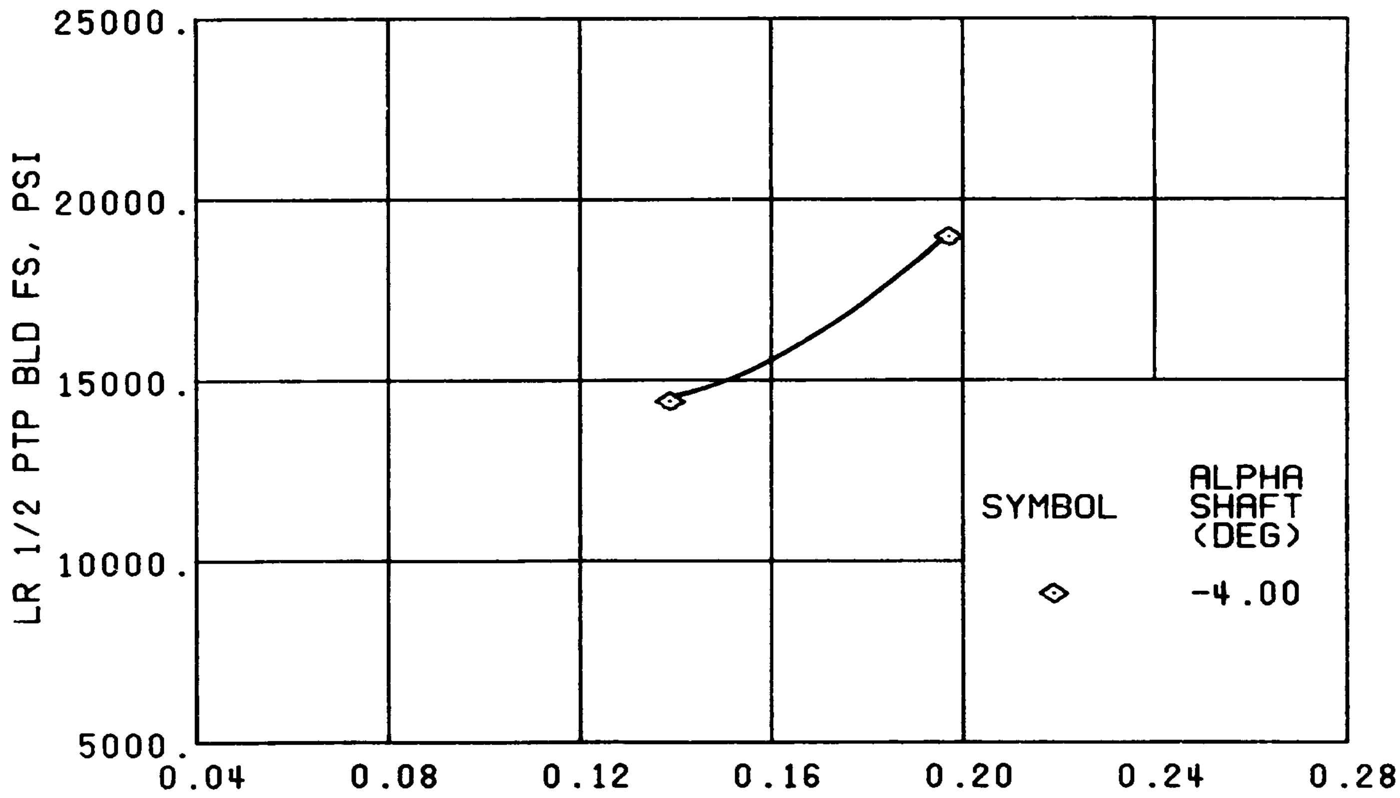

(e) GAGE 93 R132

Figure 58. Continued.
$\mu = 0.70$ $B'_{1s} = 8$ Deg

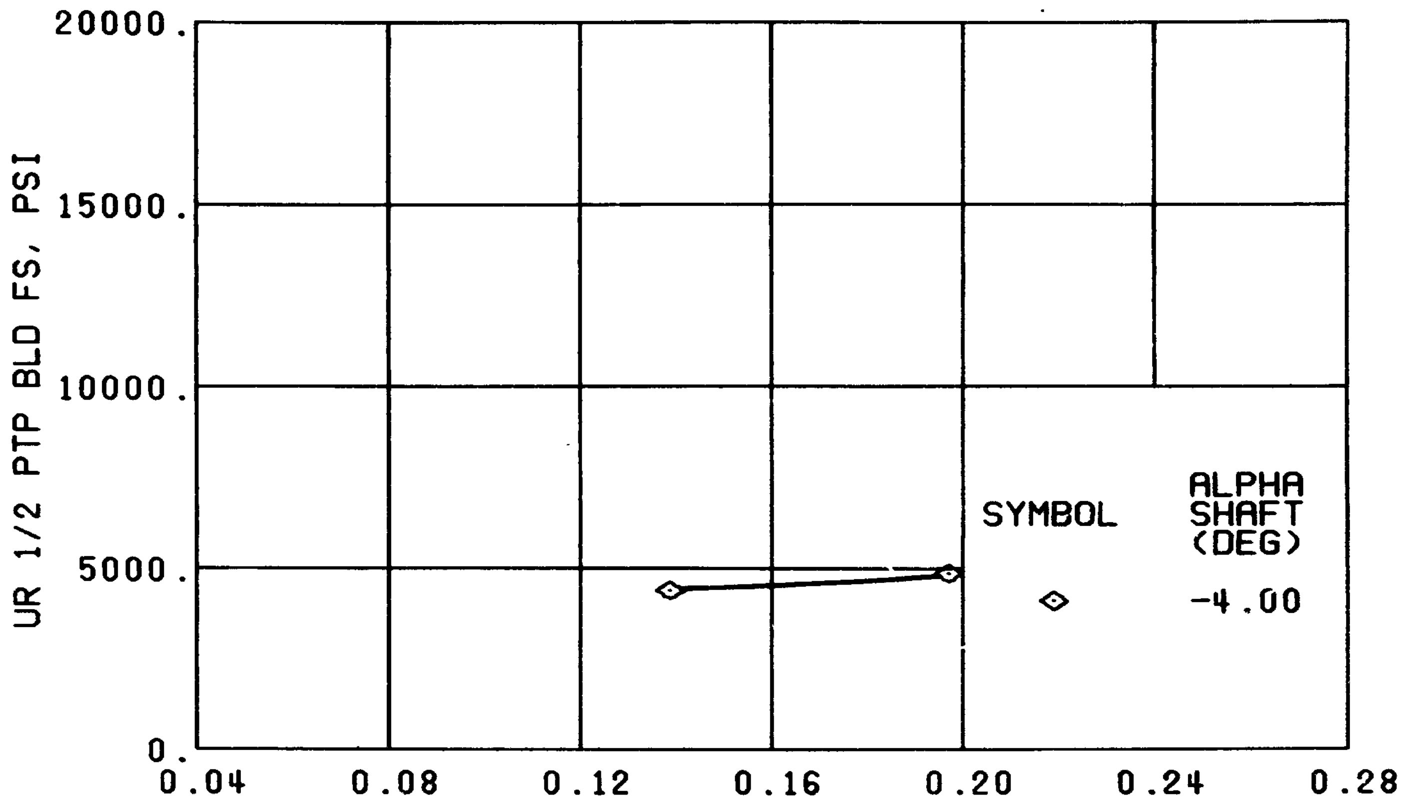

(f) GAGE 55 R204

Figure 58. Continued.
$\mu = 0.70$ $B'_{1s} = 8$ Deg

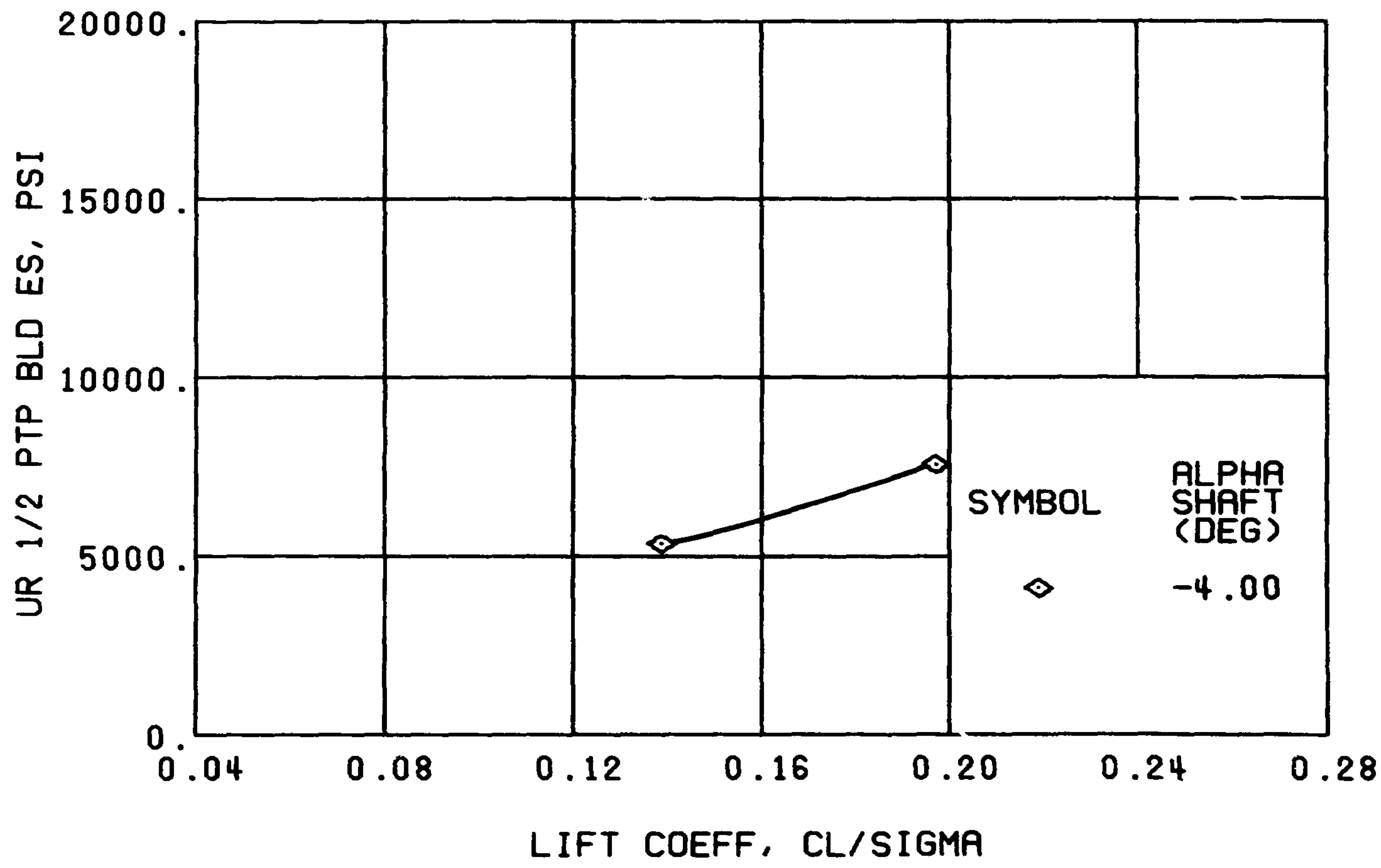

(h) GAGE 40 R84

Figure 58. Continued.
$\mu = 0.70 \quad B'_{1s} = 8$ Deg

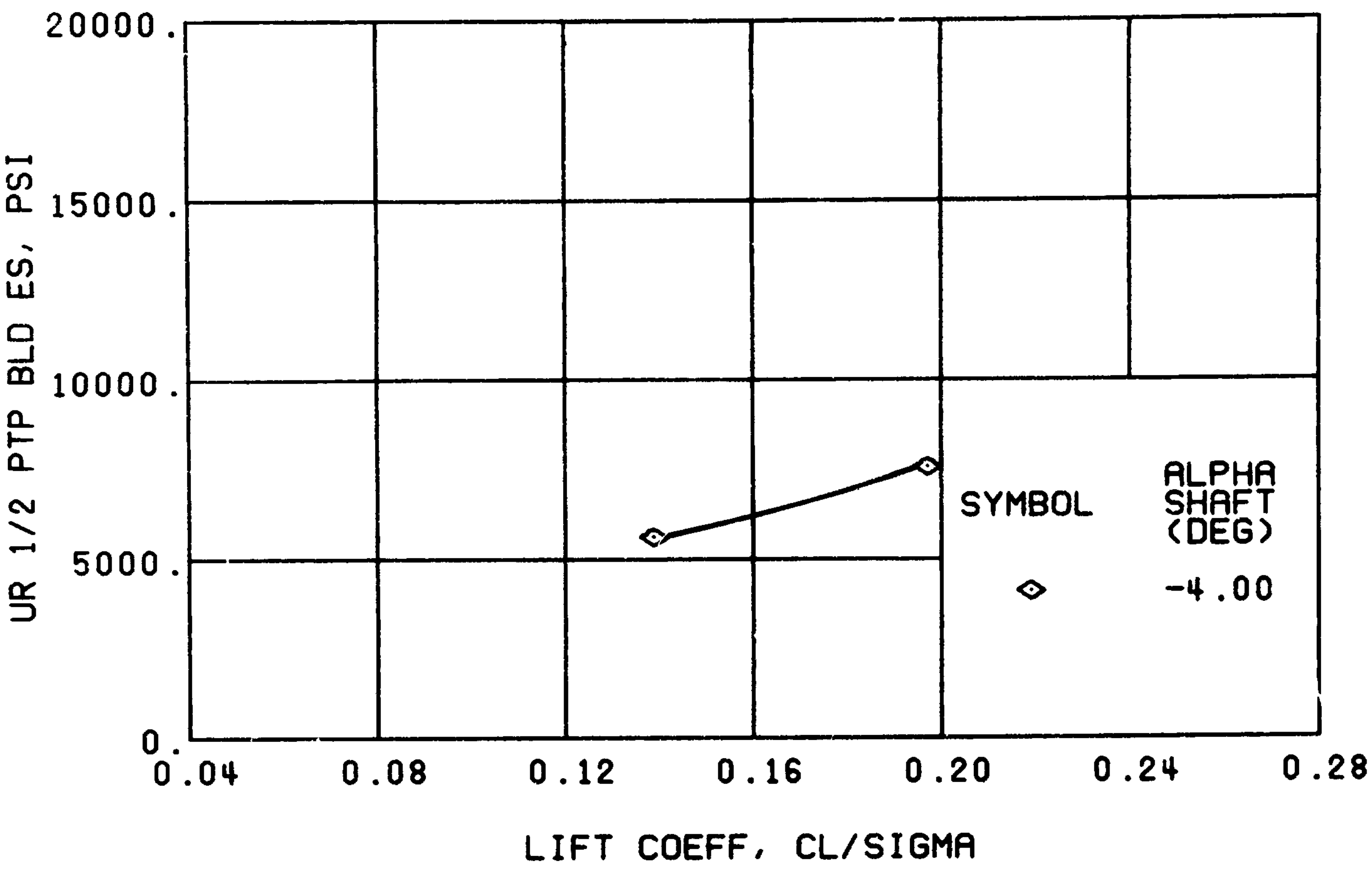

(j) GAGE 42 R132

Figure 58. Continued.
$\mu = 0.70$ $B'_{1s} = 8$ Deg

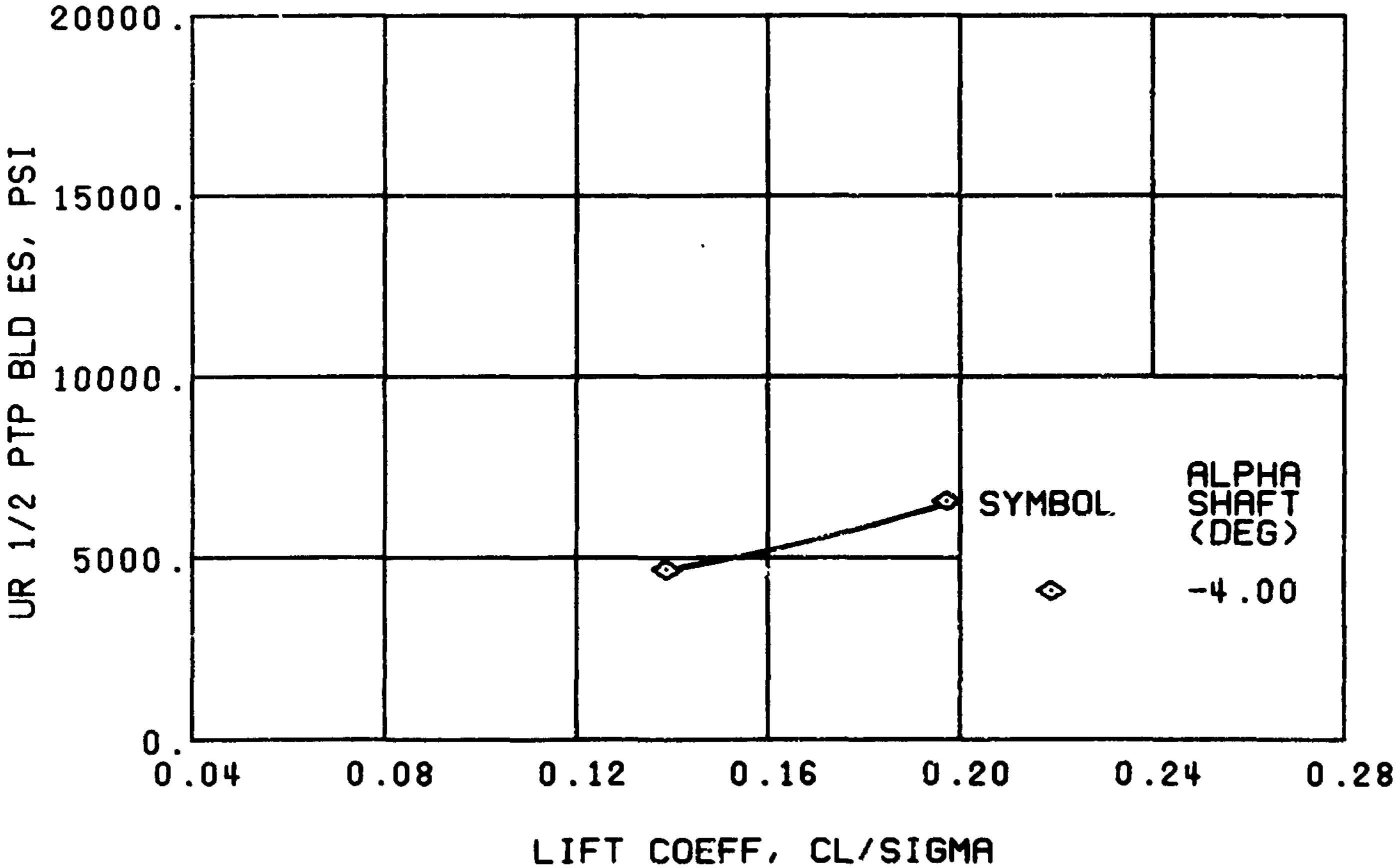

(k) GAGE 43 R168

Figure 58. Continued.
$\mu = 0.70$ $B'_{1s} = 8$ Deg

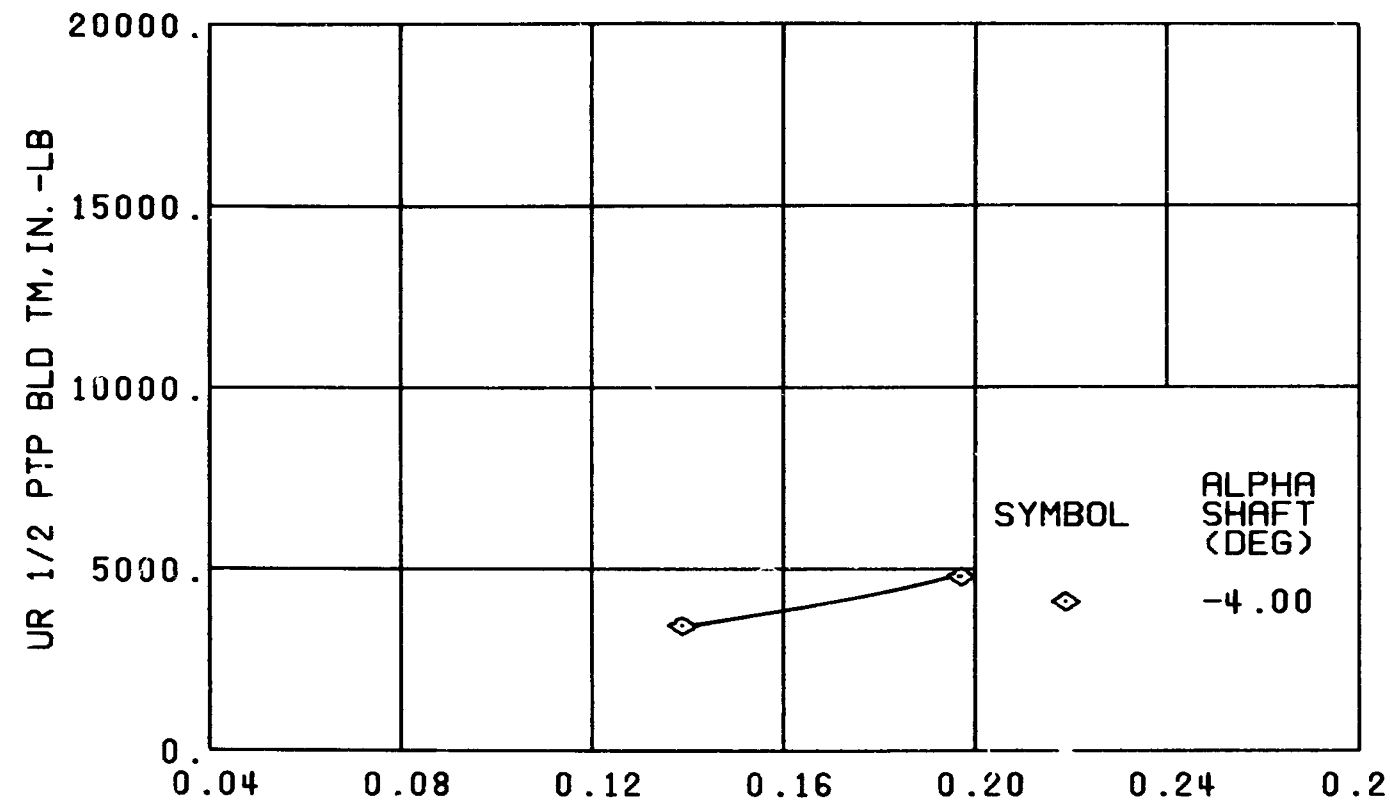

(m) GAGE 46 R130

Figure 58. Continued.
$\mu = 0.70 \quad B_{1s}' = 8$ Deg

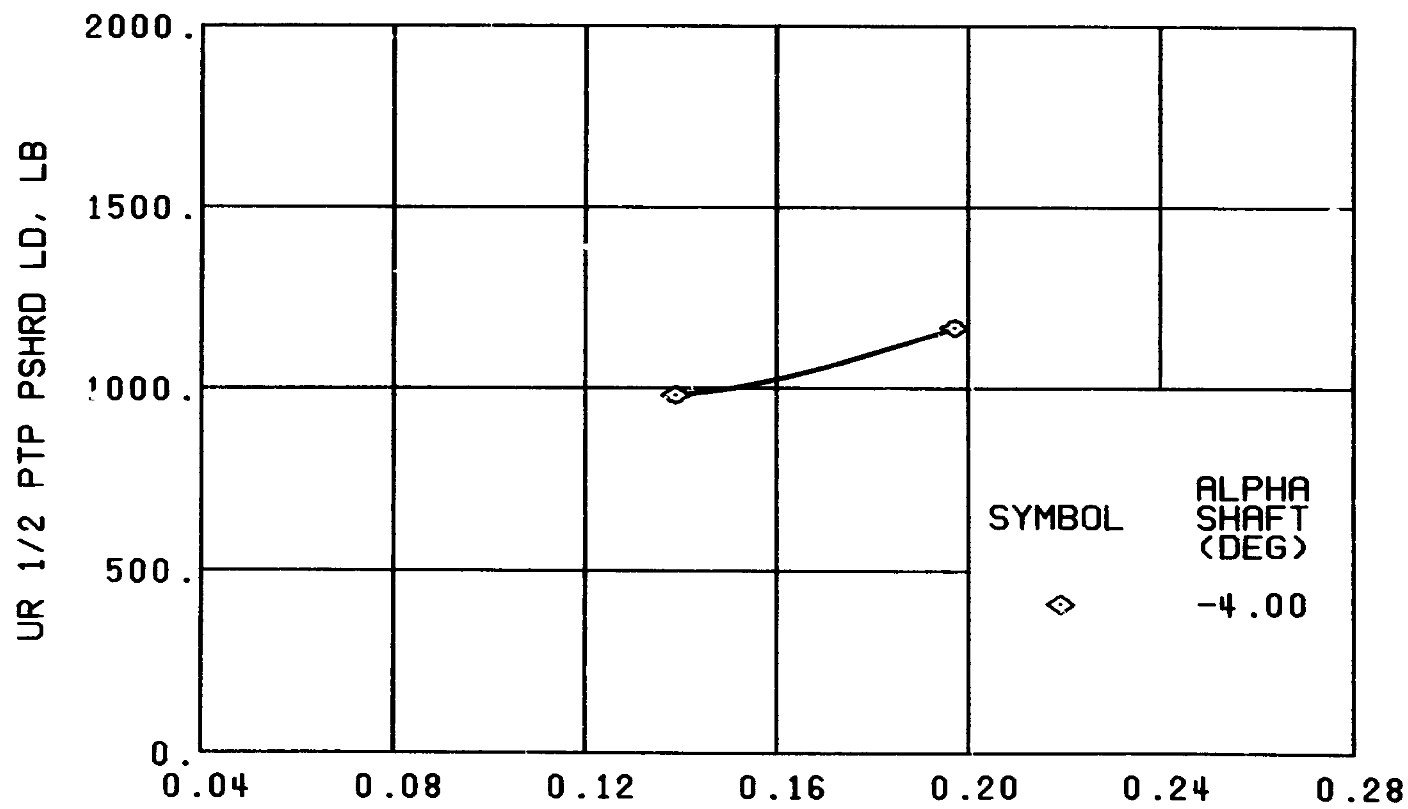

(n) GAGE 37

Figure 58. Continued.
μ = 0.70 B'_{1s} = 8 Deg

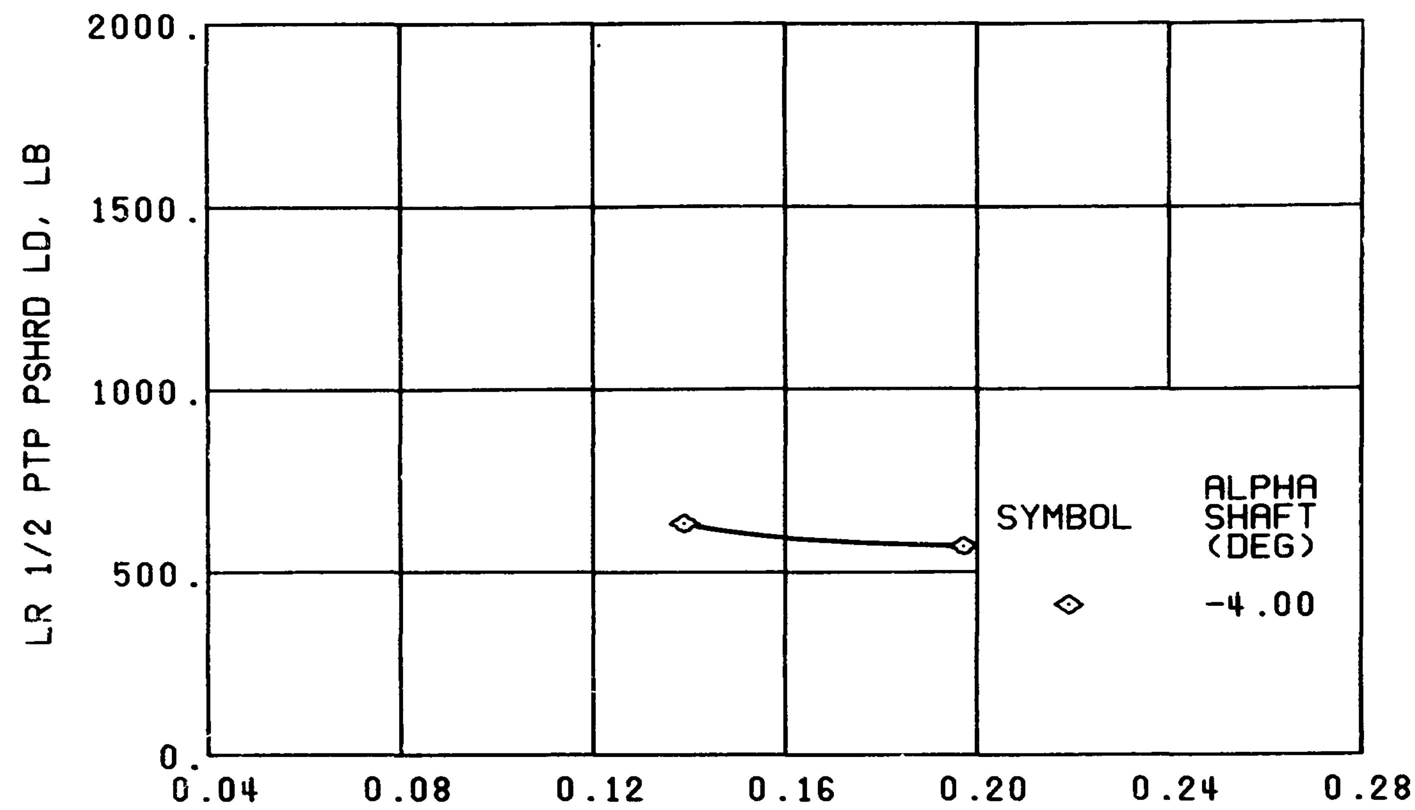

(o) GAGE 34

Figure 58. Continued.
$\mu = 0.70 \quad B'_{1s} = 8$ Deg

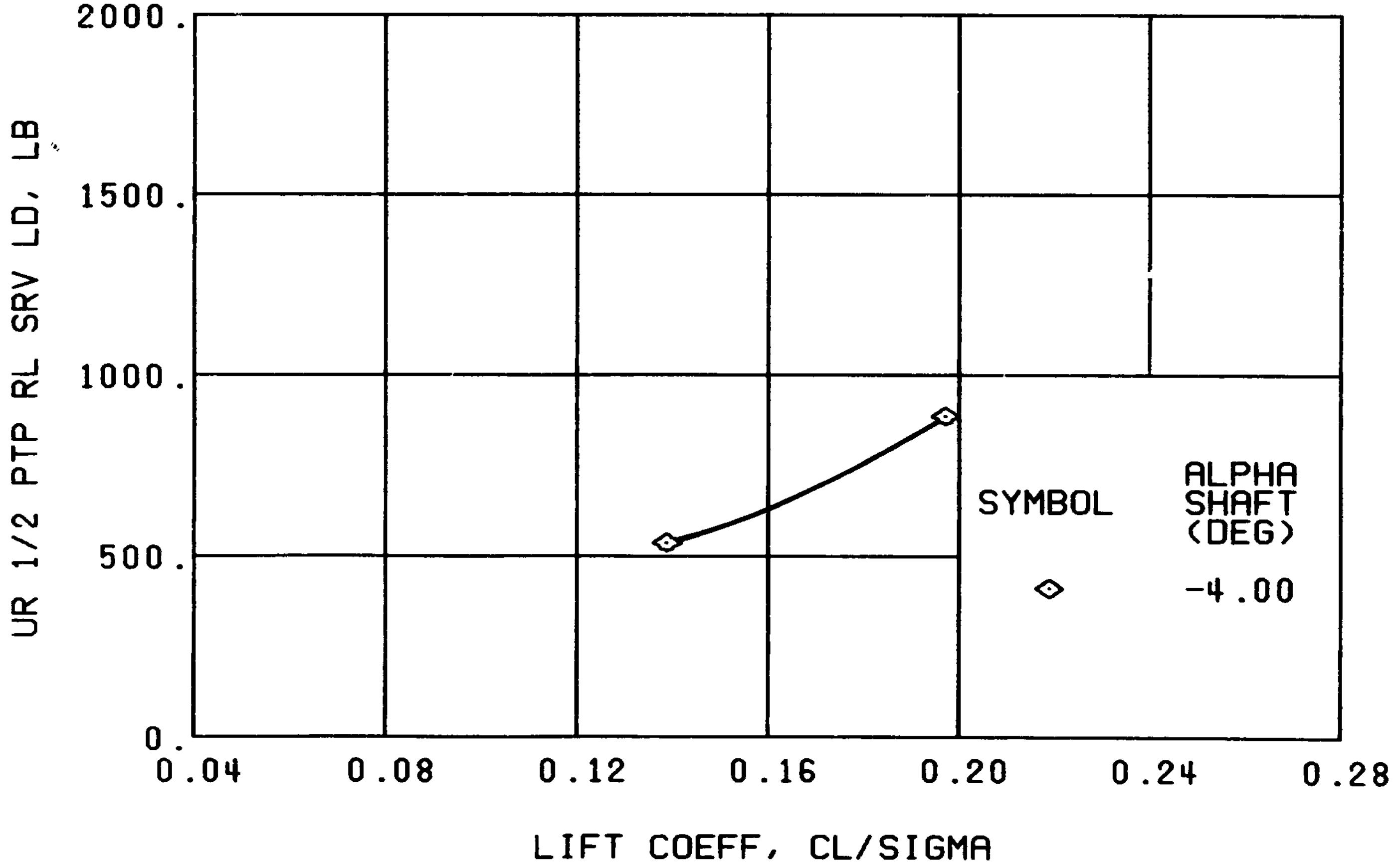

(p) GAGE 22

Figure 58. Continued.
$\mu = 0.70 \quad B'_{1s} = 8$ Deg

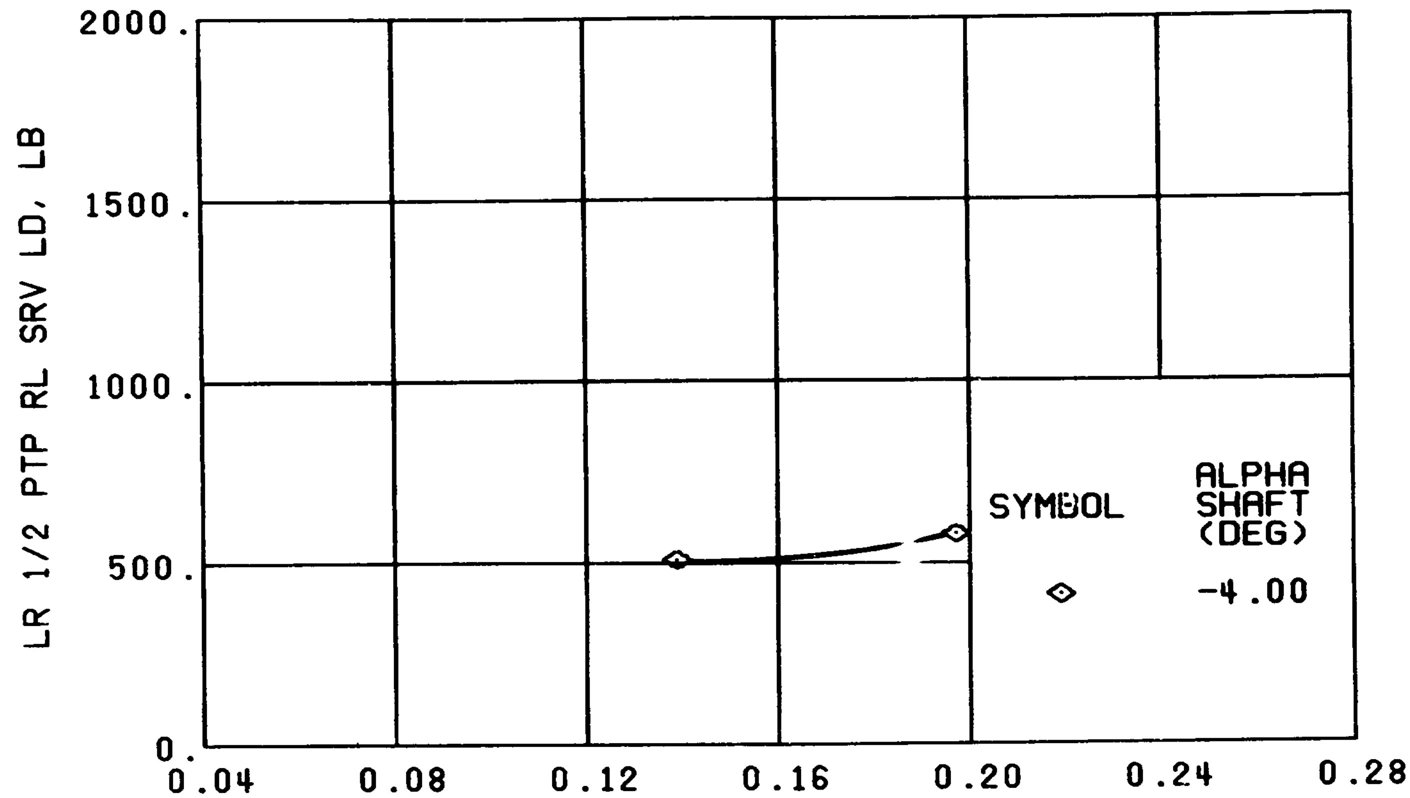

(q) GAGE 25

Figure 58. Continued.
$\mu = 0.70 \quad B'_{1s} = 8$ Deg

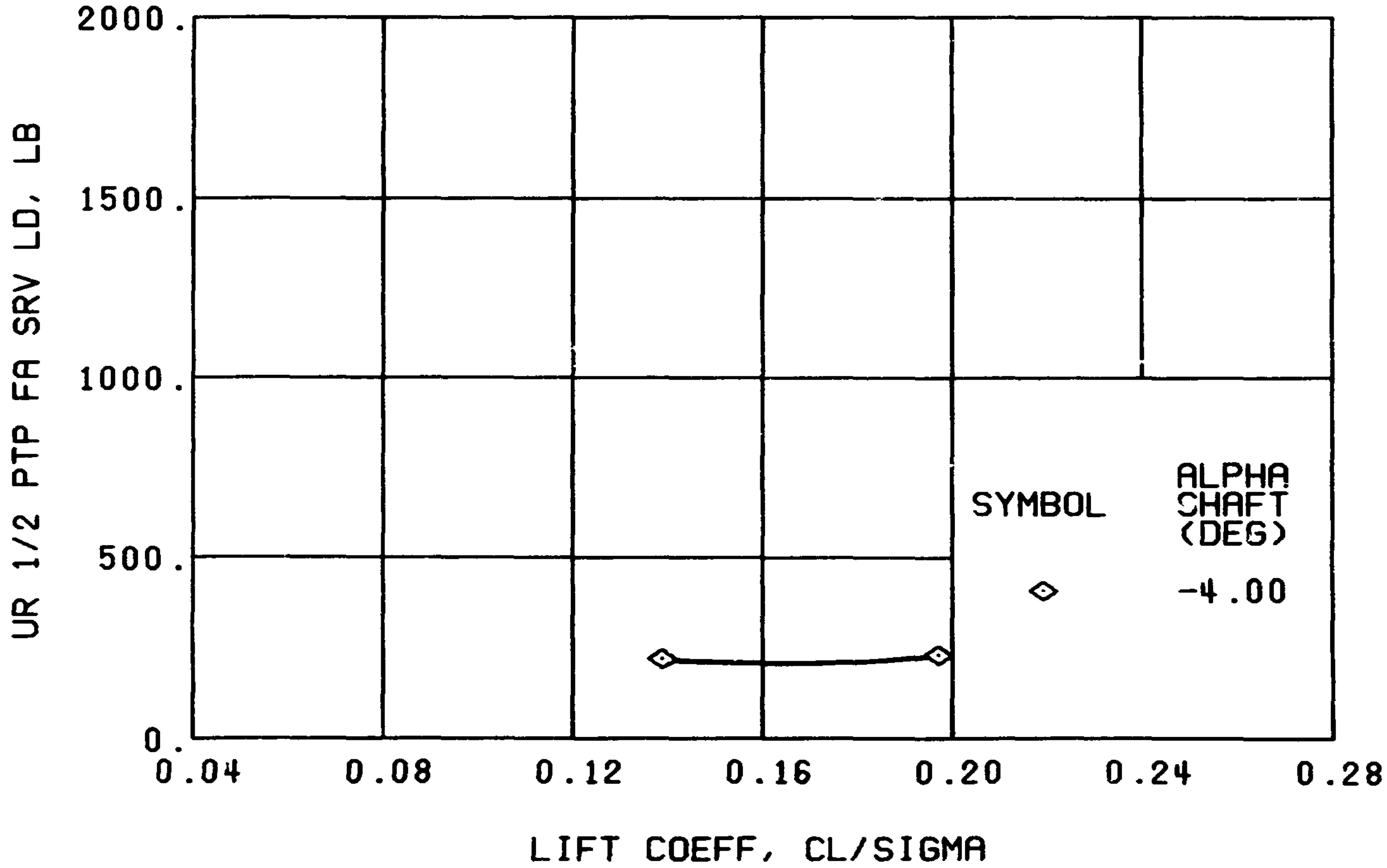

(r) GAGE 24

Figure 58. Continued.
$\mu = 0.70$ $B'_{1s} = 8$ Deg

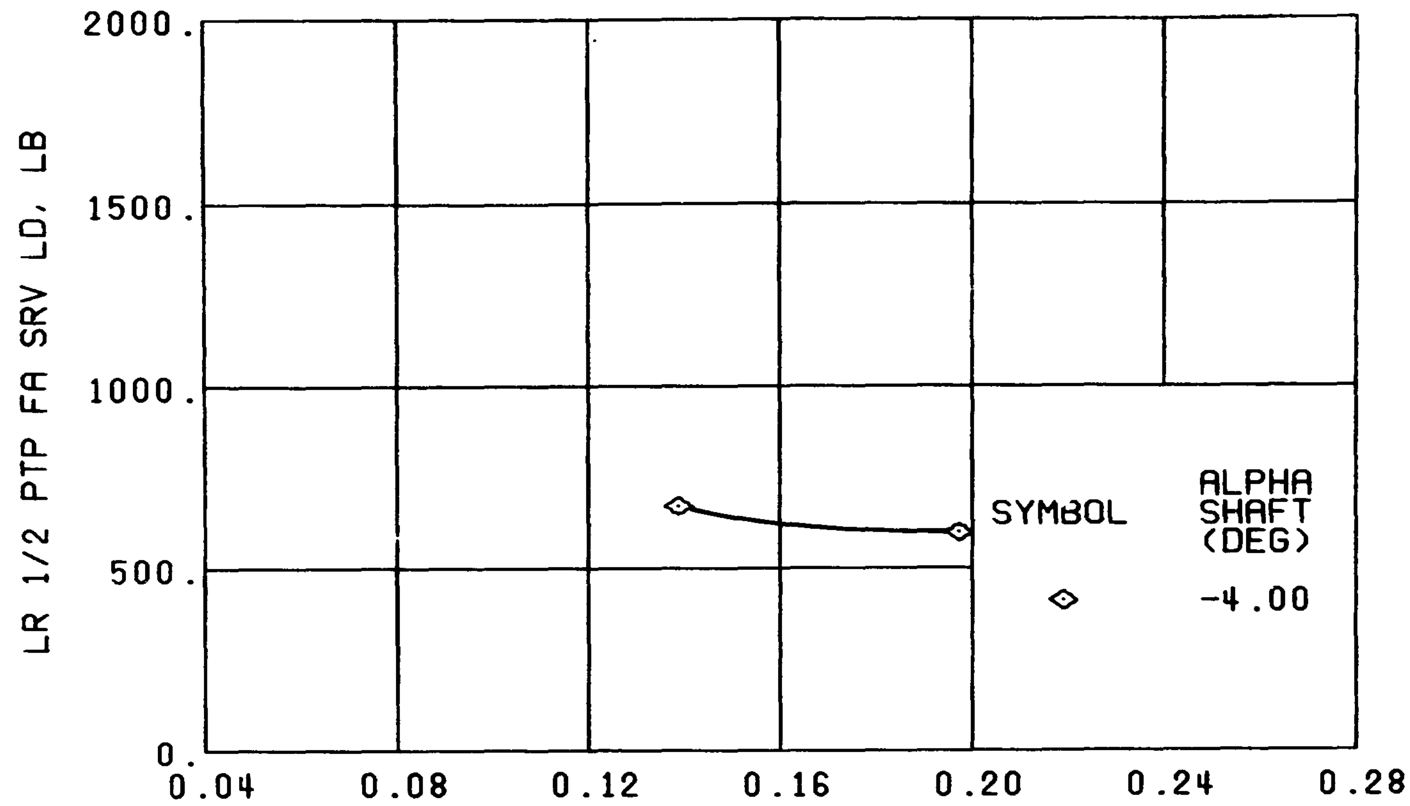

(s) GAGE 27

Figure 58. Continued.
μ = 0.70 B'_{1s} = 8 Deg

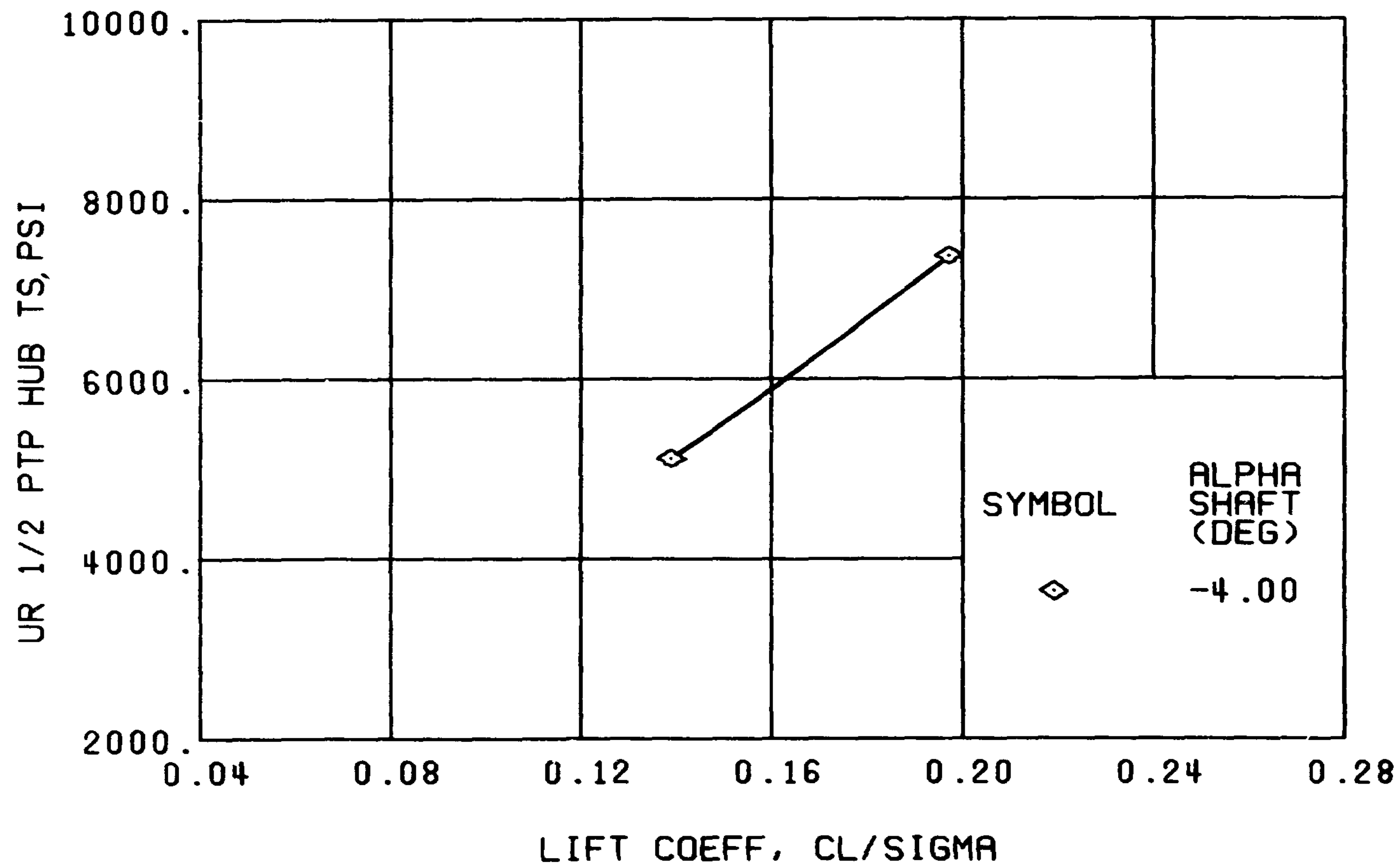

(f) GAGE 65

Figure 58. Continued.
$\mu = 0.70 \quad B'_{1s} = 8$ Deg

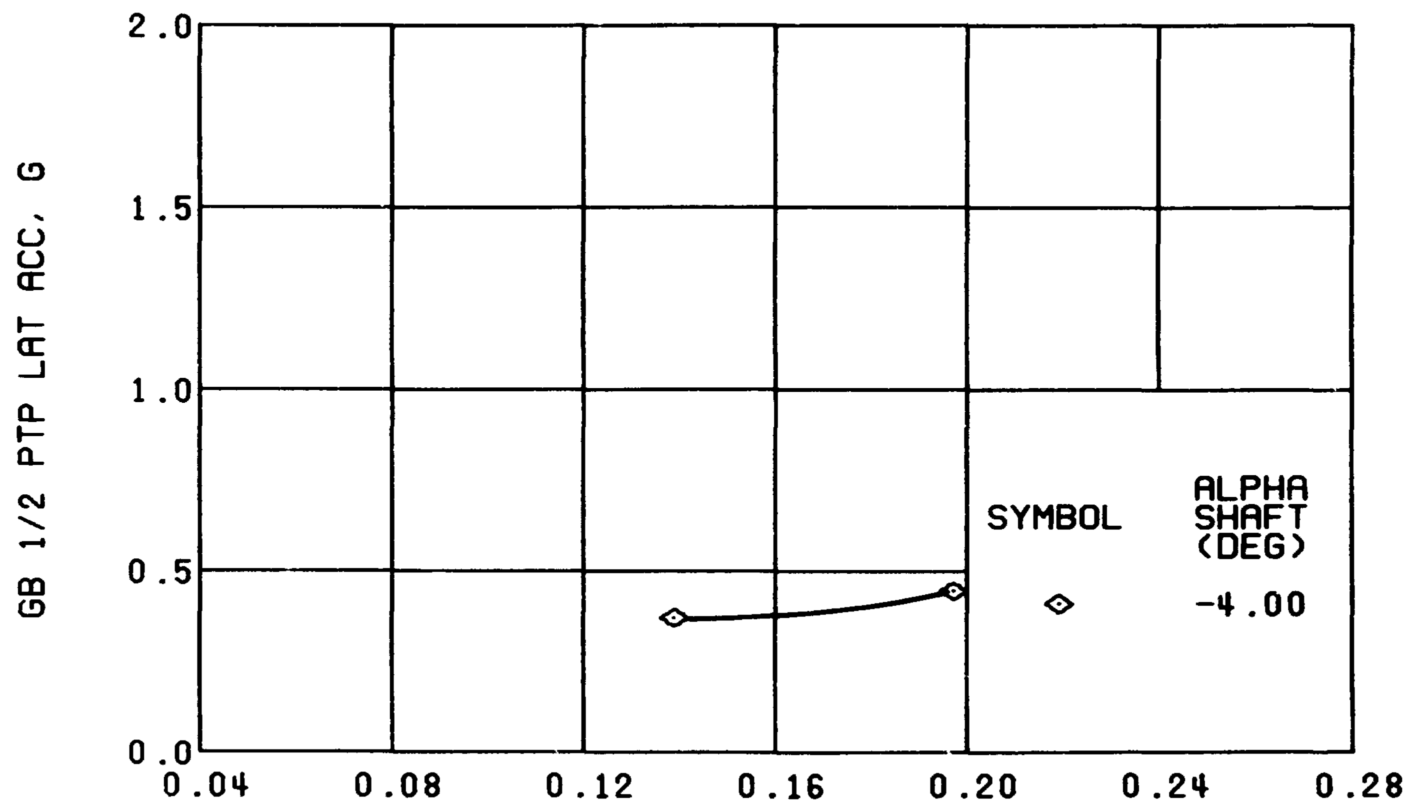

(u) GAGE 15 STA 76, BL 30

Figure 58. Continued.
$\mu = 0.70 \quad B'_{1s} = 8$ Deg

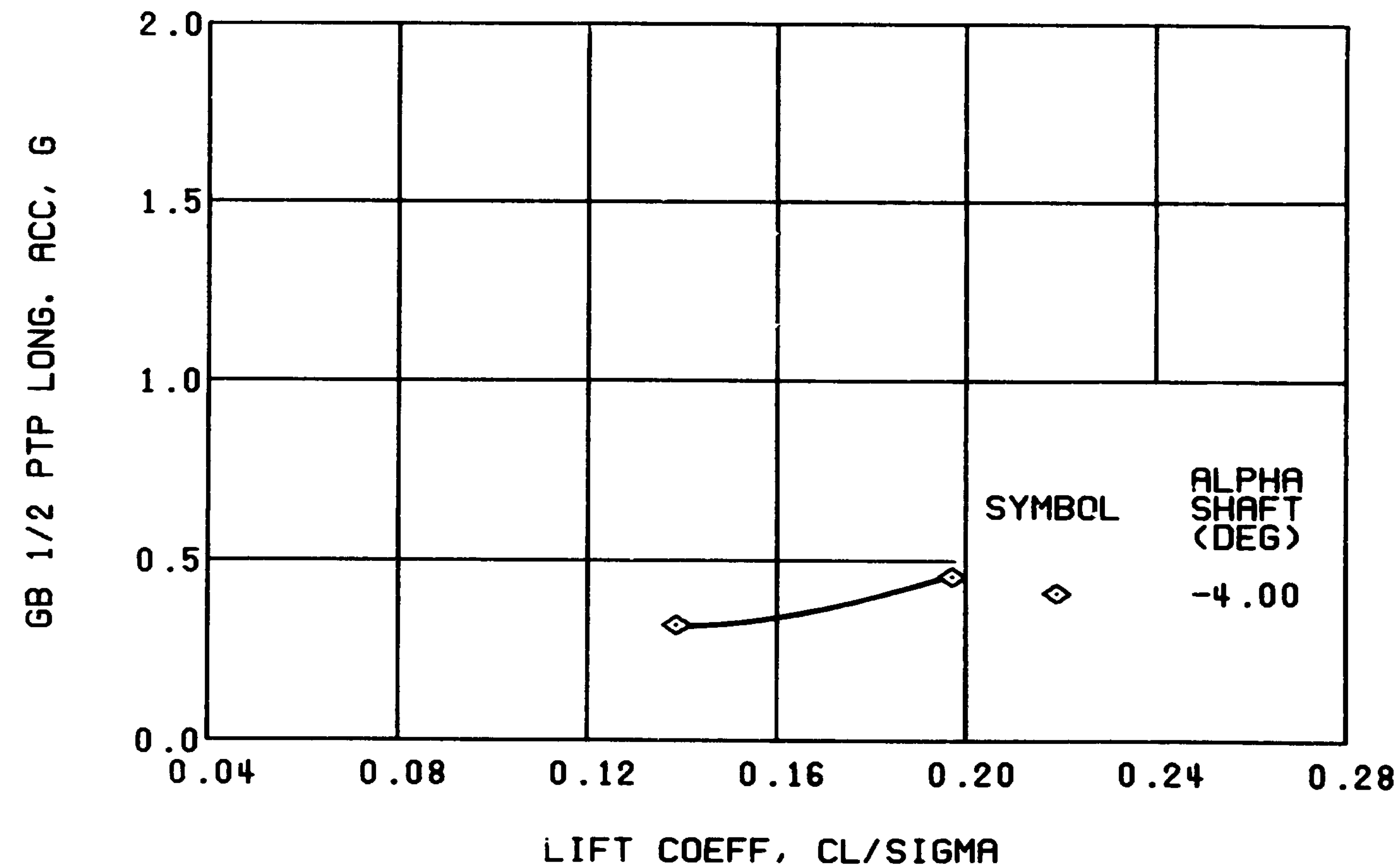

(v) GAGE 14 STA 61, BL 0

Figure 58. Continued.
$\mu = 0.70 \quad B'_{1s} = 8$ Deg

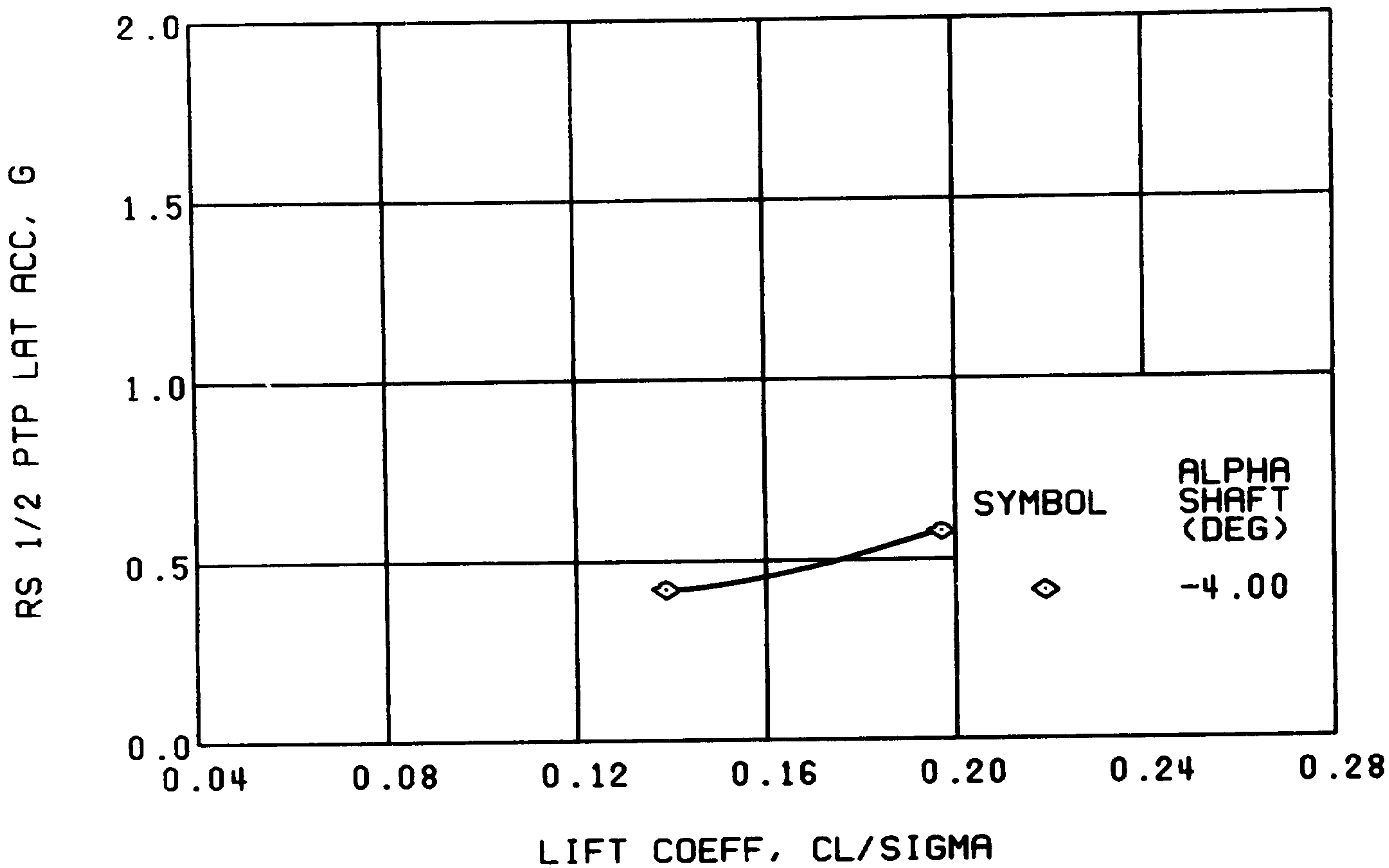

(w) GAGE 16 ROVER 3

Figure 58. Continued.
$\mu = 0.70 \quad B'_{1s} = 8$ Deg

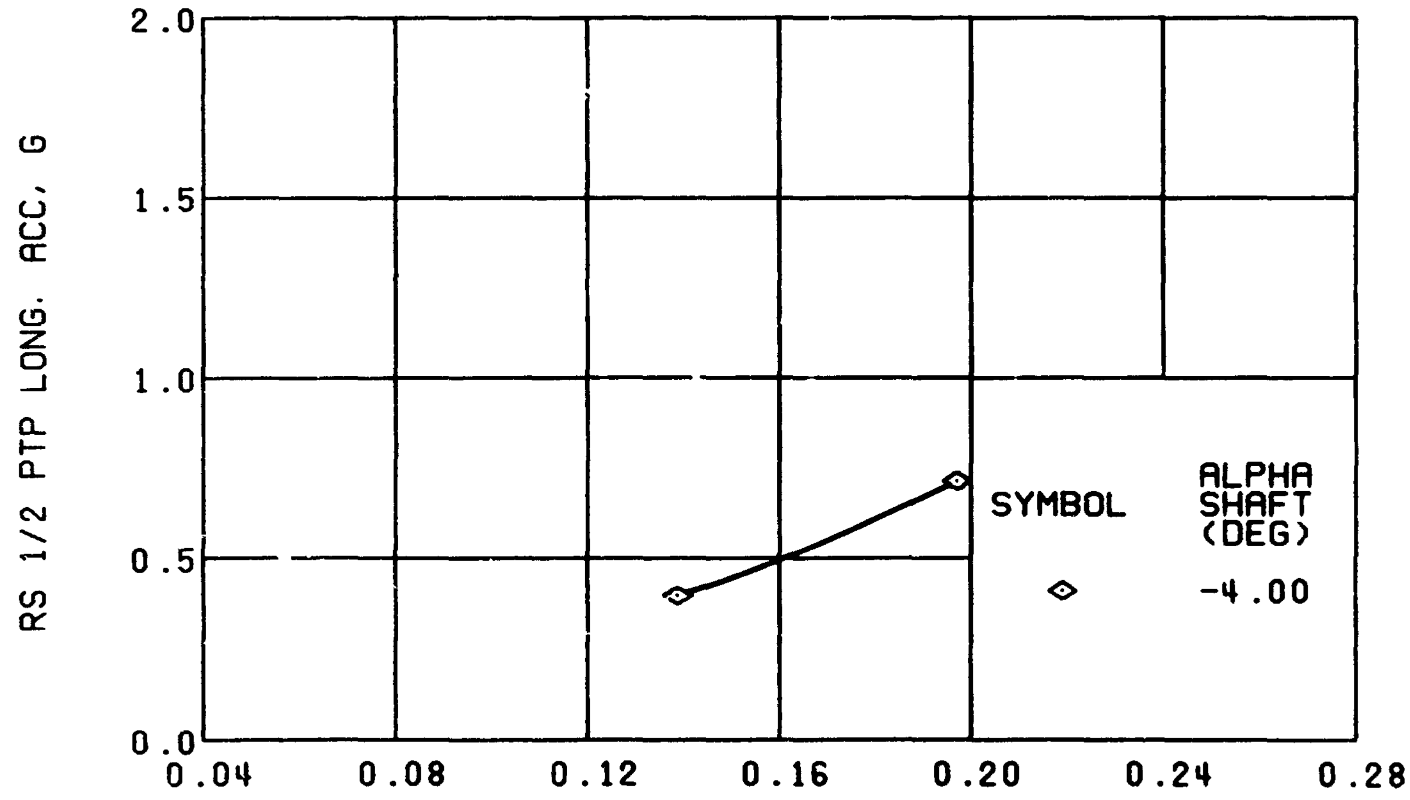

(x) GAGE 17 ROVER 4

Figure 58. Concluded.
$\mu = 0.70 \quad B'_{1s} = 8$ Deg

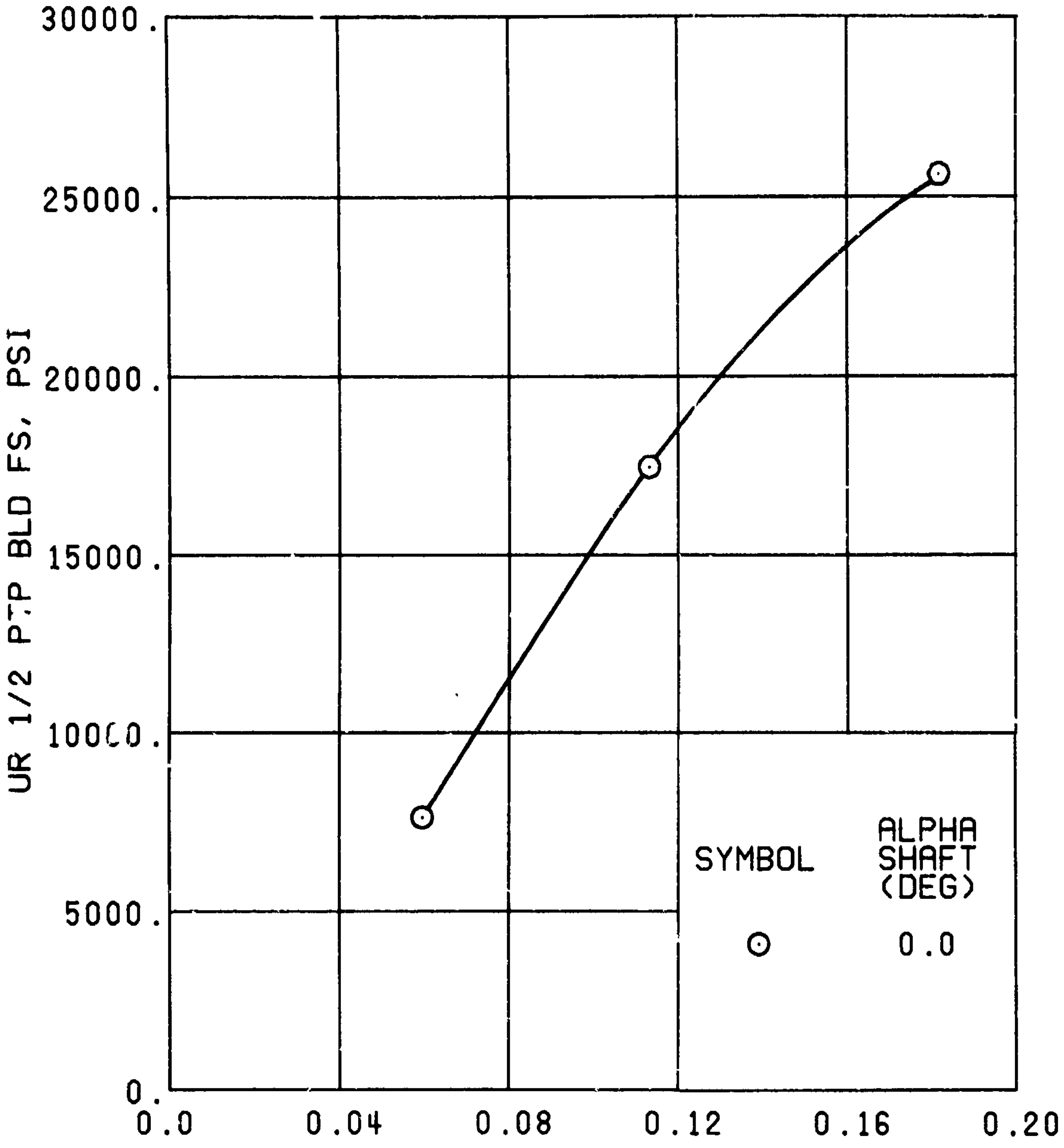

(a) GAGE 51 R84

Figure 59. Stress, Load, and Vibration Data at an Advance Ratio of 0.91 With the Lateral Displacement Control (B'_{1s}) Set at 2 Degrees.

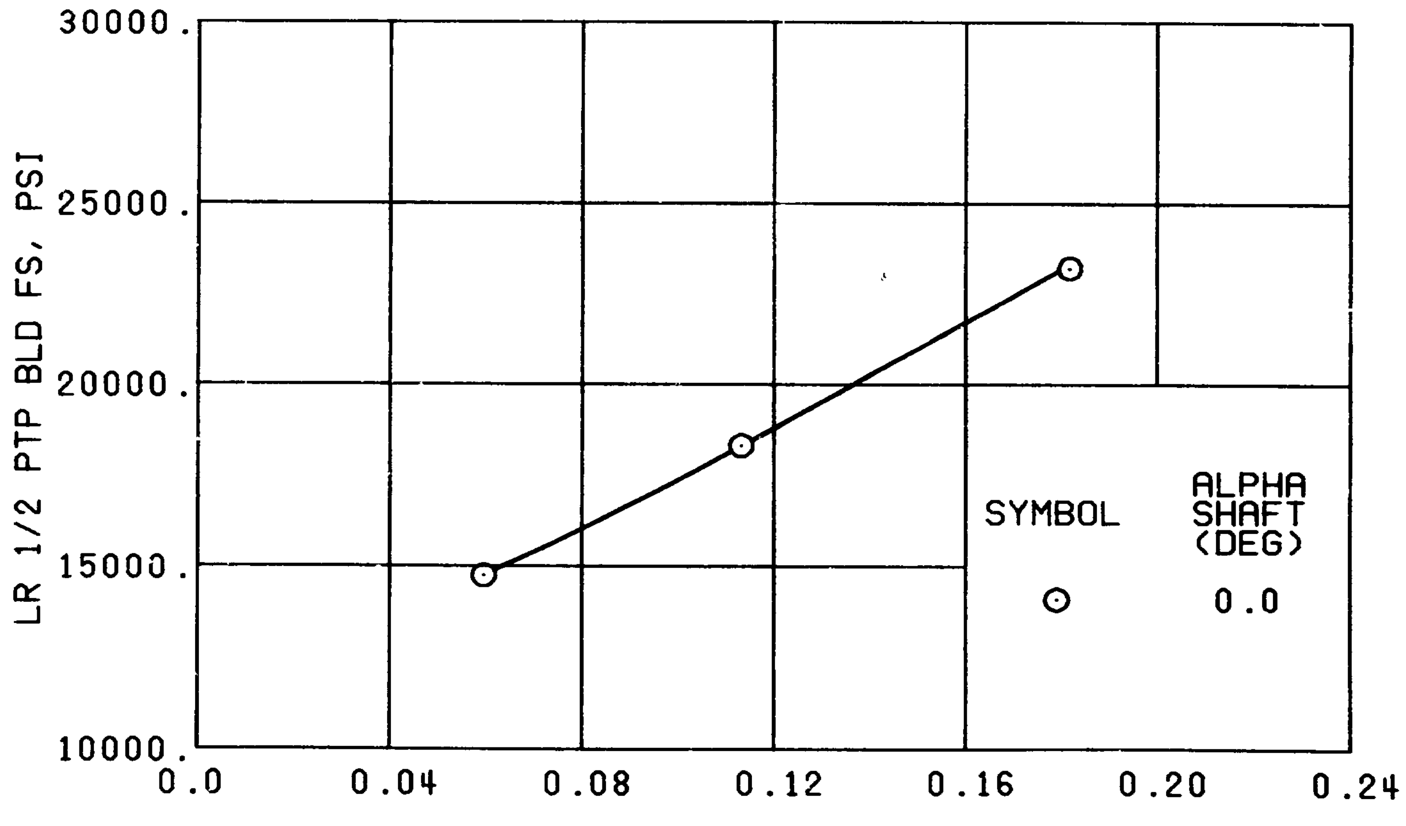

(b) GAGE 1 R84

Figure 59. Continued.
$\mu = 0.91$ $B'_{1s} = 2$ Deg

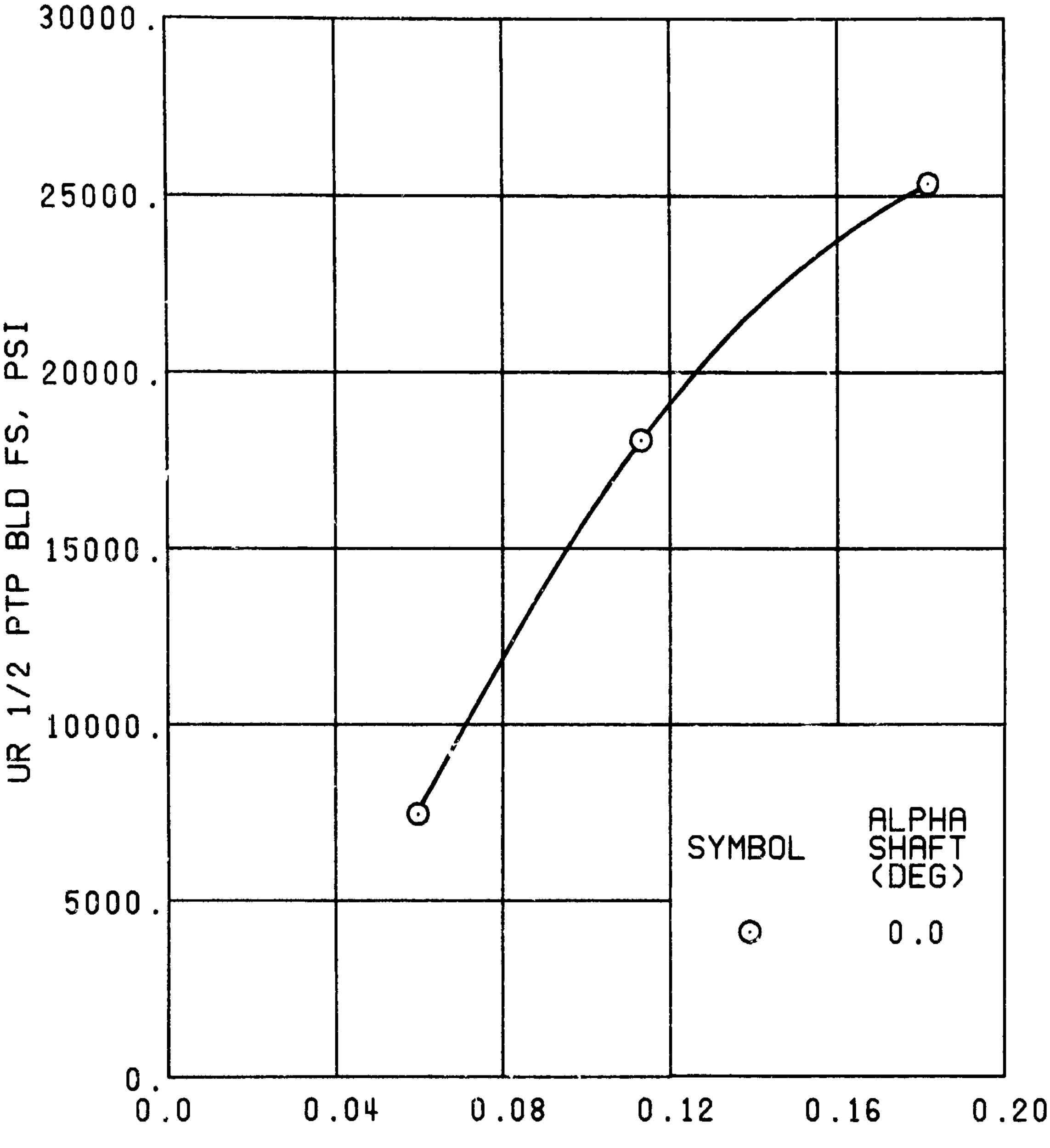

(c) GAGE 52 R108

Figure 59. Continued.
$\mu = 0.91 \quad B'_{1s} = 2$ Deg

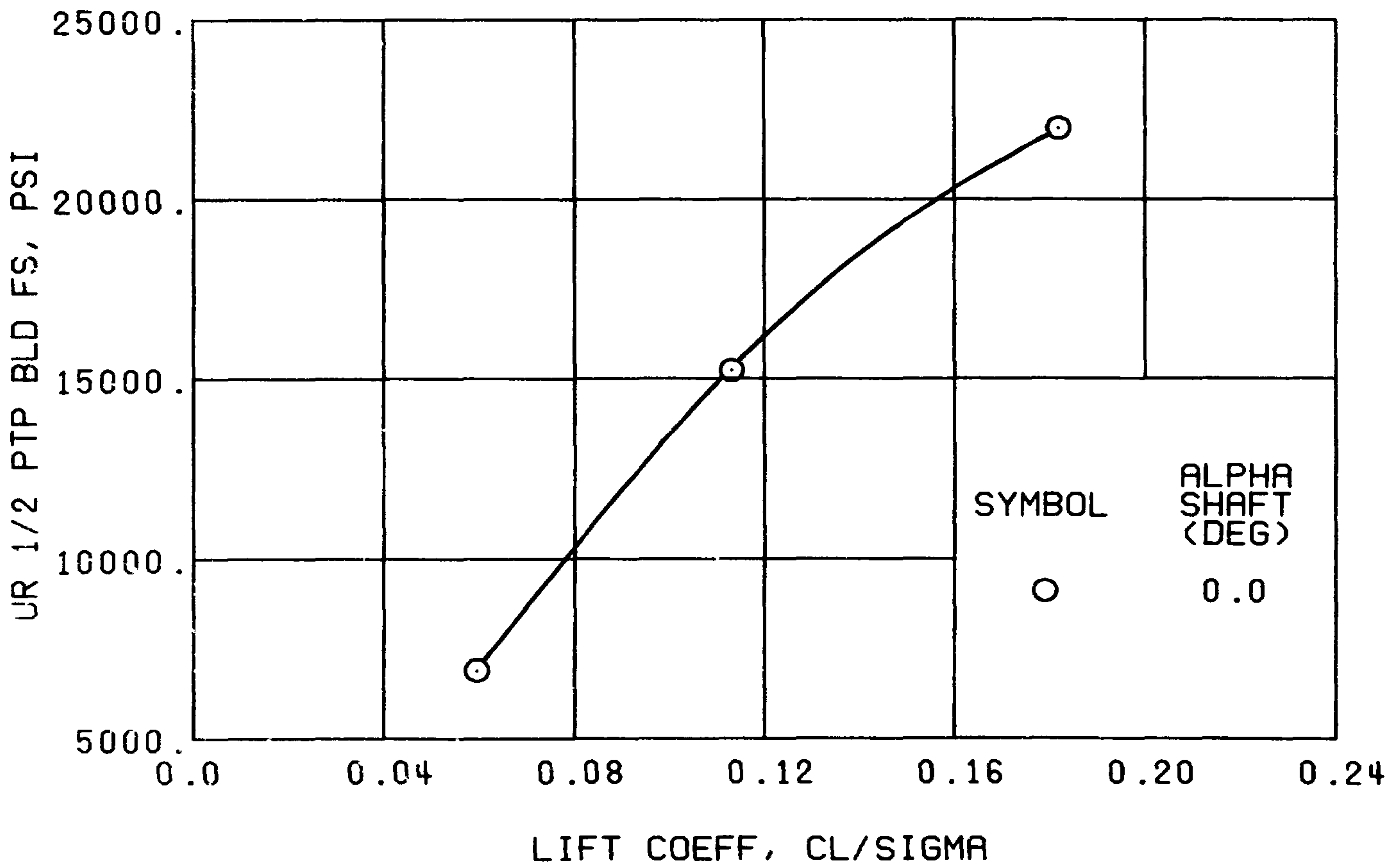

(d) GAGE 53 R132

Figure 59. Continued.
$\mu = 0.91$ $B'_{1s} = 2$ Deg

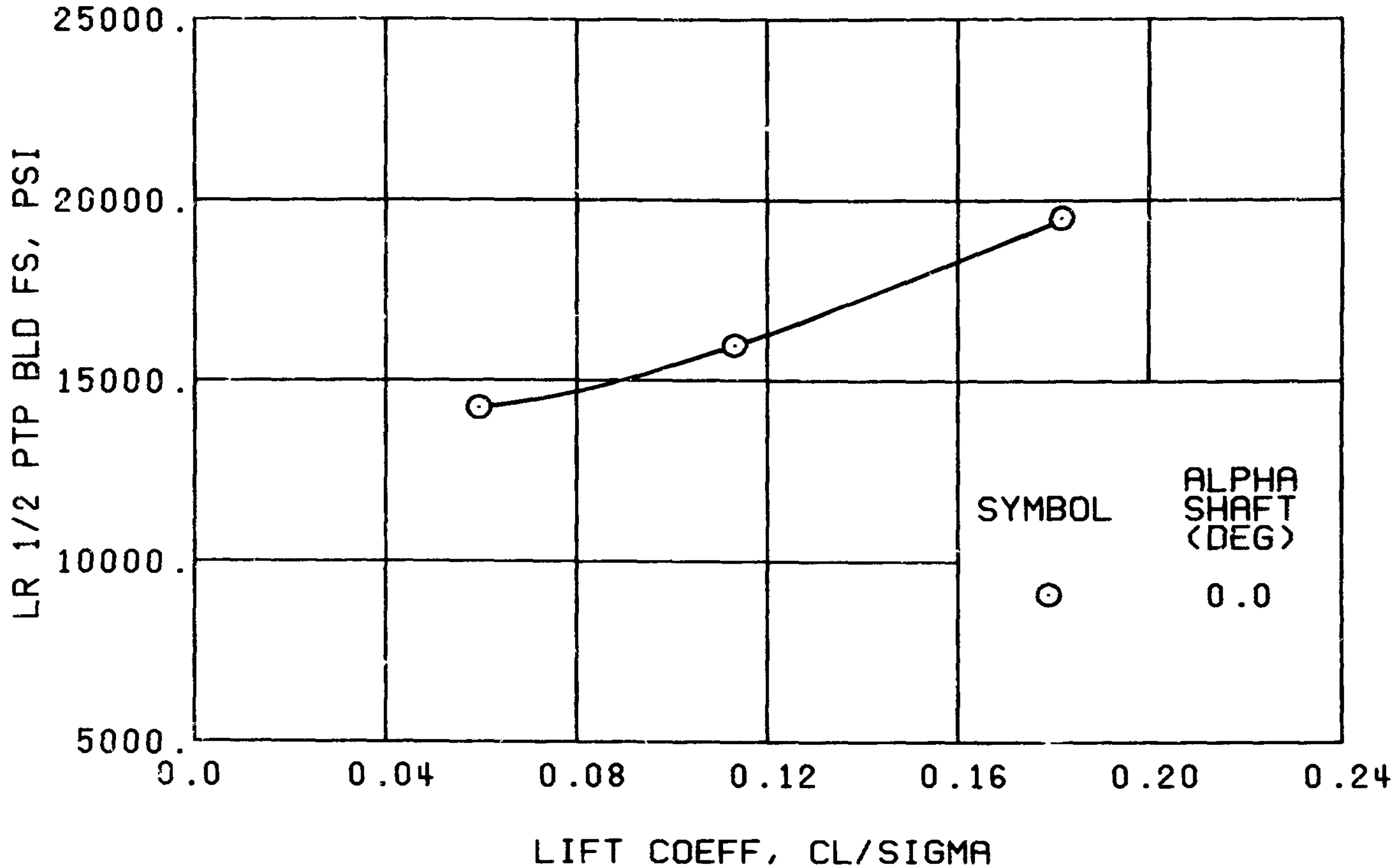

(e) GAGE 93 R132

Figure 59. Continued.
$\mu = 0.91$ $B'_{1s} = 2$ Deg

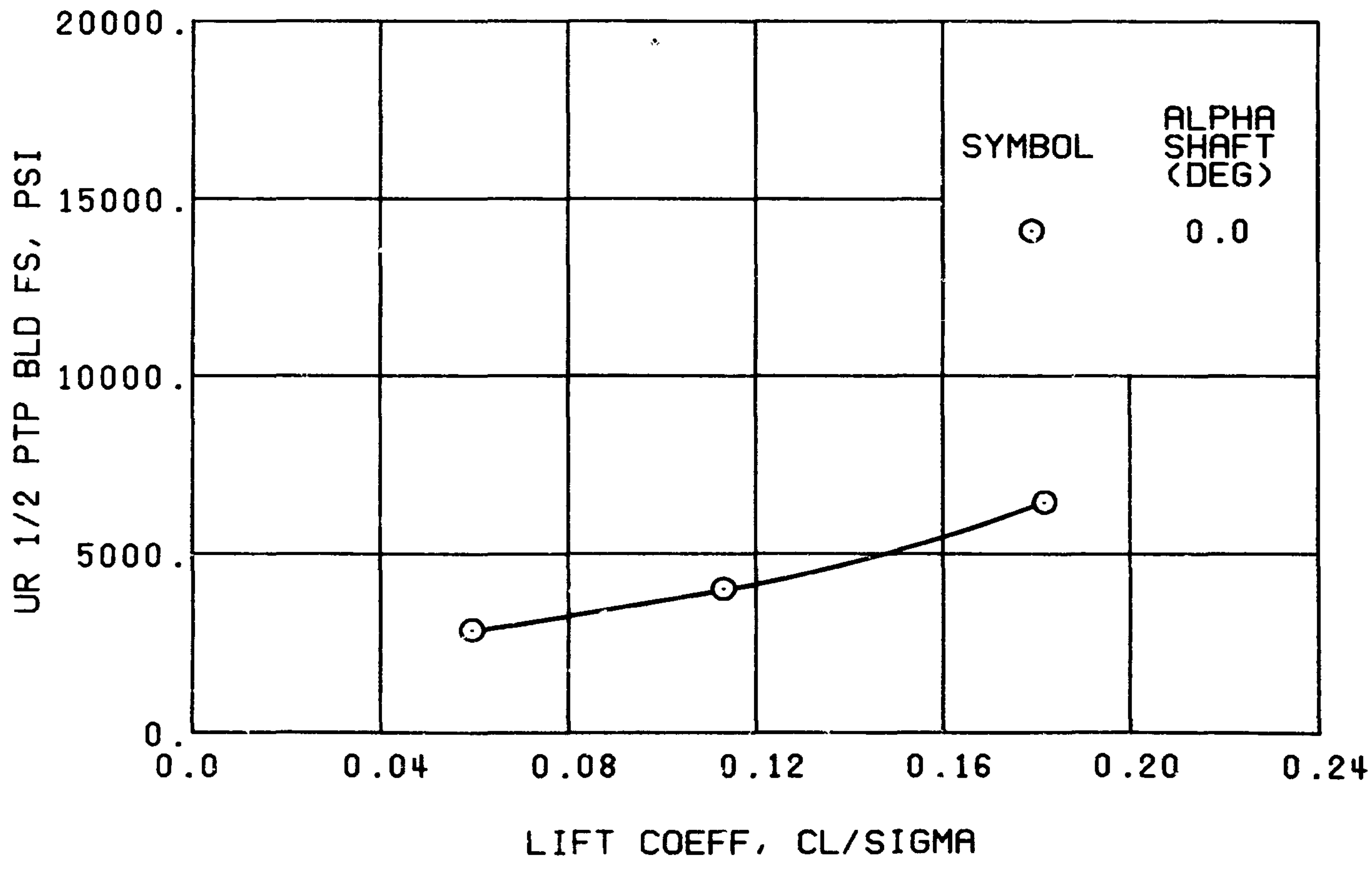

(f) GAGE 55 R204

Figure 59. Continued.
$\mu = 0.91$ $B'_{1s} = 2$ Deg

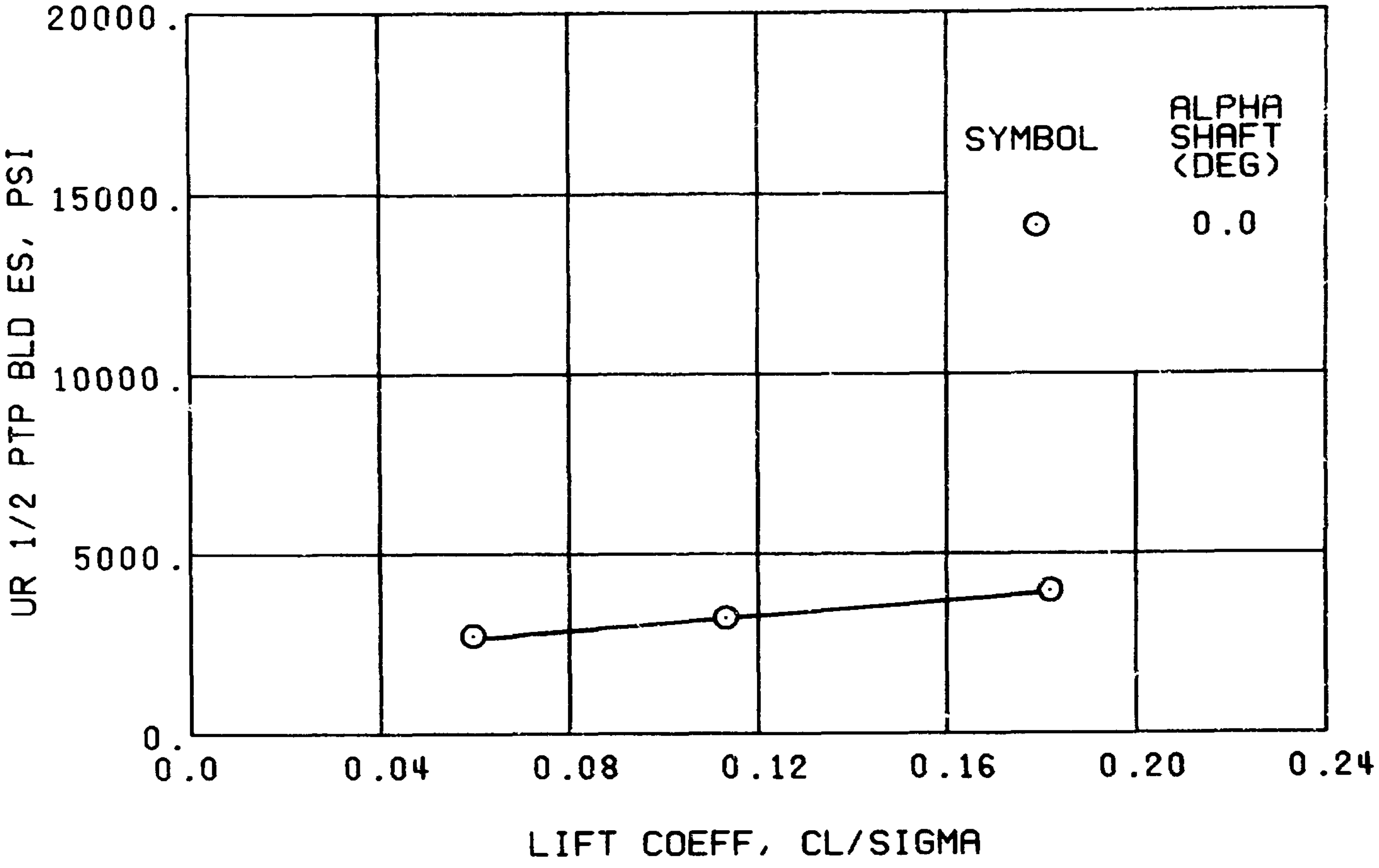

(h) GAGE 40 R84

Figure 59. Continued.
$\mu = 0.91$ $B'_{1s} = 2$ Deg

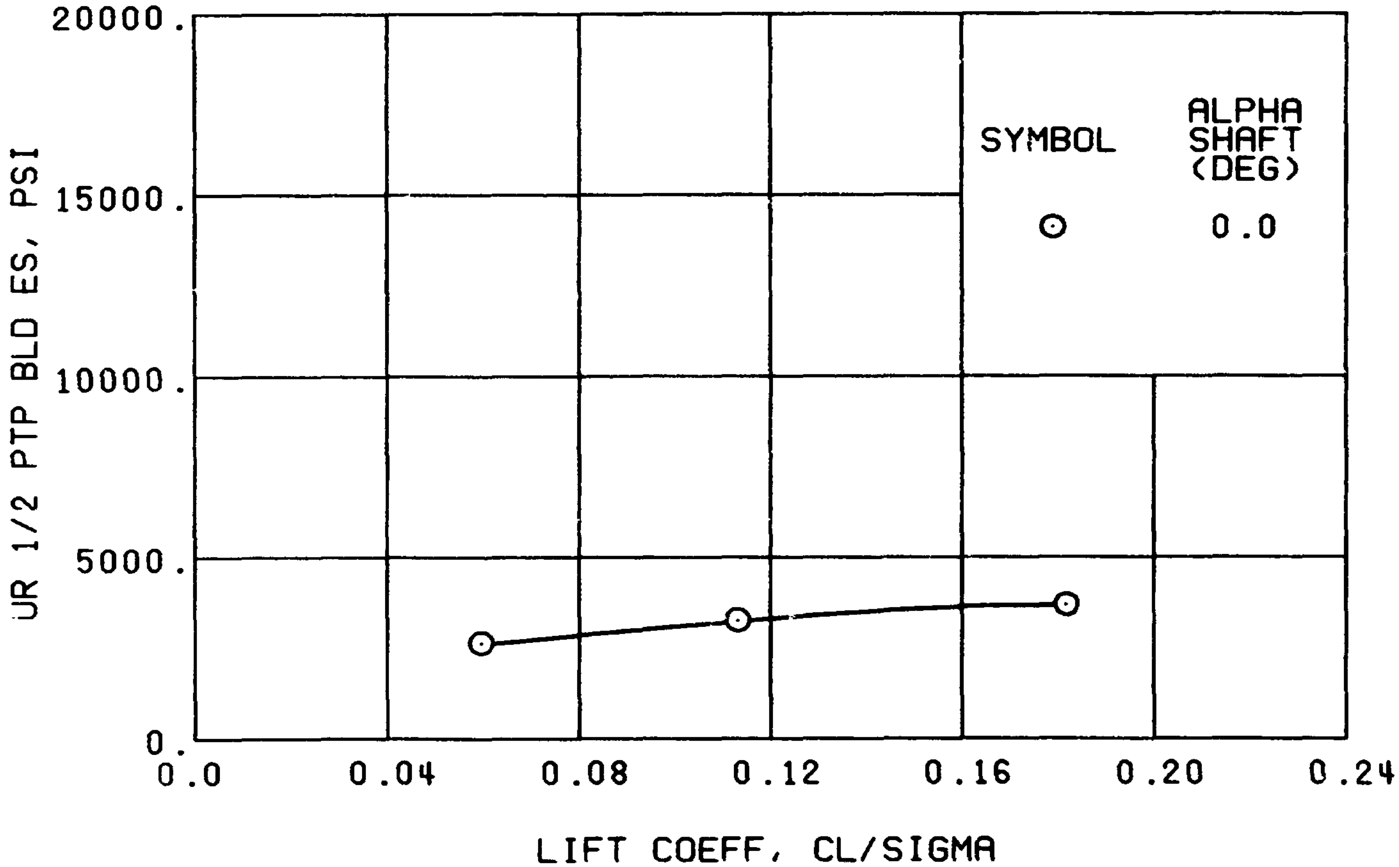

(j) GAGE 42 R132

Figure 59. Continued.
$\mu = 0.91$ $B'_{1s} = 2$ Deg

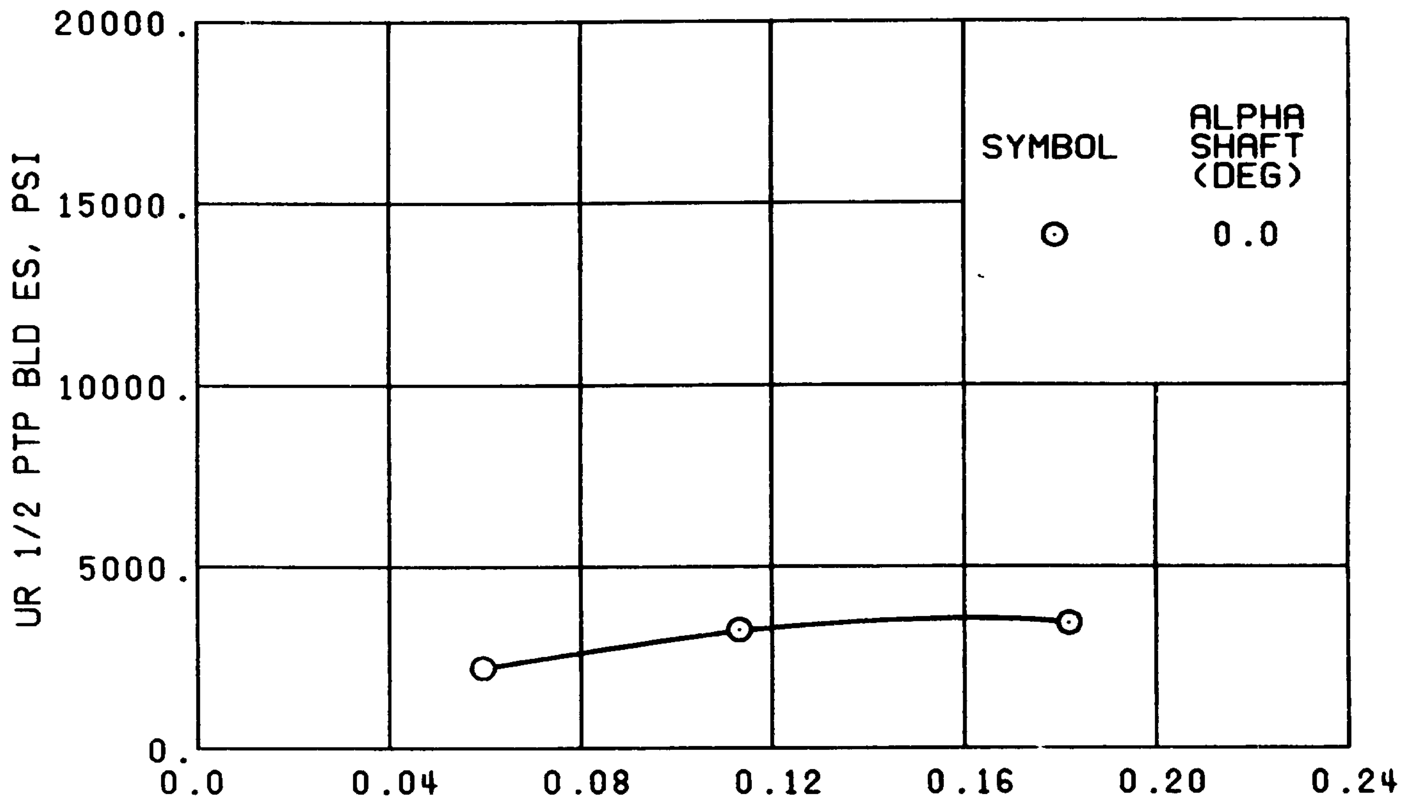

(k) GAGE 43 R168

Figure 59. Continued.
$\mu = 0.91$ $B'_{1s} = 2$ Deg

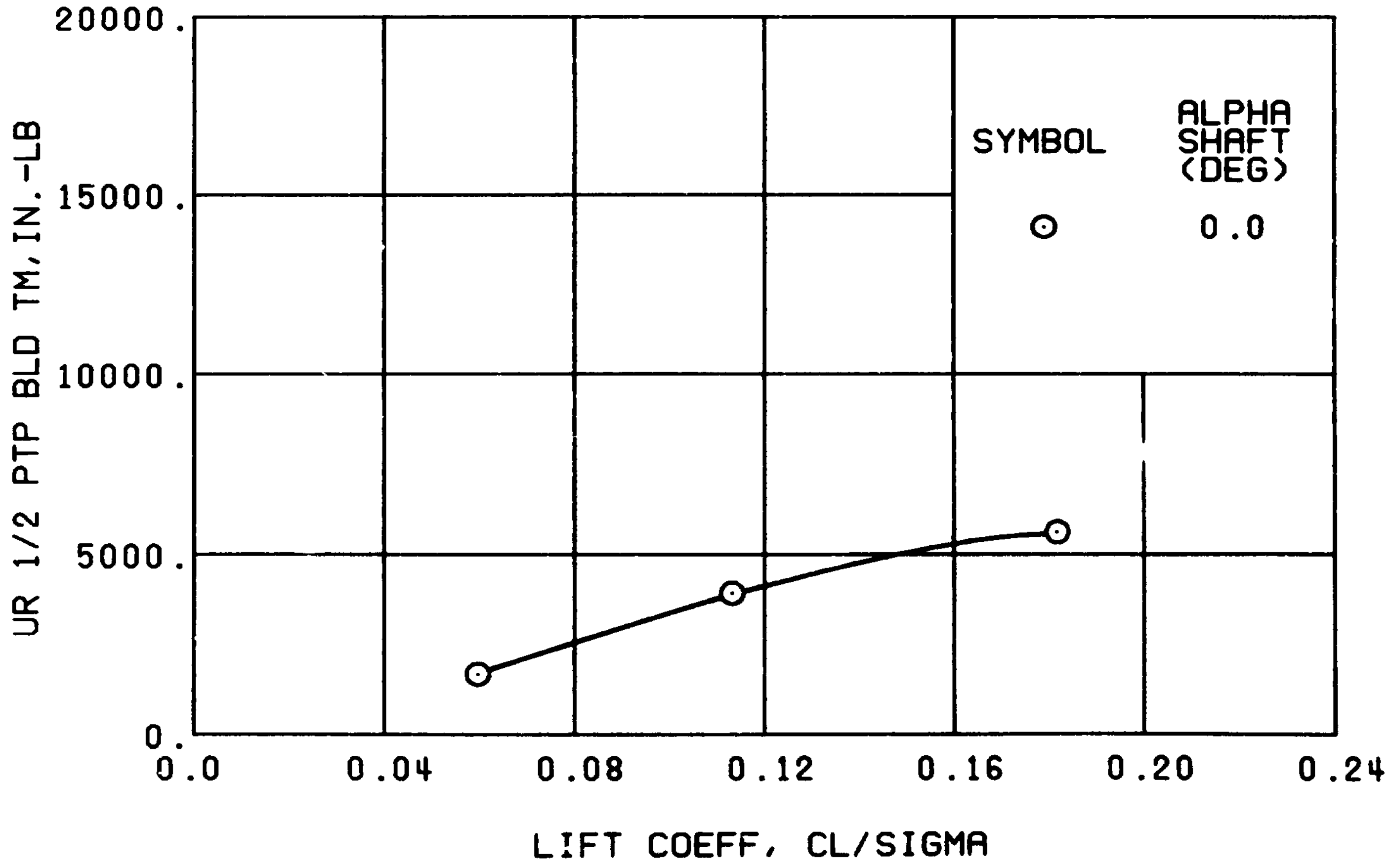

(m) GAGE 46 R130

Figure 59. Continued.
μ = 0.91 B'_{1s} = 2 Deg

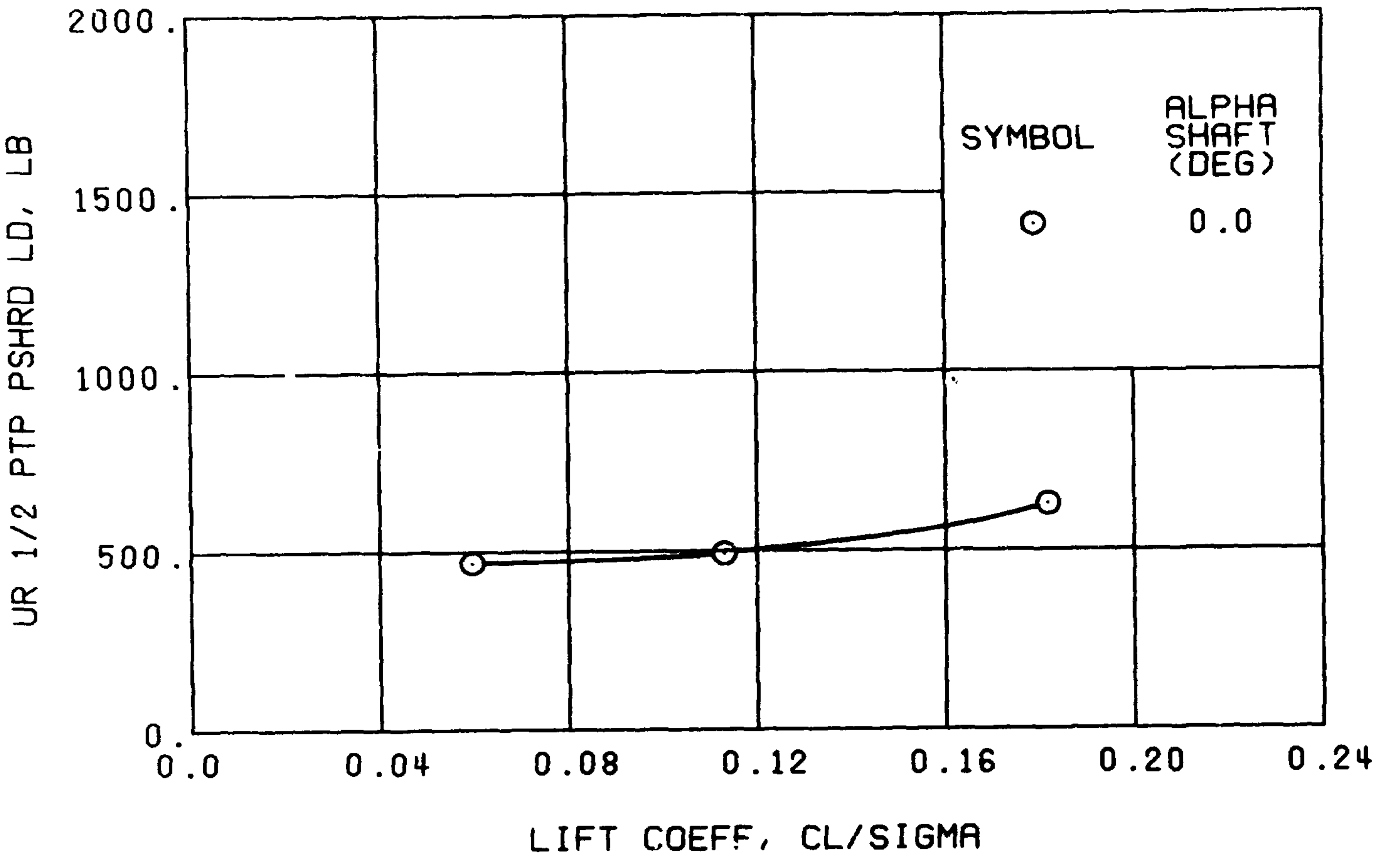

(n) GAGE 37

Figure 59. Continued.
$\mu = 0.91$ $B'_{1s} = 2$ Deg

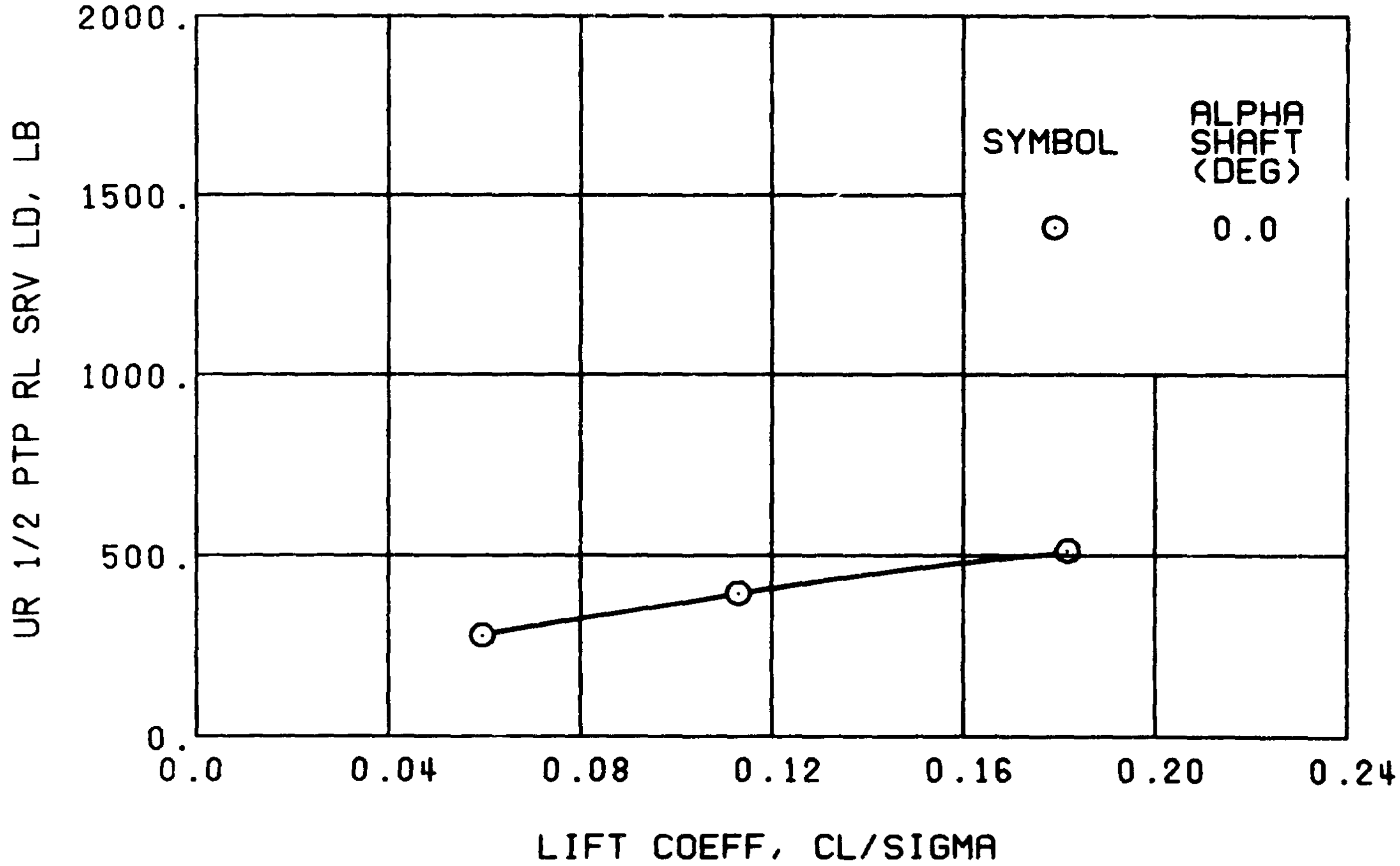

(p) GAGE 22

Figure 59. Continued.
$\mu = 0.91 \quad B'_{1s} = 2$ Deg

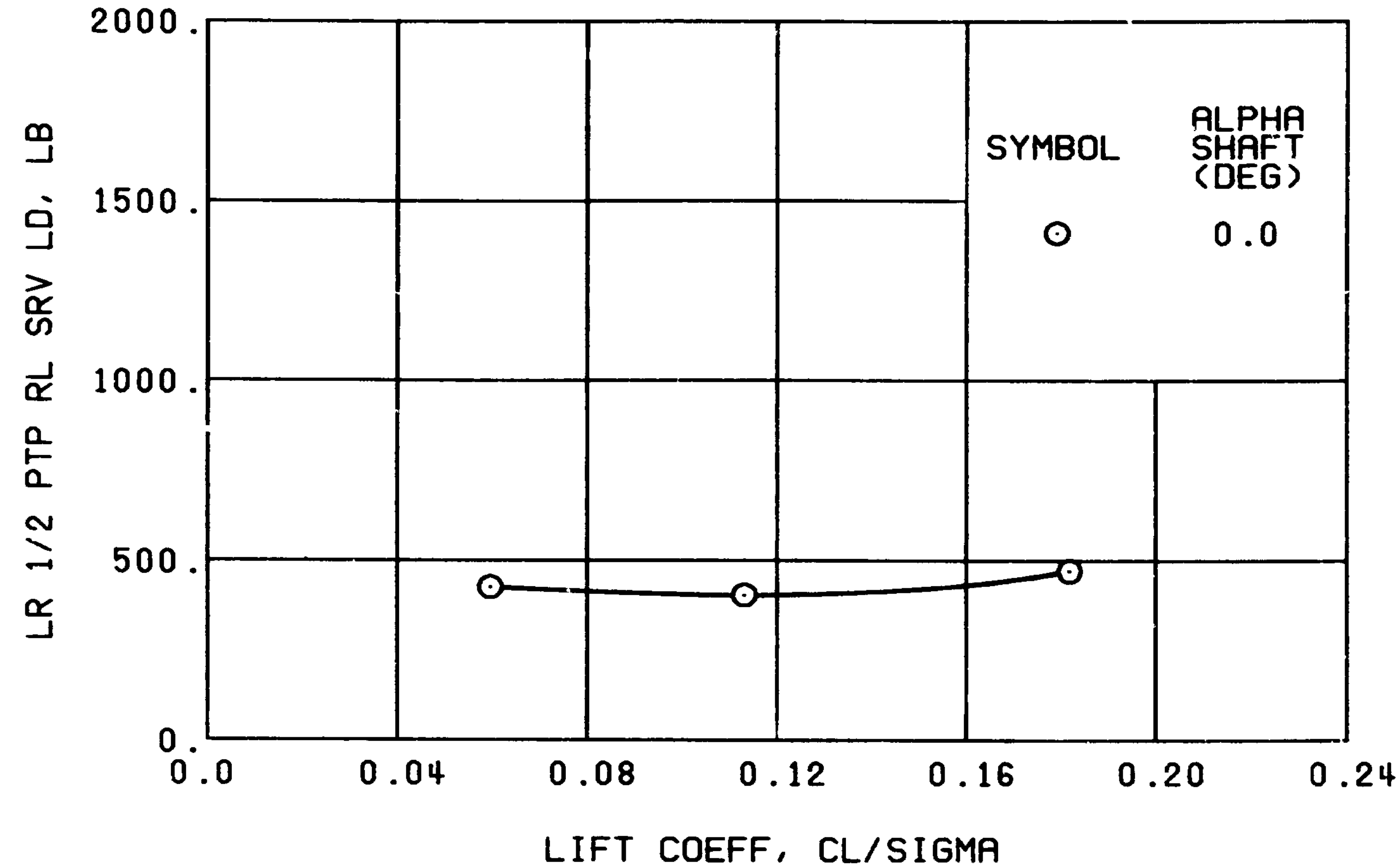

(q) GAGE 25

Figure 59. Continued.
$\mu = 0.91 \quad B'_{1s} = 2$ Deg

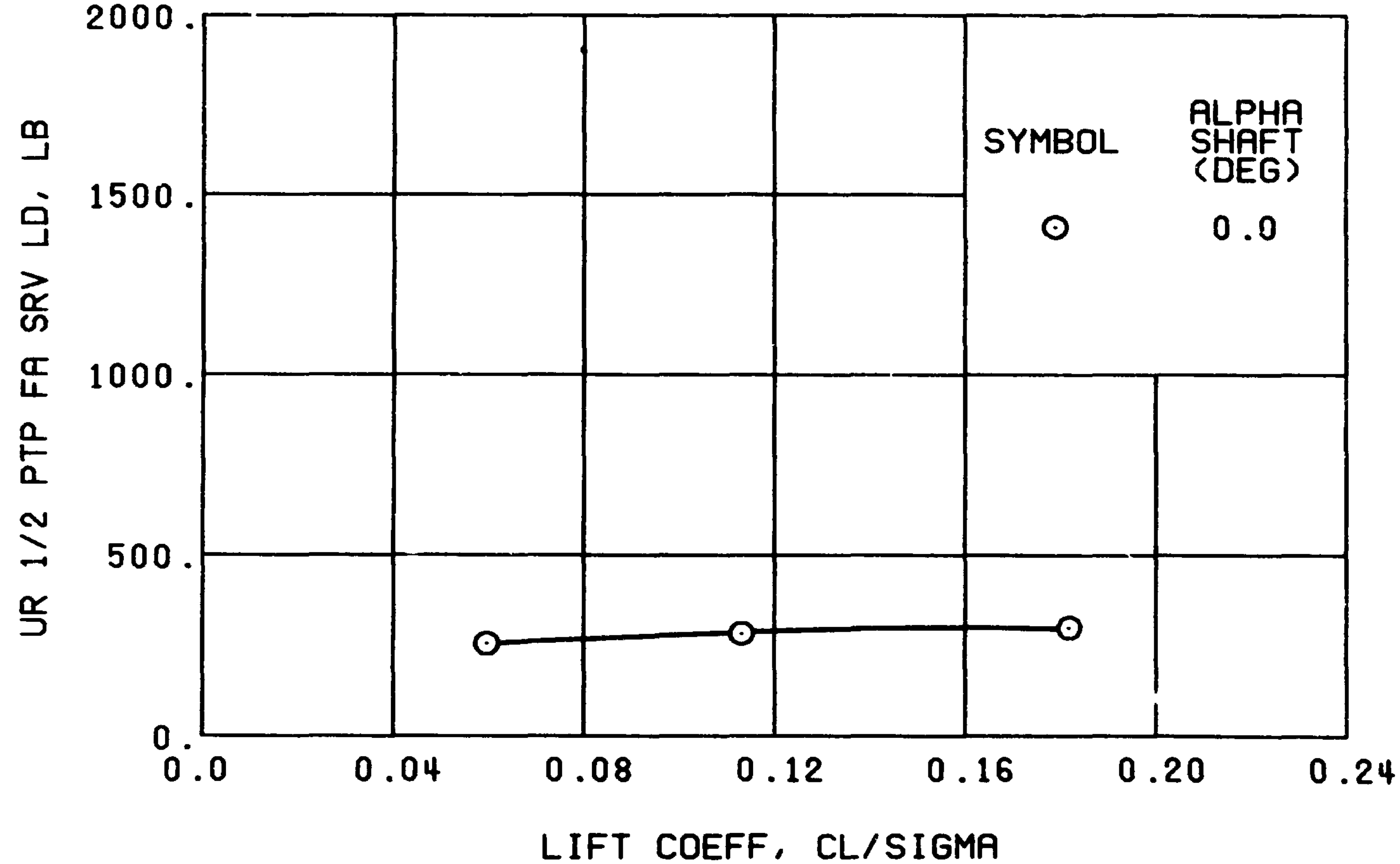

(r) GAGE 24

Figure 59. Continued.
$\mu = 0.91 \quad B'_{1s} = 2$ Deg

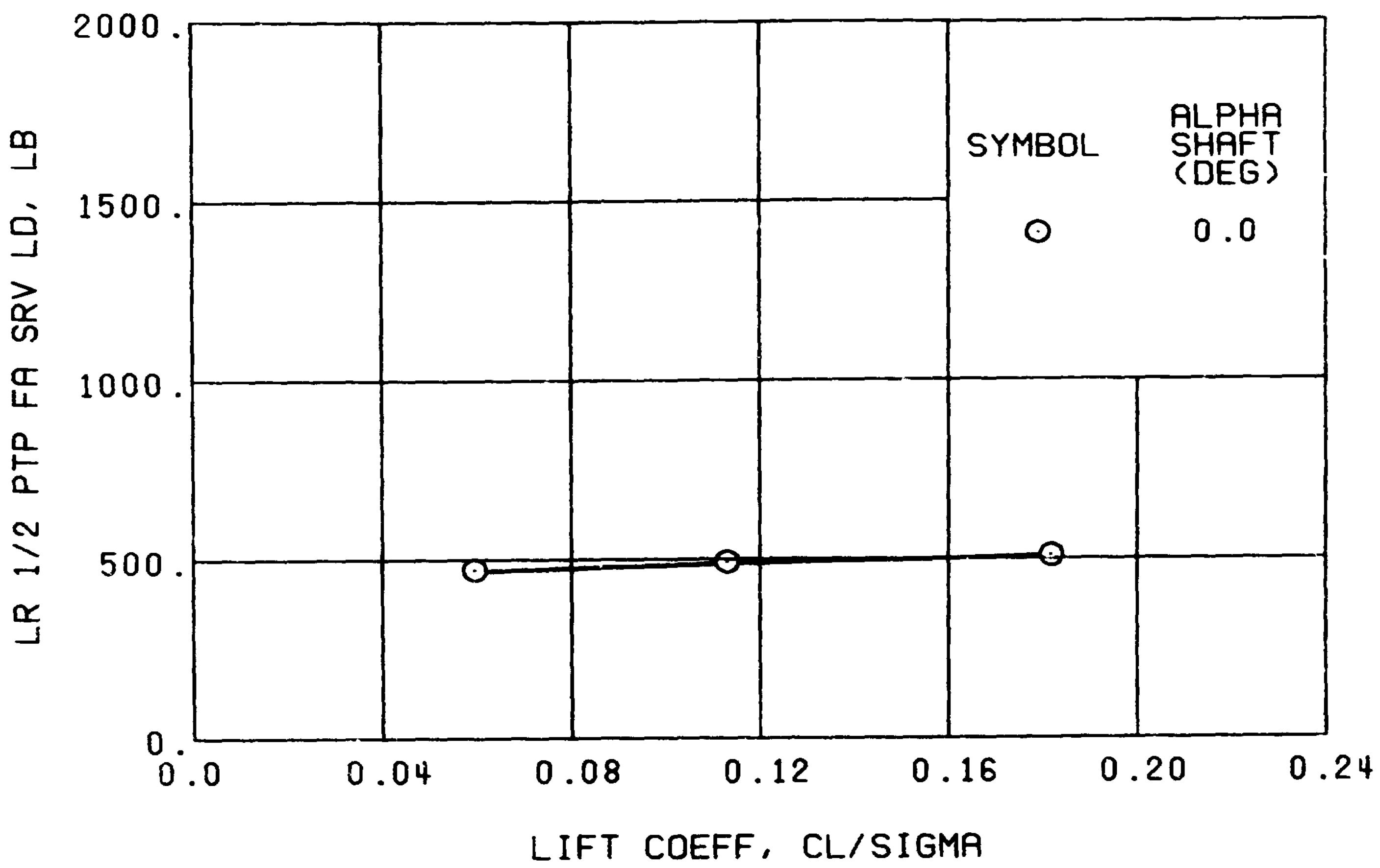

(s) GAGE 27

Figure 59. Continued.
$\mu = 0.91 \quad B_{1s}' = 2$ Deg

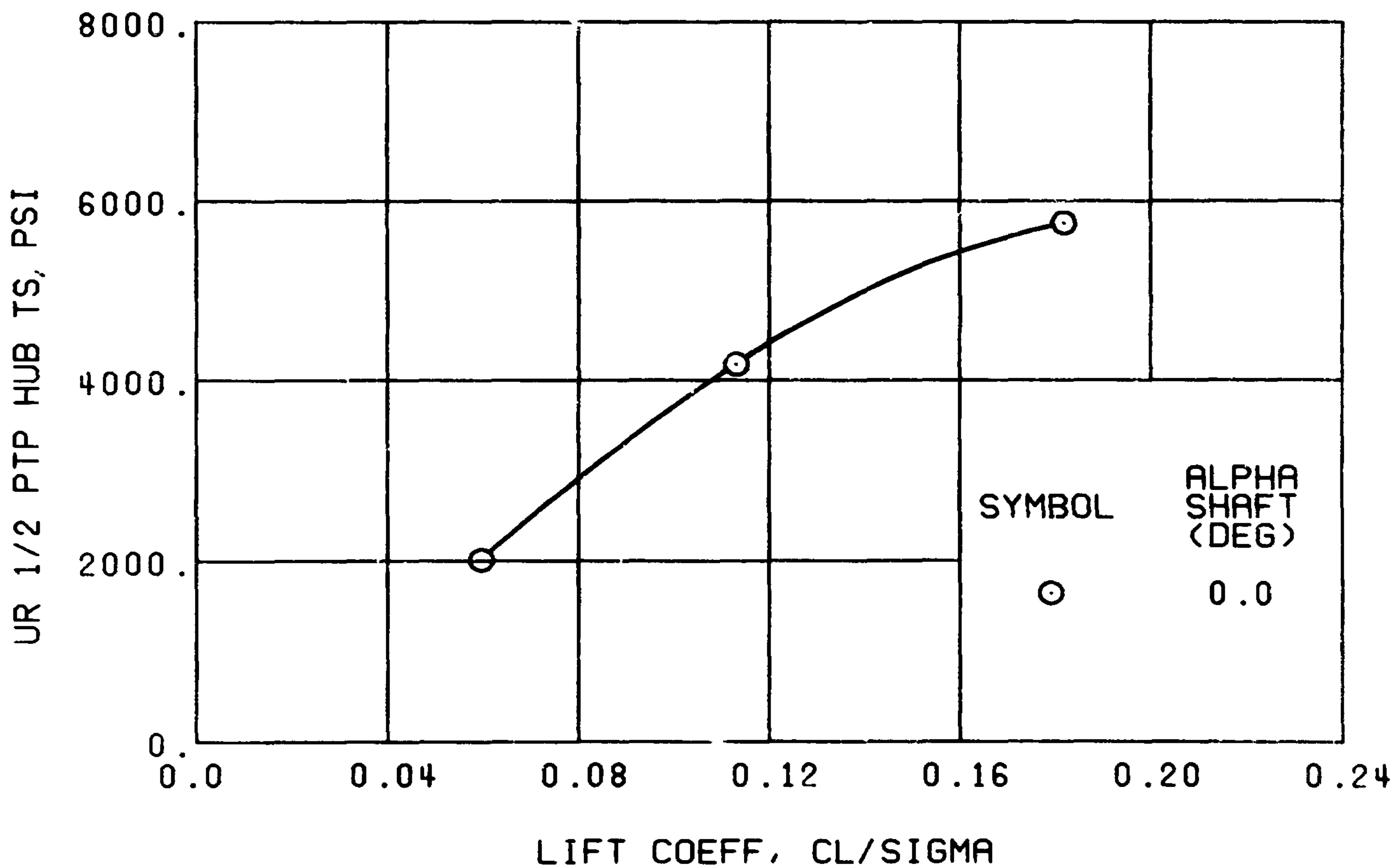

(t) GAGE 65

Figure 59. Continued.
$\mu = 0.91$ $B'_{1s} = 2$ Deg

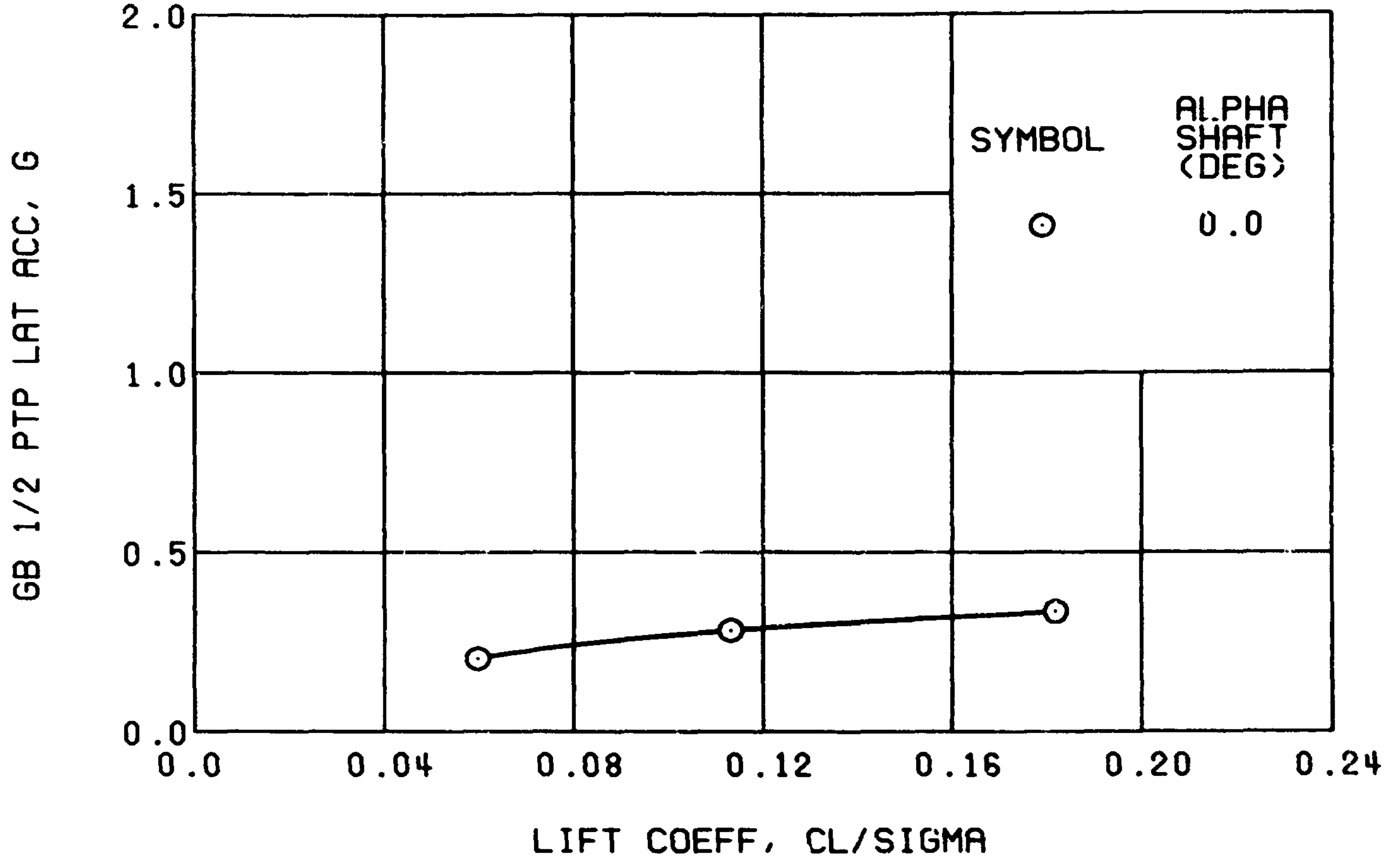

(u) GAGE 15 STA 76, BL 30

Figure 59. Continued.
$\mu = 0.91$ $B'_{1s} \approx 2$ Deg

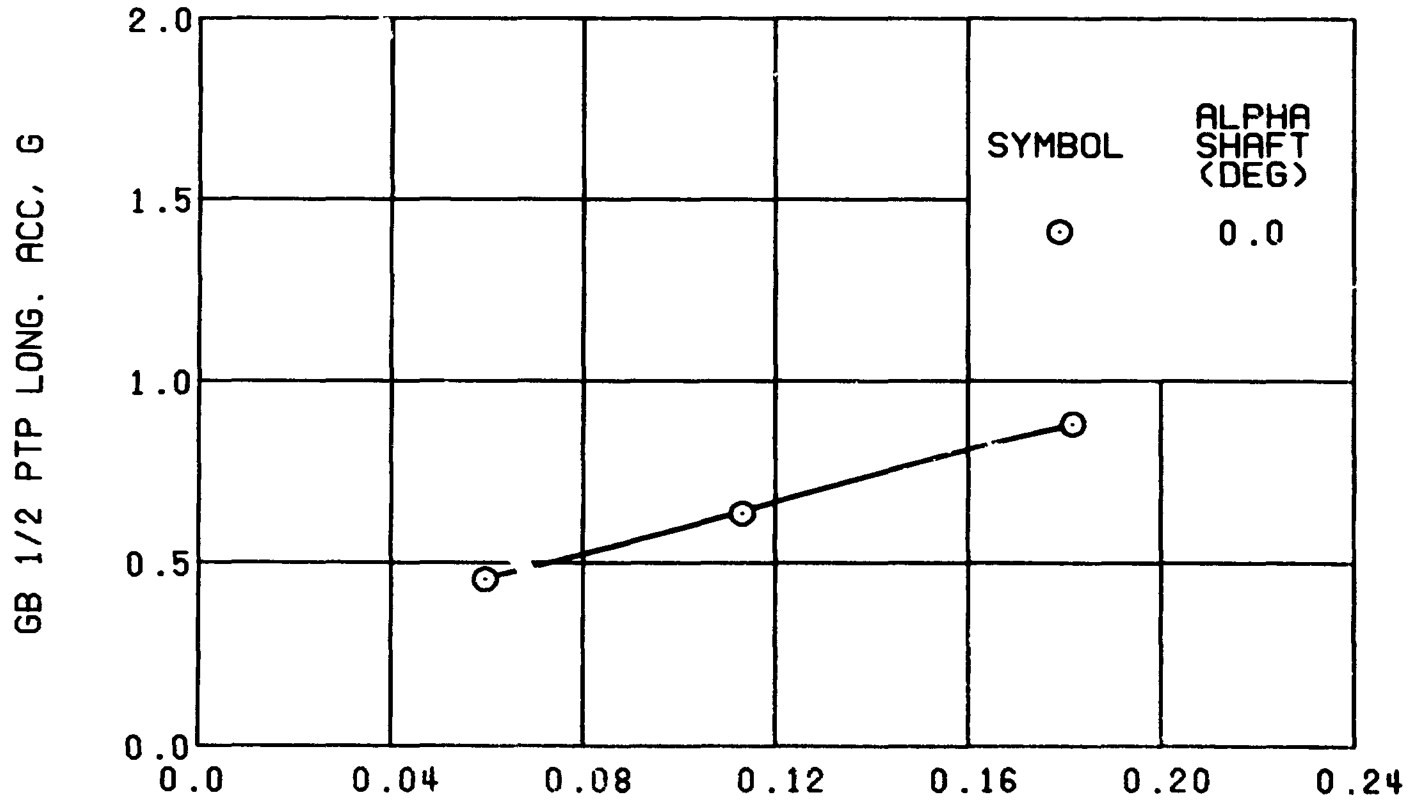

(v) GAGE 14 STA 61, BL 0

Figure 59. Continued.
$\mu = 0.91$ $B'_{1s} = 2$ Deg

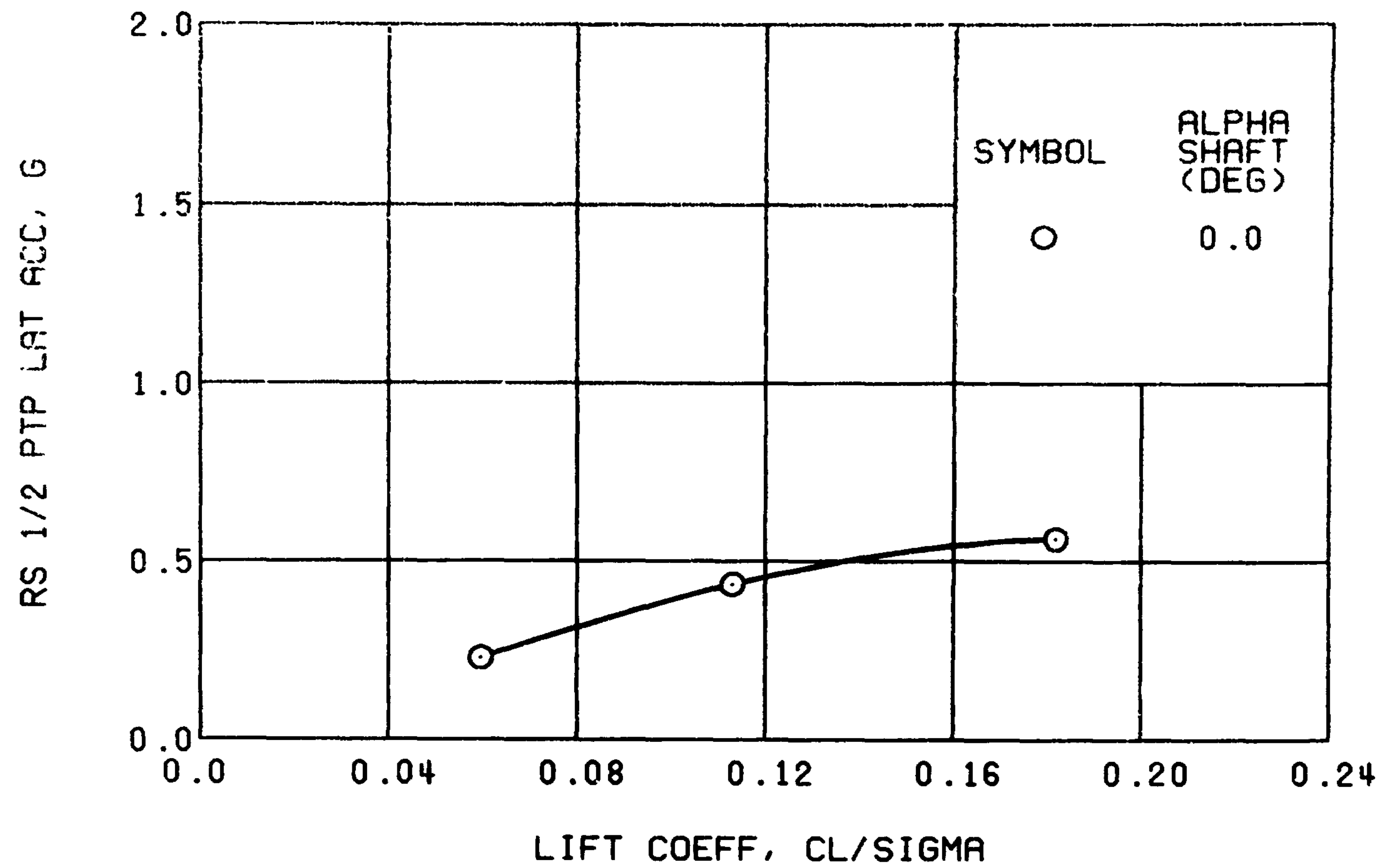

(w) GAGE 16 ROVER 3

Figure 59. Continued.
$\mu = 0.91$ $B_{1s} = 2$ Deg

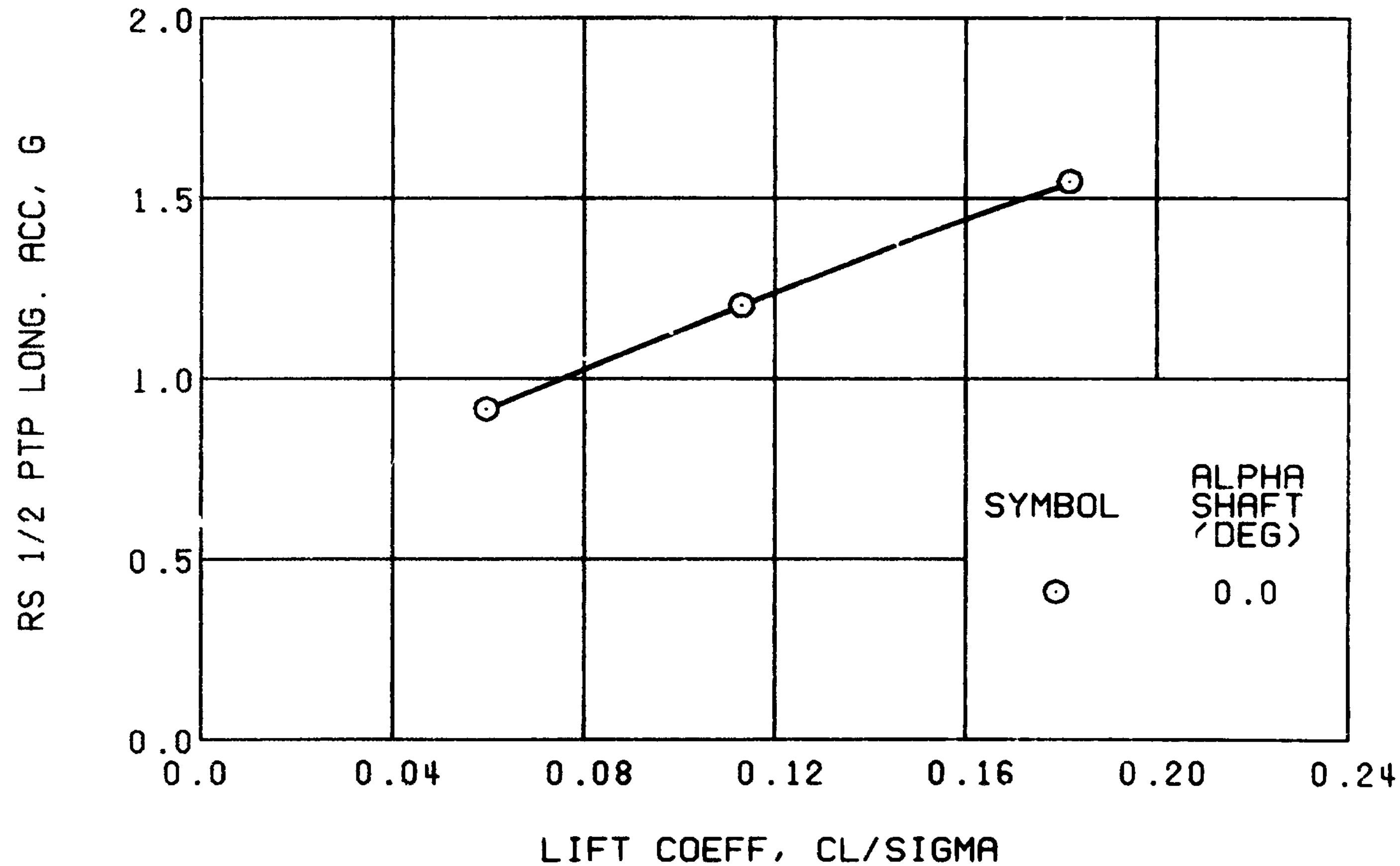

(x) GAGE 17 ROVER 4

Figure 59. Concluded.
$\mu = 0.91 \quad B'_{1s} = 2$ Deg

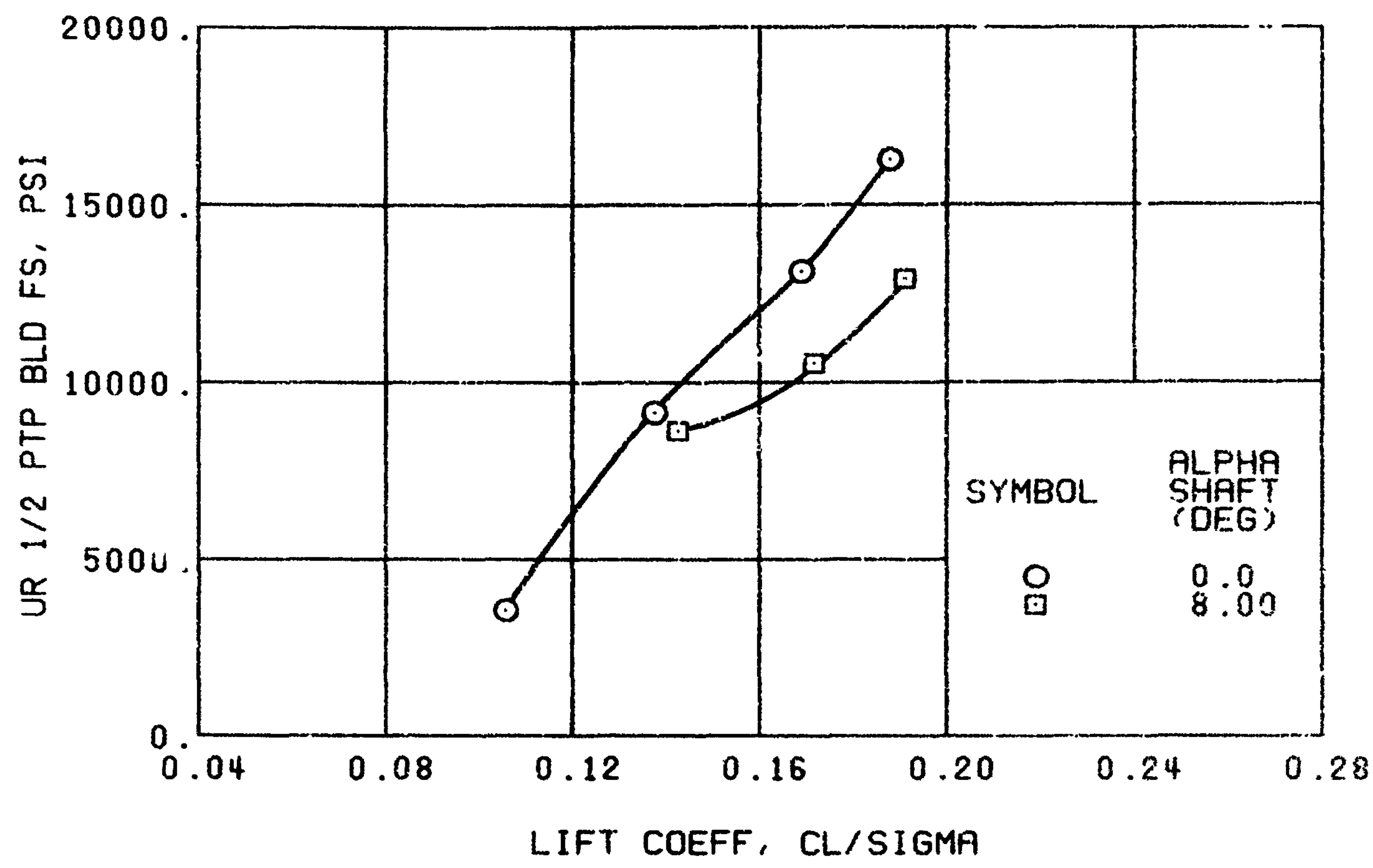

(a) GAGE 51 R84

Figure 60. Stress, Load and Vibration Data at an Advance Ratio of 0.21 With the Lateral Displacement Control (B'_{1s}) Set at 2 Degrees (Single-Rotor Configuration).

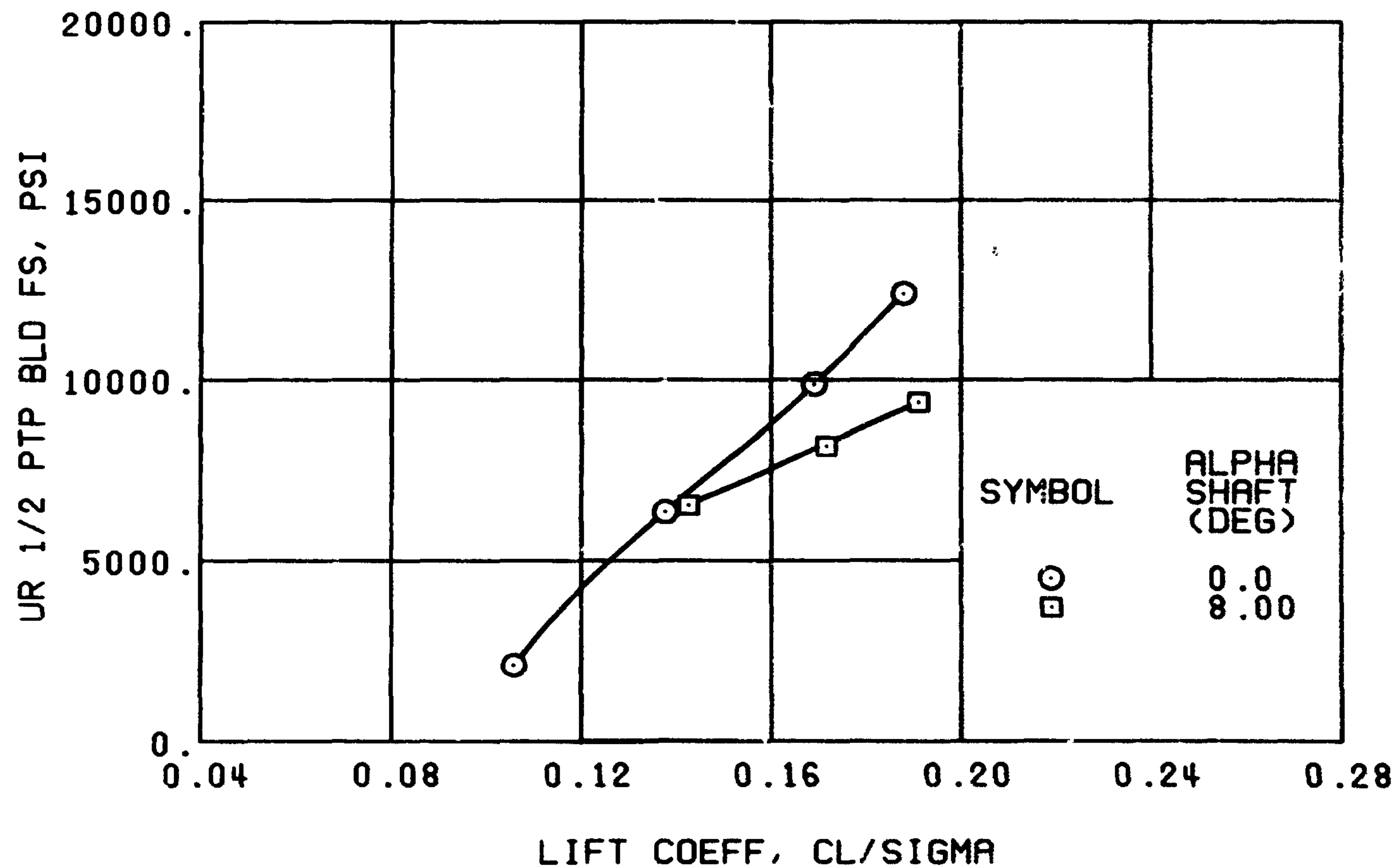

(c) GAGE 52 R108

Figure 60. Continued.

$\mu = 0.21$ $B'_{1s} = 2$ Deg (Single-Rotor Configuration)

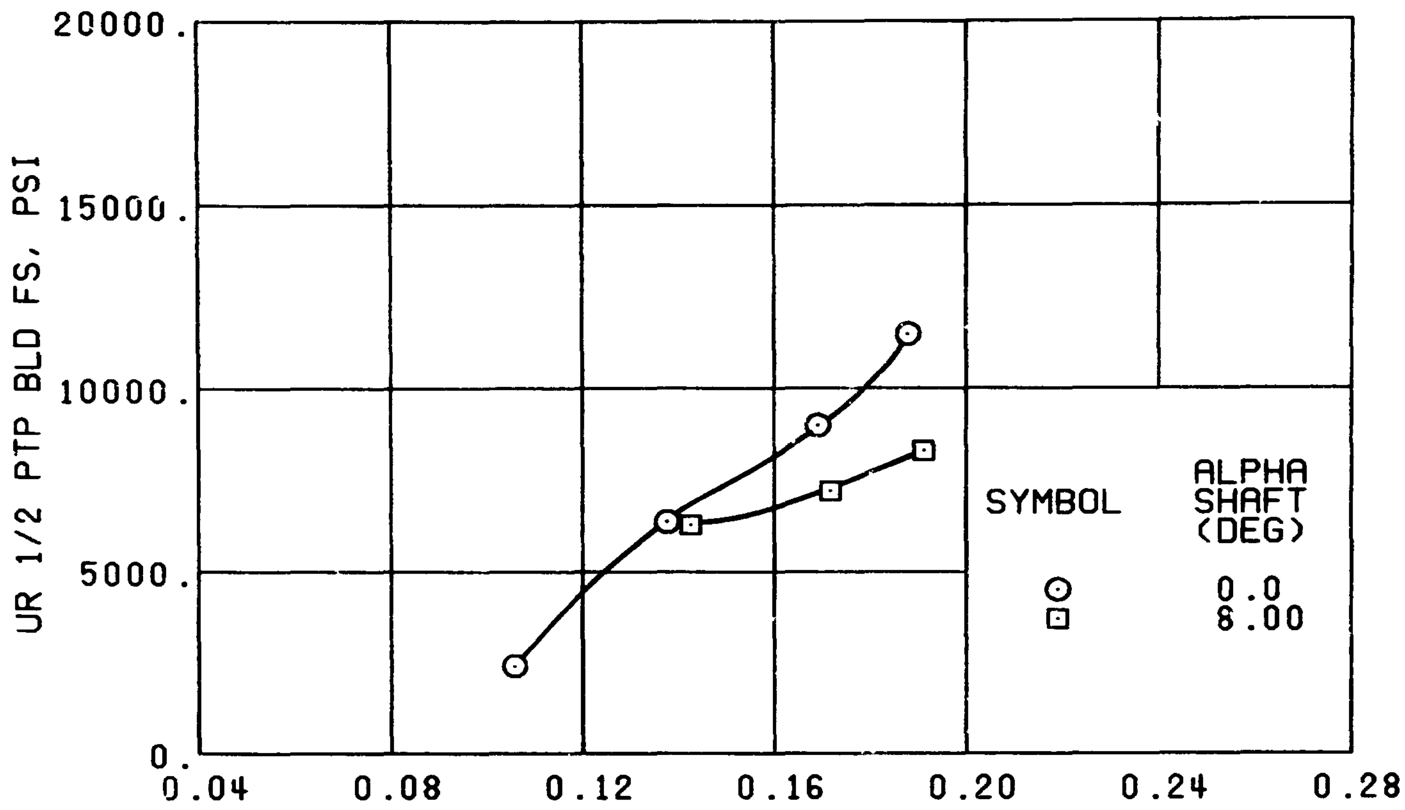

(d) GAGE 53 R132

Figure 60. Continued.

μ = 0.21 B'_{1s} = 2 Deg (Single-Rotor Configuration)

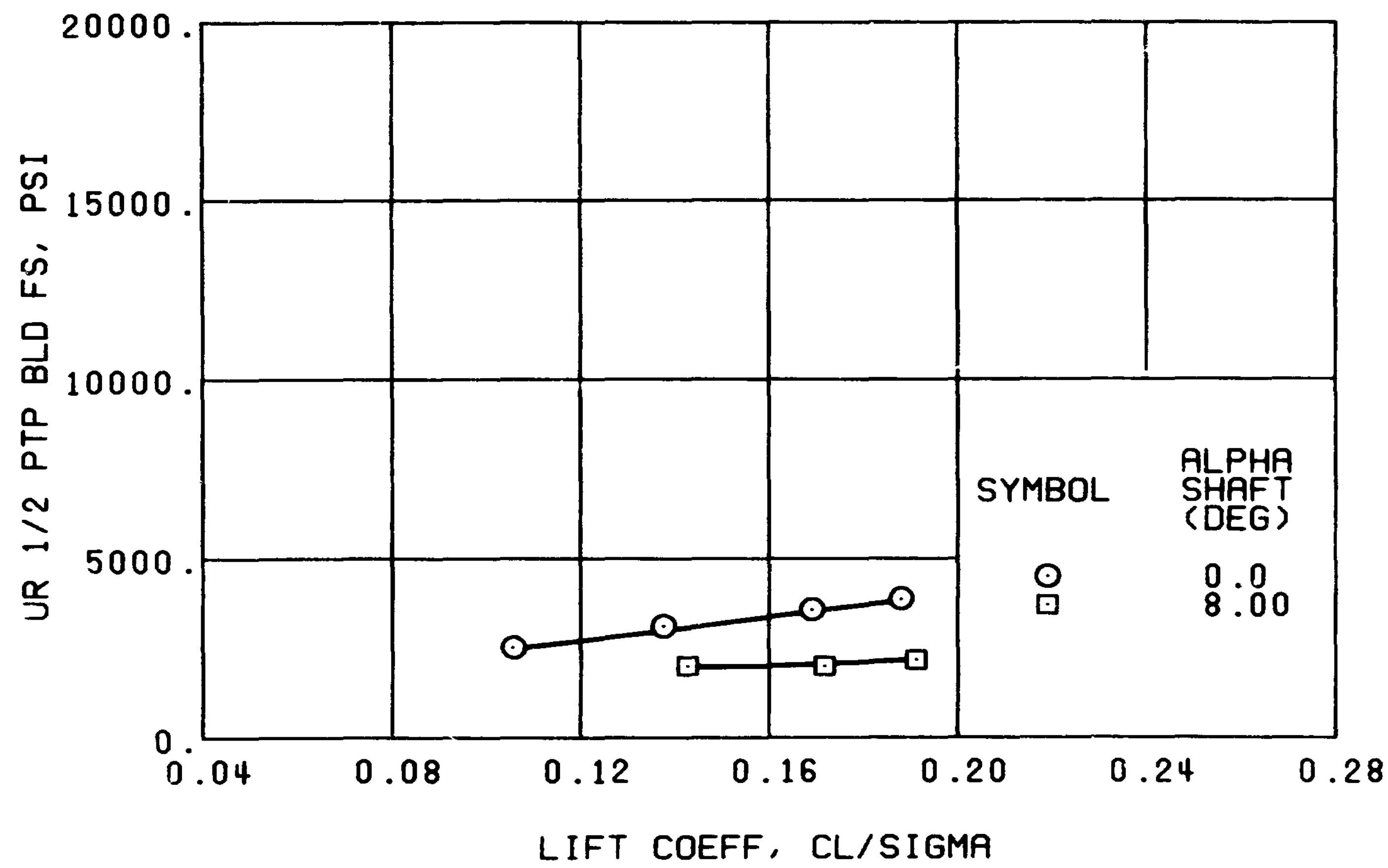

(f) GAGE 55 R204

Figure 60. Continued.

μ = 0.21 B'_{1s} = 2 Deg (Single-Rotor Configuration)

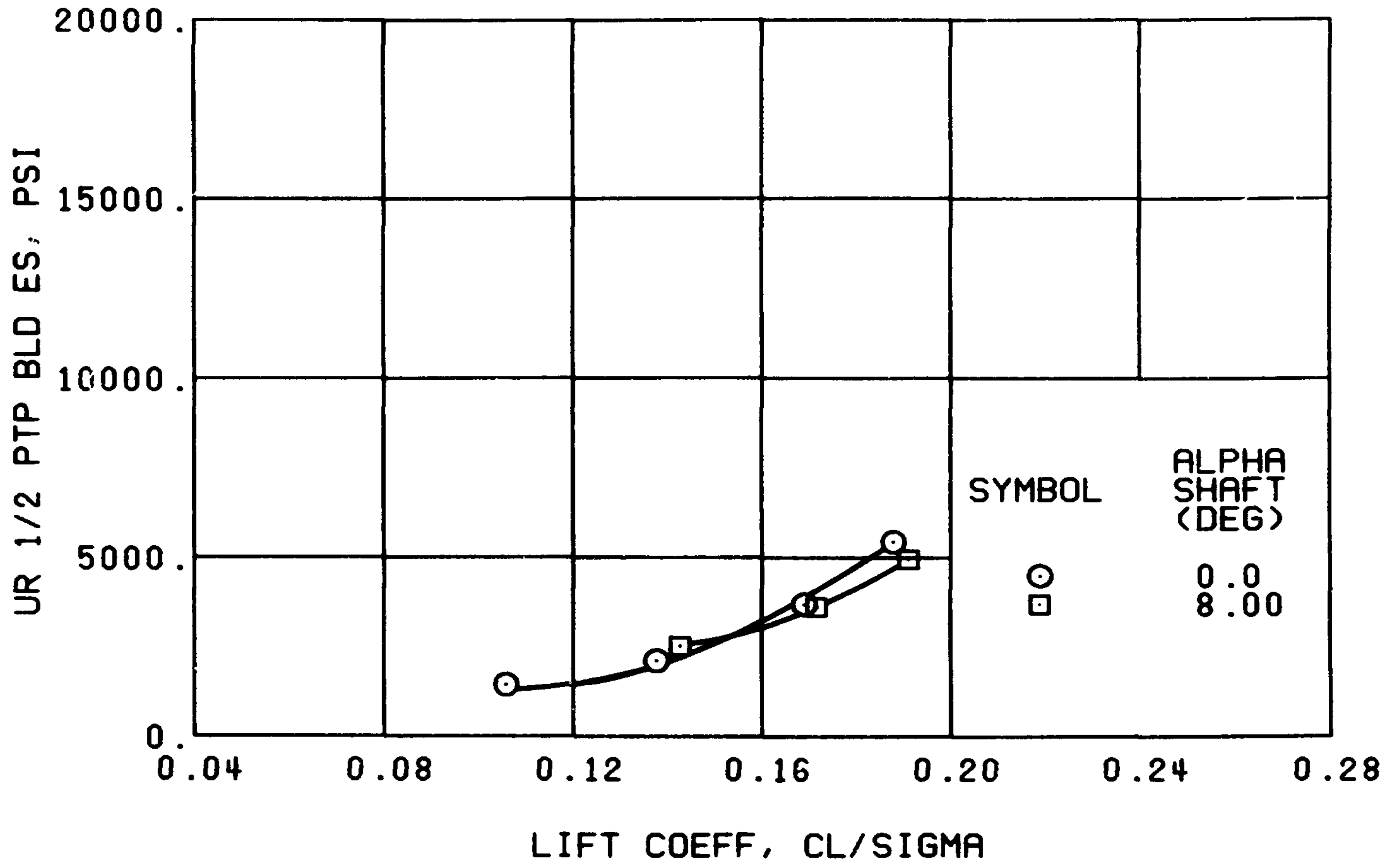

(h) GAGE 40 R84

Figure 60. Continued.

μ = 0.21 B'_{1s} = 2 Deg (Single-Rotor Configuration)

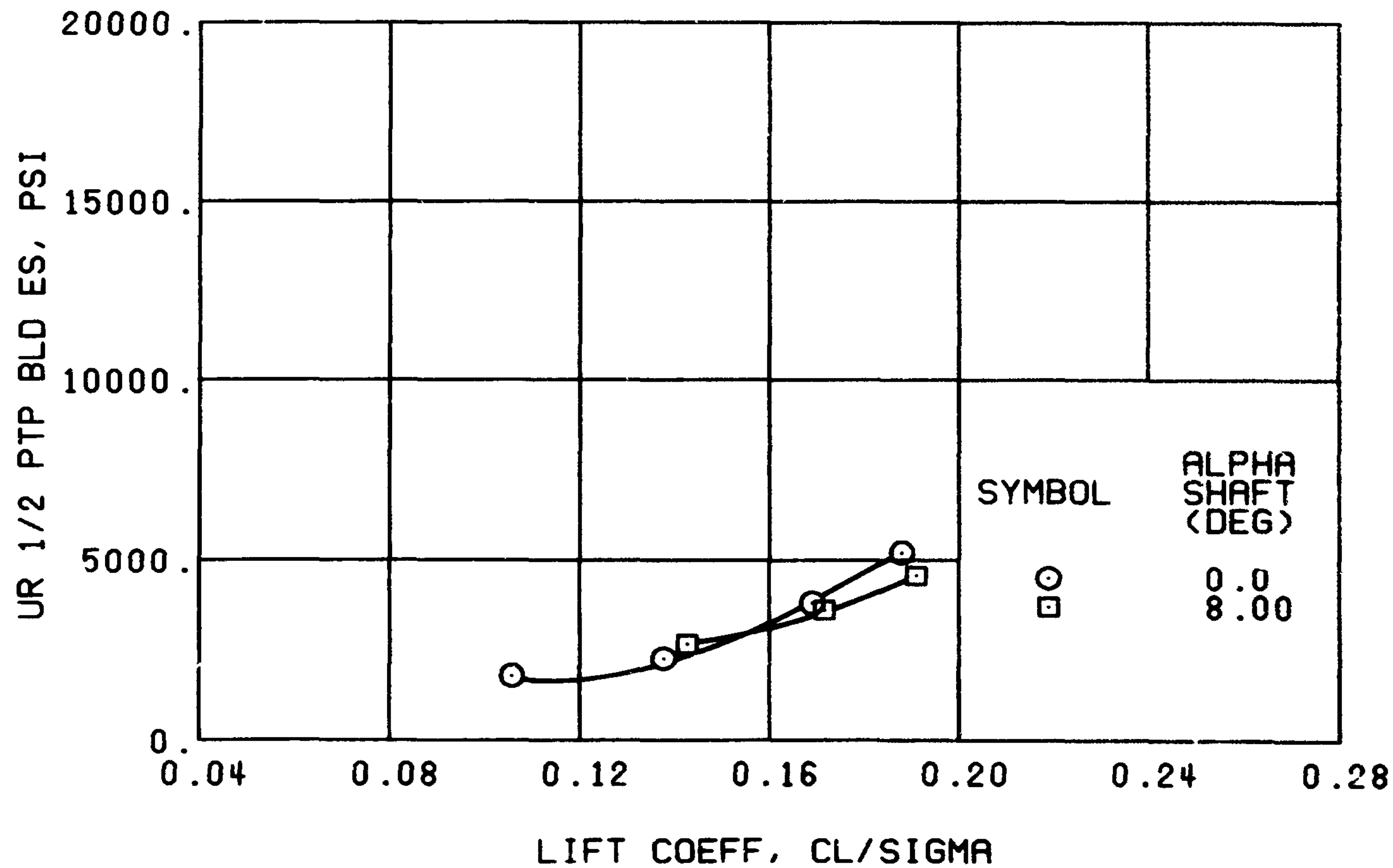

(j) GAGE 42 R132

Figure 60. Continued.

μ = 0.21 B'_{1s} = 2 Deg (Single-Rotor Configuration)

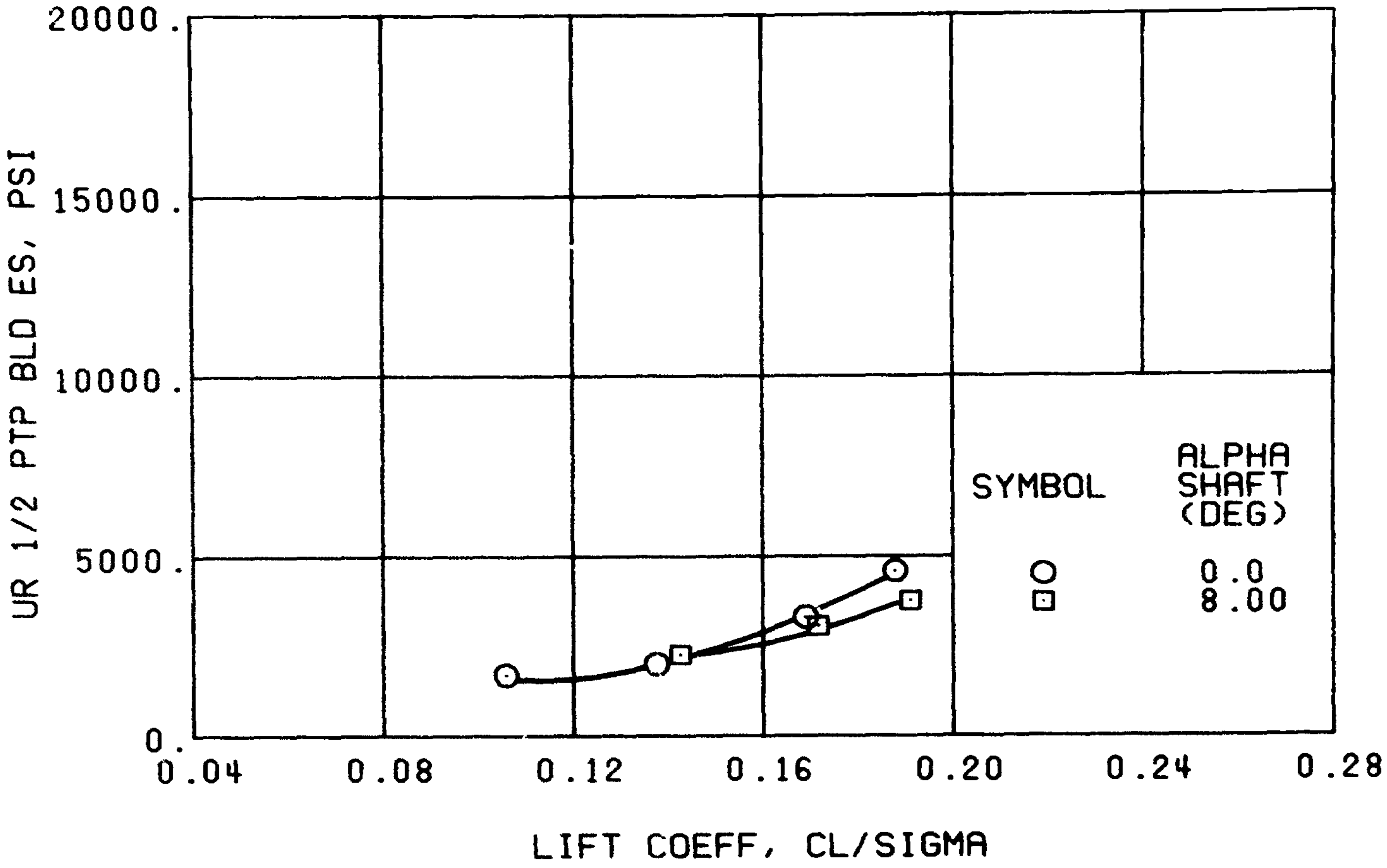

(k) GAGE 43 R168

Figure 60. Continued.

$\mu = 0.21$ $B'_{1s} = 2$ Deg (Single-Rotor Configuration)

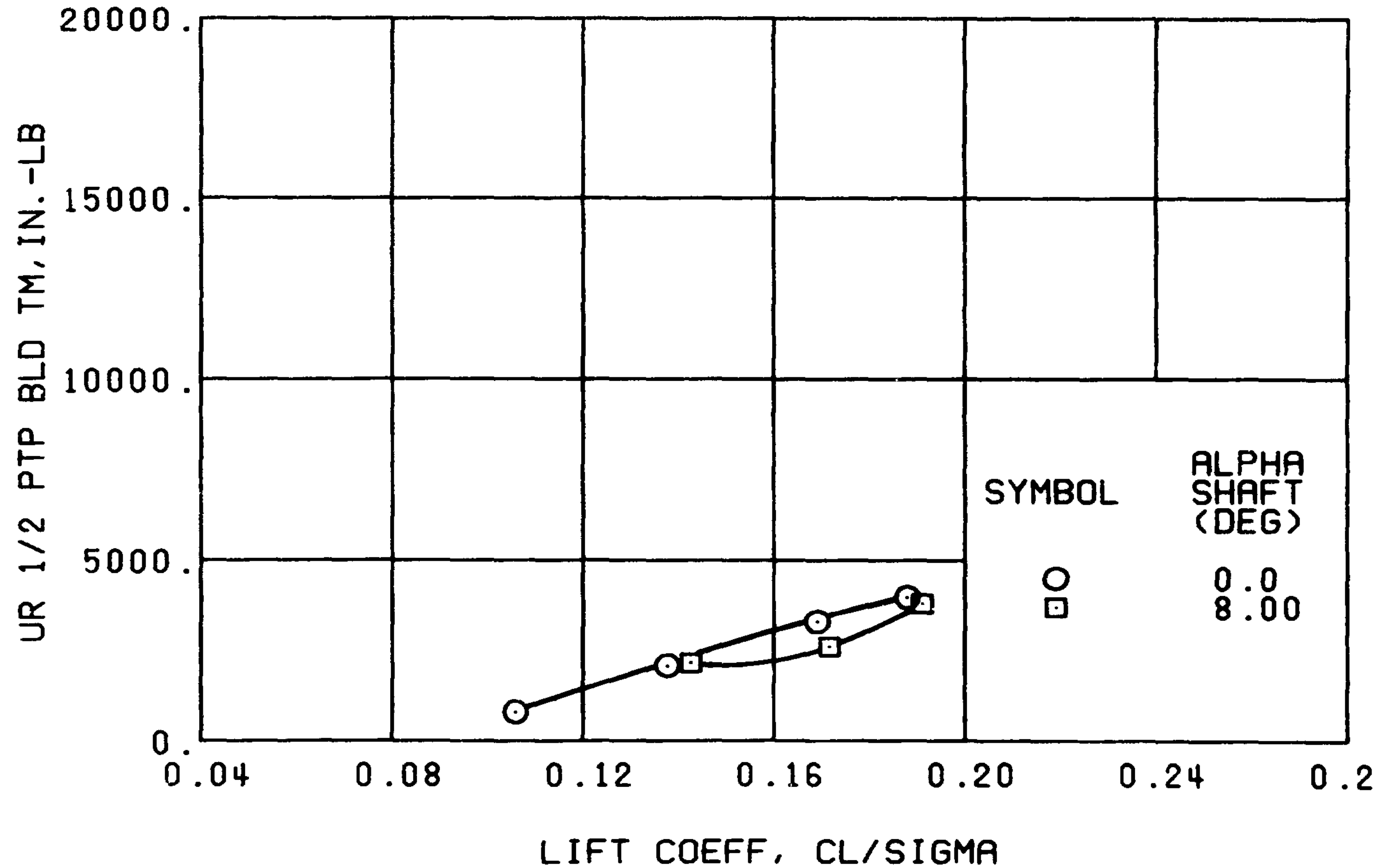

(m) GAGE 46 R130

Figure 60. **Continued.**

μ = 0.21 B'_{1s} = 2 **Deg (Single-Rotor Configuration)**

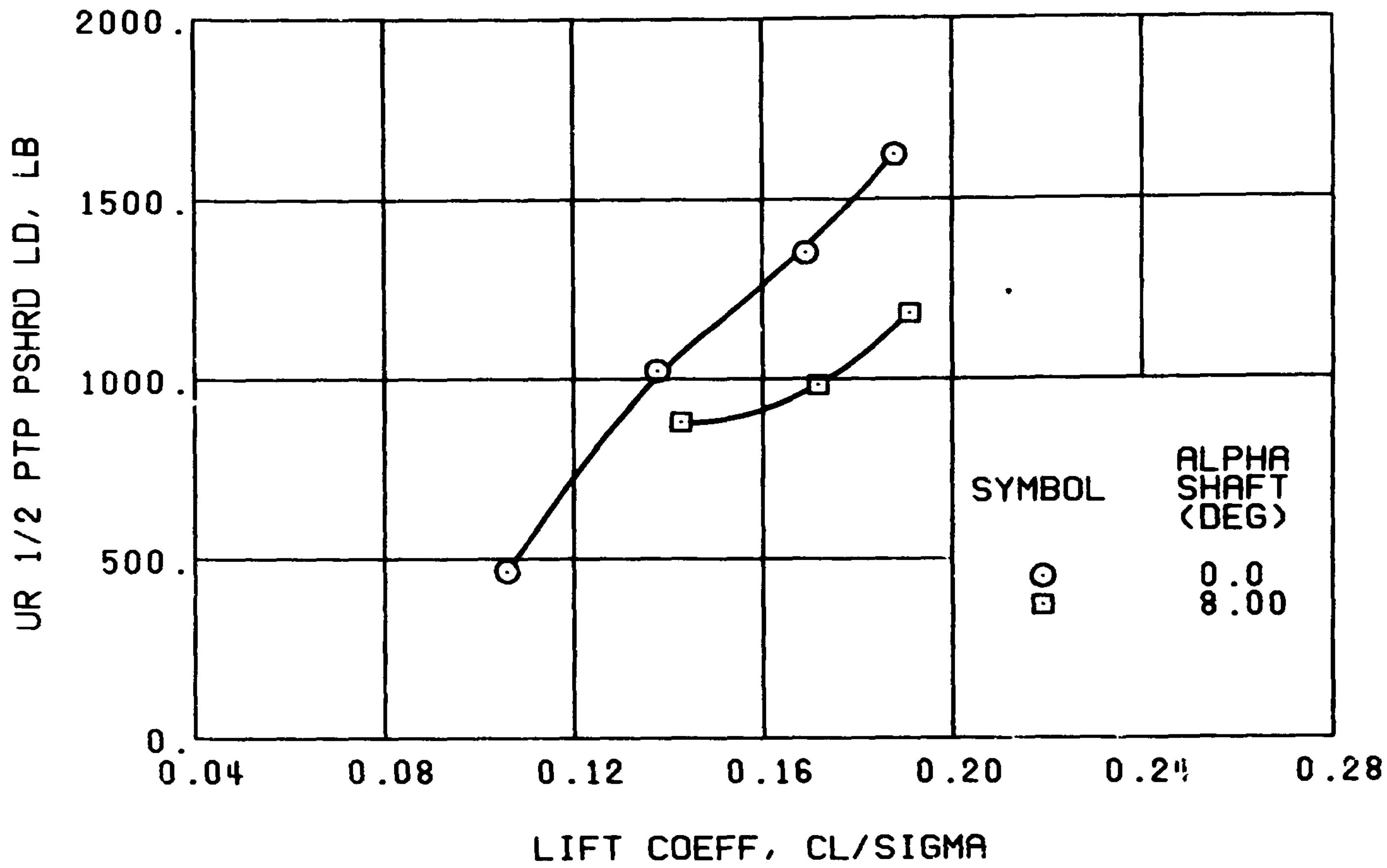

(n) GAGE 37

Figure 60. Continued.

$\mu = 0.21 \quad B'_{1s} = 2$ Deg (Single-Rotor Configuration)

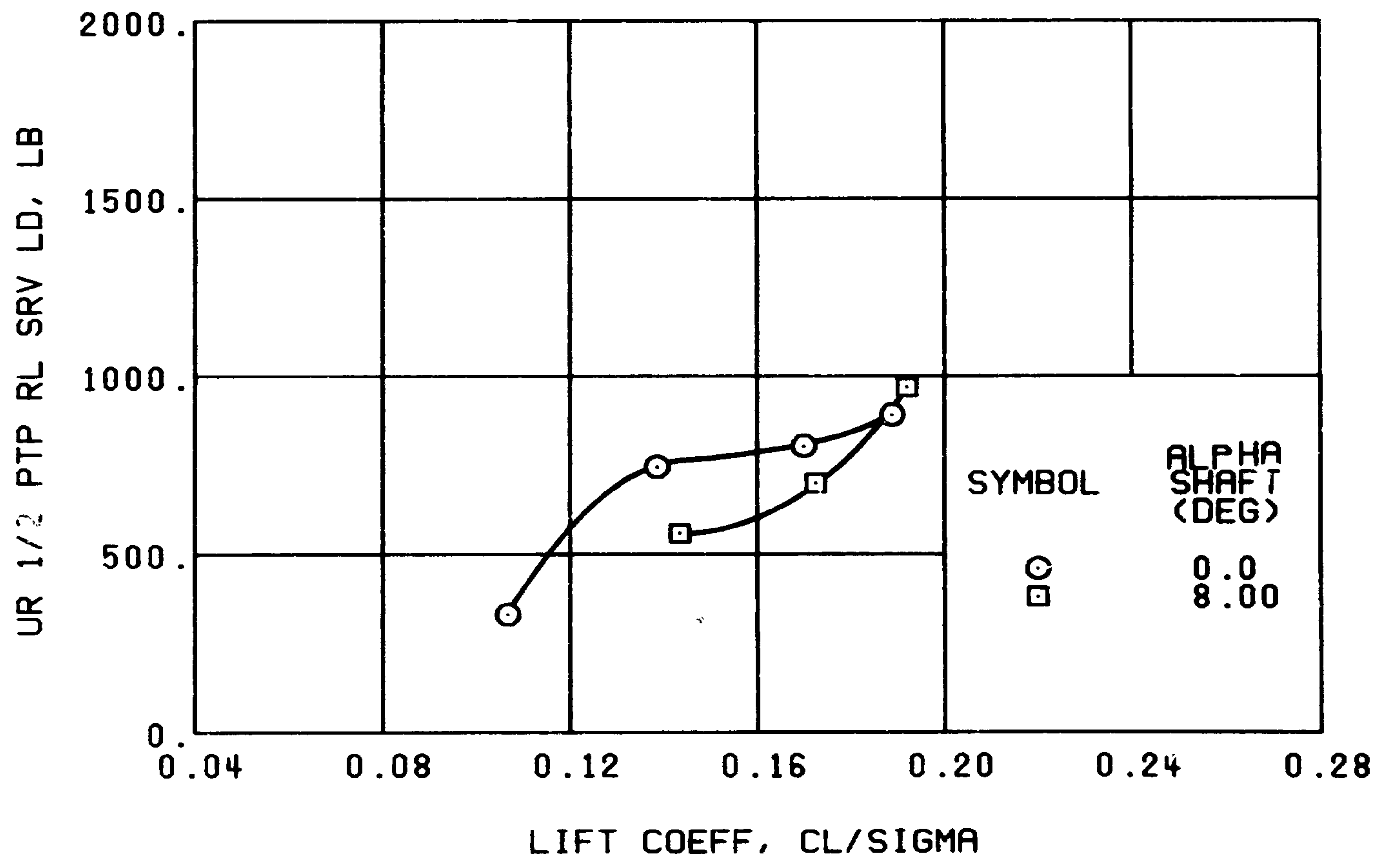

(p) GAGE 22

Figure 60. **Continued.**

$\mu = 0.21$ $B'_{1s} = 2$ Deg (Single-Rotor Configuration)

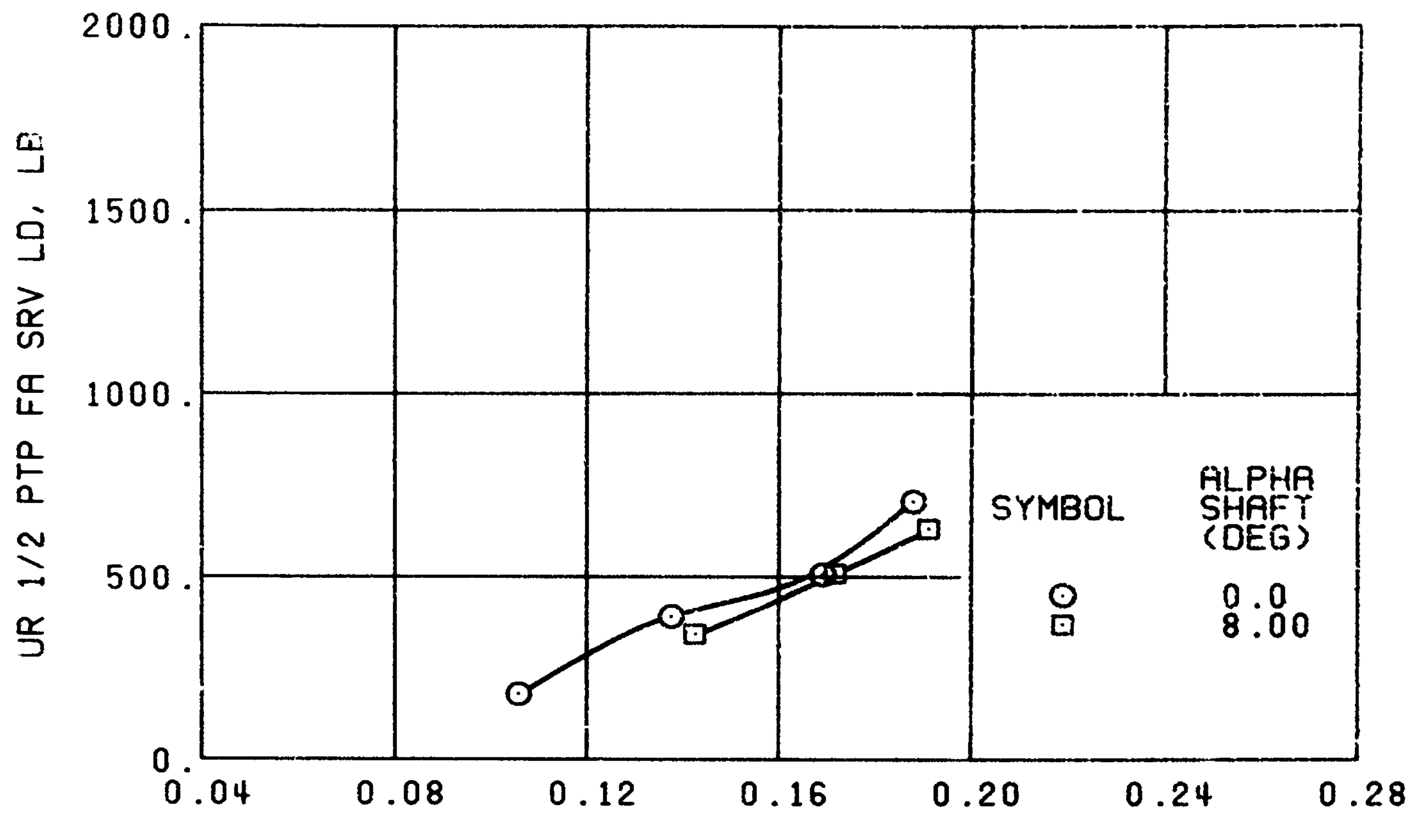

(r) GAGE 24

Figure 60. Continued.

$\mu = 0.21 \quad B'_{1s} = 2$ Deg (Single-Rotor Configuration)

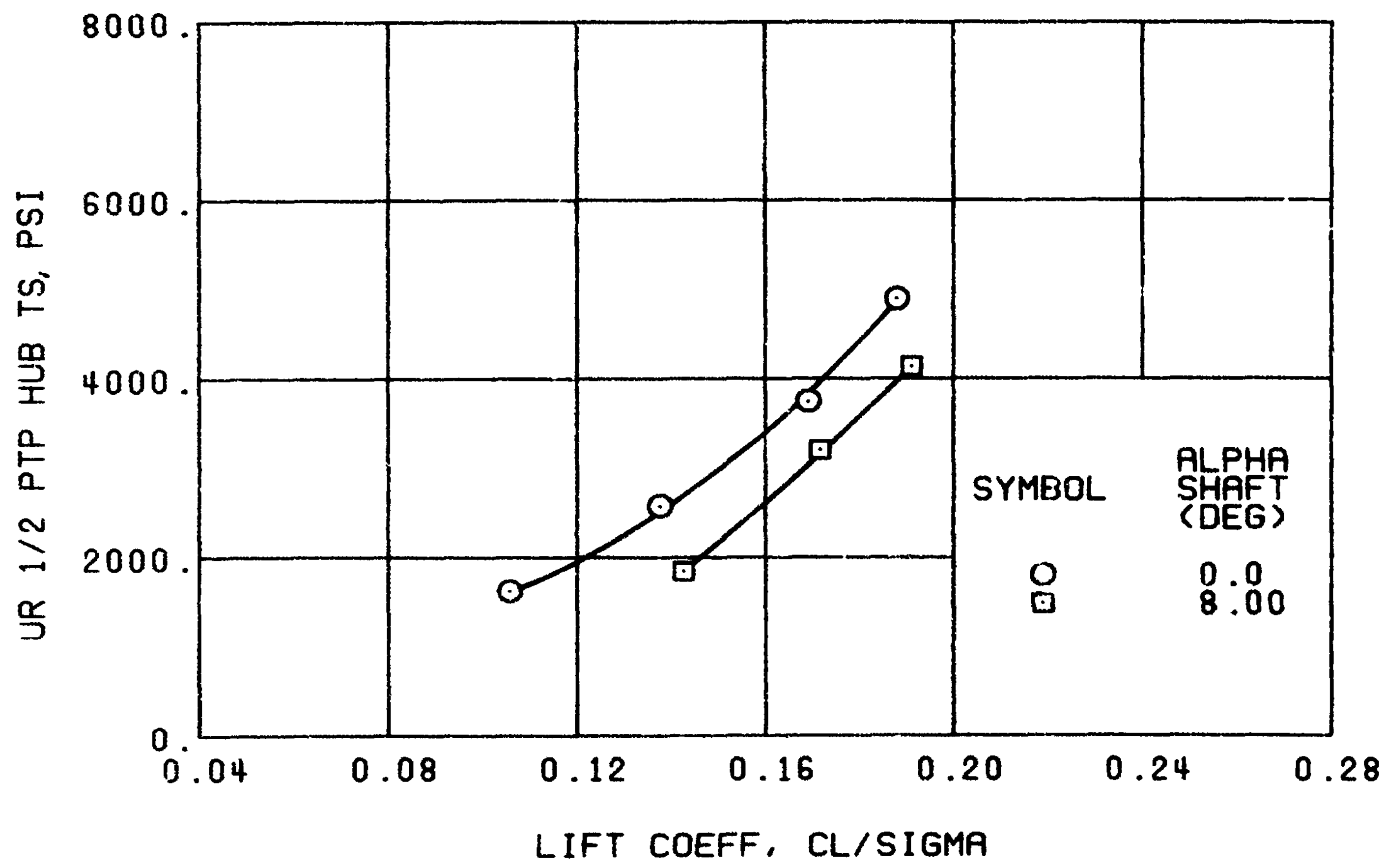

(f) GAGE 65

Figure 60. Continued.

$\mu = 0.21$ $B'_{1s} = 2$ Deg (Single-Rotor Configuration)

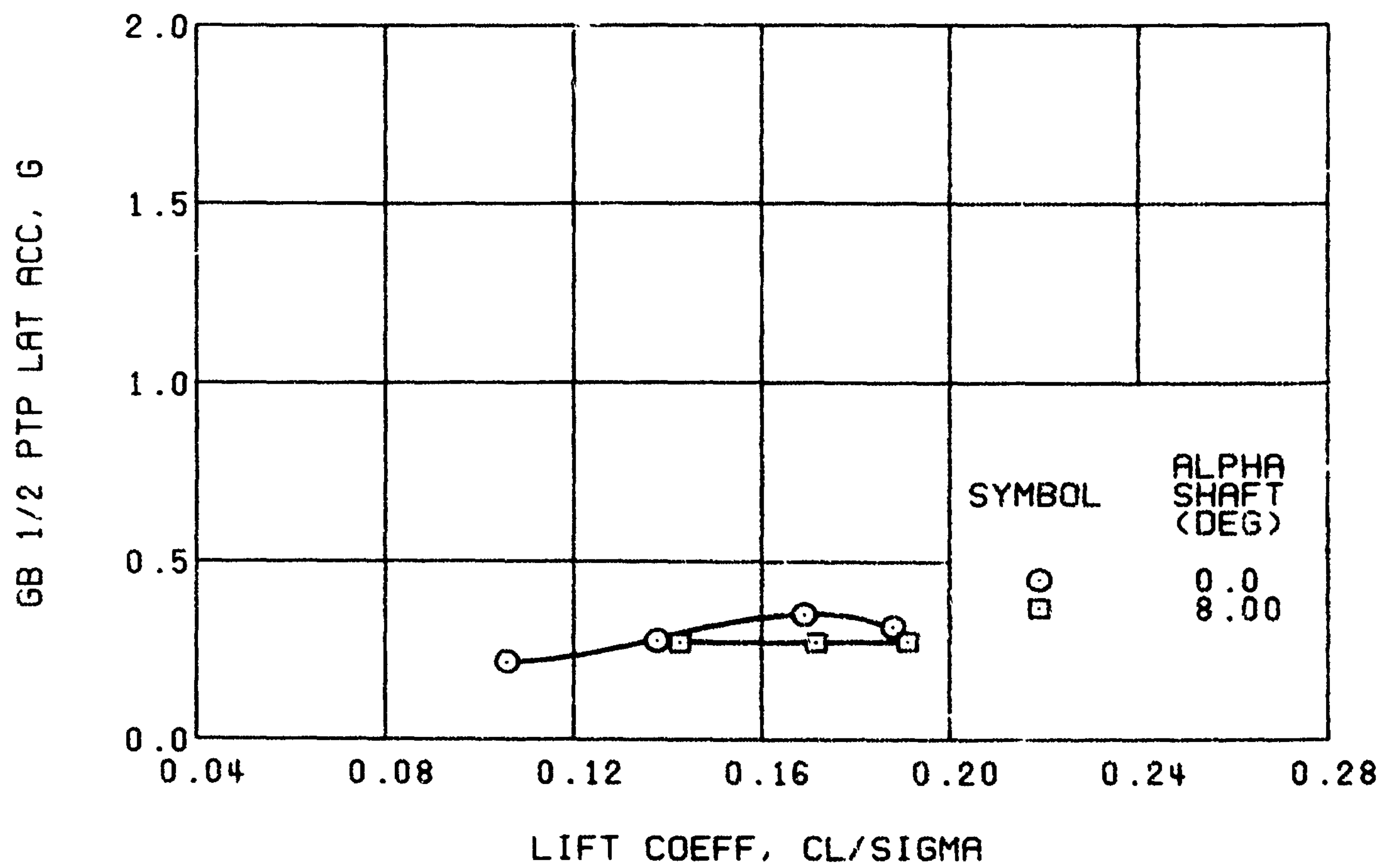

(u) GAGE 15 STA 76, BL 30

Figure 60. Continued.

$\mu = 0.21$ $B'_{1s} = 2$ Deg (Single-Rotor Configuration)

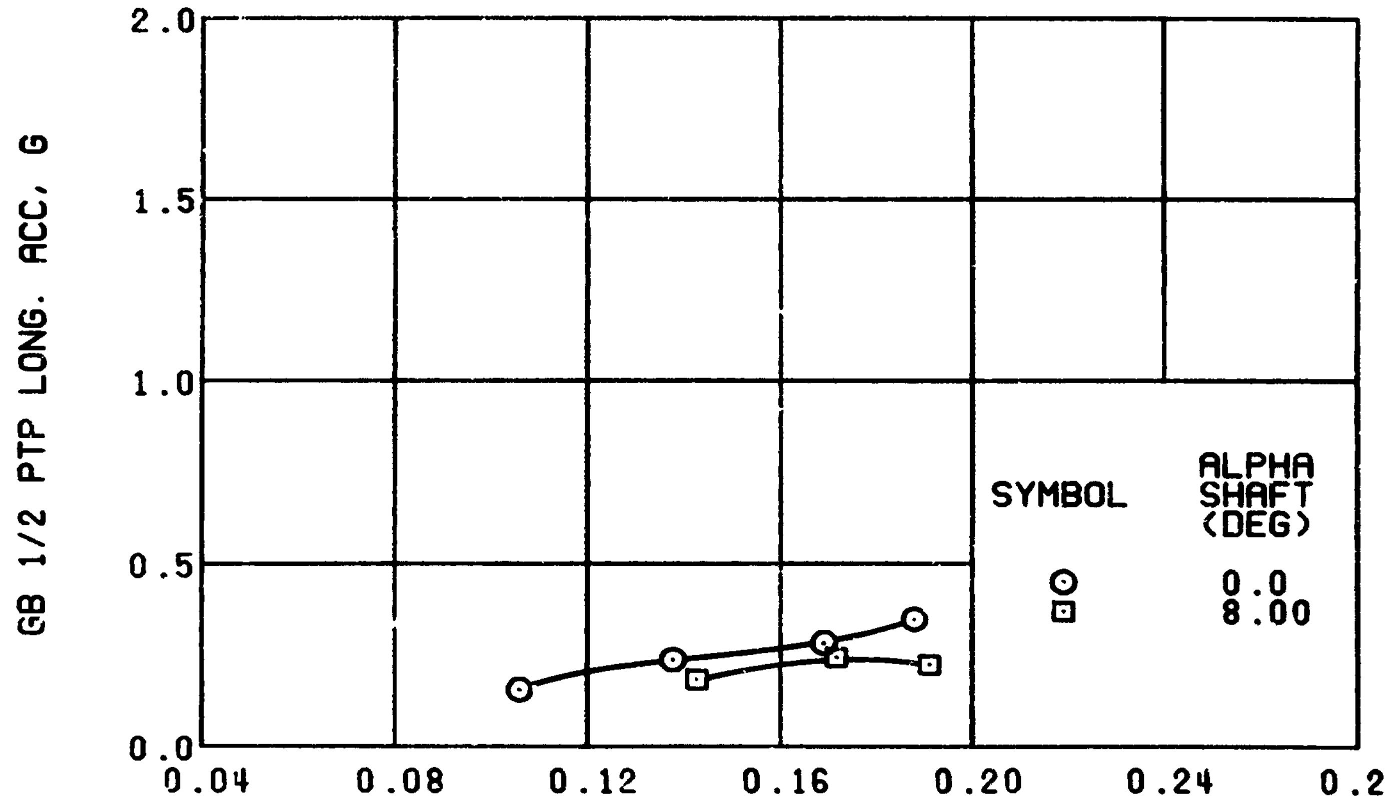

(v) GAGE 14 STA 61, BL 0

Figure 60. Continued.

μ = 0.21 B'_{1s} = 2 Deg (Single-Rotor Configuration)

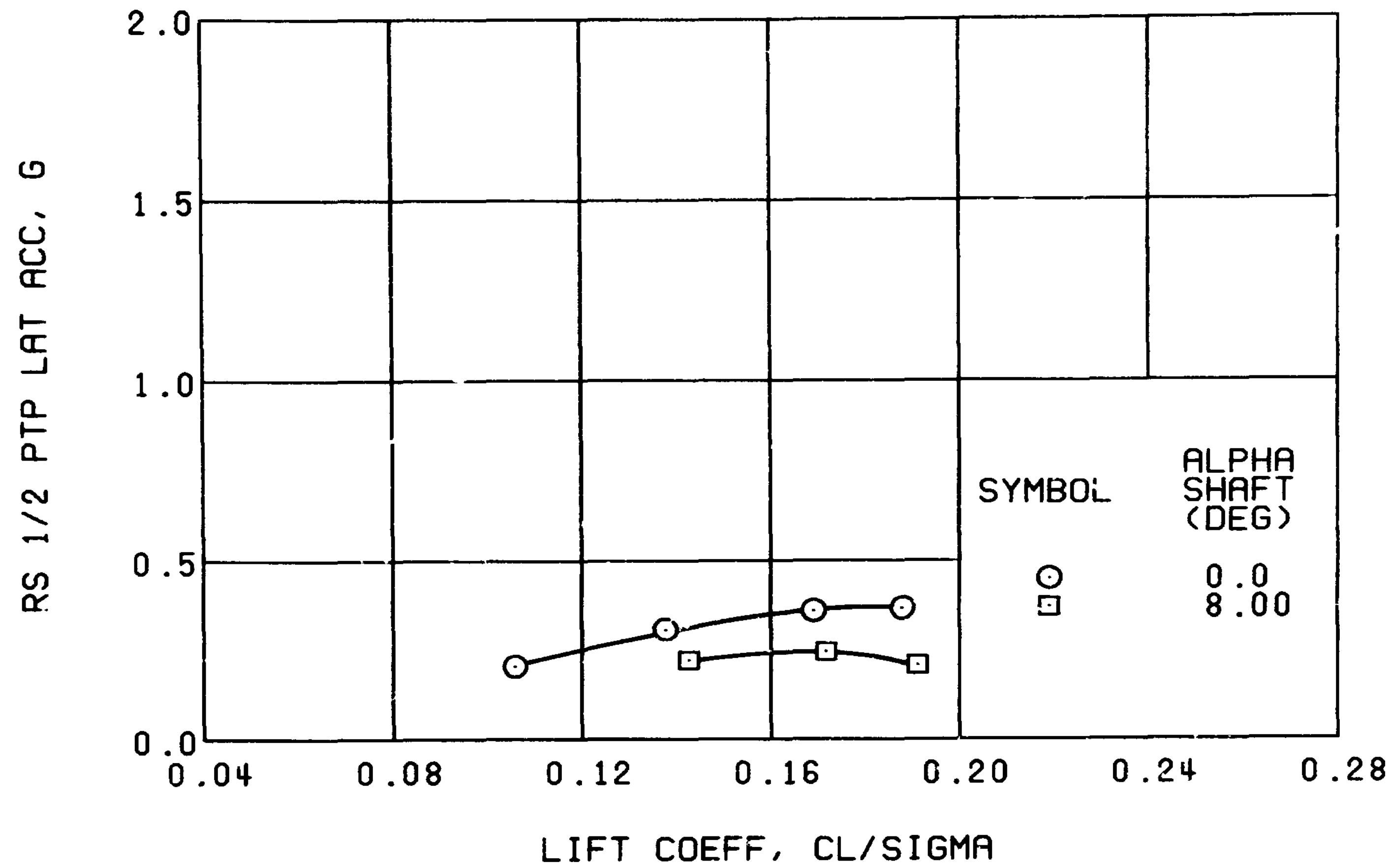

(w) GAGE 16 ROVER 3

Figure 60. Continued.

$\mu = 0.21$ $B'_{1s} = 2$ Deg (Single-Rotor Configuration)

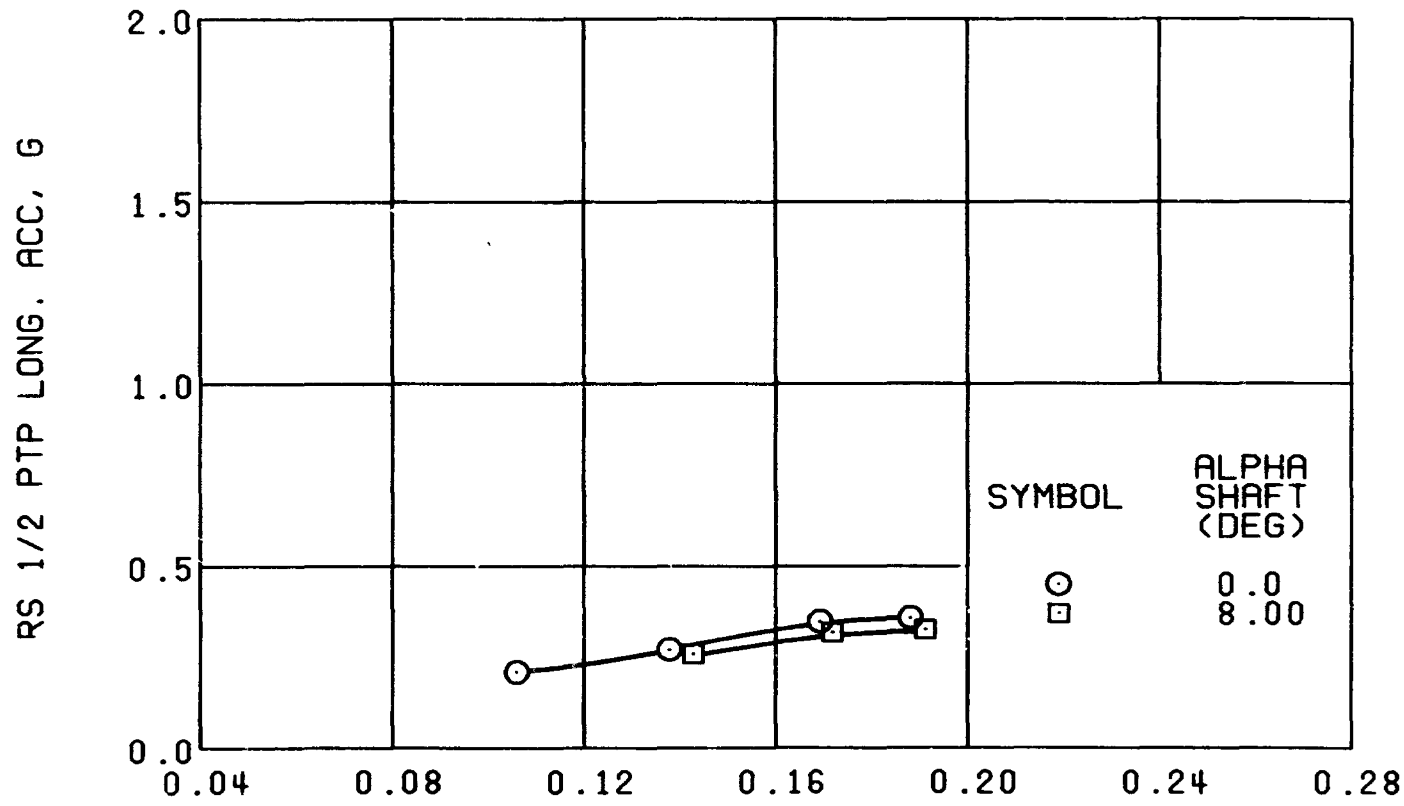

(x) GAGE 17 ROVER 4

Figure 60. Concluded.

$\mu = 0.21$ $B'_{1s} = 2$ Deg (Single-Rotor Configuration)

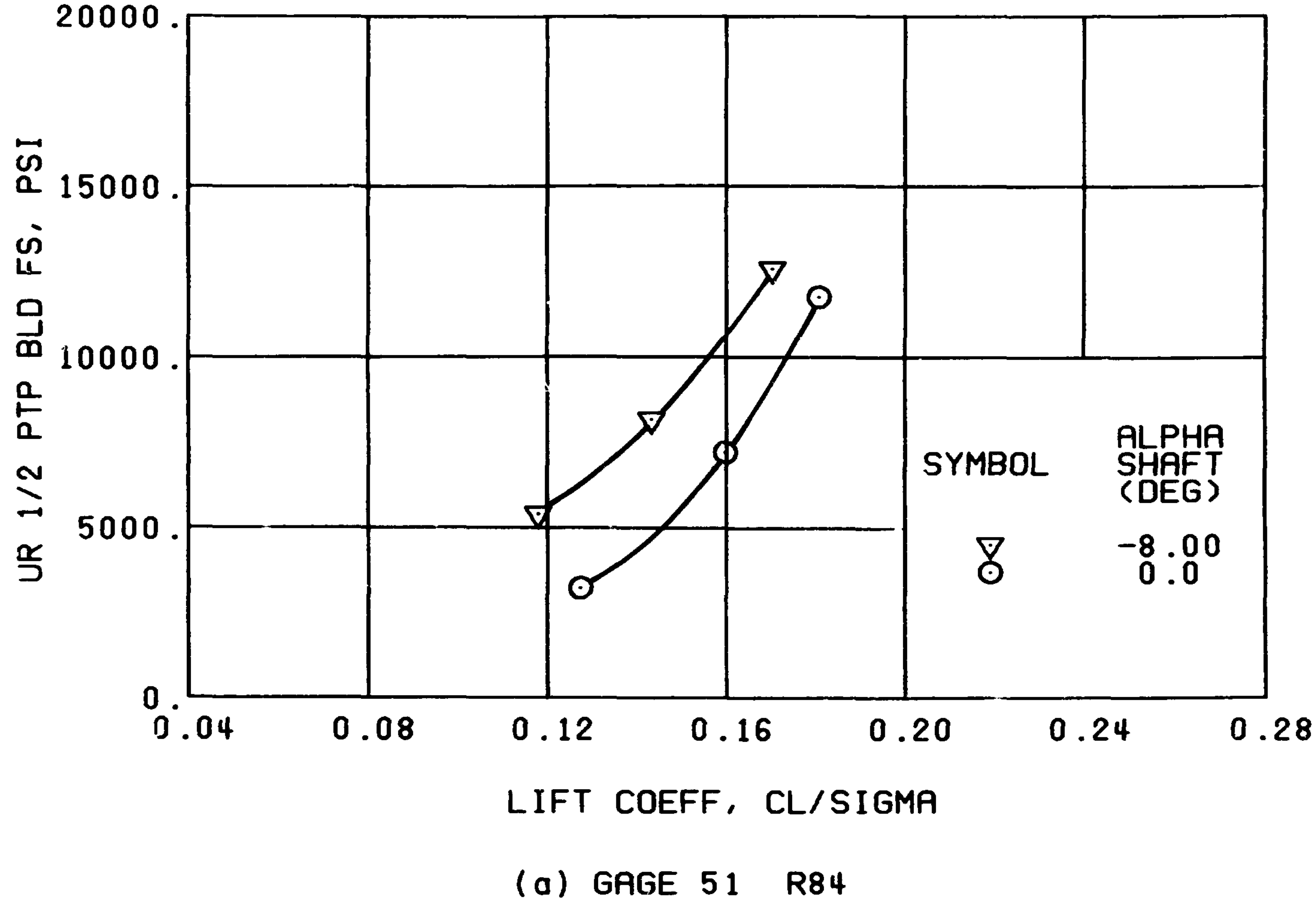

Figure 61. Stress, Load, and Vibration Data at an Advance Ratio of 0.21 With the Lateral Displacement Control (B'_{1s}) Set at 4 Degrees (Single-Rotor Configuration).

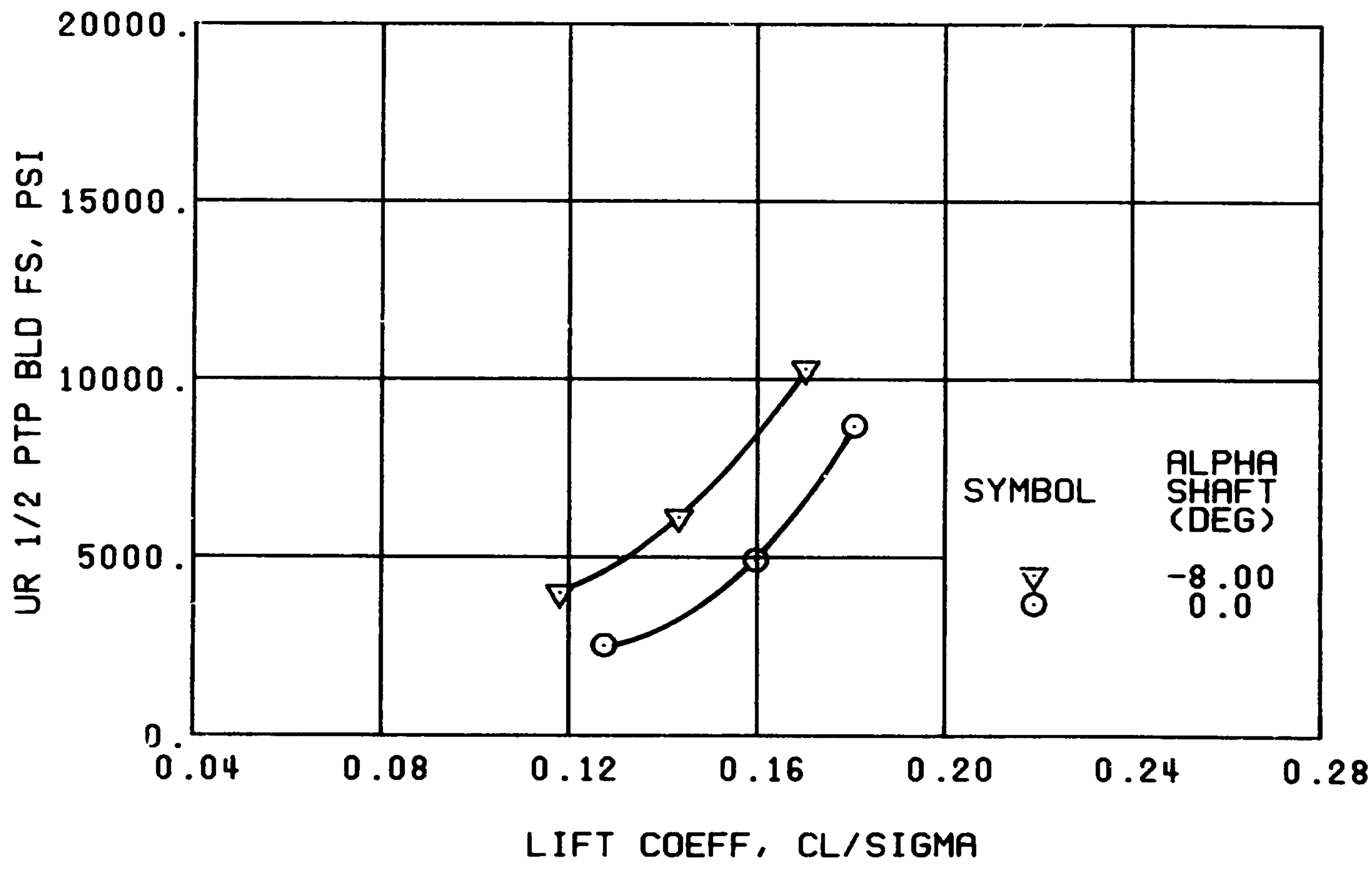

(c) GAGE 52 R108

Figure 61. Continued.

μ = 0.21 B'_{1s} = 4 Deg (Single-Rotor Configuration)

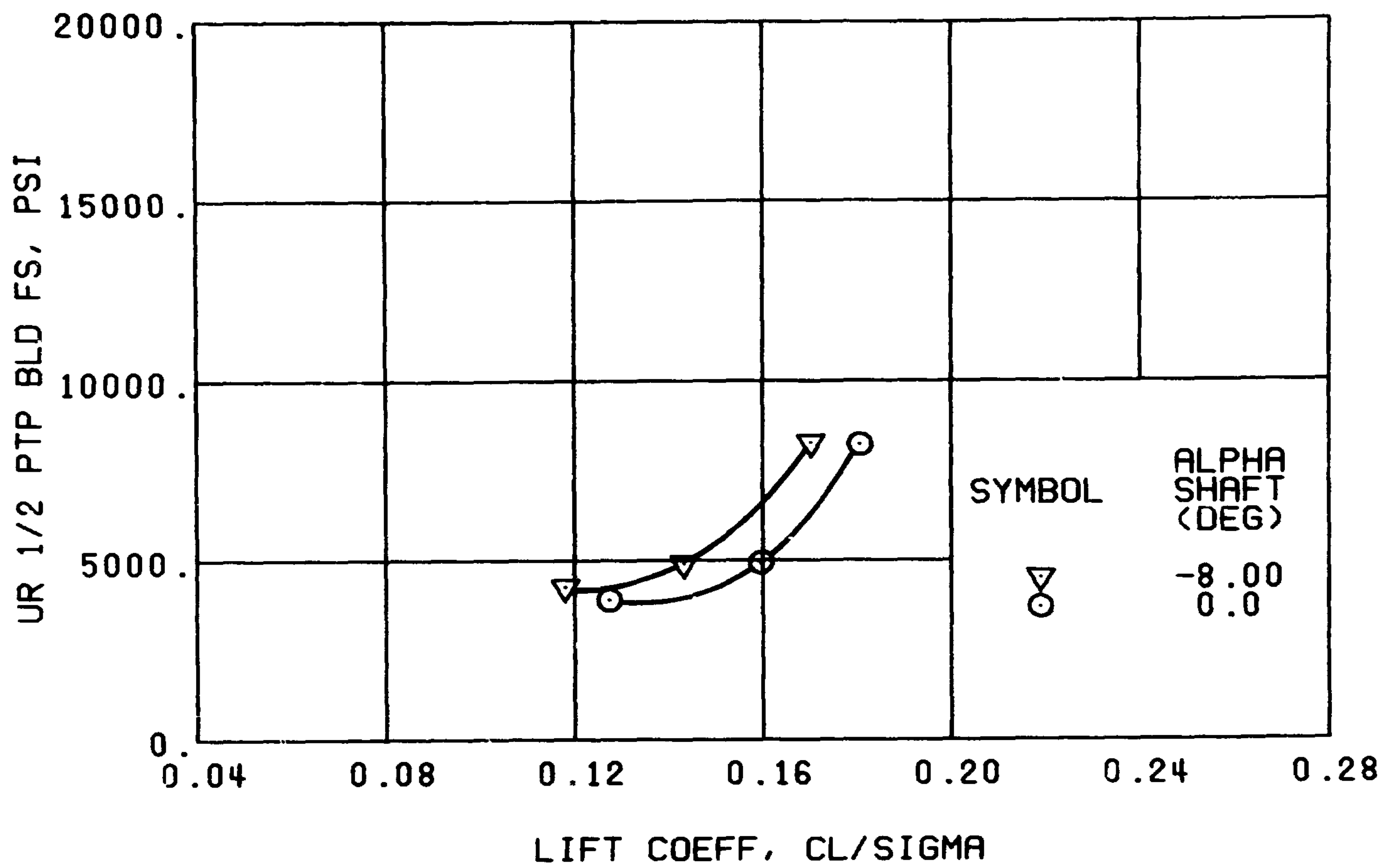

(d) GAGE 53 R132

Figure 61. Continued.
$\mu = 0.21$ $B'_{1s} = 4$ Deg (Single-Rotor Configuration)

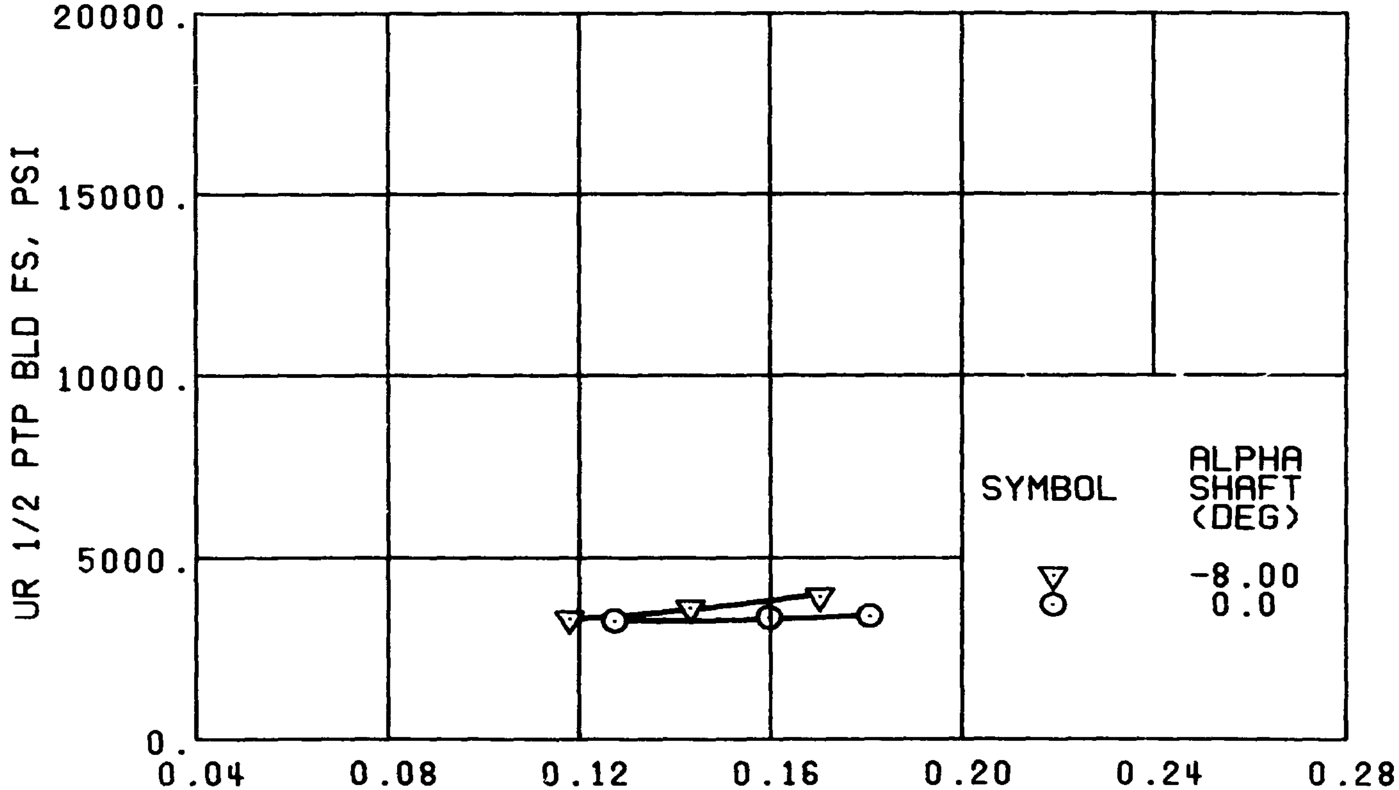

(f) GAGE 55 R204

Figure 61. Continued.
μ = 0.21 B'_{1s} = 4 Deg (Single-Rotor Configuration)

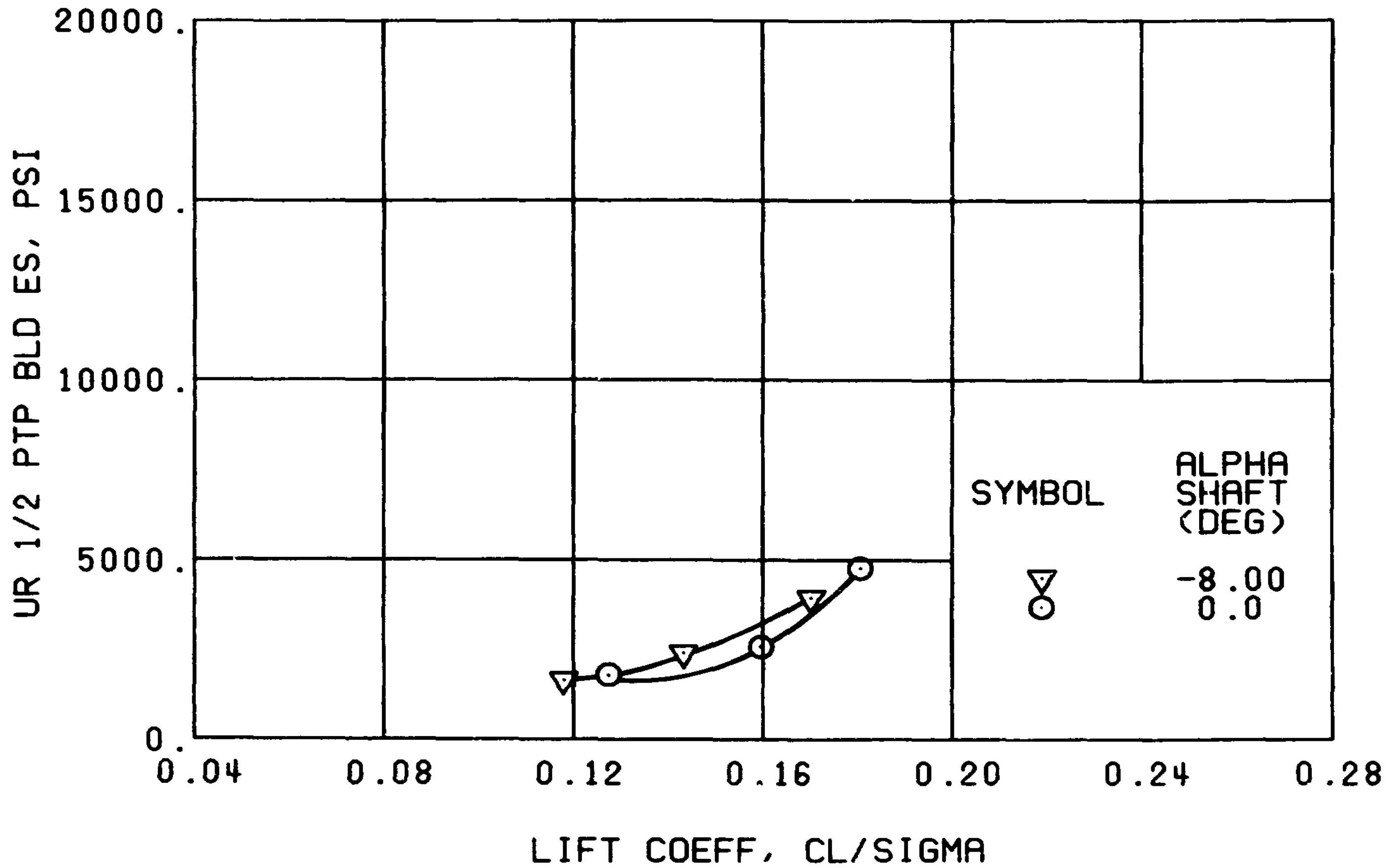

(h) GAGE 40 R84

Figure 61. Continued.
$\mu = 0.21$ $B'_{1s} = 4$ Deg (Single-Rotor Configuration)

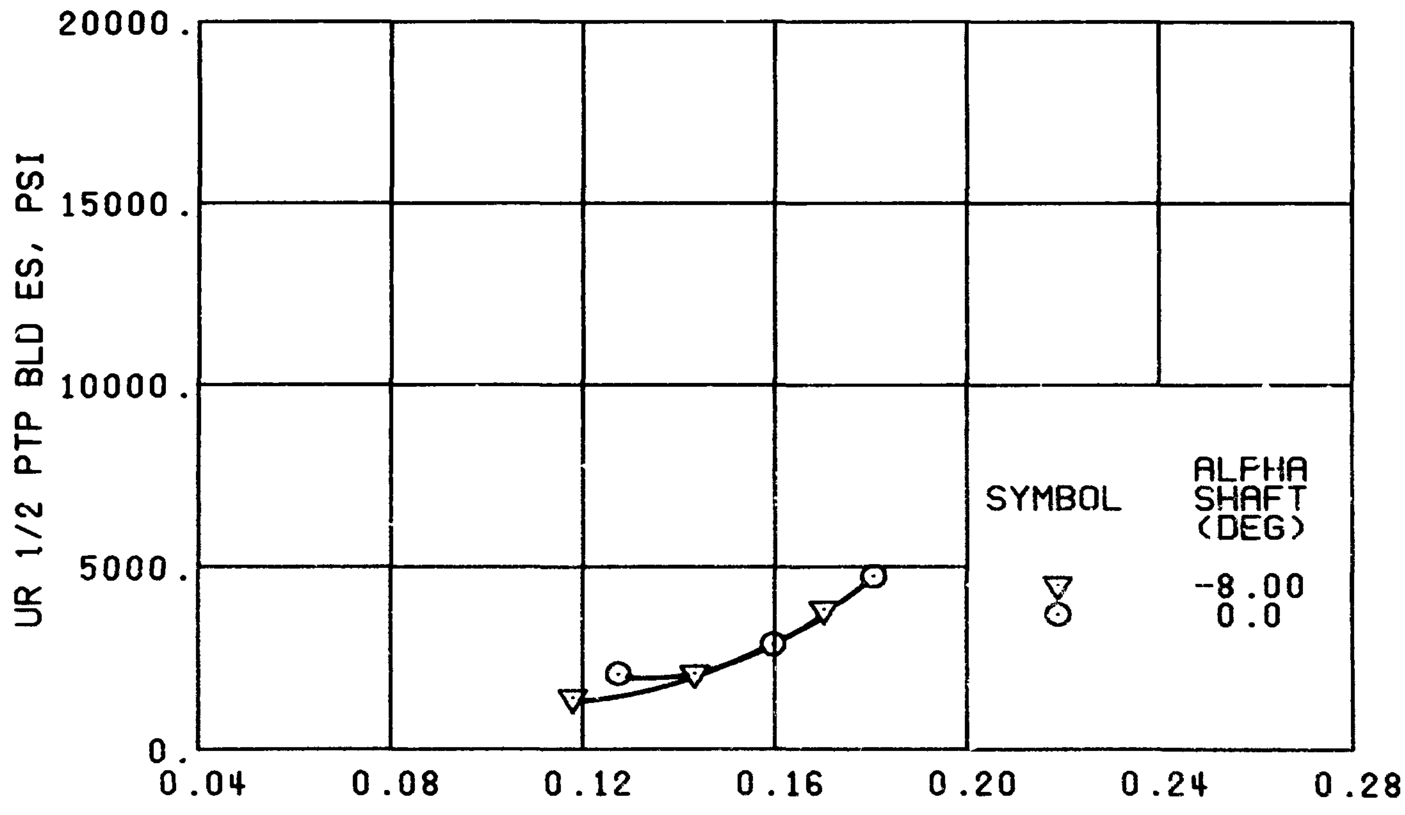

(j) GAGE 42 R132

Figure 61. Continued.
μ = 0.21 B'_{1s} = 4 Deg (Single-Rotor Configuration)

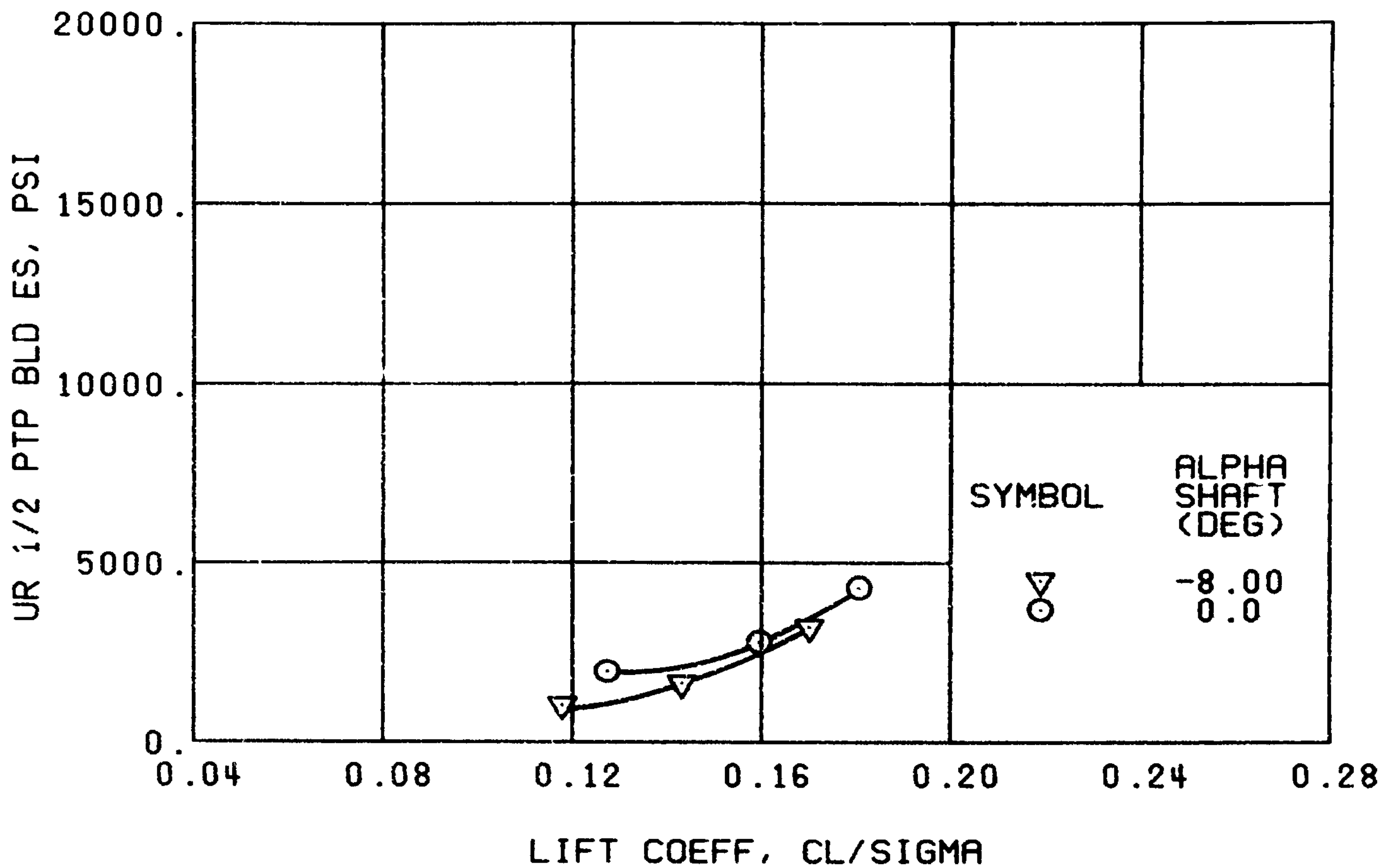

(k) GAGE 43 R168

Figure 61. Continued.
$\mu = 0.21$ $B'_{1s} = 4$ Deg (Single-Rotor Configuration)

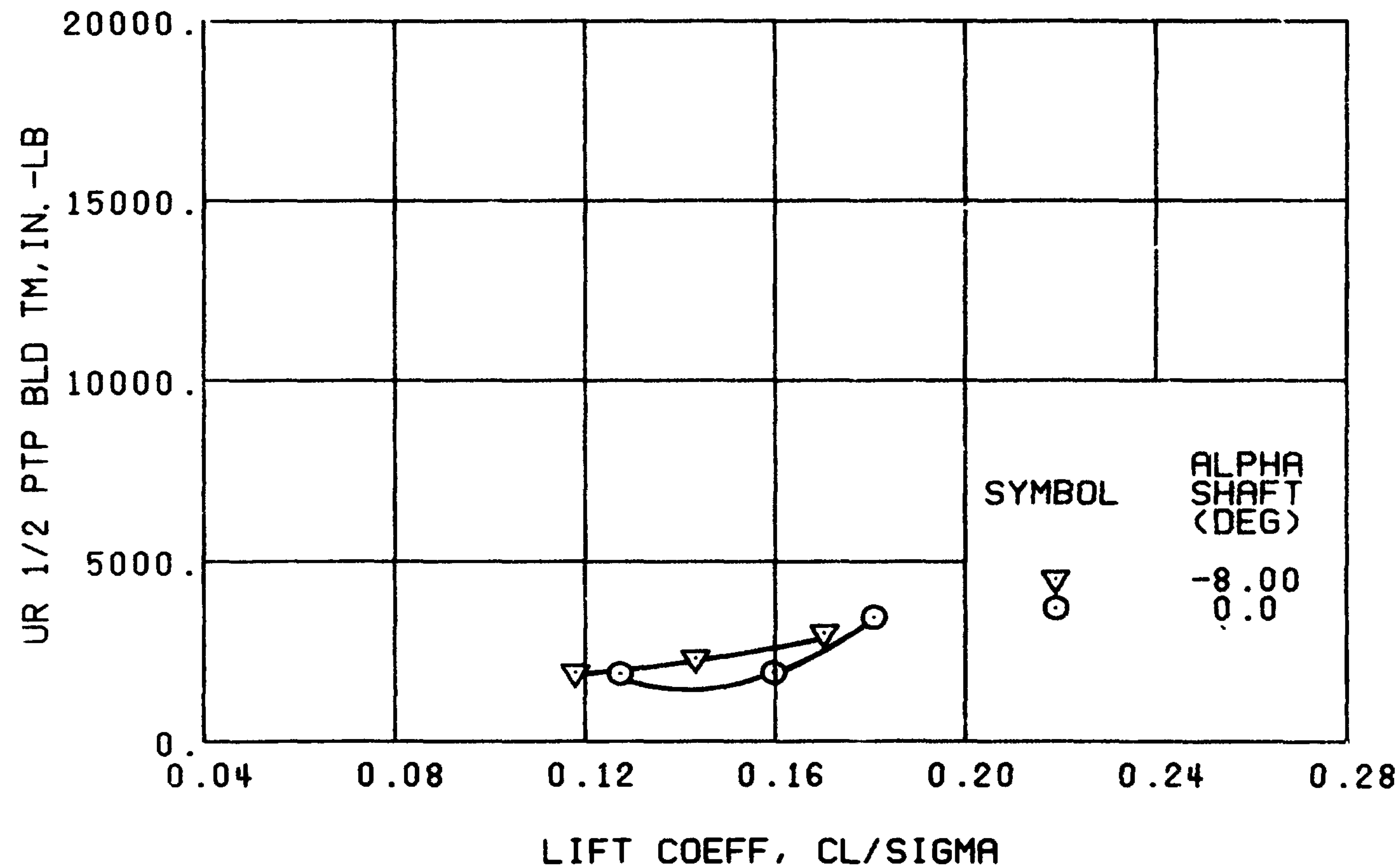

(m) GAGE 46 R130

Figure 61. Continued.
$\mu = 0.21$ $B'_{1s} = 4$ Deg (Single-Rotor Configuration)

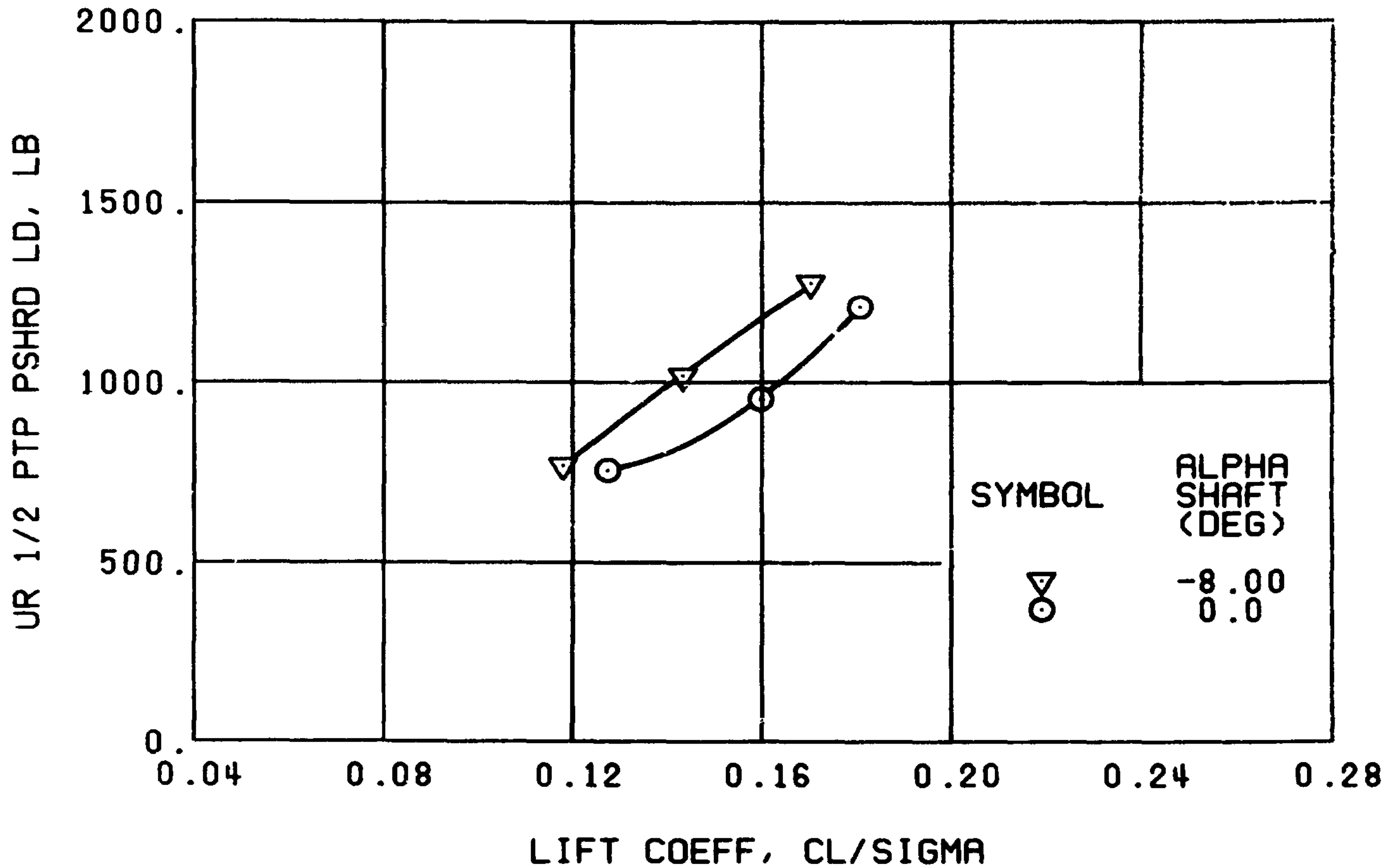

(n) GAGE 37

Figure 61. Continued.
μ = 0.21 B'_{1s} = 4 Deg (Single-Rotor Configuration)

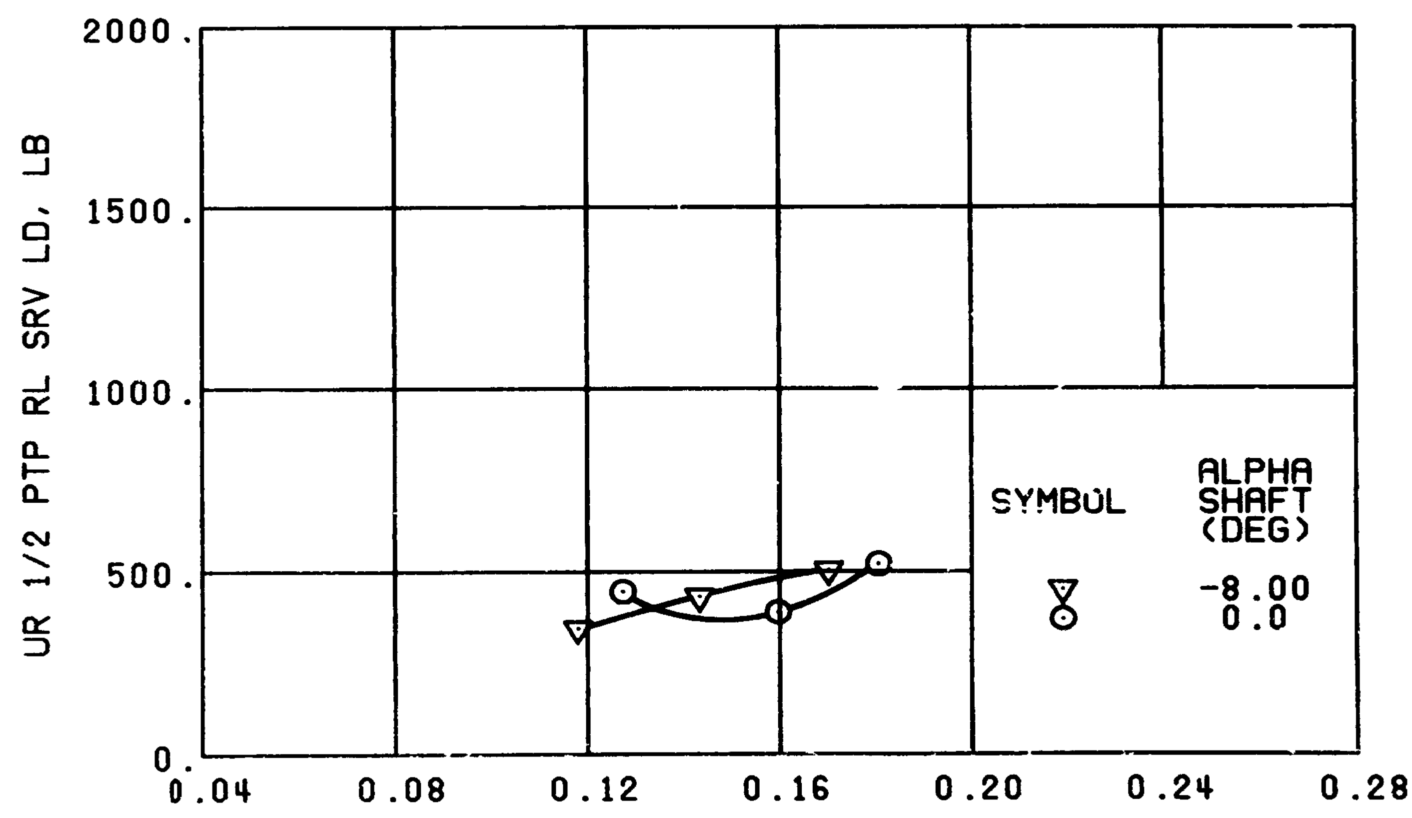

(p) GAGE 22

Figure 61. Continued.
μ = 0.21 B'_{1s} = **4 Deg (Single-Rotor Configuration)**

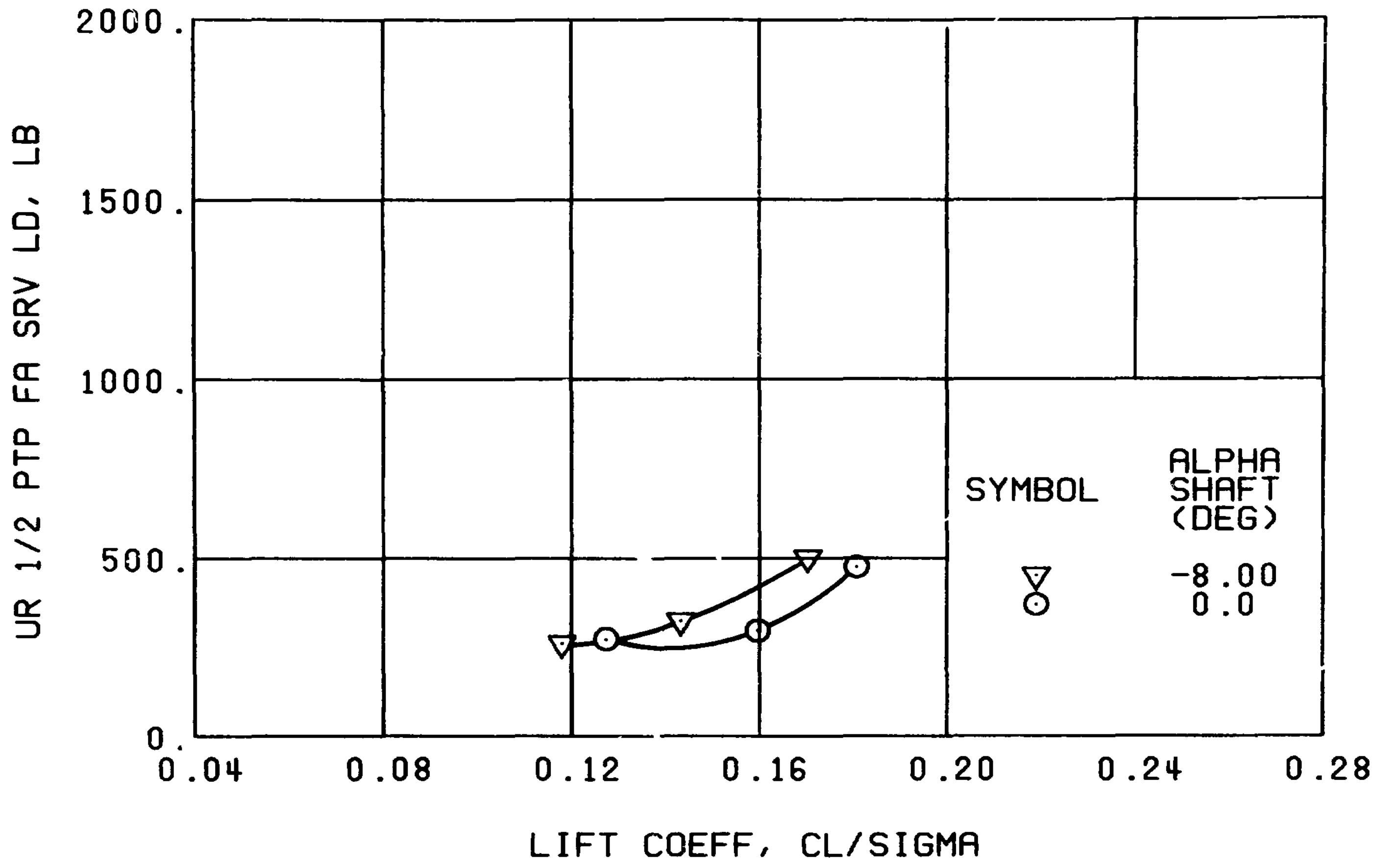

(r) GAGE 2

Figure 61. Continued.
$\mu = 0.21$ $B'_{1s} = 4$ Deg (Single-Rotor Configuration)

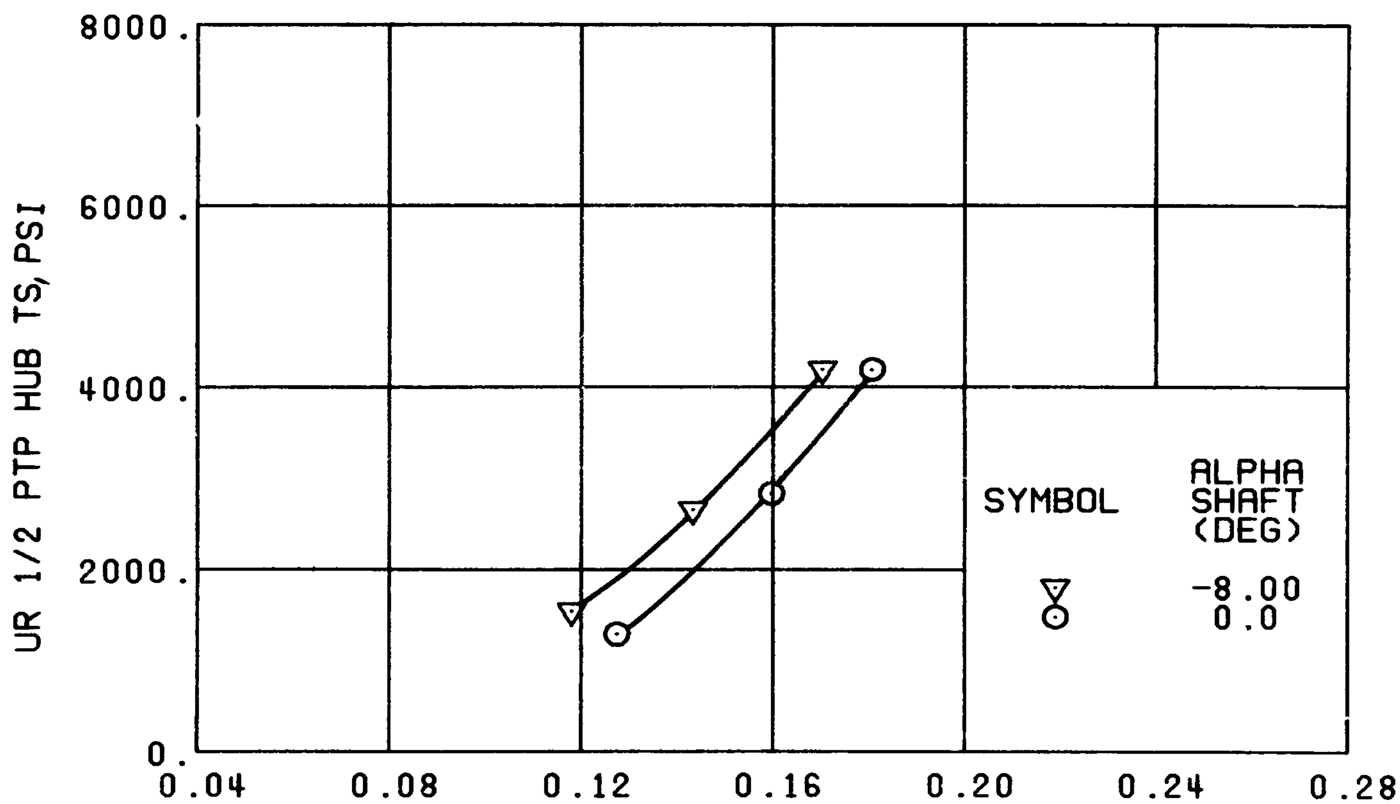

(f) GAGE 65

Figure 61. Continued.
μ = 0.21 B'_{1s} = 4 Deg (Single-Rotor Configuration)

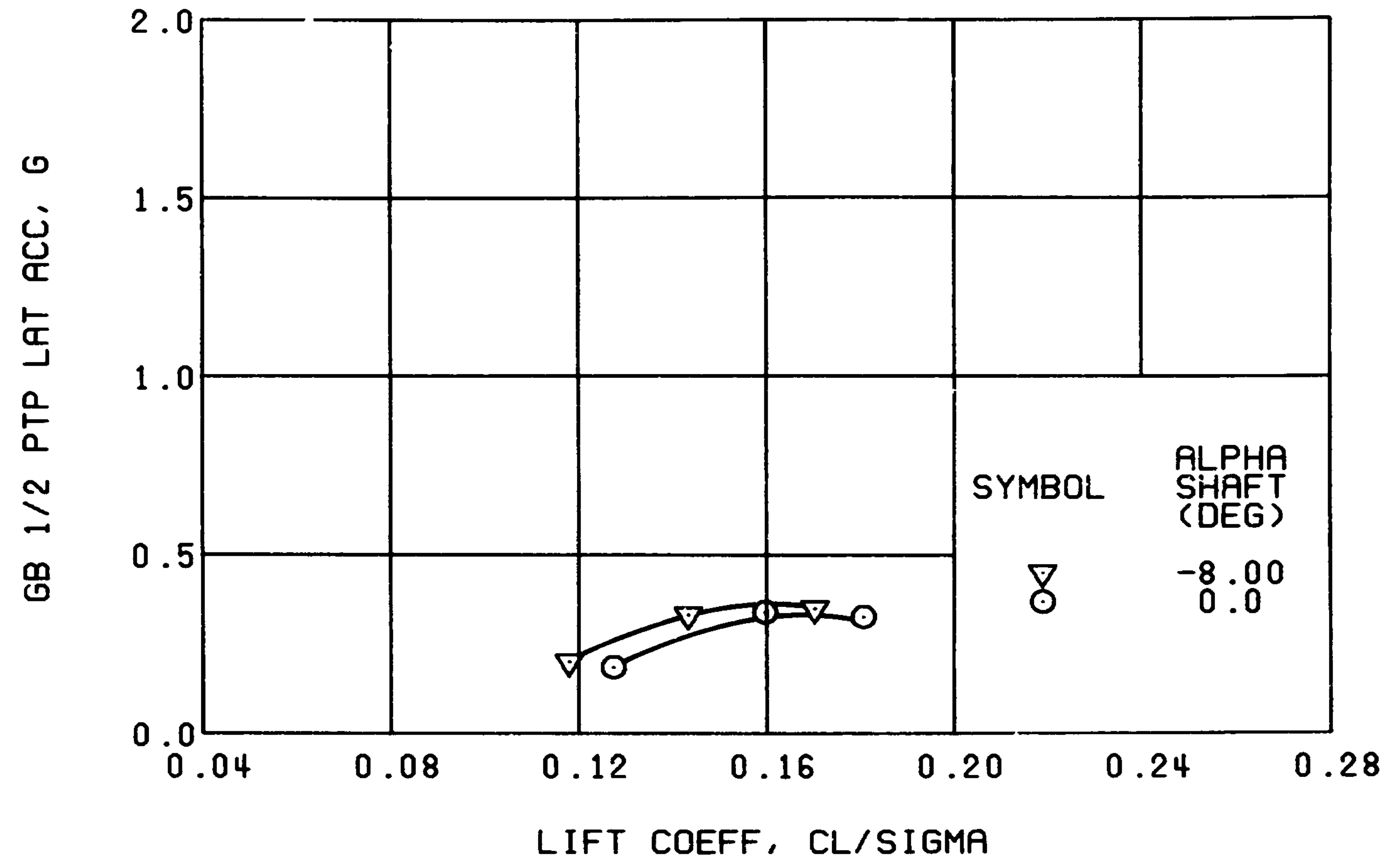

(u) GAGE 15 STA 76, BL 30

Figure 61. Continued.
$\mu = 0.21 \quad B'_{1s} = 4$ Deg (Single-Rotor Configuration)

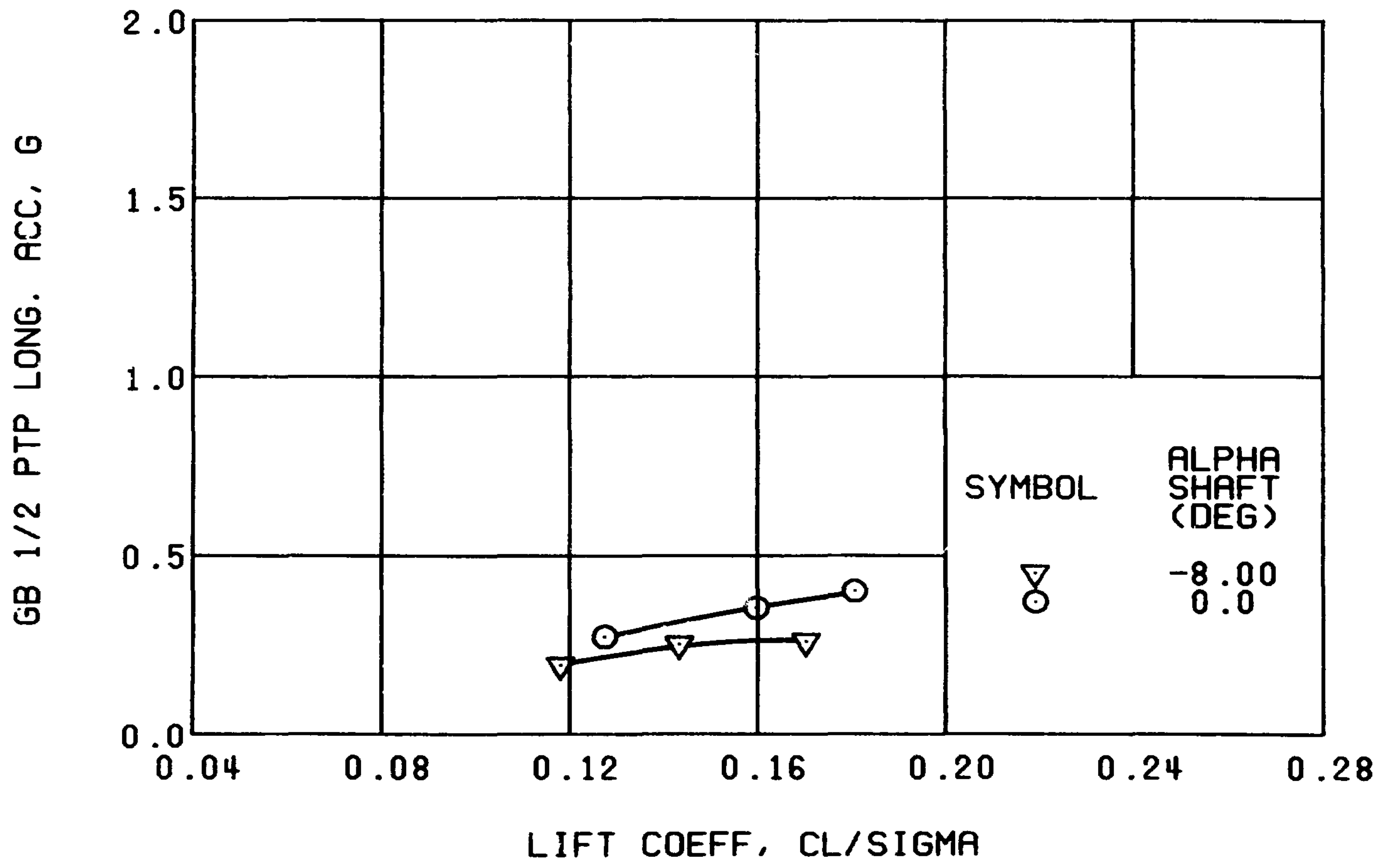

(v) GAGE 14 STA 61, BL 0

Figure 61. Continued.
$\mu = 0.21$ $B'_{1s} = 4$ Deg (Single-Rotor Configuration)

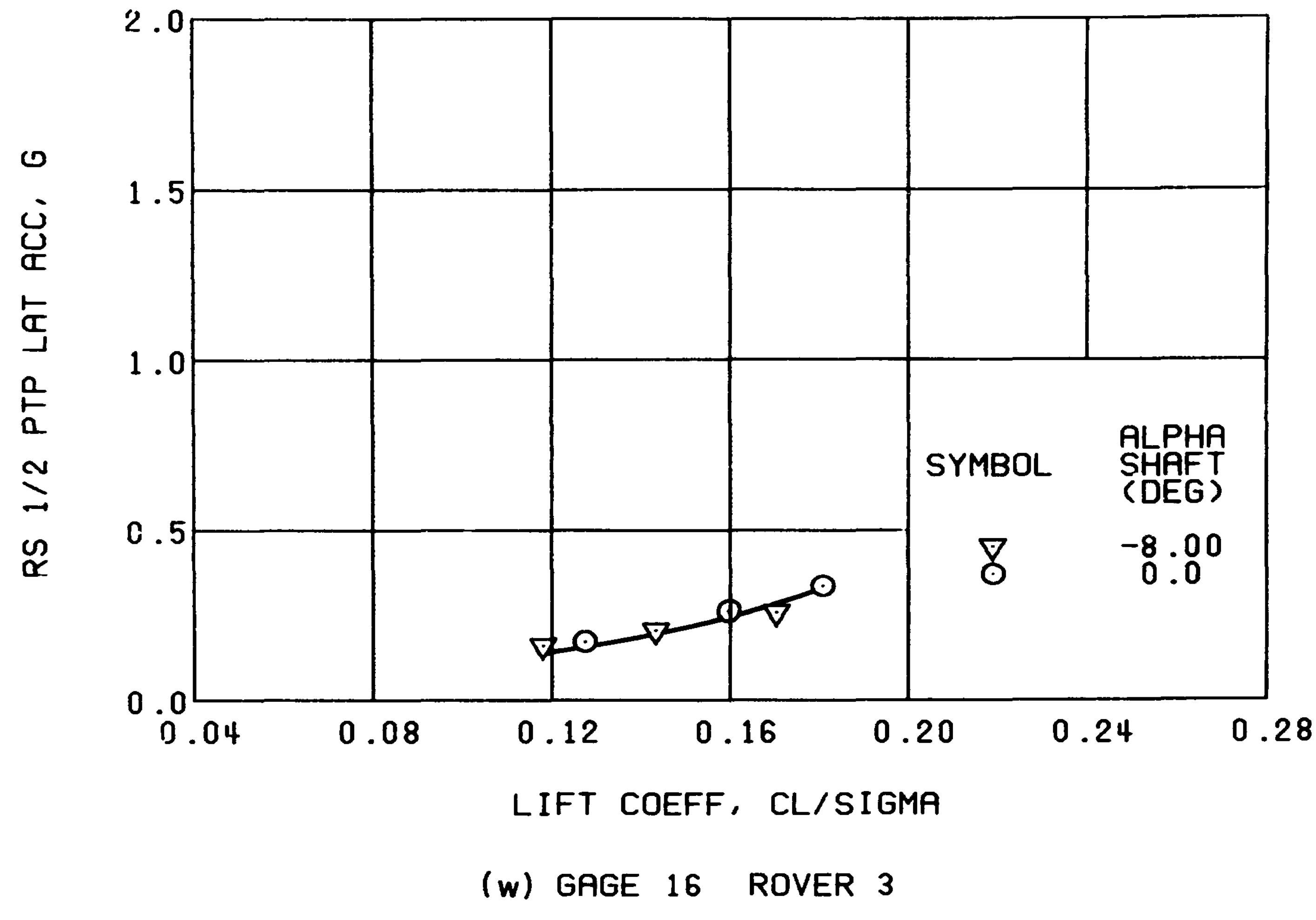

Figure 61. Continued.
μ = 0.21 B'_{1s} = 4 Deg (Single-Rotor Configuration)

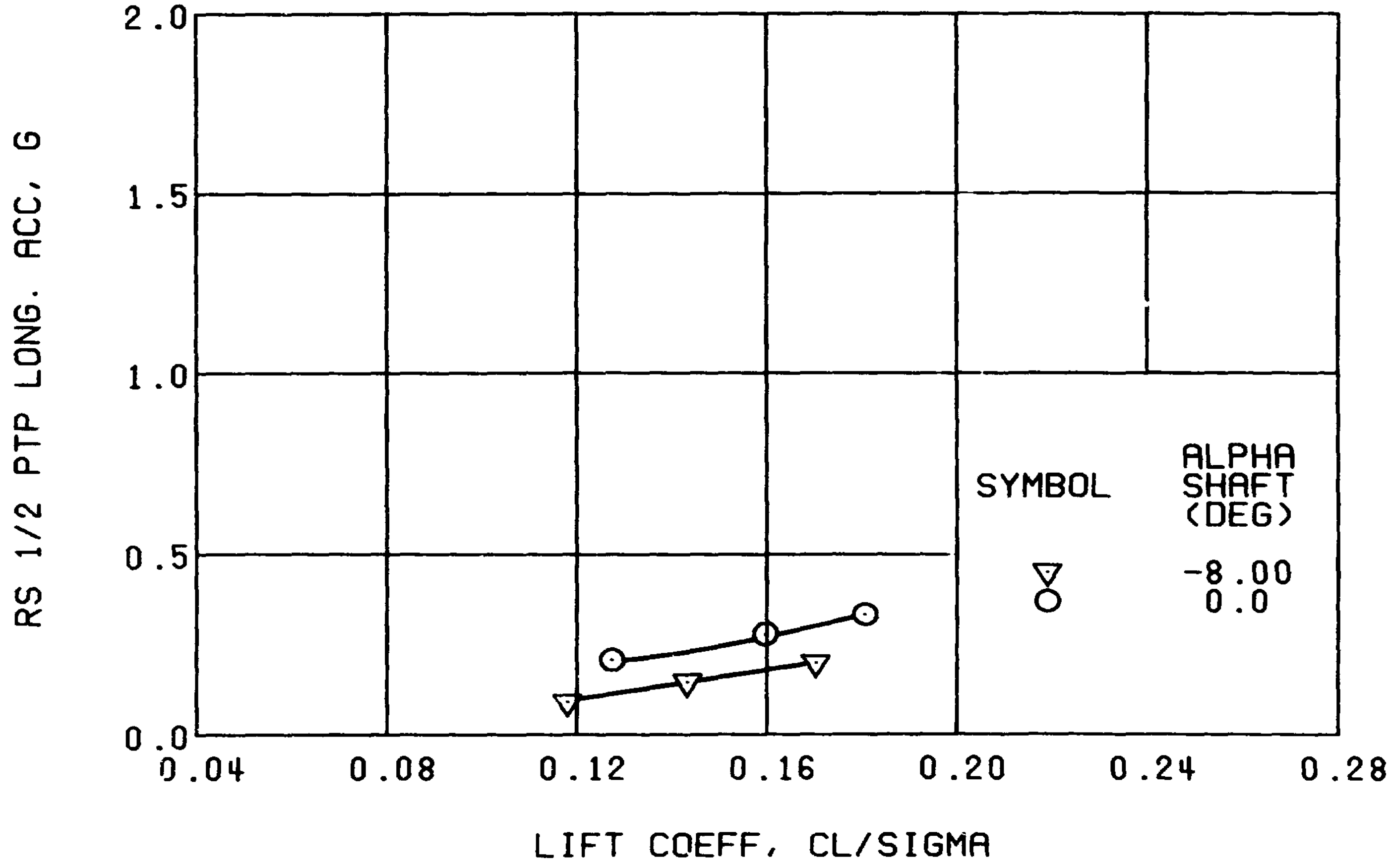

(x) GAGE 17 ROVER 4

Figure 61. Conclude .

μ = 0.21 B'_{1s} = 4 Deg (Single-Rotor Configuration)

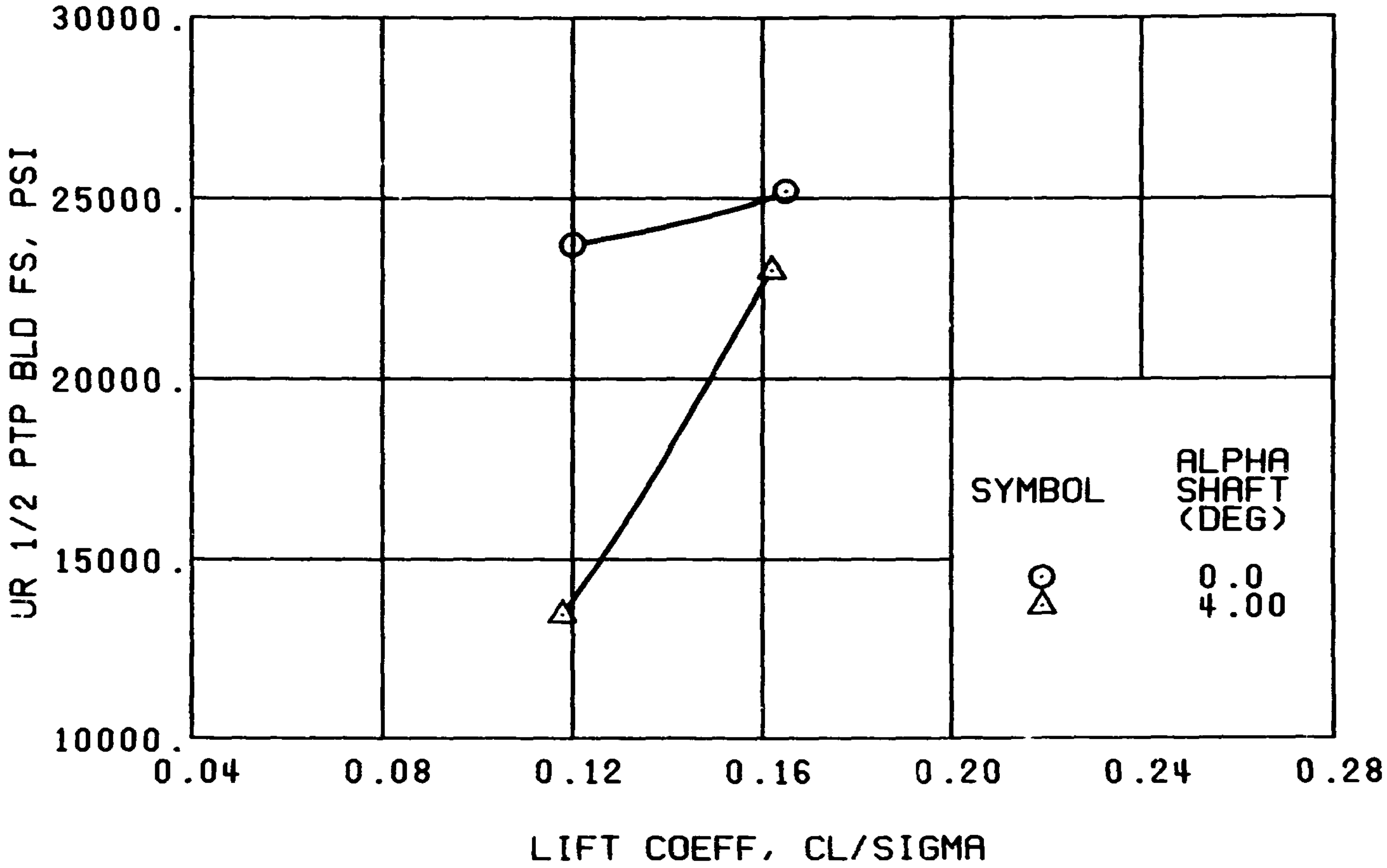

(a) GAGE 51 R84

Figure 62. Stress, Load, and Vibration Data at an Advance Ratio of 0.35 With the Lateral Displacement Control (B'_{1s}) Set at 2 Degrees (Single-Rotor Configuration).

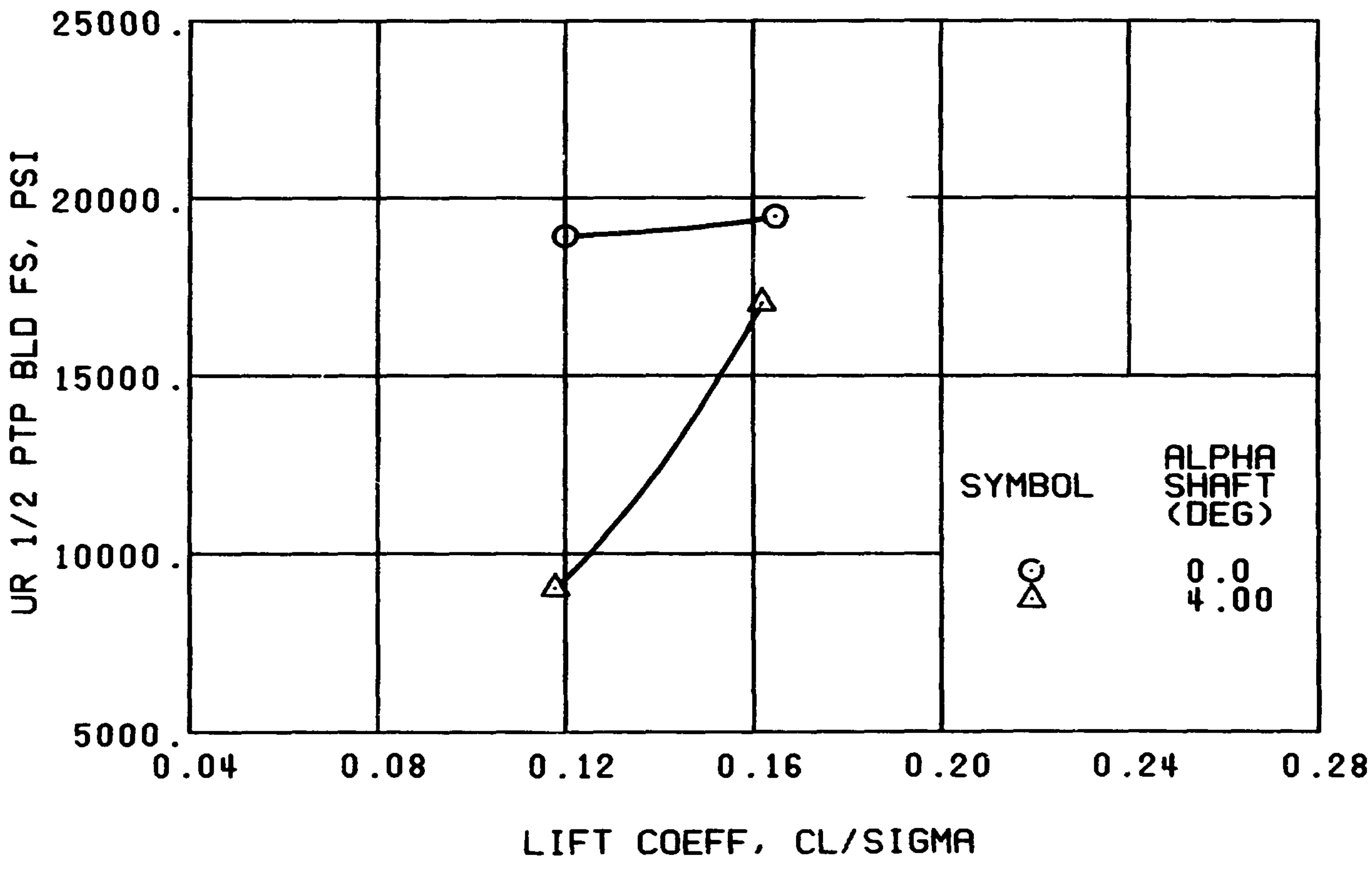

(c) GAGE 52 R108

Figure 62. Continued.
μ = 0.35 B'_{1s} = 2 Deg (Single-Rotor Configuration)

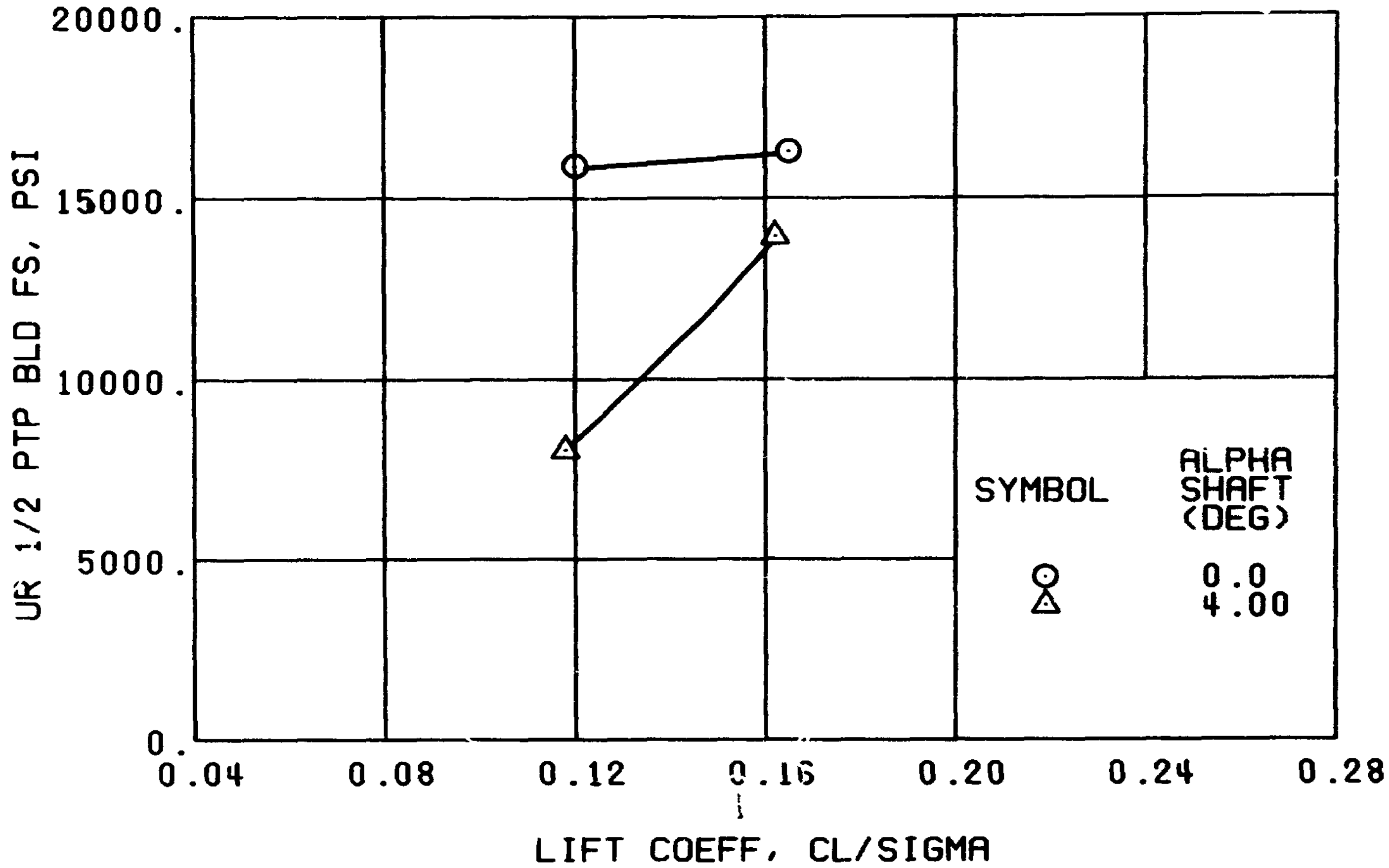

(d) GAGE 53 R132

Figure 62. Continued.
μ = 0.35 B'_{1s} = 2 Deg (Single-Rotor Configuration)

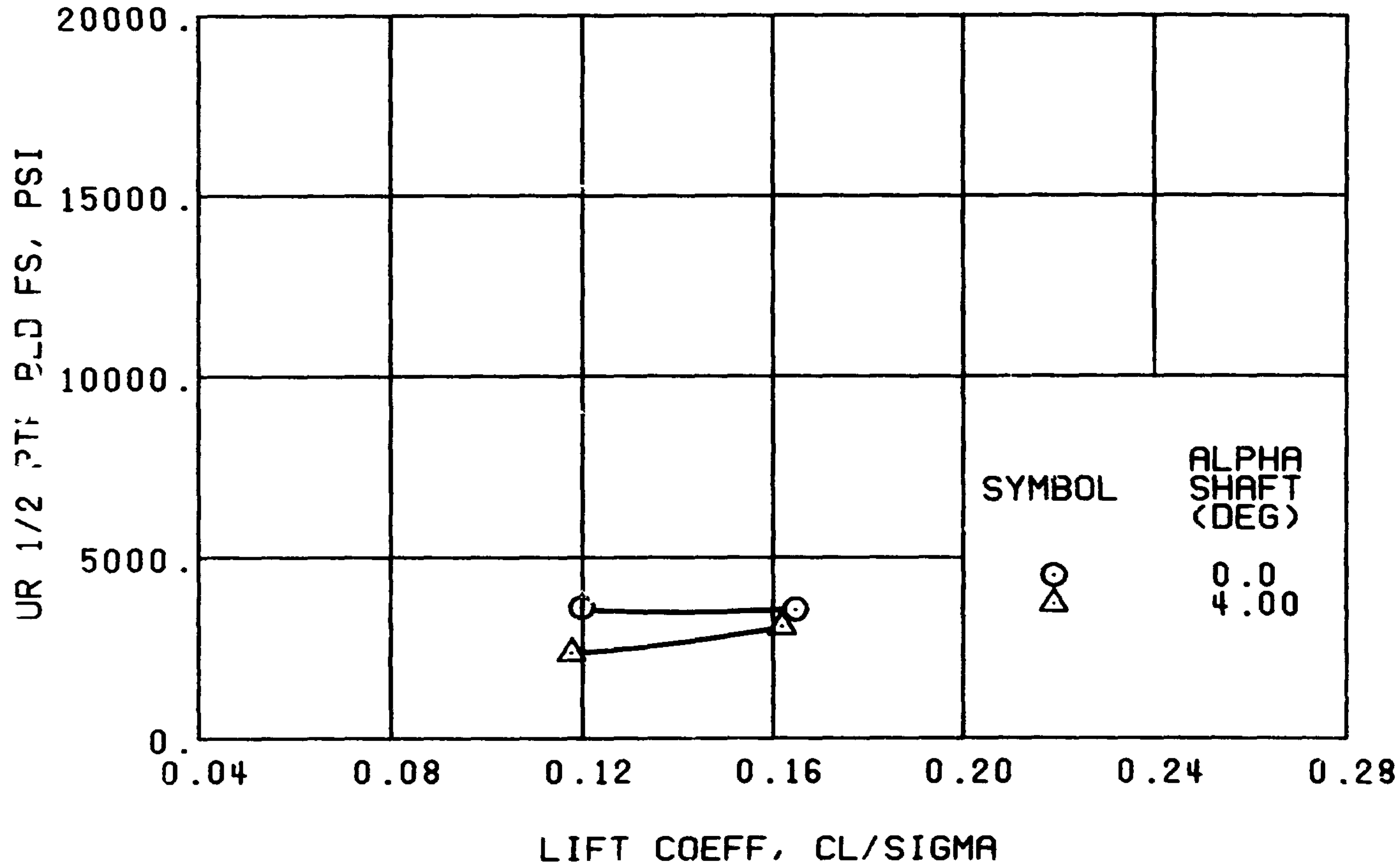

(f) GAGE 55 R204

Figure 62. Continued.
μ = 0.35 B'_{1s} = 2 Deg (Single-Rotor Configuration)

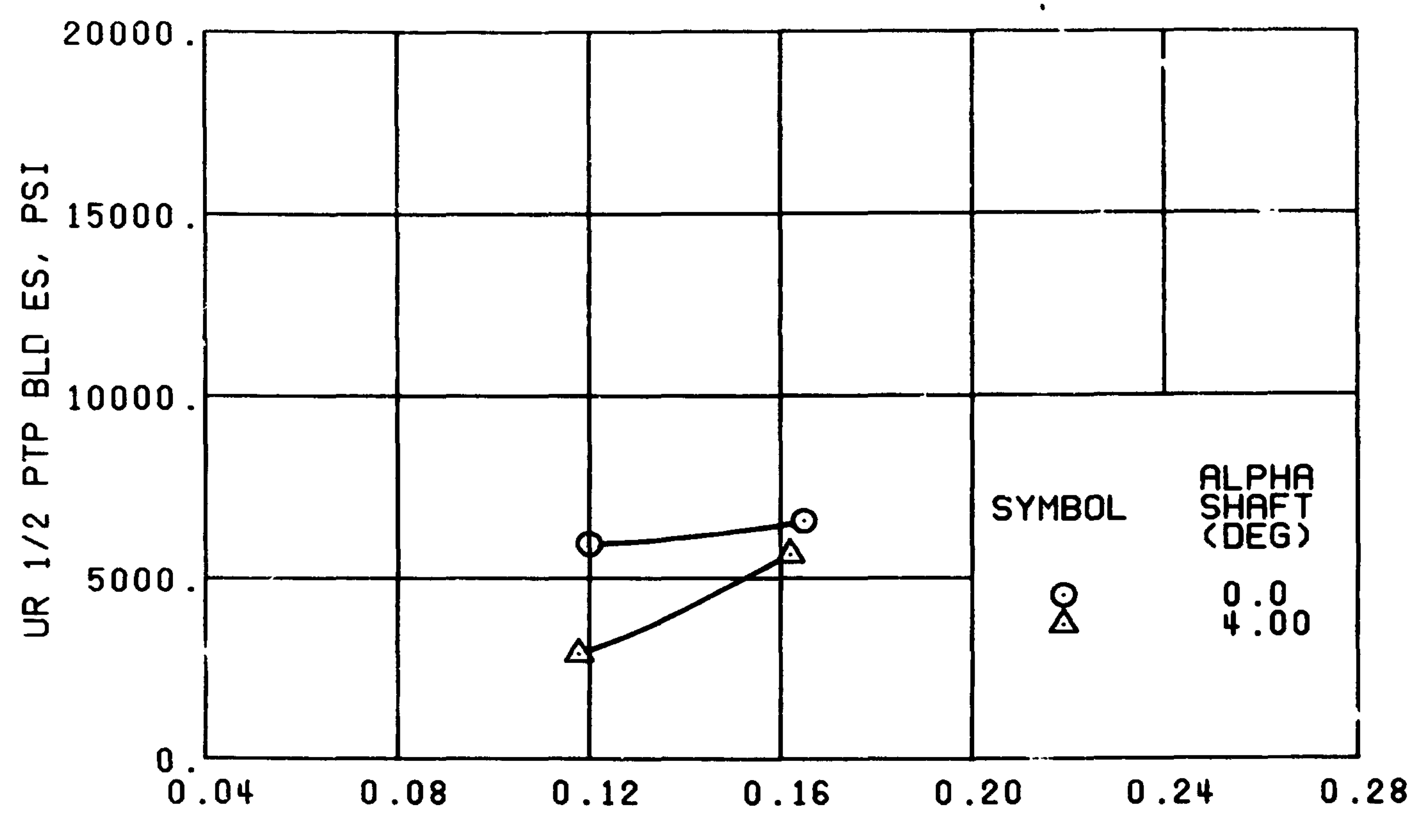

(h) GAGE 40 R84

Figure 62. Continued.
$\mu = 0.35$ $B'_{1s} = 2$ Deg (Single-Rotor Configuration)

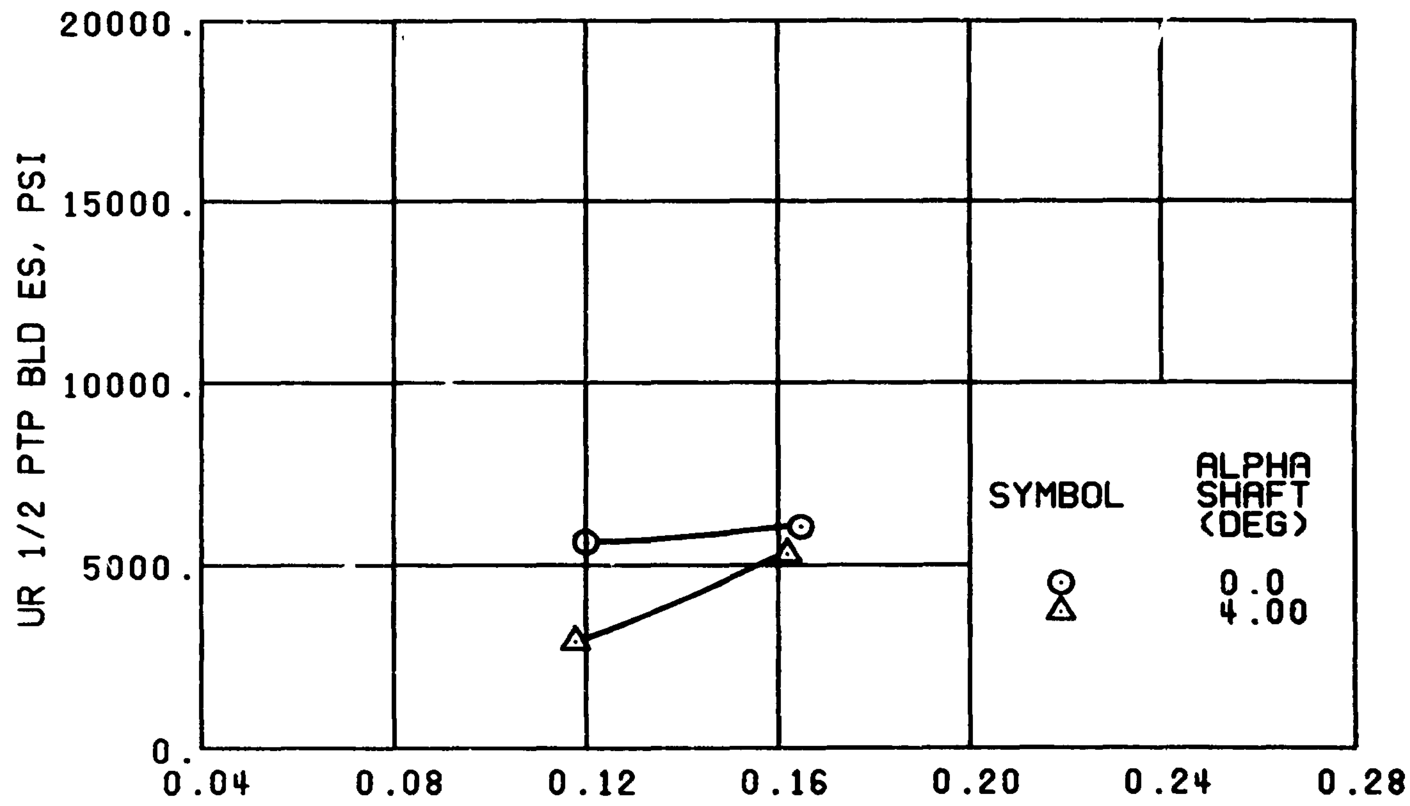

(j) GAGE 42 R132

Figure 62. Continued.
$\mu = 0.35$ $B'_{1s} = 2$ Deg (Single-Rotor Configuration)

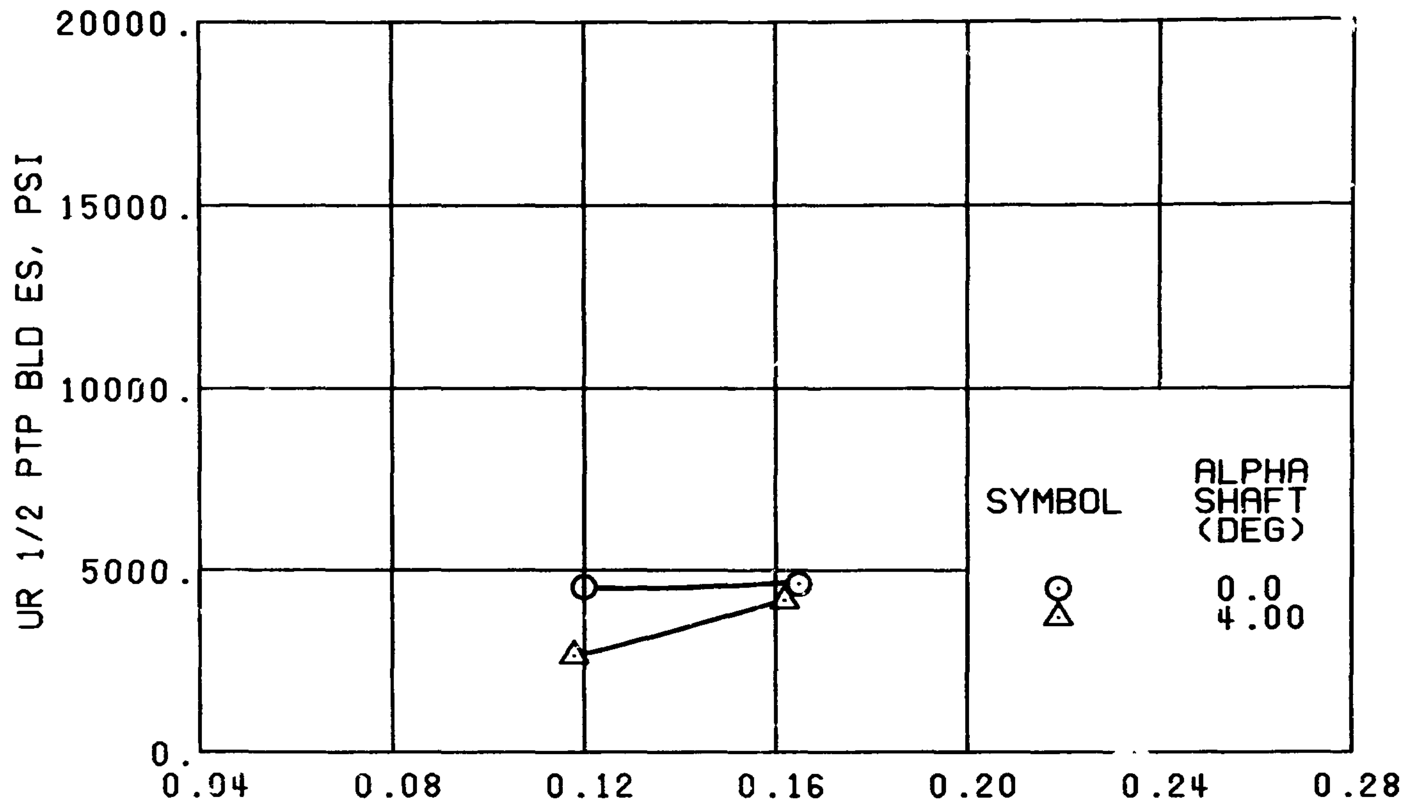

(k) GAGE 43 R168

Figure 62. Continued.
$\mu = 0.35$ $B'_{1s} = 2$ Deg (Single-Rotor Configuration)

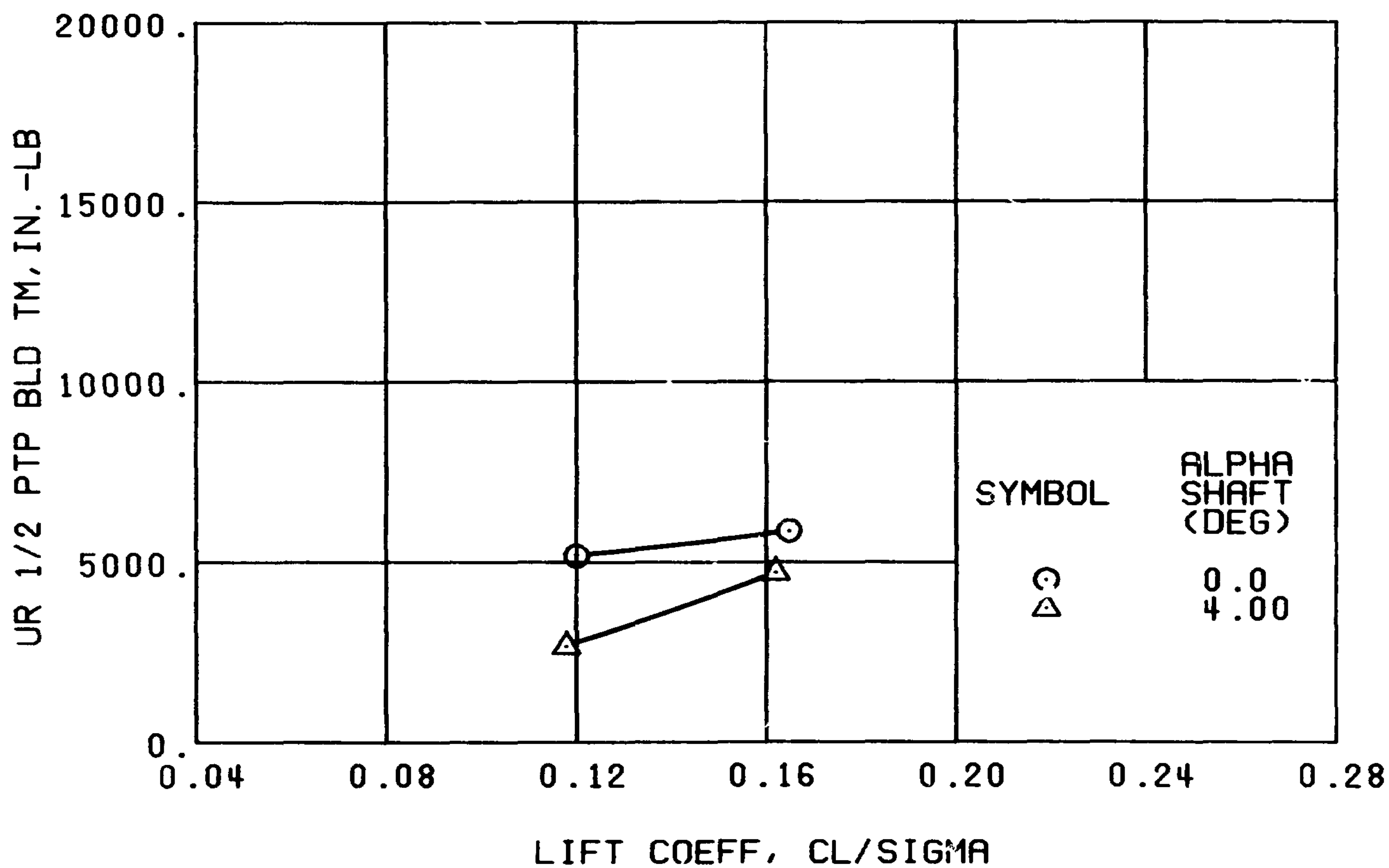

(m) GAGE 46 R130

Figure 62. Continued.
$\mu = 0.35$ $B'_{1s} = 2$ Deg (Single-Rotor Configuration)

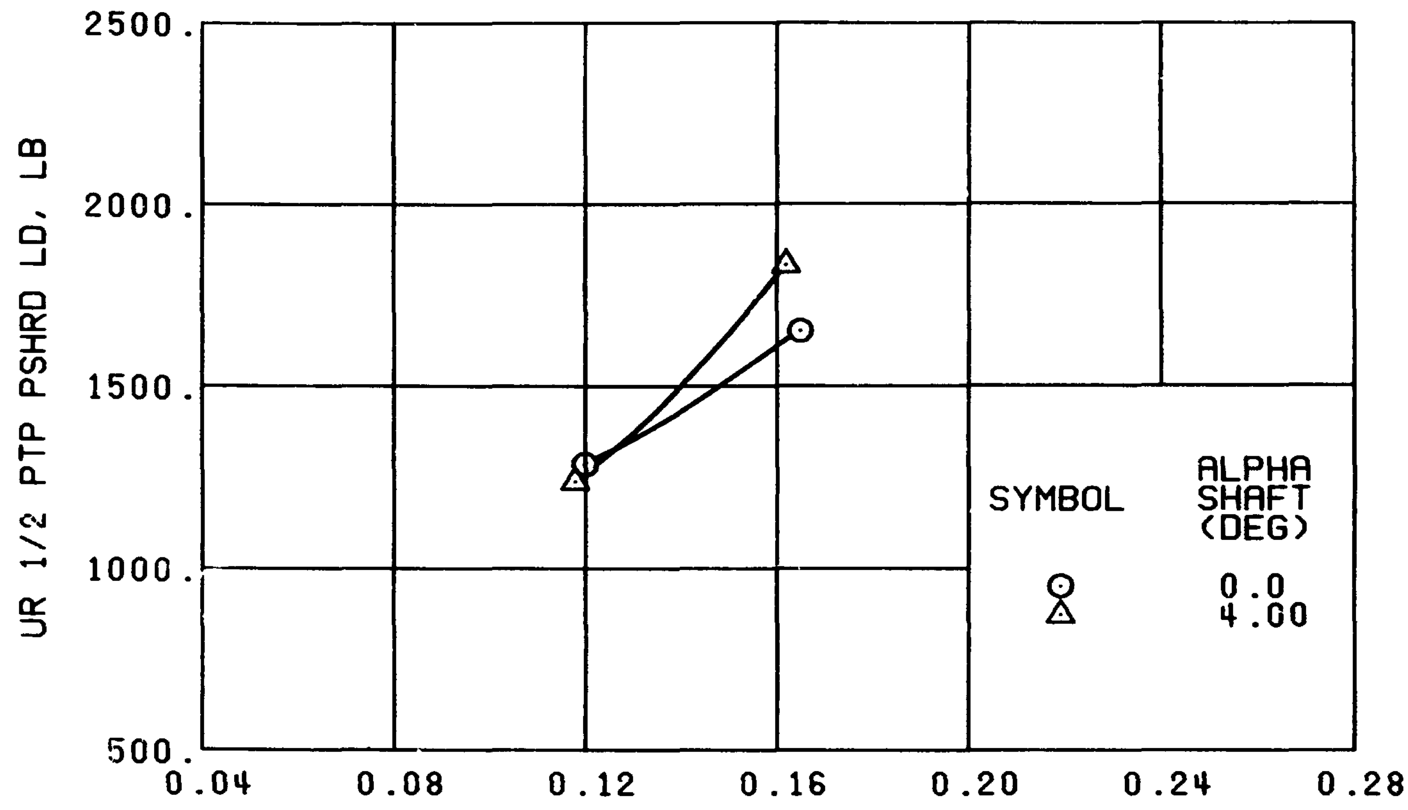

(n) GAGE 37

Figure 62. Continued.
$\mu = 0.35$ $B'_{1s} = 2$ Deg (Single-Rotor Configuration)

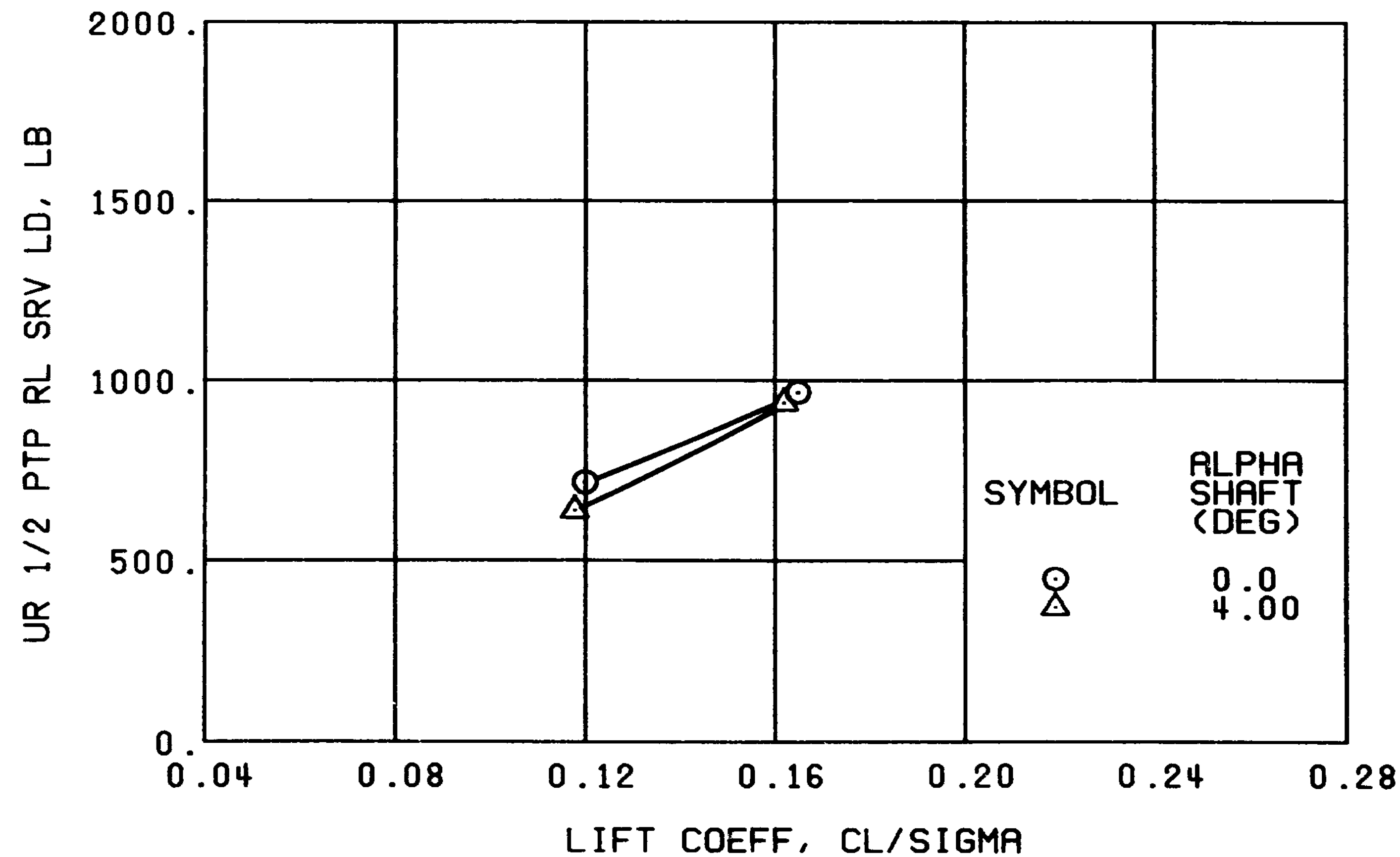

(p) GAGE 22

Figure 52. Continued.
$\mu = 0.35$ $B'_{1s} = 2$ Deg (Single-Rotor Configuration)

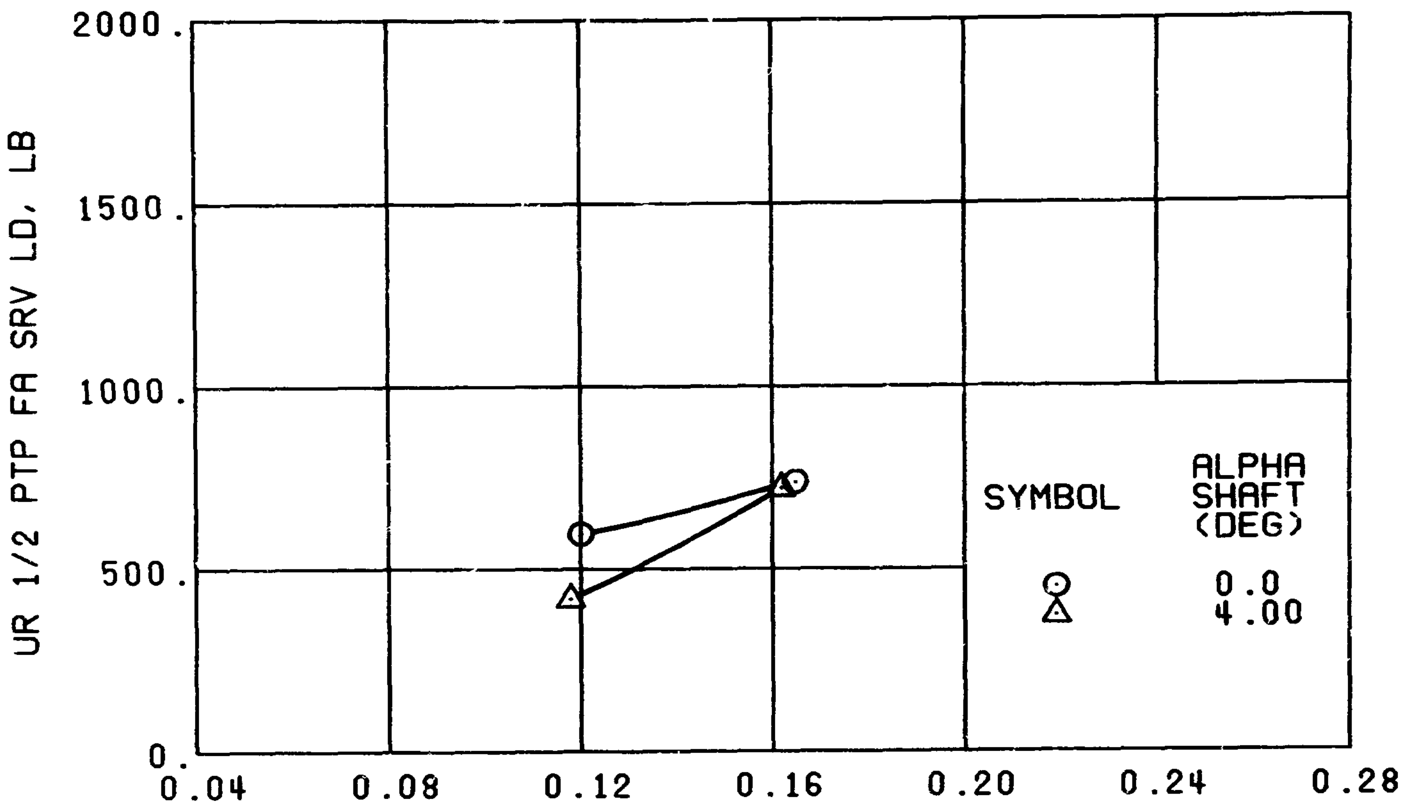

(r) GAGE 24

Figure 62. Continued.
$\mu = 0.35$ $B'_{1s} = 2$ Deg (Single-Rotor Configuration)

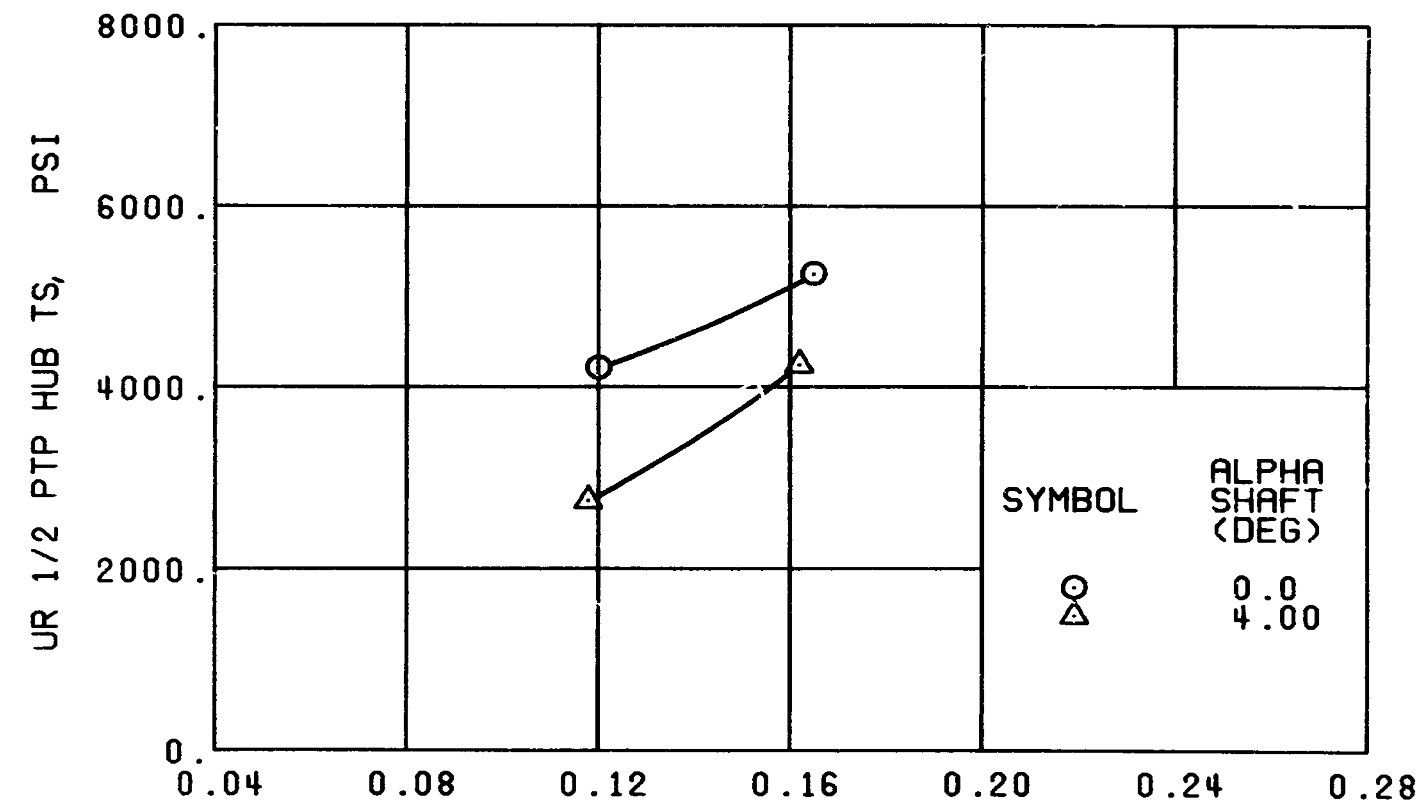

(f) GAGE 65

Figure 62. Continued.
$\mu = 0.35$ $B'_{1s} = 2$ Deg (Single-Rotor Configuration)

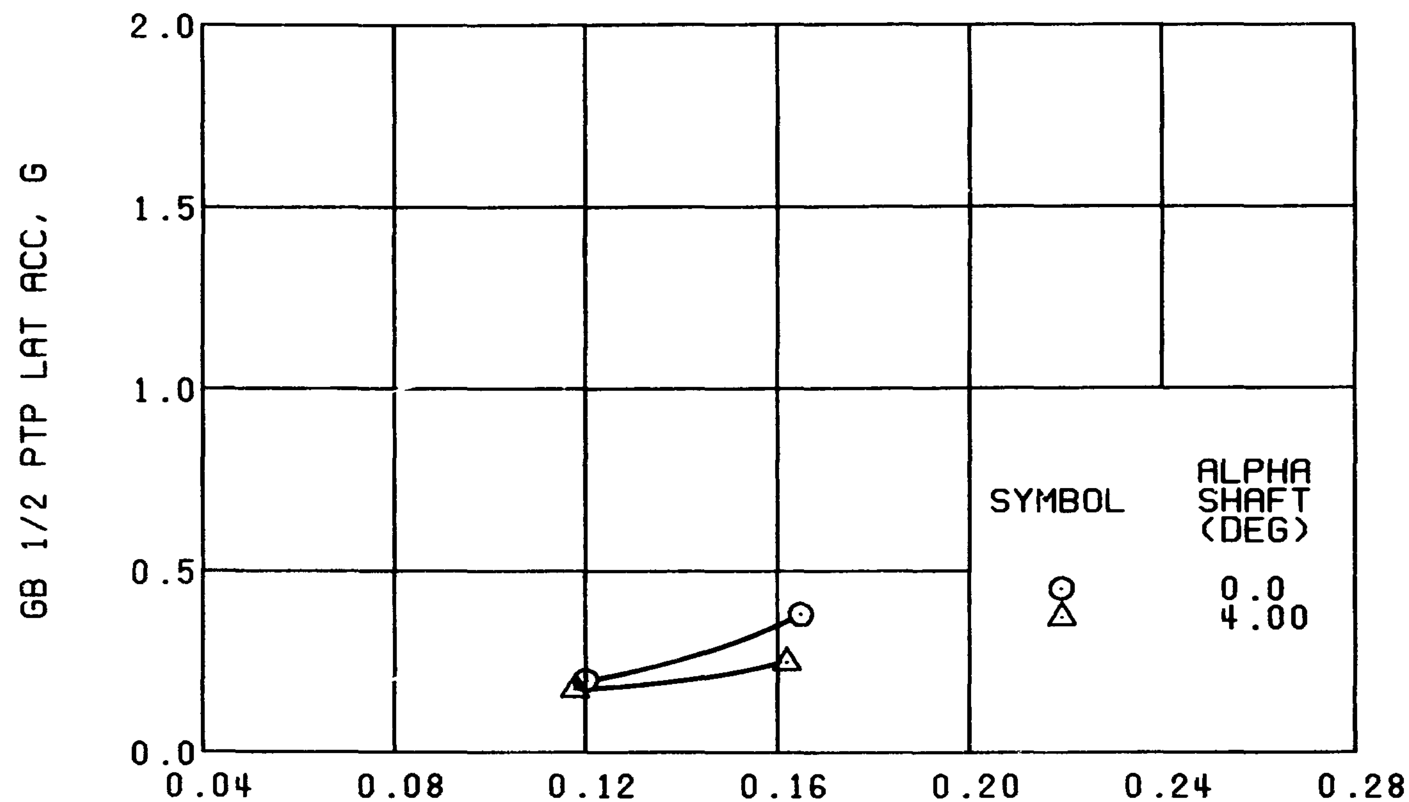

(u) GAGE 15 STA 76, BL 30

Figure 62. Continued.
$\mu = 0.35$ $B'_{1s} = 2$ Deg (Single-Rotor Configuration)

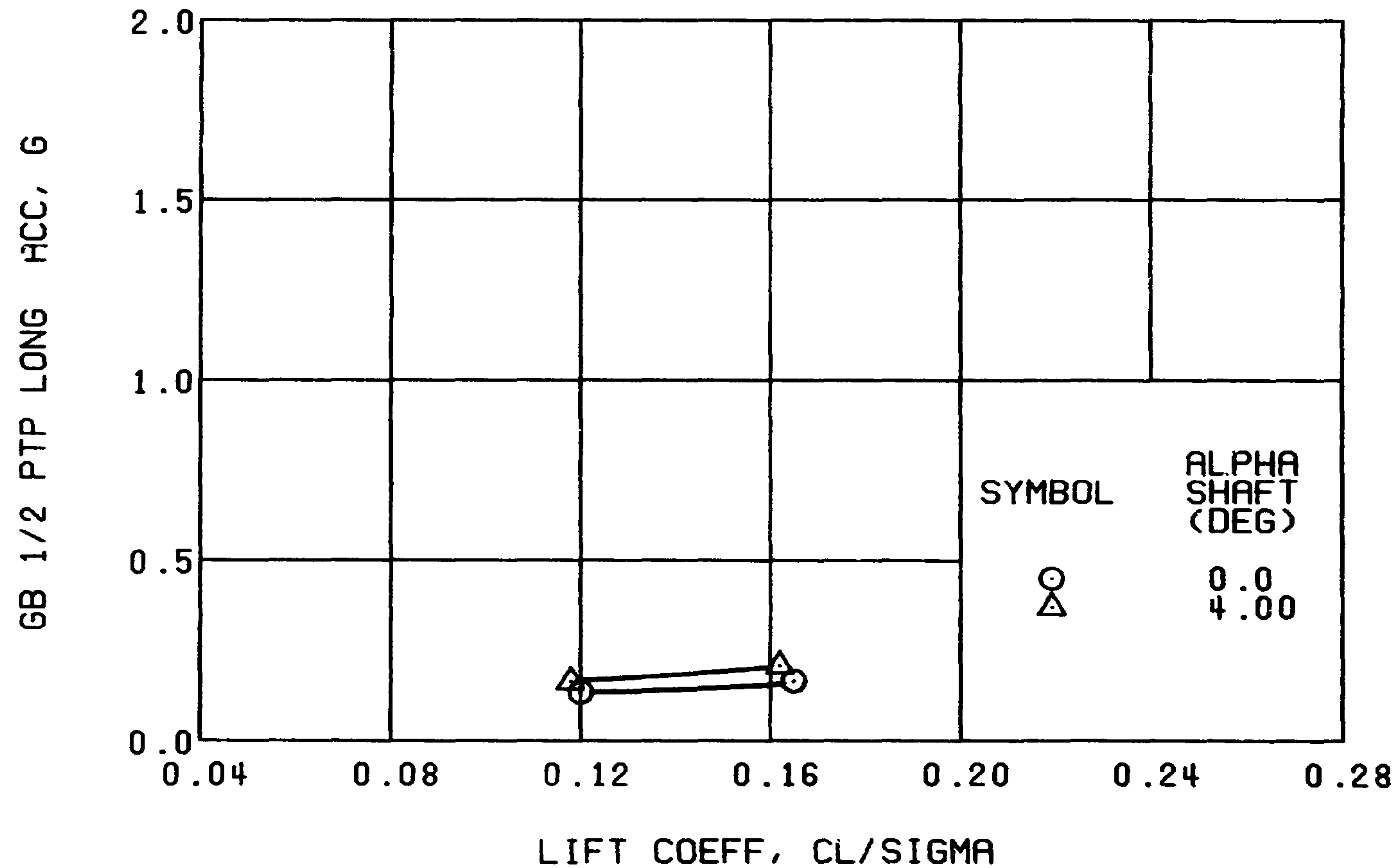

(v) GAGE 14 STA 61, BL 0

Figure 62. Continued.
μ = 0.35 B'_{1s} = 2 Deg (Single-Rotor Configuration)

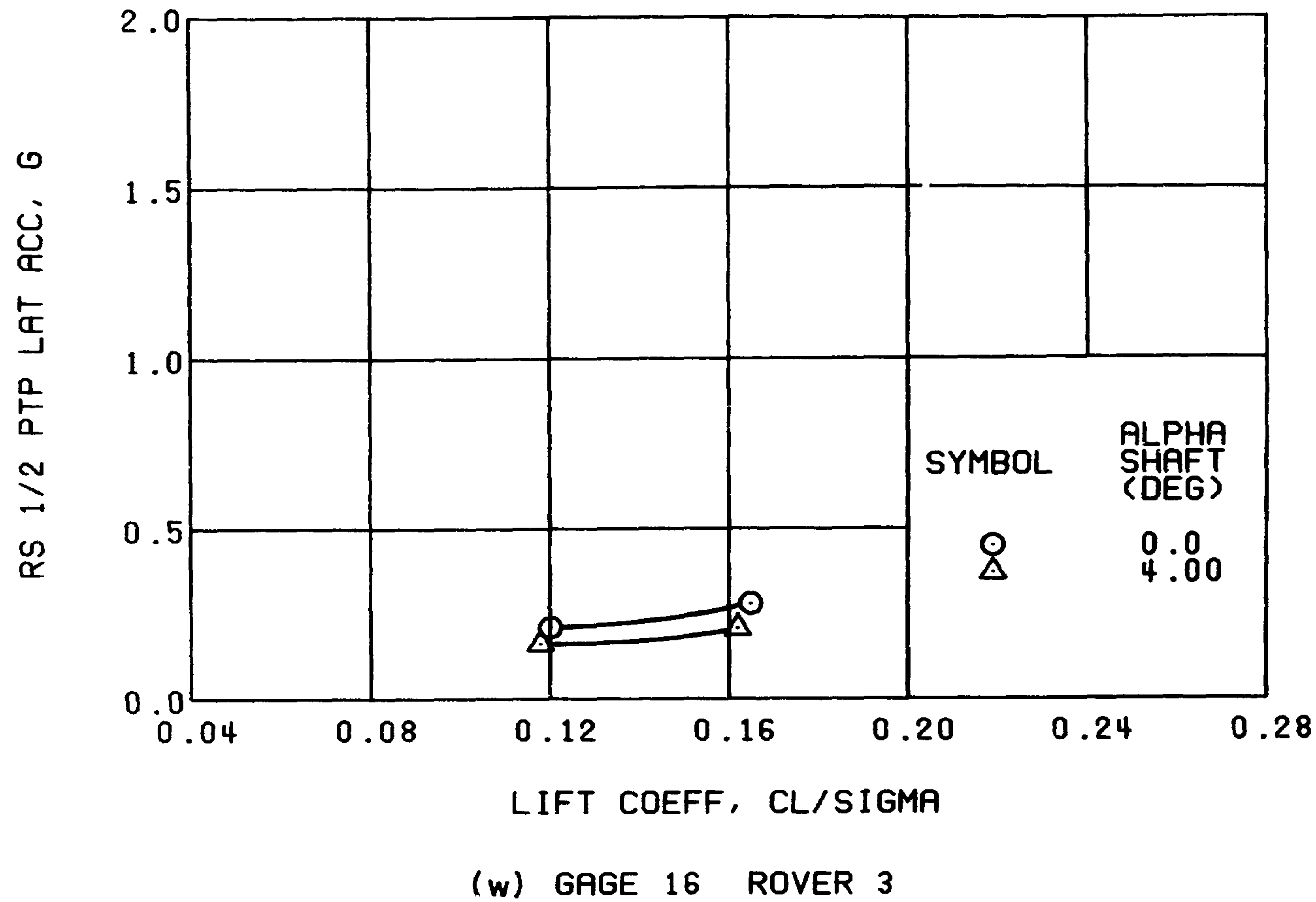

Figure 62. Continued.
$\mu = 0.35$ $B'_{1s} = 2$ Deg (Single-Rotor Configuration)

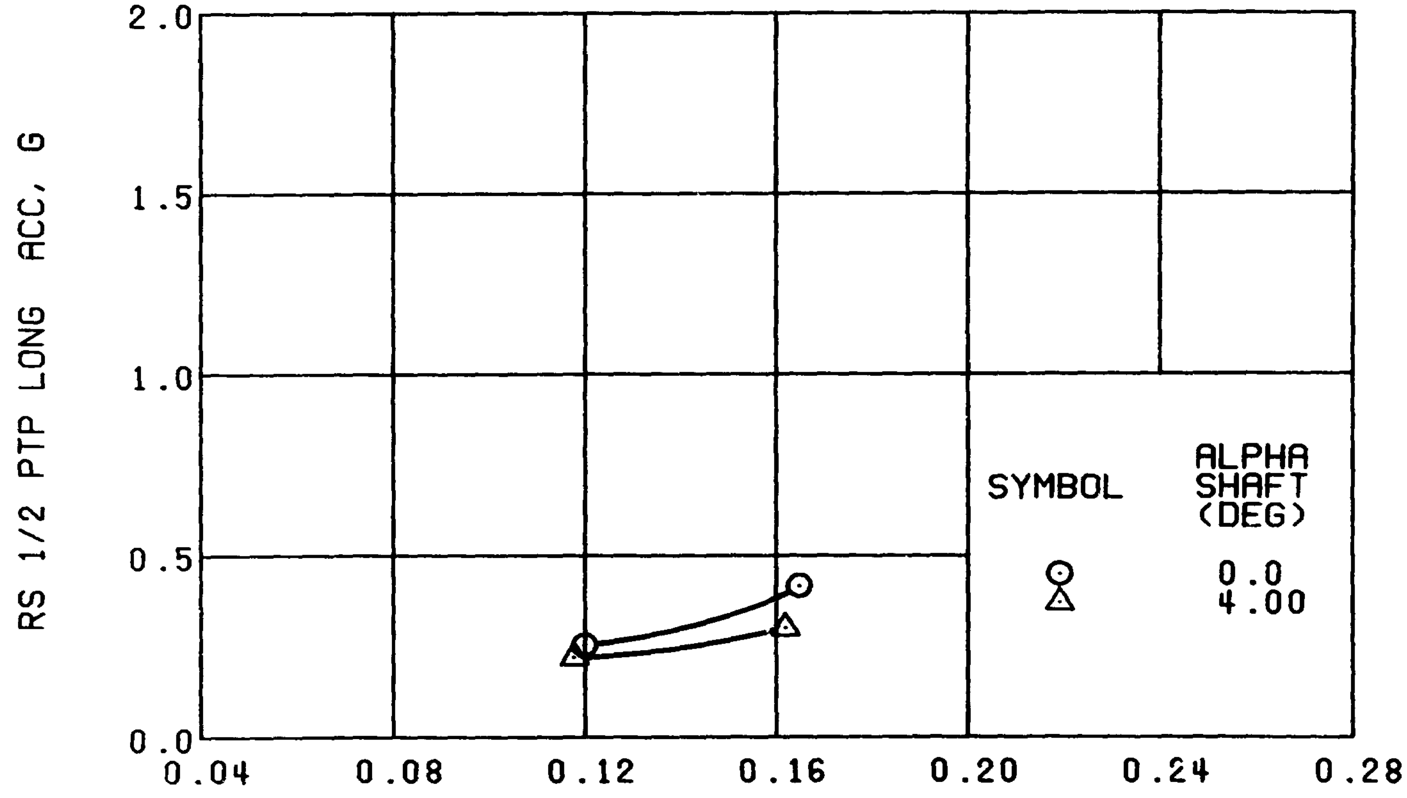

(x) GAGE 17 ROVER 4

Figure 62. Concluded.

$\mu = 0.35$ $B'_{1s} = 2$ Deg (Single-Rotor Configuration)

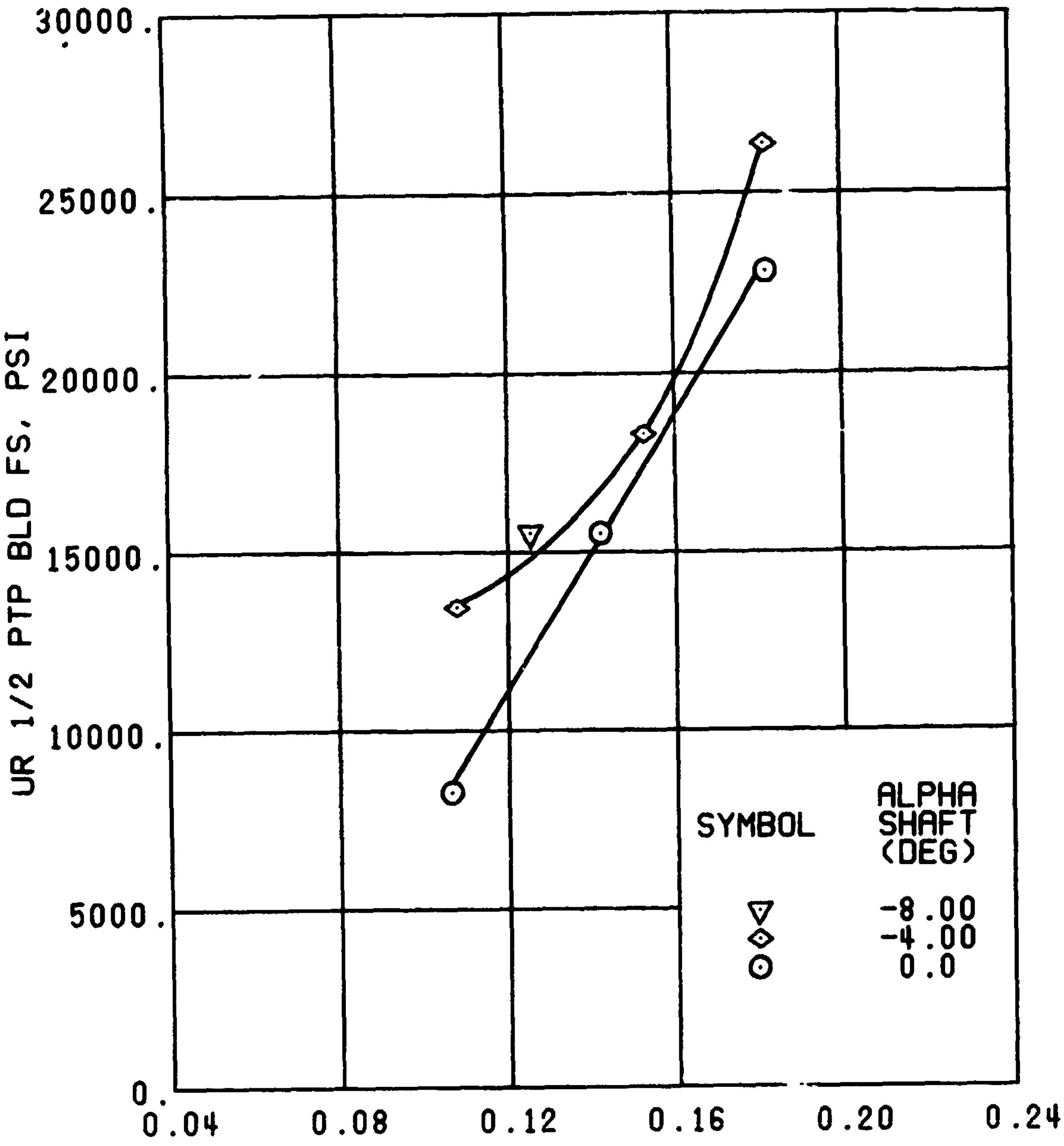

(a) GAGE 51 R84

Figure 63. Stress, Load, and Vibration Data at an Advance Ratio of 0.35 With the Lateral Displacement Control (B'_{1s}) Set at 4 Degrees (Single-Rotor Configuration).

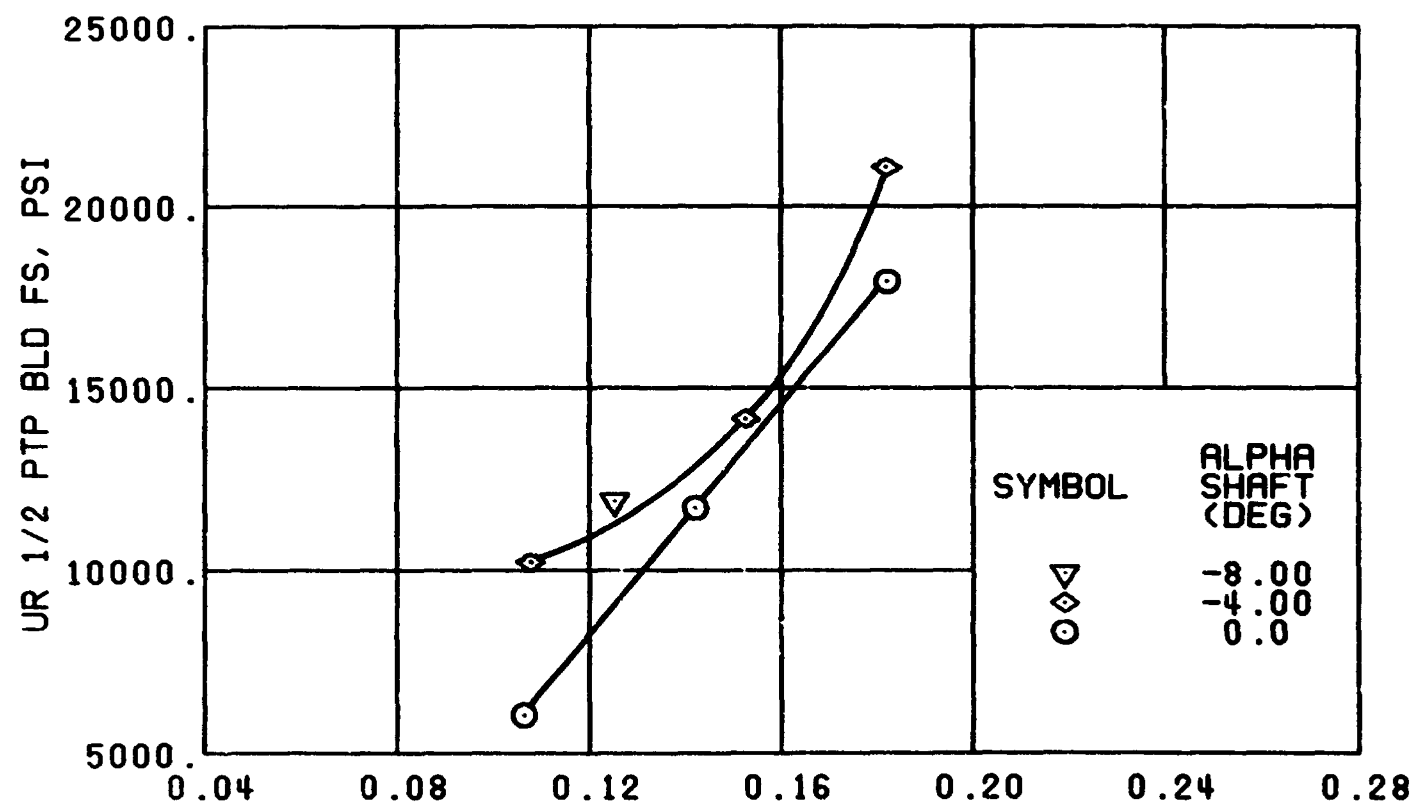

(c) GAGE 52 R108

Figure 63. Continued.
$\mu = 0.35$ $B'_{1s} = 4$ Deg (Single-Rotor Configuration)

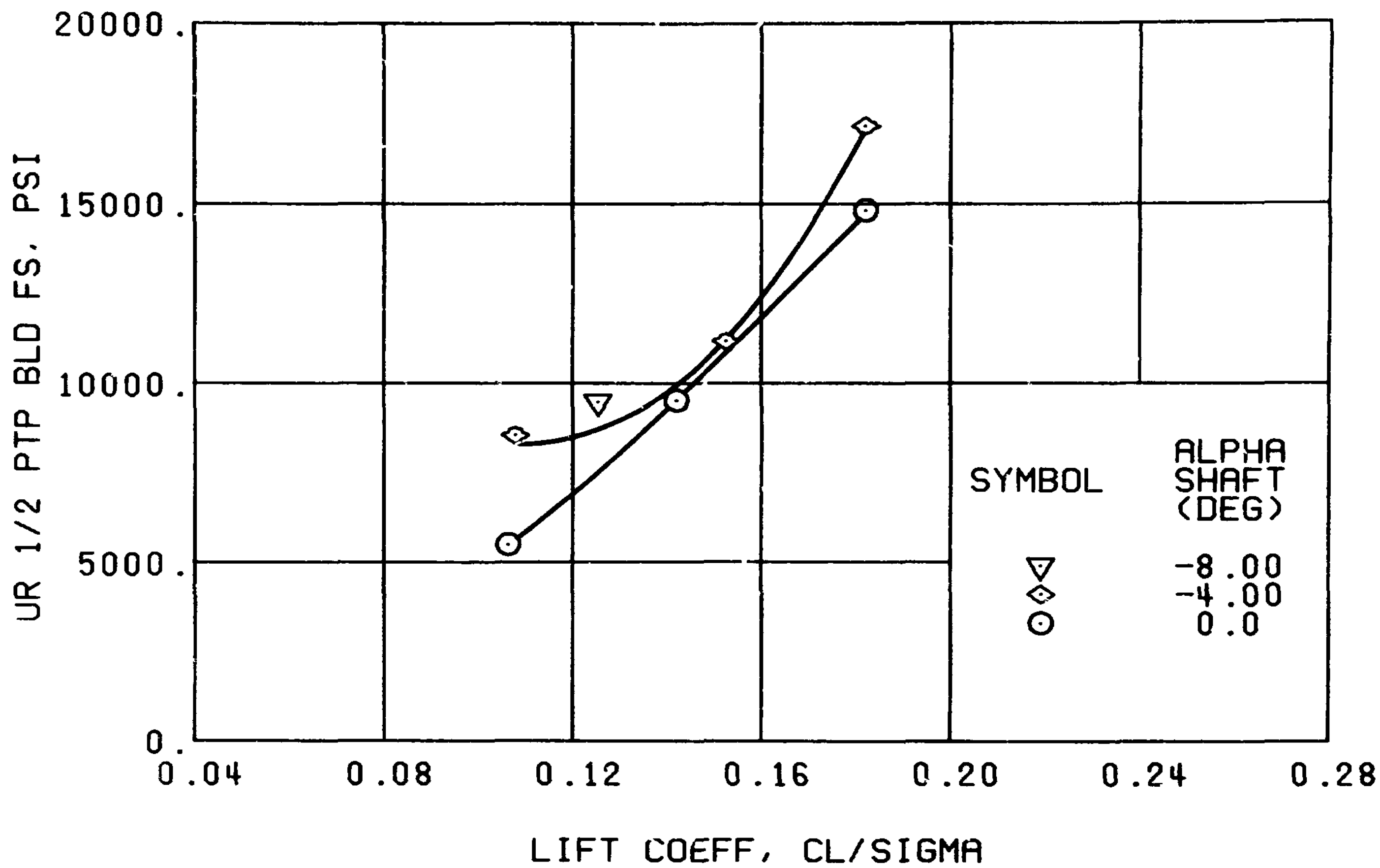

(d) GAGE 53 R132

Figure 63. Continued.
$\mu = 0.35$ $B'_{1s} = 4$ Deg (Single-Rotor Configuration)

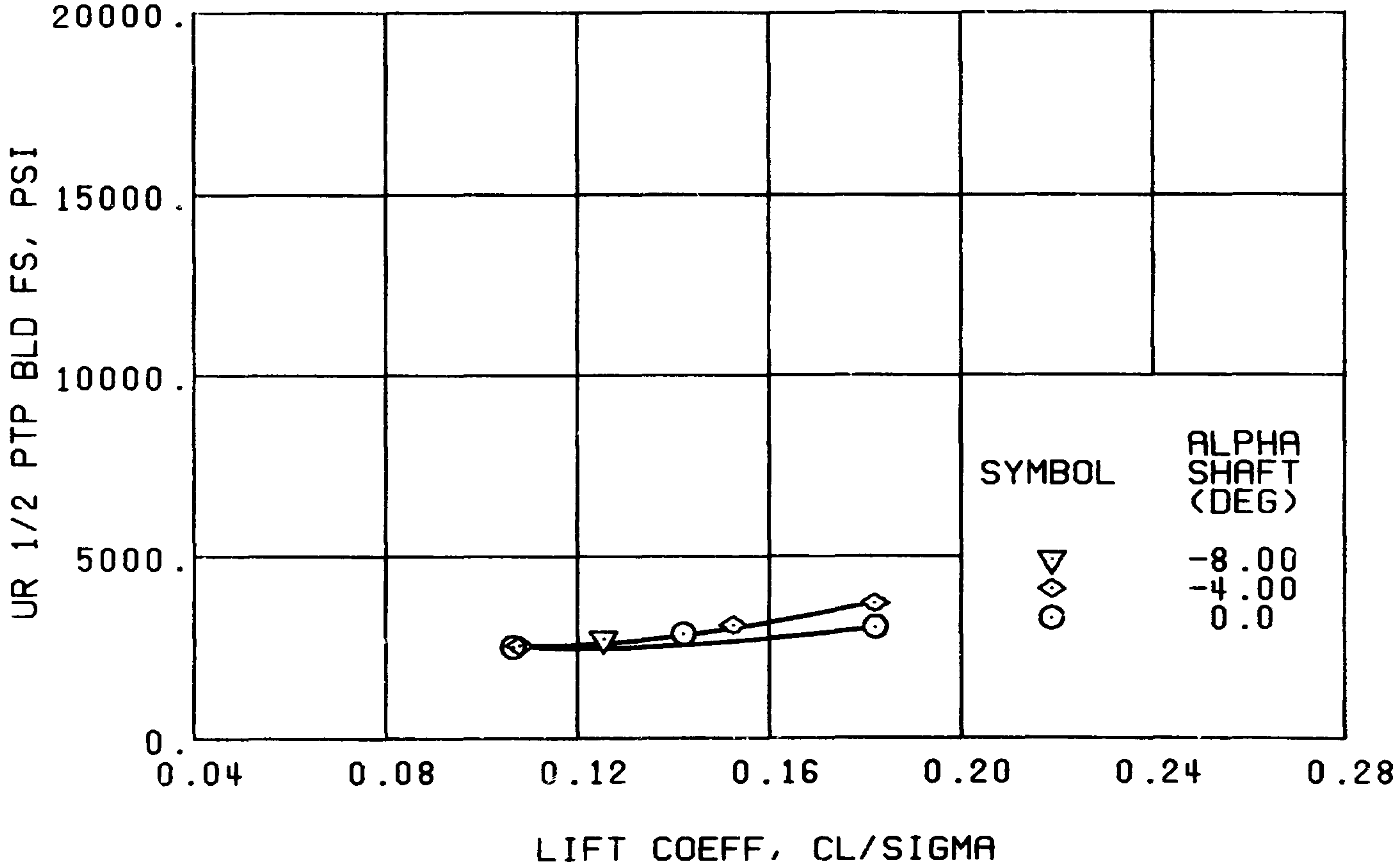

(f) GAGE 55 R204

Figure 63. Continued.
μ = 0.35 B'_{1s} = 4 Deg (Single-Rotor Configuration)

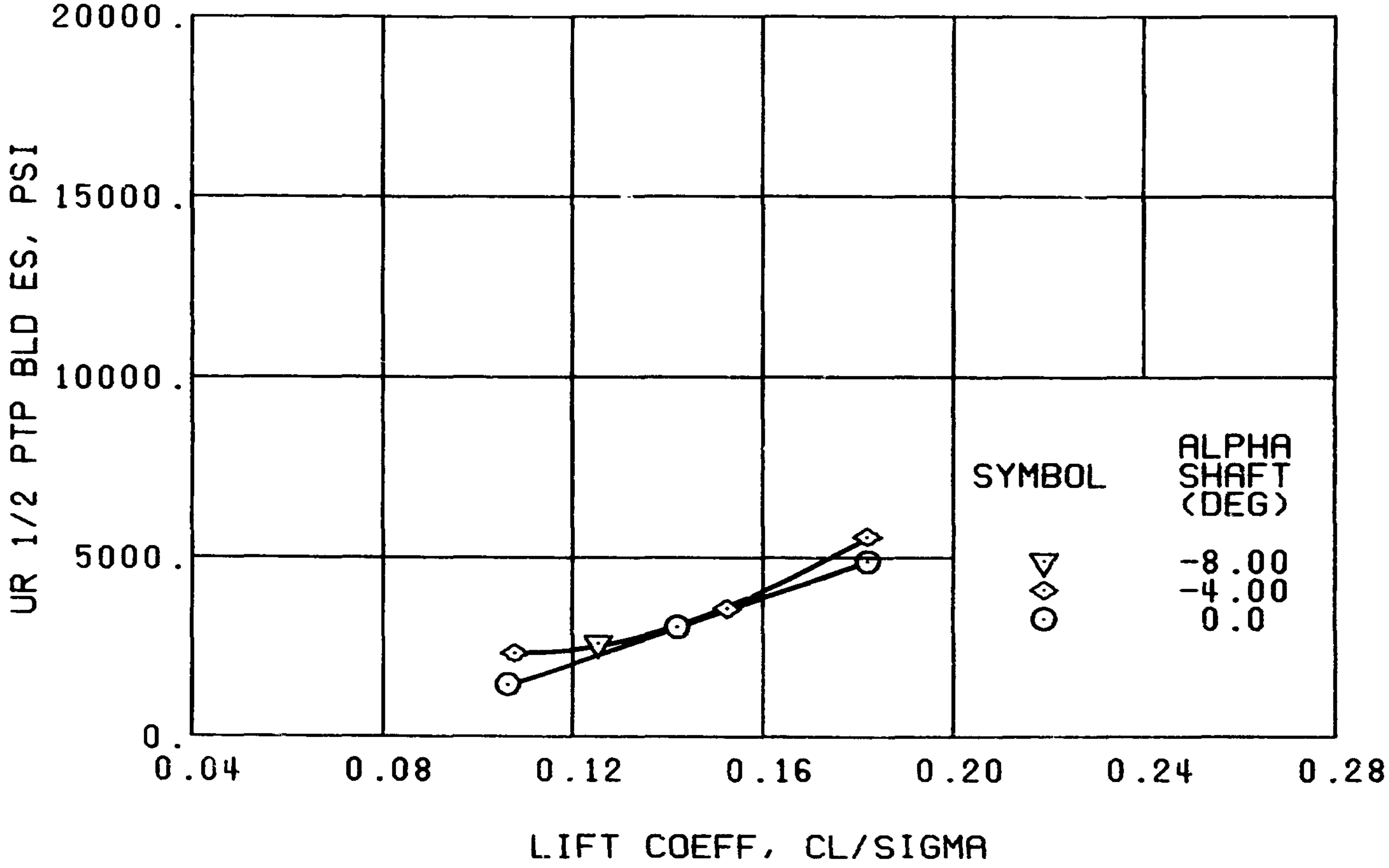

(h) GAGE 40 R84

Figure 63. Continued.
$\mu = 0.35 \quad B'_{1s} = 4$ Deg (Single-Rotor Configuration)

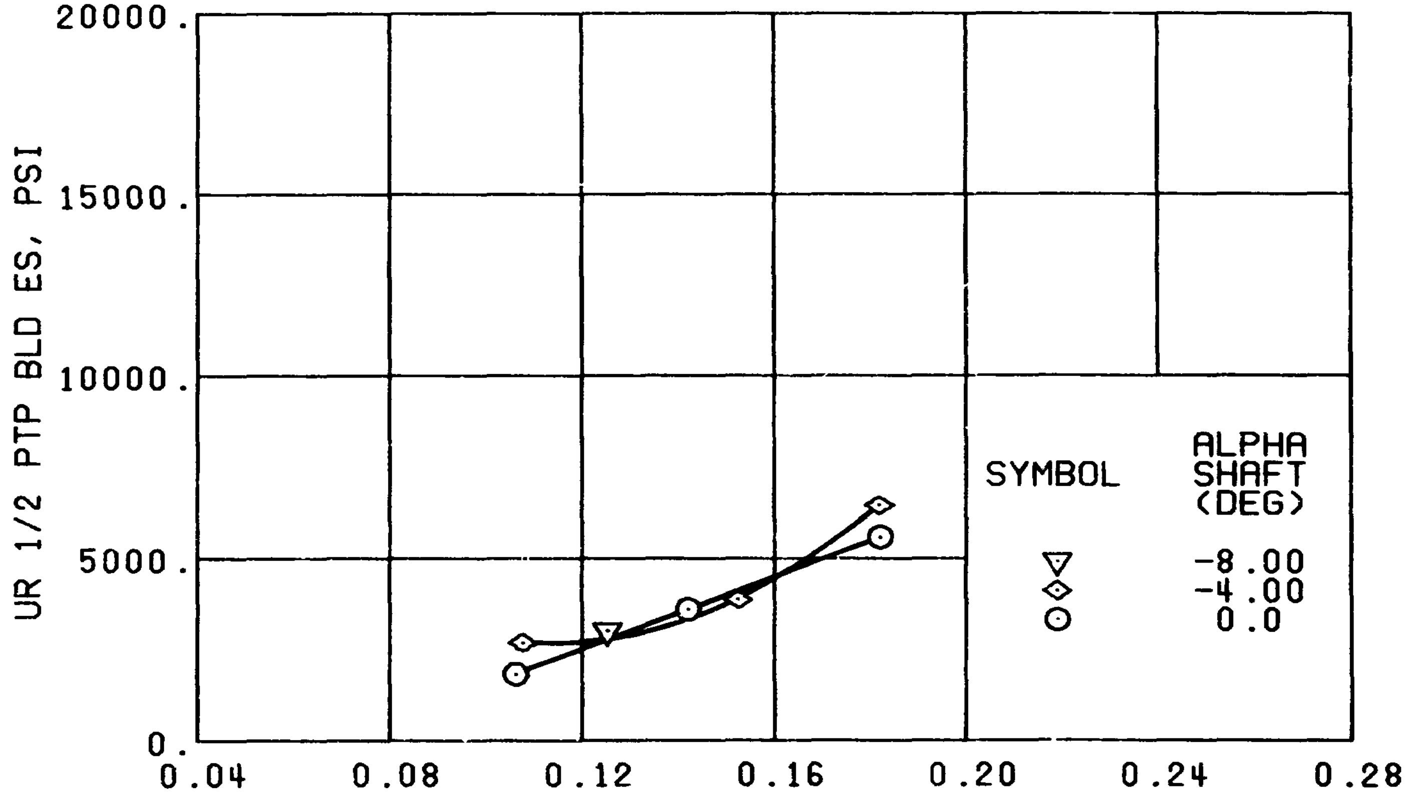

(j) GAGE 42 R132

Figure 63. Continued.
$\mu = 0.35$ $B'_{1s} = 4$ Deg (Single-Rotor Configuration)

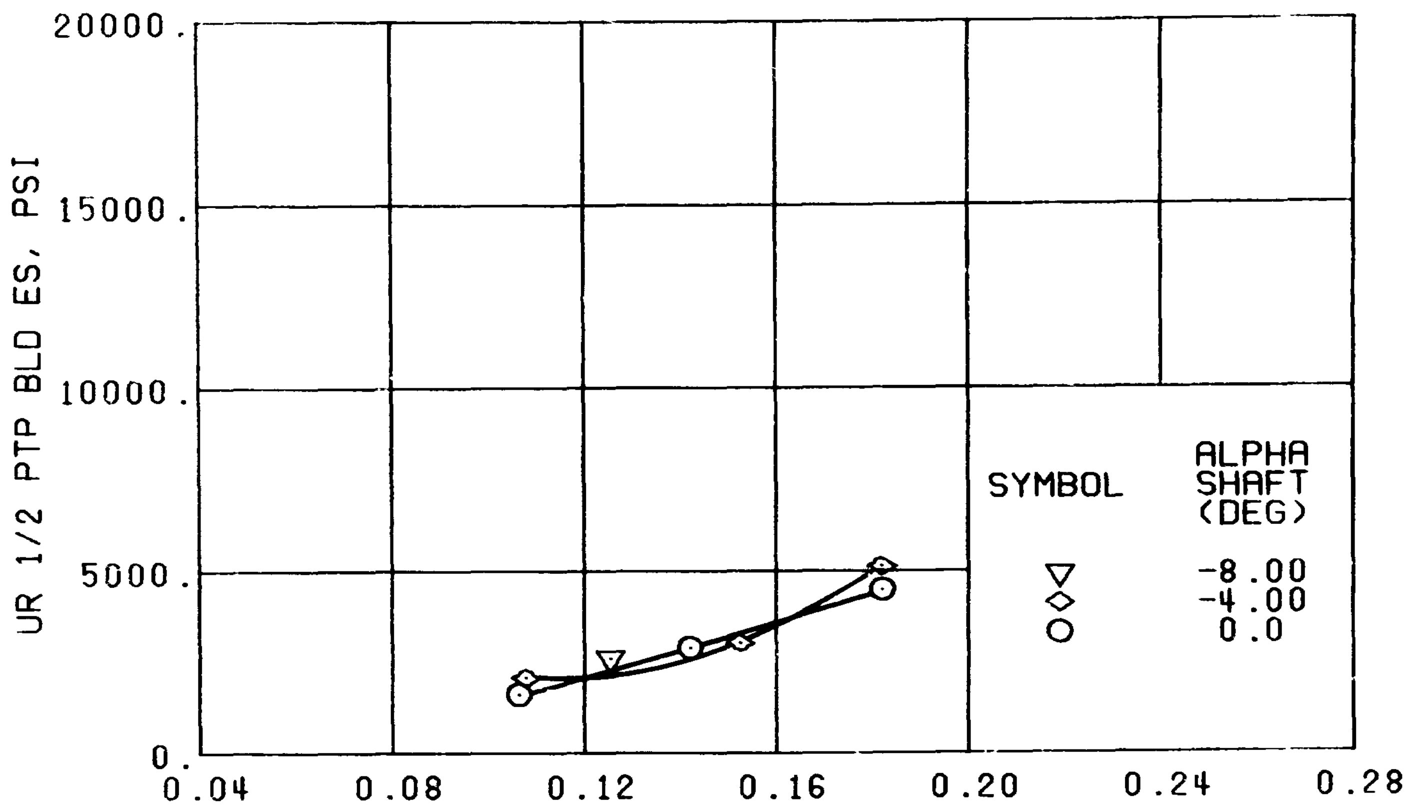

(k) GAGE 43 R168

Figure 63. Continued.
$\mu = 0.35$ $B'_{1s} = 4$ Deg (Single-Rotor Configuration)

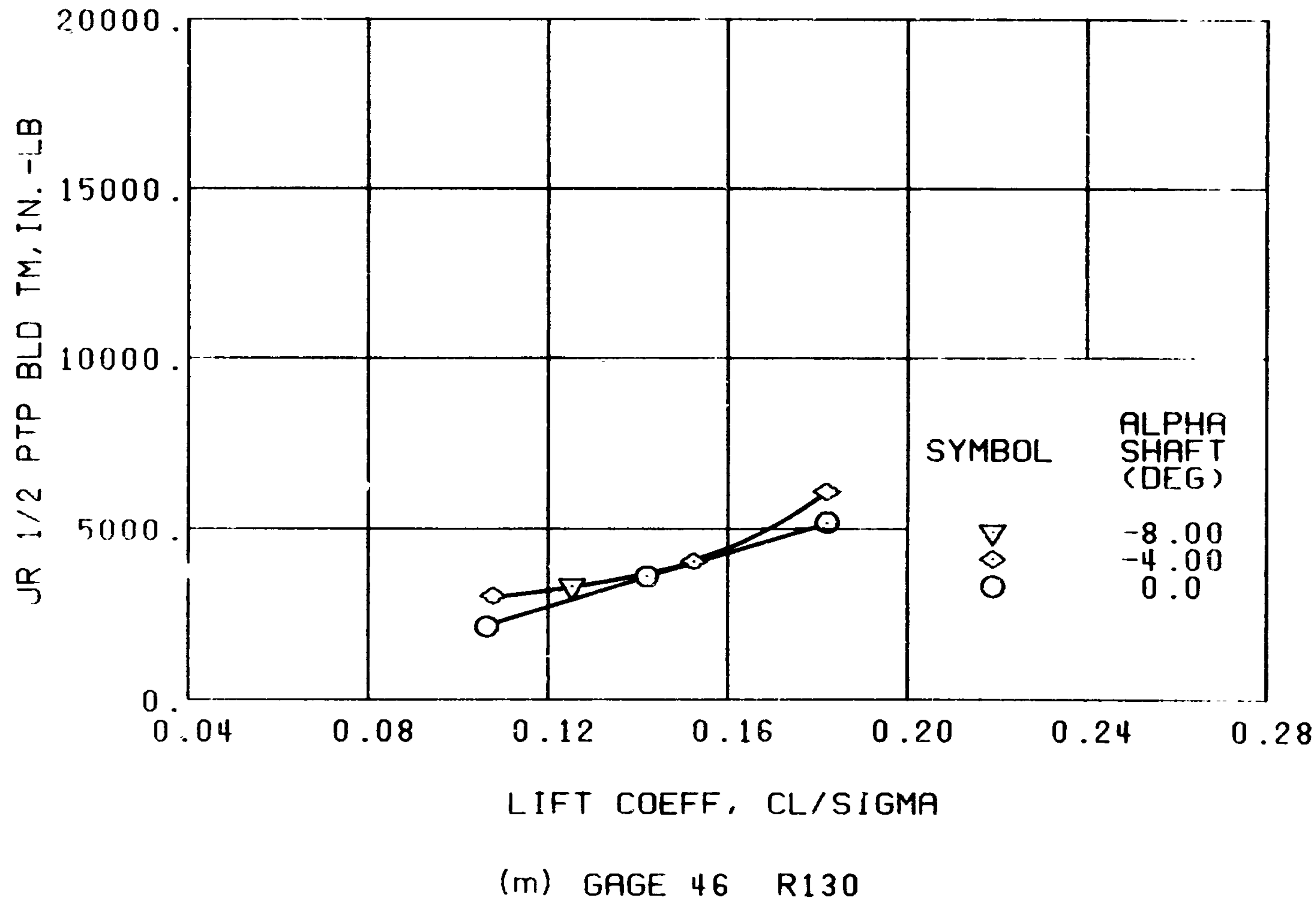

Figure 63. Continued.

μ = 0.35 B'_{1s} = 4 **Deg** (Single-Rotor Configuration)

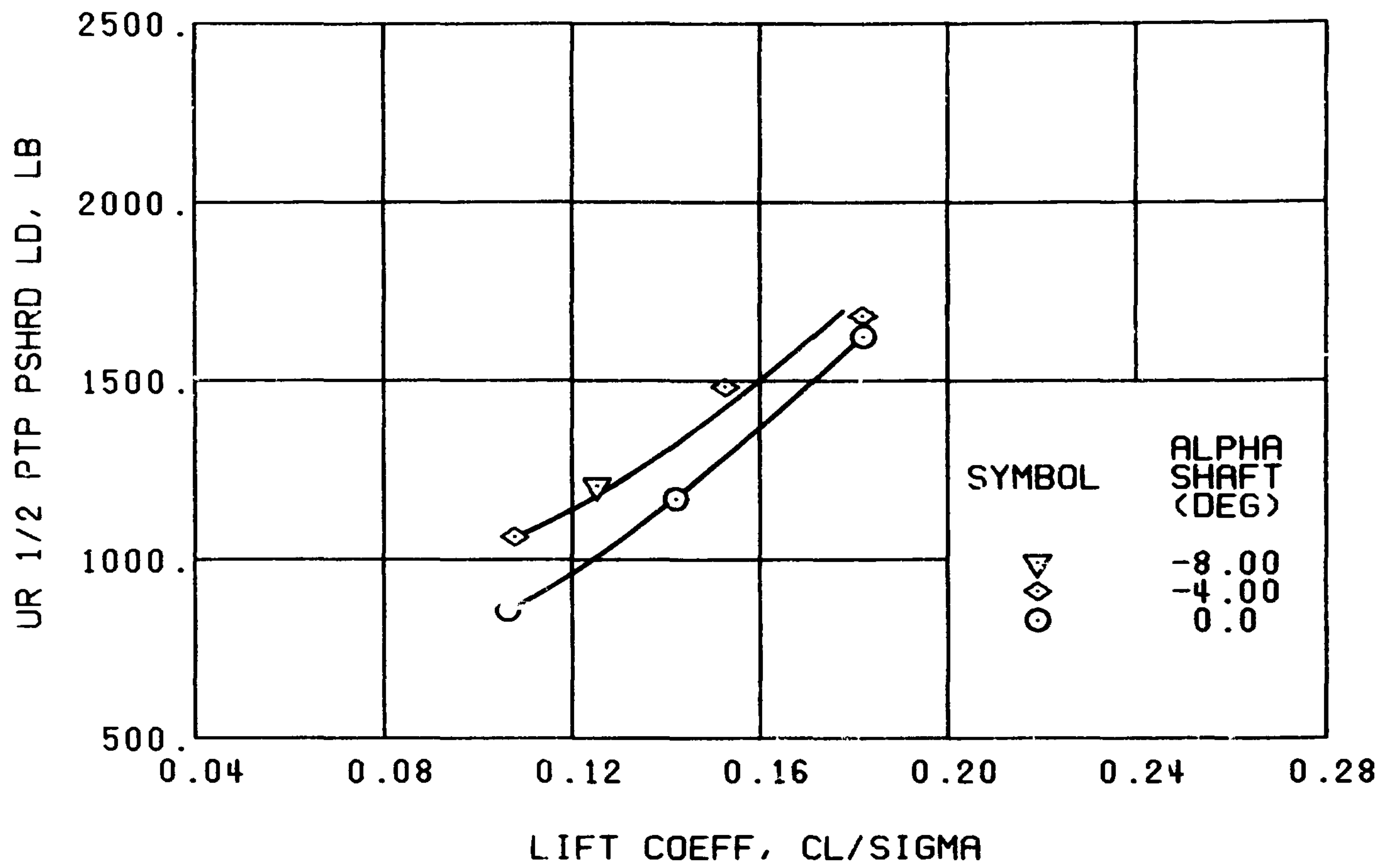

(n) GAGE 37

Figure 63. Continued.
$\mu = 0.35$ $B'_{1s} = 4$ Deg (Single-Rotor Configuration)

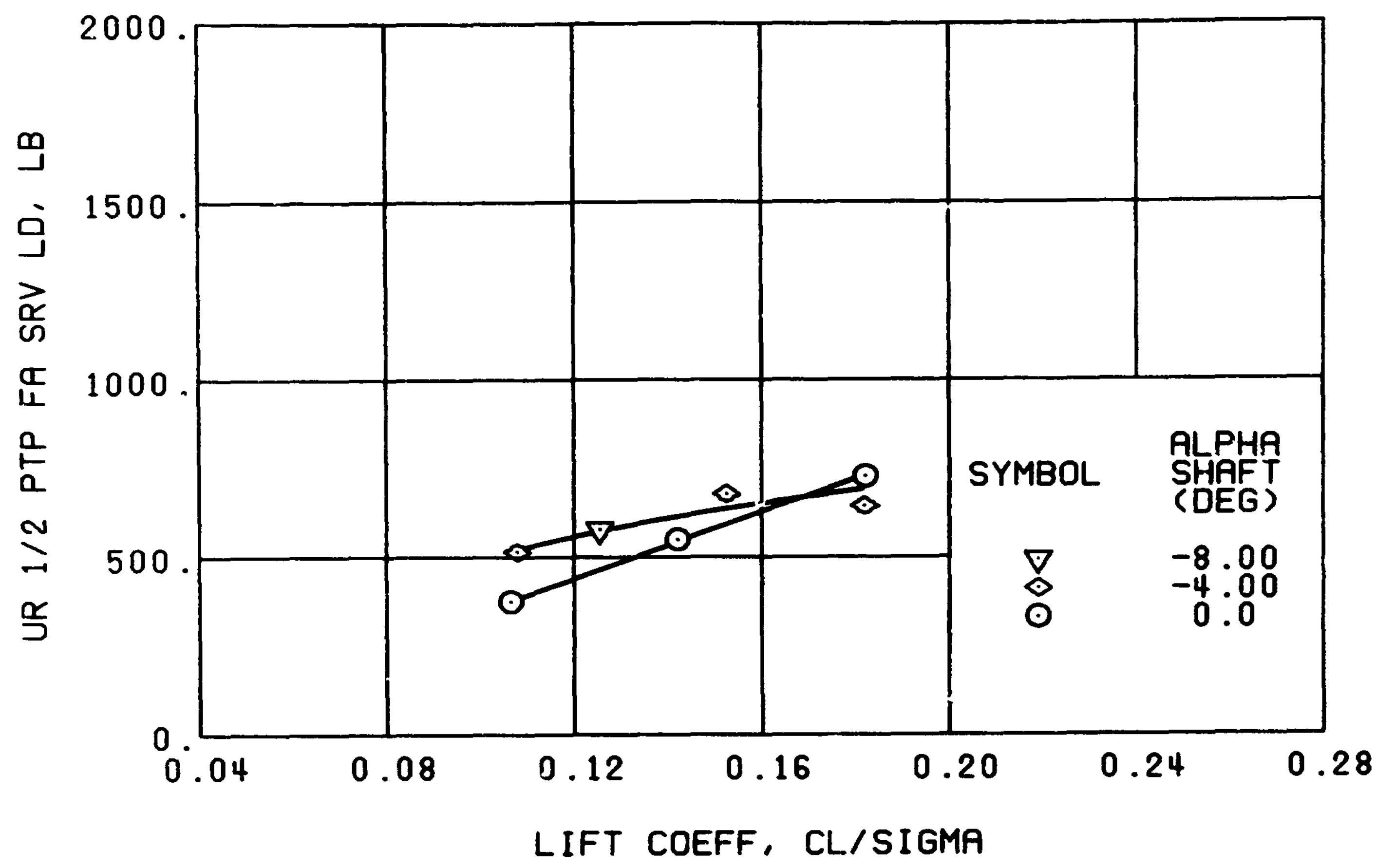

(r) GAGE 24

Figure 63. Continued.

$\mu = 0.35 \quad B'_{1s} = 4$ Deg (Single-Rotor Configuration)

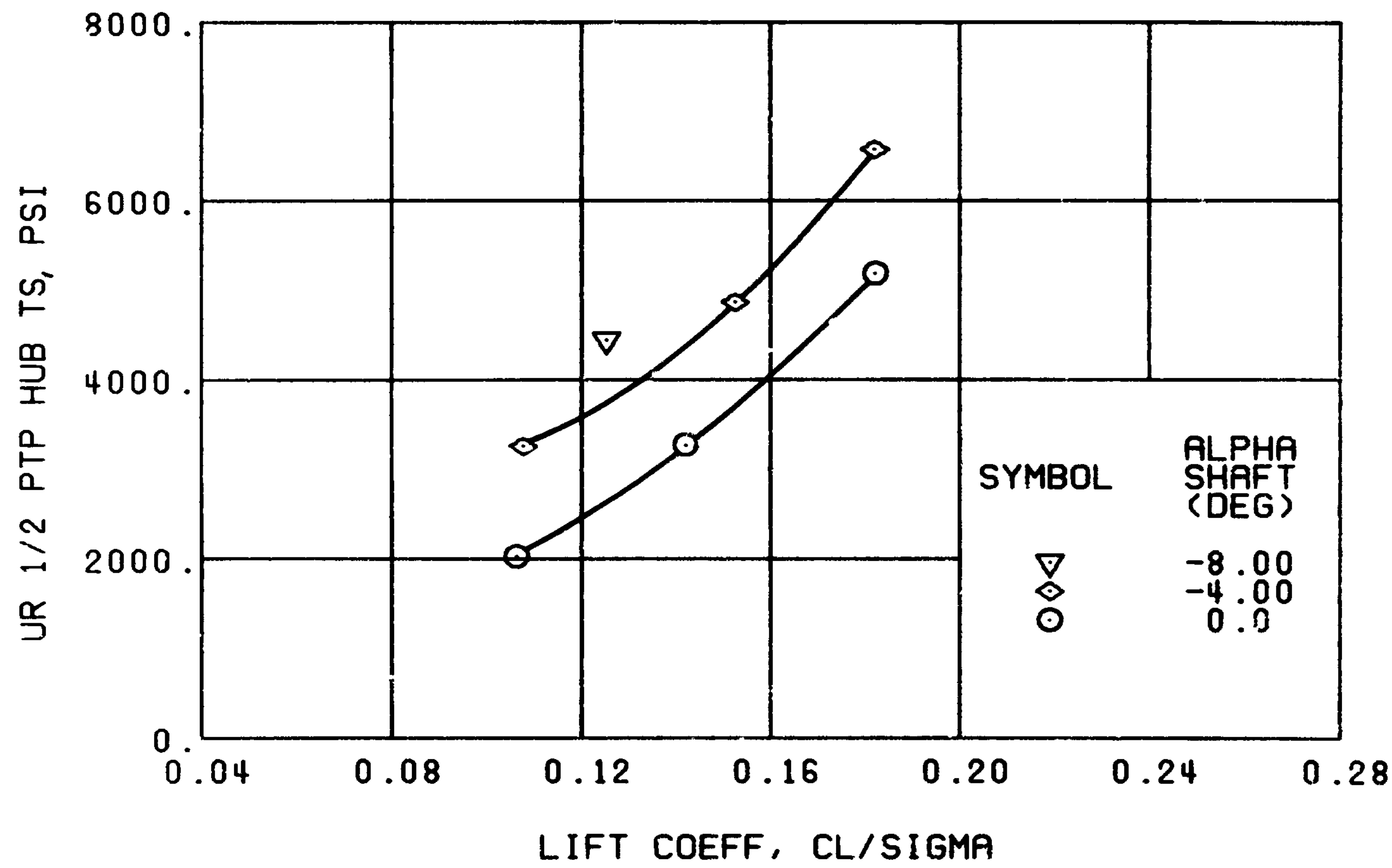

(f) GAGE 65

Figure 63. Continued.
$\mu = 0.35$ $B'_{1s} = 4$ Deg (Single-Rotor Configuration)

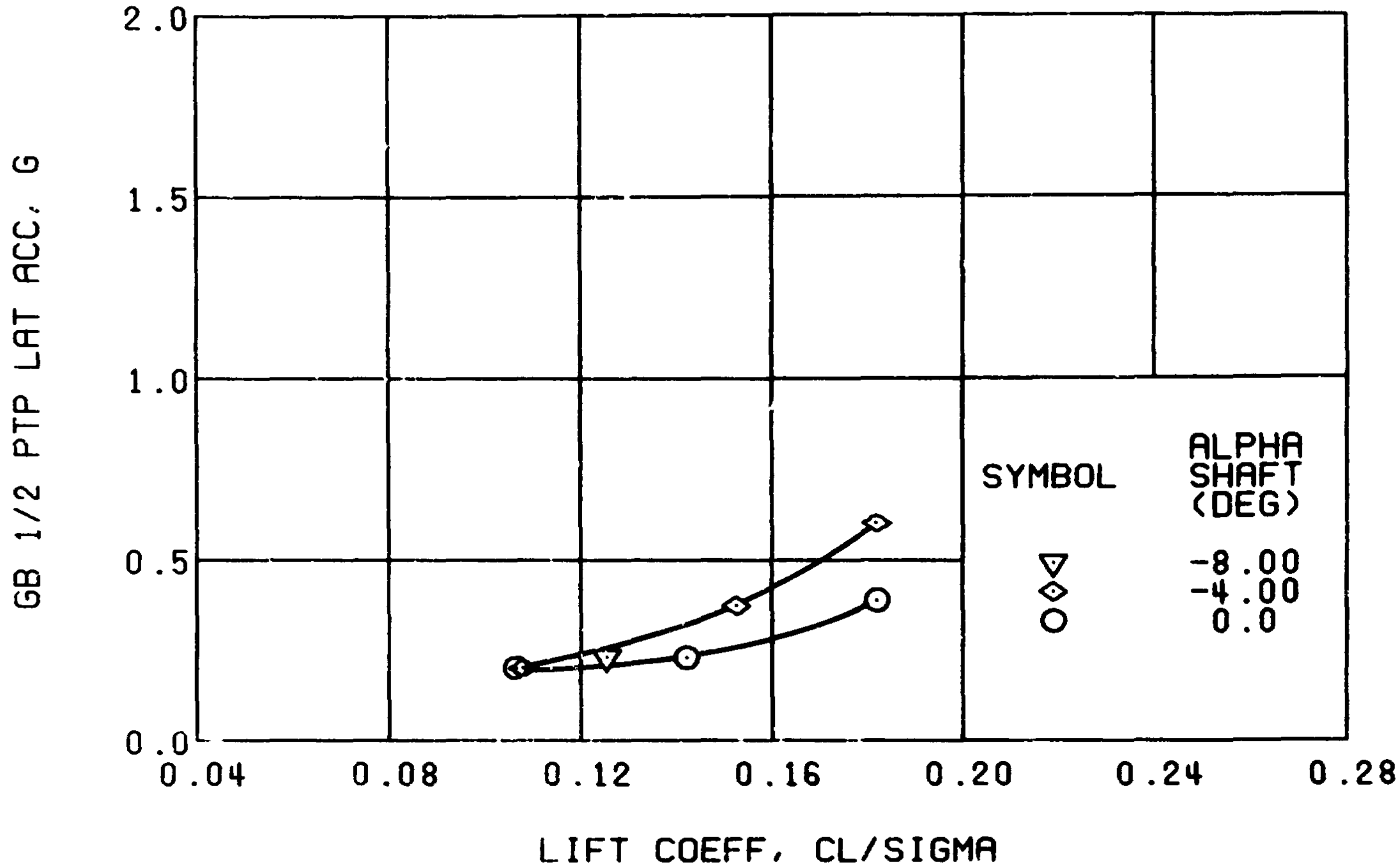

(u) GAGE 15 STA 76, BL 30

Figure 63. Continued.
$\mu = 0.35 \quad B'_{1s} = 4$ Deg (Single-Rotor Configuration)

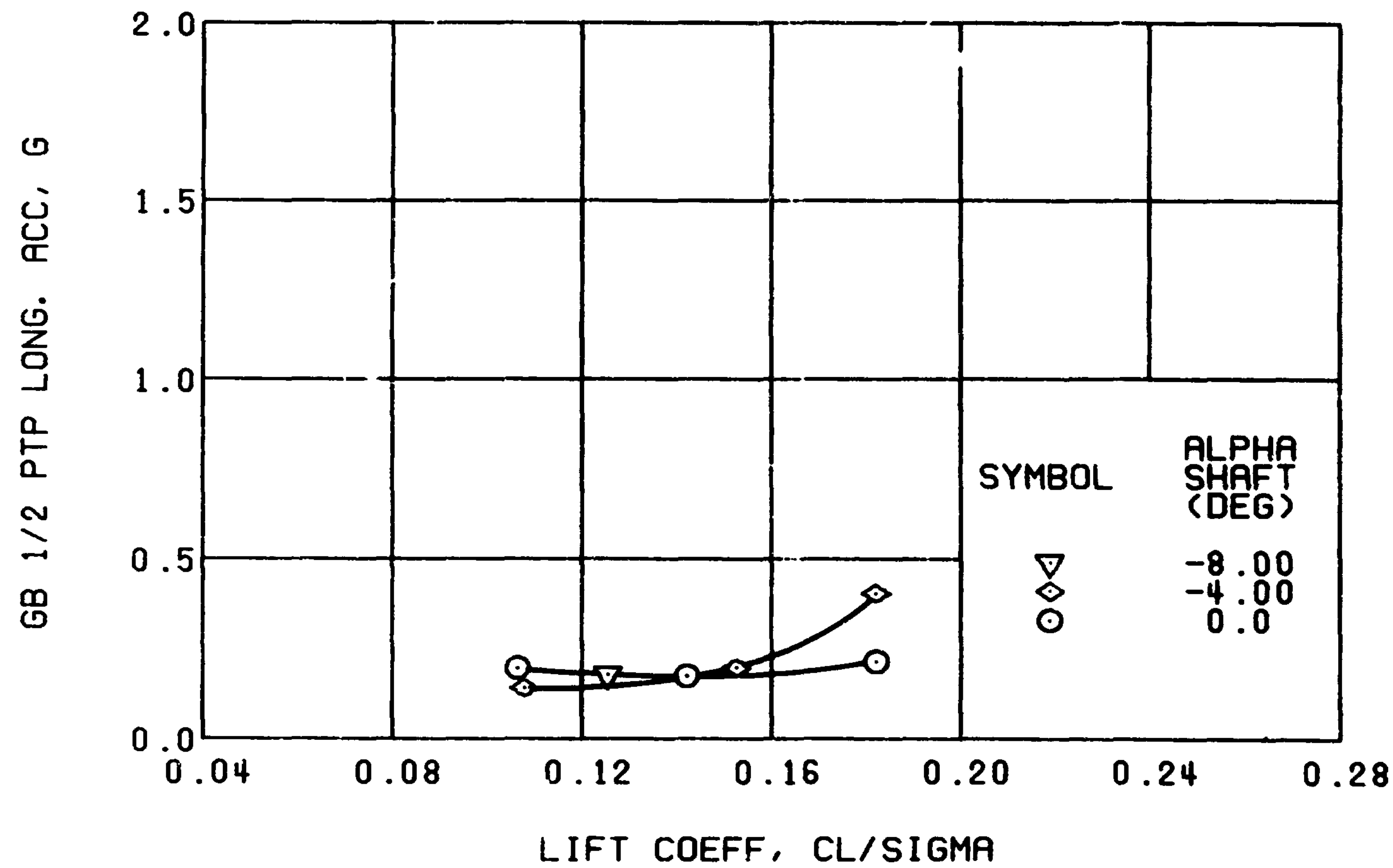

(v) GAGE 14 STA 61, BL 0

Figure 63. Continued.
$\mu = 0.35$ $B'_{1s} = 4$ Deg (Single-Rotor Configuration)

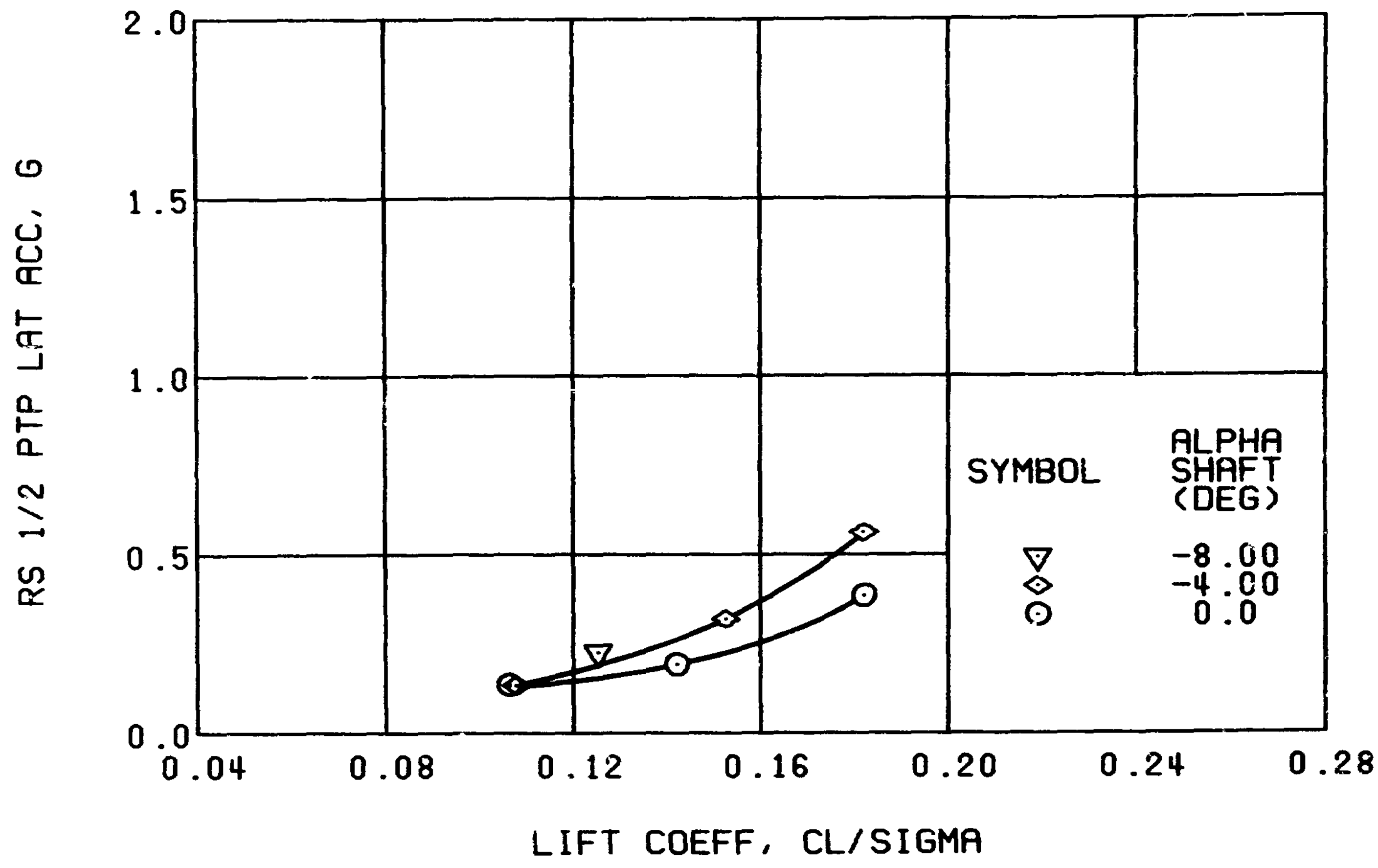

(w) GAGE 16 ROVER 3

Figure 63. Continued.
$\mu = 0.35$ $B'_{1s} = 4$ Deg (Single-Rotor Configuration)

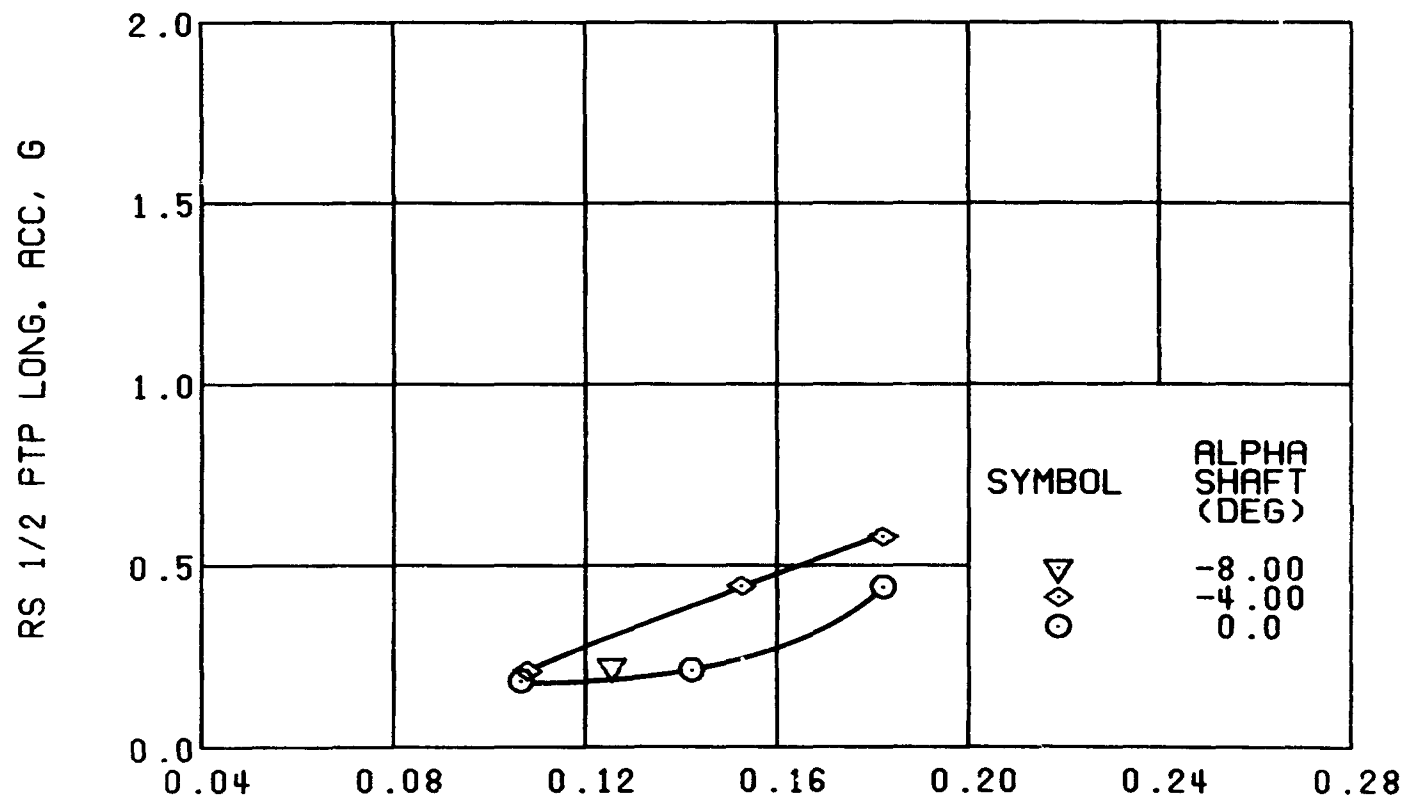

(x) GAGE 17 ROVER 4

Figure 63. Concluded.

$\mu = 0.35$ $B'_{1s} = 4$ Deg (Single-Rotor Configuration)